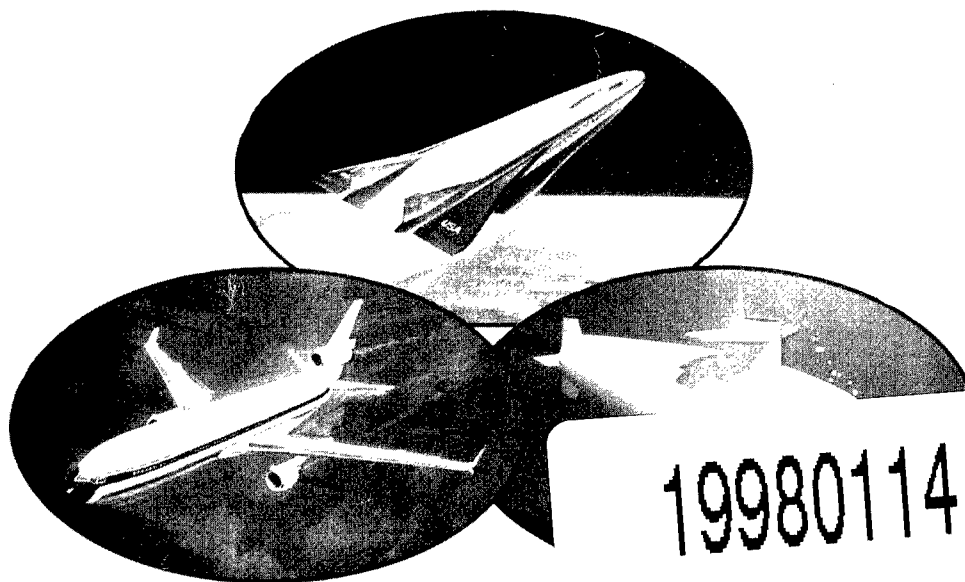


FAA TECHNICAL CENTER  
Atlantic City International Airport  
New Jersey 08405

*secs. VI, paper G, p. 1097*

# Proceedings Of The Ninth DoD/NASA/FAA Conference On Fibrous Composites In Structural Design

Lake Tahoe, Nevada  
November 4-7, 1991



19980114 035

**DISTRIBUTION STATEMENT A**  
Approved for public release  
Distribution Unlimited

## NOTICE

### FOR EARLY DOMESTIC DISSEMINATION

Because of its significant early commercial potential, this information, which has been developed under a U.S. Government program, is being disseminated within the United States in advance of general publication. This information may be duplicated and used by the recipient with the express limitation that it not be published. Release of this information to other domestic parties by the recipient shall be made subject to these limitations.

Foreign release may be made only with prior Federal Aviation Administration approval and appropriate export licenses. This legend shall be marked on any reproduction of this information in whole or in part.

Review for general release November 30, 1994

**DTIC QUALITY INSPECTED 3**



U.S. Department of Transportation  
Federal Aviation Administration

**FAA TECHNICAL CENTER**  
Atlantic City International Airport  
N.J. 08405

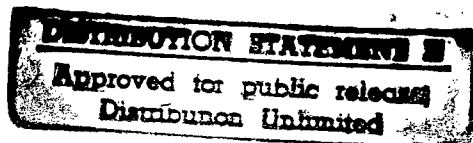
# **Ninth DoD/NASA/FAA Conference on Fibrous Composites in Structural Design**

*Compiled by*

Joseph R. Soderquist  
*Federal Aviation Administration  
Washington, DC*

Lawrence M. Neri  
*Federal Aviation Administration  
Technical Center  
Atlantic City International Airport, NJ*

Herman L. Bohon  
*Galaxy Scientific Corporation  
Hampton, VA*



Proceedings of a conference sponsored by the  
Department of Defense, the National Aeronautics  
and Space Administration, and the Federal  
Aviation Administration, and held in  
Lake Tahoe, Nevada on November 4-7, 1991

**DTIC QUALITY INSPECTED 3**

September, 1992



#### NOTICE

This document is disseminated under the sponsorship of the U. S. Department of Transportation in the interest of information exchange. The United States Government assumes no liability for the contents or use thereof.

The United States Government does not endorse products or manufacturers. Trade or manufacturers' names appear herein solely because they are considered essential to the objective of this report.



## CONFERENCE ORGANIZATION

Joseph R. Soderquist  
General Chairman  
Federal Aviation Administration  
Washington, DC

Lawrence M. Neri  
Conference Technical Coordinator  
FAA Technical Center  
Atlantic City International Airport, NJ

Herman L. Bohon  
Technical Chairman  
Composites Consultant  
Galaxy Scientific Corporation  
Hampton, VA

## CONFERENCE ORGANIZATION COMMITTEE

Joseph R. Soderquist  
James H. Starnes, Jr  
Thomas E. Hess  
Donald W. Oplinger  
J. David Oetting  
Dan E. Good

Federal Aviation Administration  
NASA Langley Research Center  
Naval Air Development Center  
Federal Aviation Administration  
Wright Research and Development Center  
Army Aviation Applied Technology Directorate

## PREFACE

The Ninth DoD/NASA/FAA Conference on Fibrous Composites in Structural Design is one of a series of conferences jointly sponsored by the Federal Aviation Administration, the National Aeronautics and Space Administration, the U.S. Air Force, the U.S. Army, and the U.S. Navy (Department of Defense). The purpose of this series of conferences is to convene periodically key government and industry research and design engineers to present and discuss the status, problems, and requirements in the technical disciplines related to the design of composite structures. This series of conferences provides a forum for the scientific community to exchange composite structures design and technology.

The Ninth DoD/NASA/FAA Conference on Fibrous Composites in Structural Design was hosted by the Federal Aviation Administration and held at Lake Tahoe, Nevada during November 4-7, 1991. The conference offered 91 presentations by senior managers and experts in the field of composite structures, organized into a total of 11 sessions. These included: one overview session on perspectives in composites; seven discipline sessions in applications (two sessions); innovative design/manufacturing (one session); methodology (two sessions); reliability (one session); damage tolerance (one session); and two focused sessions on thick structures and space structures. The conference also hosted the second industry briefing on the NASA Advanced Composites Technology (ACT) program. This publication contains (in three volumes) the technical material presented in these sessions.

*Certain materials are identified in this publication in order to specify adequately which materials were used in the structural design or research efforts. In no case does such identification imply recommendation or endorsement of a product by FAA, NASA, or DoD, nor does it imply that the materials are necessarily the only ones or the best ones available for the purpose. In many cases, equivalent materials are available and would probably produce equivalent results.*

The Conference Organizers would like to take this opportunity to thank all the authors and presenters for their outstanding contributions to the conference technical program, as well as the conference attendees whose contributions to the conference discussions helped to make the conference a successful technology exchange forum for current composite structural design issues.

Joseph R. Soderquist  
Lawrence M. Neri  
Herman L. Bohon

James H. Starnes, Jr.  
Thomas E. Hess  
Donald W. Oplinger  
J. David Oetting  
Dan E. Good

# TABLE OF CONTENTS

## VOLUME I\*

<b>PREFACE</b> .....	i
<b>CONFERENCE ORGANIZATION</b> .....	iii
<b>TABLE OF CONTENTS</b> .....	v

### **SESSION I - Perspectives in Composites**

Chairman: Joseph R. Soderquist, Federal Aviation Administration

A. Reliable Composites, Reliable Manufacturing and Materials: A Perspective .....	3
<i>John C. Halpin, Wright Aeronautical Systems Division</i>	
B. Utilization of Composite Materials by the U.S. Army: A Look Ahead .....	7
<i>Richard Chait, U.S. Army Materiel Command</i>	
C. Benefits and Limitations of Composites in Carrier-Based Aircraft .....	35
<i>Donald P. McErlean, Naval Air Development Center</i>	
D. Advanced Materials Requirements and Needs for Future Aerospace Applications ...	93
<i>Samuel L. Vennneri, NASA Office of Aeronautics, Exploration and Technology</i>	

### **SESSION II - Aircraft Design Methodology (A)**

Chairman: James H. Starnes, Jr., NASA Langley Research Center

A. Mechanical Properties of Triaxially Braided Composites: Experimental and .....	99
Analytical Results	
<i>John E. Masters, Lockheed Engineering and Sciences Company, NASA Langley Research Center; Raymond L. Fay, Lockheed Engineering and Sciences Company, North Carolina A&amp;T State University; and Christopher M. Pastore and Yasser A. Gawayed, North Carolina State University</i>	
B. Mechanisms of Compressive Failure in Woven Composites and .....	125
Stitched Laminates	
<i>B. N. Cox, M. S. Dadkhah, R.V. Inman, W. L. Morris and S. Schroeder, Rockwell International Science Center</i>	
C. Effect of the Fiber-Matrix Interphase on the Transverse Tensile Strength .....	139
of the Unidirectional Composite Material	
<i>H. C. Tsai and A.M. Arocho, Naval Air Development Center</i>	
D. The Effect of Material Heterogeneity in Curved Composite Beams for .....	157
Use in Aircraft Structures	
<i>Brendan J. O'Toole and Michael H. Santare, University of Delaware</i>	
E. Investigation of Static and Cyclic Bearing Failure Mechanisms .....	167
for GR/EP Laminates	
<i>R. W. Walter and M. M. Tuttle, The Boeing Company</i>	
F. Compression Failure of Angle-Ply Laminates .....	185
<i>L. D. Peel, Mirage Carrier Works; M. W. Hyer, Virginia Polytechnic Institute and State University; and M.J. Shuart, NASA Langley Research Center</i>	

\*Published in companion document

## **SESSION II - Aircraft Design Methodology (A) (continued)**

- G. Analysis of Composite Structures with Delaminations Under Combined ..... 197  
Bending and Compression  
*Han-Pin Kan, Northrop Corporation; Edward Kautz, Naval Air Development Center; and Larry Neri, Federal Aviation Administration Technical Center*
- H. Mechanics of Composites Research at ONR ..... 219  
*Yapa D. S. Rajapakse, Office of Naval Research*
- I. Post-Buckling Analysis of Curved, Stiffened Composite Panels with ..... 223  
Central Cut-Outs  
*U. Mbanefo, Northrop Corporation*
- J. Buckling Behavior of Long Symmetrically Laminated Plates ..... 227  
Subjected to Combined Loads  
*Michael P. Nemeth, NASA Langley Research Center*
- K. Compressive Residual Strength of Graphite/Epoxy Laminates ..... 253  
After Impact  
*Teresa A. Guy and Paul A. Lagace, Massachusetts Institute of Technology*

## **SESSION III - DESIGN APPLICATIONS (A)**

Chairman: Dan Good, Aviation Applied Technology Directorate, U.S. Army

- A. Application of Advanced Material Systems to Composite Frame Elements ..... 277  
*Steven Llorente, Pierre Minguet and Russell Fay, Boeing Defense and Space Group; and Steven Medwin, E.I. Du Pont De Nemours and Company (Incorporated)*
- B. Design, Analysis and Testing of a Metal Matrix Composite ..... 297  
Web/Flange Intersection  
*S. B. Biggers and N. F. Knight, Jr., Clemson University; S. G. Moran, NASA Headquarters; and R. Olliffe, Lockheed Aeronautical Systems Company*
- C. Characteristics of Laminates with Delamination Control Strips ..... 329  
*C. T. Sun, Purdue University; J. C. Goering, McDonnell Aircraft Company; and J. M. Alper and L. W. Gause, Naval Air Development Center*
- D. Vibrational Behavior of Adaptive Aircraft Wing Structures ..... 361  
Modelled as Composite Thin-Walled Beams  
*O. Song, L. Librescu and C. A. Rogers, Virginia Polytechnic Institute and State University*
- E. Unique Considerations in the Design and Experimental Evaluation ..... 383  
of Tailored Wings with Elastically Produced Chordwise Camber  
*Lawrence W. Rehfield, Peter J. Zischka, Michael L. Fentress and Stephen Chang, University of California, Davis*
- F. C-130 Advanced Technology Center Wing Box Conceptual Design/Cost Study ..... 401  
*R. S. Whitehead, Northrop Corporation; C. R. Foreman, LTV Advanced Products Group; and K. Silva, Wright Laboratories/FIBAC*
- G. Development of Composite Carrythrough Bulkhead ..... 421  
*R. J. Ehlen, McDonnell Aircraft Company, and M. Libeskind, Naval Air Development Center*
- H. Effects of Floor Location on Response of Composite Fuselage Frames ..... 443  
*Huey D. Carden and Lisa E. Jones, NASA Langley Research Center, and Edwin L. Fasanella, Lockheed Engineering and Sciences Company*

#### **SESSION IV - Design Criteria, Reliability, Supportability**

Chairman: Thomas E. Hess, Naval Air Development Center

- A. A Critical Review of Evolving Qualification Approaches for ..... 461  
Contemporary Composite Airframes  
*Keith R. Kedward, University of California; John C. Halpin, Wright  
Aeronautical Systems Division; and John E. McCarty, Consultant*
- B. Structural Design Optimization with Survivability Dependent Constraints ..... 465  
Application: Primary Wing Box of a Multi-Role Fighter  
*Douglas J. Dolvin, Wright Patterson Air Force Base*
- C. Reliability Analysis of Composite Structures ..... 489  
*Han-Pin Kan, Northrop Corporation*
- D. Uncertainties in Obtaining High Reliability from Stress-Strength Models ..... 503  
*Donald M. Neal, William T. Matthews and Mark G. Vangel,  
U.S. Army Materials Technology Laboratory*
- E. Probabilistic Design of Advanced Composite Structure ..... 523  
*P. M. Gray and M. G. Riskalla, LTV Aerospace and Defense*
- F. Probabilistic Evaluation of Fuselage-Type Composite Structures ..... 535  
*Michael C. Shiao, Sverdrup Technology, Incorporated, and  
Christos C. Chamis, NASA Lewis Research Center*
- G. Proof Test Methodology for Composites ..... 549  
*Edward M. Wu and David K. Bell, Naval Postgraduate School*
- H. Materials and Processes Used for Bonded Repairs of F/A-18 ..... 561  
Advanced Composite Honeycomb Sandwich Structures  
*Douglas R. Peri, Naval Aviation Depot North Island*
- I. Navy Composite Maintenance and Repair Experience ..... 565  
*T. M. Donnellan, R. C. Cochran, E. L. Rosenzweig and R. E. Trabocco,  
Naval Air Development Center*

### **VOLUME II**

#### **SESSION V - NASA Advanced Composites Technology (ACT)**

##### **SESSION V-A - Supporting Technology**

Chairman: John G. Davis, Jr., NASA Langley Research Center

- A. Overview of the ACT Program ..... 577  
*John G. Davis, Jr., NASA Langley Research Center*
- B. Designers' Unified Cost Model ..... 601  
*W. Freeman, NASA Langley Research Center; L. Ilcewicz and G. Swanson,  
Boeing Commercial Airplanes; and T. Gutowski, Massachusetts  
Institute of Technology*
- C. COINS: A Composites Information Database System ..... 621  
*Shahid Siddiqi, Louis F. Vosteen, Ralph Edlow and Teck-Seng Kwa,  
Analytical Services and Materials, Incorporated*
- D. Composite Fuselage Shell Structures Research at NASA ..... 631  
Langley Research Center  
*James H. Starnes, Jr. and Mark J. Shuart, NASA Langley Research Center*
- E. Structural Testing of the Technology Integration Box Beam ..... 659  
*C. F. Griffin, Lockheed Aeronautical Systems Company*
- F. Technology Integration Box Beam Failure Study: Status Report ..... 673  
*M. J. Shuart, D. R. Ambur, D. D., Davis, Jr., R. C. Davis, G. L. Farley,  
C. G. Lotts and J. T. Wang, Lockheed Aeronautical Systems Co.*

### **SESSION V-B. - Stitched RTM Technology**

Chairman: Marvin B. Dow, NASA Langley Research Center

- A. Development of Stitched/RTM Composite Primary Structures ..... 689  
*Susan M. Kullerd, Lockheed Engineering and Sciences Company, and  
Marvin B. Dow, NASA Langley Research Center*
- B. Resin Transfer Molding Technology for Composite Primary ..... 715  
Wing and Fuselage Structures  
*A. Markus, Douglas Aircraft Company*
- C. Test and Analysis Results for Composite Transport Fuselage ..... 719  
and Wing Structures  
*Jerry W. Deaton, NASA Langley Research Center; Susan M. Kullerd,  
Lockheed Engineering and Sciences Company; and Ram C. Madan  
and Victor L. Chen, Douglas Aircraft Company*

### **SESSION V-C. - Automated Fiber Placement technology**

Chairman: William T. Freeman, NASA Langley Research Center

- A. Tension Fracture of Laminates for Transport Fuselage ..... 747  
Part I: Material Screening  
*T. H. Walker, W. B. Avery and L. B. Ilcewicz, Boeing Commercial Airplane  
Group, and C. Poe, Jr. and C. E. Harris, NASA Langley Research Center*
- B. Indentability of Conventional and Negative Poisson's Ratio Foams ..... 789  
*R. S. Lakes and K. Elms, University of Iowa*
- C. Local Design Optimization for Composite Transport Fuselage Crown Panels ..... 795  
*G. D. Swanson, L. B. Ilcewicz and T. H. Walker, Boeing Commercial  
Airplane Group, and D. Graesser, M. Tuttle and Z. Zabinsky, University of  
Washington*
- D. Composite Fuselage Crown Panel Manufacturing Technology ..... 815  
*K. Willden and S. Metschan, Boeing Commercial Airplanes, and  
C. Grant and T. Brown, Hercules Aerospace*

### **SESSION V-D. - Textile Preform Technology**

Chairman: Randall C. Davis, NASA Langley Research Center

- A. Recent Progress in NASA Langley Textile Reinforces Composites Program ..... 845  
*H. Benson Dexter, Charles E. Harris and Norman J. Johnston,  
NASA Langley Research Center*
- B. Advanced Textile Applications for Primary Aircraft Structures ..... 875  
*Anthony C. Jackson, Ronald E. Barrie, Bharat M. Shah and  
Jay G. Shukla, Lockheed Aeronautical Systems Company*
- C. Comparison of Resin Film Infusion, Resin Transfer Molding and ..... 903  
Consolidation of Textile Preforms for Primary Aircraft Structure  
*J. Suarez and S. Dastin, Grumman Aircraft Systems*
- D. Characterization and Manufacture of Braided Composites for Large ..... 935  
Commercial Aircraft Structures  
*Mark J. Fedro, Boeing Defense and Space Group, and Kurtis Willden,  
Boeing Commercial Airplane Group*

### **SESSION VI - Damage Tolerance**

Chairman: J. David Oetting, Wright Research Development Center

- A. The Use of Impact Force as a Scale Parameter for the Impact ..... 981  
Response of Composite Laminates  
*Wade C. Jackson, U.S. Army Aerostructures Directorate, and  
C. C. Poe, Jr., NASA Langley Research Center*



## **SESSION VI - Damage Tolerance (continued)**

- B. Application of Damage Tolerance Methodology in Certification of the ..... 999  
Piaggio P-180 Avanti  
*Jerry Johnson, Dow-United Technologies Composite Products, Incorporated*
- C. Effect of Low-Speed Impact Damage and Damage Location ..... 1013  
on Behavior of Composite Panels  
*Dawn Jegley, NASA Langley Research Center*
- D. Impact Damage Resistance of Composite Fuselage Structure, Part I ..... 1037  
*E. F. Dost, W. B. Avery, L. B. Ilcewicz and D. H. Grande, Boeing Commercial  
Airplane Group, and B. R. Coxon, Integrated Technologies, Incorporated*
- E. Applications of a Damage Tolerance Analysis Methodology in Aircraft Design ... 1071  
*M. R. Woodward, S. D. Owens, G. E. Law and L. A. Mignery, General  
Dynamics Corporation*
- F. Compressive Strength of Damaged and Repaired Composite Plates ..... 1083  
*Scott R. Finn and George S. Springer, Stanford University*
- G. Post Impact Compressive Strength in Composites ..... 1097  
*Edvins Demuts, Raghbir S. Sandhu and John A. Daniels,  
Wright Laboratory, U.S. Air Force*
- H. Fundamental Concepts in the Suppression of Delamination ..... 1105  
Buckling by Stitching  
*B. N. Cox, Rockwell International Science Center*
- I. Damage Tolerance of a Geodesically Stiffened Advanced ..... 1111  
Composite Structural Concept for Aircraft Structural Applications  
*Marshall Rouse and Damodar R. Ambur, NASA Langley Research Center*
- J. Advanced Wing Design Survivability Testing and Results ..... 1123  
*J. Bruno, Grumman Aircraft Systems, and M. Tobias,  
Naval Air Development Center*
- K. NASA-ACEE /Boeing 737 Graphite-Epoxy Horizontal Stabilizer Service ..... 1139  
*J. T. Quinlivan, J. A. Kent and D. R. Wilson, Boeing  
Commercial Airplane Group*

## **VOLUME III\***

## **SESSION VII - Innovative Design/Manufacturing**

Chairman: Larry Kelly, Wright Research Development Center

- A. Process and Control Systems for Composites Manufacturing ..... 1153  
*T. H. Tsiang and J. L. Wanamaker, Lockheed Aeronautical  
Systems Company*
- B. Development of a Low-Cost, Modified Resin Transfer Molding ..... 1163  
Process Using Elastomeric Tooling and Automated Preform Fabrication  
*William J. Doane and Ronald G. Hall, General Dynamics Convair Division*
- C. Design of Fabric Preforms for Double Diaphragm Forming ..... 1175  
*Steven Luby and Edward Bernardon, Charles Stark Draper  
Laboratory, Incorporated*
- D. Static and Fatigue Testing of Full-Scale Fuselage Panels Fabricated Using a ..... 1185  
Therm-X® Process  
*Albert J. DiNicola, Christos Kassapoglou and Jack C. Chou,  
United Technologies-Sikorsky Aircraft Division*
- E. Advanced Tow Placement of Composite Fuselage Structure ..... 1211  
*Robert L. Anderson and Carroll G. Grant, Hercules Aerospace Company*
- F. Service Tough Composite Structures Using the Z-Direction ..... 1223  
Reinforcement Process  
*Glen Freitas, Constance Magee and Joseph Boyce, Foster-Miller, Incorporated  
and Richard Bott, Naval Weapons Center*

\* Published in companion document

## **SESSION VII - Innovative Design/Manufacturing (continued)**

- G. Through-the-Thickness® Braided Composites for Aircraft Application ..... 1231  
*Richard T. Brown, Atlantic Research Corporation*
- H. Thermoplastic Pultrusion for Future Aerospace Application ..... 1249  
*Hsin-Nan Chou, McDonnell Douglas Missile System Company*
- I. ACT/ICAPS - Thermoplastic Composite Activities ..... 1253  
*M. P. Renieri, S. J. Burpo, L. M. Roundy and S. M. Roundy and S. M. Todd,  
McDonnell Aircraft Company*
- J. Composite Intermediate Case Manufacturing Scale-Up for Advanced Engines ..... 1289  
*Rowena H. Ecklund, Pratt and Whitney Group, United Technologies Corporation*
- K. Resin Transfer Molding of Textile Preforms for Aircraft ..... 1303  
Structural Applications  
*Gregory H. Hasko, Lockheed Engineering and Sciences Company;  
H. Benson Dexter, NASA Langley Research Center; and Mark H. Weideman,  
Virginia Polytechnic Institute and State University*

## **SESSION VIII - Design Applications (B)**

Chairman: Donald W. Oplinger, Federal Aviation Administration Technical Center

- A. Analysis of Aircraft Engine Blade Subject to Ice Impact ..... 1319  
*E. S. Reddy and G. H. Abumeri, Sverdrup Technology, Incorporated  
and C. C. Chamis and P. L. N. Murthy, NASA Lewis Research Center*
- B. Application of Fiber-Reinforced Bismaleimide Materials to ..... 1333  
Aircraft Nacelle Structures  
*Vasilios Peros, John Ruth and David Trawinski, Martin Marietta  
Aero and Naval Systems*
- C. Innovative Design and Fabrication of Composite Canopy Frames ..... 1349  
*Robert L. Chu and Michael C. Y. Niu, Lockheed Aeronautical  
Systems Company*
- D. Assembly Induced Delaminations in Composite Structures ..... 1353  
*J. Goering, R. Bohlmann and S. Wanthal, McDonnell Aircraft Company;  
E. Kautz, Naval Air Development Center; and L. Neri, Federal  
Aviation Administration Technical Center*
- E. Stress Analysis and Failure of an Internally Pressurized ..... 1379  
Composite-Jacketed Steel Cylinder  
*Peter C. T. Chen, U.S. Army Armament Research, Development  
and Engineering Center*
- F. Composite Flight-Control Actuator Development ..... 1389  
*Richard Bott, Naval Weapons Center, and Fred Ching, HR Textron Incorporated*

## **SESSION IX - Thick Structures Technology**

Chairman: Michael F. Card, NASA Langley Research Center

- A. Higher Order Finite Element Analysis of Thick Composite Laminates ..... 1407  
*J. Goering and H. J. Kim, McDonnell Aircraft Company*
- B. An Improved Plate Theory of Order {1,2} for Thick Composite Laminates ..... 1417  
*A. Tessler, U.S. Army Materials Technical Laboratory*
- C. Failure Analysis of Thick Composite Cylinders Under External Pressure ..... 1431  
*A. Caiazzo and B. W. Rosen, Materials Sciences Corporation*
- D. On the Thermally-Induced Residual Stresses in Thick Fiber-Thermoplastic ..... 1447  
Matrix (PEEK) Cross-Ply Laminated Plates  
*Shoufeng Hu and John A. Nairn, University of Uta*
- E. Advanced Fabrication Processes for Thick Composite Submarine Structure ..... 1455  
*James J. Kelly, DARPA; George Leon, GD/Electric Boat;  
and Diana Holdinghausen, McDonnell Aircraft Corporation*
- F. Low-Cost Design and Fabrication of Composite Ship Structures ..... 1459  
*Milton O. Critchfield and Thomas D. Judy, Davis Taylor Model Basin*

## **SESSION X - Aircraft Design Methodology (B)**

Chairman: Donald W. Oplinger, Federal Aviation Administration Technical Center

- A. Analysis of Stresses in Finite Anisotropic Panels with ..... 1485  
Centrally Located Cut-Outs  
*Vickie O. Britt, NASA Langley Research Center*
- B. The Role of Biaxial Stresses in Discriminating Between Meaningful ..... 1507  
and Illusory Composite Failure Theories  
*L. J. Hart-Smith, Douglas Aircraft Company*
- C. Static and Dynamic Strain Energy Release Rates in Toughened Thermosetting .... 1529  
*Douglas S. Cairns, Hercules Advanced Materials and Systems Company*
- D. Analysis Techniques for the Prediction of Springback in Formed and ..... 1539  
Bonded Composite Components  
*Michael F. Gasick and Gary D. Ranieri, McDonnell Aircraft Company*

## **SESSION XI - Space Structures**

Chairman: Michael F. Card, NASA Langley Research Center

- A. Stiffness and Strength Tailoring in Uniform Space-Filling Truss Structures ..... 1561  
*Mark S. Lake, NASA Langley Research Center*
- B. Design Prediction for Long Term Stress Rupture Service ..... 1589  
of Composite Pressure Vessels  
*Ernest Y. Robinson, The Aerospace Corporation*
- C. Designing for Time-Dependent Material Response in Spacecraft Structures ..... 1617  
*M. W. Hyer and Lynda L. S. Oleksuk, Virginia Polytechnic Institute  
and State University, and D. E. Bowles, NASA Langley Research Center*
- D. Composite Flexible Insulation for Thermal Protection of Space Vehicles ..... 1631  
*S. Amanda Chiu, Sterling Software, Incorporated*

**SESSION V**

**NASA ADVANCED COMPOSITES TECHNOLOGY (ACT)**

**THIS PAGE INTENTIONALLY BLANK**

**SESSION V-A**  
**SUPPORTING TECHNOLOGY**

**THIS PAGE INTENTIONALLY BLANK**

## OVERVIEW OF THE ACT PROGRAM

John G. Davis, Jr.  
NASA Langley Research Center  
Hampton, Virginia

### INTRODUCTION

NASA'S Advanced Composites Program (ACT) was initiated in 1988. A National Research Announcement was issued to solicit innovative ideas that could significantly contribute to development and demonstration of an integrated technology data base and confidence level that permits cost-effective use of composite primary structures in transport aircraft. Fifteen(15) contracts were awarded by the Spring of 1989 and the participants include commercial and military airframe manufacturers, materials developers and suppliers, universities and government laboratories. The program approach is to develop materials, structural mechanics methodology, design concepts and fabrication procedures that offer the potential to make composite structures cost-effective compared to aluminum structure. Goals for the ACT program included 30-50 percent weight reduction, 20-25 percent acquisition cost reduction, and provided the scientific basis for predicting materials and structures performance.

This paper provides an overview of the ACT program status, plans and selected technical accomplishments. Sixteen(16) additional papers, which provide more detailed information on the research and development accomplishments, are contained in this publication.

Gratitude is expressed to the Program Selection Committee for the Ninth DOD/NASA/FAA Conference on Fibrous Composites in Structural Design for allocating one day of the agenda for presentations on the ACT Program.

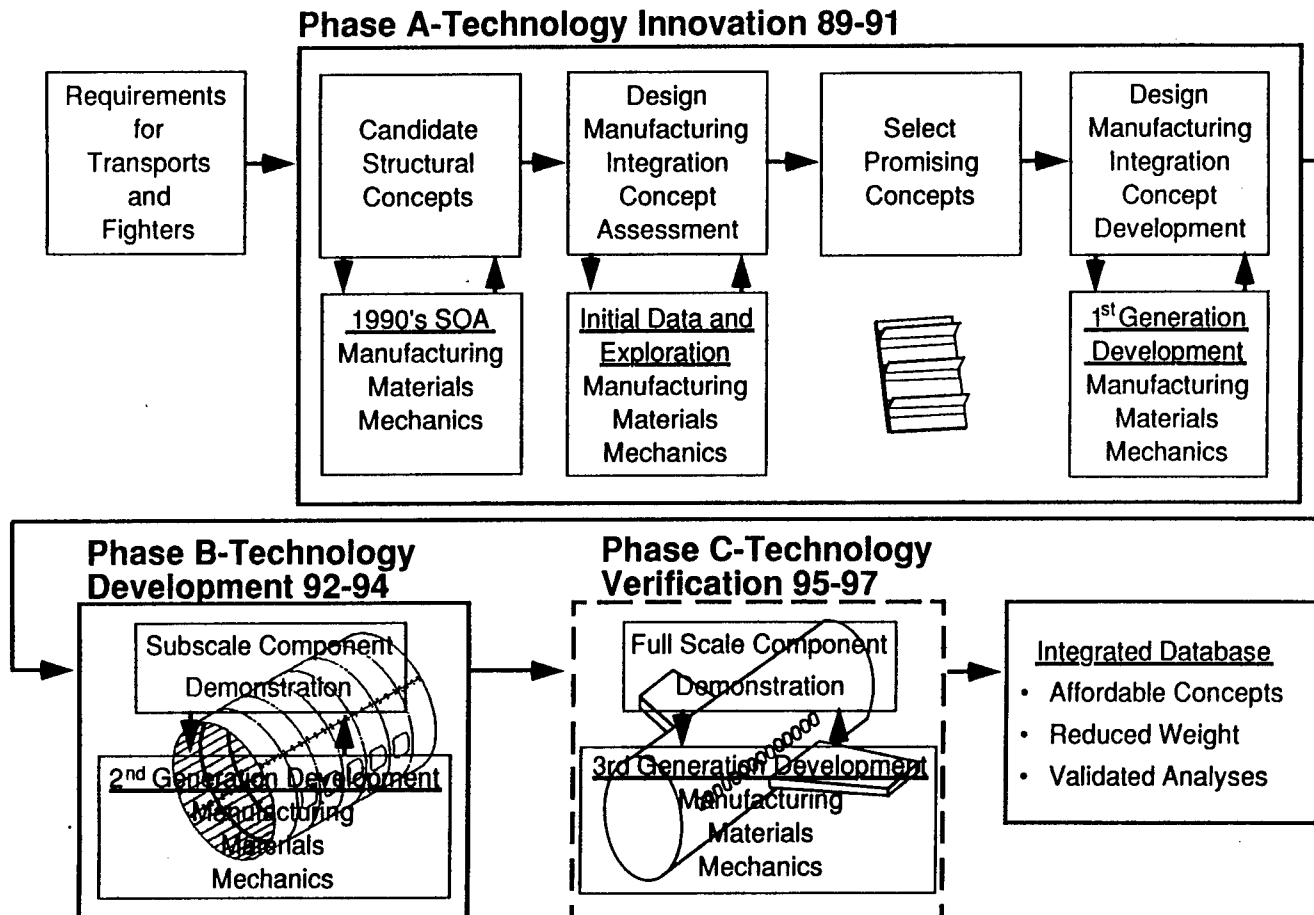


## ACT PROGRAM LOGIC

The program plan began with definition of requirements for military and transport aircraft contains three phases, and ends with a verified integrated database. Phase A is complete and several candidate materials, concepts and fabrication methods that offer the potential for cost-effective composite structures were identified. Materials coupons, small panels and elements, and fabrication articles have been tested. Cost-effectiveness is the most challenging goal.

Focus of Phase B is a wing concept that exploits through-the-thickness stitching of dry fiber material and resin transfer molding and a fuselage concept that exploits a combination of automated fiber placement and textile preforms. A semi-span wing box for a 200 passenger aircraft will be developed and ground tested. Large panels representative of the crown, window belt and keel areas of Boeing-777 size aircraft will be developed and tested.

Phase C is not fully defined but the anticipated focus is large components at the wing body intersection and a full barrel with doors and windows aft of the wing.

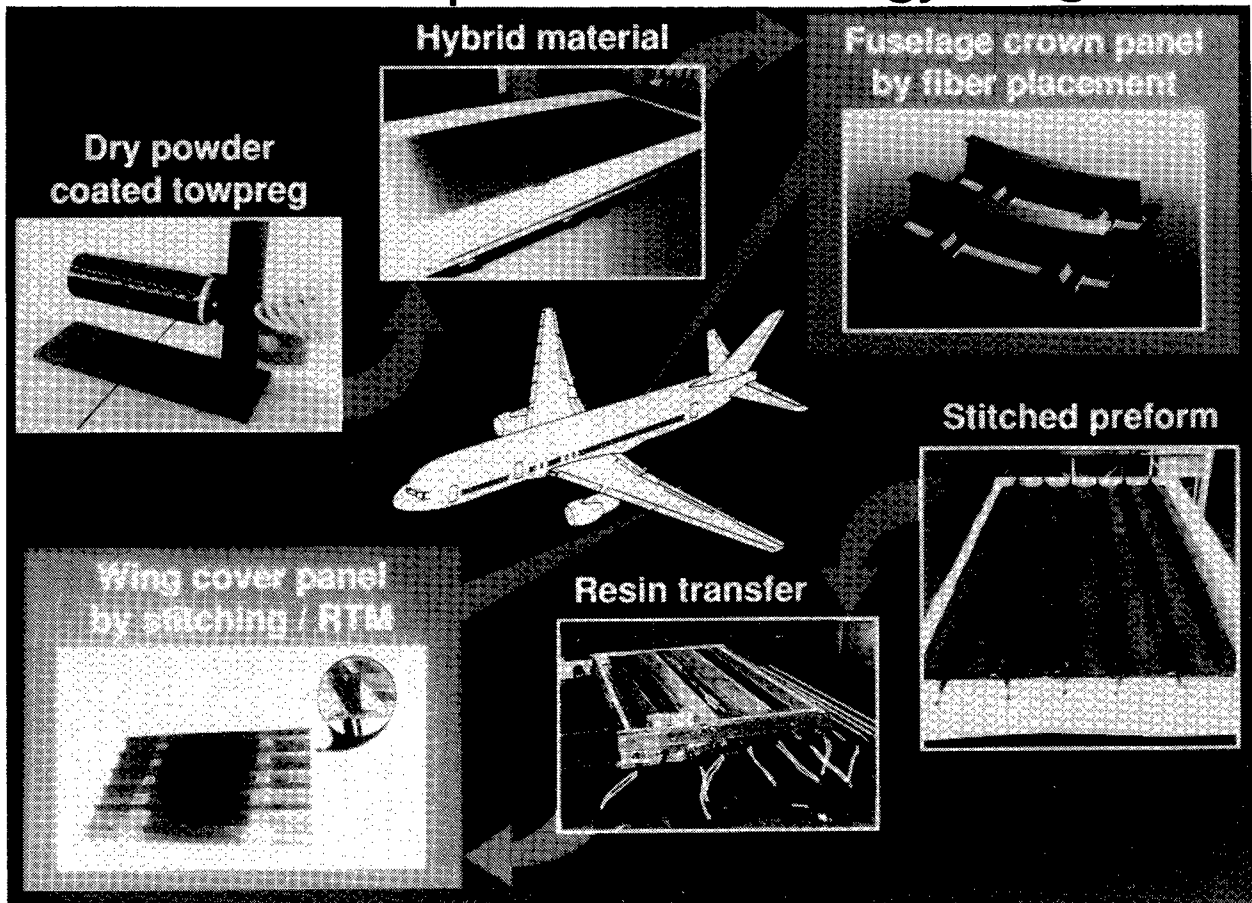


## PHASE A SELECTED HIGHLIGHTS

Dry powder coated towpreg has been identified as a potential low cost method for producing material for use in weaving or fiber placement of structural components. Other advantages of the process are that solvents are not required and shelf life can be greatly extended. Use of intermediate strength and stiffness graphite/glass hybrids in tension-tension design applications such as the fuselage crown area appears to offer cost advantages compared to use of high modulus/high strength graphite. A crown panel design that is cost-effective relative to aluminum panels has been identified. Eliminating fasteners and reducing assembly cost are key features.

Wing panels up to six (6) feet in length have been fabricated and tested. Use of through-the-thickness preforms and resin transfer molding with state-of-the-art untoughened resins have produced panels which meet damage tolerance requirements. Test results indicate that delamination and stiffener separation are eliminated or greatly reduced compared to panels without through-the-thickness stitching. Resin transfer is through the thickness and thus major technical barriers to scale-up are not anticipated.

## Advanced Composites Technology Program

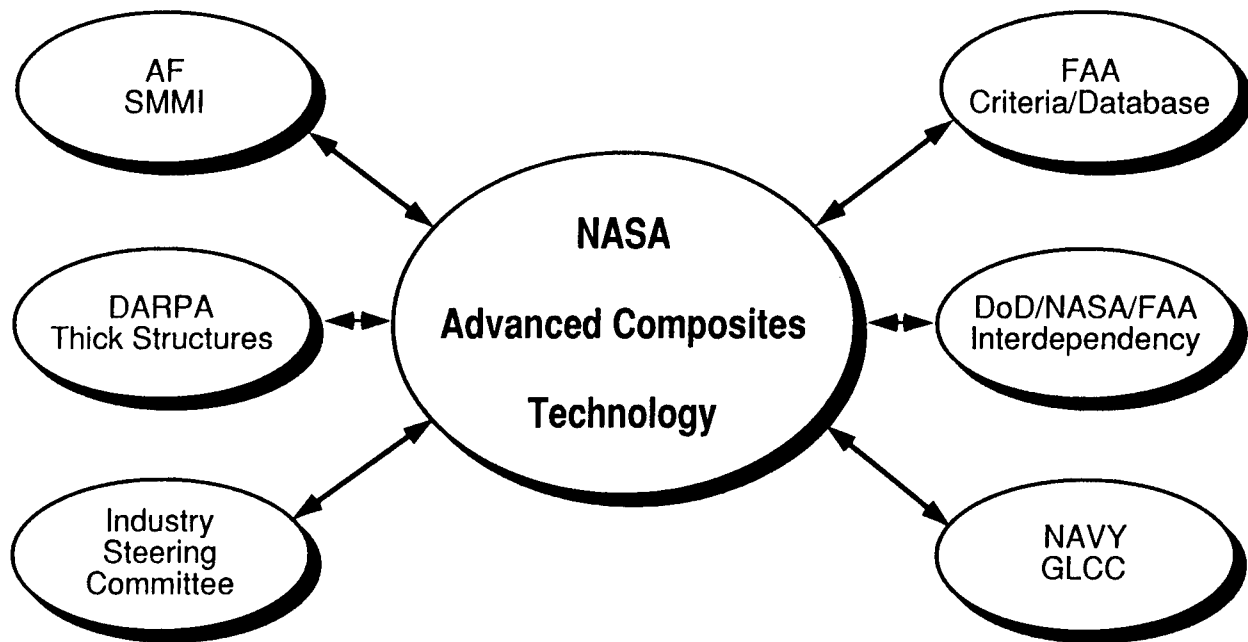


## GOVERNMENT/INDUSTRY INTERFACE

NASA has established and maintained a strong interface with industry and other government agencies that are developing composite materials and structures technology for application to primary structures. This will insure that maximum synergism is obtained for each program, the maximum possible advancement in the state-of-the-art is achieved with the available budget, that lessons learned are shared between the participants, and the possibility of overlooking major technical obstacles is minimum.

It is anticipated that formal cooperative agreements will evolve from several of these interfaces. Joint conferences are already occurring and are planned for the future. Representatives from the various organizations have participated in several technical workshops. Common interest in developing cost models and common formats for collecting cost data have been identified.

## Advanced Composites Technology Program



## ACT STEERING COMMITTEE

The ACT Steering Committee was formed in 1990 and includes representatives from airframe manufacturers, a materials company, a commercial airline company, the U. S. Air Force, the Federal Aviation Administration and NASA Headquarters. Several members of the Langley Research Center staff serve an ex-officio role. These include the Director for Structures, Chiefs of the Materials and Structures Divisions and Manager of the Structures Technology Program Office.

The Committee has been charged to periodically critique the ACT Program and to provide recommended improvements. Technical, resource allocation and schedules are reviewed with the Committee. Three meetings have been held: November 1990, June 1991 and November 1991. The committee recommended that the focus of the ACT Program be narrowed to emphasize structural concepts that exploit stitched dry fiber/resin transfer molding, textile preforms and automated fiber placement. The recommendation has been implemented.

<b>Members:</b>	Jack McGuire	Boeing (Chairman)
	Dale Warren	Douglas
	Cecil Schneider	Lockheed
	Sam Dastin	Grumman
	Robin Whitehead	Northrop
	John DeVault	Hercules
	Terry Hertz	NASA
	Robert Neff	U.S. Air Force
	Joe Soderquist	FAA
	Jim Epperson	American Airlines
<b>Ex-Officio Members:</b>	Charles Blankenship	NASA
	Darrel Tenney	NASA
	John Malone	NASA
	John Davis	NASA

## NASA/ACT FOCUSED RESEARCH TEAMS

Four primary research teams have been established. Three are in response to the ACT Steering Committee recommendation. Each of the specific technical thrust areas has a lead airframe contractor. The other organizations perform a supporting role.

Boeing is the lead contractor for the Automated Fiber Placement team and Hercules, Stanford, University of Utah(B), LaRC Materials Division and Structural Mechanics Division are supporting members.

Douglas is the lead contractor for the RTM/Stitched team and Dow, LaRC Materials and Structural Mechanics Divisions are supporting members. Lockheed is the lead contractor for the Textile Preforms team and Grumman, Rockwell, BASF, LaRC Materials, Structural Mechanics, and Structural Dynamics Divisions are Supporting members.

A portion of the research and development that was initiated early in the program is generic, and performing organizations are listed under Supporting Technology.

### **Automated Fiber Placement**

Boeing Commercial Airplanes  
Hercules  
Stanford University  
University of Utah (B)  
LaRC Materials Division  
LaRC Structural Mechanics Division

### **RTM/Stitched**

McDonnell Douglas  
Dow Chemical  
LaRC Materials Division  
LaRC Structural Mechanics Division

### **Textile Preforms**

Lockheed Aeronautical Systems  
Grumman  
Rockwell International  
BASF  
LaRC Materials Division  
LaRC Structural Mechanics Division  
LaRC Structural Dynamics Division

### **Supporting Technology**

University of Utah (N)  
Sikorsky  
University of Cal-Davis  
University of Delaware  
Northrop  
LaRC STPO  
LeRC Structures Division

## TOTAL FUNDING BY FISCAL YEAR

Funding for each specific thrust area is shown. Taking into account the applicability of some of the textile preform research and development to the RTM/stitched thrust, the funding for each of the three specific thrust areas is approximately the same. Funding for the generic supporting technology is less and reflects the decision to narrow the program focus. The funding shown does not include ACT Program resources that have been redirected to support research and development of materials and structures for high speed civil transport type aircraft.

## ACT Focused Research Program

Research Areas	Prior Years	$\phi A \longrightarrow$		$\longleftarrow \phi B$		Total
		FY91	FY92	FY93	FY94	
Automated Fiber Placement	7441	8076	6179	4986	5897	32579
RTM/Stitched	5670	4284	5672	5292	5183	26099
Textile Preforms	3715	9158	9016	9900	9350	41138
Supporting Technology	6572	3360	3435	4505	4870	22742
<b>Total</b>	<b>23398</b>	<b>24877</b>	<b>24301</b>	<b>24682</b>	<b>25300</b>	<b>122558</b>

## **RESPONSIBILITY FOR NASA/ACT RESEARCH TEAM FOCUSING ON AUTOMATED FIBER PLACEMENT (AFP)**

Boeing is responsible for overall design, analyses, fabrication and testing of transport fuselage concepts that exploit the AFP process. Hercules is responsible for the fabrication of panels that will be used to validate structural and cost performance. Stanford University is conducting tests and developing compression damage tolerance analysis methods. University of Utah is investigating failure mechanisms that affect tension damage tolerance. University of Delaware is developing technology to design and predict the response of Long Discontinuous Fiber(LDF) frame concepts. The Materials Division of the NASA Langley Research Center is investigating new material forms that offer potential for cost savings. The Structural Mechanics Division of the NASA Langley Research Center is conducting advanced analyses and performing tests to verify the performance of the AFP concepts and to insure that the technology basis is sufficiently mature to predict the response under load.

### **Boeing Commercial Airplane Group (ATCAS Program)**

- Coordinate team efforts to concentrate on critical technical issues
- Lead DBT studies to optimize quadrant designs and manufacturing plans
- Formulate preliminary design cost model
- Create process and test plans for development and validation tasks
- Demonstrate composite fuselage manufacturing technology
- Develop analyses/perform tests to link material and structural performance
- Validate composite fuselage performance using analyses and tests
- Document technology databases (design, process, test, and analysis)

### **Hercules Incorporated**

- Support DBT on design, process, and performance issues with emphasis on AFP
- Process manufacturing demos and test articles as specified by DBT decisions

### **Stanford University**

- Damage tolerance analysis methods and "Impact" software
- Impact tests database

### **University of Utah**

- Characterize failure mechanisms affecting the tension damage tolerance of AFP laminates
- Identify relationships between AFP process variables and critical failure mechanisms

### **University of Delaware**

- Identify a BCA frame design for demonstrating LDF manufacturing approach
- Process, analyze, & test frames to validate LDF technology

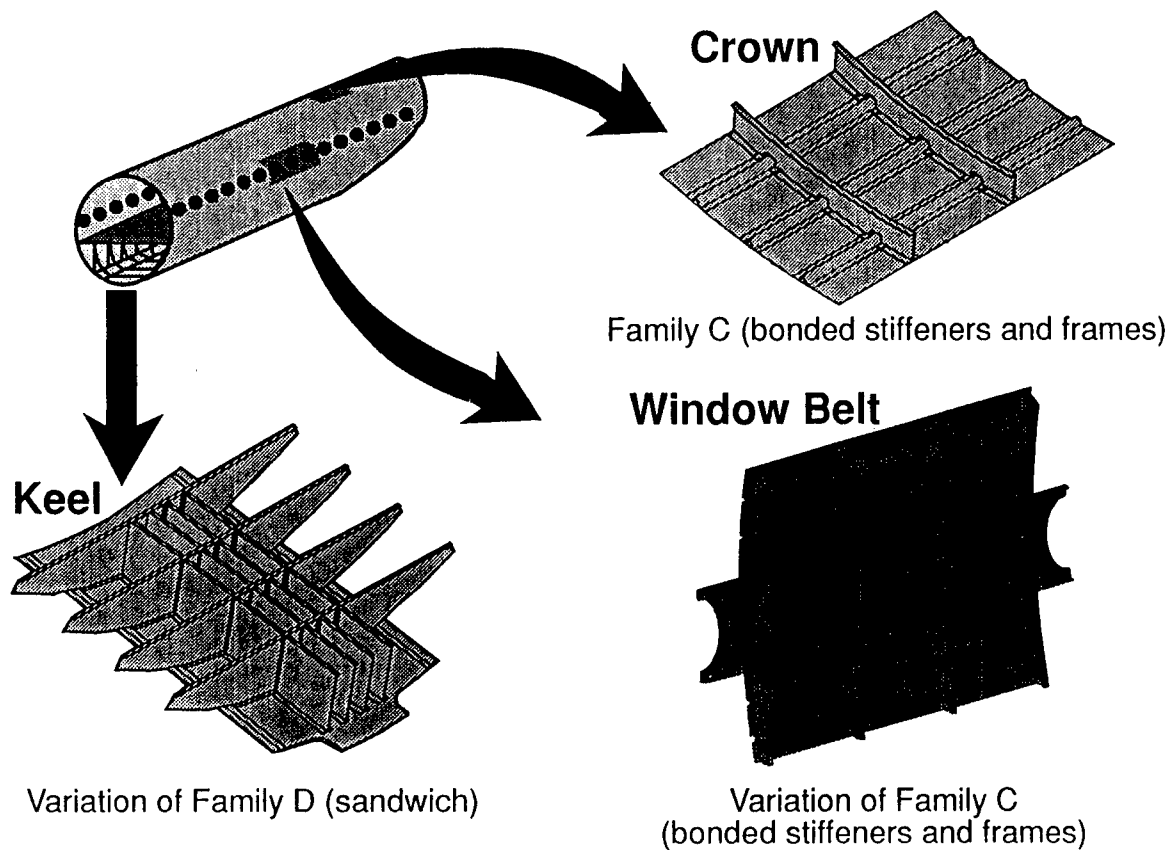
### **NASA (MD, SMD)**

- Conduct research on mechanics of advanced materials
- Conduct advanced studies on damage tolerance for transport fuselage

## BASELINE FUSELAGE CONCEPTS

Boeing Design-To-Build-Team(DBT) studies early in Phase A of the ACT Program concluded that the most probable approach for achieving cost-effective fuselage structure is to build the barrel in quadrants. Variation in design load requirements in the crown, side and keel areas, fabrication and assembly considerations, inspection and repair requirements lead to this conclusion. The skins for all panels will be fabricated by continuous AFP. Three cylindrical mandrels will be used to AFP four crown, four side and ten keel panels. The skins will be cut, removed from the mandrel, and laid into a tool for subsequent cure and bonding of stringers and frames. The baseline frames are textile preforms that are impregnated by RTM.

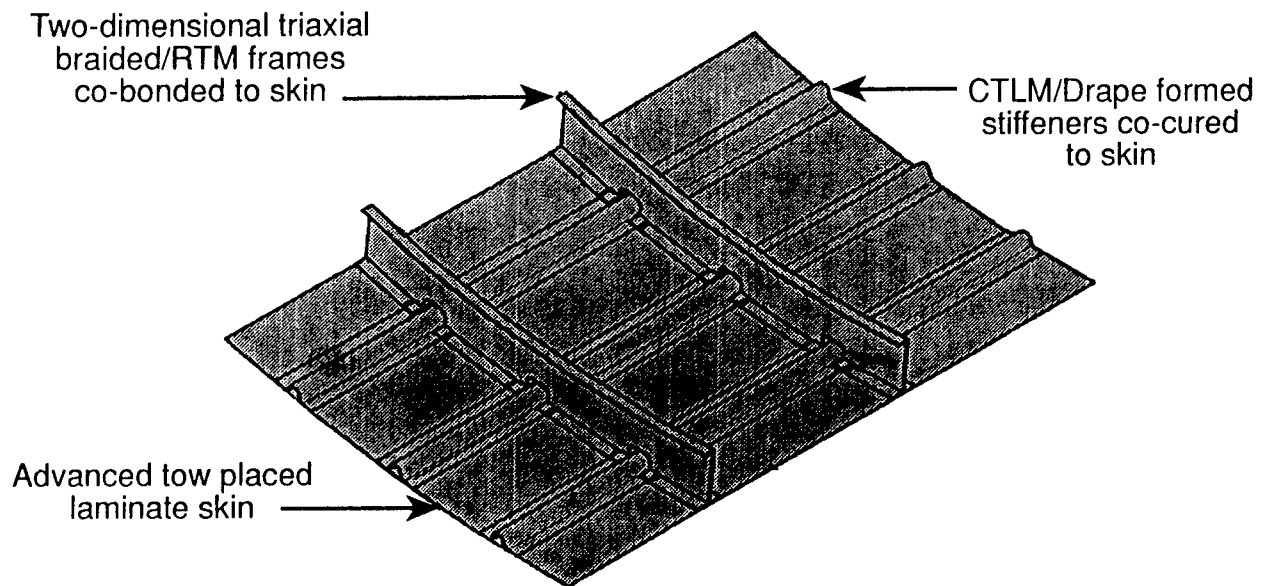
The baseline window belt frames are also textile preforms/RTM and will be developed by Lockheed under contract to NASA.





## BASELINE CROWN QUADRANT

The baseline design for the crown quadrant section of the fuselage contains a mixture of technologies that was selected on the basis of Design to Build Team (DBT) meetings that addressed cost, weight, maintenance, inspection and repair. AFP was selected for the skin. The hat-shaped stiffeners will be fabricated using the Contour Tape Layed Mold (CTLTM)/Drape forming process. A two-dimensional triaxial braided textile preform that will be impregnated with the resin transfer molding process will be used to build frames. The frames will be co-bonded to the skin whereas the stiffeners will be co-cured with the skin. Current estimates indicate a fifty percent reduction in weight and approximately thirty percent reduction in cost compared to aluminum aircraft structure. A significant portion of the cost savings is attributed to the size of one composite panel (approximately twenty five percent of the fuselage circumference and 30 feet in length) compared to numerous aluminum panels required. Elimination of thousands of fasteners compared to the metal panels also contributes to the cost savings. Graphite/epoxy material remains as a major cost center.



### Notes from Global Optimization

Comparison with aluminum 767-X

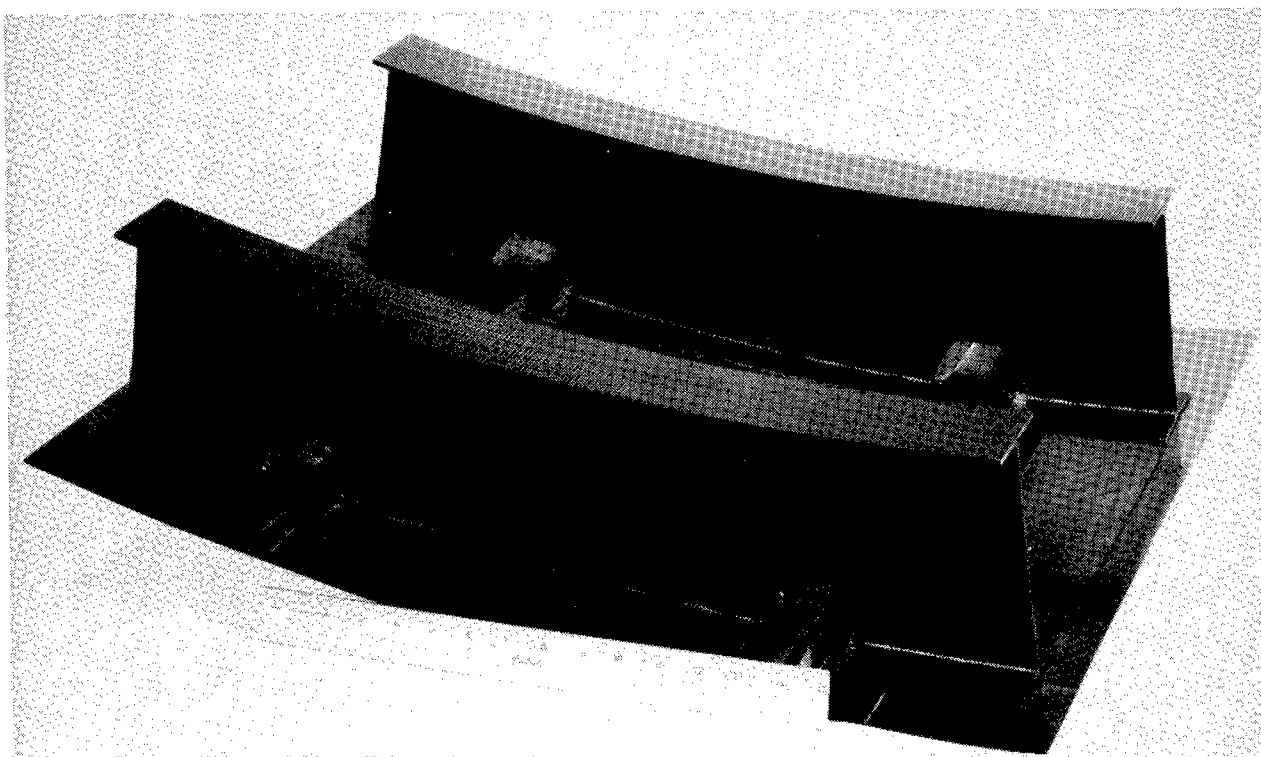
50% weight savings

Potential for up to 30% cost savings in local optimization

Major cost center: Material

## INITIAL TOOL PROOF ARTICLE FOR AFP CROWN PANEL

The first tool proof panel fabricated by Boeing is shown. A small curved panel with two "I" frames and two hat stringers was fabricated and cured with the a soft tooling concept. The radius of curvature for the panel is 74 inches. The panel was cured under 150 psi pressure on a steel outer mold line tool. The purpose of the tool proof article was to evaluate dimensional accuracy and bond quality for the fabrication approach. Additional trials are planned for 3 feet x 5 feet panels and the 7 feet x 10 feet crown verification panels. The soft tooling concept uses silicon rubber bag material that is selectively reinforced with graphite fiber to provide stiffness for dimensional stability at cure temperatures. The flexible caul concept provides a low cost way to accurately locate stringer cross sections and panel taper in the composite panel. Additional papers on this subject are included in the proceedings of this conference.



## **RESPONSIBILITY FOR NASA/ACT RESEARCH TEAM FOCUSING ON RESIN TRANSFER MOLDING(RTM) TECHNOLOGY**

Douglas is responsible for overall design, analyses, fabrication and testing of transport wing and fuselage concepts that exploit the stitched dry fiber/RTM process. William and Mary College and Virginia Polytechnic Institute and State University are developing flow and cure models and performing related experiments. Ketema and Pathe are developing automated high speed sewing machines to stitch the cover panels and to attach stiffeners to the cover panels. The Materials Division of the NASA Langley Research Center is conducting tests on specimens and small panels to assess mechanical properties and environmental effects. The Structural Mechanics Division of the NASA Langley Research Center is conducting advanced analyses and performing tests to verify the performance of the stitched dry fiber/RTM concepts and to insure that the technology basis is sufficiently mature to predict the response under load. Hercules will build an AFP fuselage panel that will provide a direct comparison with a RTM panel.

### **Douglas Aircraft Company**

- Develop through-the-thickness stitching concepts for damage tolerant structures
- Create processes and tooling for RTM of stitched preforms
- Develop analyses/perform tests to link material and structural performance
- Demonstrate composite wing and fuselage manufacturing technology
- Validate composite structures performance using tests and analyses
- Document technology databases (Design, Process, Test and Cost)

### **William and Mary College**

- Measure cure kinetics of RTM resins
- Devise manufacturing thermal cycles
- Develop instrumentation for monitoring RTM processes

### **Hercules Incorporated**

- Support Douglas on ATP process and tooling issues
- Fabricate tooling for ATP fuselage panels designed by Douglas
- Build panel test articles for process demonstration

### **Ketema, Inc. and Pathe**

- Stitch dry carbon fabric preforms for concept developments
- Develop high speed stitching machines for structural preforms
- Demonstrate new machines on panel preforms

### **V.P.I. and State Univ.**

- Develop RTM flow and cure models
- Characterize flow properties for stitched preforms
- Devise optimum heat and pressure cycles

### **NASA (MD, SMD)**

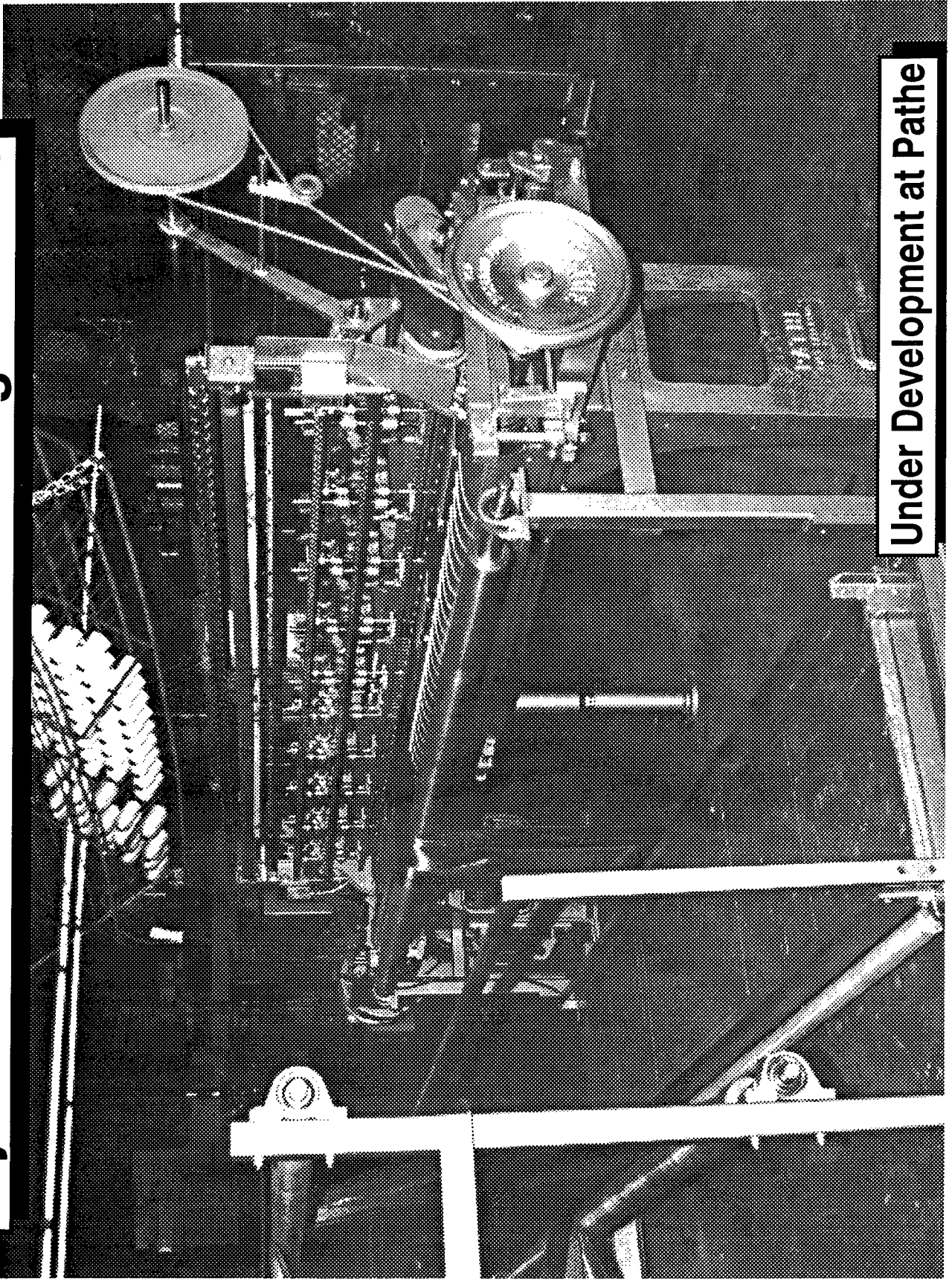
- Test stitched/RTM laminates for properties and CAI strength
- Perform studies on mechanics of stitched composite materials
- Test ATP and RTM fuselage panels

## **DRY PREFORM MULTINEEDLE STITCHING MACHINE**

The multineedle machine, with up to 256 needles, is mechanically controlled and can accommodate up to a 128 inch wide preform. Material up to one-half inch thick or 72-ply nominal 0.006 inch per ply preforms can be sewn. The machine will perform a wide range of stitching densities (light-1 inch on center with 100 denier thread to heavy-3/16 inch on center with 1500 denier thread). Capability is limited to lock stitching. Speed varies according to stitch density but the machine is expected to be capable of stitching a wing cover panel 8 feet by 12 feet in size in one hour. The machine is scheduled to be fully operational in the first quarter of calendar year 1992.

(See photograph on following page)

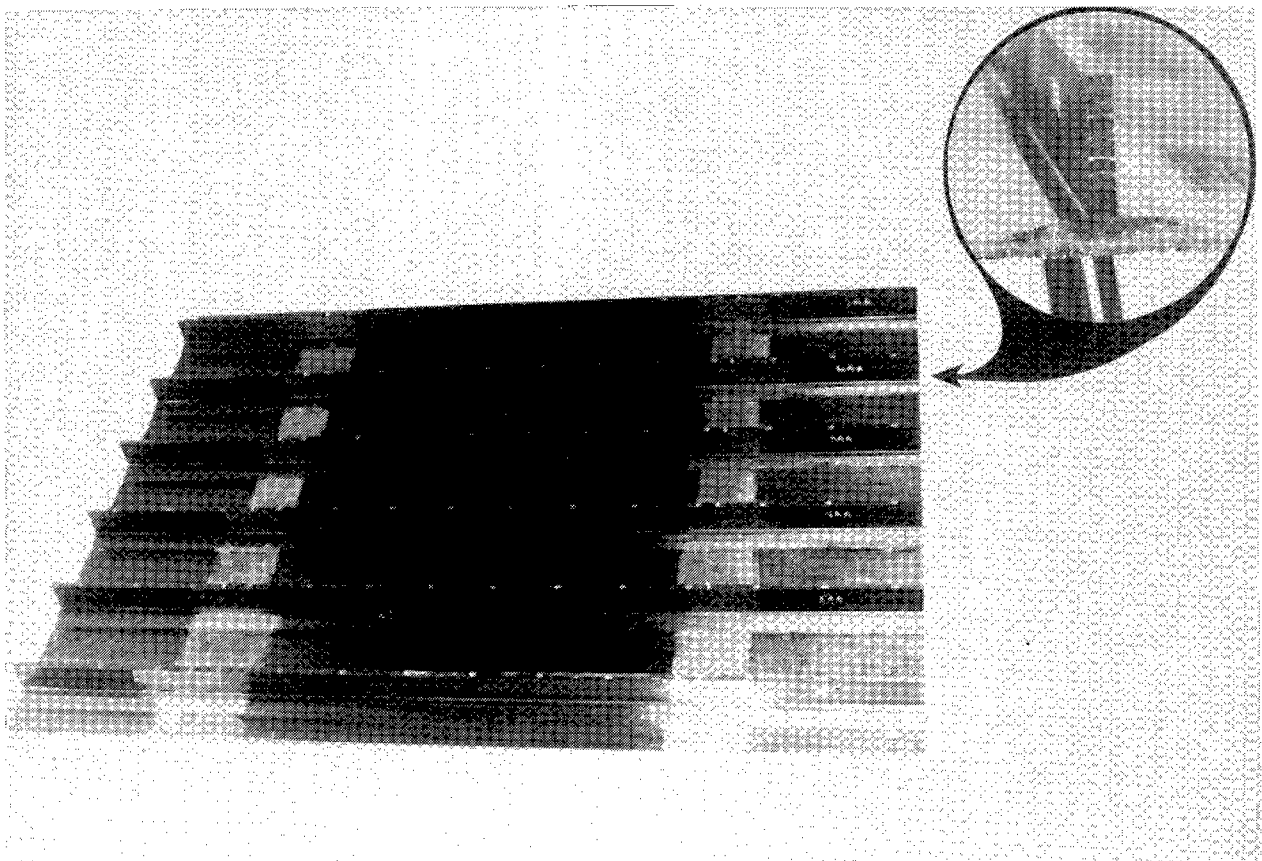
# Dry Preform Multineedle Stitching Machine



Under Development at Pathe

## DAC STITCHED/RTM WING PANEL

A six foot by four foot six stringer wing panel is shown. The cover panel was fabricated as follows: a dry preform was stitched throughout the planform area, stiffeners were next attached to the planform by stitching, and the dry preforms were subsequently placed in a mold, compacted, impregnated by resin film infusion and cured formed. Fabrication of this panel represents a significant step in the scaleup of the RTM process for skin stiffened structural components. Through-the-thickness stitches which provide enhanced damage tolerance and resistance to skin stiffener separation are visible in the enlarged section of the photograph. Mechanical tests are being conducted on these types of panels to verify the load carrying capacity and the analyses capability to predict structural response. Future research and development will include building and ground testing a semispan wing box for a 200 passenger size transport aircraft to verify weight savings, cost savings and integrated technology base.



## **RESPONSIBILITY FOR NASA/ACT RESEARCH TEAM FOCUSING ON TEXTILE PREFORM TECHNOLOGY**

Lockheed is responsible for overall design, analyses, fabrication and testing of fuselage components that exploit textile preform technology. Lockheed and Boeing are working together in DBT's to select a window belt design that Lockheed will develop. The window belt will subsequently be incorporated into a side panel that Boeing will test. Rockwell is conducting a basic investigation on the fatigue response of woven materials. BASF is developing powder coated tow that will be woven into textile preforms. Grumman is focusing on cross-stiffened elements and an integrally woven fuselage panel. The Materials and Structural Mechanics Divisions of the NASA Langley Research Center are conducting fundamental studies on mechanics of materials and will perform tests to verify capability to predict structural response.

### **Lockheed Program**

- Develop advanced resin systems
- Demonstrate preform fabrication and processing methods
- Develop low cost preform fabrication techniques and equipment
- Design and fabricate crown and lower side quadrant fuselage components
- Document databases for design, process and analysis
- Validate structural response and failure analysis methods

### **Rockwell**

- Fatigue characterization of woven materials

### **BASF**

- Powder coated tow-preg material development

### **Grumman Aircraft**

- Support DBT to design, fabricate and test a cross-stiffened integrally woven element
- Fabricate and deliver to LaRC for test, an integrally woven fuselage panel

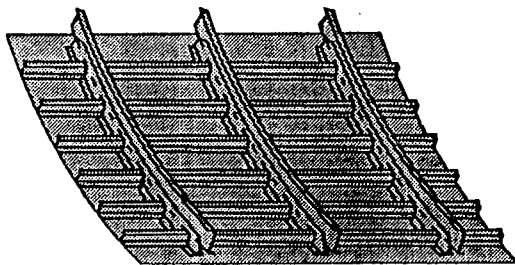
### **NASA (AMB, PMB, MeMB, ASB)**

- Lead studies on mechanics for advanced textile architecture
- Develop RTM inplane flow models
- Conduct benchmark panel tests
- Demonstrate weaving of powdered tow-preg
- Develop analytical methods, modeling and test standardization
- Develop micromechanics for fatigue and test standards

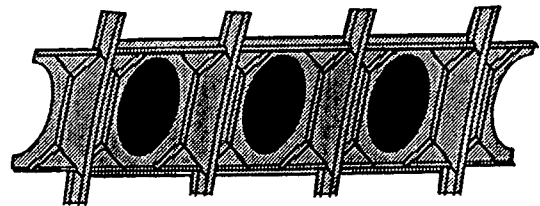
## TEXTILE REINFORCED COMPOSITE STRUCTURAL COMPONENTS

Four basic types of fuselage structural components have been selected to focus the technology development for textile preforms: integrally woven stiffened panels, circumferential frames, window belt insert and keel beam frame intercostals. These components must support out of plane loads and can benefit from the improved damage tolerance potential of textile preforms. All material, fabrication methods and analytical development will be directed at achieving lower cost and lower weight components compared to metallic structure. Full scale panels, approximately 6 feet in length and with a circumferential arc length sufficient to include five stiffeners will be built and tested to verify the cost and weight savings compared to metal components. The circumferential frames will have a radius equal to that of a large transport aircraft and be at least 8 feet in arc length.

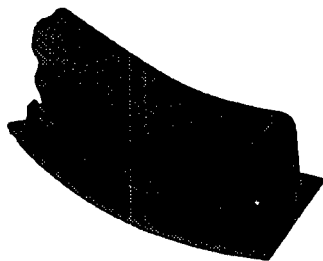
**Benchmark/Crown Lower/Side Panels**



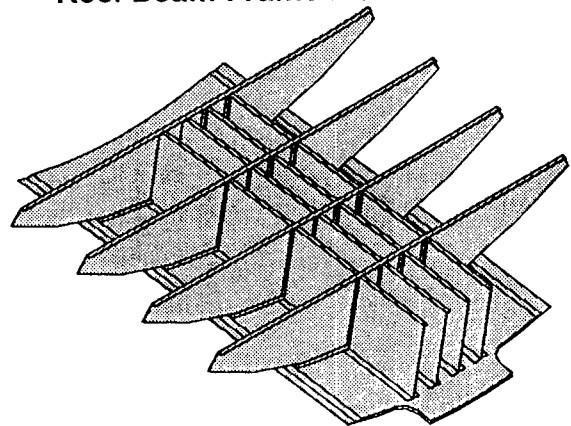
**Window Belt Insert**



**Circumferential Fuselage Frames**



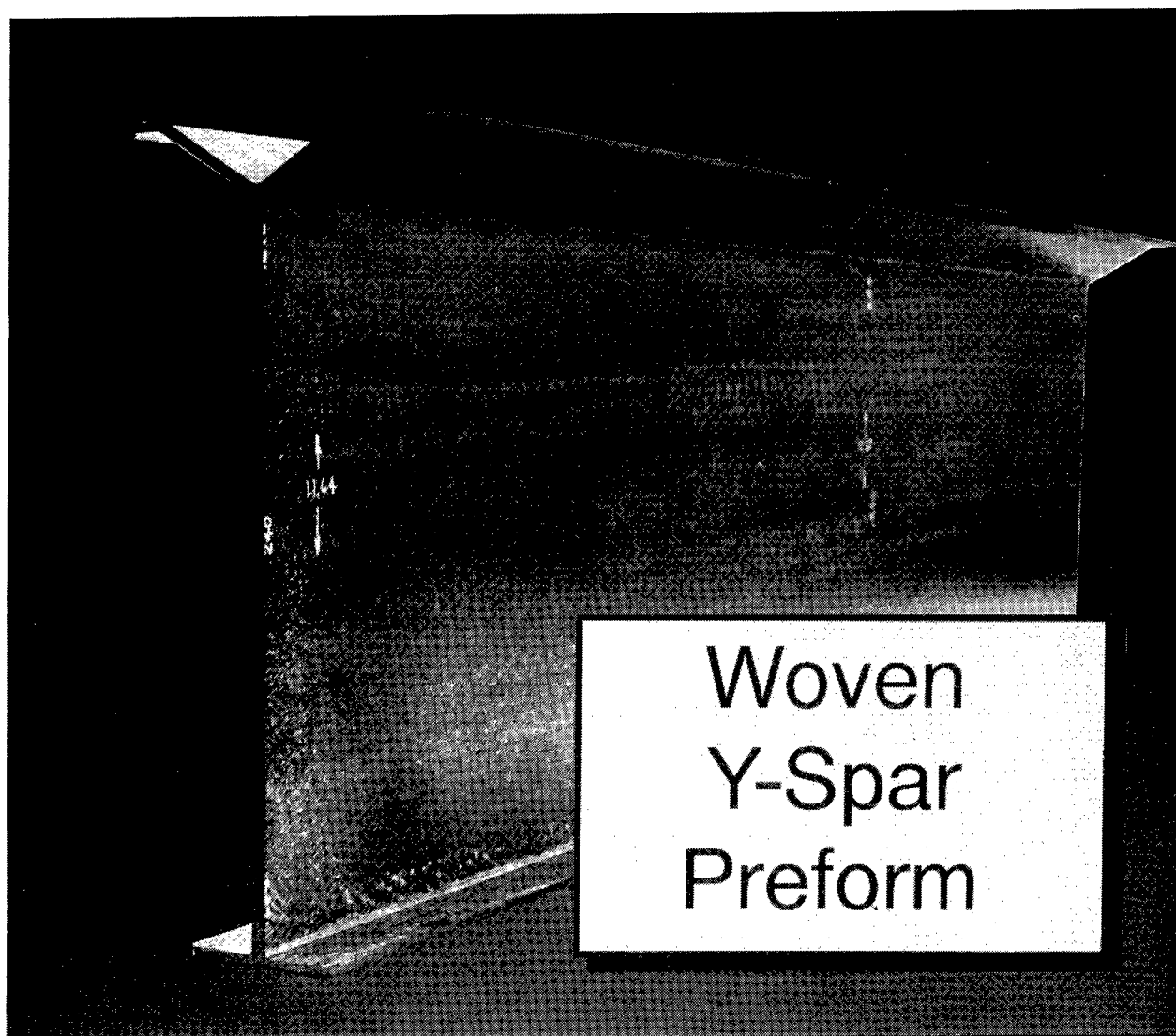
**Keel Beam Frame Intercostals**





## WOVEN Y-SPAR PREFORM

The 40 inch long Y-spar shown in the photograph was fabricated by Textile Technologies on a Jacquard loom using angle-interlock fiber architecture. AS4 is the graphite reinforcing fiber and PEEK 150-g tows formed the matrix for the angle interlock layers. 0/90-degree weave and  $\pm 45$ -degree fabric layers were stitched to the interlock layer with fiberglass threads. The commingled preform was consolidated at 720°F and 160 psi. Percent fiber volume percent, resin volume, and void content were 56.1, 42.8 and 1.1, respectively. The spar was subsequently tested in four point bending and failed when the tensile stress in the upper cap exceeded the open-hole tensile strength. Details can be found in the paper by Suarez and Dastin.



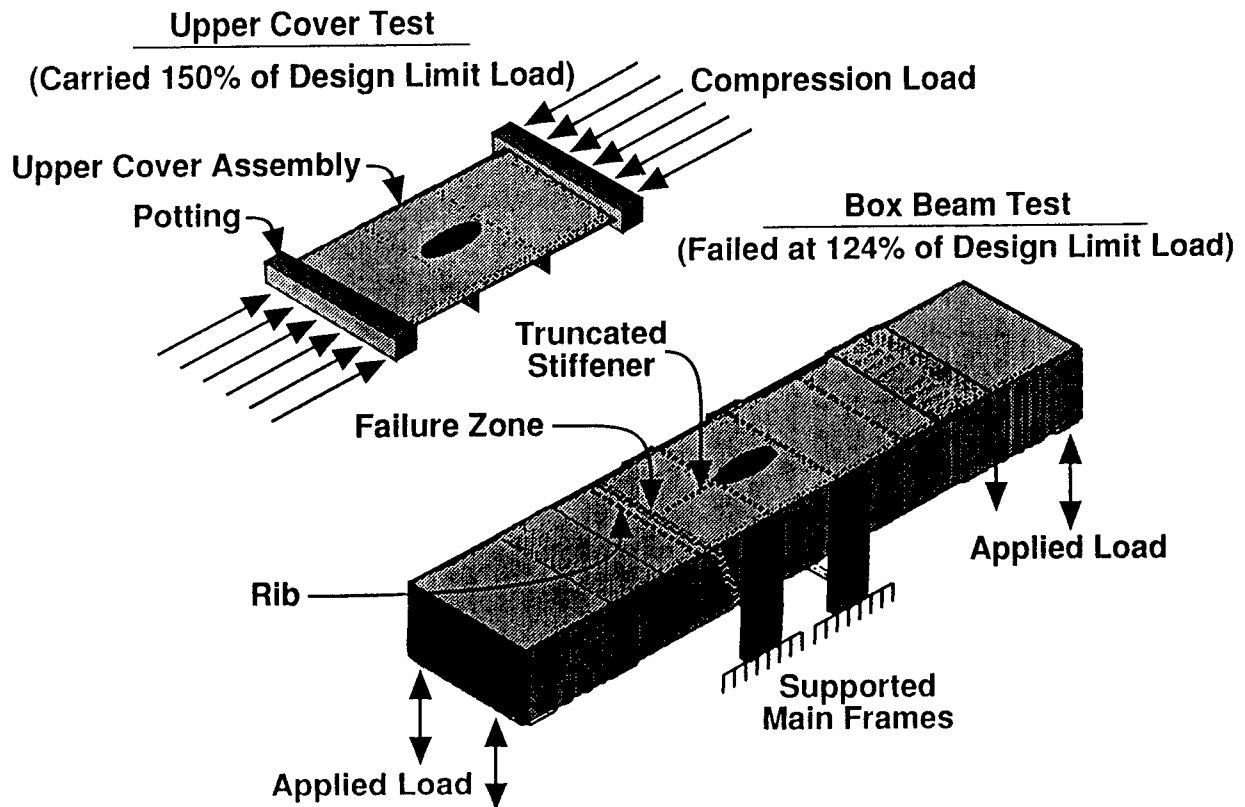
## ACT FOCUSED PROGRAM SUPPORTING TECHNOLOGY

In addition to the specific focused technology development that is underway for the three areas described herein before, there are a number of tasks underway that are applicable to a wider range of technical approaches or concepts. These items include laminate failure analyses by University of Utah, development of the Therm-X tooling process by Sikorsky, use of composite structures to achieve aeroelastic tailoring of wing box structure by University of California at Davis, analyses and tests of Long Discontinuous Fiber(LDF) beams by University of Delaware, testing of an integrated technology wing box structure by Lockheed, development and application of structural mechanics methodology by NASA organizations and development of cost models and cost database for composite structures.

Performing Organization	Deliverables
Utah (N)	Laminate Failure Analyses
Sikorsky	4' x 6' Therm-X Window-Belt Panel
Cal-Davis	Aeroelastic Tailoring Methodology
Delaware	LDF Frame Demo
Lockheed	Box Beam Tests
LeRC Probabilistic Mechanics	Probabilistic Mechanics
LaRC Impact Dynamics Branch	Crash Dynamics Tests
LaRC Applied Materials Branch	Micromechanics Analyses Tools
LaRC Aircraft Structures Branch	Cylinder Response Under Combined Loads
LaRC Computational Structures Branch	Performance Analysis Test Bed Demo
LaRC Structures Technology Program Office	Cost Model Tracking/Demo

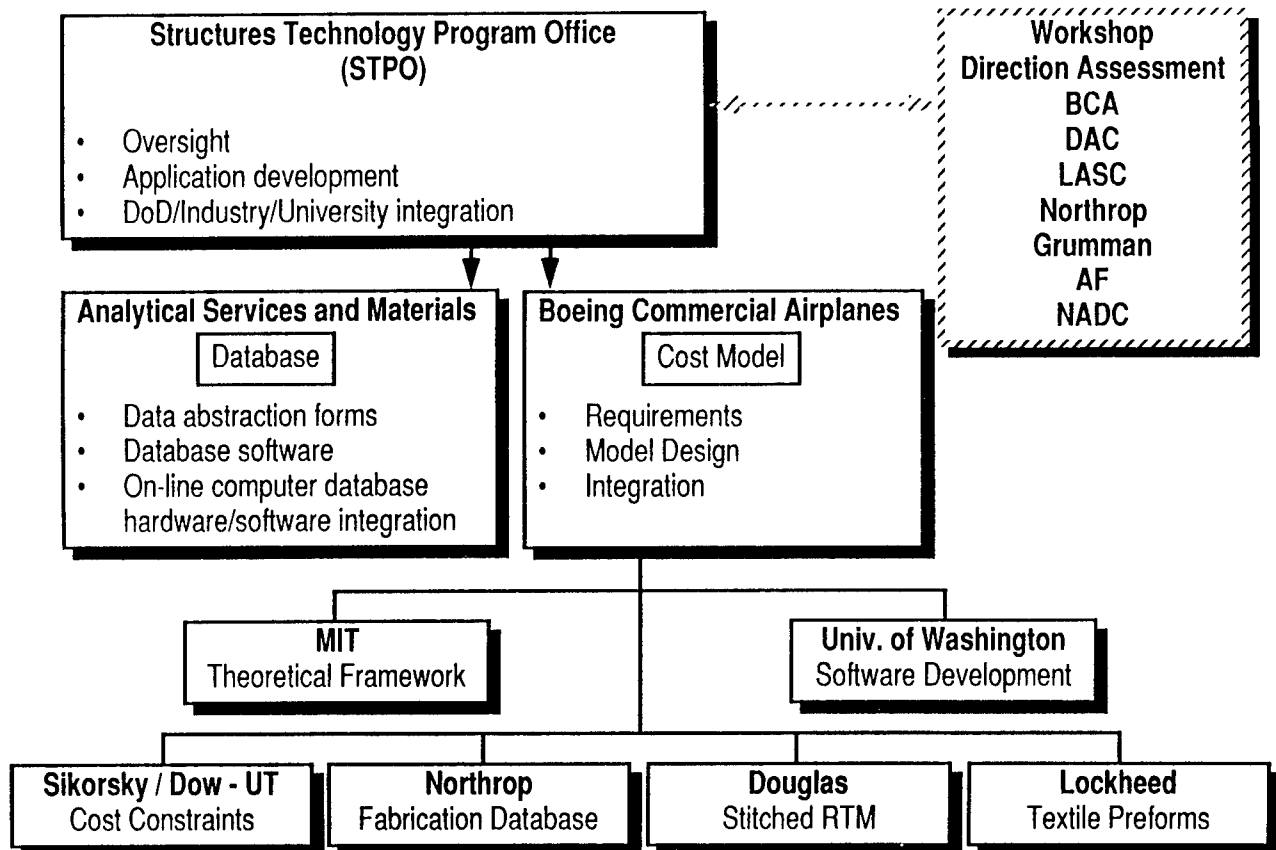
## TECHNOLOGY INTEGRATED BOX BEAM TEST DEMONSTRATES IMPORTANCE OF LOAD INTERACTION

A comprehensive experimental and analytical investigation is under way to quantify the mechanisms that led to the failure of the Technology Integration Box Beam (TIBB) at a load level less than 150% of design ultimate load. Overall dimensions of the composite test section of the box are 150 inches long, 50 inches wide and 28 inches deep. Development tests prior to final fabrication of the box included an upper cover panel which supported design ultimate load. The panel was potted at the ends and this tended to restrain rotation at the ends. Experimental results from the box test indicate significant bending deformation of the hat stiffener and upper cover in the box. Preliminary analyses and study of the experimental results suggest that failure initiated in the upper cover skin due to severe bending in the region of the hat stiffener termination. A stiffener run out specimen is being defined and will be machined from the side of the box that did not fail. The specimen will be used to simulate the TIBB response and failure mechanisms. Further details are provided in the paper by Shuart, et al..



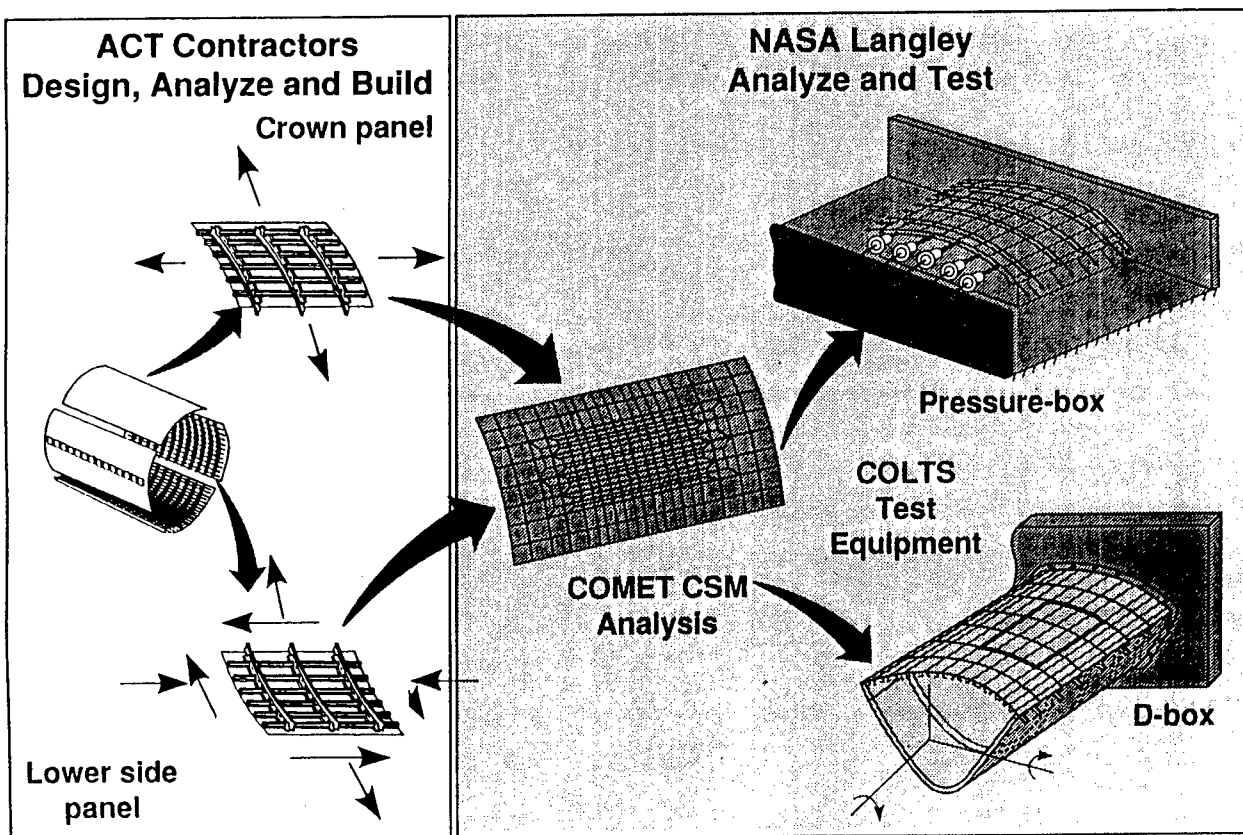
## COST DATABASE AND MODEL DEVELOPMENT

A collaborative effort involving industry, university and government is being used to develop a database and cost model that conceptual and preliminary airframe designers can utilize to predict the relative cost of composite and metallic structures. The database has been designed to include important details that influence cost and can be accessed by personal computer. The cost model will be based on a theoretical framework that estimates cost as a function of the geometric features and the processes required to produce the design concept under study. Relationships developed will allow evaluation of the effect of design variables on the cost for individual components and the fully assembled structure. Additional details are found in the papers by Freeman, Ilcewicz and Swanson and Siddiqi, Vosteen, Edlow, and Kwa.



## TECHNOLOGY BENCHMARK PLAN INTEGRATES INDUSTRY AND NASA ROLES

The technology benchmark components will be used to assess progress in materials, structural mechanics and manufacturing technologies. ACT Program contractors are designing fuselage crown, window belt and lower side panels. A set of common design criteria, loads and overall geometry has been defined. Boeing and Douglas are scheduled to build crown panels. Lockheed and Boeing are collaborating to build a window belt panel that is not depicted in the sketch. Grumman will also build a window belt panel. Boeing, Douglas and Grumman are scheduled to build lower side panels. Each design will utilize different combinations of materials, structural concepts and fabrication methods. NASA researchers will perform in-depth analyses and will test the panels. The first of nine planned Boeing crown panels is scheduled to be tested in the pressure-box in 1992. Subsequent tests will include different types of damage and some panels will be damaged and repaired prior to testing. Cost data on fabrication of the nine panels will be used to verify portions of the cost model under development in the ACT Program. Design of the remaining test fixtures has begun. All panels will be extensively instrumented to aide in determining load interaction between skin, stiffeners and frames and failure modes. Both pretest and post test analyses will be conducted to assess the capability to predict failure modes and response of the panels under simulated flight scenarios.



## SUMMARY

Phase A of the ACT Program is nearly complete. The program has been focused to fully exploit structural concepts and materials combinations that may be fabricated by Advanced Fiber Placement, from Dry Fiber Stitched/RTM and /or Textile Preforms. Results obtained to date indicate that these fabrication methods used singly or jointly offer the best potential for achieving cost-effective primary structures. Experience thus far has indicated that concurrent engineering which integrates design and manufacturing in the beginning of the development cycle is essential to achieving the required cost-effectiveness. A collaborative effort with industry, university and government laboratory personnel has been initiated to develop methodology for predicting costs for fabrication and assembly of composite primary structures. A format for collecting the data has been established. Phase B of the ACT program will scale-up the materials, mechanics, fabrication methods and concepts defined in Phase A. The current plan is to design, fabricate and ground test a semispan wing box for a 200 passenger size aircraft and large fuselage panels for a Boeing 777 size aircraft.

- Phase A Technology Innovation is Nearing Completion
- Three Major Areas of Focus Have Been Selected:
  - Advanced Fiber Placement
  - Dry Fiber Stitched/RTM
  - Textile Preforms
- Cost Effectiveness of Design/Manufacturing Integration Has Been Demonstrated
- Methodology for Predicting Cost and Collecting Cost Data is Under Development
- Phase B Technology Development Has Been Initiated

**THIS PAGE INTENTIONALLY BLANK**

## DESIGNERS' UNIFIED COST MODEL

W. Freeman, NASA Langley Research Center  
L. Ilcewicz and G. Swanson, Boeing Commercial Airplanes  
T. Gutowski, Massachusetts Institute of Technology

### Abstract

The Structures Technology Program Office (STPO) at NASA Langley Research Center has initiated development of a conceptual and preliminary designers' cost prediction model. The model will provide a technically sound method for evaluating the relative cost of different composite structural designs, fabrication processes, and assembly methods that can be compared to equivalent metallic parts or assemblies. The feasibility of developing cost prediction software in a modular form for interfacing with state-of-the-art preliminary design tools and computer aided design programs is being evaluated.

The goal of this task is to establish theoretical cost functions that relate geometric design features to summed material cost and labor content in terms of process mechanics and physics. The output of the designers' present analytical tools will be input for the designers' cost prediction model to provide the designer with a database and deterministic cost methodology that allows one to trade and synthesize designs with both cost and weight as objective functions for optimization. This paper presents the team members, approach, goals, plans, and progress to date for development of COSTADE (Cost Optimization Software for Transport Aircraft Design Evaluation).

### Introduction

The preliminary design process has been identified as the most critical period of opportunity for substantial cost reduction during an airframer's hardware production cycle. Boeing has experienced that 70% of airplane fabrication costs are fixed by the time the drawings are frozen, and the influence of engineering on fabrication cost reductions is significantly reduced once the detailed design is completed. Concurrent engineering interdisciplinary teams are now emphasizing cost evaluation during early stages of the development cycle in the preliminary design process, and the advent of powerful low-cost work stations now provides the designer with the possibility of including cost as a complimentary variable in the design process. A comparative cost algorithm, which can function purely as an engineering design tool to evaluate different design concepts, would be exceptionally valuable to concurrent engineering teams.

Accurate cost prediction is considered a high-priority issue to assure a valid comparison of cost-effective structural concepts, material forms, and assembly methods being developed by the Advanced Composites Technology (ACT) program participants. The Structures Technology Program Office (STPO) has initiated the development of a conceptual and preliminary designers' cost prediction model based on workshop results and objectives that are detailed in Reference 1. Affordable composite technology for pressurized transport fuselages is currently being developed under Boeing's Advanced Technology Composite Aircraft Structure (ATCAS) contract NAS1-18889. The ATCAS contract was modified to initiate development and verification of the designers' cost prediction model. The model software acronym will be **COSTADE** (Cost Optimization Software for Transport Aircraft Design Evaluation). This software will be written to incorporate the cost model, appropriate mechanics constraints, and optimization capabilities. Cost and mechanics modules will be self-contained, allowing the user to run them separately or in combination with the optimizer.



This paper is divided into four main sections describing the proposed development and verification of a designer's cost prediction model. The first section reviews the goals, requirements, and applications for such a model. The next section describes an integrated approach involving industry, university, and government. The third section describes major technology issues and outlines the detailed plans which will be used to solve these issues. Progress to date and conclusions are highlighted in the final section.

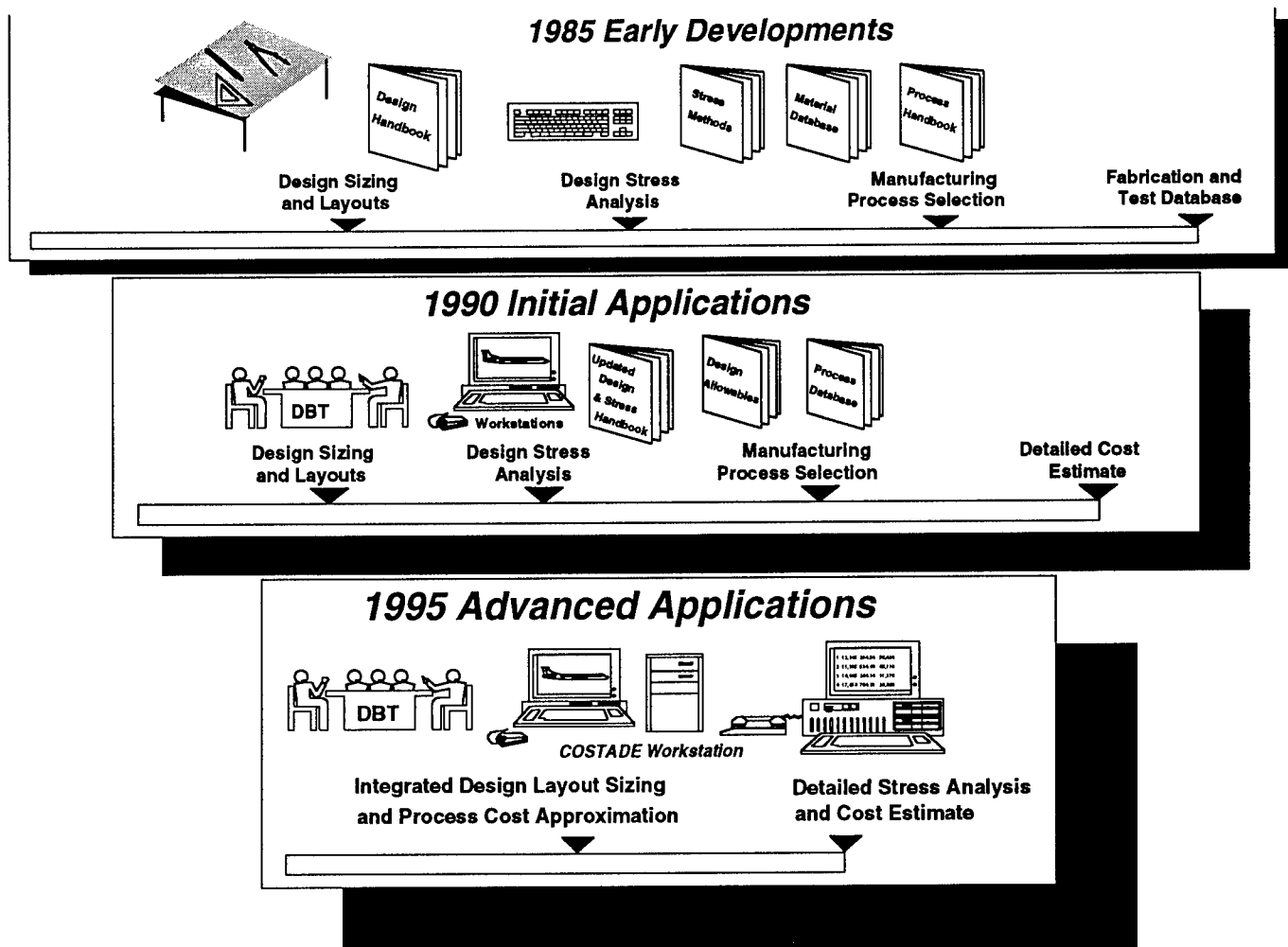
### **Designer-Specific Cost Prediction Model Goals, Requirements, and Applications**

"Designers, accountants, estimators, managers, manufacturing engineers, etc. are interested in different details and economic conditions that imply a numerical value to the term "cost." Unifying the way the composites design community represents hardware and assembly cost for composites and metallics is perhaps as much a communication problem as it is a demanding engineering challenge. This program will determine the feasibility of establishing theoretical cost functions that relate design variables (size, shape, tolerances, geometric complexity, and material properties) to summed material cost and computed labor content in terms of process mechanics and physics. STPO's objective in attempting to develop a designer's cost prediction model is not to replace company accountants or estimators, or to develop more efficient bookkeeping tools that are now used by estimators, but rather to develop a cost model that will provide the designer with a user-friendly tool that relates cost to terms the designer normally uses. A model for designers must be structured to have input that can be coupled directly to a preliminary design module. Such input relates cost to panel thickness, stringer spacing, stiffener height, laminate ply orientation stacking sequence, etc. The cost-related issues a designer can influence usually are related to selections of tolerances, simple-versus-complex shape or geometry, and process-dependent features that contribute to automation potential and tooling complexity. The designers' model should provide definitive assistance in identifying the cost implications of these choices and have sufficient fidelity to distinguish between concepts that have significantly different costs. This fidelity implies the need for adequate detail in the description of the part/assembly labor and material cost at any stage of the fabrication and assembly process. A cost methodology that sums the cost for each element of the fabrication process and allows for parallel as well as serial operations may be required to achieve the needed fidelity. One goal is to provide the designer with the ability to relate the value of a new composite design to an equivalent aluminum structure at similar stages in the fabrication or assembly process.

The ability to fabricate a very large one-piece composite structure to eliminate thousands of fasteners in equivalent aluminum hardware requires assembly-level cost estimating to establish a fair comparison during preliminary design. The exceptional fatigue life and resistance to environmental degradation of composites should be considered since they provide favorable maintenance and supportability comparisons. Large weight savings associated with extensive use of composites in wing and fuselage structure would also result in significant fuel savings over the operational life of each aircraft. Ideally the designer should be aware of the cumulative effects of operational and supportability cost savings, but his influence on lowering the acquisition cost generally dictates the success of a replacement part or new design being committed to a production application.

After the designer has screened a multitude of concepts and fabrication/assembly methods employing the COSTADE model, he would forward the details and drawings of final design trades to the professional cost analyst who has to interpret company policy regarding labor rates, return on investment, capital equipment purchase, etc., for a management accepted cost estimate/comparison.

Figure 1 illustrates how technology for advanced composite transport primary structures has evolved at The Boeing Company in past years. Developments during the 1980's were performed by co-located engineering and manufacturing personnel. Despite co-location, 1985 technology development efforts occurred in series, and the relationships between design, performance, and manufacturing costs were not understood. Early supporting technology efforts included process trials, analysis development, database



**Figure 1: Evolution of Design Tools and Advanced Composite Technology Timelines for Primary Transport Structures**

generation, and the documentation of design and process guidelines. By 1990, a concurrent engineering design/build team (DBT) approach was adopted to allow various engineering and manufacturing disciplines to influence decisions made early in the design process. The 1990 DBT consisted of many individuals with composites experience; however, rigid schedules and the continued lack of comprehensive databases limited cost and weight optimization efforts.

Figure 1 also shows an estimated timeline for 1995 advanced DBT activities that are supported by a computing workstation incorporating COSTADE software. The COSTADE design tool is expected to substantially reduce the DBT time needed to select concepts by integrating sizing exercises and cost approximation. This will enable the DBT to give early consideration to details which have traditionally lead to design changes and increased cost. As in current design practices, more detailed stress analyses and cost estimates will still be used to validate the selected concepts.

The COSTADE design tool is intended to be suitable for several applications. First and foremost, it must give timely support to a DBT by efficiently projecting the effects of preliminary design decisions on manufacturing and assembly costs. Calculations performed during sizing exercises will be matched with an approximation of the effect of structural details on process costs. The model is intended to help the DBT quickly trade cost and weight of numerous design details prior to concept selection. This would enhance the DBT's ability to select design variables (e.g., stiffener spacing, material type, skin gage) that:

(a) are cost effective for available manufacturing processes; and (b) meet performance requirements for the particular application. As with any model, the accuracy of COSTADE predictions is dependent on data input by the DBT; therefore, the cost and weight savings potential will increase as composite databases grow.

Additional applications for the designer's cost model would include trade studies to guide research and development (R&D) programs in manufacturing, structures, and materials. Relationships between structural design guidelines, criteria, and manufacturing cost can be used to judge which areas should be studied in greater detail to avoid the unnecessary costs associated with overly restrictive design rules. Trade studies with the model may also be used to estimate when added material cost is acceptable for enhanced performance.

### **Approach**

In early 1991, the Boeing ATCAS contract was modified for development and verification of a design technology tool for assessing the cost and weight of transport aircraft structures. Deliverables described in the modified work statement include: (1) theoretical formulations of structural design relationships to manufacturing cost; (2) design analysis methods to estimate structural performance and constrain design decisions affecting manufacturing tolerances; (3) software for predicting design performance, cost, and weight; (4) optimization algorithms to efficiently perform trade studies; and (5) documentation on design tool usage, including results from applications to composite aircraft structures.

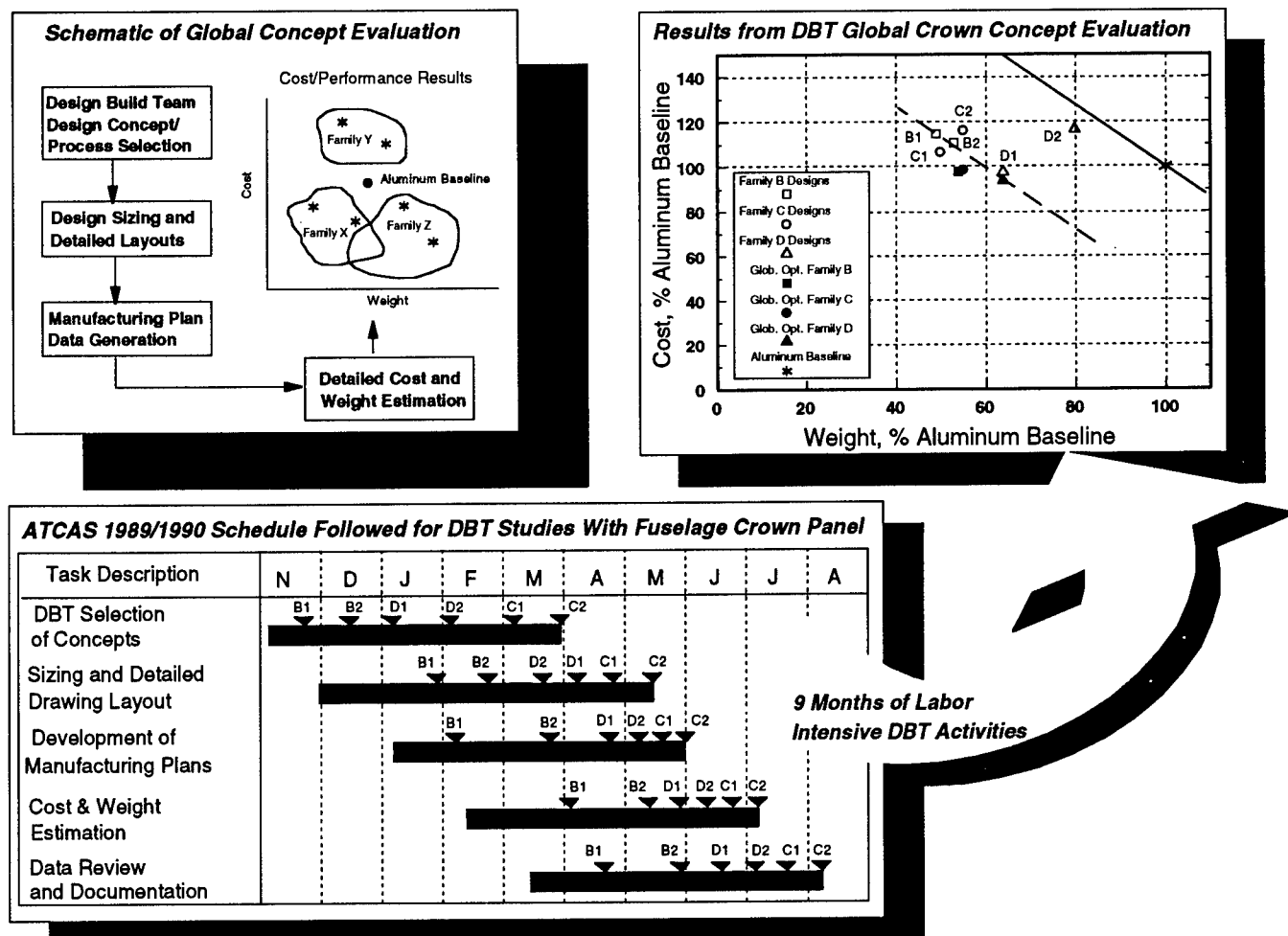
Several requirements for the design cost model have been established. The proposed four-year effort will be closely tied to existing NASA ACT contracts with progress reviewed annually at cost workshops. Recommendations from other ACT contractors will be solicited to help guide model development and integrate technologies (e.g., design sizing methods, databases, and manufacturing cost relationships) developed and validated during the course of the NASA ACT program. Formulation of the theoretical cost model will be general enough to simulate the design/cost relationships of new manufacturing technologies as they evolve. Finally, all data considered sensitive by industry will be treated as user inputs to the model, allowing the user to retain proprietary rights.

The ATCAS DBT approach for global/local design optimization was described in detail in References 2 and 3. To date, this approach has been successfully used to select (Refs. 2 and 4) and optimize (Ref. 5) fuselage crown panel concepts that are projected to have both cost and weight savings relative to 1995 metals technology.

The upper left portion of Figure 2 shows the global concept evaluation steps used for selecting a design family. Design families arose out of the DBT's desire to efficiently perform cost and weight trade studies. Each design family consisted of concepts having unique features from a manufacturing perspective. For example, in the ATCAS global evaluation exercise (Ref. 2), Family A differed from Family B in that stiffeners were mechanically attached for A and bonded for B. During global evaluation, concepts representing a limited number of families are analyzed and the results are used by the DBT to select a family having the best potential for cost and weight savings.

The ATCAS program is considering large integrated composite panels for potential cost savings in fuselage applications. Large integrated panels will reduce assembly labor and joint complexity which has traditionally been identified as a cost center for aluminum structure. Large panels will facilitate composite automation and greatly reduce the number of fasteners required compared to metallic assemblies (Refs. 6-9).

In order to project the cost and weight of large curved composite panels, a labor intensive screening process was adopted for global evaluation. The bottom of Figure 2 shows the schedule which was used for crown global evaluation, resulting in more than 12,000 manhours of effort. Two concepts for each of three families were evaluated (Refs. 2 and 4). The six concepts had different materials, processes, and design details, allowing trades to be performed down to the element level. An exhaustive study was deemed necessary due to the lack of experience in designing and manufacturing composite transport fuselage structure. Detailed drawings were used to develop a manufacturing plan of the process steps needed to fabricate and install a 15-ft. by 31-ft. crown panel for a fuselage with a 20-ft. diameter. A factory of the future, capable of producing five shipsets a month, had to be envisioned. Finally, detailed cost estimates were used to project manufacturing costs.



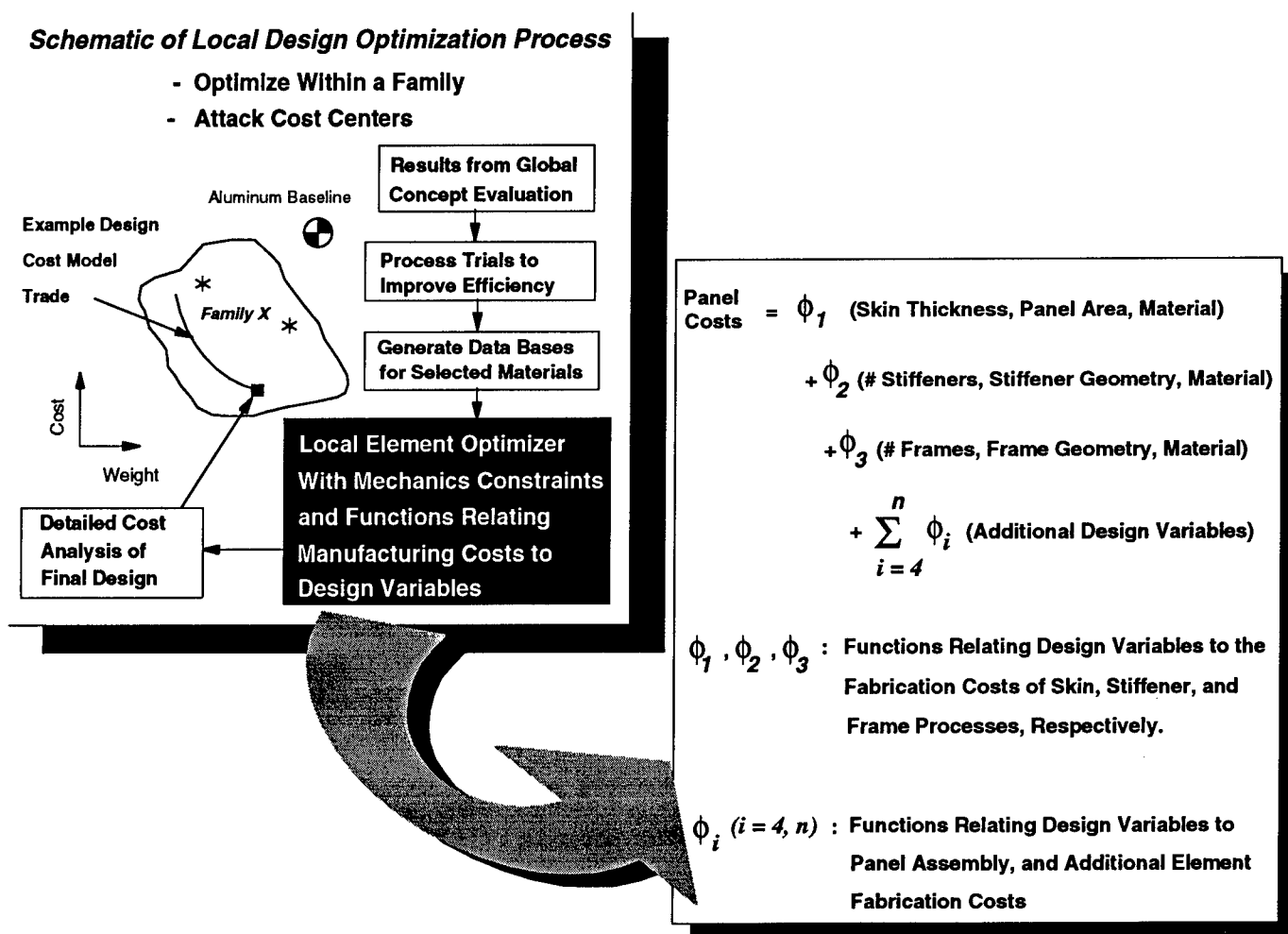
**Figure 2: Results from Global Evaluation of ATCAS Fuselage Crown Concepts**

The upper right portion of Figure 2 shows results from global crown evaluation. A sloped line is drawn through the aluminum baseline to represent an acceptable added cost per unit weight savings. Since all composite concepts fall below this line, each would be considered to have advantages in crown applications. After considering the design, material, and process trades performed at the element level, globally optimized concepts were selected for each family (marked by filled symbols in Figure 2). Family C was selected for local design optimization, fabrication, and test as described in References 2 and 4.

The DBT activities supporting ATCAS global evaluation will be used to help develop the design cost model. As discussed earlier, the model is required to be general enough to account for emerging

technologies. By projecting the layout and costs of future factories capable of producing advanced composite fuselage structures, ATCAS studies will provide insight on the theoretical formulation needed for a general designers' cost model. With this foundation, methods will exist for converting fabrication data into suitable input data for the design cost model as new technologies emerge in the factory. A large database relating design, material, and manufacturing variables to the cost of fully assembled structure was initiated for the crown. Cost centers for fuselage crown panels were identified in this effort. Future ATCAS global evaluation studies for keel and side panels will provide results for additional fuselage design details (e.g., large cutouts) that affect manufacturing costs.

Local optimization in ATCAS is used to focus design efforts. After using global evaluation to select a design family, the cost and weight relationships within that family are analyzed in greater detail during ATCAS local optimization. As shown in Figure 3, local optimization includes several activities, one of which is directly associated with the application of a design cost model. Initial ATCAS efforts with crown panels used a computer program called UWCODA which was developed in cooperation with an ATCAS subcontract to the University of Washington (Ref. 10).



**Figure 3: Role of Design Cost Model During Local Optimization of ATCAS Fuselage Concepts**

Functions relating manufacturing costs to design variables for crown structures were developed and added to UWCODA in order to perform cost and weight optimization (Ref. 5). As shown schematically in Figure 3, the functional form of these equations treats design parameters as independent variables. Constants in the equations characterize the manufacturing cost relationship for a specific set of processes.

Separate functional relationships quantify fabrication and assembly components of the cost; however, it is important to obtain the sum to judge how complex interactions (i.e., design variables that affect several components of cost) affect total costs (Ref. 6).

Results from applying UWCODA to crown local optimization are documented in Reference 5. Some of these results will also be discussed later in this paper. The crown design cost relationships and UWCODA serve as a starting point for COSTADE. Generalizations are needed to develop the design cost model suitable for analyzing other fuselage structures and manufacturing processes.

The ATCAS global/local DBT approach is currently being applied in a research and development mode. From a hardware program perspective, the global evaluation step could be used during product development to help make major economic decisions (e.g., composite versus metal, equipment purchase, factory and manpower needs). Local optimization would be applied during detail design to ensure that an existing factory is utilized efficiently. A design cost model would directly support local optimization; however, parametric studies could be performed with such a tool to globally evaluate different factories.

The designer's cost prediction model development and verification tasks will interface with the ATCAS global/local DBT in two ways. First, global evaluation of future factories will support design cost model development by helping to generalize the theory for emerging technologies. Second, the model will be verified during ATCAS local optimization.

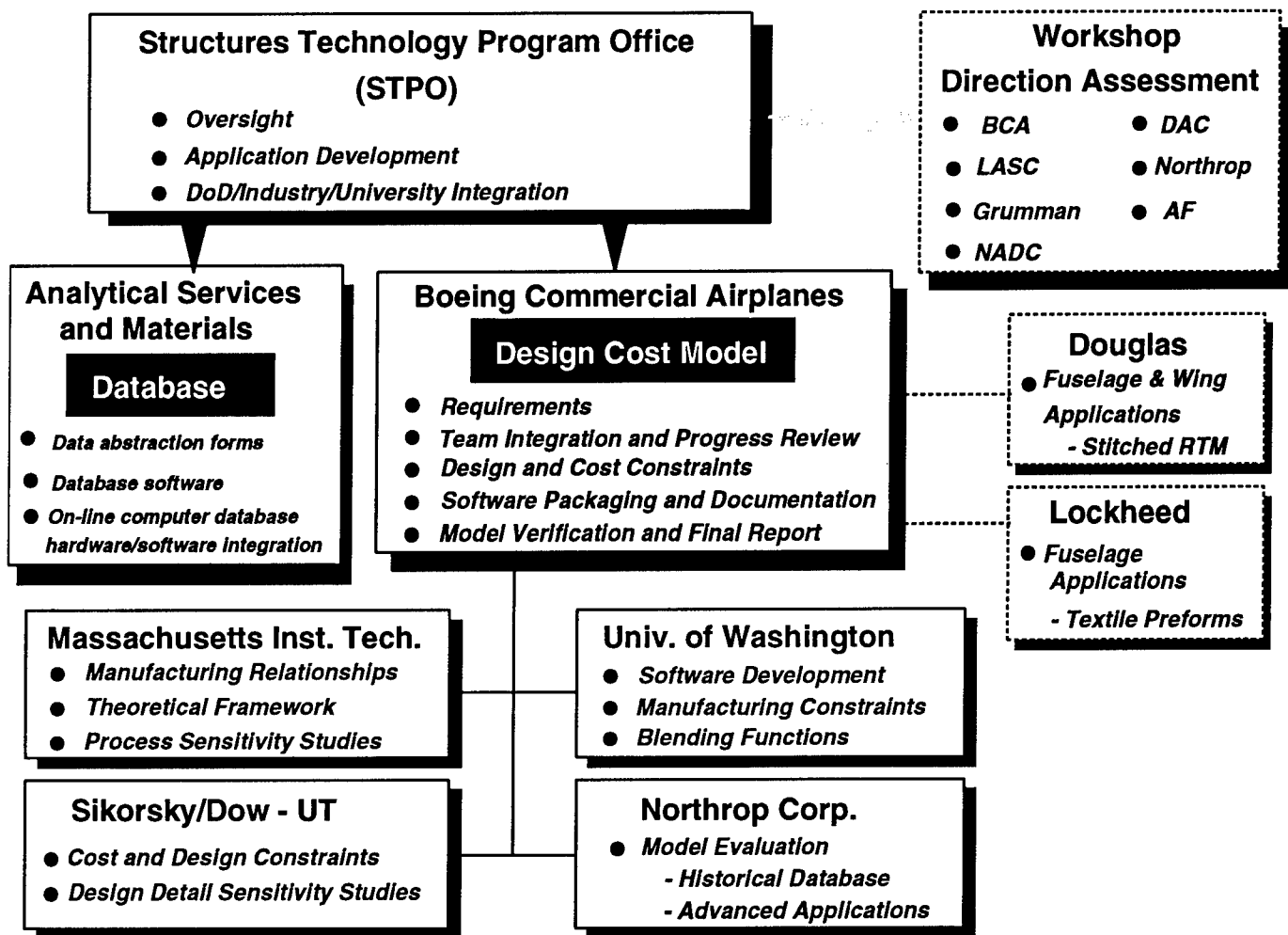
A collaborative effort involving industry, university, and government will be used to develop and demonstrate the capabilities of COSTADE. Subcontracts are currently planned to include Massachusetts Institute of Technology (MIT), University of Washington, Sikorsky Aircraft, Dow-United Technologies Composite Products Inc., and Northrop Corporation. Figure 4 shows these team members and some of their responsibilities.

### Issues and Plans

Several technical issues will be addressed during the course of designers' cost prediction model development and verification. Table 1 lists seven objectives for solving the major technical issues.

- 
- |     |   |
|-----|---|
| 1.) | <i>Develop an Understanding of Design Details Critical to Manufacturing Costs</i>   |
| 2.) | <i>Develop a Theoretical Framework, General Enough to Model Design/Cost Relationships for Both Current &amp; Evolving Processes</i>       |
| 3.) | <i>Incorporate Design Constraints in the Model to Help Ensure that Concepts Analyzed for Cost Are Also Structurally Sound</i>             |
| 4.) | <i>Develop Methods to Analyze the Effects of Design Details On Manufacturing Tolerances and Add Appropriate Model Constraints</i>         |
| 5.) | <i>Develop &amp; Adapt a "Blending Function" Which Enables the Model to Cost-Effectively Blend Design Details Over Variations in Load</i> |
| 6.) | <i>Combine Design Cost Model Technology as Software (COSTADE) Suitable for Performing Design Trade Studies in a Timely Manner</i>         |
| 7.) | <i>Verify the Design Cost Model and COSTADE With ACT Fabrication Data, Detailed Estimates for Future Factories, and Past Databases</i>    |
- 

**Table 1: Technical Issues to Solve, Expressed as Objectives for Design Cost Model Development and Verification**

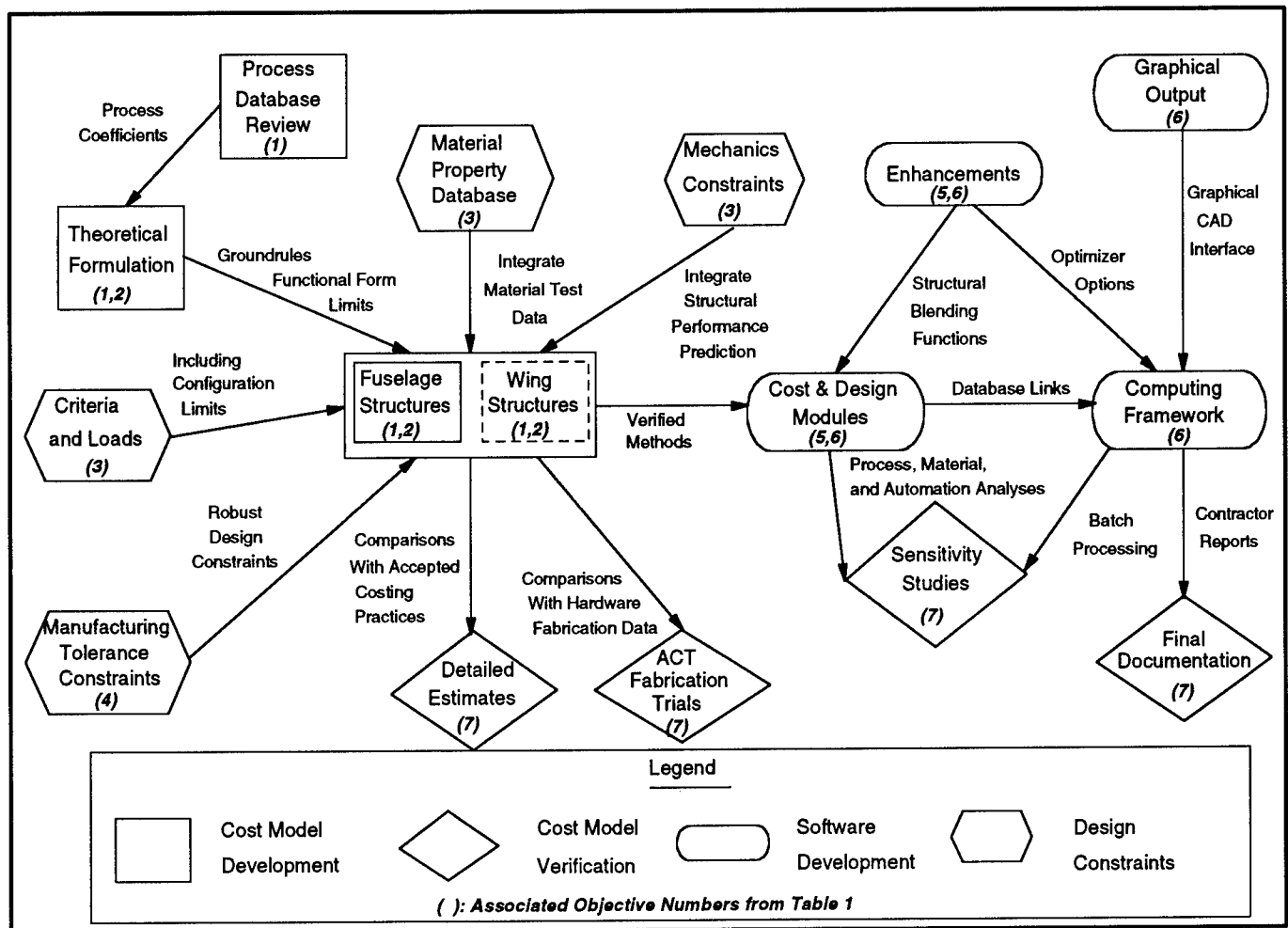


**Figure 4: ACT Team Interactions for Database and Design Cost Modeling Tasks**

The plan developed to achieve objectives listed in Table 1 involves four main areas of work. These include cost model development, design constraints, software development, and cost model verification. Tasks associated with each area of work are shown in Figure 5. This figure also shows the interactions between individual tasks and a critical path to achieving goals. The objective numbers from Table 1 that relate to specific tasks in Figure 5 appear in the associated flow chart symbols.

Figure 5 shows that the theoretical formulation will make use of existing database and process experience. Data considered to be of a proprietary nature may be used for model development, but won't be included in documentation that demonstrates the model. Despite the link with past data, the design cost model must have a theoretical framework based on scientific principles. Such a formulation will be derived based on process modeling and industrial engineering, as opposed to purely empirical relationships with data from existing factories. An empirical approach would not meet the requirement for a general model that can be used for emerging technologies. Since the primary focus of the ACT program is composite primary structures for transport aircraft, reliable data for an empirical approach is also not likely to be available for several years.

Model verification will include comparison of the model predictions with detailed cost estimates and fabrication trials from the ACT program. The "ACT Costing Groundrules" (Refs. 1 and 2) will be adopted as default values to portray how the model is utilized. The remaining tasks will incorporate design criteria, material databases, manufacturing tolerances, and mechanics constraints. These tasks



**Figure 5: Critical Path Flow Diagram for the Design Cost Model**

include integrating ACT technologies including automated tow placement, textile preforms, resin transfer molding, etc. An additional major task will involve development of the computer program, COSTADE.

Theoretical characteristics of the model will be determined in coordination with team members during the first year of work. The model will be capable of relating design features (e.g., material type, skin gage, stiffener spacing, etc.) and processing parameters (e.g., material cost, ply lay-up speeds, tooling costs, etc.). Initial efforts will concentrate on design details for fuselage structures. The model will also be generalized for wing structures with the help of other ACT contractors. A number of composite fabrication methods and material forms which are suitable for the various hardware elements will be studied. These will include automated tow placement, resin transfer molding, textiles, and conventional hand lay-up.

Inputs to the cost model will need to be predetermined in a manner analogous to material moduli for a solid mechanics analysis. For example, cost data may be used to determine the coefficient relating stiffener fabrication cost to stiffener geometry; whereas, a mechanics model requires coupon tests to determine a material property that relates tensile stress to strain. In each case, a combination of simple relationships (i.e., process/design cost equations or material constitutive laws) is used to determine more complex behaviors (i.e., total structural cost or stiffness, respectively).



One prerequisite for a cost-effective design is that it is also a structurally sound design. Most cost models which compare different processing methods for a structural element have made the assumption that design performance and the manufacturing process are uncoupled. This is clearly not the case in the real world where structural properties can vary depending on process and material form (e.g., filament winding with oven cure and hand lay-up with autoclave cure will not generally produce panels having equivalent performance characteristics). In order to perform efficient cost and weight trades for numerous designs, the designer must have tools that enable him to quickly evaluate both performance and cost. As shown in Figure 5, design criteria, loads, and mechanics constraints will be linked to the design cost model to facilitate trade studies. Process-related properties will be included in supporting material databases.

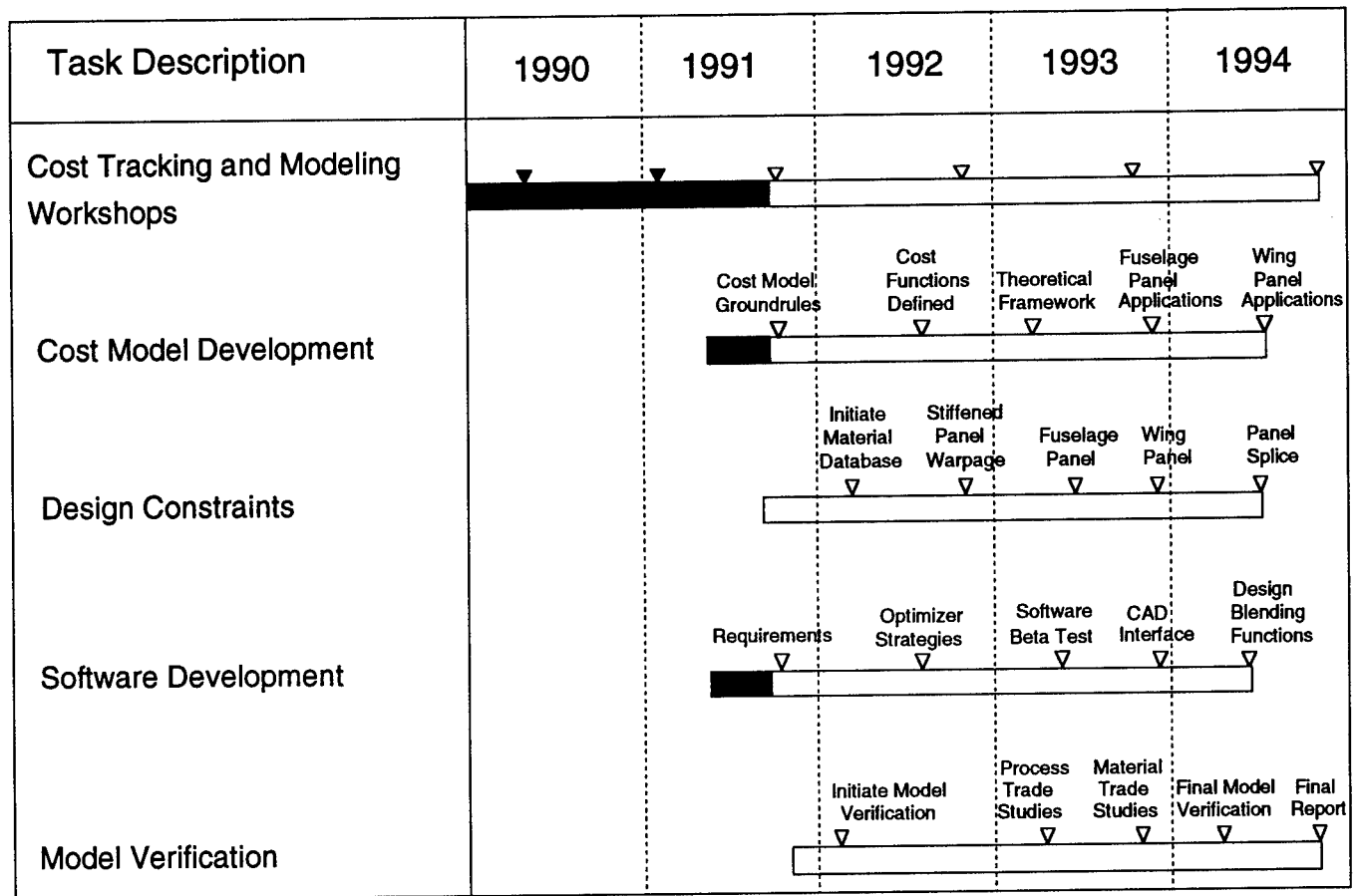
Another interface between product cost and performance comes in the form of design decisions which affect manufacturability. For example, it is crucial to limit a designer from tailoring part geometry and skin gage such that they have a severe effect on factory automation and efficiency. In addition, designs which are not robust (e.g., those tending to warp or are sensitive to manufacturing tolerances) may lead to additional costs during assembly. Methodologies will be developed that help constrain design selection and avoid designs prone to assembly problems.

As shown in the software development symbols of Figure 5, COSTADE software will be written to incorporate the cost model, appropriate design constraints, and optimization capabilities. Advanced optimization modules, capable of blending design details over variations of load, will be developed and added to COSTADE. Cost and mechanics modules will be self-contained, allowing the user to run them separately or in combination with the optimizer. The COSTADE design modules will also evaluate whether a design is robust for assembly by analyzing the combined effects of manufacturing tolerance variations for individual details. Sensitivity studies will be used to check software and to identify critical variables affecting cost. The computer code entitled UWCODA (Refs. 5 and 10), which was developed as a design optimization tool for Boeing's ATCAS program, will be used as the initial basis for COSTADE.

The diamond-shaped boxes in Figure 5 show four tasks supporting cost model verification. The cost data collected for ACT fabrication trials will provide some verification, although none of the hardware currently planned will allow a direct comparison for full-scale structures fabricated with the production rates of a dedicated factory. Detailed estimating, which is an approach currently used to forecast the costs of future composite structures, will help to evaluate the model for future factories. The final two verification tasks, sensitivity studies and documentation, will be used to screen for critical factors and report results.

Figure 6 shows a schedule of major milestones for the design cost model. Discussions with individual groups to support this effort are currently underway. As shown at the top of Figure 6, workshops are planned during each year of cost model development and verification.

*Cost model development:* Work in this area will concentrate on the formulation of analyses to relate design variables and manufacturing costs for transport aircraft composite structures. Groundrules for this effort will be determined by team member meetings and through a consensus reached at a future NASA ACT cost workshop. The theoretical basis for relating design variables and manufacturing costs will be established by the end of 1992. This will include documentation of a functional form for the theory that, in general, will allow nonlinear interactions between design parameters and cost components. During the following year, specific design/cost equations will be formulated. Documentation will be required to give variable and coefficient distinctions to each parameter in the equations. A theoretical framework is scheduled to be completed by early 1993. The capabilities and limits of the theory will also be documented at that time.



**Figure 6: Schedule of Major Milestones for the Design Cost Model**

The design model will allow for manufacturing cost components such as material, fabrication labor, assembly labor, and tooling. As shown in Figure 4, MIT will take the primary role in understanding the manufacturing relationships and in developing the design/cost theoretical framework. Relationships developed will allow evaluation of the effect of design variables on fabrication cost for both an individual component and the fully assembled structure. Close collaboration between MIT and industry team members will be needed during model development since a perception of assembly and tooling relationships is not readily available outside industry.

Fuselage structures will be the primary focus for design/cost model development and verification in ATCAS. As discussed earlier, much of the fuselage cost constraint data needed for such a model will become available during the course of global evaluation studies involving ATCAS quadrants (i.e., crown, keel, and side). This data includes the identification of cost centers and critical design variables. The schedule for applications of the design/cost model to each fuselage quadrant will trace ATCAS local optimization activities.

The ATCAS fuselage study section is directly aft of the wing to body intersection (Refs. 2 and 3). Loads in this area include internal pressure and additional axial tension, compression, and shear-for-flight maneuvers that induce body bending. Development of methods for analyzing design/cost relationships for crown, keel, and side quadrants of the ATCAS study section will result in capabilities for most of the

fuselage shell. Much of the crown quadrant consists of the minimum gage panels also representative of upper and lower regions of barrel sections located away from the wing-to-body intersection. The keel quadrant is characteristic of heavily loaded compression panels found at the bottom of the fuselage, in sections directly forward and aft of the wing-to-body intersection. Side panels include design details for door and window cutouts found along the full pressurized length of the fuselage.

The design cost model will be generalized to include wing structures with the help of other ACT programs. Activities in this area will be initiated at the design/cost model workshop scheduled for the end of 1992. Model developments for wing panel applications will be completed by mid-1994.

*Design Constraints:* Work in this area will integrate the tools that a designer needs to efficiently consider multiple design concepts during COSTADE analysis. As shown in Figure 6, the information needed in a material database for transport fuselage and wing applications will be identified first. One objective of the ACT program is to establish a database of properties for advanced material forms processed with low-cost manufacturing methods. Results from such activities will be used with design and cost constraints to evaluate cost/performance relationships. The process/material property database used during model verification will be reviewed periodically at workshops.

The loads, design criteria, and limits on structural configuration will be established as guidelines for development and verification of the COSTADE tool. Sensitivity studies will be performed with the cost model in order to judge how criteria (e.g., damage tolerance, defect allowances) affect the cost of composite structures. Results from such studies will be reviewed at workshops.

Design and mechanics constraints will be added to the design cost model to analyze transport fuselage and wing structures. Most of this sub-task will concentrate on integrating design sizing methods that exist or were developed in other ACT activities. Typical mechanics constraints include stiffness requirements, panel stability, crippling, damage tolerance, bolted joints, cutouts, combined load criteria, and load redistribution guidelines. All constraints used for this effort will be suitable for screening multiple designs. Constraints for fuselage zones characteristic of ATCAS crown panels will be established during the first year. Methods for other fuselage and wing locations will be added, resulting in more complete capabilities by the end of 1993. The final mechanics constraints generated will relate to panel splice details.

Manufacturing tolerance constraints will be developed to address the effects of design decisions on costs associated with manufacturing tolerances. The constraints will be added to COSTADE to help the designer in developing robust design concepts that avoid assembly problems. An analysis method will be developed to evaluate the effects of element design details (e.g., geometry and lay-up) on co-cured/co-bonded panel warpage. The effects of cured panel manufacturing sensitivities such as resin content tolerances, resin content distribution, and ply misalignment tolerances will be considered in this effort.

*Software Development:* The computer program COSTADE will incorporate design and cost constraints that enable a DBT to efficiently perform cost and weight trade studies. Most of the work on this task will be performed at the University of Washington and Boeing. Software and hardware requirements will be established first. Software decisions on language, framework, and computational architecture will be subject to approval by NASA and participants at future cost workshops. Hardware compatibility requirements will be set after identifying which computing tools are projected to be used by designers in future years.

A modular programming style will be used for COSTADE. The software will be written to allow links with databases for input parameters related to process cost, material properties, and mechanical performance. A number of input/output options will be added including: (1) switches to run cost and

mechanics modules with or without optimization features; (2) user-written subroutines for performing sensitivity studies; and (3) macros for batch job processing and output data reduction. A software manual will be created that includes case studies.

Initial software for cost and design modules is planned for completion after associated *cost model development* and *design constraint* activities. The proposed timeline to develop the cost model and to integrate design constraints was set based on availability of input from current ATCAS schedules. Cost and design software modules developed for each area of the aircraft will have features that allow improvements to be made as technology matures (e.g., innovative design concepts).

A number of optimization capabilities will be developed for COSTADE and made optional to the user. These enhancements will help to trade a larger range of design details and consider possible interactions. Although current structural guidelines limit the number of composite variables considered by designers, a properly constrained optimization scheme is still an advantage. As composite technologies mature and databases expand, additional cost and weight savings will be possible by removing unwarranted constraints. Some cost and weight optimization capabilities have already been established for the original code, UWCODA (Refs. 5 and 10). The ability to perform cost/weight optimization will be added. This feature will require an input from the user to determine the cost he is willing to pay per unit weight savings.

Other optimization capabilities which will be developed for COSTADE include "panel and splice blending functions." Currently, designers apply point analyses to size each portion of the structure and then make changes in design details to meet requirements for compatibility at adjacent points. This activity, referred to as blending, results in continuity for an entire configured panel. The key to a blending function algorithm is to model how design details selected at one point of the structure affect the requirements at neighboring points. The desired result is a tool that performs cost/weight optimization for a complete fuselage or wing panel.

The cost of a configured structure depends on the success of a blending scheme, manual or otherwise. Considering the large panel sizes that are projected to be cost effective for composites and the complex nature of anisotropic materials, the task of blending a composite structure can be laborious when performed manually. In the past, the time needed to blend a composite design has often limited trade studies and resulted in increased cost because schedule-driven design selections result in costly details. For example, local laminate lay-up and thickness tailoring may be adapted to meet performance or weight requirements, at the penalty of an adverse effect on manufacturing automation.

Panel blending functions will be developed as enhancements for optimization performed with COSTADE. These functions will enable a designer using COSTADE to minimize total costs while considering a design space with variable load distribution and design criteria. Without the blending module, COSTADE will still be able to analyze the relationship between local design details and total structural costs. The addition of a blending function will enhance this capability by guiding the selection of local design details to minimize total structural costs.

The effects of splice design details will initially be programmed in COSTADE as design constraints. The "splice blending function" will be added as an option to combine panel and splice optimization schemes. This is scheduled to be added after work is completed on adding splice modules to the cost and mechanics models.

A visual presentation of ideas and results from design trade studies can often help members of a DBT make decisions. This is true provided the graphics can be produced in a timely manner. An effi-

cient method of creating graphics from COSTADE results will be considered in the form of a computer-aided design (CAD) graphics interface. The first step in this effort is to define the industry CAD which will be most suitable. Most the work on a CAD interface will occur after other software developments have been completed.

**Model Verification:** The overview schedule shown in Figure 6 indicates that cost model verification milestones are dispersed throughout the four-year plan, yielding direct measures of the success of cost model developments as they evolve. Since verification occurs continuously, each step of cost model development will benefit from previous findings. Industry team members (Boeing, Northrop, and Sikorsky/Dow UTC) will take a lead role in model verification. As was the case with many work tasks on *Design Constraints*, results from current ACT contracts will also be used to support some of the model verification tasks. Contractor proprietary data will not be included in the deliverables documenting model verification and demonstration; however, such data will be useful when individual companies evaluate the model.

Sensitivity studies will be used to demonstrate the cost model capabilities. Such studies are crucial to checking sensitivities to input data used for simulating process relationships (Ref. 7). This is particularly critical to interpreting the results for new processes which lack sufficient databases. Additional process and material trade studies will be performed to evaluate cost relationships for different transport fuselage and wing design details. Sensitivity studies will be used to identify the most critical variables to consider during optimization.

The model can be used to estimate the influence of process automation and large material volumes on the cost of composite structures. The capital cost of advanced process and assembly equipment will be traded against costs saved through automation. Finally, the model will be used to compare the projected costs for manufacturing composite structures against those of aluminum for the same time frame. A detailed cost-estimating approach used in the ATCAS program for projecting the costs of transport fuselage structures will be compared to the cost model predictions. This will provide direct comparisons with an industry-accepted approach to cost estimating.

Another form of cost model verification will be possible with proper interpretation of results from ACT fabrication trials. Several contractors have plans to produce composite fuselage and wing subcomponents during the course of the ACT program. Although these subcomponents will not be produced with the automation of a full-scale production hardware program, the cost model should still be general enough to scale for smaller sized panels and reduced production rates.

### **Progress to Date**

Preliminary ATCAS work on a design cost model started during a one-year subcontract with the University of Washington in 1990. Design optimization software (UWCODA) was initially developed with mechanics constraints for minimizing the structural weight of fuselage crown panels (Ref. 10). Following crown global evaluation, it became desirable to enhance UWCODA to include design/cost constraints and an objective function for minimizing cost. Previous sections of this paper described the proposed plans to further generalize the design cost model and its software package. This work will eventually lead to an enhanced version of UWCODA which has been referred to as COSTADE.

Reference 5, which is included in the proceedings for this conference, documents the use of an enhanced version of UWCODA to optimize the fuselage crown panel design. Significant cost and weight savings were projected for design details selected with the help of the design cost model. The cost con-

straint equations for this effort were developed using manufacturing plans and detailed cost-estimating results for a specified factory. Hardware programs are expected to make use of a design cost model in a manner similar to that demonstrated in Reference 5 (i.e., optimize design details for selected manufacturing processes).

Design cost equations developed in Reference 5 treat design details as variables. Constants input to the model are used to characterize manufacturing processes. These variable and coefficient distinctions are consistent with a primary desire to use the model to predict the effects of design details on manufacturing cost. The cost model formulation will also allow analysis of the inverse problem (i.e., effects of process variations on the cost of a given design detail). This can be achieved in parametric studies by trading values of the associated constants for different manufacturing processes.

The geometric design variable found to have the strongest effect on fuselage crown panel cost and weight in Reference 5 was found to be stiffener spacing. The reduced manufacturing cost associated with wider stiffener spacing was traded against the increased weight of a thicker skin gage needed to satisfy loads and design criteria. Initial cost modeling results by Sikorsky Aircraft indicated similar trends for curved stiffened composite panels (Ref. 11).

A detailed evaluation of ATCAS crown panel design/cost relationships indicated that the number of stiffeners affects the cost of numerous fabrication and assembly processing steps. The relatively complex geometry of stiffeners makes them more costly to fabricate than skin; however, this effect was found to be relatively small in comparison to the total costs affected by the number of stiffeners. Stiffener design details increase panel bonding costs due to increased labor during panel sub-assembly, bagging, and inspection. The number of stiffeners also affects the costs associated with the intersections at frame elements (e.g., mouse-hole design details). Fabrication and assembly tooling costs increase with the number of stiffeners. Finally, the cost of circumferential panel joints increases with the number of stiffeners due to a larger number of splice elements and additional assembly labor. The potential for assembly problems (e.g., shimming) also increases with the number of stiffening elements expected to align at major joints.

Sensitivities to design criteria and guidelines were found to have a strong effect on the cost and weight of fuselage crown panel designs. For example, the value of a minimum load level used to constrain skin buckling was found to dominate costs associated with the trade between stiffener spacing and skin gage. Decreased values in the buckling constraint were found to decrease cost and weight until a point at which a new design driver became dominant. Studies such as these suggest that arbitrary guidelines established for composites should be challenged. In many cases, guidelines are used to constrain composite designs within the range of a database. As the database expands, the guidelines should be updated to reflect new insight and avoid adding unnecessary cost and weight.

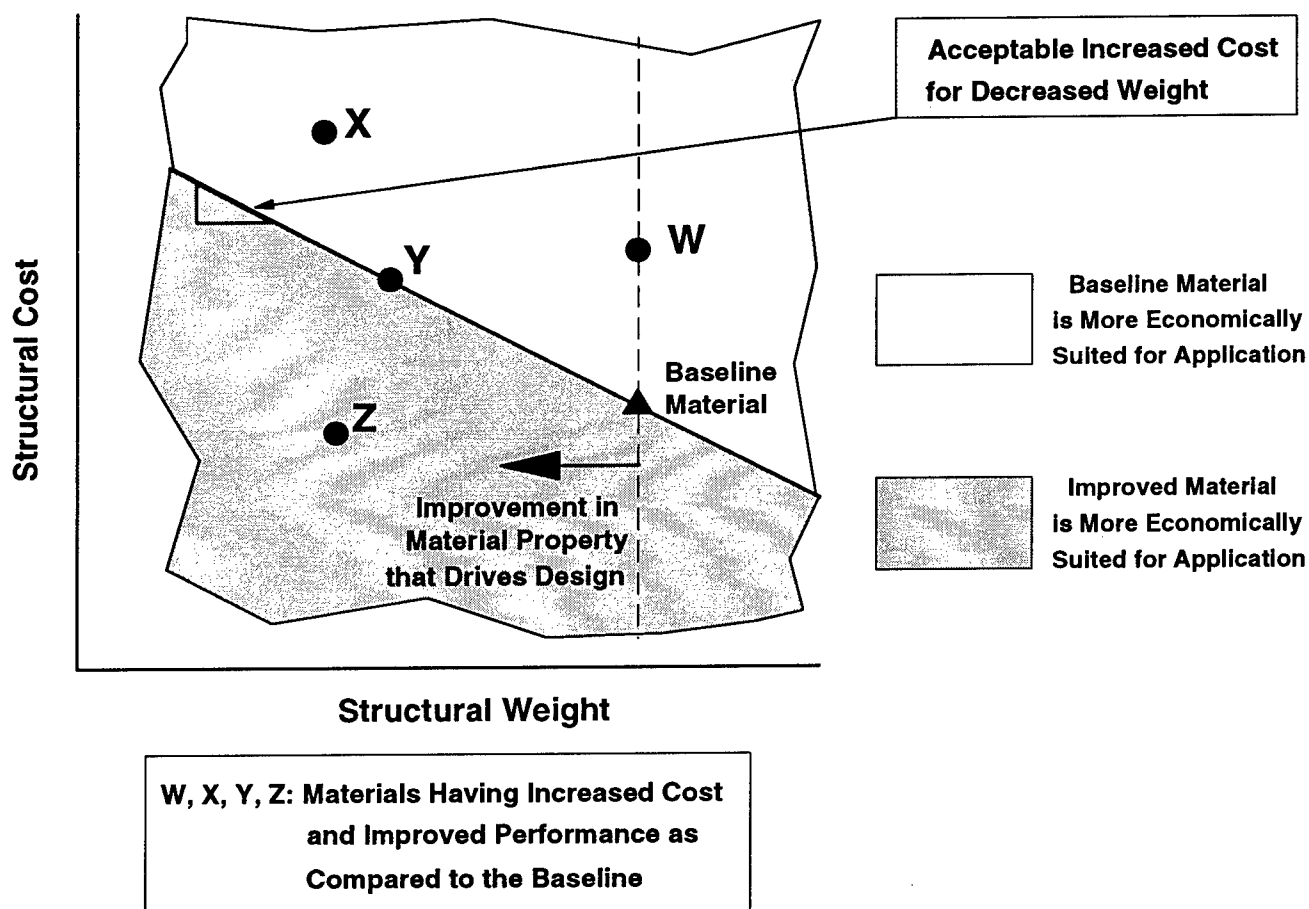
The design sizing task of blending structural details to satisfy load and design criteria over the full crown panel appeared to influence cost and weight (Ref. 5). This effect was quantified by evaluating the total cost difference between a blended and optimized point design. The blended design appeared more expensive because the total cost of optimized point designs was simply calculated using a sum. In practice, design details will require some blending to avoid affecting automation and adding cost. For example, point-to-point compatibility of the skin laminate lay-up must be maintained to avoid the cost of local ply adds and drops.

One can surmise that the method used for blending designs will have a strong impact on cost and weight. In general, current designs are blended manually with the help of computing tools capable of sizing individual points. As discussed earlier, the development of mathematically based blending functions is proposed to enhance the design cost model. These functions are expected to optimize structural

details for a space containing variable loads and criteria. The blending function should be capable of incorporating advantages of some advanced technologies. For example, automated tow placement will allow greater freedom in ply tailoring (e.g., ply add/drop on the fly and angle changes over a distance).

The material variables considered during ATCAS crown design cost trade studies included graphite fiber type and hybridization. As expected, composite materials having higher modulus fibers were found to have improved performance and some weight savings. However, a material with lower modulus graphite fiber was selected as the most promising candidate for crown applications after comparing cost per unit weight savings (Ref. 5).

Figure 7 schematically illustrates how material cost and weight trade studies are performed using a design cost model. The results of such trades are application specific and depend on interactions with design variables. Therefore, the "best material" will change depending on several factors. Examples of these factors include the structural location, basic design concept, associated design drivers, and the value for an acceptable increased cost per unit weight savings.



**Figure 7: Schematic Diagram of a Trade Between Material Cost and Performance**

The example given in Figure 7 compares four materials having both improved performance and increased cost, relative to a baseline material. An isovalue line is drawn in the figure to indicate an acceptable increased cost per unit weight savings. In general, this line will depend on specific hardware program goals. The baseline material would be selected over both materials X and W. Materials Y and Z are shown to have a value equal to and better than that of the baseline material, respectively. The

improved properties of material W are not design drivers, and the design cost increased directly with material cost. Material X is shown to have improved performance for a design driver; however, the weight savings does not warrant increased cost according to specified program goals. Material Z is the obvious choice over all materials shown in Figure 7 since the improved performance yielded both minimum cost and weight.

Cost-versus-performance trades can also be used in a research program to guide material developments for specific applications. This can be done by considering improvements in material properties known to drive design. As discussed in Reference 5, AS4/938 towpreg was selected for ATCAS fuselage crown panel applications. Considering this as the baseline material form, a study was performed for the current paper to determine how changes in the longitudinal ply modulus ( $E_{11}$ ) affects performance. The acceptable increased material cost per unit weight savings was also determined using the same isovalue design lines applied in the ATCAS crown study.

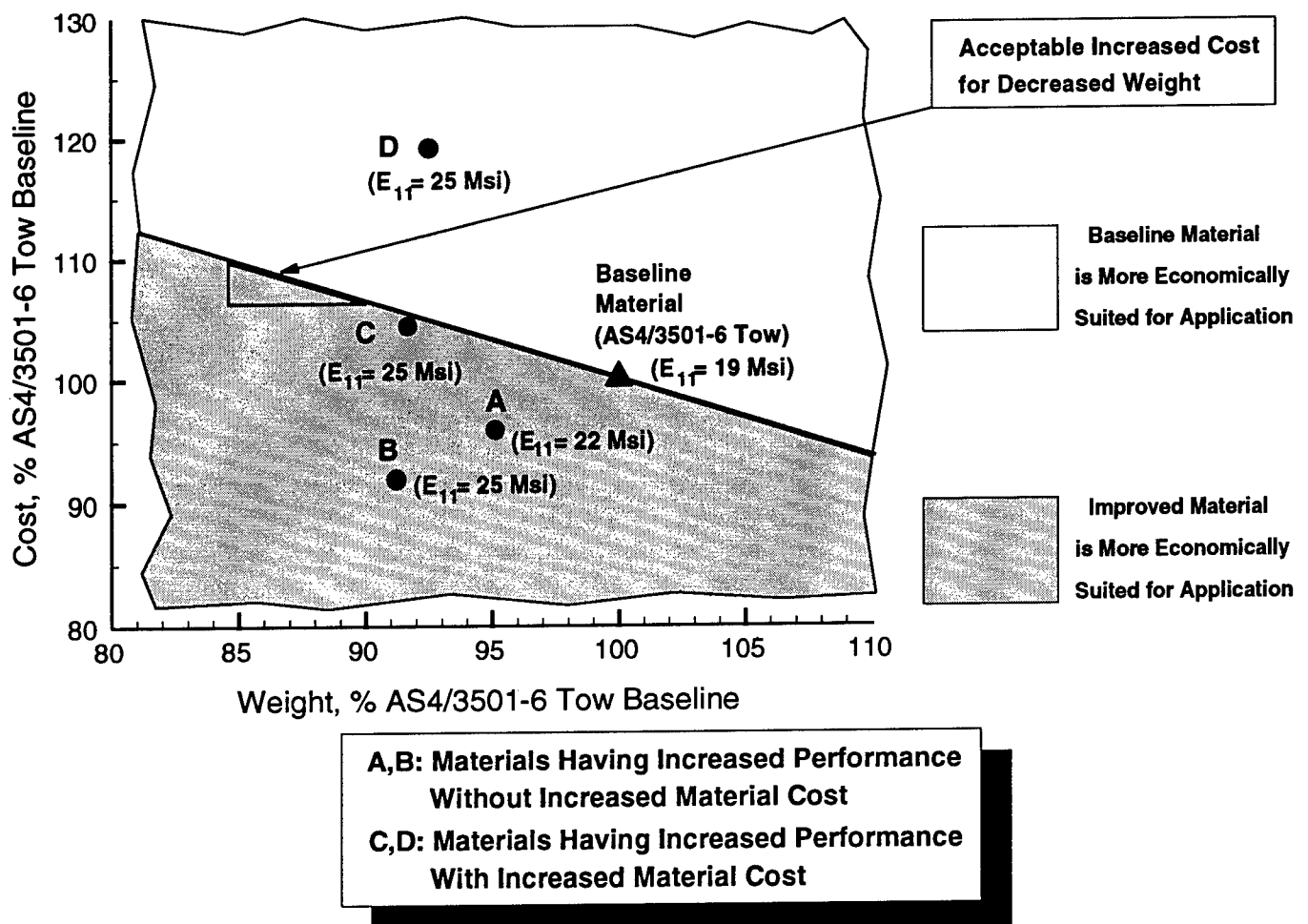
Figure 8 shows theoretical results for crown panel designs consisting of materials with three different values of  $E_{11}$ . For purposes of simplicity, all other properties were assumed to remain the same as that of the baseline material. Material types A and B have the same material cost as the baseline, while C and D have increased costs. The increased  $E_{11}$  for materials A and B result in design variations that decrease cost and weight. When the technology required to enhance material performance also increases material cost, it would still be desirable to pursue such developments to the extent that design costs remain below the isovalue line. Material C represents such a case. The material cost for C is approximately twice that of the baseline material, but the value of weight savings possible in crown applications using such a material would be deemed acceptable. The material cost for D is approximately three times that of the baseline material. The crown design cost and weight trade indicate that the baseline material is more economically suited for crown applications than material D.

As discussed at the start of this section, results from References 5 and 11 suggest that cost savings are possible with increased stiffener spacing. Figure 8 showed that improvements in  $E_{11}$  allow increased stiffener spacing for a given skin thickness, resulting in lower design weights. As discussed with the help of an isovalue line, the economic value of the design may also be lower, depending on an interaction with material cost.

Another laminated material form which could theoretically allow wider stiffener spacing and reduced costs is one having a constant fiber aerial weight, increased ply thickness, and decreased density. Such a material may also yield a number of structural advantages for fuselage applications because the skin's bending stiffness per unit weight would increase. The material would conceivably have intra-layers consisting of continuous fibers and matrix with volume fractions consistent with current tape prepreg or towpreg. A porous matrix material with discontinuous fiber additives would constitute inter-layers having thicknesses on the order of 1/3 to 1 times that of the intra-layer. The density of the inter-layer would be on the order of high density core materials (e.g., 20 to 30 lb/ft<sup>3</sup>). Interlaminar shear strength requirements would likely control development of the inter-layers. Future ATCAS studies will consider the cost advantages, manufacturing concerns, and technical issues associated with a low density material having thicker plies.

The trade study shown in Figure 8 was simple in the sense that new materials were conceived to have changes in a single critical property. Cost and weight savings from improving a single material property are limited because a new design driver quickly becomes critical. In general, new materials have unique properties for several different performance issues. In some cases, material characteristics that increase one property can even decrease others. Based on fuselage design studies performed to date, materials having balanced performance attributes are desirable. Advances with new materials should be measured by considering the full range of properties critical to the design and application.





**Figure 8: Skin Material Performance Versus Cost Trade for ATCAS Fuselage Crown Applications**

### Conclusions

The NASA Langley STPO has initiated a program to develop and verify a designer's cost prediction model that will aid engineers in trading the cost and weight of composite transport aircraft structures. Such a model is intended to be used in hardware applications to help design build teams select structural details with projections of their overall effect on manufacturing cost. Research programs may also use the model to guide advanced developments in processes, materials, structural concepts, and design guidelines.

The Boeing Company was selected to develop the designer's cost prediction model. Other industry and university subcontractors will include Sikorsky, Dow-UT, Northrop, MIT, and University of Washington. The Boeing ATCAS design-build-team approach will support model development and verification for fuselage structures. Seven objectives to address major technical issues were identified and a detailed plan was completed to pursue solutions for each of these issues.

Design cost relationships will be developed with the help of existing databases. However, the model's theoretical framework will be general enough to analyze both current and evolving technologies. This requirement is crucial to making the model suitable for predicting the cost of large composite transport fuselage and wing structures assembled in future aircraft factories. The designer's cost prediction

model will be developed to incorporate cost, design, and manufacturing constraints. This tool will be packaged as a computer program entitled Cost Optimization Software for Transport Aircraft Design Evaluation (COSTADE). An optimization algorithm which cost-effectively blends structural details over variations in load and design criteria will be derived as an option for COSTADE. Verification tasks to demonstrate the design cost model are planned throughout the four-year period of study.

Initial design cost model developments have concentrated on fuselage crown panel applications. To date, a software tool was developed for crown panel local optimization and used to perform sensitivity studies on factors critical to the projected cost of a future factory. Results are documented in References 5 and 12, which can be found in these proceedings.

### References

- 1.) Freeman, W.T., Vosteen, L.F., and Siddiqi, S., "A Unified Approach for Composite Cost Reporting and Prediction in the ACT Program," First NASA Advanced Composites Technology Conference, NASA CP-3104, Part 1, 1991, pp. 357-369.
- 2.) Ilcewicz, L.B., Walker, T.H., Willden, K.S., Swanson, G.D., Truslove, G., and Pfahl, C.L., "Application of a Design-Build-Team Approach to Low Cost and Weight Composite Fuselage Structure," to be Published as a NASA Contractor's Report, 1991.
- 3.) Ilcewicz, L.B., Smith, P.J., Walker, T.H., and Johnson, R.W., "Advanced Technology Commercial Fuselage Structure," First NASA Advanced Composites Technology Conference, NASA CP-3104, Part 1, 1991, pp. 127-155.
- 4.) Walker, T.H., Smith, P.J., Truslove G., Willden, K.S., Metschan, S.L., and Pfahl, C.L., "Cost Studies for Commercial Fuselage Crown Designs," First NASA Advanced Composites Technology Conference, NASA CP-3104, Part 1, 1991, pp. 339-356.
- 5.) Swanson, G.D., Ilcewicz, L.B., Walker, T.H., Graesser, D., Tuttle, M., and Zabinsky, Z., "Local Design Optimization for Transport Fuselage Crown Panels," presented at the Ninth DoD/NASA/FAA Conf. on Fibrous Composites in Structural Design, Lake Tahoe, NV, November 1991.
- 6.) Krolewski, S., and Gutowski, T., "Effect of the Automation of Advanced Composite Fabrication Processes on Part Cost," SAMPE Quarterly, Vol. 18, No. 1, 1986, pp. 43-51.
- 7.) Foley, M., and Bernardon, E., "Cost Estimation Techniques for the Design of Cost Effective Automated Systems for Manufacturing Thermoplastic Composite Structures," in Proceedings of the SAMPE 35th International Sym., April, 1990, pp. 1321-1335.
- 8.) Gutowski, T., Henderson, R., and Shipp, C., "Manufacturing Costs for Advanced Composites Aerospace Parts," SAMPE Journal, Vol. 27, No. 3, May/June, 1991, pp. 37-43.
- 9.) Shipp, C.T., "Cost Effective Use of Advanced Composite Materials in Commercial Aircraft Manufacture," M.S. Thesis (Mechanical Engineering and Management), M.I.T., May 1990.
- 10.) Zabinsky, Z., Tuttle, M., Graesser, D., Kim, G., Hatcher, D., Swanson, G., and Ilcewicz, L., "Multi-Parameter Optimization Tool for Low-Cost Commercial Fuselage Crown Designs," First NASA Advanced Composites Technology Conference, NASA CP-3104, Part 2, 1991, pp. 737-748.
- 11.) Kassapoglou, C., DiNicola, A.J., Chou, J.C., and Deaton, J.W., "Structural Evaluation of Curved Stiffened Composite Panels Fabricated Using a THERM-X<sup>SM</sup> Process," First NASA Advanced Composites Technology Conference, NASA CP-3104, Part 1, 1991, pp. 207-232.

- 12.) Willden, K., Metschan, S., Grant, C., and Brown, T., "Composite Fuselage Crown Panel Manufacturing Technology", presented at the Ninth DoD/NASA/FAA Conference on Fibrous Composites in Structural Design, Lake Tahoe, NV, November 1991.

## **COINS: A Composites Information Database System**

Shahid Siddiqi, Louis F. Vosteen, Ralph Edlow, and Teck-Seng Kwa  
Analytical Services & Materials, Inc., Hampton, Virginia

Presented at  
9th DoD/NASA/FAA Conf. Fibrous Composites in Structural Design,  
Lake Tahoe, NV, Nov 1991.

### **Abstract**

An automated data abstraction form (ADAF) has been developed to collect information on advanced fabrication processes and their related costs. The information will be collected for all components being fabricated as part of the ACT program and included in a COMposites INFORMATION System (COINS) database. The aim of the COINS development effort is to provide future airframe preliminary design and fabrication teams with a tool through which production cost can become a deterministic variable in the design optimization process. The effort was initiated by the Structures Technology Program Office (STPO) of the NASA Langley Research Center to implement the recommendations of a working group comprised of representatives from the commercial airframe companies. The principal working group recommendation was to re-institute collection of composite part fabrication data in a format similar to the DoD/NASA Structural Composites Fabrication Guide. The fabrication information collection form has been automated with current user friendly computer technology. This work in progress paper describes the new automated form and features that make the form easy to use by of an aircraft structural design-manufacturing team.

### **Introduction**

The U.S. transport aircraft industry has over two decades of experience in manufacturing composite secondary structures. These applications, including elevators, rudders, spoilers, landing gear doors, fairings, etc., use approximately 400,000 pounds of composite materials per year.

Despite the fact that composite materials offer design advantages in terms of weight, corrosion resistance and fatigue life, their application in commercial aircraft has been limited relative to metals. A modest leap forward will occur when the new Boeing 777 is manufactured with carbon fiber horizontal and vertical stabilizers. High cost and the uncertainty in the cost prediction for composite structures are the main factors holding back more extensive use of these materials in commercial aircraft

One goal of the NASA Advanced Composites Technology (ACT) program is to have several airframe manufacturers design and fabricate composite structures with superior performance compared to equivalent aluminum structures and significantly lower in cost than that of earlier composite concepts. New and automated manufacturing processes will be used. The fabrication labor hours and costs involved will be tracked and reported to NASA. For a number of past DoD and NASA composite structures development programs, such information was submitted to the Air Force for inclusion in the DoD/NASA Advanced Composites Fabrication Guide using the "Fabrication Guide Data Abstraction Form" or "DAF", Reference 1. The NASA/DoD program to collect fabrication cost information ended in 1983. A working group of commercial airframe industry representatives recommended that NASA collect information on the actual costs of fabricating composite components being made as part of the ACT program. This information could be used to compare and evaluate various composite fabrication techniques and provide a technical database for 21st century aircraft structures.

Coupling fabrication cost information with an improved cost estimating model for composites (Reference 2) is the first step toward providing future concurrent engineering teams with a tool that can be used to include cost as a design variable during the preliminary design stage. Such a tool will have exceptional value since industry experience shows that 70% of airplane fabrication costs are fixed when the design is frozen.

The current status of the development of the automated data acquisition form (ADAF) for collection of fabrication cost information will be described in this paper. The fabrication cost information will become a part of the COMposites INFORMATION System (COINS).

### **COINS and Automated Data Abstraction Form Development**

The COINS database will be implemented with a commercially available relational database software package. The software selected is Informix-OnLine® with the WINGZ™ spreadsheet as an interface. This software was selected because it is used, supported and accepted in the commercial environment. Furthermore, the interface is user friendly and the database takes advantage of emerging technology for storing and retrieving images and text files as well as data fields. It also has a demonstrated capability to operate with MS-DOS®, Macintosh®, UNIX®, and other common operating systems.

The recommendations of the commercial airframe industry representatives from two workshops organized by STPO were reported in Reference 3. A third workshop was held in January 1991 and was devoted to a detailed evaluation of the DAF referred to above. As a result of this workshop, the form was modified to reflect current composites fabrication technology and the recommendations were incorporated in the new automated data acquisition form (ADAF). The input fields included in the new form are listed in Table 1.

The ADAF will be used to provide input data for COINS and has been designed to interface with a database update module. Initially, ADAF information will be submitted to NASA on a floppy disk where it will be checked by a software module for format and for "sanity" or "reasonableness" of the data. The data will then be transferred to the COINS database by AS&M personnel. Selected data from the DoD/NASA Advanced Composites Fabrication Guide will also be transferred to COINS to provide direct comparison of current data with that from past programs.

At present, the data base will reside on a Silicon Graphics IRIS™ workstation (operating under the UNIX operating system). The IRIS is connected to the NASA Larcnet. In the future, ACT contractors will be given access to this machine for submitting data by electronic mail. The transfer of ADAF data into the COINS database will still be performed by AS&M personnel. Users will have read only access to the database to avoid inadvertent changes or contamination of the data. The data will be accessible through user friendly database search procedures that can be built up with menu driven functions or that respond to direct user input queries such as "retrieve material types and labor hours for wing ribs manufactured with autoclaves". The retrieval modules will also interface with the WINGZ spreadsheet whose color graphics capabilities provide the user with a variety of form, graph and chart layouts. A user manual will be provided by AS&M for the ADAF and retrieval software.

The ADAF and the data retrieval procedures via WINGZ is almost identical in appearance on MS-DOS or Macintosh microcomputers. Similarly, they are compatible with UNIX environment workstations. This feature should be attractive for interfacing with the CAD/CAM capability available in the industry. Users will be computer platform independent and only one user manual will be required no matter what computer is used to host the WINGZ spreadsheet package. The only requirement is that users will have to purchase WINGZ software for the operating system they choose to use. WINGZ is available for the MS-DOS, Macintosh or UNIX operating

systems, the WINGZ software has also been ported to some other operating systems.

The ADAF form is expected to require input from more than one member of a preliminary design/fabrication engineering team. The form is arranged so that each input screen/page can be completed by an appropriate member of the team. The software is intelligent enough to prompt the user for only the required input choices on the basis of previously entered input. A Glossary function that explains the fabrication terms and processes will always be available to the user via a pull down menu. Figure 1 shows a block diagram of the screen pages in the ADAF.

Following an opening screen, the user is presented with the general information screens/forms shown in Figures 2 and 3. These screen/forms collect information about the part and the aircraft in which the structural part or assembly will be used. A typical fabrication data input screen is shown in Figure 4. The descriptors in the upper right-hand corner of each screen suggest which team member might fill out that page of the form.

The following control features (see Figure 3a) are available for each ADAF screen:

- (1) Pull down menus.
- (2) User activated hidden buttons.
- (3) Paging buttons in the lower right hand corner labeled HOME, NEXT, BACK, and ACCEPT.

The pull down menus provide overall WINGZ software control that allow the user to enter or exit the ADAF and access the Help information available. The set-up should be familiar to users of window-type software on workstations and micro computers.

Hidden buttons are used to provide user friendly input assistance. The required input fields on the ADAF screens are displayed in blue (underlined in the figures included in this paper) or in red (not underlined in the figures). There are hidden buttons located under the blue input text (the text itself may be thought of as the button) are activated when the user clicks the computer mouse button on any area of this text. For example if the button below *Aircraft Type* was activated, the options displayed in Figure 3b would appear. The user must make selections regarding the aircraft classification by positioning the mouse cross-hairs on the selection squares and clicking. This selects that text and records it as input for the active field.

The red input prompt text (denoted by the text that is not underlined on the figure) requires direct user input from the keyboard into the dashed prompt box that appears adjacent to this text. The user types text into the box and presses the enter/return key to terminate and record the input. The user may also use the arrow keys to move between such input boxes.

The paging buttons in the lower right hand side have the following functions and allow the user to move to different screens of the ADAF:

- |      |   |
|------|---|
| NEXT | Advances the user to the next screen without saving the input entered on the current screen/page. This button allows users to skip input screens that may be more appropriately addressed by another team member. |
|------|---|

- ACCEPT Functions like the NEXT button described above except that the input for the current screen/page is saved. This button should be used to advance screens after completing the appropriate input.
- BACK Functions like the NEXT button; skips or positions the user to the previous screen without saving (or altering) the input.
- HOME Returns the user to the first screen/page.

The ADAF is being designed to serve the needs of the preliminary design/fabrication teams in industry. The DoD/NASA DAF only required fabrication data input. Future needs of the airframe industry may best be served if design information is collected simultaneously. Screens will be proposed for including design related information to the ADAF to expand it beyond the original DAF. These design screens will prompt the user for information such as loading type, design strain level, etc..

### Summary Remarks

The work in progress status of the Advanced Composites Technology program Composites Information System (COINS) effort has been described. An automated data acquisition form (ADAF), based on the DoD/NASA Advanced Composites Fabrication Guide data abstraction form, has been developed. The form is available for use on Macintosh, MS-DOS and UNIX systems. A test version of the ADAF has been distributed to ACT contractors and is currently being evaluated. Evaluators comments and recommendations will be incorporated into a production version of the ADAF that will be made available for ACT program distribution.

### References

- (1) Meade L. E., DoD/NASA Structural Composites Fabrication Guide-3rd Edition, Vol 1-2, Air Force Wright Aeronautical Laboratories, 1982.
- (2) Freeman W. T., Ilcewicz L., Swanson G., and Gutowski T., Designer's Unified Cost Model, Proc. 9th DoD/NASA/FAA Conf. Fibrous Composites in Structural Design, Lake Tahoe, NV, Nov. 1991.
- (3) Freeman W. T., Vosteen L. F., and Siddiqi S., A Unified Approach for Composite Cost Reporting and Prediction in the ACT Program, Proc. of the 1st NASA ACT Meeting, Seattle, Wash., Nov. 1990.

Informix-OnLine and WINGZ are registered trademarks of Informix Software, Inc.  
 IRIS is a trademark of Silicon Graphics, Inc.  
 Macintosh is a registered trademark of Apple Computer, Inc.  
 MS-DOS is a registered trademark of Microsoft Corp.  
 UNIX is a registered trademark of AT&T Corp.

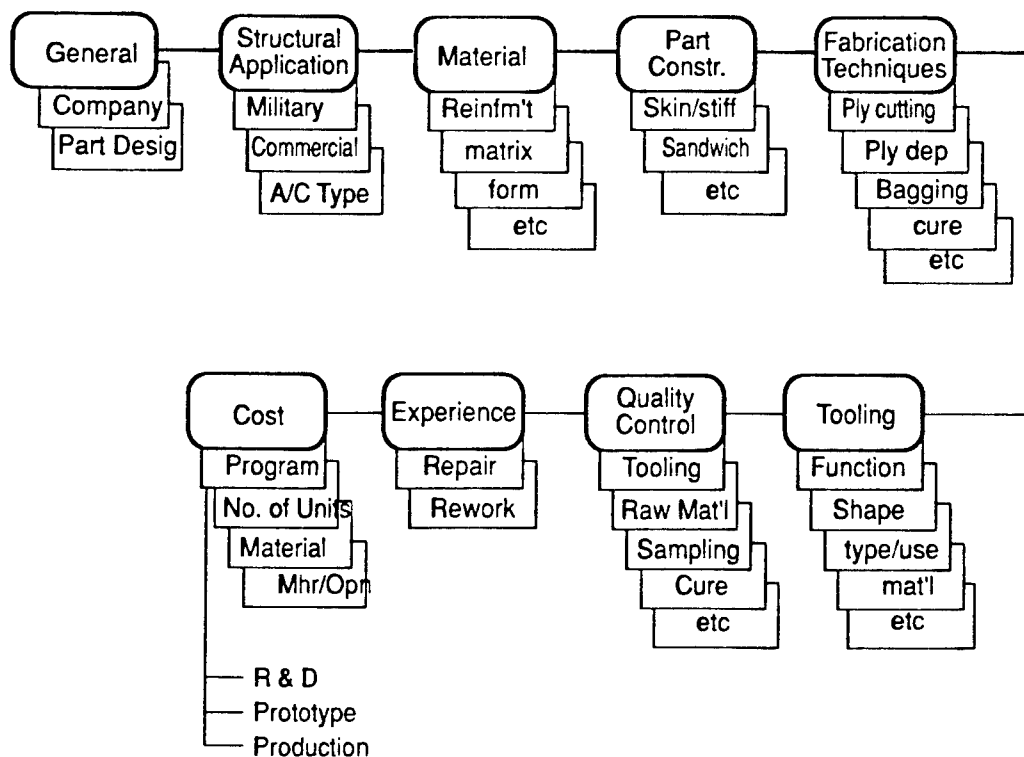


Figure 1. A Block Diagram of the ADAF.

## 1.GENERAL

General

Company: STPO Inc

Division: Structural Design

Recorder\*: Designer A C  
(Last Name, - First Initial)

Aircraft  
(Org./Dept.)

804-827-8000  
(Phone Number)

Fabrication Date: 08-23-91  
(Month/Day/Year)

\*If information is provided by more than one person, show name of principal point of contact>

Test	Accept
------	--------

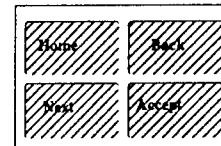
Figure 2. The ADAF General Information Screen.



## 2.AIRCRAFT APPLICATION

Designer

**Application:** Commercial  
**Aircraft Type:** Transport  
**Role:** utility  
**PowerPlant:** Turbofan  
**Structural Level:** Primary  
**Vehicle Model No.:** C-11-30D  
**Part Number or Description:** W123/45-P(C-11-30D) Wing rib  
**List Dimensions & Weight:** 6ft chord, 2ft thick, 20 lb  
**Quantity per assembly (of this part):** 10  
**Next Assembly:** wing inboard section 3  
**Maximum Service Temperature:** 200 deg. f  
**Total Accumulated Test Hours to Date:** 255 hrs  
**Type of Test:** Destructive  
**Equivalent Life Times:** 2  
**Total Accum. Flight Hrs. to Date:** 50 hrs



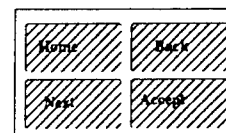
(a) The ADAF Aircraft Information Screen.

## 2.AIRCRAFT APPLICATION

Designer

A screenshot of a software dialog box titled 'Application'. It features a list box on the left labeled 'Aircraft Type' with the following options: Transport (selected), Helicopter, Trainer, and Sea Plane. On the right, there is a section labeled 'Type Application' with two radio buttons: 'Commercial' (selected) and 'Military'. At the bottom right of the dialog box are two buttons: 'OK' and 'Cancel'.

Total Accumulated Test Hours to Date: 255.00  
Type of Test: Destructive  
Equivalent Life Times: 0.01  
Total Accum. Flight Hrs. to Date: 50.00



(b) The ADAF Aircraft Information Screen with the Dialog Box Display.

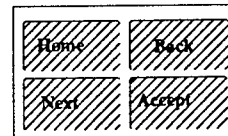
Figure 3. Example screens for "Aircraft Application".

## **7.FABRICATION TECHNIQUES**

*Fabricator*

Ply Deposition: RTM  
Deposition Mode: Semiautomatic  
Deposition Method: Ply-By-Ply In On Tool  
Ply Cutting: Water Jet  
Cutting Mode: Manual  
Compaction: Pressure  
Bag Material: Elastomeric  
Seal: Permanent  
Bleeder: Fiberglass Cloth  
Curing Consolidation: Self -Contained  
Atmosphere: Air Vented Bag  
Max Cure Temp.: 350 (degrees Farenheit)  
Max Cure Pressure: 200 psi  
Total Cure Time: 20 (hours)  
Max. Heating Rate: 10 (degrees Farenheit/min.)  
Post Cure Heat Treat: 10 (degrees Farenheit/min.)  
Heat Treat. Time: 10 (hours)

Cure Profile



**Figure 4. The ADAF Fabrication Information Screen.**

Table 1. Data fields included in automated data abstraction form.

<u>GENERAL</u>	
1. Company	
2. Division	
3. Recorder	
4. Date Recorded	
<u>APPLICATION</u>	
5. Commercial/Military	
6. Aircraft Type	
7. A/C Role	
8. Power Plant	
9. Structural Level	
10. Vehicle Model No.	
11. Part Number or description	
12. Dimensions	
13. Weight	
14. Quantity per Assy (of this part)	
15. Next Assembly	
16. Maximum Service Temperature, °F	
17. Total Cum Test Hours to Date	
18. Type of Test	
19. Equivalent Life Times	
20. Total Cum. Flight hrs. to Date	
<u>MATERIAL</u>	
21. Matrix	
22. Reinforcement	
23. Reinforcement Type	
24. Product Form	
25. Material Type	
26. Width, in.	
27. Length, in.	
28. Thickness, in.	
29. Discontinuous fiber type	
30. Fiber Diameter, mils	
31. Tow Diameter, mils	
32. Tow fiber count	
33. Supplier Code No.	
34. Specifications (if applicable)	
<u>TOOLING</u>	
Fabrication Tooling	
35. Function	
36. Shape	
37. Surface	
38. Surface Support	
39. Type	
40. Tool Surface Material	
41. Elastomer type (if used)	
42. Supplier (if applicable)	
43. Designation (Name or Code No.)	
44. Fabrication Technique	
45. Life Expectancy, parts per tool	
46. Surface Preparation	
47. Maintenance Experience	
<u>Assembly Tooling</u>	
48. Assembly Parts	
49. Next Assembly	
50. Function	
51. If Bonded Fixture . . .	
52. Adhesive Tradename & No.	
53. Braze Alloy Name & No., if used	
54. Fastener Tradename & No.	
55. Number of fasteners	
56. High Temperature Exposure	
57. (If Yes) Type	
58. Max. Temperature, °F.	
59. Material	
60. Life Expectancy, units	
61. Maintenance Experience	
<u>PART CONSTRUCTION</u>	
62. Shape	
63. Construction Method	
64. Substructure	
65. Core	
66. Stitching	
67. Molding method	
68. Leading Edge Protection	
69. Leading Edge/Airfoil Bond	
70. X-Section Shape	
<u>Ply Information</u>	
71. Max. Number of Plies	
72. Min. Number of Plies	
73. Ply Layout 0° 45° 90°	
74. Other Orientation (specify)	
<u>Weights</u>	
75. Raw Material Purch for Part, pd	
76. Total Part (incl. noncomp.), pd	
77. Noncomposite Part, pd	
78. Trimmed Material, pd	
79. Test Material, pd	
80. Completed Part, pd (comp. only)	
81. Assembly, pd	
<u>Dimensions</u>	
82. Max. Width, in.	
83. Max. Thickness, in.	
84. Max. Length, in.	
85. Wetted Area, sq in	
86. Outside Diameter, in.	
87. Wall Thickness, in.	
88. Taper Ratio, in./inch	
<u>FABRICATION TECHNIQUES</u>	
89. Ply Deposition	
90. Deposition Mode	
91. Deposition Method	
92. Ply Cutting	
93. Compaction	
94. Bag Material	
95. Seal	
96. Bleeder	
97. Curing /Consolidation	
98. Max. Cure Temp., °F	
99. Max. Cure Pressure, psi	
100. Total Curing Time, hrs.	
101. Max. Heating Rate, °F/min.	
102. Atmosphere	
103. Post Cure/Heat Treat, °F	
104. Post cure time, hrs.	
105. Cure Profile	

Table 1. (concluded)

<u>FABRICATION TECHNIQUES (cont.)</u>		
<u>Secondary Fabrication Operations</u>		
106. Final Sizing/Mat'l Removal		
107. Holes/Penetrations		
108. Cutting Tool Material		
<u>Surface Preparation (for Bonding)</u>		
109. Metal		
110. Resin Matrix		
111. Bonding type		
112. Adhesive bonded and/or fastened?		
113. Adhesive Tradename & No.		
114. Fastener Tradename & No.		
115. No. of Fasteners		
116. Fastener Pitch		
117. Braze Alloy Name & No., if used		
<u>Finishing Operation</u>		
118. Surface Treatment		
119. Painting		
120. Erosion Protection		
121. Lightning Protection		
<u>QUALITY CONTROL</u>		
122. Primary Tool/Part Process Qual.		
123. Periodic Inspection		
124. Inspection Frequency		
<u>Part Raw Material Inspection</u>		
125. Initial Inspection		
126. Reinspection During Production		
<u>Sampling Technique</u>		
127. In process (Fab.) Controls		
128. Orientation and Number of Piles		
129. Inserts/Attachments/Tag Ends		
130. Test Panels		
131. Leak Check		
<u>Curing Consolidation</u>		
132. Continuous/intermittent Record		
133. Dielectrometry		
	<u>Finished Part Inspection</u>	
	134. Visual	
	135. Ultrasonic	
	136. Destructive	
	137. Acoustic Emission	
	138. Radiographic	
	139. Infrared	
	140. Microwave	
	141. Phototropic	
	142. Proof Loading	
	143. Other	
	144. Acceptance Rate, %	
	<u>COST</u>	
	145. Cost basis	
	146. Development Status	
	147. Production Rate, units/month	
	148. Total Number Produced to Date	
	149. Total Number Planned	
	150. Time Span of Manufacture	
	151. Price of Part Raw Material \$/Pound	
	152. Yr. Purchased	
	153. Price of Purchased Components \$/Part	
	<u>Direct Fabrication Labor (manhours/unit) by operation</u>	
	154. Tool Preparation	
	155. Composite Orientation	
	156. Pattern Cutting	
	157. Layout/Detail Installation	
	158. Honeycomb Preparation	
	159. Instrumentation	
	160. Bagging/Tool Closure	
	161. Cure/Consolidation	
	162. Post Cure	
	163. Part Removal/Cleanup	
	164. Machining/Trimming/Drilling	
	165. Finishing	
	166. Assembly	
	167. Total Fabrication Hours	
	<u>Direct Assy Labor (MH/unit) by operation</u>	
	168. Fixture Setup	
	169. Detail Installation	
	<u>Tooling Costs</u>	
	179. Material, \$	
	180. Design Labor, manhours	
	181. Fabrication Labor, manhours	
	182. Inspection Time, manhours	
	<u>Assembly Costs</u>	
	183. Price of Purch. Components, \$/Assy	
	184. Learning Curve Projected, %	
	185. Learning Curve Actual, %	
	<u>Fixture</u>	
	186. Material, \$	
	187. Design Labor, manhours	
	188. Fabrication Labor, manhours	
	189. Inspection Time, manhours	
	<u>EXPERIENCE</u>	
	190. Repair Documentation Reference	
	191. Is Mil-P-9400 used?	
	192. Problems/Rework	
	193. Other References	
	194. User Recommendations	
	195. Learning Curve Projected, %	
	196. Learning Curve Actual, %	

**THIS PAGE INTENTIONALLY BLANK**

Composite Fuselage Shell Structures Research at  
NASA Langley Research Center

James H. Starnes, Jr. and Mark J. Stuart  
NASA Langley Research Center  
Hampton, VA 23665-5225

Introduction

Fuselage structures for transport aircraft represent a significant percentage of both the weight and the cost of these aircraft primary structures. Composite materials offer the potential for reducing both the weight and the cost of transport fuselage structures, but only limited studies of the response and failure of composite fuselage structures have been conducted for transport aircraft. Before composite materials can be applied safely and reliably to transport fuselage structures, the behavior of these important primary structures must be understood and the structural mechanics methodology for analyzing and designing these complex stiffened shell structures must be validated in the laboratory. Methods for accurately predicting the nonlinear response and failure of structurally efficient, cost-effective stiffened composite shell structures must be developed and validated. The effects of local gradients and discontinuities on fuselage shell behavior and the effects of local damage on pressure containment must be thoroughly understood before composite fuselage structures can be used for commercial transport aircraft.

The present paper describes the research being conducted and planned at NASA Langley Research Center to help understand the critical behavior of composite fuselage structures and to validate the structural mechanics methodology being developed for stiffened composite fuselage shell structure subjected to combined internal pressure and mechanical loads. Stiffened shell and curved stiffened panel designs are currently being developed and analyzed, and these designs will be fabricated and then tested at Langley to study critical fuselage shell behavior and to validate structural analysis and design methodology. The research includes studies of the effects of combined internal pressure and mechanical loads on nonlinear stiffened panel and shell behavior, the effects of cutouts and other gradient-producing discontinuities on composite shell response, and the effects of local damage on pressure containment and residual strength. Scaling laws are being developed that relate full-scale and subscale behavior of composite fuselage shells. Failure mechanisms are being identified and advanced designs will be developed based on what is learned from early results from the Langley research activities. Results from combined load tests will be used to validate analytical models of critical nonlinear response mechanisms as well as shell scaling laws.

## **COMPOSITE FUSELAGE SHELL STRUCTURES RESEARCH**

The objectives of the Langley composite fuselage shell structures research program are to develop the structural mechanics methodologies needed to predict reliably the response and failure of composite fuselage shell structures that are subjected to combined internal pressure and mechanical loads, and to understand the effects of local damage on the damage tolerance and residual strength of these structures. These structural mechanics methodologies include structural analysis methods, structural sizing procedures and structural scaling methods. The structural analysis methods will be used to predict the nonlinear response of internally pressurized fuselage shells and the local stress and deformation gradients that cause failure in composite shells with discontinuities. The structural sizing procedures will be used to conduct minimum weight design studies for candidate shell design concepts and to determine the sensitivity of the response and structural weight of a design to changes in structural parameters. The structural scaling methods will be used to study subscale models of candidate design concepts in an attempt to reduce the cost of design development by minimizing the amount of full-scale development testing needed for a new structural design. The structural mechanics methodologies developed by this research effort will be verified in the laboratory by conducting experiments with curved stiffened composite panels and pathfinder pressurized composite shells. These experiments will also identify critical failure modes and the effects of local damage and stress and deformation gradients on composite shell behavior.

**Objectives:** Develop verified structural mechanics methodologies for reliably predicting the response and failure of composite fuselage structure subjected to combined internal pressure and mechanical loads and to local damage

**Approach:**

- Develop and apply structural analysis methods that predict the nonlinear response and failure of composite fuselage shell structures with combined loads
- Develop structural sizing procedures and conduct parametric studies for structurally efficient composite fuselage shell structures with combined loads
- Develop scaling methodology for composite fuselage shells with combined loads
- Test benchmark curved panels and pathfinder stiffened shells to identify critical failure modes, to verify structural analysis methods, and to understand the effects of local damage and gradients on composite shell behavior

Figure 1

## PRESSURIZED COMPOSITE FUSELAGE SHELL

An important effect of internal pressure on a stiffened composite shell structure is suggested in figure 2. The relatively thin skin of a pressurized frame-stiffened fuselage shell expands outward in the radial direction more than the stiffer frames and a local bending gradient is generated in the skin where the skin is attached to a frame. The radial deflections in the thin skin can be large enough that the behavior of the shell is nonlinear. The local bending gradients will cause local three-dimensional interlaminar stress gradients in the skin which could be large enough to cause failure to occur. Inplane compression and shear stress resultants in the skin that are caused by mechanical loads may increase the magnitudes of these local interlaminar stress gradients due to the coupling of the inplane stress resultants and the out-of-plane deflection gradients associated with nonlinear thin shell behavior.

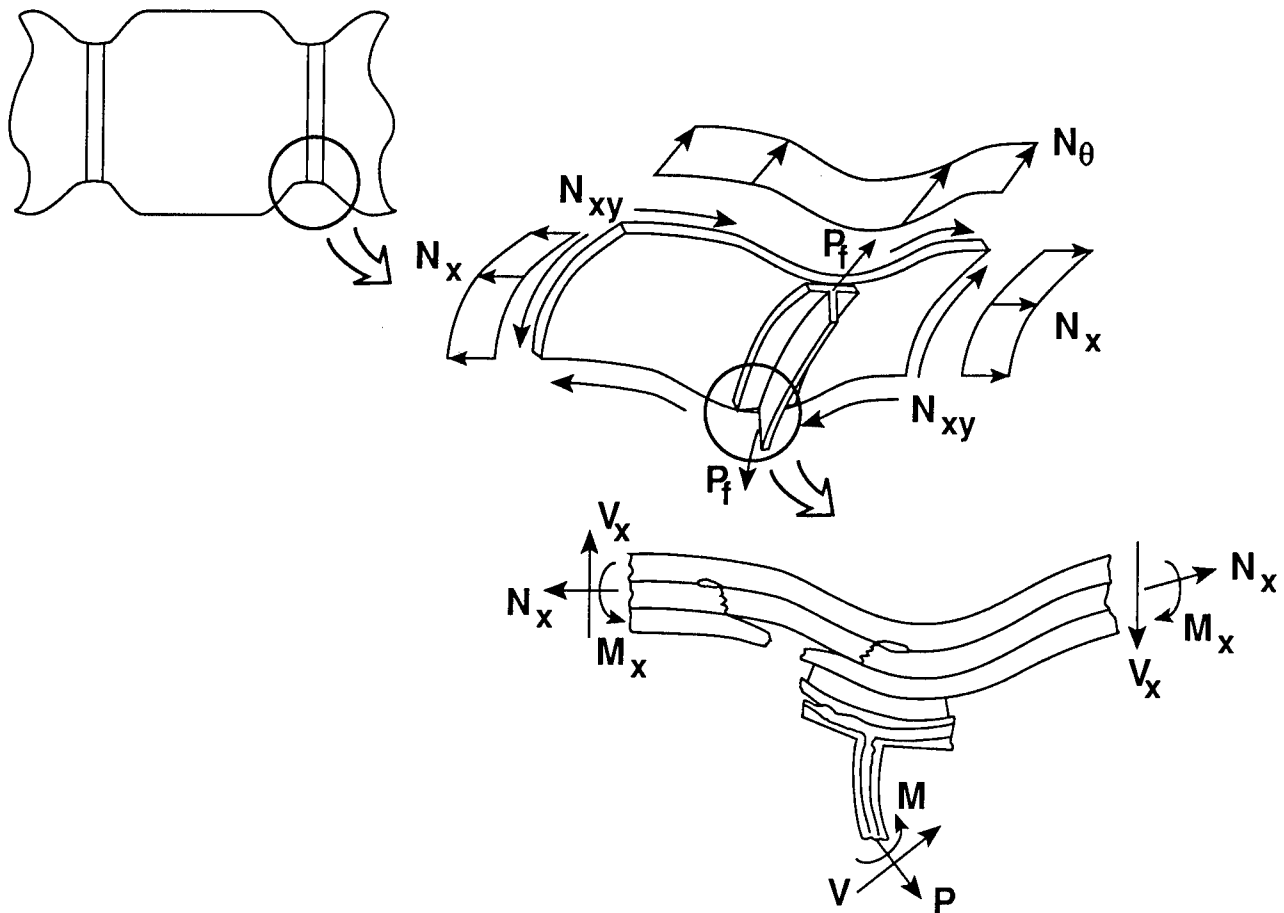


Figure 2



## **COMPOSITE FUSELAGE SHELL STRUCTURES RESEARCH SHELL ANALYSIS AND SIZING STUDIES**

Nonlinear shell analysis and structural sizing studies for the Langley composite fuselage shell structures research program are indicated in figure 3. The effects of combined internal pressure and mechanical loads on nonlinear structural response will be studied analytically. The postbuckling response of the skin and the redistribution of internal loads associated with stiffness changes due to nonlinear skin buckling response and damage propagation will be included in the nonlinear analyses. The local stress and deformation gradients associated with local details, discontinuities and eccentricities will be determined for accurate failure analyses and the effects of shell curvature on nonlinear behavior and local gradients will also be studied. Structural design studies will be conducted to determine minimum-weight designs for candidate design concepts subjected to combined internal pressure and mechanical loads. Studies will also be conducted to determine the sensitivity of the response and failure of candidate minimum-weight design concepts to changes in structural parameters.

- **Nonlinear Shell Analysis**
  - Stiffened shell response to pressure and mechanical loads
  - Postbuckling response
  - Local deformation and stress gradients caused by local details, discontinuities and eccentricities
  - Curvature effects
  - Local stress fields for failure predictions
  - Internal load redistribution associated with stiffness changes due to nonlinear response and damage
- **Structural Sizing Studies**
  - Minimum-weight design studies for pressure and mechanical loads
  - Parametric studies

Figure 3

## COMPOSITE FUSELAGE SHELL STRUCTURES

Hierarchical shell models that represent three levels of structural modeling refinement for the Langley composite fuselage shell structures studies are shown in figure 4. Relatively coarse stiffened shell models will be used to determine the global structural response and internal load distributions due to combined internal pressure and mechanical loads. These models will also be used to determine the redistribution of internal loads due to a local stiffness change caused by skin buckling and damage propagation. Refined curved stiffened panel models will be used to determine more accurately the local gradients caused by the interaction of skin and frame elements and to predict the behavior of stiffened panel specimens of selected concepts. More highly refined shell element and structural detail models will be used to predict the local stress and deformation gradients associated with local discontinuities, eccentricities and other details and these gradients will be used to predict local failure.

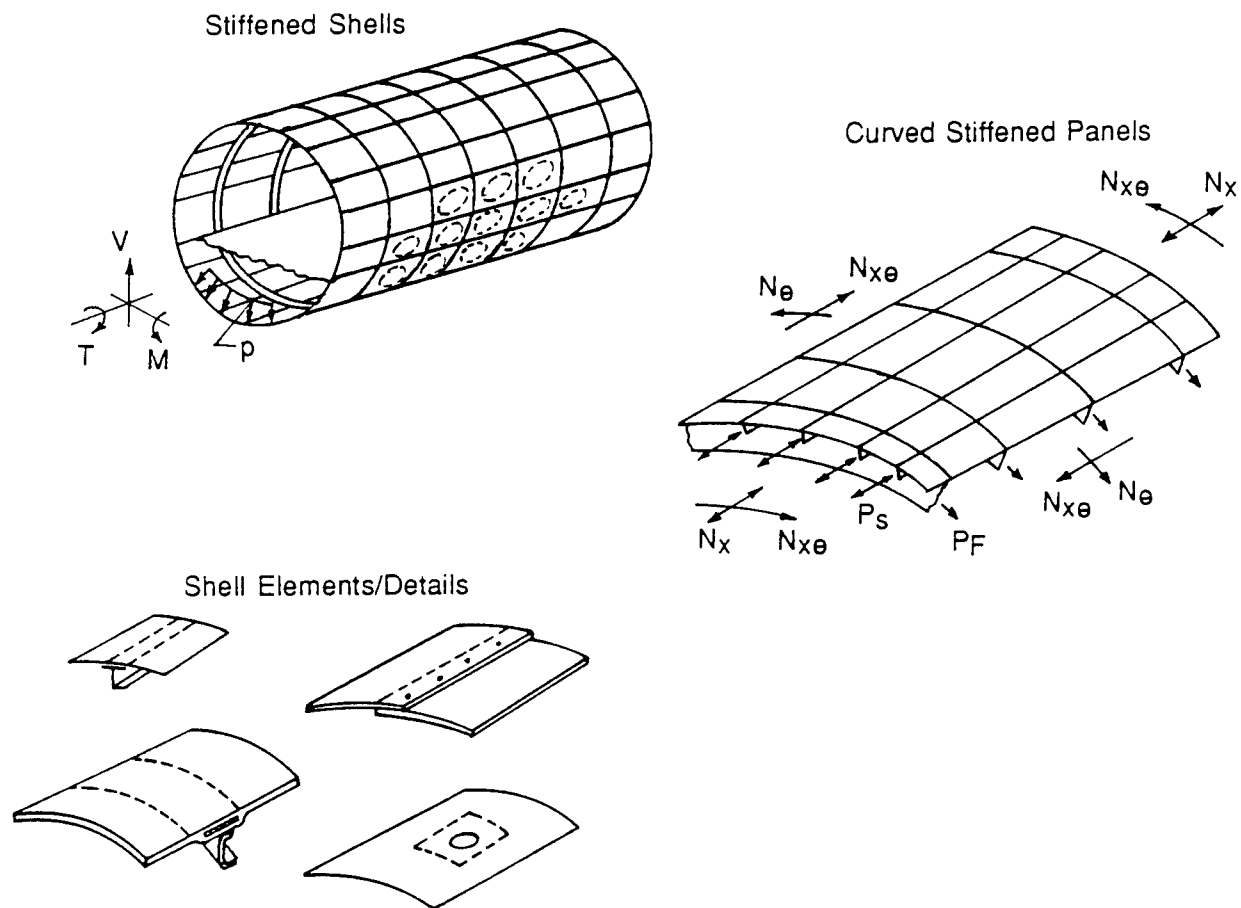


Figure 4

## EFFECT OF INTERNAL PRESSURE ON COMPOSITE SHELL STRUCTURES

An example of results for a stiffened shell analysis model currently being studied is shown in figure 5. The shell model is based on the current Boeing design being developed under NASA contract NAS1-18889 and is being used to develop the Langley pathfinder half-scale stiffened shell design. The shell radius is 122 inches, the shell length is 264 inches and the shell skin is made from a  $[\pm 45/90/0/\pm 60/90]_s$  graphite-epoxy laminate. The shell is loaded by an internal pressure of 10.35 psi. The model includes 3 skin bays with discrete stringers, frames and floor beams. The figure shows the effects of the stringers, frames and floor beams on the hoop stress resultant distribution in the skin. These results indicate that the value of the hoop stress resultant is significantly affected by the interaction of the skin and the frames, stringers and floor beams.

**Radius = 122 in., Length = 264 in.**  
**Shell Laminate  $[\pm 45/90/0/\pm 60/90]_s$**   
**Pressure = 10.35 psi**

### Reference Design Based on Current Boeing Design

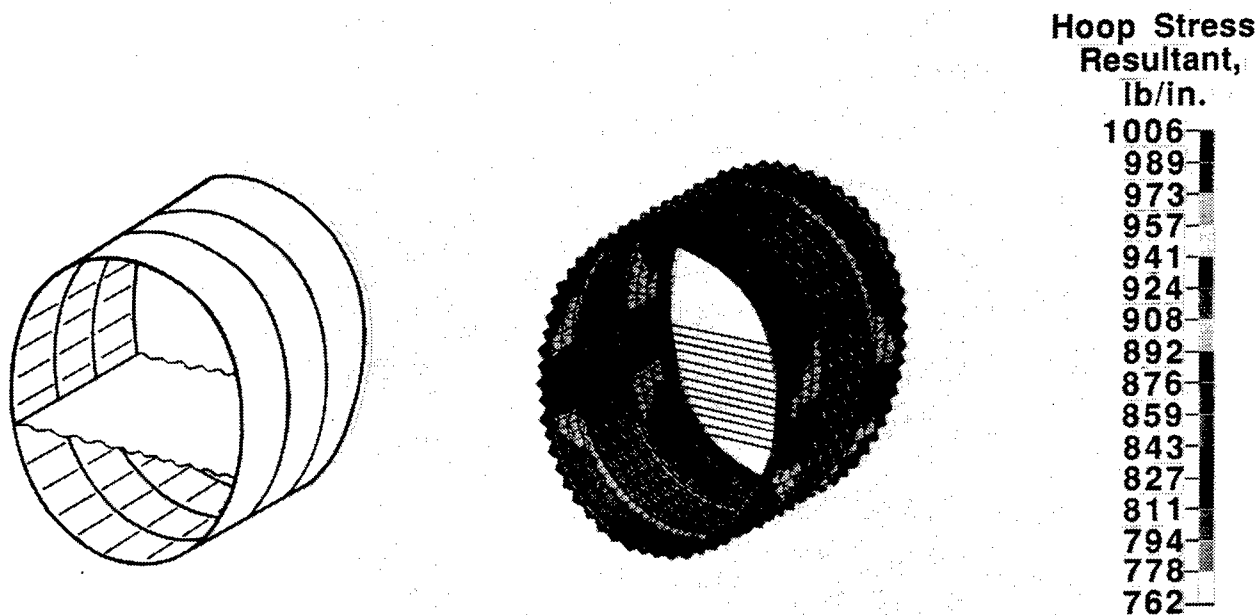


Figure 5

## EFFECT OF INTERNAL PRESSURE ON UNSTIFFENED CURVED GRAPHITE-EPOXY PANEL RESPONSE

An example of the effects of internal pressure on the response of curved unstiffened graphite-epoxy panels is taken from ref. 1 and shown in figure 6. The panels are 20 inches long, 8 inches wide and have a 60 inch radius. Analytical and experimental out-of-plane deflections  $w$  at the center of the panel are shown in the lower left figure as pressure increases for 5-, 8- and 16-ply-thick panels. These results show that the panels stiffen as the pressure is increased and that the pressure-deflection response curves are nonlinear. The circumferential or hoop strain distribution along the  $x$  or circumferential coordinate from the center of the panel to a panel edge is shown in the lower right figure for an 8-ply-thick panel with 50 psi internal pressure. Inside and outside surface strain results indicate that a significant bending strain gradient exists near the panel edge. This bending strain gradient is severe enough to cause the panel to fail along this edge as shown in the upper right photograph.

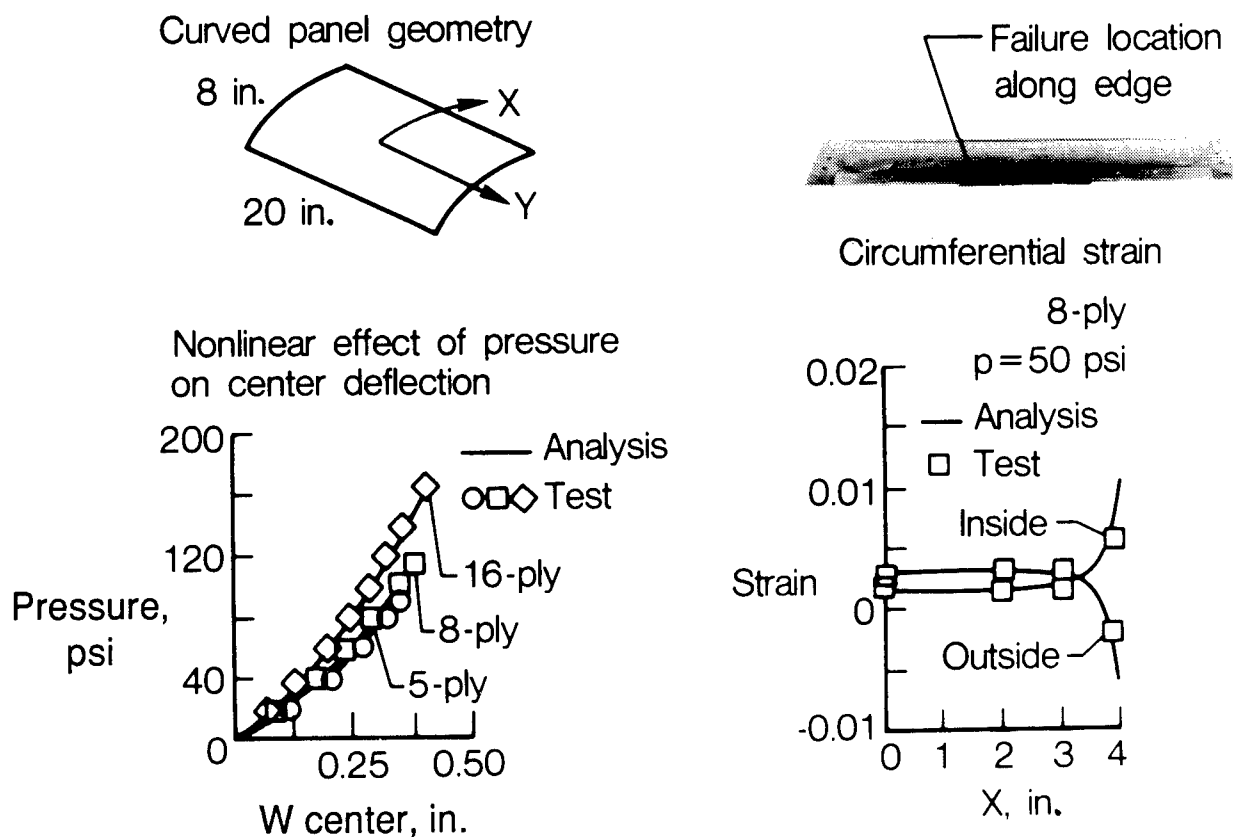


Figure 6

## FIRST MAJOR FRACTURE EVENT AND ULTIMATE FAILURE LOAD

Failure results for 4-, 5-, 8- and 16-ply-thick graphite-epoxy panels loaded by internal pressure are taken from reference 1 and are shown in figure 7. The graphite-epoxy panels are made from  $[\pm 45]_S$ ,  $[\pm 45/90]_S$  and  $[\pm 45]_{2S}$  laminates and  $[\pm 45/0/90]_S$  and  $[\pm 45/0/90]_{2S}$  quasi-isotropic laminates. Results are also shown for 0.020- and 0.040-inch-thick aluminum panels for comparison. Strain gage data from back-to-back strain gages near the edge of a panel where the bending strain gradient is severe (see figure 6) are shown in the upper right figure as pressure is increased and the results indicate that local failure can occur in this region before ultimate failure. The ultimate failure pressures of the graphite-epoxy panels are not a linear function of panel thickness. All failure events for the graphite-epoxy panels occurred above 50 psi of internal pressure which is well above the operating pressure of a transport fuselage.

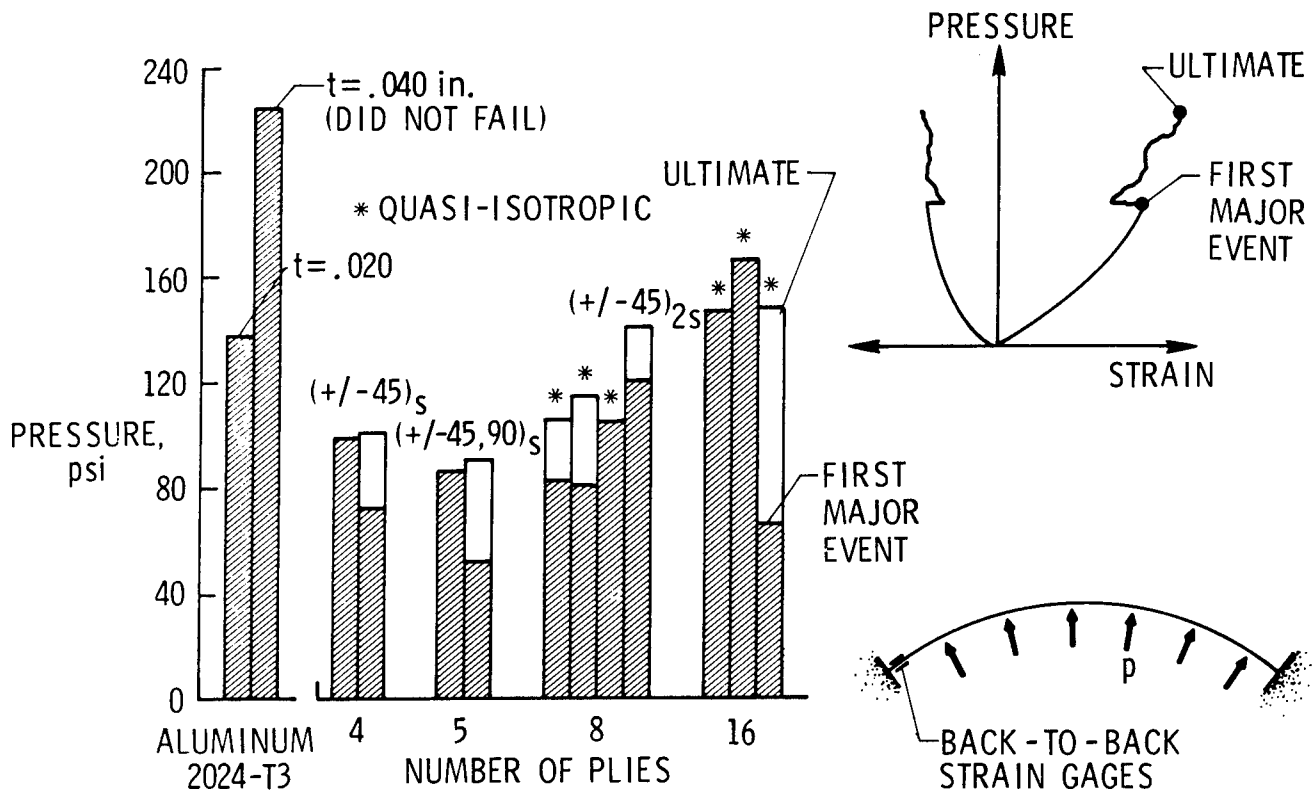


Figure 7

## EFFECT OF STIFFENER BENDING STIFFNESS ON PRESSURIZED GRAPHITE-EPOXY PANEL RESPONSE

The influence of stiffener bending stiffness on the response of a stiffened graphite-epoxy panel subjected to pressure loading was studied in reference 2 and some results of that study are shown in figure 8. The middle left and upper right figures show the out-of-plane deflection  $w$  distribution across the panel at midlength for 14 psi applied pressure. The middle left figure shows the effect of changing the stiffener height on the skin deflections. The shorter stiffener has relatively low bending stiffness and has relatively little effect on the deformation shape of the skin. The taller stiffener has relatively high bending stiffness and causes the skin to deform into a different shape than for the shorter stiffener. The upper right figure shows the effect of changing the stiffener attachment flange bending stiffness on the deformation shape of the skin for the taller stiffener. Increasing the thickness of the stiffener attachment flange changes the shape of the skin deformation near the stiffener. These results indicate that the deformation shapes of stiffened panels can be significantly influenced by the bending stiffnesses of the stiffener. These deformation shapes suggest that the stresses in the skin are also significantly influenced by the stiffener bending stiffnesses. An example of the interface normal stress between the flange and the skin of one of these panels near the edge of the flange was taken from reference 3 and is shown in the lower right figure. These results indicate that the interface stress gradients are influenced by the nonlinear response of the skin.

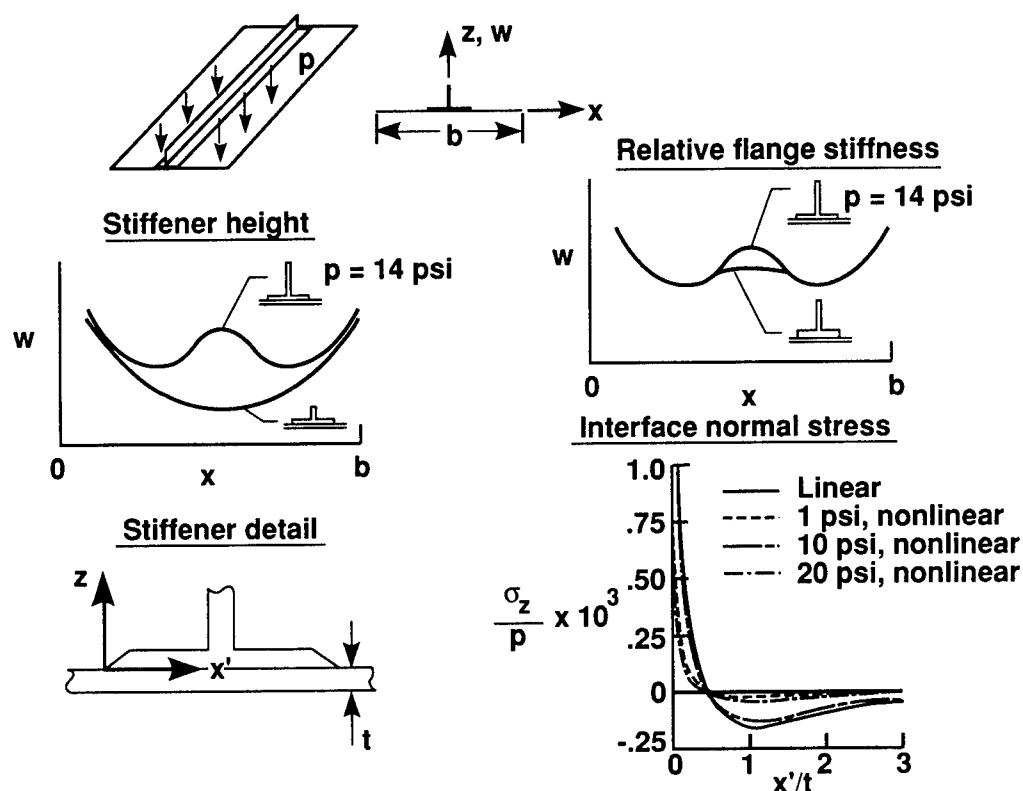


Figure 8

## NONLINEAR EFFECTS INFLUENCE BENDING RESPONSE OF COMPOSITE CYLINDERS

The effect of bending loads on graphite-epoxy cylinders is being studied by Mr. Hannes Fuchs under NASA Grant NAG1-343 with VPI and some results of nonlinear analyses from this study for  $[\pm 45/0/90]_S$  quasi-isotropic cylinder with length-to-radius ratio of 2 and radius-to-thickness ratio of 150 are shown in figure 9. The distribution of the radial deflection  $w$  normalized by the shell thickness  $t$  for different values of applied bending moment  $M$  normalized by the buckling moment  $M_{Cr}$  are shown in the right-hand figures for the generators with maximum compression and tension stresses. The contour plot shows the radial deflection pattern for the entire shell. These results indicate that the bending in the skin at the ends of the shell grows significantly on the compression side of the shell as the value of  $M$  is increased. These results suggest that high values of stresses will occur in this local region of high deformation gradients.

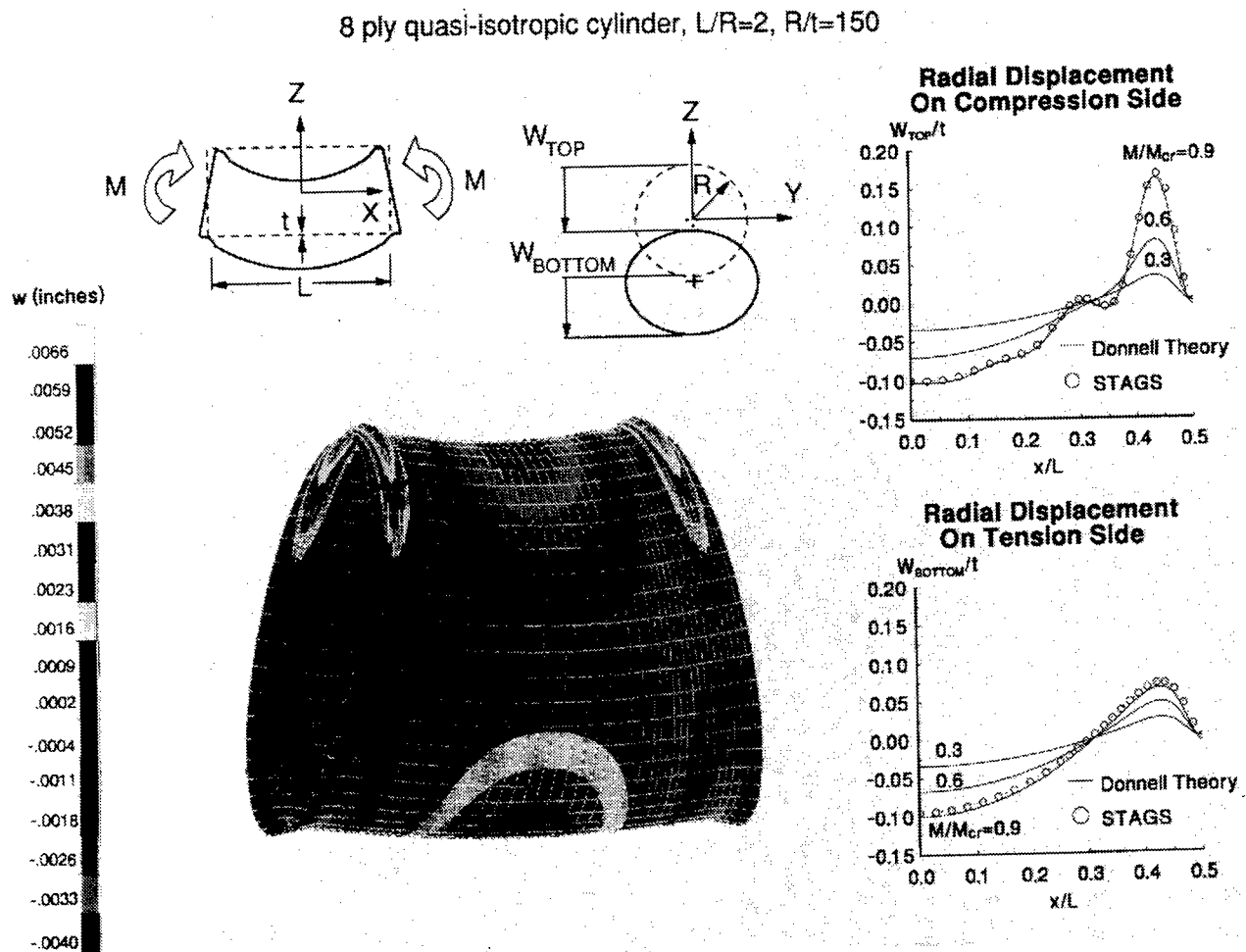
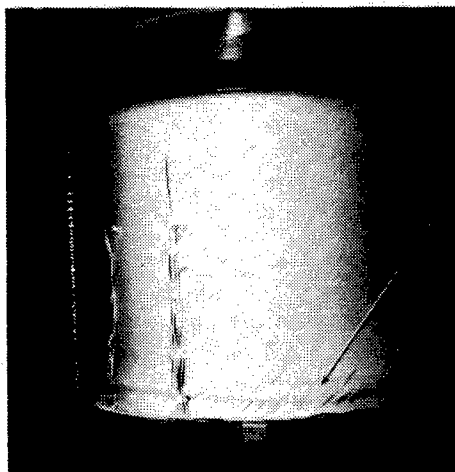
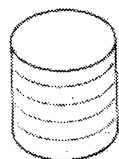


Figure 9

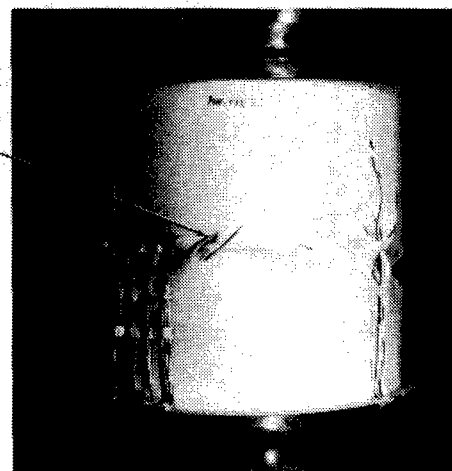
## COMPOSITE SHELL FAILURE MODE AFFECTED BY BUCKLING MODE SHAPE

The results of buckling tests for two graphite-epoxy cylindrical shells with different skin laminates are shown in figure 10. These shells are 16 inches long, 0.08 inches thick and have an 8-inch radius. The two shells buckled into different buckling mode shapes; the  $[\pm 45/\mp 45]_{2s}$  shell buckled into an axisymmetric mode shape with larger local bending deformations at the ends and the  $[\pm 45/0/90]_{2s}$  shell buckled into an asymmetric diamond-pattern mode shape with larger bending deformations along the nodal lines at midlength. Failure occurred for both shells where the local bending deformations were the largest. The results in figures 9 and 10 suggest that regions of a shell with significant local bending deformations should be considered potential failure locations. The results in figures 7 and 8 indicate that significant local bending deformations can also be caused by internal pressure. The combination of internal pressure and mechanical loads with compression and shear components may amplify the local bending deformations in a shell which may affect failure loads and locations.

Axisymmetric mode  
 $[\pm 45/\mp 45]_{2s}$



Asymmetric mode  
 $[\pm 45/0/90]_{2s}$



Failure  
location

- Failure initiates in zones with severe bending gradients
  - End bending boundary layer for axisymmetric mode
  - Interior nodal line for asymmetric mode

Figure 10



## EFFECT OF CIRCULAR CUTOUTS ON COMPOSITE CYLINDER COMPRESSION STRENGTH

The results of tests for four graphite-epoxy cylindrical shells with 1-inch-diameter cutouts and different skin laminates are shown in figure 11. The shells are 14 inches long, 0.08 inches thick and have an 8-inch radius. For the  $[\pm 45/0/90]_{2s}$ ,  $[\pm 45/0_4/\mp 45]_s$  and  $[\pm 45/90_4/\mp 45]_s$  shells, failure occurred at buckling. For the  $[\pm 45/\mp 45]_{2s}$  shell, failure occurred after buckling and at a lower load than the failure loads for the other laminates. Failure was influenced by the cutout for all four shells regardless of the mode shape. The curvature of the shell induces out-of-plane deformation and stress gradients near the cutout which cause interlaminar failures to occur near the cutout. These failures can propagate circumferentially around the shell as shown in the upper left sketch for the  $[\pm 45/0/90]_{2s}$  shell. Interlaminar failures also occurred near the cutout for the  $[\pm 45/0_4/\mp 45]_s$  shells, but interlaminar failures along the asymmetric buckling modal lines also occurred as shown in the upper right sketch. These results suggest that the local deformation and stress gradients associated with a local discontinuity in the shell, such as a cutout, can significantly influence the response and failure of the shell.

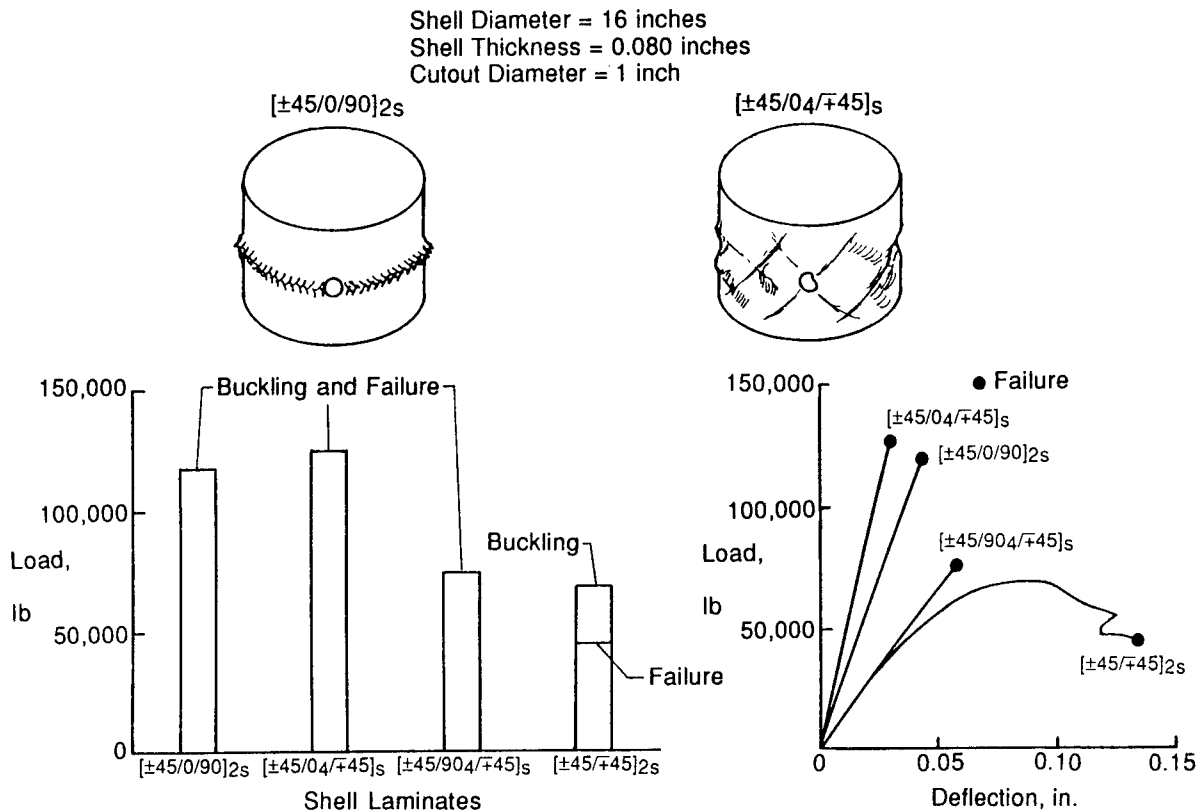


Figure 11

## **SCALING METHODOLOGY FOR COMPOSITE FUSELAGE SHELL STRUCTURES**

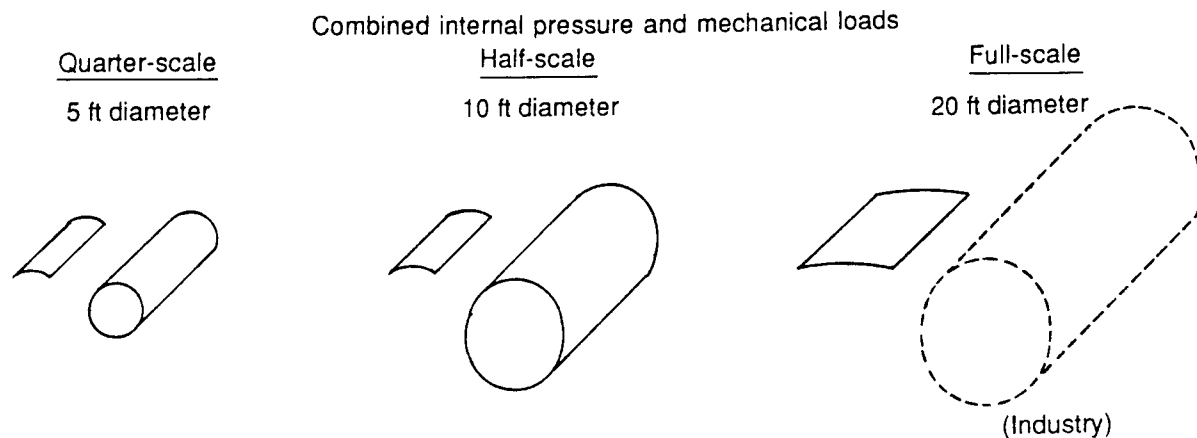
A part of the Langley composite fuselage shell structures research program is the development of structural scaling methodology for composite shells subjected to combined loads. One of the benefits of verified structural scaling methodology includes a reduction in specimen and testing costs during the research and development phases of a new structural design concept. Properly designed subscale models of an advanced design concept should identify some of the critical issues associated with the design before full-scale verification testing is begun. A subscale model, say half or quarter scale, could be used to understand the effects of changing structural parameters on structural behavior. Properly formulated structural scaling methodology should be based on the governing principles of structural mechanics and, as such, should help develop the underlying science and technology base for composite shell structures. Analysis methods verified by testing will be used to formulate the appropriate structural scaling methodology for composite shell structures and parametric studies will be conducted to determine the range of applicability of this structural scaling methodology.

- **Benefits**
  - **Reduced specimen and testing costs during R and D phases**
  - **Improved understanding of parameters that govern structural behavior**
  - **Helps provide underlying science and technology**
- **Scaling methodology based on verified analysis methods and parametric studies**

Figure 12

## SCALING METHODOLOGY FOR COMPOSITE FUSELAGE SHELL STRUCTURES

The Langley structural scaling methodology for composite fuselage shell structures will focus on the relationships between full-scale, half-scale and quarter-scale shells with a 20-foot-diameter shell taken as the full-scale shell. Both complete stiffened cylindrical shells and stiffened curved panels will be studied to understand the relationships between complete shells and panels and the effects of changes in geometric parameters on panel and shell behavior. These studies will help to determine what can and cannot be scaled effectively. These studies will also help to identify the interaction between structural parameters, loads and structural response characteristics when geometric parameters are changed. The effect of changing structural scale on failure mechanisms will also be studied. This analysis-based scaling methodology will be verified in the laboratory with test results.



- Determine what can be scaled
- Determine critical failure mechanisms and how they change with scaling
- Determine interaction between structural parameters, loads and structural response mechanisms for scaling methodology
- Verify analysis-based scaling methodology with test results

Figure 13

## NONDIMENSIONAL CURVATURE PARAMETER FOR BUCKLING OF ANISOTROPIC SHELLS

An example of analysis-base structural scaling methodology for curved composite panels is shown in figure 14 and is based on the analysis presented in reference 4. The buckling coefficients  $K_S$  for a curved panel loaded by a shear stress resultant  $N_{xy}$  is shown for an isotropic and an anisotropic panel in the figure as a function of the curvature parameter  $Z$ . The parameter  $Z$  is a function of the geometric parameters and mechanical properties of the curved panel. The isotropic curvature parameter is a simple function of radius  $R$ , width  $b$ , thickness  $t$  and Poisson's ratio  $\nu$  as shown in the left equation. The buckling results for an isotropic panel are shown in the left figure and the results indicate that  $K_S$  increases as  $Z$  increases beyond a value of about 10. The effect of changing any of these parameters can be determined from the curve shown in the lower left figure. The anisotropic curvature parameter is a function of radius  $R$ , width  $b$  and the membrane and bending stiffnesses of the panel laminate as indicated in the right equation. The buckling results for a  $[(\pm 45)_N]_S$  family of composite panels is shown in the right figure. These results indicate that thinner composite panels (i.e., those with low values of  $N$ ) are affected by the anisotropy of the panel, and buckling results depend on the direction of the applied shear load relative to the panel coordinate axes. Anisotropic coupling can increase or decrease the panel buckling load depending on the direction of the applied load as indicated by the dashed curves in the right-hand figure. Thicker panels (i.e., larger values of  $N$ ) approach orthotropic panel behavior, and the buckling results are represented by the single solid curve in the right-hand figure.

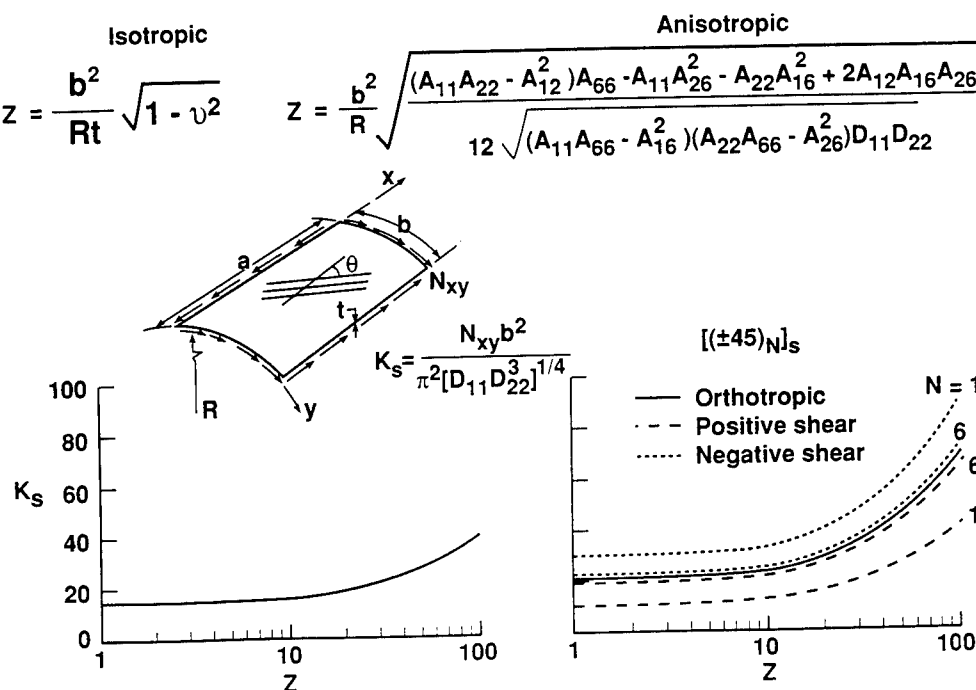


Figure 14

## **COMPOSITE FUSELAGE SHELL STRUCTURES EXPERIMENTS**

Experiments will be conducted as part of the Langley composite fuselage shell structures program to understand the response and failure characteristics of stiffened panels, stiffened shells and structural elements for the panels and shells. Full-scale technology benchmark curved stiffened panels from the Langley Advanced Composites Technology (ACT) program will be tested to verify the behavior of candidate shell design concepts and half-scale pathfinder stiffened shells will be subjected to combined internal pressure and mechanical loads to identify and verify shell behavioral characteristics that cannot be studied at a panel level. These experiments will also be used to verify structural scaling methodology for composite shell structures.

- **Experiments to understand response and failure of stiffened shells, panels and elements**
- **Benchmark curved stiffened panels**
- **Pathfinder stiffened shell structures**
- **Experiments to verify scaling methodology**

Figure 15

## PRESSURE BOX

Stiffened panels subjected to combined hoop and axial loads will be tested in the pressure-box fixture shown schematically in figure 16. Internal pressure will be applied to the panel which will generate hoop stress reactions where the panel is attached to the fixture. Hydraulic actuators will be used to generate the axial stresses.

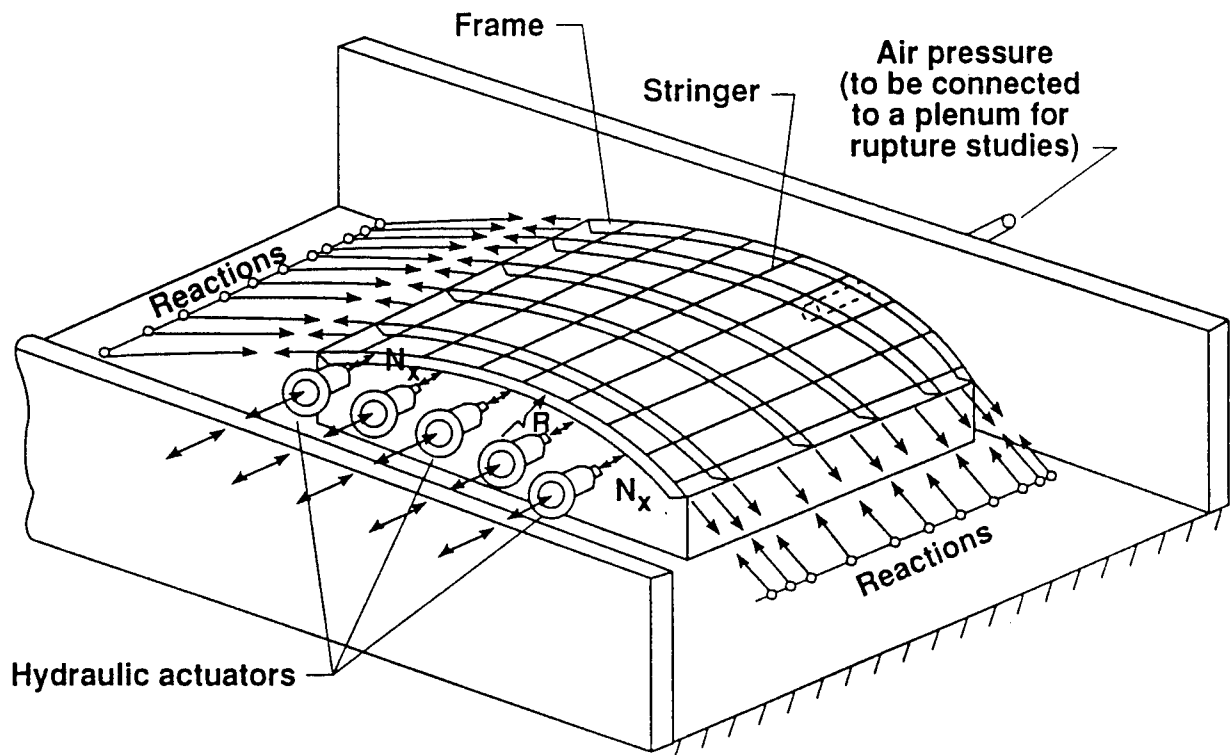


Figure 16

## CYLINDER TEST APPARATUS

Stiffened panels and shells subjected to combined loads with a shear component will be tested in the cylinder test apparatus shown schematically in figure 17. A closed-cell test section will be mounted to a rigid backstop at Langley with load introduction adaptor fixtures between the test specimen and the backstop and loading platen. Hydraulic jacks will be used to apply axial, bending, torsion and vertical shear loads to the load platen. Internal pressure will be applied using hydraulic and pneumatic pressure as appropriate.

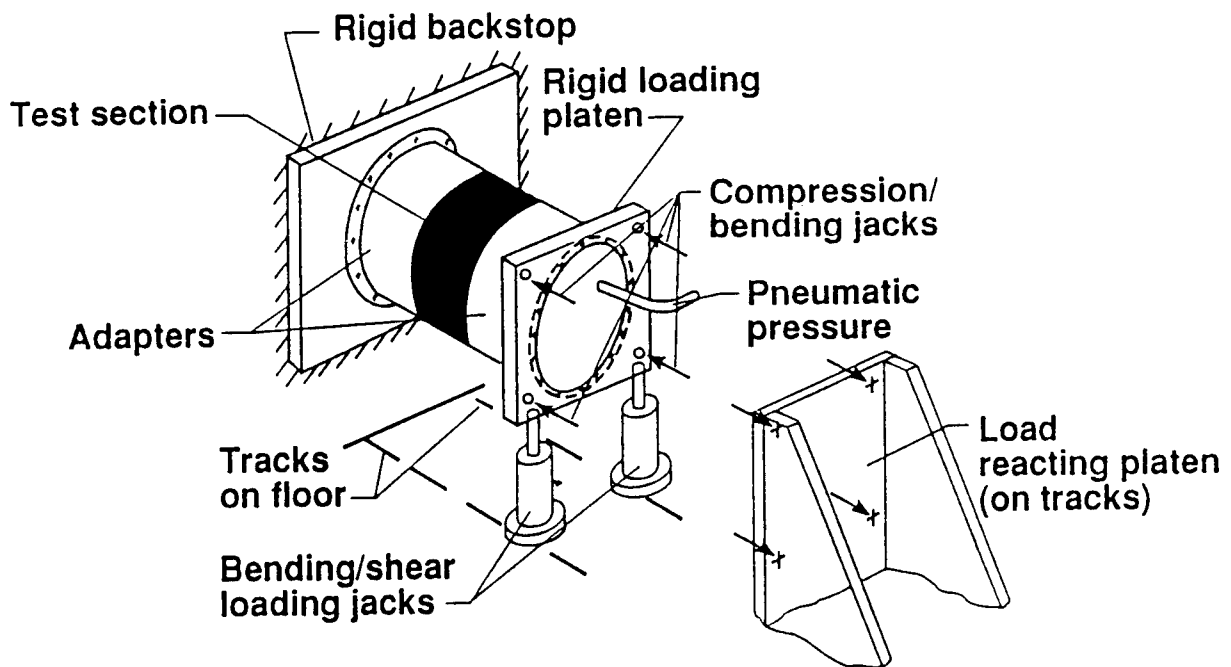


Figure 17

## ANALYSIS OF COMPOSITE FUSELAGE SHELL TEST

An aluminum load-introduction adaptor shell is currently being designed and some analytical results for a composite shell loaded by internal pressure and axial tensile loads are shown in figure 18. Attention is being focused on the interaction between the composite test specimen and the aluminum load-introduction adaptor shell to assure that the composite shell behavior is what is expected and that no premature failures at the interface between the composite and aluminum shells occur. The geometrically nonlinear behavior of the composite shell specimen is being considered in the design of the aluminum adaptor shell.

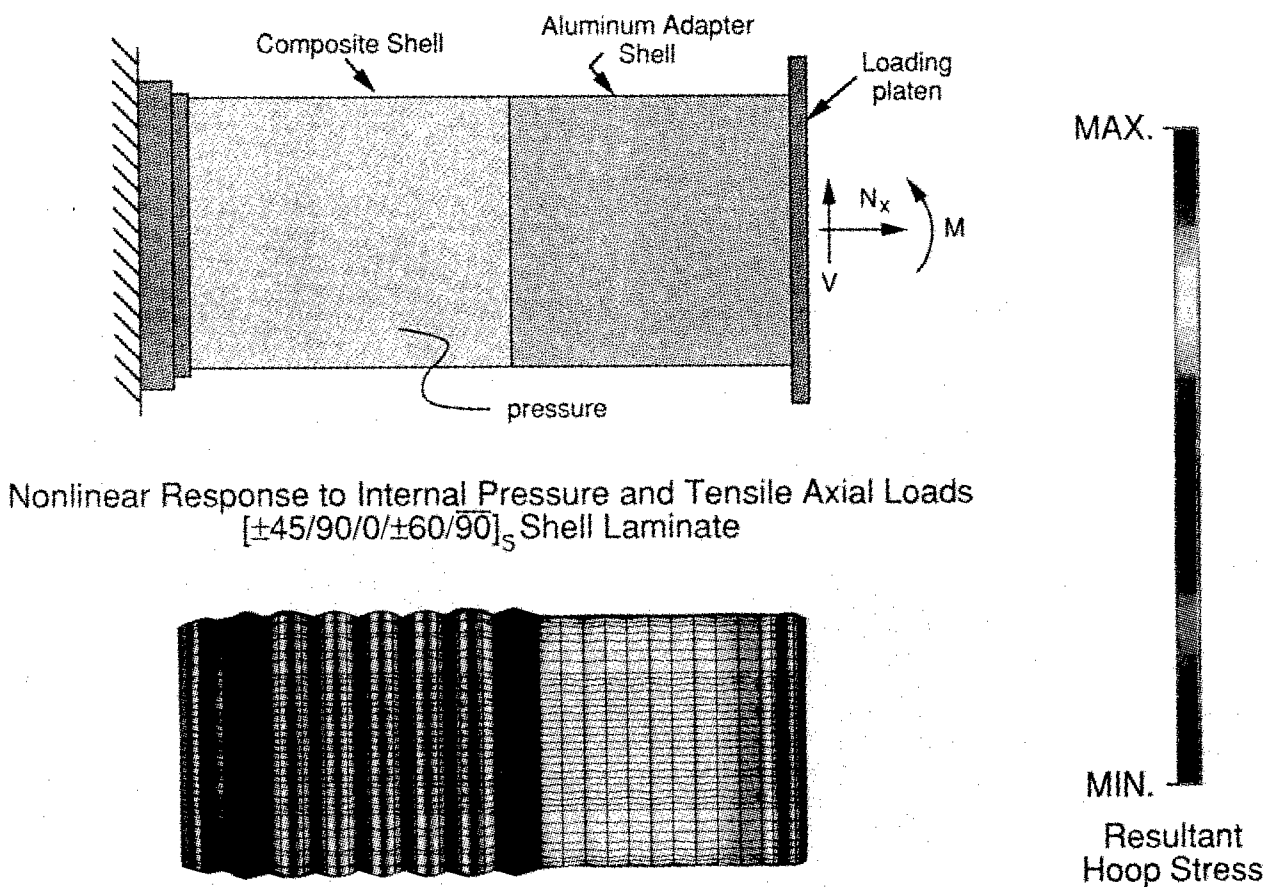


Figure 18



## D-BOX FOR CURVED PANEL TESTS

Large-scale curved stiffened panels subjected to combined loads with a shear component will be tested in the closed-cell D-shaped box fixture shown schematically in figure 19. The test panel will be attached to a larger load-introduction or "dummy" panel with the same radius of the test specimen. Analytical studies of the test panel and load-introduction panel configuration will be conducted to quantify the test panel loading including the shear stress resultant  $N_{xy}$  and the normal stress resultants and loads in the skin, axial stiffeners and frames  $N_{skin}$ ,  $N_s$ , and  $N_f$ , respectively.

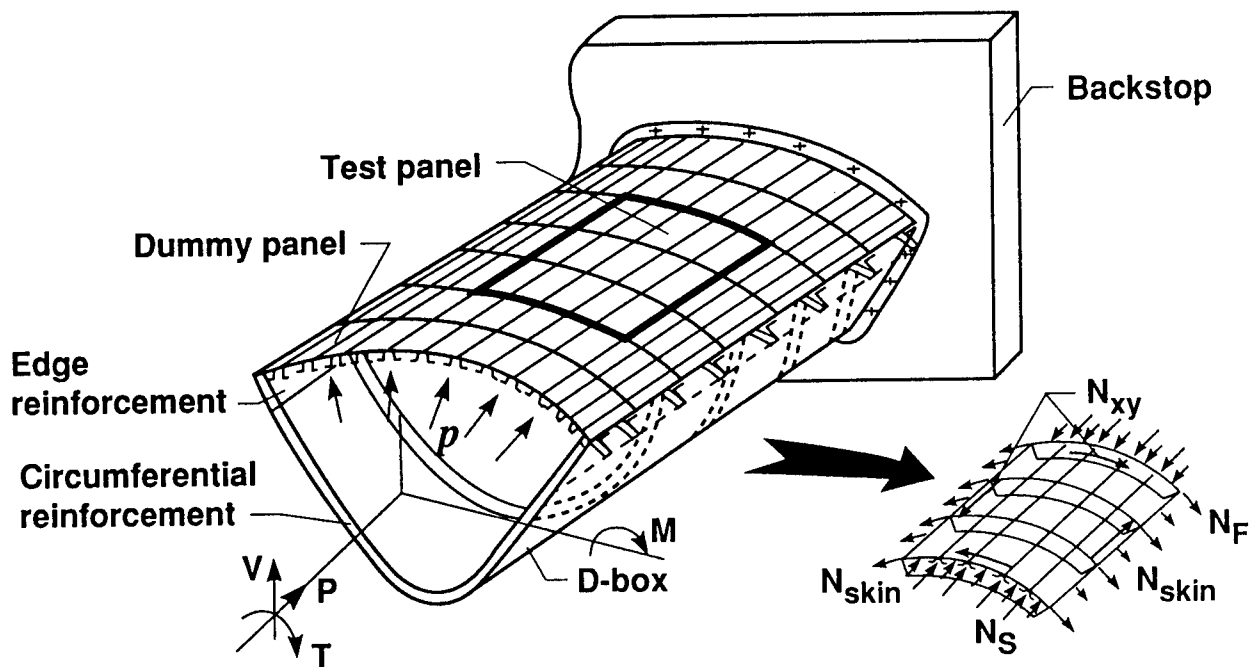


Figure 19

## **DAMAGE TOLERANCE AND PRESSURE CONTAINMENT FOR THIN-WALLED COMPOSITE SHELL STRUCTURES**

Damage tolerance studies in the Langley composite fuselage shell structures research program will focus on low-energy impact damage and crack growth issues and a limited assessment of high-energy impact damage issues will also be conducted. For low-energy impact damage, a study is being conducted to determine the level of impact damage necessary to cause leaks to occur in thin-walled pressurized composite shells. Studies will be conducted to determine the residual strength of locally damaged shell structures that are subjected to combined internal pressure and mechanical loads. Damage growth characteristics will be identified for curved stiffened panels and shells to help identify critical damage parameters. Damage containment concepts will be developed and evaluated to help provide safer designs. The results of the studies should help define damage tolerance design criteria for thin-walled shells that leak before they burst. A limited high-energy impact damage study will also be conducted to assess the sensitivity of pressurized composite shell structures to very severe damage conditions.

- **Low-energy impact damage and cracks**
  - **Determine damage necessary to cause leaks in pressurized shells**
  - **Determine residual strength of damaged panels and shells subjected to combined loads**
  - **Determine damage growth characteristics and critical damage parameters**
  - **Evaluate damage containment concepts**
  - **Determine damage-tolerance and leak-before-burst criteria**
- **High-energy impact damage**
  - **Assess sensitivity of pressurized composite shell structures to high-energy impact damage**

Figure 20

## EFFECTS OF SLITS ON FAILURE OF COMPOSITE SHELLS SUBJECTED TO INTERNAL PRESSURE

Some results of a study of the effects of damage on the burst strength of 12-inch-diameter graphite-epoxy cylindrical shells are shown in figure 21. These results were obtained by Massachusetts Institute of Technology under NASA grant NAG1-991 and are reported in reference 5. Thirty-inch-long unstiffened cylinders with  $[90/0/\pm 45]_S$ ,  $[\pm 45/0]_S$  or  $[\pm 45/90]_S$  laminates were pressurized to failure with slits of length  $2a$  machined into the shell at midlength. The figure shows that the burst pressure of the shells decreases as the slit length  $2a$  increases and that laminate stacking sequence affects the burst strength.

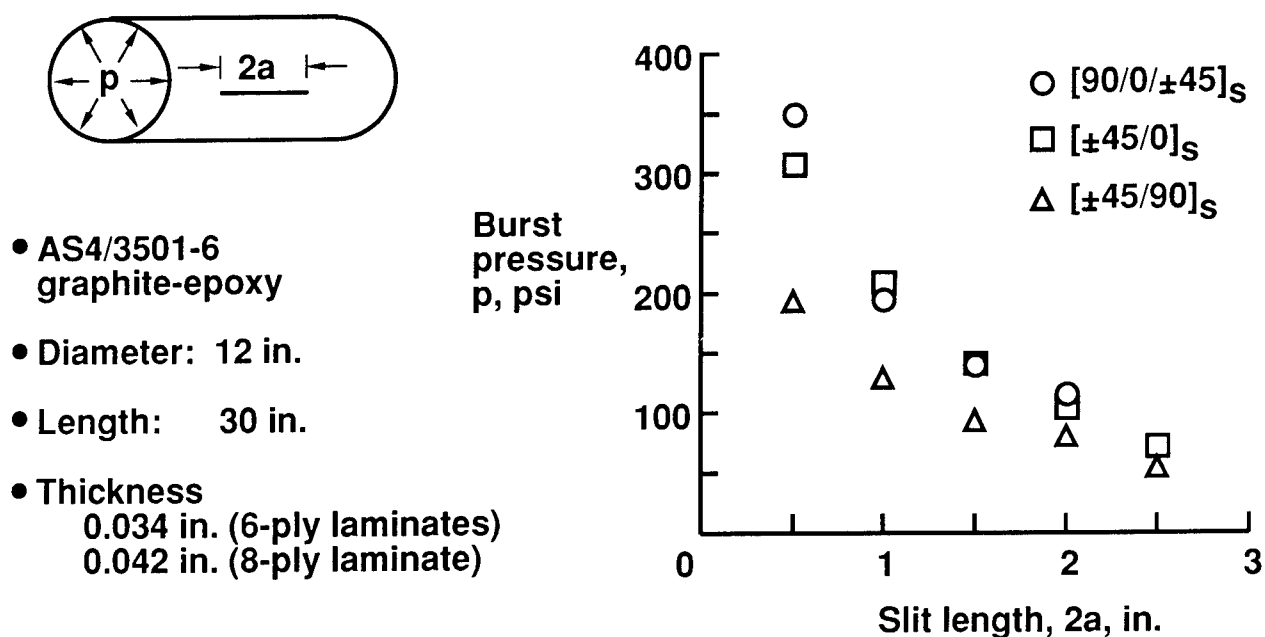


Figure 21

## HOOP STRESSES IN COMPOSITE FUSELAGE SHELL WITH DAMAGE

The effect of damage on a full-scale frame and stringer stiffened composite shell subjected to internal pressure and axial tensile loads is shown in figure 22. The shell model is based on the current Boeing design being developed under NASA contract NAS1-18889 and has a 122 inch radius and a 264 inch length and the skin is made from a  $[\pm 45/90/0/\pm 60/90]_s$  graphite-epoxy laminate. The hoop stress resultant distribution for the undamaged shell is shown in the left figure. A 22-inch-long crack was modeled in the skin of the fuselage crown with 11 inches of the crack on either side of the frame at midlength and this frame was also modeled as being broken. The hoop stress resultant distribution for the damaged shell is shown in the right figure. The results indicate that severe hoop stress gradients are present in the vicinity of the damage and the effect of the damage beyond the 2 frames on either side of the crack is shown in detail in the right-hand inset of the right figure. The local bulging of the skin associated with the local radial deflection gradient near the crack is shown in the left-hand inset of the right figure.

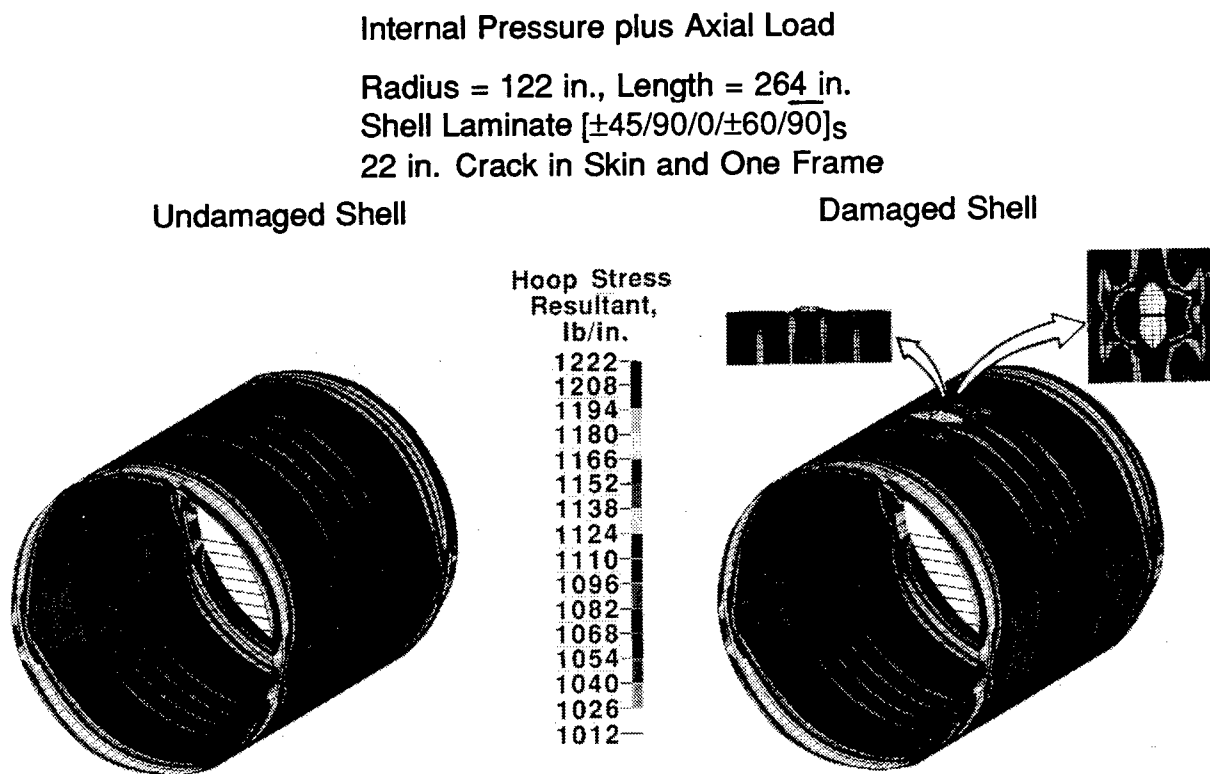


Figure 22

## COMPOSITE FUSELAGE SHELL STRUCTURES RESEARCH

The principal activities for the Langley composite fuselage shell structures research program are shown in figure 23 by fiscal year from FY92 to FY95.

### Principal Activities by Fiscal Year

#### FY92

- Develop and evaluate panel and shell concepts and designs
- Analyze response of panels with design details and conduct design studies
- Test panels for effects of discontinuities, impact damage, and internal pressure

#### FY93

- Conduct nonlinear analyses and design studies for panels and shells
- Test panels subjected to combined loads for response and failure mechanisms
- Analyze response of panels and shells with design details and combined loads
- Test shells for effects of discontinuities, impact damage

#### FY94-FY95

- Test shells subjected to combined loads for response and failure mechanisms
- Verify damage containment analyses and concepts for pressurized shells
- Verify scaling methodology for panels and shells and conduct nonlinear analyses

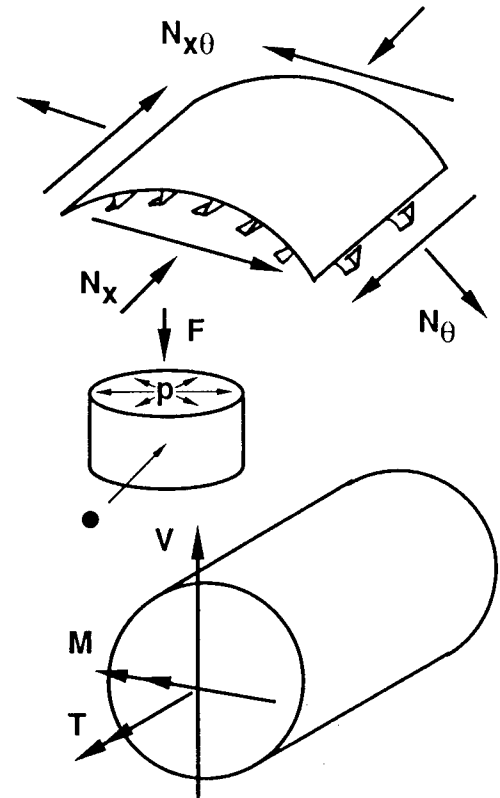


Figure 23

## COMPOSITE FUSELAGE SHELL STRUCTURES RESEARCH SCHEDULE

The planned schedule for the Langley composite fuselage shell structures program is shown in figure 24 through fiscal year FY95.

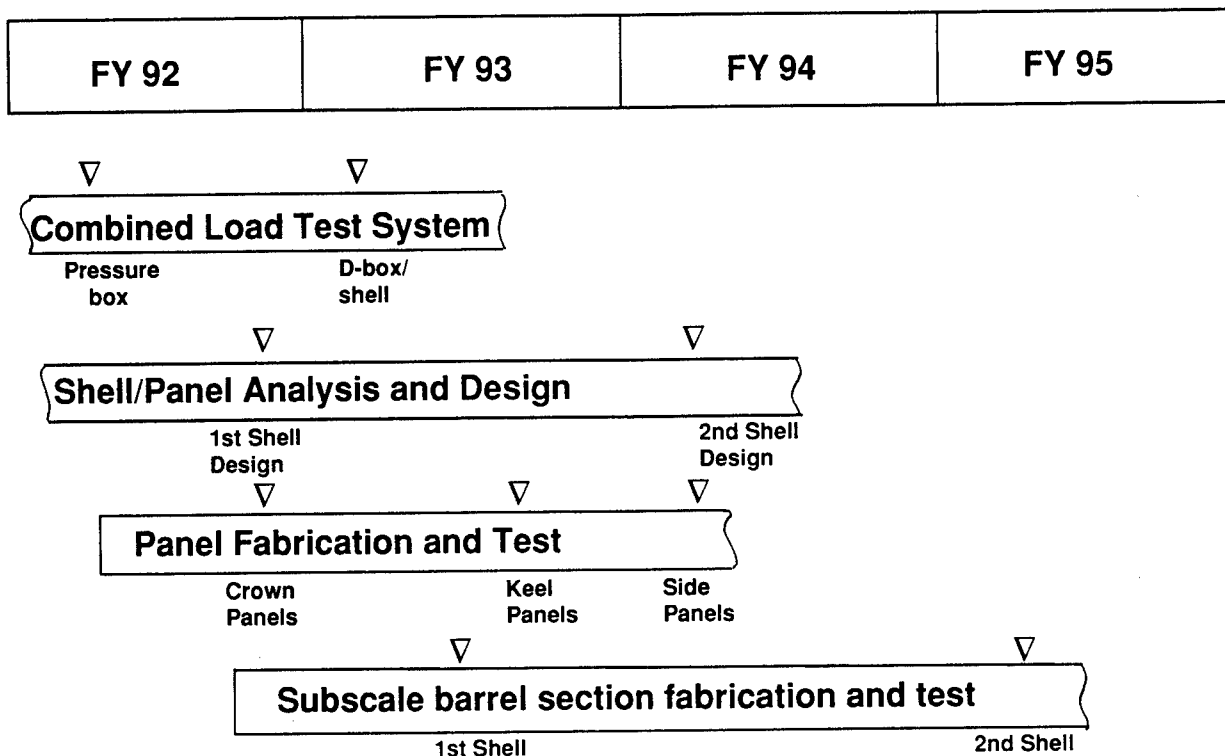


Figure 24

## CONCLUDING REMARKS

The composite fuselage shell structures research program at the NASA Langley Research Center will develop verified structural mechanics methodologies for reliably predicting the response and failure of composite frame- and stringer-stiffened shell structures and curved stiffened panels subjected to combined internal pressure and mechanical loads and to local damage. The mechanical loads will include compression, tension, bending, vertical shear and torsional loads. Structural analysis methods that predict the nonlinear response and failure of composite fuselage shell structures subjected to combined loads will be developed and applied to candidate shell designs. Geometrically nonlinear behavior associated with the effects of internal pressure on skin deformation and postbuckling behavior will be included in the analysis and design of candidate shell structures. Structural details, discontinuities and eccentricities that generate local stress and deformation gradients and the interaction between the subcomponents of stiffened shell structure will be studied in the program. Structural sizing procedures that provide minimum-weight designs for stiffened composite fuselage shells subjected to combined loads will be developed and used to conduct parametric studies to determine the sensitivity of the shell behavior to changes in structural parameters. Structural scaling methodology will be developed for composite fuselage shells subjected to combined loads to relate full-scale designs to half-scale and quarter-scale models of these designs. Tests will be conducted on technology benchmark curved stiffened panels and pathfinder stiffened shells to identify critical failure mechanisms, to verify structural analysis methods, and to understand the effects of local gradients and local damage on composite shell behavior. Studies will be conducted to determine the damage tolerance and propagation characteristics and residual strength of damaged composite stiffened shells subjected to combined internal pressure and mechanical loads and damage containment concepts will be explored. The Langley composite fuselage shell structures research program will contribute to the development of the structures technology necessary to develop full-scale pressurized composite stiffened fuselage structures for future transport aircraft.

## REFERENCES

1. Boitnott, R. L.; Starnes, J. H., Jr.; and Johnson, E. R.: Nonlinear Response of Internally Pressurized Graphite-Epoxy Cylindrical Panels. AIAA Paper No. 84-0955, May 1984.
2. Hyer, M. W.; Loup, D. C.; and Starnes, J. H., Jr.: Stiffener/Skin Interactions in Pressure-Loaded Composite Panels. AIAA Journal, Vol. 28, No. 3, March 1990, pp. 532-537.
3. Hyer, M. W.; and Cohen, D.: Calculation of Stresses and Forces Between Skin and Stiffener in Composite Panels. AIAA Journal, Vol. 26, No. 7, July 1988, pp. 852-857.
4. Nemeth, M. P.: Nondimensional Parameters and Equations for Buckling of Symmetrically Laminated Thin Elastic Shallow Shells. NASA TM 104060, March 1991.
5. Ranniger, C. U.: Damage Tolerance and Arrest Characteristics of Pressurized Graphite/Epoxy Tape Cylinders. M. S. Thesis, Massachusetts Institute of Technology, June 1991. TELAC Report 91-11.



**THIS PAGE INTENTIONALLY BLANK**

# **STRUCTURAL TESTING OF THE TECHNOLOGY INTEGRATION BOX BEAM**

**C. F. GRIFFIN**

**LOCKHEED AERONAUTICAL SYSTEMS COMPANY  
MARIETTA, GEORGIA**

## **SUMMARY**

A full-scale section of a transport aircraft wing box was designed, analyzed, fabricated and tested. The wing box section, which was called the technology integration box beam, contained blade stiffened covers and T-stiffened channel spars constructed using graphite/epoxy materials. Covers, spars and the aluminum ribs were assembled using mechanical fasteners.

The box beam was statically tested for several loading conditions to verify the stiffness and strength characteristics of the composite wing design. Failure of the box beam occurred at 125% of design limit load during the combined upbending and torsion ultimate design load test. It appears that the failure initiated at a stiffener runout location in the upper cover which resulted in rupture of the upper cover and portions of both spars.

## **INTRODUCTION**

Current applications of composite materials to transport aircraft structure, most of which are stiffness critical secondary structural components, have demonstrated weight saving from 20 to 30 percent. The greatest impact on aircraft performance and cost will be made when these materials are used for fabrication of primary wing and fuselage structures that are 30 to 40 percent lighter than their metal counterparts and have a reduced acquisition cost. Achievement of this goal requires the integration of innovative design concepts, improved composite materials, and low cost manufacturing methods.

In 1984, the Lockheed Aeronautical Systems Company began a program to develop engineering and manufacturing technology for advanced composite wing structures on large transport aircraft. The program was sponsored by the National Aeronautics and Space Administration (NASA) under contracts NAS1-17699 and NAS1-18888 and Lockheed Aeronautical Systems Company independent research and development funds.

The selected baseline component is the center wing structural box of an advanced version of the C-130 aircraft. A preliminary design of a composite wing box was completed as were many design development tests. A full-scale section of the wing box was designed in detail, analyzed, fabricated and tested. This paper will summarize the major technical achievements of the box beam test program.

## **BOX BEAM DESIGN AND ANALYSIS**

### **Geometry**

The technology integration box beam, shown in Figure 1, represents a highly loaded section of the C-130 center wing box. The test section of the box is 150 inches long, 50 inches wide, and 28 inches deep, and contains a large access hole in the upper cover, wing box to fuselage mainframe joints, and center wing to outer wing joints.

### **Design Loads and Criteria**

Design loads for the box beam were based on baseline aircraft requirements. Maximum ultimate loads are 26,000 lb/inch compression in the upper covers and 24,000 lb/inch tension in the lower covers. Ultimate spar web shear flow is 4,500 lb/inch. These loads were combined with the appropriate pressure loads due to beam bending curvature and fuel. The stiffness requirements for the wing were established to meet the commercial flutter requirements specified in FAR Part 25. Stated briefly, at any

wing station the composite wing bending stiffness and torsional stiffness could not be less than 50 percent of the baseline wing, and the ratio of the bending to torsional stiffness must be greater than one but not more than four.

Structural requirements for damage tolerance considered civil as well as military criteria. Thus, the criteria used for this program requires the structure to have ultimate strength capability with the presence of barely visible impact damage anywhere within the structure. Barely visible impact damage is defined as either the kinetic energy required to cause a 0.1 inch deep dent or a kinetic energy of 100 ft-lb with a 1.0 inch diameter hemispherical impactor, whichever is least.

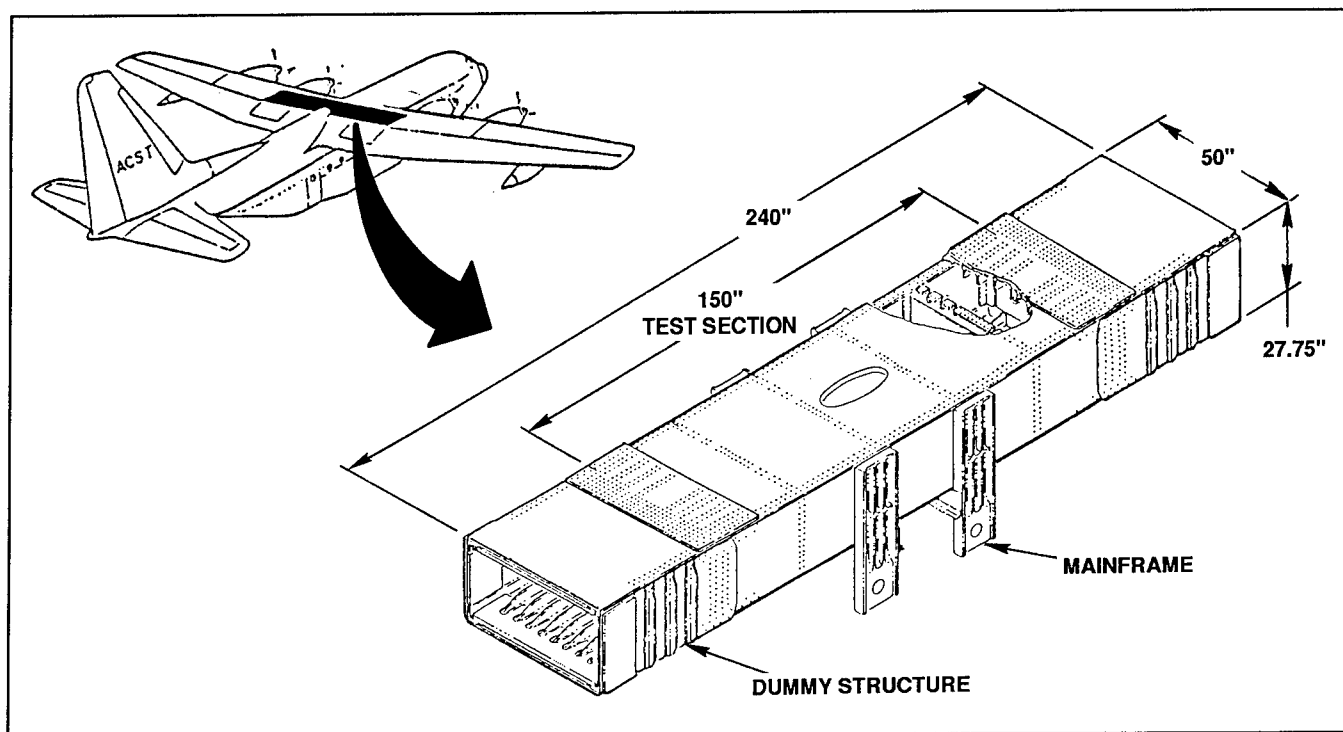


Figure 1. Technology Integration Box Beam  
Cover Design

The lower cover design, shown in Figure 2, consists of back-to-back channels laid up on a skin laminate to form a blade stiffened panel. Note that the flanges of the channels contain additional 0 degree plies compared to the web, resulting in a blade containing 67 percent 0 degree plies, 29 percent plus/minus 45 degree plies, and 4 percent 90 degree plies. The blades, which are spaced at 5 inches, are tapered in height to account for the increased axial loading from the outboard joint to the wing centerline. A constant thickness laminate containing 27 percent 0 degree plies, 64 percent plus/minus 45 degree plies, and 9 percent 90 degree plies makes up the skin.

The configuration of the upper cover, shown in Figure 3, is similar to the lower cover with the exception that the blades are slightly taller. Also, the central bay of the upper cover is reinforced by a hat stiffener which is terminated at each rib location. An 8 inch wide strip of the cover laminate below the hat stiffener has a lay-up of 44 percent 0 degree plies, 46 percent plus/minus 45 degree plies and 9 percent 90 degree plies. The remainder of the upper skin is the same laminate as was used for the lower skin. The covers were constructed using three types of AS4/974 fabric; unidirectional, bi-directional and plus/minus 45 degree bias.

### Spar Design

A T-stiffened channel configuration, shown in Figure 4, was selected for the front and rear spars. Spar webs and caps are of constant thickness with the exception of the doublers located at the mainframe

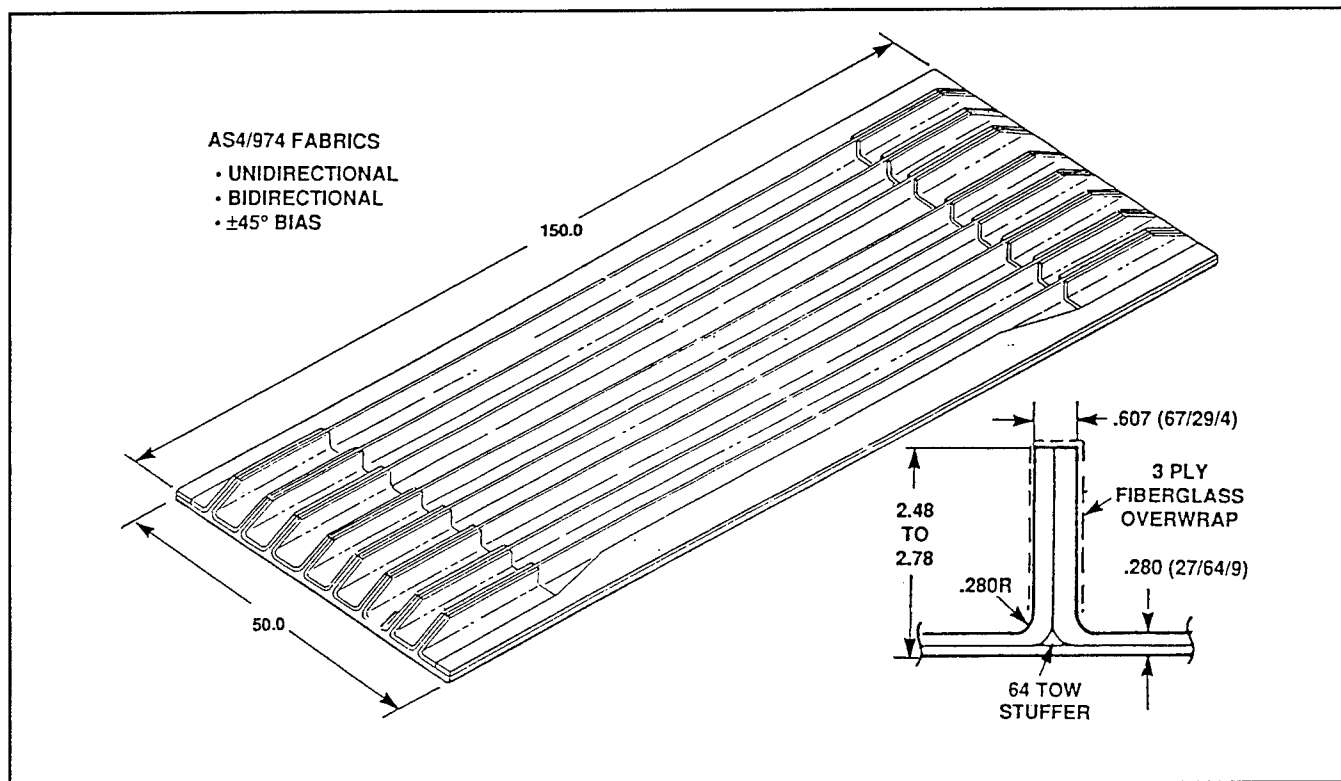


Figure 2. Lower Cover Box Beam Design

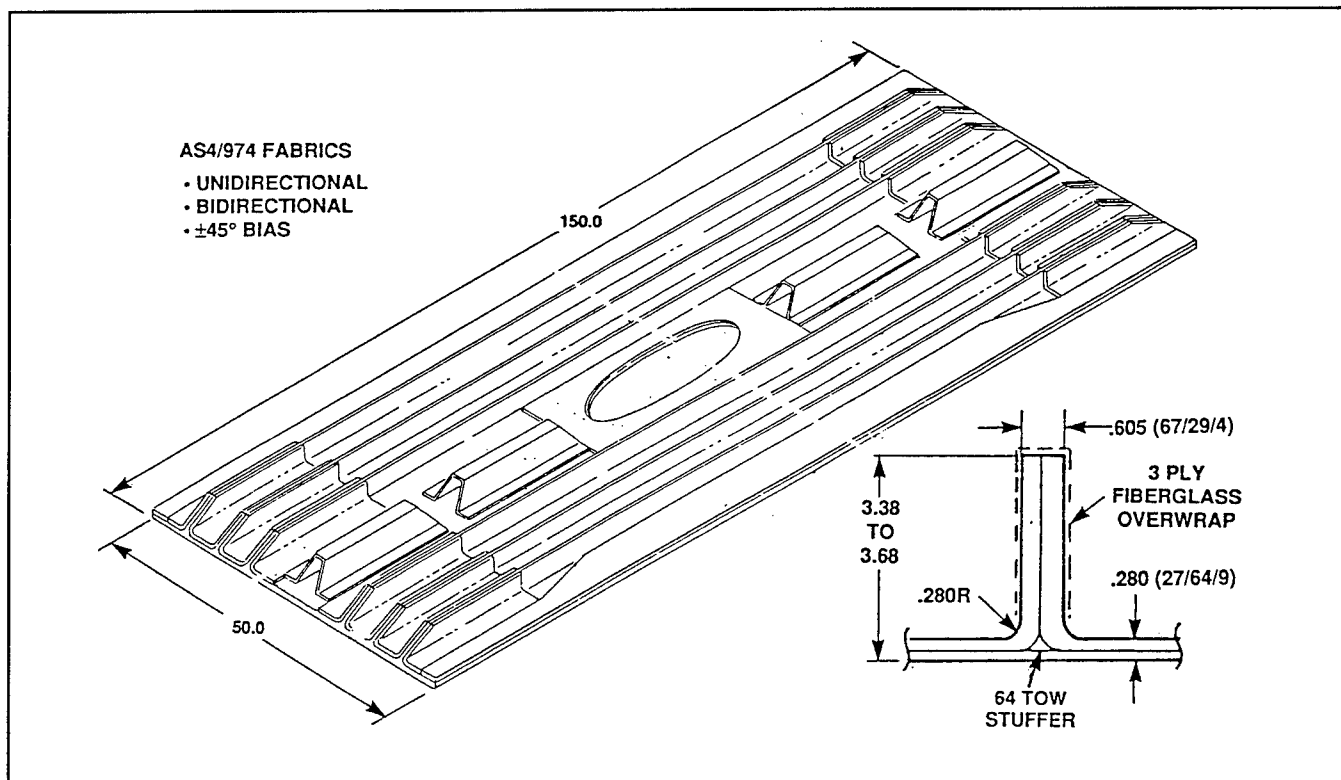


Figure 3. Upper Cover Box Beam Design

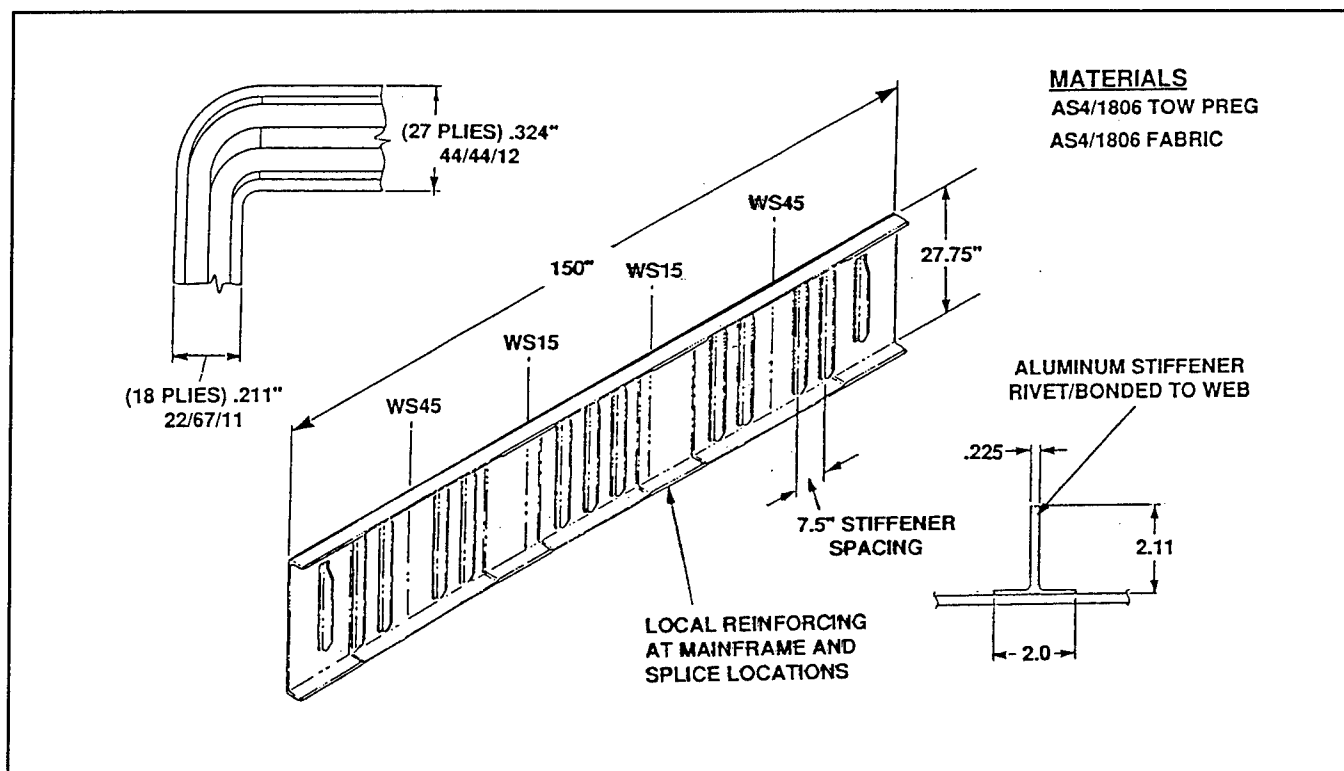


Figure 4. Spar Assembly

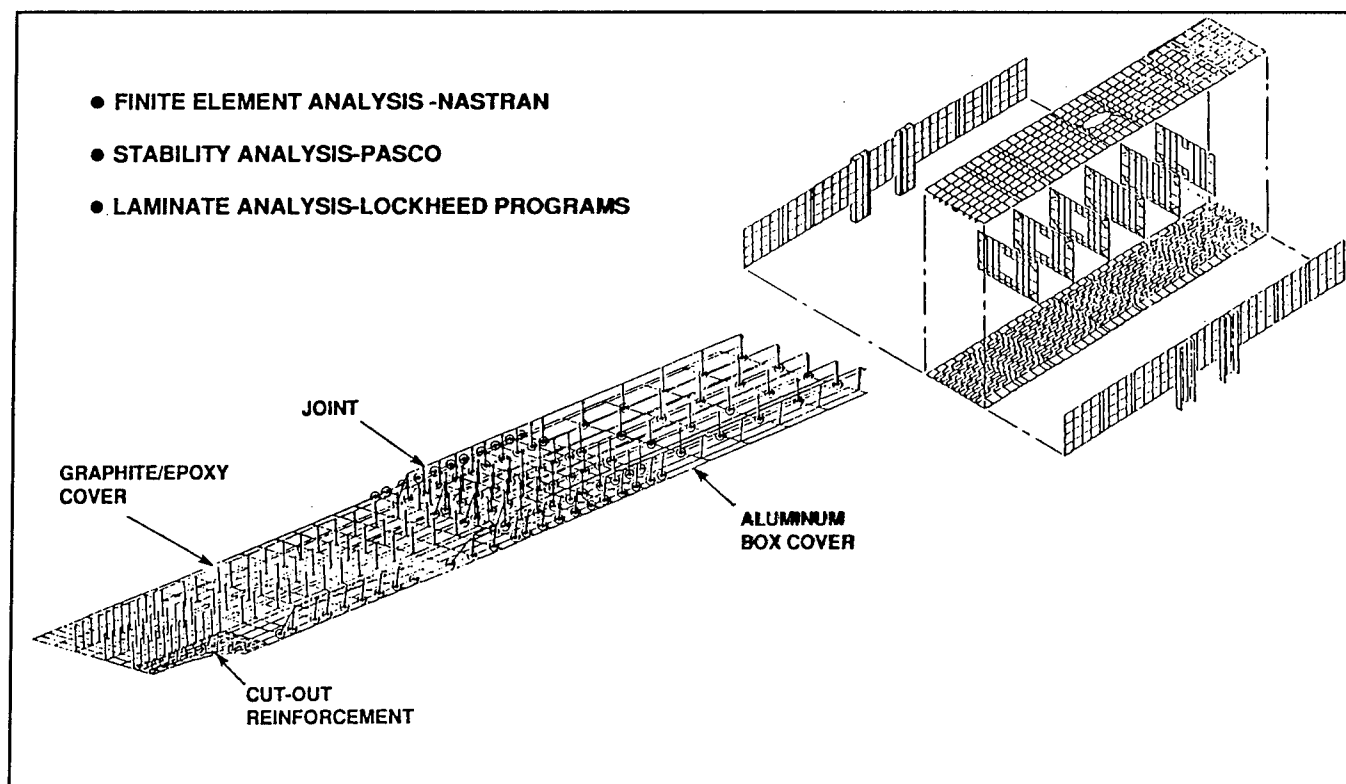


Figure 5. Structural Analysis Methods

attachment and spar splice locations. The spars were filament wound using AS4/1806 towpreg with unidirectional, bidirectional, and bias fabrics used for the spar cap inserts, and doublers. The stiffeners were made of aluminum and were bolted and bonded to the spar webs.

### Ribs and Box Assembly

For the box beam, a J-stiffened skin configuration constructed of aluminum was used for all of the ribs. T-shaped shear ties connect the rib webs and rib caps to the covers. All ribs were mechanically fastened to the spar webs and covers. The spar caps were mechanically fastened to the covers using a double row of fasteners.

### Structural Analysis

A detailed structural analysis was completed on the box beam using the methods shown in Figure 5. A three-dimensional finite element model was constructed and used to obtain internal loads for sixteen loads cases. Detailed two-dimensional models were used to analyze the cover chordwise joint, cover cut-out area, and the mainframe to spar joint. The compression stability of the covers was predicted using the PASCO computer code obtained from NASA. Several Lockheed computer programs were used to obtain local stresses and strains using the internal loads obtained from the NASTRAN models.

Figure 6 presents the typical design allowables obtained for the AS4/1806 and AS4/974 materials. These allowables were computed based on laminate tests, and in the case of the impacted laminate allowables, stiffened panel tests. Note that allowable strain is plotted as a function of the percentage of plus/minus 45 degree plies within the laminate minus the percentage of 0 degree plies. This value is called the AML for angle minus longitudinal plies. For example, a quasi-isotropic laminate has an AML value of 25. The blade stiffener on the cover has an AML of -38 and the majority of the cover skin a value of 37.

Margins of safety were computed for numerous locations on the covers and spars using applied strains and design allowable strains. Minimum margins of safety are presented in Figure 7. Both the upper cover and spar webs have a 0 margin of safety for the impact damaged condition. The lower cover and the spar caps are critical for bearing/bypass and net tension, respectively.

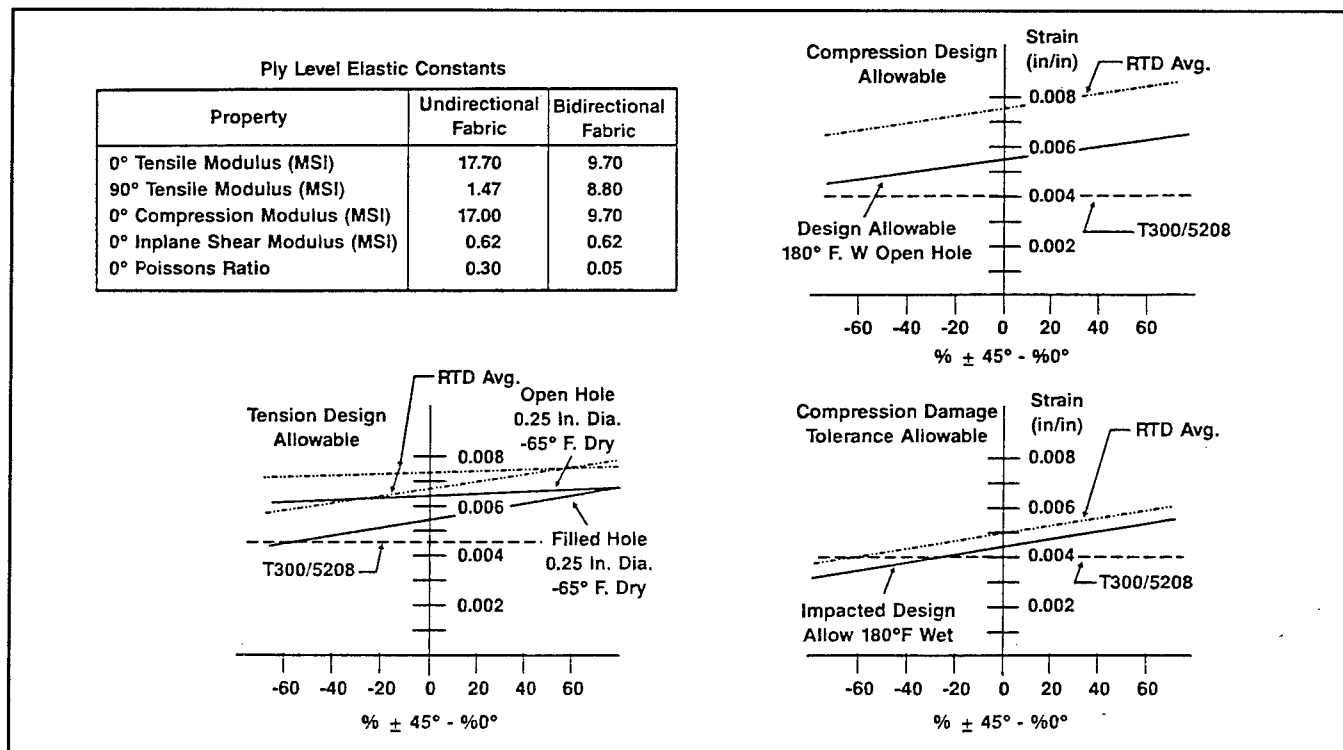


Figure 6. Design Allowables

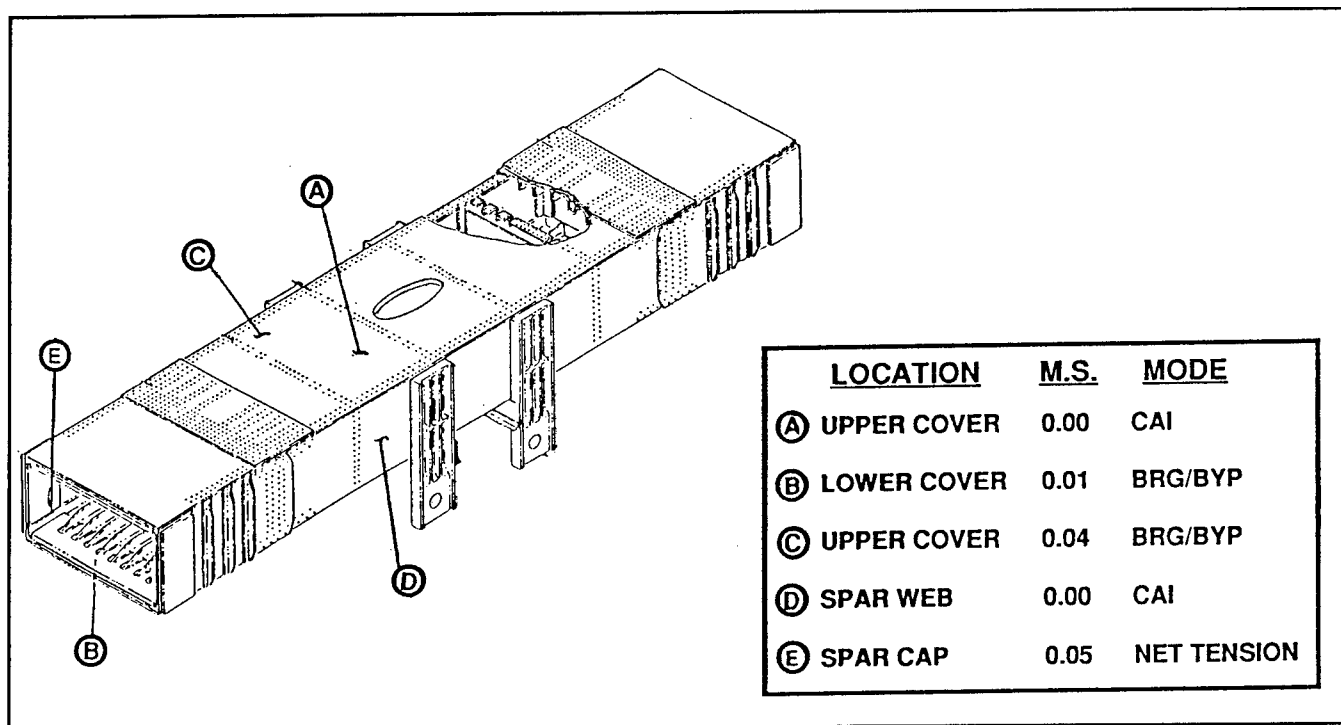


Figure 7. Minimum Margins of Safety

## BOX BEAM TEST PROGRAM

### Box Beam Test Set-Up

Since the box beam was tested for combined bending and torsion loads, metal extensions were attached to the ends of the composite material box to obtain the desired vertical shear and bending moment distributions. As shown in Figure 8, the vertical shear loads were applied by two hydraulic jacks at each end of the beam. These loads were reacted at the four mainframe locations near the center of the beam. Axial strain gages, rosette strain gages and deflection gages were utilized to measure the deflections and strains of the box beam during the tests. Strain gages were also applied to the reaction struts to measure the vertical shear load reactions.

### Stiffness Tests

After conducting an upbending test to 20 percent of design ultimate load to verify the performance of the instrumentation, a series of stiffness tests were performed. For these tests, the box beam was loaded to 30% of design ultimate for the upbending, downbending and torsion design conditions. Deflection gages, mounted spars at various positions along the span were used to measure the vertical displacements of the test specimen. For the beam bending conditions and the torsional loading condition the deflections agreed with the predicted values. The results of these tests verified that the design met or exceeded the stiffness requirements for the center wing box.

### Strength Tests

The test plan for strength verification included the following: a) limit load downbending plus torsion, b) limit load upbending plus torsion, c) ultimate load upbending plus torsion, and d) a residual strength to failure test with upbending plus torsion loads after the box had been impact damaged in several locations. Premature failure of the box beam occurred at 125% of the design limit load during the ultimate load test condition. The following paragraphs will discuss the test results obtained and describe the box failure.

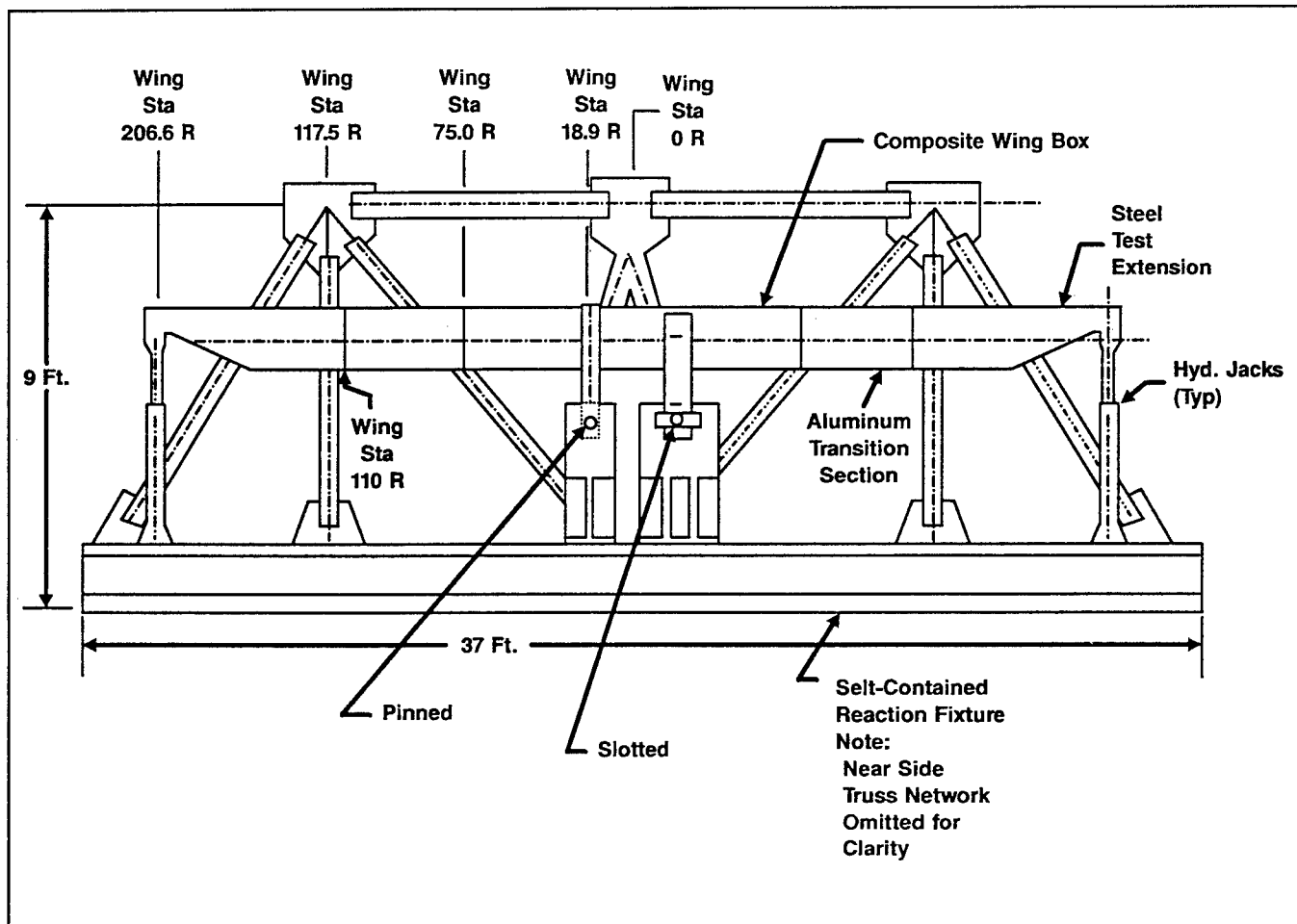


Figure 8. Box Test Set-up

For the downbending combined with torsion condition, the box was loaded to limit load. A review of the load-strain data indicated that the maximum strains, which were less than 3000 micro inch/inch, were slightly greater than predicted. No indications of local buckling were detected; however, local bending strains of the upper cover panels in the vicinity of the access hole and hat stiffeners were slightly greater than anticipated.

An upbending combined with torsion loading condition was conducted to limit load followed by the ultimate load test for the same combined load condition. During the ultimate load test the box failed at 125% of design limit load. The failure location was in the upper cover and spars at wing station 45. Figure 9 presents the average axial loads for the upper and lower covers and the axial strains in the covers at the failure load. The measured strains are the averages for the gages mounted back-to-back on the cover skin located approximately 4 inches from the spar web. Compared to strains predicted by finite element analysis, the measured strains are considerably greater in the mid-span locations of the box. From W.S. 30 inboard, the measured strains on the lower cover were 16 percent greater than predicted and 22 percent greater than predicted on the upper cover.

A review of the load-strain information for the upbending condition indicated that no local buckling occurred in the covers or spars prior to failure. However, as shown in Figure 10, a significant amount of local bending was measured in the central section of the upper cover in the area surrounding the cutout. The 5500 microinch/inch compressive strain recorded near the edge of the cutout was also the largest strain measured on either upper or lower covers. Most of the local bending which occurred in this region is due to the axial load path eccentricity caused by the access hole and its reinforcement.



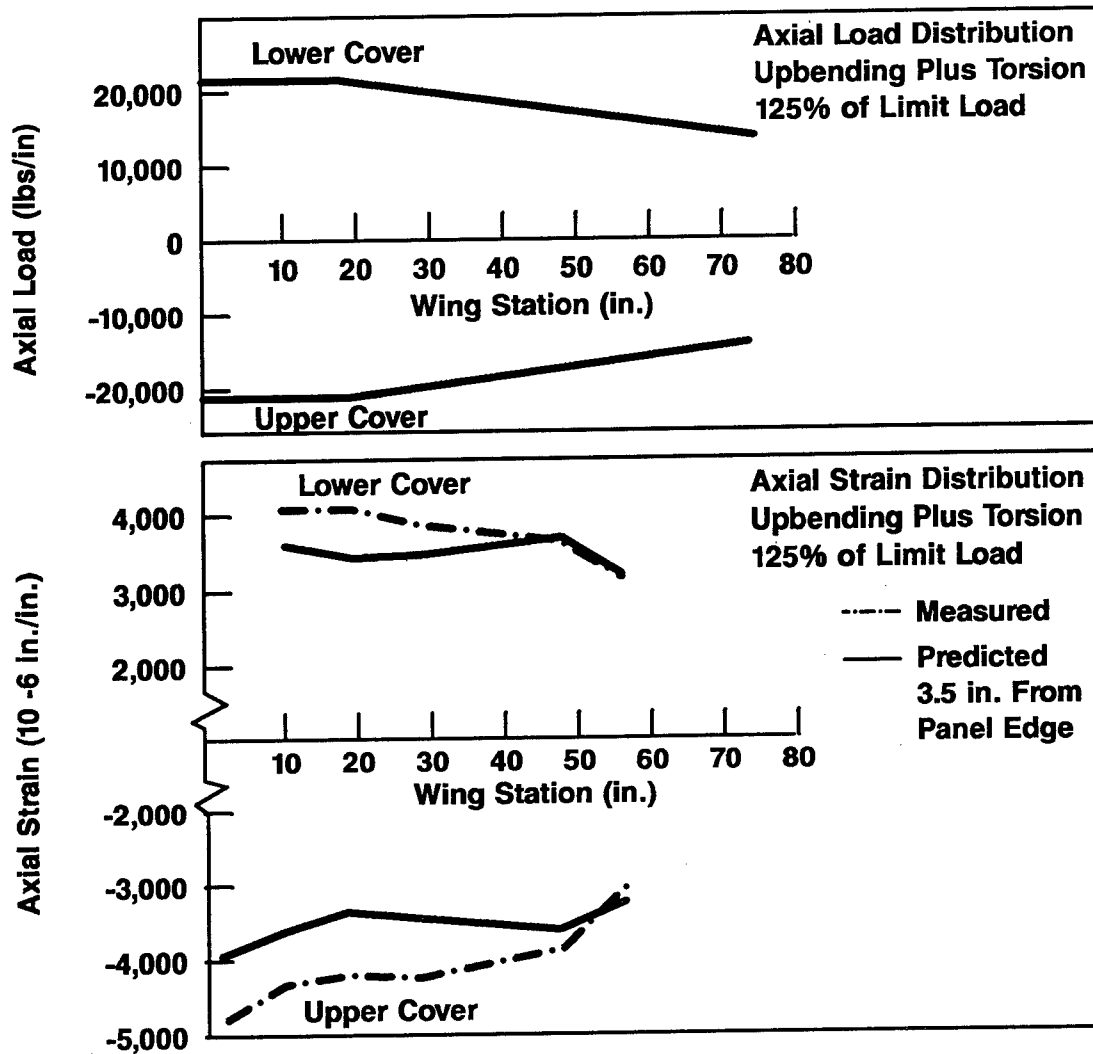


Figure 9. Cover Loads and Strains at Box Failure Load

Failure of the upper cover occurred at W.S. 45. The failure location and axial strains measured in the location just prior to failure are shown in Figure 11. Note that all of these strains are much less than the compression design allowable for the cover material, and as shown previously in Figure 9 are close to predicted values. However, the hat runout at the rib cap does cause a load path eccentricity in the central section of the cover which causes a local bending moment as indicated by the strains measured on the skin and hat crown gages at W.S. 31.5. It is hypothesized that local bending on the skin laminate at the hat runout precipitated failure of the upper cover through the last row of fasteners attaching the hat flanges to the skin. Figure 12 shows the upper cover failure as viewed from outside of the box. The photograph in Figure 13 presents the upper cover failure viewed from inside the box. Note that the modes of failure seen in the cover skin and blade stiffeners were similar to those seen in stiffened panel tests previously conducted to evaluate compression load carrying performance of this type of construction.

A review of the load-strain plots for the front and rear spars indicated no local buckling had occurred prior to failure. Measured strains on the front spar web at the failure load, shown in Figure 14, averaged 18 percent greater than the predicted values at W.S. 10 and W.S. 27.5. At W.S. 48 the measured strains were equal to the predicted strains. Note that the maximum strain at plus/minus 45 degrees on

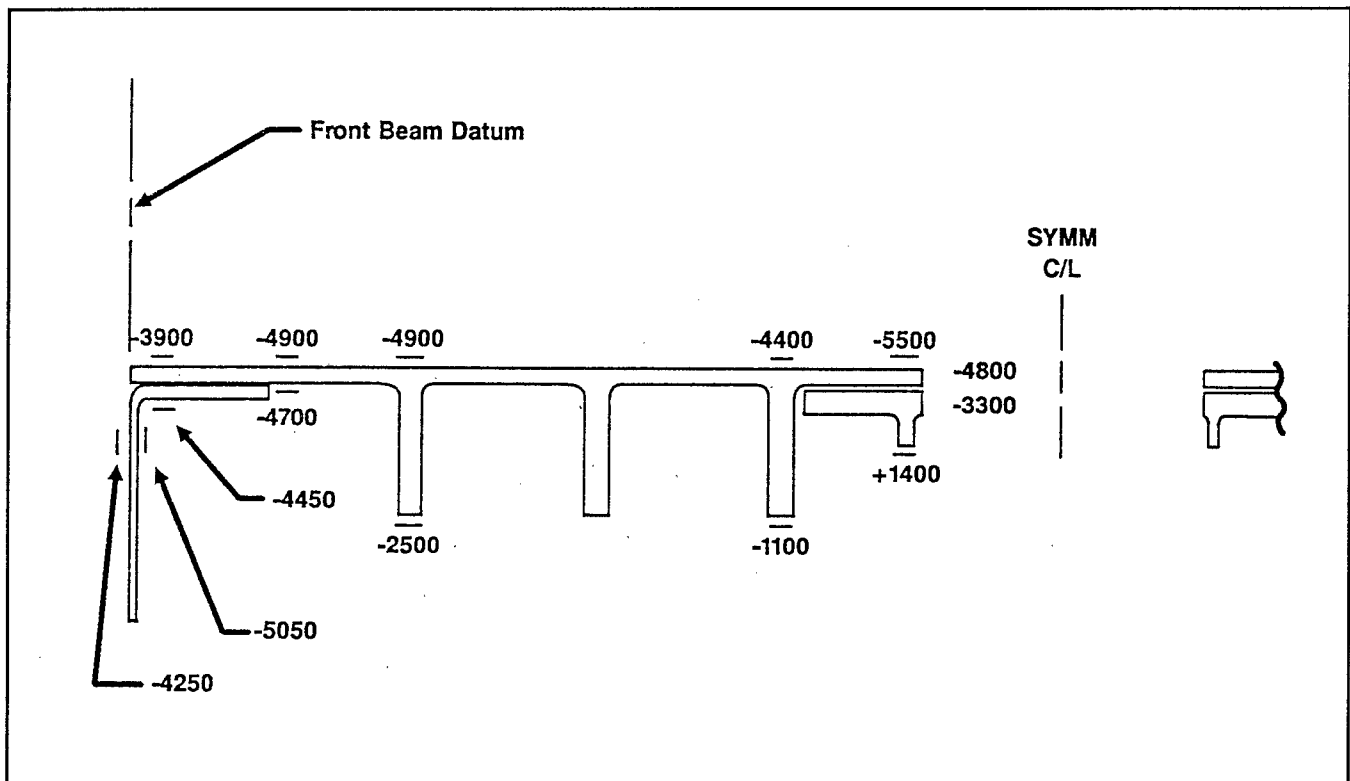


Figure 10 Measured Axial Strains of Upper Cover at W.S. 0 at Failure Load (All Strains  $10^{-6}$  In./In.)

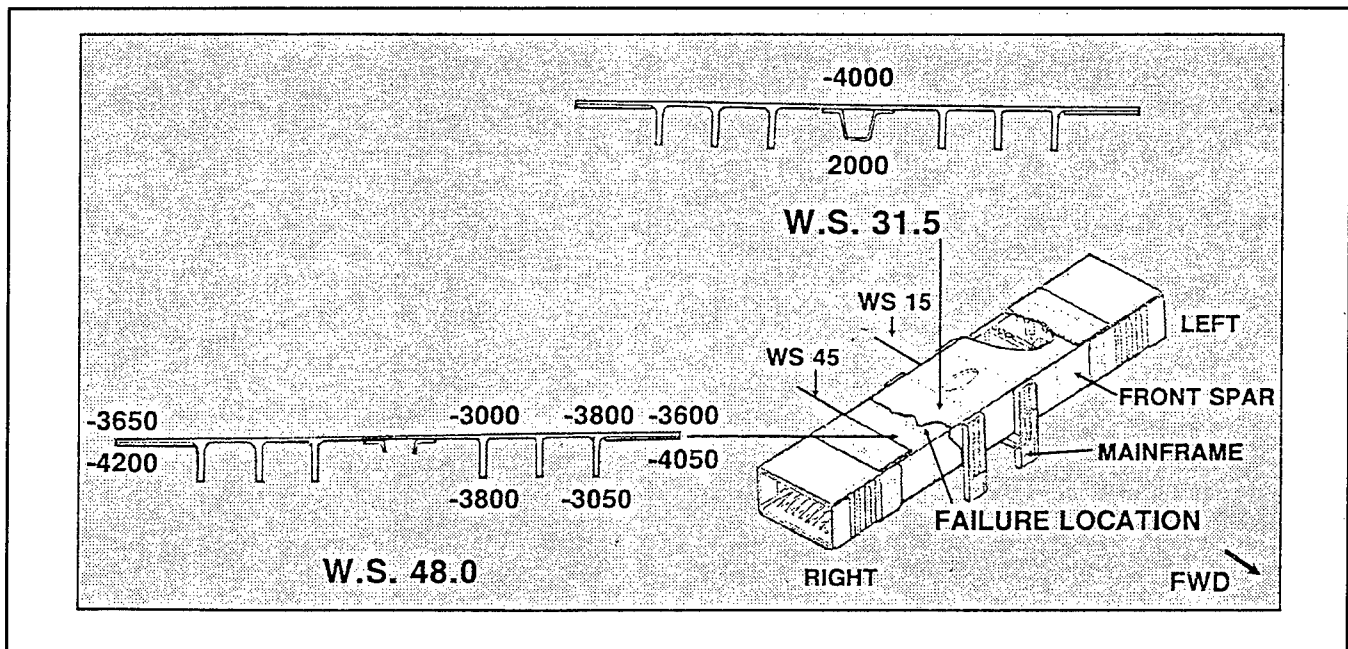


Figure 11. Axial Strains Near Failure Location (All Strains are  $10^{-6}$  In./In.)

the web is -2500 microinch/inch. Figure 15 shows the failure of the front spar web which starts at the upper cap at about W.S. 42 and runs to the edge of the mainframe at W.S. 25. The failure of the rear spar was similar to that shown for the front spar.

### Post Test Investigations

Upon completion of the test program, a review was made of the load-strain data, and the box failure locations were visually inspected from the exterior and interior of the box. For the no-impact damage condition, structural analysis had predicted that the minimum margin of safety for the upper cover was at W.S. 45 for a bearing/bypass failure mode at the cover to spar cap joint (see Figure 7). However, all of the axial strains measured near the failure location, previously presented in Figure 11, were considerably less than the average open hole compression strength for this material and laminate orientation. A review of the inspection records indicated there were no anomalies in the covers or spars at the failure location. The spar cap and spar web had higher margins of safety than the cover at this location.

Additional structural analysis, quality assurance tests and panel tests are being conducted on the box to determine the cause of the premature failure. Analysis completed to date points to the hat runout as the most likely detail which initiated the failure.

### CONCLUDING REMARKS

Design studies indicated that the use of advanced composites for construction of a transport wing box would result in a 25 percent weight savings compared to a metal wing box. A full-scale section of the composite wing was designed in detail, analyzed, fabricated and tested. The box failed prematurely at 125 percent of design limit load during the combined upbending and torsion ultimate design load test. Based on the post test investigations completed thus far, it appears that the failure initiated at a hat

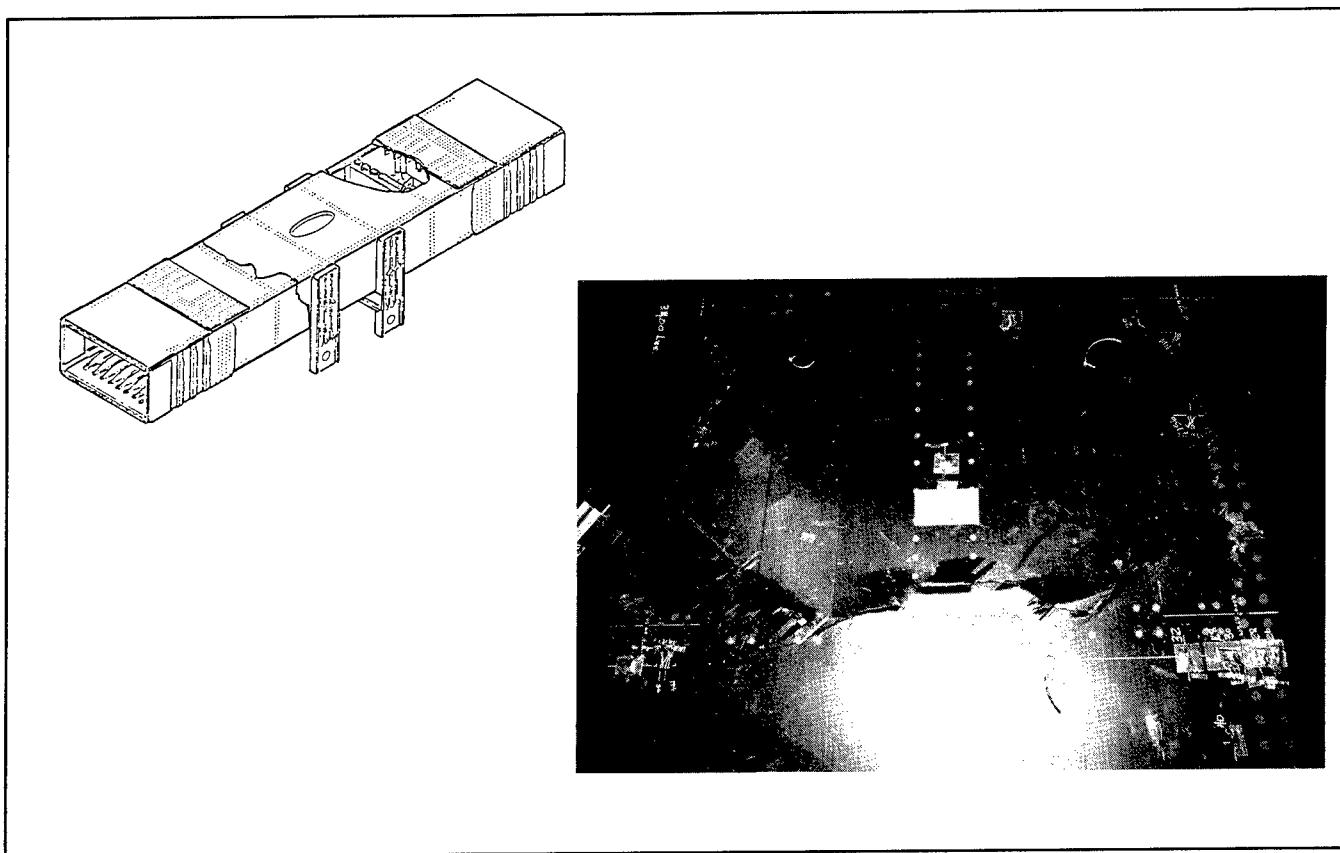


Figure 12. Upper Cover Failure at W.S. 45

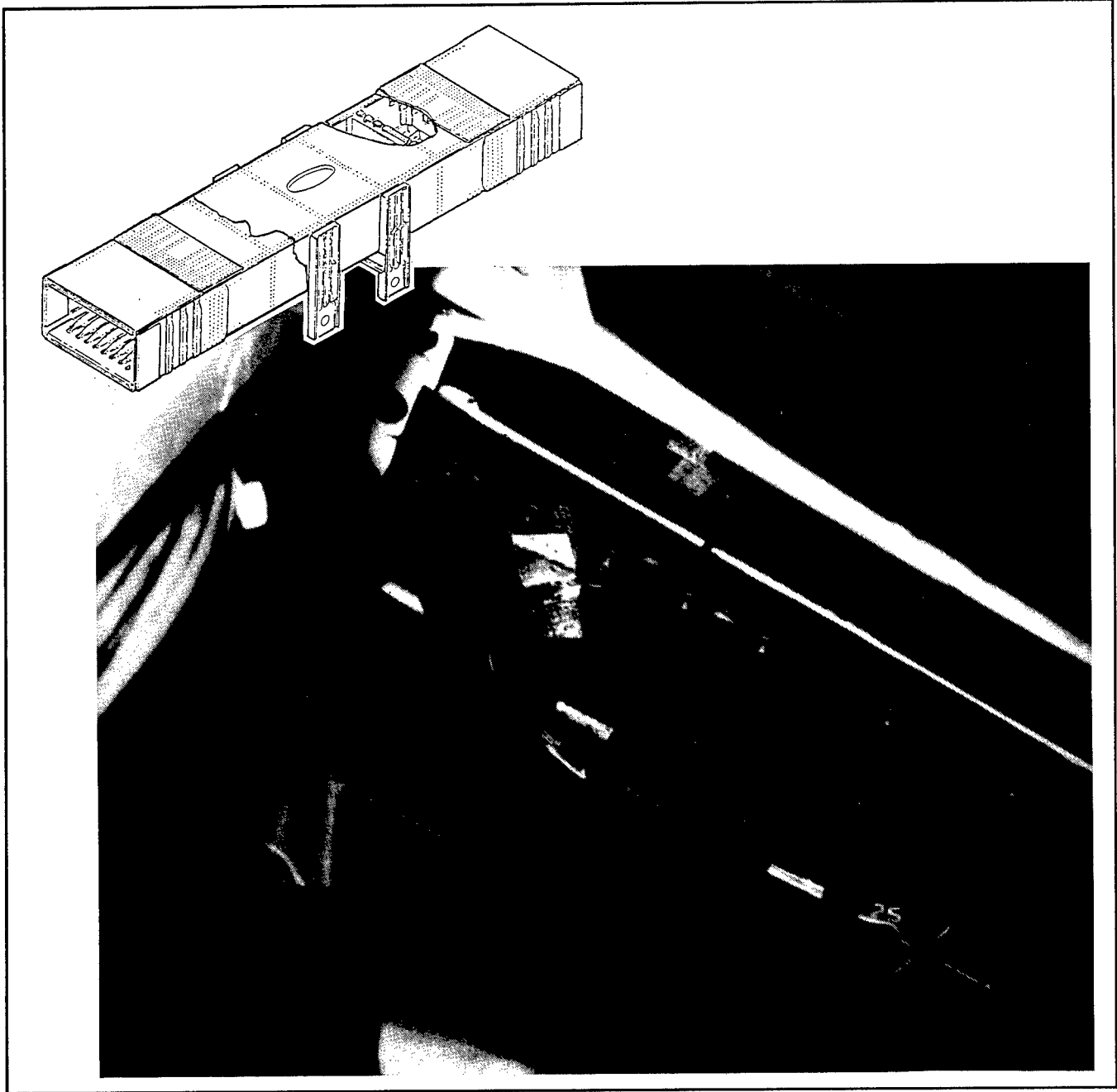


Figure 13. Interior View of Upper Cover Failure at W.S.. 45

stiffener runout in the central section of the cover. It is hypothesized that the load path eccentricity at the stiffener runout caused higher than predicted local bending stresses which resulted in a premature failure in the upper cover. Additional structural analysis and tests are continuing to substantiate this hypothesis.

In addition to the suspected design detail problem at the hat runout in the upper cover, data from the test program also indicated a local bending around the access hole in the upper cover. The access hole reinforcement design concept should be revised to minimize the load path eccentricities in that area. Another design change recommended is to use an intermediate modulus fiber such as IM7 in place of the AS4 for the spanwise plies in the covers and spar caps. Trade studies have indicated that this change would result in a substantial weight savings compared to the current design and more than offset the weight added to modify the design details associated with the hat stiffener runout and access hole reinforcement.

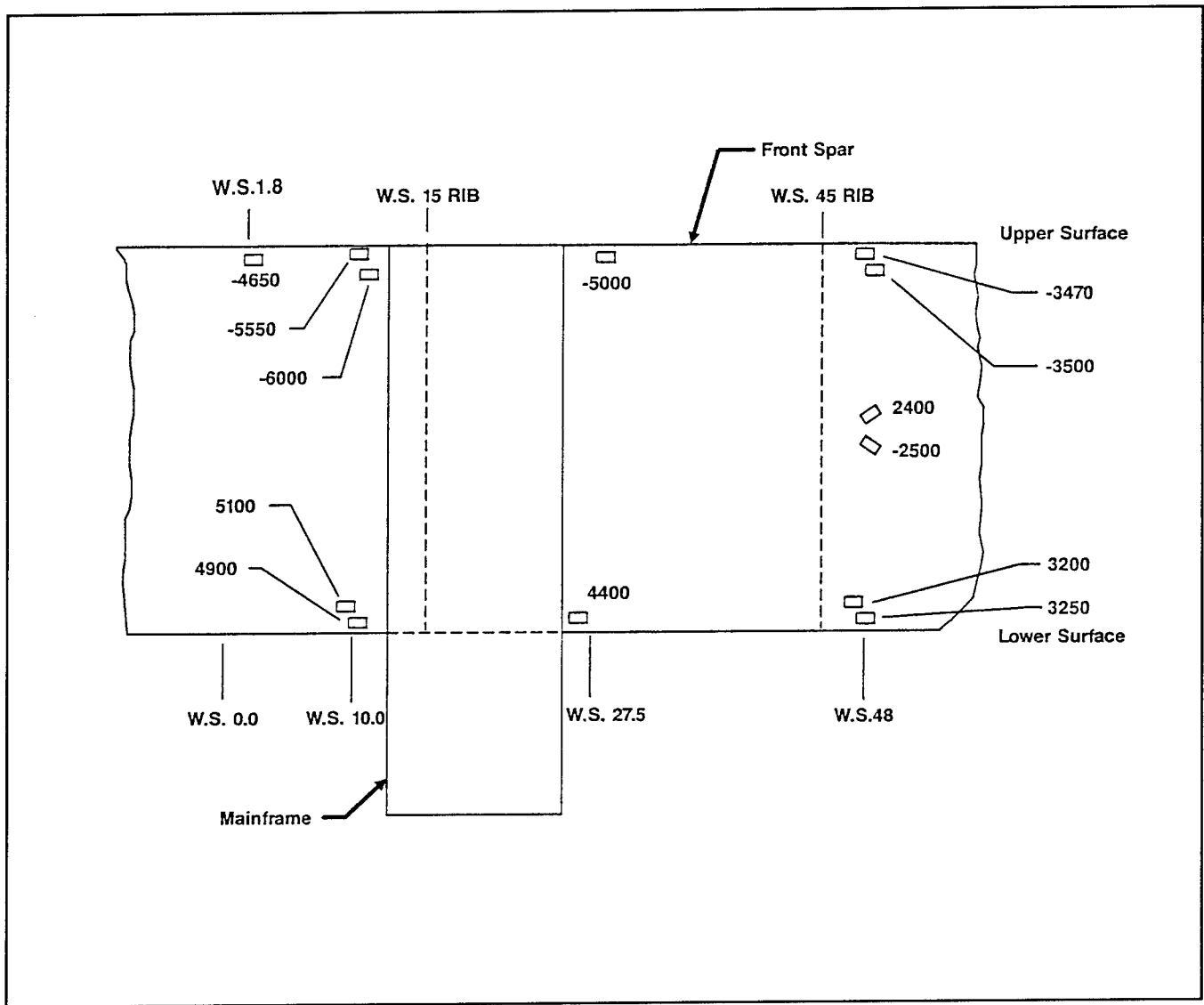


Figure 14 Front Spar Measured Strains at Failure Load

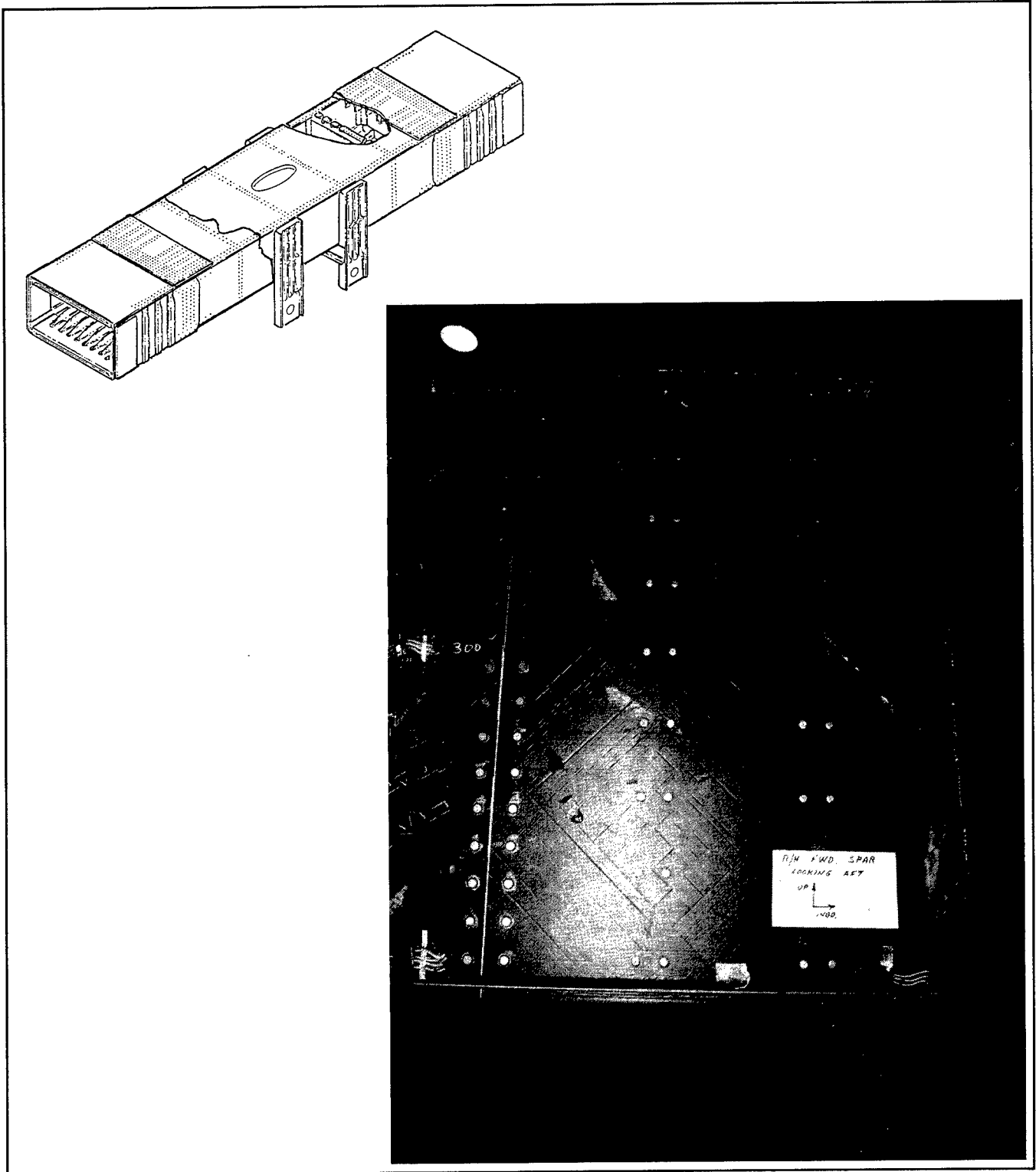


Figure 15. Exterior View of Front Spar Failure

**THIS PAGE INTENTIONALLY BLANK**

# TECHNOLOGY INTEGRATION BOX BEAM FAILURE STUDY: STATUS REPORT

M. J. Shuart, D. R. Ambur, D. D. Davis, Jr.,  
R. C. Davis, G. L. Farley, C. G. Lotts, and J. T. Wang

## Introduction

Composite structures have the potential to be cost-effective, structurally efficient primary aircraft structures. The Advanced Composites Technology (ACT) Program has the goal to develop the technology to exploit this potential for heavily loaded aircraft structures. As part of the ACT Program, Lockheed Aeronautical Systems Company completed the design and fabrication of the Technology Integration Box Beam (TIBB, ref. 1). The TIBB is an advanced composite prototype structure for the center wing section of the Lockheed C-130 aircraft. Lockheed tested the TIBB for downbending, upbending, torsion, and combined upbending and torsion load conditions to verify the design (ref. 2). The TIBB failed at 83 percent of design ultimate load for the combined upbending and torsion load condition.

The objective of this paper is to describe current results from an on-going study of the mechanisms that led to the failure of the TIBB. Experimental and analytical results are presented. Experimental results include load, strain, and deflection data for the TIBB. An analytical investigation was conducted to compliment the experimental investigation and to gain additional insight into the TIBB structural response. Analytical results include strain and deflection results from a global analysis of the TIBB. A local analysis of the failure region is being completed. These analytical results are validated through comparisons with the experimental results from the TIBB tests. The experimental and analytical results from the TIBB tests are used to determine a sequence of events that may have resulted in failure of the TIBB. A potential cause of failure is high stresses in a stiffener runout region. Typical analytical results are presented for a stiffener runout specimen that is being defined to simulate the TIBB failure mechanisms. The results of this study are anticipated to provide better understanding of potential failure mechanisms in composite aircraft structures, to lead to future design improvements, and to identify needed analytical tools for design and analysis.



## Applied Loads and Reactions for Failure Load Case

The TIBB loading conditions were thoroughly examined as a precursor to understanding the TIBB response and failure mechanism. The TIBB was loaded at both ends of the beam and was supported by mainframes in the middle of the beam as illustrated at the top of figure 1. Loads were applied to the TIBB using hydraulic actuators located at four corners of the TIBB. Applied loads measured during the test are shown on the left side of the figure. The applied loads for the forward right and left actuators were equal, and the applied loads for the aft right and left actuators were equal. The applied loads for the forward actuators were 230 percent greater than the applied loads for the aft actuators to simulate a combined upbending and torsion wing-loading condition. This loading condition will be referred to herein as the failure load case. Loads were applied to the TIBB incrementally during the test, and selected strain and displacement results were evaluated at each load level. The "stair-step" trend for the applied load data is a result of the applied loading procedure.

Results for the reaction forces in the TIBB mainframe supports are shown on the right side of figure 1. Each reaction force was calculated using results from strain gages located on the corresponding mainframe support. Results for the reaction forces are shown on the figure as percentages of the total load. The percentage of the total load for each reaction force varied significantly for total loads below 50 kips. The variations are due to settling of the test fixture and TIBB during loading. At failure (i.e., 301 kips total applied load) the forward right and left reaction loads were approximately 50 and 20 percent, respectively, of the total load, and the aft right and left reaction loads were approximately 20 and 5 percent, respectively, of the total load. The calculated reaction forces were expected to have a load distribution similar to that for the applied loads. The results for the calculated reaction forces may be affected by the boundary conditions at the supports, deformation of the test fixture, and/or rigid body motions of the TIBB.

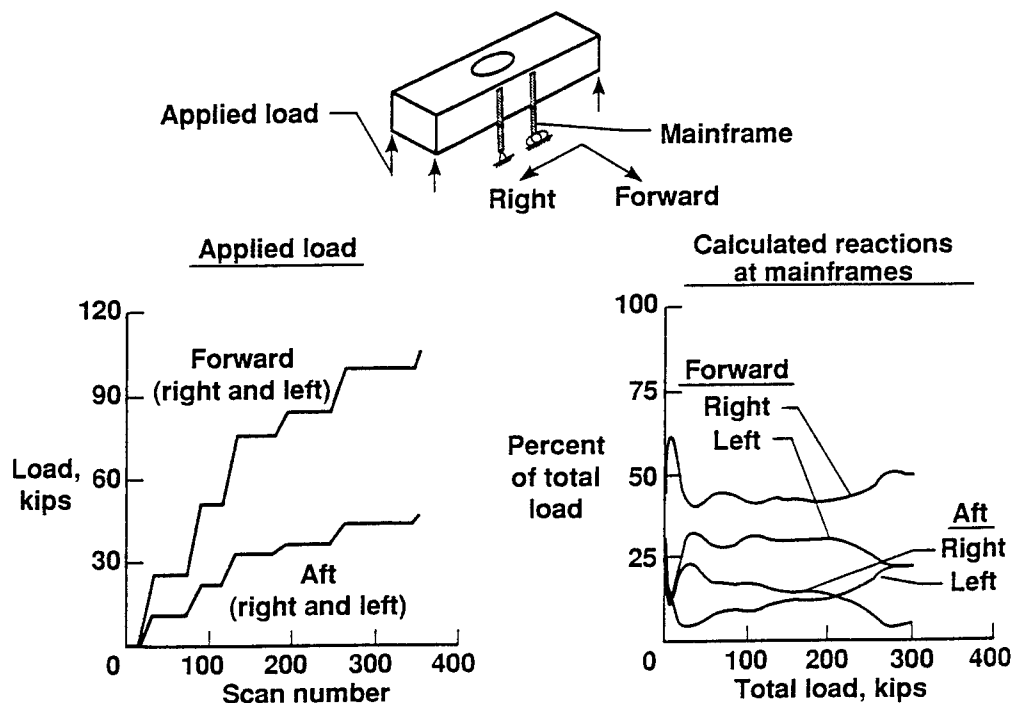


Figure 1

## Typical Strains in the Upper Cover

Measured axial strains for the failure load case from the upper cover of the TIBB are shown in figure 2. Strain gage locations are identified by the letters A through F and are indicated by a parallelogram on the schematic at the top of the figure and by the sketch of stiffener cross sections at the lower right of the figure. The approximate location of the TIBB failure across the upper cover is also indicated on the schematic. The strain gages at location C are in the vicinity of a hat stiffener, and the strain gages at location D are in the vicinity of a blade stiffener. The subscripts i and e for the letters C and D designate strain gage locations on the interior and exterior surfaces, respectively, of the TIBB.

Axial (spanwise) strain results are plotted on the figure as a function of the total applied load. The strains at locations A, B, E, and F are consistent with the expected deformation of the TIBB for this load case. The largest axial compressive strain is approximately  $-0.0045$  in./in. and occurs at location E. The differences between the interior surface strains and the exterior surface strains at locations C and D indicate stiffener bending. Severe bending in the hat stiffener at failure is caused by local bending moments near the termination of the hat stiffener.

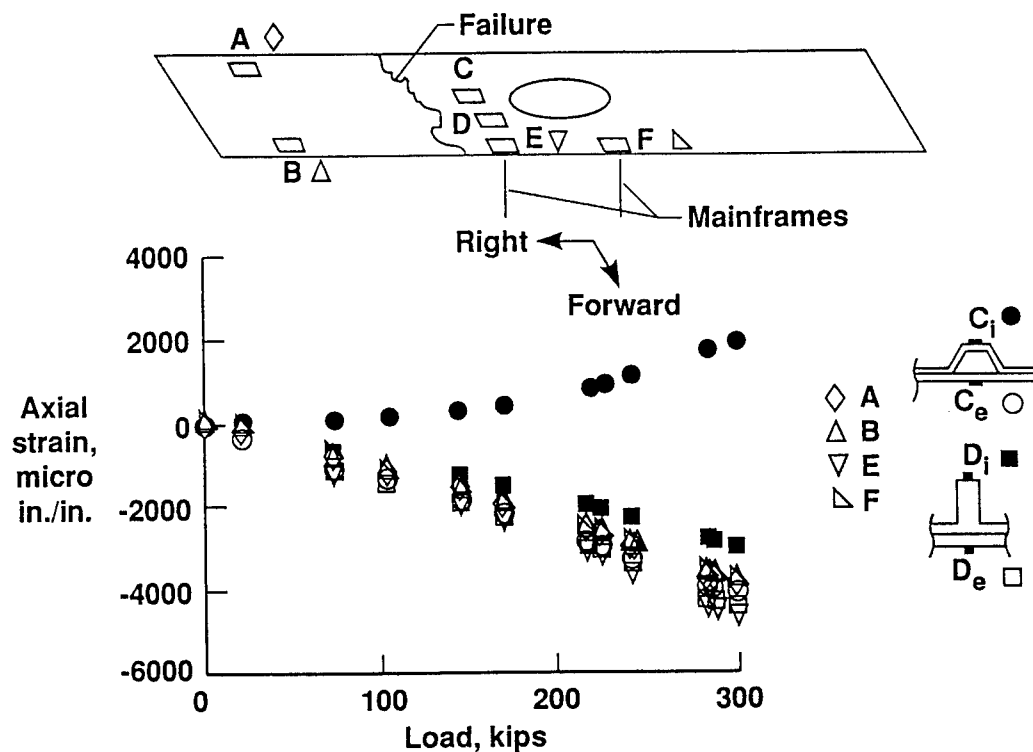


Figure 2

### Typical Strains in the Forward Spar

Measured axial strains for the failure load case from the forward spar of the TIBB are shown in figure 3. Strain gage locations are identified by the letters A through F and are indicated by a rectangle on the schematic at the top of the figure. The schematic also includes the approximate location of the TIBB failure across the forward spar. Strain results are plotted using the symbol identified for each letter in the legend on the right side of the figure. The open symbols correspond to results for gages located near the upper cover of the TIBB, and the filled symbols correspond to results for the gage located near the lower cover. Strain results for locations A and B indicate upbending of the spar which is consistent with this load case. The maximum compressive strain at location A is approximately -0.0046 in./in. The maximum measured compressive strain for the forward spar is at location C and is approximately -0.006 in./in. This maximum compressive strain is too low to cause failure of this undamaged structure. Furthermore, the TIBB failure propagates through a region of the spar where the compressive strains are even lower. These experimental results and similar results for the aft spar indicate that the TIBB failure may have initiated in the upper cover.

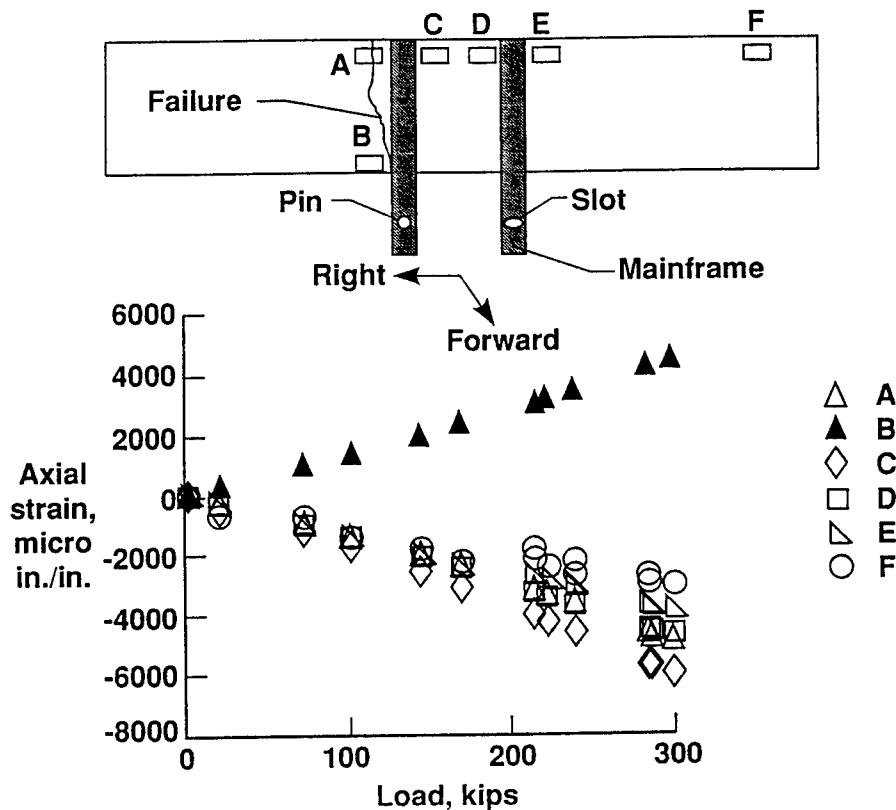


Figure 3

## **Analytical Approach**

An analytical investigation of the TIBB is being conducted to complement the experimental investigation and to gain additional insight into the TIBB structural response. The analytical approach used in this study is summarized in figure 4. Analyses are being conducted using the MSC/NASTRAN (ref. 3) and the Computational Mechanics Testbed (COMET, refs. 4, 5) finite element computer codes. Global analyses for the entire TIBB are being performed using MSC/NASTRAN. The results from the global analyses are being verified using the available experimental results. Displacement results from the verified global analyses will be used as input to a local analysis of the upper cover failure region. The local analysis is being performed using COMET. The local analysis will be used to obtain detailed deformation and strain distributions. The local analysis results will be verified using available experimental results.

A potential test specimen for this TIBB study will also be analyzed. This specimen is referred to herein as the stiffener runout specimen and will be described subsequently in this paper. Analyses for the stiffener runout specimen will be conducted to determine the specimen's response to compression loading for comparison to the TIBB's response to the failure load case. Specimen geometry and loading conditions for the stiffener runout specimen will be evaluated analytically to determine the response that best approximates the TIBB's response at failure. The deformation and strain distributions for the stiffener runout specimen will be predicted prior to testing.

- Use the Computational Mechanics Testbed (COMET) and MSC/NASTRAN
- Conduct global analysis of TIBB; verify global analysis with experimental results
- Use displacement results from verified global analysis as input boundary conditions for local analysis of upper cover
- Conduct local analysis of failure region to determine deformations, strains; verify local analysis with experimental results
- Analyze stiffener runout specimen
  - simulation of TIBB failure mode
  - specimen geometry, test conditions
  - predict deformations, strains

Figure 4

## Axial Surface Strain for Failure Load Case from Modified Global Analysis

Axial surface strain distributions obtained from a modified MSC/NASTRAN global model of the TIBB are shown in figure 5 for the failure load case. The model used for the present analysis was based on a model developed by Lockheed for the TIBB and has been modified to include stiffener runouts and flanges of hat stiffeners. The present global finite element model is more detailed than the original Lockheed model. The present model contains 3,885 quadrilateral, triangular, and bar elements and has 16,578 degrees of freedom.

The global analyses were used to calculate strains in regions near the observed failure. The exterior surface strain distribution is shown on the TIBB global model near the top of the figure. These results do not indicate any unusually high exterior surface strains. A portion of the interior surface strain distribution is shown in the lower half of the figure. The interior surface strain distribution is presented for the upper cover region near the observed failure. These results show strains for the skin of the upper cover that are greater than  $-0.01$  in./in. in the region of the hat stiffener termination. The high skin strains are caused by an eccentric load path that induces local bending. The observed TIBB failure extends through the region of the hat stiffener termination.

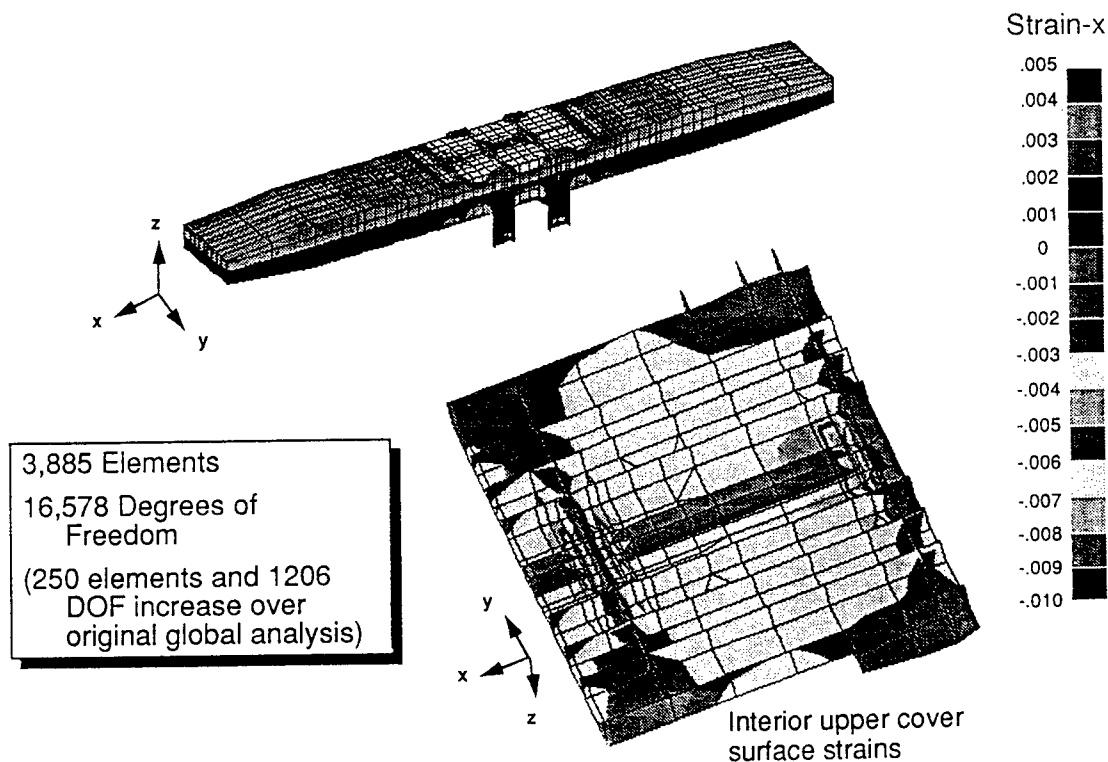


Figure 5

### Vertical Spar Deflections for Failure Load Case

The vertical deflections for the forward and aft spars predicted by the global analysis are compared with experimental results in figure 6. Measured deflections for the left and right ends of the TIBB ( $\eta = \pm 206.6$  in., respectively) and for the mainframes were used as boundary conditions for the global analyses. The composite test section of the TIBB is located between wing stations  $\eta = \pm 75$  in. Correlation between the measured and predicted deflections is excellent.

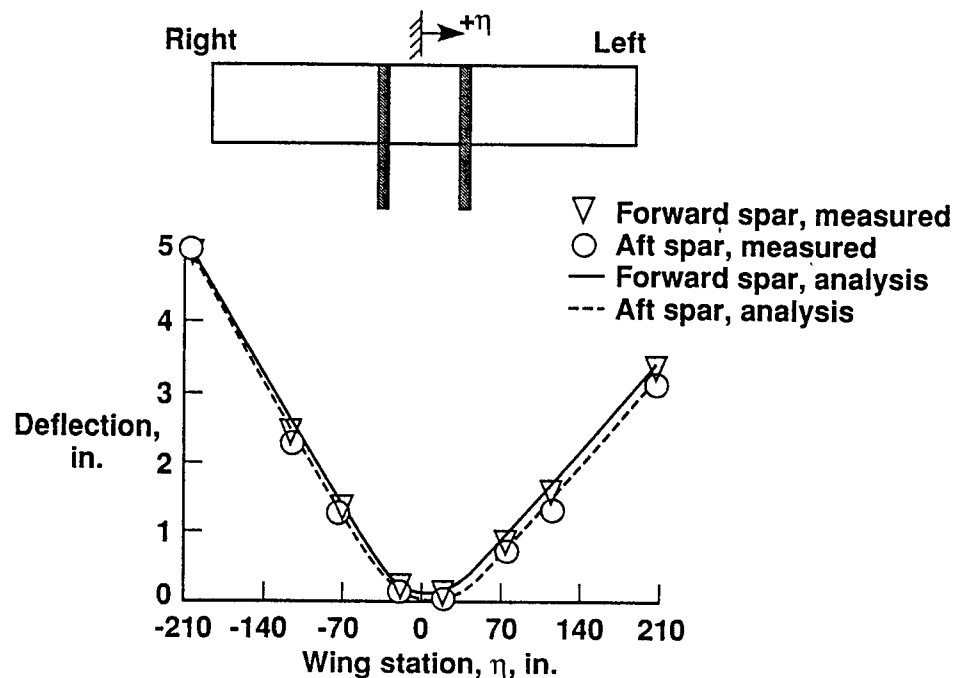


Figure 6

## Upper Cover Axial Strains at Failure

A comparison of upper cover strains at failure of the TIBB is presented in figure 7. Measured strains are compared to predicted strains from the global analysis, and all strains are given in units of micro-in./in. The experimental and predicted strains are shown in the figure at the approximate strain gage location on a schematic of the upper cover. The results on the figure indicate good agreement between test and analysis strains for gages located near the center of the upper cover. The results indicate poor agreement between test and analysis strains for gages located near the ends of the upper cover. These differences between experimental and predicted results may be due to modeling approximations for the TIBB load introduction structure. The results on the figure also indicate poor agreement between test and analysis strains for gages located near the mainframe supports that may be due to modeling approximations for the mainframe, spar, and upper cover connections. Despite the modeling approximations, the experimental and analytical results for the global model agree reasonably well in the center of the upper cover.

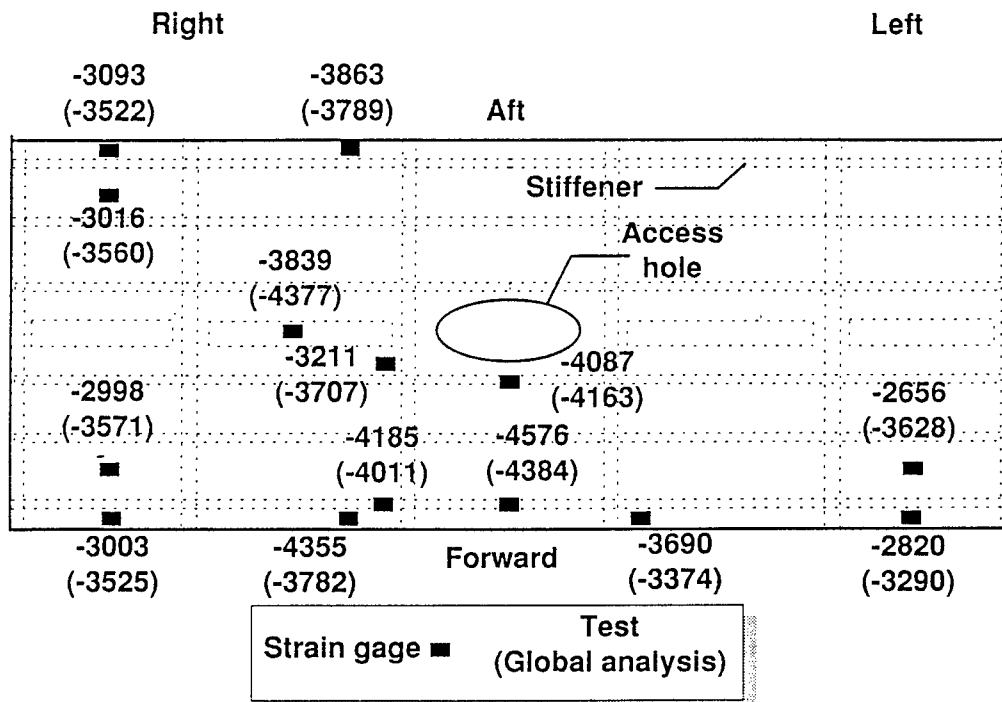


Figure 7

### Finite Element Model for Local Analysis

A detailed local finite element model of half of the upper cover was developed to determine the deformations and strains near the TIBB failure. The local model shown in figure 8 consists of 4,338 9-noded assumed natural-coordinate strain elements (ref. 6) resulting in approximately 88,000 degrees of freedom. Several loading conditions will be used to investigate the behavior of the upper cover. Displacements and rotations from the global analysis will be applied along all four edges of the local model and at the locations where the transverse ribs attach to the cover skin.

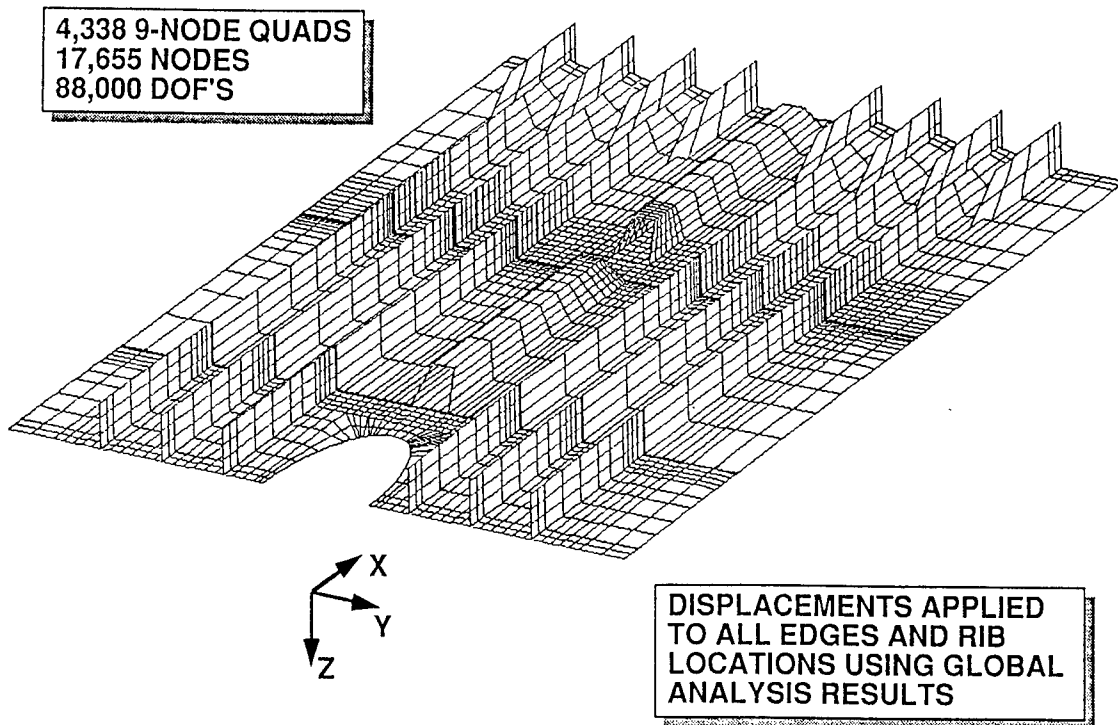


Figure 8



### **Preliminary Failure Scenario**

Experimental and analytical results from this study have been combined to determine a preliminary failure scenario that is summarized in figure 9. When the TIBB was subjected to the failure load case, the eccentric load path at the hat stiffener termination resulted in local bending moments. These bending moments produced severe bending deformations in the hat stiffener and in the unsupported skin near the hat stiffener termination. The unsupported skin also experienced large axial strains due to the thickness discontinuity caused by termination of the stiffener flanges. A combination of large axial and bending strains in the unsupported skin at the hat stiffener termination initiated the failure of the skin of the TIBB upper cover. This failure propagated in the chordwise direction across the TIBB upper cover and caused the forward and aft spars to fail.

- Combined bending/torsion loading applied to TIBB
- Hat stiffeners subjected to severe bending
- Unsupported skin at hat stiffener runout subjected to severe bending
- Strains in skin at stiffener runout initiated TIBB failure
- Upper cover failure led to forward and aft spar failures

Figure 9

## Stiffener Runout Test Specimen

A stiffener runout test specimen (SRTS) was cut from the undamaged portion of the TIBB upper cover as illustrated by the schematic in the upper left of figure 10. The SRTS is approximately 60 in. long and 33 in. wide and will be tested in uniaxial compression to verify the preliminary failure scenario. The unloaded edges of the SRTS will be constrained with knife edges to simulate a simple support boundary condition. The out-of-plane deflection  $w$  will be constrained to be zero along the transverse rib connection located near the center of the specimen. Approximately 150 strain gages and 10 direct current differential transformers (DCDT's) will be used to measure the SRTS response to the applied load. Strains in the critical region of the unsupported skin between the hat stiffener termination and the transverse rib flange will be measured using strain gages and full-field laser interferometry techniques.

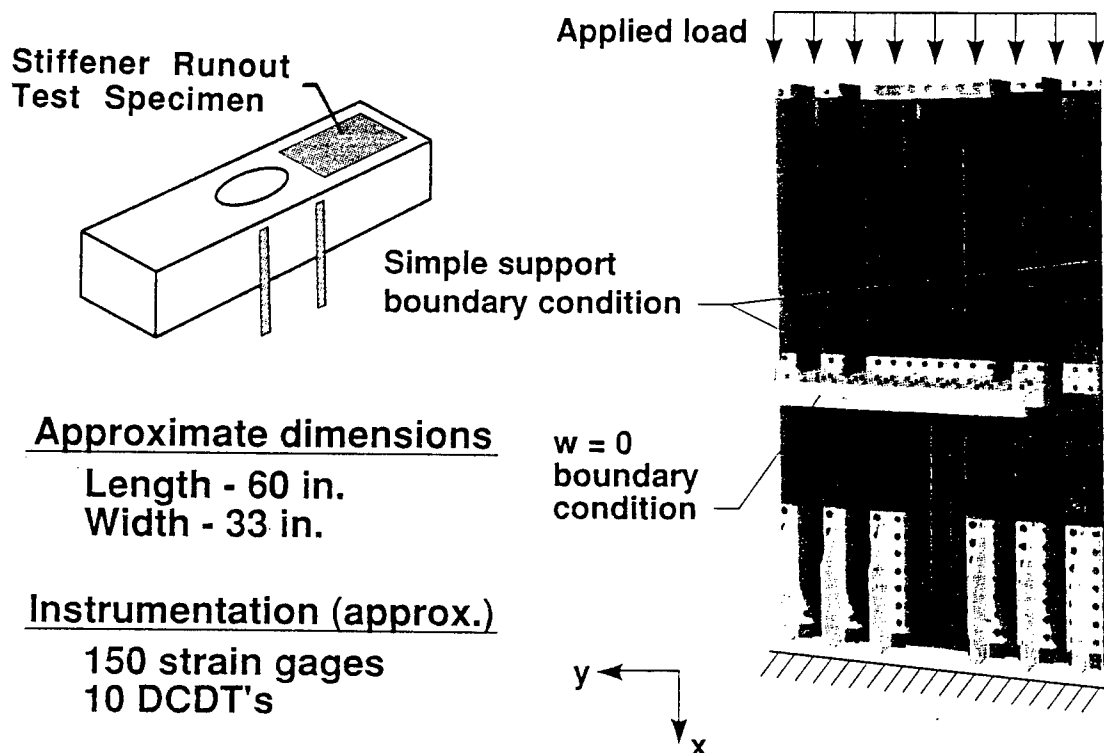


Figure 10

## Typical Response of Stiffener Runout Test Specimen

The stiffener runout test specimen (SRTS) will be tested to simulate the TIBB response and failure mechanisms and thereby verify the TIBB failure scenario. A finite element analysis of the SRTS is being conducted to study the effects of specimen geometry, intermediate supports, end fixity, and depth of end potting on the specimen behavior. A half-model of the SRTS is being developed. Preliminary results from these analyses indicate that regardless of end fixity or depth of end potting, very high strains exist in the unsupported skin near the hat stiffener termination. A typical response for the SRTS is shown in figure 11. Deformed geometry and load-shortening response are shown on the figure. Significant bending deformation of the hat stiffener and the upper cover skin are illustrated.

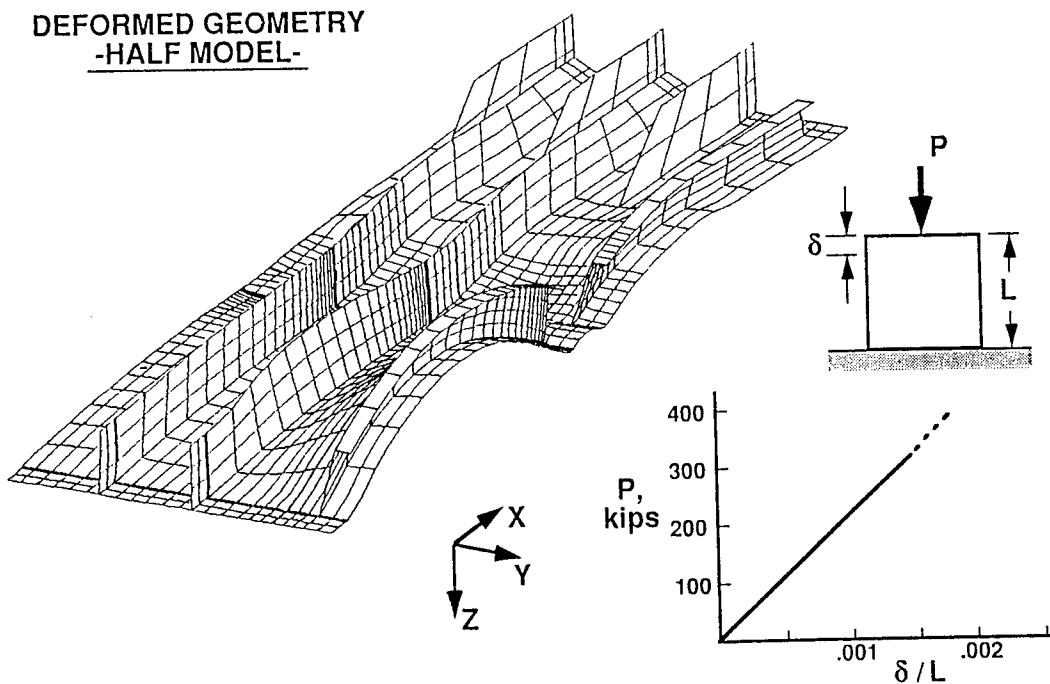


Figure 11

## **Concluding Remarks**

A comprehensive experimental and analytical study is underway to quantify the mechanisms that led to the failure of the Technology Integration Box Beam (TIBB). The experimental results indicate significant bending deformation of the hat stiffener and upper cover skin. Analytical results from a modified global model of the TIBB agree reasonably well with experimental results. Additional analysis is being conducted using a local model of the TIBB upper cover which includes the failure region. Preliminary results from this study suggest that failure of the TIBB initiated in the upper cover skin due to severe bending of the upper cover skin in the region of the hat stiffener termination. A stiffener runout specimen is being defined to simulate the TIBB response and failure mechanisms.

## **References**

1. Griffin, C.; and Meade, L.: Design, Analysis and Fabrication of the Technology Integration Box Beam. Proceedings of the First NASA Advanced Composites Technology Conference, Seattle, WA, October 29-November 1, 1990, NASA CP-3104, Part 1, 1991, pp. 157-178.
2. Griffin, C. F.: Structural Testing of the Technology Integration Box Beam. Presented at the 9th DoD/NASA/FAA Conference on Fibrous Composites in Structural Design, Lake Tahoe, NV, November 4-7, 1991.
3. MSC/NASTRAN User's Manual, Version 65, Vols. 1 and 2. The MacNeal-Schwendler Corporation.
4. Knight, N. F., Jr.; and Stroud, W. J.: Computational Structural Mechanics: A New Activity at the NASA Langley Research Center. NASA TM 87612, 1985.
5. Lotts, C. G.; Greene, W. H.; McCleary, S. L.; Knight, N. F.; Paulson, S. S.; and Gillian, R. E.: Introduction to the Computational Structural Mechanics Testbed. NASA TM 89096, 1987.
6. Park, K. C.; and Stanley, G. M.: A Curved  $C^\circ$  Shell Element Based on Assumed Natural-Coordinate Strains. Journal of Applied Mechanics, vol. 53, 1986, pp. 278-290.

**THIS PAGE INTENTIONALLY BLANK**

**SESSION V-B**  
**STITCHED RTM TECHNOLOGY**

**THIS PAGE INTENTIONALLY BLANK**

## DEVELOPMENT OF STITCHED/RTM COMPOSITE PRIMARY STRUCTURES

Susan M. Kullerd  
Lockheed Engineering & Sciences Company  
Hampton, Virginia

Marvin B. Dow  
NASA Langley Research Center  
Hampton, Virginia

### INTRODUCTION

The goal of the NASA Advanced Composites Technology (ACT) Program is to provide the technology required to gain the full benefit of weight savings and performance offered by composite primary structures. Achieving the goal is dependent on developing composite materials and structures which are damage tolerant and economical to manufacture. Researchers at NASA Langley Research Center and Douglas Aircraft Company are investigating stitching reinforcement combined with resin transfer molding (RTM) to create structures meeting the ACT program goals. The Douglas work is being performed under a NASA contract entitled Innovative Composites Aircraft Primary Structures (ICAPS). The research is aimed at materials, processes and structural concepts for application in both transport wings and fuselages. Empirical guidelines are being established for stitching reinforcement in primary structures and test data are reported in reference 1. New data are presented in this paper from evaluation tests of thick (96-ply) and thin (16-ply) stitched laminates, and from selection tests of RTM composite resins. Tension strength, compression strength and post-impact compression strength data are reported. Elements of a NASA Langley program to expand the science base for stitched/RTM composites are discussed.



## Evaluation of Stitch-Reinforced Composites

Although great advances have been made in carbon fiber-reinforced composites, innovative concepts are needed to overcome the performance and cost barriers that limit the application of composites in aircraft primary structures. Thermoplastics and toughened epoxies provide improved damage tolerance and structural efficiency, but are considered too expensive for widespread application. Composite manufacturing methods used on production aircraft are still costly and labor intensive. In an effort to enable affordable and damage tolerant composite structures, Douglas Aircraft Company has adopted the approach shown in figure 1. Layers of dry carbon fabric are stacked in the desired ply orientation and the plies are stitched together using Kevlar or glass thread for through-the-thickness reinforcement. The stitched preform is then impregnated with resin and cured in a resin transfer molding (RTM) process.

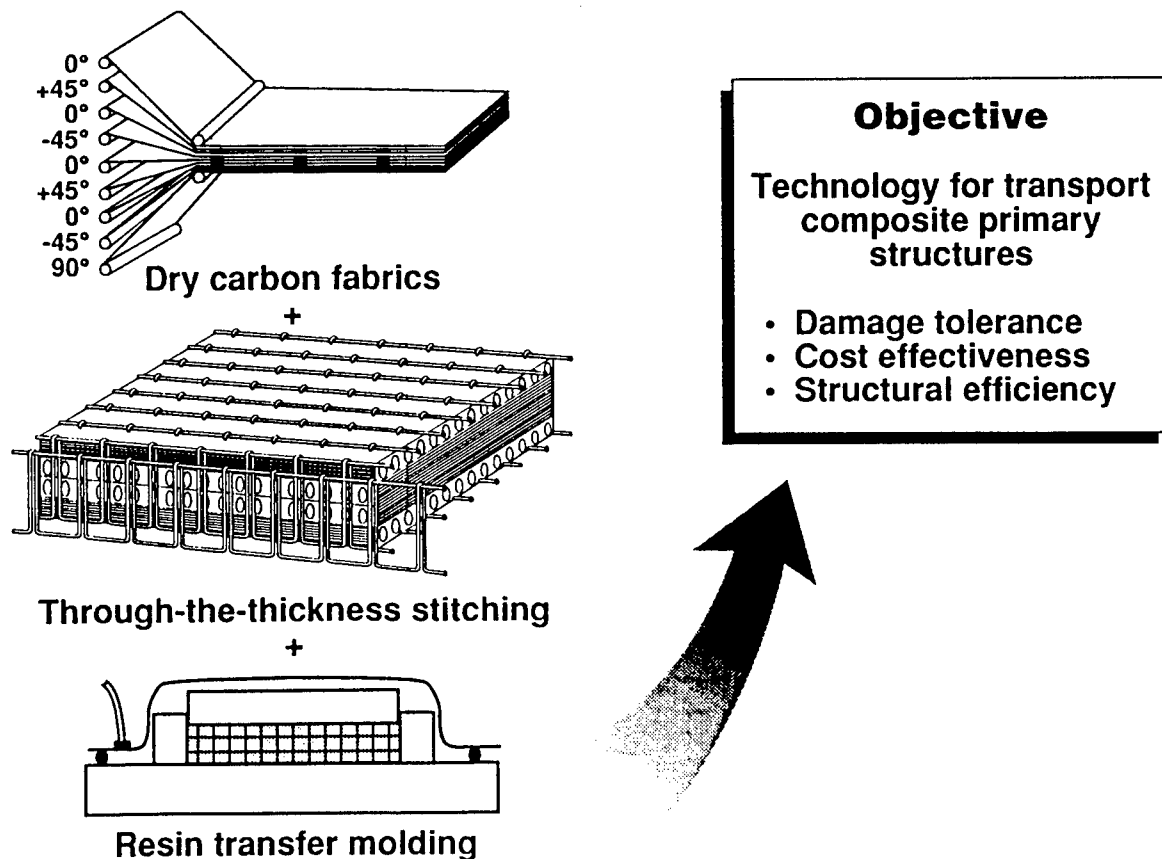


Figure 1

## Development of Stitched/RTM Primary Structures

As part of the NASA Advanced Composites Technology (ACT) Program, Douglas Aircraft Company is developing unique composite materials and processes for transport aircraft primary structures. An outline of the Douglas contract is shown in figure 2. Phase A - Concepts Development is currently in progress and involves stress analysis of stitched composite aircraft structures and the establishment of a supporting database of stitched/RTM composite properties. Two RTM processes are being developed, one for wings and one for fuselage structures. For heavy wing structure, the process is resin film infusion with autoclave curing. For fuselage structure, the process involves fixed volume tooling and pressure RTM. Details of these RTM processes are given in the paper by A. Markus titled "Resin Transfer Molding Technology for Composite Primary Wing and Fuselage Structures." Testing of the wing and fuselage elements is currently in progress.

The planned Phase B - Technology Verification will consist of building and testing a 12 ft. by 8 ft. wing box with stitched upper and lower cover panels. A fuselage barrel section (150 inches long by 100 inches in diameter) will be built and tested. Two benchmark fuselage panels, a lower side panel and a crown panel, will be built for testing at NASA Langley Research Center. Two other major airframe manufacturing companies will also build benchmark panels for NASA Langley tests.

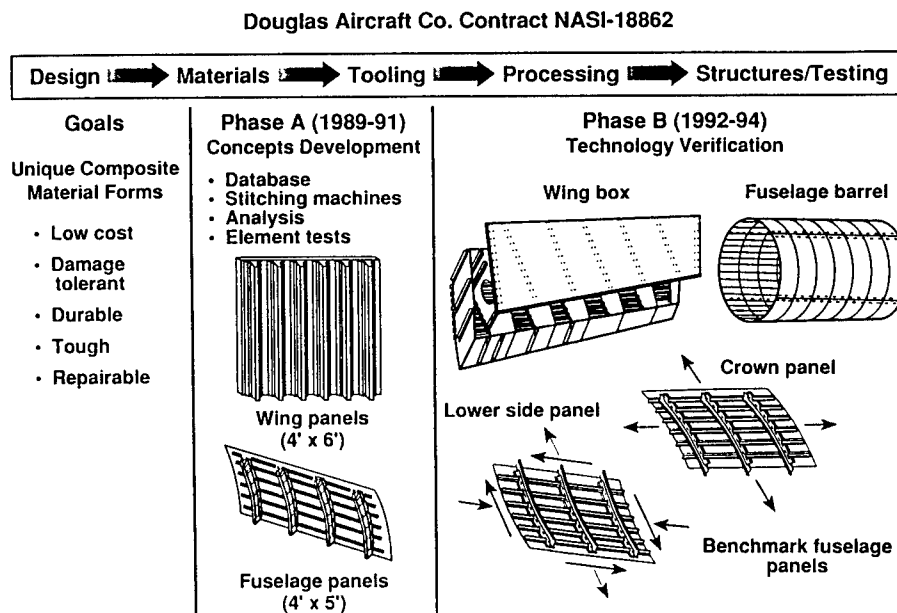


Figure 2

## Candidate Concepts for Transport Wing and Fuselage Structures

Design concepts selected by Douglas for stitched/RTM wing and fuselage panels are shown in figure 3. The wing panels incorporate blade stiffeners which were selected for structural efficiency combined with manufacturing simplicity. The design was developed under a previous NASA contract and details are presented in reference 2. In the stitched/RTM wing panels, the skins have a dense array of through-the-thickness stitching and flange-to-skin stitching is used with the stiffeners and intercostals. All elements have the same layup of 44 percent  $0^\circ$  plies, 44 percent  $\pm 45^\circ$  plies and 12 percent  $90^\circ$  plies.

Like the wing panels, the fuselage design was also developed under a previous NASA contract, see reference 3 for details. Fuselage longerons are "J" sections selected for structural efficiency. In the current stitched/RTM design, only the longeron flanges are stitched to the skin. The layup for skin and longerons has equal percentages, or 33.3 percent each of  $0^\circ$ ,  $\pm 45^\circ$  and  $90^\circ$  plies.

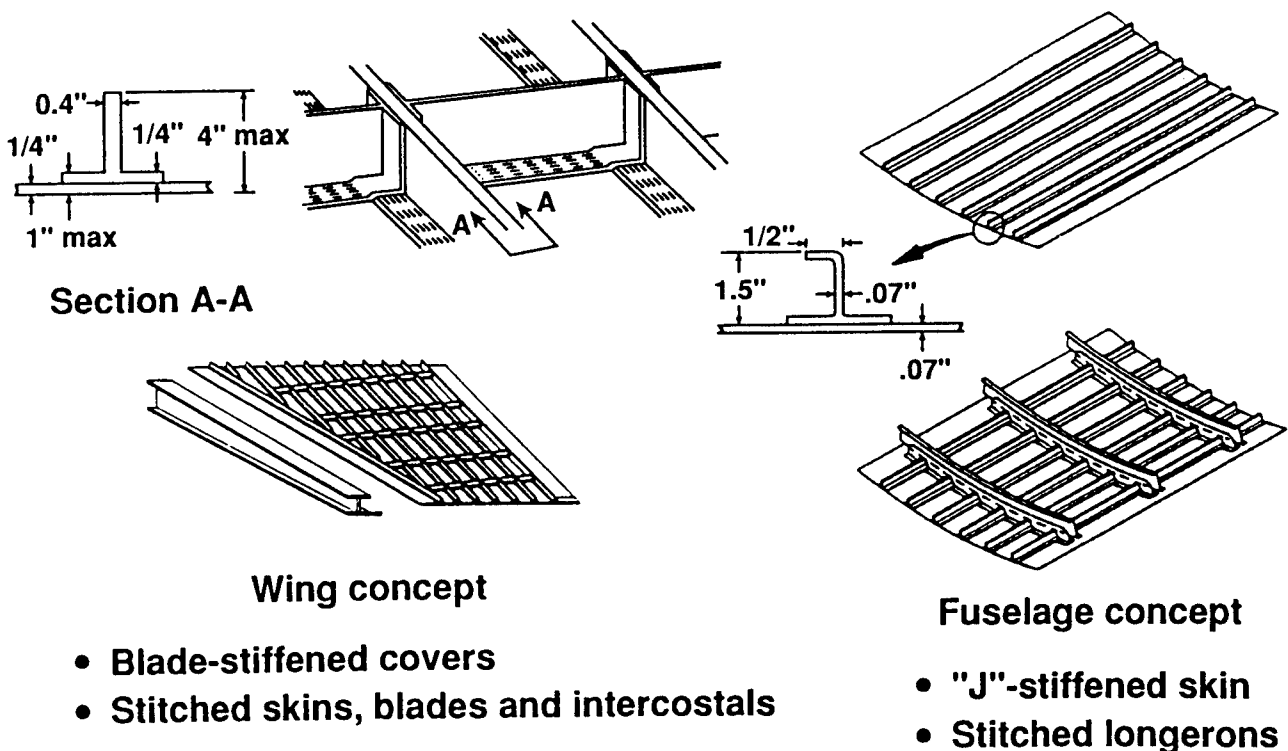


Figure 3

## NASA/ACT Research on Stitched/RTM Materials and Structures

Organizations involved in the NASA/Douglas ICAPS effort are shown in figure 4. Douglas has the lead role in the design, fabrication and stress analysis of stitched/RTM structures, as well as the tabulation of cost data and program documentation. The Materials Division at NASA Langley has a major role in database testing. In addition, Langley has a sizable program to advance the mechanics and technology of stitched composites. The elements of this program are described later in this paper. Under a subcontract to Douglas, researchers at William and Mary College and Virginia Polytechnic Institute are developing RTM process and flow models and processing guidelines for various resin systems, in addition to designing cure monitor instrumentation. Ketema, Inc., another Douglas subcontractor, stitched the fabric preforms for the database test coupons. Pathe, Inc., a third Douglas subcontractor, is designing and building new automated single needle and multi-needle stitching machines.

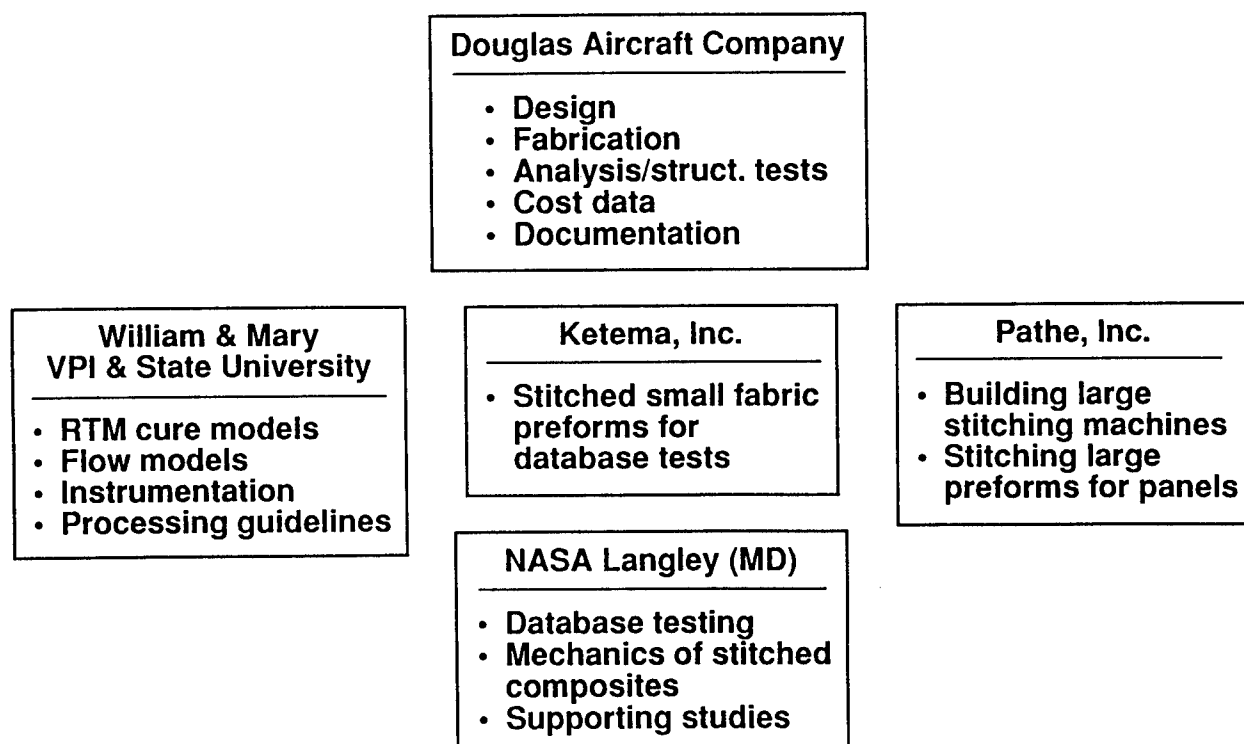


Figure 4

## **Stitched Materials and Structures Database Work in Progress**

Figure 5 shows work in progress at Douglas and NASA Langley under the ACT contract. Douglas work includes fabrication of stitched and resin transfer molded coupons for database testing, as well as wing and fuselage elements and subcomponents. Douglas is also performing compression tests of thick wing panels and single stringer crippling tests. For structural analysis of stitched composites, Douglas has adopted a modified laminate theory and a macro-mechanics/semi-empirical approach. Douglas is using NASTRAN to model the behavior of "J" stiffened fuselage panels. Douglas is also responsible for checkout of the single-needle and multi-needle stitching machines being developed at Pathe.

Laminate coupon testing is being done at NASA Langley and the data is provided to Douglas for their structural analysis. Tests include tension, compression and compression after impact as well as stiffener pull-off tests and compression testing of fuselage "J" stiffened panels. Tests in progress include stitched stiffener pull-off specimens and stitched "J" stiffened panels.

- **Under the ACT Contract:**
  - Fabrication of stitched coupons, elements and subcomponents
  - Compression testing of thick wing panels
  - Single stringer crippling tests
  - Structural analysis
  - Checkout of new stitching machines
- **At Langley:**
  - Lamina coupon testing for analysis data
  - Strength tests of wing and fuselage coupons (tension, compression, CAI)
  - Stiffener pull-off tests
  - Compression testing of fuselage element panels (21 in. x 15 in.)

Figure 5

### Six Stringer and Three Stringer Wing Panels

Douglas has built several three-stringer structural element panels, figure 6(a), using the resin film infusion process. These element panels will be tested in compression to investigate damage tolerance and to provide data for correlation with structural analysis. The test panels are 21 in. wide by 15 in. long.

The first six stringer wing panel successfully built by Douglas using the resin film infusion process is shown in figure 6(b). The skin has 54 plies with ply orientation of  $[0^\circ/45^\circ/0^\circ/-45^\circ/90^\circ/-45^\circ/0^\circ/45^\circ/0^\circ]_{3s}$ , and the stringers are 72 ply laminates with the same layup as the skin. The panels were resin transfer molded using 3501-6 epoxy resin. The lightly shaded areas visible in Figure 6(b) have been sanded and cleaned for secondarily bonding the intercostals to the wing skin and stringers. In all future panels, the intercostal preforms will be stitched to the skin and the entire assembly will be resin transfer molded.



Figure 6(a)

## SIX-STRINGER WING PANEL

AS4/3501-6 Dimensions: 72 in. long x 42 in. wide

Lock stitched with S-2 glass thread at 1250 yd/lb

Skin 54 plies [0/45/0/-45/90/-45/0/45/0]<sub>3s</sub>

Stringer 72 plies - same layup as skin

Intercostal  
(rib clip)  
locations

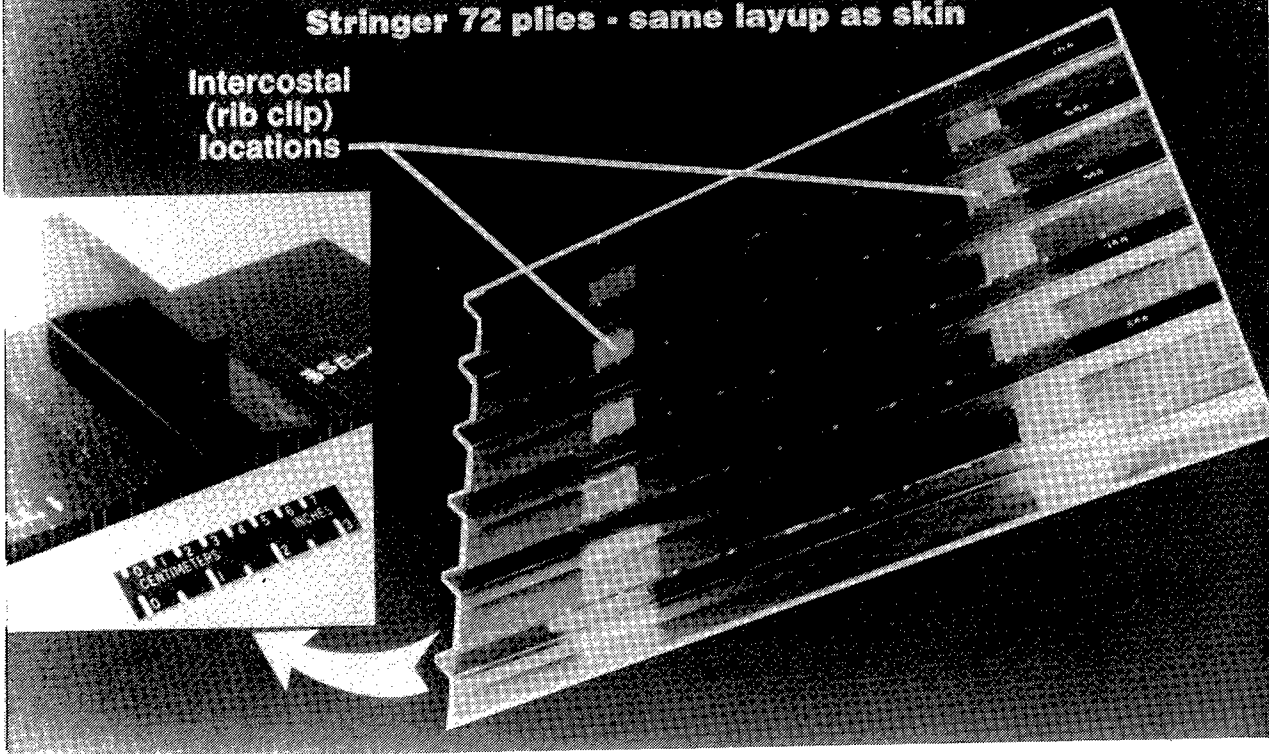


Figure 6(b)

## Damage Tolerant Stiffened Panel Concept

Figure 7(a) shows the fabrication procedure for making preforms for wing panels. The 54-ply skin is made by stitching together six 9-ply subelements in the desired orientation of  $0^\circ$ ,  $\pm 45^\circ$  and  $90^\circ$  plies. The stiffener is made by stitching together eight 9-ply subelements to form the web section. The flanges are formed by folding out 4 subelements on each side and cutting them at varied lengths to provide taper. A filler of prepreg tape is placed in the flange to web joint and the flanges are then stitched to the skin. A completed AS4 fabric single stringer preform is shown in figure 7(b), ready for resin impregnation and cure.

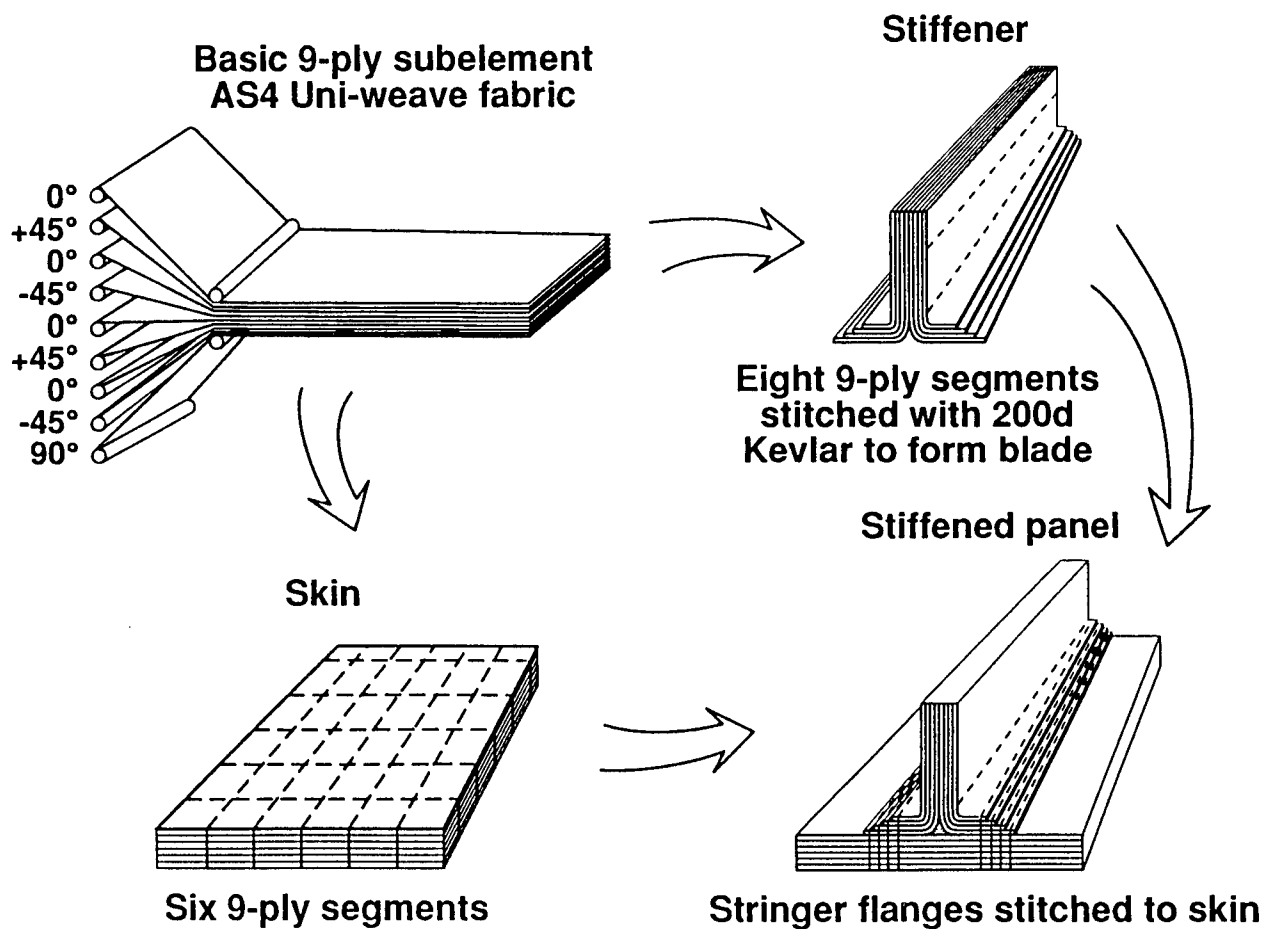


Figure 7(a)



## DRY STITCHED CARBON FABRIC PREFORM

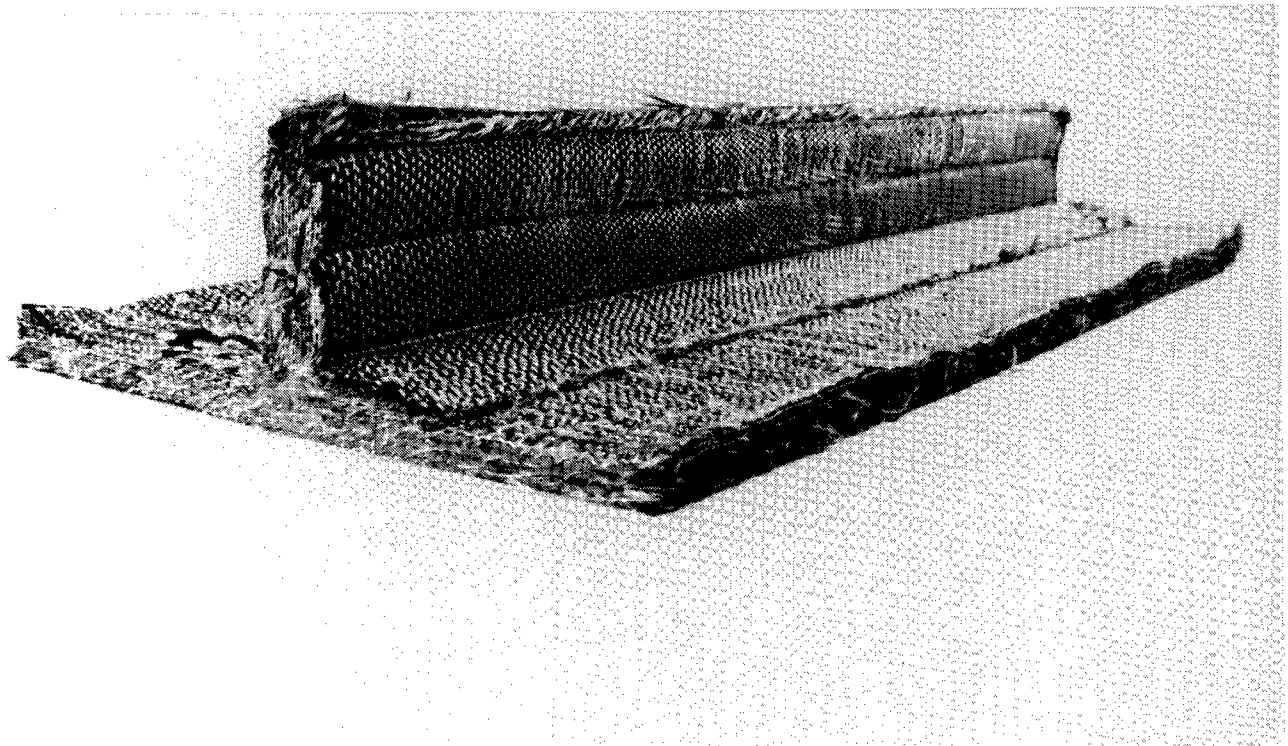


Figure 7(b)

## Single Needle Lock Stitch Machine

Preforms for all database laminates and the stiffened panels, figure 6, were stitched on the manual single needle lock stitching machine shown in figure 8. The machine features adjustable needle and bobbin thread tensions and variable stitch pitch and stitch speed. An adjustable guide rail reset after each pass controls the row spacing. With an arm reach of five feet, the machine can accommodate a 0.5 inch thick by 5 feet wide dry preform of any length. Because the stitching speed is slow and the operator must move the preform by hand, this machine is not suitable for the economical stitching of large preforms.

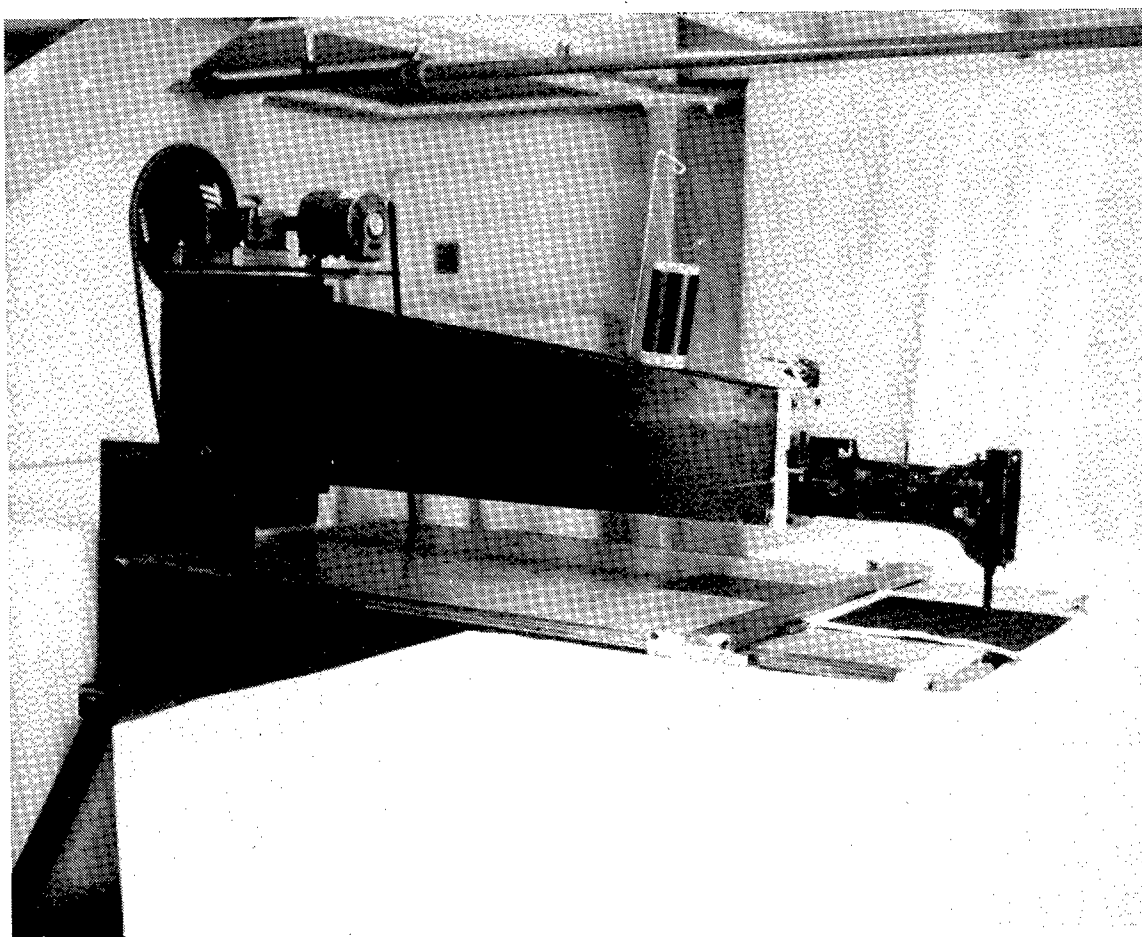


Figure 8

## Automated Single Needle and Multi-Needle Stitch Machines

Single needle manual stitching machines have proven to be invaluable tools in the development of damage tolerant stitched composite structures, but more efficient and cost effective methods of stitching preforms must be developed. Figures 9(a) and 9(b) show two stitching machines being developed by Pathe under the Douglas ICAPS contract. The multi-needle stitching machine with up to 256 needles, is mechanically controlled and can accommodate a 128 inch wide preform. In its current design, the multi-needle machine will perform both light and heavy density stitching. The single needle stitching machine features computer controlled motion of the stitching head with a work area of eight feet by fifteen feet. Both machines are limited to lock stitching only. In the overall scheme, the multi-needle machine will stitch together single plies to make a wing skin, for example; then stiffeners will be stitched to the skin using the single needle machine. The current manual machine, figure 8, would require about 400 hours to stitch an eight by twelve foot preform, whereas the new automated multi-needle machine would reduce that time to about one hour (ref. 4).

### DRY PREFORM MULTI-NEEDLE STITCHING MACHINE

Cam/Gear Control - 256 Needles in Two Rows  
Stitching Width 128 Inches - Lock Stitching

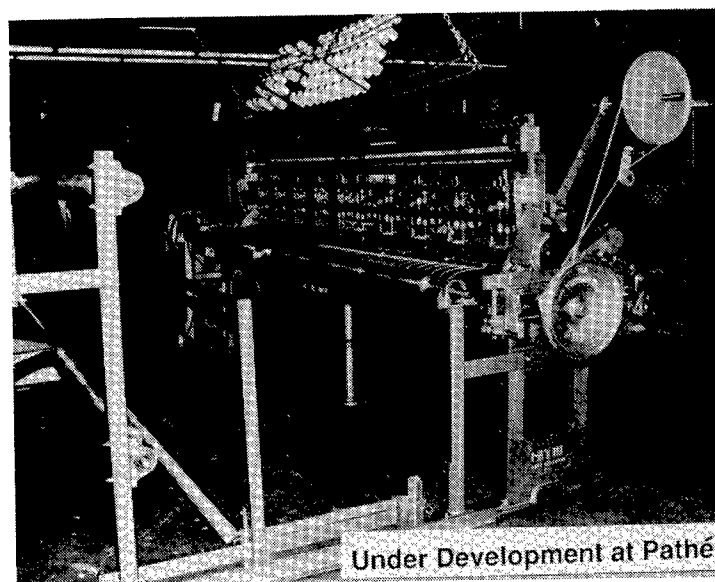


Figure 9(a)

## DRY PREFORM SINGLE NEEDLE STITCHING MACHINE

Computer Controlled X-Y Motion of Stitching Head  
Working Area 8' x 15' - Lock Stitching

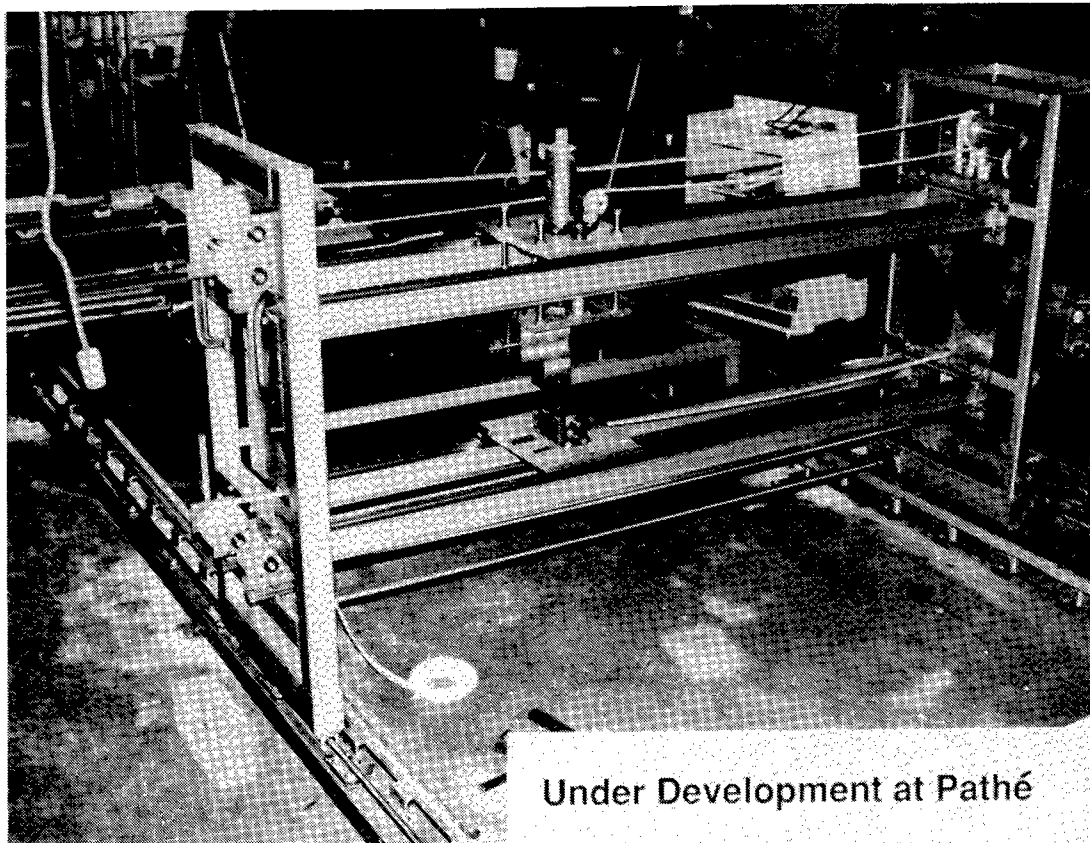


Figure 9(b)

## Specimen Fabrication for Database Testing

The overall scheme for fabricating and testing specimens for the stitching/RTM database is shown in figure 10. Laminates were made with AS4 uniweave fabric that contained 97.5 weight percent 0° (warp) carbon fibers and 2.5 percent 90° (fill) glass fibers. The glass fill fibers were used merely to stabilize the 0° carbon fibers and facilitate handling of the fabric. Individual plies of the uniweave fabric were cut and stacked in a  $[45^\circ/0^\circ/-45^\circ/90^\circ]_{2S}$  sequence to form a 16-ply, quasi-isotropic laminate and in a  $[45^\circ/0^\circ/-45^\circ/90^\circ]_{12S}$  sequence to form a 96-ply laminate. The 16-ply laminates were chosen for testing to simulate fuselage structure and the 96-ply laminates were chosen to represent built-up areas of the wing skins. The dry fabric preform stacks were lock stitched with S-2 fiberglass and Kevlar 29 threads of various weights, then resin transfer molded with 3501-6 resin. The AS4 fabric and 3501-6 epoxy resin were chosen as the baseline materials because they have been well characterized and, compared with other fiber/resin systems, are among the least expensive. The resin evaluation specimens were quasi-isotropic unstitched laminates of uniweave fabric that were resin transfer molded using either Shell 1895 or 862 resins or the British Petroleum E905L resin.

Test specimen configurations are shown in the lower left quadrant of figure 10. The 1.75-inch by 1.5-inch short block compression specimen is a NASA Langley configuration suitable for tests of angle ply laminates. For the tension tests, a tabbed 9-inch by 1-inch specimen was used and the compression after impact tests were performed using the 10-inch by 5-inch specimen shown, as recommended by reference 5. Results of previous laminate property and stitching guideline tests are given in reference 1.

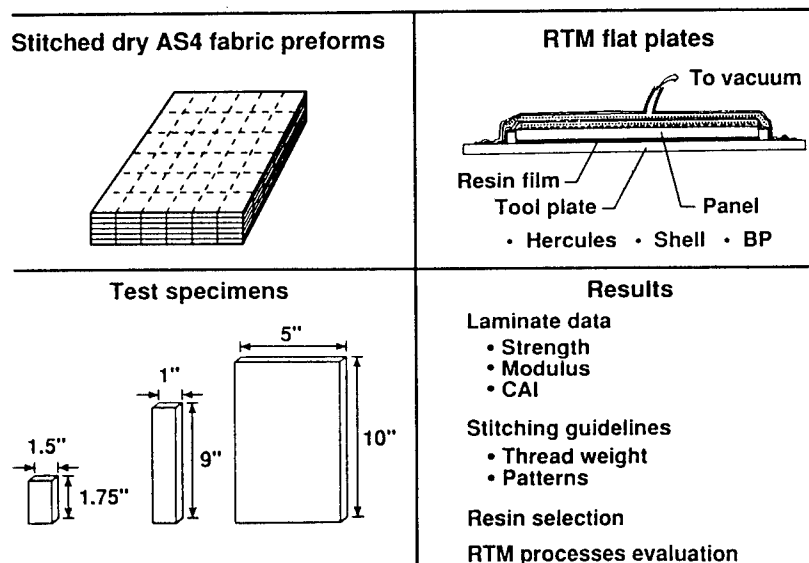


Figure 10

## Effect of Laminate Thickness on Stitched Composite Properties

Strength and stiffness data for tension and compression tests of thin (16-ply, 0.096-inch nominal thickness) and thick (96-ply, 0.576-inch nominal thickness) stitched laminates are shown in figure 11. Values shown represent the average of three test specimens. Two different stitching patterns were used: 1/8" and 3/16" row spacing each with eight penetrations per inch and stitch rows parallel to the 0° carbon fibers, (designated 0° stitching). The thick compression specimens were stitched using the same two patterns, but with an additional pattern having stitch rows perpendicular to the 0° carbon fibers (90° stitching). All specimens were stitched with a 200 denier (d) Kevlar 29 needle thread and with bobbin threads as indicated in figure 11. Denier is the weight in grams of a 9000 meter length of thread. In the designation for S-2 glass, the number '449' refers to the epoxy compatible sizing on the fibers, and '1250' refers to the thread weight in yards per pound.

For the thin laminates, the data show that using S-2 glass bobbin thread, which is six times heavier than the 600d (7448 yards/pound) Kevlar bobbin thread, gives much lower in-plane properties. The highest strengths were obtained using the 3/16" x 8 x 0° stitch pattern and Kevlar 29 600d bobbin thread. For the thick laminates, compressive properties of thick laminates with 0° stitching were higher than for 90° stitching. Additionally, better properties were obtained using the 3/16" x 8 x 0° stitch pattern and 3000d (1488 yards/pound) Kevlar bobbin thread. These results are in agreement with data presented in reference 1.

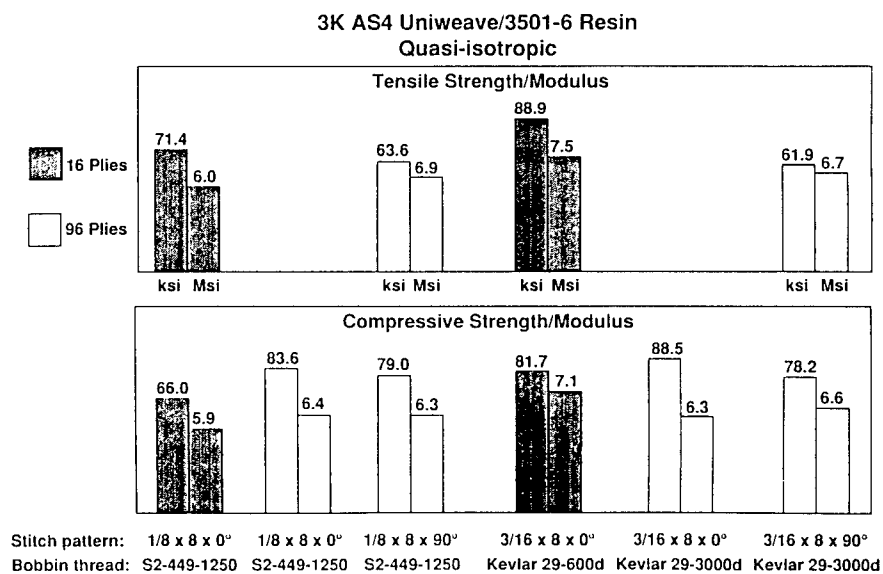


Figure 11

## Post-Impact Compression Strength Retention of Stitched Composites

Figure 12 shows the results of compression after impact (CAI) tests on thin (16-ply) and thick (96-ply) stitched laminates. The thin specimens were impacted using a 0.5-inch diameter steel tup attached to a 10-pound drop weight at the energy levels indicated. The thick laminates were impacted using a 1.0-inch diameter steel tup attached to a 20-pound drop weight at the energy levels shown. These energy levels were chosen to assess the damage tolerance of stitched laminates under severe conditions.

The results for the thin laminates show that using the stronger S-2 glass bobbin thread (breaking strength: 59 pounds) and the 1/8" x 8 x 0° stitching gives outstanding CAI strength retention when compared to laminates stitched with 600d Kevlar bobbin thread (breaking strength: 24 pounds) and 3/16" x 8 x 0° stitching. However, as shown in figure 11, lower in-plane properties were obtained using S-2 glass and 1/8" x 8 x 0° stitching. Based on results presented here and in reference 1, the best compromise for stitching thin laminates would be the 3/16" x 8 x 0° stitch pattern and 600d Kevlar thread.

C-scans (not shown) of the thick panel with 1/8" x 8 x 90° stitching indicated the presence of manufacturing defects prior to being impacted at 100 ft-lbs, and would explain the lower CAI strength than those impacted at higher energies. There were no indications of manufacturing defects in the other thick panels. The results for the thick laminates indicate that there is no real advantage in using either one of the thread/stitch pattern combinations tested. When compared to the results presented in figure 11, however, the best combination of in-plane properties and CAI strength retention was obtained using 3000d Kevlar thread (breaking strength: 124 pounds) and the 1/8" x 8 x 90° stitch pattern. These results are in agreement with those presented in reference 1.

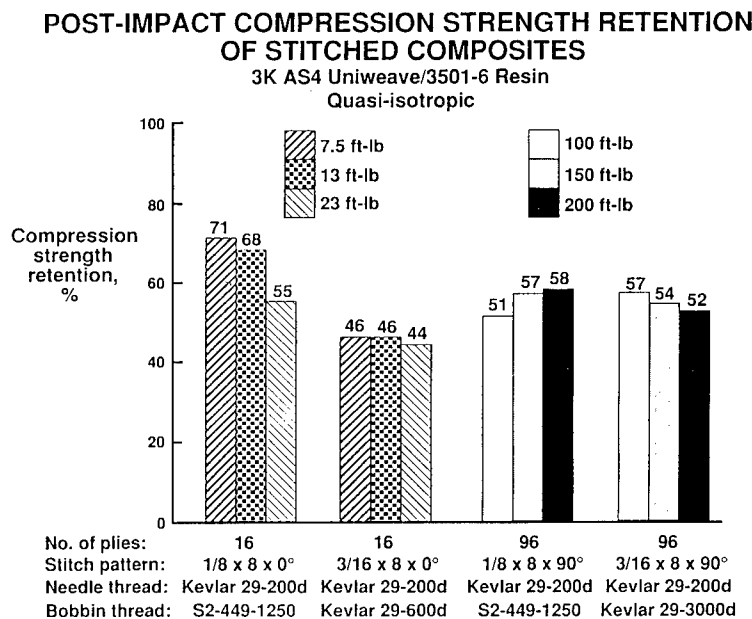


Figure 12

## RTM Resin Evaluation and Selection for Pressure RTM

The purpose of this investigation was to select a low viscosity resin for resin transfer molding fuselage panels. The 3501-6 resin used in wing structure was not considered for the pressure RTM process because of its short pot life at elevated temperature. Selection was focused on two-component resins formulated specifically for resin transfer molding. Figure 13 shows the results of tension and compression tests on quasi-isotropic unstitched laminates. The 8-ply test specimens were fabricated from AS4 uniweave fabric with ply orientation of  $[45^\circ/0^\circ/-45^\circ/90^\circ]_s$ , then resin transfer molded using the three resins shown. Both Shell resins, 1895 and 862, showed comparable tension properties, but the 1895 resin had the best room temperature, dry (RTD) and hot, wet compression properties of the three resins tested. The 1895 and 862 laminates, each with an average thickness of 0.051 inch, were thinner than the E905L laminate, which was 0.059 inches thick. The difference in thickness might indicate that the E905L laminate had a lower fiber volume fraction and thus explain its lower properties. Both Shell resins, at five and ten dollars per pound, are more economical when compared with 3501-6 resin (\$36 per pound) or toughened resins (\$100 or more per pound). The best combination of performance and cost was provided by the Shell 1895 resin, which was selected by Douglas for pressure RTM of the fuselage elements. Ongoing RTM resin evaluation tests at Langley will further verify these results.

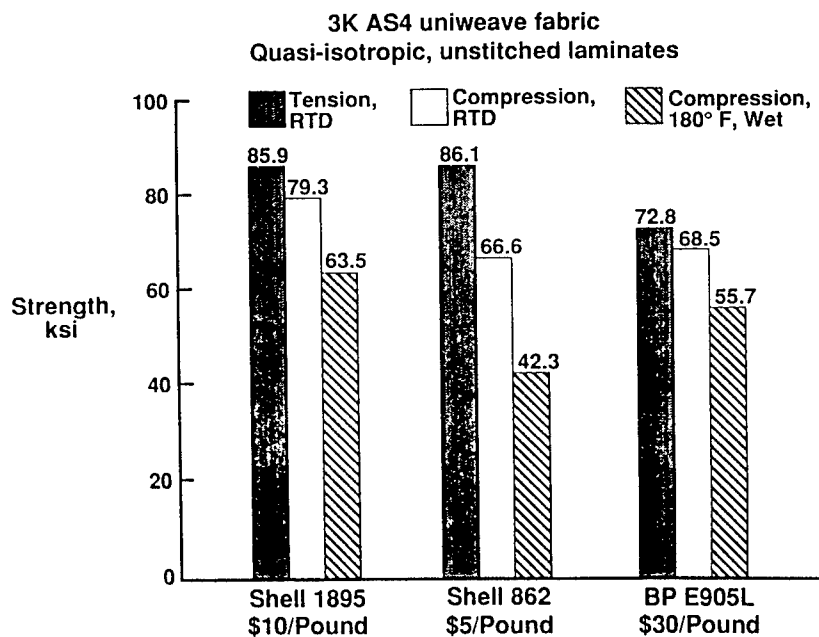


Figure 13



## Expanding the Technology for Stitched/RTM Structures

NASA Langley Research Center's in-house program to expand the science-based technology for stitched/RTM composite structures is outlined in figure 14. Within the Materials Division, the Mechanics of Materials Branch will be involved with Douglas in cooperative research to model the mechanics of stitched laminates. The Applied Materials Branch will investigate the effects of stitching parameters on structural performance, new stitched materials concepts, and environmental effects on stitched laminates. Each element of the program will be discussed further in succeeding figures.

- **Mechanics modeling of stitched composites**
- **Effects of stitching parameters on structural performance**
- **Effects of moisture and thermal cycles**
- **New stitched material concepts**

Figure 14

## Mechanics of Stitched Laminates

Figure 15 shows the areas to be investigated in a NASA/Douglas cooperative research program on mechanics of stitched composites. Researchers will study failure modes such as Euler buckling, "micro" buckling and sublamine buckling, as well as bolted joint failure modes such as net tension and bearing. Interlaminar toughness testing will also be included, along with the effects of ply drops on fatigue properties.

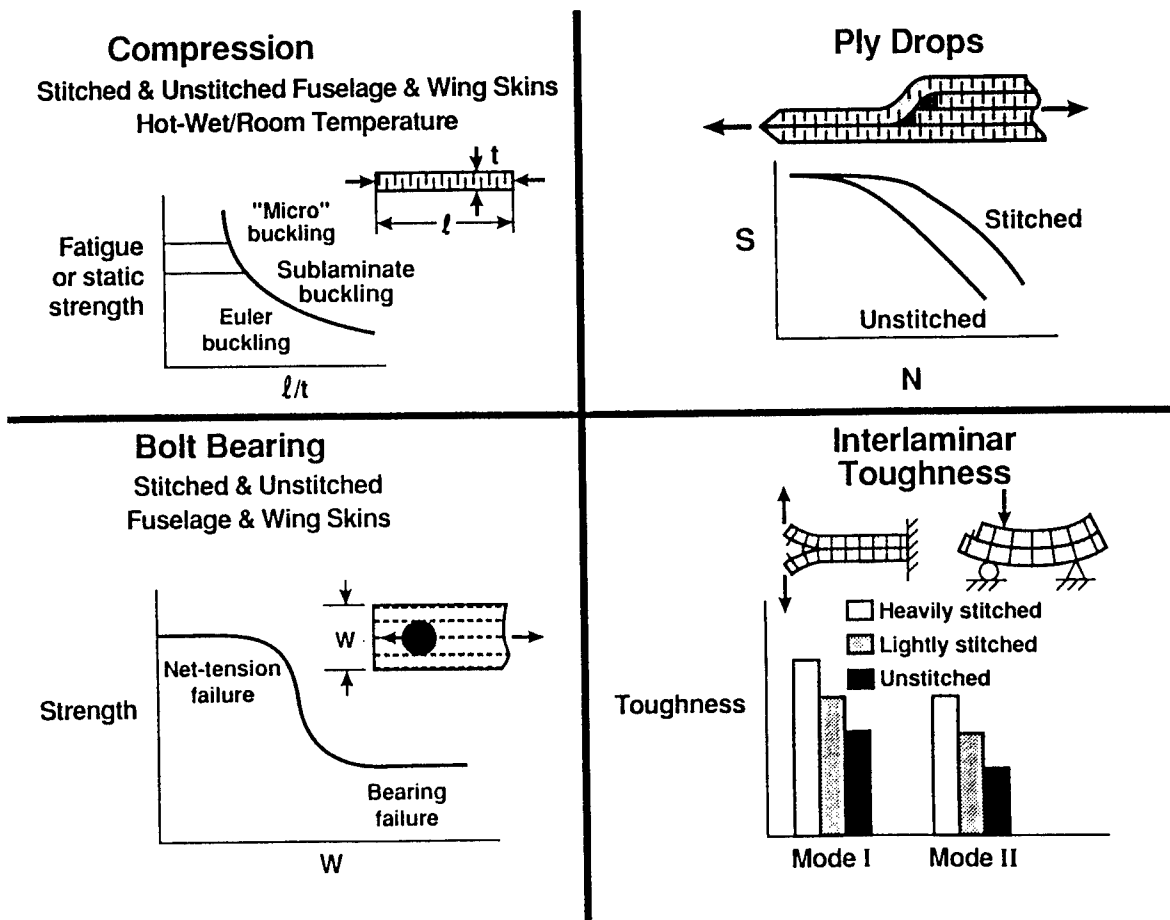


Figure 15

## Stitched Composites Parametric Investigation

A test program shown in figure 16 will investigate five different stitched composite parameters: laminate thickness (number of plies), stitch pitch, row spacing, thread material and thread strength. Tension, compression and compression after impact tests will be performed. A design of experiments (Taguchi) approach will be employed to provide significant information with a minimum number of tests. The resulting parametric database will be used to develop predictive models and stitching guidelines. The guidelines will include the laminate thickness/stitch parameter interactions and the trade-offs between in-plane strength loss and improved damage tolerance. British Petroleum E905L resin was chosen for this study before the RTM resin evaluation results presented in figure 13 were available. Additional resins may be included in this work as more resin evaluation tests are completed.

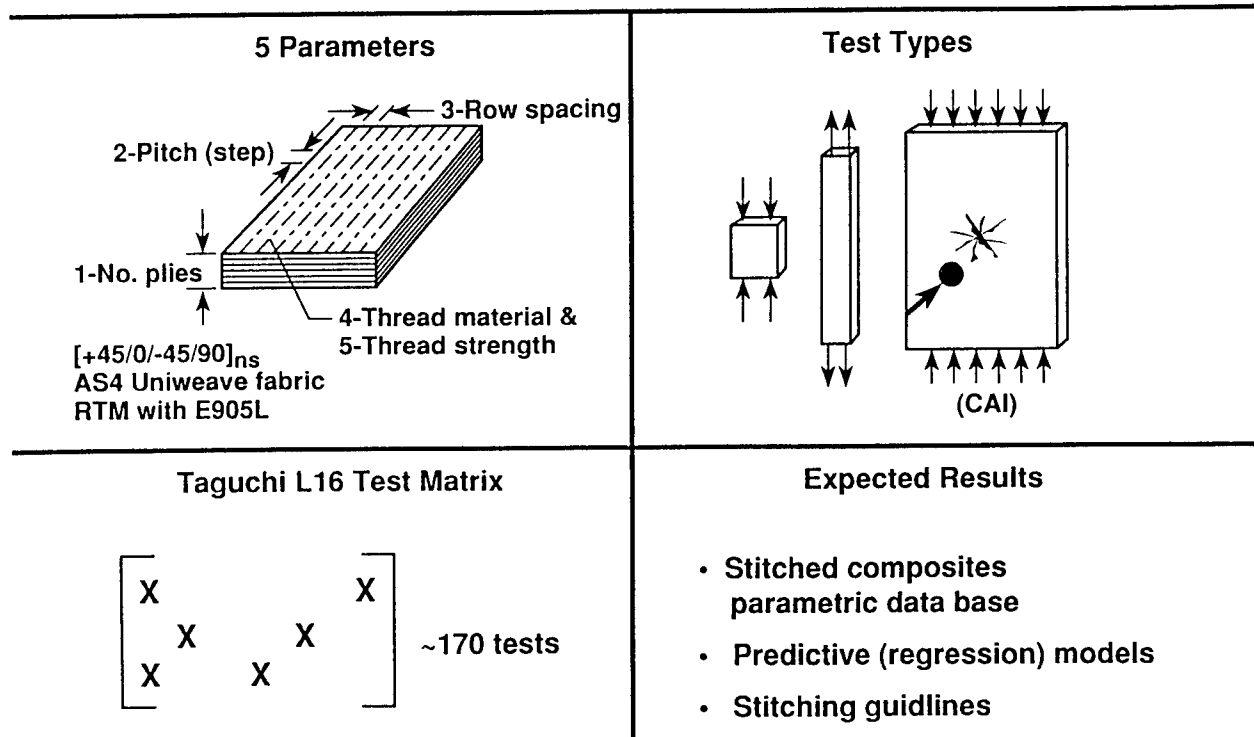


Figure 16

## Environmental Effects on Stitched Composites

Figure 17 illustrates another Langley research program that is currently investigating environmental effects on stitched composites. Test panels are 32-ply quasi-isotropic laminates of AS4 uniweave fabric, with ply orientation of  $[45^\circ/0^\circ/-45^\circ/90^\circ]_{4s}$ . Three groups of specimens will be tested: unstitched laminates, and laminates stitched with 1500 yd/lb S-2 glass thread or 1000d Kevlar 29 thread. All test panels have been resin transfer molded with 3501-6 resin, cut into test coupons as shown, and are being subjected to an environmental cycling regime of  $+60^\circ\text{C}$  to  $-54^\circ\text{C}$  and 0 to 100 percent relative humidity. The 3501-6 resin was chosen because it has been well-characterized, and it is the resin selected for thick, heavily loaded wing panels of the type shown in figure 6. The expected results of this study include diffusion coefficients that will better define the moisture absorption of stitched composites, a greater understanding of microcracking mechanisms, especially around the stitch threads, and residual strength properties as a function of environmental history. A companion study that investigates the effects of jet fuels, hydraulic fluids, and other chemicals on RTM resins is nearly completed.

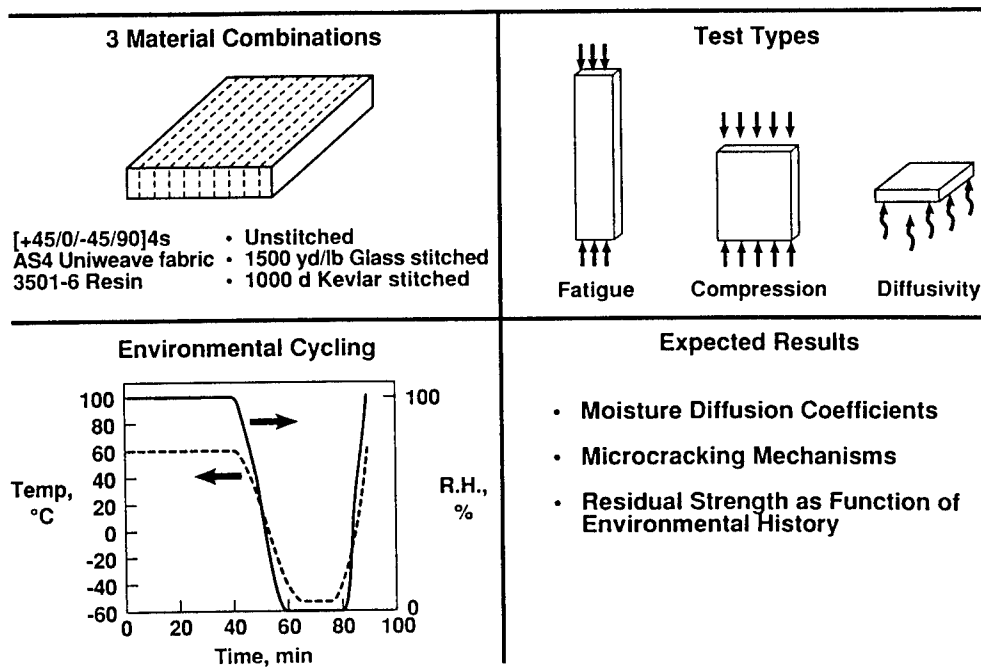


Figure 17

## Improved Damage Tolerance of Composites Using Glass Buffer Strips

Figure 18(a) illustrates a third Langley research program aimed at utilizing existing materials combined with stitching and resin transfer molding to create innovative damage tolerant materials. This research will use glass buffer strip fabric made of AS4 uniweave, with half-inch strips of the 0° carbon (warp) fibers replaced with S-2 glass as shown in Figure 18(b). The glass "softening" buffer strips, less stiff than the surrounding carbon fibers, have been shown to effectively arrest crack growth in composites (ref. 6), but their compression properties have not been adequately characterized. The 40-ply quasi-isotropic laminates will be laid up with glass buffer strips in every layer and ply orientation of  $[45^\circ/0^\circ/-45^\circ/90^\circ]_{5s}$ . The panels will then be stitched, resin transfer molded and cut into test specimens as shown in Figure 18(a). British Petroleum E905L resin was chosen for this study before the RTM resin evaluation results presented in figure 13 were available. Additional resins may be included in this work as more resin evaluation tests are completed. Tension, short block compression, open hole compression, compression after impact and bearing test results are expected to demonstrate the best combination of buffer strip orientation and stitching for improved damage tolerance and bearing strength.

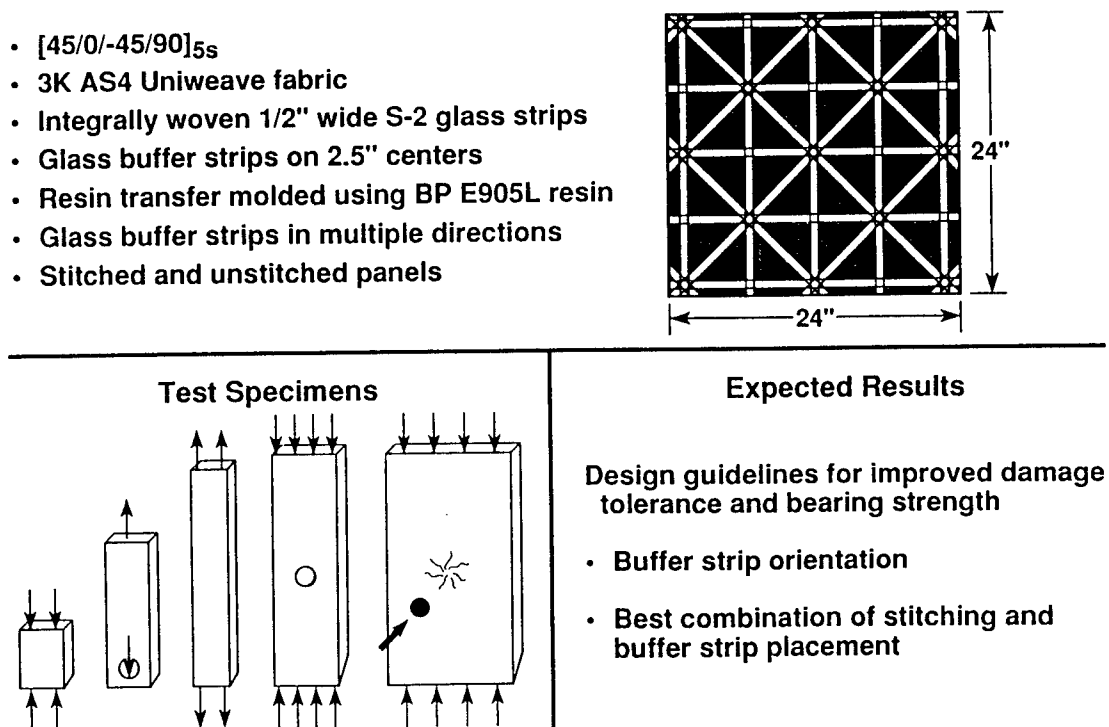


Figure 18(a)

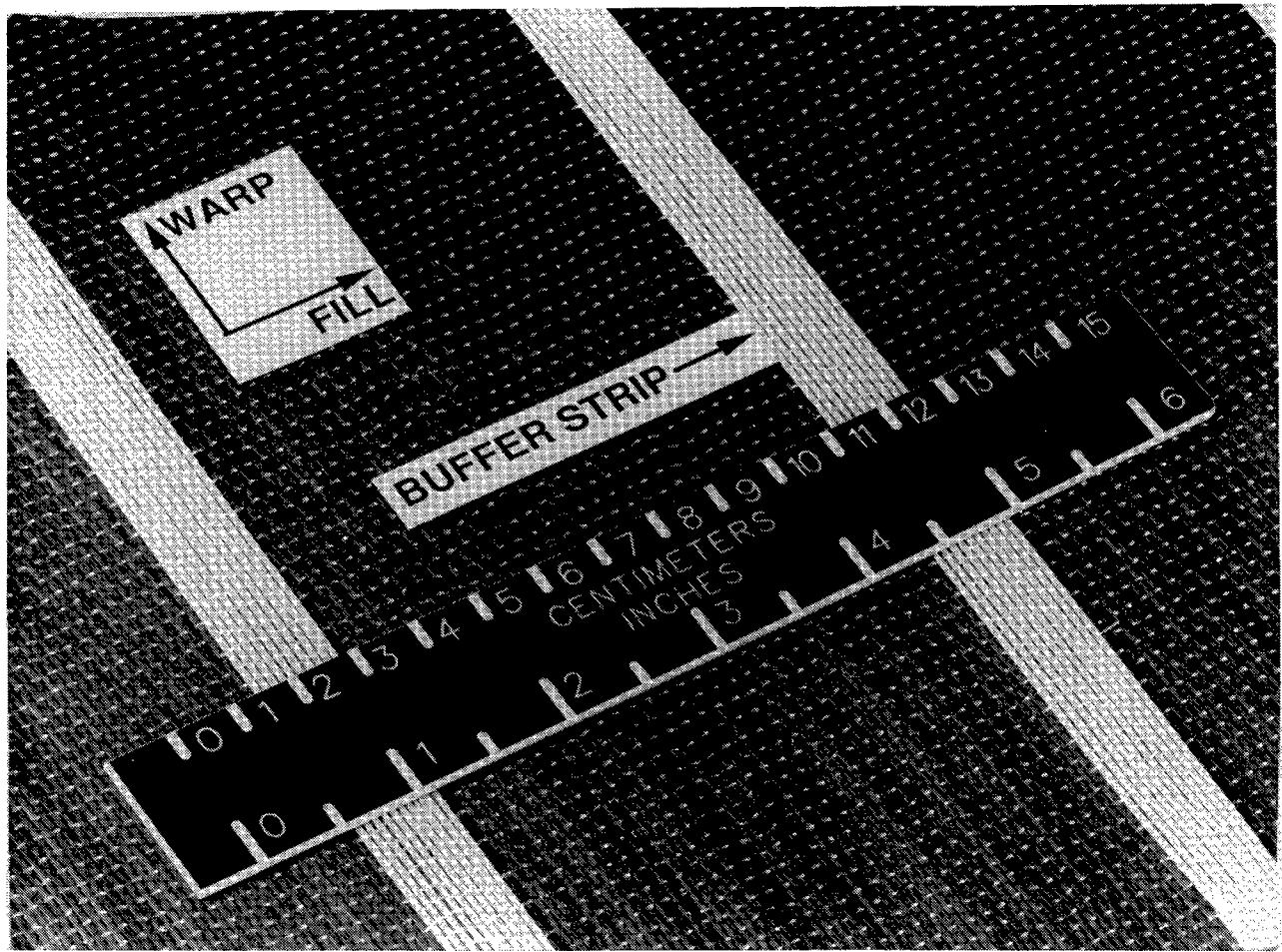


Figure 18(b)

## **Concluding Remarks The Case for Stitching**

The research to date on stitched/RTM composites supports the conclusions listed in figure 19. Stitched composites show outstanding damage tolerance, as indicated by their post-impact compression strength retention. Stitched composites also demonstrate acceptable fatigue behavior and hot, wet performance as reported in reference 1. Stitching and resin transfer molding provide near net shape molding of integral structures requiring very little machining to final size and reduce the need for mechanical fasteners. Lower cost fibers and resins can be used in stitched and resin transfer molded structures, making them more cost-effective than toughened resin composites and traditional prepreg tape composites. In summary, stitched and resin transfer molded composites afford strong potential to achieve the benefits of weight savings and performance offered by composite primary aircraft structures.

- **Completed tests on stitched laminates showed:**
  - Outstanding damage tolerance
  - Acceptable fatigue behavior
  - Acceptable hot, wet performance
- **Provides near net shape molding of integral structures**
- **Accommodates lower cost fibers and resins**
- **Reduces need for mechanical fasteners**
- **Potential breakthrough technology for composite primary structures**

Figure 19

## References

1. Palmer, Raymond J., Dow, Marvin B., and Smith, Donald L.: Development of Stitching Reinforcement for Transport Wing Panels, *First NASA Advanced Composites Technology Conference*, Seattle, WA, Oct. 29-Nov.1, 1990. NASA CP-3104, Part 2, pp. 621-646.
2. Madan, Ram C.: Composite Transport Wing Technology Development, NASA CR 178409, Feb., 1988.
3. Sumida, R. C., Madan, R. C., and Hawley, A. V.: Test Results for Composite Specimens and Elements Containing Joints and Cutouts, NASA CR 178246, Aug., 1988.
4. Chen, Victor L., et. al.: Composites Technology for Transport Primary Structure, *First NASA Advanced Composites Technology Conference*, Seattle, WA, Oct. 29-Nov.1, 1990. NASA CP-3104, Part 1, pp. 71-126.
5. Standard Tests for Toughened Resin Composites - Revised Edition. NASA RP-1092, July 1983.
6. Poe, C. C., and Kennedy, J. M.: An Assessment of Buffer Strips for Improving Damage Tolerance of Composite Laminates, *Journal of Composite Materials Supplement*, 1980, vol. 14, pp. 57-70.



**THIS PAGE INTENTIONALLY BLANK**

**Resin Transfer Molding Technology for  
Composite Primary Wing and Fuselage Structures**

A. Markus  
Douglas Aircraft Company

**THIS PAGE INTENTIONALLY BLANK**

# TEST AND ANALYSIS RESULTS FOR COMPOSITE TRANSPORT FUSELAGE AND WING STRUCTURES

Jerry W. Deaton  
NASA Langley Research Center  
Hampton, VA

Susan M. Kullerd  
Lockheed Engineering & Sciences Company  
Hampton, VA

Ram C. Madan and Victor L. Chen  
Douglas Aircraft Company  
Long Beach, CA

## INTRODUCTION

Automated tow placement (ATP) and stitching of dry textile composite preforms followed by resin transfer molding (RTM) are being investigated by researchers at NASA Langley Research Center and Douglas Aircraft Company as cost-effective manufacturing processes for obtaining damage tolerant fuselage and wing structures for transport aircraft. The Douglas work is being performed under a NASA contract entitled "Innovative Composites Aircraft Primary Structures (ICAPS)." Data are presented in this paper to assess the damage tolerance of ATP and RTM fuselage elements with stitched-on stiffeners from compression tests of impacted three-J-stiffened panels and from stiffener pull-off tests. Data are also presented to assess the damage tolerance of RTM wing elements which had stitched skin and stiffeners from impacted single stiffener and three-blade-stiffened compression tests and stiffener pull-off tests.

The design concepts for stitched/RTM fuselage and wing panels were developed under previous NASA contracts and details are presented in references 1 and 2. The design criteria that the selected fuselage and wing concepts must satisfy are given in reference 3.

## ICAPS TEST ARTICLES

The ICAPS test articles being evaluated are outlined in figure 1. The ATP fuselage elements include three-J-stiffened compression and J-stiffened pull-off specimens. The ATP crown panels were fabricated by Hercules, Inc., Magna, Utah, under contract to Douglas Aircraft Company using Hercules IM7/8551-7 graphite fiber reinforced toughened epoxy composite material. The skins and stiffeners were fabricated separately and cocured together. The skin and stiffener had the same layup  $[0/90/45/0/-45/90]_s$ . The RTM fuselage elements also include three-J-stiffened compression and J-stiffened pull-off specimens. The RTM crown panels had the same stacking sequence for the skin and stiffener as the ATP fuselage elements and utilized AS4 graphite uniweave fabric. Stiffeners were stitched to the skin and the assembly was pressure resin transfer molded with Shell 1895 epoxy resin using fixed volume tooling.

The damage tolerance of the fuselage elements was determined from impact tests performed on the compression and pull-off specimens. The impact energy for all fuselage elements was between 10 and 20 ft-lbs, which was the range of impact energy levels needed to obtain barely visible damage, and was accomplished by using either a 0.5-inch diameter or 1.0-inch diameter hemispherical drop weight impactor.

The RTM wing elements tested include single stiffener compression, three-blade-stiffened compression, and blade-stiffener pull-off specimens. The wing panels were fabricated from stitched skins and stiffeners utilizing AS4 graphite uniweave fabric. The skin has 54 plies with ply orientations of  $[0/45/0/-45/90/-45/0/45/0]_{3s}$ , and the stiffeners are 72 plies with the same layup as the skin. The stiffeners are stitched to the skin and then resin transfer molded with 3501-6 epoxy resin.

The damage tolerance of the wing elements was also determined from impact tests performed on wing element specimens. The impact energy for all impacted wing specimens was 100 ft-lbs, which is the cut off energy level for detectability, and was accomplished by using a 1-inch diameter hemispherical drop weight impactor.

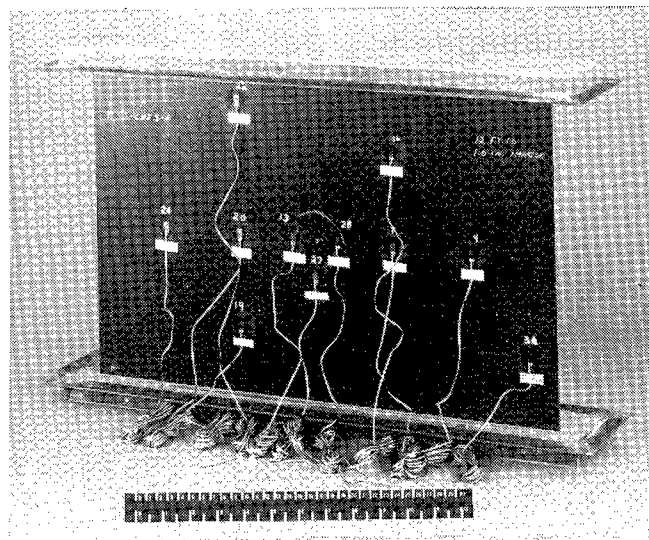
All RTM fuselage and wing elements were fabricated by Douglas Aircraft Company. All testing was performed at NASA Langley Research Center except as noted.

- **Auto tow placed (ATP) fuselage elements**
  - IM7/8551-7
  - Three-J-stiffened compression tests
  - J-stiffened pull off tests
- **Resin transfer molded (RTM) fuselage elements**
  - AS4 Uniweave fabric/Shell 1895
  - Stitched stiffener
  - Three-J-stiffened compression tests
  - J-stiffened pull off tests
- **Resin transfer molded wing elements**
  - AS4 Uniweave fabric/3501-6
  - Stitched skin and stiffeners
  - Three blade stiffened compression tests
  - Single stiffener compression tests
  - Blade stiffened panel pull off tests

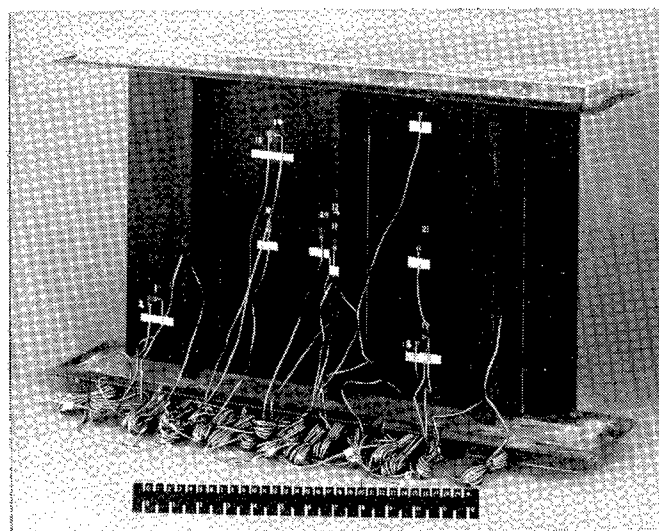
Figure 1

### THREE-J-STIFFENED COMPRESSION PANEL

A typical fuselage compression panel is shown in figure 2. Specimens were nominally 21-inches wide and 15-inches long. The ends of each panel were potted using a room temperature potting compound. The ends of the panels were then machined flat, square, and parallel to each other. All impacted panels were impacted (prior to the potting procedure) from the skin side, midway between the specimen ends which were clamped during impact. Impact locations were either mid-bay, over the center stiffener, or at the flange edge of the center stiffener. Impact energy levels were selected which resulted in barely visible damage at each impact location. Each specimen was strain gaged as shown in figures 2a and 2b. The skin side of each compression panel was then spray painted white in order to use Moiré fringe interferometry to obtain buckling loads, mode shapes, and mode changes during the compression tests.



(a) Skin side



(b) Stiffener side

Figure 2

## TEST SETUP FOR J-STIFFENED COMPRESSION TESTS

A 300 kip hydraulic test machine was used to apply compression loads to the specimens; see figure 3. In addition to the strain gages, seven LVDT's were used to monitor specimen displacements. One was used to monitor overall specimen shortening and two were used on each stiffener, one for out-of-plane displacements and one for stiffener rolling. Most specimens were tested at 0.02 in./min and strains and displacements were recorded continuously using an IBM PC-based data acquisition system.

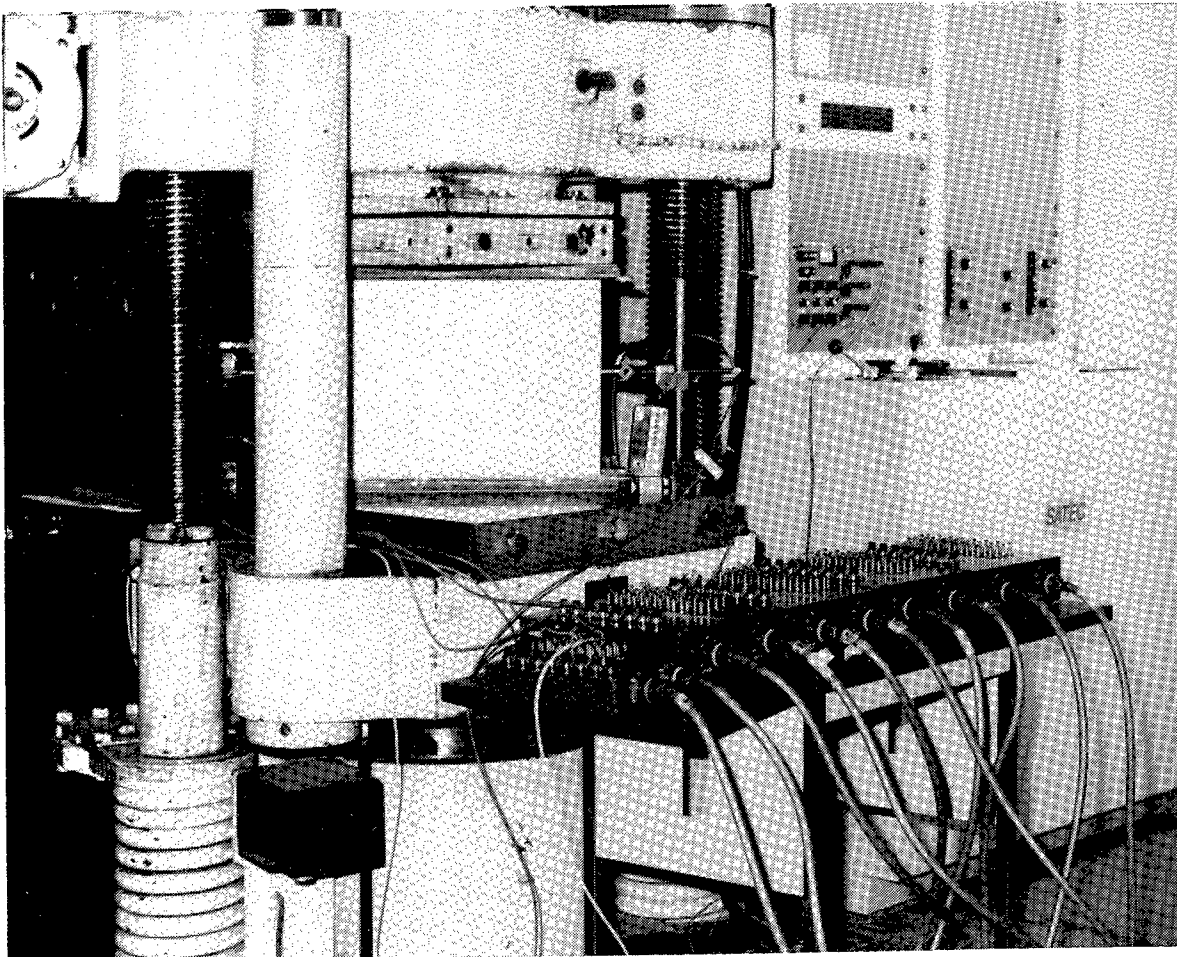
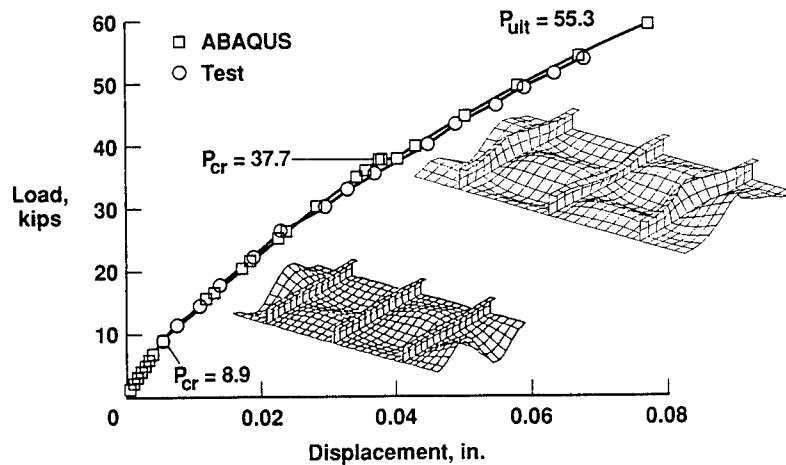


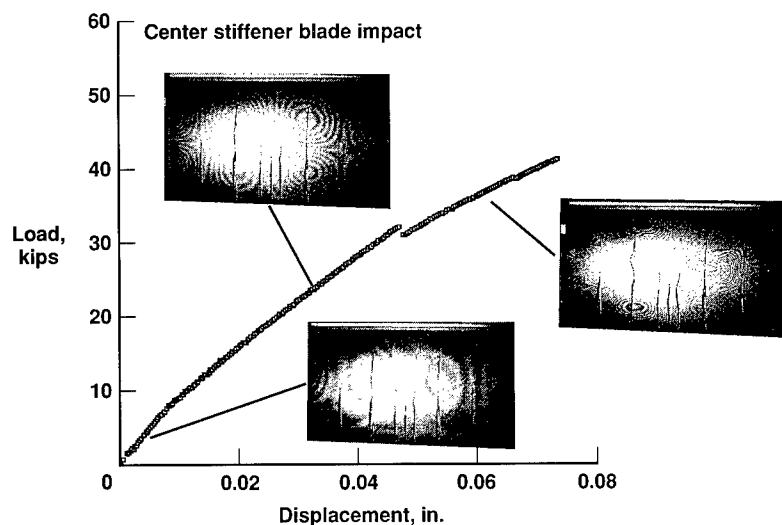
Figure 3

## LOAD-SHORTENING OF FUSELAGE J-STIFFENED PANELS

Figure 4 shows typical load-shortening data plots for the ATP and stitched/RTM fuselage J-stiffened panels under compression. Also shown in figure 4a are finite element simulation results obtained for the ATP panel using the ABAQUS code. Numerical predictions are shown to agree very well with test results. The ATP panel behaved linearly up to about 9 kips, then buckled into a one-half-wave mode (not shown) due to wide free edges. This mode smoothly grew into a two-half-wave mode slightly above the first  $P_{cr}$ , but the FEA showed lack of convergence and a nonlinear buckling (bifurcation) procedure was adopted. A three-half-wave mode was found numerically at 37-38 kips while tests showed this mode occurred around 35 kips with a loud popping sound. The FEA provided convergent results beyond 60 kips but predicted crippled stiffeners at about 55 kips, which is the measured failure load. Finite element simulation for the stitched/RTM fuselage panel has not been conducted because all necessary property data for the AS4 uniweave fabric/Shell 1895 material is not yet available. However, the load-shortening curve along with the Moiré fringe photographs, figure 4b, indicates that the stitched/RTM fuselage panel behaved similarly to the ATP panel under compression loading.



(a) ATP



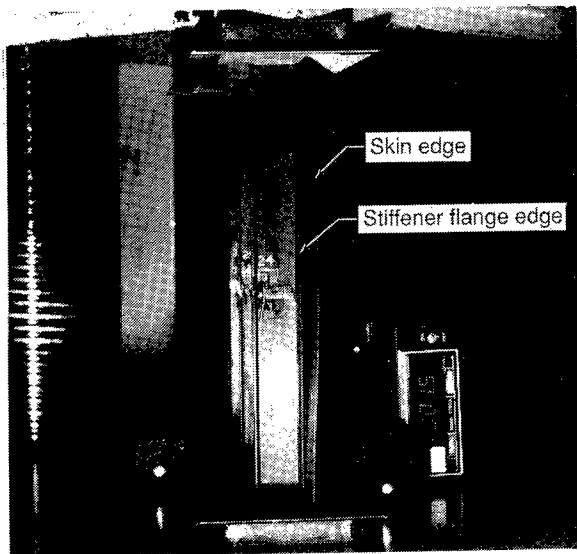
(b) RTM

Figure 4

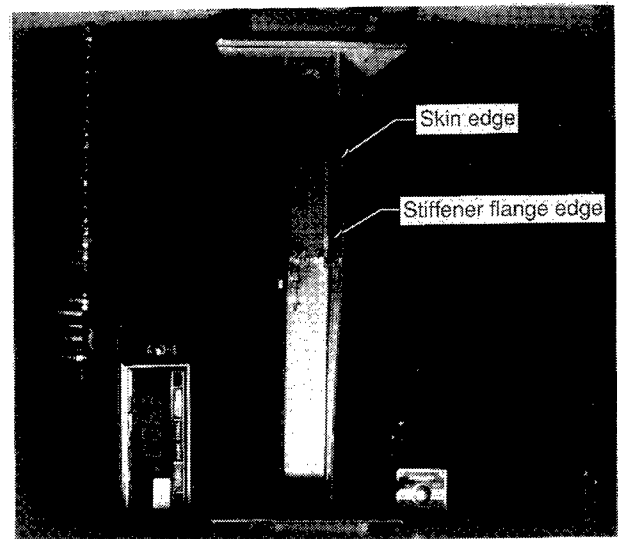


## J-STIFFENED COMPRESSION PANEL FAILURE - SIDE VIEW

Figure 5 shows panel failure viewed from the side of the compression specimens. Figure 5a is for the ATP fuselage panel and illustrates stiffener crippling and skin/stiffener separation. Note that the stiffener flange edge is essentially straight whereas the skin edge is curved, which indicates that the buckled skin has separated from the stiffener. The load meter shown indicates a 1.5 kip load, which was applied to the specimen to better show the skin/stiffener separation. Figure 5b is for the stitched/RTM fuselage panel and illustrates a stiffener crippling failure but no skin/stiffener separation (both stiffener flange and skin are buckled) even with a 6.3 kip load applied as indicated by the load meter. All impacted stitched/RTM fuselage panel failures resulted in crippling failure of one stiffener without any skin/stiffener separation. Most impacted ATP panel failures involved crippling failures of all three stiffeners with accompanying skin/stiffener separation along with some degree of skin failure.



(a) ATP

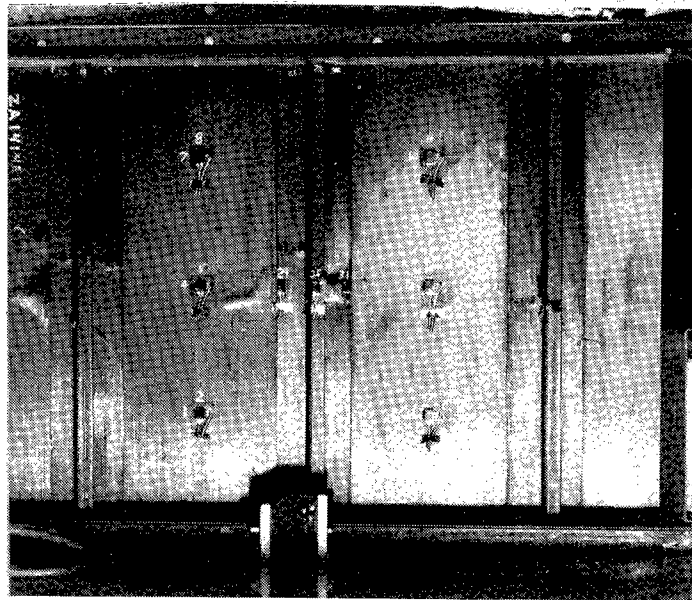


(b) RTM

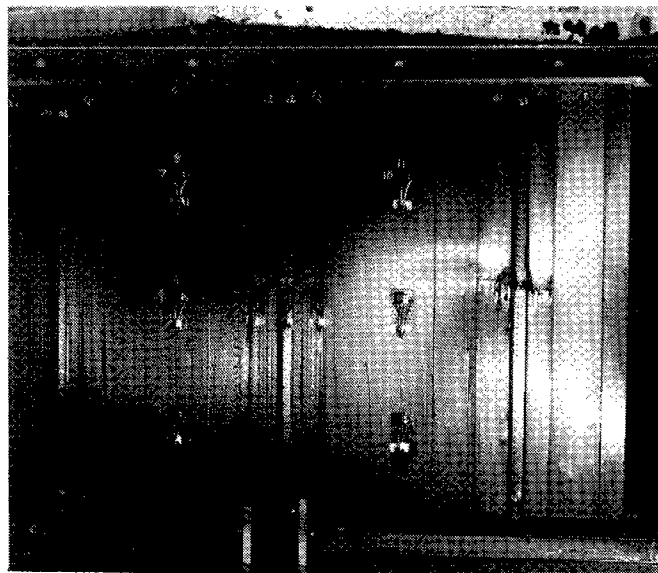
Figure 5

## J-STIFFENED COMPRESSION PANEL FAILURES - STIFFENER SIDE

Additional photographs were obtained from the stiffener side of the failed panels. Figure 6a shows the same failed ATP fuselage panel shown in figure 5a, again, with a compression load of 1.5 kips applied. Crippling failure of all three stiffeners is evident along with some outer ply skin failure. Figure 6b shows the failed stitched/RTM fuselage panel shown in figure 5b with a 6.3 kip load applied. The stiffener on the right has failed in crippling, but the flanges remain attached to the skin. The failures shown in figures 5 and 6 are typical for all impacted J-stiffened compression panels.



(a) ATP

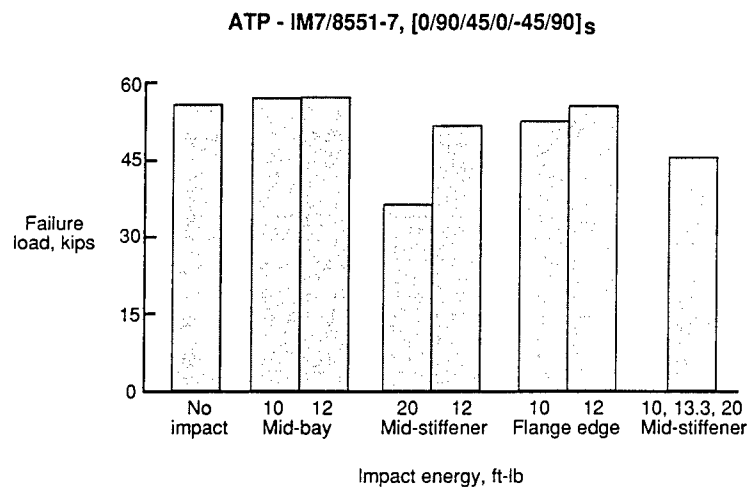


(b) RTM

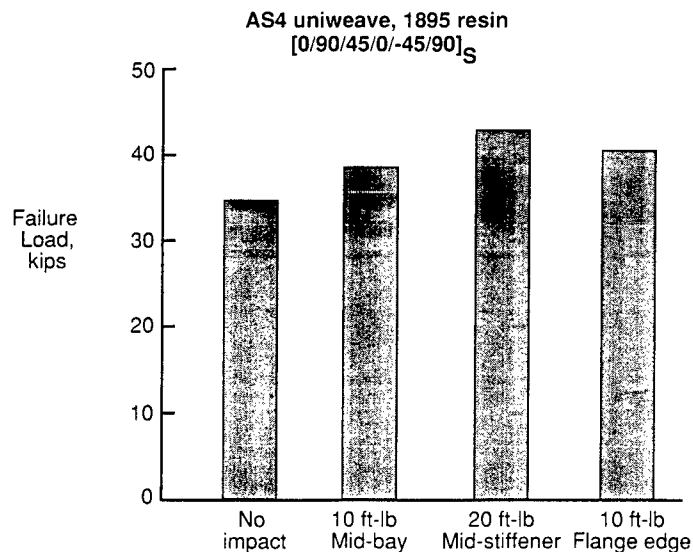
Figure 6

## POST-IMPACT COMPRESSION STRENGTH OF J-STIFFENED FUSELAGE PANELS

The failure load of each J-stiffened fuselage panel tested is shown plotted in figure 7 for each impact location and impact energy level evaluated. The ATP and stitched/RTM data are shown in figures 7a and 7b, respectively. The lowest failure load (denoted by asterisk) shown on each plot was obtained from tests which were conducted at a displacement rate 2.5 times faster than all other tests. At this loading rate, the panel may not have had sufficient time to redistribute loads between skin and stiffeners when the panel underwent buckling and mode shape changes, thus causing a premature failure. Design criteria (ref. 3) for the fuselage panels requires an ultimate compression loading of 1700 lb/in. or about 35 kips for the specimens being evaluated. All impacted specimens exceeded this requirement. The higher failure loads obtained for the impacted ATP fuselage panels compared to the stitched/RTM fuselage panels can be attributed to the higher strength fiber and toughened resin system used in their fabrication.



(a) ATP



(b) RTM

**Figure 7**  
**726**

## ATP FUSELAGE STIFFENER PULL-OFF SPECIMEN

Cabin design pressure differential for the baseline aircraft fuselage is 9.1 psi limit, ref. 3. This is associated with flight loads to provide a limit condition at which there should be no detrimental structural deformation. This can be interpreted conservatively as no initial stiffener separation in the pull-off case due to pressure alone. Figure 8 shows an ATP fuselage stiffener pull-off specimen which was used to assess the effects of impact on stiffener pull-off load. Impacted pull-off specimens were machined from impacted three-J-stiffened panels as previously described for the compression tests. Pull-off specimens were 11.5-inches long and 4.5-inches wide and had 0.125-inch thick aluminum doublers bonded on each end on both sides with a room temperature curing adhesive. The bottom of the "J" stiffener was machined off to facilitate the introduction of pull-off loads into the specimen. Initial pull-off specimens utilized numerous strain gages (figure 8) to ensure that a uniform load distribution was obtained with the pull-off fixtures. After ensuring that the fixture was performing as desired, either 2 or 4 strain gages were used to aid in detecting the load at which initial skin/stiffener separation occurred.

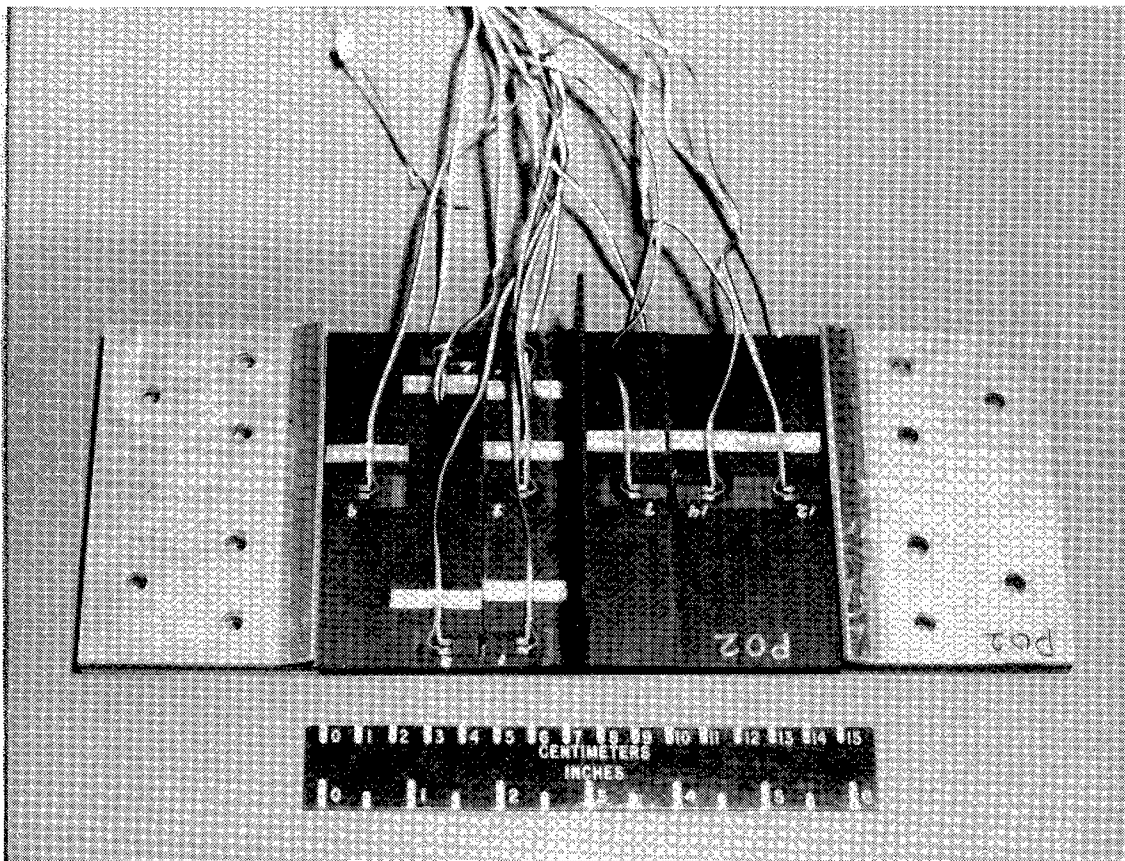


Figure 8

## TEST SETUP FOR FUSELAGE STIFFENER PULL-OFF TEST

The setup for fuselage stiffener pull-off tests is shown in figure 9. The specimen was bolted to the loading fixture and 0.25-inch thick aluminum splice plates were bolted to the stiffener as shown in the figure. All bolts were torqued to a value of 60 in.-lb. and the assembly was placed inside an environmental chamber. Load was introduced into the loading fixture and splice plates through 0.75-inch diameter pins. Most tests were performed at room temperature; however, three ATP pull-off tests were performed at 180°F after the specimens were soaked in 160°F water for 13 days. For these three tests, strain gages were installed and then sealed by applying three layers of silicone waterproofing compound. All tests were performed at a displacement rate of 0.05 in./min and strain was recorded continuously throughout the tests. Photographs were taken during the tests to document the failure sequence.

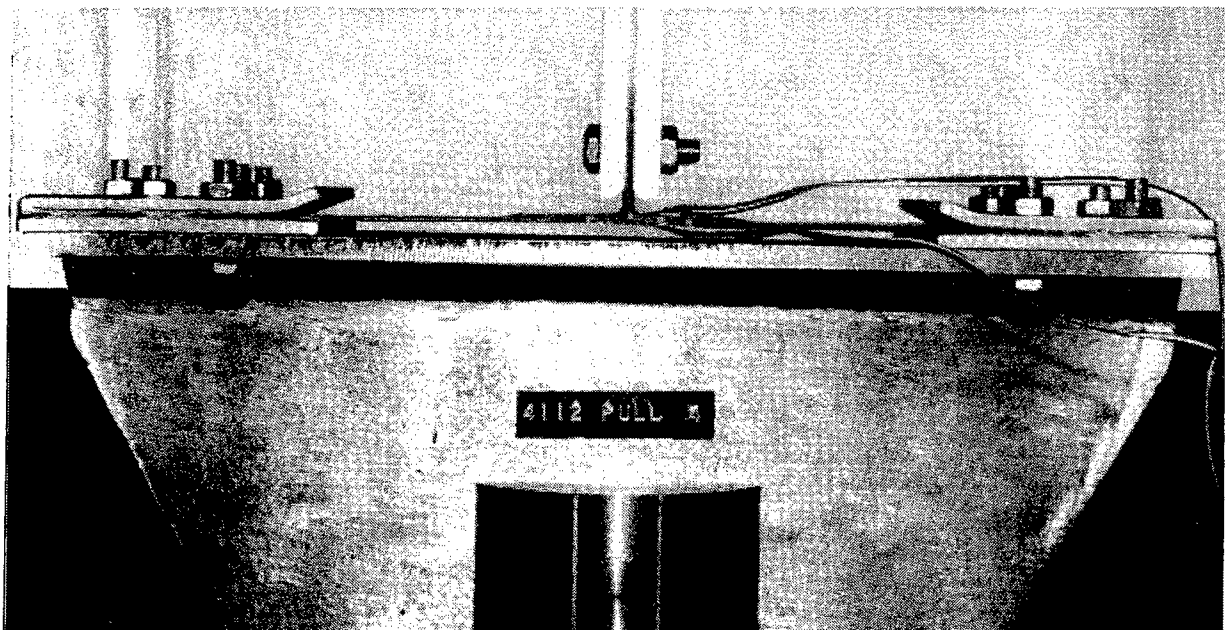


Figure 9

## STITCHED/RTM FUSELAGE STIFFENER PULL-OFF TESTS

A typical load/strain plot for one of the stitched/RTM fuselage stiffener pull-off tests is shown in figure 10. Only two gages were installed on this specimen; gage 1 was located on the stiffener flange next to the upright portion of the stiffener, and gage 2 was located on the skin side of the specimen directly beneath the center of the stiffener. Both gages were oriented in the long dimension of the specimen. Load was applied continuously until the stiffener separated from the skin for the ATP specimens or until all stitches failed in one of the flanges for the stitched/RTM specimens. Initial skin/stiffener separation load was determined from a loud popping sound, visually (door to chamber was open except for hot, wet pull-off test), or from strain gage data. Photographs at 600, 800, and 1000 pounds of applied load are shown in the figure to illustrate the typical failure sequence; note the increase in skin deflection and crack growth between skin and stiffener with increasing load.

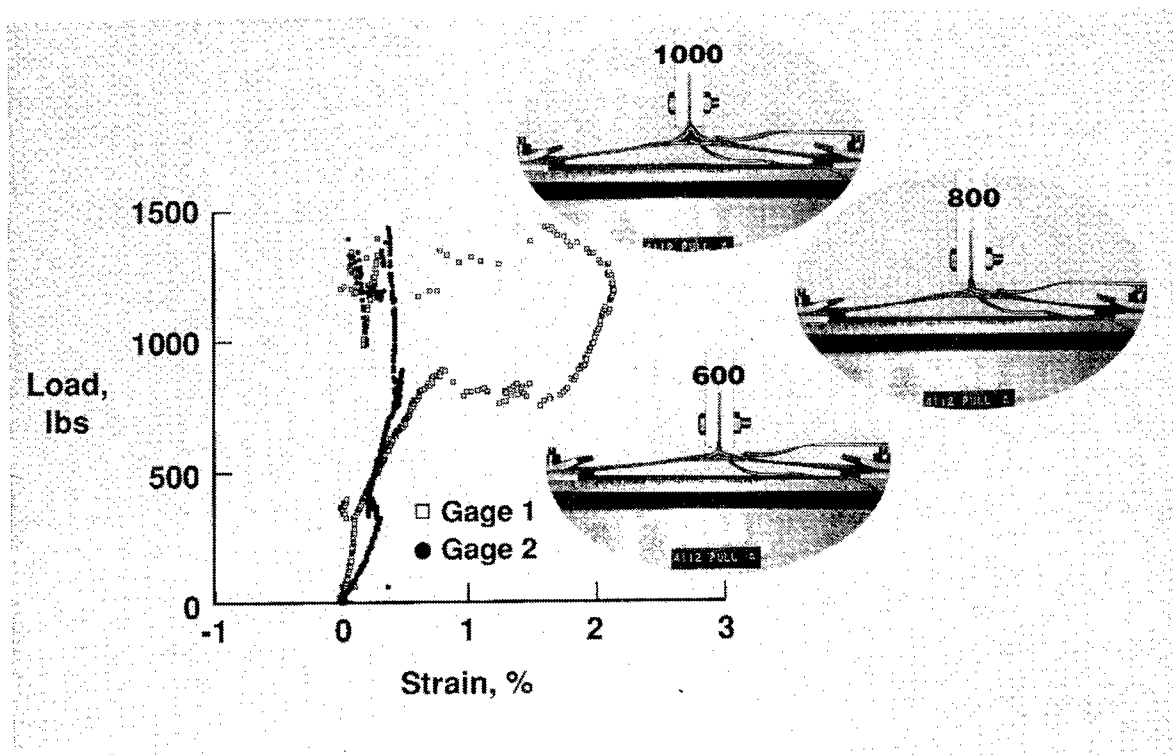


Figure 10

## STITCHED/RTM FUSELAGE STIFFENER PULL-OFF FAILURE

Figure 11 shows a stitched/RTM fuselage stiffener pull-off specimen after failure. For this specimen, the photograph was taken with zero load indicated on the test machine. The skin deflection shown in the photograph was not permanent: the skin straightened out when it was removed from the loading fixture.

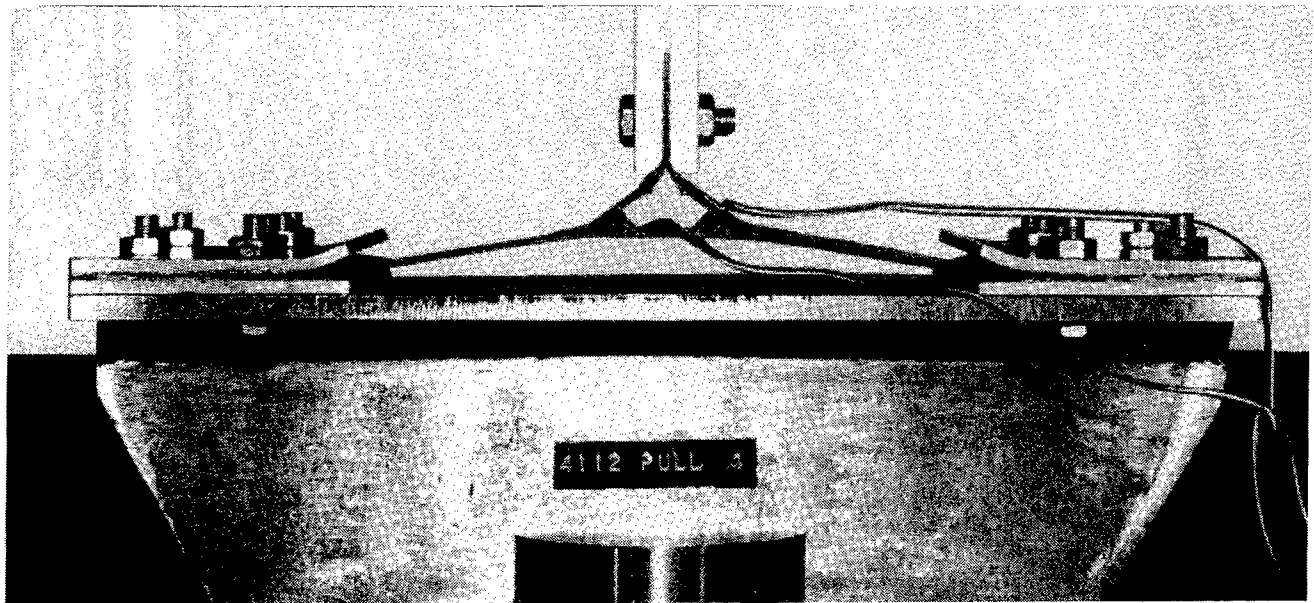


Figure 11

## EFFECT OF IMPACT ON FUSELAGE STIFFENER PULL-OFF LOAD

Results obtained from the stiffener pull-off tests are shown in figure 12a and 12b for the ATP and stitched/RTM fuselage stiffener pull-off specimens, respectively. It should be noted that the ordinate shown for the ATP data is only one-half of that shown for the stitched/RTM fuselage pull-off data. The shaded bars correspond to the pull-off load at which skin/stiffener separation initiated and the open bars represent failure load. Results shown for the ATP specimens which were not impacted are the average of three tests at room temperature (RTD) and the average of three tests at 180°F after a 13-day water soak in 160°F water (HW). The data indicate that the ATP specimens subjected to the water soak and elevated temperature test conditions had reduced failure and skin/stiffener separation loads of about 20 and 40 percent of the RTD values, respectively. All other data shown in figure 12a and 12b represent individual test results. The data indicate that the flange edge impact for the ATP specimens is the critical impact location for both skin/stiffener separation and failure load where a reduction of about 80 percent occurs. For the stitched/RTM specimens, no reduction in pull-off load or initiation of skin/stiffener separation is indicated due to impact energy level or impact location. Superior stiffener-to-skin integrity is indicated for the stitched/RTM fuselage concept where twice the ATP strength is indicated without damage and ten times the ATP strength with flange edge impact damage.

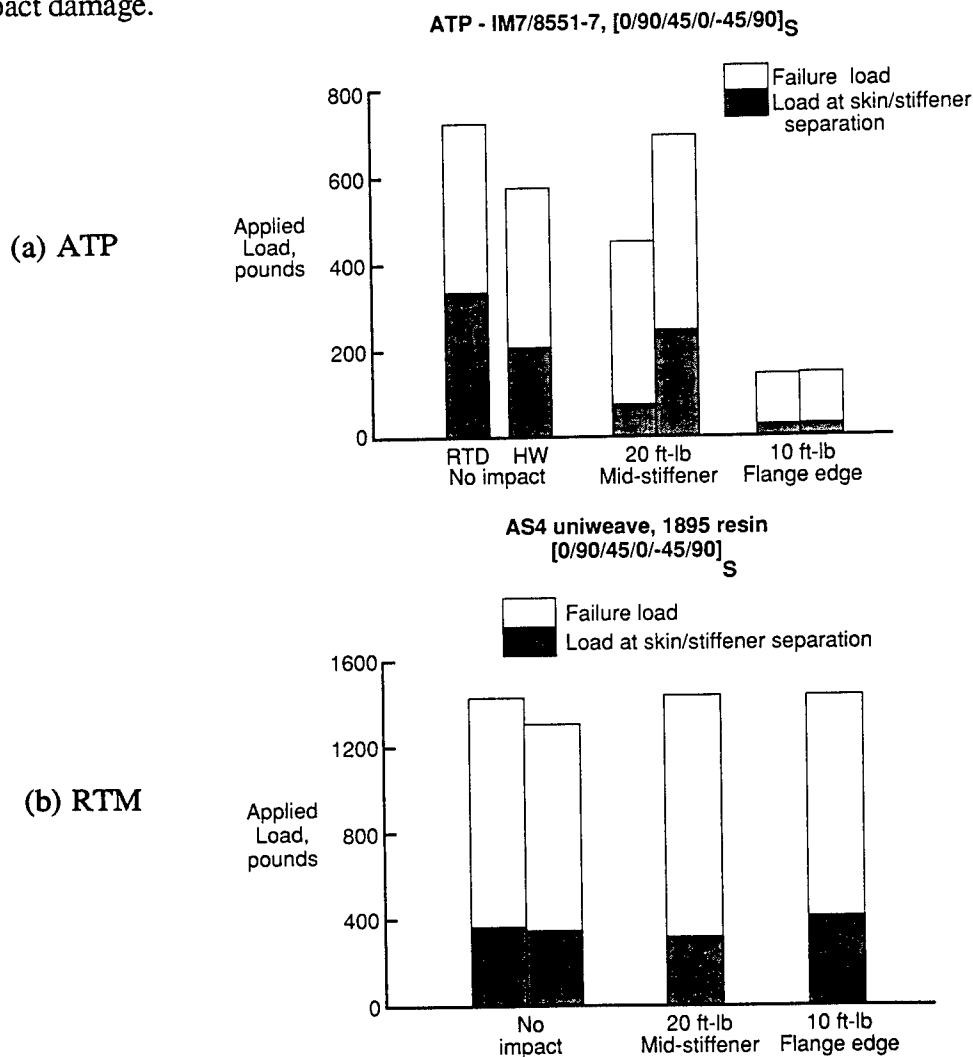


Figure 12



## DAMAGE TOLERANT STIFFENED PANEL CONCEPT

Figure 13 shows schematically the fabrication procedure for making preforms for wing panels. The 54-ply skin is made by stitching together six of the basic 9-ply subelements of AS4 uniweave fabric having the layup shown. The stiffener is made by stitching together eight of the 9-ply subelements to form the blade. Flanges are formed by folding out 4 subelements on each side and cutting them at different lengths to provide taper. A filler of prepreg tape is placed in the flange-to-blade joint and the flanges are then stitched to the skin. Additional information on this concept is detailed in the paper by S. Kullerd and M. Dow, titled "Development of Stitched/RTM Composite Primary Structures," also presented at this conference. The preform is placed in a tool and resin transfer molded with 3501-6 epoxy resin.

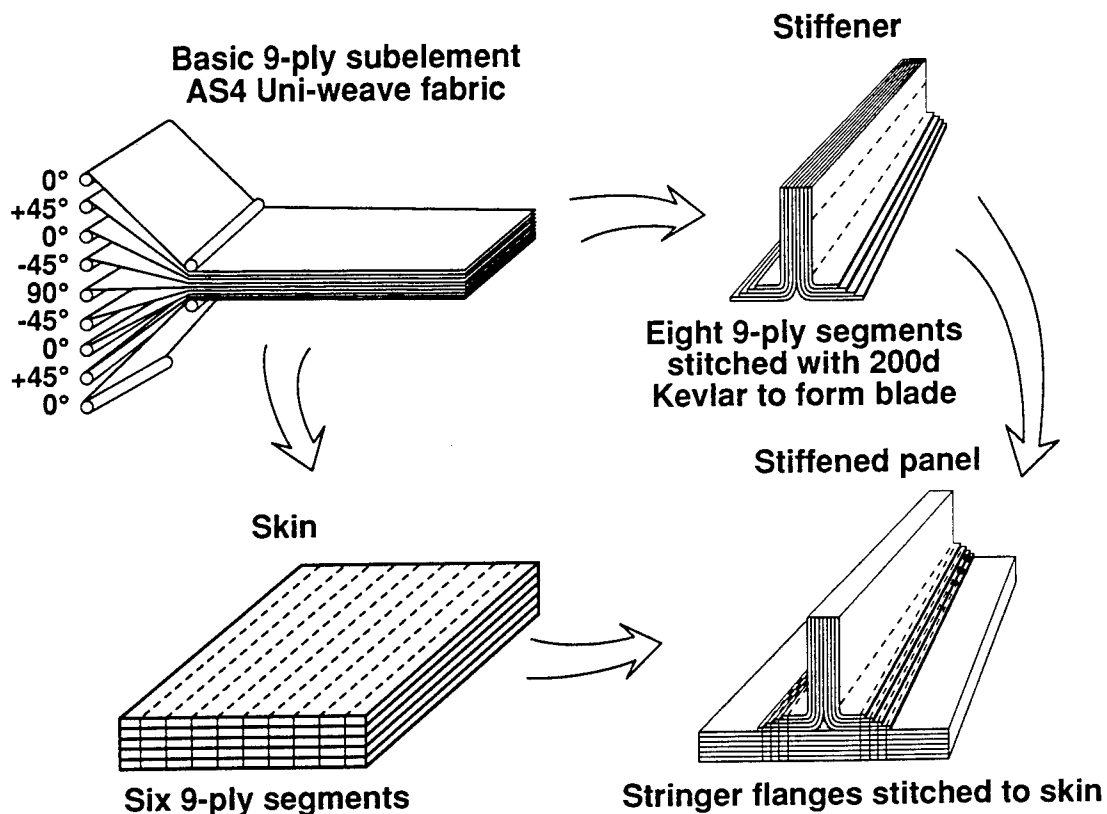


Figure 13

## DAMAGE TOLERANT COMPRESSION PANELS

Compression panels used to assess the damage tolerance of stitched/RTM composite primary wing structures are shown schematically in figure 14. Six single-stringer specimens were machined from one 3-stringer panel after impact. Impacts were made on the skin side directly beneath a stringer or at the flange edge of a stringer in such a way that the impact location for single-stringer specimens was at the center length during compression testing. The impact energy for all impacted specimens was 100 ft-lbs, which is the cut off energy level for detectability, and was accomplished by using a 1-inch diameter hemispherical drop weight impactor. The panel was C-scanned before machining the single-stringer test specimens. Each single-stringer specimen was instrumented with three pairs of back to back strain gages.

The skin side impact locations for the three-stringer panels include mid-bay, mid-stringer, and flange-edge of the middle stringer. The ends of each three-stringer panel was supported along its width and clamped to a table during impact. Each end of the three-stringer compression specimens was potted in a room temperature potting compound. The ends were then machined flat, square and parallel to each other. Each three-stringer panel was instrumented with 15 strain gages and included back-to-back pairs on both the skin and center stringer. The compression tests were performed at a displacement rate of 0.05 in./min by Douglas Aircraft Company or their subcontractor.

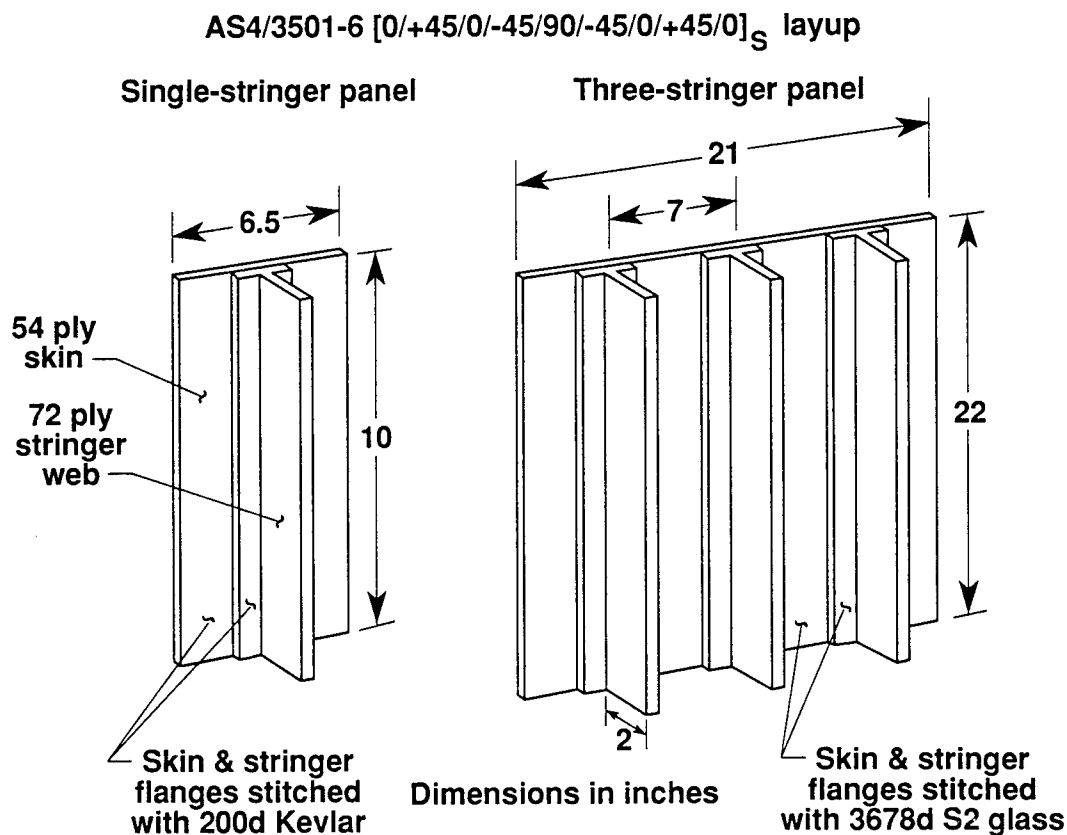


Figure 14

## POST-IMPACT CRIPPLING STRENGTH OF SINGLE-STIFFENER WING ELEMENTS

The effect of a 100 ft-lb impact on the crippling strength of single-stiffener compression specimens is shown in figure 15. The shaded bars are the average obtained from two specimens. The flange-edge impacted specimens failed at a lower load than unimpacted and mid-stiffener impacted specimens. However, the reduction was less than 10 percent for individual specimens. All single-stiffener compression tests were performed by Douglas Aircraft Company.

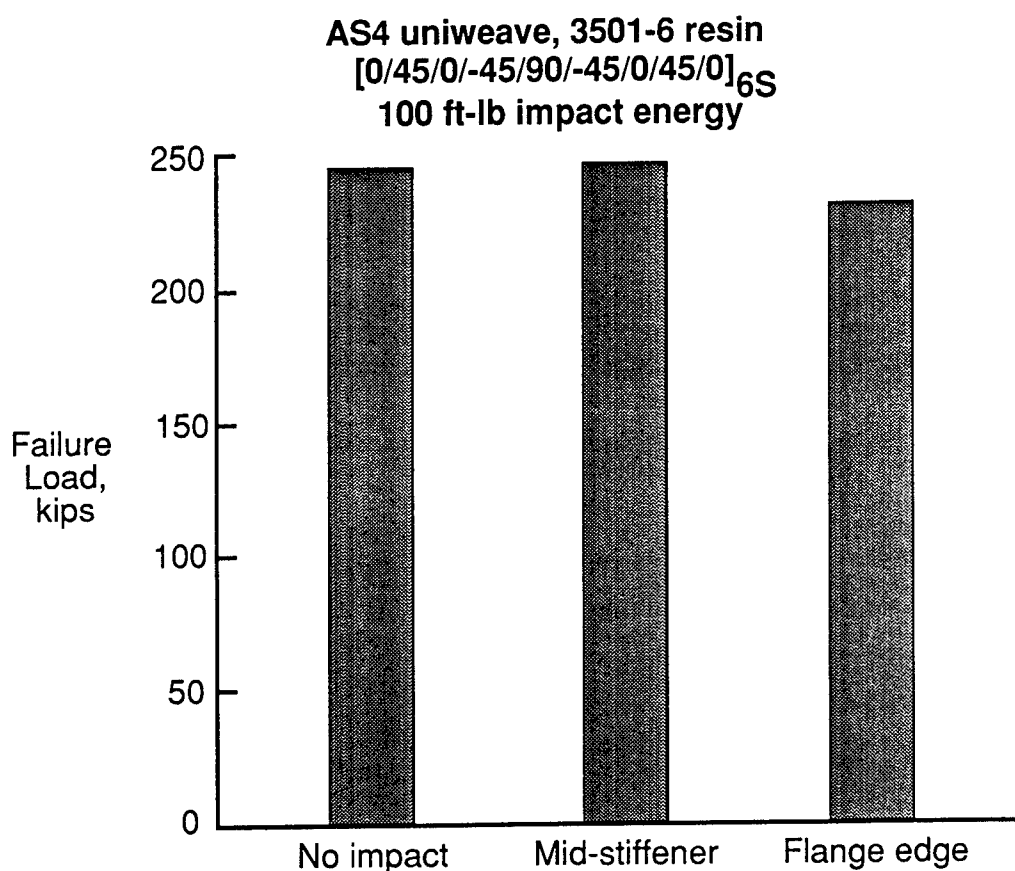
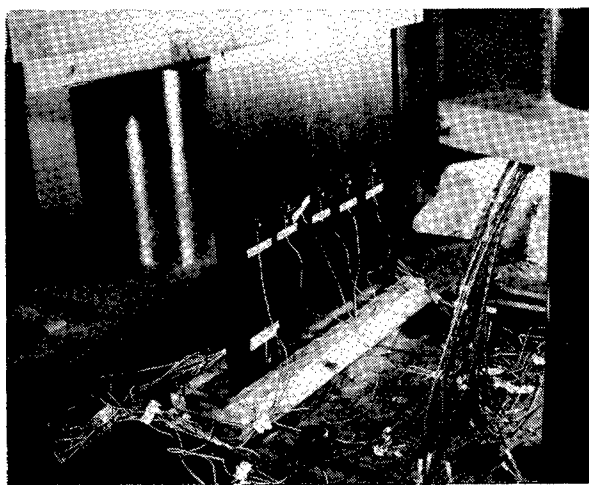


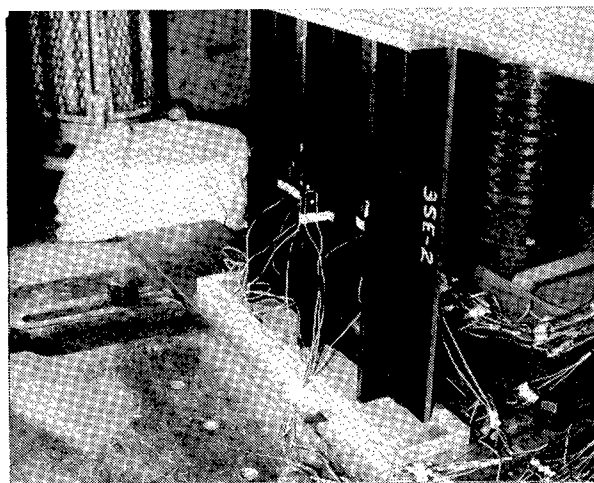
Figure 15

## TEST SETUP FOR COMPRESSION TEST OF 3-STIFFENER WING PANEL

The test setup for the 3-stiffener wing panel is shown in figure 16. The panel shown (figure 16a) has been impacted at the mid-bay location. Figure 16b shows the same panel as viewed from the stiffener side. The panel was tested in DAC's 1.1-million pound capacity test machine at a displacement rate of 0.05 in./min. Three additional panels were tested at Hercules' Magna, Utah, test facility using their 1.5-million pound capacity MTS machine. All panels failed without any skin/stiffener separation and a slight bending (buckling) was observed just before panel failure.



(a) Skin side

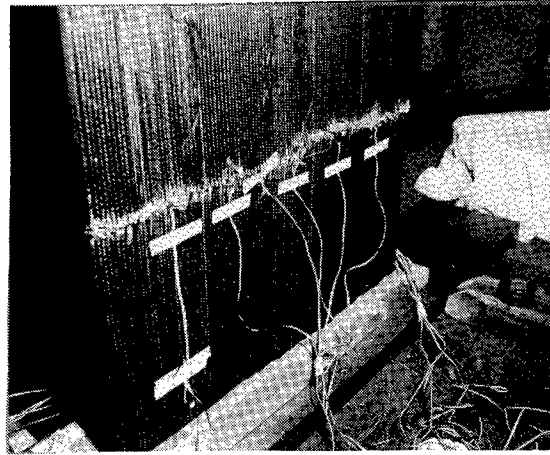


(b) Stiffener side

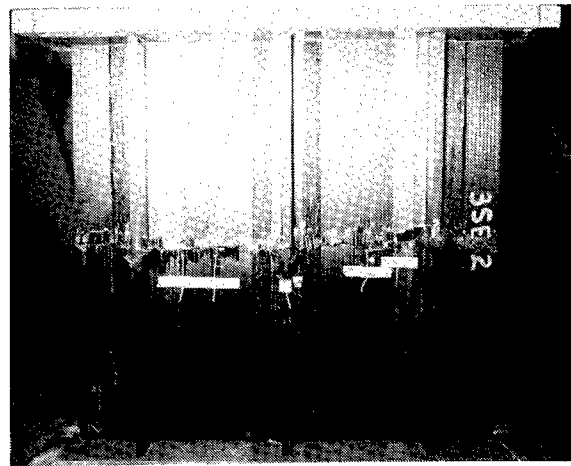
Figure 16

### 3-STIFFENER WING PANEL COMPRESSION FAILURE

Photographs of the mid-bay panel failure are shown from the skin side and stiffener side in figures 17a and 17b, respectively. The skin (figure 17a) failed through the impact location and all three stiffeners (figure 17b) failed. The stitching pattern used to fabricate the skin and stiffeners can be seen in these figures.



(a) Skin side



(b) Stiffener side

Figure 17

## POST-IMPACT COMPRESSION STRENGTH OF 3-STIFFENER WING ELEMENTS

The failure load of each blade-stiffened wing panel tested is shown plotted in figure 18. Data are shown for panels impacted at mid-bay, mid-stiffener, and center stiffener flange-edge at an impact energy of 100 ft-lbs and are compared to the failure load of a panel without impact damage. Design criteria (reference 3) for the wing panels requires an ultimate compression loading of 23.6 kips/in. or about 496 kips for the 21-inch wide specimens being evaluated. All impacted specimens exceeded this requirement. The data indicate that the mid-bay impact is the most critical location for stitched panels subjected to compression loading where a reduction of about 20 percent in the failure load is indicated compared to the specimen which was not impacted. The panels impacted at the mid-stiffener and stiffener flange-edge at the 100 ft-lb energy level did not experience a reduction in load capability compared to the panel which was not impacted. The results shown in figure 18 are very encouraging when compared to the results obtained in reference 2 for mid-bay impacted panels fabricated from 1808I/IM6, a very damage tolerant material. The referenced panel was also 21-inches wide and had a 54 ply skin and 72 ply stiffeners of the same ply orientation as the stitched/RTM wing panel. The mid-bay impacted 1808I/IM6 panel of reference 2 failed at a load of 363 kips and the failure sequence consisted of skin/stiffener separation, skin buckling, and catastrophic failure.

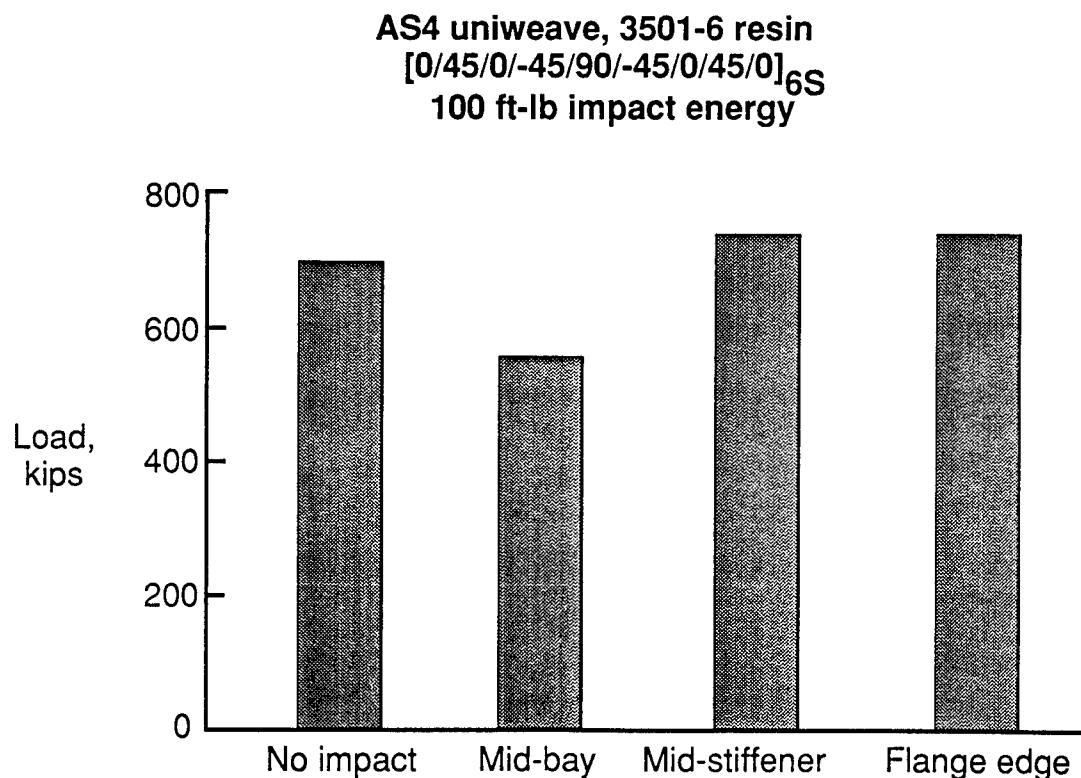


Figure 18

## STITCHED/RTM WING STIFFENER PULL-OFF SPECIMEN

The ultimate design load for wing fuel tankage corresponds to the highest fuel pressure which is projected to occur during a 9g crash. Although the only criterion for this situation is not to rupture the tank, it is desirable not to experience total separation of skin and stiffener. The highest fuel pressure combined with the stiffener spacing results in a 327 lb/in. ultimate pull-off loading. Figure 19 shows a stitched/RTM wing stiffener pull-off specimen which was used to assess the effects of 100 ft-lb impacts on stiffener pull-off load. Pull-off specimens were machined from impacted 3-blade-stiffened panels as previously described for the compression tests. Wing stiffener pull-off specimens were 10.5-inches long and 4.5-inches wide. Each end of the specimen had a 0.125-inch and 0.5-inch thick aluminum doubler bonded to the bottom and top of the specimen, respectively. Wing pull-off specimens were instrumented with either 2 or 4 strain gages to aid in detecting the load at which initial skin/stiffener separation occurred.

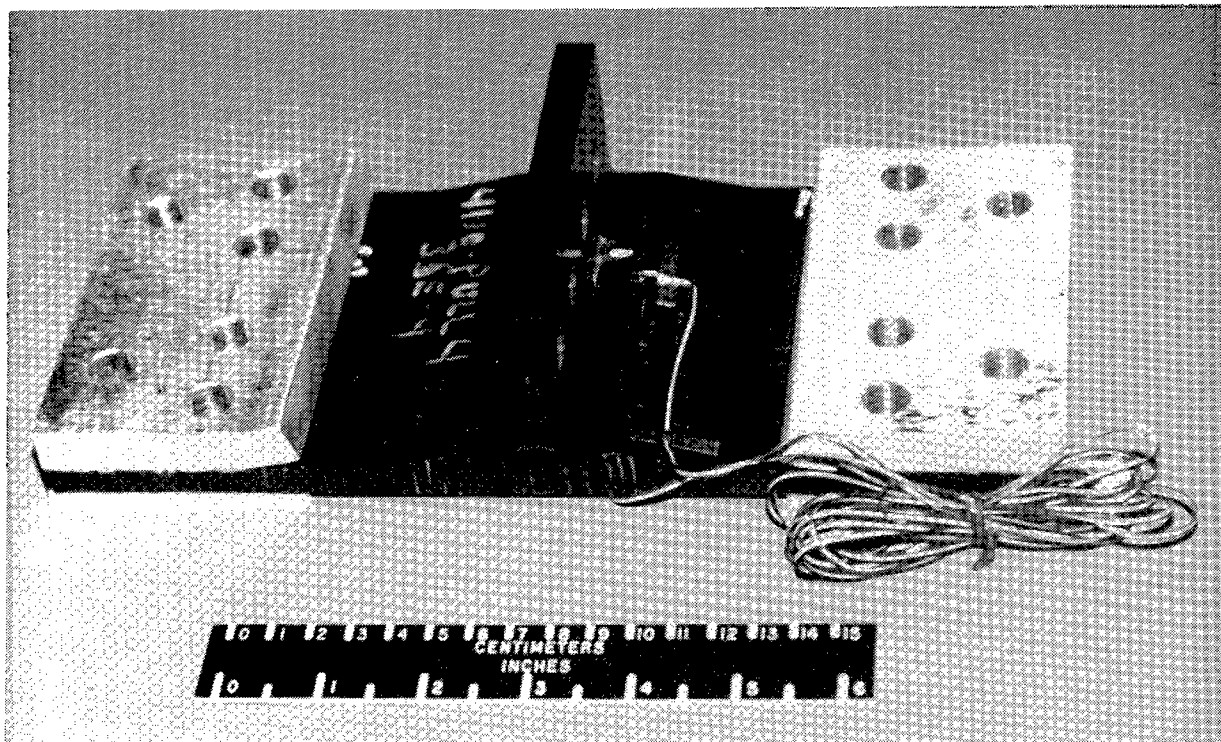


Figure 19

## TEST SETUP FOR WING STIFFENER PULL-OFF TEST

The set up for wing stiffener pull-off tests is shown in figure 20. The setup is similar to that used for the fuselage pull-off tests; however, the loading fixture and splice plates were much thicker. The specimen was bolted to the loading fixture and 0.5-inch thick steel splice plates were bolted to the stiffener with 0.5-inch diameter bolts as shown in the figure. All bolts were torqued to a value of 75 ft-lbs and the assembly was pinned to the loading rods inside the environmental chamber. All wing pull-off tests were performed at room temperature at a displacement rate of 0.05 in./min and strain was recorded continuously throughout the tests. Photographs were taken during each test to document the failure sequence.

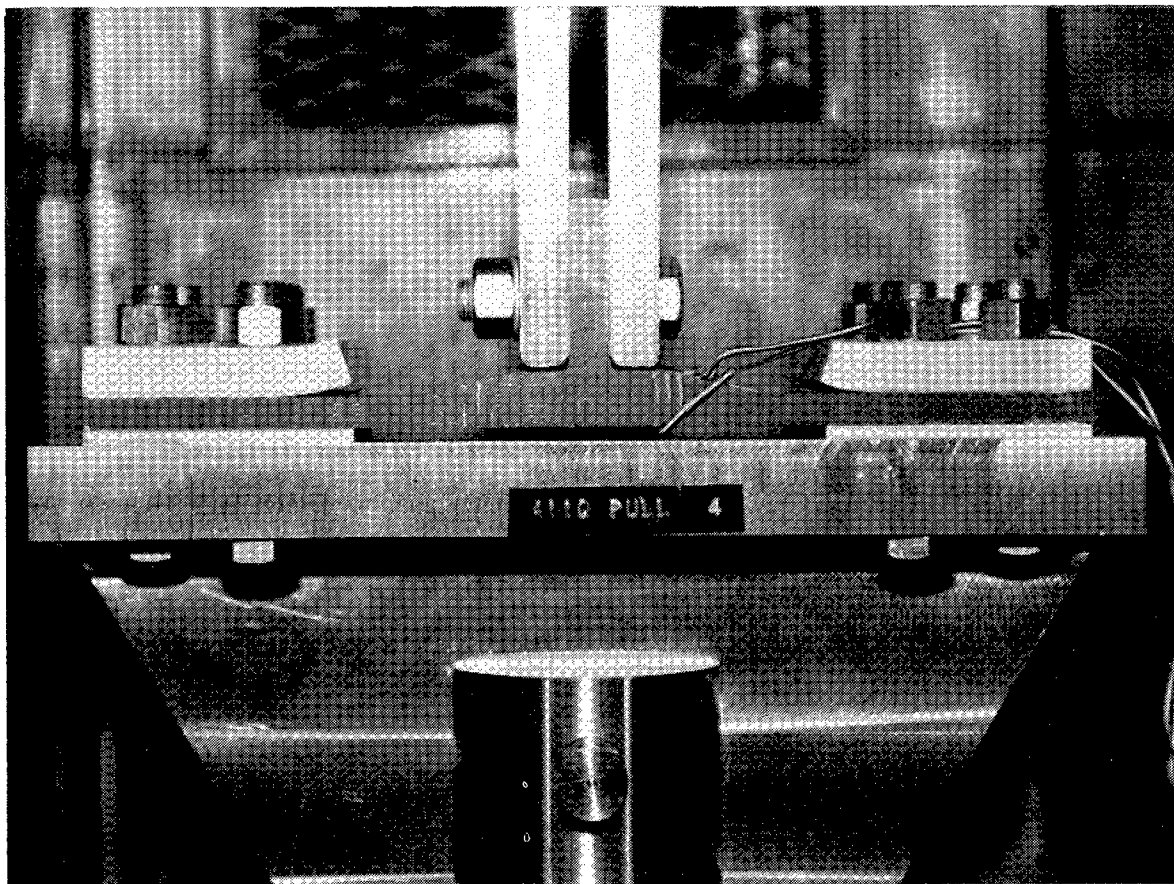


Figure 20



## STITCHED/RTM WING STIFFENER PULL-OFF TESTS

A typical load/strain plot for one of the stitched/RTM wing stiffener pull-off tests is shown in figure 21. For the data shown, gage 1 was located on the stiffener flange and gage 2 was located on the skin side of the specimen directly beneath the center of the stiffener. Both gages were oriented perpendicular to the blade stiffener. Load was applied continuously until failure of all stitching on one of the flanges. Initial skin/stiffener separation load was determined visually, audibly, or from strain gage data. Photographs taken at 4000, 6000, and 8000 pounds of applied load are shown in the figure to illustrate the failure sequence at loads corresponding to failure of a line of stitching through the flange.

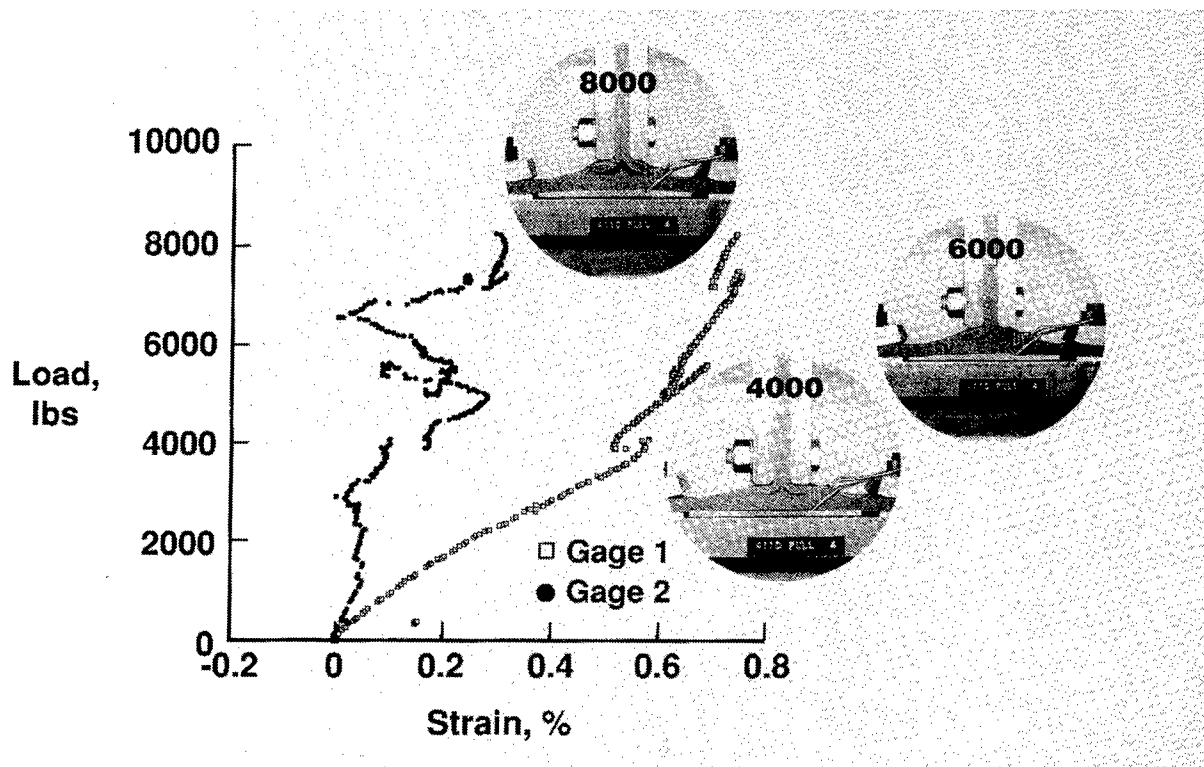


Figure 21

## STITCHED/RTM WING STIFFENER PULL-OFF FAILURE

Failure of a stitched/RTM wing stiffener pull-off specimen is shown in figure 22. Failure consists of stitching breakage in each flange along with delamination between the 9-ply subelements of AS4 uniweave fabric. Note that the skin has returned to the straight preloading condition. A total of six wing pull-off specimens were tested and the failure shown in figure 22 is typical for both non-impacted and impacted specimens.

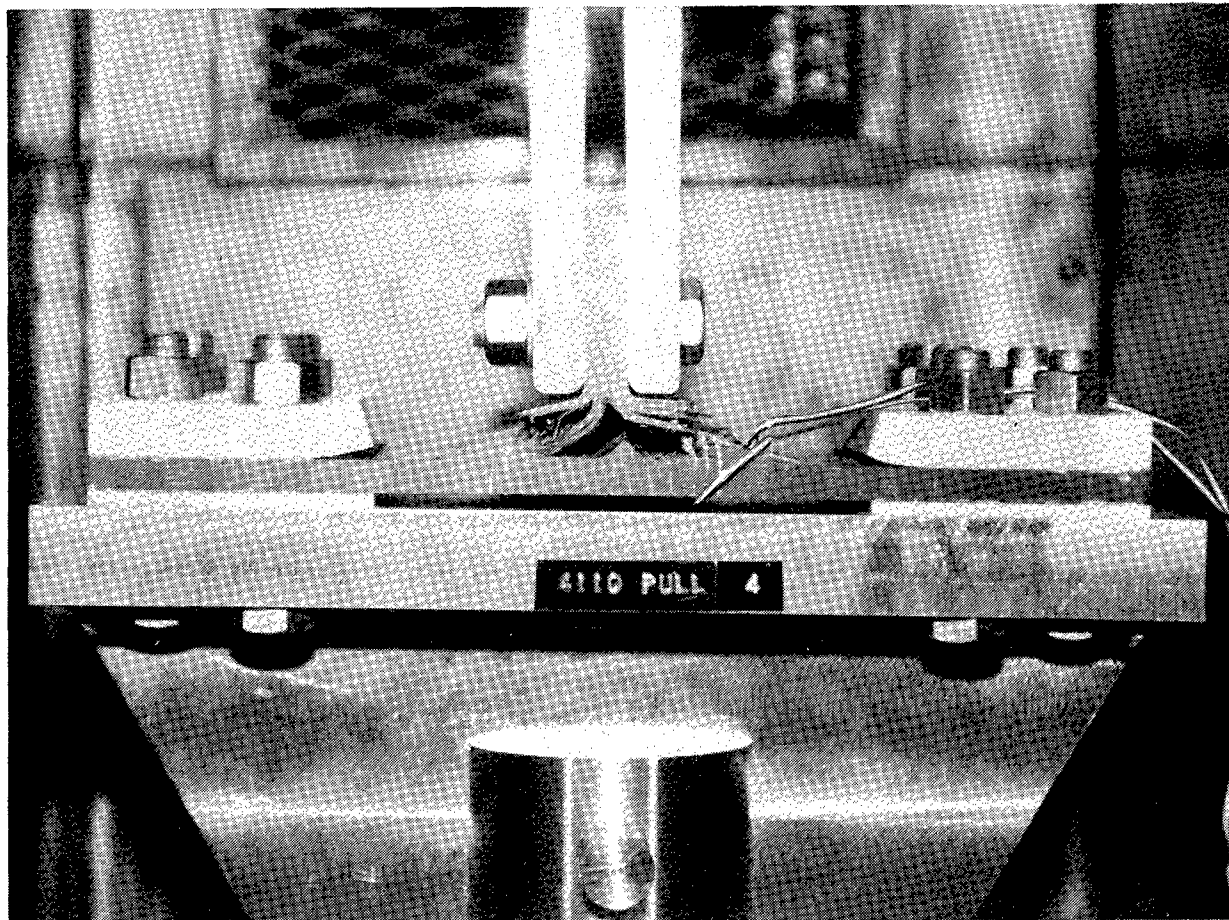


Figure 22

## EFFECT OF IMPACT ON WING STIFFENER PULL-OFF LOAD

Results obtained from the wing stiffener pull-off tests are shown in figure 23. The shaded bars correspond to the pull-off load at which skin/stiffener separation initiated and the open bars represent the maximum failure load. Each bar represents an individual test. Recall that the ultimate pull-off load associated with the highest fuel pressure in the wing was 327 lb/in. which corresponds to approximately 1500 pounds of applied load for the 4.5-inch wide wing stiffener pull-off specimens. The data indicate that all specimens exceeded the ultimate load requirement without experiencing initial skin/stiffener separation. The failure load data indicate that the flange-edge is the critical impact location for this test where a reduction of approximately 37 percent in the pull-off load is noted. However, failure load exceeded the design ultimate requirement by a factor of three.

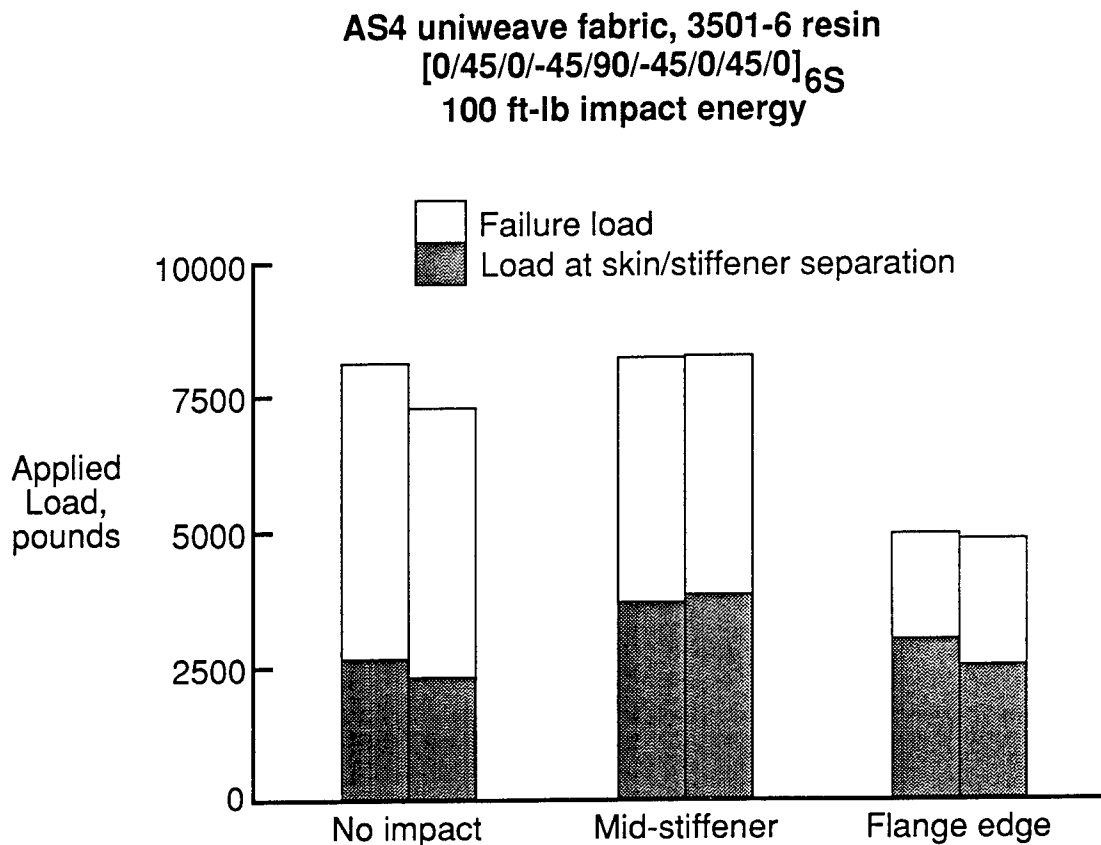


Figure 23

## CONCLUSIONS

The damage tolerance of automated tow placement (ATP) and resin transfer molded (RTM) fuselage elements with stitched-on stiffeners has been determined from compression tests of impacted three-J-stiffened panels and from impacted stiffener pull-off tests. The damage tolerance of RTM wing elements which had stitched skin and stiffeners was also determined from impacted single-stiffener and three-blade-stiffened compression tests and impacted stiffener pull-off tests. The results of this investigation lead to the following conclusions:

- Fuselage Structural Elements
  - Both fuselage concepts met compression design goals with impact damage present.
  - Critical impact sites were identified for both ATP and stitched/RTM fuselage concepts: mid-stiffener for ATP and mid-bay for stitched/RTM compression tests.
  - Analysis correlated well with test results for ATP panel: predicted buckling and non-linear bifurcation load within 5 and 10 percent, respectively. Stitched/RTM laminate properties are being obtained for FEM analysis.
  - Stiffener pull-off failure load of ATP specimens were reduced 20 percent for hot-wet condition. No hot-wet pull-off test performed on stitched/RTM concept.
  - Superior stiffener-to-skin integrity for stitched stiffener fuselage concept demonstrated through pull-off tests: factor of 2 stronger than ATP without damage and factor of 10 stronger than ATP with damage.
- Wing Structural Elements
  - All three-stiffener and single-stiffener specimens met compression design goal after 100 ft-lb impact.
  - Mid-bay critical impact site for 100 ft-lb impact energy for three-stiffener compression panel test: 20 percent reduction in compression strength.
  - Flange edge critical impact site location for 100 ft-lb impact energy from stiffener pull-off tests where a 37 percent reduction in pull-off load was obtained. Failure load still exceeded the design requirement by a factor of three.
- The test results demonstrate that wing and fuselage structure meeting damage tolerance goals can be designed and fabricated using stitching and RTM processes.

## REFERENCES

1. Sumida, P. T.; Madan, R. C.; and Hawley, A. V.: Test Results for Composite Specimens and Elements Containing Joints and Cutouts. NASA CR-178246, Aug. 1988.
2. Madan, R. C.: Composite Transport Wing Technology Development. NASA CR-178409, Feb. 1988.
3. Chen, Victor L., et. al.: Composite Technology for Transport Primary Structure. First NASA Advanced Composites Technology Conference, Seattle, WA, Oct. 29-Nov. 1, 1990, NASA CP-3104, Part 1, pp. 71-126.

**THIS PAGE INTENTIONALLY BLANK**

**SESSION V-C**

**AUTOMATED FIBER PLACEMENT TECHNOLOGY**

**THIS PAGE INTENTIONALLY BLANK**

# **TENSION FRACTURE OF LAMINATES FOR TRANSPORT FUSELAGE**

## **PART I: MATERIAL SCREENING<sup>1</sup>**

**T. H. Walker, W. B. Avery, L. B. Ilcewicz**  
**Boeing Commercial Airplane Group**  
**Seattle, Washington**

**C. C. Poe, Jr., and C. E. Harris**  
**NASA Langley Research Center**  
**Hampton, Virginia**

### **ABSTRACT**

Transport fuselage structures are designed to contain pressure following a large penetrating damage event. Applications of composites to fuselage structures require a database and supporting analysis on tension damage tolerance. Tests with 430 fracture specimens were used to (1) identify critical material and laminate variables affecting notch sensitivity, (2) evaluate composite failure criteria, and (3) recommend a screening test method. Variables studied included fiber type, matrix toughness, lamination manufacturing process, and intraply hybridization. The laminates found to have the lowest notch sensitivity were manufactured using automated tow placement. This suggests a possible relationship between the stress distribution and repeatable levels of material inhomogeneity that are larger than found in traditional tape laminates. Laminates with the highest notch sensitivity consisted of toughened matrix materials that were resistant to a splitting phenomena that reduces stress concentrations in major load bearing plies. Parameters for conventional fracture criteria were found to increase with crack length for the smallest notch sizes studied. Most material and laminate combinations followed less than a square root singularity for the largest crack sizes studied. Specimen geometry, notch type, and notch size were evaluated in developing a screening test procedure. Traditional methods of correcting for specimen finite width were found to be lacking. Results indicate that a range of notch sizes must be tested to determine notch sensitivity. Data for a single small notch size (0.25 in. diameter) was found to give no indication of the sensitivity of a particular material and laminate layup to larger notch sizes.

### **INTRODUCTION**

Boeing's program for Advanced Technology Composite Aircraft Structure (ATCAS) is studying manufacturing and performance issues associated with a wide body commercial transport fuselage (Ref. 1). Tension damage tolerance and pressure containment are major technical issues to solve for fuselage structures. Although composites are generally thought to have excellent tension properties, there is limited data on the performance of configured composite shell structures with large through-penetrating damage and subjected to combined load conditions, including pressure. A collaborative effort between Boeing and NASA is committed to collecting a database and solving the technical challenges associated with composite fuselage damage tolerance.

---

<sup>1</sup> This work was funded by Contract NAS1-18889, under the direction of J. G. Davis and W. T. Freeman of NASA Langley Research Center.



During the last year, much of the work in ATCAS has concentrated on local cost and weight optimization of crown panels (Ref. 2). The minimum gage structures that constitute crown panels in ATCAS are characteristic of up to 70% of the fuselage surface area. Depending on material selection and design details, both hoop and axial tension damage tolerance can be design drivers for the ATCAS crown panels. The crown local optimization task which is the subject of this paper involved the collection of a tension fracture database for candidate skin materials. During the course of achieving this task, a process-related characteristic was found to increase tension fracture performance of automated tow-placed laminates. As discussed at the start of Reference 2, the improved fracture strength lead to projections for significant reductions in structural cost and weight.

Most of the published tension fracture work performed to date has concentrated on relatively small notches, having sizes less than 1 in. (see Ref. 3 for a review of work up to 1985). A previous NASA-funded program at Boeing included tests with larger cracks, characteristic of transport fuselage damage tolerance criteria (Ref. 4). Some modification to classical fracture analyses (e.g., addition of a semi-empirical characteristic dimension in failure criteria or a change in the order of crack tip singularity) was used in most past studies to predict tension fracture in composite laminates. More recent work has considered the effects of pre-catastrophic damage growth on stress redistribution at the crack-tip. Results from both small and large cracks indicate that numerous variables affect tension fracture, including laminate thickness, ply stacking sequence, fiber type, and matrix type.

With the multitude of variables affecting tension fracture for composite materials (Ref. 5), it is desirable to screen performance at the coupon level. One material screening test, used extensively by the aerospace industry over the past few years, is uniaxial tension loading of a notched specimen having a 0.25 in. diameter open hole. Little work has been performed to indicate that test results from this narrow specimen are suitable for material screening of tension fracture for transport fuselage damage tolerance. In order for the test to have qualitative meaning, there needs to be an experimental correlation established between small and large notch data. Supporting analyses are also needed to quantify fuselage damage tolerance based on specimen data available during preliminary design.

The current paper reviews the "small notch" ATCAS tension fracture specimen database collected for ten candidate crown skin materials. The test matrix was designed to assess uniaxial tension fracture for layups and thicknesses characteristic of the skins for stiffened fuselage panel design concepts. Both traditional tape and tow-placed laminates were evaluated. Test results were analyzed to assess critical material variables such as fiber type, matrix type, and intraply hybridization. Three different notch types were studied; machined cracks, drilled holes, and through-penetrations created by subjecting the laminate to an impact event with a sharp blade. In addition to characterizing material performance, the database served three other purposes. First, there was a desire to confirm the equivalence of laminates fabricated by automated tow placement and hand layup using tow and tape material forms, respectively. Second, tension fracture analyses and failure criteria were evaluated for a range of crack lengths from 0.25 in. to 5.0 in. Third, a suitable method for material screening was derived based on experimental and analytical results.

The following text is divided into four main sections. The first section gives a detailed account of specimen fabrication and test procedures. The second section discusses trends in experimental results. Statistical data analysis was performed to judge if the trends in material performance for small cracks are indicative of those for the largest cracks tested. The accuracy of a number of failure criteria for predicting notched strength is covered in the third section. This includes a review of the importance of the scale of material inhomogeneity and order of crack tip singularity. A comparison of results for width-to-notch-size ratios of 2 and 4 is used to discuss the validity of analysis methods for correcting fracture results for finite specimen width. In the final section, recommended test procedures for fuselage material screening are discussed.

## EXPERIMENTS

### Test Matrix

The test matrix of 430 coupons is shown in Figure 1. Laminates were made from ten materials. The first two materials are the primary fiber and matrix candidates, IM6<sup>2</sup>/937A<sup>3</sup> and AS4<sup>4</sup>/938<sup>5</sup>, both in tape form (937A and 938 are resin systems nearly identical to 3501-6<sup>6</sup>). At the time the test matrix was formulated, tow and tape laminates consisting of the same constituents and volume fractions were expected to have nearly equivalent performance. The tape laminates fell into three categories: (1) angle- and cross-ply laminates (0/90, +45/-45, and +30/-30) as building blocks for predictive method development; (2) quasi-isotropic and other potential crown laminates (Quasi, Crown1, and Crown2) for evaluation of realistic performance; and (3) the Crown1 laminate rotated 15° and 30° with respect to the crack and loading orientations (Crown1 + 15, Crown1 + 30) for validation of the generality of predictive models. Other variables considered were notch size, notch type, and specimen-width-to-notch-size ratio ( $W/2a$ ). Notch sizes ranged from 0.25 to 5.00 inches, while notch types included holes, machined cracks, and penetrations (i.e., cracks created by penetrating the laminate with a chissle-like impactor). The latter notch type was included to evaluate the effects of the damage zone created by a realistic penetration event, since clean cracks, analogous to fatigue cracks in metals, do not form in composites.  $W/2a$  ratios of 2 and 4 were included.

A single laminate type (Crown1) was made from each of the remaining eight materials to allow limited comparisons with the two primary fiber and matrix candidates. The Crown1 laminate was the most likely candidate for the skin laminate in the fuselage crown when the testing was defined. Specimens for these limited comparisons were restricted to a  $W/2a = 4$ .

The IM7<sup>7</sup>/8551-7<sup>8</sup> was included as a representative toughened material system. Since tow-placement was the selected manufacturing process for the crown, AS4/938 tow was included to evaluate process-induced performance changes from the tape form. In combination with the S2<sup>9</sup>/938 tow, it also served as material endpoints for comparison with the intraply hybrids, which comprise the final five materials.

Intraply hybrids, as discussed in this paper, are materials with tows of more than one fiber type combined in a repeating pattern within each individual ply, as shown in Figure 2. These hybrid materials appeared attractive due to potential tension fracture performance improvements and reduced material costs. The materials tested in the current work were an extension of the fiberglass buffer strip

---

<sup>2</sup> IM6 is a graphite fiber system produced by Hercules, Inc.

<sup>3</sup> 937A is a resin system produced by ICI/Fiberite.

<sup>4</sup> AS4 is a graphite fiber system produced by Hercules, Inc.

<sup>5</sup> 938 is a resin system produced by ICI/Fiberite.

<sup>6</sup> 3501-6 is a resin system produced by Hercules, Inc.

<sup>7</sup> IM7 is a graphite fiber system produced by Hercules, Inc.

<sup>8</sup> 8551-7 is a resin system produced by Hercules, Inc.

<sup>9</sup> S2 is a glass fiber system produced by Owens-Corning Fiberglas, Corp.

concept, which has been widely shown to improve tension fracture strength (e.g. Ref. 6, 7), to multiple directions and a material lamina scale. The advent of the tow-placement process allows such materials to be created with little impact on the manufacturing cost. Any significant performance improvement would result in a reduction of the total material requirement, thereby reducing the structural weight, total material costs, and manufacturing costs. In addition, the use of fiberglass as the hybridizing fiber would result in lower material unit costs, since it would replace higher-cost graphite fiber, although at a slight density penalty.

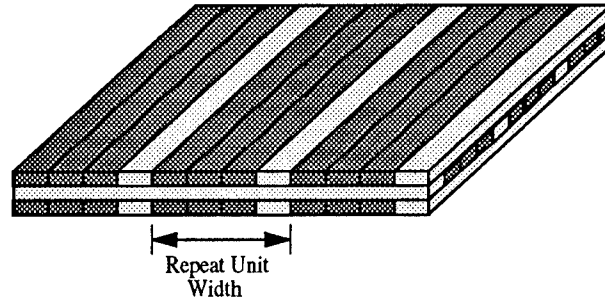
Notch Type ▶		Open Hole			Machined Slit								Penetration
Notch Size ▶		0.25	0.50	0.875	0.25	0.50		0.875		1.75	2.50	5.00	0.875
Material	Width Length	1.00	2.00	3.50	1.00	1.00	2.00	1.75	3.50	3.50	10.00	10.00	3.50
	Laminate	12.0	12.0	12.0	12.0	12.0	12.0	12.0	12.0	12.0	30.0	30.0	12.0
AS4/938 Tape	0/90		3		3	3	3	3	3		2		
	+45/-45		3		3	3	3	3	3		2		
	+30/-30		3		3	3	3	3	3		2		
	Quasi		3		3	3	3		3				3
	Crown1		3		3	3	3	6	3	3	2	2	3
	Crown1 + 15		3		3	3	3		3				
	Crown1 + 30		3		3	3	3		3		2		
	Crown2		3		3	3	3		3				3
IM6/937A Tape	0/90		3		3	3	3	3	3		2		
	+45/-45		3		3	3	3	3	3		2		
	+30/-30		3		3	3	3	3	3		2		
	Quasi		3		3	3	3		3				3
	Crown1		3		3	3	3	6	3	3	2	2	3
	Crown1 + 15		3		3	3	3		3				
	Crown1 + 30		3		3	3	3		3		2		
	Crown2		3		3	3	3		3				3
IM7/8551-7 Tape	Crown1				3		3		3		2	2	4
AS4/938 Tow	Crown1	3		3	3				3		2		3
S2/938 Tow	Crown1	3		3	3				3		2		3
Hybrid 1 / 938	Crown1			3	3						2		3
Hybrid 2 / 938	Crown1	3							3		2		3
Hybrid 3 / 938	Crown1			3	3						2		3
Hybrid 4 / 938	Crown1	3							3		2		3
Hybrid 5 / 938	Crown1	3		3	3				3		2		3








Layup Designations				Hybrid Material Definitions		
				Hybrid No.	Hybridization	Repeat Unit Width
0/90	[0/90]2S	Crown1	[+45/90/-45/0/+30/-30/0/-45/90/+45]	1	75% AS4, 25% S2	4 Tows
+45/-45	[+45/-45]2S	Crown1 + 15	[+60/-75/-30/+15/+45/-15/+15/-30/-75/+60]	2	50% AS4, 50% S2	4 Tows
+30/-30	[+30/-30]2S	Crown1 + 30	[+75/-60/-15/+30/+60/0/+30/-15/-60/+75]	3	50% AS4, 50% S2	12 Tows
Quasi	[+45/90/-45/0]S	Crown2	[+45/-45/0/90/+30/-30/0/90]S	4	75% AS4, 25% S2	12 Tows
				5	75% AS4, 25% T1000	12 Tows

**Figure 1: Specimen Configurations and Number of Replicates for Tension Fracture Testing**

The configuration of the intraply hybrid materials considered in the current program are detailed in Figure 2. AS4/938 was the baseline tow. In Hybrids 1 through 4, the AS4 was combined with a low-stiffness, high-strain fiber, S2 fiberglass. In Hybrid 5, AS4 was combined with high-stiffness/high-strain graphite fiber, T1000<sup>10</sup>. Variables evaluated for these materials were notch size and type, hybridization percentage, and repeat unit width.

<sup>10</sup> T1000 is a graphite fiber system produced by Toray Industries, Inc.



Designation	Base Mat'l Tow 	Hybridizing Mat'l Tow 	Repeating Pattern	Repeat Unit Width
Hybrid #1	AS4/938	S2/938		0.38 in.
Hybrid #2	AS4/938	S2/938		0.38 in.
Hybrid #3	AS4/938	S2/938		1.10 in.
Hybrid #4	AS4/938	S2/938		1.10 in.
Hybrid #5	AS4/938	T1000/938		1.10 in.

**Figure 2: Intraply Hybrid Material Description**

For the AS4/S2 hybrids, an eight run designed experiment was used to evaluate (1) notch sizes of 0.25 and 0.875 inches, (2) notch types of holes and cracks, (3) hybridizing percentages of 25% and 50% S2-glass, and (4) repeat unit widths of 4 and 12 tows. Within this designed experiment, the Crown1 layup and a  $W/2a$  of 4 remained constant for all specimens. Additional tests were conducted outside the designed experiment for 2.5 inch cracks and 0.875 inch penetrations. A fully crossed matrix of the above notch variables was tested for Hybrid 5, which was a 75%/25% combination of AS4 and T1000, respectively, with a 12 tow repeat unit.

All laminates in the test matrix were fabricated from material with a fiber volume of approximately 57% (corresponding to a resin content of 35% for graphite/epoxy systems). The fiber tows used in all tape materials were 12K. To maintain approximately equal tow spread for all intraply hybrid fiber types, 6K tows of AS4 and 12K tows of T1000 were used, as was 20 end 750 yd./lb. S2-glass.

### Panel Fabrication

A single panel was manufactured for each unique combination of material and laminate type. The tape panels were fabricated from 12 inch wide prepreg tape using standard hand layup techniques. The tow-placed panels were fabricated on the Hercules 6-axis fiber placement machine using a 12-tow Band Cut and Add head. All panels were autoclave cured at 350°F. Nominal cured ply thickness for both tow and tape materials was 0.0074 in. Through-transmission ultrasonics was used to non-destructively inspect each panel after cure to ensure laminate quality. Measurements of laminate thickness indicated that all panels fabricated were within specified limits.

## Specimen Machining

The coupons were cut to slightly oversized dimensions using a band saw, then sanded to final dimensions. A 125 surface finish was designated for all cut edges. The open holes were created using tapered drills. Cracks were created by drilling two 0.070 inch diameter holes at the crack tip locations, then connecting them using an abrasive waterjet cutter. X-ray inspection was used to assess machining-induced damage. Specimen thickness, width, and notch size were measured prior to testing.

The 10 in. x 30 in. coupons were tabbed with 10 in. x 3 in. tabs on both sides of each end to insure against failure in the grips. The 100% S2-glass and the S2-glass hybrid coupons utilized tabs fabricated from E-glass/5208<sup>11</sup> 8HS prepreg with a  $[0/45/0]_s$  stacking sequence. The AS4/938, IM6/937A, IM7/8551-7, and AS4/T1000 hybrid test specimens utilized tabs fabricated from T300<sup>12</sup>/5208 plain weave fabric prepreg with a  $[0]_n$  stacking sequence. All tabs had a nominal thickness of approximately 0.07 inches, and were bonded to the test specimens with a 0.010 inch thick 250°F cure film adhesive. The test specimens and tabs were prepared for bonding by lightly grit blasting the bonding surfaces, followed by a solvent wipe to remove any loose material.

## Test Procedures

The through-penetration damages were created by impacting individual specimens in an impact tower. The specimen support fixture is illustrated in Figure 3, and consists of a 0.50 inch steel plate with a 5.0 in. x 2.5 in. cutout. Specimens were held with clamps at each end of the specimen to prevent specimen rebound during impact. The test fixture approximates simply-supported boundary conditions. An instrumented impact tower was used to perform the penetration event. A steel blade with a width and thickness of 0.875 in. and 0.060 in., respectively, and a 45° thickness-taper at the tip was dropped at a velocity of 12.5 ft./sec. The weight of the impactor was approximately 13.6 lbs., thus producing an impact energy of 400 in.-lbs. Force, energy, and deflection versus time were recorded by a data acquisition system and digitally stored. After impact, the damage in each specimen was assessed ultrasonically using the pulse-echo time-of-flight technique at a frequency of 5 MHz.

Testing was conducted in two test machines. The 1-in.-wide specimens were tested in a 20 kip test frame, while all others were tested in a 56 kip hydraulic test frame. A displacement rate of 0.125 in./min. was used for the 10-inch-wide coupons, while 0.05 in./min. was used for all other specimens. All tests were conducted at room temperature and ambient humidity.

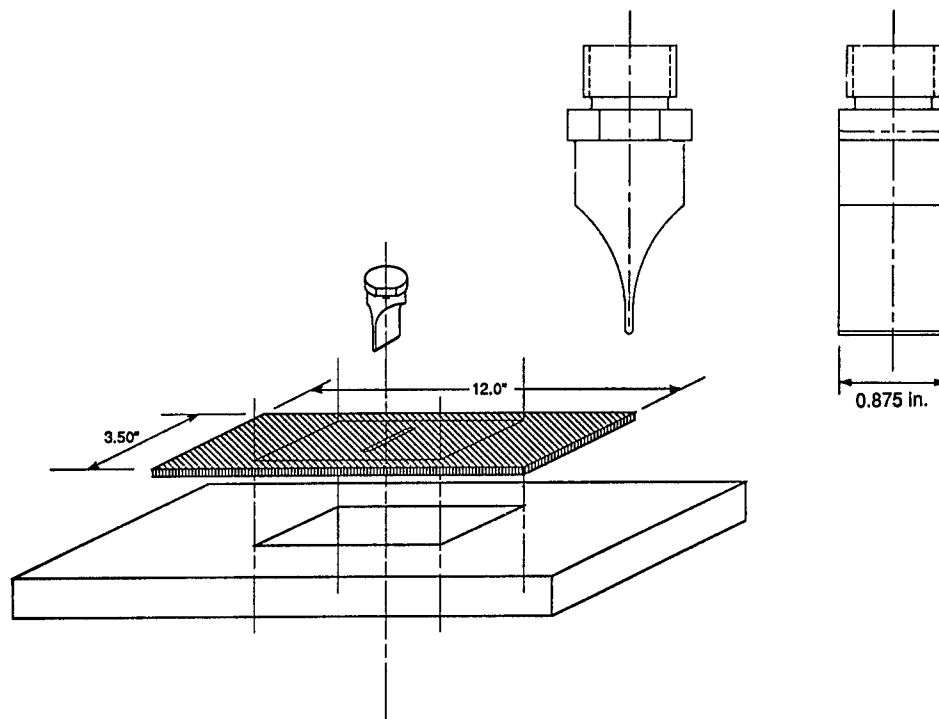
X-ray radiographs were obtained for one of the three replicates of many of the 1- and 3.5-in.-wide specimen types to document pre-failure damage progression. X-rayed specimens were loaded to between 75 and 90% of the expected failure load prior to inspection, and were subsequently loaded to failure.

Extensometers placed approximately midway between the notch and the loading frame were used to monitor far-field strains during loading. Strain gages were used on some specimens to measure far-field strain, local load redistribution and transverse buckling adjacent to the unsupported edges of the crack. Several tests were recorded on videotape to document failure mechanisms and progression.

---

<sup>11</sup> 5208 is a resin system produced by Narmco Materials, Inc.

<sup>12</sup> T300 is a graphite fiber sytem produced by Toray Industries, Inc.



**Figure 3: Penetrating Impact Support Fixture**

## TEST RESULTS

The average nominal failure stress (i.e., failure load ÷ (number of plies \* nominal ply thickness)) for each specimen configuration is listed in Figure 4. In the following subsections, the important results are presented and discussed.

### Layup

As shown in Figure 5, large variations in fracture strength with layup were observed within each material type. The relationship between layup and notched tensile strength has been shown to be complex (e.g., Refs. 8-13). Certain combinations of ply splitting and delamination that occur at a crack tip can enhance residual strength by effectively reducing the stress concentration. Delaminations that extend to the edge of finite-width specimens, uncoupling plies and allowing them to fail without fiber breaks, however, reduce the residual strength.

The laminates in Figure 5 for each material are shown in order of decreasing axial modulus. It appears that fracture strength tends to increase with increasing modulus. The 0/90 laminates had significantly higher strengths than all other laminates, and a somewhat reduced sensitivity to changes in crack length. Despite relatively low fracture strength of the +45/-45 laminates, this layup was found to be relatively notch insensitive, as seen by comparing results for different crack sizes in Figure 4. This agrees with data presented in Reference 14.

Notch Type ▶			Open Hole			Machined Slit								Penetration
Notch Size ▶			0.25	0.50	0.875	0.25	0.50		0.875		1.75	2.50	5.00	0.875
Material	Laminate	Width Length	1.00 12.0	2.00 12.0	3.50 12.0	1.00 12.0	1.00 12.0	2.00 12.0	1.75 12.0	3.50 12.0	3.50 12.0	10.00 30.0	10.00 30.0	3.50 12.0
AS4/938 Tape	0/90			50.80		59.70	34.68	49.94	35.47	49.05		45.63		
	+45/-45			17.74		17.58	11.12	18.30	12.00	17.93		17.45		
	+30/-30			40.93		49.98	31.10	45.38	28.12	35.56		26.44		
	Quasi			43.67		44.70	28.51	39.61		36.30				35.39
	Crown1			36.98		44.68	28.11	41.42	27.35	38.02	18.71	27.90	14.10	35.22
	Crown1 + 15			34.98		41.54	29.42	35.70		31.02				
	Crown1 + 30			35.34		42.49	25.73	34.14		35.82		26.35		
	Crown2			42.43		45.12	29.74	36.49		31.52				38.74
IM6/937A Tape	0/90			70.24		72.97	52.74	68.10	43.79	61.95		57.69		
	+45/-45			17.74		17.28	11.33	18.16	11.91	18.00		18.33		
	+30/-30			48.65		56.66	34.90	51.35	36.00	42.79		35.45		
	Quasi			51.04		62.08	36.98	75.26*		51.11				50.34
	Crown1			42.21		51.95	34.66	46.24	32.08	39.63	27.59	34.64	16.92	43.96
	Crown1 + 15			45.14		53.19	37.55	51.40		38.50				
	Crown1 + 30			46.22		54.53	34.35	46.82		35.22		32.18		
	Crown2			48.56		58.24	37.18	48.56		41.53				53.02
IM7/8551-7 Tape	Crown1				69.68		61.40		53.41		32.23	18.04		43.82
AS4/938 Tow	Crown1	49.87		41.48	50.45				46.33		35.27			44.04
S2/938 Tow	Crown1	51.11		54.44	53.47				52.70		45.05			49.65
Hybrid 1 / 938	Crown1			43.24	52.20						37.81			44.53
Hybrid 2 / 938	Crown1	47.91							48.83		40.35			44.08
Hybrid 3 / 938	Crown1			39.25	51.05						41.12			40.30
Hybrid 4 / 938	Crown1	47.64							46.96		36.61			43.60
Hybrid 5 / 938	Crown1	55.36		44.78	57.17				50.37		41.18			47.89

Layup Designations			
0/90	[0/90]2S	Crown1	[+45/90/-45/0/+30/-30/0/-45/90/+45]
+45/-45	[+45/-45]2S	Crown1 + 15	[+60/-75/-30/+15/+45/-15/+15/-30/-75/+60]
+30/-30	[+30/-30]2S	Crown1 + 30	[+75/-60/-15/+30/+60/0/+30/-15/-60/+75]
Quasi	[+45/90/-45/0]S	Crown2	[+45/-45/0/90/+30/-30/0/90]S

Hybrid Material Definitions		
Hybrid No.	Hybridization	Repeat Unit Width
1	75% AS4, 25% S2	4 Tows
2	50% AS4, 50% S2	4 Tows
3	50% AS4, 50% S2	12 Tows
4	75% AS4, 25% S2	12 Tows
5	75% AS4, 25% T1000	12 Tows

\* These data appear in error but no good explanation was found.

**Figure 4: Average Nominal Failure Stress Results**

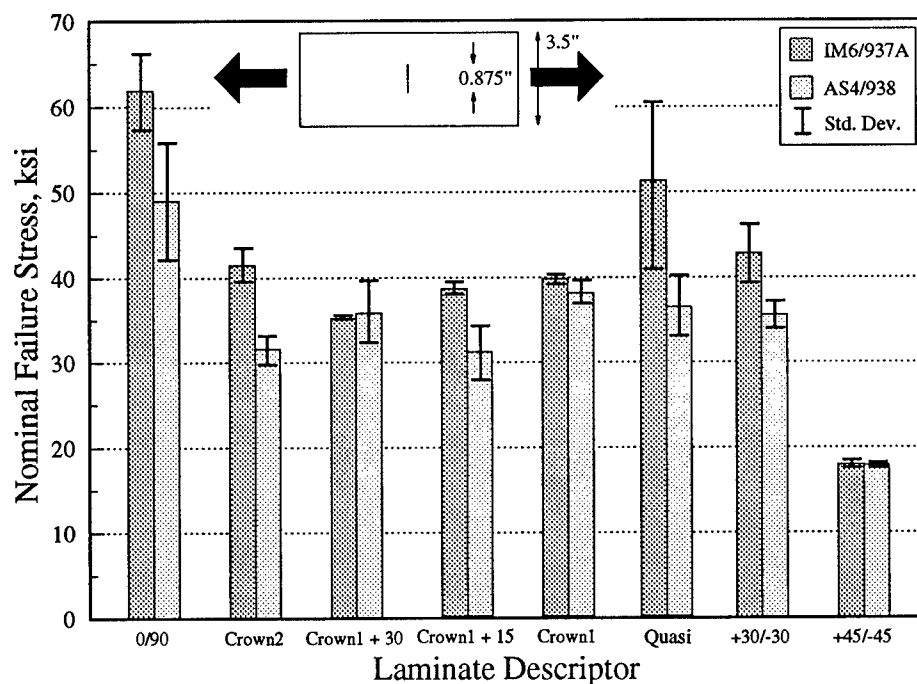
## Notch Type

The open hole and crack strengths were within approximately 10% of each other. The relative severity varied among the laminates. These results are similar to the small notch results summarized in Reference 3. For the Crown1 laminate that was used for the majority of material comparisons, holes were found to have strengths below those of cracks.

Comparison of the instrumented impact force-displacement results for the through-penetrations revealed significant differences between material types. The slope of the force-displacement curve relates to the plate bending stiffness, and the area under the curve is a measure of the event energy. This event energy is a combination of the energy absorbed by the plate during the penetration event and the energy required to bend the plate. Instrumented impact results for non-penetrating events typically subtract out the plate-bending component. For the case of a through-penetration event, however, the plate rebound energy cannot be measured since the displacement is associated with the impactor.

Force-displacement curves for Crown1 laminates fabricated from AS4/938 tape, AS4/938 tow, IM6/937A tape, and IM7/8551-7 tape are presented in Figure 6. The AS4/938 tow has a higher load than the AS4/938 tape, resulting in an approximately 60% higher event energy. This difference may

be attributed to an increase in damage formed adjacent to the penetration in the tow-placed laminate. This was confirmed by ultrasonic scans.

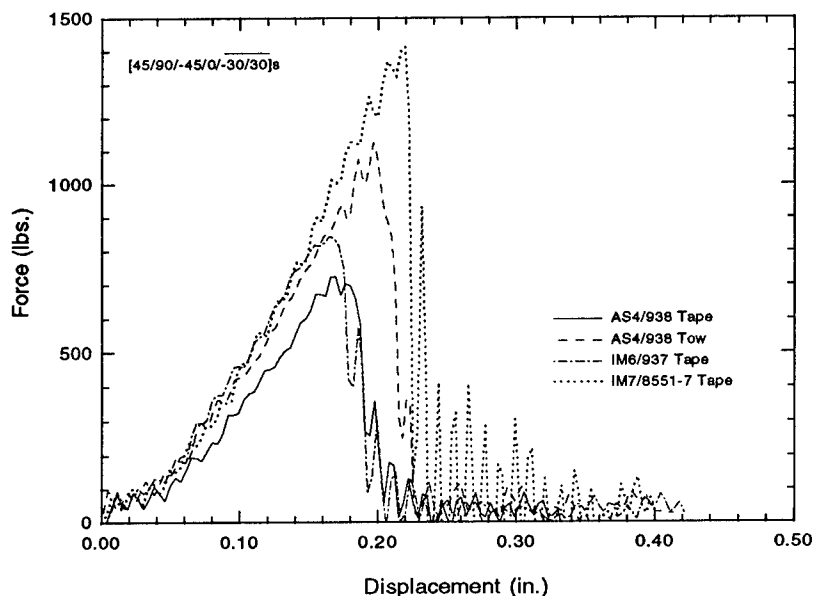


**Figure 5: Variation of Fracture Strength with Layup for IM6/937A and AS4/938 Tape**

The IM6/937A tape instrumented impact results showed a peak load and total event energy that were 20-25% above that of the AS4/938 tape. The amount of damage area created was similar for the two materials, as might be expected for equivalent resin systems. The energy differences, therefore, might be due to the slightly higher laminate bending stiffness and fiber strengths, both a result of the higher stiffness of the IM6 fiber.

As also shown in Figure 6, penetration of IM7/8551-7 tape resulted in a 40% higher maximum load and a 65% higher total event energy than IM6/937A tape. Ultrasonic scans indicated that damage created adjacent to the penetration was significantly smaller in IM7/8551-7 than in any of the other materials. Possible causes for the energy difference include (a) the slightly higher bending stiffness and fiber strength with the IM7 fiber, and (b) the increased energy absorbed per unit damage due to the higher toughness of 8551-7. Neither of these, though, appear likely to account for a majority of the energy increase. Extension of the crack beyond the net impactor length, however, would require additional fiber failure and associated energy. This scenario is plausible since 8551-7 resin is resistant to matrix damage that would reduce the stress concentration near the corners of the penetrator. Note that the ultrasonic methods used for the current study are unable to distinguish fiber failure zones.





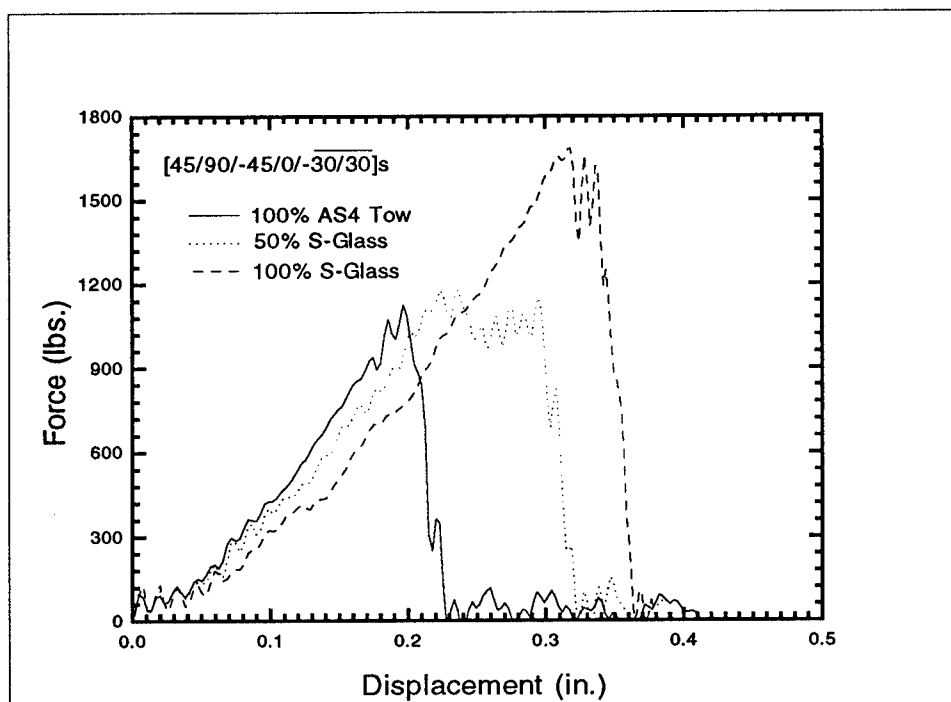
**Figure 6: Instrumented Impact Results for Through-Penetration of AS4/938 Tow and Tape, IM6/3501-6, and IM7/8551-7**

Force-displacement curves for tow-placed Crown1 laminates of 100% AS4/938, 100% S2/938, and Hybrid #3 (i.e., 50% AS4 / 50% S2 / 938, 12 tow repeat unit width) are presented in Figure 7. As expected from the fiber stiffness difference, the slope of the 100% S2/938 curve is less than that of the 100% AS4/938, and that of Hybrid #3 falls midway between. The total event energy of the S2/938 was over twice as large as that of the AS4/938, and the Hybrid #3 energy was midway between. Another conspicuous feature of the Hybrid #3 curve is the relative ductility of the failure, as compared to either the AS4/938 or S2/938.

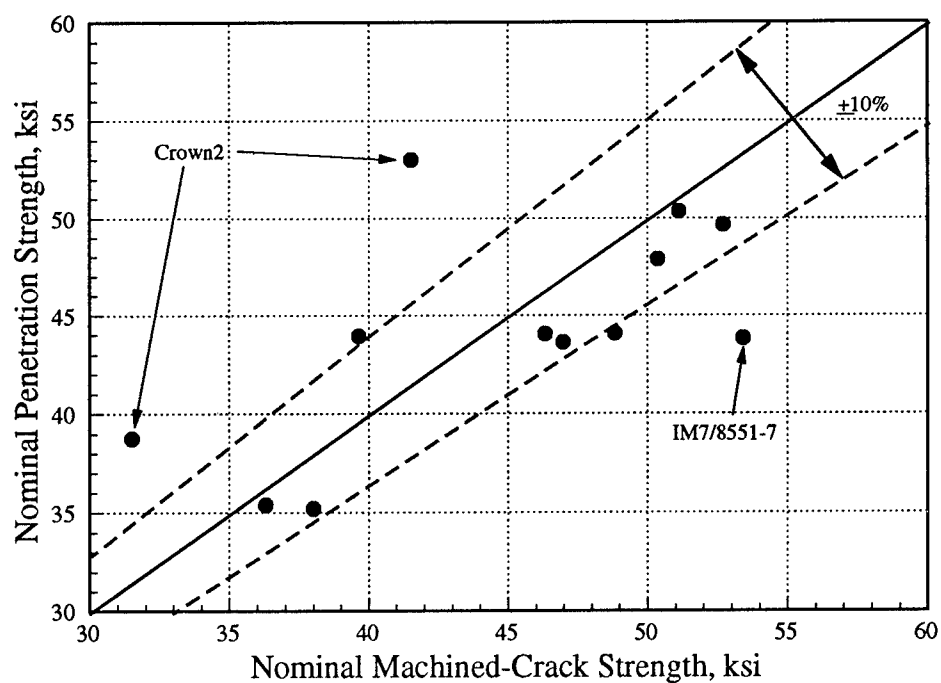
Tension fracture strengths for specimens with 0.875 in. through-penetrations were compared to specimens with 0.875 in. machined cracks. The results are shown in Figure 8. In most cases, penetration strengths were within 10% of the machined-crack strengths, with the latter being higher.

The single configuration for which the penetration strength is more than 10% below the machined-crack strength is the IM7/8551-7 Crown1 laminate. The toughness of 8551-7 resin could conceivably create crack-tip extension significantly greater than that of the 937A and 938 materials, as alluded to in the discussion of instrumented impact results. An effective crack extension of approximately 0.25 in. on each side of the penetrator would result in a fracture strength that follows the trends of the machined cracks for IM7/8551-7. Future work involving deply of through-penetrated specimens will help to quantify fiber damage caused by the impact event.

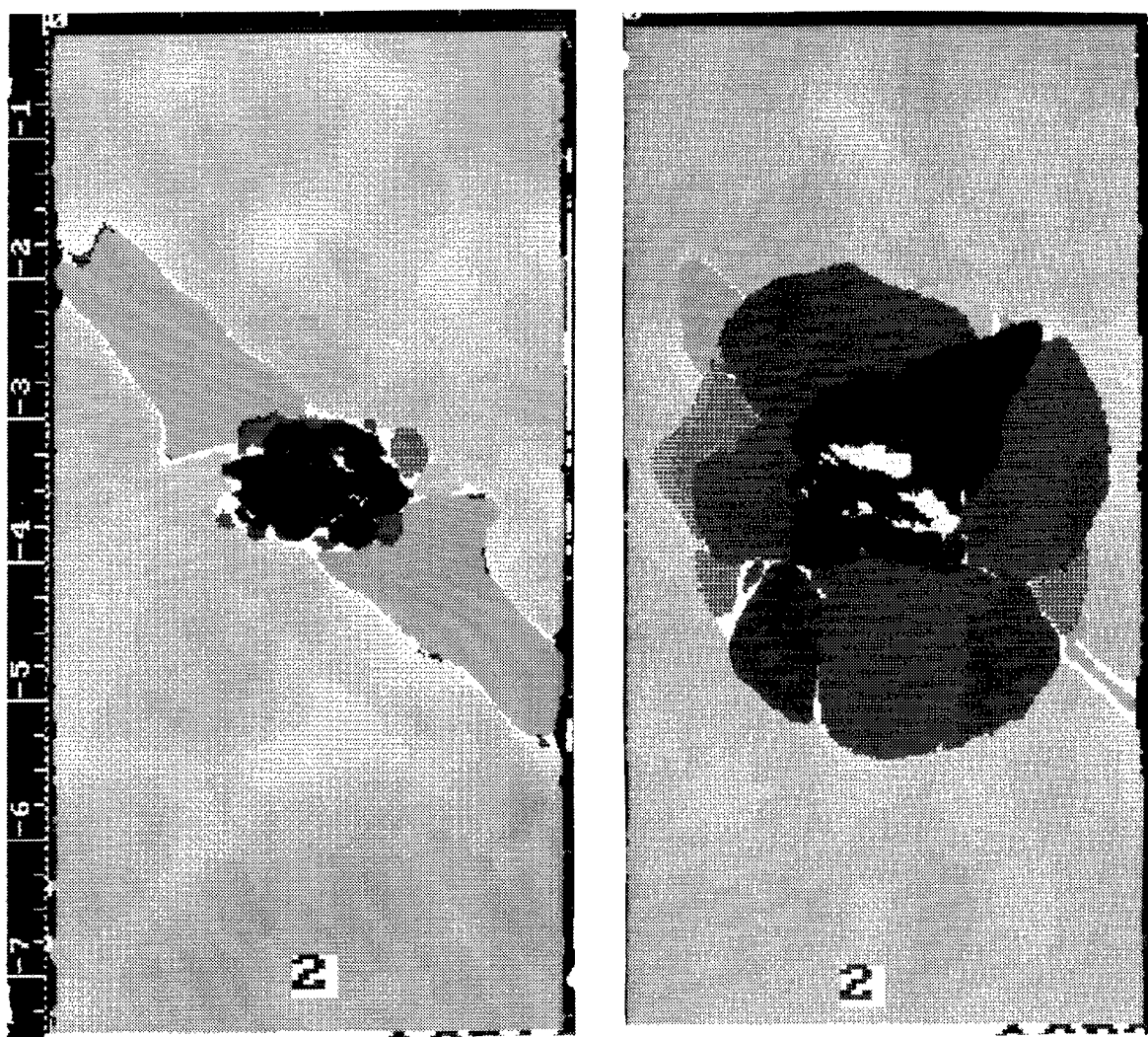
The two configurations which have penetration strengths that are more than 10% higher than machined-crack strengths are the IM6/937A and AS4/938 Tape Crown2 laminates. The relatively high bending stiffness of the 16-ply Crown2 laminate may result in the formation of larger matrix splits and delaminations near the crack tip, thereby reducing the stress concentration and increasing the strength. Ultrasonic scans (e.g., Figure 9) confirmed the existence of larger delaminations in the Crown2 specimens.



**Figure 7: Instrumented Impact Results for Through-Penetration of Tow-Placed Laminates Consisting of Various Percentages of AS4 and S2**



**Figure 8: Comparison of Penetration and Machined-Crack Strengths**



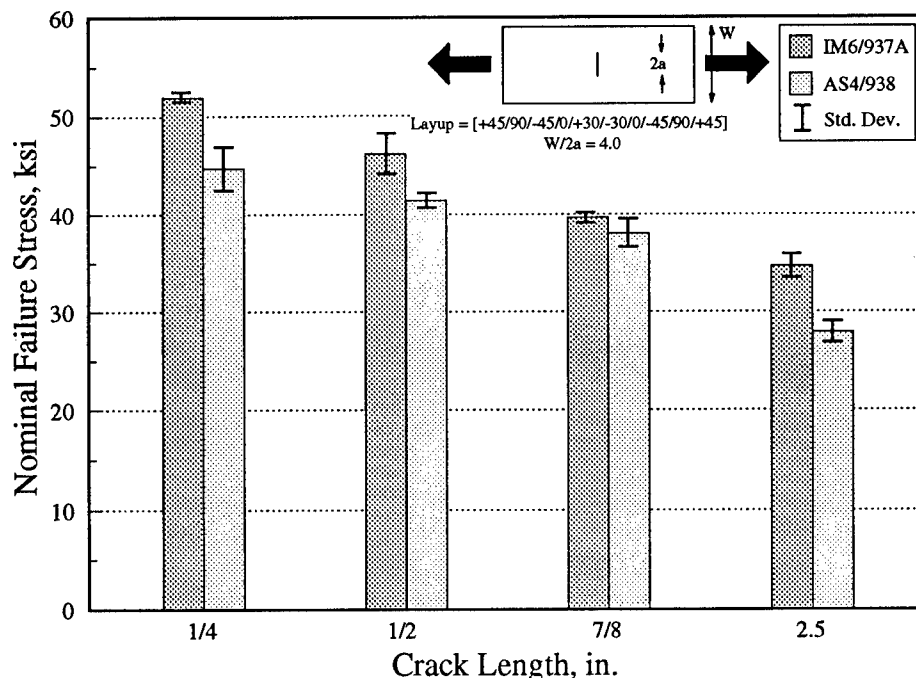
Crown1

Crown2

**Figure 9: Ultrasonic C-Scans of AS4/938 Tape Crown1 and Crown2 Through-Penetration Specimens**

### Fiber Type

A representative comparison of the tension fracture strength of IM6/937A and AS4/938 tape systems for the Crown1 laminate is contained in Figure 10. For this layup and range of crack sizes, notched strength is higher for IM6/937A than AS4/938. A similar increase was seen for other layups. The IM6 fiber provides a 20 to 25% increase over AS4 in both fiber and unidirectional ply strengths. Since the laminate notched-strength of IM6/937A ranged from 5 to 25% greater than AS4/938, the fiber strength improvement of IM6 was not realized in all cases. Although IM6 appears to have some advantage in tension fracture performance over AS4, even a 25% improvement does not result in a crown design that is more economically attractive than an AS4 design (Ref. 2).



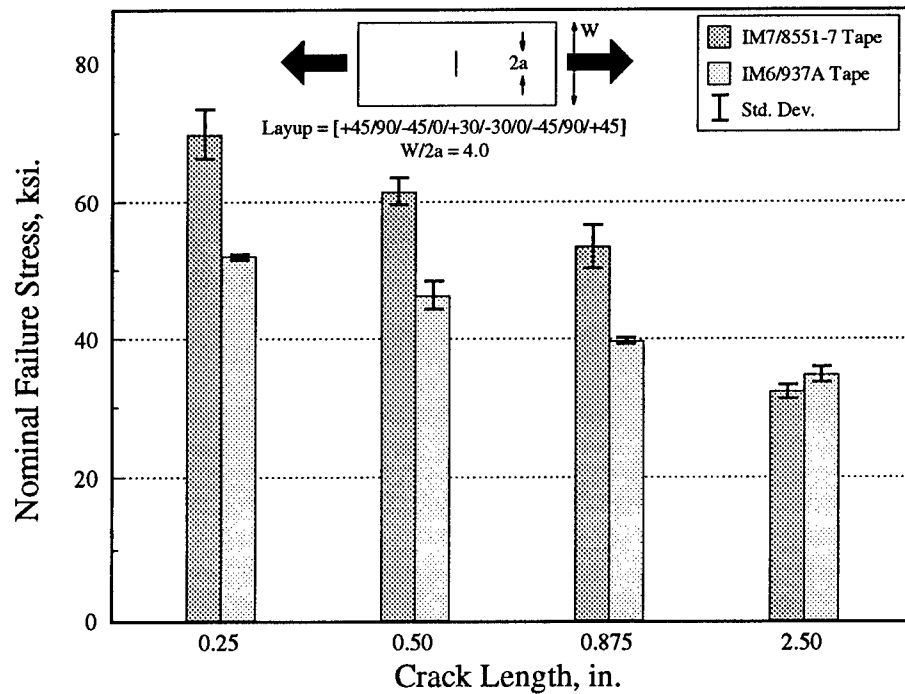
**Figure 10: Comparison of Fracture Strength for IM6/937A and AS4/938 Tape**

### Resin Type

The effect of resin type was evaluated by comparing the fracture performance of IM7/8551-7 and IM6/937A tapes. Since IM6 and IM7 fibers are essentially identical, the behavior differences shown in Figure 11 are expected to relate to the resin type and how it bonds to the fiber. The IM7/8551-7 material exhibited approximately 35% greater strength for crack sizes less than 1 inch, but with a 2.5 in. crack, its strength was 7% below that of the IM6/937A. Similar findings were reported in Reference 14 between other brittle and tough resin systems.

Data for the 2.5 in. cracks supports a hypothesis that splitting in plies oriented along the loading direction enhances tension fracture performance of laminates having larger crack sizes. A Drexel University subcontract<sup>13</sup>, supporting the ATCAS program, has studied the formation and growth of matrix splits in unidirectional specimens. The Drexel analysis and tests indicate that IM7/8551-7 is more resistant to matrix splitting than graphite fiber composites with matrices similar to 937A. The IM7/8551-7 material was also found to have  $G_{Ic}$  and  $G_{IIc}$  values for matrix damage growth that are 3 to 4 times as high as those of composites having the 937A-class resin. Despite the improved  $G_{Ic}$ , tests for mode I matrix cracking in IM7/8551-7 (Ref. 15) indicated that resin rich interlaminar layers reduce the "insitu strengthening effect" characteristic of multidirectional laminates.

<sup>13</sup> Ghaffari, S., Awerbuch, J., and Wang, A. S. D., "Temperature and Fracture Toughness Effects On Mixed Mode Matrix Splitting," Presented at the Fourth ASTM Symposium On Composite Materials: Fatigue and Fracture, 1991.

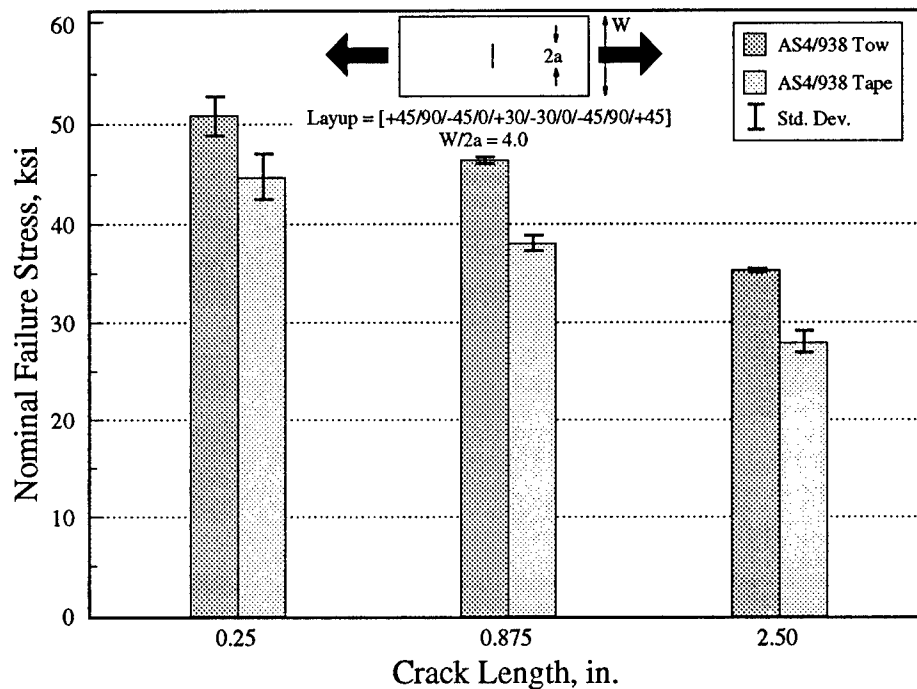


**Figure 11: Comparison of Fracture Strength for IM7/8551-7 and IM6/937A Tape**

Wang (Ref. 16) has shown that the initiation of matrix splitting in notched cross-ply laminates includes both mode I and II components of strain energy release rate, while subsequent stable growth is dominated by mode II. Conceivably, matrix splits will still form near cracks in IM7/8551-7 multidirectional laminates. However, mode II dominated split growth is resisted, leading to only minimal reduction of the stress concentration for larger cracks, and correspondingly lower tensile fracture strength. Additional discussions on this subject appear later in this paper.

### Tow Material Form

Unexpected tension fracture results were found in comparing tow-placed AS4/938 laminates with similar tape laminates. As shown for machined cracks in Figure 12, the tow material was found to have a reduced sensitivity to crack length, with fracture strength improvements of approximately 10% for crack lengths below 1 in. and 25% for 2.5 in. cracks. This could be related to an enhanced mechanism of splitting parallel to the loading axis. Photomicrographs of cross-sections showed significantly higher amounts of intraply resin-rich zones in tow-placed laminates. These zones can serve as split-initiation sites. Other differences between tow and tape material forms which may have affected tension fracture include fiber sizing (tow fibers were sized, tape fibers were unsized), fiber bundle size (tow was 6K, tape was 12K), and resin impregnation method (tow was hot melt, and tape was solvent). Discussions in the analysis section of this paper will also hypothesize that tow-placed material forms have a higher dimensional level of inhomogeneity, tending to reduce the stress concentration for a range of crack sizes.



**Figure 12: Comparison of Tension Fracture Strength of AS4/938 Tow and Tape**

### Intraply Hybridization

Results for the 8-run intraply hybrid designed experiment were analyzed (Ref. 17) using the factor levels shown in Table 1. Nominal failure stress and nominal failure strain (i.e., nominal failure stress/calculated modulus) were evaluated separately as response variables. Both measurements were corrected for finite width effects prior to data analysis. The finite width corrections were 7.6% and 3.8% for holes and cracks, respectively.

Factors	Factor Level	
	Low (-1)	High (+1)
(A) Hybrid Repeat Unit Width	0.38 in.	1.10 in.
(B) Percent S2-Glass (% by volume)	25%	50%
(C) Notch Type	Crack	Hole
(D) Notch Size	0.250 in.	0.875 in.

**Table 1: Factor Levels for Intraply Hybrid Designed Experiment**

The nominal values of failure stress and strain were found to have differing relationships with factors from the designed experiment. The following equations were generated based on regression analysis of experimental results:

Failure Stress,  $\sigma_{cr}$  (ksi)

$$\sigma_{cr} = 49.90 - 0.83A - 1.74C - 2.86D - 0.92(AB \text{ or } CD)$$

Failure Strain,  $\epsilon_{cr}$  (% in./in.)

$$\epsilon_{cr} = 0.785 - 0.014A + 0.057B - 0.028C - 0.045D \\ - 0.016(AB \text{ or } CD) - 0.014(AD \text{ or } BC)$$

where the values for A, B, C, and D are taken as +1 or -1 (see Table 1). Only those regression terms affecting results by 3% or greater were included in the above equations. Both failure stress and strain were found to depend on notch size and notch type. Percent S2-Glass was found to have the strongest effect on failure strain, while having little impact on failure stress. The hybrid repeat unit width and possible two-way interactions were found to have small effects.

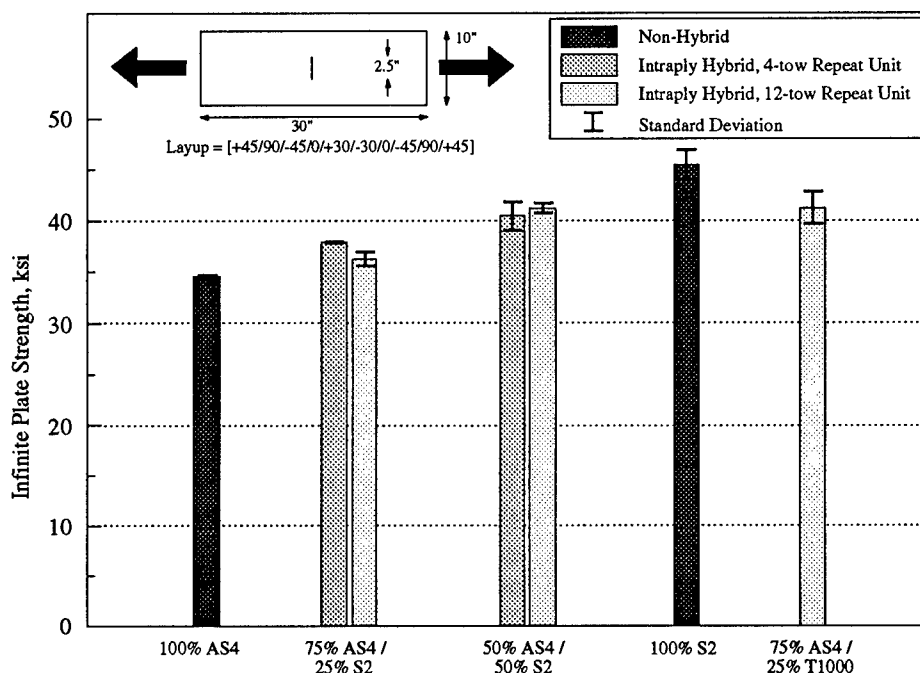
Experimental values of  $\sigma_{cr}$  and  $\epsilon_{cr}$  were found to decrease on the order of 10% with increasing notch size (from 0.25 in. to 0.875 in.). The magnitude of residual strength decrease over this range of notch sizes was much less than that of traditional tape material forms (Ref. 3). For example, current results for AS4/938 and IM6/937A tape materials with the same layup (i.e., see Crown1 results in Figure 4) indicate strength reductions on the order of 15 and 25%, respectively. The reduced notch sensitivity of hybrid materials is similar to that observed for the AS4/938 tow-placed material.

Other hybrid variables found to have a significant effect on tensile fracture performance include notch type and percent S2-glass. Both  $\sigma_{cr}$  and  $\epsilon_{cr}$  were found to be on the order of 7% lower for the specimens with holes than for those with cracks. Based on classical fracture theories, the opposite trend is expected for larger diameter holes and cracks. Future ATCAS tests will address this. The value of  $\epsilon_{cr}$  tended to increase with increasing percent S2-glass, while  $\sigma_{cr}$  remained constant. This suggests that the increased  $\epsilon_{cr}$  resulting from hybridization of AS4 (i.e., relatively low strain/high modulus fiber component) and S2-glass (i.e., relatively high strain/low modulus fiber component) was enough to counteract the drop in laminate modulus. Note that the hybrid designed experiment yielded results for relatively small notches. The ensuing paragraphs will discuss fully-crossed experimental results that show both  $\sigma_{cr}$  and  $\epsilon_{cr}$  increase with percent S2-glass for a 2.5 in. crack.

The notched strengths of the hybrid materials were found to segregate from those of the tow-placed 100% AS4/938 material as notch size increased. For the AS4/S2 hybrids, the maximum increase in  $\sigma_{cr}$  was approximately 5% for both 0.25 and 0.875 in. notches; however, as illustrated in Figure 13, significantly larger increases (i.e., up to 17%) were seen at the 2.50 in. crack size. This trend may relate to interactions between percent S2-glass, hybrid repeat unit width, and notch size. The hybrid designed experiment results for relatively small notch sizes (i.e., 0.25 and 0.875 in.) indicated some interactions for the range of repeat unit widths analyzed.

Fracture tests for the fifth tow-placed hybrid, 75% AS4/25% T1000, were not part of the designed experiment. The T1000 fiber for this all-graphite hybrid has both a higher modulus and failure strain than AS4 fiber. A relative comparison of small notch results for the graphite hybrid and the tow-placed laminate consisting of 100% AS4 indicated an increase in  $\sigma_{cr}$  on the order of 10% for the former. Relative improvements in  $\sigma_{cr}$  for the 2.5 in. crack sizes were even higher (17% as shown in Figure 13). Considering the Crown1 layup used in fracture testing, axial modulus of the graphite hybrid was calculated to be 4.6% higher than that for a laminate with only AS4 fiber. By definition,

this resulted in a greater increase in  $\sigma_{cr}$  than in  $\epsilon_{cr}$  when comparing the all-graphite hybrid and non-hybrid laminates. As was the case for tow-placed AS4/S2 hybrids, greater improvements for large notch sizes suggest possible interactions between hybridization parameters (e.g., percent T1000, hybrid repeat unit width) and notch size.



**Figure 13: Tension Fracture Strength of Intraply Hybrids for 2.5 Inch Crack**

Significant differences in failure were observed between the graphite tow-placed materials (i.e., 100% AS4 and Hybrid 5) and those containing any S2-glass (i.e., 100% S2-glass and Hybrids 1 through 4). The graphite specimens qualitatively appeared to exhibit relatively small amounts of crack-tip damage growth, while specimens with S2-glass exhibited large areas of matrix splitting and delamination prior to failure. As shown in Figure 14, the greater extent of crack-tip damage growth in S2-glass hybrids was confirmed by ultrasonic scans of failed 10 in. wide specimens with 2.5 in. initial crack length and a Crown1 layup. Note that higher failure strains correspond to greater damage levels for each of the four materials in Figure 14.

Another difference between graphite tow-placed materials and those containing any S2-glass relates to the load carrying capability of specimens after exceeding the maximum load. The all-graphite specimens exhibited brittle failures while those containing S2-glass continued to carry significant loads (often 30 to 40% of the peak load) after "failure." Evidence of this can be seen in Figure 15, which shows a failed 10 in. wide Hybrid #3 specimen with a 2.5 in. initial crack length and a Crown1 layup. The majority of the S2-glass fibers did not break, and, after failure of the graphite, rotated into the loading direction. Although the observed behavior for S2-glass hybrids depends on the use of displacement controlled tests, additional load carrying capability may better enable fuselage structures to sustain "get-home" loads following a discrete source damage event.

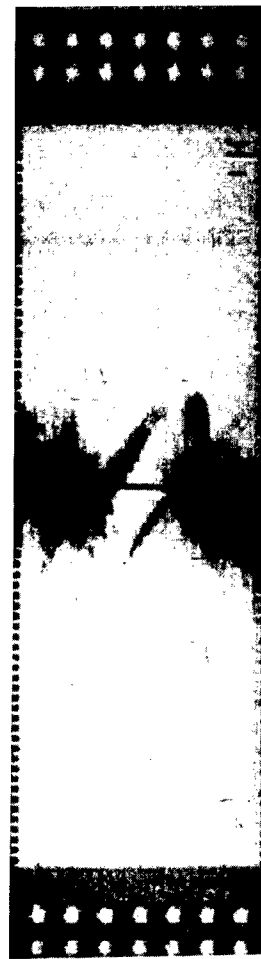




AS4/938 Tape  
 $P_{cr}/AE_x = .0039$



AS4/938 Tow  
 $P_{cr}/AE_x = .0050$



Hybrid #1  
 $P_{cr}/AE_x = .0059$



Hybrid #2  
 $P_{cr}/AE_x = .0075$

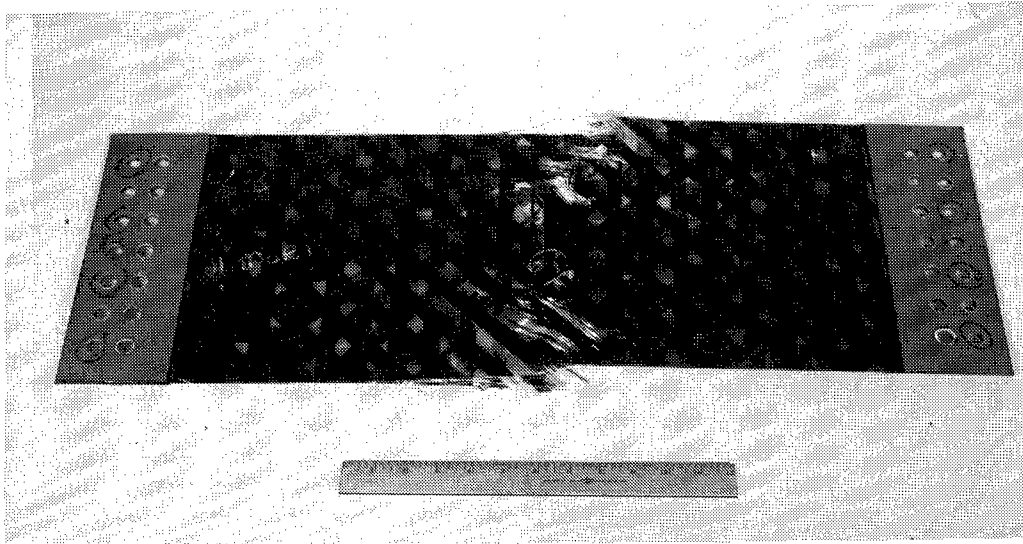
**Figure 14: Ultrasonic Scans of Failed Fracture Specimens**

### Comparisons of Notch Sensitivity

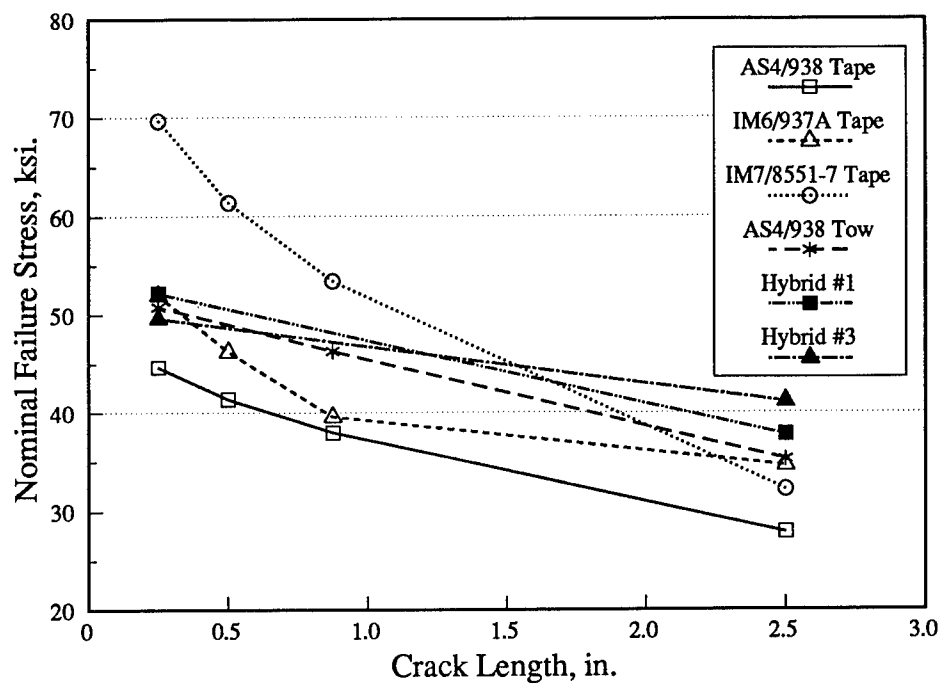
For purposes of comparison in the current paper, notch sensitivity is defined as a change in fracture strength with increasing crack length. Figure 16 shows notch sensitivity data trends for six different material types. All data in the figure corresponds to averages for machined cracks,  $W/2a = 4$ , and the Crown1 layup. The six materials in Figure 16 are shown to have large differences in notch sensitivity. For the range of cracks tested (0.25 in. to 2.5 in.), IM7/8551-7 appears to have the greatest notch sensitivity (total drop of 54%), while Hybrid #3 had the least (total drop of 18%).

Data trends in Figure 16 also suggest that there is little correlation between fracture results for the smallest and largest cracks tested. For example, IM7/8551-7 had distinctly higher fracture strength than all other materials for a 0.25 in. crack, but had close to the lowest strength for a 2.5 in. crack. A series of statistical analyses was performed with the complete data set for Crown1 layups to confirm

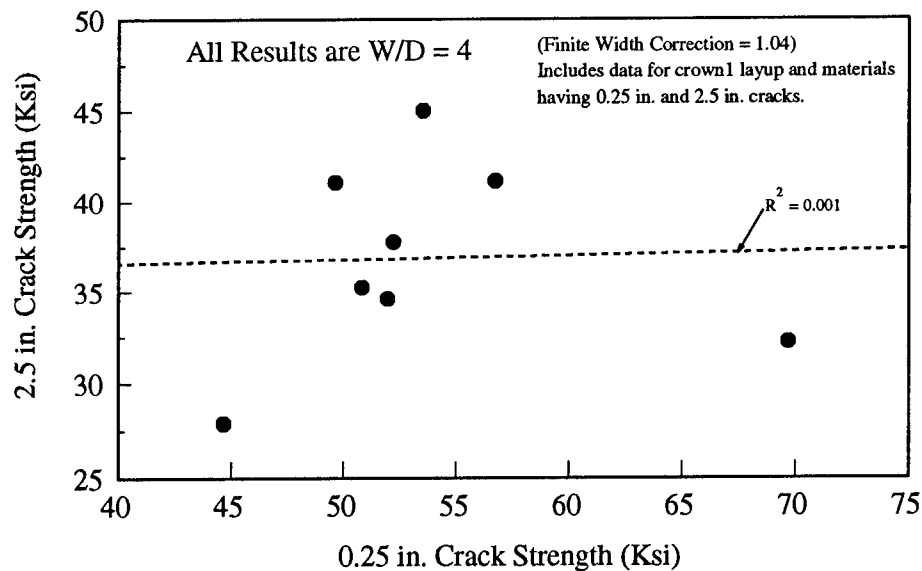
this observation. Figure 17 shows results from regression analysis comparing 0.25 in. and 2.5 in. crack data for eight of the ten material types (due to the nature of a designed experiment two hybrids did not have test data for a 0.25 in. machined crack). This figure indicates that there is no correlation between data obtained at the two crack sizes.



**Figure 15: Failed Intraply Hybrid Tension Fracture Specimen**



**Figure 16: Comparison of Notch Sensitivity for Different Materials**



**Figure 17: Statistical Relationship Between Small and Larger Crack Strengths**

Results from other regression analyses indicated more favorable statistical correlations between fracture strengths at different crack sizes. A small correlation ( $R^2 = 0.40$ ) was obtained between 0.875 in. and 2.5 in. crack test results. Better correlations ( $R^2 = 0.78$ ) were obtained when comparing notched strength differences, e.g.,

$$(\sigma_{cr\{0.25 \text{ in.}\}} - \sigma_{cr\{2.5 \text{ in.}\}}) \text{ vs. } (\sigma_{cr\{0.25 \text{ in.}\}} - \sigma_{cr\{0.875 \text{ in.}\}}) \text{ and} \\ (\sigma_{cr\{2.5 \text{ in.}\}}/\sigma_{cr\{0.25 \text{ in.}\}}) \text{ vs. } (\sigma_{cr\{0.25 \text{ in.}\}} - \sigma_{cr\{0.875 \text{ in.}\}}).$$

As mentioned earlier, an open hole specimen with a 0.25 in. diameter hole is commonly used in the aerospace industry to screen materials for notched tensile strength. Since holes and cracks are nearly equivalent for small notch sizes, results in Figures 16 and 17 suggest that the 0.25 in. notch test should not be used to screen materials for fuselage damage tolerance. An alternative procedure, involving a range of notch lengths is recommended later in this paper.

### ANALYTICAL COMPARISONS

The primary purpose of tension fracture analysis methods is to provide failure predictions beyond the notch sizes and structural geometries tested during material characterization. To ensure this extrapolation capability, suitable models must revolve around theories with a basis in the physics of the problem. It is also desirable to minimize the number of degrees-of-freedom in a model to reduce material testing requirements. The following is a discussion of previously proposed analysis methods, and an evaluation of how well they predict the test data obtained in this program. Discussions of test data will be limited to the center-crack results, since the range of open-hole configurations was insufficient to evaluate predicted trends.

## Finite Width Corrections

Correcting failure strengths for finite width effects provides the basis for comparison of different specimen configurations. Numerical methods have been employed to show that isotropic finite width correction factors (FWCF) differ from their orthotropic counterparts by less than 3% for specimen-width-to-crack-length ratios ( $W/2a$ ) greater than 2 [Refs. 3, 18]. Any of the several expressions for isotropic FWCFs may therefore be used.

The current crack test database was used to assess the validity of using isotropic FWCFs. Nominal notched strengths, corrected for finite width according to

$$\sigma_N^\infty = \text{FWCF} * \sigma_N, \quad (1)$$

where  $\text{FWCF} = 1 + 0.1282 (2a/W) - 0.2881 (2a/W)^2 + 1.5254 (2a/W)^3$ ,

were compared for all laminates fabricated from both AS4/938 and IM6/937A tape. Test data were plotted as finite-width-corrected strength versus crack length for each of  $W/2a = 4$  and  $W/2a = 2$ , as shown in Figure 18 for the AS4/938 Crown1 laminate. Properly corrected data should fall on a single curve. For every laminate, however, the  $W/2a = 2$  data was lower than that of  $W/2a = 4$ . This difference was quantified by comparing average strengths for equivalent crack lengths, and found to be between 4 and 30% of the  $W/2a = 4$  values.

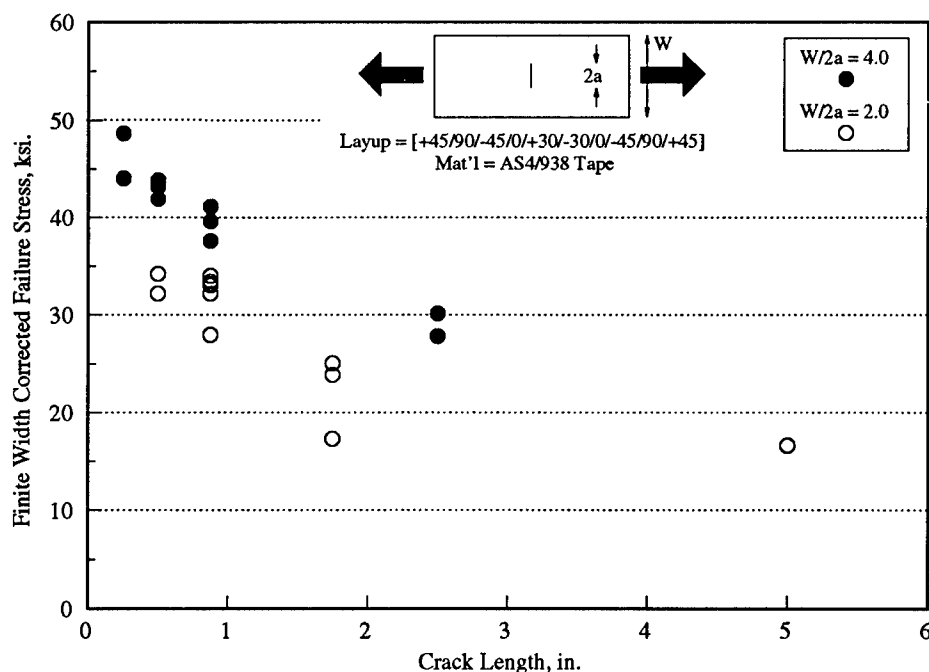
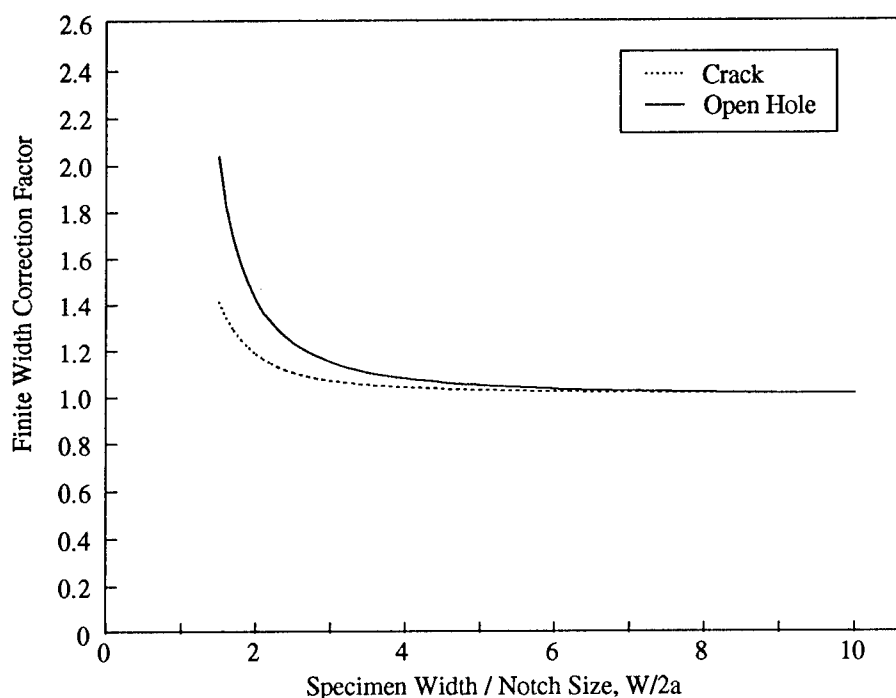


Figure 18: Comparison of Finite Width Corrected Strengths for  $W/2a = 2$  and  $W/2a = 4$

Experimental results clearly indicate that FWCFs for  $W/2a = 2$  data are consistently underpredicted. Several phenomena not considered in the development of the FWCF relationships may account for this shortcoming. These are: (a) specimen edge-delamination, (b) crack-tip softening due to matrix damage, and (c) buckling adjacent to the unsupported crack surfaces due to Poisson's-ratio-induced transverse compression.

Specimen edge delamination and crack-tip matrix damage act to increase the stress-field interaction with the boundary. Edge delamination causes an in-plane stiffness reduction in the vicinity of the delamination, resulting in load redistribution toward the center of the specimen. Similarly, crack-tip matrix damage reduces the stiffness near the crack tip, resulting in load redistribution towards the edge of the specimen. Both of these phenomena were observed to varying extents during the tests. The increased interaction with the boundary is more pronounced in lower  $W/2a$  specimens, since a higher percentage of the net area is affected. A larger increase in the actual FWCF for  $W/2a = 2$  specimens therefore results.

Transverse buckling adjacent to the unsupported crack surface was observed in both the 2.5 in. and 5.0 in. crack specimens, and was confirmed with the measurement of out-of-plane displacements of up to several times the specimen thickness at 75 to 80% of the failure load. The transverse buckling reduces in-plane stiffness in a somewhat circular region, resulting in behavior resembling that of a partially-filled hole. The FWCF for the crack with transverse buckling, therefore, increases towards that of a hole. As shown in Figure 19, the FWCF difference between a crack and a hole (Ref. 19) is much larger for  $W/2a = 2$  than for  $W/2a = 4$ .



**Figure 19: Comparison of Finite Width Correction Factors for Cracks and Open Holes**

Due to the uncertainty in correcting test data with differing  $W/2a$  values, the remainder of the comparisons with test data in this paper are limited to those data with  $W/2a = 4$ . Many of the studies in the literature (as reviewed by Ref. 3) increased crack length for a constant width specimen, with the largest cracks typically being tested in the  $W/2a = 2$  range. This results in the residual strength curve being errantly skewed downward at the larger crack lengths. Limiting comparisons to  $W/2a = 4$  reduces this problem.

## Review of Failure Criteria

Several failure criteria that have been proposed for tension fracture were evaluated. In the following discussion of the criteria,  $\sigma_N^\infty$  and  $\sigma_o$  are the notched and unnotched strengths of an infinite plate, respectively, and  $a$  is the half-crack length.

The stress distribution at a crack tip is singular for classical continuum theories. In linear elastic fracture mechanics (LEFM) for homogeneous materials, a square-root singularity exists, and failure is predicted by

$$\sigma_N^\infty = K_{Ic}/(\pi a)^{1/2} \quad (2)$$

where  $K_{Ic}$  is the critical stress intensity factor. This approach suffers from the physically unacceptable situation of infinite stresses at the crack tip. As a consequence,  $\sigma_N^\infty$  increases rapidly with decreasing  $a$  and  $\sigma_o$  becomes infinite, in the limit, as  $a$  approaches 0.

In composites, this has been addressed by several theories through the use of a characteristic dimension, inherent flaw size or critical damage zone length. The Whitney-Nuismer (WN) point-stress criteria (Refs. 20, 21), for example, predicts failure when the stress at a characteristic dimension,  $d_I$ , ahead of the crack tip equals or exceeds  $\sigma_o$ . The notched strength, then, is given by

$$\sigma_N^\infty = (1 - (a/(a + d_I))^2)^{1/2} \quad (3)$$

The two parameters in this model which must be determined are  $\sigma_o$  and  $d_I$ .

The Pipes-Wetherhold-Gillespie (PWG) model (Refs. 22, 23) extends the WN point-stress model to include an exponential variation of  $d_I$  with crack length. This provides added flexibility in predicting small crack data, but requires an additional parameter to be determined.

Another multi-parameter model, proposed by Tan (Ref. 24), uses a characteristic dimension to predict failure of a plate with an elliptical opening subjected to uniaxial loading. In this model, a high-aspect-ratio ellipse is used to simulate a crack. Notched strengths are predicted by factoring the actual unnotched laminate strength by the ratio of predicted notched to predicted unnotched strengths. Both of these predicted strengths are obtained using a quadratic failure criterion in conjunction with the first-ply-failure technique. The predicted notch strength is determined by applying the failure criterion at a characteristic dimension away from the crack. The coefficients in this criterion are the additional parameters that must be determined.

The Poe-Sova (PS) model (Refs. 25, 26) may also be formulated with a characteristic dimension,  $d_2$ , but predicts failure when the *strain* at that distance ahead of the crack tip equals or exceeds the fiber failure strain. The notched failure stress is given by

$$\sigma_N^\infty = \sigma_o / (1 + (a\xi^2/2d_2))^{1/2} \quad (4)$$

where  $\xi$  is a functional that depends on elastic constants and the orientation of the principal load carrying plies. The characteristic dimension relates to a material toughness parameter, which was found to be relatively independent of layup. The two parameters which must be determined for this model are the fiber failure strain and  $d_2$ .

Two other frequently-used models, Waddoups-Eisenmann-Kaminski (WEK) and WN average stress, each have undamaged strength as the first parameter. The second parameters for WEK and WN average stress models are referred to as critical damage size and average stress characteristic dimension, respectively. The WEK model (Ref. 27) applies LEFM to an effective crack that extends beyond the actual crack by the inherent flaw size. The WN average stress model (Refs. 20, 21)

assumes failure when the average stress across the characteristic dimension equals or exceeds  $\sigma_o$ . Both the WEK and WN average stress models were found to be functionally equivalent to the PS model if a linear strain-to-failure is assumed.

The approaches described above which use a length parameter (e.g., characteristic dimension) were formulated to account for observed experimental trends for composites. In practice, these length parameters are determined from notched strength data and given limited physical meaning in relationship to any microstructural dimension of the material. They are often thought of as classical analysis correction factors, which enable the user to account for apparent changes in the stress distribution or fracture toughness with increasing crack size. It should be noted that the length parameter calculated for the WN point stress, WN average stress, PS, WEK, and Tan models will generally take on different values for the same set of data.

A more physically acceptable approach to predicting composite fracture may involve changes in the crack tip stress distribution as a function of material length parameters that define levels of inhomogeneity. Simplified analysis performed to evaluate the effect of inhomogeneities at the fiber/matrix scale indicated that the crack size should be at least three orders of magnitude larger than the fiber diameter to vindicate the classical continuum homogeneity assumption (Ref. 28). The results of Reference 28 show that inhomogeneity tends to reduce stress intensity factors for a range of crack lengths that is related to the level of inhomogeneity. Considering the fiber/matrix dimensional scale, the crack length range affected by inhomogeneity is smaller than that for which characteristic lengths are needed to correct classical fracture analyses for graphite/epoxy composites. However, higher levels of inhomogeneity exist in tape and tow-placed laminates due to manufacturing processes. These characteristics of composite materials may be responsible for the reduced stress concentrations traditionally found for small cracks.

Solutions to fracture problems using generalized continuum theories have also yielded results consistent with experimental trends in composites, without a semi-empirical formulation. Generalized continuum theories are formulated to have additional degrees of freedom which characterize microstructural influence. The stress concentrations for such theories change as a function of relationships between notch geometry and material characteristic lengths (e.g., Refs. 29, 30, and 31). Note that the characteristic lengths of generalized continuum are different than those in models described earlier because they are fundamentally based on moduli from the theory. As a result, the moduli have relationships with other material behavior (e.g., wave propagation) and their values can be confirmed from a number of independent experimental measurements. Ultrasonic wave dispersion measurements have been used to predict the moduli and notched stress concentration for wood composite materials (Ref. 29). Unfortunately, considerably more work is needed to develop generalized continuum theories for applications with laminated composite plates.

For inhomogeneous materials, the stress distribution at the crack tip is also not limited to a square-root singularity. The Mar-Lin (ML) model (Refs. 32, 33) allows the singularity,  $n$ , to be other than square-root. The notched failure stress is given by

$$\sigma_N^\infty = H_c / (2a)^n \quad (5)$$

where  $H_c$  is the composite fracture toughness. In general,  $H_c$  and the exponent  $n$  are the two parameters that must be determined. In the Reference 32 and 33 studies, the exponent,  $n$ , was related to the theoretical singularity of a crack in the matrix, with the tip at the fiber/matrix interface. For this case, the singularity is a function of the ratio of fiber and matrix shear moduli and Poisson's ratios. Using this method, the singularities for a range of typical fiber/matrix combinations were determined to be between 0.25 and 0.35.

The Tsai-Arocho (TA) model (Ref. 34) combines the non-square-root singularity of the ML model with the inherent flaw concept of the WEK method. At the expense of another parameter, additional flexibility in predicting small-crack strengths is gained, although this effect lessens as the order of the singularity is reduced.

Other theoretical approaches which have been applied to predict tension fracture in composites include damage zone models, DZM (e.g., Ref. 35 and 36), and progressive damage analysis, PDA (e.g., Ref. 37 and 38). Both methods use finite elements to account for notch tip stress redistribution as damage progresses. The DZM utilized a Dugdale/Barenblatt type analysis for cohesive stresses acting on the surface of an effective crack extension over the damage zone length. As was the case for characteristic-length-based failure criteria described above, a Barenblatt analysis (Ref. 39) resolves the stress singularity associated with cracks. The PDA methods account for the reduced stress concentration associated with mechanisms of damage growth at a notch tip by reducing local laminate stiffness. From a practical viewpoint, both DZM and PDA methods may be more suitable in calculating the finite width effects discussed in the previous subsection and for predicting the performance of final design concepts; however, applications of finite-element-based methods during design concept selection are limited.

### Functionality of Criteria

This subsection will review the degrees of freedom in curves from two parameter models which have been used extensively to predict tension fracture for composite laminates. This background will help to interpret discussions that compare theory with the current experimental database in the following subsection. Predictions for both small crack ( $2a \leq 1.2$  in.) and large crack ( $2a$  up to 20 in.) sizes will be compared. The former crack sizes are characteristic of most data collected for composites to date. Four theories will be covered in detail; classical LEFM, WN (point stress), PS (point strain), and ML. As a baseline for comparing changes in crack length predicted by the four theories, curves will be generated based on average experimental results (finite width corrected) for the IM6/937A tape material with Crown1 layup and  $W/2a = 4$ . This will ensure that all theories agree for at least one crack length.

Figure 20 shows a comparison of the four theories for small crack sizes. Only a small difference is seen between PS and WN criteria. A close examination of the LEFM and ML curves indicates that the singularity has a significant effect on curve shape. For crack lengths less than the baseline point, ML predictions are less than those of LEFM. For crack lengths greater than the baseline point, the opposite is true, and theories tend to segregate based on singularity (i.e., WN, PS, and LEFM yield nearly the same predictions).

Figure 21 shows that singularity dramatically affects differences between predictions in the large crack length range. The ratio of notched strength predictions for theories with the same order of singularity becomes a constant. For example, WN and LEFM become functionally equivalent and the relationship:

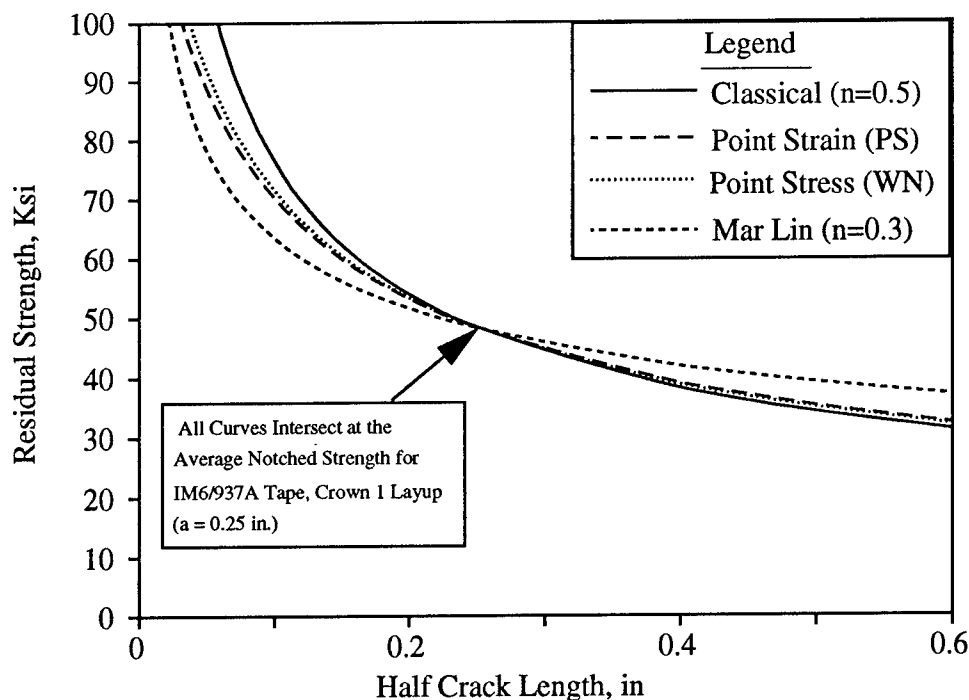
$$K_{Ic} = \sigma_o (2\pi d_I)^{1/2} \quad (6)$$

will yield a value for  $K_{Ic}$  such that the two theories compare exactly for large cracks.

In order to compare the effect of a range of singularities on notched strength predictions, curves in Figures 22 and 23 vary the value of  $n$  from 0.1 to 0.5. All curves in Figure 22 cross at the baseline point used to determine the corresponding fracture toughness values. By allowing both variations in fracture toughness and order of singularity, the ML criterion could statistically fit a wide range of notched strength data trends for small crack sizes. Such an approach is not recommended for other



than interpolation purposes, because Figure 23 clearly shows how projections to a large crack size is strongly dependent on the assumed singularity.



**Figure 20: Comparison of Curve Shapes for Notched Strength Prediction Theories in Small Crack Range**

Figures 24 and 25 show how the two parameters in the WN point stress criteria,  $\sigma_o$  and  $d_I$ , affect both the shape and relative positions of notched strength curves. Again comparisons are made with classical LEFM equations passing through common points. The lower set of curves corresponds to the baseline data point. Unlike the LEFM curves which rise sharply with decreasing crack length, the point stress theory has a finite strength,  $\sigma_o$ , at  $a = 0$ . For a given value of  $\sigma_o$ , increasing  $d_I$  tends to increase the predicted notched strength and, hence, has an effect similar to increasing  $K_{Ic}$  in LEFM (see upper curves in Figures 24 and 25).

In the small crack length range, a reduced value of  $\sigma_o$  can have the appearance of reducing the singularity. The curve shapes for lower curves in Figure 24 indicate that various combinations of  $\sigma_o$  and  $d_I$  could be selected to represent data trends that follow any of the singularities shown in Figure 22 (particularly for  $a \leq 0.25$ ). For small crack sizes characteristic of past databases, the curve-fits for WN and ML theories are nearly indistinguishable (Ref. 3). This inability to distinguish lower orders of singularity in past composite data may relate to measured values of  $\sigma_o$  that were low due to edge delamination phenomena in finite width specimens. For large crack lengths, Figure 25 shows that the magnitude of  $\sigma_o$  and  $d_I$  determine residual strength, but curve shape is dominated by the order of singularity. As discussed in reference to Figure 23, the proper order of singularity is best judged at large crack lengths.

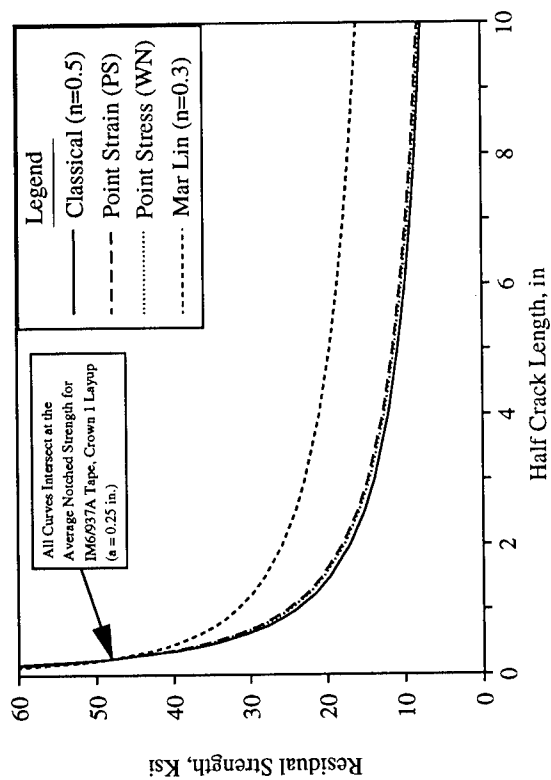


Figure 21: Comparison of Curve Shapes for Notched Strength Prediction Theories in Large Crack Range

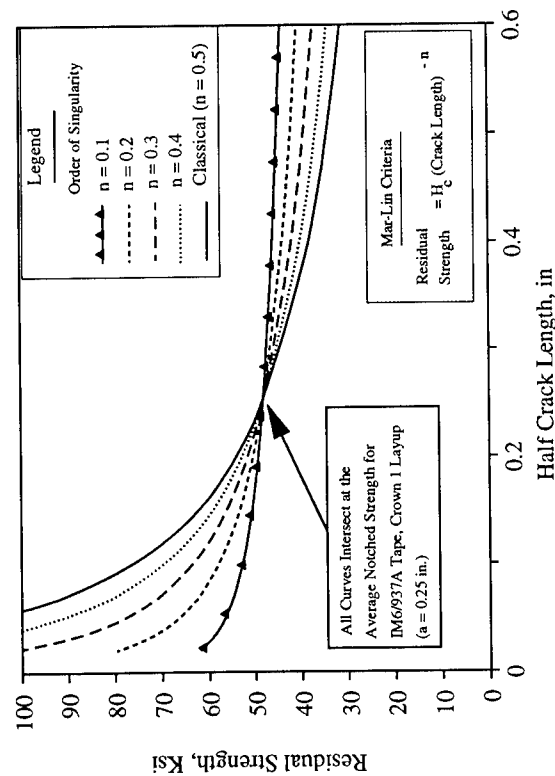


Figure 22: Effect of Singularity on Curve Shapes for Notch Strength Prediction Theories in Small Crack Range

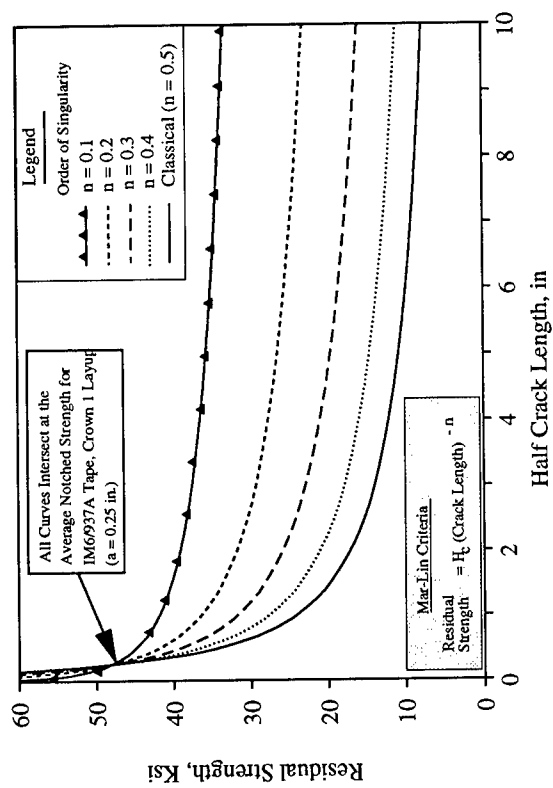


Figure 23: Effect of Singularity on Curve Shapes for Notch Strength Prediction Theories in Large Crack Range

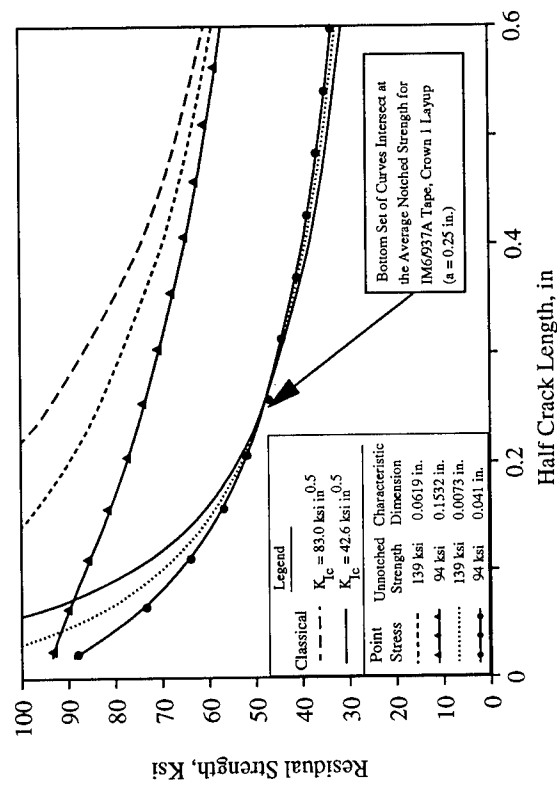
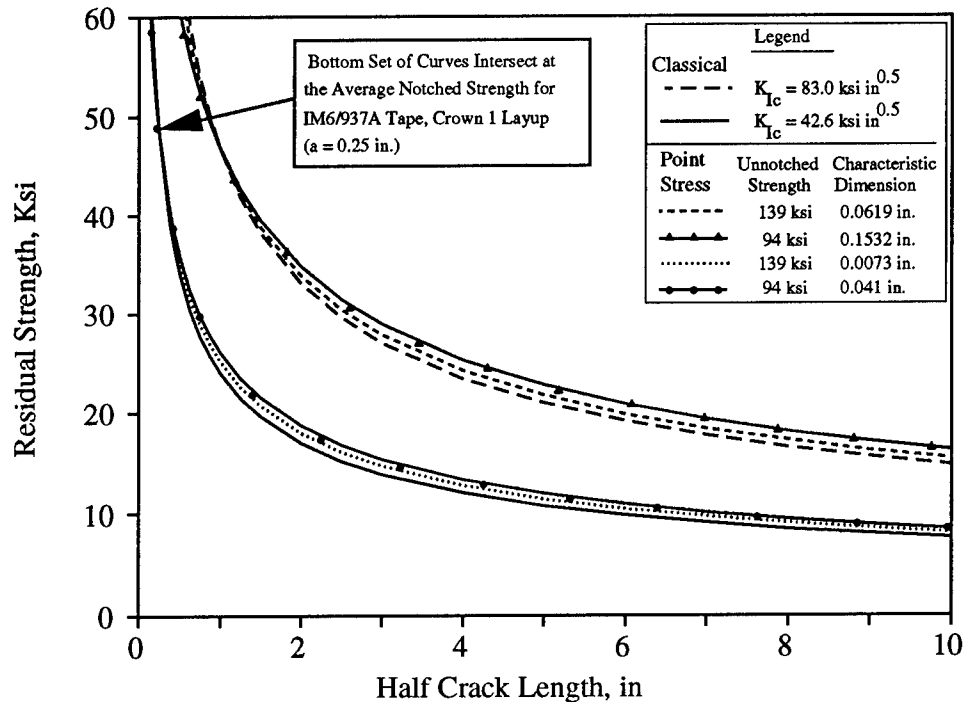


Figure 24: Effects of Characteristic Dimension and Unnotched Strength on Curve Shapes for Notch Strength Prediction Theories in Small Crack Range



**Figure 25: Effects of Characteristic Dimension and Unnotched Strength on Curve Shapes for Notch Strength Prediction Theories in Large Crack Range**

### Comparison With Test Results

Test data collected to screen materials for fuselage applications also provided a basis to evaluate the various failure criteria. Evaluations were made for laminates of practical interest to fuselage skin structures (i.e., multidirectional laminates having some percentage of both  $0^\circ$  and  $90^\circ$  plies). As in the application of fracture mechanics to metallic structures, suitable failure criteria use specimen data from material characterization tests to predict fracture of structural geometries. Structural variables are a subject of future ATCAS activities; however, the current study provides data to evaluate the theories for variable crack length.

Applications documented in the literature have advised using experimental data for a range of crack lengths to determine semi-empirical parameters in the composite notched failure criteria (e.g., Ref. 3). This may be achieved by using a least squares statistical curve fit with the proper function. Alternatively, the parameters can be determined for each crack length in the database and a scatter plot versus crack length can be used to judge if the parameter remains constant. This alternative approach was adopted for evaluating theories in the current study. Model parameters that were predetermined, independent of the notched fracture data, include the unnotched strength ( $\sigma_0$ ) and order of singularity ( $n$ ). Note that the order of singularity was set at 0.3 for the ML criteria. This reduced the number of parameters determined directly from notched test data to one for each of the four failure criteria evaluated in this section.

Due to the phenomena of edge delamination, finite specimen width is known to reduce the unnotched tensile strength measured for laminates. Tension test results from unnotched tubular specimens (Ref. 40) showed that quasi-isotropic laminates consisting of AS4/3501-6 tape materials (similar to AS4/938 used in current study) fail at a strain very close to the fiber failure strain measured in tests with

unidirectional specimens. To avoid finite width effects in determining the value of  $\sigma_o$ , it was calculated for laminates that had plies oriented in the axis of load by

$$\sigma_o = E_x \epsilon_{cr}$$

where  $E_x$  was the laminate modulus in the direction of load (calculated based on lamination theory and measured lamina properties) and  $\epsilon_{cr}$  was the measured axial fiber failure strain from unidirectional tests. In the case of hybrid materials, methods described by Chamis (Ref. 41) were used to calculate  $E_x$ . The hybrid  $\epsilon_{cr}$  was assumed to be that of the fiber with the lowest value (i.e., unidirectional laminate test data for AS4/938 in all cases).

In an attempt to minimize the width effect discussed earlier, all failure criteria evaluations were performed using data for  $W/2a = 4$ . To determine parameters for the failure criteria, the average values printed in Figure 4 were corrected for finite width (FWCF = 1.04). Scatter plots of the fracture parameters versus crack length were generated for each multidirectional layup and material type. As expected, the classical fracture mechanics approach yielded an increasing  $K_{Ic}$  with increasing crack length for all cases. In most cases, the value of  $K_{Ic}$  doubled for crack lengths ranging from 0.25 in. to 2.5 in.

Composite failure theories evaluated in the current study were all found to have better correlation with experimental data than the classical  $K_{Ic}$  approach. However, values of composite fracture parameters ( $d_1$ ,  $d_2$ ,  $H_c$ ) were also found to have significant increases with increasing crack length for most materials and layups studied. For example, values of  $H_c$  increased by up to 50% for crack lengths ranging from 0.25 in. to 2.5 in. The current authors recognize that these findings generally differ from those reported by Awerbuch and Madhukar (Ref. 3) in a review of fracture data available in the literature.

Significant differences in evaluations of the current database and those obtained in most past studies include:

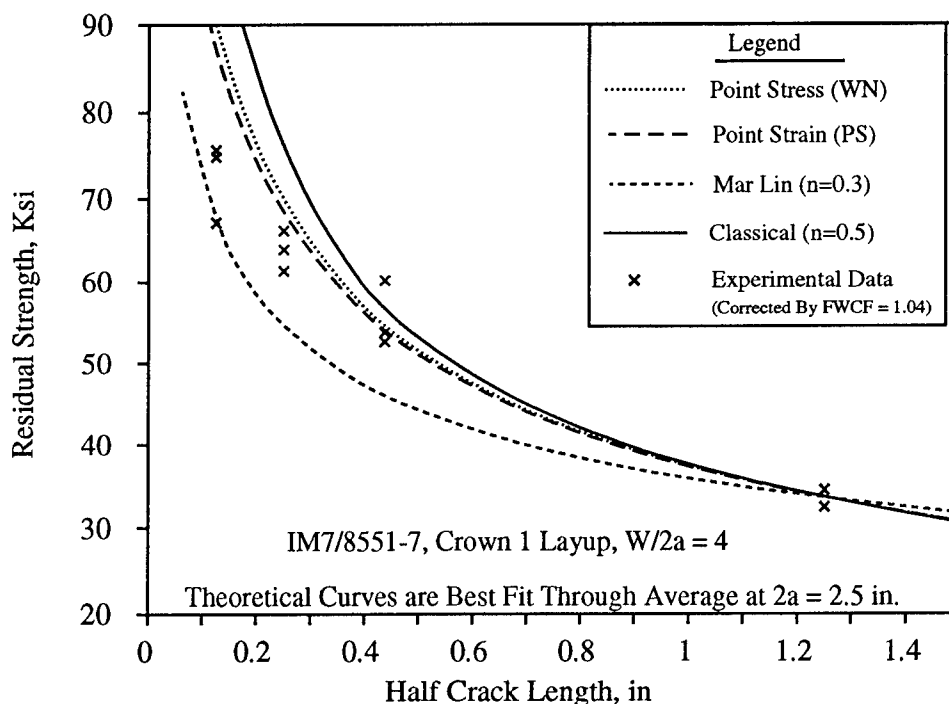
1. The longest cracks considered in the current study were larger than those considered in most past studies.
2. Current analysis comparisons were made with variable crack length data obtained from specimens having a constant  $W/2a$  (i.e., the FWCF was the same for all data).
3. Tension test values obtained for  $\sigma_o$  and used in failure criteria for past studies may have been low due to edge delamination in finite width specimens.

As illustrated in the previous subsection, a wide range of crack lengths is needed to distinguish differences in the various composite failure criteria. Results shown earlier in this paper indicated that classical FWCF for small  $W/2a$  are inaccurate. This may have resulted in misleading trends in past studies that compared theory to variable crack length data obtained for constant specimen width (i.e., the FWCF used to facilitate the comparison changed with increasing crack length). As a result, the past studies may have overlooked the effects of the assumed singularity which is dominant for larger crack lengths. Finally, low values for  $\sigma_o$  can tend to mask possible limitations of theories applied to small crack data.

A close examination of the theories and experimental data for specific layups and material types revealed several interesting trends. For some materials and layups, specific fracture parameters became constant for the two largest cracks in a data set. In agreement with theory, the fracture strength for the largest crack sizes appeared to become dependent on the order of singularity and a constant value of fracture toughness. In the case of the thickest laminates tested (16 ply), some failure

parameters were constant for the full range of crack lengths. Several graphs will be used in the remainder of this subsection to illustrate the observed trends and discuss strengths and weaknesses generally found for the failure criteria evaluated.

Figure 26 shows results for the material with a toughened matrix, IM7/8551-7. The comparison between theory and experiment was made by using fracture parameters determined from the average strength data for the largest crack length. Results suggest that a singularity of 0.5 best represents data trends for large crack lengths. Out of all the materials and layups studied, this trait was found to be unique to the IM7/8551-7 material. Note that, of the square-root singularity methods, WN and PS best follow data trends for the smaller crack lengths, but values of  $d_1$  and  $d_2$  would need to increase with crack length for a good fit of the entire data range.

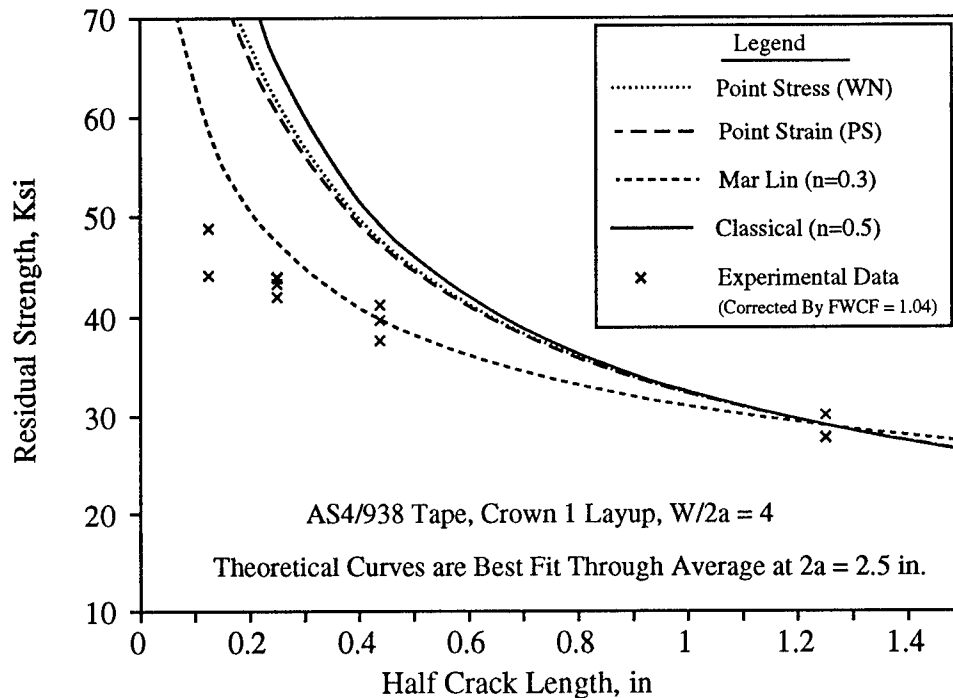


**Figure 26: Comparison of IM7/8551-7 Experimental Results With Different Failure Criteria**

Figure 27 shows results for the AS4/938 tape material and a Crown1 layup. Again the comparison is made for fracture parameters determined from the average strength data of the largest crack length. In this case, the ML criteria and a singularity of 0.3 compares well with the two largest crack lengths. In similar comparisons, most other materials and layups also compared best with the ML theory for larger crack sizes in which the singularity becomes dominant. Possible corrections to the ML theory using parameters similar to those in WN and PS (Ref. 34) would likely result in improved prediction of trends for small crack sizes.

As shown in Figure 28, the AS4/938 tape Crown2 laminate was one of the two cases in which a fracture theory compared well with the experimental data for the full crack length range. Unfortunately, specimens with 2.5 in. cracks were not tested for this layup, which limits the ability to judge the order of singularity. The IM6/937A Crown2 tape layup also compared well with the ML theory for cracks ranging from 0.25 in. to 0.875 in. Good correlations with the ML theory indicate a

constant  $H_c$  value. Although this was evident for small crack lengths and the Crown2 layup, it was not seen for other layups of either material type. The Crown1 laminate (results shown in Figure 27) had similar ply orientations as those used for Crown2.



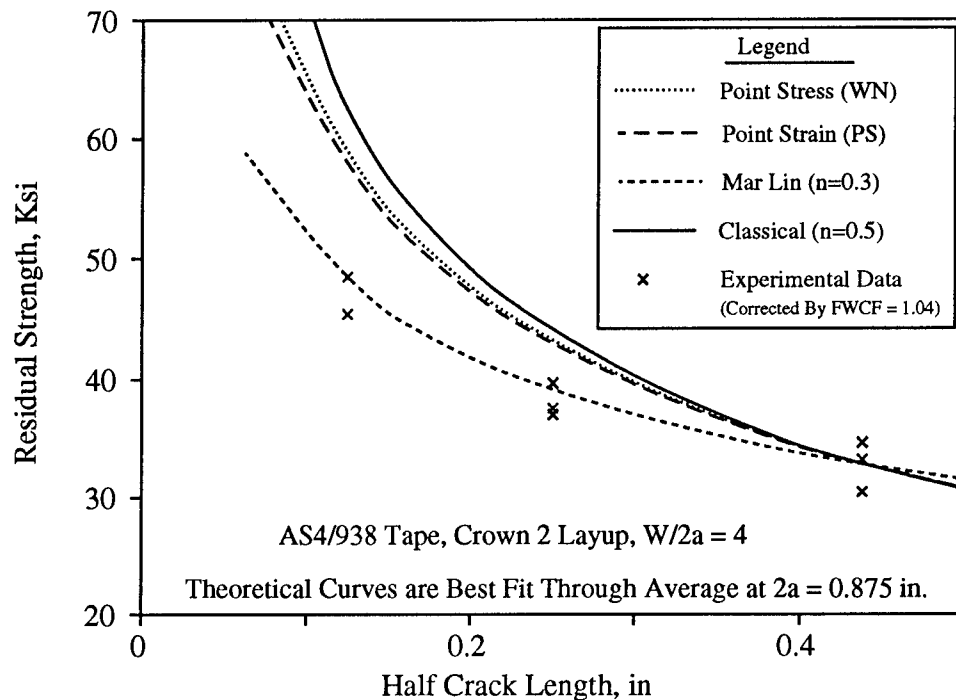
**Figure 27: Comparison of AS4/938 Tape (10 Ply Laminate)  
Experimental Results With Different Failure Criteria**

One unique feature of the Crown2 layup was that it had the largest number of plies of all laminates tested. A previous study with tape laminates (Ref. 9) showed that experimental values for the classical fracture toughness approached a constant value, independent of "small" crack lengths (i.e., ranging in size from 0.5 in. to 1.25 in.), for thick laminates that contain many plies. Perhaps laminate thickness relates to characteristics of composite materials that tend to change the small crack resistance.

Theoretical work discussed in the subsection entitled "**Review of Failure Criteria**" indicated that levels of inhomogeneity in a composite material microstructure can reduce the crack tip stress intensity (Refs. 28, 29, 30, 31). Conceivably, the inhomogeneous structure created in tape by the prepreg manufacturing processes (i.e., intralaminar regions of higher than average resin and fiber content) would become smeared as the number of plies increased. This is conceivable because fiber and resin rich regions of individual plies would tend to misalign as the number of plies increased in a hand layup process, yielding a more homogeneous inplane density distribution as laminate thickness increased. In the case of automated tow-placed laminates, a numerically controlled machine is more likely to repeat the placement of an inhomogeneous structure. This may explain why tow-placed laminates have higher fracture strengths (and associated fracture parameters) than tape laminates with the same constituents and layup.

Figure 29 shows theoretical comparisons with experimental data for the AS4/938 tow-placed Crown1 laminate. As shown in Figure 27 for AS4/938 tape material having the same laminate layup, the ML theory best represents the tow data in Figure 29. A close evaluation of the two figures indicates that

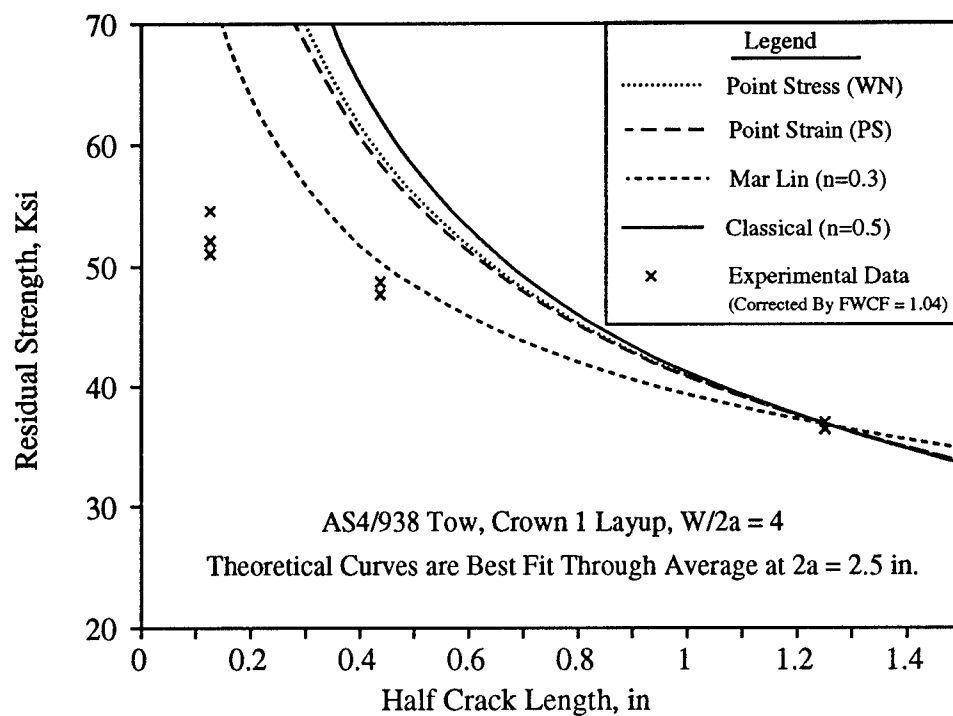
tow test results deviate further from the ML curve than does tape data. In addition to providing further evidence of the inability of the failure criteria to predict small crack effects, tape appears to be more notch sensitive than tow-placed laminates. Notch insensitivity suggests a higher level of inhomogeneity, reducing the stress concentration in the tow-placed laminates. The hypothesis posed in the previous paragraph may explain the manner in which this inhomogeneity is produced.



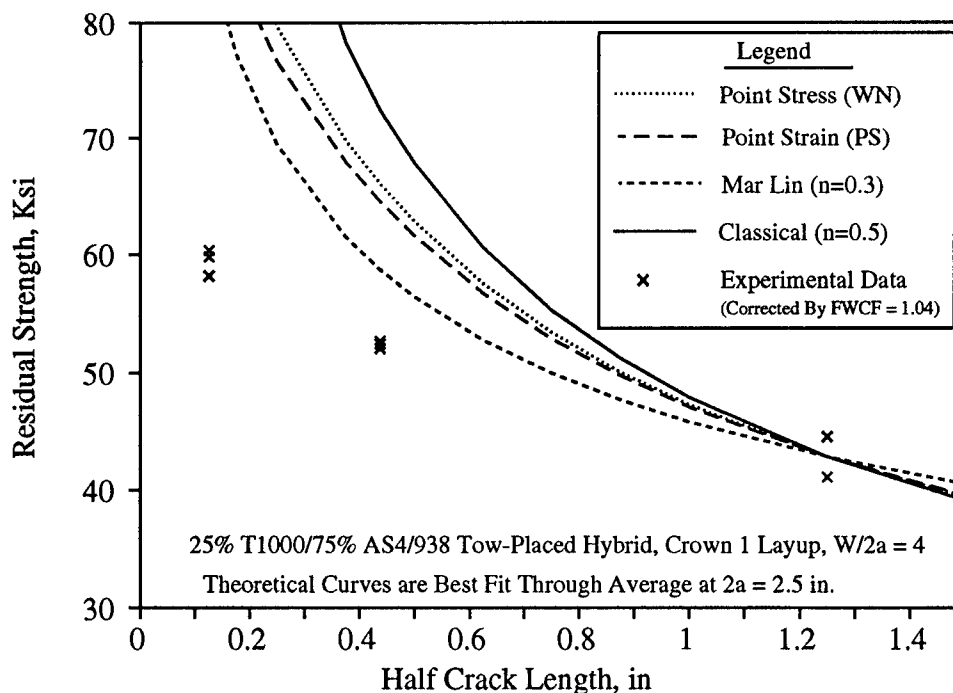
**Figure 28: Comparison of AS4/938 Tape (16 Ply Laminate)  
Experimental Results With Different Failure Criteria**

As used in the current discussions, the idea of inhomogeneous levels of microstructure relate to point-to-point changes in the laminate properties. For example, a level of inhomogeneity affecting tension fracture is perceived as inplane variations in laminate density and moduli that repeat as a function of a characteristic length. The pattern in which such variations repeat from point to point in a laminate is expected to depend on the manufacturing process, panel thickness, and fiber/matrix architecture.

Tow-placed intraply hybrid laminates are the most dramatic example of a material that has point-to-point inplane variations in properties. Figure 30 shows results for Hybrid #5 (consisting of bands of T1000 and AS4) that indicate strong deviations from theory for small crack sizes. There is no indication that the test results for a 2.5 in. crack are large enough to determine the proper singularity. For the range of cracks tested, all hybrids were found to be relatively notch insensitive as compared to tape laminates. These results suggest that this class of materials has significant changes in the stress intensity as a function of material architecture, notch size, and shape. Some form of generalized theory appears needed to help model the behavior exhibited by tow-placed hybrids.



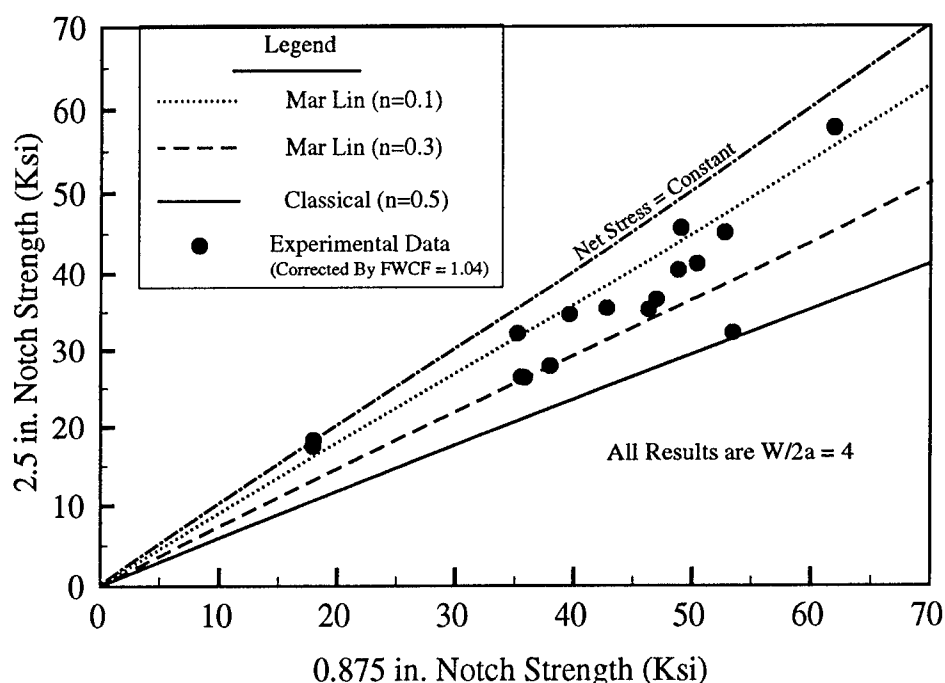
**Figure 29: Comparison of AS4/938 Tow-Placed Laminate Experimental Results With Different Failure Criteria**



**Figure 30: Comparison of AS4/T1000/938 Hybrid Tow-Placed Laminate Experimental Results With Different Failure Criteria**



It is possible to estimate the order of singularity for all theories presented in this section by comparing changes in residual strength with crack size. During the course of discussions, it was suggested that such an exercise is best performed with the largest crack sizes in the data base. In an effort to evaluate the complete data set, the average 0.875 in. notched strength results were plotted versus those for 2.5 in. crack lengths. Each point in Figure 31 represents an average data pair for a specific material and layup (including angle and cross ply laminates). The majority of points fall between theoretical curves for  $n = 0.1$  and  $0.3$ . Linear regression analysis of all the data in Figure 31 yields a slope of  $0.78$ , a small Y-intercept ( $1.77$ ), and  $R^2 = 0.82$ . The corresponding singularity for this regression slope is  $n = 0.24$ .

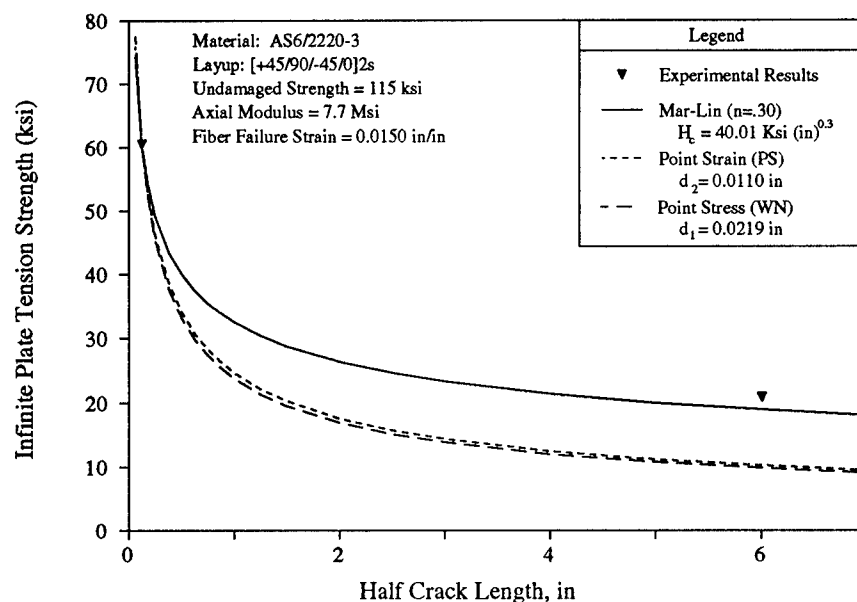


**Figure 31: Evaluation of the Order of Singularity for All Laminates Having Both 0.875 in. and 2.5 in. Notched Strength Test Data**

The single point in Figure 31 falling close to the  $n = 0.5$  theoretical line corresponds to IM7/8551-7, which has the highest resistance to splitting. This, in combination with the  $n = 0.3$  of the IM6/937A material, indicates that the singularity is not related to the idealized crack at the fiber/matrix interface. Theoretically, these two materials would have nearly identical singularities since the respective shear moduli and Poisson's ratios are very similar. The significant difference between these two materials, however, is the resin toughness, implying that the level of splitting may relate to the effective singularity.

Points in Figure 31 near the  $n = 0.1$  line correspond to crossply and angleply tape laminates, and tow-placed hybrids that may still be under the influence of "small notch" effects. Crossply tape laminates and tow-placed hybrids undergo extensive matrix damage at the crack tip, including splitting. This is further evidence that splitting has the effect of reducing the stress intensity and effective singularity.

Limited evidence suggests a reduced singularity provides improved predictions of large-crack strengths. A previous NASA/Boeing fuselage contract (NAS1-17740, Ref. 4) tested small ( $2a = 0.25$  in.,  $W = 1.5$  in) and large ( $2a = 12$  in.,  $W = 30$  in.) flat unstiffened center-crack specimens of two laminates. The panels were fabricated from AS6<sup>14</sup>/2220-3<sup>15</sup> tape material (2220-3 resin is somewhat tougher than 938 but significantly more brittle than 8551-7). Figure 32 compares the data from the 16-ply quasi-isotropic panel with the PS, WN point stress and ML ( $n = 0.3$ ) methods, all calibrated with the 0.25 in. data. The ML method slightly underpredicts the 12 in. data, with the other methods underpredicting by approximately 50%. Similar results were seen for the second laminate. Although this data is of differing  $W/2a$  values and without intermediate crack sizes, comparable results are expected for constant  $W/2a$  and other crack sizes.



**Figure 32: A Comparison of AS6/2220-3 Notched Strength Data and Three Fracture Models**

In the past NASA contract (Ref. 4), the PS method was applied incorrectly to the data in Figure 32. The characteristic dimension associated with the WN point-stress method ( $d_1$ ) obtained from the 0.25 in. data was used, and a good prediction of the 12 in. crack result was obtained merely by coincidence.

### RECOMMENDED TEST PROCEDURES FOR FUSELAGE MATERIAL SCREENING

As previously discussed, the 0.25 in. open hole tension tests currently used for material screening does not provide meaningful information for predicting notched laminate strength for cracks on the order of several inches, nor is it likely to for larger cracks in configured structure. New procedures are therefore desired to screen materials for fuselage tension damage tolerance.

<sup>14</sup> AS6 is a graphite fiber system produced by Hercules, Inc.

<sup>15</sup> 2220-3 is a resin system produced by Hercules, Inc.

Selection of a specimen configuration is influenced by several factors.

- o The notch type (e.g., penetration versus machined crack) has a significant influence on the behavior.
- o Laminate thickness and layup also have significant influence on tension fracture performance.
- o Specimen strength depends on finite width effects that are not accurately modeled by classical methods; therefore, it is desirable to use  $W/2a \geq 4$ .
- o Grouping specimens of differing  $W/2a$  values can artificially skew the strength versus crack-length curve.
- o Specimens with larger  $W/2a$  values require additional material, and therefore cost, for a given crack length than do those with smaller  $W/2a$  values.
- o Specimens wider than standard hydraulic grips (i.e., approximately 4 in.) require load introduction fixtures, resulting in increased test complexity and costs.

It is therefore recommended that all specimens be of center-crack configuration with  $W/2a = 4$ . This configuration can be used to test the notch type of interest and minimizes possible skewing of the notch sensitivity curve. In addition, the width of specimens having  $W/2a = 4$  should reduce errors associated with classical finite width correction, while minimizing material and test costs for a given crack length. Fracture tests should be performed with specimen thickness and layups characteristic of the particular application.

A compromise for initial screening is to test at least 3 crack sizes ranging from 0.25 in. to approximately 1.0 in., all with  $W/2a = 4$ . The largest specimens are those having widths equal to the maximum allowed in hydraulic grips, typically in the 4.0 in. range. From this data, comparisons can be made with analysis to judge "small notch" effects and the apparent singularity. A second level of screening, using 10 in. wide coupons with 2.5 in. cracks, can be used to confirm trends for the most promising candidates from initial screening.

As part of the screening process, failure mechanisms should be studied to help evaluate material and laminate characteristics affecting fracture. For example, matrix splitting is one phenomenon that can effectively reduce the singularity and may be thought of as a material attribute for composite fuselage damage tolerance. Experimental measurements (e.g., crack opening displacements, pre-failure radiography) should be used to enhance visual observations.

The recommended test procedure listed in this section results in the most accurate extrapolations to large-crack tension fracture performance. Several materials tested in the current work were relatively notch insensitive, resulting in 2.5 in. crack data that may not indicate the effective singularity. An assumed singularity of 0.5 and the fracture toughness associated with the largest crack in the database will, at worst, yield conservative predictions of large-crack performance.

## CONCLUSIONS

Collaborative efforts between Boeing and NASA have begun to address the issues associated with transport fuselage pressure damage tolerance. With all the composite material and laminate variables that can affect tension fracture performance, screening test and analysis procedures are needed to facilitate evaluations for fuselage applications. Tests involving 430 tension fracture specimens were performed in the current work to support ATCAS fuselage design and to develop a procedure for screening tension fracture performance. Requirements for screening tests included that the procedure

be economically feasible and recognize the effects of specimen geometry, analysis assumptions, and failure mechanisms.

Fracture tests were performed with ten candidate material types. These studies evaluated the effects of layup, notch type, specimen width, and notch size. As in past studies, large variations in notched strength were found due to layup. The strength for specimens with cracks and open holes of the same size (up to 0.875 in.) were within approximately 10% of each other, with no clear trend regarding the severity of one or the other. For a given layup, a ranking of materials based on the fracture strength of specimens with 0.25 in. cracks had no relationship with the performance observed for coupons with 2.5 in. cracks. This indicated the limits of current material screening tests involving a 0.25 in. open hole.

Material variables evaluated for tension fracture performance included fiber type, matrix toughness, and intraply hybridization of towpreg consisting of different fiber types. In addition, both hand layup tape and automated tow placement were considered as manufacturing variables for fabricating laminates. The IM6-fiber laminates provided a 5 to 25% increase in fracture strength over those consisting of AS4, compared to a 20 to 25% increase in fiber and unidirectional ply strength. Matrix toughness was found to have a major effect on increasing the notch sensitivity of the material. The toughened IM7/8551-7 material was 35% higher than IM6/937A at small cracks but 7% lower at 2.5 in. cracks. This was hypothesized to be due to the toughened materials resistance to matrix splitting. Matrix splits are believed to relieve the notched stress concentration and enhance tension fracture strength, particularly for large notches.

Tow-placed laminates were found to have 10 to 25% higher fracture strengths than tape consisting of the same volume of fiber and matrix constituents, and significantly reduced sensitivity to crack size. Hybrids consisting of AS4 and either S2-glass or T1000 graphite fibers had reduced notch sensitivity, similar to AS4 tow-placed laminates. Strengths of hybrids and non-hybrids segregate at large notch sizes, with an up to 17% increase in the former. This may relate to interactions between percent hybridizing fiber, hybrid repeat unit width, and notch size. Hybrids exhibited large amounts of matrix splitting and delamination prior to failure. The AS4/S2-glass hybrids also had significant post-failure load carrying capability.

The tension fracture performance of specimens with machined cracks and sharp penetrations created by an impact event were compared. The latter is more characteristic of the real damage threat. The instrumented impact response during the penetration event was found to depend on material and laminate variables. Post-impact damage levels and tension fracture performance were also found related to the same variables. In the case of the thickest laminates tested, the tension fracture strengths of specimens with impact penetrations were up to 20% higher than those for coupons with machined cracks. For the minimum thickness range of concern for fuselage structures (approximately 0.1 in.), the specimens with machined cracks had fracture strengths similar to those with impact penetrations. One notable exception was in the case of IM7/8551-7, which had post-impact tension fracture strengths that were 20% lower than those for specimens with machined cracks. Evidence suggests that impact penetration of IM7/8551-7 laminates may result in effective crack extension via fiber breakage.

Experimental data was used to evaluate finite width correction analysis and composite failure criteria. Comparison of finite width corrected data for specimens with the same crack lengths, but differing  $W/2a$ , indicated significant deviation. The finite width corrected strengths for specimens with  $W/2a = 2$  were up to 30% less than those for  $W/2a = 4$ . In order to minimize this finite width effect, all failure criteria were evaluated using the variable crack length data for specimens having a constant  $W/2a = 4$ .

Failure criteria that were evaluated for accuracy in predicting the effect of notch size included three theories with the classical singularity of 0.5: LEFM, point stress, and point strain. Analysis using a singularity of 0.3 was also compared to experimental results. For most materials and layups in the database, each failure criteria was found to have fracture parameters that increased with increasing crack length over a range of small crack sizes (i.e., up to 1.0 in. long). With the exception of comparisons with LEFM, these findings differ from most past studies. Differences with past evaluations were discussed in the text including the method of determining an undamaged laminate strength and the correction of fracture data with variable  $W/2a$ .

Despite the noted inaccuracy, modified analysis methods that include "characteristic dimensions" are better at predicting small crack experimental trends than LEFM. This suggests the classical crack stress intensity is inaccurate for composites and that the actual distribution has characteristics that have an effect similar to the point stress and point strain formulations (i.e., stress intensity that is generally lower and a function of notch size). A hypothesis was posed based on evidence from analysis and experiments that suggest small crack stress distribution is strongly influenced by material inhomogeneity. Reductions in stress concentration occur for cracks having a length within several orders of magnitude of the material inhomogeneity scale. For a given crack size, therefore, notched strength increases with increasing scale of inhomogeneity. Possible scales of inhomogeneity include fiber diameter, tow width, and hybrid repeat unit width.

Each fracture theory converges to a curve dominated by the order of singularity at large crack sizes. Larger crack data (i.e., up to 2.5 in. long) for several materials and laminate layups tended to converge with failure criteria having a singularity of 0.3. One notable exception was the toughened material, IM7/8551-7, that tended to converge to the classical curve for singularity of 0.5. This and other evidence suggested that the effective singularity was dependent on matrix splitting. The ability to split and relieve the notch stress concentration relates to characteristics of the material and laminate layup.

### FUTURE WORK

Several major efforts in the tension-fracture arena are targeted for continued work by ATCAS during 1991 and 1992. The major thrust in testing will be the verification of the crown panel design. These tests are outlined in Table 2. Testing of coupons with sizes on the order of specimens discussed in this paper will also continue, collecting data for additional laminates and addressing such issues as the relative strengths of holes and cracks at larger (i.e., 2.5 in.) sizes, increased strain rates, finite width effects, hybridization, and the role of material inhomogeneity. Work will be conducted with other contractors to understand the increased performance of the tow-placed material form, to enable control and maintenance of these improvements.

Curvature	Stiffening	Loading	Approximate Crack Size (in.)	Number of Specimens
flat	none	uniaxial	12	3
flat	none	biaxial	2.5	8
flat	tear straps	uniaxial	8	3
flat	hat stringers	uniaxial	14	2
curved	hoop tear straps	biaxial	20	1
curved	hat stringers, J frames	biaxial	25	3

**Table 2: Crown Verification Testing**

Analytically, efforts will focus on the further evaluation of predictive models for larger crack sizes, structural configurations, and curvature effects. In addition, work is planned in the development of analytical techniques for addressing the dynamic aspects of the pressure-release problem associated with an actual penetration of a transport fuselage.

Several suggestions for additional work, outside the scope of ATCAS, can be made based on findings in the current study. First, improved analysis methods are needed for predicting changes in small notch stress distribution as a function of notch geometry and material inhomogeneity. Experiments should be performed to separate the effects of material microstructure and progressive damage accumulation on local stress concentrations. The relationship between layup, material type, progressive damage accumulation, and the effective singularity for large notch sizes also needs to be studied. Some form of progressive damage models is needed for predicting the effects of panel width and matrix damage on stress concentration. Finally, experimental databases that include large crack sizes and combined loads for other composite materials are needed to best understand features that affect tension damage tolerance. The limited results found to date suggest a wide range of composite material performance, with the most attractive candidates having tension fracture properties better than traditional metal materials used in transport fuselage.

### ACKNOWLEDGEMENTS

The authors would like to express their appreciation to Brian Coxon (Intec, Inc.), Dodd Grande (Boeing Materials Technology), and Fu-Kuo Chang (Stanford University) for the efforts in specimen testing and evaluation of failure mechanisms.

### REFERENCES

1. Ilcewicz, L. B., Smith, P. J., Walker, T. H., and Johnson, R. W., "Advanced Technology Commercial Fuselage Structure," First NASA Advanced Composites Technology Conference, NASA CP-3104, Part 1, pp. 127-155, 1991.
2. Swanson, G. D., Ilcewicz, L. B., Walker, T. H., Graesser, D., Tuttle, M., and Zabinsky, Z., "Local Design Optimization for Transport Fuselage Crown Panels," in Proceedings of Ninth DoD/NASA/FAA Conference on Fibrous Composites in Structural Design, NASA CP-19 . . . (Paper . . . of this compilation.)
3. Awerbuch, J., and Madhukar, M. S., "Notched Strength of Composite Laminates: Predictions and Experiments -- A Review," J. of Reinforced Plastics and Composites, Vol. 4, pp. 1-159, 1985.
4. Smith, P. J., Thomson, L. W., and Wilson, R. D., "Development of Pressure Containment and Damage Tolerance Technology for Composite Fuselage Structures in Large Transport Aircraft," NASA CR-3996, 1986.
5. Kim, J. K., and Mai, Y. W., "High Strength, High Fracture Toughness Fibre Composites with Interface Control - A Review," Composites Science and Technology, Vol. 41, pp. 333-378, 1991.
6. Kennedy, J. M., "Damage Tolerance of Woven Graphite/Epoxy Buffer Strip Panels," NASA TM 102702, 1990.
7. Poe, C. C., Jr., and Kennedy, J. M., "An Assessment of Buffer Strips for Improving Damage Tolerance of Composite Laminates," Journal of Composite Materials Supplement, Vol. 14, pp. 57-70, 1980.

8. Harris, C. E., and Morris, D. H., "Fractographic Investigation of the Influence of Stacking Sequence on the Strength of Notched Laminated Composites," in *Fractography of Modern Engineering Materials: Composites and Metals*, ASTM STP 948, pp. 131-153, 1987.
9. Harris, C. E., and Morris, D. H., "Effect of Laminate Thickness and Specimen Configuration on the Fracture of Laminated Composites," *Composite Materials Testing and Design (Seventh Conference)*, ASTM STP 893, pp. 177-195, 1986.
10. Lagace, P. A., "Notch Sensitivity and Stacking Sequence of Laminated Composites," *Composite Materials Testing and Design (Seventh Conference)*, ASTM STP 893, pp. 161-176, 1986.
11. Daniel, I. M., Rowlands, R. E., and Whiteside, J. B., "Effects of Material and Stacking Sequence on Behavior of Composite Plates with Holes," *Experimental Mechanics*, Vol. 14, pp. 1-9, 1974.
12. Walter, R. W., Johnson, R. W., June, R. R., and McCarty, J. E., "Designing for Integrity in Long-Life Composite Aircraft Structures," *Fatigue of Filamentary Composite Materials*, ASTM STP 636, pp. 228-247, 1977.
13. Aronsson, C. G., "Stacking Sequence Effects on Fracture of Notched Carbon Fibre/Epoxy Composites," *Composites Science and Technology*, Vol. 24, pp. 179-198, 1985.
14. Poe, C. C., Jr., "Fracture Toughness of Fibrous Composite Materials," *NASA Technical Paper 2370*, 1984.
15. Ilcewicz, L. B., Dost, E. F., McCool, J. W., and Grande, D. H., "Matrix Cracking in Composite Laminates With Resin Rich Interlaminar Layers," in *Proc. of 3rd Symposium for Composite Materials: Fatigue and Fracture*, ASTM STP 1110, 1991.
16. Wang, A. S. D., Reddy, E. S., and Zhong, Y., "Three-Dimensional Simulation of Crack Growth in Notched Laminates," *J. of Reinforced Plastics and Composites*, Vol. 9, pp. 134-150, 1990.
17. Box, G. E. P., Hunter, W. G., and Hunter, J. S., Statistics for Experimenters, John Wiley & Sons, Inc, 1978.
18. Konish, H. J., Jr., "Mode I Stress Intensity Factors for Symmetrically-Cracked Orthotropic Strips," in *Fracture Mechanics of Composites*, ASTM STP 593, American Society for Testing and Materials, pp. 99-116, 1975.
19. Tan, S. C., "Finite-Width Correction Factors for Anisotropic Plate Containing a Central Opening," *J. of Composite Materials*, Vol. 22, pp. 1080-1097, 1988.
20. Whitney, J. M. and Nuismer, R. J., "Stress Fracture Criteria for Laminated Composites Containing Stress Concentrations," *J. Composite Materials*, Vol. 8, pp. 253-265, 1974.
21. Nuismer, R. J. and Whitney, J. M., "Uniaxial Failure of Composite Laminates Containing Stress Concentrations," in *Fracture Mechanics of Composites*, ASTM STP 593, American Society of Testing and Materials, pp. 117-142 (1975).
22. Pipes, R. B., Wetherhold, R. C., and Gillespie, J. W., Jr., "Notched Strength of Composite Materials," *J. Composite Materials*, Vol. 12, pp. 148-160, 1979.
23. Pipes, R. B., Gillespie, J. W., Jr. and Wetherhold, R. C. "Superposition of the Notched Strength of Composite Laminates," *Polymer Engineering and Science*, Vol. 19, No. 16, pp. 1151-1155, 1979.

24. Tan, S. C., "Notched Strength Prediction and Design of Laminated Composites Under In-Plane Loadings," *J. of Composite Materials*, Vol. 21, pp. 750-780, 1987.
25. Poe, C. C., Jr. and Sova, J. A., "Fracture Toughness of Boron/Aluminum Laminates with Various Proportions of  $0^\circ$  and  $\pm 45^\circ$  Plies," NASA Technical Paper 1707, 1980.
26. Poe, C. C., Jr., "A Unifying Strain Criterion for Fracture of Fibrous Composite Laminates," *Engineering Fracture Mechanics*, Vol. 17, No. 2, pp. 153-171, 1983.
27. Waddoups, M. E., Eisenmann, J. R., and Kaminski, B. E., "Macroscopic Fracture Mechanics of Advanced Composite Materials," *J. Composite Materials*, Vol. 5, pp. 446-454, 1971.
28. Chiang, C. R., "Inhomogeneity Effect on the Stress Intensity Factor," *J. Composite Materials*, Vol. 21, pp. 610-618, 1987.
29. Ilcewicz, L. B., Shaar, C., Kennedy, T. C., and Wilson, J. B., "Experimental Evidence of a Relationship Between Ultrasonic Wave Dispersion and Fracture," *Engineering Fracture Mechanics*, Vol. 26, pp. 895-908, 1986.
30. Nakamura, S. and Lakes, R. S., "Finite Element Analysis of Stress Concentration Around a Blunt Crack in a Cosserat Elastic Solid," *Computer Methods in Applied Mechanics and Engineering*, Vol. 66, pp. 257-266, 1988.
31. Eringen, A. C., Speziale, C. G., and Kim, B. S., "Crack-Tip Problem in Nonlocal Elasticity," *J. Mech. Phys. Solids*, Vol. 25, pp. 339-355, 1977.
32. Mar, J. W. and Lin, K. Y., "Fracture Mechanics Correlation for Tensile Failure of Filamentary Composites with Holes," *Journal of Aircraft*, Vol. 14, No. 7, pp. 703-704, 1977.
33. Lin, K. Y. and Mar, J. W., "Finite Element Analysis of Stress Intensity Factors for Cracks at a Bi-Material Interface," *Int. J. of Fracture*, Vol. 12, No. 2, pp. 521-531, 1987.
34. Tsai, H. C., and Arocho, A. M., "A New Approximate Fracture Mechanics Analysis Methodology for Composites with a Crack or Hole," Report NADC-88118-60, 1990.
35. Aronsson, C. G., and Backlund, J., "Tensile Fracture of Laminates with Cracks," *J. Composite Materials*, Vol. 20, pp. 287-307, 1986.
36. Aronsson, C. G., and Backlund, J., "Damage Mechanics Analysis of Matrix Effects in Notched Laminates," in *Composite Materials: Fatigue and Fracture*, ASTM STP 907, pp. 134-157, 1986.
37. Chang, F. K., and Chang, K. Y., "A Progressive Damage Model for Laminated Composites Containing Stress Concentrations," *J. Composite Materials*, Vol. 21, pp. 834-855, 1987.
38. Chamis, C. C., "Computational Simulation of Progressive Fracture in Fiber Composites," NASA TM-87341, 1986.
39. Barenblatt, G. I., "The Mathematical Theory of Equilibrium Cracks in Brittle Fracture," Advances in Applied Mechanics (Edited by Dryden, H.L. and von Karman, T.), Vol. 7, pp. 55-129, 1962.
40. Swanson, S. R., and Christoforou, A. P., "Response of Quasi-Isotropic Carbon/Epoxy Laminates to Biaxial Stress," *J. Composite Materials*, Vol. 20, pp. 457-471, 1986.
41. Chamis, C. C., and Sinclair, J. H., "Micromechanics of Intraply Hybrid Composites: Elastic and Thermal Properties," NASA-TM-79253, 1979.



**THIS PAGE INTENTIONALLY BLANK**

# INDENTABILITY OF CONVENTIONAL AND NEGATIVE POISSON'S RATIO FOAMS

R. S. Lakes

K. Elms

Department of Biomedical Engineering  
Department of Mechanical Engineering  
Center for Laser Science and Engineering  
University of Iowa  
Iowa City, IA

## Abstract

The indentation resistance of foams, both of conventional structure and of re-entrant structure giving rise to negative Poisson's ratio, is studied using holographic interferometry. In holographic indentation tests, re-entrant foams had higher yield strengths  $\sigma_y$  and lower stiffness  $E$  than conventional foams of the same original relative density. Calculated energy absorption for dynamic impact is considerably higher for re-entrant foam than conventional foam.

## Methods

Specimens of copper foam were cut from a larger block using a high speed band saw. The highest speed setting was used to avoid any plastic deformation during the cutting process. The specimens are transformed to the re-entrant structure by triaxial compression. A vise was used to apply the compression, and two 1/2 inch thick pieces of Plexiglass were placed on the faces of the vise in order to provide a smooth surface. The foam specimen was then placed in the vise and subjected to small compressions of approximately 1 mm each, in each of the three orthogonal directions. This compression sequence was repeated, on average 15-20 times, until the desired volumetric compression ratio (VCR) was reached.

The set-up of holographic equipment was designed to simplify interferometric fringe interpretation. In this set-up the light from the laser passes through a beam splitter and spatial filter which changes it from a concentrated beam to diverging light. The light then passes through two lenses to become collimated. A large glass plate acts as a beam splitter, and a portion of the light is reflected onto the object, becoming the object light. The remainder of the light passes through the plate and becomes the reference light. The object light illuminates the object and is reflected back through the beam splitter plate and onto the film. The reference light is reflected off another glass plate, which acts as a mirror, and onto the film. The observer views the reconstructed image by gazing from behind the film in the direction of the object.

The actual object consists of a foam sample mounted on a platform with cyanoacrylate glue. The indenting force is applied to the foam via a pivot device. The arm of the pivot has a platform at one end to hold the weights, and an indenter at the midpoint of the arm. The tip of the indenter contacts the surface of the foam sample to cause the indenting force. The Boussinesq solution was used for analysis. Because only the sides of the foam sample can be seen in this configuration, a tilted mirror was added so that the top surface could be viewed. The top surface is the plane of applied indenting force, and interference fringes of greatest importance will be visible in the mirror. Because the object light is perpendicular to the object, the unit vector of

illumination is simplified, and the fringe interpretation relation reduces to  $u_z = \frac{n\lambda}{2}$  in which  $u_z$  is the out-of-plane displacement. The wavelength  $\lambda$  for red helium neon laser light is 632.8 nm.

These tests used double exposure holographic interferometry, with one exposure in a stressed state, and the other in an unstressed state. The film, Agfa 8E75 or 10E75, was

sandwiched between two glass plates and loaded into the plate holder. Because the film has a curvature, it must be allowed to settle between the plates for approximately one minute.

The first exposure is made with weights on the platform of the pivot, so that the material is in the stressed state. After the exposure the weights were removed, and the second exposure was taken with the material in the unstressed state. Exposure times were 20 seconds each, with 20 seconds between exposures for removal of the weights. The film was then removed and developed with Kodak D19 Developer, followed by Kodak indicator stop bath. Extinction ratio of the hologram was measured, and the hologram was bleached with a potassium dichromate bleaching mixture. After drying, holograms were viewed.

If permanent yield has occurred in the material, it will be indicated by the presence of one or more interference fringes, encircling the region of yield or damage. Also studied is the size of the yielded region, and any patterns in its behavior. The indentation threshold tests were designed to determine plastic yield via holographic interferometry in copper foam samples subjected to an indenting load.

Tests were performed on three groups of copper foam samples. Both conventional and re-entrant samples were tested for 20 pore/inch foam with original relative density of 0.04; and 60 pore/inch foam, with original relative density of 0.08-0.09. A sample of re-entrant 40 pore/inch was tested; original relative density was 0.05. In addition, one sample of conventional Rohacell polymethylacrylamide foam was tested; relative density was 0.092.

The average applied stress was determined from the classical elasticity solution for indentation by a circular flat rigid punch.

## Results

Figure 1 plots outer yield radius against stress for samples of 20 pore/inch conventional and re-entrant foam, with original relative density of 0.04. The outer yield radius is the distance between the edge of the indenter and the circular interference fringe (there was only one fringe observed in these tests); the stress is the average bearing stress along the z axis, or direction of applied load.

The results indicate two important findings. First, the re-entrant sample yields at a higher stress. Second, the area of damage, or yield radius, is smaller in the re-entrant foam than in the conventional foam for equal applied stresses, even though the re-entrant foam material is more compliant. For both materials the graphs show that there appears to be an upper limit to the size of the damage area, which follows an initial peak value. The yield stress for the conventional foam was 0.23 MPa at a strain of 0.0021. The peak yield radius was 5.0 mm with a limiting value of approximately 3.9 mm. The re-entrant sample, with volumetric compression ratio (VCR) of 2.2, had a yield stress of 0.36 MPa at a strain of 0.0067. This sample had a peak yield radius of 2.8 mm with a limiting value of roughly 2.2 mm.

For these tests, the indenter remained in the same location on the surface of the material throughout the testing procedure. The curve for the re-entrant material in Fig. 1 shows the effects of strain hardening; yielding followed by no yield at higher stresses. An additional series of tests was performed on the re-entrant sample to investigate yield without the effects of strain hardening. Each time a hologram was made, the indenter was in a new location on the material's surface. The yield radii for the tests on the new locations are equal or nearly equal to the initial peak radius, and again there is a limiting value to the yield radius.

Two samples of 60 pore/inch copper foam with initial relative density of 0.08-0.09 were tested, one re-entrant and one conventional. Figure 2 plots the outer yield radius against applied stress for both materials. Yielding of the conventional sample occurred at a stress of 0.51 MPa and strain of 0.0030. The limiting yield radius was roughly 1.3 mm, with no initial peak radius. Holograms made at 0.98 and 1.03 MPa showed two circular yield fringes; the radius of both inner fringes is 0.9 mm. This sample also shows the effects of strain hardening, as indicated by the fluctuation in yield radius.

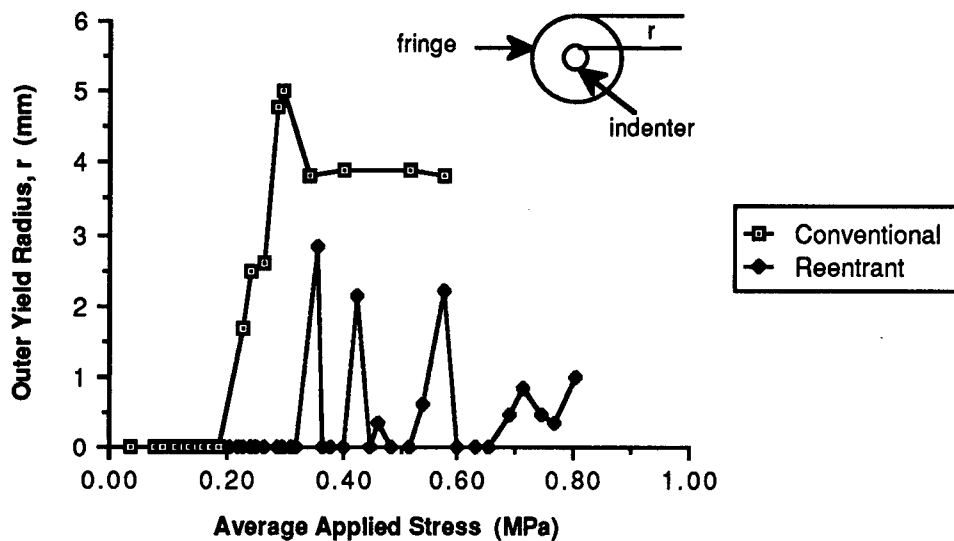


Figure 1. Outer yield radius vs. applied stress along the z axis for both conventional and reentrant (permanent volumetric compression ratio = 2.2) 20 pore/inch copper foams with initial relative density of 0.04. Stress repetitively applied to same location.

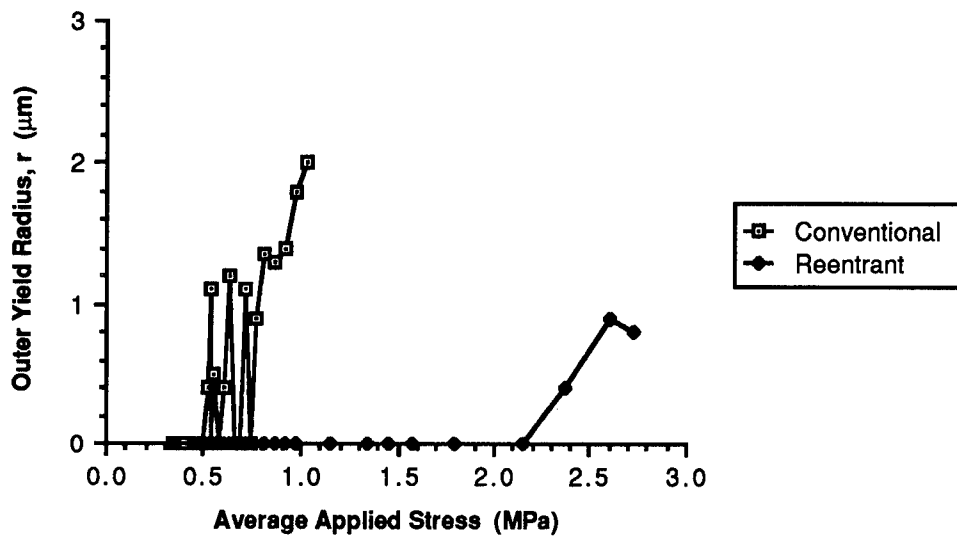


Figure 2. Outer yield radius vs. applied stress along the z axis for both conventional and reentrant (permanent volumetric compression ratio = 2.3) 60 pore/inch copper foams with initial relative density of 0.09. Stress repetitively applied to same location.

The measurement of outer yield radius is not necessarily a true measure of actual yield. It is possible for the material to yield directly under the indenter by local crushing of the foam cells, and without lateral deformation or axial motion of material outside the region covered by the indenter. Therefore, actual yield may occur in the material without causing the formation of an interference fringe on the surface of the material. This behavior can be detected and

measured from fringes that appear on the arm of the pivot device that is used to apply the indenting loads.

Conventional foam with an initial relative density of 0.09 yielded at a stress of 0.51 MPa and at a strain of 0.0030. MTS compression tests on the same type of material showed a yield stress of 0.56 MPa at a strain of 0.007, as determined by the 0.2% offset method. Holographic bending tests on similar materials determined the yield stress to be 0.42 MPa at a strain of 0.00047 [30]. The yield stress predicted by a structural model is 0.47 MPa; experimentally determined values for all methods are within the allowable range of  $0.47 \pm 0.09$  MPa.

Variation in measured values can be attributed to differing sensitivity of measurement techniques. Holography and shadow moire have greater sensitivity than the 0.2% offset method. Micro-yield can be observed holographically with a strain sensitivity of  $10^{-5}$ ; the 0.2% offset method has a strain sensitivity of only  $10^{-3}$ . As a result, yield stresses measured holographically will be lower than by 0.2% offset, as will the yield strains.

The re-entrant sample with initial relative density of 0.08 and permanent volumetric compression ratio of 2.3 had a yield stress of 2.37 MPa at a strain of 0.018. Materials testing (MTS) tests on similar materials indicate yield at approximately 2.9 MPa at a strain of 0.016, determined by 0.2% offset. The yield stress for the outer yield fringe method is less due to the increased sensitivity of the method.

The re-entrant 20 and 40 pore/inch and the conventional 60 pore/inch copper foams had roughly similar final relative densities, 0.082, 0.088, and 0.086 respectively. As a result, a comparison of properties based on cell size can be made. The re-entrant 20 pore/inch sample had a yield stress of 0.33 MPa at a strain of 0.0067, its Young's modulus was 52 MPa, and the limiting outer yield radius was 2.2 mm. The re-entrant 40 pore/inch sample had a yield stress of 0.86 MPa at a strain of 0.015; its Young's modulus was 58 MPa and it had a limiting outer yield radius of 1.4 mm. The conventional sample had a yield stress of 0.51 MPa at a strain of 0.0030, its Young's modulus was 170 MPa, and the limiting outer yield radius was 1.8 mm.

The 40 pore/inch re-entrant sample had the best yield strength and smallest damage region, although its stiffness was about one third the stiffness of the 60 pore/inch conventional foam with the same relative density. For dynamic loads, the compliance of the material can be beneficial. For a one-dimensional elastic buffer subjected to a dynamic impact force from a moving object, the maximum impact energy,  $mv^2/2$  is in terms of core geometry,

$$\frac{mv^2}{2} = \frac{1}{2} bch \left( \frac{\sigma_y^2}{E} \right)_{\text{core}}$$

To maximize the impact energy, a high  $\sigma_y$  and a low  $E$  are desirable. For the 20 and 40 pore/inch re-entrant foams and the 60 pore/inch conventional foam, which all have the same final relative density, the value of the  $\sigma_y^2/E$  term is 0.0021, 0.013, and 0.0015, respectively. Therefore, the 40 pore/inch re-entrant sample provides both increased yield strength in the static case, and higher impact energy in the dynamic case.

**Table 1**

	Pores	Compression		$\sigma_y$	$E$	Energy
Material	per inch	ratio	$\rho/\rho_{\text{solid}}$	(MPa)	(MPa)	$[\propto \sigma_y^2/E]$
copper	20	2.2	0.082	0.33	52	2.1
copper	40	1.8	0.088	0.86	58	13
copper	60	1.0	0.086	0.51	170	1.5
Rohacell	70	1.0	0.092	0.4	180	1.

## Conclusions

1. Foam core sandwich panels can be made more resistant to failure in certain modes if a re-entrant foam is used as the core material. This is based on both the increased yield strength and the negative value of the Poisson's ratio.
2. For materials with the same original relative density, re-entrant foams had a smaller outer yield radius (representing a damaged region) than conventional foams.
3. In holographic indentation tests, re-entrant foams had higher yield strengths  $\sigma_y$  and lower stiffness  $E$  than conventional foams of the same original relative density.
4. Calculated energy absorption for dynamic impact,  $\propto \sigma_y^2/E$ , was considerably higher for re-entrant foam.

**THIS PAGE INTENTIONALLY BLANK**

# **LOCAL DESIGN OPTIMIZATION FOR COMPOSITE TRANSPORT FUSELAGE CROWN PANELS<sup>1</sup>**

**G. D. Swanson, L. B. Ilcewicz, T. H. Walker**

**Boeing Commercial Airplane Group  
Seattle, WA**

**D. Graesser, M. Tuttle, and Z. Zabinsky**

**University of Washington  
Seattle, WA**

## **ABSTRACT**

Composite transport fuselage crown panel design and manufacturing plans were optimized to have projected cost and weight savings of 18% and 45%, respectively. These savings are close to those quoted as overall NASA ACT program goals. Three local optimization tasks were found to influence the cost and weight of fuselage crown panels. This paper summarizes the effect of each task and describes in detail the task associated with a design cost model.

Studies were performed to evaluate the relationship between manufacturing cost and design details. A design tool was developed to aid in these investigations. The development of the design tool included combining cost and performance constraints with a random search optimization algorithm. The resulting software was used in a series of optimization studies that evaluated the sensitivity of design variables, guidelines, criteria, and material selection on cost. The effect of blending adjacent design points in a full scale panel subjected to changing load distributions and local variations was shown to be important. Technical issues and directions for future work were identified.

## **INTRODUCTION**

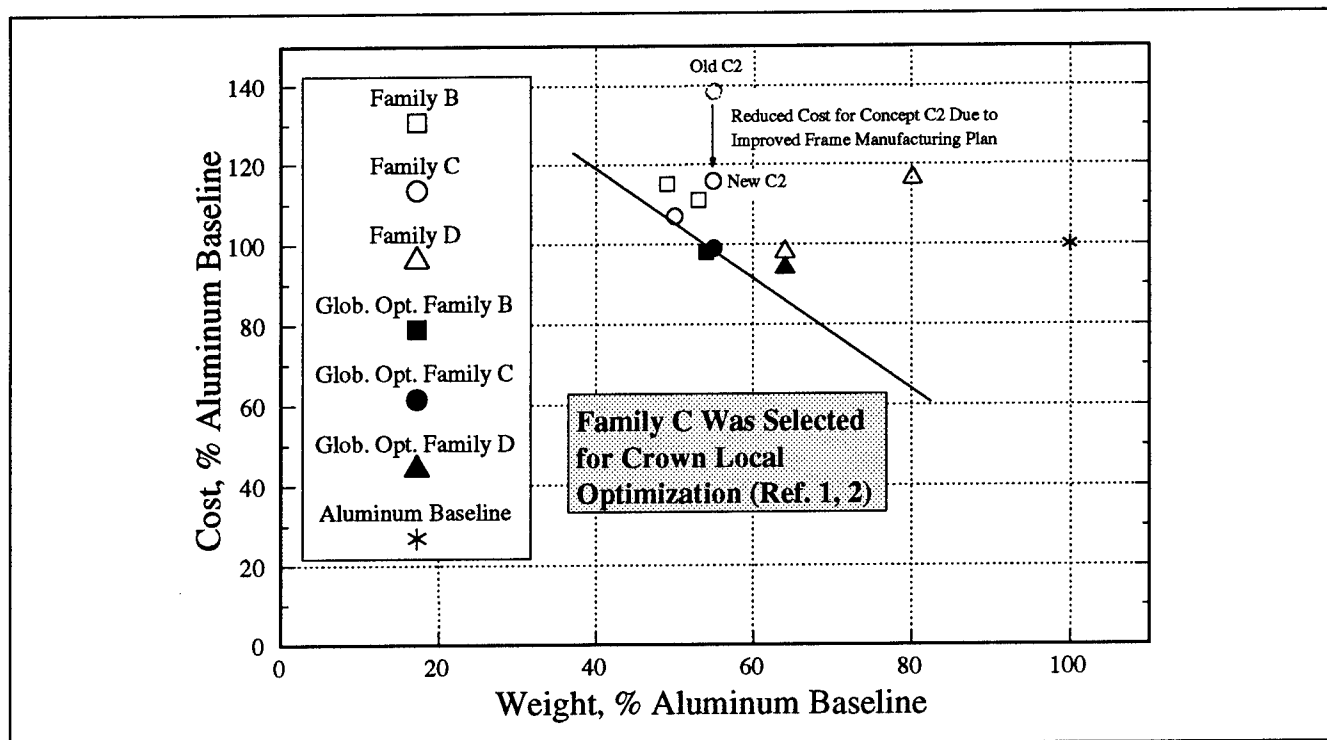
Boeing is studying transport fuselage applications in the NASA/Boeing Advanced Technology Composite Aircraft Structures (ATCAS) program. The ATCAS design build team has adopted a two phase approach for minimizing structural cost and weight that includes global evaluation and local optimization (Refs. 1 and 2). During global evaluation, the cost and weight characteristics of several "design families" are quantified. One of the families is then selected for local optimization based on cost/weight merits and the potential for additional savings. To date, both global and local design phases have been completed for a 15 ft. by 31 ft. crown quadrant in the section directly behind the wing to body intersection of a 20 ft. diameter fuselage.

For the purpose of review, final results from the crown global evaluation studies performed in 1990 are shown in Figure 1. An intricately bonded skin/stringer/frame design (i.e., Family C) was selected by ATCAS for local optimization studies.

---

<sup>1</sup> This work was funded by Contract NAS1-18889, under the direction of J. G. Davis and W. T. Freeman of NASA Langley Research Center.





**Figure 1: Results of the ATCAS Global Crown Panel Evaluation (Refs. 1 and 2)**

The beginning of this paper summarizes how three tasks supporting local optimization of crown panels affected cost and weight. Two of the tasks are detailed in other papers appearing in this proceedings (Refs. 3 and 4). The third task, involving the development and application of a design tool for assessing the effects of design details on cost and weight will be described in this paper. Discussions will include (a) the steps to develop the design tool, (b) the sensitivity studies performed to identify the critical crown panel variables, and (c) the technique used to arrive at a final optimum crown panel design.

### ATCAS FUSELAGE CROWN STUDIES

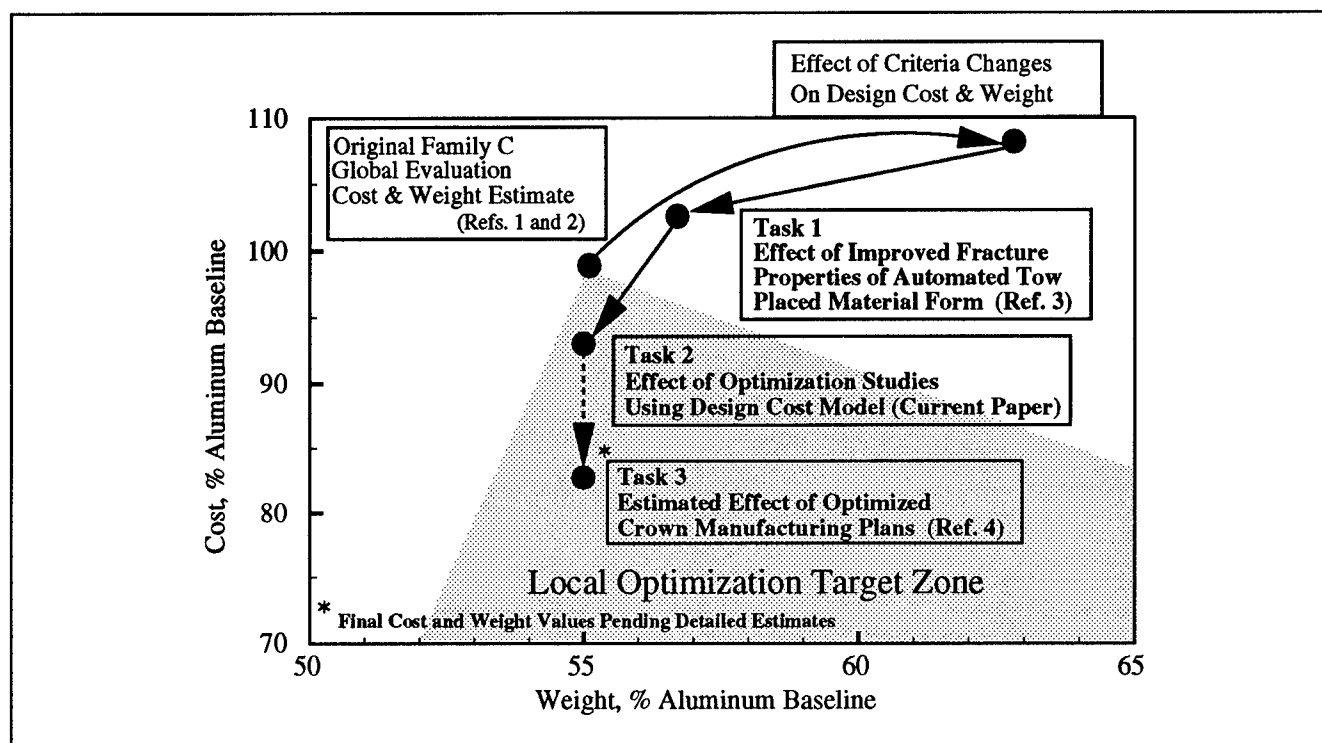
Local optimization in the ATCAS program is essentially a more detailed study of a given design. The three tasks that support local optimization include:

1. perform tests for selected materials to augment the database on critical performance issues
2. develop design/cost analyses to be used to optimize design details for selected processes
3. perform fabrication trials and optimize manufacturing plans to improve process efficiency.

In general, the cost and weight of the design can either increase or decrease depending on results generated in task 1. Task 3 attacks cost centers by exploring possible improvements in manufacturing process steps. Task 2 attempts to minimize the cost and weight by evaluating the effects of design details. This task makes use of results from tasks 1 and 3.

Figure 2 summarizes how each local optimization task affected the manufacturing cost and weight of the ATCAS crown quadrant. The final crown design was found to have a projected cost and weight

savings (relative to 1995 aluminum technology) of 18% and 45%, respectively. These savings are close to those quoted as overall NASA ACT program goals.



**Figure 2: Effects of the Criteria, Material Properties, Design Details, and Manufacturing Processes on ATCAS Crown Panel Local Optimization**

Referring to Figure 2, the cost and weight of the original design sized for global evaluation changed due to modifications in design criteria. Criteria were changed to include larger through penetration damage sizes, minimum stiffness requirements (axial and shear), and a minimum skin buckling load level. Initial global sizing efforts used a relatively small penetration for the failsafe damage condition, and had no minimum skin buckling or stiffness criteria imposed. After applying the additional criteria to obtain an acceptable design, both cost and weight were found to increase. Of the three criteria changes, a larger damage size was found to have the strongest effect on this initial shift in structural cost and weight.

Collection of tension fracture test data for candidate skin materials was the focus of task one for local crown optimization. Laminate fracture test results for the automated tow placed material form were found to be superior to the tape properties assumed during global evaluation. As shown in Figure 2, the improvement resulted in lower cost and weight due to a reduced skin gage. In this case, the generation of a tension fracture database was found to help reduce design cost and weight, essentially counteracting some of the effect of the design criteria for larger damage size. It was not possible to take full advantage of the improvements because other criteria, such as minimum stiffness and skin buckling constraints, were found to become design drivers as the skin gage decreased. The improved fracture properties and their effect on the design are discussed further in another paper included in these proceedings (Ref. 3).

The third task for crown local optimization considered changes in the manufacturing plans to reduce cost. As shown in Figure 2, the total effect of several changes was projected to decrease cost by approximately 10%. Cost centers that were attacked included the fabrication of skin, stringer, and frame elements, and panel cure. Modifications having the strongest impact on cost related to automation, reduced numbers of tools, elimination of processing steps, and deletion of unnecessary design details. Fabrication of curved braided frames and panel cure trials using soft tooling concepts provided supporting data for changes in the manufacturing plans. The changes in crown manufacturing plans and supporting data from process trials are discussed further in another paper included in these proceedings (Ref. 4).

The remainder of this paper will focus on task 2 of crown local optimization, namely the development and application of a design cost model for the Family C, intricately bonded, panel concept. A software design tool was developed to support this effort. The tool combined a random search optimization routine with software modules containing design/cost relationships, structural mechanics sizing tools, and design criteria. Analyses were performed with the tool to determine the cost drivers and design sensitivities. The overall effect of optimizing design details for the crown concept can be seen in Figure 2. As shown in the figure, task 2 efforts decreased the relative cost and weight of the crown panel design such that it is within a target zone identified at the start of local optimization (Ref. 1).

## DESIGN TOOL DEVELOPMENT

A computer program was developed to evaluate the effects of design details on cost and weight. The design tool combines three components: cost and performance constraints and a random search optimization algorithm. The optimization algorithm is capable of minimizing cost and weight objective functions in a global, discontinuous space. The cost constraint algorithm relates the manufacturing process costs to the detailed design variables. This algorithm provides for the ability to optimize for minimum cost. The performance constraint module accounts for load conditions, design criteria, material properties, and design guidelines. The three design tool components complement each other to insure structural integrity while optimizing for both cost and weight (Ref. 5).

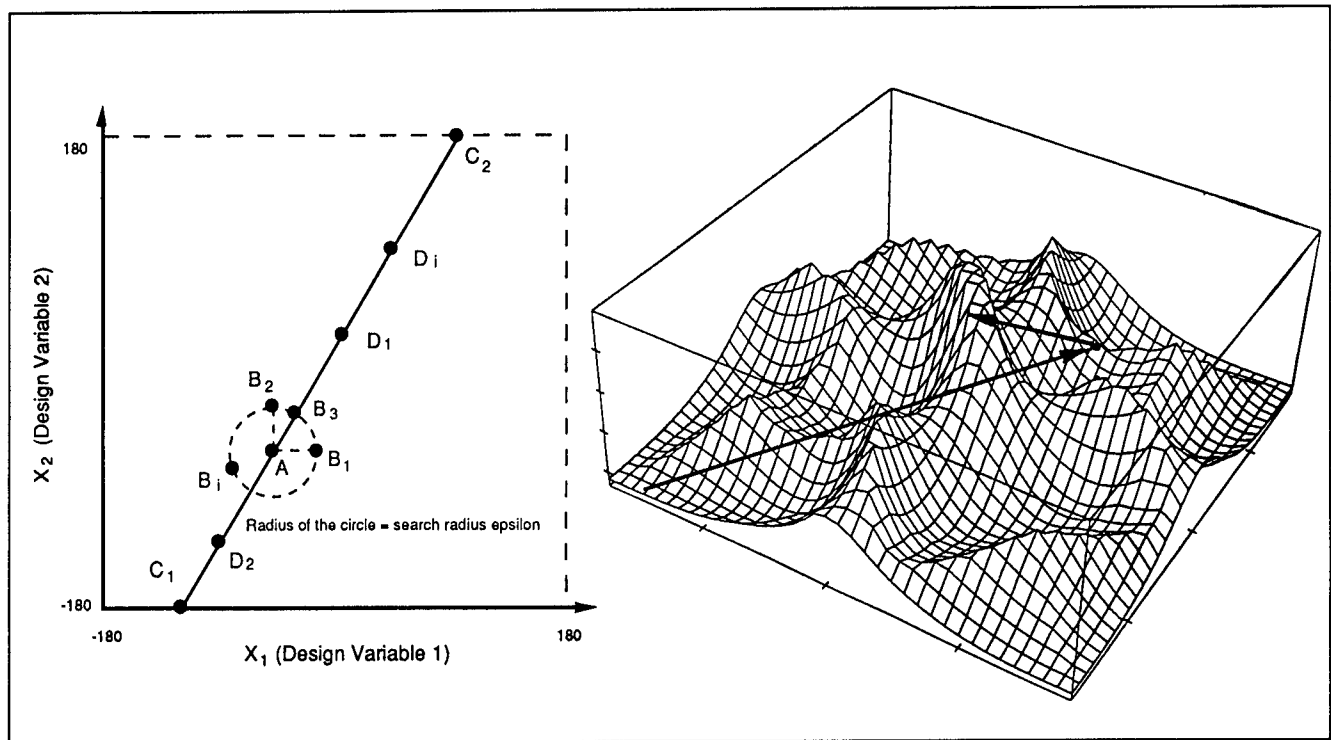
### Optimization Routine

The design tool uses a sequential random search algorithm which globally searches the design space to find the optimum configuration.<sup>2,3</sup> The global nature of this algorithm is different from the more common gradient search methods in that it is not dependent on the initial starting point. Gradient search methods require multiple runs with varying starting points to ensure that an optimum design has been located. Figure 3 shows a schematic of how the random search optimization method considers the entire design space. This approach is efficient for composite structures applications that include many variables and a design space having discontinuous functions. Since laminates contain an integer number of plies, an optimizer that is insensitive to discontinuous functions is a benefit.

---

<sup>2</sup> Z. B. Zabinsky, D. L. Graesser, M. E. Tuttle, G. I. Kim, "Global Optimization of Composite Laminates Using Improved Hit and Run", Recent Advances in Global Optimization, edited by C. A. Floudas and P. M. Pardalos, Princeton University Press, to appear 1991.

<sup>3</sup> D. L. Graesser, Z. B. Zabinsky, M. E. Tuttle, G. I. Kim, "Designing Laminated Composites Using Random Search Techniques", Journal of Composite Structures, to appear 1991.



**Figure 3: Random Search Method Schematic Diagram**

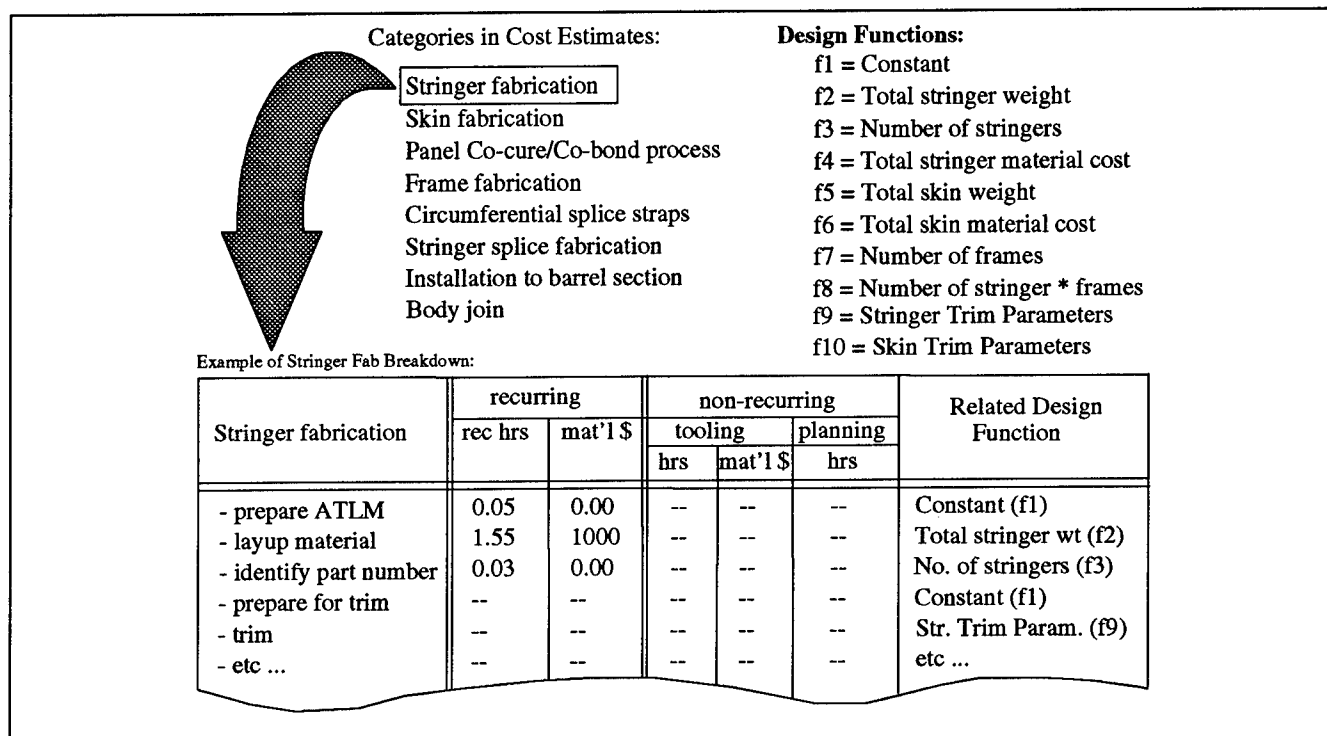
The results given in this paper utilize the random search algorithm to determine the optimum design. In practice, however, the global nature of the random search method becomes computationally inefficient because it continues to search a large design space as the optimum solution is approached. Current work is considering the combination of the random search algorithm with an efficient gradient based optimization code to search the entire design space and then converge to the solution more effectively. This work supports the larger optimization problems envisioned for a tool which blends the design for multiple load points in a large aircraft structure. The framework for this advanced development is discussed in further detail in Reference 6.

### Cost Constraints

Design/manufacturing cost relationships were developed in order to optimize crown panels for cost. These relationships were added to the optimization tool as cost constraints. They were based on data collected during the crown global evaluation process (Refs. 1 and 7), when a comprehensive manufacturing plan was compiled for each design to support a detailed cost estimate. Focussing on the design concept chosen for local optimization, individual cost drivers were determined from the detailed cost breakdown. This was accomplished by evaluating the detailed cost steps in terms of how they relate to the design details. By considering how each step may be affected by variables relating to the design, relationships were determined and the costs were normalized to the baseline design. Using this approach, any variance in a given design detail can be accounted for in the part cost.

Figure 4 shows an example of how design/manufacturing cost relationships were derived from detailed estimating data. The figure includes a list of the processes considered in the crown panel development, a list of the design functions used in the cost breakdown, and an example of how the functions were assigned to each detailed process step. As shown in Figure 4, each detailed process step was coupled with the design function that directly affects the cost. If none of the design functions were perceived to have a direct effect, that individual step was assumed to be constant. Following this analysis, all

terms were summed to obtain a single equation for total crown panel costs. A representation of this cost equation for the skin/stiffener/frame cobonded crown panel assembly is shown in Figure 5. The coefficients in this equation are valid only for this particular design family, panel size, and associated manufacturing processes. Using this equation, small variations in the design details from the baseline design could be evaluated from a cost standpoint and the major cost drivers exploited. Any major design differences from the global design or any process changes are likely to result in changes to the equation coefficients. A more generalized cost evaluation analysis is envisioned for future work to evaluate different types of structures. Again, the framework for this is discussed in Reference 6.

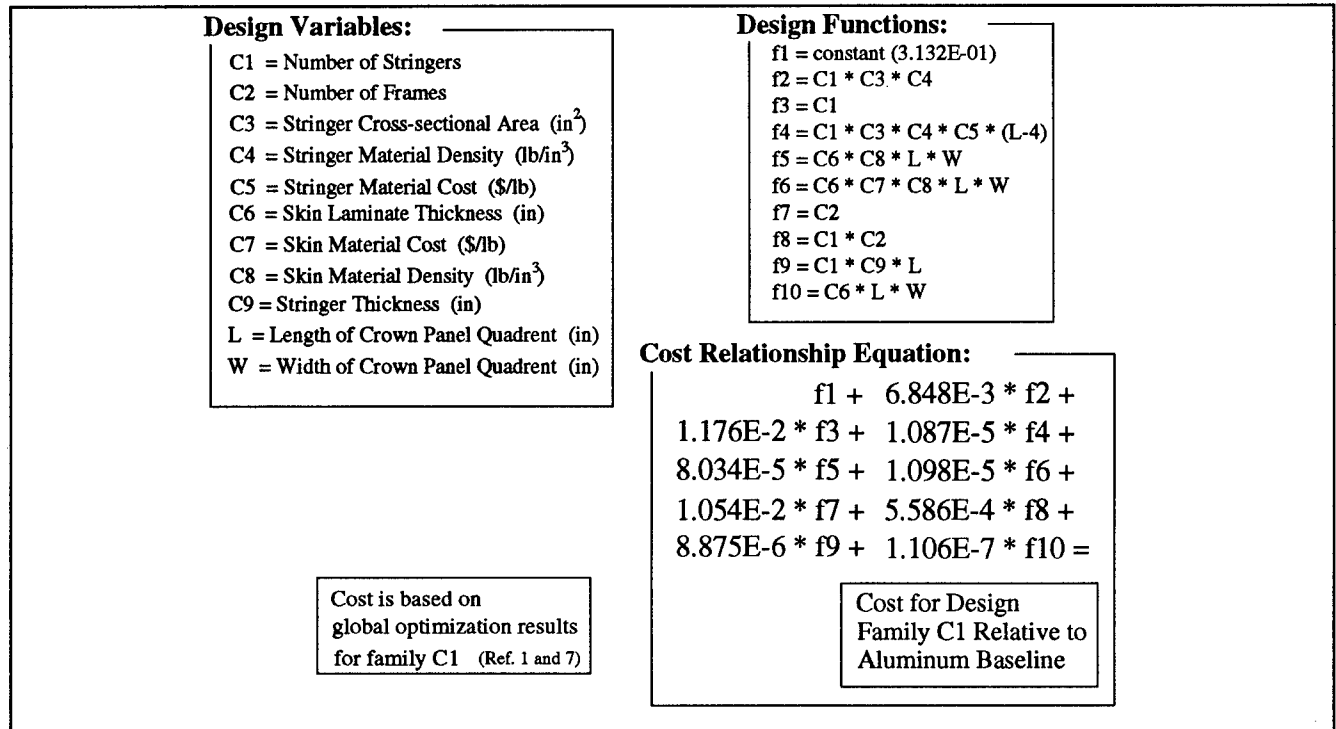


**Figure 4: Design Variables and Their Relationship to the Manufacturing Cost**

### Performance Constraints

The criteria used to design a composite fuselage crown panel are very similar to those used for its aluminum counterpart since both structures perform the same function. Many design checks were made to evaluate structural performance for each loading condition. A summary of the constraints used during local optimization are shown in Table 1. Using these criteria to constrain investigations to a feasible design space, structural cost and/or weight was used as an objective function in the optimization routine to find the best possible design.

Of the constraints and guidelines listed in Table 1, the minimum skin buckling, minimum stiffness, and tension damage tolerance constraints tended to be the most critical. The minimum skin buckling criteria was initially limited to be no less than 40% of the ULTIMATE compression load (i.e., skin buckling was not allowed to occur below this load level). This effectively limited the amount of post-buckling that occurred in the structure. It was later reduced to 33% of the ULTIMATE load, as discussed in "Criteria and Guideline Sensitivities". The minimum stiffness criteria used was based on



**Figure 5: Cost Relationship Used During Local Optimization**

90% of the baseline aluminum airplane fuselage stiffness. The aluminum design is heavier in the forward end due to the higher load levels. This directly corresponds to a higher stiffness in that region. The minimum stiffness was lower in the aft crown panel where the skin gages are smaller due to the lighter loads. The stiffnesses used to constrain the composite crown designs may not be the absolute minimum fuselage stiffness allowed for this type of structure. Without extensive analysis of the effects of fuselage stiffness on aerodynamic control, ride quality, and flutter limitations, however, it was assumed to be sufficient. A longitudinally oriented through penetration that included a central failed frame element was used to evaluate hoop tension damage tolerance. Analytical corrections for configuration, stiffness, pressure, and curvature were included.

The loading conditions applied to the crown panel include both flight loads and internal pressure loads. The critical flight loads are derived from a 2.5g symmetric maneuver, factored by 1.5 to an ULTIMATE load condition, with a 13.56 psi internal pressure differential applied simultaneously. This loading combination gives the maximum axial tension load in the crown panel. The tension load distribution and the associated shear loads are shown in Figure 6. The maximum compression load in the crown comes from a -1.0g symmetric maneuver and was derived from the 2.5g case by using a 40% reversal assumption, again factored by 1.5 to achieve an ULTIMATE load condition. Two pressure cases are also used to design the fuselage structure. An ULTIMATE pressure load case (18.2 psi pressure differential) is applied without any additional flight loads. This case is critical in the crown for frame loads and for the longitudinal splices. A FAILSAFE pressure load (10.3 psi pressure differential) is used to evaluate the tension damage tolerance in the hoop direction.

**Structural Criteria Related Design Checks**

- o Ultimate failure strains
- o Tension damage tolerance (axial and hoop directions)
- o General panel stability
- o Local buckling/crippling

**Structural Guidelines**

- o Minimum overall axial and shear stiffness no less than 90% of an aluminum counterpart stiffness
- o Minimum skin buckling percentage of 33% ULTIMATE load
- o Maximum of 60% of the total load in either the skin or stringer element
- o Maximum stringer spacing based on skin area between adjacent stringers and frames
- o Minimum skin gage based on impact damage resistance data

**Composite Laminate Guidelines**

- o Poisson ratio mismatch between skin and stringer laminate less than 0.15
- o A minimum of four  $\pm 45^\circ$ , two  $0^\circ$ , and two  $90^\circ$  plies in any laminate.
- o Ply angle increments of  $15^\circ$  in final laminate

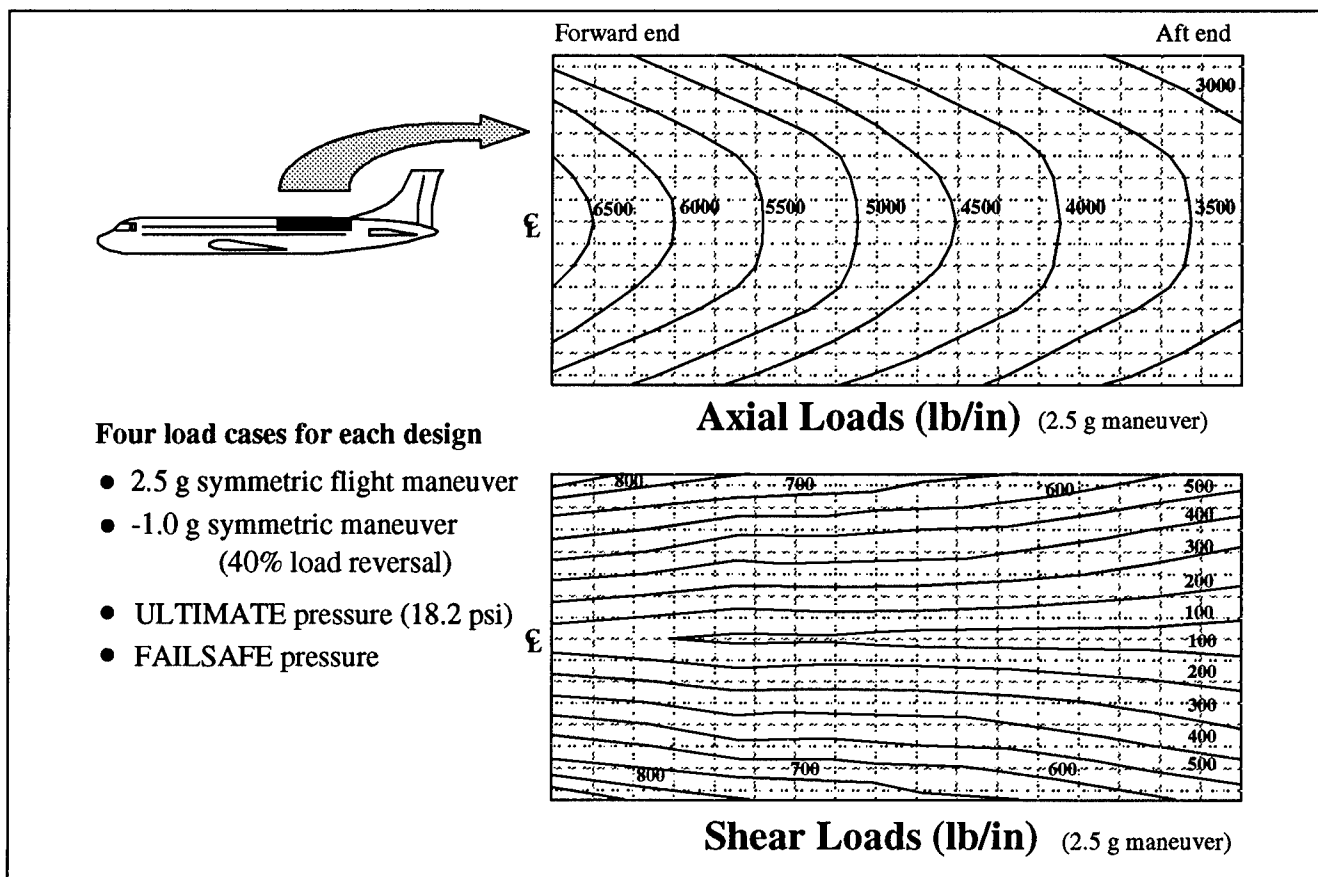
**Geometric, Configuration, or Manufacturing Constraints**

- o Maximum stringer height
- o Minimum stringer flange widths
- o Stringer web angle limitations

**Table 1: Structural Performance Constraints and Guidelines**

The design criteria, structural guidelines, and loading conditions were all included in the design tool for crown panel applications. When appropriate, each criteria was checked for the four load cases applied at a given point on the crown panel. Only designs that met all of the design criteria and constraints were evaluated for weight and cost using the objective function. Seven different locations on the crown panel were evaluated, each having unique load requirements. Combined, these seven load points were used to optimize the entire crown panel. The blending of the individual design points is discussed in the section entitled "Blending Function".

During the course of crown panel local optimization, many different design combinations were considered. Certain cost trends and sensitivities to specific design variables and constraints were observed. A few of the trends and relationships stood out as being significant. The effects of structural geometry, namely stringer spacing, was found to have a large impact on the total panel cost. In addition to the geometry, the material type chosen for use also impacted the final cost significantly. The materials traded in this study included a low cost, low modulus graphite/epoxy system, a higher cost, intermediate modulus graphite/epoxy system, and a graphite/fiberglass hybrid system. In addition, the panel design and cost were found to be sensitive to small changes in the critical structural guidelines. The structural guidelines considered for this sensitivity study included the minimum initial skin buckling load level and the minimum axial fuselage stiffness.



**Figure 6: Crown Panel Loads**

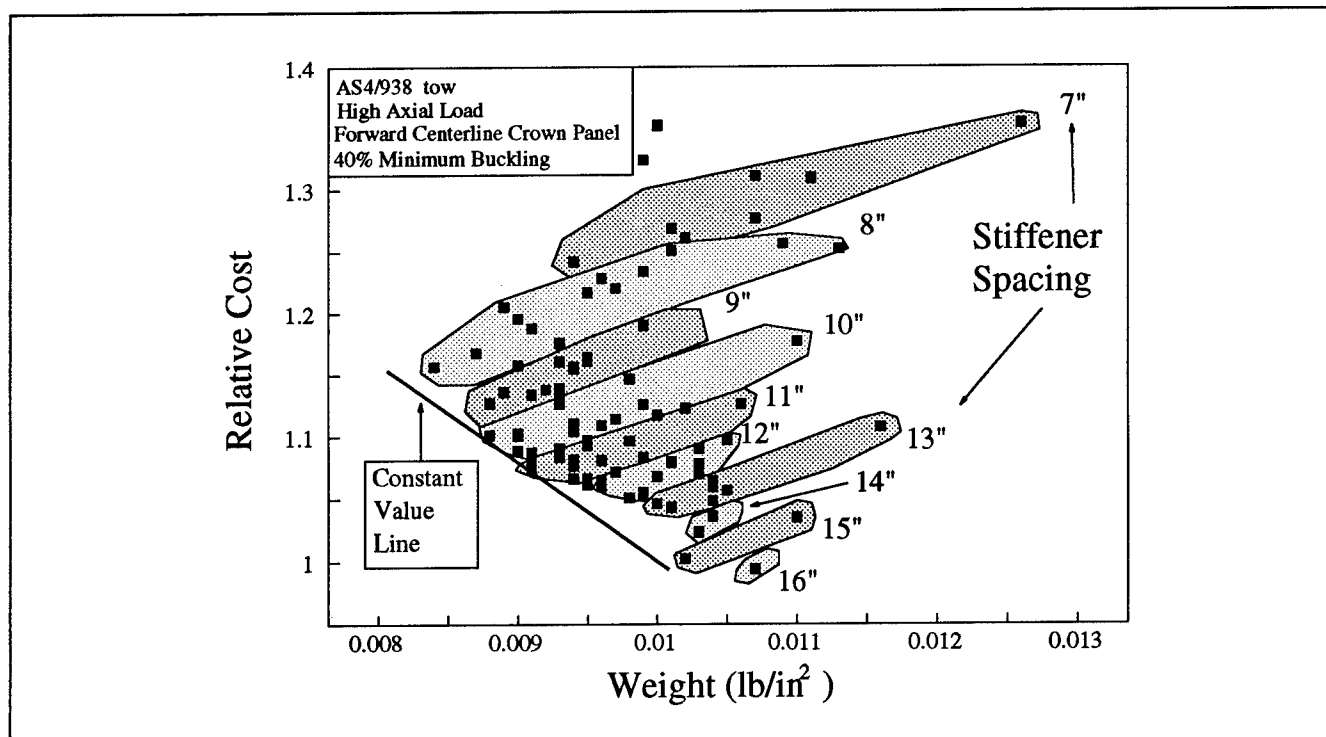
## SENSITIVITY STUDIES

### Geometric Parameters

For a given load point on the crown panel, the optimum design was determined by considering a wide range of skin and stringer thicknesses. For each individual design, the analyst defined the number of skin and stringer plies. The design tool was used to determine the cross-sectional geometry and spacing of the stringers, and the skin and stringer ply angles that simultaneously meet the design criteria and minimize the cost. For a given load condition, this involved hundreds of combinations of skin and stringer laminate thicknesses. As an example, a thin skin and thin stringer tended to be relatively inefficient and expensive since the required stringer spacing was very small and the design was relatively heavy. A thicker skin and stringer laminate, however, was more efficient in terms of cost due to a wider stringer spacing. Note that the stringer spacing became limited by a trade with skin weight, minimum skin buckling, and maximum stringer spacing guidelines.

The results of this design exercise are shown in Figure 7. Each point represents the best design for a given skin and stringer laminate thickness. From the scatter of points shown in Figure 7, a trend relating to the stringer spacing is shown by grouping the points with similar stringer spacings. These groupings are shown in the shaded areas. The wider stringer spacings typically correspond to a lower cost and higher weight. The optimum design for this load condition is defined by a constant value line, which corresponds to the value of a pound of weight savings.

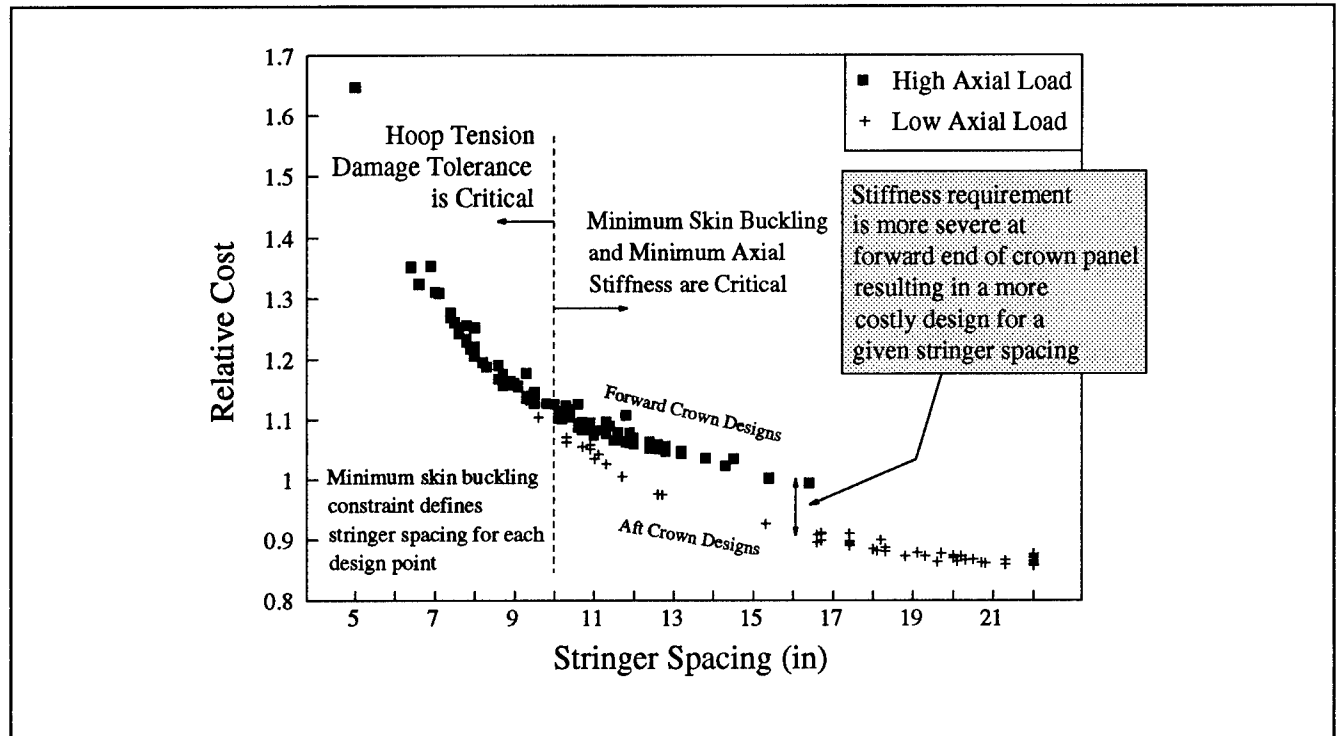




**Figure 7: Design of the Forward Crown Panel - Designs for All Practical Combinations of Skin and Stringer Thickness Combinations**

The relationship between stringer spacing and cost can also be seen in Figure 8. The high axial load case shown in Figure 8 is the same data presented in Figure 7. A similar design exercise was performed for an aft crown panel case and is included to show the effects of a lower axial load on the cost. The design points for the lower load case tend to have larger stringer spacings due to the lower loads. The minimum skin buckling constraint limits the maximum stringer spacing for both load cases.

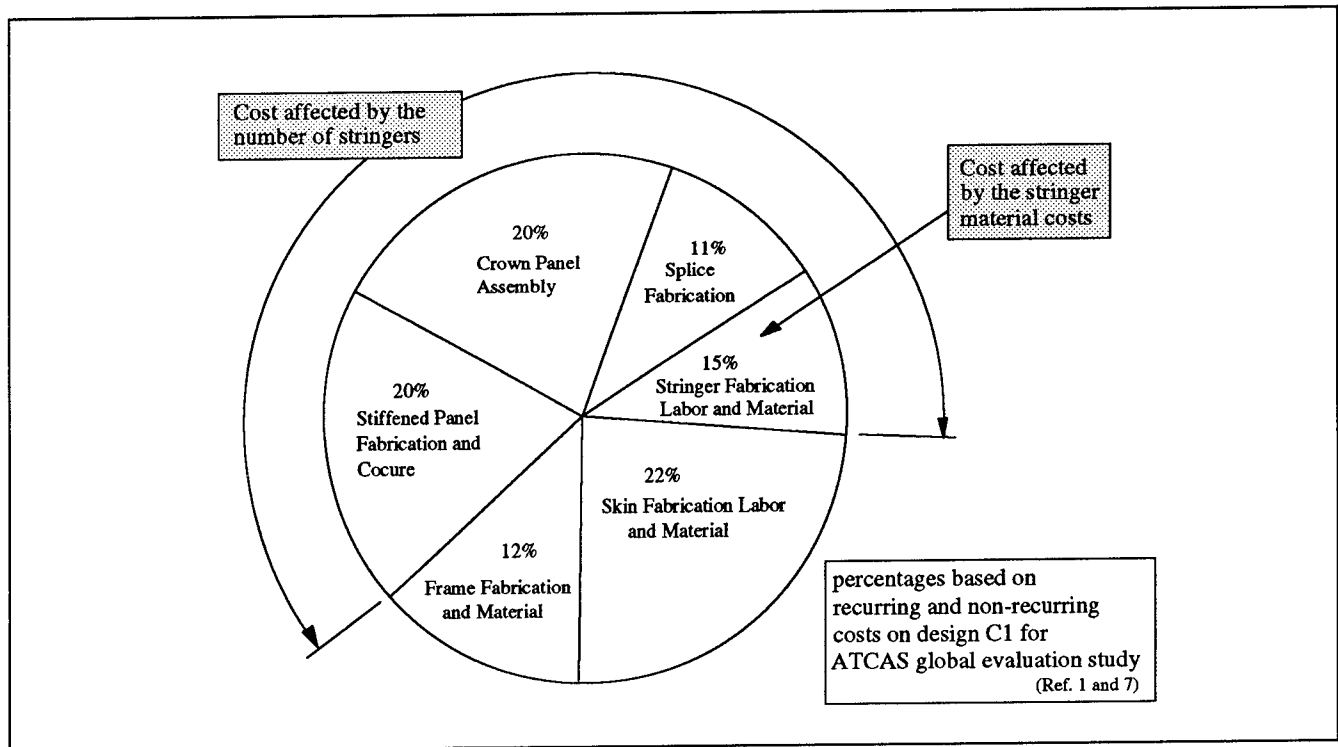
The effects of the design constraints and guidelines on the results can also be seen in Figure 8. For almost every design point, the minimum skin buckling constraint defined the stringer spacing. For stringer spacings less than 10 inches, the designs were also limited by tension damage tolerance issues. The smaller stringer spacings typically had thinner skins which directly affect the hoop damage tolerance properties. The larger stringer spacings are affected by the minimum stiffness constraint. In the forward crown panel, where the axial loads are highest, a heavier, and therefore stiffer, structure is required than in the aft section where the axial loads are less severe. For stringer spacings greater than 10 inches, the tendency for the high load, forward crown designs to be higher in cost than similar designs in the aft crown panel can be attributed to the different stiffness constraints for these load conditions. The effect of the stiffness constraints is significant in that it can penalize the cost of the design by requiring either smaller stringer spacing or additional material to meet the required minimum target. As discussed earlier, this particular constraint needs to be evaluated further to avoid any arbitrary penalties to the cost and weight of a composite fuselage by requiring it to be stiffer than is necessary.



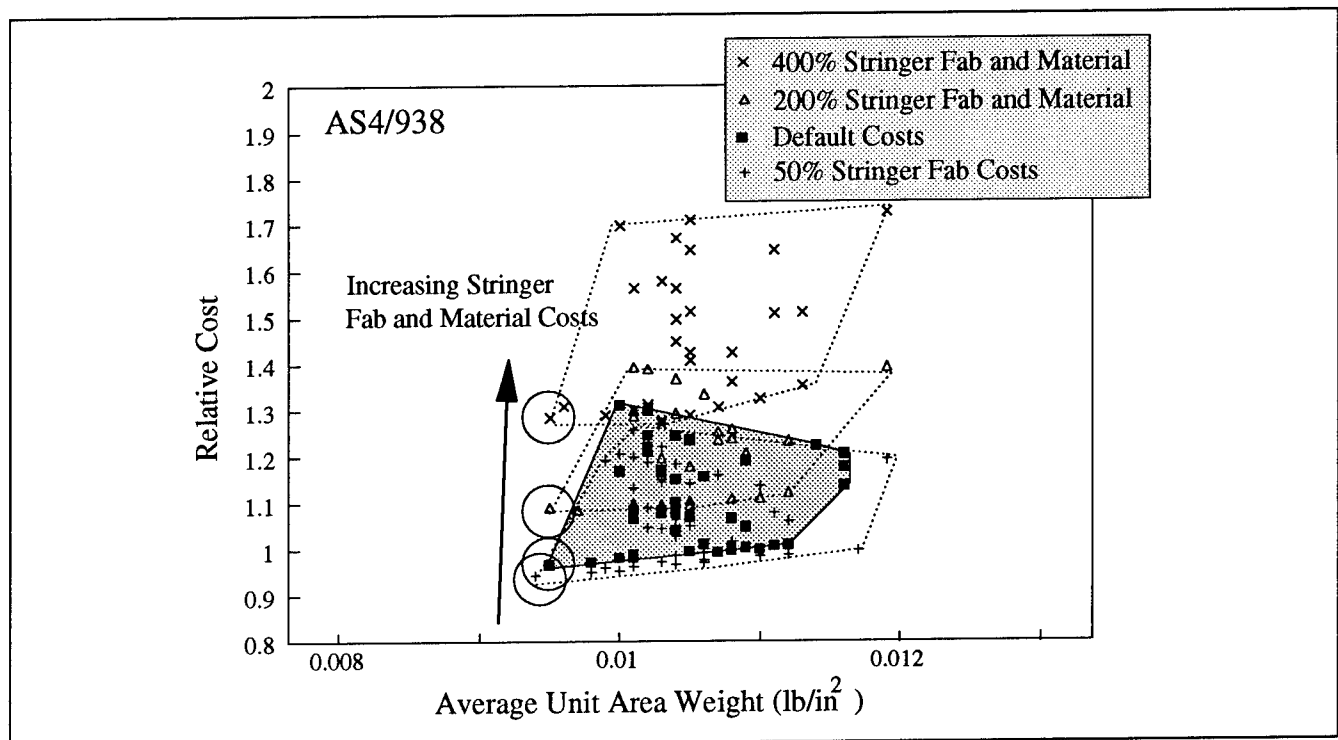
**Figure 8: Relationship Between Stringer Spacing and Cost**

Strong relationships with stringer design variables can be explained by looking closer at the cost breakdowns. Figure 9 shows the breakdown of total crown panel cost in percentages. The categories shown that are affected by the number of stringers account for 61% of the total cost. The effect of the number of stringers on each category may not be directly proportional, but is still significant. For example, in the case of the crown panel assembly, both longitudinal and circumferential splices are included in the cost breakdown. The number of stringers affects this cost center only through the stringer splices in the circumferential splice operation. A significant part of the assembly cost is therefore directly proportional to the number of stringers, yet the remaining part is unaffected.

Sensitivity of the optimum design configuration to changes in individual element costs provides further insight into design/cost relationships. As an example, a study considering a range of stringer costs was conducted, with the results shown in Figure 10. It is evident that the original trend to eliminate as many stringers as possible to minimize cost is true for stringer element costs varying from 50% to 400% of the original assumptions. For this range, the details for each optimum design point were nearly identical and cost differences directly related to the assumed change in stringer costs. The current study indicates that from a geometric standpoint, the most significant variable is stringer spacing.



**Figure 9: Cost Breakdown for Baseline Crown Panel From Global Evaluation Study**



**Figure 10: Effect of Increased Stringer Element Costs on Design**

## Material Parameters

The final crown panel design used an AS4/938<sup>5</sup> material system. This choice was made based on a comparison of cost/performance relationships with other material systems. These relationships were determined by using the appropriate material properties during design/cost optimization studies. Some important properties for fuselage performance, such as tension fracture strength, have complex relationships with fiber stiffness, matrix properties, and material form. Reference 3, which is included in this proceedings, discusses results from ATCAS tension fracture material characterization tests.

Design optimization results are shown for two material systems in Figure 11. The higher modulus of the IM6<sup>6</sup>/938 material system is evident in that the best IM6 design case is lower in weight than the best AS4/938 design; however, the AS4 design was found to be more attractive after considering the value of a unit weight savings. A discussion of optimization studies involving the graphite/fiberglass hybrid appears later in the subsection entitled "Criteria and Guideline Sensitivities".

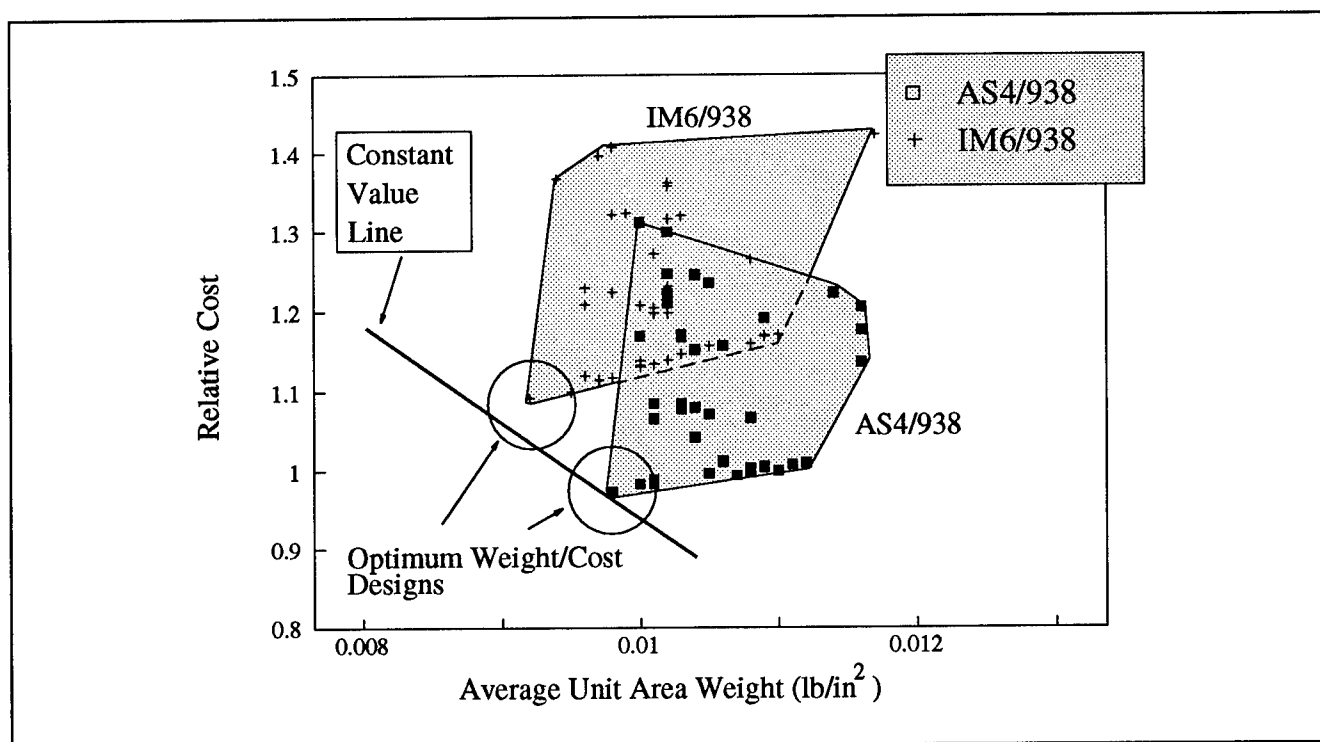


Figure 11: The Effect of Material Choice on the Design

## Blending Function

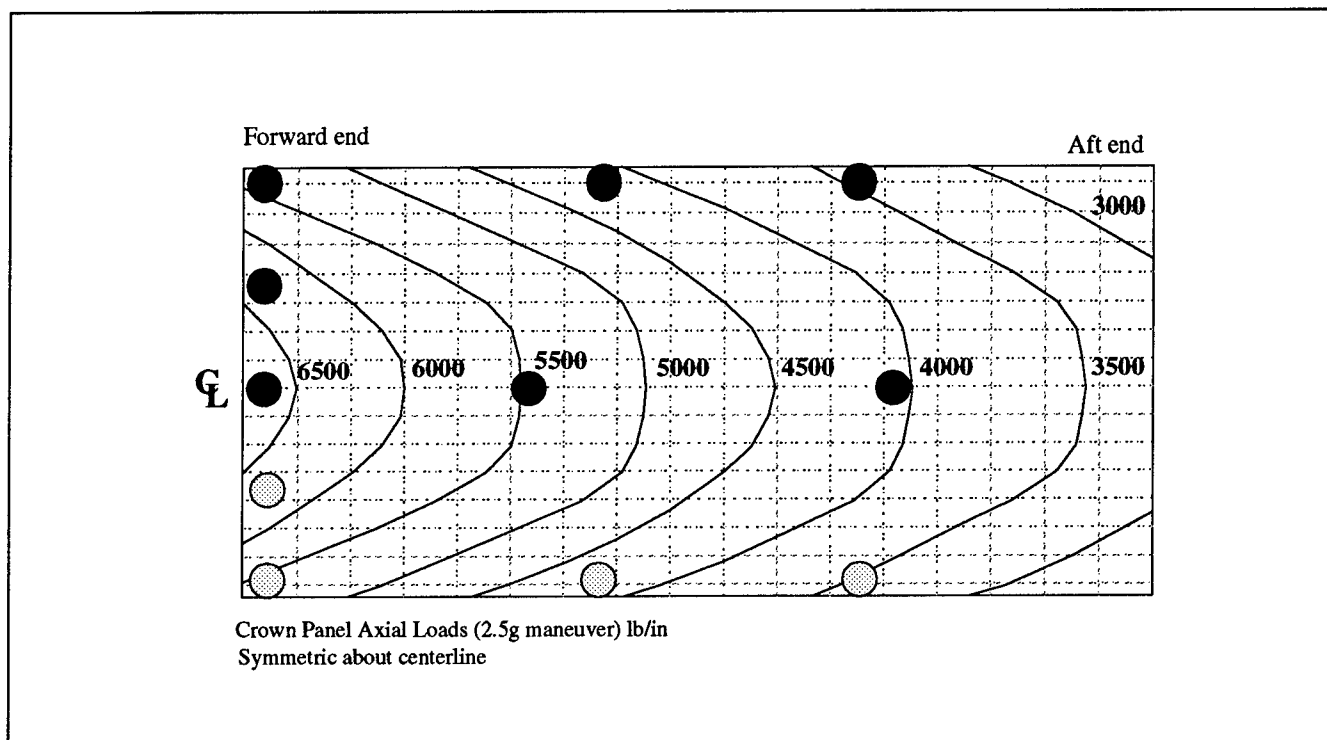
In order to transition from a number of point designs into a final, cohesive design, the individual points must be blended together. For the current study, the seven load points shown in Figure 12 were considered, each having unique load requirements. In order to blend the individual points in the crown

<sup>4</sup> AS4 is a graphite fiber system produced by Hercules, Inc.

<sup>5</sup> 938 is a epoxy resin system produced by ICI/Fiberite.

<sup>6</sup> IM6 is a graphite fiber system produced by Hercules, Inc.

panel without changing the cost relationships, a number of manufacturing constraints were imposed. The first imposed constraint is that the stringers remain straight and, therefore, the stringer spacing between two adjacent stringers is constant along the length of the crown panel. Stringer spacing was, however, allowed to vary across the crown panel width (i.e., the stringer spacing at the edge of the panel could be different than at the center). In addition to the stringer spacing constraint, it was also assumed that the individual ply angles will remain constant, forcing the laminates at any adjacent points to be consistent. Ply dropoffs were allowed between design points, as long as fabrication rates were unaffected and the remaining laminate was a reasonable subset of the adjacent laminates.

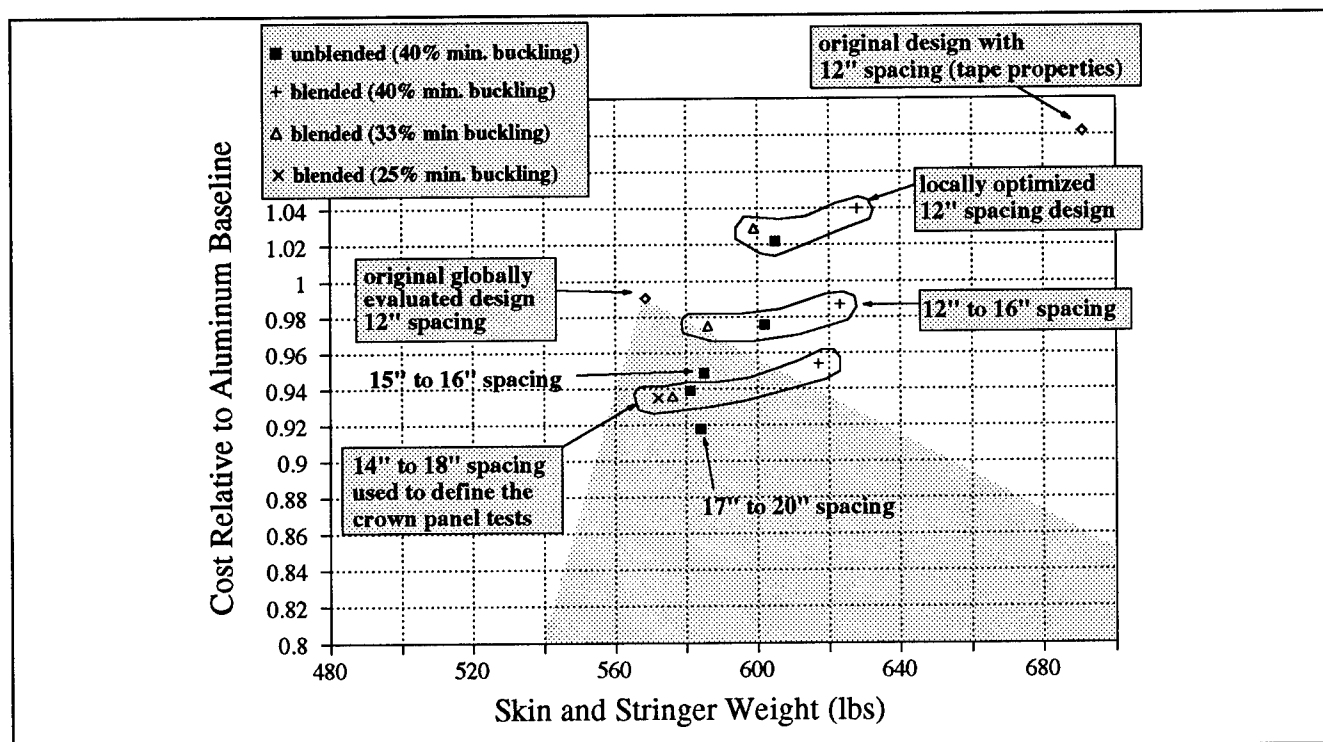


**Figure 12: Load Points Used to Design the Crown Panel During Blending**

Many interesting combinations of design variables result from trying to blend an entire design. For example, the optimum stringer spacing at the more highly loaded forward end of the crown panel tended to be smaller than the stringer spacing at the lightly loaded aft end. This was seen in Figure 8. The dominating reason for this difference was the effect of the minimum skin buckling constraint that was imposed. When blending the stringer spacings, the larger stringer spacing possible in the aft end would penalize the forward end for both cost and weight. Likewise, the smaller spacing trend in the forward end would penalize the aft end of the crown. After considering both of these scenarios, it was determined that the penalty of the larger stringer spacing on the forward end was smaller than the penalty imposed by forcing a smaller stringer spacing on the aft end. This result is reasonable if one considers the cost breakdown and stringer effects of the baseline design shown in Figure 9.

Based on results from the initial point design optimization exercise, a series of blended crown panel designs were developed. The stringer spacings obtained from the initial study were imposed for the entire crown panel. The results of this study are shown in Figure 13. Initially, the laminate layups were not constrained and were still somewhat inconsistent between adjacent design points. This

condition is labeled as "unblended". Three stringer spacing scenarios were chosen for further consideration. These three designs were further blended to achieve consistency between adjacent laminate design points and are labeled as "blended". Figure 13 shows that blended designs generally have higher cost and weight since additional plies were needed to satisfy the requirements.



**Figure 13: Local Crown Panel Optimization and the Effects of Blending**

The development of advanced tow placement technology which allows some point to point variation in fiber angle within a ply would help minimize this effect. In addition, the generalization of optimization schemes used for the design cost model would enable analysis of blended designs, resulting in lower costs and weights than achieved in current efforts.

### Criteria and Guideline Sensitivities

Initially, a minimum skin buckling constraint was imposed that limited the design such that no skin buckling could occur below 40% of the ULTIMATE load levels. This constraint was critical to the cost of most designs in that it controlled the maximum stringer spacing. To determine the effect of this criteria, the crown panel was redesigned with the same stringer spacings, but with a minimum buckling load of 33% of the ULTIMATE load. This lower constraint, along with no change in the stringer spacing, resulted in thinner laminates and different design drivers, essentially lowering the cost and weight of the design. The design was no longer limited by minimum buckling but was critical for minimum stiffness and hoop damage tolerance. Further reduction of the minimum buckling criteria had no effect on the design and only increased the margin of safety on the minimum buckling since this criteria was no longer critical. The effects of the minimum buckling criteria can be seen in Figure 13 by the points labeled "blended (33% minimum buckling)".

Since the cost of the crown panel is sensitive to the minimum skin buckling guideline, research is needed to better understand the effects of design on this requirement. The current guideline assumes a

concept is at risk when skin buckling occurs below a cut-off level, independent of design details. This is likely not the case and a better definition of the requirement is needed to avoid overly conservative and costly designs.

It can be seen that an increase in stringer spacing significantly improves both the cost and weight of the structure. Other design guidelines that limit the stringer spacing will become critical as the stringer spacing increases. One of these guidelines is often referred to as a blowout panel. The blowout panel is defined as the maximum skin area between adjacent stringer and frame elements and is limited to a given size defined by the aircraft's environmental system capabilities. Using typical values for this guideline from existing aircraft, a maximum stringer spacing for the composite hat stiffened crown panel is about 18 inches. Therefore, for the final crown panel design, the maximum stringer spacing was limited by this value.

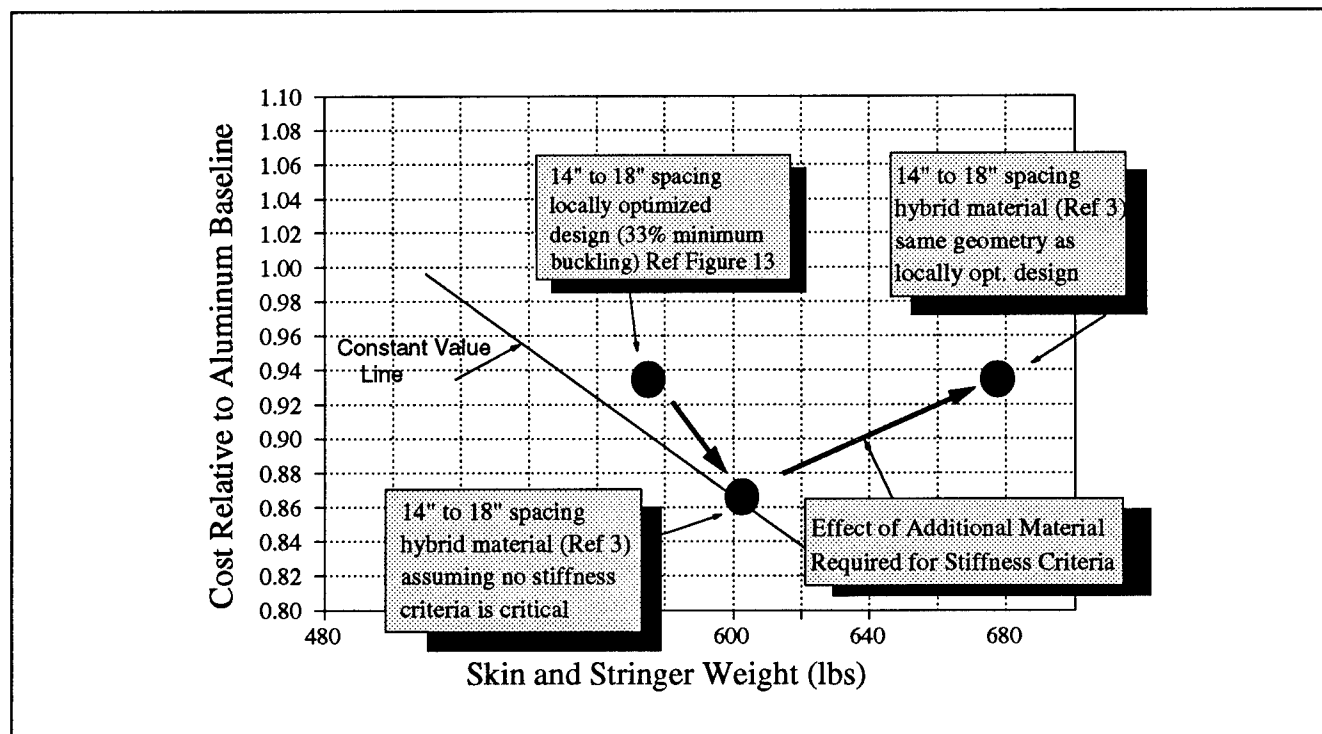
The effect of the fuselage stiffness was discussed previously and is shown graphically in Figure 8 by comparing the trends for the two load conditions considered. The difference in these trends can be attributed to a difference in the overall stiffness requirements between the forward and aft crown panel.

The only remaining design criteria that was consistently a critical design driver in the crown panel is tension damage tolerance. The effect of this criteria on the design is most apparent when a material system that has superior tension damage tolerance properties is considered in the design. An intraply graphite/fiberglass hybrid material system is a good example of a material system with excellent damage tolerance properties and low material cost, but lower modulus. This material is discussed in detail in Reference 3. Using a minimum skin buckling criteria of 33%, the 14- to 18-inch design in Figure 13 was designed using the hybrid material system. The results of this exercise are shown in Figure 14. Assuming for a moment that no stiffness criteria existed, the improved tension damage tolerance of the hybrid material reduced the crown panel cost about 6% with a small weight penalty due to the increased density of the hybrid material. When the stiffness criteria are imposed, a number of additional plies are required, increasing the cost of the hybrid crown panel close to that of the graphite design, with a significant weight penalty. Looking at the entire airplane, however, there are many locations on the fuselage where the hoop tension damage tolerance criteria are critical. For certain fuselage sections forward of the wing and immediately forward of the empennage, stiffness may not be a critical design guideline as it is in the highly loaded center sections. In these more lightly-loaded sections, a hybrid material design may provide for cost-effective structure.

### LOCALLY OPTIMIZED CROWN PANEL DESIGN

The many sensitivity studies and design combinations performed during local optimization resulted in a final design for the crown panel. A sketch of the details of this final design are shown in Figure 15. The stringer spacings chosen were based on the results of the blending exercise and were limited by the blowout panel criteria discussed earlier. A stringer spacing of 14 inches at the center of the crown was determined by the higher axial load at the center of the panel. Lower axial loads at the edge allowed for a wider spacing resulting in a lower total panel cost. The stringer laminate ply angles tended towards  $0^\circ$ . A minimum number of  $\pm 45^\circ$  and  $90^\circ$  plies were included to satisfy laminate layup guidelines. The skin plies were also constrained to have a minimum number of  $0^\circ$ ,  $\pm 45^\circ$ , and  $90^\circ$  plies. In the aft end, the remaining plies at the center of the panel tended towards  $90^\circ$  to resist the hoop tension damage tolerance criteria. Towards the side of the aft crown panel, laminate thickness increased, with the remaining plies tending towards  $\pm 45^\circ$  to resist the minimum shear buckling criteria. A compromise was found that minimized the total cost and incorporated  $\pm 60^\circ$  plies to resist shear buckling at the edge and hoop tension damage tolerance at the center. In the forward end, this same base laminate required additional plies to resist the increased axial and shear loads. In the center of the

panel, longitudinal plies were required to resist the additional axial loads. However, at the edge, the higher shear loads required more angle plies. The final  $\pm 15^\circ$  plies added to the forward crown provided the shear requirements at the edge and the axial requirements at the center. Additional details to account for the joints and frames were included in the final design and cost estimates, but there was no attempt to optimize these details.



**Figure 14: Effect of Hybrid Material on Crown Panel Design**

The criteria and guidelines that drove the final crown panel design are shown in Figure 16. Hoop tension damage tolerance was more critical in the aft crown panel where the skin laminate was thinner. The axial stiffness tended to be critical almost everywhere, suggesting that this particular criteria be studied to ensure that the design is not arbitrarily over-constrained. The minimum buckling guideline was not as critical in the aft crown as it was in the highly loaded forward crown panel. Any increase in stringer spacing or a higher minimum buckling, however, would quickly make this criteria a dominant design driver. Finally, the shear stiffness criteria was critical only in the forward part of the panel towards the lower side, where the shear loads were highest and the stiffener spacing largest.



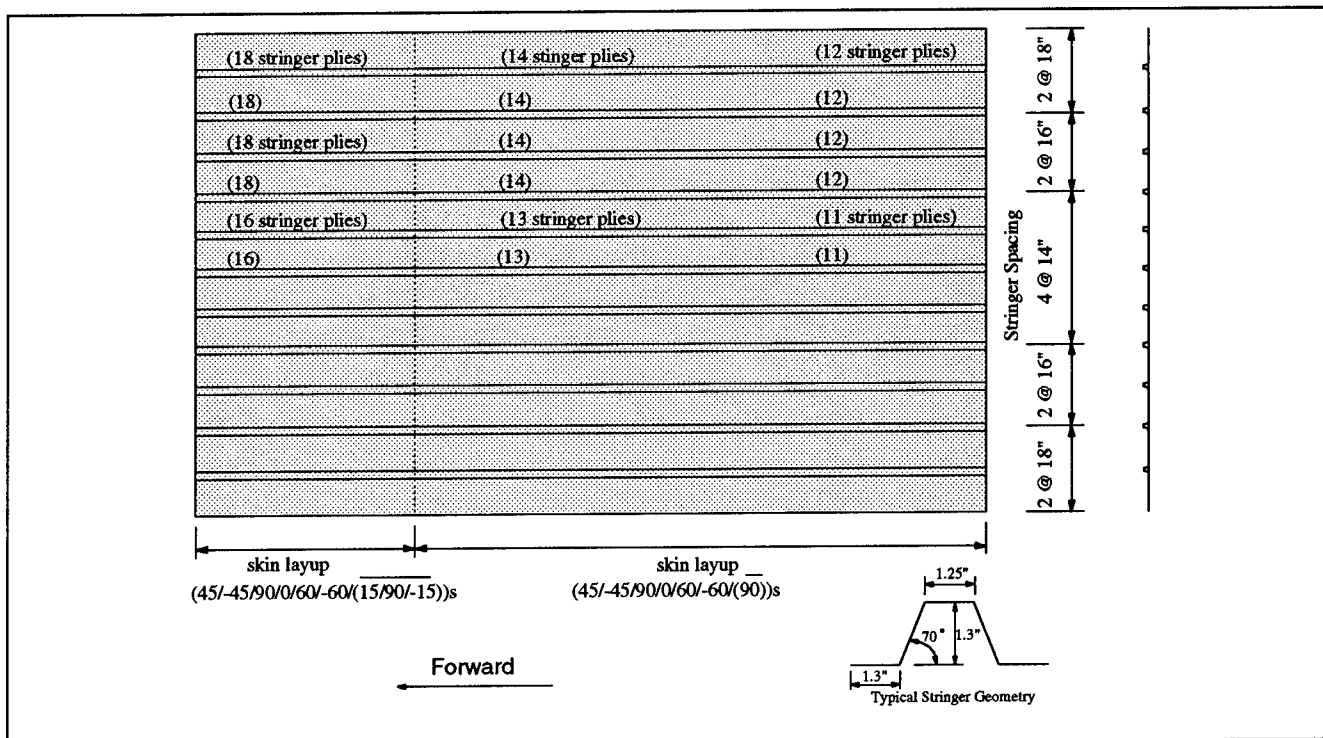


Figure 15: Final Crown Panel Design

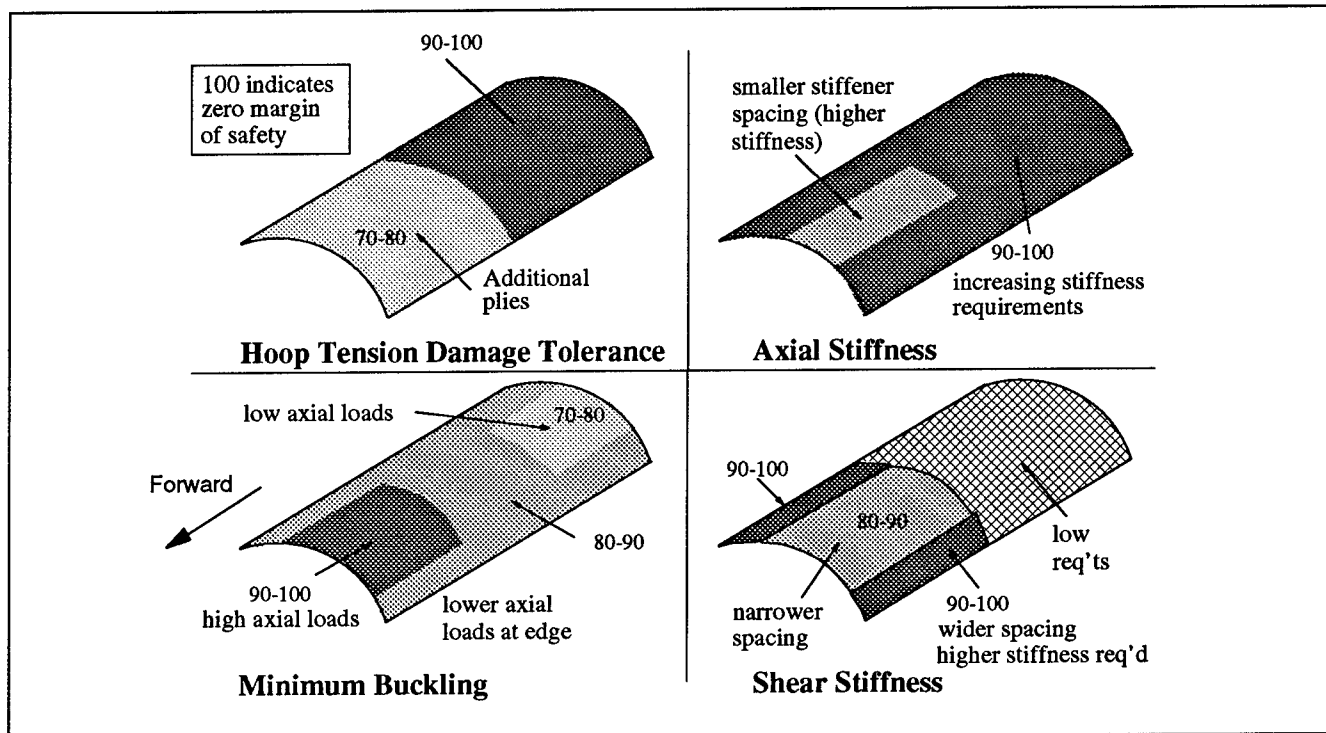


Figure 16: Design Drivers for Locally Optimized Crown Panel

## **LESSONS LEARNED DURING LOCAL OPTIMIZATION**

The usefulness of a design tool that combines optimization with realistic design criteria and an ability to evaluate the manufacturing cost has been shown to be quite effective in understanding the sensitivities of the design details to the criteria and cost. Many improvements have been identified during the course of this initial work with a design tool of this type. The most significant is the need to design the entire panel, combining the different design trends and loading levels in each part to make the design consistent and feasible for manufacturing. The current point optimization characteristics of the design tool, typical of most structural sizing tools, makes the job of blending the point-to-point variations in a real design very labor intensive. Future work with the design tool will develop algorithms and optimization approaches to effectively blend designs for a full scale panel subjected to changing load distributions and local variations in the design such as joints, splices, and cutouts.

An understanding of the effect of the design criteria on an optimized design is another important feature that a design tool of this type can provide. As with all optimization, the algorithm will take advantage of the criteria or constraints to minimize its objective function. As is often true, if a design is constrained by a given criteria, there is another criteria that will quickly dominate the design should an improvement be made which relieves the initial constraint. With the many interactions that occur in a design study such as this, careful attention to the trends and criteria can define the direction of future work that would be of benefit to the design.

## **CONCLUSIONS AND RECOMMENDATIONS FOR FUTURE WORK**

The local optimization study for composite fuselage crown panels revealed many insights into the relationship between manufacturing cost and design details. A design tool was developed to aid in these investigations. Steps taken in developing the design tool, the sensitivity studies that were performed to identify critical variables, and the technique used to arrive at a final optimum crown panel design were discussed.

It was concluded that design constraints used to limit the design can be very important when optimizing a real structure for cost. Constraints such as minimum stiffness and skin buckling can be a significant cost driver. The tension damage tolerance design criteria are also a significant design driver in many parts of the crown panel.

The benefits of a design tool that combines structural constraints and manufacturing costs were also shown. Sensitivity studies showed the effect of different constraints on the cost and weight of optimized designs. Material trade studies showed that many interactions affect the cost effectiveness of improved material properties. Hybrid materials were shown to have promise in a significant portion of the airframe.

A final optimized crown panel design was completed utilizing the data obtained from these sensitivity studies. Stringer spacings ranging from 14 to 18 inches were selected. The optimized design showed significant cost savings relative to the original global evaluation study.

During the course of the study, it became apparent that there are many research areas that need to be addressed. A summary of these items are listed below:

Stiffness criteria for a composite fuselage must be evaluated further to avoid overly conservative designs. This is a potential cost driver for composite fuselage structure.

Stringer spacing is a dominant design driver in the crown panel. The minimum load below which skin buckling is not allowed needs to be addressed for different design configurations to avoid unnecessary cost penalties.

Blending of adjacent points during an optimization cycle is the key to a realistic structural optimization problem. The development of an automated blending function is critical.

## REFERENCES

1. T. H. Walker, P. Smith, G. Truslove, K. Willden, S. Metschan, C. Pfahl, "Cost Studies for Commercial Fuselage Crown Designs", First NASA Advanced Composite Technology Conference, Seattle, WA, October 29 - November 1, 1990, NASA-CP-3104.
2. L. B. Ilcewicz, P. Smith, T. Walker, R. Johnson, "Advanced Technology Composite Aircraft Structures", First NASA Advanced Composite Technology Conference, Seattle, WA, October 29 - November 1, 1990, NASA-CP-3104.
3. T. H. Walker, W. B. Avery, L. B. Ilcewicz, C. C. Poe, C. E. Harris, "Tension Fracture of Tow-Placed Laminates For Transport Fuselage Applications", In Proceedings of the Ninth DoD/NASA/FAA Conference on Fibrous Composites in Structural Design, FAA Publication, 1991. (Paper of this compilation.)
4. K. S. Willden, S. Metschan, J. Koontz, "Composite Fuselage Crown Panel Manufacturing Technology", In Proceedings of the Ninth DoD/NASA/FAA Conference on Fibrous Composites in Structural Design, FAA Publication, 1991. (Paper of this compilation.)
5. Z. B. Zabinsky, M. E. Tuttle, D.L. Graesser, G. I. Kim, D. Hatcher, G. D. Swanson, L. B. Ilcewicz, "Multi-Parameter Optimization Tool for Low-Cost Commercial Fuselage Crown Designs", First NASA Advanced Composites Technology (ACT) Review, October 29 - November 1, 1990, Seattle, WA, NASA-CP-3104.
6. W. T. Freeman, L. B. Ilcewicz, G. D. Swanson, T. Gutowski, "Designer's Unified Cost Model", In Proceedings of the Ninth DoD/NASA/FAA Conference on Fibrous Composites in Structural Design, FAA Publication, 1991. (Paper of this compilation.)
7. L. B. Ilcewicz, T. H. Walker, K. S. Willden, G. D. Swanson, G. Truslove, and C. L. Pfahl, "Application of a Design-Build-Team Approach to Low Cost and Weight Composite Fuselage Structure," to be Published as a NASA Contractor's Report, 1991.

# Composite Fuselage Crown Panel Manufacturing Technology<sup>1</sup>

K. Willden, S. Metschan  
Boeing Commercial Airplanes  
Seattle, Washington

and C. Grant, and T. Brown  
Hercules Aerospace  
Magna, Utah

## ABSTRACT

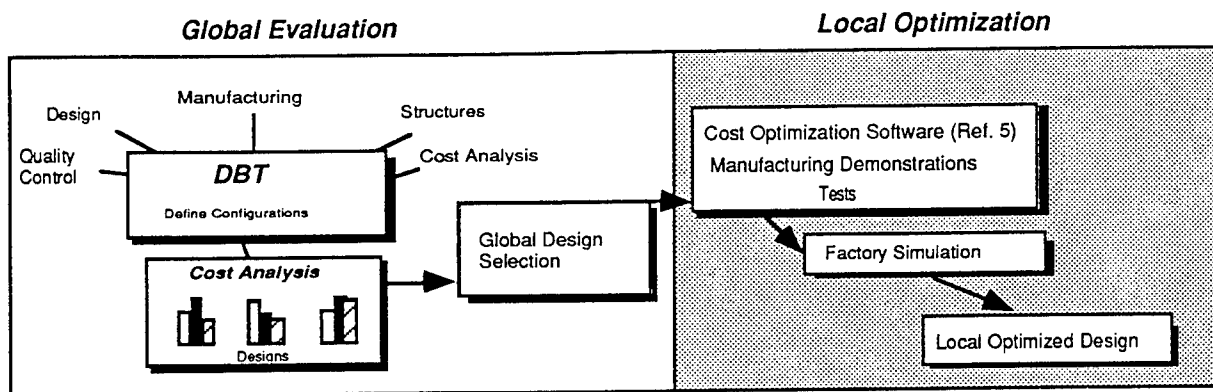
Commercial fuselage structure contains significant challenges in attempting to save manufacturing costs with advanced composite technology. Assembly issues, material costs, and fabrication of elements with complex geometry are each expected to drive the cost of composite fuselage structure. Boeing's efforts under the NASA ACT program have pursued key technologies for low-cost, large crown panel fabrication. An intricate bond panel design and manufacturing concepts were selected based on the efforts of the Design Build Team (DBT) (Ref.1). The manufacturing processes selected for the intricate bond design include multiple large panel fabrication with Advanced Tow Placement (ATP) process, innovative cure tooling concepts, resin transfer molding of long fuselage frames, and utilization of low-cost material forms. The process optimization for final design/manufacturing configuration included factory simulations and hardware demonstrations. These efforts and other optimization tasks were instrumental in reducing cost by 18% and weight by 45% relative to an aluminum baseline. The qualitative and quantitative results of the manufacturing demonstrations were used to assess manufacturing risks and technology readiness.

## INTRODUCTION

Under the NASA/ Boeing Advanced Technology Composite Aircraft Structures (ATCAS) program, design / process trade studies were performed using low cost manufacturing technology for a 15 ft. by 31 ft. crown panel. Through a down selection process which incorporated the DBT approach, several design configurations, representing efficient manufacturing processes, were evaluated. Detailed costs and manufacturing requirements were established for six crown panel configurations. The best combination of stringers, frames, and skin for weight, cost, and performance were chosen as the global design (Refs. 2 and 3). Further optimization of the selected intricate bond design was conducted with structural performance analysis, cost optimization software, manufacturing hardware demonstrations, and tests. Throughout the local optimization process, DBT efforts ensured that the final design complied with all criteria (structural, manufacturing, design, etc.).

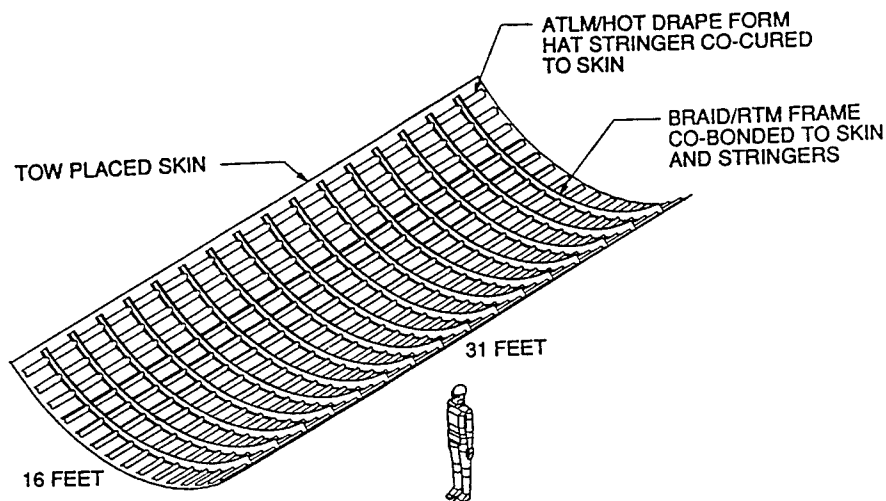
---

<sup>1</sup> This work was funded by Contract NAS1-18889, under the direction of J.G. Davis and W.T. Freeman of NASA Langley Research Center.



**Figure 1: Flow Chart of Crown Panel Optimization Process**

The global design configuration shown in Figure 2 represents key cost effective processes used for the intricate bond design. When evaluating the manufacturing cost of large aluminum structure, costs drivers that could be minimized with composite materials were identified and targeted for reduction (Ref. 4). These cost centers include; 1) minimize labor intensive shimming and fasteners installation by producing large elements and assemble using co-curing/co-bonding operations, 2) automate and control processes to reduce inspection while increasing production efficiencies, 3) use automated equipment that efficiently produces quality structure with low cost material forms, and 4) increase part size and commonality as indicated in Figure 3. Since the intricate bond panel is very stiff, assembly issues must be addressed in all phases of process and tooling developments to minimize panel warpage and maximize panel dimensional accuracy.



**Figure 2: Global Intricate Bond Configuration**

Aluminum			Composite (Global Evaluation)		Composite (Local Optimized)	
	<u>Number</u>	<u>Types</u>	<u>Number</u>	<u>Types</u>	<u>Number</u>	<u>Types</u>
Skin	3	3	1	1	1	1
Frame	16	3	16	3	16	1
Stingers	23	5	15	5	11	2
Clips	368	5	0		0	
Fasteners*	11,770		0		0	

\* Fasteners for quadrant panel assembly not included

Figure 3: Comparison of Crown Panel Elements

### Global Manufacturing Plans

The global evaluated crown panel configuration used the cost advantages of the ATP, braiding/resin transfer molding and unique bonding of skin, stringer, and frames with innovative tooling as shown in Figure 4 (Refs. 3 and 4). The skins are produced four at a time to maximize cost advantage for tooling and labor. The resin transfer molded 16 ft. long frames were produced sixteen at a time to realize the same benefits. The stringers were fabricated with an over-head gantry ATP to take advantage of the cheaper tow material form and batch sizes. The global crown panel design dictated a reverse assembly process, which required a rotisserie to assemble the frames and stringers and then transfer the subassembly onto the skin. Challenges for the reverse assembly process and cure tooling required unique concepts and tooling developments to minimize risk and cost. The reduction of cost and risk were realized in the local optimization process through hardware demonstrations.

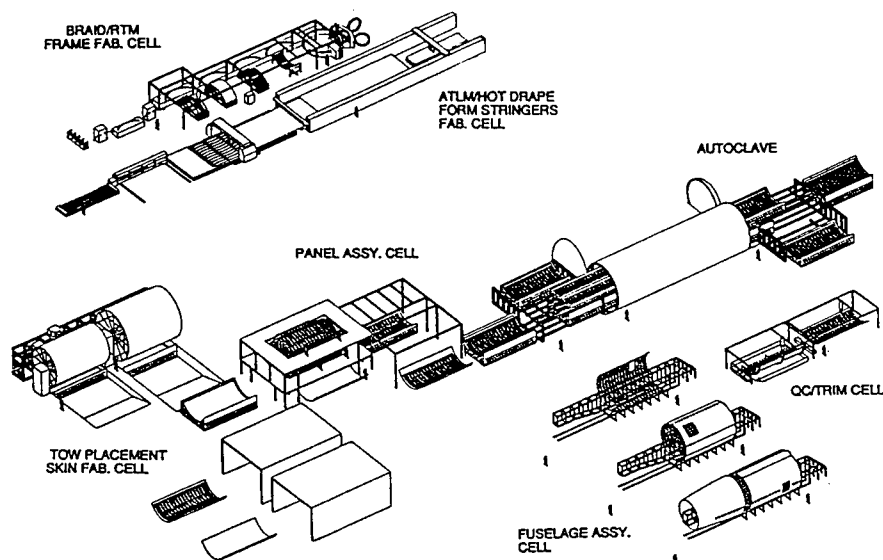
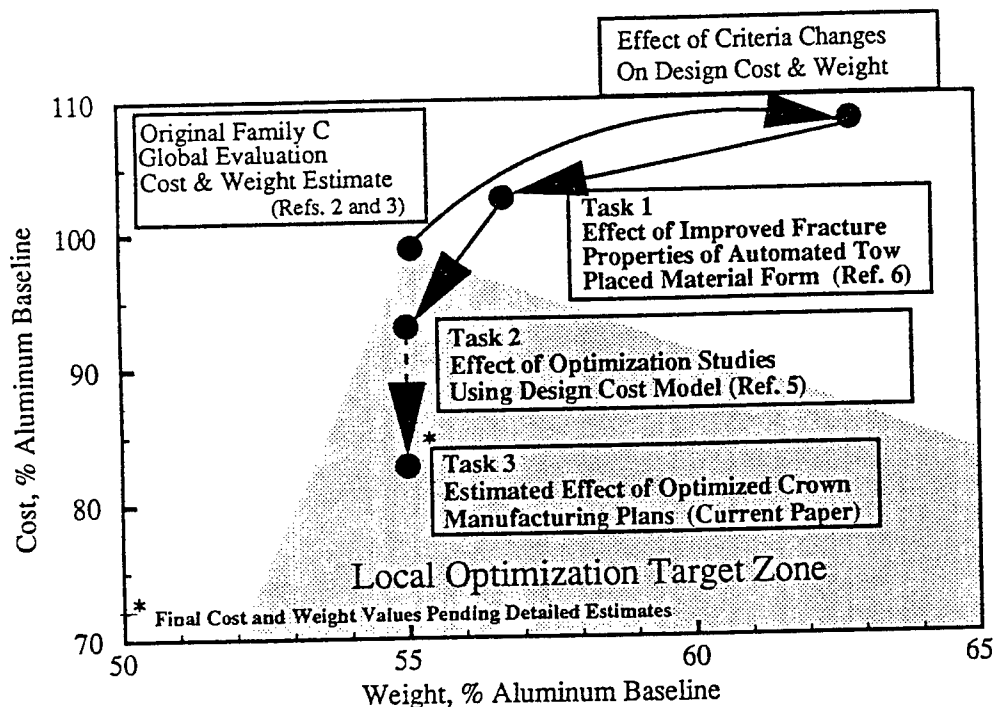


Figure 4: Factory of Global Configuration

## Local Manufacturing Optimization

Figure 5 shows the history of the intricate bond design from global selection through local optimization. Once the cost data for global intricate bond configuration was established, further optimization was conducted through several tasks. Design requirements were reviewed and the initial global point was shifted to reflect an increase in weight to meet changes in criteria (Ref. 5). The efforts of task 1 increased weight savings with improved fracture toughness of tow placed material forms (Ref. 6). Cost and weight were further reduced with the aid of software which optimized cost and weight based on known manufacturing cost relationships and structural performance criteria (Ref. 5). The current software optimization is based on known manufacturing processes selected for a particular design and is not capable of selecting an alternative lower cost process for a given design variation. These types of qualitative manufacturing process selections were assessed for further cost benefits through manufacturing demonstrations and factory simulations. The hardware demonstration and factory simulations were also used to verify and reduce cost of each manufacturing process, assess / minimize manufacturing risks, and conduct tests to verify structural performance. Under task three, the manufacturing hardware demonstrations and factory simulation reduced cost an additional 10.7%.

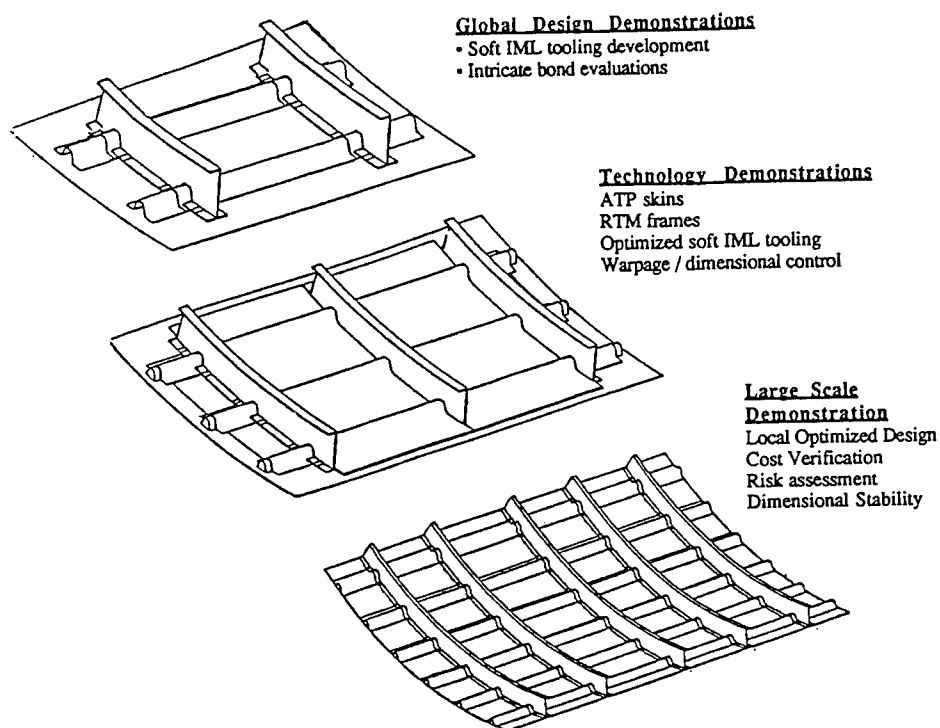


**Figure 5: Effects of the Criteria, Material Properties, Design Details, and Manufacturing Processes on the ATCAS Crown Panel Local Optimization**

## Manufacturing Hardware Demonstrations

To meet ATCAS program objectives, large manufacturing demonstration panels were identified to access manufacturing risk, technology readiness for the intricate bond configuration, and verify cost for an optimized configuration. New innovative cure tooling concepts, which were critical to the success and cost reduction of the intricate bond configuration, were optimized through a series of tool trials to not only reduce manufacturing risk but to increase the part quality / performance. Scale-up issues were considered such that manufacturing concepts demonstrated on small panels

would accommodate large panels without increasing manufacturing risks. Several types of manufacturing demonstration panels were identified to validate the tooling and intricate bond process ( Figure 6). First, two-frame/two stringers flat and curved panels were fabricated at Boeing to develop the soft IML tooling concept. The results were used to fabricate 3 ft. by 5 ft. panels at Hercules to evaluate the technology integration of the ATP skins and stringers, RTM frames, and innovative soft IML tooling. Tooling and manufacturing processes modifications from these trials support the large scale demonstrations.



**Figure 6: Series of Manufacturing Demonstrations to Validate Local Optimization**

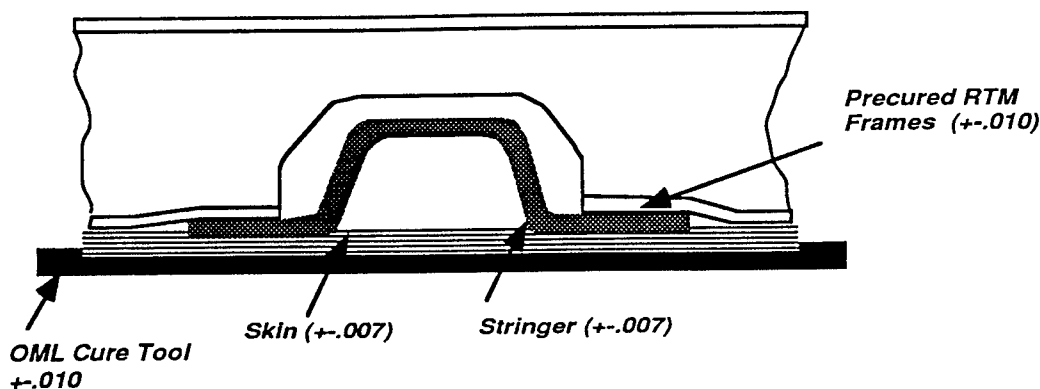
One of the main challenges of the selected global crown panel was to ensure bond integrity of a precured frame cobonded with a green skin and stringer on a contoured surface. The capability to cobond precured frames onto a contoured surface may eliminate fasteners, but the risk to control tolerance build-up and part location for subsequential assembly is increased. Figure 7 shows the tolerances associated with each structural element for the intricate bond configuration.

It is evident that either a clearance or interference situation may occur. Since these conditions are too costly to control with precise machining or manufacturing methods, the manufacturing trials assessed the ability of the adhesive and uncured skin and stringer material to flow and accommodate either condition with the aid of soft IML tooling.

### **Intricate Bond Tooling Considerations**

The success of the intricate bond also depends on the tooling material and tool contour accuracy to minimize gaps and interference between elements, control panel warpage, and reduce production maintenance. One main consideration for the type of tooling used to fabricate the intricate bond panel is the compatibility of the OML cure tool, stringer tooling, and resin transfer mold for frames. If the same tooling material is used for both the OML cure tool and frame tool, then the skin and





**Figure 7: Intricate Bond Element Tolerances**

precured frame mismatch during cure is minimized. Invar 36<sup>2</sup> was selected as the material for the hard tooling because the coefficient of thermal expansion (CTE) is very close to that of the composite laminate (1.7 in/in./ F°). Since Invar 36 can be machined with precision by typical machining operations master tooling, which is typical for composite tools, is eliminated. The reusable stringer cure tooling had to accommodate skin thickness variations and be extractable after cure. Therefore, silicon mandrels were originally selected for stringer tooling. To avoid the typical labor intensive bagging procedures and risks associated with bag failures, soft IML reusable tooling was developed. The soft tooling was required to assist in locating elements during panel assembly and control resin bleeding.

### Manufacturing Demonstration of Soft Tooling

The first demonstration panel was fabricated to develop the reusable net shape soft IML tooling concept and to evaluate the reverse assembly process. The flat two stringer / two frame panel was constructed of precured fabric frames, tape hand laid skin, and drape formed stringers. Variations of frame mandrel inserts and no frame mandrel inserts were evaluated as shown in Figure 8. To make a net shape soft IML tool, a mock-up of the stringer-frame-skin panel was constructed. Next, calendered fluoroelastomer material, reinforced with graphite cloth for thermal stability, was placed on the mock-up surface and cured. The continuous fluoroelastomer bag has integral vacuum ports and breathing paths to avoid volatile entrapment. Silicon frame mandrels were fabricated and used to provide support to one of the frames during final cure. To transfer autoclave pressure to the stringer in the mouse hole area and prevent resin pooling, pressure pads that mated with the fluoroelastomer bag were inserted.

To assemble the panel for cure, precured frames and mandrel inserts were located into the soft IML tool cavities. Adhesive was placed along the base of the frame and then the uncured drape formed stringer charges and silicon cure mandrels were located into the soft IML tool. The skin and cure caul plate were then placed on the frame / stringer subassembly.

The soft IML tool produced a net shape surface and controlled resin flow as shown in Figure 9. Pressure pads were successful in preventing the resin bleed in the mouse hole areas and provided pressure to cure the stringer section directly underneath the frame.

<sup>2</sup> Invar 36 is a steel with 36% nickel content produced by Inconol Inc.

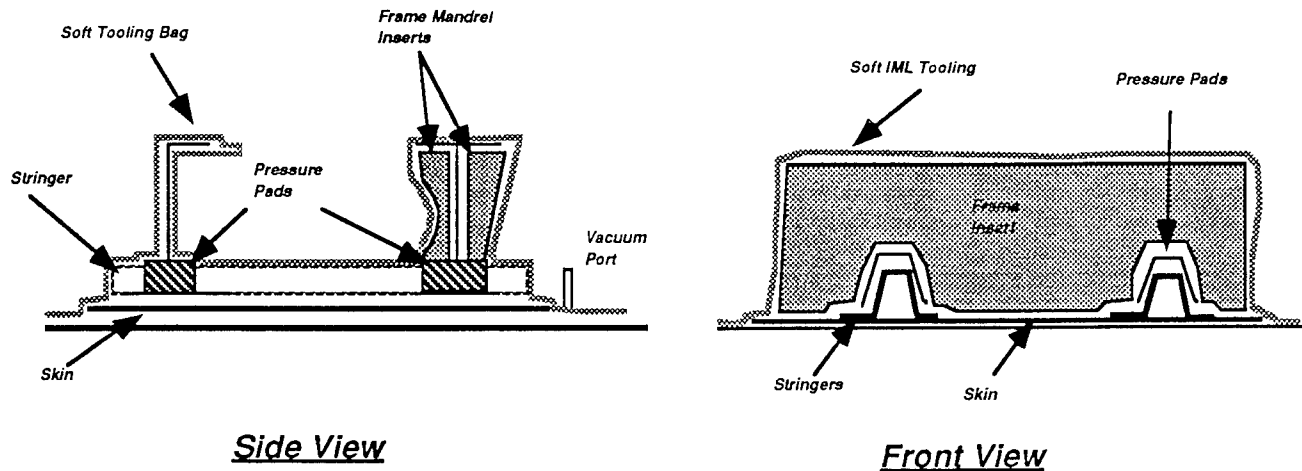


Figure 8: First IML Soft Tooling Configuration

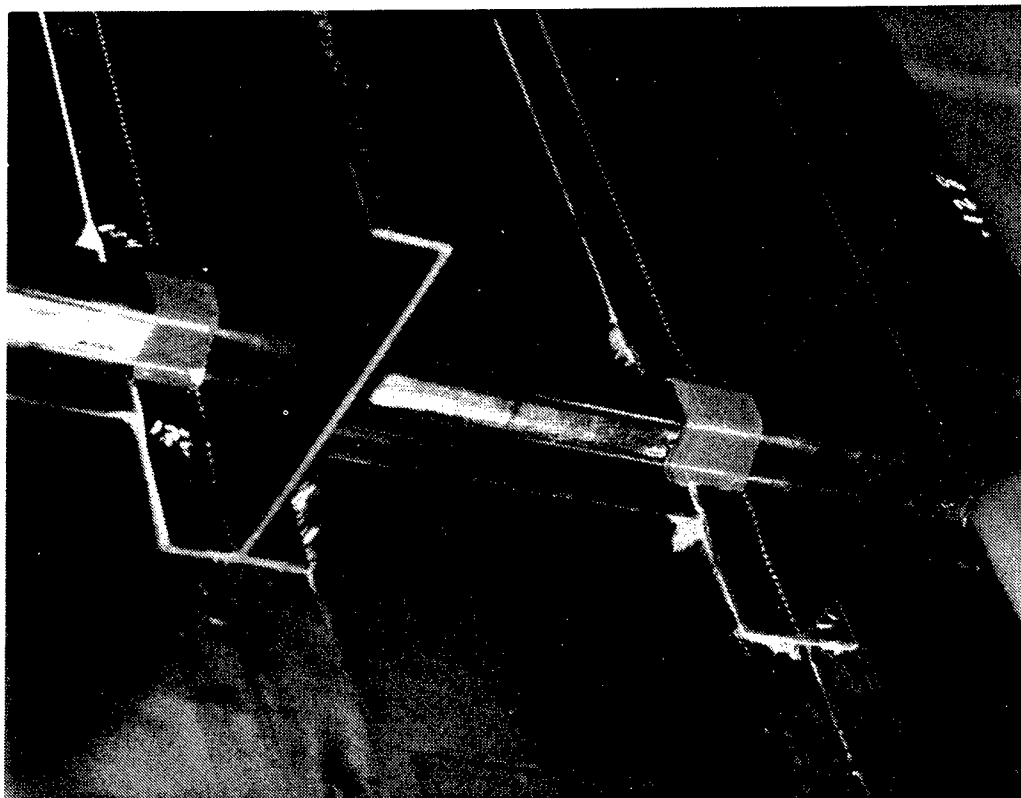
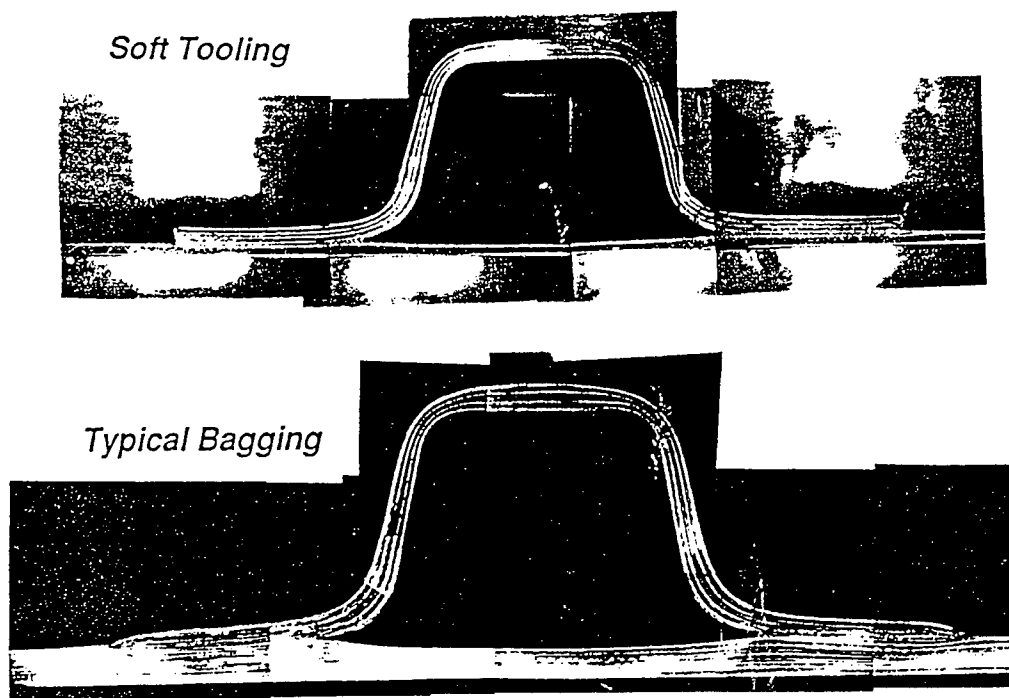


Figure 9: Cure Panel with Soft IML Tooling

Inspection of the panel indicated a good bond line with small voids caused by improper nesting of the soft IML tooling near the frame base flanges. The adhesive, skin, and stinger material did flow as expected to compensate for the interference/gap condition of the stringer-frame intersections. The soft IML tooling also trapped resin from bleeding up onto the frame flanges. A cross section of the stringers indicated that more stringer wall thickness control was achieved with the soft IML tooling when compared to a typical bagging process as shown in Figure 10.



**Figure 10: Stringer Effects of Soft IML Tooling and Typical Bagging Approach**

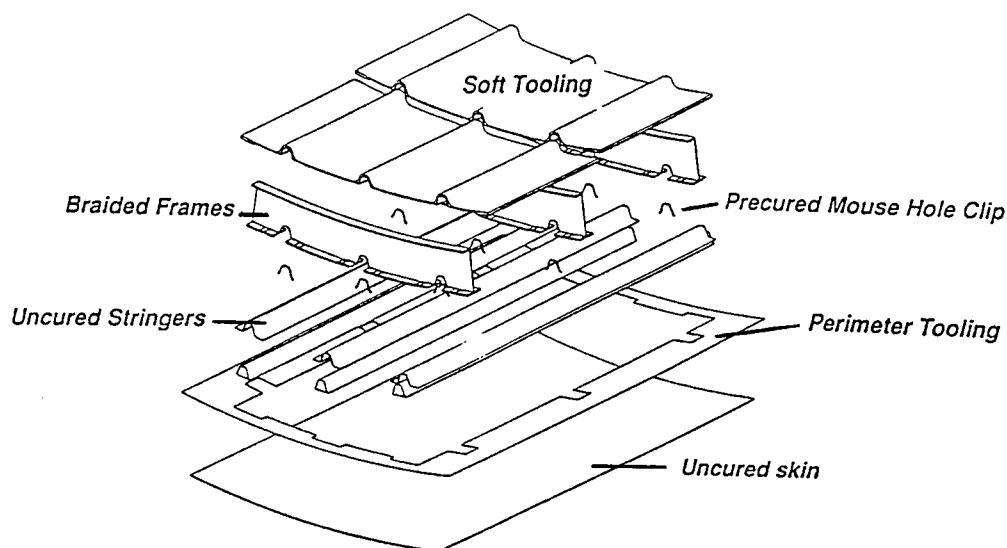
During and after the demonstration of the reversible assembly process with the soft IML tooling, problems were identified that required additional tooling modifications. Table 1 indicates the problems and solutions that were verified on the second tooling trial demonstration.

<i><b>Problem</b></i>	<i><b>Solution</b></i>
Difficult to manage one piece bag. Fit of multiple large parts with soft IML tooling bag is difficult.	Develop a two piece system 1. a continuous silicon bag for the cure bag 2. separate fluoroelastomer soft IML tooling for each frame bay
Parts did not nest properly with IML soft tooling causing resin pooling and cure pressure variations.	Taper the frame and stinger flanges to avoid tooling interference.
Mouse hole pressure pads can be misplaced easily causing resin rich areas or stringer tooling depressions.	Eliminate pressure pads with fly-away tooling.
The uncontrolled expansion of the stringer cure mandrels produced stringer thickness variations.	Develop a low CTE flexible extractable mandrel
Thickness variations of the soft IML tooling produced surface resin rich areas.	Construct soft IML tooling with uniform thickness

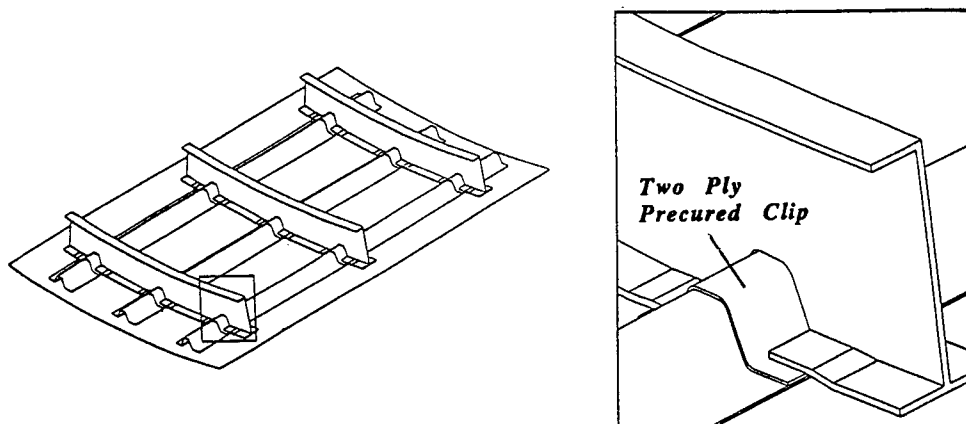
**Table 1: Results and Solutions for the Development of Soft IML Tooling**

## Optimization of the Soft Tooling Concept

A two piece soft IML tooling system was designed to meet the global assembly requirements. This concept involves the use of segmented soft IML tooling between each frame and a near net shape continuous silicon cure bag that covers the whole assembly (Figure 11). The silicon bag is textured so that there is a continuous air path across the panel. The mouse hole pressure pads were replaced with a two-ply precured hat shaped clip as shown in Figure 12. The clip accomplishes the same tooling requirements, but remains as part of the structure. The clip extends underneath the frame sections and beyond the edge of the frames so that resin is trapped and not permitted to bleed into the mouse hole area. The new clip concept not only reduced the number and complexity of the soft IML tooling, but eliminated the manual labor associated with locating the pressure pads. The revised soft IML tooling still retained the cost advantage by eliminating recurring bagging material (i.e. breather, separator film, etc.).



**Figure 11: Revised Soft IML Tooling Concept**

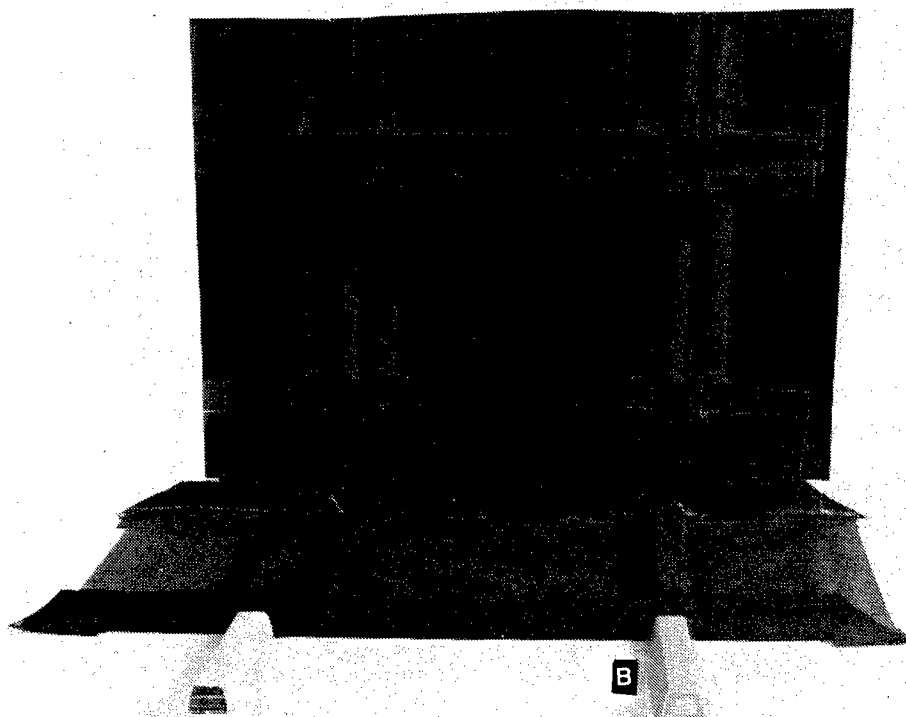


**Figure 12: Mouse Hole Clip Configuration**

To minimize the stringer gage thickness variations, a low CTE flexible mandrel was developed. The flexible mandrel is comprised of thin laminates constrained to flex only along the length of the mandrel. The mandrel is encapsulated with a silicon tube to prevent resin bleed between the laminates and aid in mandrel extraction.

### **Demonstration of the Revised Soft IML Tooling**

The second tooling trial was used to verify the new tooling concept with a curved panel. Since the large cure tool for the 3 ft. by 5 ft. and 7 ft. by 10 ft. panels was not completed, an existing steel 76 in. radius tool was used to cure a two frame / two stringer panel. The soft IML tooling was fabricated with a flat mock-up rather than a curved mock-up since the tooling is flexible enough to accommodate the radius bend without increasing manufacturing risks. The tooling trial included frames that were constructed of fabric and precured on steel tooling. After the panel was assembled onto the OML cure tool, a gap of 0.020" between the frames and skin was detected. This was attributed to a partially debulked skin and stringer lay-ups. To ensure that the skin, stringer, and frames were completely bonded without gaps, a 150 psi cure pressure was used. Figure 13 shows the cured panel and soft IML tooling used between frames. Point A is the soft IML tooling that is located between frames; point B is the silicon stringer cure mandrel, and point C is the new low CTE flexible stringer mandrel.



**Figure 13: Intricate Bond Panel and Soft IML Tooling**

Visual inspection of the panel showed that the IML soft tooling imparted a smooth net shape surface. Some resin pooling occurred along the non-tapered frame flange due to a gap between the soft IML tooling and frame flange. The fly-away mouse hole clip tooling performed as expected but some resin bled into the mouse hole area due to an error in the mock-up tool used to fabricate the soft IML tooling. The panel was inspected with through transmission and pulse-echo ultrasonic methods. No porosity was indicated in the panel or bond interfaces. Further sectioning of the stringers and frames revealed a few small voids near the skin-frame-stringer intersection ( see Figure 14). Point A shows voids in the precured fabric frames. These voids were eliminated in the precured resin transfer molded frames. The microphotographs indicate that both skin-frame-stringer intersections showed signs of an under-fill condition (compare points B and C). The actual under-fill condition prior to cure is difficult to determine since some resin bled into the mouse hole area. The tapered stringer flanges conformed more naturally minimizing the degree of skin movement (point B). The stringers were slightly mislocated but compensated by tapered stringer flanges and flexibility of the soft IML tooling to minimize resin pooling and skin wrinkles (point D). The flexibility of the soft IML tooling did not prevent resin bleeding of the non-tapered stringer flange (point E). Further inspection of the stringer cross section indicates that the low CTE flexible mandrel minimized the thickness variations and skin thinning under the hat stringer (compare points F and G). Point H shows a laminate wrinkle caused by an oversized radius filler. Although the flexible mandrel requires radius fillers that increase cost, the risk to extract the mandrel without damage is minimized.

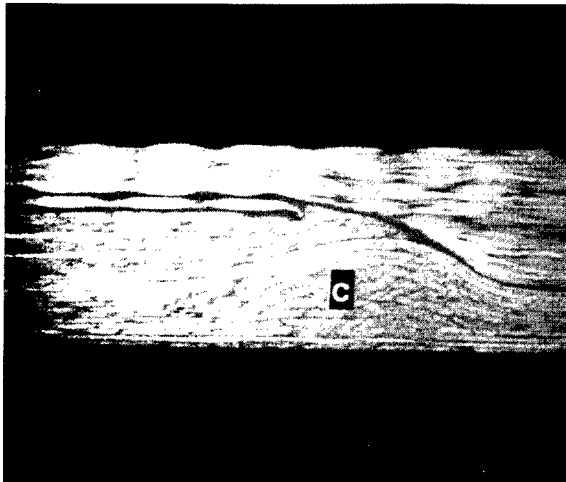
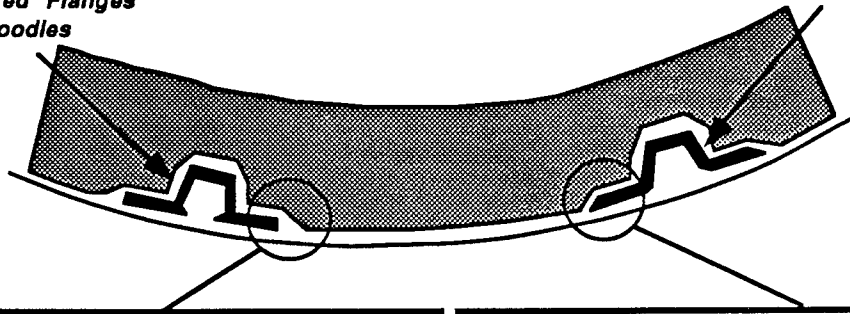
To fully address the assembly risks of the intricate bond design, causes and effects of panel warpage must be understood. During the development of the soft IML tooling, measurements were used to isolate causes of the panel warpage and minimize them through tooling modifications. Figure 15 shows transverse and longitudinal measurements from demonstration panels with and without frame elements.

Warpage data indicated that kinks in the panel occurred near the edges of the stringer flanges where resin pooling occurred. By tapering the stringer flanges and modifying the soft IML tooling, resin pooling on the outer flanges of the stringer was eliminated. Tooling changes and frame stiffening effects minimized the transverse panel warpage to 0.035 inch. Longitudinal warpage was minimized to 0.015 inch. Without the soft IML tooling and frame stiffening effects, larger deviations for a simple hat stiffened panel will occur.

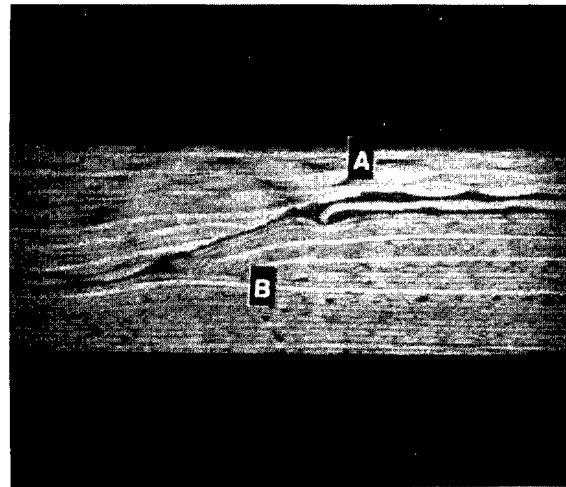
The revised soft tooling trial demonstrated that tapers on all stringers and frames are required to minimize the manufacturing anomalies with soft IML tooling. The low CTE flexible stringer mandrel controlled stringer and skin resin flow which is critical to minimizing panel warpage. The results of these tooling demonstrations will support the fabrication of the 3 ft. by 5 ft. and 7 ft. by 10 ft. intricate bond demonstration panels.

- Low CTE Cure Mandrel
- Non-tapered Flanges
- Radius Noodles

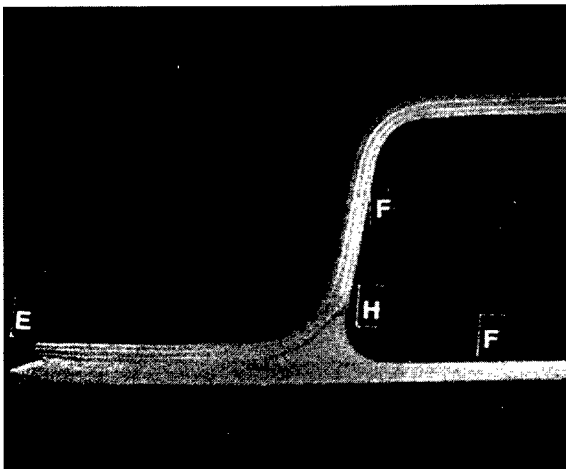
- Silicon Cure Mandrel
- Tapered Flanges



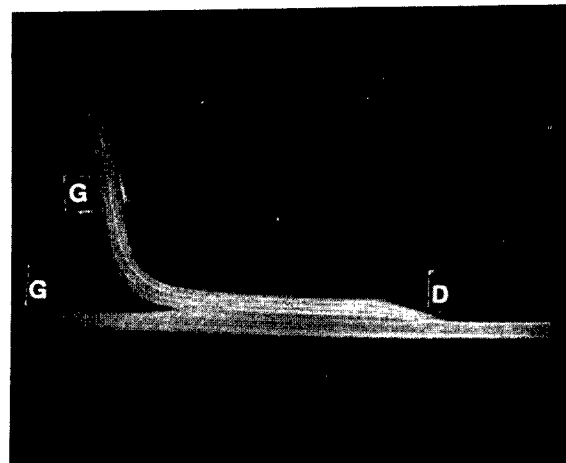
*Skin-Stringer-Frame Intersection*



*Skin-Stringer-Frame Intersection*

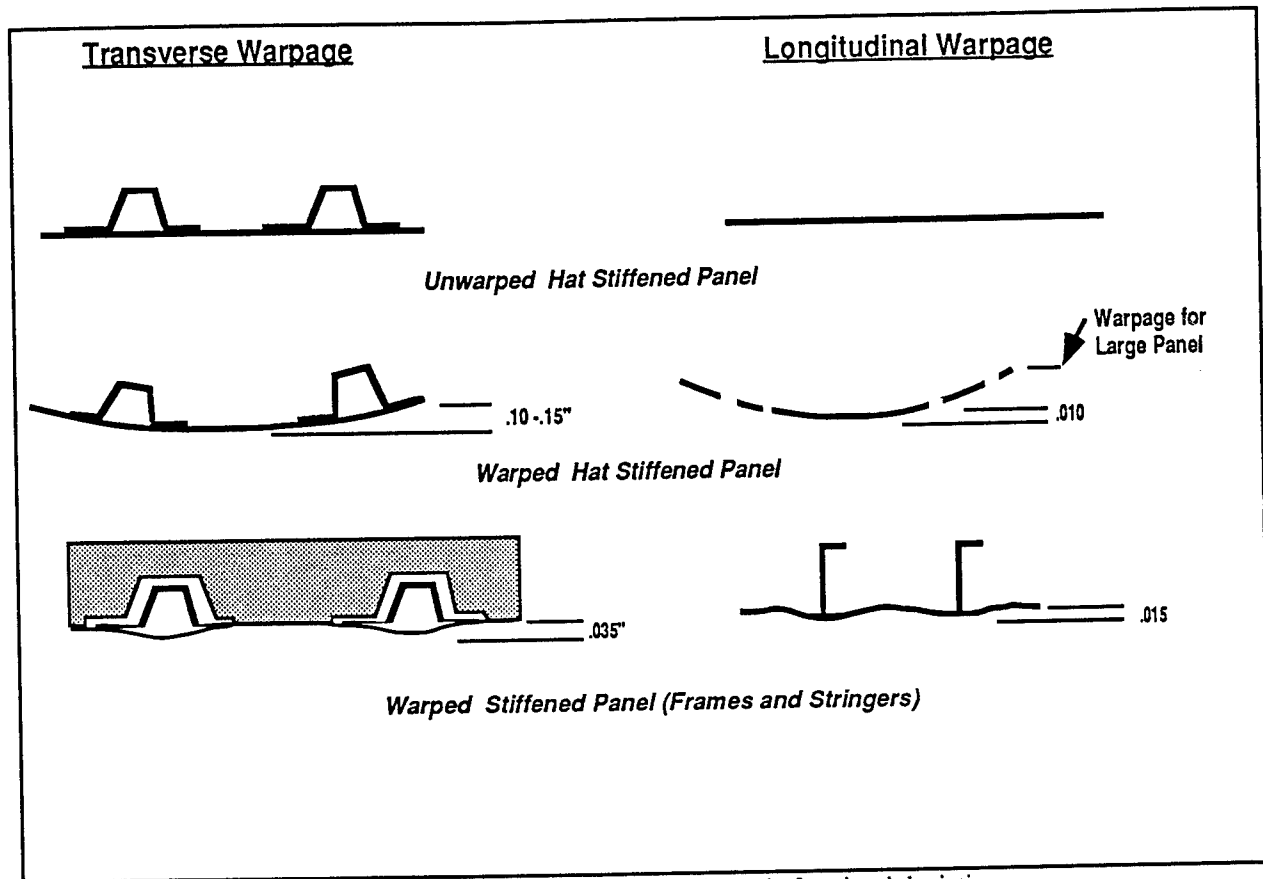


*Low CTE Flexible Mandrel*



*Low CTE Flexible Mandrel*

**Figure 14: Inspection of the Composite Panel Using the Revised Soft IML Tooling Concepts**

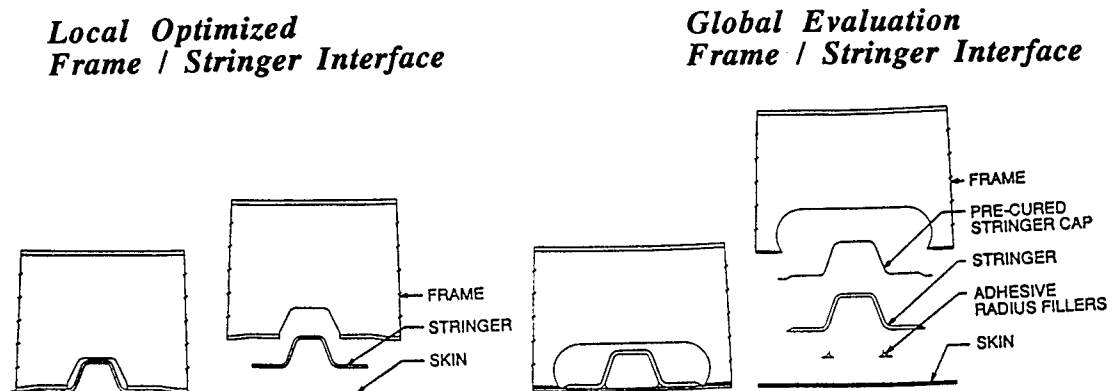


\* Illustrations exaggerate the warpage anomalies only for visual depiction

**Figure 15: Panel Warpage of Manufacturing Demonstrations**

### Local Optimization / Demonstration

During the local optimization process for the intricate bond configuration, manufacturing costs and risks were assessed and several design modifications were identified for additional cost benefits. One of the most significant modifications was a larger frame mouse hole (see Figure 16) that reduced tolerance build-up at the stringers-frame-skin interfaces and opportunities for lower cost assembly methods could now be utilized.

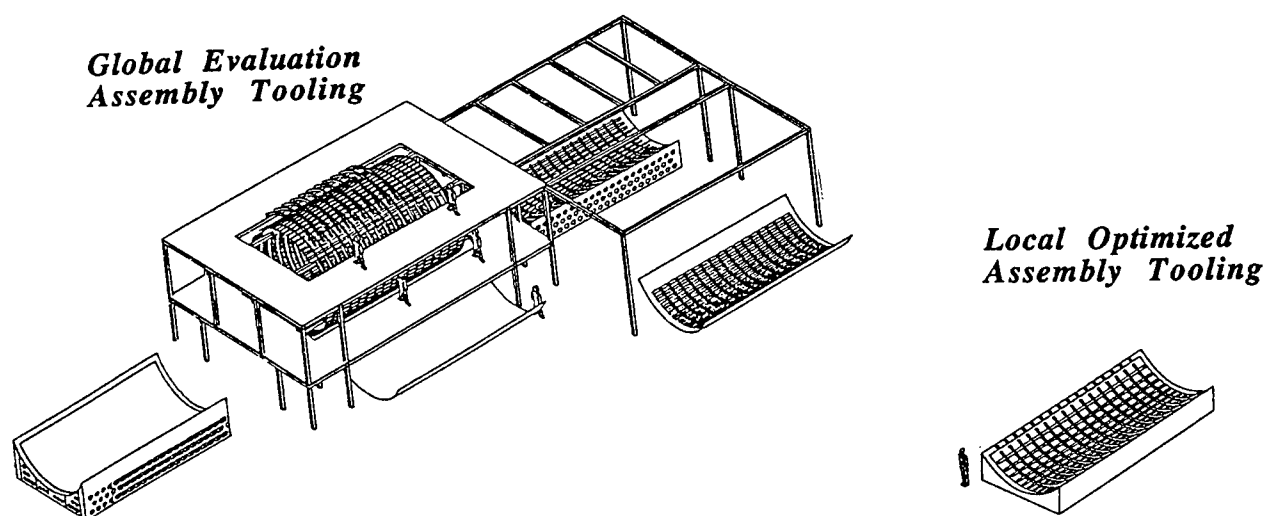


**Figure 16: Mouse Hole Designs**



The reverse assembly method for the global configuration was driven by the fact that the mouse hole size restricted the ability to place frames on a preassembled skin-stringer panel. The larger mouse hole eliminates this restriction and a new panel assembly method was evaluated. Assembly costs were reduced by eliminating the need for the rotisserie assembly tool. Initial design assessment of the new mouse hole configuration reduced the frame weight by 8.5% without increasing the cost. The DBT determined that the modification to a larger mouse hole would require further testing to evaluate the structural performance impact.

The optimized panel is assembled on the OML cure tool with clamps to locate and secure the frames for cure. First, the skin and stringers are located onto the OML cure tool. Then the frames are located and clamped. The frame clamp design is critical so that the frames are only constrained to maintain frame spacing. The inability of the frames to adjust to skin and stringer debulking during cure may increase the risk of bond line voids due to inadequate skin cure pressure. Therefore, the clamps were designed with two degrees of freedom to eliminate these risks. The new assembly method as shown in Figure 17 not only reduced the number of assembly tools, but reduced manufacturing risks by eliminating panel assembly transfers and potential high risk factory flow problems.

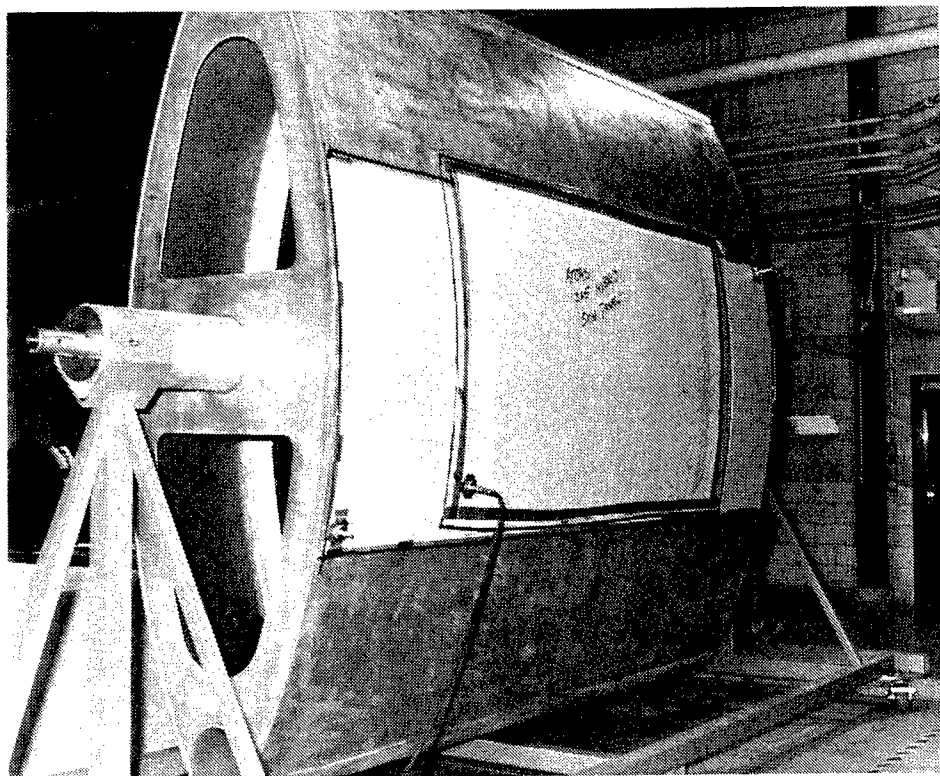


**Figure 17: Comparison of the Global and Local Panel Assembly Tooling**

The new mouse hole and finalized soft IML tooling configuration was demonstrated on a two frame / three stringer curved panel. The panel included resin transfer molded triaxial braided frames with a 20° tapered flange. The frame fabrication procedures were optimized by Boeing and Fiber Innovations and are summarized in reference 7.

## Demonstration of Key Low Cost Manufacturing Technologies

The local optimization key manufacturing technologies were integrated and demonstrated with the fabrication of two 3 ft. by 5 ft. panels. For proper verification of the optimized manufacturing plans, critical tooling for skin fabrication and cure of the intricate bond assembly were designed and constructed. A winding mandrel was designed for parts up to 10 ft. by 14 ft. long and was constructed with aluminum to minimize weight. To demonstrate the tow placement of multiple large skins, a double lobed mandrel was designed to meet the ATP work space limitations (see Figure 18).



**Figure 18: ATP 122" Radius Winding Mandrel**

The OML cure tool for 3 ft. by 5 ft. and 7 ft. by 10 ft. demonstration panels was designed by Hercules and Boeing and fabricated by Ebco, Vancouver, B.C. with Invar 36 material. The skin gage is 3/4 inches and the support structure is 3/8 inches thick. Since Invar 36 material has a lower heat up rate than steel or composite, the support structure was designed with large air passages to increase heat transfer by convection. This has been proven to be very effective in reducing tool weight without sacrificing rigidity critical for tool dimensional stability. To ensure tool quality, Boeing used a computerized advanced theodolite system (CATS) to measure the surface irregularities as shown in Figure 19. About 250 points on the tool surface were digitized and compared to a cylindrical surface of a 12 inch radius. The standard deviation was  $\pm 0.007$  inch which satisfies the requirement of  $\pm 0.010$  inches.

### Local Optimized Fabrication Demonstration

The two 3 ft. by 5 ft. demonstration panels were fabricated as part of the scale-up process for the final crown 7 ft. by 10 ft. demonstration panels. One of the 3 ft. by 5 ft. panels was constructed

with a hybrid material form consisting of 25% S-2 glass and 75% AS4 fiber. The skin and stringer charges were tow placed onto the double lobed winding mandrel and debulked (Figure 20). After the skins were wound with the 32 tow placement band head, the skins were placed into the Invar OML cure tool. The skin was oriented to the OML cure tool with the aid of a S-2 tow that was tow placed along the edge of the panel. The tow placed stringer charges were then trimmed and drape formed over the low CTE flexible mandrels. The stringers and cure tooling were then located onto the skin with the aid of a mylar template. The precured mouse hole clips and adhesive were then compacted onto the stringers at the frame-stringer intersection. Next, the three precured resin transfer molded frames were located and the soft IML tooling was placed between the frames. After the silicon bag had been secured and vacuum tested the panel was cured.

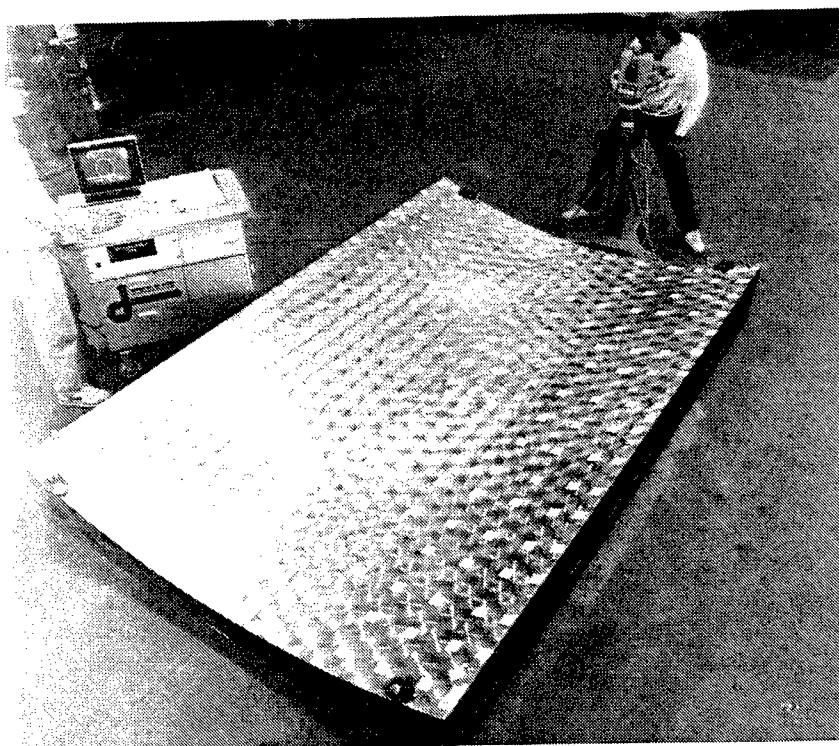


Figure 19: 122" Radius Invar Cure Tool

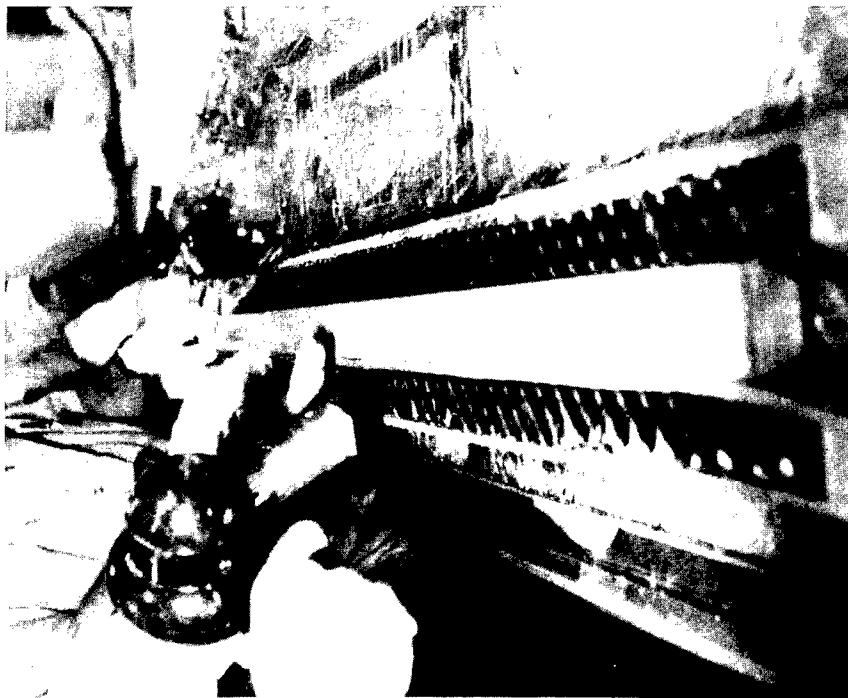


Figure 20 Stringer Drape Formed onto Mandrels



Figure 21 Locating Frames

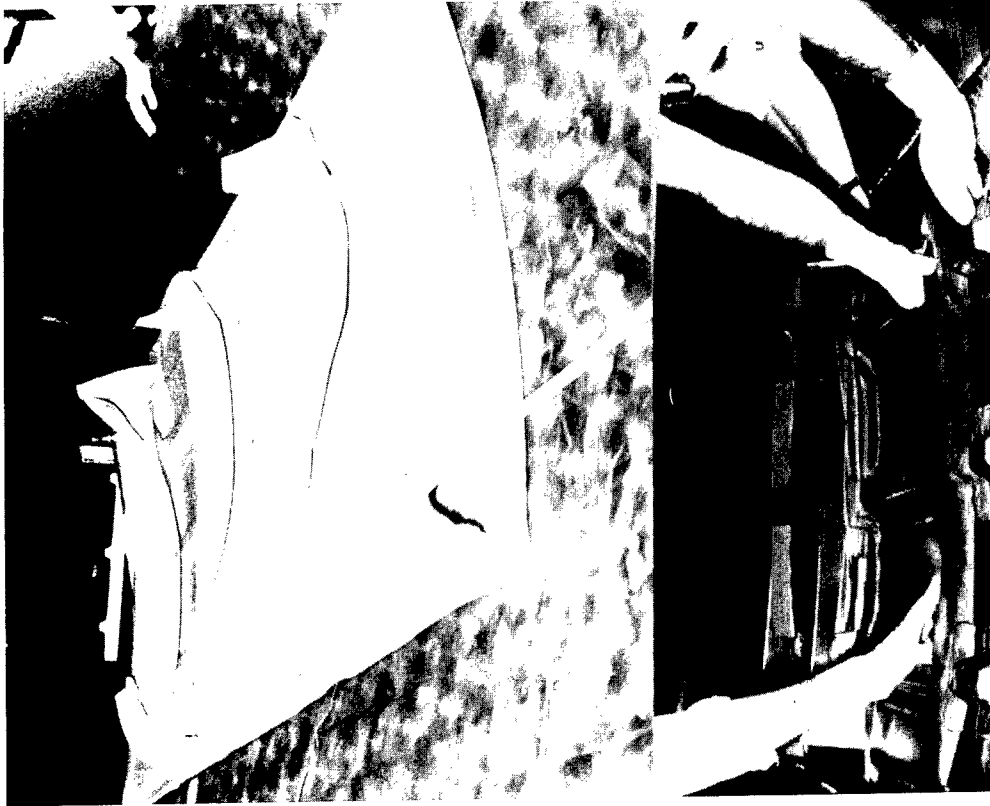


Figure 23 Placement of Silicon Cure Bag



Figure 22 Locating Soft IML Tooling

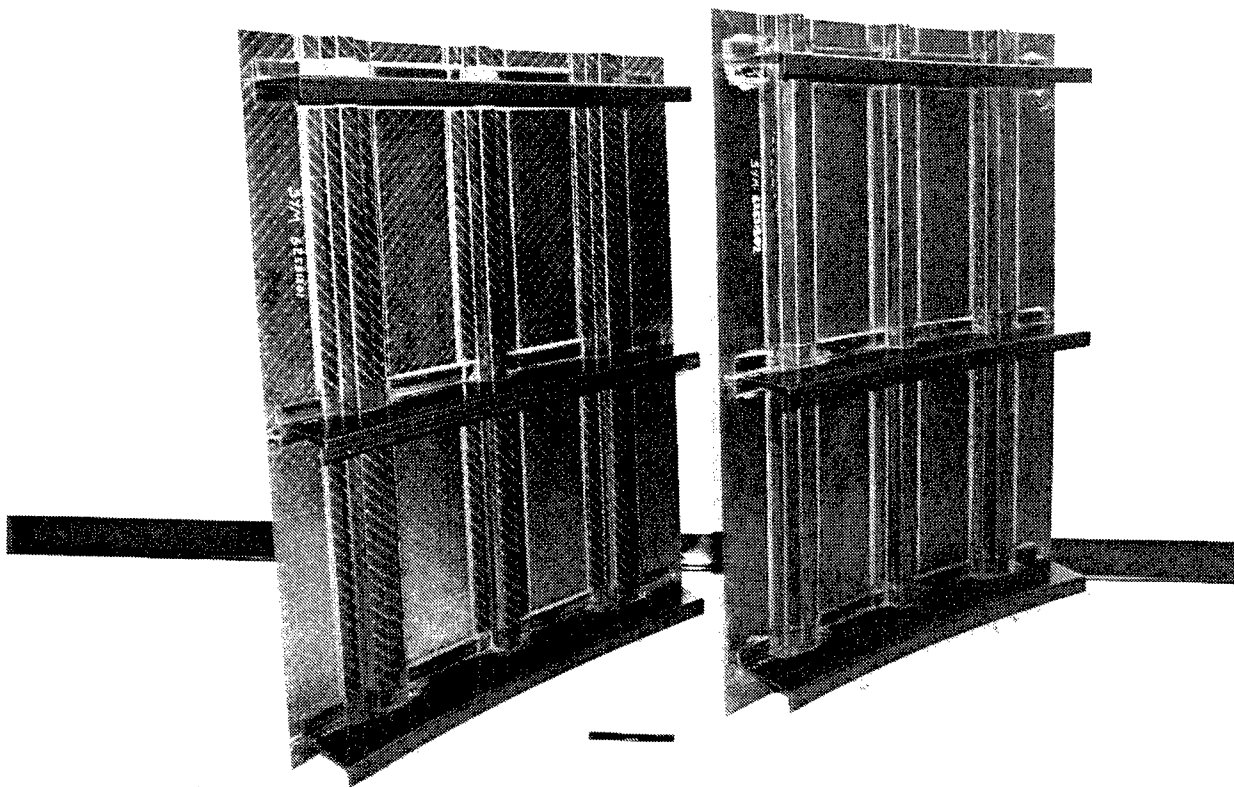


Figure 24 Cured Panels

## Cost Reduction by Manufacturing Demonstrations and Factory Simulation

Through the optimization process, the DBT minimized risk and cost for the intricate crown panel configuration. In conjunction with the manufacturing demonstrations, the factory was simulated for producing crown panels according to the NASA ACT ground rules (Ref. 1). The simulation process identified additional savings by optimizing tooling and batch sizes to reduce high risk factory flow problems. The following cost, weight, and risk savings represent the final local optimized design as shown in Figure 5.

Tables 2-4 represent the results of the local optimization process for the crown panel. The results of either design or manufacturing changes and how they impact cost, manufacturing risk and structural performance are summarized. It should be noted that additional optimization will be required beyond the local optimization which integrates the side and keel panel fabrication requirements.

### Cost Savings of Local Optimized Frames

A 30% savings in frame fabrication costs was realized from two major effects (see Table 2). One effect is the elimination of the bottom ply cap which reduced the number of preform elements and labor costs to fabricate and place (see Figure 25). The cap was initially a manufacturing criterion, but through the manufacturing demonstrations, its need was eliminated.

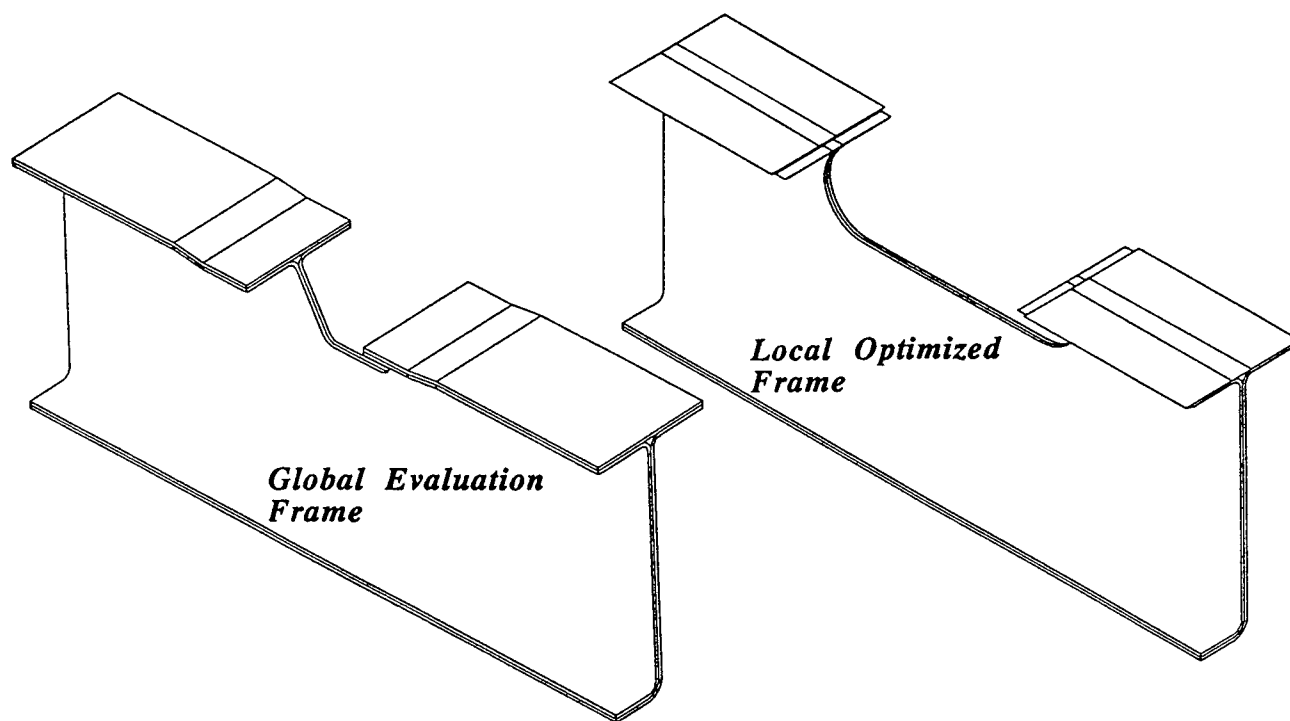


Figure 25: Global and Local Optimized Frame

The other major cost savings for the frames related to a reduction in tooling costs. Factory simulation results showed that sixteen RTM tools could be reduced to five and still meet the desired crown panel production rate. This reduced the total panel costs by 3.2% as indicated in Table 2. Some frame design modifications were identified that minimized manufacturing risks. Although costs saving were not projected for these modifications, risk of manufacturing anomalies were reduced.

<u>Global</u>	<u>Local</u>	<u>Purpose</u>	<u>Optimization Method</u>	<u>Impact</u>		
				Savings	Manuf. Risk	Struct. Perform.
Small Mouse Hole	Wider Mouse Hole	o Reduce tolerance build-up o Reduce tooling cost	- DBT - Demonstration	.6 %	Reduced	TBD
16 tools	5 tools	o Reduce tooling cost	-Factory Simulation	16.2 %	NA	NA
Bottom Cap	No Cap	o Increase Performance o Reduce cost o Reduce weight	- DBT - Demonstration	13.3 %	Reduced	Increased
Braided Noodle	Adhesive Noodle	o Increase damage tolerance	- Design Analysis - Demonstration	0 %	Reduced	Increased
Flange edge	Tapered Edge	o Minimize resin pools o Lower cure bagging risks o Increase pull-off strength	- Structural Tests - Demonstration	0 %	Reduced	Increased

Total Frame Savings 30.1%

Total Panel Savings	3.2 %
---------------------	-------

Table 2: Savings of Local Optimized RTM / Braided Frames

### Cost Savings of Optimized Panel Assembly/Cure

One of the high risk areas identified with the crown panel configuration was the ability to bag and cure the frames, stringers, and skin together. The larger mouse hole design eliminated the rotisserie tool and allowed the use of the OML cure tool as an assembly tool. These changes reduced tooling costs, factory floor space, and the potential for factory flow problems. A panel assembly cost of 22.2% savings was gained which reduced the total panel cost by 4.9% (see Table 3).

<u>Global</u>	<u>Local</u>	<u>Purpose</u>	<u>Optimization Method</u>	<u>Impact</u>		
				Savings	Manuf. Risk	Struct. Perform.
1-piece reusable cure bag	2- piece Bag	o Reduce Labor costs o Reduce tooling costs o Robust for tolerance o Uniform Pressure control	- Factory Simulation - Demonstration	18.5 %	Reduced	Reduced anomalies
Reverse Panel Assembly	Assembly on OML cure tool	o Eliminate tooling o	-Design Optimizer -Factory Simulation	3.7%	Reduced	NA
Bag-frame stringers-skin	Skin-frames stringers-bag					

Panel Assembly Savings 22.2%

Total Panel Cost Savings	4.9%
--------------------------	------



**Table 3: Savings of Local Optimized Panel Assembly**

**Cost Savings of Optimized Skin and Stringers**

The major cost savings for stringers was accomplished by reducing the number of processing steps with the flexible low CTE mandrels and automated trimming operations. When the tow band width was increased from four inches to six inches, a 2.6% cost savings was realized for the skin and stringer fabrication costs. The stringer and skin cost savings was 17.8% which reduced the total crown panel cost by 2.2% as shown in Table 4. The combination of all cost savings generated a total panel savings of 10.7 % (Tables 2-4).

<u>Global</u>	<u>Local</u>	<u>Purpose</u>	<u>Optimization Method</u>	<u>Impact</u>		
				Savings	Risk	Struct. Perform.
4" Tow band width	6" Tow band width	o Reduce Labor costs	Factory Simulation	Skins 2.6 %  Stringers 5.6%	Reduced	TBD
16 stringers	10 Stringers	see Ref. 5	-Design Optimizer -Factory Simulation	see Ref. 5	NA	NA
Manual Trimming	Automated trimming	o Reduce labor costs	- Factory Simulation - Demonstration	14.4 %	Reduced	NA
Stringer non-tapered edge	Tapered Edge	o Minimize resin pools o Lower cure bagging risks o Increase pull-off strength	- DBT - Demonstrations	0 %	Reduced	Increased
Rubber cure tooling	Flexible low CTE cure tooling	o Minimize resin pools o Lower cure bagging risks o Increase pull-off strength o Reduce tooling costs o Reduce processing steps o Increase part tolerance control	- Factory Simulation - Demonstration	.1 %	Reduced	Increased
Drape Forming	Optimized procedures	o Reduce processing steps o Optimize procedures	Simulation	3.3%	Reduced	NA

**Total Skin and Stringer Savings      17.8 %**

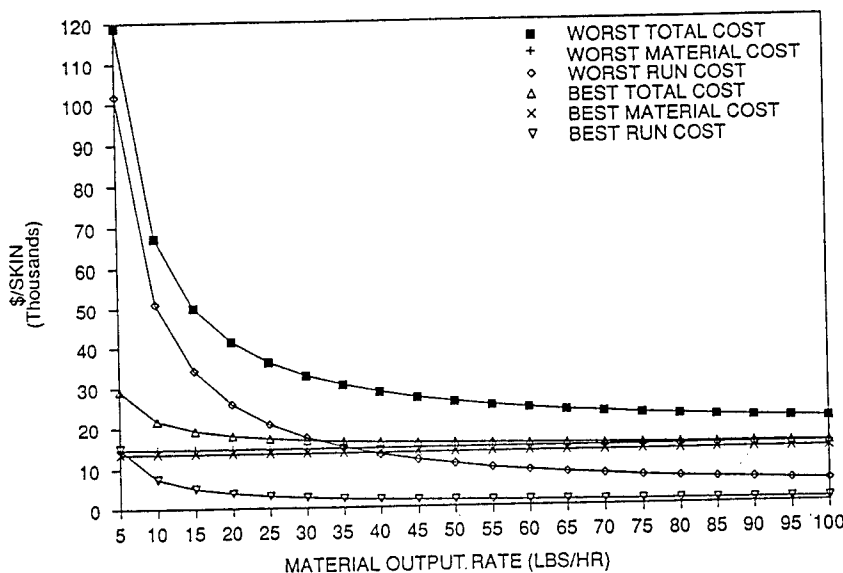
<b>Total Panel Cost Savings</b>	<b>2.2 %</b>
---------------------------------	--------------

**Table 4: Savings of Local Optimized Skin and Stringers**

## Sensitivity Studies of the ATP Process

The ATP process was chosen early on as a promising fabrication process for the manufacturing of crown skins in the ATCAS program. One of the benefits of the ATP process is the low cost material form 938<sup>3</sup>/AS4<sup>4</sup> tow. A model was constructed for the ATP process to understand process sensitivities and how the affects of processing assumptions on cost and risk. ATP payout rate, down time, crew size, and capital investment for a variety of production rate requirements were evaluated for cost impact.

Figure 26 shows the range of crown skin costs as a function of machine pay out rates (see appendix for assumptions made in best and worst case scenarios). The pay out rate is the amount of material in pounds per hour that can be placed for a given design. In this figure, the unutilized capacity of the tow placement equipment was assumed to be used on other parts (i.e. side or keel panels), minimizing the effect of capital equipment costs. Output rates of 50 lbs/hr or more tend to isolate risks associated with the ATP process. Design details such as adding local reinforcement on skin panels affects both the total costs and cost variability due to a lower material output rate. If the design details affect the material output rate enough, the ATP process could no longer be cost effective. The effects of capital equipment costs can be important due to the relationship between material output rate and final cost. This trend may be true for other processes as well.



**Figure 26: Composite Skin Panel Costs vs. Machine Rates**

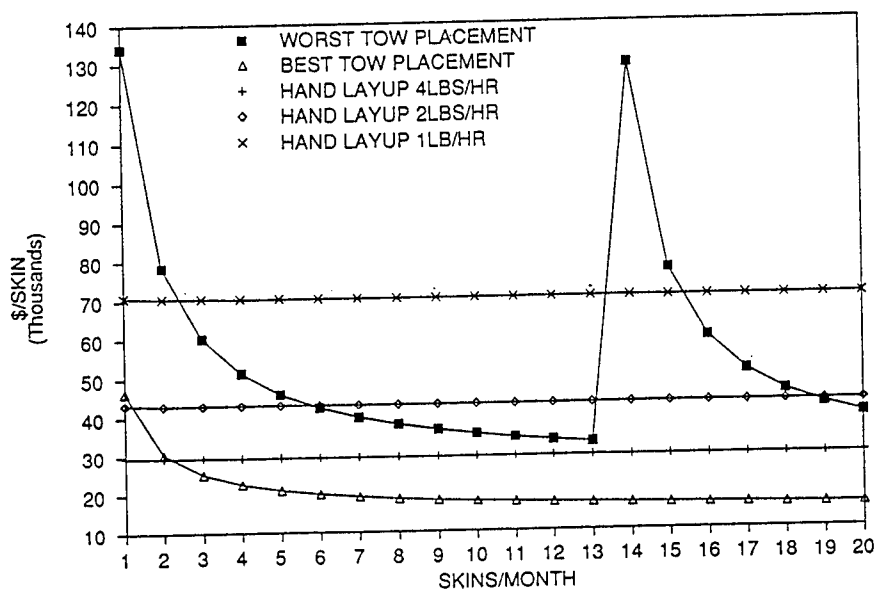
The effects of production volume on cost are shown in Figure 27. Unlike Figure 26, unused capacity of the tow placement equipment was burdened over the crown skins produced. The best and worst tow placement scenarios were evaluated and compared to a hand layup process with various output rates.

As the worst case tow placement curve approaches full utilization, additional equipment must be purchased, resulting in a spike in the curve. The curve representing the best tow placement scenario assumes a much higher material output rate and the point at which full utilization of the equipment is reached is far off the scale of crown skins/month. Again, the relationship between design details,

3 938 is an epoxy resin system produced by ICI Fiberite

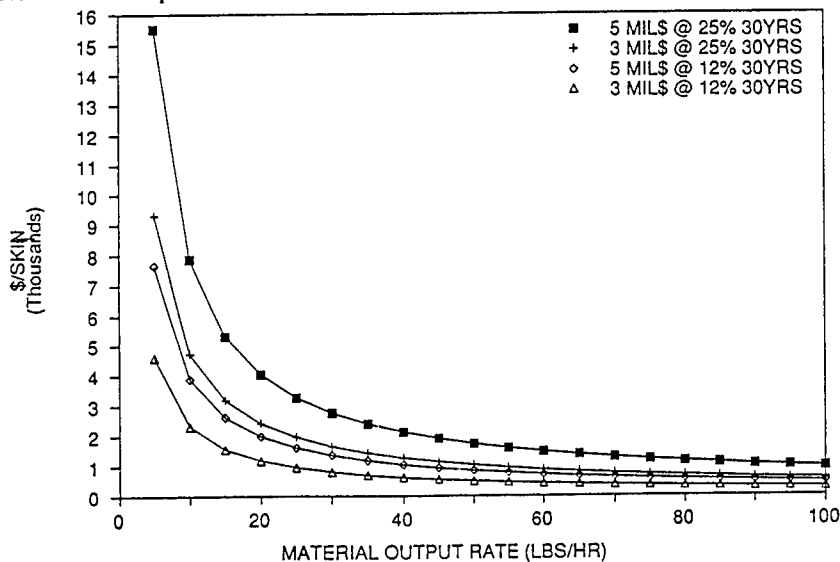
4 AS4 is a graphite fiber system produced by Hercules Inc.

material output rate, and production volume can influence the cost of implementing a given manufacturing process.



**Figure 27: Skin Panel Cost vs. Production Rates**

The effects of capital costs and rates of return burden on the production cost of crown skins are shown in Figure 28. This relationship is the dominant reason for the increased costs for low material output rates shown in Figure 26 and 27. Many factors can influence the cost of the equipment, including variable tax incentives, national interest rates, and company resources. Higher material output rates reduce the cost and risk of capital equipment related issues which dominate the costs for a low production rate or a low material output rate.



**Figure 28: Panel Costs vs. Machine Cost Rate of Return**

The evaluations shown in Figure 26-28 depict trends for ATP manufacturing risk and cost. Additional evaluations that include the effects of machine down time, machine crew sizes, and hourly pay wages must be conducted to better understand their impact to the manufacturing process.

## CONCLUSIONS AND RECOMMENDATIONS

The manufacturing technologies identified for the global crown panel configuration were demonstrated and optimized to reduce cost by 10.7 %. The demonstration panels provided warpage and panel dimensional accuracy information that is critical for determining cost and risk for fuselage assembly. Tow placed skins, resin transfer molded frames, and drape formed stringers were assembled and cured with innovative soft IML tooling and cure mandrels. The development of the innovative tooling required several manufacturing trials to minimize anomalies that would impact structural performance. Although the first manufacturing demonstrations were relatively small compared to the full size crown panel, tooling and processing parameters were selected and developed for scale-up to the 15 ft. by 31 ft. crown panels. The local optimized panel design was also evaluated with factory simulation software that further reduced cost by determining batch sizes and machine requirements. To fully realize the cost of a quadrant panel or full barrel section, additional optimization must be performed to include the keel and side quadrants. This cost optimization must include the equipment utilization for all quadrants.

The ATP technology offers significant cost advantages for fabricating large composite fuselage skins. The ATP process is capable of batch mode processing, tow placing low cost material forms, and can add / drop material on the fly. The processing rates of the ATP process can be modified depending on the required production rate with the use of multiple heads or wider material band widths. In order to maximize the cost benefits associated with the ATP automation, manual or frequent interruptive inspection tasks must be eliminated with the use of Statistical Process Control (SPC) or other automated non-interruptive inspection methods.

Use of automated composite fabrication processes must be justified by an improvement in the total part cost. The determination of which set of fabrication processes is best for a structural application is possible only after gaining some understanding of the fabrication process, structural requirements, and production rates. Given the amount of interaction between fabrication processes, design variables, and production rate ranges, computer based design models appear to be the best way to perform trades due to the many competing and reinforcing interrelationships.

Verification of crown panel processes for production readiness must be supported by additional large scale assembly demonstrations. These additional demonstrations must include evaluations of fully automated manufacturing processes to determine actual processing rates to determine final costs.

## REFERENCES

1. L.B. Ilcewicz, T.H. Walker, G. Truselove, K. Willden, G.D. Swanson, and C. Pfahl, "Application of a Design-Build-Team Approach to Low Cost and Weight Composite Fuselage Structure," to be Published as a NASA Contractor's Report 1991
2. T.H. Walker, P. Smith, G. Truselove, K. Willden, S. Metschan, C. Pfahl, " Cost Studies for Commercial Fuselage Crown Designs", First NASA Advanced Composite Technology Conference, Seattle, WA, October 29-November 1, 1990, NASA-CP-3104
3. L.B. Ilcewicz, P. Smith, T.H. Walker, R. Johnson, " Advanced Technology Composite Aircraft Structures", First NASA Advanced Composite Technology Conference, Seattle, WA, October 29-November 1, 1990, NASA-CP-3104
4. K.S. Willden, S. Metschan, V. Starkey, " Process and Assembly Plans for Low Cost Commercial Fuselage Structure", First NASA Advanced Composite Technology Conference, Seattle, WA, October 29-November 1, 1990, NASA-CP-3104

5. G.D. Swanson, L.B. Ilcewicz, T.H. Walker, "Local Design Optimization for Transport Fuselage Crown Panels", presented at the Ninth DoD/NASA/FAA Conference on Fibrous Composites in Structural Design, Lake Tahoe, Nevada, November 4-7, 1991
6. T.H. Walker, W.B. Avery, L.B. Ilcewicz, C.C. Poe, C.E. Harris, "Tension Fracture of Tow Placed Laminates For Transport Fuselage Applications", presented at the Ninth DoD/NASA/FAA Conference on Fibrous Composites in Structural Design, Lake Tahoe, Nevada, November 4-7, 1991
7. M.J. Fedro, K.S. Willden " Characterization and Manufacture of Braided Composites for Large Commercial Aircraft Structures", presented at the Ninth DoD/NASA/FAA Conference on Fibrous Composites in Structural Design, Lake Tahoe, Nevada, November 4-7, 1991

## Appendix

### Assumptions for Figure 28

	<u>Best</u>	<u>Worst</u>
Cost of Capital Equipment:	\$ 3M	\$5M
Rate of Return:	12%	25%
Life:	30 yrs.	30 yrs.
Utilization:	Unused capacity used by other parts	
Production		
Hours / Month:	700	325
Skins / Month:	5	5
Material Output Rate:	Variable	Variable
Down Time:	10%	40%
Material Waste	8%	16%
Crew Size:	1	2
Hourly Rate:	\$100 / hr.	\$ 200 / hr.

### Assumptions for Figure 29

Same as above except

Utilization	Unused capacity burdened over production	
Production		
Skins / Month:	5	5
Material Output Rate:	78 lbs / hr.	30 lbs /hr

### Assumptions for Figure 30

Cost of Capital Equipment:	Variable
Rate of Return:	Variable
Life:	30 yrs.
Utilization:	Unused capacity used by other parts
Production	
Hours / Month:	700
Skins / Month:	5
Material Output Rate:	Variable
Down Time:	10%
Material Waste	8%
Crew Size:	1
Hourly Rate:	\$100 / hr.

**THIS PAGE INTENTIONALLY BLANK**

**SESSION V-D**  
**TEXTILE PREFORM TECHNOLOGY**



**THIS PAGE INTENTIONALLY BLANK**

## **RECENT PROGRESS IN NASA LANGLEY TEXTILE REINFORCED COMPOSITES PROGRAM**

H. Benson Dexter, Charles E. Harris, and Norman J. Johnston  
NASA Langley Research Center  
Hampton, Virginia

### **INTRODUCTION**

The NASA Langley Research Center is conducting and sponsoring research to explore the benefits of textile reinforced composites for civil transport aircraft primary structures. The objective of this program is to develop and demonstrate the potential of affordable textile reinforced composite materials to meet design properties and damage tolerance requirements of advanced aircraft structural concepts. In addition to in-house research, the program was recently expanded to include major participation by the aircraft industry and aerospace textile companies. The major program elements include development of textile preforms, processing science, mechanics of materials, experimental characterization of materials, and development and evaluation of textile reinforced composite structural elements and subcomponents. The NASA Langley in-house focus is as follows: development of a science-based understanding of resin transfer molding (RTM), development of powder-coated towpreg processes, analysis methodology, and development of a performance database on textile reinforced composites. The focus of the textile industry participation is on development of multidirectional, damage-tolerant preforms, and the aircraft industry participation is in the areas of design, fabrication, and testing of textile reinforced composite structural elements and subcomponents.

Textile processes such as 3-D weaving, 2-D and 3-D braiding, and knitting/stitching are being compared with conventional laminated tape processes for improved damage tolerance. Through-the-thickness reinforcements offer significant damage tolerance improvements. However, these gains must be weighed against potential loss in in-plane properties such as strength and stiffness. Analytical trade studies are underway to establish design guidelines for the application of textile material forms to meet specific loading requirements. Fabrication and testing of large structural components are required to establish the full potential of textile reinforced composite materials. The goals of the NASA Langley-sponsored research program are to demonstrate technology readiness with subscale composite components by 1995 and to verify the performance of full-scale composite primary aircraft structural components by 1997.

## TEXTILE REINFORCED COMPOSITES

### - RESEARCH TEAM -

The team that has been assembled to conduct research on textile reinforced composites is shown in figure 1. The current team includes NASA Langley in-house personnel, numerous universities, textile fabricators, and major aerospace contractors. The team will expand to meet program needs as required. Recent program emphasis has been on development of aircraft quality textile preforms, development of science-based processes, development of mechanics methodologies, and experimental characterization of textile reinforced composite materials. As these technologies mature, future emphasis will shift to design, analysis, fabrication, and test of structural elements and subcomponents. The recent addition of Lockheed to the team and the redirection of Grumman will provide a much needed aircraft structures focus to the textile reinforced composites program.

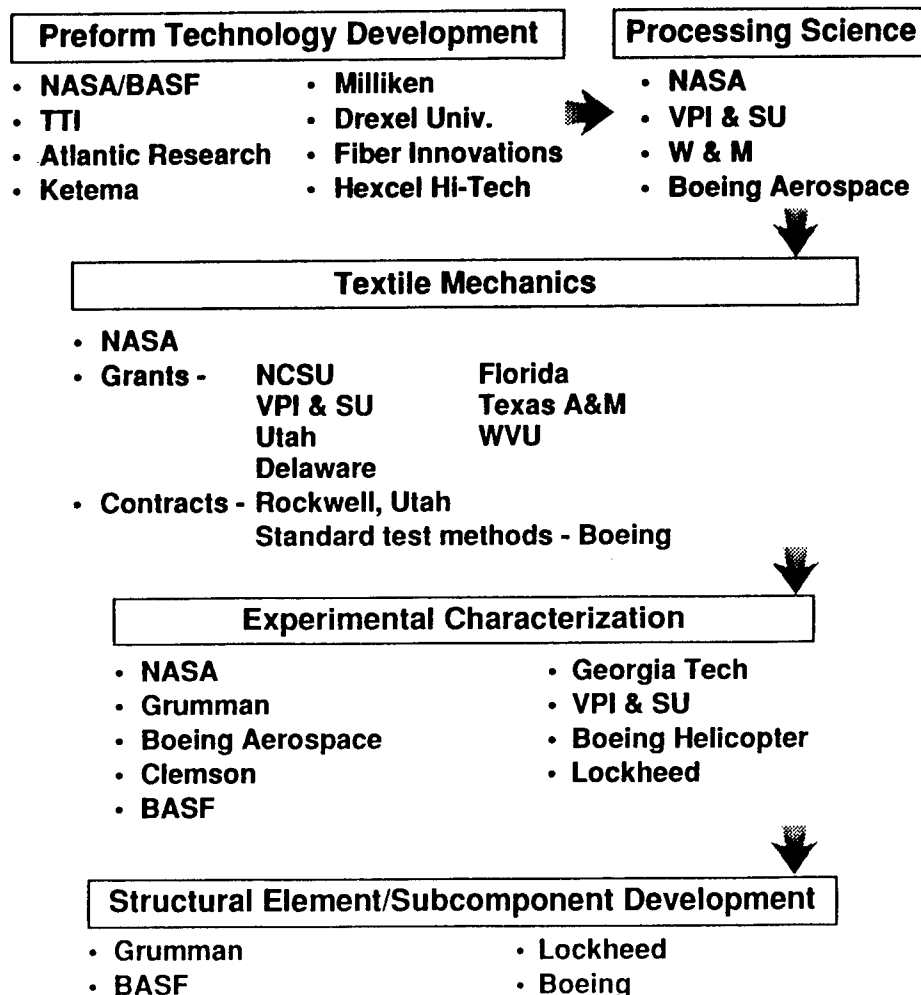


Figure 1

## ACT CONTRACTS FOCUSED ON TEXTILE REINFORCED COMPOSITES

The four Advanced Composites Technology (ACT) contracts that are focused on textile reinforced composites are summarized in figure 2. The Lockheed Aeronautical Systems contract is focusing on the application of textile materials to aircraft fuselage structures. Textile preforms, RTM and powdered epoxy resins, and innovative tooling concepts will be developed for four types of fuselage structural subcomponents. Included will be circumferential frames, window-belt insert, keel beam/frame intersection, and crown panels. Composite subcomponents will be tested at Lockheed, NASA Langley, and Boeing Commercial Airplane Co.

The Grumman contract is focusing on cross-stiffened integrally woven fuselage elements and lower side quadrant fuselage panels. The evaluation of integrally woven wing Y-spars has been completed. In addition, Grumman will focus on developing design guidelines and analysis methods for through-the-thickness reinforced composite structural elements. The Rockwell contract is focusing on the fatigue response of woven composites. Experiments are being conducted and micromechanics models are being developed to characterize damage initiation and growth. Strength and fatigue life prediction methods are also being developed for textile reinforced composites.

The BASF contract is focusing on commingled thermoplastic/carbon yarns and powder-coated towpreg for fabrication of woven and braided structural elements. Innovative tooling concepts and fabrication studies will be conducted for woven and braided panels. The powder-coated towpreg process is in its early stages of development. BASF will investigate scale-up feasibility for production of large quantities of powder-coated towpreg. Towpreg characteristics will be optimized to achieve cost-effective preform fabrication in conventional weaving and braiding machines.

<b>Lockheed Aeronautical Systems</b>	<b>Grumman Aircraft Systems</b>
<ul style="list-style-type: none"> <li>• Preform development and processing</li> <li>• RTM and powdered epoxy resins</li> <li>• Innovative tooling and fab. development</li> <li>• Circumferential fuselage frames</li> <li>• Fuselage window-belt insert</li> <li>• Keel beam/frame intersection</li> <li>• Fuselage crown panel</li> <li>• Design/analysis methodology</li> </ul>	<ul style="list-style-type: none"> <li>• Design guidelines/analysis methods</li> <li>• Integrally woven wing Y-spar</li> <li>• Cross-stiffened integrally woven fuselage element</li> <li>• Lower side quadrant fuselage panel</li> </ul>
<b>Rockwell International</b>	<b>BASF Structural Materials</b>
<ul style="list-style-type: none"> <li>• Static and fatigue response of woven composites</li> <li>• Micromechanics models of damage initiation and growth</li> <li>• Strength and fatigue life prediction methodologies</li> </ul>	<ul style="list-style-type: none"> <li>• Commingled thermoplastic/carbon yarns</li> <li>• Powder-coated towpreg</li> <li>• Weaving and braiding studies</li> <li>• Tooling and consolidation studies for woven panels and braided frames</li> <li>• Scale-up of towpreg and composite processing</li> </ul>

Figure 2

## TEXTILE MATERIAL FORMS OF INTEREST

Textile material forms that have the most potential for primary aircraft structural applications are indicated in figure 3. The ultimate goal is to minimize the number of individual plies required to build-up part thickness. Integral weaving and braiding will result in near-net structural shapes that require only minimal machining and fastening. Multilayer-multiaxial knitted fabrics are being investigated as a cost-effective replacement for biaxial woven broadgoods. The knitted fabrics can be postformed to achieve selected structural shapes. If high concentrations of 0-degree reinforcements are required, low crimp uniweave fabric can be added to woven, knitted, or braided material forms. Through-the-thickness stitching has been used to provide improved out-of-plane strength, damage tolerance, and delamination resistance. It is expected that continued developments in automation of textile processes will result in significant cost savings in fabricating textile preforms for aircraft structures.

- **Low crimp uniweave fabric**
- **Integrally woven fabric shapes (2-D, 3-D)**
- **Multiaxial knitted fabric (0, 90,  $\pm\theta$ )**
- **Braided preforms (2-D, 3-D, interlock)**
- **Stitched combinations of woven, knitted and braided preforms**

Figure 3

## TEXTILE MATERIALS BEING EVALUATED

The textile materials that are currently being investigated in the NASA Langley program are shown in figure 4. Quasi-isotropic (+45, 0, -45, 90) multiaxial warp knit fabrics have been produced by Hexcel Hi-Tech and Milliken. Tests are underway to assess performance differences between 3, 6, and 12K tows. Kevlar and polyester knitting yarns and Kevlar and carbon stitching yarns are being investigated. Triaxial ( $0 \pm 30$ ) braids produced by Fiber Innovations are currently being evaluated. Both stitched and unstitched materials are being tested. Atlantic Research has produced 3-D braids for improved impact resistance. Several different 3-D interlock weave configurations have been produced by Textile Technologies, Inc. All of these materials are being tested to assess mechanical properties and impact damage tolerance.

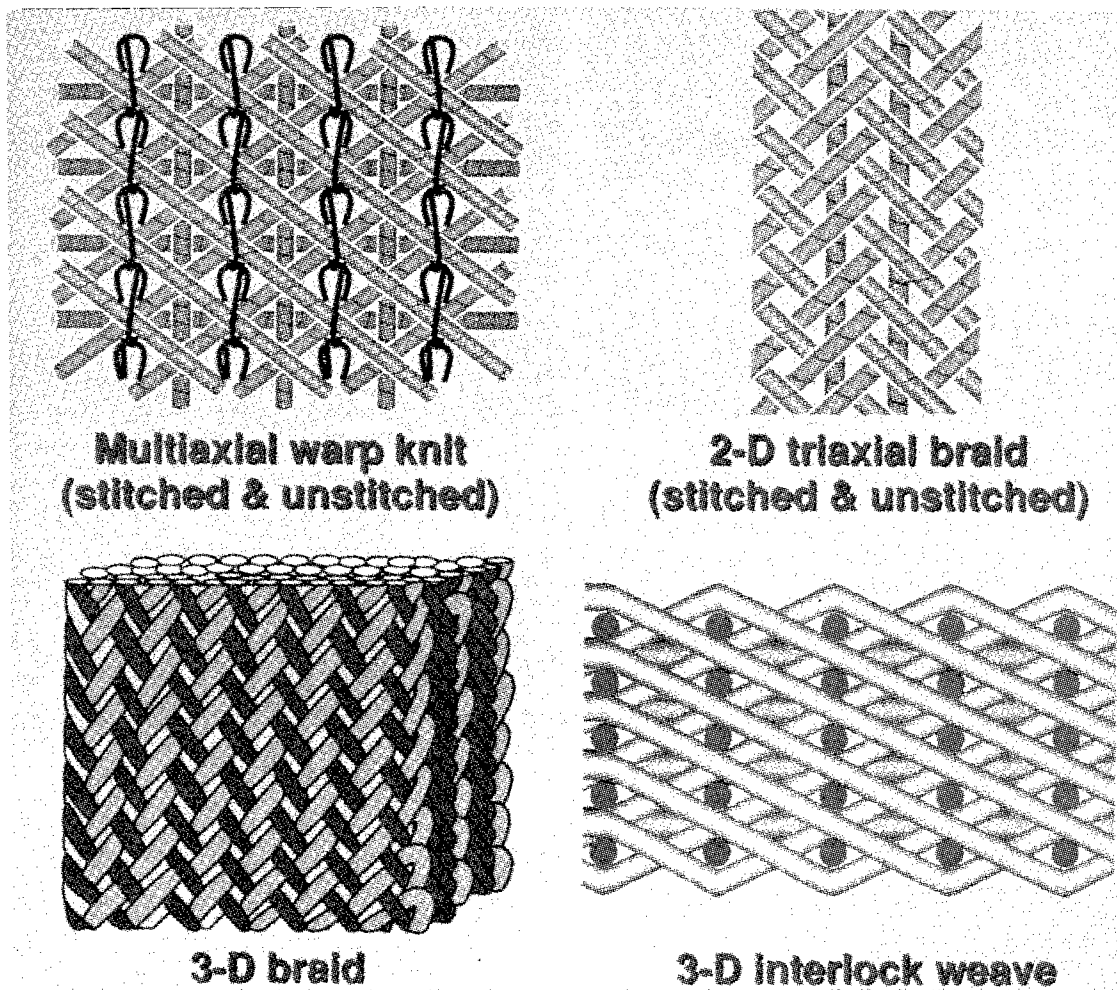


Figure 4

## NET-SHAPED TEXTILE PREFORMS

Some of the textile preforms that are being considered for structural applications are shown in figure 5. Weaving is well-suited for production of stiffened panels. However, automated weaving processes are currently limited to (0/90) fiber orientations in the skin and stiffening elements. Off-axis reinforcement, if required, must be bonded or stitched onto the surfaces of the (0/90) preform. Two-dimensional multilayer braiding is being used to produce complex curved shapes such as fuselage frames. The braiding process provides multidirectional fiber continuity throughout the preform structural shape. Both 2-D and 3-D braiding processes can produce structural shapes that are difficult or inefficient to achieve by other processes.

The knitted sine wave beam shown in figure 5 was produced by postforming knitted fabric to a specified shape. Epoxy powder tackifiers or stitching can be used to tack layers together. The integrally woven Y-spar shown in figure 5 can be produced in continuous lengths. As with the hat-stiffened panel, off-axis reinforcement must be added to the spar as a secondary operation.

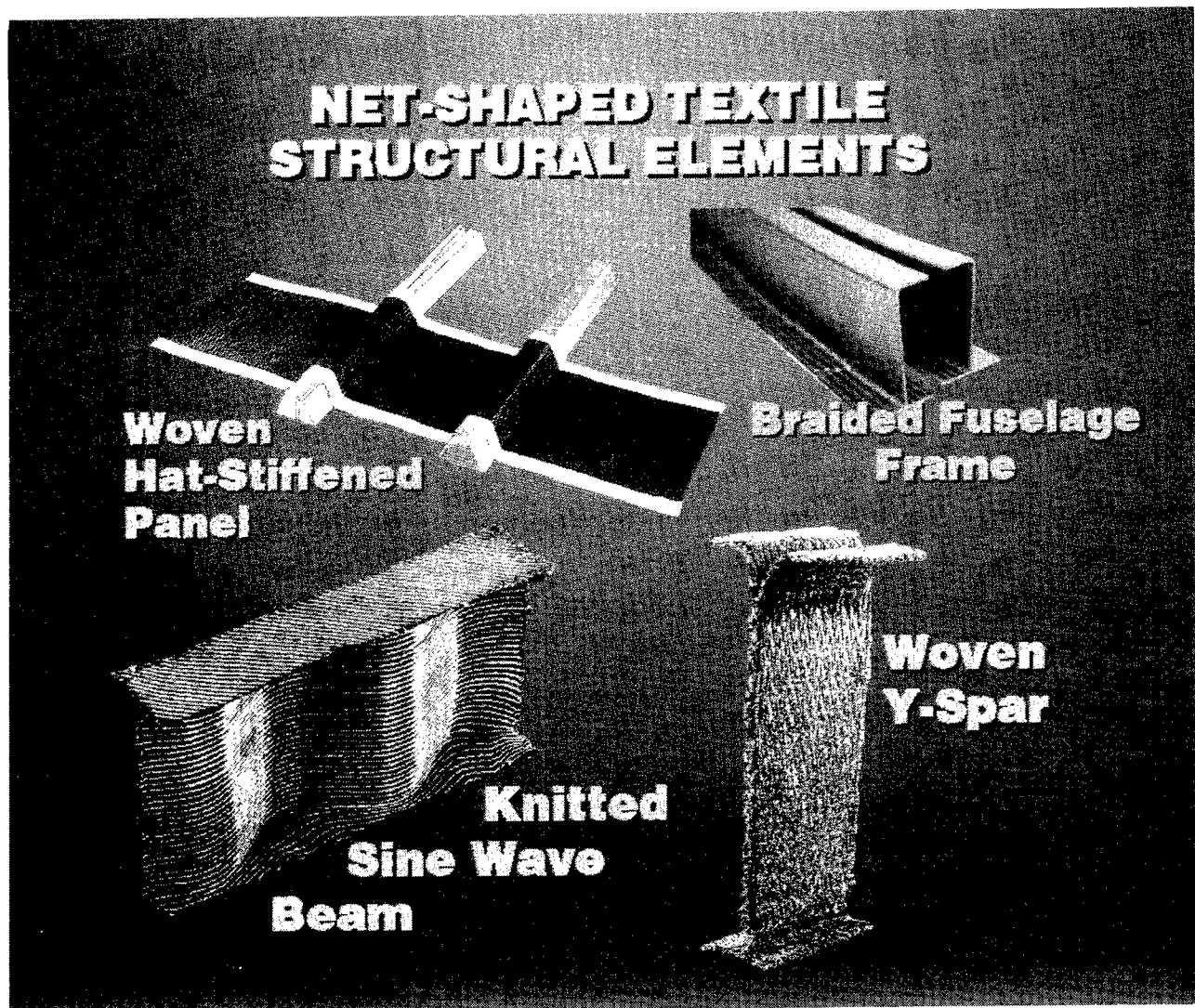


Figure 5

## COST-EFFECTIVE PROCESSES AND FABRICATION METHODS

Cost-effective processes and fabrication methods must be developed to produce cost-competitive aircraft-quality composite structures from the preforms discussed previously. The objectives and program elements for this research are shown in figure 6. Two major areas of research focus are resin transfer molding (RTM) and powder-coated towpreg. RTM is one of the most promising processes to achieve cost-effective structures because it uses resins and fibers in their lowest cost form. RTM has been used for many years but previous applications did not have stringent performance requirements. New resins with enhanced flow properties, higher strength, and improved toughness are currently under development. Appropriate tooling concepts must be developed to make cost-effective use of RTM. Analytical models are being developed to understand the RTM process and to eliminate trial-and-error procedures that are commonly used.

Powdered resins are a potential alternative to RTM. Powder-coated tows, if properly prepared, can be used in textile processes such as a weaving and braiding. Hence, pumping of resin into the preform, as with RTM, can be eliminated. The powder coating process is in its infancy and significant research is required before aircraft-quality composite structures can be produced. The research program elements shown in figure 6 are currently being pursued by NASA Langley, aerospace contractors, and universities.

- **Objectives**

- **Develop innovative processes and tooling concepts for RTM**
- **Optimize powder coating techniques, demonstrate weaving and braiding characteristics, and develop fabrication processes**

- **Program elements**

- RTM**

- **Improved RTM resins with high modulus, strength and toughness**
  - **Analytical processing science models for liquid, semi-solid and paste resins**
  - **Innovative compaction and tooling concepts for structural elements**

- Powdered resins**

- **Optimized powder coating techniques**
  - **Weaving and braiding trials**
  - **Fiber wet-out and preform consolidation models**
  - **Tooling concepts for complex structural shapes**
  - **Technology demonstration through structural element fabrication**

Figure 6



## PROCESSING SCIENCE OF TEXTILE REINFORCED COMPOSITES

Science-based processing studies are underway for textile reinforced composites. Analytical and experimental studies are being conducted to characterize preform and resin behavior for RTM. Major program elements are shown in figure 7. To model the RTM process, preform properties such as permeability and compaction, and resin viscosity as a function of temperature and time, must be known. Experimental studies are underway to determine preform permeability and compaction coefficients as a function of preform architecture. Resin infiltration studies are underway to predict how various resins flow through porous fiber preforms. Infiltration is affected by preform porosity, resin viscosity, flow direction, and applied pressure. Once the preforms are infiltrated, a cure kinetics analysis is performed to predict the degree of cure. A finite element analysis that utilizes preform and resin characteristic data has been employed to predict initial resin mass required, resin front position and time required for preform infiltration, resin viscosity and degree of cure, and final part thickness and fiber volume fraction.

Dielectric sensors are being used to track resin behavior as a function of time and to verify the RTM simulation model discussed above. The sensors can monitor infiltration position, resin viscosity, and degree of resin cure. The in-situ sensors can be used for real-time feedback control so that processing parameters can be modified if required. Flow visualization studies will be conducted to verify flow front position and to substantiate sensor output.

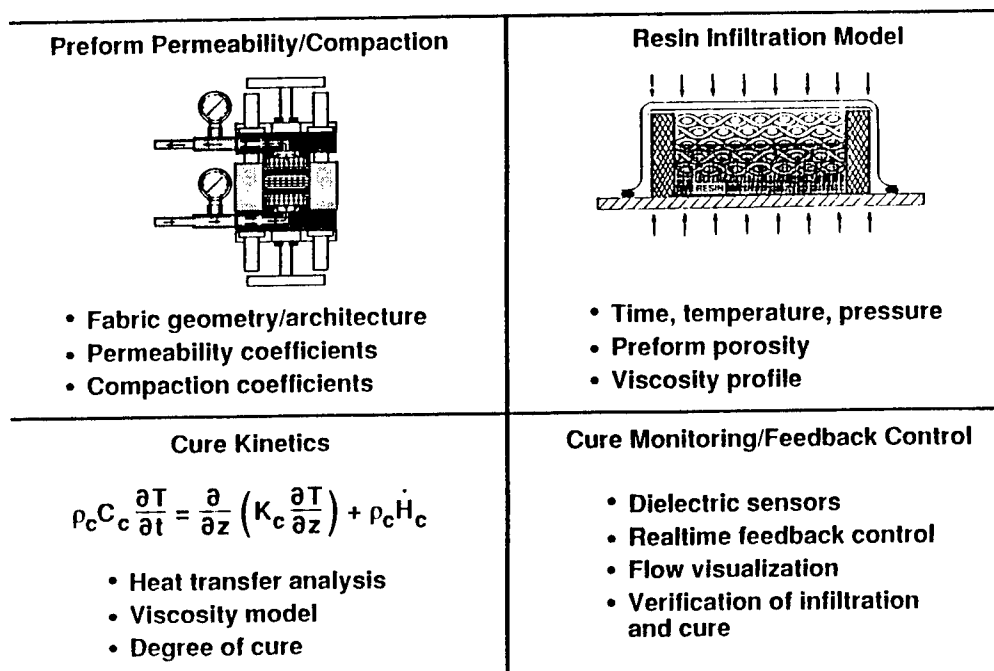


Figure 7

## COMPACTION AND PERMEABILITY CHARACTERISTICS OF HEXCEL HI-TECH KNITTED FABRIC

An important part of resin transfer molding textile material forms is understanding the compaction and permeability characteristics of the material. Compaction and permeability coefficients can be used to predict fiber volume fraction and ease of resin infiltration. As shown in figure 8, fiber volume fraction and fabric thickness are nonlinear functions of compaction pressure. The Hexcel Hi-Tech knitted fabric had a nominal uncompact fiber volume fraction of approximately 37 percent and a thickness of approximately 0.39-inch. To achieve a fiber volume fraction of 60 percent and a final thickness of 0.250-inch, a compaction pressure of approximately 35 psig is required.

Also shown in figure 8 is the effect of fiber volume fraction on permeability. Permeability is a function of fabric architecture, compaction, porosity, and fluid flow direction. Permeability along a fiber bundle can be an order of magnitude greater than transverse to the fiber bundle. Permeability for the Hexcel knitted fabric is approximately 5 in<sup>2</sup> for a fiber volume fraction of 60 percent. At a fiber volume fraction of 50 percent, the fabric would be much easier to infiltrate at a permeability of 14 in<sup>2</sup>.

(+45/0/-45/90)<sub>2s</sub>

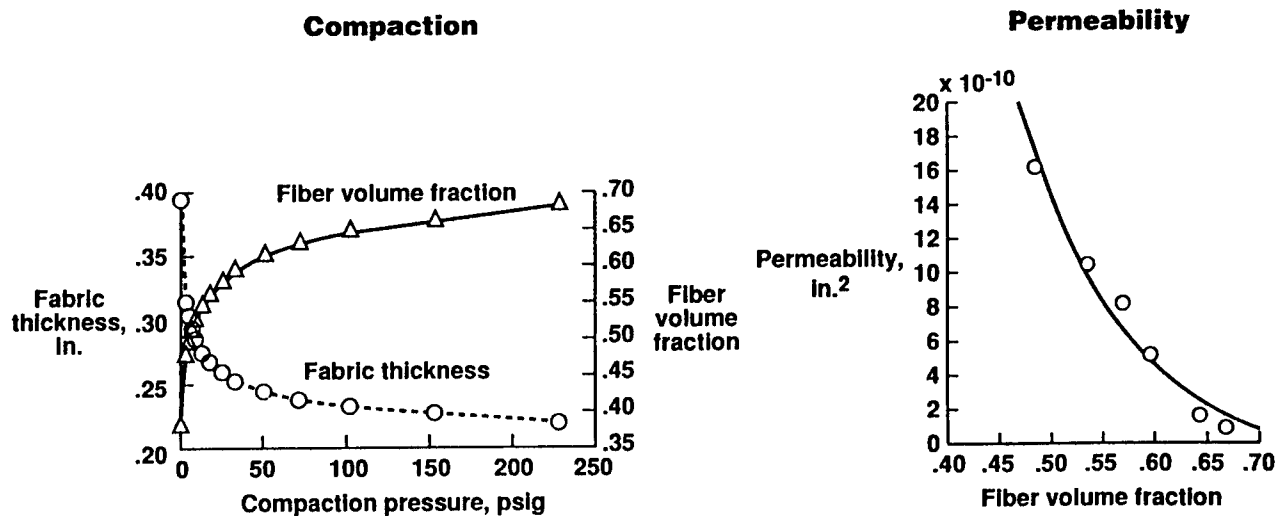


Figure 8

## POWDER-COATED TOWPREG TECHNOLOGY FOR TEXTILE REINFORCED COMPOSITES

As indicated in figure 9, the objective of powder-coated towpreg research is to investigate the viability of powder coating as an alternate to RTM for fabrication of textile reinforced composites. To achieve this objective, the approach shown in figure 9 is being followed. First generation powder-coated towpreg is currently being woven into flat panels to evaluate mechanical properties and damage tolerance. Stiffened panels will be evaluated to address fabrication issues and to assess structural performance. After weaving trials are completed, braiding studies will be conducted to assess other textile processing methods. On a continuing basis, processing studies will be conducted at the powder application level to optimize application techniques. Processing science studies will be conducted to understand compaction and consolidation issues specific to particular fiber forms and types of powder.

- **Objective:**
  - **Develop powder-coated towpreg technology as a viable alternate to RTM for fabrication of textile composites**
- **Approach:**
  - **Verify weave capability of powder-coated towpreg by systematically fabricating and evaluating flat composite panels of increasing complexity**
  - **Verify braid capability of powder-coated towpreg by fabricating and evaluating braided flat composite panels**
  - **Fabricate and evaluate single and three-stringer panels from powder-coated towpreg**
  - **Conduct process optimization studies to determine the important physical properties and processing characteristics of powder-coated towpreg**
  - **Conduct detailed compaction/consolidation studies to determine the proper fabrication procedures for preforms made from powder-coated towpreg**

Figure 9

## POWDER-COATED TOWPREG TECHNOLOGY FOR TEXTILE REINFORCED COMPOSITES

### - RESEARCH TEAM -

The research team that has been assembled to conduct research on powder-coated towpreg technology is shown in figure 10. NASA Langley is conducting in-house research and is sponsoring grant and contract research to advance powder-coated towpreg technology. Powders are being developed by 3M, Dow, Shell, and Mitsui Toatsu Chemicals. Basic powder application technology is being developed by Old Dominion University research associates at NASA Langley, Georgia Institute of Technology, and Clemson University. BASF Structural Materials is focusing on optimizing the towpreg process and processing scale-up for production quantities of towpreg. NASA Langley and BASF are sponsoring weaving and braiding studies to produce aircraft quality textile preforms. The textile companies that are currently involved in the program include Textile Technologies Inc., Fabric Development, J. B. Martin, and Fiber Innovations.

As part of the Lockheed ACT contract refocus, weaving and braiding will be investigated for fabrication of aircraft fuselage structural elements such as curved frames and stiffened panels. Powder-coated towpreg structural elements will be compared with similar elements fabricated with RTM processes.

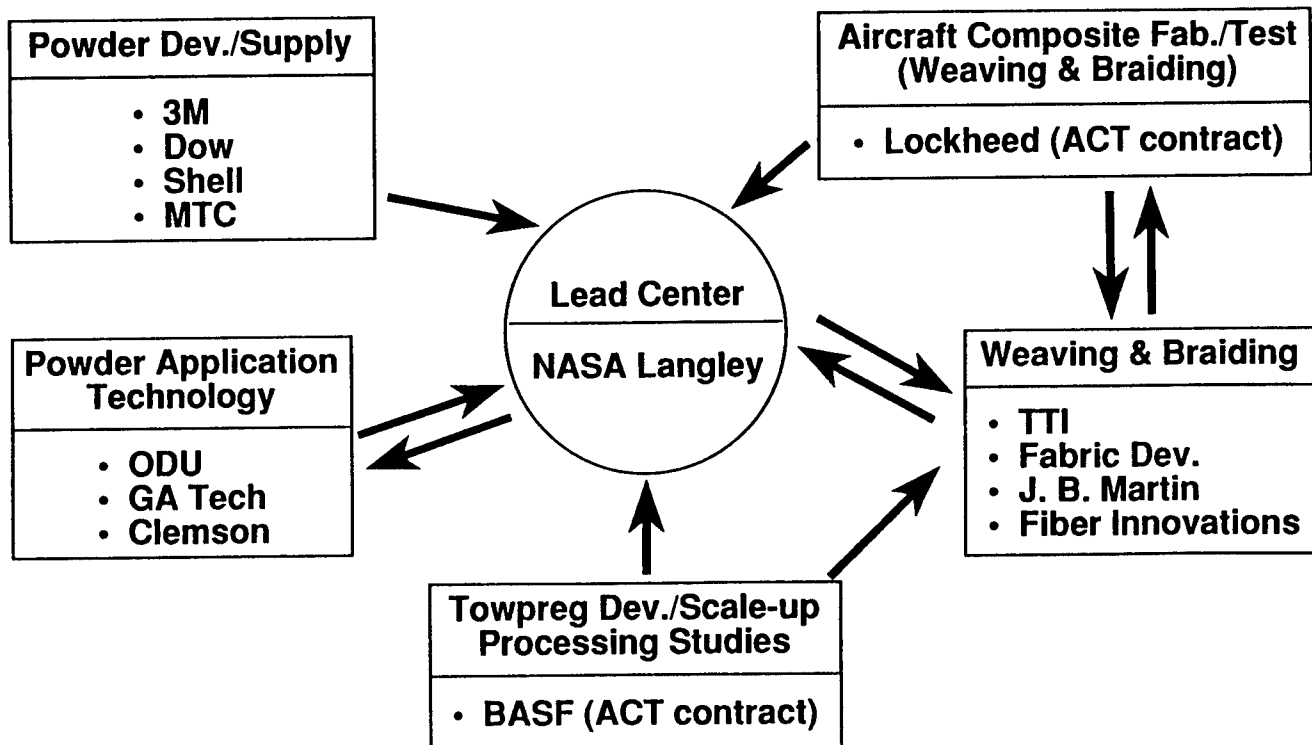


Figure 10

## NASA LARC ADVANCED POLYMER POWDER TOWPREG FACILITY

The powder-coated towpreg facility that is operational at NASA Langley Research Center is shown in figure 11. The experimental system is composed of five components: (1) fiber feed with tension brake, (2) air jet tow spreader, (3) fluidization/ polymer deposition chamber, (4) electric heater for polymer fusion onto tow bundles, and (5) towpreg take-up with tow speed and twist control. The LaRC facility operates routinely at line speeds up to 30 ft./min. Both 3K and 12K carbon tows have been coated successfully with the NASA LaRC system.

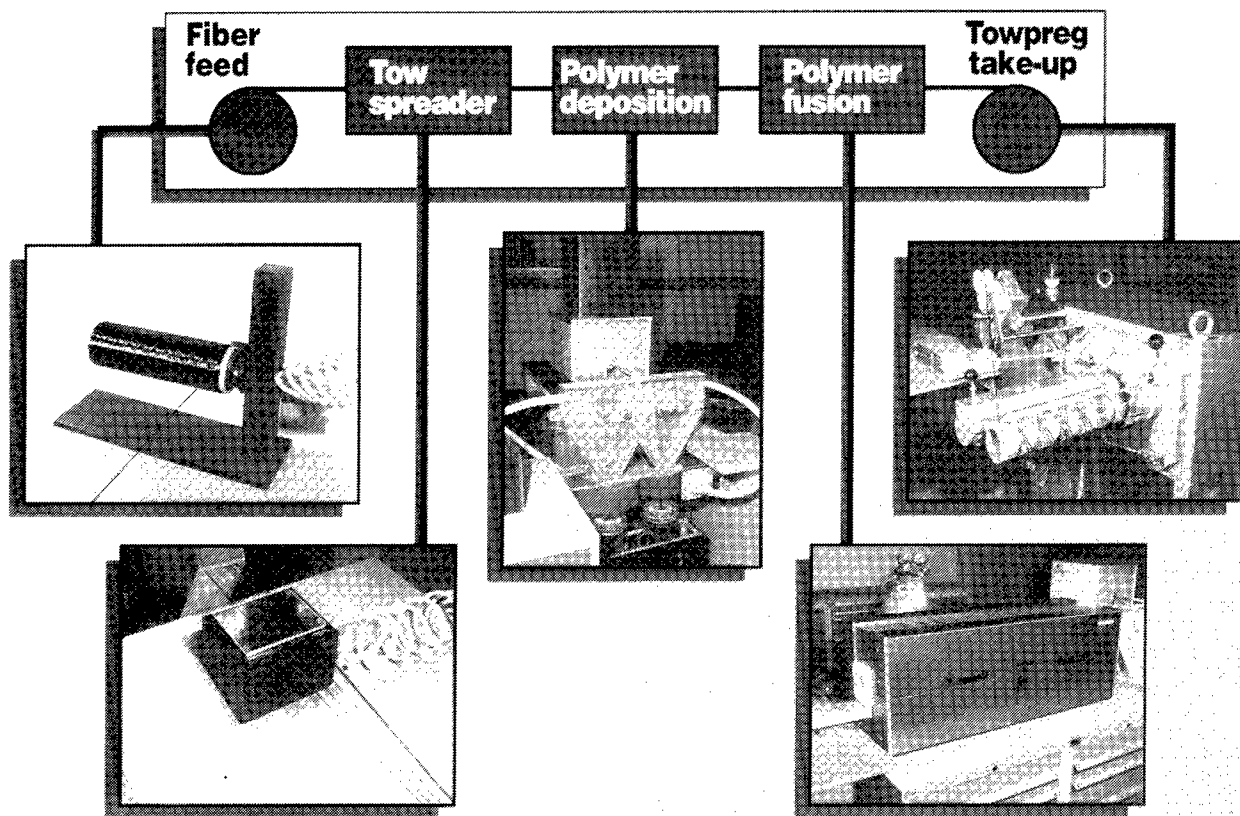


Figure 11

## IMPORTANT FEATURES OF THE POWDER COATING PROCESS

The dry powder coating process under development at NASA LaRC overcomes many of the difficulties associated with melt, solution, and slurry prepregging. Some of the important features of the powder coating process are shown in figure 12. The process is versatile in that it is applicable to thermoplastic and thermoset matrix materials. The powder application process operates at room temperature and no solvents are required. Since refrigeration is not required, the powders do not have "out-time" problems that are inherent with state-of-the-art prepreg. As a result, less waste and spoilage should be a significant benefit for powder-coated towpreg. Preliminary engineering studies indicate that powder-coated towpreg can be used in conventional textile processes. Significant research is currently underway to demonstrate that the powder process is a viable alternative to RTM processing of textile reinforced composites.

- **Versatile: Thermoplastics and thermosets**
- **Operates at room temperature**
- **No solvents involved**
- **Manageable exposure to toxic materials**
- **Prepreg requires no significant refrigeration:  
reduces waste/spoilage**
- **Prepreg can be woven, filament wound, pultruded,  
thermoformed**
- **Viable alternative to RTM processing of textile  
preform composites**

Figure 12

## POLYMER POWDER RESEARCH

Some of the powders and product forms that are being investigated in the NASA LaRC program are listed in figure 13. Five different epoxy powders and two polyarylene ether powders are being investigated for subsonic commercial transport applications. Several polyimide and bismaleimide powders are being considered for application to future high-speed civil transport aircraft. The uniformity of powder deposition is indicated in the photograph of powder prepreg. Eight harness satin fabric that was woven with powder-coated towpreg is shown in the lower left of figure 13. Processing/consolidation studies are underway with this fabric. Mechanical properties will be compared with properties obtained with conventional prepreg fabric.

Some of the powder-coated product forms that are being investigated include uniweave prepreg tape, woven broadgoods, 2-D/3-D woven and braided textile preforms, and towpreg ribbon for use in advanced tow placement machines.

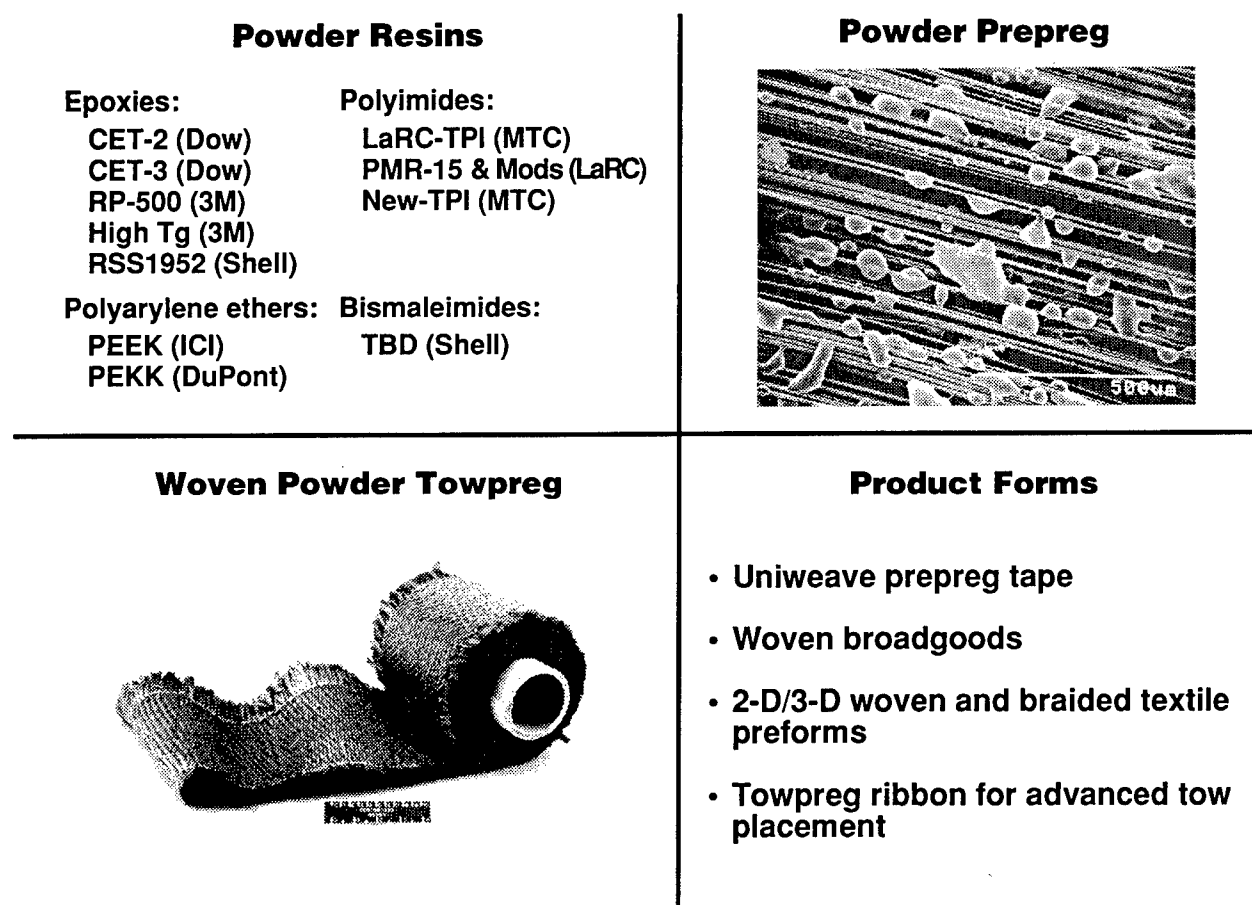


Figure 13

## LONGITUDINAL FLEXURE STRENGTH AND MODULUS OF POWDER-COATED TOWPREG UNIDIRECTIONAL LAMINATES

Longitudinal flexure strength and modulus data for unidirectional composites fabricated with four different powders are shown in figure 14. Flexure strength ranges from 256 ksi for the LaRC TPI material to 300 ksi for the Shell RSS-1952 material. Flexure modulus ranges from 17.5 Msi for the 3M PR-500 material to 18.7 Msi for the Dow CET-2 material. These results for powder-coated G30-500 carbon fiber are similar to results expected for conventional preimpregnated tape materials. The results shown in figure 14 are normalized to a fiber volume fraction of 0.60.

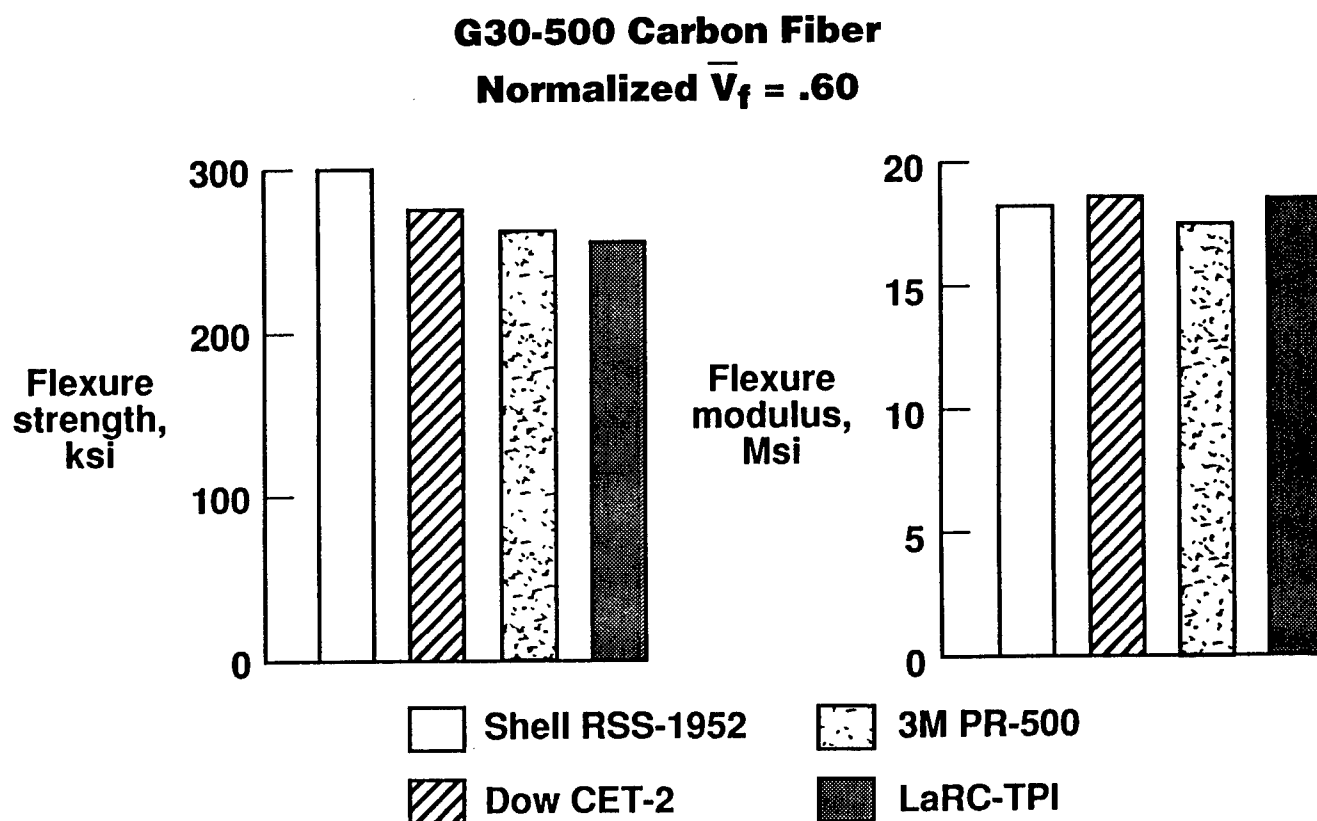


Figure 14



## POWDER-COATED TOWPREG WEAVING STUDIES

Weaving studies are underway to determine powder-coated towpreg characteristics that will allow the towpreg to be woven on conventional looms. An outline of the weaving studies is shown in figure 15. During powder application, the following towpreg characteristics must be considered: degree of powder adhesion, tow flexibility, tow dimensional tolerance, tow twist, and damage during the coating process. All of these factors can affect the quality of woven product forms. Some of the weaving parameters that may require attention include loom/equipment modifications to accommodate towpreg, loom speed, tow abrasion/powder loss, and tow damage as a result of weaving operations.

The textile architectures that are being considered include 2-D uniweave and satin weaves, 3-D layer-to-layer interlock, and 3-D net-shape preforms. Once high-quality fabrics are achieved, processing studies must be conducted to arrive at optimum composite properties. One concern is the uniformity in resin content throughout the woven preform. Other issues such as towpreg bulk factor and compaction must be addressed. These issues are related to tool designs that will produce well-consolidated composites. Processing science studies will be conducted to aid in cure cycle development and to minimize the time required to arrive at optimum processing conditions.

Towpreg Characteristics	Weaving Parameters
<ul style="list-style-type: none"> <li>• Degree of powder adhesion</li> <li>• Tow flexibility</li> <li>• Tow dimensional tolerance</li> <li>• Tow twist</li> <li>• Damage during coating process</li> </ul>	<ul style="list-style-type: none"> <li>• Loom/equipment modifications required to accommodate towpreg</li> <li>• Loom speed</li> <li>• Tow abrasion/powder loss during weaving</li> <li>• Tow damage during weaving</li> </ul>
Textile Architectures	Processing Technology
<ul style="list-style-type: none"> <li>• 2-D Uniweave</li> <li>• 2-D Satin weaves</li> <li>• 3-D Layer-to-layer interlock</li> <li>• 3-D Net shape preforms</li> </ul>	<ul style="list-style-type: none"> <li>• Optimum resin content</li> <li>• Towpreg bulk factor/compaction</li> <li>• Tool design/composite consolidation</li> <li>• Processing science/cure cycle development</li> </ul>

Figure 15

## MECHANICS OF MATERIALS MODELS FOR TEXTILE COMPOSITES

NASA Langley has assembled a team of mechanics experts to develop methodologies and models to predict performance of textile reinforced composites. The major program elements are outlined in figure 16. An accurate description of the fiber architecture is required to adequately predict mechanical response. Mathematical formulations are being developed to describe yarn path and geometry of repeating unit cells. Stress-strain relationships will be developed from the homogeneous or continuum mechanics viewpoint. The upper right schematic in figure 16 illustrates a strategy that is mathematically similar to the finite element discretization method. Master subcells that reflect the essence of the repeating geometry are arranged in the pattern necessary to model the unit cell. The stiffness matrix for the unit cell is computed by standard matrix manipulations of the stiffness matrices of the master subcells. This type of model may be used to directly define the A, B, D coefficients or to calculate effective elastic moduli by imposing the correct boundary conditions on the unit cell.

Continuum level strength models will be developed in conjunction with the stress-strain models. This will allow a first approximation of load carrying capacity to be obtained from the average stresses computed by a global structural analysis using the homogenized stiffness properties. The average stresses will then be evaluated in a tensor polynomial failure criterion, for example, using phenomenological strength parameters determined from simple coupon tests.

A methodology will be developed to predict damage progression and residual strength using global/local analysis strategies to address damage tolerance requirements. Initial emphasis will be on modeling impact damage. Fatigue behavior will be experimentally characterized and then treated analytically. Fatigue life prediction methodologies will be developed for in-plane tension and compression loads and for out-of-plane loads.

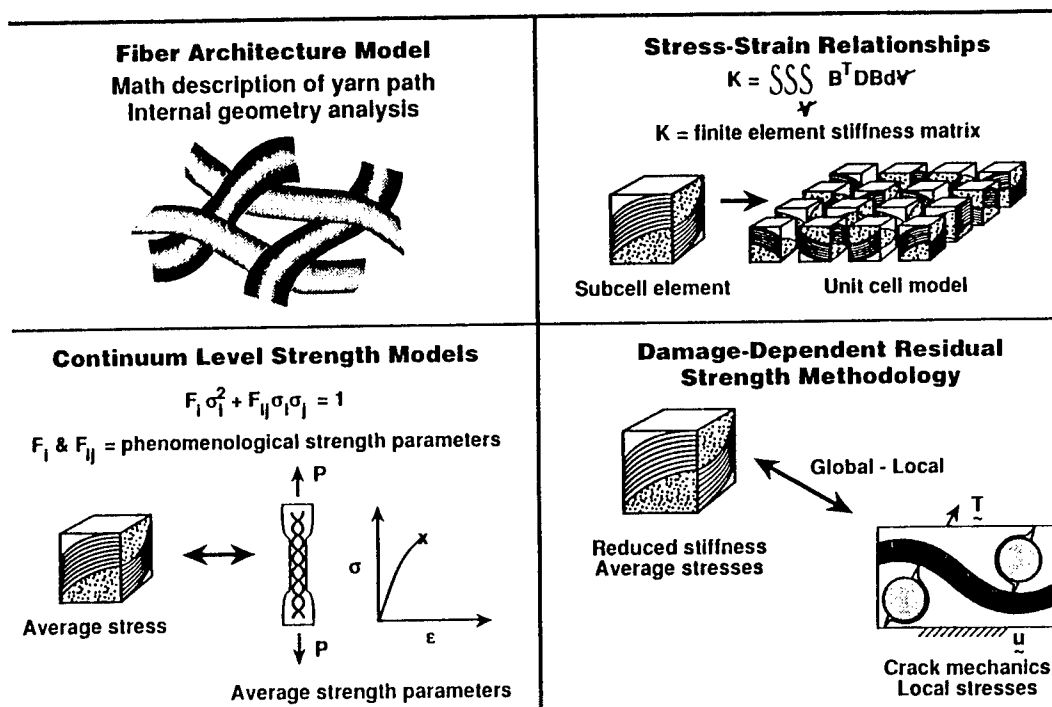


Figure 16

## TEXTILE MECHANICS

### - RESEARCH TEAM -

The Mechanics of Materials Branch (MEMB) at NASA Langley has the lead role in developing mechanics methods for performance prediction of textile reinforced composites. A "textile mechanics working group" has been formulated to ensure program coordination and cooperation among the participants in a synergistic environment. The working group is comprised of the MEMB in-house research team, all program contractors and grantees, and ACT contract representatives from Lockheed, Grumman, Douglas, and Boeing. The working group meets quarterly for 1- or 2-day informal work-in-progress reviews. Co-location of team members at NASA Langley for various periods of time is encouraged to facilitate technology transfer.

The research topics that are currently being addressed are indicated in figure 17. Fiber architecture math models are being developed at North Carolina State University. Stiffness and strength models for stitched laminates are being developed at the University of Florida. Global/local analysis methodologies and fatigue response of braided composites are being developed at Virginia Polytechnic Institute and State University. Notch effects in braided composites are being studied at West Virginia University.

The Rockwell Science Center is conducting research on impact and fatigue response of 3-D woven fabrics and knitted/stitched materials. The University of Utah is studying failure of textile reinforced composites under combined stress states. Texas A&M University is focusing on micromechanics analysis of compression failure in textile materials. The University of Delaware is conducting a design study for an out-of-plane strength test specimen. Development of standard test methods will be discussed in a subsequent figure.

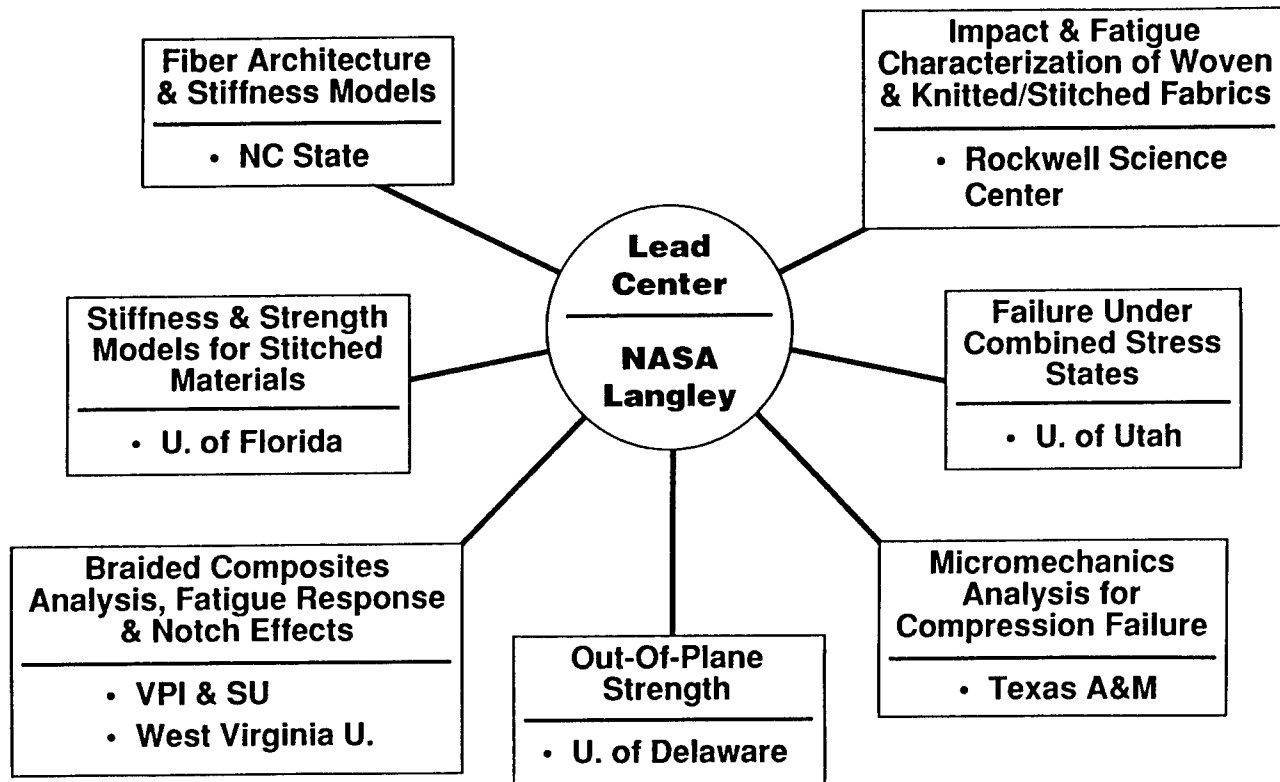


Figure 17

## TEXTILE FIBER ARCHITECTURE MODEL

In order to perform an accurate stress analysis of textile reinforced composites, the textile fiber architecture must be accurately defined. One approach that is being studied is shown in figure 18. First, models of the yarn path must be formulated. The reinforcing structure is modeled as a set of fixed points in space that represent the position of the center of the yarn. These points are "hard points" in that they are determined by the manufacturing process. In order to develop a realistic model of the yarn as it moves through space, the center-line points are smoothed with a B-spline to create a minimal strain energy curve. The cross-sectional shape of the yarn is then swept along this smoothed center-line, maintaining appropriate bending and twisting. The surface is then constructed by applying a Bezier patch to the surface points generated from this sweep. The resulting model represents the surface of the yarns within the fibrous structure.

The second step is to conduct an internal geometric analysis of the fiber architecture. The yarns are sectioned numerically to compute yarn orientations and cross-sectional areas. These mathematical models must be validated and adjusted as necessary by comparing with photomicrographs of the consolidated composite. Once the geometric model is verified, the mathematical description of the architecture can be applied to various analytical techniques, ranging from homogenization to detailed finite element approaches.

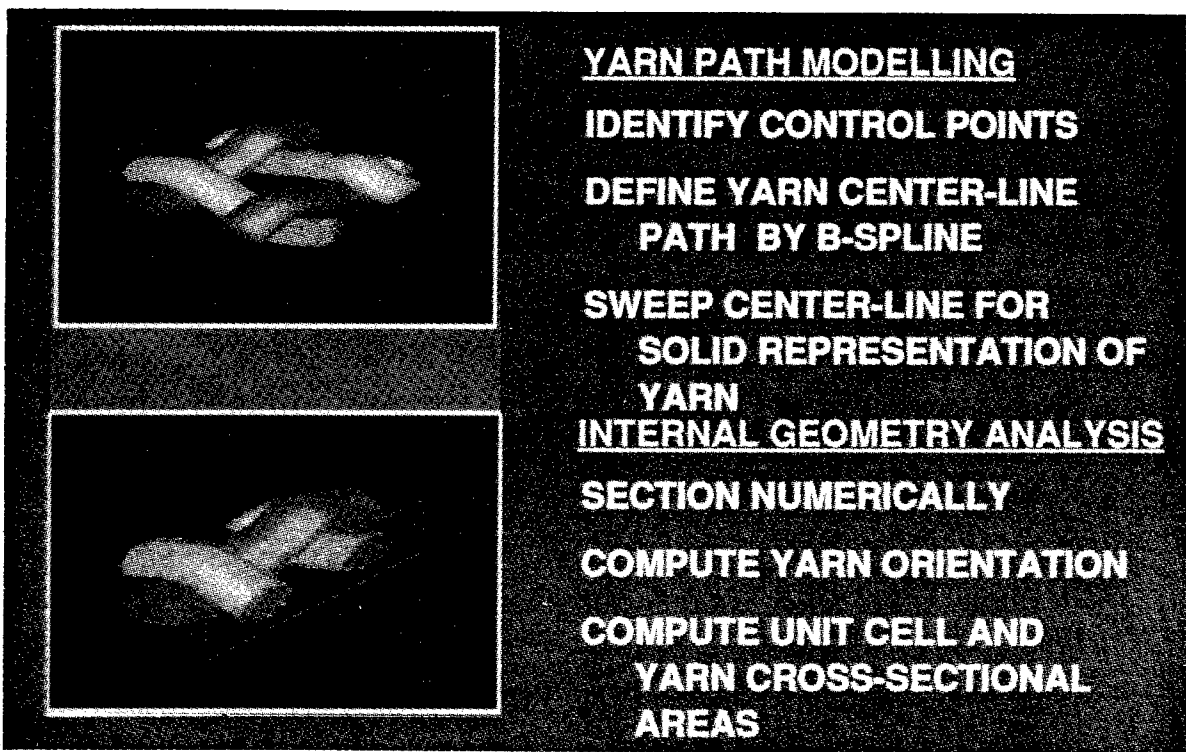


Figure 18

## EXPERIMENTAL CHARACTERIZATION AND PRELIMINARY DESIGN PROPERTIES

An experimental characterization program is underway at NASA Langley to develop mechanical properties, damage tolerance, and preliminary design properties for textile reinforced composites. The objectives and program elements are shown in figure 19. Materials being characterized include woven, braided, knitted, and stitched fiber architectures. Most of the tests conducted to date have focused on in-plane mechanical properties and impact damage tolerance. A limited amount of fatigue tests have been conducted under compression-compression constant amplitude loading. Additional fatigue tests that include tension-tension and tension-compression cyclic loading will be conducted. The test matrix will also be expanded to include bearing and out-of-plane strength. Structural element level tests such as crippling, stiffener pull-off, and panel buckling will be expanded in the near future. Special fixtures and load introduction techniques will be developed as necessary. These tests will provide preliminary design properties and a database for comparison with analytical models.

- **Objectives**
  - **Develop experimental data base to characterize the mechanical behavior and damage tolerance of selected textile architectures**
  - **Develop preliminary design properties to support design of selected structural elements and subcomponents**
- **Program elements**
  - **In-plane mechanical properties data base for woven, braided and knitted/stitched composites**
  - **Out-of-plane strength and delamination resistance**
  - **Impact damage tolerance and notch effects**
  - **Bearing/mechanical fasteners**
  - **Tension and compression fatigue response**
  - **Preliminary design properties for specific structural elements and subcomponents**

Figure 19

## TEST SPECIMENS

The test specimens that are currently being used in the NASA Langley in-house test program are shown in figure 20. The specimens have a nominal thickness of 0.250-inch with length and width as indicated in the sketches. Test results obtained to date indicate that strain gages must be selected to match particular fiber architectures. Factors such as tow size, tow spacing, and textile unit cell dimensions must be accounted for in making strain measurements. For example, a material braided with 3K tows will have a smaller unit cell than a material braided with 12K tows. The local strain response of these materials may be different, and different size strain gages may be required to accurately measure material response. Strain gages that are located directly over a through-the-thickness stitch could be affected by local material response. The size and location of resin pockets could also affect local material response. Additional research on development of standard test methods for textiles will be discussed in a subsequent figure.

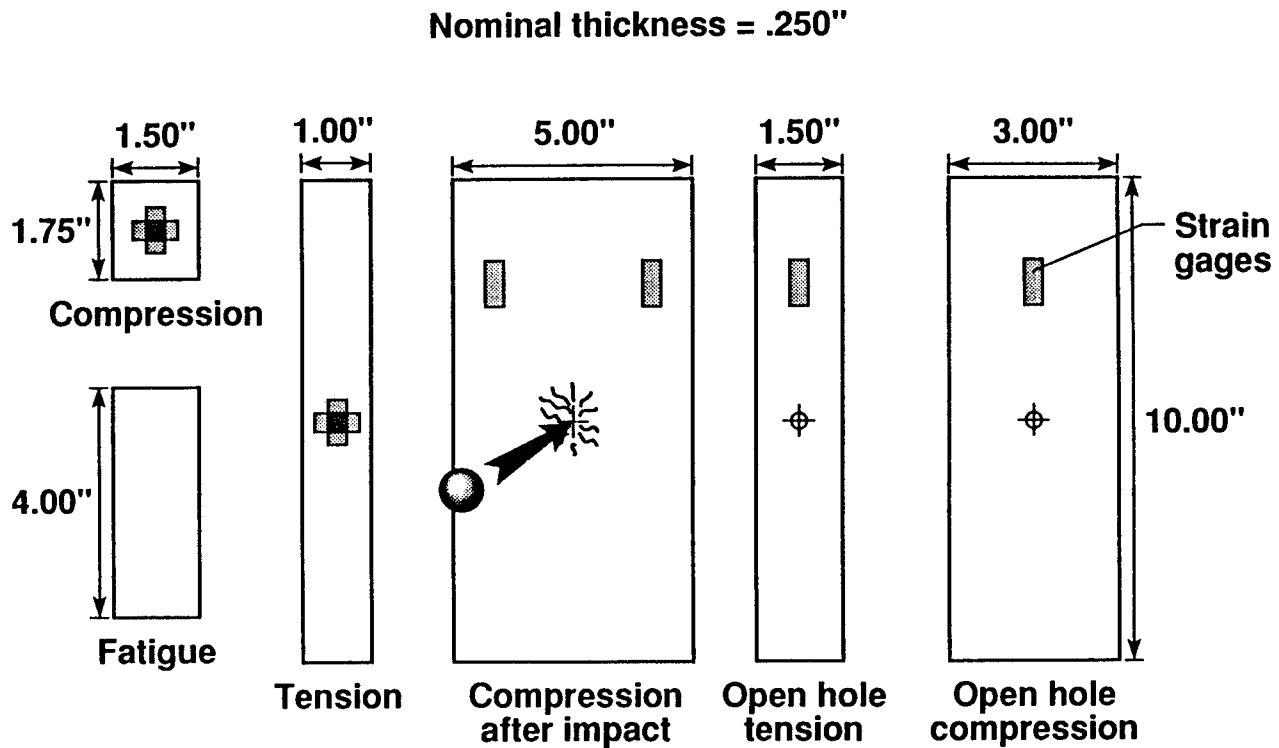


Figure 20

## COMPRESSION AND COMPRESSION-AFTER-IMPACT STRENGTH OF QUASI-ISOTROPIC AS4/EPOXY LAMINATES TESTED IN THE 0° DIRECTION

Compression and compression-after-impact (CAI) strengths of knitted/stitched composites are compared with those of laminated composites fabricated with prepreg tape, figure 21. The knitted/stitched fabrics were infiltrated with three different resin systems: Hercules 3501-6, British Petroleum E905L, and 3M PR500. The prepreg tape was fabricated with Hercules 3501-6 epoxy resin. The knitted fabric was produced by knitting four layers of AS4 carbon fibers together with a 70 denier polyester yarn. The knitted subgroups were stacked to form a 16-ply quasi-isotropic (+45, 0, -45, 90)<sub>2s</sub> preform. The 16-ply preforms were subsequently stitched together with a carbon stitching yarn using a modified lock stitch. The knitted/stitched fabric was produced by Hexcel Hi-Tech.

Test results indicate that the knitting/stitching process reduced the compression strength of the fabric by 25 to 30 percent compared to prepreg tape laminates. However, the major benefits of knitting and stitching are in delamination suppression and damage tolerance. The results shown in figure 21 for a 30 ft.-lb. impact indicate the benefits of through-the-thickness reinforcement. The compression strength for the prepreg tape laminate was reduced from 80 ksi to below 20 ksi as a result of the impact. However, a 150 percent improvement in CAI strength was achieved with the knitted/stitched fabric compared to the prepreg tape laminate. Additional research is underway to identify fiber damage mechanisms due to knitting/stitching so the fabrication process can be optimized to minimize fiber damage and resultant strength loss.

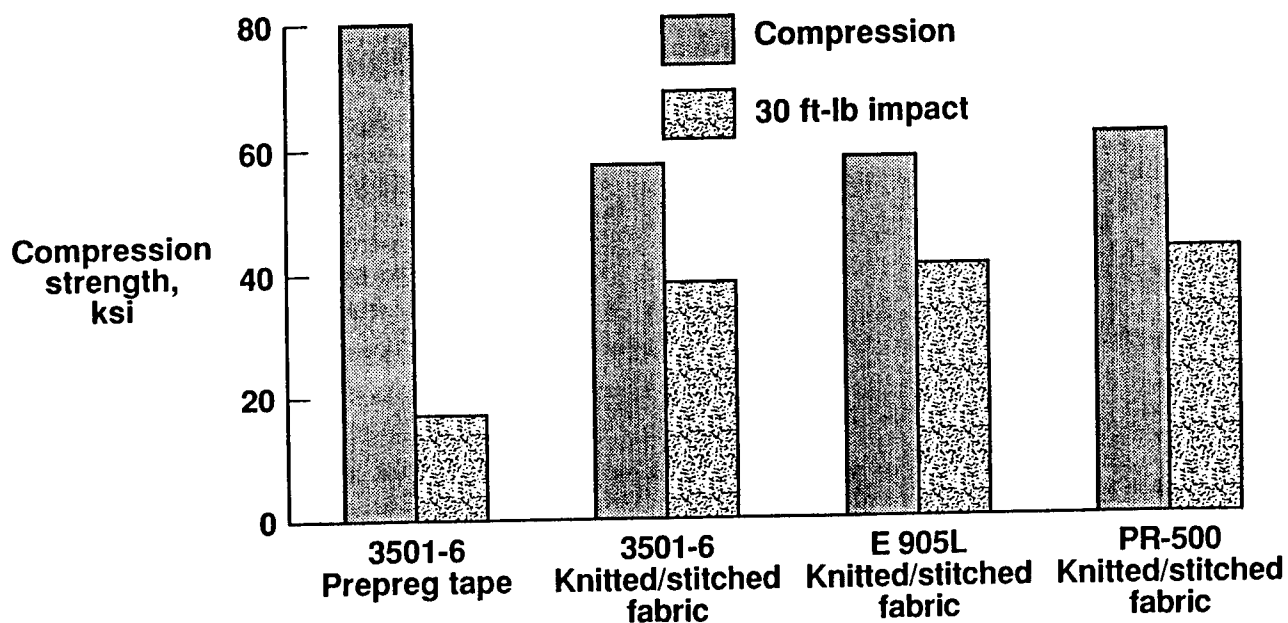


Figure 21

## COMPRESSION AND COMPRESSION-AFTER-IMPACT STRENGTH OF BRAIDED COMPOSITE PANELS TESTED IN THE 0° DIRECTION

Compression and compression-after-impact (CAI) strengths of 2-D braided, 2-D braided/stitched, and 3-D braided composites are compared in figure 22. The braided preforms were fabricated with AS4 carbon fibers with a ( $\pm 30/0$ ) fiber architecture. The preforms were infiltrated with British Petroleum E905L epoxy. An impact energy of 30 ft.-lb. was used to impact the panels, which had nominal thicknesses of 0.24-inch.

Test results indicate that the 3-D braided panels had the highest undamaged strength, over 60 ksi, whereas the 2-D braided/stitched panels had the highest CAI strength, over 40 ksi. It is somewhat surprising that the CAI strength for the 3-D braided panels was only slightly better than the CAI strength for the 2-D braided panels which have no through-the-thickness reinforcement. Additional testing is underway to further understand the behavior of braided materials.

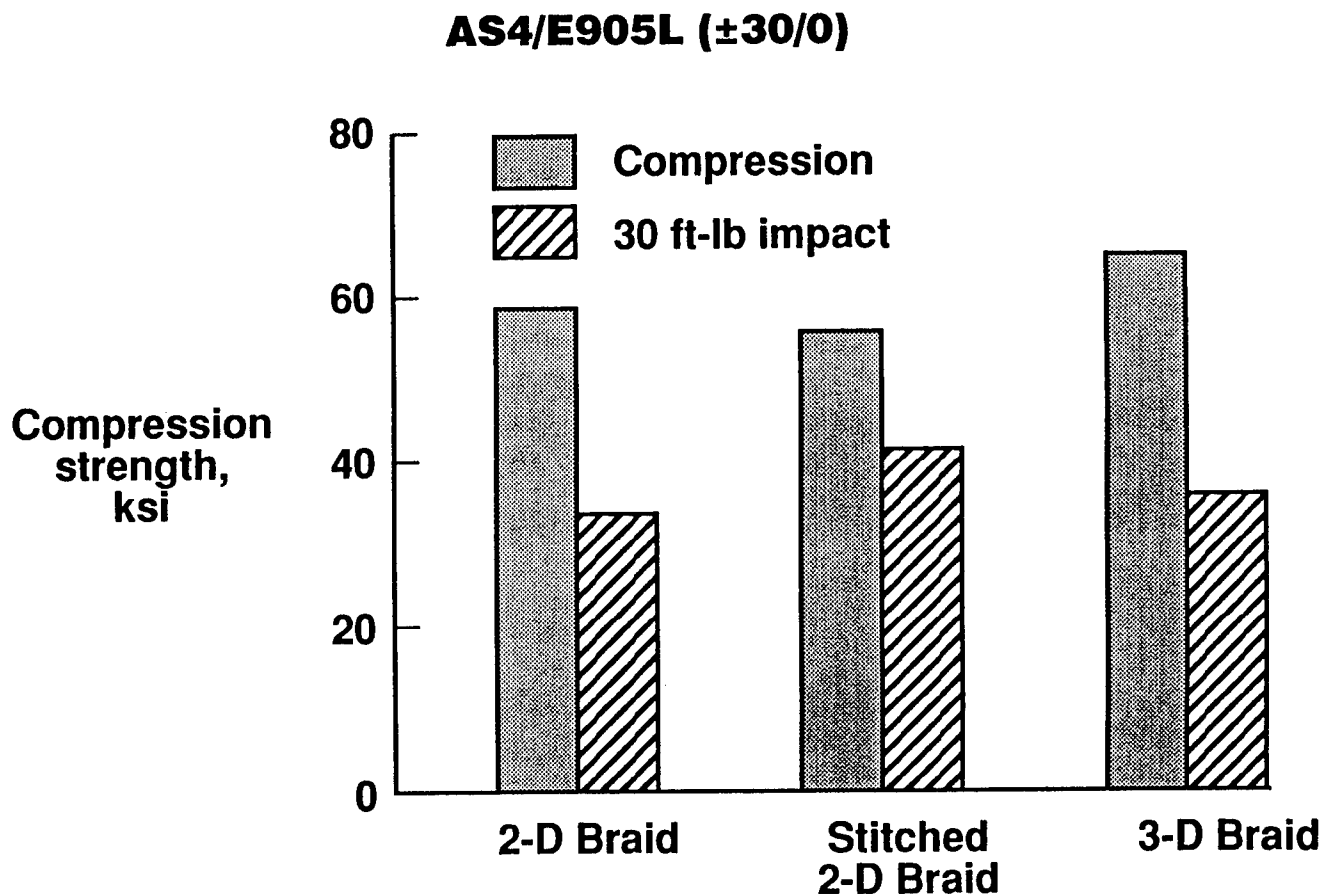


Figure 22



## STANDARD TEST METHODS FOR TEXTILES

New test techniques will be required to characterize some of the unique properties of textile reinforced composites. The sketches shown in figure 23 indicate some of the types of tests that must be conducted to explore the benefits of textile material forms. Some of the currently used in-plane test methods may be adequate for textile materials. However, modification of specimen dimensions and strain measurement techniques may be required for some textile architectures. The effect of textile unit cell dimensions on mechanical behavior must be characterized. Since textile materials with through-the-thickness reinforcement offer significant improvement in out-of-plane load capability, adequate test methods must be developed to assess performance improvements. Subelement level tests such as stiffener pull-off must also be developed. Analytical studies, in conjunction with experiments, must be performed to assure that stress states are understood and that local effects are representative of global material response. Available standard test methods in the composites industry will be investigated and used where appropriate.

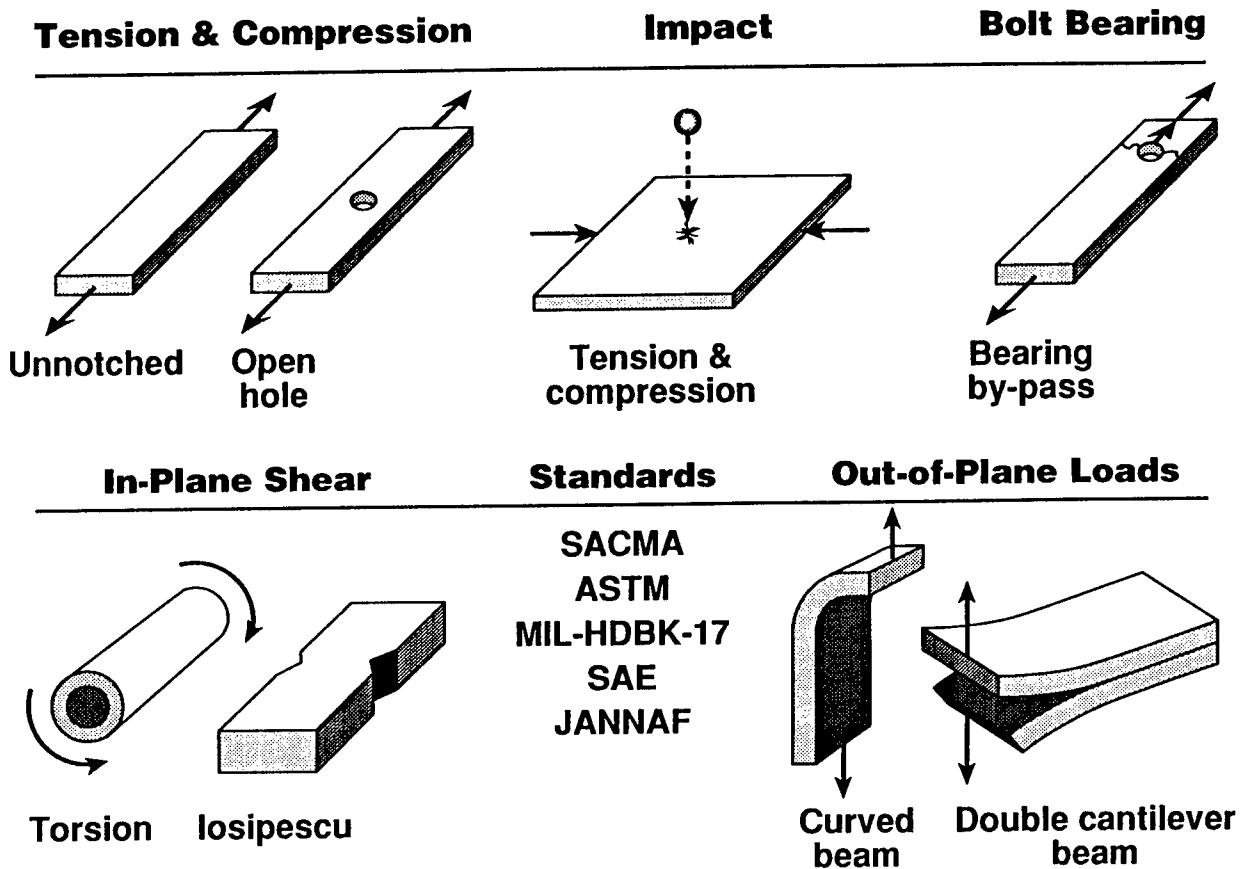


Figure 23

## AIRCRAFT FLUIDS EXPOSURE OF RTM COMPOSITES

As part of the resin selection process for resin transfer molding (RTM) of textile materials, Boeing Aerospace is conducting aircraft fluids exposure of several composite systems. The materials that are being evaluated, specimen types, and fluid exposure conditions are indicated in figure 24. Five different resins with AS4 uniweave fabric were selected for the initial test program. The selected exposure conditions and fluids are as follows: (1) 160°F water, (2) room temperature (RT) JP-4 jet fuel, (3) 160°F hydraulic fluid, (4) 160°F turbine oil, (5) RT MEK, (6) RT methylene chloride, and (7) RT deicing fluid. These fluids are representative of those that composite materials may be exposed to during realistic aircraft operational service. Tension (+45/-45)<sub>2s</sub> and short beam shear (0)<sub>16s</sub> test specimens were selected to represent matrix dominant failure modes. Room temperature and 180°F test temperatures were selected. Test results are incomplete at this time but should be available in the latter part of calendar year 1991.

### 14 Day Exposure

<u>Composite Systems</u>	<u>Fluids - Exposure Conditions</u>
<ul style="list-style-type: none"><li>• AS4/Hercules 3501-6</li><li>• AS4/Shell 862</li><li>• AS4/BP E905L</li><li>• AS4/Dow CET-2</li><li>• AS4/Ciba Geigy 5292</li></ul>	<ul style="list-style-type: none"><li>• Water - 160°F</li><li>• JP-4 Jet fuel - RT</li><li>• Hydraulic fluid - 160°F</li><li>• Turbine oil - 160°F</li><li>• MEK - RT</li><li>• Methylene chloride - RT</li><li>• Deicing fluid - RT</li></ul>
<u>Test Specimens/Conditions</u>	
<ul style="list-style-type: none"><li>• (+45/-45)<sub>2s</sub> Tension</li><li>• (0)<sub>16s</sub> Short beam shear</li><li>• Room temperature</li><li>• 180°F</li></ul>	

Figure 24

## EFFECTS OF MOISTURE AND TEMPERATURE ON RTM COMPOSITES

Results from hot/wet compression tests conducted at NASA Langley on six different RTM composite material systems are presented in figure 25. Since different fabric architectures were used in the six materials, strength retention results are compared to their respective room temperature baseline strength. The specimens were soaked in a 160°F water bath in an air circulating oven for 45 days prior to testing. After exposure, the specimens were tested at 180°F. The best performance was achieved with Dow CET-2 and 3M PR 500 resins, a strength loss of only 15 percent. The Shell 862/763 resin lost about 35 percent in strength due to hot/wet exposure. Additional tests will be conducted on emerging resins as they become available for RTM processing studies.

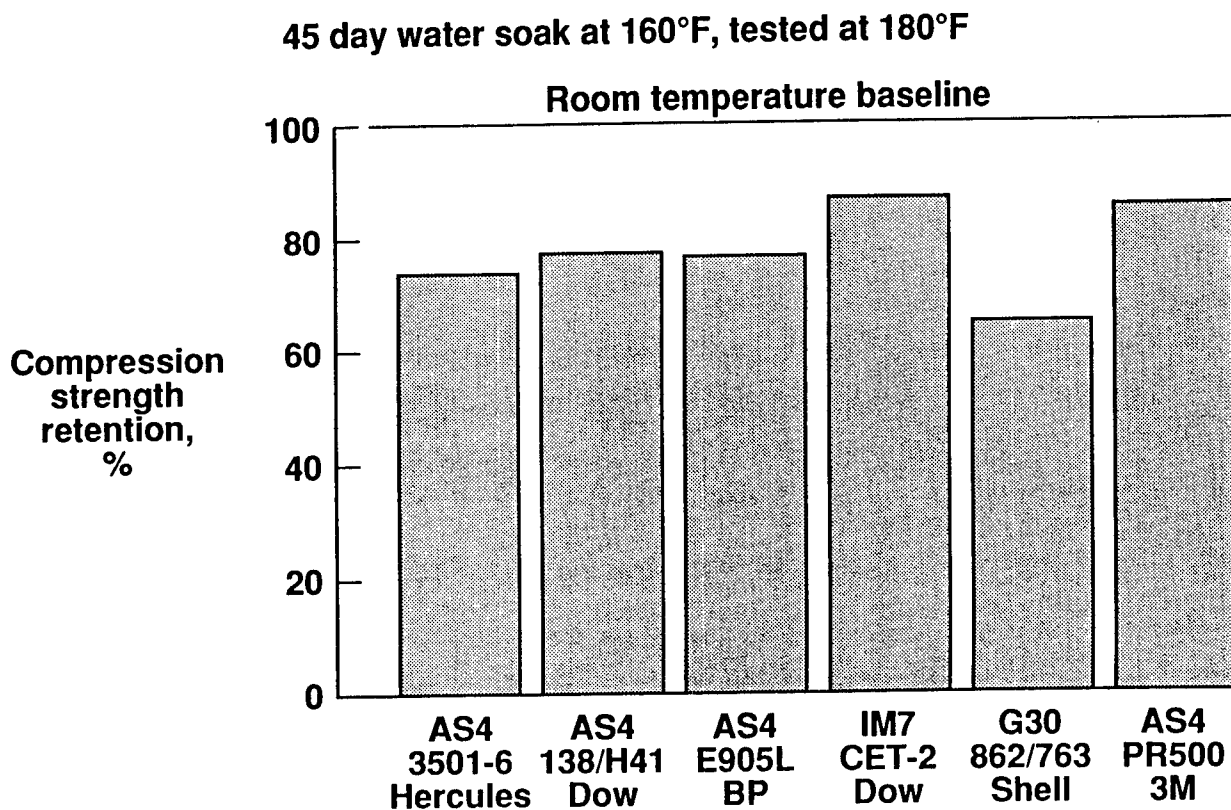


Figure 25

## TEXTILE REINFORCED COMPOSITE STRUCTURAL SUBCOMPONENTS

As part of the redirection of the Lockheed and Grumman ACT contracts, specific fuselage subcomponents were selected as candidates for application of textile material forms. Based on discussions between NASA Langley, Lockheed, Grumman, and Boeing, the four subcomponents shown in figure 26 were selected. These structural subcomponents were selected to exploit damage tolerance and through-the-thickness strength capability of textile materials. Structural tests will be conducted on each structural subcomponent to verify the performance of textile architectures. Analytical predictions will be performed and results will be correlated with experimental behavior.

Particular design issues associated with each subcomponent are indicated in figure 26. It is anticipated that several textile processes such as integral weaving, braiding, knitting, and stitching will be used to produce near net-shaped structural subcomponents. Some obvious candidates include continuously braided circumferential frames, integrally woven stiffened panels, and stitched reinforcement around window openings. An integrated design-build-team effort will be conducted by Boeing, Lockheed, and Grumman. This is necessary since some of the subcomponents will be delivered to Boeing for test in their fixtures. Additional test articles will be delivered to NASA Langley for testing in new combined load machines/fixtures that are under development.

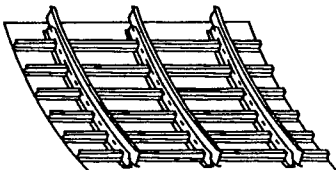
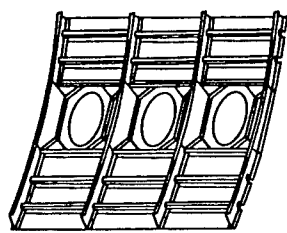
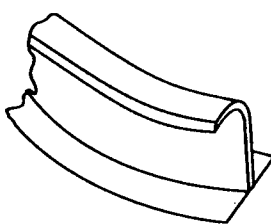
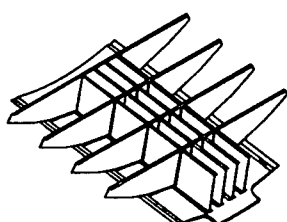
<b>Skin/Stiffened Fuselage Panels</b>  <ul style="list-style-type: none"><li>• Damage tolerance</li><li>• Buckling/postbuckling</li><li>• Pressure pillowing</li><li>• Combined cyclic loads</li></ul>	<b>Fuselage Window Belt</b>  <ul style="list-style-type: none"><li>• Out-of-plane/interlaminar stresses</li><li>• Stability under combined loads</li><li>• Damage tolerance/pressure containment</li></ul>
<b>Circumferential Fuselage Frames</b>  <ul style="list-style-type: none"><li>• Combined loads</li><li>• High interlaminar stresses</li><li>• Durability of frame/stringer/skin attachments</li><li>• Frame splices</li></ul>	<b>Keel Beam/Frame Intersections</b>  <ul style="list-style-type: none"><li>• Impact damage tolerance</li><li>• Through penetration/damage containment</li><li>• Durability of beam/frame splices</li></ul>

Figure 26

## STRUCTURAL ELEMENT AND SUBCOMPONENT EVALUATION

Key structural element and subcomponent tests must be conducted to assess performance of textile reinforced composites. Tests that measure out-of-plane load capability and damage tolerance are required to demonstrate the attributes of textile material forms. Some of the tests that are planned by the NASA ACT contractors are shown in figure 27. It is expected that textile reinforced composite structural elements will demonstrate significant improvements in compression and shear postbuckling strength, post-impact compression strength, and combined compression and shear load capability. Analytical methods will be developed to predict structural response. Predicted behavior will be compared with experimental results.

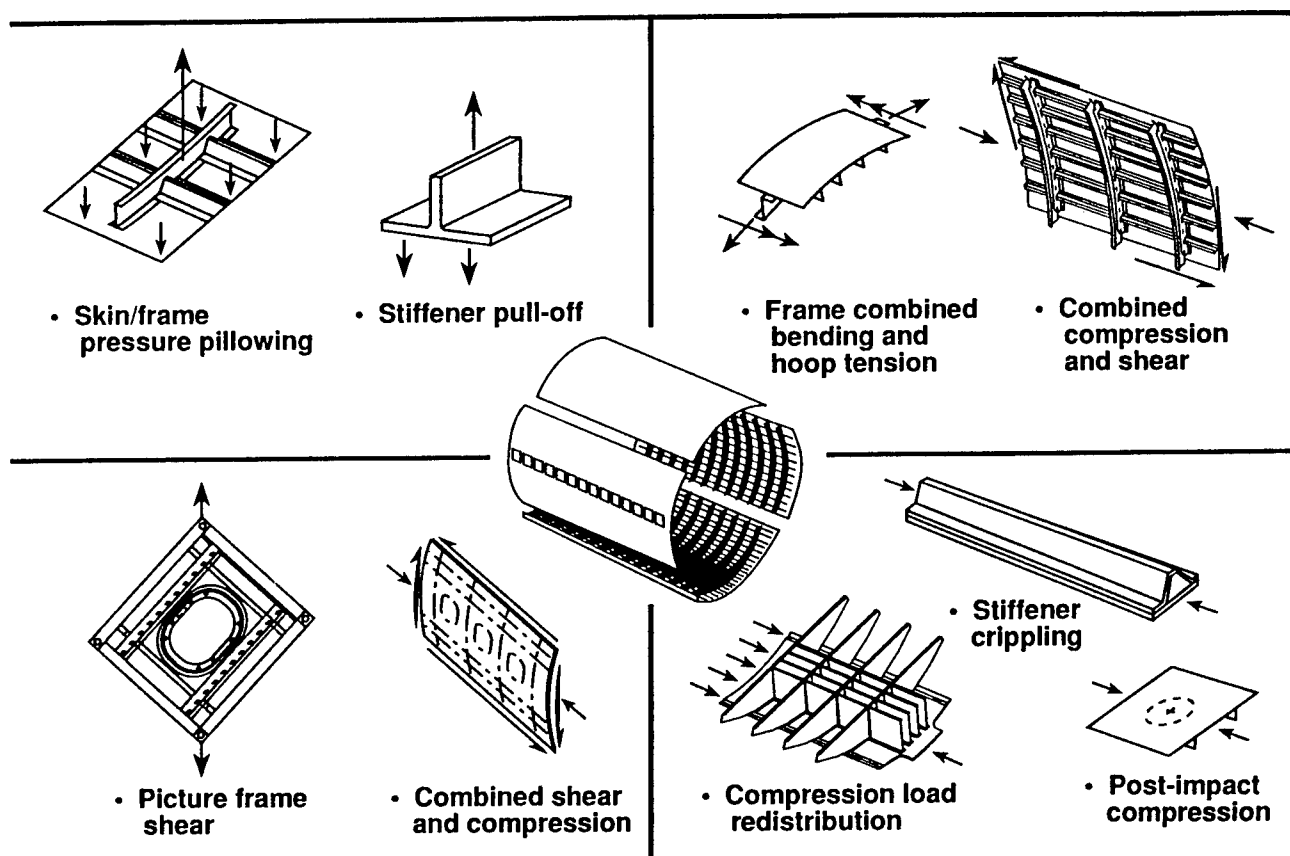


Figure 27

## NEAR-TERM RESEARCH DIRECTIONS

Redirection of some of the NASA ACT contracts on textile reinforced composites has provided an aircraft structures focus to the textile program. This focus will allow textiles to be applied to specific structural elements where textiles offer a clear advantage over more conventional material forms. The near-term research directions for the NASA Langley textile reinforced composites program are indicated in figure 28. Engineering design guidelines and performance requirements for application of textile to aircraft structures will be established. Analytical models will be developed to predict material behavior and structural performance.

Processing and fabrication studies that focus on science-based understanding of processing parameters and tooling concepts will be accelerated. Trial-and-error processing studies that have been conducted in the past are too costly and must be minimized. New test methods are required to establish an accurate assessment of textile material performance. Design property databases for applicable textile material forms must be generated so that designers can conduct accurate trade studies.

Structural elements and subcomponents that exploit the full potential of textile material forms will be designed, fabricated, and tested. An integrated team that includes textile preformers, structural designers, analysts, process engineers, and tool designers has been established to work together for cost-effective structural application of textile materials.

- **Establish engineering design guidelines and performance requirements for aircraft applications**
- **Develop analytical models to predict material behavior and structural performance**
- **Develop science-based processing/fabrication methods for aircraft-quality structures**
- **Expand design property data base for most promising material forms**
- **Design, fabricate, test and analyze structural elements that exploit properties of textile material forms**

Figure 28

**THIS PAGE INTENTIONALLY BLANK**

## **ADVANCED TEXTILE APPLICATIONS FOR PRIMARY AIRCRAFT STRUCTURES**

Anthony C. Jackson\*, Ronald E. Barrie, Bharat M. Shah, and Jay G. Shukla  
Lockheed Aeronautical Systems Company  
Marietta, Georgia

### **SUMMARY**

Advanced composite primary structural concepts have been evaluated for low cost, damage tolerant structures. Development of advanced textile preforms for fuselage structural applications with resin transfer molding and powder epoxy materials is now under development.

### **INTRODUCTION**

As part of the NASA Advanced Composite Technology Program, Lockheed Aeronautical Systems Company (LASC) is under contract to develop low cost, light weight primary aircraft structures. This contract, NAS1-18888, "Advanced Composite Structural Concepts and Material Technologies for Primary Aircraft Structures", consists of two phases.

Phase I has been underway since May 1989 and will be completed in March 1992. This phase consists of five tasks. Task 1, "Design/Manufacturing Concept Assessment", is complete. This task consisted of design trade studies for wing and fuselage structures. The results of these studies were presented at the NASA ACT Conference in Seattle, Washington in November of 1990. Task 2, "Structural Response and Failure Analysis", involved the development of generic structural models and postbuckling analysis. Task 3, "Advanced Material Concepts", develops and evaluates polyisoimide and SIPN materials for High Speed Civil Transport applications. Task 4, "Advanced Concepts Assessment Review", involved the preparation and presentation of the plans for Phase II for NASA approval. Task 5, "Composite Transport Wing Technology Development", involved fabrication and assembly of a transport wing center box. This box was tested by LASC earlier this year and the results are the subject of another paper at this conference.

Phase II, "Development and Verification of Technology", is now underway and will run to early 1995. This phase involves the development of advanced textile preforms, with resin transfer molding (RTM) and powder epoxy technology, to provide low cost, damage tolerant fuselage structures.

This phase consists of four tasks. Task 1, "Advanced Resin Systems for Textile Preforms", evaluates and selects RTM and powder epoxy systems. Task 2, "Preform Development and Processing", develops near-net-shape textile preforms for fuselage applications. Task 3, "Design, Analysis, Fabrication, and Test", covers four structural components: fuselage frames, window belt insert, keel beam/frame intersections, and a skin/stiffened fuselage panel. This task also includes supporting analytical methodology development and validation. Task 4, "Low-Cost Fabrication Development", explores innovative tooling concepts and advanced textile machine requirements.

This paper summarizes Phase I progress, the work underway in Phase II, and the plans to completion.

### **PHASE I EVALUATION AND INITIAL DEVELOPMENT**

This phase is nearing completion. The remaining tasks are Task 2 which covers analytical methods development, and Task 3 which involves the development of advanced polymers for supersonic transport applications in the High Speed Research program.



## Task 2 - Structural Response and Failure Analysis

The primary objective of this task is to develop analysis methods and modeling techniques to accurately evaluate the global response of stiffened structures to combined in-plane and out-of-plane loadings.

The finite element solution based approach was taken to address the complex interaction of nonlinearities due to pressurization, postbuckling, and geometric configurations for stiffened structures representative of wing cover panels, fuselage shells, spar webs, bulkheads, and ribs.

To produce an efficient solution and effective computer utilization during non-linear analysis, the Arc Length method due to Riks (1) was implemented in the DIAL finite element code. This method eliminates singularity in the tangent stiffness matrix at the critical point that causes major computational difficulties in a conventional trial and error approach. This method allows the unstable branch of the postbuckling response to be predicted. The implementation of the arc-length solution method has several unique features such as: automatic shifting between load and displacement control to ensure numerical stability and trace out of the full response curve.

To illustrate this capability, for the spherical cap under a point load at the apex, a load/deflection curve is shown in Figure 1. The solution curve has two limit points - a local maximum (A) and a local minimum (B). Using only load control, the cap would dynamically snap to the inverted shape as soon as the point A is reached. The portion of the solution curve between the first limit point and the dynamic snap could not be traced. Using the Arc Length solution method - the solution starts off with the load control, switches automatically to the displacement control as the limit points are approached, and then back to the load control as limit points are passed. Figures 1 and 2 shows the DIAL non-linear solution capabilities with a test problem consisting of an axisymmetric, shallow spherical cap under a point load at the apex. The DIAL results are compared with published solution by Mescall (2), for pinned-roller support in Figure 1, and by other finite element programs (3,4), for clamped conditions in Figure 2.

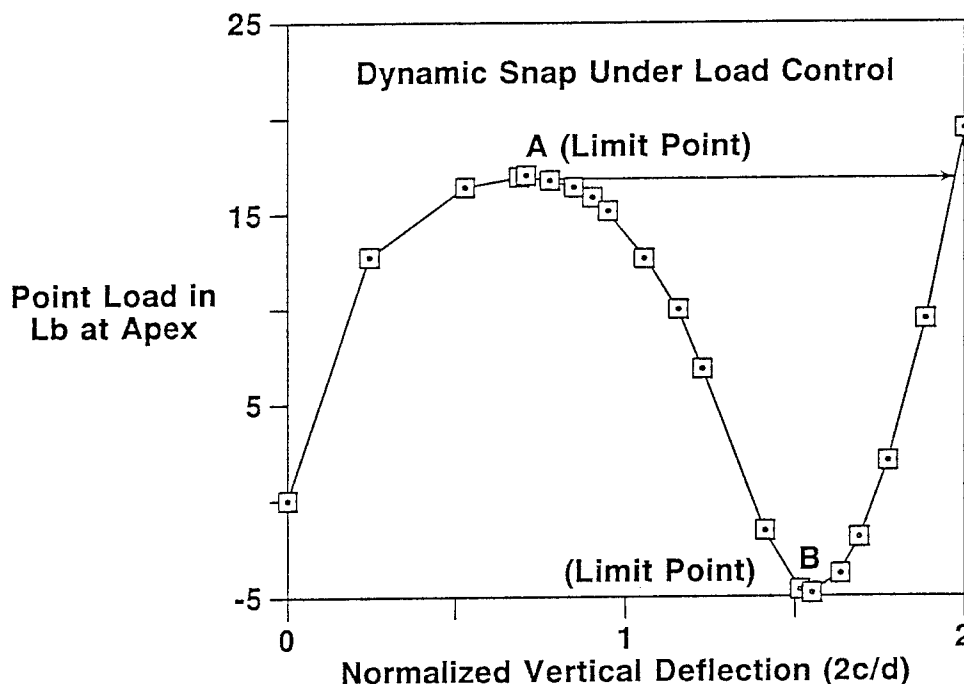


Figure 1. Load Deflection Curve and Limit Point Prediction for Spherical Cap

To develop a relatively simple analysis method for bonded structures, a new material model has been implemented in the DIAL finite element code for use with the 2-D and 3-D interface elements. This material model enables the interface elements to model a thin layer of bonding material with its shear stress-strain relationship to be generally non-linear. The stress field for interface elements consists of a normal stress perpendicular to the plane of the element and interlaminar shear stress(es). The verification of this upgrade was accomplished by comparing the DIAL results for a 3-D lap joint to those obtained by Sharifi and Sable (5). Figure 3 is a plot of the bond peel stresses at the failure load (P) of 4200 lb/in, from both the analyses. It can be seen that the agreement, is very good.

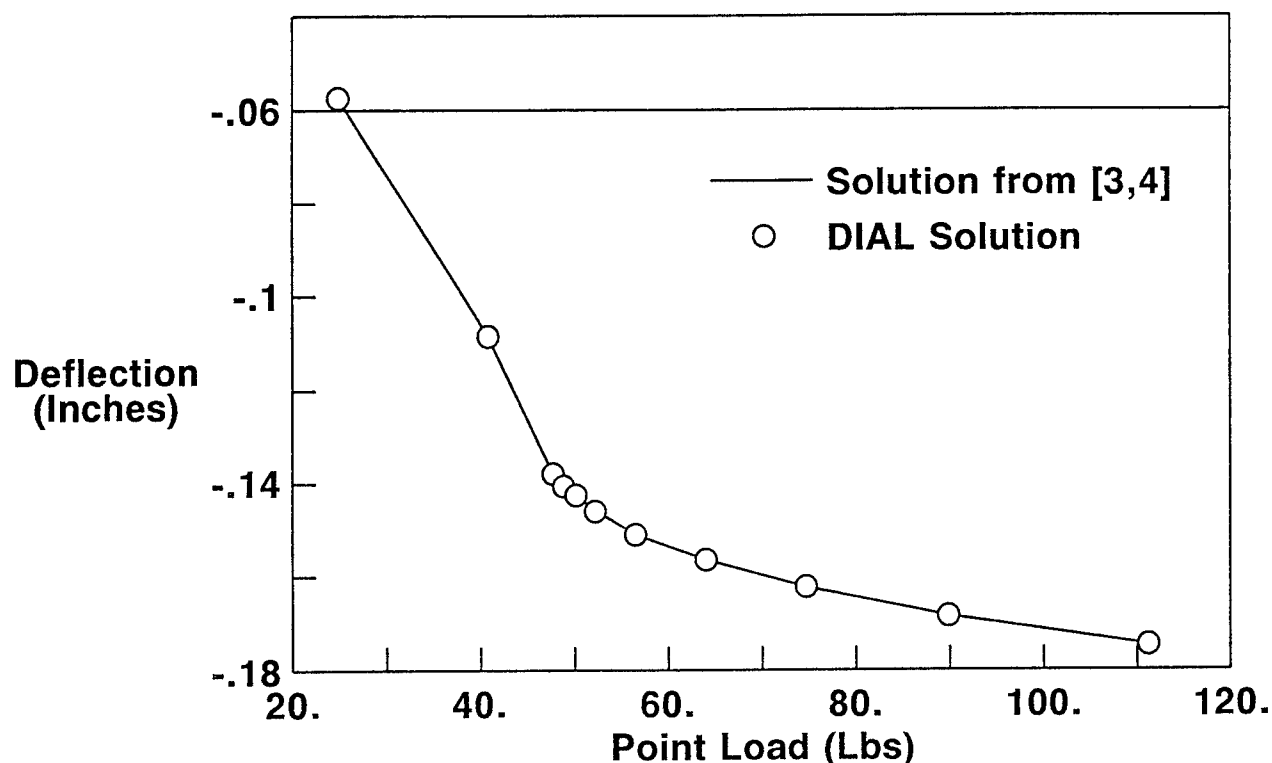


Figure 2. Displacement of Apex vs. Load for Example 2.

The AML (% Angle plies Minus % Longitudinal plies) laminate failure methodology has been implemented in the DIAL code. The AML method is a simplified approach to obtain the design allowable strain which account for fastener holes, barely visible impact damage, and internal defects in a symmetric and balanced laminate. Based on the user supplied AML values for tension and compression, the SCOPE post-processor in the DIAL computes margin of safety using AML failure strain at each integration point, in four fiber directions (0,+/- 45, 90) at the top, middle, and bottom of laminate. The minimum of the twelve margins at each integration point is used to generate a plot. As an illustration, a tubular panel, in Figure 4(a), subjected to a uniform compression loading was analyzed and contour plots of the AML margin of safety for each element of the panel were generated. Figure 4(b) shows one of the contour plot margin of safety of the bottom face sheet.

For streamlining the analyst's work during a concepts analysis/trade study, a series of DIALMATIC programs are developed. These programs combine a series of modules with the finite element code DIAL as its backbone, hence it is called DIALMATIC. Each DIALMATIC program is an interactive design tool that is intended to provide the means of performing a self-initiated preliminary analysis of specific primary composite structures, such as: flat stiffened panel, corrugated flat sandwich panel, curved stiffened fuselage panel, and curved geodesic fuselage panel. The DIALMATIC program requires the user to simply specify basic geometry, material properties,

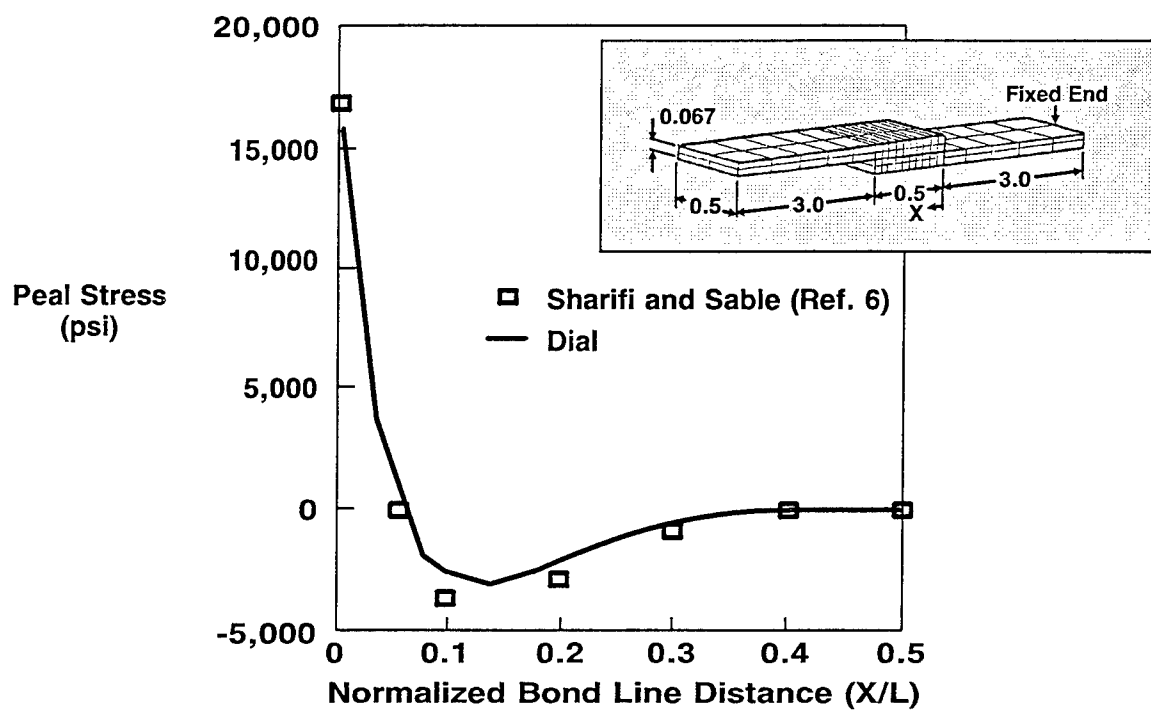


Figure 3. Peel Stresses in Adhesive at Failure

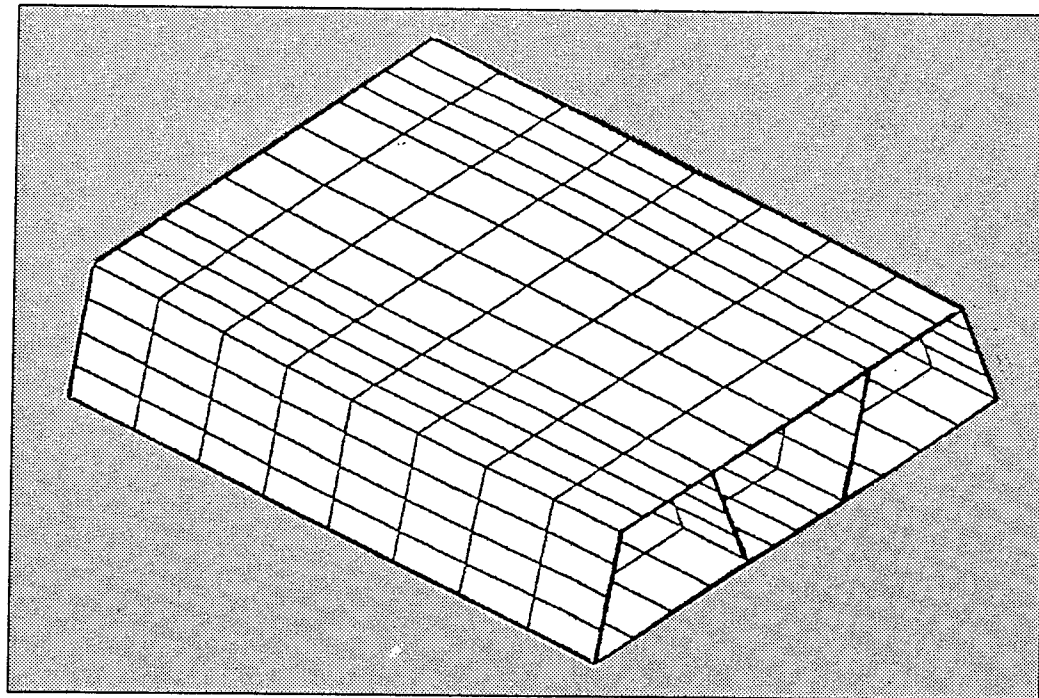


Figure 4(a). Tubular Sandwich Panel Model

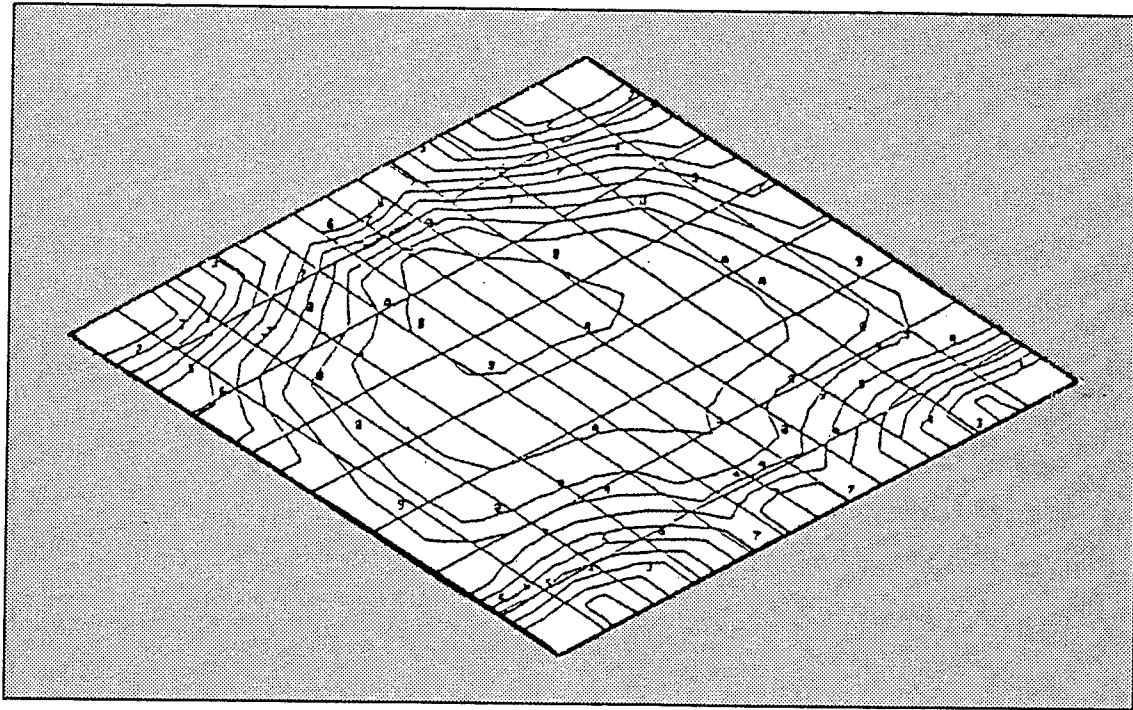


Figure 4(b). Contour Plot of AML Margin-of-Safety - Bottom Face Sheet

loads information, boundary conditions, and types of analysis. The program utilizing this information generates the finite element model automatically and performs the analysis. The output in the form of summary tables of stress or margin of safety, contour plots of loads or stresses or strains and deflected shape plots which may be used to determine the adequacy of the specific design concept. Figure 5 illustrates the mesh generated by the four modules, each with different types of stiffening elements.

The last part of this task concerns the development of bolted composite joint strength prediction methodology. The motivation of this task was in direct response to the need for an accurate strength prediction for multifastener composite joints and to alleviate significant costs associated with obtaining strength data through testing. The methodology developed is a 2-D non-linear finite element based analysis considering material and geometrical non-linearity. It also conducts an in-situ strength failure analysis and applies material degradation models. To date significant progress has been made in the development of the analysis code. The developed code is interactive and has the capacity to analyze matrix tension and compression failure, shear-out failure, and fiber failure. Work is in progress to include a bearing failure model. Validation of the code (called TEXTJOINT-X) developed to date is in progress and the predicted versus test results for a T300/1034 doubler shear joint with 100 percent load transfer.

### Task 3, Materials Development

The objective of this task is to establish the feasibility of bridging the current polymer composites technology with future technologies for supersonic transport systems.

Current research is concerned with the high-performance attributes of polymer materials, which include: high level of thermal and thermo-oxidative stability, high level of fracture toughness, high modulus and strength, especially in compression and environmental durability.

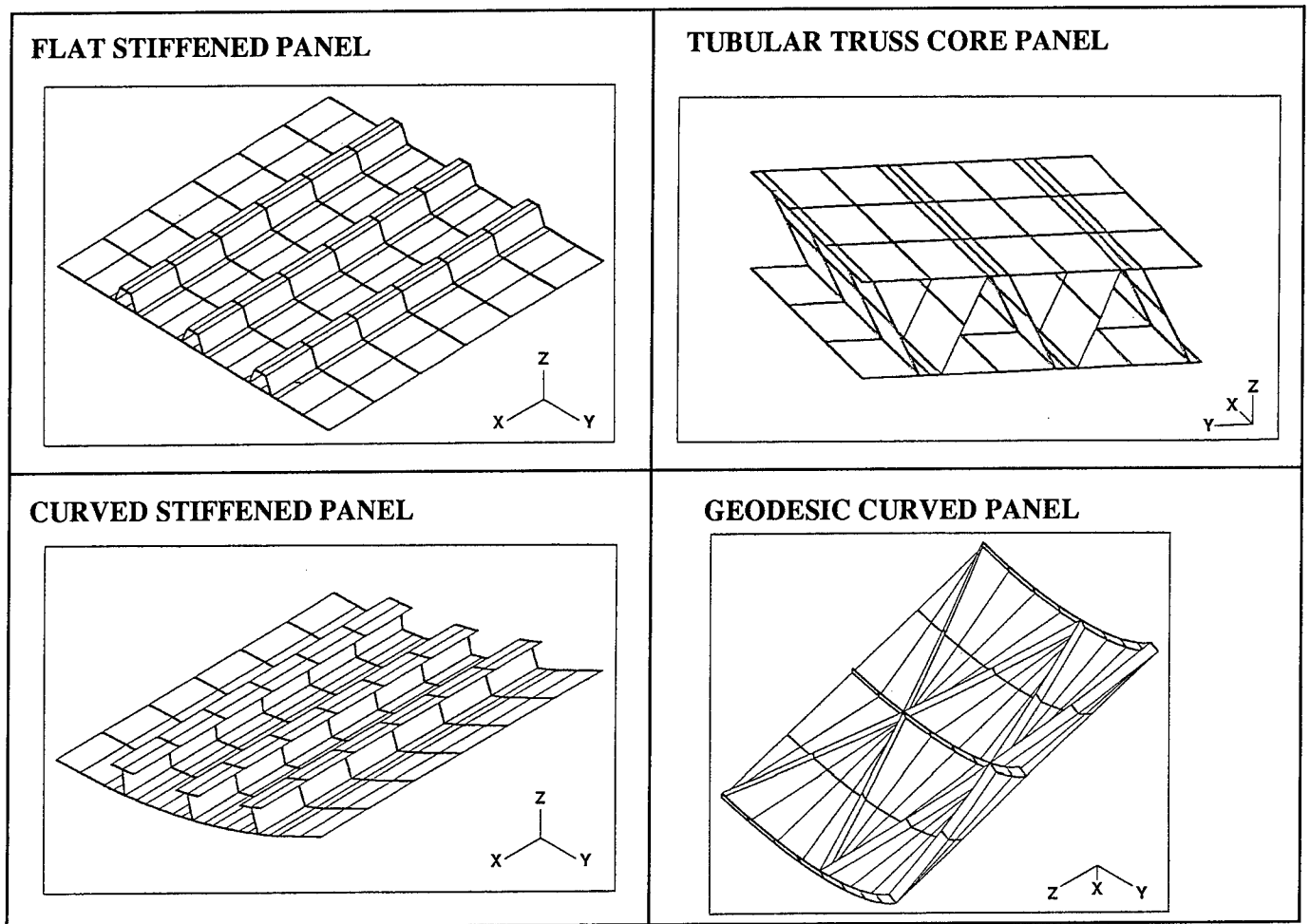


Figure 5. Mesh Generated for Four Typical Modules

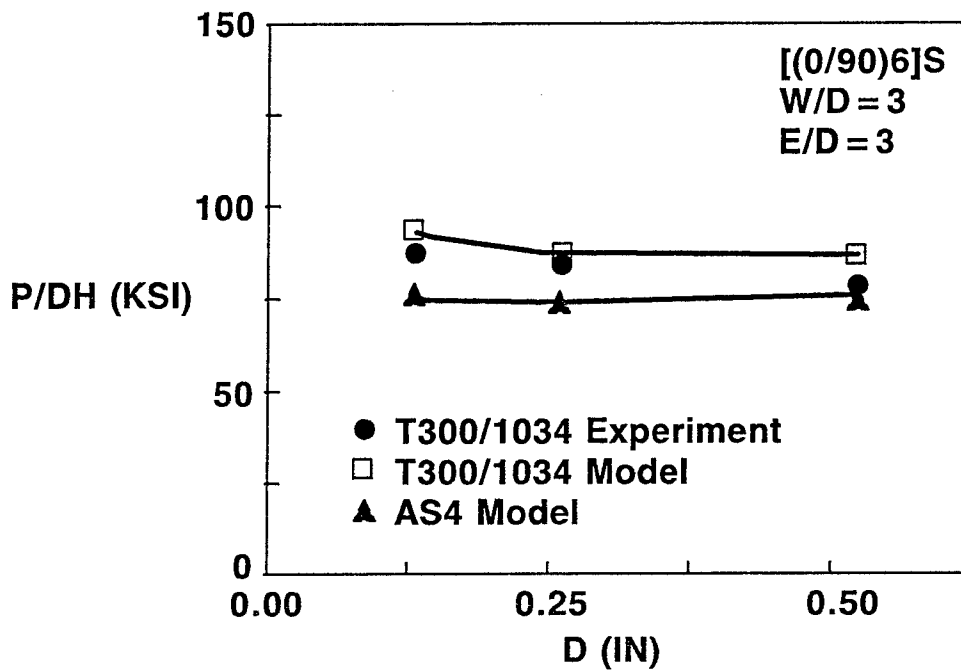


Figure 6. Comparison of Failure Load of Bolted Joints

The emphasis is on an interdisciplinary study, involving chemistry, mechanics, and processing of imide based copolymers which are amenable to chemical modification through the isoimide technique for processability enhancement. Property tailoring is examined through polymer blending and copolymer techniques. Various polymer blends can be designed for different operating temperature ranges.

Isoimide modification of polyimides generally improves melt and solution processability of imide containing thermoplastics, such as polyimides, poly(imide-sulfones), poly(ether-imides), poly(ether-ketone-imides), and imide-hetrocycle hybrids. The isoimide form permits easier processing. The isoimide then converts to the imide during cure without the generation of volatiles. The chemical transformation from monomers to polyamic acid, which in turn forms the isoimide and imide, is well defined chemistry and providesreproducible synthesis and thus easy quality control.

Polyimides are ideal candidates due to there overall high performance. The key issues, however, are processability and cost-effectiveness. The supply of monomers allows permutations of these monomers to generate new polymers and copolymers. Using these available monomers, NASA developed such thermoplastic polyimides as LARC-TPI, LARC-ITPI, LARC-CPI, and LARC-PIS. The constructive monomers of a variety of high performance polyimides are commercially available to synthesize these polymars.

Other high-temperature resistant polyimide systems include Ube's Upilex polyimides andoxybis (3,4-dicarvoxyphenyl) dianhydride based polyimides. The semicrystalline nature of LARC-CPI and Upilex permits molecular orientation to achieve modulus enhancement.

Table 1 summarizes the rankings of the various polyisoimides studied. LARC-ITPI is the most attractive material system for near-term applications. A strong second choice is the copolymers of poly(TDA-APB)isoimide and poly(BTDA-3,4'-ODA)isoimide.

The three systems currently being prepregged and tested are LARC- ITPI isoimide, Copolyisoimide 0-11, and Copolyisoimide 0-13.

Table 1, Ranking of Polyimide candidates

Final Ranking	Trivial Name	Polymer Constituent		Criteria		
		Dianhydride	Diamine	Cost Comp	Ease of Synth	Good Prelim Results
1	LARC-ITPI Polyisoimide	IPDA	MPDA	1	1	Yes
4	Polyisoimide O-10	BTDA	3,4'-ODA	2	2	Yes
2	Copolyisoimide O-13	BTDA	APB(3) 3,4'-ODA(1)	2	1	Yes
2	Copolyisoimide O-11	BTDA	APB(1) 3,4'-ODA(1)	2	1	Yes
5	Polyisoimide B-10	BTDA	BAPP	1	2	need more evaluation
6	OPDA-based Polyisoimides	OPDA	Various Diamines	2	-	need evaluation

## PHASE 11 DEVELOPMENT AND VERIFICATION OF TECHNOLOGY

This phase has been entirely rescoped as a result of the ACT Steering Committee recommendations late last year. The objectives of this phase are: to develop and exploit textile preform technology, resin transfer molding and powder resin technology, to produce low-cost components for fuselage structures. Lockheed is working closely with Boeing and will produce the textile preform components to be incorporated into the large Boeing test panels. To this end Lockheed is participating in the Boeing Design Build Teams for the keel and window belt structures on the Boeing 767X baseline airplane.

This phase is just getting underway, Initial evaluation of the resins and textile technologies is proceeding. A resin transfer molding machine is being ordered. Lockheed personnel have been participating in the Design Build Team for keel structure.

This phase is scheduled to cover 42 months and will provide parts in a building block approach for testing up to the final curved fuselage panels, 85 inches long by 60 inches wide.

### Task 1, Advanced Resin Systems for Textile Preforms

The epoxy resin systems currently used for resin transfer molding (RTM) fall short in their performance for aircraft primary structures. In particular their damage tolerance characteristics and environmental resistance are inadequate. These deficiencies can be offset by exploiting 3-D textile woven and braided preforms. New toughened resin systems offer an opportunity to significantly improve these properties when combined with the textile preforms. The use of near net preforms and non-autoclave processes offers a substantial cost reduction potential for aircraft primary structures.

An alternative approach is to fabricate the preforms from a powder coated tow which can be processed by pultrusion, compression molding, autoclave molding, and if additional resin is needed then by RTM.

The resin selection criteria for RTM and for powder resins are different. Figure 7 shows the flow of resin evaluation. The emerging toughened resin systems are currently being evaluated by NASA and the Aerospace Industry for potential applications in aircraft primary structures. Much of these data will be available to aid in resin selection for this program.

#### Resin selection criteria for RTM

- o Low viscosity (300 500 cps)
- o Long pot life (6-8 hours)
- o Processibility
- o Environmental resistance (180°F wet)
- o Toughness for damage tolerance
- o Cost and performance

The following systems have been selected for initial screening:

- o PR-500 (3M)
- o RSL-1895 (Shell Chemical)
- o E-905L (BP Chemical)
- o CET-3 (Dow)

Screening will be accomplished by fabricating 8-harness satin fabric laminates by RTM with each of the resins. Each laminate will be cut up and tested according to the test matrix shown in Table 2. The ease of processing static and dynamic test performance and cost will be the primary factors for selection. The selected system will be used in Task 2 to evaluate the textile preforms.

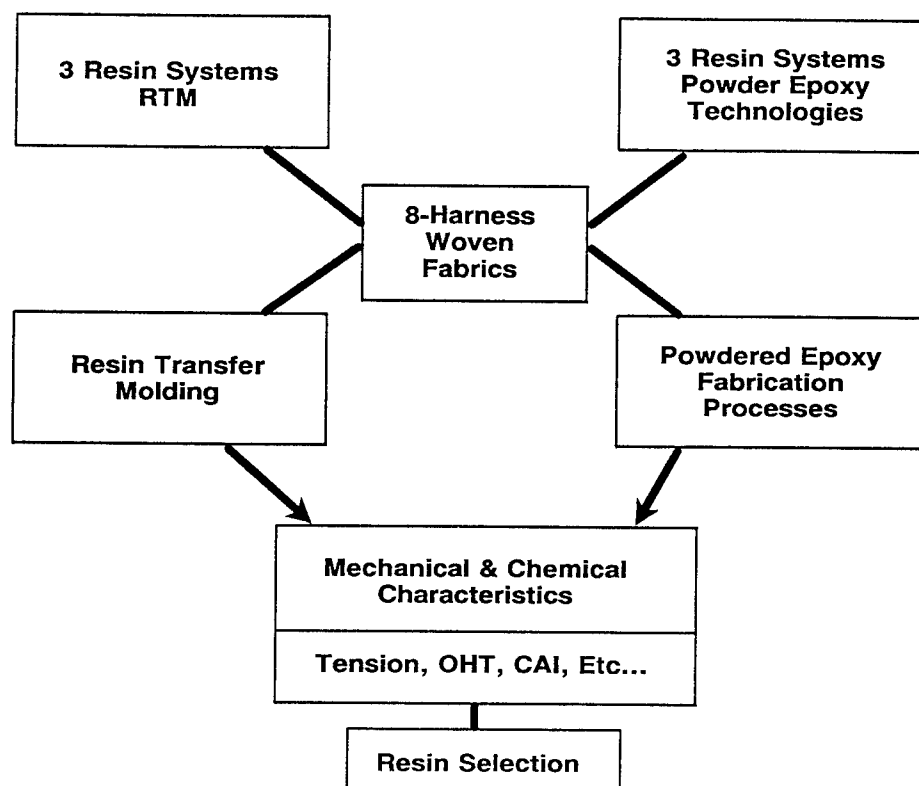


Figure 7. Task 1 Evaluation Approach

Table 2. Material Screening Test Matrix

Laminate Orientation	Test Type/Loading	Specimen Size	No. of Specimens @ t °F				Test Method
			t (in)	-65°F	RTA	180°F Wet	
0°	UNT	1.0 x 12.00	0.045	3	3	3	ASTM D-3039
0°	UNC	1.0 x 5.50	0.12		3		ASTM D-3518
±45°	UNT	1.0 x 10.00	0.08		3		
QI	UNT	1.25 x 12.00 DB	0.12	3	3	3	ASTM D-3039
QI	OHT	1.25 x 12.00	0.12		3		ASTM D-3039
QI	UNC	1.25 x 12.00 DB	0.12		3		Modified A-11
QI	OHC	1.25 x 12.00	0.12		3		Modified A-11
QI	CAI	4 x 6 (Boeing)	0.16		4		Boeing



Powder technology offers major potential benefits for the fabrication of near net shape composite structures at reduced cost. Labor intensive hand layup is eliminated, improved fiber/resin interface will allow tight weaving and braiding to be maintained.

The powder towpreg can be converted into preforms by 3-D weaving, braiding, knitting, and stitching processes. These preforms can be processed into parts by compression molding, pultrusion, and autoclave molding.

Two types of powder coating processes will be evaluated for low cost towpreg. The first is a solution coating with a water base slurry and the second is an electrostatic coating process. Selection will be based on the adhesion of the resin to the fibers, coated tow flexibility and weavability and braidability of the coated tows.

Powder resin selection criteria:

- o Shelf-life at room temperature
- o Particle size
- o Environmental resistance
- o Toughness for damage tolerance
- o Viscosity
- o Glass transition temperature
- o Cost and performance

The shelf life of the resins at room temperature is of prime importance not only in the powder form but more importantly when coated on the fibers and tows, because the towpreg will go through various room temperature processes in the weaving, braiding, and knitting before processing into its final form. Thermal and chemical stability will be acceptance criteria.

Particle size is also a critical element in achieving good coating. For example, the slurry bath requires particle sizes ranging from 30 to 100 microns and for electrostatic coating 100 to 200 microns. A low glass transition temperature (60 C) and low moisture absorption is needed for the slurry process. Low moisture absorption is also required for the electrostatic process along with large particle size for uniform high cloud formation. The degree of fusion and fibre/resin interface is also extremely important for subsequent textile operations and part fabrication. The handlability and flexibility of the powder towpreg will be dependent on the degree of fusion and will require tailoring to meet specific textile processing criteria.

The following resins were selected for initial screening:

- o PR-500 (3M)
- o RSS-1892 (Shell Chemical)
- o CET-3 (Dow Chemical)

These resin systems meet the basic criteria for powder coating processes. Flat laminated will be made from 8-harness satin fabric woven from powder towpregs. The screening test matrix is shown in Table 2. Processability in powder coating and textile operations, performance and cost will be the determining factors in selection of one resin system for Task 2.

## **Task 2, Preforms Development and Processing**

The objective of this task is to evaluate advanced textile preform technologies which provide improved damage tolerance and lower overall cost of advanced composite structures by reducing part count and assembly operations. Recent advances in textile processing have heightened interest in low cost fabrication methods such as RTM, pultrusion, resin film infusion (RFI), and compression molding for near net shaped structures. The following textile processes will be evaluated in this task:

- o 3-D interlock weaving/stitching

- o 3-D weaving
- o 2-D braiding
- o 3-D interlock braiding
- o 3-D through the thickness braiding
- o 3-D multi-axial warp knitting/stitching
- o 3-D Near Net Fiber Placement (N<sup>2</sup>FP), stitching

Flat laminates will be produced from dry tow and from powdered tow with the above processes and used for screening. The size and process limitations will be determined for subsequent use in task 3 for the fabrication of fuselage subcomponents. These laminates will be fabricated by RTM, compression molding, or autoclave molding and will be tested as shown in Table 2. The evaluation criteria and process are shown in Figure 8.

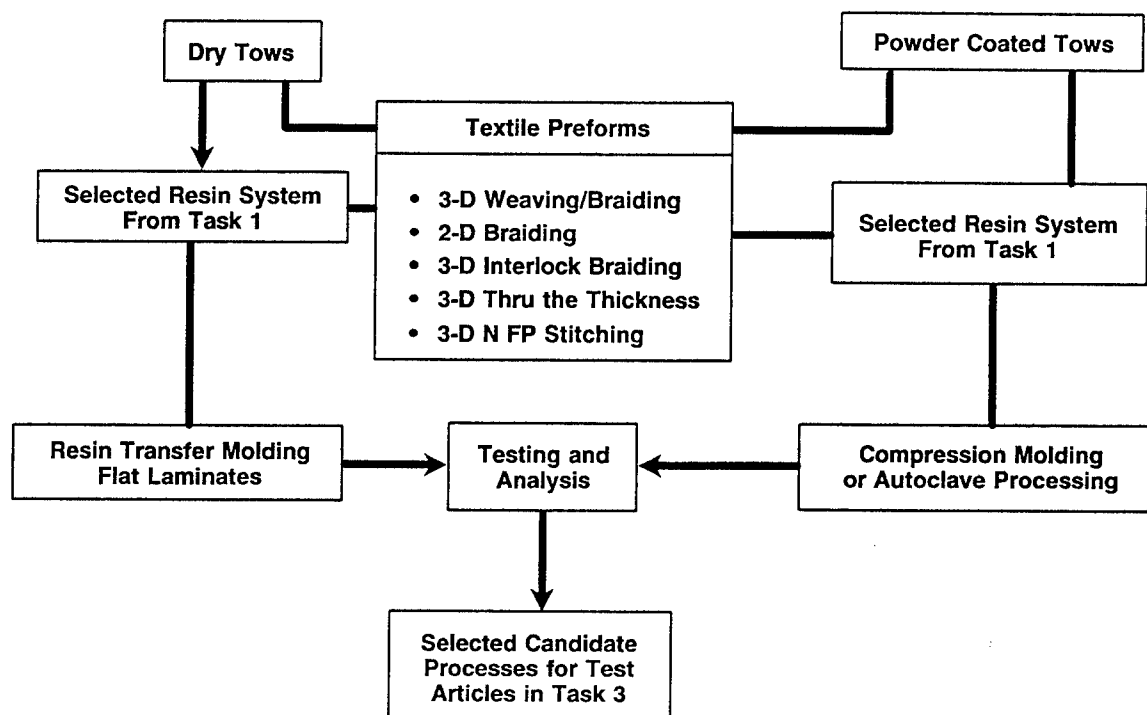


Figure 8. Task 2 - Evaluation Approach

### Current Status of Textile Processes

Figure 9 shows textile processes being evaluated and typical yarn paths. The current status and limitations of these processes are briefly reviewed.

#### (1) 3-D Weaving

3-D interlock weaving has been used to produce cruciforms, nose cones, and other aerospace components. However, it can only produce 0°/90° multi-layer fabric. It is therefore limited in its use for aircraft structures since biased (45°/135°) plies cannot be woven. Efforts are underway in the textile industry to overcome this deficiency. The 3-D weaving of quasi-isotropic, multi-layer fabric has been attempted by a manual process. In this task we will screen 3-D interlock woven/biased ply stitched materials.

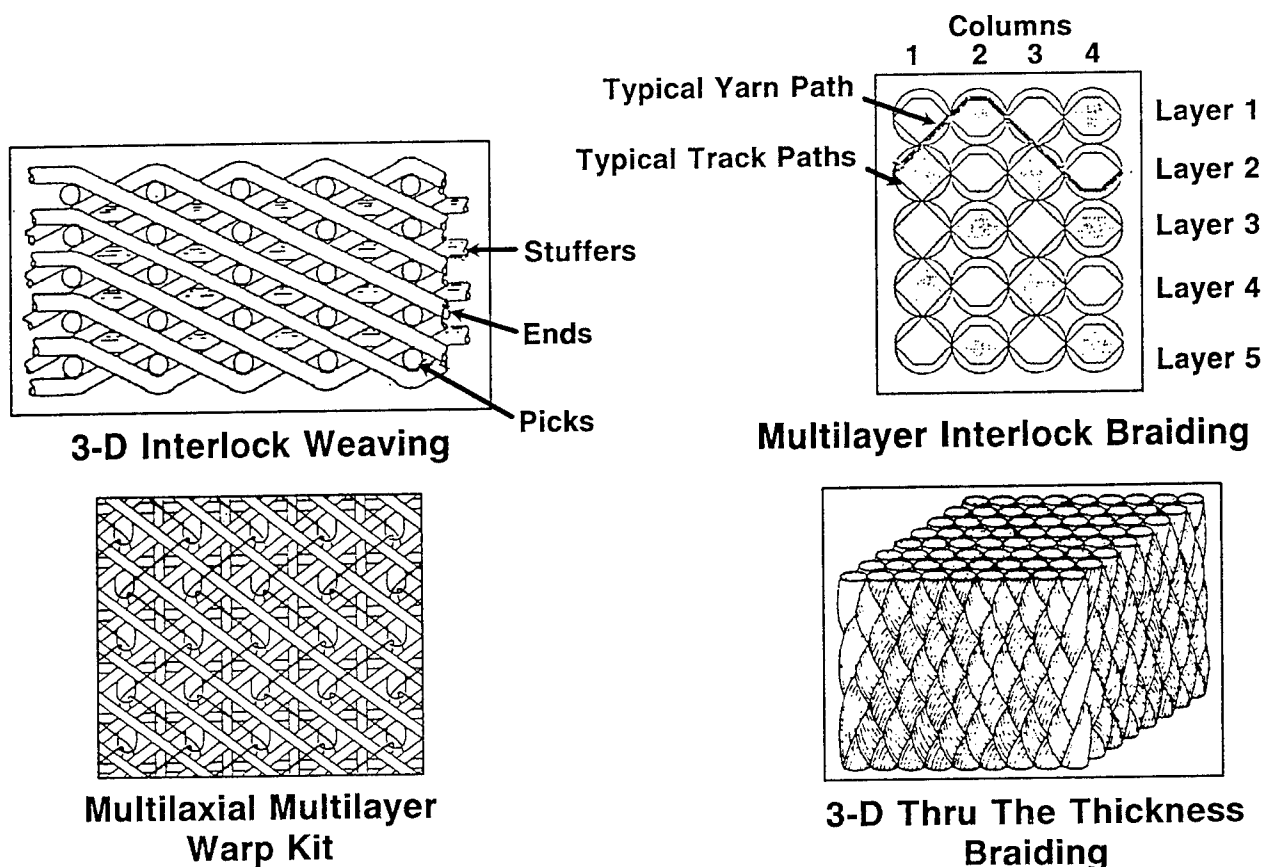


Figure 9. Textile Architectures

## (2) 3-D Braiding

2-D braiding/stitched preforms such as frames and stiffeners have been explored for aircraft structures. Size limitations, yarn coverage and manual operations limit this process to narrow parts. Advances in 3-D through-the-thickness braiding offer potential benefits in producing stiffened panels and other complex shapes. 3-D interlocking flat braiding has potential applications in near net size components such as 'J' frames, hats, and floor beams.

## (3) Multi-axial Warp Knitting/Stitching

Quasi-isotropic 4 to 7 multi-layer fabrics can be produced by this process. Stiffened panels and window frames can be produced.

## (4) $N^2$ FP Stitching

Preforms using this process can be made in any orientation, but may have some limits in thickness. The yarn path can be programmed for various shapes. Potential candidates include window frames and window belts.

The textile preform screening conducted in this task will aid in the selection of the textile processes to selected for the Task 3 elements and subcomponents.

### Task 3. Design, Analysis, Fabrication and Test

The baseline article selected for Lockheed's Phase II studies is an aft fuselage segment of the Boeing 767X commercial passenger airplane shown in Figure 10. This segment, which is also the Boeing ACT baseline article represents the latest in design and manufacturing technology for aluminum airplanes, thus providing an excellent baseline with which to compare the advanced composite structural concepts being developed under this program. The selection of a common baseline for the Boeing and the various textile processes being pursued by Lockheed and (2) components incorporating textile p[reforms] can be supplied to Boeing for incorporation in larger test articles (see Figure 11).

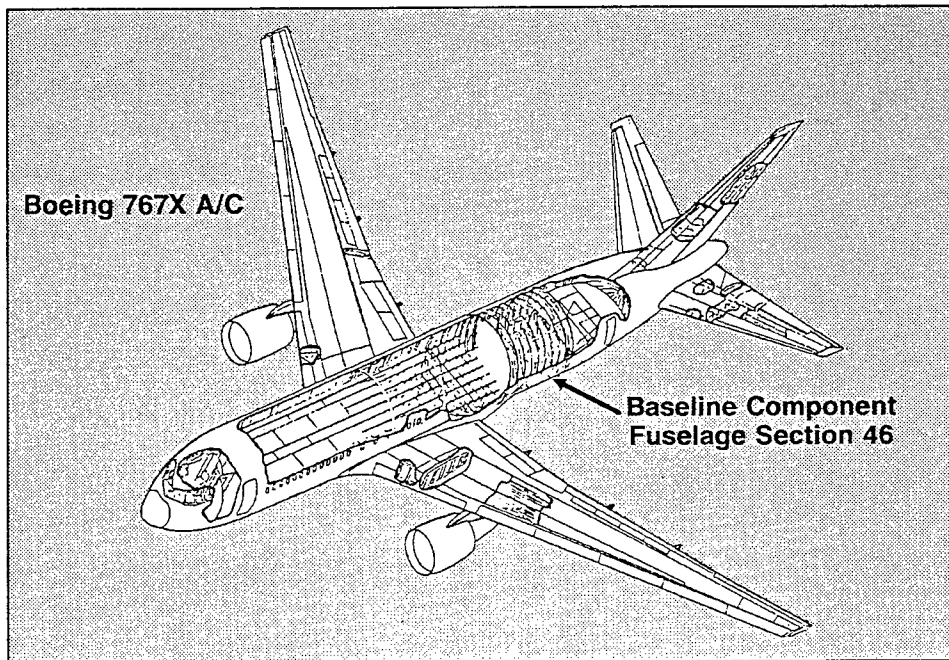


Figure 10. Baseline Airplane and Segment

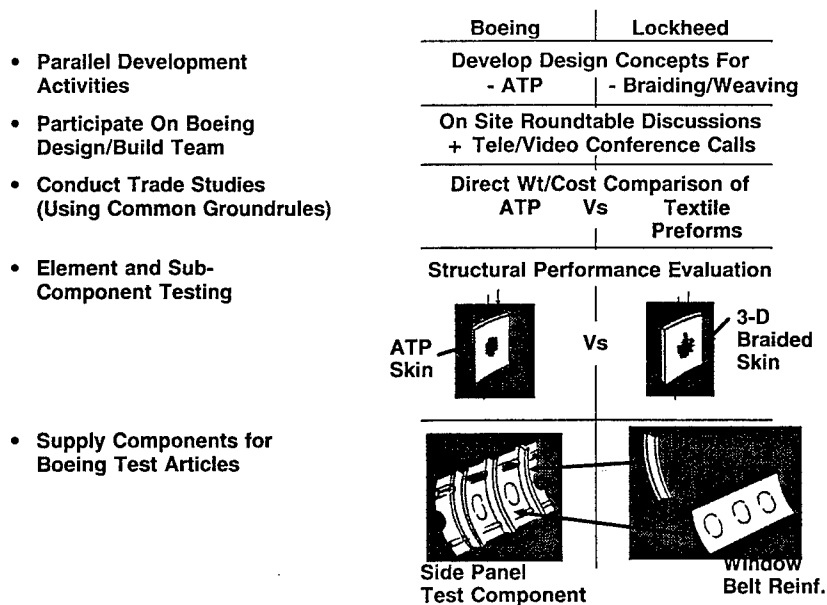


Figure 11. The Boeing Connection

The total scope of Lockheed's Task 3 activities is shown in Figure 12. It covers the design, analysis, fabrication, and test of four structural components: circumferential frames, window belt reinforcement, cargo floor support structure, and stiffened skin fuselage panel (The NASA Technology Benchmark Test Article). For each of these test components, innovative design concepts amenable to automated textile fabrication processes will be developed and evaluated with respect to structural efficiency and low cost. Those concepts judged to have a high potential for achieving the program objectives will be further evaluated through element and subcomponent testing (see Figure 13).

## **Design, Analysis, Fabrication and Test of:**

- **Circumferential Frames**
  - **Window Belt Reinforcement**
  - **Cargo Floor Support Structure**
  - **Stiffened Skin Fuselage Panel**
- (NASA Technology Benchmark Test Article)**

Figure 12. Task 3, Scope

### **For Each Component**

- **Establish Baseline Requirements**  
(767X Drawings, Loads, Environment, Interfaces, etc.)
- **Evaluate Alternative Material Systems and Textile Processes**
- **Evaluate Fabrication Methods and Tooling Concepts**
- **Develop Innovative Design Concepts Incorporating Textile Preforms**
- **Conduct Trade Studies**
- **Select Concepts for Further Development**
- **Conduct Element, Subcomponent and Panel Tests**

Figure 13. Development Approach

## Circumferential Frames

A wide variety of design/manufacturing approaches will be evaluated for fuselage circumstantial frames. Figure 14 shows the major options being considered. They range from discrete detail parts to design concepts which are totally integrated with the skin. Here the potential benefits of one-piece components (where part and fastener counts are minimized) will be weighed against process and tooling complexity. To support the Boeing test program, only discrete frame concepts which can be used in conjunction with ATP skins will be considered. Two advanced textile fabrication processes currently being evaluated for these components are shown in Figure 15. Both of these concepts employ 3-D tri-axial braiding. Various fabrication methods including RTM and pultruding powder prepreg will be investigated. Proposed element and subcomponent testing for these design concepts are shown in Figure 16.

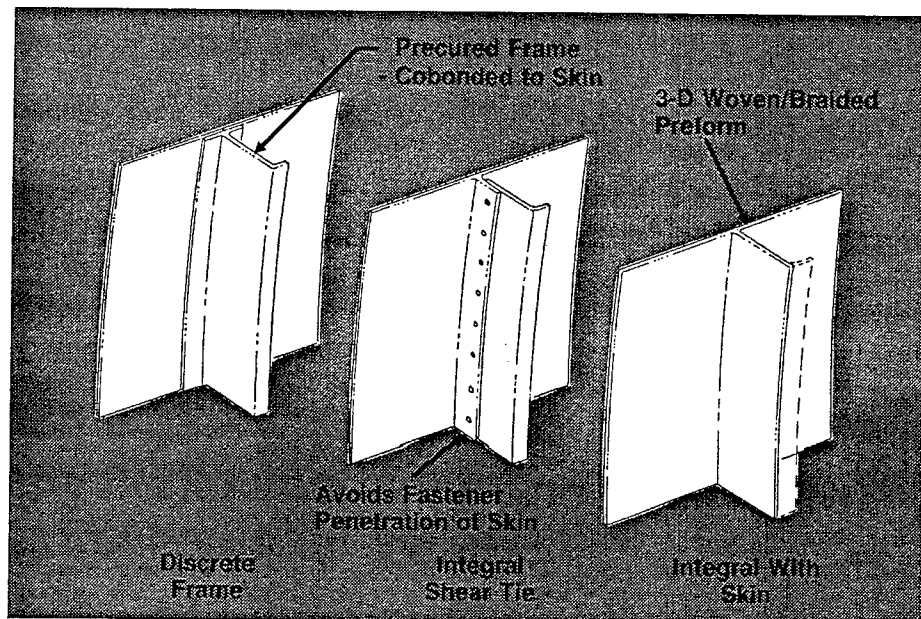


Figure 14. Frame Design Options

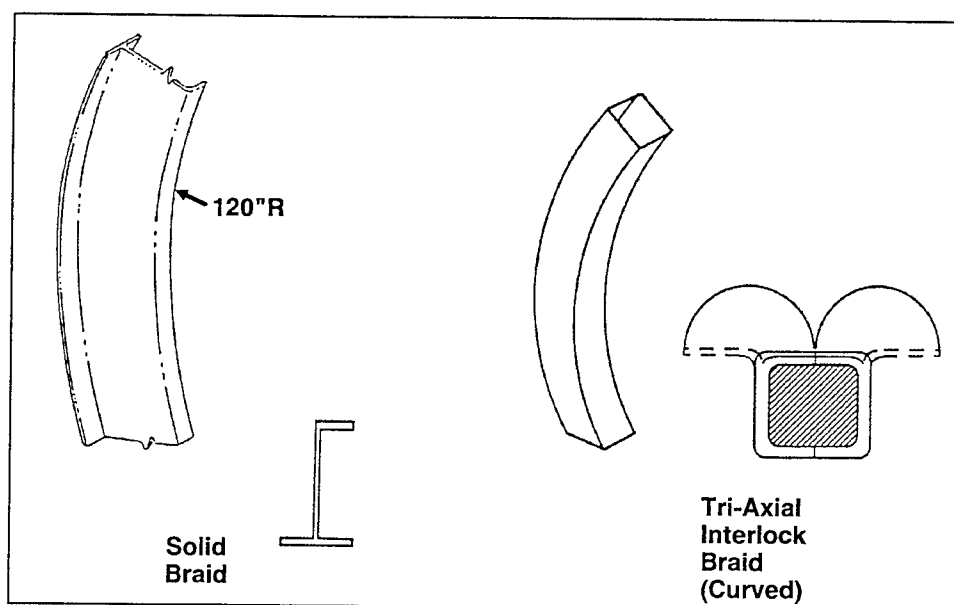


Figure 15. Fuselage Frame Concepts

## Window Belt Reinforcement

The use of textile preforms is being evaluated as an efficient method of reinforcing the window belt cutout area in composite fuselage side panels. In metallic fuselages the window belt is generally reinforced by significantly increasing the skin thickness and mechanically attaching window frames. This approach is inefficient for conventionally laid up composite structures due to the discontinuity of fibers and the interlamina stresses induced in a weak direction. The use of textiles offers an opportunity to provide continuous fibers around the cutout and through-the-thickness reinforcement, thereby providing a much more efficient structure. One such design concept currently being considered is shown in Figure 17.

this concept uses 3-D braided techniques to provide a continuous band of reinforcement as well as for individual window frames. By using powder prepreg material in the braiding process these components may be cured together with an ATP skin in a single molding operation.

Two other promising concepts being evaluated are shown in Figures 18 & 19. In the first a textile process called Near Net Fiber Placement (NFP), which allows fibers to be placed in any prescribed orientations is being considered. In the second a 3-D braiding technique is used to form the window frame from a basic belt preform. Details of a comprehensive test plan to investigate these concepts is shown in Figure 20.

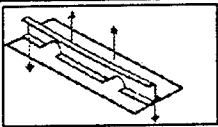

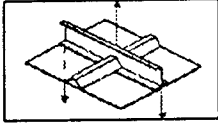
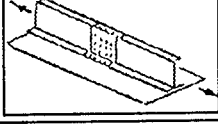
Test	Test Configuration	Specimen Configurations (Replicates)	Total Number Of Tests Planned	Conditions
Frame Bending		2 (2)	4	4 Point Bending RTD
Combined Bending And Hoop Tension		2 (1)	2	RTD
Frame/ Stringer Attachment		2 (1)	2	Cyclic Loads RTD
Frame Splice		2 (1)	2 1	RTD Cyclic Loads

Figure 16. Fuselage Frames, Test Plan

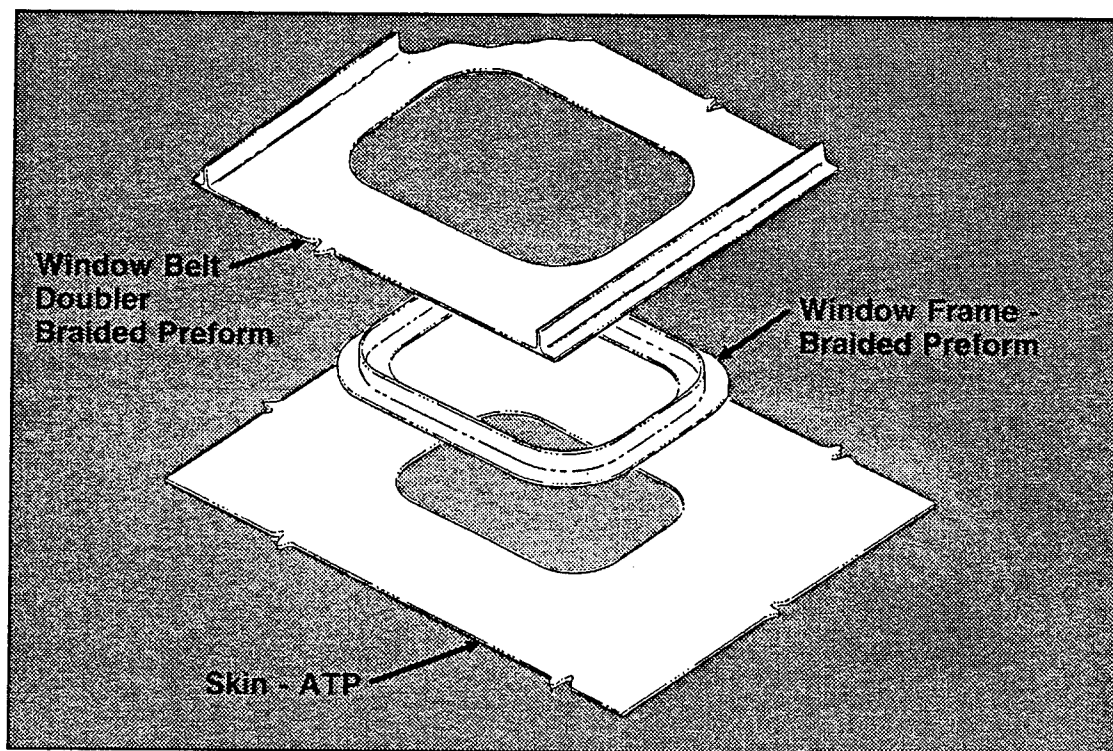


Figure 17. Window Belt Reinforcement Concept

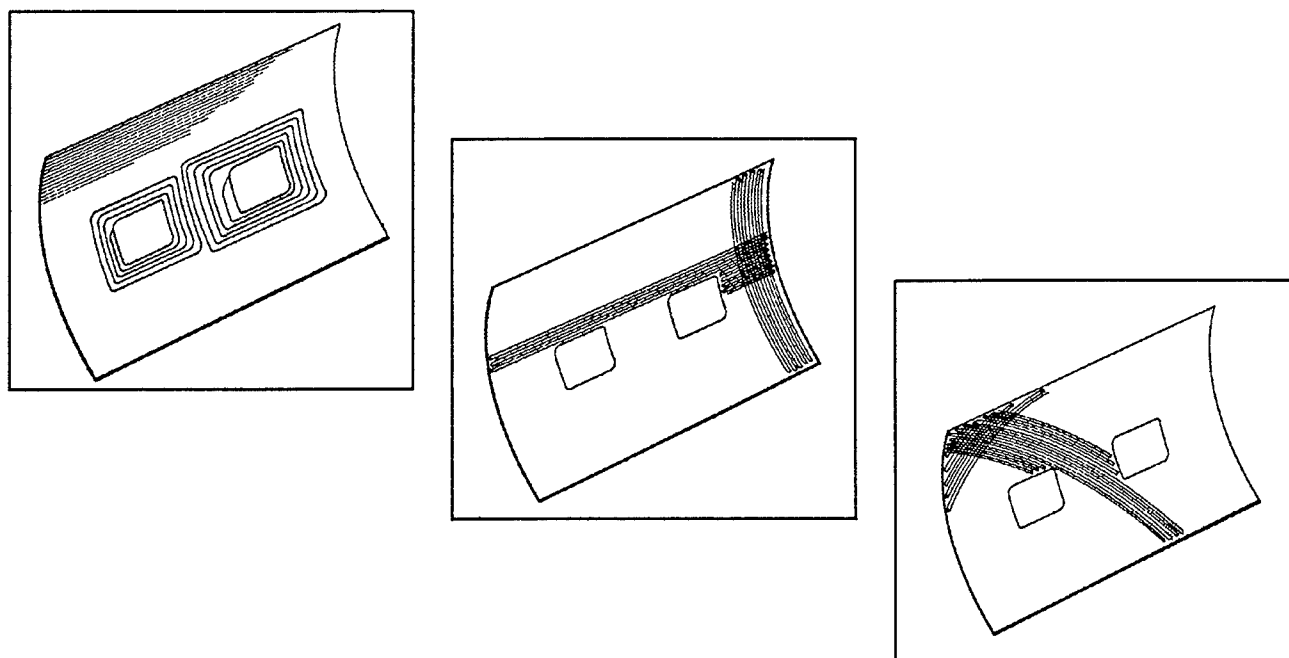


Figure 18. Window Belt Concept Using Near Net Fiber Placement



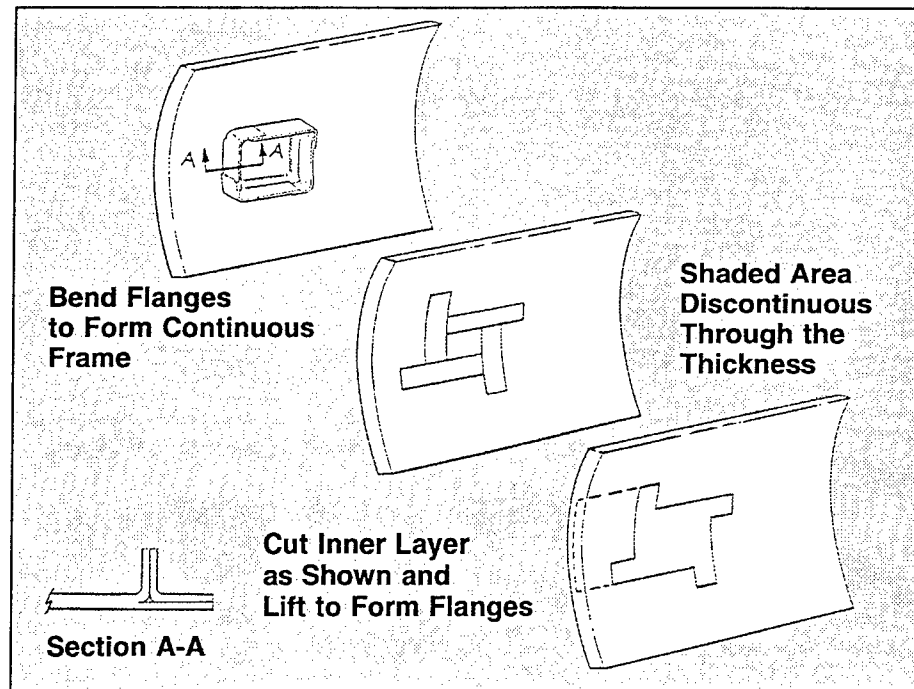


Figure 19. Window Belt Concept Using 3-D Braiding Technique

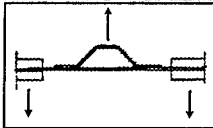
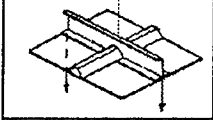
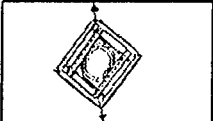
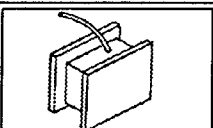
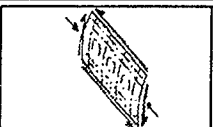
Test	Test Configuration	Specimen Configurations (Replicates)	Total Number Of Tests Planned	Conditions
Stringer Pull-off		3 (2)	6	RTD (4) ETW (2)
Frame Pull-off		2 (2)	4	RTD
Picture Frame Shear		3 (2)	6	RTD
Pressure Integrity		2 (2)	4	Impact Damage
Combined Compression And Shear		2 (2)	2	Impact Damage

Figure 20. Window Belt, Test Plan

## Cargo Floor Support Structure

The configuration of the various components constituting the cargo floor support structure offers several possible applications for textile preforms as shown in Figure 21. Some frames are of a stiffened web design while other less highly loaded frames have a beam and post configuration. The stiffened web frame design shown in Figure 22 uses 3-D woven and braided details to produce a structurally efficient cocured assembly. A major benefit realized through the use of braided cruciform members is that fiber continuity is maintained in both the web and the intercostal direction. A rather more ambitious concept is shown in Figure 23. In this concept stiffeners, cap and web are produced from a single textile preform. Several concepts for post type frame applications are shown in Figure 24. A wide variety of fabrication techniques has been proposed for these concepts. They will be fully evaluated in the trade studies and through subcomponent testing as outlined in Figure 25.

### Technology Benchmark Test Component

This component was introduced into the ACT programs to provide a direct comparison of cost and structural efficiency for a variety of fabrication processes. The Lockheed test article will highlight the latest textile processes. This large component shown in Figure 26 is approximately 85 inches by 60 inches and includes 3 frames and 4 different stiffener segments. A major goal of this subtask is to provide a one-piece co-cured assembly which does not rely on stitching to provide the out-of-plane performance. Two such concepts are shown in Figures 27 and 28. These designs together with other promising concepts will be fully evaluated through cost/weight trade studies and the test plan shown in Figure 29.

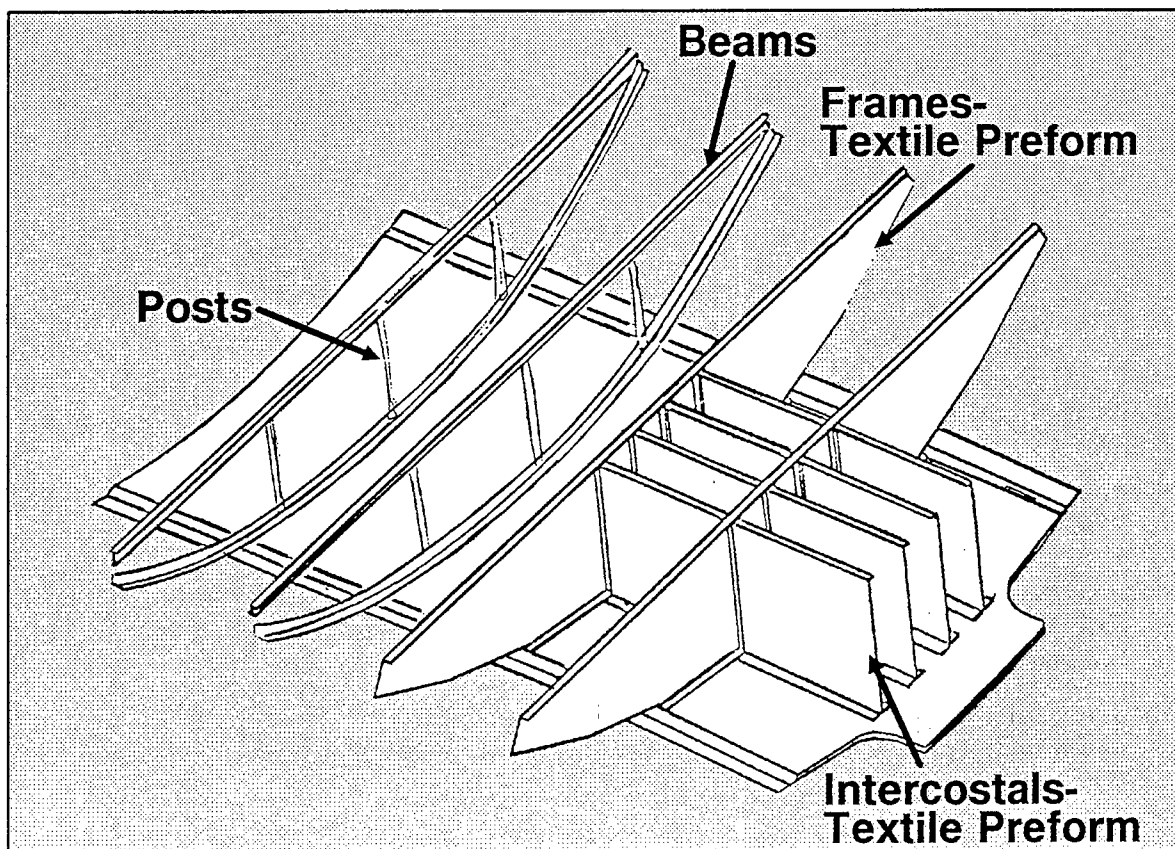


Figure 21. Keel structural configuration

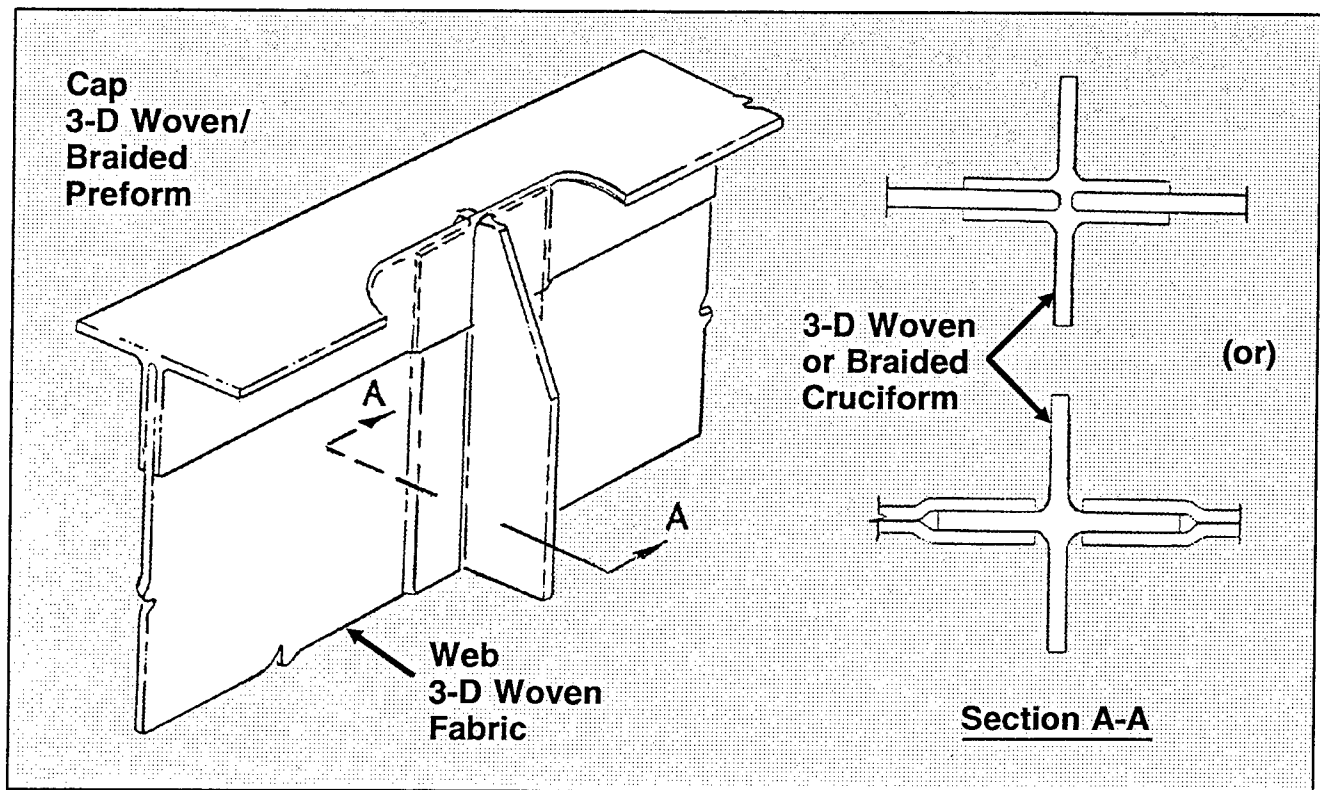


Figure 22. Configuration for Underfloor Frame Built with Woven and Braided Preforms

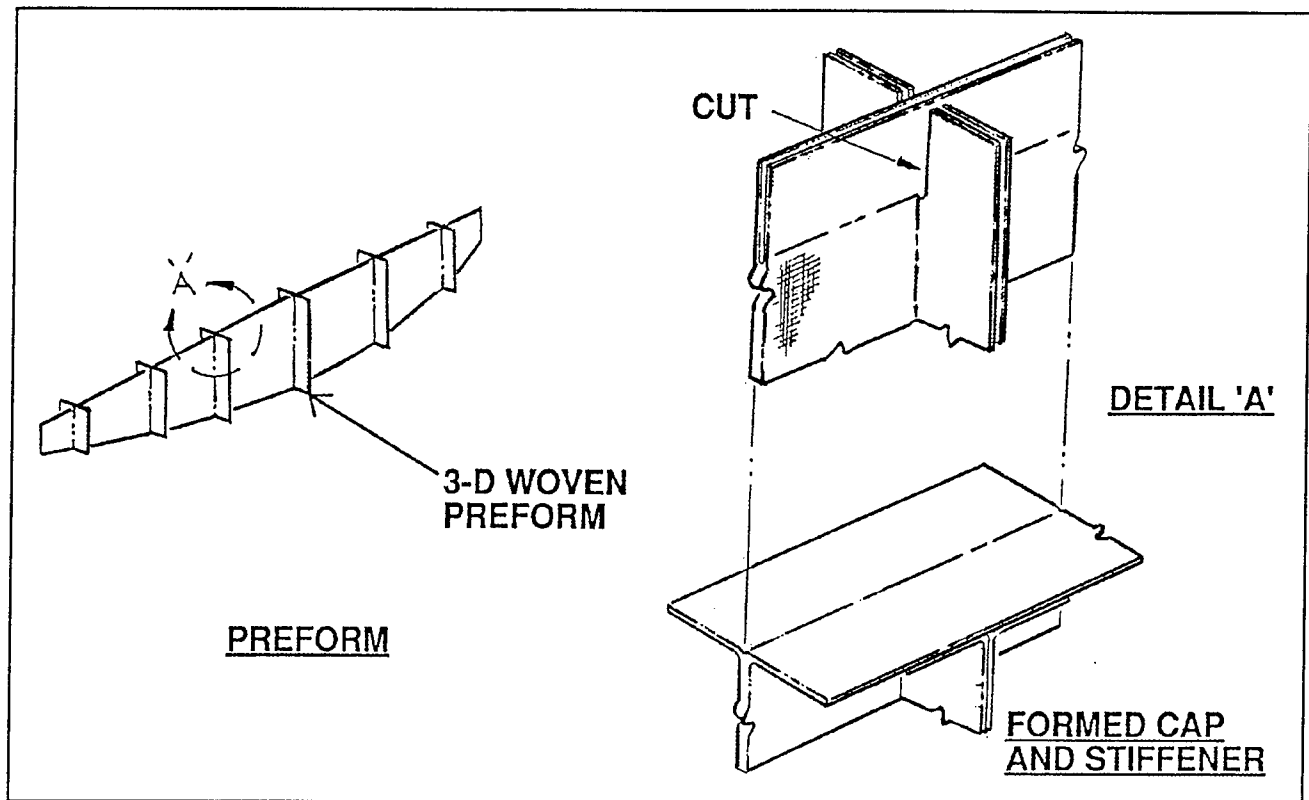


Figure 23. Configuration for Underfloor Frame Using Single Textile Preform

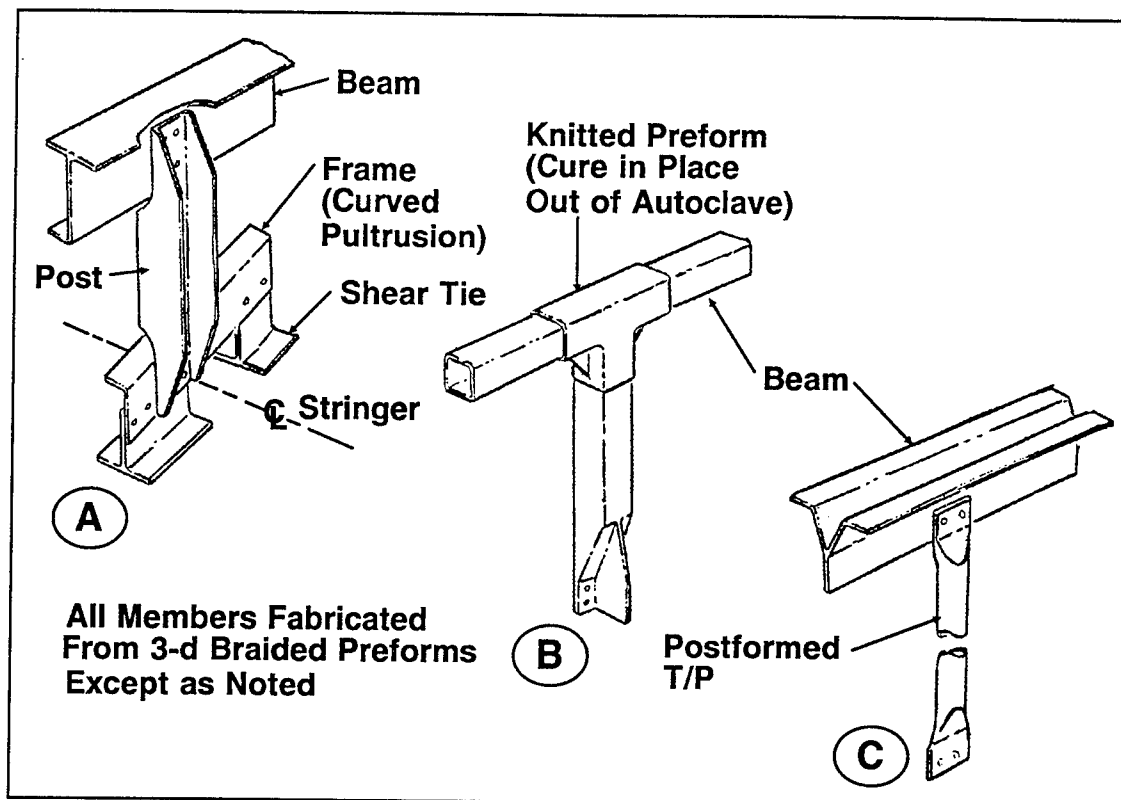


Figure 24. Concepts for Post/Beam Underfloor Frames

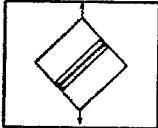
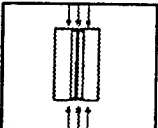
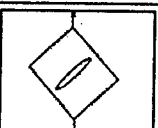
Test	Test Configuration	Specimen Configurations (Replicates)	Total Number Of Tests Planned	Conditions
Frame Shear Panel		2 (2)	4	RTD
Frame Crippling Panel/Stiff		2 (2)	4	RTD
Intercostal Shear Panel		2 (2)	4	RTD

Figure 25. Keel Test Plan

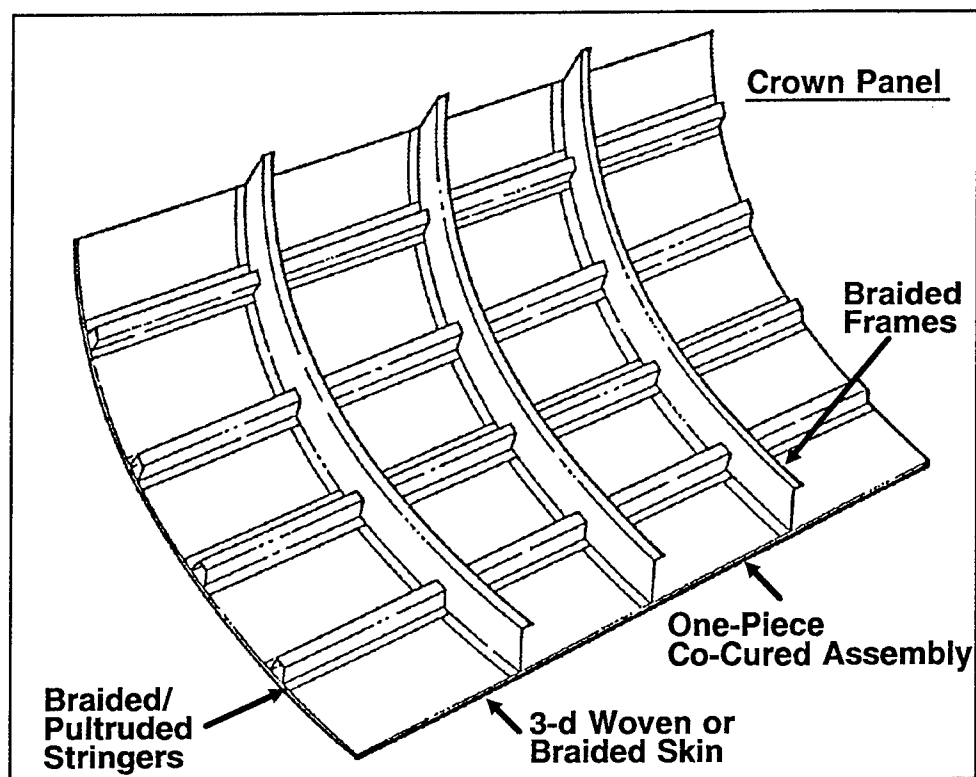


Figure 26. Technology Benchmark Test Component

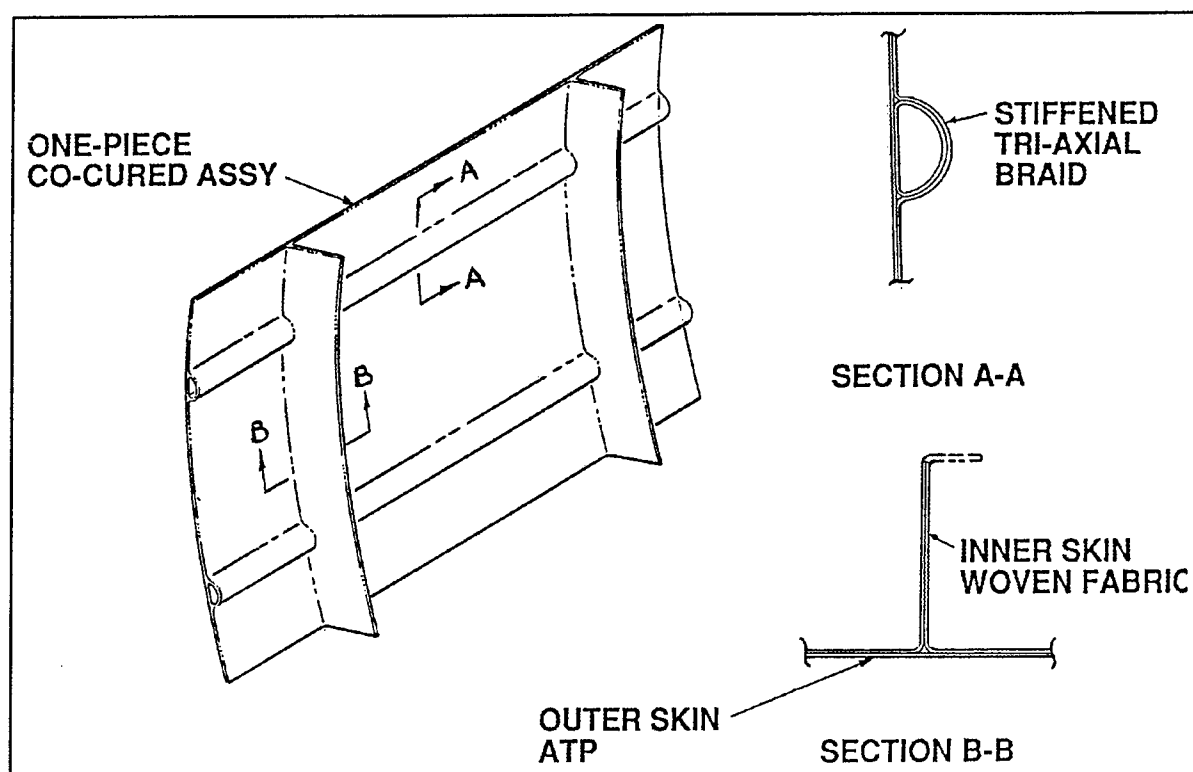


Figure 27. Fuselage Side Panel Concept

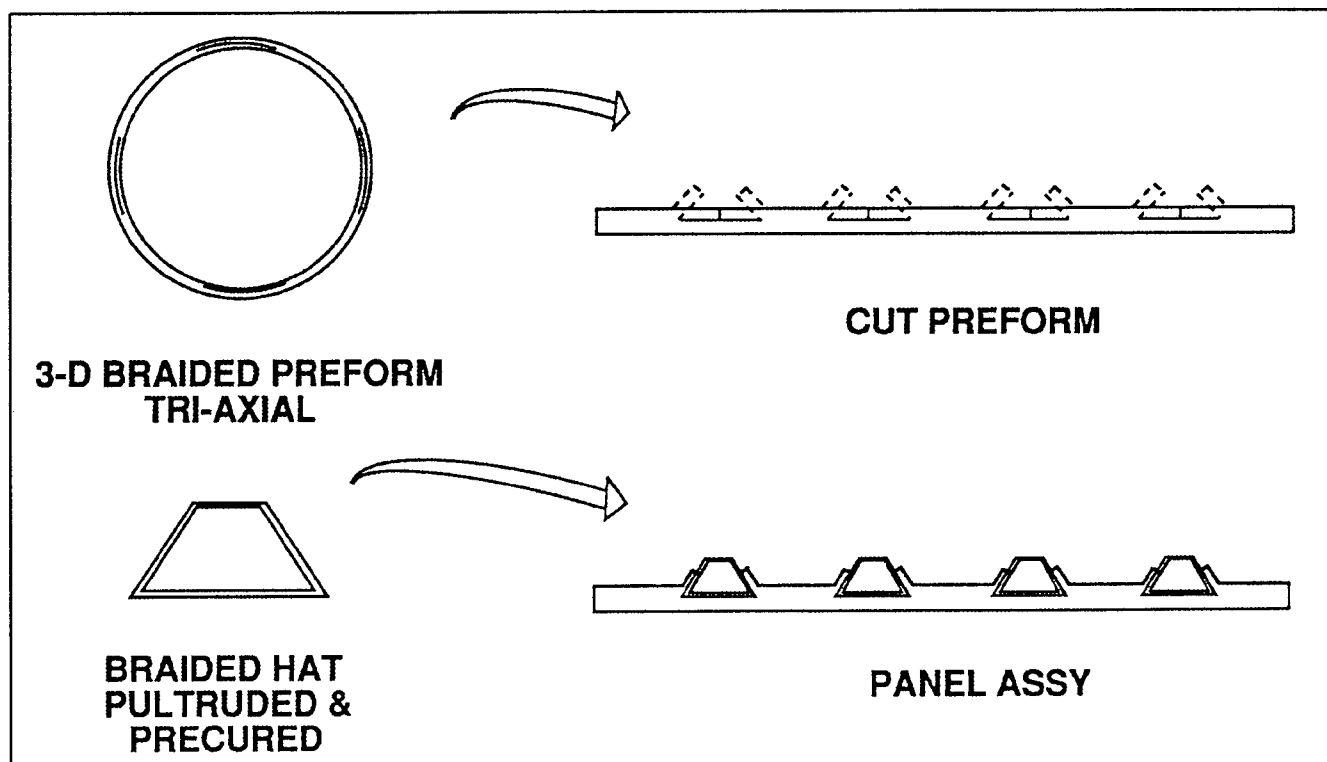


Figure 28. Braided Stiffed Skin Concept

### Task 3.5 Supporting Design Analysis Methodology

In support of the design development of the four structural components, in the task three of NASA/LASC - ACT program, analytical techniques/methods applicable to textile reinforced composites are planned to be developed and validated through component tests. Also included in this task is the element testing for obtaining design-to mechanical properties of the potential textile architectures.

Use of the textile reinforced composites in primary structure applications have potential for reducing costs and increasing damage tolerance. Unlike in a conventional laminated composite where fiber distribution is highly uniform, the textile reinforced composite is highly nonuniform, as it is effected by the size of the individual yarn and "Unit Cells". Such nonuniformity in textile composites presents a problem in the measurement and analysis of stresses at the "local" scale for the prediction of damage evolution, requiring development of mechanics methods to predict: the thermo-mechanical properties, the out-of-plane strength, durability, impact damage resistance and tolerance, damage repair method, and mechanically fastened joint strength.

As illustrated in Figure 30, the textile composites "performance prediction" will be a systematic and integrated approach encompassing preform microstructure design, preform processing science, composite fabrication, and performance characterization. The aim of the effort is to establish the "performance maps" of the textile composites through development of analytical models, theoretical predictions, and experimental verification. This effort will include 2D & 3D braids, angle inter-lock weaving, and stitching. The maximum use of the test data generated under Task 2, Preform Development, will be made in the characterization.

The following fundamental behaviors of the textile composites will be modeled: 1) Non-linear Stress-Strain - behaviors under uniaxial tension and compression, off-axis tension and compression, and shear. 2) Residual Strength - analytical methodology will be developed to quantify the residual strength of textile composites as a function of damage size and damage mode. The interaction of tension and compression induced defects is also

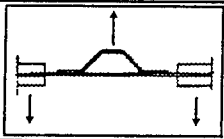
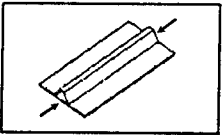
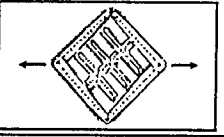
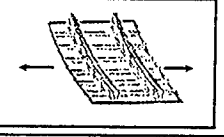
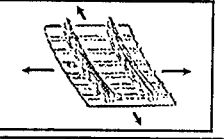
Test	Test Configuration	Specimen Configurations (Replicates)	Total Number Of Tests Planned	Conditions
Stringer/Shell Pull-off		3 (3)	9	RTD
Stringer Compression		3 (3)	9	RTD
Picture Frame Shear		3 (1)	3	RTD (2) ETW (1)
Combined Tension And Shear		1 (1)	1	Impact Damage Cyclic Loads
Biaxial Tension		1 (1)	1	Damage Tolerance Cyclic Loads

Figure 29. Common Structural Component, Test Plan

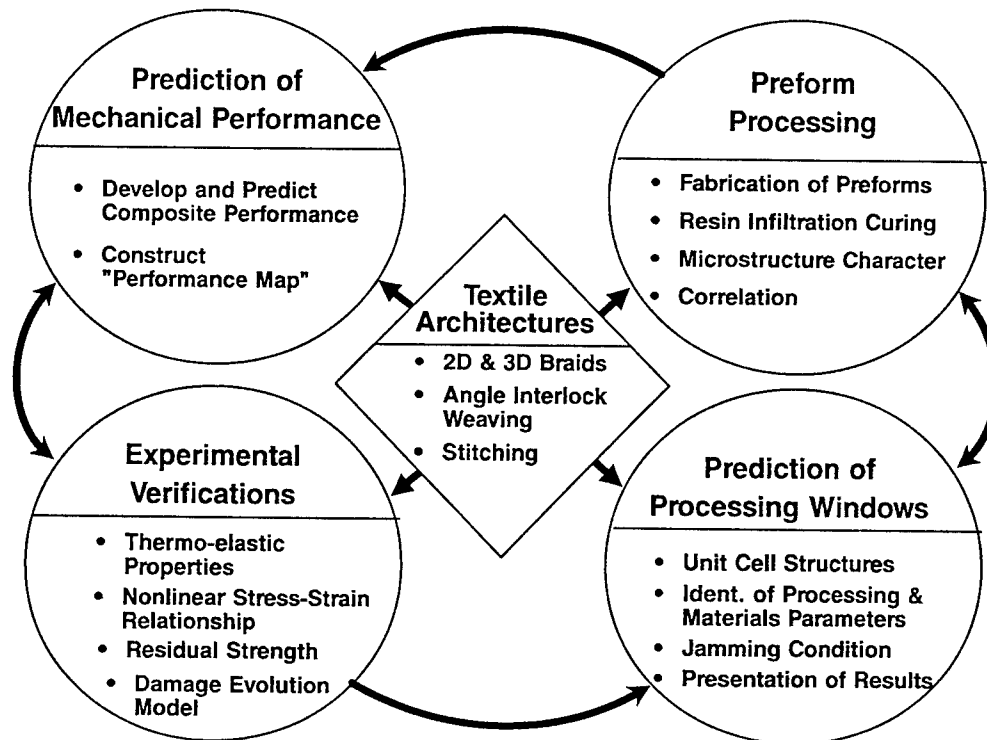


Figure 30. Textile Composite Performance Prediction

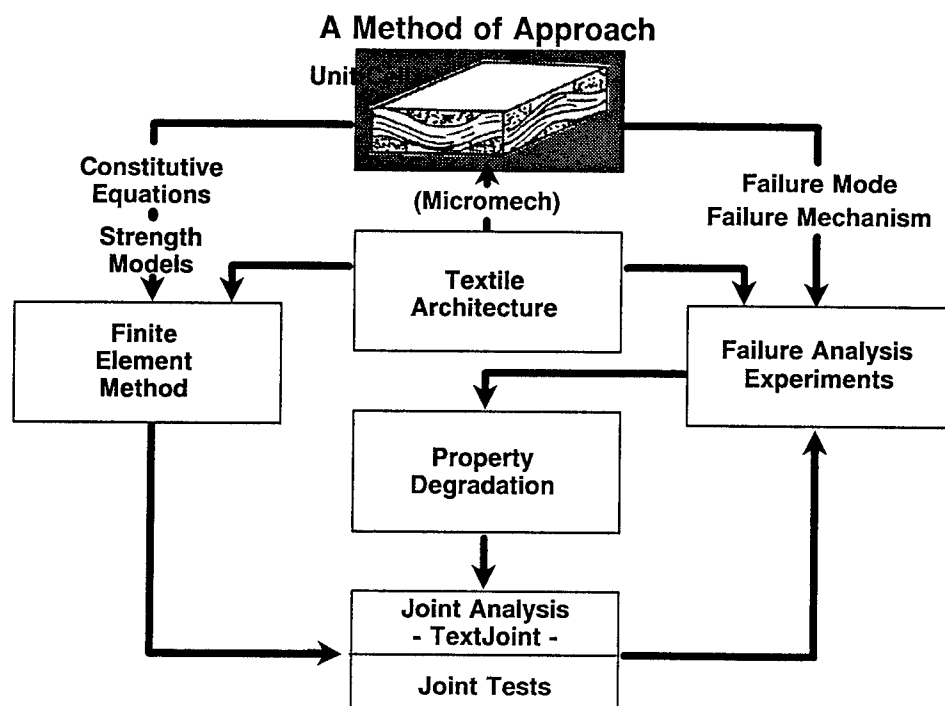


Figure 31. Textile Bolted Joint Strength Prediction - A Method of Approach



essential to the study of biaxial loadings and tension-compression fatigue. 3) Fracture Toughness - The crack driving force, or strain energy release rate, of 3-D composites is sharply reduced owing to through-the-thickness reinforcement. The fracture toughness of 3-D textile composite is greatly enhanced compared to 2-D laminates. The crack fiber interactions in Mode I and Mode II fracture will be investigated by finite element analysis.

TEXTJOINT code developed in Phase I will be extended to bolted joint strength prediction for textile composites. The method of approach, shown in Figure 31, includes modifying an in-situ failure analysis with observed failure and postmortem characterization, constructing constitutive equations for textile preform architectures, extending 2-D finite elements to 3-D, and verification through the test and the analysis correlation.

#### Task 4, Low Cost Fabrication and Automation

The specific objectives of this task area follows:

- o Develop analytical methods to predict parameters for RTM part/tool combinations.
- o Purchase RTM equipment, evaluate fabricability of various preforms and develop a data base to aid in selection..
- o Evaluate powder coated epoxy towpreg for fabricating standard elements and develop a data base.
- o Survey textile industry developments to determine automation requirements.

Resin flow through a preform can be predicted using analytical models developed for flow through a porous media using Darcy's law. The permeability of the fiber is dependent on the wetted surface area and free volume for resin flow. Analytical modes will be used to permeability and flow through preforms. The resin flow front analysis will aid in the design of the tools. Similarly, thermokinetic and viscosity models will be used to predict the degree of cure and viscosity as a function of time and temperature. Analytical modelling will be carried out in house. The University of Delaware will flow front work for 3-D textile preforms to be evaluated in Task 2. A flow chart showing thermokinetic and viscosity models and a model for permeability predictions is shown in Figures 32 and 33.

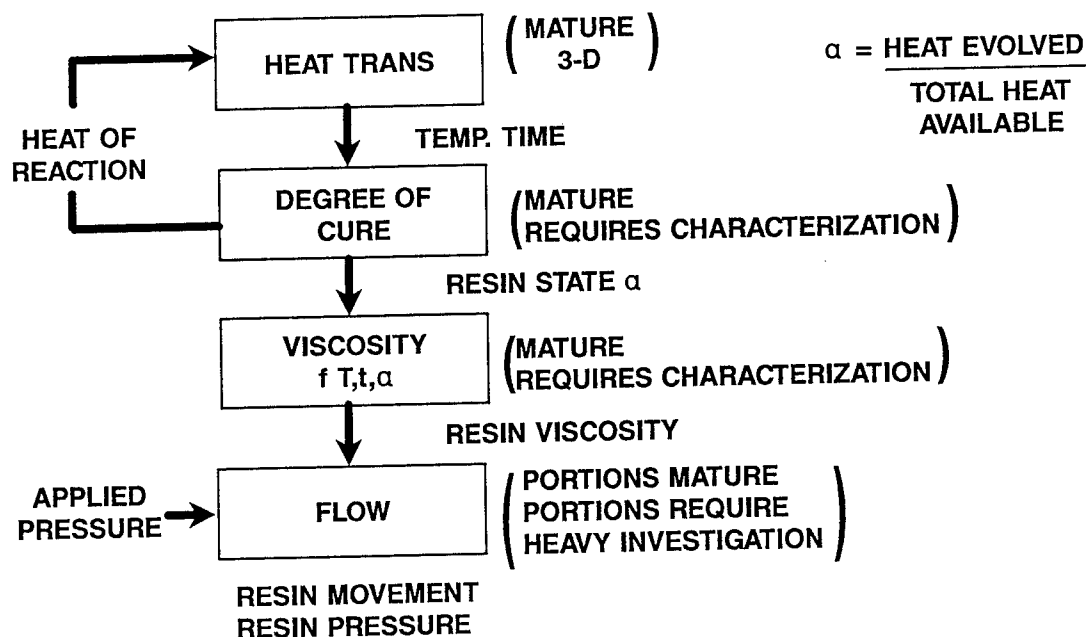


Figure 32. Science Base Modeling Concept, Modular Approach

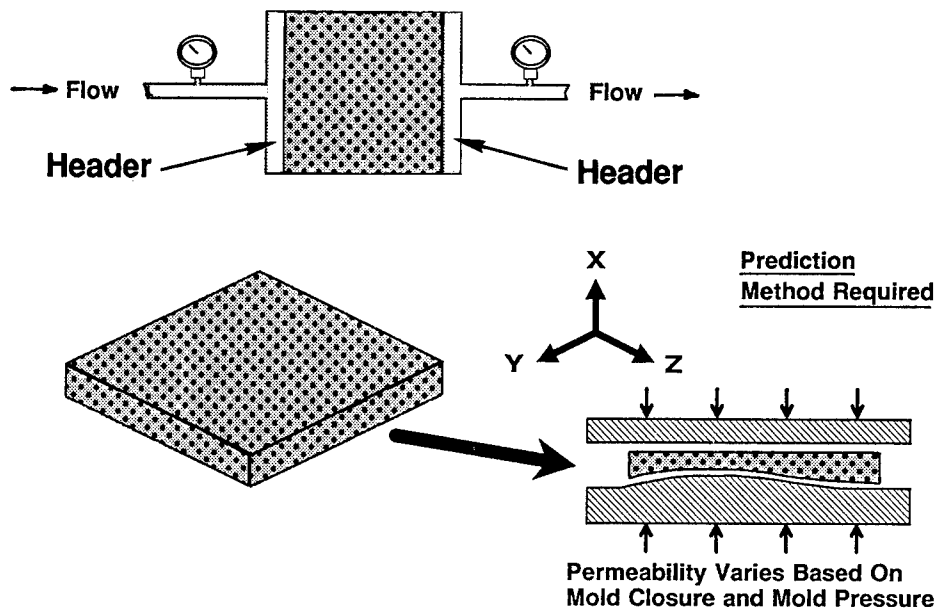


Figure 33. Measuring Permeability

Compaction studies for textile preforms made with both dry tow and powder coated tows will be carried out. High bulk factors in textile preforms will require innovative tooling approaches be developed in order to meet part tolerance requirements.

New developments in textile processing will be surveyed and automation requirements for cost-effective textile processing will be determined. This effort will be tied closely to work on-going in the Composite Automation Consortium.

A specification for resin transfer molding equipment has been completed and quotes are currently being solicited.

## SUMMARY

Work is now underway to develop advanced textile technology to fulfill the needs of the Aerospace Industry. Initial efforts are focussing on RTM, because this technology is the more mature. Several RTM resin systems are available for evaluation in this program immediately. Only one powder resin system is sufficiently advanced to be used immediately, however. Powder coated tows for textiles have a high potential for meeting the low cost goals of this program.

## REFERENCES

1. Riks, R., "Progress in Collapse Analysis," Collapse Analysis of Structures, ASME PVP Vol. 84, pp 51-67
2. Mescall, J.F., "Large Deflections of Spherical Shells Under Concentrated Loads", Journal of Applied Mechanics, Vol. 32, pp 936-938, Dec. 1965.
3. ABAQUS Example problems Manual, Hibbit, Carleson, and Sorensen, Inc. Oct. 1982.
4. Bathe, K.J. Ozdemer, H., and Williams, E.L., "Static and Dynamic Geometric and Material Nonlinear Analysis", Report No. UCSESM 74-4, Structural Engineering Laboratory, University of California, Berkeley, CA. pp 127-129. Feb. 1974.
5. Sable, W.W., Sharifi, P., "Structural Analysis of Bonded Joints Using the Finite Element Method", International Conference on Composite Materials, Honolulu, HI, July 14-19, 1991.

COMPARISON OF RESIN FILM INFUSION,  
RESIN TRANSFER MOLDING AND  
CONSOLIDATION OF TEXTILE PREFORMS  
FOR PRIMARY AIRCRAFT STRUCTURE

J. Suarez and S. Dastin  
Grumman Aircraft Systems  
Bethpage, NY

SUMMARY

Under NASA's Novel Composites for Wing and Fuselage Applications (NCWFA) Program, Grumman is developing innovative design concepts and cost-effective fabrication processes for damage-tolerant primary structures that can perform at a design ultimate strain level of 6000 micro inch/inch ( $\mu\text{in./in.}$ ). Attention has focused on the use of textile high-performance fiber-reinforcement concepts that provide improved damage tolerance and out-of-plane load capability, low-cost resin film infusion (RFI) and resin transfer molding (RTM) processes, and thermoplastic forming concepts. The fabrication of wing "Y" spars by four different materials/processes methods is described: "Y" spars fabricated using IM7 angle interlock 0-/90-deg woven preforms with  $\pm 45$ -deg plies stitched with Toray high-strength graphite thread and processed using RFI and 3501-6 epoxy; "Y" spars fabricated using G40-800 knitted/stitched preforms and processed using RFI and 3501-6 epoxy; "Y" spars fabricated using G40-800 knitted/stitched preforms and processed using RTM and Tactix 123/H41 epoxy; and "Y" spars fabricated using AS4(6K)/PEEK 150-g commingled angle interlock 0-/90-deg woven preforms with  $\pm 45$ -deg commingled plies stitched using high-strength graphite thread and processed by consolidation. A comparison of the structural efficiency, processability, and projected acquisition cost of these representative spars is presented.

INTRODUCTION

A wider application of state-of-the-art composites to primary aircraft structure has been inhibited by the materials' intrinsic low damage tolerance, low fracture toughness, low notch strength, and low out-of-plane strength. In addition, the materials' high acquisition cost and high manufacturing costs have not helped. To overcome these deficiencies, we have embarked on a NASA-sponsored program to develop damage-tolerant primary structures that can operate at a design ultimate strain level of 6,000  $\mu\text{in./in.}$  via innovative design concepts and cost-effective fabrication processes.

The NCWFA Program is performed by Grumman Corporation Aircraft Systems Division and its subcontractors, Textile Technologies, Inc., and Compositek Corporation, under the sponsorship of NASA Langley

Research Center (LaRC), Hampton, VA 23665-5225. Mr. H. Benson Dexter is the NASA/LaRC Contracting Officer Technical Representative.

## OBJECTIVE

The primary objective of the NCWFA Program is to integrate innovative design concepts with cost-effective fabrication processes to develop damage-tolerant primary structures that can perform at a design ultimate strain level of 6000  $\mu\text{in./in.}$  This is being investigated through: (1) optimum wing and fuselage design concepts; (2) the use of textile processes with high-performance fiber architecture that provide improved damage tolerance and durability, high-notch strength and increased out-of-plane load capability; and (3) the use of cost-effective fabrication processes such as RTM, RFI, and consolidation forming of hybrid Gr/Ep fiber forms.

## WING DESIGN CONCEPTS

To achieve the objective of the NCWFA Program, innovative composite design concepts were incorporated into the baseline wing. The baseline aircraft selected for this program is a subsonic patrol VSTOL, Grumman design 698-420. This design is a high-wing, T-tail, turn-tilting nacelle configuration that combines both power plant and control vanes immersed in the fan stream. The wing has a span of 44 ft and a fold span of 16 ft and is sized to allow installation of the conformal radar. The thickness ratio is 14% at the root and 12% at the tip, with a maximum depth of 14.4 in. at the centerline. Fuel is carried in the wing box from fold joint to fold joint. Roll control in conventional flight is provided by spoilers mounted on the rear beam.

The multi-spar and multi-rib structural arrangement considered spar/stiffener orientation, spar/stiffener spacing, and rib pitch. The structural geometry was varied to achieve a least-weight/cost cross-section of detail structural elements. For the multi-spar structural concepts, the two types of wing cover configurations that were evaluated have the potential of successfully increasing the working strain to levels at least 50% higher than those of the baseline. The two types evaluated were plain panel-spread and discrete cap. The plain panel-spread is essentially a monolithic skin of approximately constant thickness at any chordwise cut. In addition, the laminate consists of the same family of lamina orientations (0, 90, and  $\pm 45$ -deg) at any point. The second type, discrete cap, utilizes a skin of two distinct laminate orientations. Between spars, the skin panel consists of a high-strain-to-failure laminate of 90- and  $\pm 45$  deg layers. The absence of 0-deg layers in this panel has two additional advantages: first, for a given thickness, it will possess a higher resistance to buckling loads; second, the laminate's EA (extensional stiffness) is very low as compared to the total section, resulting in a lesser axial load applied to the unsupported segment of skin. At each spar, 0-deg layers are added to the panel laminate, resulting in a local pad. The

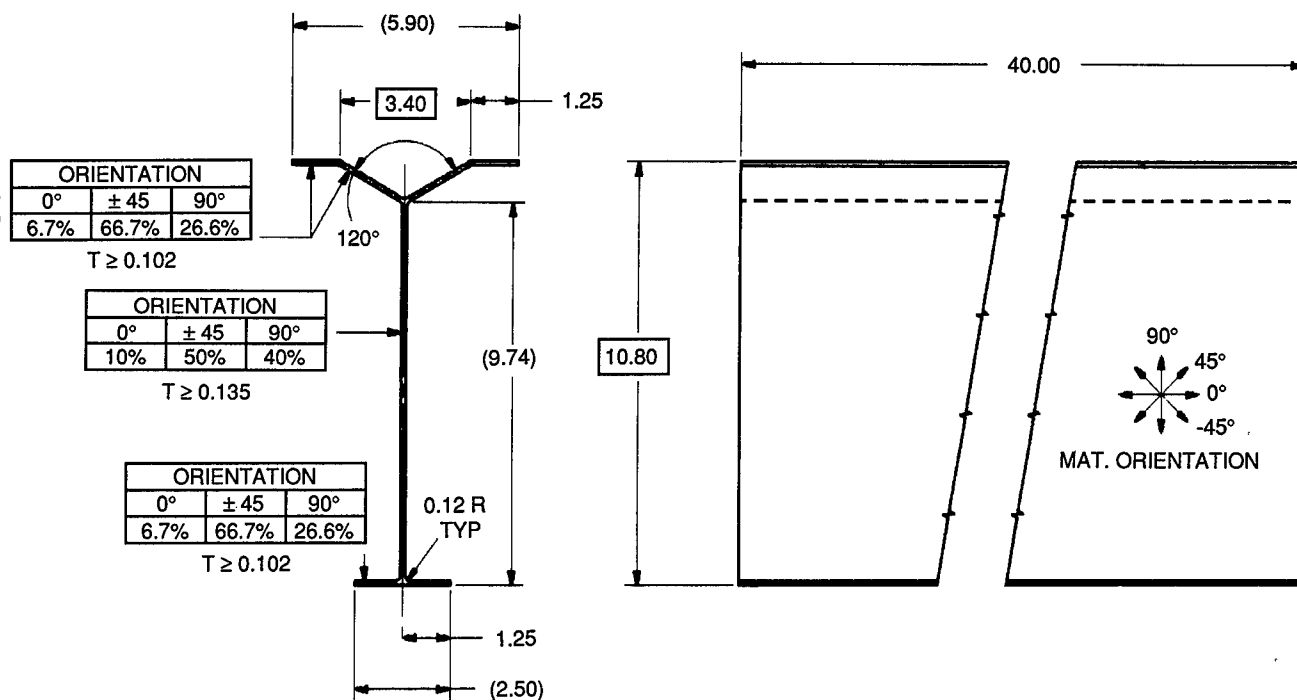
0-deg layers provide the axial filament control to the laminate and carry the preponderance of axial load. Located over the spar, the high loads are rigidly supported minimizing any instability problems. For the multi-rib concepts, stiffeners parallel to the front spar were selected as the preferred stiffener orientation because of relatively high structural efficiency and potential ease of manufacture.

The development of combined material/configuration concepts involved the use of Y spars and Y stiffeners to support the covers. The basic philosophy in using Y spars is that they reduce panel widths and required thickness on the upper cover. Although an increase in weight is expected for the intermediate spars, the weight savings produced by the upper cover will adequately compensate for it, and yield an overall weight savings. For all Y-spar designs, the angle was set at 120 deg to provide equilibrium and balance. The distance between the legs of the Y spar at the attachment to the upper cover depends on the spar spacing. To obtain the maximum benefit from the Y-spar configuration, the fastener spacing is half that of the spar. The weight savings generated by these concepts showed significant improvement over the baseline. The multi-rib design, using G40-800/F584 with Y stiffeners, provided the greatest savings (573 lb, or 46% of the metal torque box weight of 1233 lb). The multi-spar design using Y spars and discrete caps was a close second in weight savings (537 lb, or 44% of the metal torque box weight). Each design concept was rated in terms of the following parameters: weight risk, manufacturing and production costs, durability/damage tolerance, repairability, inspectability, and operation and support costs before the final selection.

#### Y-SPAR SELECTION

Based on the results of the evaluation of the combined material/configuration concepts, the Y spar was selected for further study. A Y spar representative of an intermediate wing spar segment in size, complexity, and load-carrying capability (shear flow of 1,015 lb/in. in five-spar wing configuration) was designed (figure 1). The material preforms were:

- Three 40-in. Y spars woven by Textile Technologies, Inc. (TTI) on NASA Jacquard loom using angle-interlock fiber architecture
  - Commingled AS4 (6K)/PEEK 150-g Tows
  - 0-/90-deg weave and  $\pm 45$ -deg fabric stitched with Fiberglass/Toray H.S. thread
- Four 40-in. Y spars knitted/stitched by Compositek Corporation using G40-800 fiber
- Four 40-in. Y spars woven by TTI on NASA Jacquard loom using angle-interlock fiber architecture
  - IM7 (12K) Tows
  - 0-/90-deg weave and  $\pm 45$ -deg fabric stitched with Fiberglass/Toray H.S. thread.



R91-6880-001

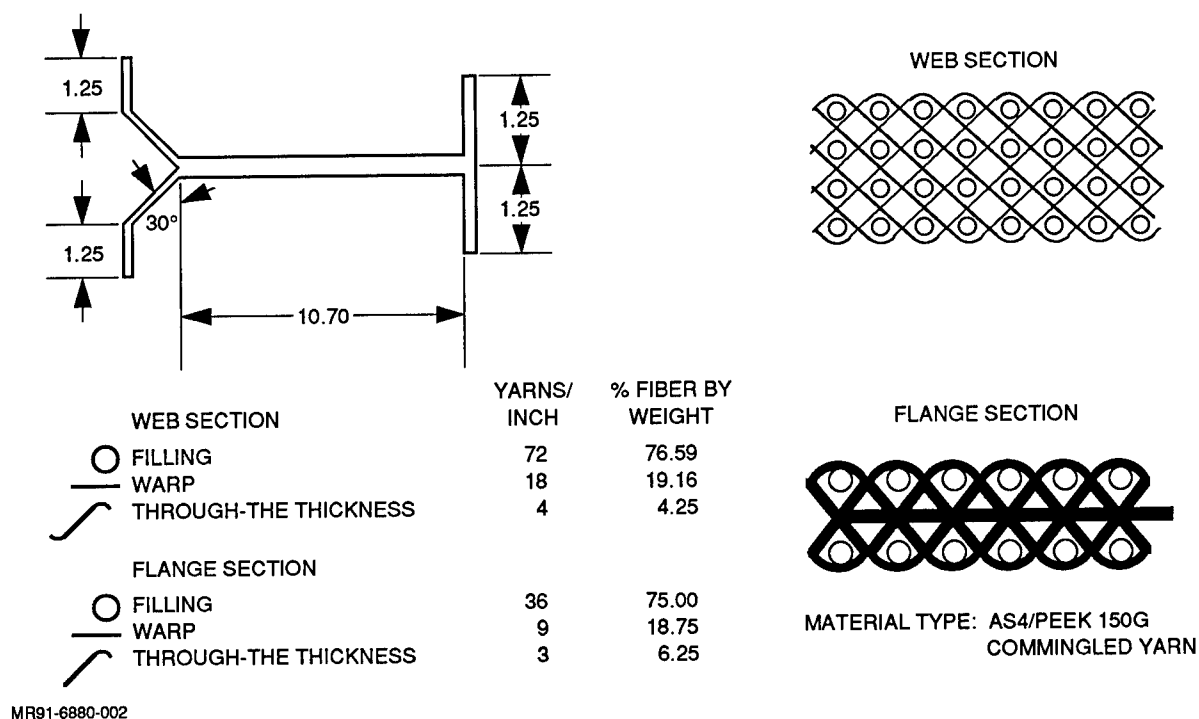
Figure 1 Y-Spar Configuration

## MANUFACTURING EFFORT OVERVIEW

- Commingled AS4/PEEK 150-g Y spars
  - Design and fabrication of woven commingled AS4/PEEK 150-g Y-spar preforms
  - Consolidation/forming of Y-spar preforms
  - NDI and dimensional analysis of Y spars
  - Structural test of Y spar
- G40-800/3501-6 Gr/Ep Y spars
  - Design and fabrication of knitted/stitched G40-800 preforms
  - RFI/autoclave-processed Y-spar preforms
  - NDI and dimensional analysis of Y spars
  - Structural test of Y spar
- G40-800/Tactix 123 Gr/Ep Y spars
  - Design and fabrication of knitted/stitched G40-800 preforms
  - RTM processed with Tactix 123/H41
  - NDI and dimensional analysis of Y spar
  - Structural test of Y spar
- IM7/3501-6 Gr/Ep Y spar
  - Design and fabrication of IM7 12K angle-interlock woven Y-spar preforms
  - RFI/autoclave-processed Y spar
  - NDI and dimensional analysis of Y spar
  - Structural test of Y spar.

## CONSOLIDATION OF WOVEN COMMINGLED Y SPARS

The effort involved the consolidation (thermoforming) of three woven/stitched AS4 6K/PEEK 150-g Y spars. The architecture of the woven commingled AS4/PEEK 150-g 0-/90-deg preforms is presented in figure 2. The preform webs consist of 76.59% fill yarns, 19.16% warp stuffers, and 4.25% through the thickness warp weavers. The preform flanges consist of 75.00% fill yarns, 18.75% warp stuffers, and 6.25% through the thickness warp weavers. The PEEK resin in these preforms was commingled in the proper proportion with the AS4 graphite fiber yarns prior to weaving and stitching.



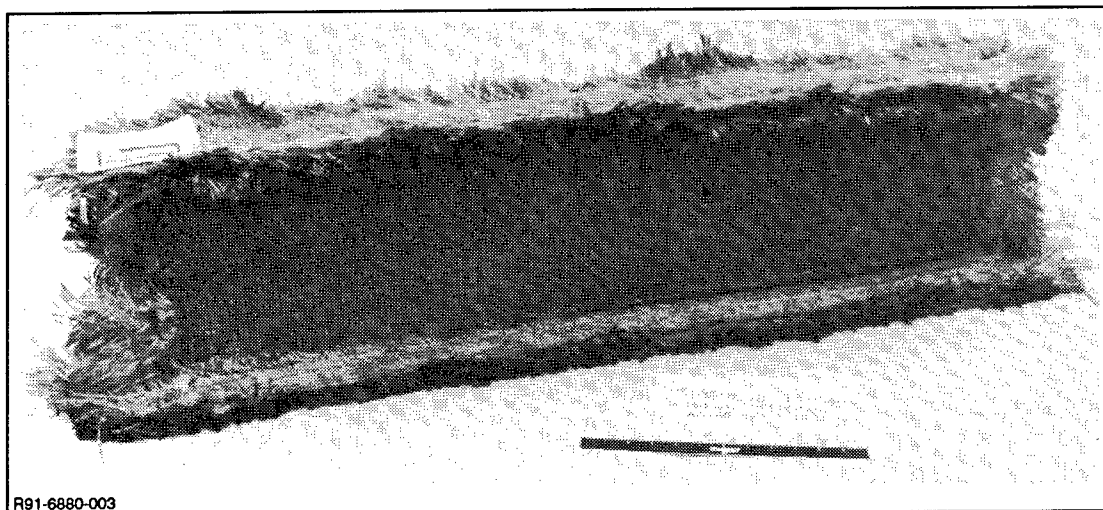
**Figure 2 Architecture of Woven Commingled AS4/PEEK 150G 0-/90-Deg Preform**

The 0-/90-deg carcasses were first woven by TTI on a Jacquard loom. Next, the  $\pm 45$ -deg ply material was located on the outside faces of both the webs and the flanges of the completed carcasses and semi-automatically stitched in place by Sewing Machine Exchange (SMX), Chicago, IL, using Toray T900-1000A fiber. The completed preforms were then shipped back to TTI for inspection; then to Grumman for consolidation.

Because of errors in the loom setup, the preforms were dimensionally incorrect. The 0-/90-deg carcasses were woven at 22 picks per inch (ppi) instead of 11 ppi, as required. In addition, the web height was 10.7 in., instead of 9.7 in., as specified.



The required 45-/135-deg fabric reinforcement was stitched to the woven 0-/90-deg commingled AS4/PEEK 150-g Y-spar carcasses by SMX (figure 3). The preform was stitched using a cross-hatch pattern with a row spacing of 1/4 in. In the radius areas, however, three rows of stitches were installed, with a row spacing of 1/8 in.



**Figure 3 Preform of Woven 0-/90-Deg Commingled AS4/PEEK with Stitched 45-/135-Deg Fabric**

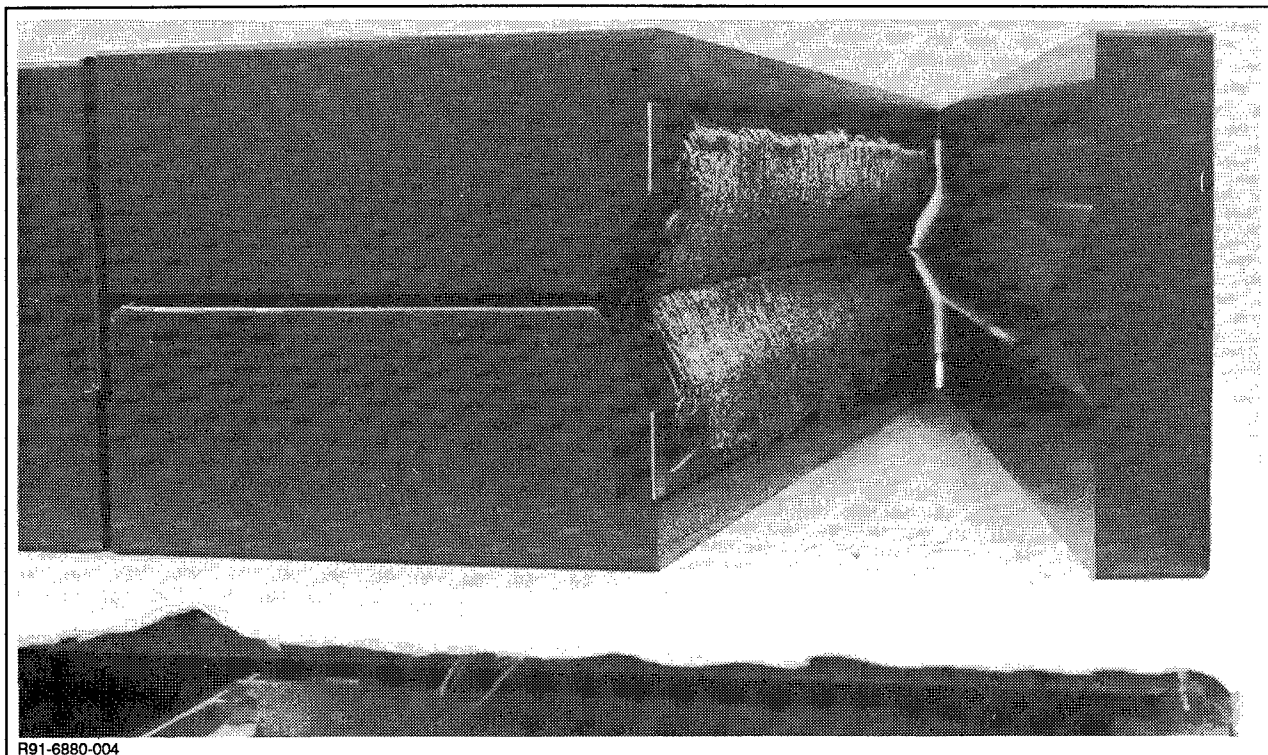
It was intended that the preform be stitched using only Toray T-900-1000A carbon fiber; SMX, however, required the use of fiberglass loops in combination with the carbon fiber thread in the radii and flanges of the preform. The carbon stitching equipment was too large to be conveniently used for the Y-spar flanges. In addition, this equipment lacked the sensitive feeding characteristics required for the flange stitching operation. Ultimately, the Y-spar preform flanges were stitched manually.

Monolithic graphite was chosen for the tooling, based on the following advantages over more conventional materials:

- Coefficient of thermal expansion (CTE) near that of the part
- Fairly high thermal conductivity
- Excellent surface finishes possible for good part finish and ease of release
- Relatively low cost.

The tool consists of four machined details: two matching left and right halves for the web, and top and bottom details for the flanges. The tool's details are pictured in figure 4.

The consolidated commingled AS4/PEEK 150-g woven/stitched Y spar was consolidated for 4 hr at 720°F ( $\pm 10^\circ$ ), 160 psi fluid pressure, plus full vacuum bag pressure. The prolonged hold at elevated temperature was required to accommodate the relatively large mass of the monolithic graphite mandrels that acted as heat sinks. In production, integrally



**Figure 4 AS4/PEEK Y-Spar Preform in Graphite Tool**

heated and cooled tools would be used in combination with cold-wall autoclave procedures to provide a low-cost consolidation methodology. The high-temperature autoclave run was performed without any processing difficulties. The consolidated Y spar was visually acceptable (figure 5).

All three completed spars were ultrasonically inspected for voids. Both the first and third spars processed showed several minor void areas--particularly in the flanges--whereas the second spar tested almost void-free, with only small areas of interstices in the angular sections of the Y flanges. Based on these results, all further testing was done on the second Y spar only.

Resin content and fiber volume determinations for the consolidated Y spar where:

- Percent fiber volume - 56.1
- Percent resin volume - 42.8
- Percent void volume - 1.1.

Figure 6 presents a comparison of the three spars' target, preform, and final part dimensions. (The target dimensions are adjusted for the oversize and overthickness conditions of the preforms.) Also given in the figure is the percentage of consolidation for each Y spar. This is a measure of how the bulk factor of each preform related to each finished part's final thicknesses. Ideally, the consolidation percentages should be fairly closely matched within each part and among the three parts.

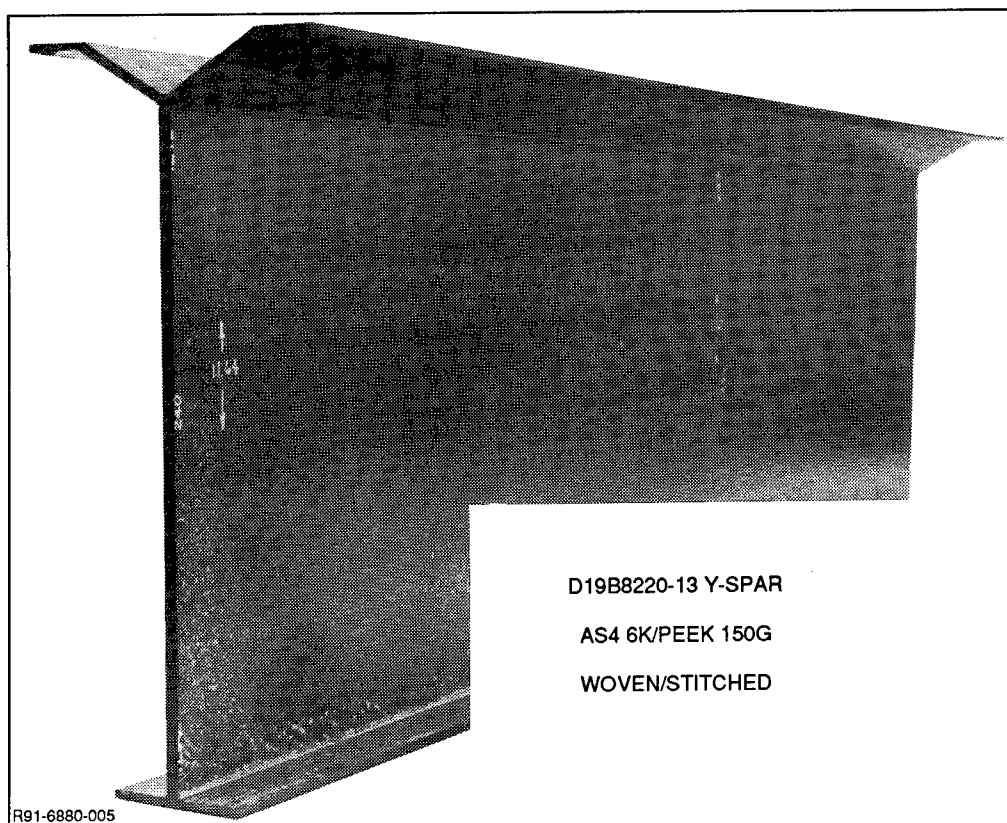


Figure 5 Consolidated Y Spar

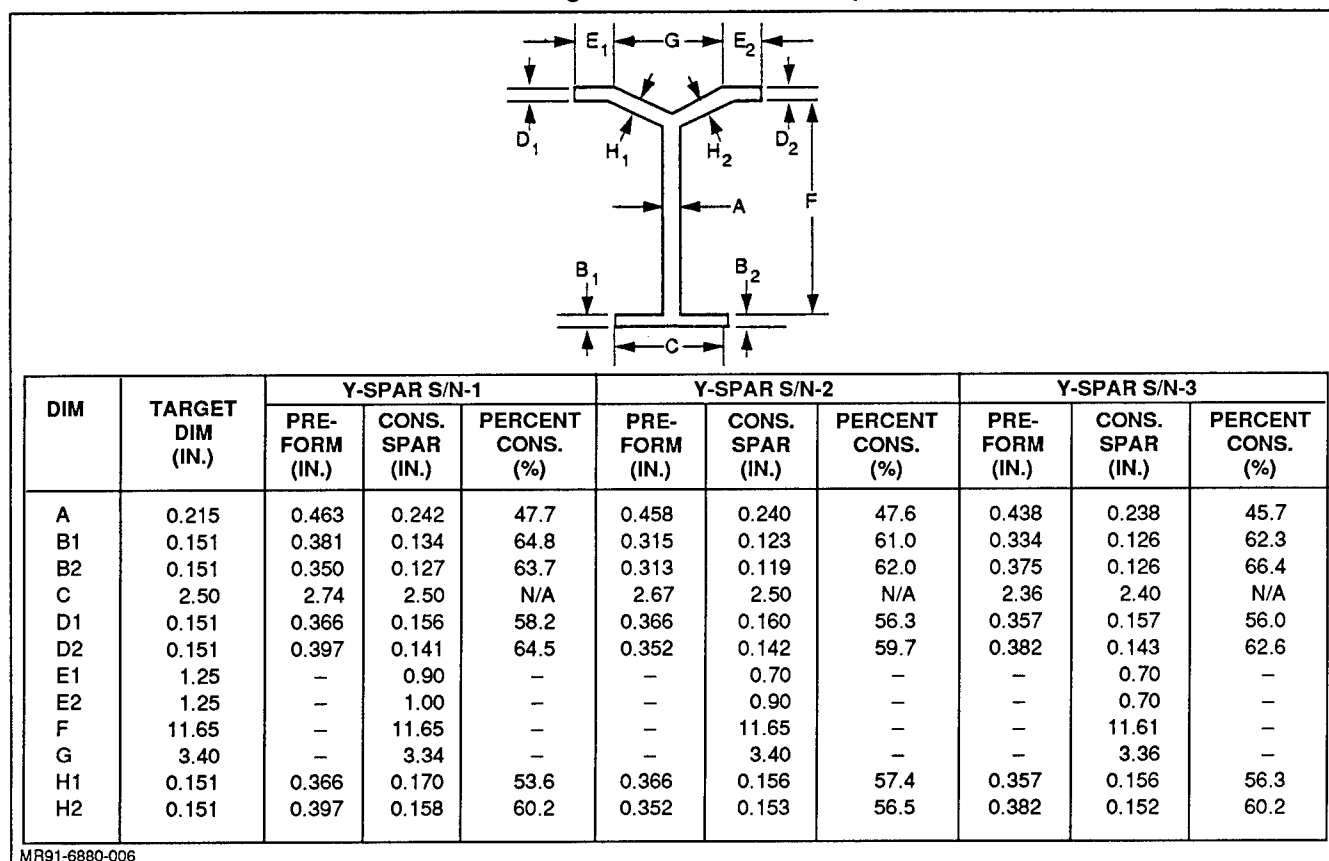


Figure 6 Comparison of Consolidated Preforms S/Ns 1, 2, and 3 Target, Preform, and Final Part Dimensions

Again, the second spar--S/N 2--provided the best results dimensionally. With the exception of the web thickness (letter A, of 0.240 in.) and a consolidation percentage of 47.6, the other thickness dimensions have consolidation percentages between 56.3 and 62.0. This is the tightest range of the three spars, and is reflected in the better NDI results mentioned earlier. The raw dimensions of spar S/N 2 also are the most consistent among the three spars. Both the angular and horizontal areas of the Y flange (for example, letters D1, D2, H1 and H2) have thicknesses ranging from 0.142 to 0.160 in. And although the thicknesses of the two legs of the T flange (letters B1 and B2) are somewhat less (0.123 and 0.119 in., respectively), this condition exists in all the spars. It is a reflection of the greater thickness of all the preforms in the Y end.

With regard to the spars' web thicknesses (letter A, of 0.242, 0.240, and 0.238 in., respectively) and their corresponding low consolidation percentages, it is apparent that the bulkiness of the preforms' webs, combined with the large area of web, made it impossible to compact these areas down to the target value of 0.215 in.

#### RFI OF KNITTED/STITCHED Y SPAR

Four G40-800 knitted/stitched graphite Y-spar preforms were fabricated by Composittek Corporation. The Y-spar architecture was:

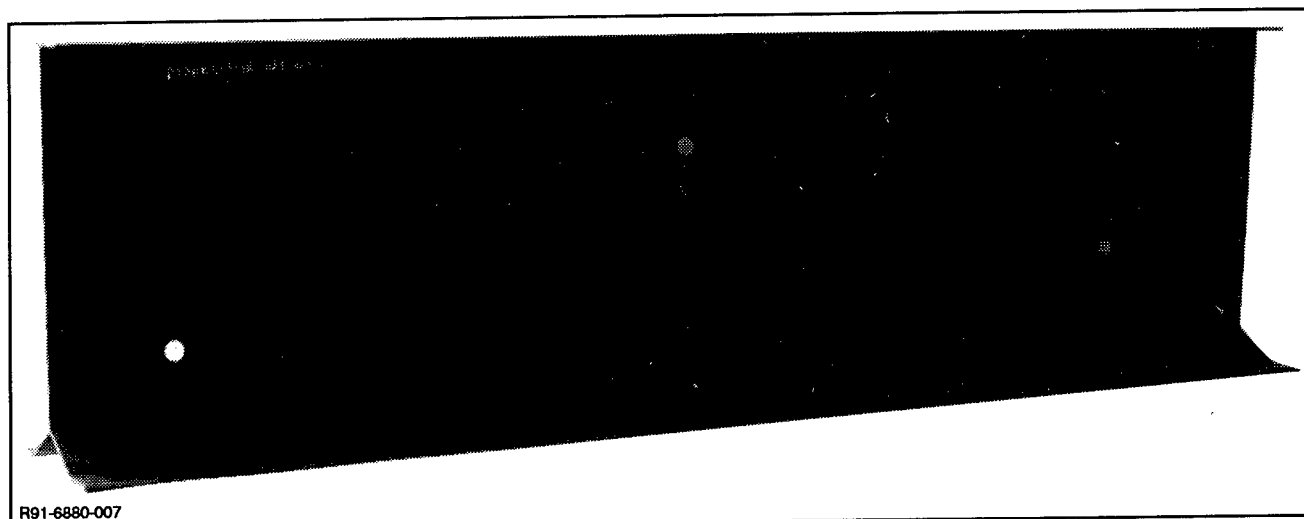
- Flanges:
  - 0 deg, 6%
  - $\pm 45$  deg, 55%
  - 90 deg, 39%
- Web:
  - 0 deg, 9%
  - $\pm 45$  deg, 62%
  - 90 deg, 29%.

Three of the knitted/stitched preforms were (RFI) impregnated and autoclave processed using Hercules 3501-6 resin film. In this proprietary process, resin in film form is positioned within the fiber preform as the preform is being constructed. The fiber and resin are then heated in a vacuum chamber, thus impregnating the preform by gravity and capillary wetting. During the infusion, the vacuum is pulsed to remove entrapped air and volatiles from the resin.

The impregnated preform was then to be processed by Composittek using their Autocomp technique. This proprietary procedure combines aspects of compression molding and autoclave molding in one process. The preform is installed in an integrally heated, matched mold, and the setup is located inside a reusable vacuum bag contained within the Autocomp pressure vessel. Vacuum is then drawn on the part while the tool is heated. At the proper temperature for the particular resin system, vacuum is shut down and fluid pressure is applied to fully close the tool, and to complete the part's processing. Due to setup problems with Composittek's Autocomp pressure vessel and related

equipment, the three spars were conventionally consolidated in an autoclave.

From an initial visual standpoint, RFI S/N 1 was of poor appearance overall, with large, obviously dry areas throughout the spar. On the other hand, both RFI S/Ns 2 and 3 looked quite good, with no apparent bad areas. As a result, it was decided to further analyze only RFI S/Ns 2 and 3; no further examinations or analyses were made of RFI S/N 1. Figure 7 shows the completed Y spar RFI S/N 2.



**Figure 7 RFI S/N 2 G40-800/3501-6 Y Spar**

Both RFI S/Ns 2 and 3 were ultrasonically inspected via C scan, with results indicating that RFI S/N 2 was void free, and that RFI S/N 3 contained only a small void in one horizontal leg of the Y flange.

Figure 8 compares the target and part dimensions of RFI S/Ns 2 and 3. It is apparent that although the spars are dimensionally consistent, they are both thicker than as targeted (with the exception of dimensions H1 and H2, the angular component of the Y flange, which in both parts is slightly undersize). Whether this general oversizing is due to the tool itself or is process dependent is not known at this time.

Both RFI S/Ns 2 and 3 were trimmed to length, and RFI S/N 3 was subjected to destructive testing under four-point beam bending. The dropoff from each spar was sectioned into physical properties coupons. Results of these analyses are: S/N 2 fiber volume: 52.8%, resin volume: 46.0%; S/N 3 fiber volume: 57.3%, resin volume: 41.2%.

#### **RTM OF KNITTED/STITCHED Y SPAR**

The last of the four G40-800 knitted/stitched graphite Y-spar preforms fabricated by Compositex Corporation was RTM processed. The resin system chosen for the preform's impregnation was Dow Tactix 123/H41.

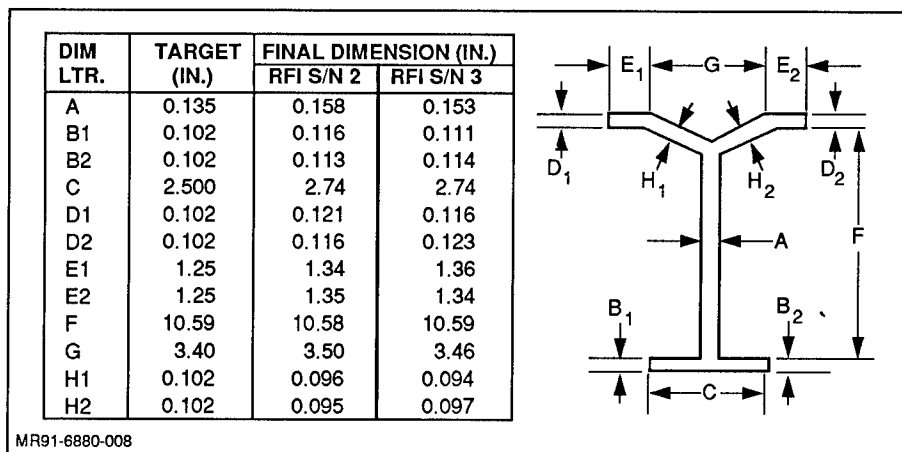


Figure 8 Comparison of RFI S/Ns 2 and 3 Target and Final Part Dimensions

Overall, this operation produced good results, yielding a part with only minimal resin richness along its periphery in localized areas. The completed Y spar is shown in figure 9. The only major anomalies exhibited in the part were localized dry areas in the angular segments of the Y flange. These resulted from a blown O-ring seal in the Y flange during processing. Results of the ultrasonic inspection of this spar confirmed that these areas were unsatisfactory. However, the remainder of the part was predominantly free of sonic indications.

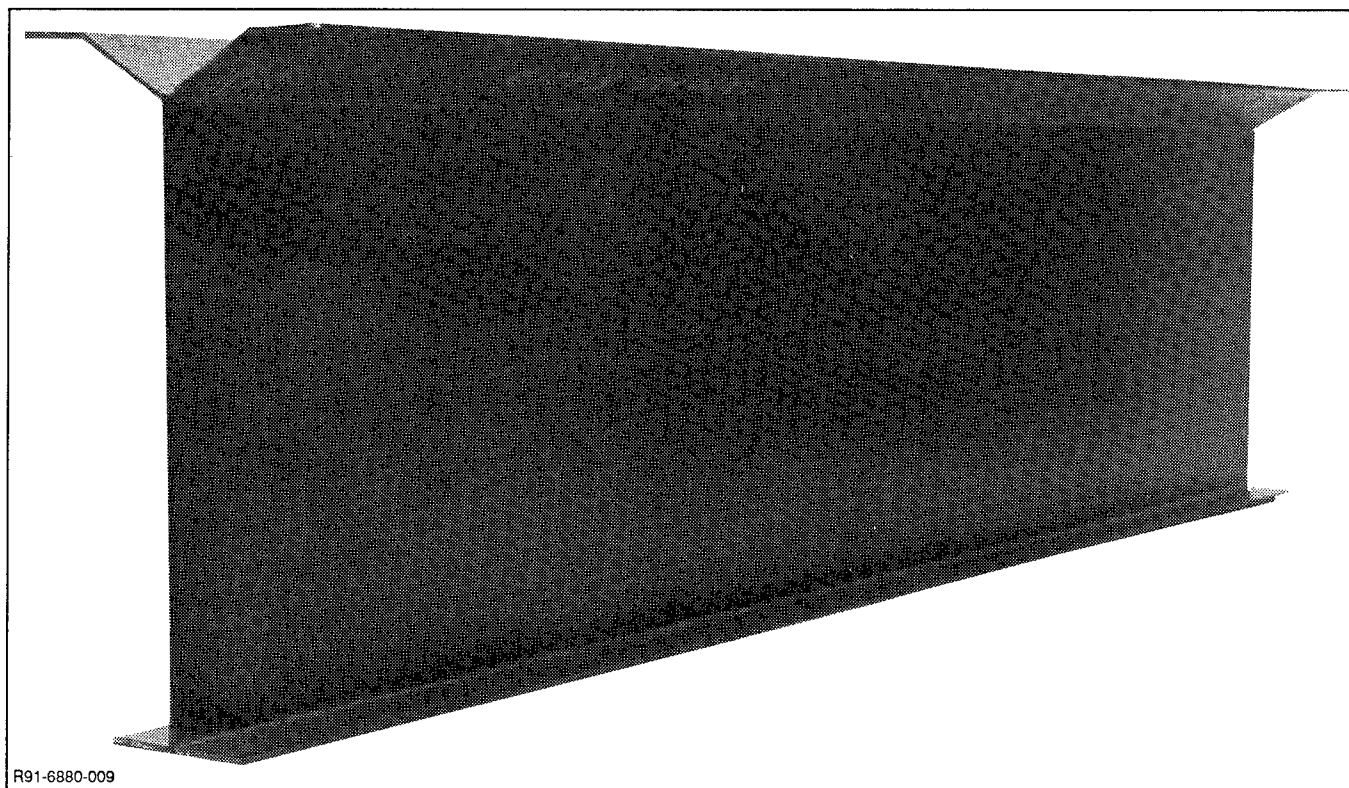


Figure 9 Completed Knitted/Stitched (RTM) Y Spar No. 1

A preliminary dimensional analysis of the RTM-processed Y spar provided the results shown in figure 10. Again, overall results are excellent. There are two potential causes for concern, however. The first is the somewhat-thin angular faces of the Y end, dimensions H1 and H2. This condition is undoubtedly due to the previously discussed seal failure.

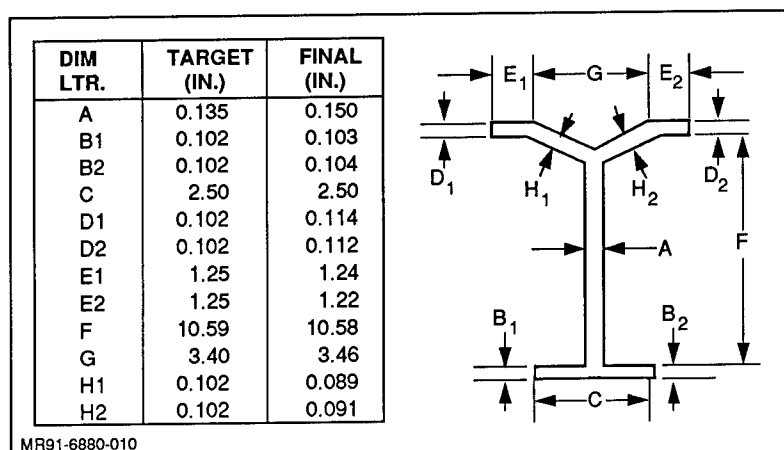


Figure 10 Knitted/Stitched G40-800/Dow TACTIX 123/H41Y Spar  
S/N 1 (RTM Processed) Target and Final Part Dimensions

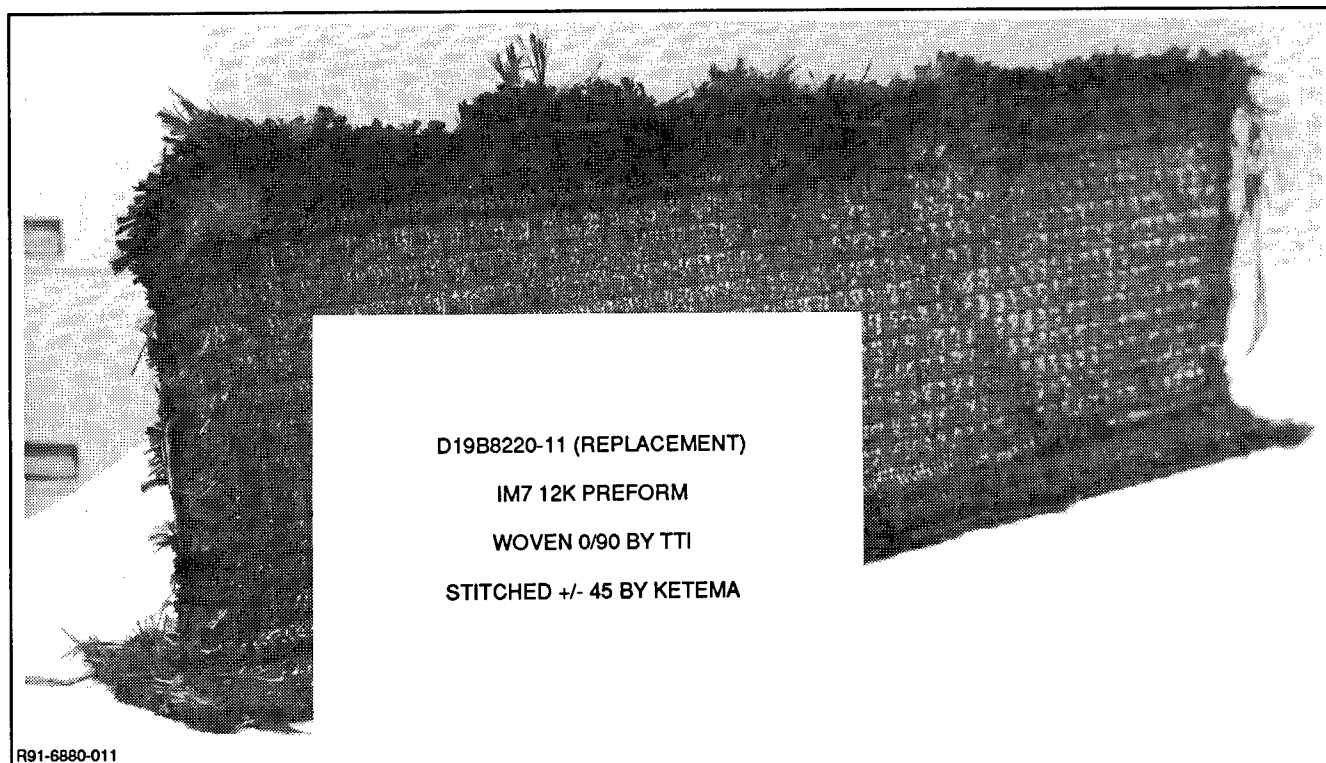
The other concern is the inconsistency in the thickness of the web, dimension A. Although shown in figure 10 as only a 0.015-in. deviation from the target value (0.150 vs 0.135 in.), the difference is in fact the result of an increase in the web thickness toward the spar's center. The ends of the web measure 0.138 in. and 0.142 in. thick, whereas the center measures 0.170 in. It is not clear whether this condition was caused by a tooling problem [localized thickness (bulkiness) in the preform], or is somehow related to the seal failure experienced during resin injection. Physical property analysis yielded an average fiber volume of 52.5% and an average resin volume of 47.4%.

#### RFI OF ANGLE INTERLOCK WOVEN Y SPAR

The 0-/90-deg IM7(12K) carcasses were woven by TTI, Hatboro, PA, on a Jacquard loom. This fully automatic weaving system involves a series of punched cards to control the carcass's architecture based on engineering requirements. The  $\pm 45$ -deg ply material was then located on the outside faces of both the webs and the flanges of the completed carcasses by TTI. The  $\pm 45$ -deg plies were then semiautomatically stitched in place by Ketema Textile Products Div., Anaheim, CA, using Toray T900-1000A fiber. (The stitching operation was necessitated by the fact that weaving is currently limited to 0- and 90-deg orientations.) This completed the preforms, which were then shipped back to TTI for removal of a PVA serving from the yarns. This serving, required to maintain integrity of the yarns during the weaving operations, was boiled off in multiple steps in large tanks. After TTI's quality checks, the preforms were shipped to Grumman for inspection.

Unfortunately, during inspection of the first three preforms, it was discovered that the TTI woven carcasses were not correct. Dimensional checking revealed that they were oversize and too thick. Specifically, the web heights, targeted to be 9.7 in., were woven between 10.5 and 11.0 in. Additionally, both the webs and the flanges of the carcasses were thicker than originally called for. TTI's investigation of their processing records indicated that the IM7 spar carcasses (0-/90-deg), were woven at 22 ppi, not 11, as was called for by these structures' architecture.

The fourth carcass was woven by TTI with the proper number of ppi based on the specified architecture, resulting in a Y-spar preform conforming to the engineering requirements. The completed preform is shown in figure 11. After inspection, it was sent to Composittek Corporation for processing via RFI and Autocomp.



**Figure 11 D19B8220-11 Replacement Preform Prior to Processing**

The woven/stitched IM7 3-D preform Y spar was processed by Composittek using RFI and Hercules 3501-6 resin. NDI of the Y spar revealed significant porosity. It was decided to test the spar in four-point beam bending to assess the importance of porosity in its structural performance. Specimens were cut from each end of the spar to obtain photomicrographs of the web and flange cross-sections (see figure 12). The dimensional analysis of this replacement Y spar is presented in figure 13.



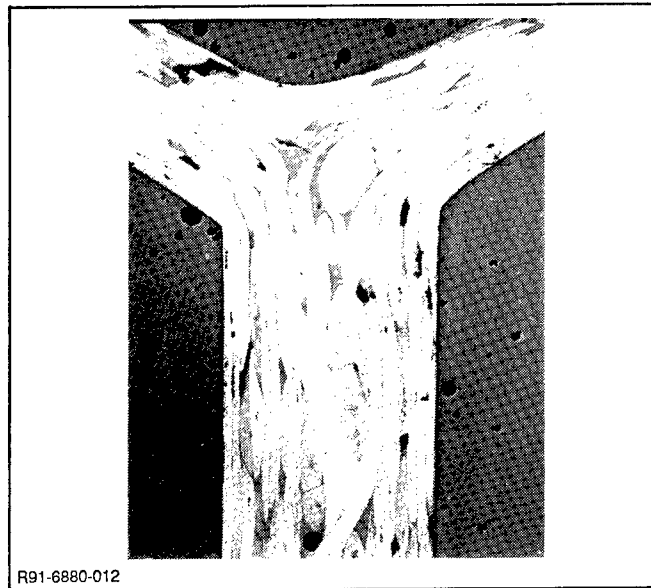


Figure 12 Photo Micrograph of IM7/3501-6 Y Spar (RFI)

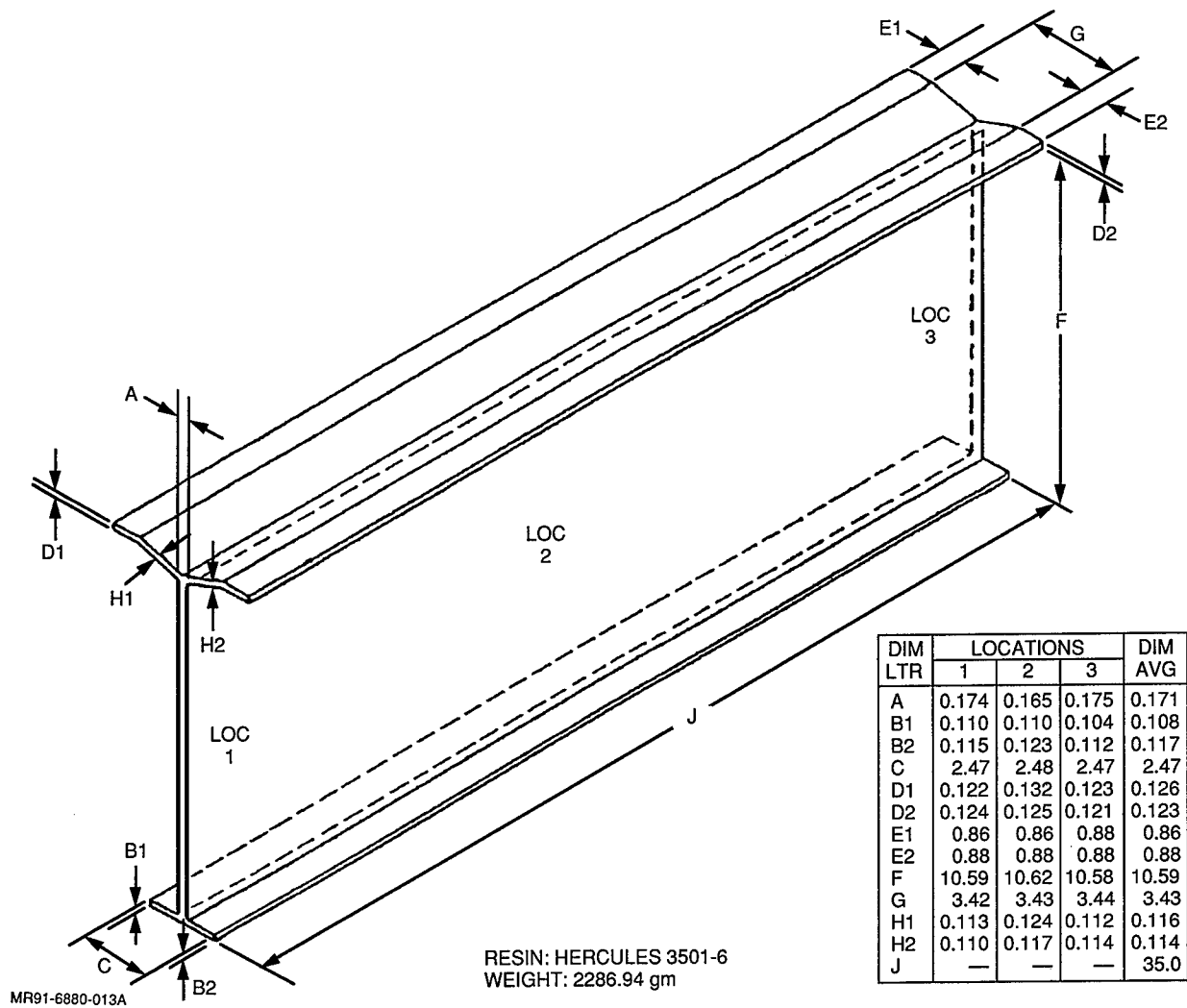


Figure 13 Dimensional Analysis of D19B8220-11 Y Spar (Replacement) RFI Processed

Resin content and fiber volume determinations for the RFI woven/stitched Y spar were:

	<u>WEB</u>	<u>FLANGES</u>
Percent fiber volume	56.1	53.2
Percent resin volume	41.1	45.0
Percent void volume	2.8	1.8

### Y-SPAR TESTS

The Y-spar element was configured as a 35-in.-long by 10.8-in.-high beam. The beams have IM6/3501-6 graphite epoxy caps mechanically fastened to the top of the Y web. Load introduction was via aluminum attachment fittings sandwiched around the spar web and bolted in place. The specimen was loaded as a four-point bending beam by the fixture shown in figure 14. Two concentrated loads were applied 3.0 in. away from both sides of the midpoint of the 30.0-in. test span to provide a moment arm of 12 in. Strain measurements were obtained via 10 axial and 4 three-element rosettes located back to back along the center line of the beam (figure 15), except for the consolidated Y spar. The AS4/PEEK commingled Y spar had 8 three-element rosettes and eight axial gages (figure 16). Concurrent with load application midspan deflection was recorded with a dial gage. The spars were loaded to 50% limit load, unloaded, loaded to limit load, unloaded, loaded to ultimate load, held, and then loaded to failure.

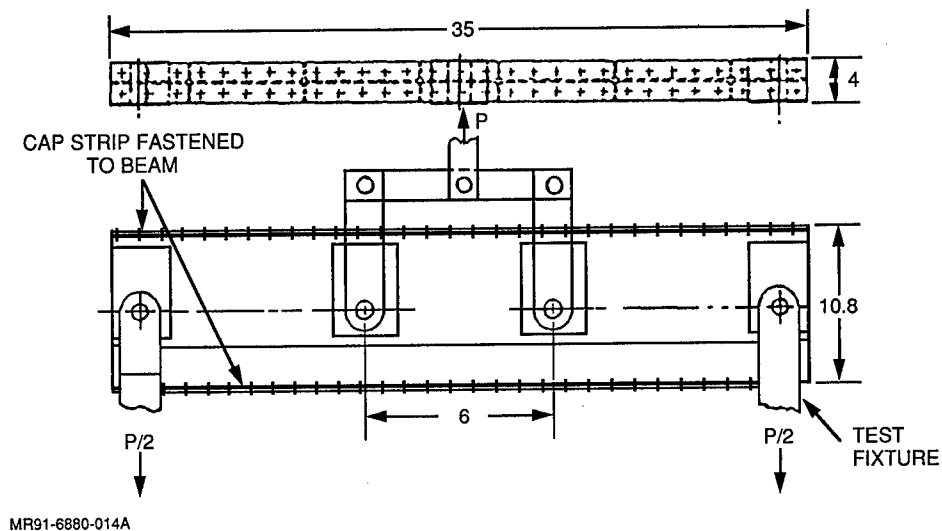
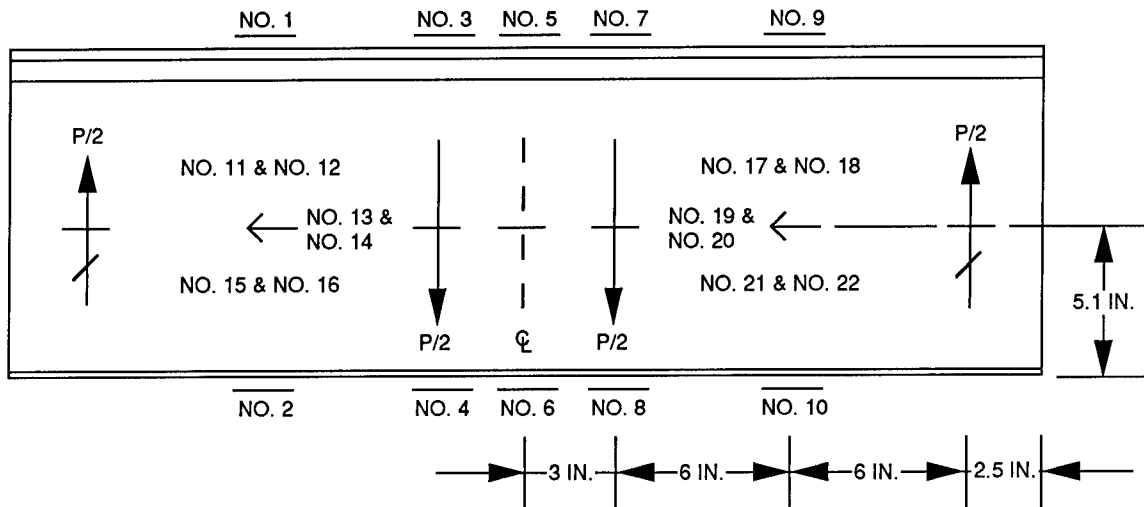
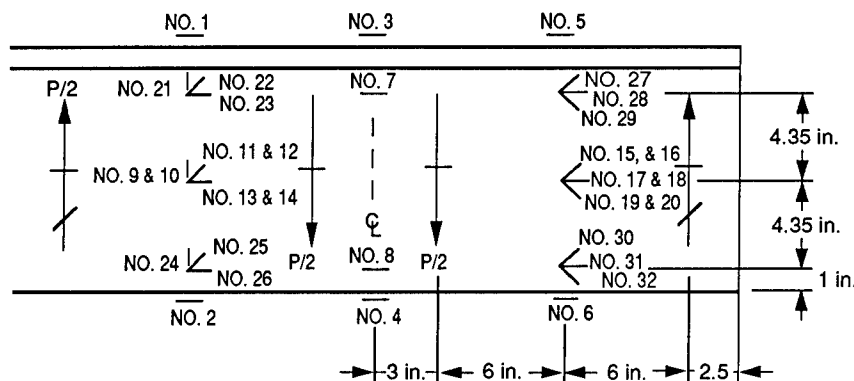


Figure 14 Y-Spar 4-Point Bending Test Setup



MR91-6880-015

Figure 15 Strain Gage Locations (Except for Woven AS4/PEEK Commingled Y Spar)



MR91-6880-016

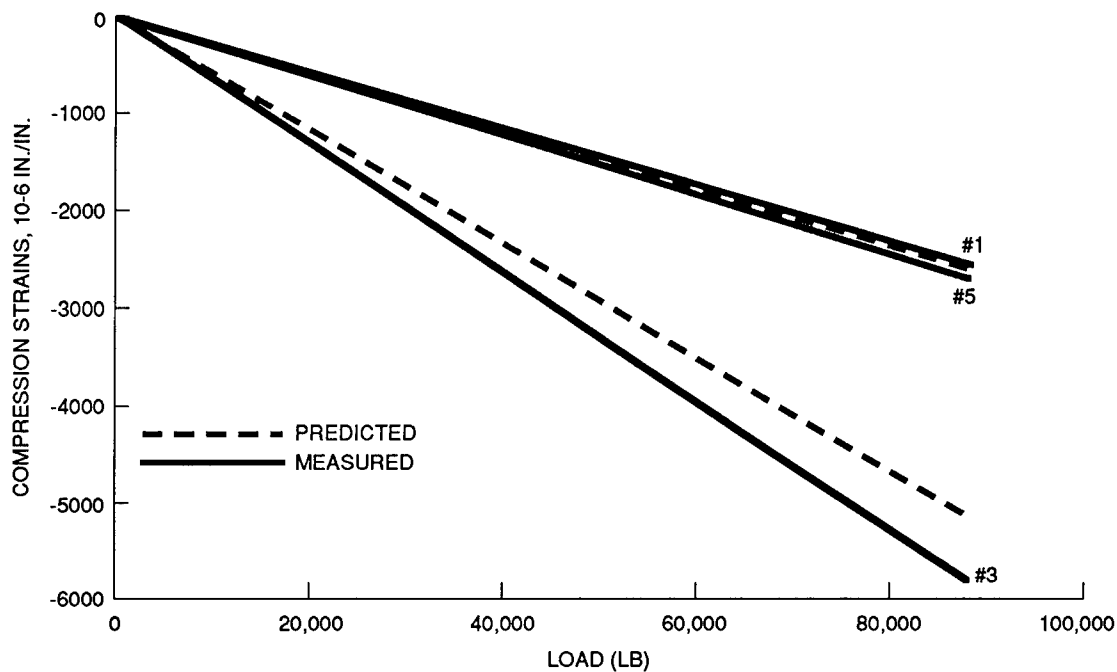
Figure 16 Strain Gage Locations for Woven AS4/PEEK Commingled Y Spar

## TEST RESULTS

In general, the measured strains agreed well with the predictions. This is significant when one considers that the stiffness properties were derived from unidirectional tape properties with corrections made for fiber volume and the woven nature of the AS4 preform. Spar bending strains at failure were close to or exceeded  $\pm 6000 \mu\text{in./in.}$  in all cases. Whereas only the G40-800/Tactix 123 test specimen failed due to the load in the spar itself, this failure compared well with the average predicted value for an IM6/3501-6 unidirectional tape prepreg laminate, autoclave cured. The structural aspects of each test spar are briefly discussed below.

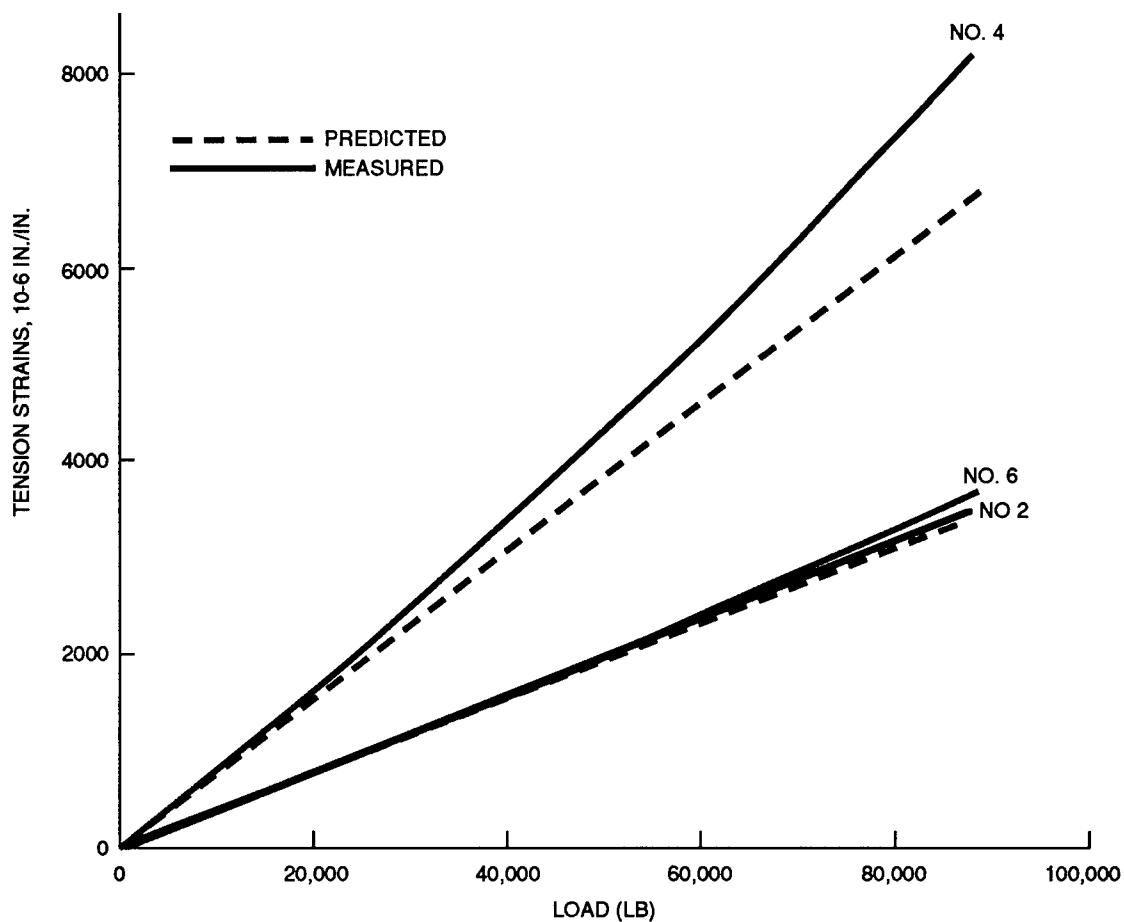
### Woven AS4/PEEK Commingled

Although this spar had problems during the preform fabrication, and the final product was oversize in height and thickness, its performance during the test was predictable. Figures 17 to 19 show



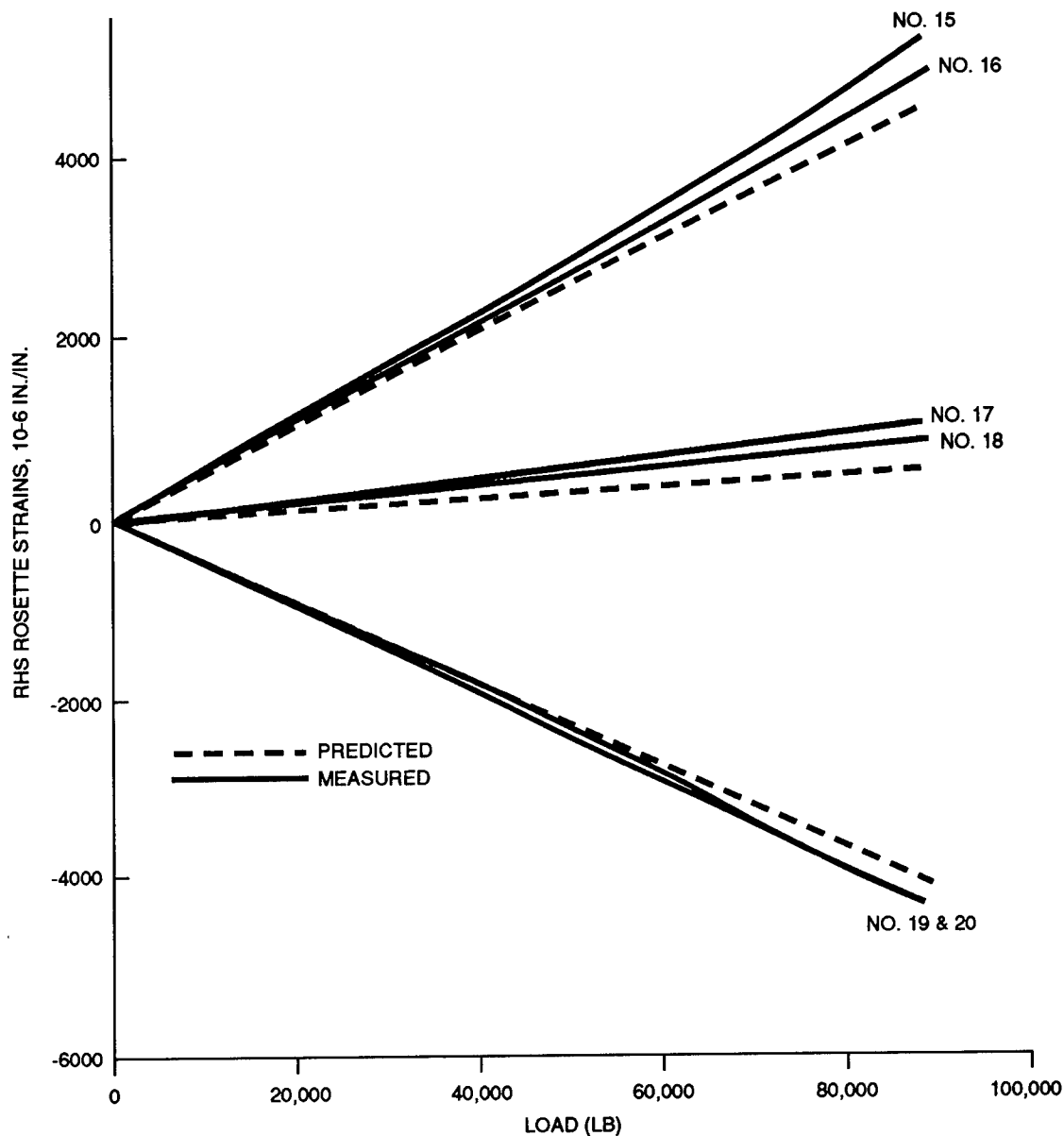
MR91-6880-017

Figure 17 Compression Strain vs Applied Load for Woven AS4/PEEK Commingled Y Spar



MR91-6880-018

Figure 18 Tension Strain vs Applied Load for Woven AS4/PEEK Commingled Y Spar



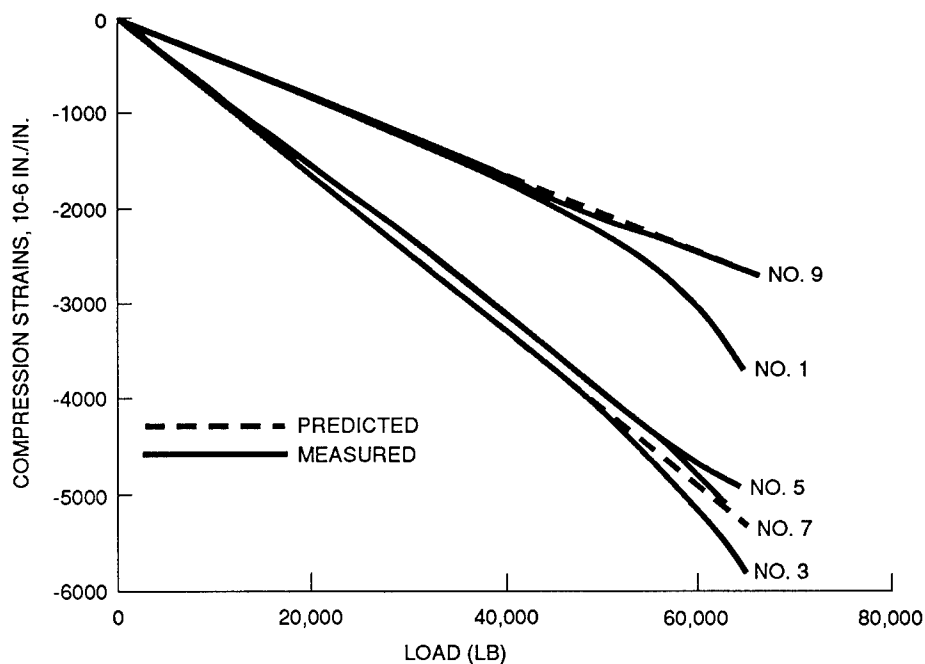
MR91-6880-019

**Figure 19 Strain vs Applied Load for Woven AS4/PEEK Commingled Y Spar**

measured and predicted strain vs applied load. Predictions are based on a 11.8/41/47.2% (0-/±45-/90-deg) laminate obtained from the results of coupon testing. Due to the increased thickness, web buckling and a web shear failure were precluded. Failure at an applied load of 89,000 lb occurred because the tensile load in the cap exceeded the open-hole strength. The bending strains at failure were +8270  $\mu\text{in./in.}$  and -5940  $\mu\text{in./in.}$ , showing that this manufacturing approach met the program goal of  $\pm 6000$   $\mu\text{in./in.}$  in bending. See figure 16 for gage locations.

## Knitted/Stitched G40-800/Tactix 123 (RTM)

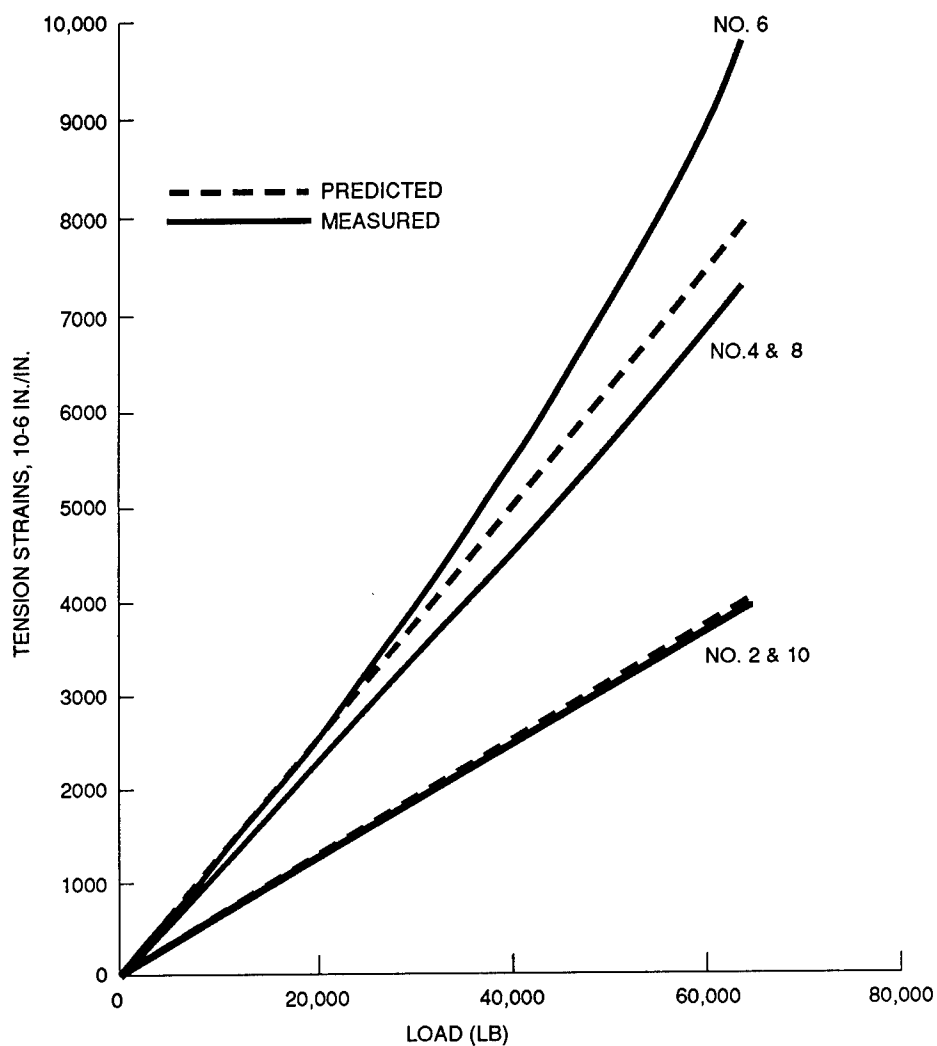
The strain response of this spar is plotted in figures 20 to 22. The maximum tension strain was 9577  $\mu\text{in./in.}$  and the maximum compression strain was -5716  $\mu\text{in./in.}$  Whereas the bending strains are in good agreement with the predictions, the shear strain is higher than expected. This is probably because of a lower effectiveness of the surface plies as a result of surface dryness noted in the spar. Using the measured shear strain and the analytical shear flow implies an effective 0.120-in.-thick, 10/56/34% laminate as opposed to the 0.138-in.-thick, 9/62/29% laminate expected. This revised laminate has an  $E_t$  of  $0.704 \times 10^6 \text{ lb/in.}$  and a  $G_t$  of  $0.440 \times 10^6 \text{ lb/in.}$ ; whereas the laminate used for pre-test analysis had an  $E_t$  of  $0.778 \times 10^6 \text{ lb/in.}$  and a  $G_t$  of  $0.548 \times 10^6 \text{ lb/in.}$  As a result, the net change in bending stiffness is small, while the change in shear strain is high. Web buckling occurred at an applied load of ~60,000 lb or an average flat web shear flow of 2840 lb/in. Predicted buckling varied from 2070 lb/in. for simply-supported edge conditions, to 3190 lb/in. for clamped edges. In both cases, a reduction in stiffness was taken for the surface plies only and the actual thickness was used. At the failure load of 65,300 lb, the calculated maximum shear stress in the web was 31,200 lb per sq in. on the effective thickness and normalized to 62%



MR91-6880-020

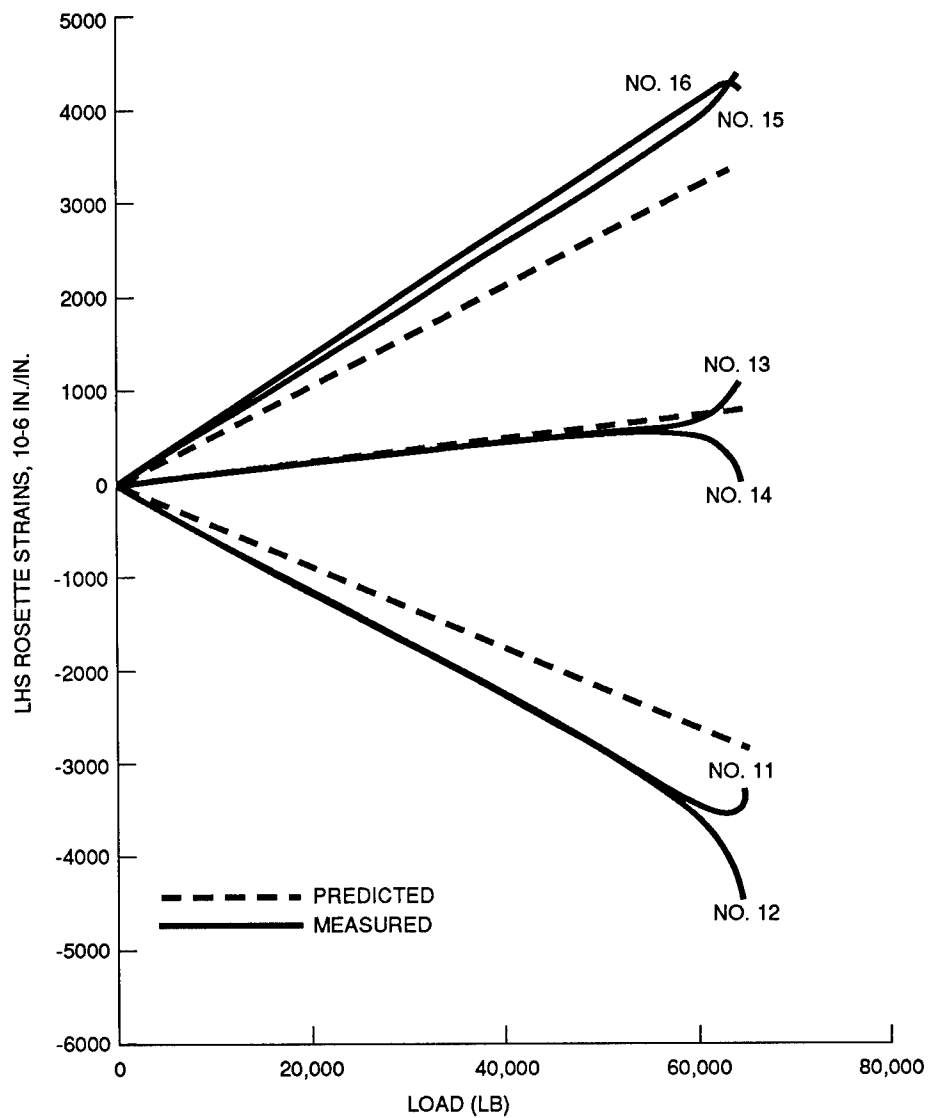
**Figure 20 Compression Strain vs Applied Load for G40-800/Tactix 123 (RTM) Y Spar**

fiber volume. Compared to a design allowable for IM6/3501-6 prepreg tape of 27,000 lb per sq in. and an average strength of 33,750 lb per sq in., the RTM process is considered structurally viable once provisions are made to ensure that all the fibers are rendered effective.



MR91-6880-021

Figure 21 Tension Strain vs Applied Load for G40-800/Tactix 123 (RTM) Y Spar



MR91-6880-022

Figure 22 Web Strain vs Applied Load for G40-800/Tactix 123 (RTM) Y Spar



### Knitted/Stitched G40-800/3501-6 (RFI)

This spar, shown in figure 23, performed very well as seen from the strain plots in figures 24 and 25. The maximum tension strain was 11,550  $\mu\text{in./in.}$  and the maximum compression strain was -6128  $\mu\text{in./in.}$  Buckling of the web occurred at ~70,000 lb of applied load, or an average shear flow of 3320 lb/in. Analytical buckling predictions were 3530 lb/in. for simply-supported edges and 4780 lb/in. for clamped edges. Examination of the failed beam revealed that the stacking sequence of the web was not symmetric and hence, the premature buckling. The test beam failed at an applied load of 76,000 lb, due to local bending of the compression cap. At this load, the maximum calculated web shear stress was 36,540 lb per sq in. on the effective thickness and normalized to 62% fiber volume. Thus, the RFI process also proved to be very structurally acceptable.

### Woven IM7/3501-6 (RFI)

The IM7 woven Y spar impregnated with 3501-6 resin by RFI was tested as a beam in four-point bending. The beam-bending specimen was instrumented with 22 strain gages. Mid-span deflection was measured with a dial gage. After installation into the test machine, the beam was loaded to 7000 lb (50% limit load) in 1000-lb increments, and then unloaded. Measured strains were compared with predictions, and checked for any anomalies. The beam was then loaded to limit load and unloaded. The measured strains were generally lower than the predictions, but repeatable and linear. The beam was loaded to ultimate (21,000 lb), held, and then loaded to failure. Failure occurred at a load of 69,200 lb and was due to the tensile stress in the cap, as shown in figure 26. The maximum tension strain was 8470  $\mu\text{in./in.}$  and the maximum compression strain was -4770  $\mu\text{in./in.}$  Maximum mid-span deflection was 0.258 in. Figures 27 through 30 are plots of predicted and measured strain vs test load for the compression gages, the tension gages, and the two pairs of rosettes. The predictions were made using a slightly modified laminate that accounted for the measured fiber volume (56.1%) and thickness of the web.

The failure was the result of combined bolt load and passing tension in the IM6/3501-6 tension cap laminate ~12 in. from the end of the spar. Based on strain gage no. 8, the strain at failure was 6600  $\mu\text{in./in.}$  The predicted average tensile failure strain determined from HOLES program was 7070  $\pm 1410$   $\mu\text{in./in.}$  Therefore, actual and predicted failure agreed within the scatter of the test data.

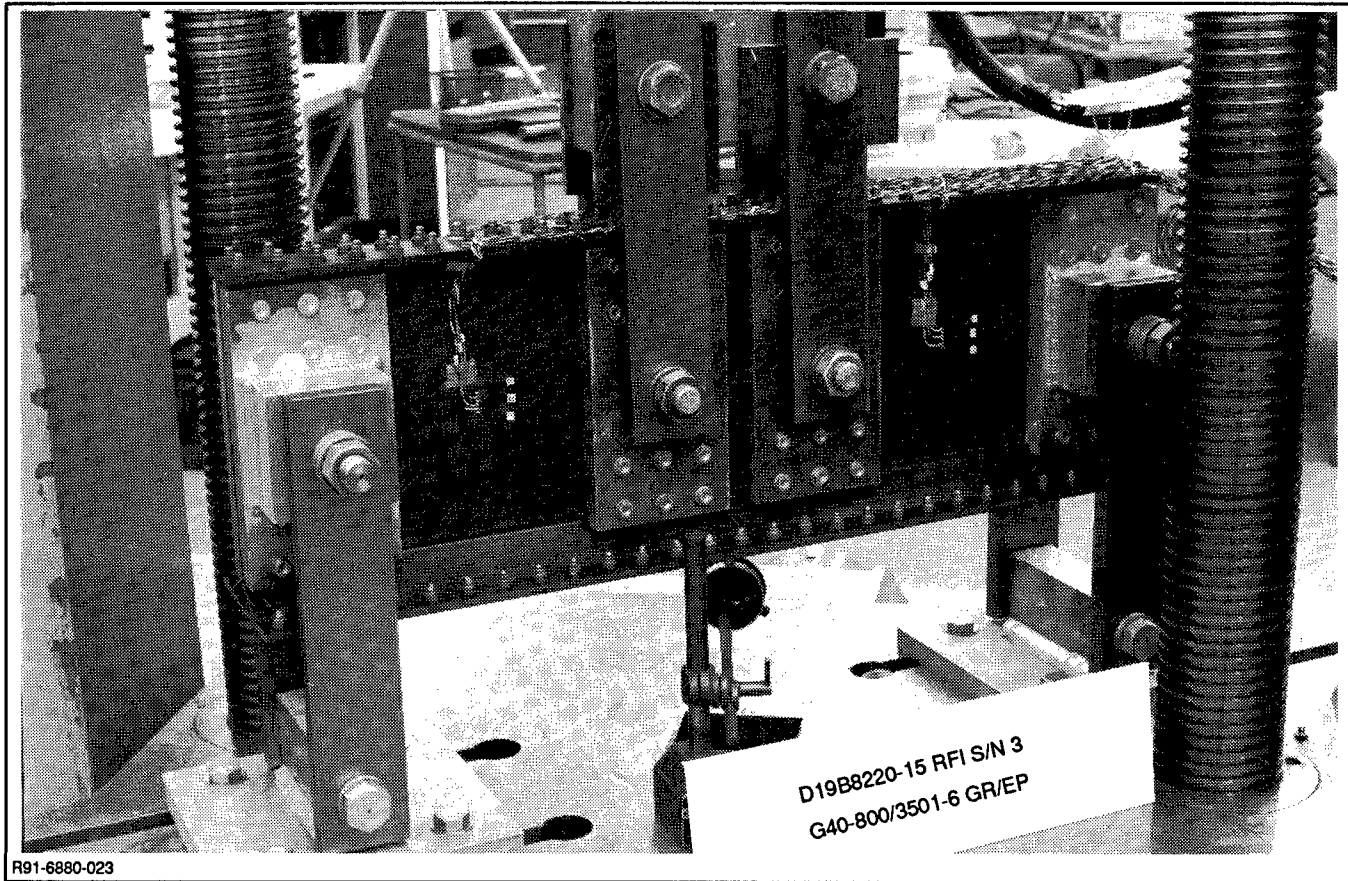
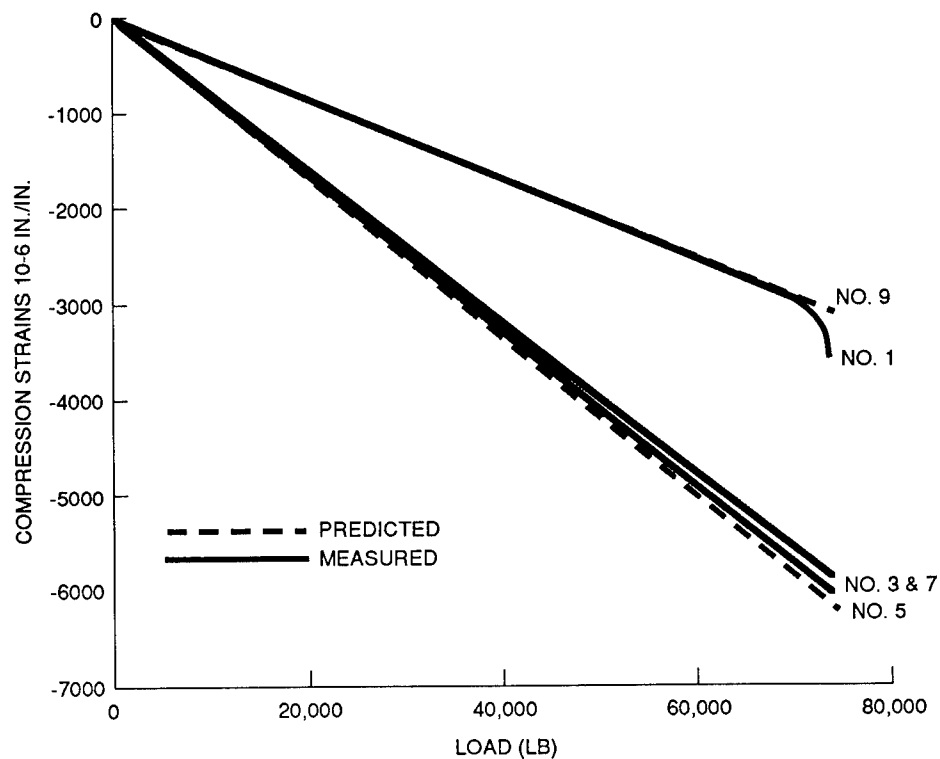
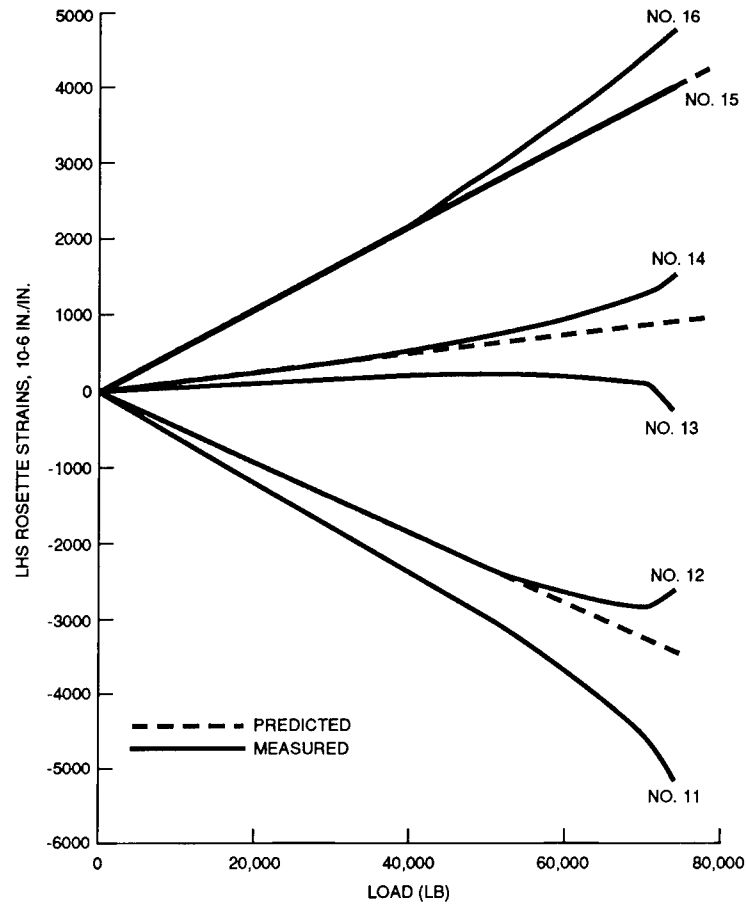


Figure 23 Test Setup for G40-800/3501-6 (RFI) Y Spar



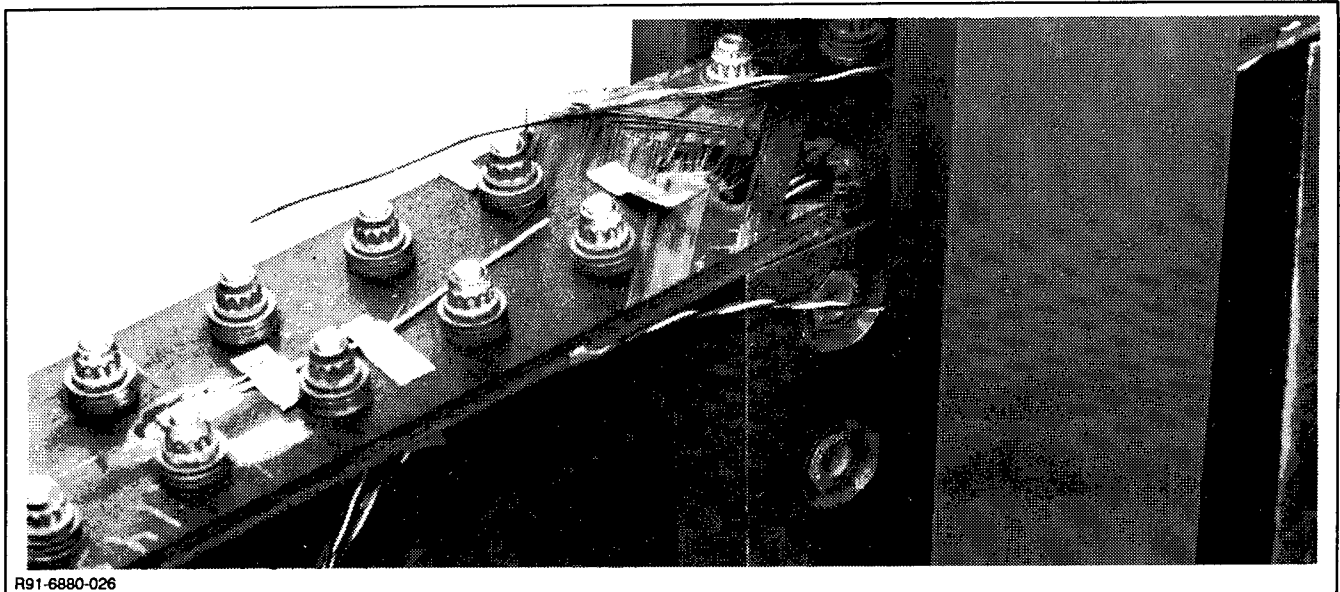
MR91-6880-024

Figure 24 Compression Strain vs Applied Load for Knitted/Stitched G40-800/3501-6 (RFI) Y Spar



MR91-6880-025

Figure 25 Web Strain vs Applied Load for Knitted/Stitched G40-800/3501-6 (RFI) Y Spar



R91-6880-026

Figure 26 Woven IM7/3501-6 (RFI) Y Spar Showing Cap (IM6/3501-6 Gr/Ep Tape) Tensile Failure

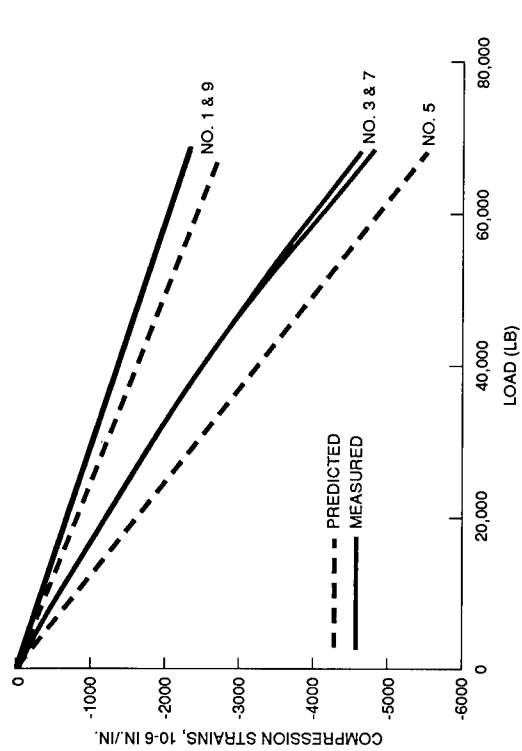


Figure 27 Compression Strain vs Applied Load for Woven IM7/3501-6 (RFI) Y Spar

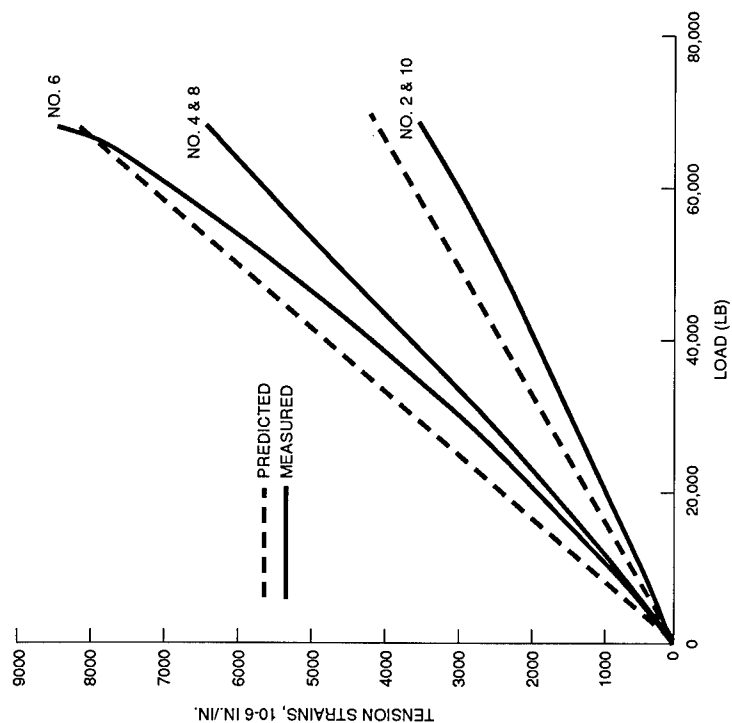


Figure 28 Tension Strain vs Applied Load for Woven IM7/3501-6 (RFI) Y Spar

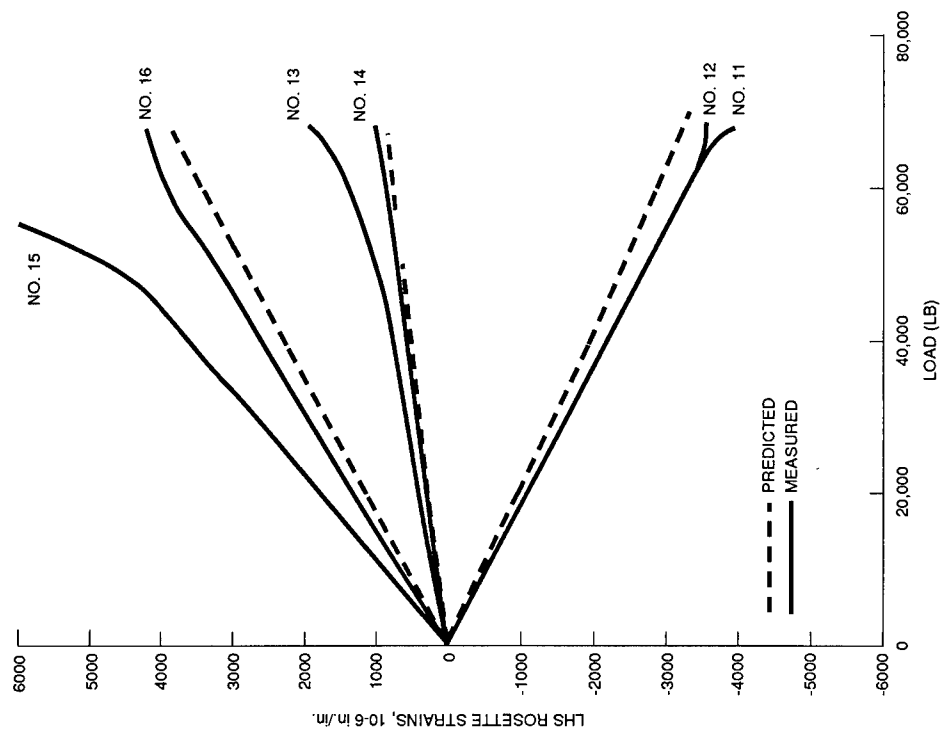
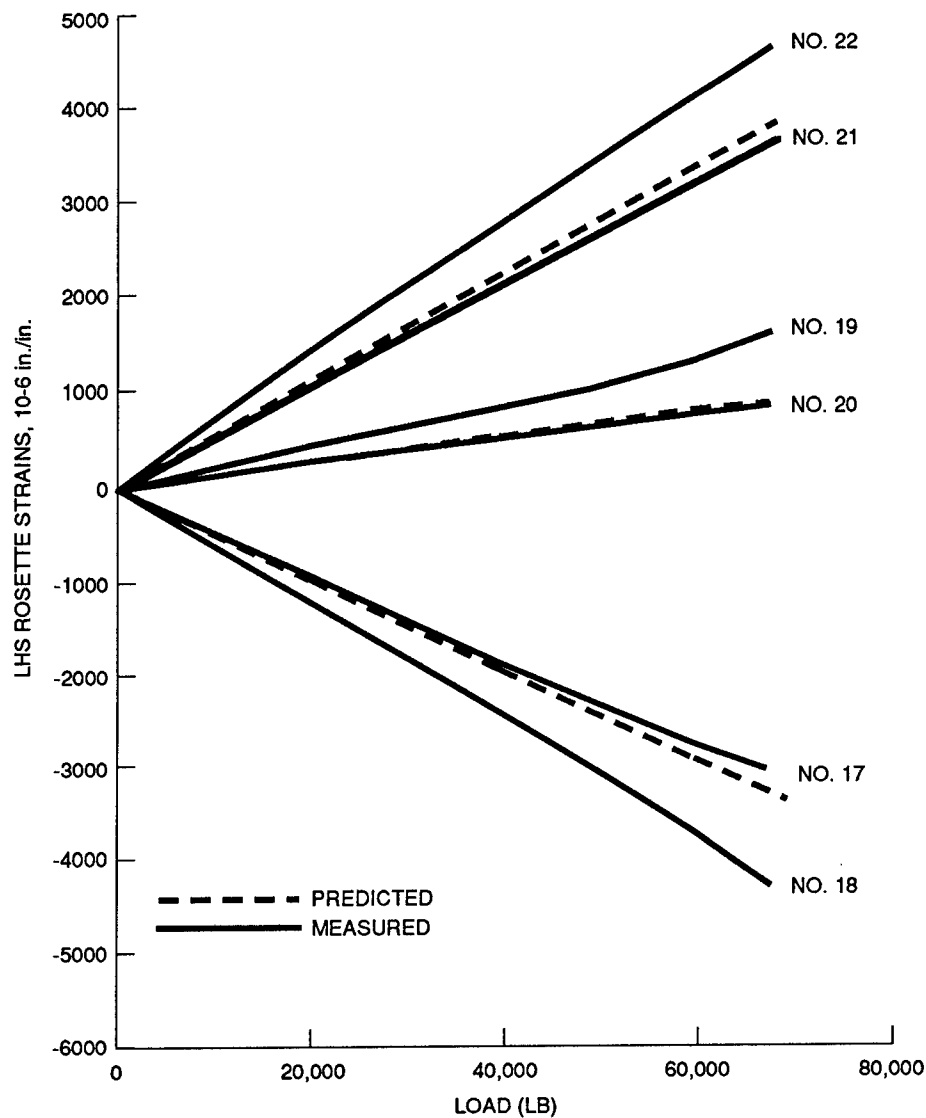


Figure 29 Strain vs Applied Load for Woven IM7/3501-6 (RFI) Y Spar (LHS Rosette)

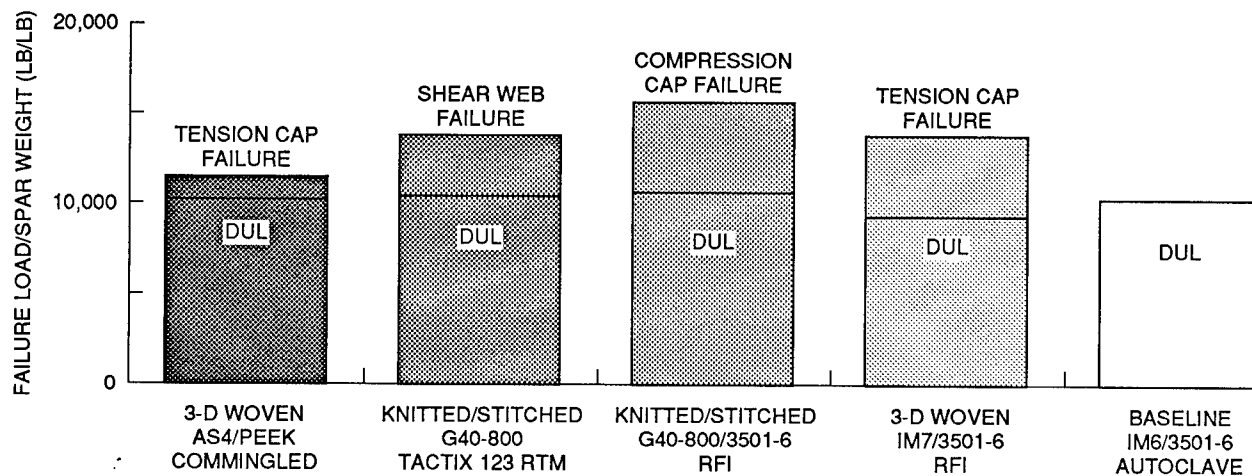


MR91-6880-030

Figure 30 Strain vs Applied Load for Woven IM7/3501-6 (RFI) Y Spar (RHS Rosette)

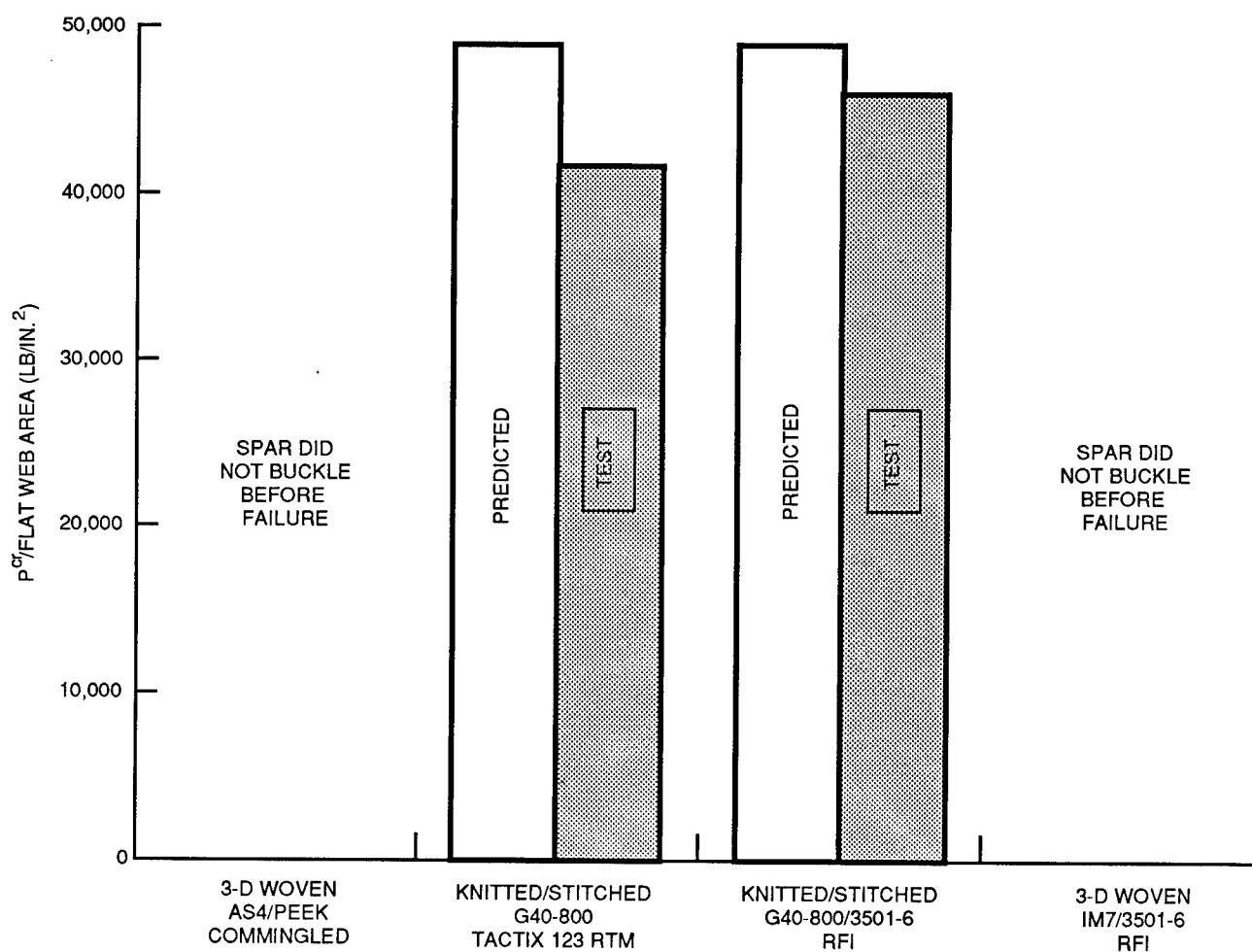
### STRUCTURAL EFFICIENCY

The various material form/processing combination Y spars were rated for their structural efficiency. As shown in figure 31, the knitted/stitched G40-800/3501-6 RFI Y spar is superior to all the others in terms of failure load per spar weight. The worst performer is the woven AS4/PEEK commingled Y spar, which was manufactured oversize. The knitted/stitched RFI spar also exhibited the highest ratio of web buckling to web area (figure 32), and the highest cap compression strain per unit weight, as shown in figure 33.



MR91-6880-031

Figure 31 Y Spar Failure Load per Unit Weight



MR91-6880-32A

Figure 32 Y Spar Web Buckling

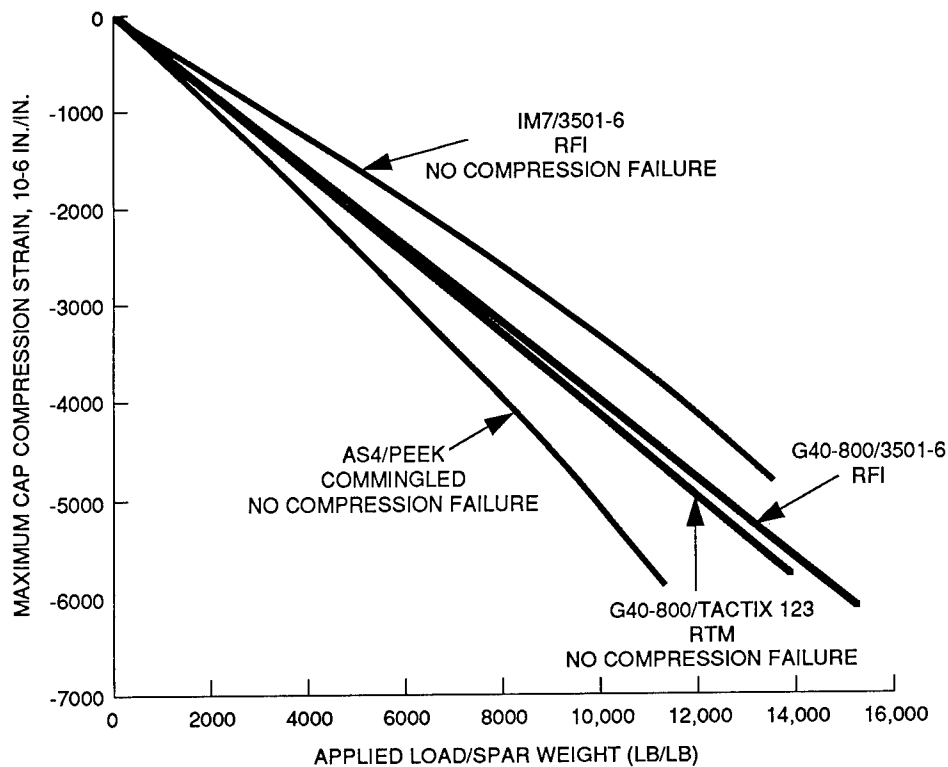


Figure 33 Compression Strain vs Applied Load

### PROJECTED COSTS

Manufacturing costs to produce the various Y spars were estimated for each of the four material form/processing combinations. These approaches are:

- Woven/stitched AS4/commingled PEEK preform thermoformed (consolidated) via autoclave/vacuum bag procedures
- Knitted/stitched G40-800 preform impregnated with Dow Tactix 123/H41 resin system via RFI, then autoclave processed
- Woven/stitched IM7 preform impregnated with Hercules 3501-6 resin system via RFI, then autoclave processed
- Knitted/stitched G40-800 preform impregnated with Hercules 3501-6 resin system via RFI, then autoclave processed.

Comparative manufacturing costs were based on actual costs for tooling (non-recurring costs), and estimates for labor and materials (recurring costs). These cost comparisons were developed for the fabrication of one Y spar of each type, based on a production run of 100 units.

## Tooling Costs

Tooling for each of the three processes was designed and fabricated by outside subcontractors, each of whom specializes in the particular materials and processes involved in the tools. Actual tool fabrication costs are presented below, for each of the three tools:

- Aluminum RTM tool for D19B8220-11 Y spar: \$18,932.00
- Monolithic Graphite tool for D19B8220-13 Y spar: \$10,869.00
- Aluminum RFI/autoclave tool for D19B8220-15 Y spar: \$20,000.00.

To generate the prorated hours to reflect the design and fabrication cost of the 100-unit production run scenario, each of the above dollar figures was converted to an equivalent number of hours by dividing by a labor rate of \$100.00/hr. These prorated person-hour requirements are presented in Table I, along with the recurring labor hours for each of the three processes.

**TABLE I. - QUANTITATIVE COMPARISON OF PERSON HOURS REQUIRED TO FABRICATE Y SPAR UNDER THREE MANUFACTURING APPROACHES**

MANUFACTURING ACTIVITY	CANDIDATE MANUFACTURING PROCESSES			REMARKS
	RTM HR	AUTOCLAVE CONSOLIDATE HR	RFI/AUTOCLAVE HR	
TOOL DESIGN & FABRICATION	1.89	1.09	2.00	TOOL DESIGN/FABRICATION HR ARE PRORATED FOR 100 UNITS
PREFORM FABRICATION:				
• WEAVING 0-/90-DEG CARCASS	68.85	68.86	N/A	BASED ON TOTAL COST; 6 FOR \$41,310.00 BASED ON COST OF \$1758.22 EACH BASED ON COST OF \$3480.00
• STITCHING ±45-DEG PLIES	17.58	17.58	N/A	
RTM FABRICATION:	34.80	N/A	N/A	
• TRIM TO FIT TOOL; LOAD IN TOOL; MIX, METER, INJECT RESIN; CURE PART; REMOVE PART				
AUTOCLAVE CONSOLIDATION:	N/A	38.00	N/A	BASED ON ACTUAL HOURS EXPENDED AT GRUMMAN
• TRIM TO FIT TOOL; LOAD IN TOOL; APPLY ALL BREATHER & BAGGING MATERIALS; AUTOCLAVE CONSOLIDATE PART; REMOVE PART; TRIM TO FINISH DIMENSIONS				
RFI/AUTOCLAVE PROCESSING:	N/A	N/A	100.00	BASED ON COST OF \$10,000.00, WHICH INCLUDES THE COST OF THE KNITTED/STITCHED PREFORM
• KNIT/STITCH PREFORM, APPLYING FILM RESIN; RFI PROCESS; PRE-PARE FOR AUTOCLAVE PROCESSING; AUTOCLAVE CONSOLIDATE PART; REMOVE PART; TRIM TO FINISH DIMENSIONS				
TOTALS	123.12	125.53	102.00	

NOTE: THE STANDARD AUTOCLAVE TAPE FABRICATION OF Y SPAR REQUIRES 129 PERSON HR



## Labor Costs

Manufacturing hours to produce the individual Y spars are also tabulated in Table I. Person-hour estimates for the autoclave-consolidated-13 Y spar are based on a single autoclave cycle being required, including an overnight preheating at 350°F. Person hours for the RTM and RFI/autoclave processes performed at a subcontractor were derived by dividing the vendor's cost to Grumman by a labor rate of \$100.00/hr. Similarly, person hours listed for the weaving and stitching of the -11 and -13 preforms were derived from the subcontractors' dollar costs to Grumman. The person-hour estimates given in Table I are average values, and do not reflect a learning curve.

Based on the tabulated data, person-hour requirements for the three fabrication approaches are:

- RTM processing of knitted/stitched Y spar: 123.12
- Autoclave consolidation of woven commingled PEEK Y spar: 125.52
- RFI/autoclave processing of knitted/stitched Y spar: 102.00.

## Material Costs

Most material costs for the Y spars under the three competing processing techniques were included in the data summarized in Table I. Therefore, Table II includes only the material costs associated with the autoclave consolidation of the woven commingled PEEK Y spars at Grumman. These include costs of all breather and bagging materials required to support the autoclave operation itself, as well as the liquid nitrogen consumed in the autoclave cycle. The data are estimates based on observation of material usage during the bagging operation, or on average consumption of gas. From Table II, the material costs for the autoclave manufacturing approach are \$1767.00.

## Facility Costs

The full-scale production of Y spars, using each of the candidate manufacturing approaches, would require the following equipment:

- High-temperature/high-pressure autoclave
- Hydraulic press
- Vacuum pumps
- Metering/injection equipment to support RTM
- Other miscellaneous facilities to support the above capital equipment.

Isolating the costs of these types of facilities was beyond the scope of this program.

**TABLE II. - MATERIAL COST FOR AUTOCLAVE CONSOLIDATION  
OF -13 Y SPAR**

MATERIAL (DESCRIPTION)	UNIT COST (\$)	USAGE	COST (\$)
BREATHER FABRIC (STYLE 181 FIBERGLASS)	1.50/YD <sup>2</sup>	10 YD <sup>2</sup>	15.00
VACUUM BAG SEALANT (HIGH-TEMPERATURE) (LOW-TEMPERATURE)	25/ROLL 5/ROLL	6 ROLLS 2 ROLLS	150.00 10.00
VACUUM BAG FILM (KAPTON)	6/YD	4 YDS	24.00
KAPTON TAPE	28/ROLL	1 ROLL	28.00
INDUSTRIAL GAS (LIQUID NITROGEN) & RELATED COSTS	28/GAL	55 GAL	1540.00
TOTAL COST			1767.00

MR91-6880-035

### Comparative Manufacturing Costs

Labor costs for the three manufacturing approaches, assuming a labor rate of \$100.00/hr, would be as follows:

- RTM-processed knitted/stitched Y spar: \$12,312.00
- Autoclave-consolidated woven commingled PEEK Y spar: \$12,552.00
- RFI/autoclave-processed knitted/stitched Y spar: \$10,200.00.

Adding to the autoclave consolidation approach the separate material costs of \$1767.00, as identified above and in Table II, would provide the following total comparative costs for the three processes:

- RTM-processed knitted/stitched Y spar: \$12,312.00
- Autoclave-consolidated woven commingled PEEK Y spar: \$14,319.00
- RFI/autoclave-processed knitted/stitched Y spar: \$10,200.00.

Based on the comparative manufacturing costs for each Y spar and assuming applicability to future aerospace components, the RFI/autoclave process could provide 17 and 29% lower fabrication costs, respectively, than the other competing processes.

## CONCLUSION

The study conducted as herein described has led to the following various conclusions:

- Textile polymer matrix composites (PMC) can be designed and fabricated for primary aircraft structural components with equivalent efficiency and reduced acquisition costs compared with current day PMC components (approximately 20% reduction)
- The various PMC materials, along with various processing methods, are all suitable for wing spar applications and thus provide for design/manufacturing flexibility
- Although the various processes have not yet been developed to a fully reliable state, with continued study it appears that full-scale components will be production implemented in the future.

# **Characterization and Manufacture of Braided Composites for Large Commercial Aircraft Structures<sup>1</sup>**

**Mark J. Fedro**

**Boeing Defense and Space Group - Philadelphia, PA**

**Kurtis Willden**

**Boeing Commercial Airplane Group - Seattle, WA**

## **ABSTRACT**

Braided composite materials, one of the advanced material forms which is under investigation in Boeing's ATCAS program, have been recognized as a potential cost-effective material form for fuselage structural elements. Consequently, there is a strong need for more knowledge in the design, manufacture, test, and analysis of textile structural composites. The overall objective of this work is to advance braided composite technology towards applications to a large commercial transport fuselage. This paper summarizes the mechanics of materials and manufacturing demonstration results which have been obtained in order to acquire an understanding of how braided composites can be applied to a commercial fuselage. Textile composites consisting of 2-D, 2-D triaxial, and 3-D braid patterns with thermoplastic and two RTM resin systems were investigated. The structural performance of braided composites was evaluated through an extensive mechanical test program. Analytical methods were also developed and applied to predict the following: internal fiber architectures, stiffnesses, fiber stresses, failure mechanisms, notch effects, and the entire history of failure of the braided composite specimens. The applicability of braided composites to a commercial transport fuselage was further assessed through a manufacturing demonstration. Three foot fuselage circumferential hoop frames were manufactured to demonstrate the feasibility of consistently producing high quality braided/RTM composite primary structures. The manufacturing issues (tooling requirements, processing requirements, and process/quality control) addressed during the demonstration are summarized. The manufacturing demonstration in conjunction with the mechanical test results and developed analytical methods increased the confidence in the ATCAS approach to the design, manufacture, test, and analysis of braided composites.

## **INTRODUCTION**

Textile structural composites represent a class of advanced materials in which a light-weight matrix material is reinforced with a textile fiber preform. The potential for significant cost savings for textile reinforced composites through automated preform fabrication and low-cost resin transfer molding (RTM) has increased the commercial airplane industry interest in these materials. As the use of composites is being expanded to large scale structural components, textile reinforcements are being considered for providing adequate structural integrity as well as process flexibility for near-net-shape manufacturing.

Boeing's program for Advanced Technology Composite Aircraft Structures (ATCAS) has focused on the manufacturing and performance issues associated with a wide body commercial transport fuselage. The main ATCAS objective is to develop an integrated technology and demonstrate a confidence level that permits cost- and weight-effective use of advanced composite materials in future primary aircraft structures with the emphasis on pressurized fuselages. An aft fuselage section directly behind the wing-to-body intersection is used for technology development and verification purposes in ATCAS. This section of fuselage (shown in Figure 1) has many design details and associated technology issues that pose a test of advancements in composite primary structures.

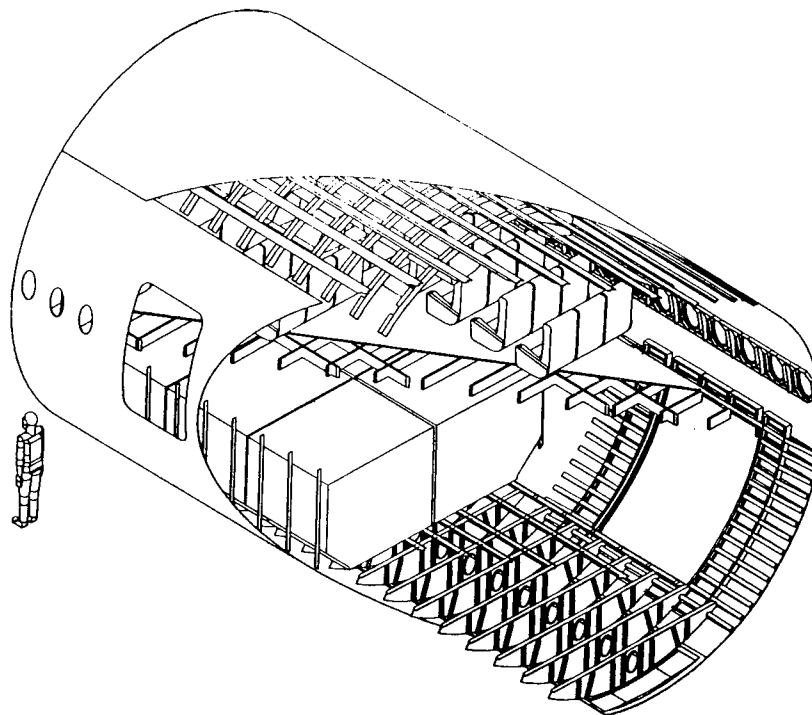
---

<sup>1</sup> This work was funded by Contract NAS1-18889, under the direction of J.G. Davis and W.T. Freeman of NASA Langley Research Center.

The ATCAS Program uses a Design Build Team (DBT) Approach and a 3-step design process. The first step in the design process is the selection of Baseline Concepts as those design and manufacturing ideas having an apparent potential for cost and weight savings, combined with an acceptable risk; technology issues are also identified during this phase of design. The second step is Global Evaluation where cost and weight savings are evaluated by performing detailed studies for the baseline and a limited number of alternative concepts. The final step in the design process is Local Optimization in which cost centers and major technology barriers established during the first two design steps are attacked. The design families chosen during the design process are shown in Figure 2.

During the ATCAS design process, the DBT recognized that textile composites have a great potential for many applications to primary structural components in a fuselage. The potential structural applications of textile composites (shown in Figure 2) are the circumferential hoop frames, the window belt, and the underfloor cargo frames.

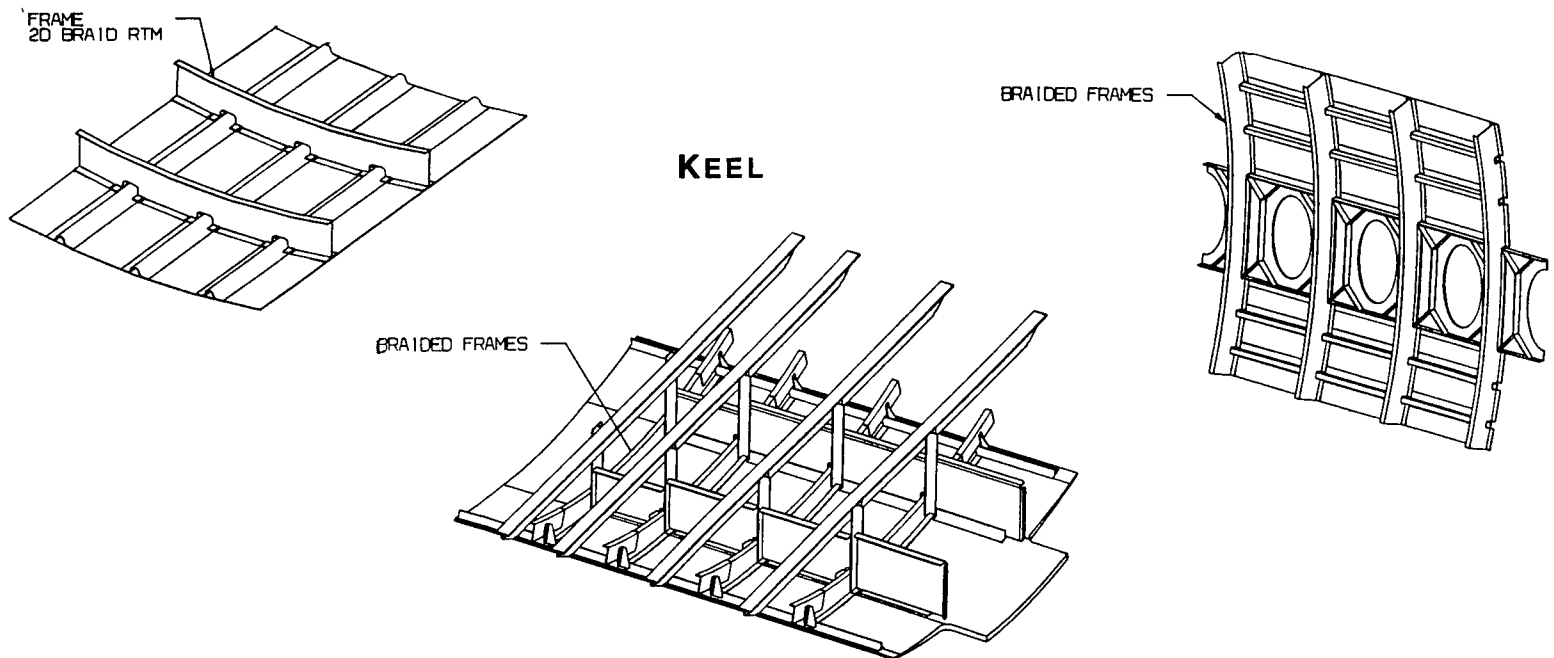
The crown panel section was the first quadrant of focus in the ATCAS Program. The ATCAS DBT performed several comparative studies of different potential textile material systems for the circumferential hoop frames. Using the results of the comparative studies, 2-D triaxially braided/RTM material systems exhibited the most promise. The focus of this paper is the characterization and manufacture of braided composites for the crown panel frames. A detailed outline of this paper is shown in Figure 3. The first section of this paper describes the global selection and requirements of the crown panel circumferential hoop frames. Section 2 details the braided/RTM technology development in the areas of materials, manufacturing, analysis, and test. Section 3 describes the details of the 3 ft. frame manufacturing demonstration and the technology that supported the demonstration. Section 4 gives the details on the Local Optimization of the frame design. Finally, the scale-up issues for a half-length manufacturing demonstration are identified and discussed in the final section of the paper.



**Figure 1: ATCAS Fuselage Design**

## CROWN PANEL

## SIDE PANEL



**Figure 2: Potential Fuselage Applications for Textile Composites**

### 1. GLOBAL SELECTION AND REQUIREMENTS

- A. Material and Manufacturing Cost Evaluation
- B. Design Requirements
- C. Manufacturing Requirements

### 2. BRAIDED/RTM TECHNOLOGY DEVELOPMENT

- A. Braided Composite Material Systems
- B. Manufacturing of Braided Composites
- C. ATCAS Textile Composites Analysis (TECA)
- D. Mechanical Characterization of Braided Composites

### 3. CIRCUMFERENTIAL HOOP FRAME DEVELOPMENT

- A. Material Selection
- B. Frame Fiber Architecture Design
- C. Manufacturing of Braided Composite Specimens
- D. Material System Performance Evaluation
- E. 3 ft Frame Manufacturing Demonstration

### 4. FRAME DESIGN LOCAL OPTIMIZATION

- A. Dimensional Accuracy Optimization
- B. Frame-to-Skin Bond Issue
- C. Mouse Hole Configuration
- D. Manufacturing Process Optimization
- E. Cost and Weight Impact of Local Design Optimization
- F. Summary of Current Circumferential Hoop Frame Design

### FUTURE WORK / KEY ACCOMPLISHMENTS

**Figure 3: Paper Outline**

# 1. FRAME GLOBAL SELECTION AND REQUIREMENTS

## A. Material and Manufacturing Cost Evaluation

Four different material systems and fabrication techniques were screened as possible candidates for the circumferential hoop frames during the detailed cost and weight studies. The four material systems and the fabrication techniques were: 1) stretch forming long discontinuous fibers (LDF), 2) compression molding fabric prepreg, 3) pultruding dry fiber through a resin bath, and 4) RTM 2-D braided preforms. A price per pound comparison of frame fabrication processes and material systems is found in Reference 1. Results of this study show that the 2-D braided/RTM material system was the most attractive process in terms of cost, weight, and manufacturability for the circumferential hoop frames; the cost of the braided RTM frames was approximately \$85/lb. This material system and fabrication technique uses the constituent materials in their lowest cost form. Braiding is a continuous, high-rate automated preform process that provides net-shape manufacturing which minimizes machining and trimming and produces preform dimensional accuracy. The fiber architecture of the preforms can also be tailored to meet design criteria. RTM provides batch-mode capabilities and repeatable closed-mold tolerances. Braided/RTM material systems tend to be more dimensionally stable than other systems such as tape, in addition the flexibility inherent to both braiding and RTM is advantageous in fabricating large complex structural composite components.

The skin/stringer/frame design was based on the use of automated systems that were considered highly efficient. Computer automated advanced tow placement was selected to lay-up the skins. A contoured tape lamination machine (CTLM), followed by a drape forming process was selected to lay-up and shape the hat stiffeners. Finally, the autoclave fabrication of full crown quadrant segments is envisioned as wet skin and stiffener, co-bonded with frames [2].

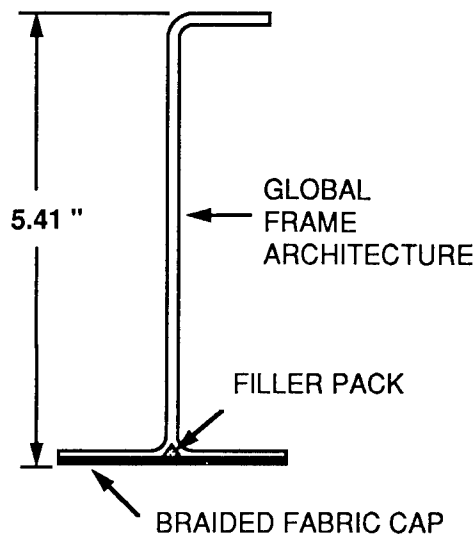
## B. Design Requirements

Fuselage frames serve a number of different functions. They maintain the cross sectional shape of the fuselage, resist the pressure-induced hoop loads (in conjunction with the skin), distribute concentrated loads, redistribute shear loads around structural discontinuities, and limit the column length of the longitudinal stringers to prevent general instability. The frames with flanges attached to the fuselage skin also act in a fail safe capacity as circumferential tear straps to restrict damage propagation.

### 1.B.1 Frame Configuration

The current configuration of the frame is a J-section with its wide flange (or cap) co-bonded to automated tow-placed skin. An I-section was considered for the frames, but was dismissed due to the difficulty of allowing attachments. A Z-section is undesirable for bonded structure due to peel stresses which develop with loads normal to the skin. A J-section, however, can easily accommodate attachment details and is not as prone to peel stresses because its web is located symmetrical with respect to the bonded flange. A limit for the total depth of the frame, including the attached skin, was assumed at 5.5 inches to maximize the useful space inside the fuselage. The J frames are mouse holed to accommodate the stringers. The frame configuration selected during global evaluation is shown in Figure 4.

The bending stiffness of the frame cap must be less than the bending stiffness of the skin to prevent excessive peel stresses from occurring during pressure pillowing of the skin. Since the frame-to-skin intersection is designed for failure to occur at the bond line, the cap must be designed to resist internal crack initiation. The frame configuration selected during global evaluation contains 3 layers of braided fabric on the frame cap to aid in manufacturing. The filler pack shown in Figure 4 must be added to the cap of the frame to fill the void caused by the splitting and separation of braided layers during frame fabrication. The filler pack material must be tough enough to resist crack initiation and propagation during frame loading.



**Figure 4: Frame Configuration Selected During Global Evaluation**

### 1.B.2 Critical Stiffness Design Criteria

The four critical load cases for the fuselage crown panel were determined to be: 1) ultimate internal pressure, 2) 6G up gust, 3) 9G forward crash condition, and 4) 3G down gust. Of these four cases, the ultimate pressure loading condition is the most critical condition for the circumferential hoop frames located in the crown panel. The ultimate pressure of 18.2 psi represents two times the normal operating pressure and corresponds to hoop direction line load of 2220 lb/in for a fuselage with a 122 inch radius. The hoop load puts the frame in axial tension, but bending loads also result as the pressure tries to stretch the frame to a larger radius. The frame spacing on the crown panel is typically 22 inches which was determined by stiffener stability, crown panel weight, and fuselage geometry requirements (ex. doors, window belt, etc.).

The pressure case also produces pull-off loads to balance the axial tension in the curved frames. The magnitude of the pull-off loads is proportional to the percentage of the load in the frame relative to the skin. These loads are critical to the strength and durability issues of the frame-to-skin bond line.

The frame loads are critical at the location of the mouse hole cut-outs where the cross sectional properties are significantly reduced. The critical ultimate pressure condition includes bending loads which produce a maximum strain at the inner flange of the frame. Design strains at ultimate load were limited to 0.5% tension and 0.4% compression for damage tolerance considerations. The effect of stress concentrations at the mouse holes is not a design driver since the edge of the mouse hole cut-out is in the middle of the bending section, away from the highly stressed frame inner flange.

The stiffness of the frames was checked to ensure that general instability of the fuselage does not occur. The criterion establishes a minimum bending stiffness of the frame as follows [3]:

$$(EI)_{\text{frame}} = \frac{MD^2}{16000 L} \quad \text{where: } M = \text{bending moment on fuselage} \quad (1)$$

$$D = \text{diameter of fuselage}$$

$$L = \text{frame spacing}$$



### 1.B.3 Mouse Hole Configuration

The frames incorporate mouse hole cut-outs to allow the continuous stringers through the frame-to-stringer intersections. The size of the cut-outs must be kept as small as possible to minimize the reduction of frame cross-sectional properties and still meet assembly requirements. In the crown section of the fuselage, the mouse holes span the entire width of the hat stringers for ease of assembly.

The column stability of the stringers requires the frames to provide enough stiffness normal to the stiffened skin such that a node point is achieved at each frame-to-stringer intersection. The mouse holes at these locations reduce the stiffness and compromise the ability of the frames to force a node point. Due to this reduction in stiffness, sections of the fuselage which are subjected to high axial compression loads often require a clip which forms a direct attachment between the stringer and the web of the frame at the mouse hole. In the crown, however, the axial compression loads are relatively small and the stringer clips were determined to be unnecessary. This conclusion will be verified later by large scale stability tests. The mouse hole detail selected during global evaluation is shown in Figure 5.

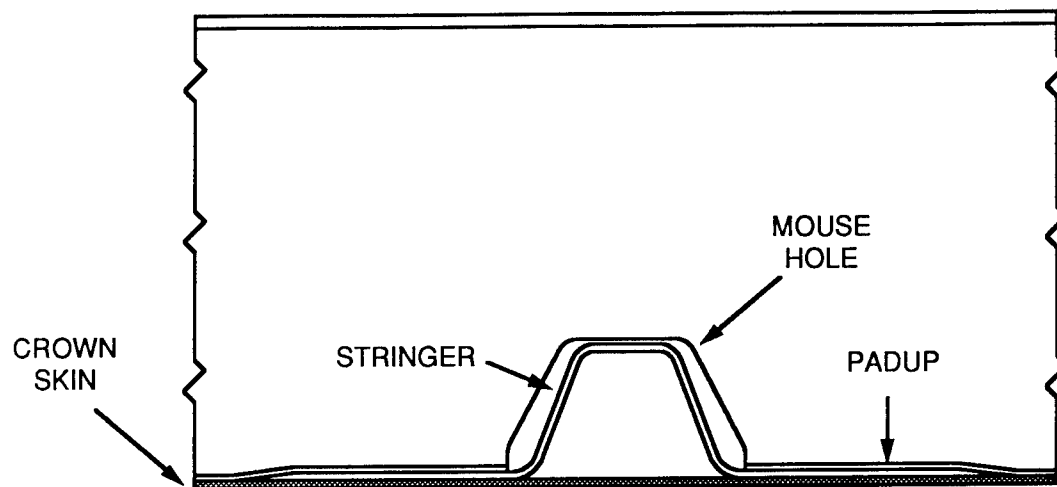


Figure 5: Mouse Hole Configuration Selected During Global Evaluation

### 1.B.4 Frame-to-Skin Bondline

One major technical issue identified for the crown panel design is the strength and durability of adhesively bonded frame elements. The crown frame bond line is subjected to pull-off forces from cabin pressure and post-buckled skins. Real time aspects of the problem needed to be considered since bond line stresses change as a function of cyclic pressure conditions. The strength and durability of adhesive bond lines that attach braided frames to automated tow-placed skins must be studied using both test and analysis.

## C. Manufacturing Requirements

The manufacturing requirements selected for RTM braided frames include: suitable RTM resin system, repeatable high quality part producibility and process control, batch mode manufacturing, and integration of process automation.

### 1.C.1 RTM Resin Requirements

In choosing an RTM resin system for the circumferential hoop frames, the ATCAS DBT screened RTM resin systems using 3 criteria: 1) manufacturability, 2) structural performance, and 3) cost. To manufacture circumferential frames the desired pot life is one hour with a viscosity of less than 50 centipoise (typical injection time is under 15 minutes). Processing anomalies are minimized with a resin system that offers low injection viscosity and a long pot life. Since the RTM frames are co-bonded to the

skin, the resin must be stable for an additional 5 hours at temperature greater than 350°F without property loss, therefore the glass transition temperature of the resin must be above 350°F. The structural performance of the resin must meet the necessary ATCAS stiffness, strength, damage tolerance, and environmental resistance requirements. Finally, the cost of the resin must be reasonable in order for composite design to compete with aluminum design.

### **1.C.2 Producibility and Process Control**

The RTM operation must achieve full wet-out conditions in order to satisfy the ATCAS criteria of less than a 2% void content of a finished composite part. In order to meet this requirement, accurate process control is needed to ensure that the resin is injected at the right viscosity and pressure. A constant resin viscosity must be maintained by accurate temperature control of the mixing pot and the entire RTM tool to avoid premature gelation and exothermal reactions. Feedback control of the temperature is essential and is considered a major parameter for SPC (Statistical Process Control) of part producibility. Optimization and control of injection ports, vacuum ports, and the resin system cure cycle are required to assist in the proper wet-out of the preforms.

### **1.C.3 Batch Mode Requirements**

To increase process efficiency, batch mode processing must be employed to reduce tooling and processing labor costs. Two batch mode processes were considered for the 2-D braided/RTM material system. Both processes use the mandrel containing the braided layers as part of the RTM tooling to minimize handling and inspection. In the first type of batch mode process, several mandrels containing the braided preforms are stacked side-by-side in a mold cavity and then the preforms are cut and folded into the desired frame geometry. In the second batch mode process, the mandrels containing the braided preforms are placed into individual mold cavities followed by the cutting and folding. The second method was chosen because the batch size is adjustable for any production requirement without tooling modifications and dimension stability can be accurately controlled with individual mold cavities. In addition, the second process requires fewer mandrels and the braided preform is more accessible which is advantageous during preform assembly.

### **1.C.4 Process Automation**

To maximize the effectiveness of the RTM and braiding operations, automation concepts must be employed for high production rates. Careful selection must be made to ensure that the selected concepts minimize the sensitivity to frame design changes. One of the main limitations of the braiding operation that needs to be overcome is the machine material capacity. Currently, a 144 carrier braider contains spools that are designed to carry less than 0.3 pound of graphite fiber. A fully loaded braider operating at a high speed (4 ft/min) must be reloaded in approximately two hours. To minimize reloading time, future spool sizes should be designed to store 2-3 pounds of graphite. Another requirement of the automation process is that handling should be kept to a minimum in order reduce inspection.

### **1.C.5 Dimensional Stability**

Dimensional stability of the circumferential hoop frames is critical because the crown panel design involves the assembly of large stiff fuselage structures. Large panel structures must be spliced together, therefore tight tolerances must be achieved on each structural component to minimize assembly problems. In addition to panel splices, the assembly of the crown panel design involves co-bonding precured structural components to uncured components and dimensional stability is extremely important in this type of operation. In addition to assembly concerns, dimensional stability is required to avoid problems with residual stresses.

As previously mentioned, the dimensional stability and accuracy of the frames are critical to the success of the skin/stringer/frame assembly. Two dimensions that influence the performance of the bond line are the

122 inch radius of the frame and the bottom flange-to-web perpendicularity. The frame bottom flange radius must be accurate to minimize the gap that may occur due to tolerance build-up at the skin/stringer/frame intersection. The tolerances of the flange radius must be controlled by proper tool design and optimization of the RTM processing parameters. The spring-in condition of the flanges must be compensated by the proper tool design.

## **2. BRAIDED/RTM TECHNOLOGY DEVELOPMENT**

The original goals of the Technology Development Phase were: 1) to acquire an understanding of the state-of-the-art in braided composite technology, 2) to conduct a general screening of braided composites, and 3) to identify potential applications (such as shear clips, shear ties, or stringers) for braided composites in a large commercial transport fuselage. Shortly after this Phase started, the ATCAS DBT identified braided composites as a potential cost-effective material system for primary fuselage structures. It was also discovered that braided composite technology had not progressed to the point where braided composites could be designed into an aircraft fuselage. The Technology Development Phase then refocused its overall goal to advance the state-of-the-art in braided composite technology and build a confidence level to support the design efforts of the baseline fuselage concepts containing textile composites. The four main areas of focus of this Phase were refocused to the following: 1) Braided Composite Material Systems, 2) Manufacturing of Braided Composites, 3) Textile Composite Analysis, and 4) Mechanical Characterization of Braided Composites.

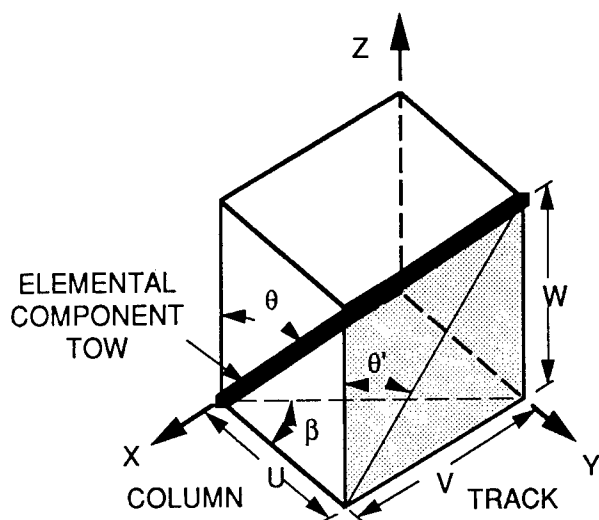
### **A. Braided Composite Material Systems**

#### **2.A.1 Material Selection**

Two material systems were investigated in the Technology Development Phase, a graphite/thermoplastic material system and a graphite/RTM resin material system. The graphite/thermoplastic material system chosen for this study was AS4/PEEK. The preform material used in this system was a commingled AS4/PEEK hybrid yarn; the graphite contained in this yarn was an AS4 3K fiber tow and the grade of PEEK was 150G. The graphite/RTM resin material system chosen was AS4/DPL-862; the preform material used in this system was an AS4 3K fiber tow and the resin system was Shell's DPL-862 and curing agent "W". This resin system was chosen for its cost (\$2.65/lb) and its manufacturability (viscosity profile suitable for RTM).

#### **2.A.2 Fiber Architectures/Braiding Techniques**

Two types of fiber architectures were investigated in the Technology Development Phase. The first fiber architecture was a fully braided architecture (100% braided tows) and the second architecture consisted of a triaxial braid in which longitudinal tows were in-laid among the bias tows. The fiber architectures were optimized for axial loading and shear loading [4]. The optimization process consisted of a combination of analytical parametric studies and the knowledge of braided preform manufacturing envelopes. The fiber architecture that was optimized for axial loading consisted of a triaxial braided structure containing 60% braided tows at a braid angle of  $20^\circ$  with 40% longitudinal tows; this fiber architecture is referred to as Architecture A. The fiber architecture that was optimized for shear loading consisted of a fully braided structure containing 100% braided tows at a braid angle of  $35^\circ$ ; this fiber architecture is referred to as Architecture B. A summary of the set-up variables for preform fabrication, the unit cell (fundamental repeated building block of a braided fiber architecture shown in Figure 6) characteristics of the architectures, and the preform characteristics of the architectures are found in Tables 1 and 2.



U = thickness  
V = width  
W = height

$\theta'$  = predetermined surface angle  
 $\theta$  = through the thickness angle  
 $\beta$  = azimuthal angle

Braiding Ratio:

$$K = \frac{V}{U} = \frac{\text{track move}}{\text{column move}}$$

Figure 6: Unit Cell of 3-D Braided Preform

FIBER ARCHITECTURES	A	B
<b>Manufacturing Set-up</b>		
Braided Tow Size	3K	3K
Longitudinal Tow Size	3K	NA
Number of Braiding Carriers	144	144
Number of Fixed Carriers	48	NA
Mandrel Diameter (inches)	0.96	0.96
<b>Unit Cell Characteristics</b>		
Width of Unit Cell (inches)	0.021	0.021
Length of Unit Cell (inches)	0.057	0.030
Thickness of Unit Cell (inches)	0.026	0.019
Surface Area of Unit Cell (inches**2)	1.20e-3	0.63e-3
Yarn Spacing on First Ply (inches)	0.039	0.034
Full Coverage Architecture (yes/no)	YES	YES
Amount of Spacing/Compaction (inches)	0.021	0.026
<b>Preform Characteristics</b>		
Number of Plies (inches)	5	7
Braiding Angle	20°	35°
Percentage of Braided Tows	61.5%	100.0%
Percentage of Longitudinal Tows	38.5%	0.00%
Thickness of Inner Ply (inches)	0.026	0.019
Thickness of Outer Ply (inches)	0.025	0.018
Total Thickness of Preform (inches)	0.129	0.127
Vf of Preform (%)	57.9	57.2

Table 1: Characteristics of the 2-D Braided Preforms

	TYPE 1	TYPE 2
<b>FIBER ARCHITECTURE A</b>		
Braiding Ratio	1.43	1.00
Width of Unit Cell (inches)	0.056	0.048
Length of Unit Cell (inches)	0.156	0.134
Thickness of Unit Cell (inches)	0.042	0.050
Surface Area of Unit Cell (inches**2)	8.74e-3	6.43e-3
Length of Bias Tow in Unit Cell (inches)	0.171	0.151
Through-the-Thickness Angle (degrees)	24.0	27.2
Azimuthal Angle (degrees)	35.0	45.0
<b>FIBER ARCHITECTURE B</b>		
Braiding Ratio	1.43	1.00
Width of Unit Cell (inches)	0.047	0.042
Length of Unit Cell (inches)	0.069	0.060
Thickness of Unit Cell (inches)	0.036	0.043
Surface Area of Unit Cell (inches**2)	3.24e-3	2.52e-3
Length of Bias Tow in Unit Cell (inches)	0.091	0.085
Through-the-Thickness Angle (degrees)	40.5	44.7
Azimuthal Angle (degrees)	35.0	45.0

**Specimen Type 1:** Tension, Open-Hole Tension, Compression, Bearing, CAI, Out-of-Plane Tension

**Specimen Type 2:** In-Plane Shear, Out-of-Plane Shear

**Table 2: Characteristics of the 3-D Braided Preforms**

In addition to investigating different fiber architectures, two preform fabrication techniques were investigated: 2-D braiding and 3-D braiding. All preforms used in the Technology Development Phase were manufactured to net shape. The 2-D braided materials employed for this study were formed by laminating several layers of braided fabric. The fabrics were formed with a 144 carrier braider incorporating 48 longitudinal yarns for the triaxial construction. The braids were formed on cylindrical mandrels, cut to the desired length, and stacked to achieve the desired thickness. The 3-D braiding process achieved a 3-D fully integrated fiber structure. Fibers were loaded on yarn carriers mounted on a Cartesian braiding bed. Each carrier moved in a predetermined path about the bed resulting in continuously interlaced fiber structures with no weak ply interfaces (i.e. a solid part with no layers was obtained). It is noted that the preforms contained a copper-coated graphite tracer tow. All preforms for the Technology Development Phase of the ATCAS Textile Composites Program were designed and fabricated at the Fibrous Materials Research Center at Drexel University.

## **B. Manufacturing of Braided Composites**

### **2.B.1 Fabrication of Braided Composite Specimens**

The overall manufacturing goal of the Technology Development Phase of the ATCAS Textile Composites Program was to develop a consolidation process and RTM process that consistently produced high quality braided composite test specimens. The processing challenge using the commingled AS4/PEEK material system was to achieve complete uniform wet-out of a preform made with commingled yarns. The

processing challenge of the RTM fabrication technique was to uniformly move resin through a highly interlaced structure with a high fiber volume fraction (60%). The approach taken to overcome these challenges and the optimized processing cycles is described in Reference 4.

### **2.B.2 Quality Control Procedures**

The quality of the braided composite test specimens was evaluated via both destructive and non-destructive evaluation (NDE) techniques. The destructive techniques included photomicrographs and resin digestion tests; the NDE techniques included X-rays, coordinate measurements, and C-scans.

Photomicrographs were used to determine the extent of specimen wet-out, the distribution of tows throughout the composite, the percentage of longitudinal fibers in a cross-section, and the extent of fiber damage due to processing. Photomicrographs were extremely helpful in understanding the physical representation of the internal fiber architectures of the specimens. Resin digestion tests were performed (in accordance with ASTM D3171-76 [5]) to determine specimen void content and fiber volume fraction. Results from the resin digestion tests are discussed in Section 2.D. It is observed from these tests that the measured fiber volume fraction was  $60\% \pm 9\%$ .

X-rays were performed to evaluate the braid angle tolerances of the braiding process and to observe the effect of processing on the internal fiber architecture of the braided composite specimens. Measurement of the apparent braid angle from the surface of each specimen preform showed some variation between coupons and within a single coupon. Both style braids showed large variations between coupons and in some cases within individual coupons; the average braid angles varied as much as  $\pm 5.0^\circ$ . Coordinate measurements were made after fabrication to evaluate the dimensional stability of the braided composites. Dimensional stability of the RTM composite specimens was much higher than the PEEK specimens. The tolerances on the thickness of the RTM specimens were held to  $\pm 0.005$  inches as compared with  $\pm 0.025$  inches for the PEEK specimens. C-scans were performed on the braided composite specimens for NDE characterization. Ultrasonic inspection of the braided specimens generally followed conventional procedures used with laminated materials but with reduced gain. This was necessary due to the basic character of braided materials where the crossover points of the yarns in the fiber architecture are dominated by fiber properties in the thickness direction, and the open portion of the mesh is practically pure resin [6]. There is a nearly a 10 to 1 attenuation difference between these two areas on the C-scan output, causing a distinct picture of the braid pattern to be drawn during panel canning. As a result of these differences, C-scans are currently of marginal value in the NDE of braided composites; work to overcome the C-scan limitations is underway in the ATCAS Program.

Overall, the quality of the braided coupons was adequate for this initial mechanical characterization. It is expected that the first few batches of any new material will see large physical variations as methods for processing and manufacturing are developed and refined. All of the problems identified above were eliminated with manufacturing experience during the ATCAS Program; these details are discussed in the Circumferential Hoop Frame Development section of this paper.

## **C. ATCAS Textile Composites Analysis (TECA)**

The ATCAS Textile Composites Analysis (TECA) Model was developed to support the Technology Development and Direct Application Phases of the ATCAS Textile Composites Program. In general, TECA predicts the stiffnesses and strengths of both 2-D and 3-D braided composites under a variety of loading conditions. TECA produces a detailed description of the unit cell geometry for braided composites. The model is capable of performing analysis for a wide variety of loading conditions including: in-plane tension, in-plane compression, in-plane and transverse shear, bending, twisting, and hygrothermal loading. The model can predict the composite moduli (taking into account fiber bending and waviness), composite

Poisson's ratios, and composite coefficients of thermal expansion. TECA is also capable of producing material cards for finite element models in which complex shapes can be represented. And finally, the failure criterion contained in TECA can predict the history of failure in a braided composite. The five modules that are listed in the following section are complete. Correlation between experimental results and predicted values from TECA is ongoing; upon completion of the correlation studies, TECA will be documented in detail. The following sections describe the general content of TECA.

## 2.C.1 Model Modules

### 2.C.1.a FIBER ARCHITECTURE GEOMETRY MODULE

The analysis of textile composite structures requires the knowledge of the internal fiber architecture of the structures. The overall purpose of the Fiber Architecture Geometry Module is to produce a detailed physical representation of the fiber architecture in a braided composite structure. The types of architectures that can be represented by this module include 2-D braids, 2-D triaxial braids, 3-D braids, and woven fabrics.

The main assumption contained in this module is that one can assume that the internal fiber architecture of a braided structure can be represented by a series of repeating building blocks called unit cells. A unit cell is comprised of elemental component tows representing the braided and in-laid longitudinal tows; the physical properties of the unit cell are dependent on the manufacturing set-up and the tow characteristics. The input variables and output parameters for both 2-D and 3-D braided structures are listed in Table 3.

2-D BRAIDED ARCHITECTURE	3-D BRAIDED ARCHITECTURE
<b>INPUT:</b> <ul style="list-style-type: none"> <li>Loom Set-up <ul style="list-style-type: none"> <li>Machine Size</li> <li>Number of Carriers</li> <li>Number of Tows per Carrier</li> <li>Mandrel Size</li> <li>Braiding Ratio</li> </ul> </li> <li>Tow Characteristics <ul style="list-style-type: none"> <li>Fiber Area</li> </ul> </li> <li>Preform Characteristics <ul style="list-style-type: none"> <li>Desired Fiber Volume Fraction</li> <li>Desired Cross-Sectional Area</li> <li>Desired Braiding Angle</li> </ul> </li> </ul>	<b>INPUT:</b> <ul style="list-style-type: none"> <li>Loom Set-up <ul style="list-style-type: none"> <li>Machine Size &amp; Shape</li> <li>Number of Carriers</li> <li>Number of Tows per Carrier</li> <li>Braiding Ratio</li> </ul> </li> <li>Tow Characteristics <ul style="list-style-type: none"> <li>Fiber Area</li> </ul> </li> <li>Preform Characteristics <ul style="list-style-type: none"> <li>Desired Fiber Volume Fraction</li> <li>Desired Cross-Sectional Area</li> <li>Desired Braiding Angle</li> </ul> </li> </ul>
<b>OUTPUT:</b> <ul style="list-style-type: none"> <li>Unit Cell Dimensions</li> <li>Degree of Coverage</li> <li>Percentage of Braided Tows</li> <li>Percentage of Longitudinal Tows</li> <li>Thickness per Ply</li> <li>Final Fiber Volume Fraction</li> <li>Number of Unit Cells within a Structure</li> </ul>	<b>OUTPUT:</b> <ul style="list-style-type: none"> <li>Unit Cell Dimensions</li> <li>Angles within a Unit Cell</li> <li>Percentage of Braided Tows</li> <li>Percentage of Longitudinal Tows</li> <li>Final Fiber Volume Fraction</li> <li>Number of Unit Cells within a Structure</li> </ul>

**Table 3: Input and Output Parameters for the Preform Architecture Module**

### **2.C.1.b ELASTIC RELATIONSHIPS MODULE**

The overall objective of this module is to predict the effective elastic constants or nonlinear constitutive relationships of textile preforms for structural analysis. Non-linear response mechanisms such as shear deformation of the preform, matrix properties, and the effect of matrix cracking are taken into consideration when determining the nonlinear constitutive relationships.

The global stiffness matrix of a braided structure is calculated through the following steps: 1) the stiffness matrix for each elemental component tow is calculated through micromechanics relationships, 2) the local stiffness matrices of the elemental component tows are transformed in space to fit the composite axes, and 3) a volume averaging approach is applied to determine the global stiffnesses [7].

Stiffness modifications were introduced into the model to account for fiber bending because a tow experiences waviness around areas of interlacing and turn-around points as it traverses through a preform. The stiffnesses were modified by an elastic strain energy approach which uses beam elements to represent the bending behavior of a braided tow [4]. The total strain energy includes the strain energy due to bending and extension of the beam elements, and compression in the region of contact in tow cross-over areas.

### **2.C.1.c STRESS ANALYSIS MODULE**

Since most engineering problems are set-up for plate or shell analysis, properties are required in a form compatible with this type of analysis. The third module of TECA performs the necessary analysis utilizing the 3-D stiffness matrix determined in the previous module. First, a plane stress condition is applied (via static condensation) to the 3-D stiffness matrix. Next, integration is performed to obtain the extensional and bending stiffness matrices. Following this step, the stress field in the composite can be calculated using shear-deformable plate analysis or shell analysis.

### **2.C.1.d STRENGTH MODULE**

The overall objective of the Strength Module is to predict the history of failure of a textile composite from average stresses obtained from global structural analysis.

The Strength Module is set-up for a progressive failure analysis using the following sequence of steps: 1) the failure mechanism for the loading condition is identified, 2) the average and principal stresses and strains in the matrix are determined on a local level, 3) the matrix cracking criterion is applied via either an average stress or principal strain criterion (if matrix cracking is detected, the necessary adjustments are made to the local stress field and component stiffnesses), and 4) the failure criteria is applied via either a maximum stress or maximum strain criteria.

## **2.C.2 Support of Technology Development Activities**

The capabilities of TECA were utilized in a variety of ways in the Technology Development Phase. These roles were: fiber architecture optimization, parametric studies, material cards for finite element modelling, efficient material characterization, failure mechanism prediction, and insight to potential problem areas.

Braid pattern optimization studies were performed using TECA to aid in the development of the mechanical characterization test matrix. The analysis provided the necessary insight to which fiber architectures would be optimum for shear and axial loading [4].

TECA was also used to perform parametric studies to study the mechanical response of a wide range of fiber architectures. The model was used to relate the following: 1) composite strengths as a function of braiding angle, 2) composite moduli as a function of braiding angle, 3) the unit cell physical dimensions as a function of braiding angle and braiding ratio, 4) the coefficients of thermal expansion as a function of the unit cell geometry, and 5) design envelopes to aid designers in choosing a fiber architecture for a given ratio of in-plane to out-of-plane loading. Some of the parametric studies performed with TECA are contained in Reference 5.



TECA was also used as a tool for creating material cards for finite element modeling of braided composite tests specimens; one example of this application was the modeling of the Iosipescu test specimen [4]. TECA was also used to reduce mechanical testing and enhance data evaluation. Predicted values from TECA are currently being correlated with experimental results. If data points can successfully be correlated over a wide range of fiber architectures, TECA will be used to produce reliable predictions between correlated data points.

## D. Mechanical Characterization of Braided Composites

### 2.D.1 Objective and Test Program Issues

The overall objective of the braided composite material characterization study during the Technology Development Phase was to provide a data base of mechanical properties for development of an analytical model (TECA) and evaluation of potential applications of braided composites. Some of the more specific issues that were addressed during this study include: 1) the selection of appropriate testing procedures, 2) braided composite specimen design, 3) characterization of the mechanical response and possible failure mechanisms of braided composite material systems, 4) the effect of different fiber architectures on mechanical behavior, and 5) a comparison between the mechanical properties of braided composite systems and laminated composites (this quantified the advantages in out-of-plane strength and damage tolerance of braided composites and determined at what cost to in-plane properties these enhancements were achieved). The mechanical testing is being performed via a cooperative effort between Boeing Helicopters and the NASA Langley Research Center.

### 2.D.2 Test Matrix Identification

The test matrix assembled for the Technology Development Phase is shown in Table 4. This 114 specimen test matrix was designed to obtain a variety of data necessary for a preliminary material characterization study. The Technology Development Test Matrix was used to obtain data for braided composites consisting of two different preforms (2-D and 3-D), two different braided fiber architectures (Architectures A & B), and two different resin systems (thermoplastic - PEEK and RTM epoxy - DPL-862).

TYPE OF TEST	2-D BRAIDED SPECIMENS				3-D BRAIDED SPECIMENS			
	A		B		A		B	
	PEEK	RTM	PEEK	RTM	PEEK	RTM	PEEK	RTM
UNNOTCHED TENSION	3	6	3		3		3	3
OPEN HOLE TENSION	3	5	3		3		3	3
UNNOTCHED COMPRESSION	3	5	3		3		3	3
COMPRESSION AFTER IMPACT	3				3			
IN-PLANE SHEAR			3				3	
TRANSVERSE SHEAR			3	3			3	3
TRANSVERSE TENSION				3				5
BEARING	3	6	3		3		3	3
<b>TOTALS</b>	<b>15</b>	<b>22</b>	<b>18</b>	<b>6</b>	<b>15</b>	<b>0</b>	<b>18</b>	<b>20</b>

#### NOTES:

A - BRAIDING GEOMETRY OPTIMIZED FOR END LOAD [60% BRAIDED AT 20 DEGREES, 40% 0 DEGREES]

B - BRAIDING GEOMETRY OPTIMIZED FOR SHEAR [100% BRAIDED AT 35 DEGREES]

**Table 4: Braided Composite Technology Development Test Matrix**

In addition to the braided composite Technology Development Test Matrix, an additional test matrix was developed to directly compare the performance of braided composites with tape laminates composites. The properties that will be directly compared include: tensile strength and modulus, compression strength and modulus, in-plane shear, open-hole tension, CAI strength, and bearing strength. The lay-ups of the laminated specimens were designed to be as close as possible to the braided fiber architectures. The lay-up to simulate Architecture A was [+45/-45/0/+45/-45/0<sub>2</sub>]<sub>5S</sub> while the lay-up to simulate Architecture B was [+35/-35]<sub>17S</sub>. The material system contained in the laminated test matrix is AS4/PEEK. The testing of the specimens contained in this test matrix is currently being performed.

### 2.D.3 Specimen Configurations and Design

The unnotched tension, open-hole tension, and unnotched compression specimens were 10.00 inches long, 1.50 inches wide, and had a nominal thickness of 0.125 inches; the open-hole tension specimens had 0.25 inch diameter holes drilled through their centers. The CAI specimens were 5.00 inches long, 3.00 inches wide, and had a nominal thickness of 0.25 inches. The end edges of the specimens were ground to ensure that they were parallel prior to testing. The Iosipescu shear specimens varied in size; the length of all specimens was 3.00 inches, while the height of the specimens ranged from 0.50 to 0.75 inches and the thicknesses varied from 0.10 inches to 0.50 inches. The top and bottom surfaces (along the 3.00 inch length) of the Iosipescu specimens were also ground prior to testing to ensure dimensional accuracy. The bearing specimens were 3.50 inches long, 1.50 inches wide, and had a nominal thickness of 0.125 inches. Two 0.25 inch diameter holes were drilled through the center of the longitudinal axis 2.00 inches apart. The fasteners included 0.50 inch diameter washers which were required to perform clamp-up condition bearing tests. The specimens contained two failure sites to obtain a lower bound on the bearing strengths. The flange bending specimen was L-shaped with leg dimensions of 4.00 inches and 2.00 inches. The two critical parameters in this test method are the radius and thickness of the specimen which were 0.25 inches and 0.50 inches respectively. In order to properly design this specimen, the bending strength, in-plane strengths, and out-of-plane strength of the material must be known. At the time of test matrix identification and specimen design, these properties were not known, so the specimen configuration previously used at Boeing Helicopters with tape laminates was utilized. The procedure for future design of a flange bending specimen is outlined below:

The criterion for out-of-plane tension failure to occur before in-plane failure is:

$$\frac{\sigma_z}{\sigma_z^U} \geq \frac{\sigma_\theta}{\sigma_\theta^U} \quad (2)$$

where  $\sigma_z$  = through-the-thickness stress  
 $\sigma_z^U$  = through-the-thickness strength  
 $\sigma_\theta$  = circumferential stress  
 $\sigma_\theta^U$  = lower of in-plane compression and tension strength

Using the following isotropic relationships:

$$\sigma_z = \frac{3 M}{2 R t} \quad \sigma_\theta = \frac{6 M}{t^2} \quad (3)$$

where M = applied moment  
R = inner radius  
t = specimen thickness

Substituting (3) into (2) gives the following criterion :

$$\sigma_z^U \leq \sigma_\theta^U \left[ \frac{t}{4R} \right] \quad (4)$$

#### 2.D.4 Coupon Testing Procedures/Methods

All testing was performed on room temperature-dry specimens. All specimens were tested in a 50 kip MTS testing machine and ramped to failure using a constant cross-head deflection rate of 0.01 inches per minute. Failure strains and axial modulus measurements were made using strain gages and/or an extensometer. Poisson's ratio measurements were made with strain gages.

The unnotched tension and open-hole tension specimens were tested in accordance with ASTM D3039-76 [6]. The unnotched compression specimens were tested in the Boeing compression test fixture; the test fixture and method are described in detail in the Boeing Specification Support Standard BSS 7260. The compression after impact specimens were tested in the Boeing CAI compression test fixture (BSS 7260). The test specimens were first impacted at 1500 in-lbs/in with a hemispherical 0.5 inch diameter tup using a drop-weight impact testing machine and then compression loaded to failure in the test fixture. Although the specimens were impacted at 1500 in-lb/in (the Boeing specification) and the Boeing CAI test fixture was used, the specimen size was not the same as what is required in BSS 7260. The dimensions were different from the Boeing specification because the 3-D CAI specimen could not be made 4.00 inches wide at the FMRC at Drexel University. The Iosipescu shear specimen was used to test both the in-plane and out-of-plane shear specimens. The Iosipescu shear test method and test fixture are described in Reference 8; the test configuration is shown in Figure 7. A flange bending test procedure was used to conduct the testing of the out-of-plane tension specimens. One leg of radius bend specimen was securely clamped while a force was applied to the other leg creating a moment, and thus out-of-plane tension stresses, in the radius of the specimen. The flange bending test configuration is shown in Figure 7. The bearing specimens were tested in a double shear test configuration (Figure 7). The double shear test configuration was chosen because the test applies uniform bearing loads across the specimen.

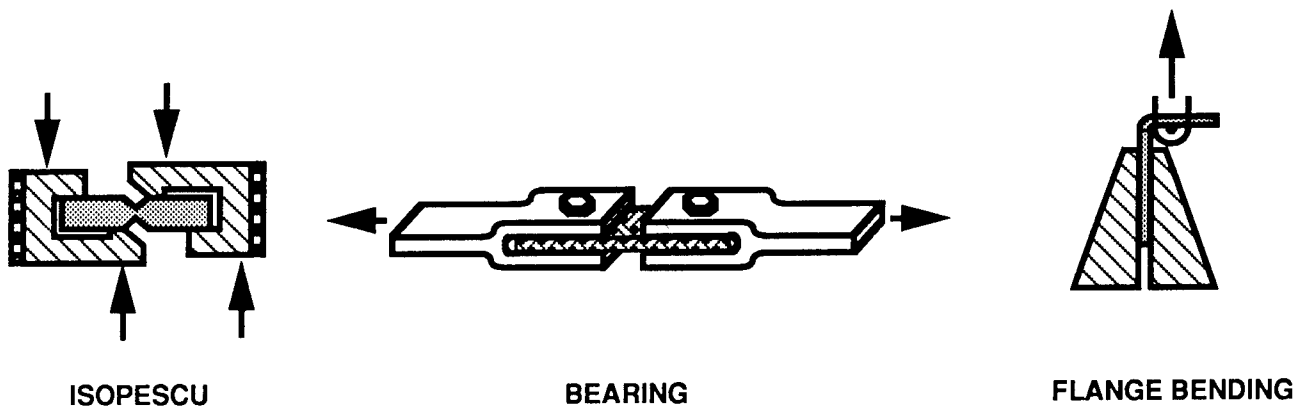


Figure 7: Braided Composite Test Specimen Configurations

#### 2.D.5 Test Instrumentation, Results , and Discussion

##### 2.D.5.a TENSION

Unnotched tension tests were performed to supply strength, modulus, Poisson's ratio, and possible failure mechanisms for the various fiber architectures tested. The specimens had (0/90) 3/16-inch long by 1/8-inch wide strain gages bonded at their mid-length. Because of the surface texture of the braided specimens,

there was an initial concern as to the accuracy of the strain gage measurements. If the gage lengths are of the same dimensional scale as the unit cell size of the braided composite, the gages may measure local variations depending on whether the gages are placed over a fiber or resin pocket. In the Technology Development Test Matrix, use of large gage sizes (as compared to the unit cell dimensions and area) were employed to ensure that the strain gage measurements averaged-out these local differences. A comparison of strain gage sizes versus unit cell dimensions for the tension tests is shown in Table 5. An extensometer was also used to measure moduli and to determine whether or not the strain gages used were sufficiently larger than the dimensions of the unit cell.

Specimen Type/Direction	Unit Cell Direction Along Gage Length (Inches)	Ratio of Gage Length to Unit Cell Dimension (Inches)
2D-A Longitudinal	0.057	3.3
2D-A Transverse	0.021	6.0
2D-B Longitudinal	0.030	6.3
2D-B Transverse	0.021	6.0
3D-A Longitudinal	0.156	1.2
3D-A Transverse	0.056	2.2
3D-B Longitudinal	0.069	2.7
3D-B Transverse	0.047	2.7

**Table 5: Strain Gage Size versus Specimen Unit Cell Size**

Results of the tension tests and average specimen fiber volume fraction and void content are summarized in Table 6. The triaxially braided architecture (Architecture A) exhibited higher tensile strength and modulus than the fully braided architecture (Architecture B) in both the 2-D and 3-D braided material systems as expected. It was observed that the in-plane tensile properties of the 3-D braided composites were significantly degraded compared with the properties of the 2-D braided composites. A summary of the reduction of in-plane tensile properties is given in Table 7. The one exception to the property degradation was the tensile modulus of the 3-D fully braided specimens which was actually 3% larger than the 2-D fully braided specimens. Moduli obtained from the strain gages and extensometer showed no significant differences in measured values indicating that the size of the strain gages was adequate; all modulus results reported in this study were calculated using a Least Squares Fit of the stress versus strain curve up to 2000 microstrain. The strain-to-failure and Poisson's ratio of Architecture B were larger than that of Architecture A due to the higher braid angle and absence of zero degree reinforcement; the Poisson's ratios were evaluated at 2000 micro strain and calculated using a secant and tangent method. The Poisson's ratio of the composites containing the DPL-862 RTM epoxy were higher than the thermoplastic braided composites. Both the 2-D and 3-D braided composites experienced high initial Poisson's ratios. The values of Poisson's ratios for the 2-D architectures ranged from 0.43 to 0.92, and the 3-D architectures ranged from 0.5 to 1.00. In general, the Poisson's ratios of braided composites, especially 3-D braided composites, tends to be higher than traditional laminated composites. It was also observed that there was a great variance in the Poisson's ratio during a test.

Specimen Type	Strength (psi)	Failure Strain ( $\mu$ Strain)	Strain Gage Modulus (Msi)	Extensometer Modulus (Msi)	Poisson Ratio (Tan/Sec )	Ave. Vf (%)	Ave. Void Content (%)
2D-A PEEK	137,900	10,300	12.96	12.61	0.562/0.533	66.3	4.1
2D-B PEEK	53,600	16,000	5.81		0.654/0.644	58.3	4.3
2D-A RTM	106,200	8,600	11.81	10.17	0.920/0.904	55.6	0.2
3D-A PEEK	109,600	9,700	10.48	10.07	0.488/0.483	59.8	3.3
3D-B PEEK	43,700	11,700	5.97		0.435/0.429	58.9	4.9
3D-B RTM	77,800	11,100	7.72	6.87	0.765/0.752	61.9	3.4

**Table 6: Braided Composite Axial Tension Test Results**

Architecture	Property	Percent of 2-D Property
Architecture A	Tensile Strength	- 20%
	Tensile Modulus	- 19%
	Compression Strength	- 10%
	Compression Modulus	- 17%
Architecture B	Tensile Strength	- 18%
	Tensile Modulus	+ 3%
	Compression Strength	- 18%
	Compression Modulus	+ 34%

**Table 7: In-Plane Properties Reduction of 3-D versus 2-D Braided Composites**

The failure surface of the braided tensile specimens was a saw-tooth pattern that propagated across the width of the specimen along a line whose shape was dependent on the length of the unit cell. The failure mechanism of the fully braided composites was a shear-out mechanism that occurred along tow boundaries. The history of failure occurred across the specimens in the following repeating sequence: 1) braided tow failure, 2) cracks forming at the broken tow boundary and propagating until a braided cross-over point, 3) failure of an intersecting tow at the cross-over point, 4) cracks forming at the intersecting broken tow boundary and propagating until the next braided cross-over point. This failure sequence was responsible for the saw-tooth pattern of the failure surface. The failure mechanism of the triaxially braided composites started with longitudinal tow failure, followed by load redistribution into the braided tows, followed by the shear-out failure just described. The failure surface of the specimens with a small unit cell length (2-D Type A and B, and 3-D Type B) propagated straight across the width of the specimens. The failure surface of the specimens with a larger unit cell length (3-D Type A) propagated diagonally across the specimen width because the cracks could propagate further along broken tows to braided cross-over points. The failure path of the AS4/DPL-862 braided composites that contained resin rich areas along the specimen

edges propagated towards these weaker areas. The saw-tooth failure pattern was also observed through-the-thickness of both the 2-D and 3-D braided composite specimens. The reason that this pattern and shear-out failure mechanism was observed through-the-thickness in the 2-D specimens was the tight nesting of fibers between braided layers.

#### 2.D.5.b Open-Hole Tension

Open-hole tension tests were performed to supply strength, modulus, and failure mechanisms for the braided fiber architectures in this study. The specimens had a 3/16-inch long by 1/8-inch wide axial strain gage bonded 1.5 inches above the center of the 0.25 inch diameter hole.

Results of the open-hole tension tests and average specimen fiber volume fraction and void content are summarized in Table 8. The ultimate strength and modulus comparisons between the different fiber architectures and material system used in the study are similar to those discussed in the unnotched tension section. Test results show that the triaxially braided architecture was more notch sensitive than the fully braided architecture; this is due to the higher stress concentration of this architecture (see Table 8) and the higher strain energy release rate. Results also show that the AS4/DPL-862 epoxy material system is more notch sensitive than the AS4/PEEK thermoplastic material system; this is due to the brittle nature of the epoxy. It was also observed from the data that the 3-D braided specimens possessed a much lower notch sensitivity than the 2-D braided specimens of the same architecture. This is not due to the assumption that braided composites lower the stress concentration around a cut-out, but due to the fact that both 2-D and 3-D braided composites offer more restraint to crack propagation once local failure initiates at the edge of the hole; 3-D braided composites resist crack propagation more than the 2-D braided composites because of more fiber interlacing.

Specimen Number	Strength (psi)	Failure Strain ( $\mu$ Strain)	Strain Gage Modulus (Msi)	Percentage of Unnotched (%)	Average Vf (%)	Ave. Void Content (%)	Stress Concentration Factor
2D-A PEEK	81,700	5,600	14.61	59.3	62.1	2.2	4.60
2D-B PEEK	41,800	11,100	4.91	78.0	55.9	4.3	2.52
2D-A RTM	73,300	5,300	13.64	69.0	55.5	0.3	4.60
3D-A PEEK	67,800	5,300	13.06	73.7	60.0	3.0	4.60
3D-B PEEK	42,200	6,400	7.27	96.6	60.2	4.5	2.52
3D-B RTM	57,000	11,400	6.33	74.3	59.7	0.8	2.37

**Table 8: Braided Composite Open-Hole Tension Test Results**

The failure surface pattern of the open-hole tension specimens was the same as the failure surface pattern of the unnotched tension specimens. Failure of the open-hole specimens progressed as follows: 1) the moduli started to drop at the vicinity of the hole (plastic deformation in fully braided composites, or local tow failure in triaxial composites), 2) the local load redistributes away from the hole, followed by 3) the same failure mechanisms that were discussed in the unnotched tension section then occur.

### 2.D.5.c Compression

Unnotched compression test results were performed to supply strength, modulus, and failure mechanisms for the various fiber architectures tested. The specimens had a single axial gage bonded at their mid-length that was the same size as the gages used in the axial tension tests.

A summary of the results obtained from the compression tests along with the average specimen fiber volume fraction and void content are summarized in Table 9. The compression strength and modulus of Architecture A were much higher than that of Architecture B as expected. Similar to the in-plane tension properties, the in-plane compression properties of the 3-D braided specimens were lower than the 2-D braided specimens (Table 7). The compression strain-to-failure of Architecture B was higher than Architecture A due to the higher braid angle and absence of axial reinforcement.

Specimen Number	Strength (psi)	Failure Strain ( $\mu$ Strain)	Strain Gage Modulus (Msi)	Average Vf (%)	Ave. Void Content (%)
2-A PEEK	69,500	5,300	14.58	58.7	3.4
2-B PEEK	37,200	6,000	6.72	57.8	5.5
2-A RTM	36,300	3,400	10.90	51.4	0.3
3-A PEEK	62,300	5,600	12.04	60.9	5.1
3-B PEEK	31,400	5,600	8.99	58.7	5.5
3-B RTM	20,900	3,200	6.55	63.5	2.1

**Table 9: Braided Composite Unnotched Compression Test Results**

The failure surface of the braided compression specimens was a saw-tooth pattern that propagated straight across the width of the specimens. The failure mechanism of the fully braided composites was a shear-breakage mechanism that occurred along tow boundaries. The history of failure occurred across the specimens in the following repeated sequence: 1) braided tow waviness exerts stresses on surrounding matrix causing cracking along the tow boundary, 2) localized fiber-matrix debonding 3) the fiber tow fails due to compression and/or localized bending, 4) matrix crack propagates along broken tow boundary until a braided cross-over point, 5) failure of an intersecting tow at the cross-over point, and 6) cracks form at the intersection broken tow boundary and propagate until the next braided cross-over point. The failure mechanism of the triaxially braided composites occurred in the following sequence: 1) longitudinal fibers exert stresses on the surrounding matrix causing cracking, 2) localized fiber-matrix debonding, 3) fiber tow failure due to compression and/or localized bending, 4) load redistribution into the braided tows, and 5) the shear-breakage failure just described. The triaxially braided specimens did not exhibit the brooming failure observed in traditional laminates because the longitudinal tows are tightly nested within the architecture. The saw-tooth failure pattern was also observed through-the-thickness of both the 2-D and 3-D braided composite specimens. As with the 2-D braided tensile specimens, this shear failure mechanism was observed through-the-thickness because of the tight nesting of fiber tows between braided layers. The delaminations inherent to laminated composite compression specimens were not observed because of the nesting. The global delaminations and sub-laminate buckling that contribute to laminated composite

compression failure did not occur in the 2-D braided composites. Local delaminations in the 2-D braided composites did not propagate beyond the unit cell level.

#### 2.D.5.d Shear

Iosipescu shear tests were performed to measure the in-plane and out-of-plane shear stiffness and strength of the braided material systems.

The specimens had  $(0 \pm 45)$  1/16-inch long by 1/16-inch wide strain gages bonded in the test section back-to-back. Gages this size had to be used because of the dimensions of the Iosipescu shear specimen configuration. The gages were not larger than the characteristic dimensions of the unit cell for the Iosipescu test specimens and thus measured local variations depending on whether the gage was applied over a fiber or resin pocket. After analyzing strain gage data, it was concluded that an initial shear modulus is the only braided composite property that can be measured with the Iosipescu shear test. The technique of calculating initial modulus is itself questionable; it is obtained by averaging the readings of four strain gages ( $\pm 45^\circ$  gages on the front and back of the specimens); the in-plane and out-of-plane shear data is not included because of this uncertainty. The following characteristics of the Iosipescu shear test method make it unattractive for shear testing of braided composites: the specimen has a small test section which requires small gages which do not measure the degree of homogeneity that is desired, the specimen edges must be ground so they are perfectly parallel, the load path changes during loading in both the longitudinal and transverse directions, a stress gradient exists across the width (i.e. through-the-thickness effects) which is not taken into consideration, and coupling exists due to material anisotropy.

#### 2.D.5.e Out-of-Plane Tension

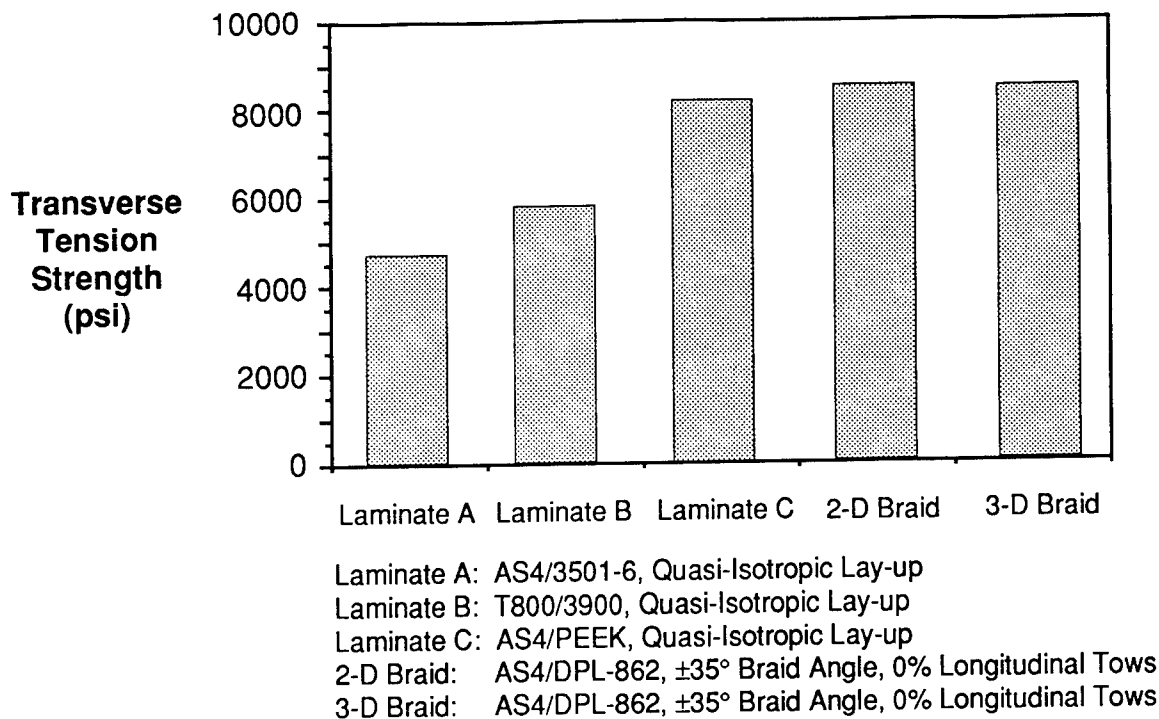
Flange bending tests were performed to measure the out-of-plane tension failure stresses and to observe failure mechanisms of the braided material systems.

A summary of the results from the out-of-plane tension tests is given in Table 10. The transverse strengths shown in the table were calculated using isotropic methods (equation 3); calculations using curved composite methods are currently being performed. The results show that both 2-D and 3-D braided material systems exceed the out-of-plane tension strengths of quasi-isotropic tape laminates; a comparison of the transverse tension strengths can be found in Figure 8. Justification for the high transverse tension strength in the 2-D braided specimens stems from the fact that the braided layers of the 2-D braided specimens are nested tightly together and do not have resin rich inter-ply planes through which cracks easily propagate. Some through-the-thickness reinforcement provided by the inter-ply nesting and fiber crimp also aided in the out-of-plane strength. The high percentage of through-the-thickness tows is justification for the high transverse tension strength in the 3-D braided specimens.

Specimen Number	Failure Load (lb)	Moment (in-lb)	Strength (psi)	Average V <sub>f</sub> (%)	Ave. Void Content (%)
2D-A RTM	720	690	8,450	64.1	0.6
3D-B RTM	600	718	> 8,610	64.1	1.9

**Table 10: Braided Composite Out-of-Plane Tension Test Results**





**Figure 8: Transverse Tension Strength Comparison of Braided and Laminated Composites**

The 2-D braided specimens failed in an out-of-plane tension failure mode. The first crack to appear in the 2-D braided specimens was a circumferential crack found between braided plies at a distance approximately 40% of the bend thickness measured from the inner radius; this is the location of maximum radial stress [9]. This crack propagated until the strain energy release rate dropped below the critical strain energy release rate needed to propagate the crack. Once crack propagation has stopped, the thickness can be viewed as two sub-laminates each having a peak stress. Theoretically the peak stress on the inner sub-laminate is greater than the peak stress of the outer [9]. Experimental results of this study contradict this theory because immediately following load redistribution, a second circumferential crack appeared in the middle of the outer sub-laminate. It is believed that the location of the second crack is dependent on the fiber architecture configuration and material anomalies (i.e. resin rich areas). Due to the nature of the manufacturing process used to fabricate the braided specimens, the fiber volume fraction is greater in the inner sub-laminate than the outer possibly explaining why the second crack appeared at this location in the specimens used in this study. The 3-D braided test specimens experienced in-plane failure due to bending and not an out-of-plane tension failure mode; this was due to the large amount of through-the-thickness fibers (and thus strength) in the specimens and the inadequate strength of the composite in the circumferential direction (i.e. equation 4 was violated). The 3-D out-of-plane tension specimens could not be designed properly due to the lack of braided composite material properties that were available at the time of specimen design. Failure of the 3-D braided specimens was in the form of transverse cracking along the inner radius of the bend.

#### *2.D.5.f Compression After Impact*

Damage size and post-impact strength were measured in compression-after-impact tests. CAI tests were performed on 2-D and 3-D triaxially AS4/PEEK braided specimens.

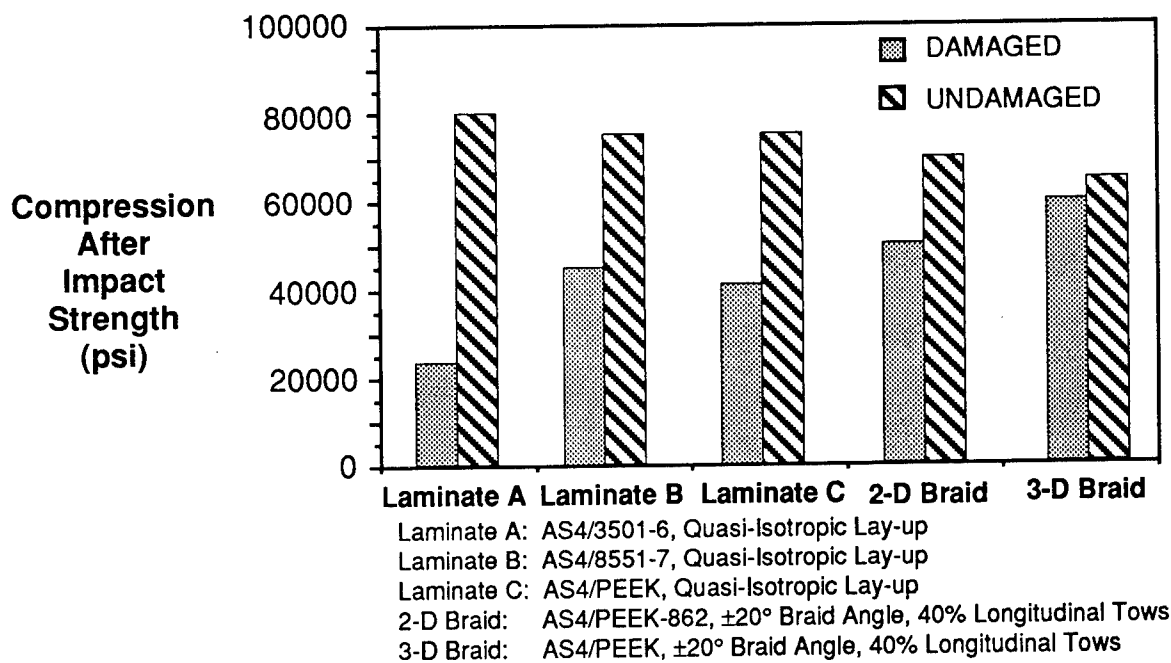
C-scans of the impacted specimens were performed to observe the shape and extent of damage. The shape of the damage area for both the 2-D and 3-D braided specimens were similar. All specimens possessed an elliptical damage area with extensive back-side fiber break-out damage; the fiber break-out damage was dome-shaped. The damage was elliptical due to the high axial stiffness of the specimens. The elliptical

damage area of the 2-D braided specimens extended to the clamped boundary conditions along the 5.00 inch length. The damage area of the 3-D braided specimens was not as severe as the 2-D braided specimens for the following reasons: 1) the through-the-thickness reinforcement and the tightly interlaced structure prevented crack propagation and delaminations, and 2) the reduced in-plane stiffness of the 3-D architecture reduced the peak impact force during impact.

A summary of the results obtained from the CAI tests along with the average specimen fiber volume fraction and void content are summarized in Table 11. The average CAI strength of the 2-D braided specimens was 49 ksi (~ 71% of the undamaged compression strength) while the average CAI strength of the 3-D braided specimens was 58 ksi (~ 92% of the undamaged compression strength). A comparison of CAI strengths between the braided material systems and three quasi-isotropic laminated tape material systems is shown in Figure 9.

Specimen Number	Strength (psi)	Percentage of Unnotched (%)	Average Vf (%)	Average Void Content (%)
2D-A PEEK	49,000	70.5	60.3	3.1
3D-A PEEK	57,700	92.6	61.2	3.9

**Table 11: Braided Composite Compression After Impact Test Results**



**Figure 9: CAI Strength Comparison of Braided and Laminated Composites**

The failure surface pattern of the CAI specimens was the same as the unnotched compression specimens. The curvature of the dome area and the small area of fiber breakage reduced the stiffness across the damage area causing some load to be redistributed into the undamaged region and thus increasing stresses around the damage site. Failure initiated in the damaged area of the specimens by a combination of the in-plane

stress concentration and localized bending moment in the fiber break-out dome area, although the bending deformation that occurred in the dome area contributed more to the initiation of failure than the stress concentration. Failure initiated on the inside (concave surface) of the dome because the compression and bending stresses are superimposed to give the maximum stresses in the damage area. Global failure of the CAI specimens occurred through a shear-breakage mechanism that occurred along tow boundaries. The complete failure mechanism of the CAI specimens was the same as the unnotched compression specimens previously discussed. The excellent performance of both the 2-D and 3-D braided specimens was caused by the interlaced structure which prevented both delamination and back fiber pull-out across the whole length of the specimen (i.e. the fibers are constrained from pulling free at the braid crossover points) as is the case with conventional laminates. Once again, local delaminations in the braided composites did not propagate beyond the unit cell level.

#### 2.D.5.g Bolt Bearing

Bearing tests were performed using a zero clamp-up condition to supply bearing strength data for the various fiber architectures.

A summary of results obtained from the bolt bearing tests is given in Table 12. The bearing strength of Architecture A was greater than that of Architecture B for all material systems tested. The low bearing strength of Architecture B was caused by the lack of longitudinal fibers. The bearing strength of the AS4/PEEK braided material systems was higher than the bearing strength of the AS4/DPL-862 braided material system; the lower compression strength of the RTM epoxy and areas of resin richness around the drilled holes are possibly accountable for the lower bearing strength. In comparing the 2-D and 3-D braided composites, the 3-D braided specimens exhibited a higher bearing strength than the 2-D braided specimens with the same fiber architecture; this was due to a larger percentage of fibers tangential to the fastener hole in the 3-D braided systems. Overall, the braided specimens tested during this study exhibited poor ultimate bearing strengths as compared to tape laminates; ultimate stresses ranged from 40 ksi to 65 ksi (compared 110 ksi for quasi-isotropic tape laminates). The poor performance of these specimens was caused by braided preform characteristics, fiber architecture, preform quality, and resin rich areas in the vicinity of the fasteners. In general, bearing strengths of textile composites do not compare favorably with bearing strengths of tape laminated composites because of the excessive fiber crimp in the textile preforms. In addition to fiber crimp, the shallow braid angles of architectures A and B offered little resistance to fastener movement. It is noted that these fiber architectures were not optimized for bearing strength.

Specimen Number	Failure Load (lb)	Bearing Strength (psi)	Average V <sub>f</sub> (%)	Average Void Content (%)
2-A PEEK	1,840	63,960	61.2	3.3
2-B PEEK	880	49,820	60.2	5.2
2-A RTM	1,550	47,540	53.6	0.5
3-A PEEK	2,300	71,600	65.1	5.8
3-B PEEK	1,760	55,600	59.9	5.1
3-B RTM	1,360	42,360	54.5	5.7

**Table 12: Braided Composite Bolt Bearing Test Results**

The failure mechanism for each specimen tested was a brooming failure directly outside of the fastener. The geometry of the washers restricted the failure mode directly around the hole.

### 2.D.6 Preliminary Correlation between Experimental Results and Analysis

Correlation between experimental data and analytical predictions from TECA is underway. Net-shape tension and compression data from the Braided Composite Technology Development Matrix were correlated for both the 2-D and the 3-D AS4/PEEK braided material systems. Correlation of the experimental data obtained for the AS4/DPL-862 braided materials systems has not begun because sufficient data has not been obtained for the RTM resin system. A test plan to obtain the necessary resin properties for analytical model input is currently being conducted.

Results from the preliminary correlation studies are shown in Figure 10. The TECA predicted values are within 6% of the tensile strength data and 9% of the compression strength data; the predicted values for the tensile and compression moduli are both within 5% of the measured values.

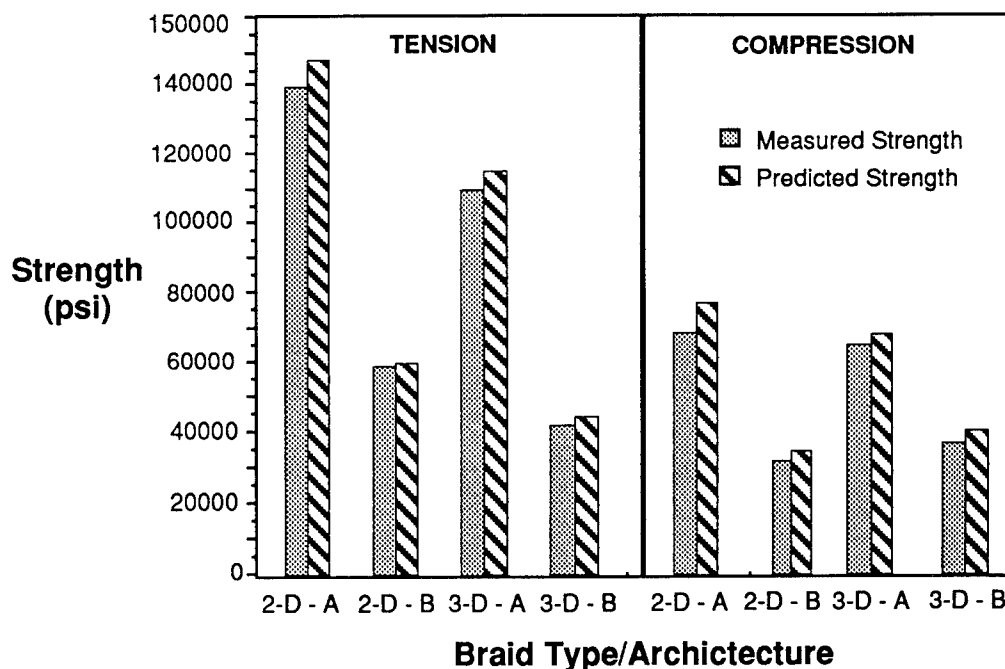


Figure 10: Correlation Between Experimental Results and TECA Predicted Values

## 3. CIRCUMFERENTIAL HOOP FRAME DEVELOPMENT

### A. Material Selection

The RTM resin system used in the Technology Development Phase was not used in the development of the circumferential hoop frames. The structural properties of the DPL-862 resin system, specifically the room temperature/dry compression and hot-wet compression performance, were not acceptable for commercial aircraft applications. However, it is noted that DPL-862 did serve its purpose in RTM process development and the initial screening of the mechanical performance of braided composites. After a detailed comparison study of various RTM resin systems from Shell, 3M, Dow, and British Petroleum, Shell's 1895 resin with curing agent W was chosen. The 1895 resin system costs \$12.50/lb, its structural performance is slightly better than 3501-6, and its viscosity profile is suitable for RTM. It is also noted that this resin system possesses a high glass transition temperature (420°F) which produces high hot-wet retention properties and is necessary for co-bonding precured structures. The combined AS4/1895 material system cost is approximately \$21/lbs (waste not included).

## B. Frame Fiber Architecture Design

As discussed in Section 1.B.2, the ultimate pressure loading condition is the most critical loading condition for the circumferential hoop frames located in the crown panel. Using the ATCAS design criteria, the minimum axial stiffness of the frames was determined to be 6.6 Msi (based on loads as of 2/91). TECA was then utilized to produce a tensile modulus design space (Figure 11) for the triaxially braided/RTM material system as a function of percentage of longitudinal tows and braiding angle; the design space provided an envelope of valid fiber architectures for a 55% fiber volume fraction. Once the design space was defined, other critical design issues inherent to the circumferential hoop frames were addressed. These critical issues included: thermal dimensional stability, mouse hole cut-outs, out-of-plane tension strength, bearing performance, and damage tolerance. Using the design space and taking into consideration the critical design issues listed above, the frame fiber architecture was chosen to consist of 37.5% longitudinal fibers with a braid angle of 66.5°; this fiber architecture is referred to as the "B1" or the "frame" architecture. Six plies of this braided fabric were used to produce a thickness of 0.141 inches. This architecture consists of 6K size tows which were chosen because they are easy to braid and produce preforms with high inter-ply nesting.

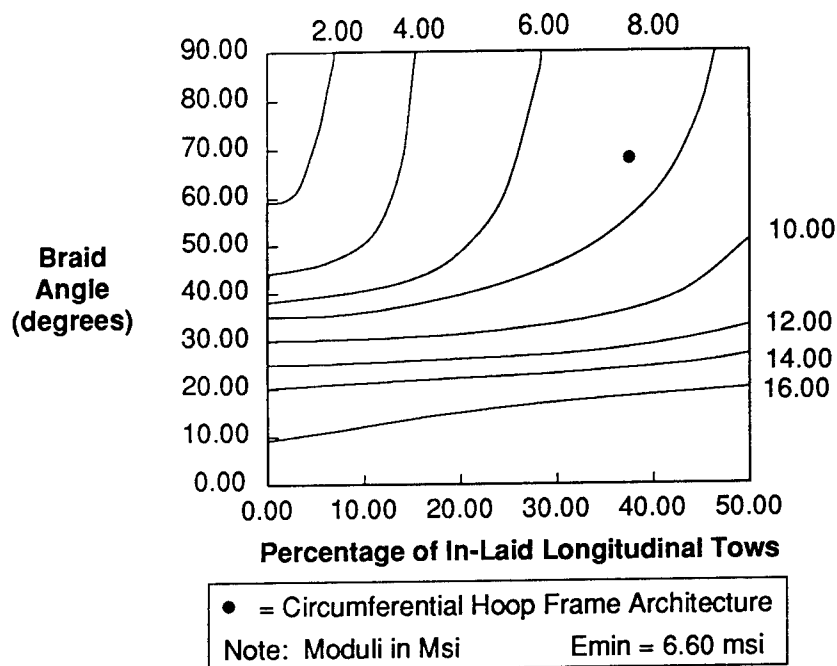


Figure 11: TECA Tensile Modulus Design Space

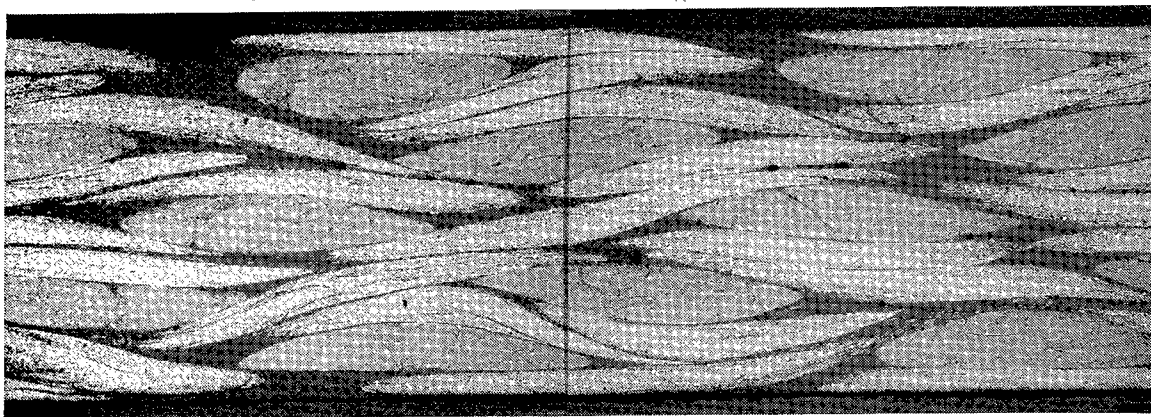
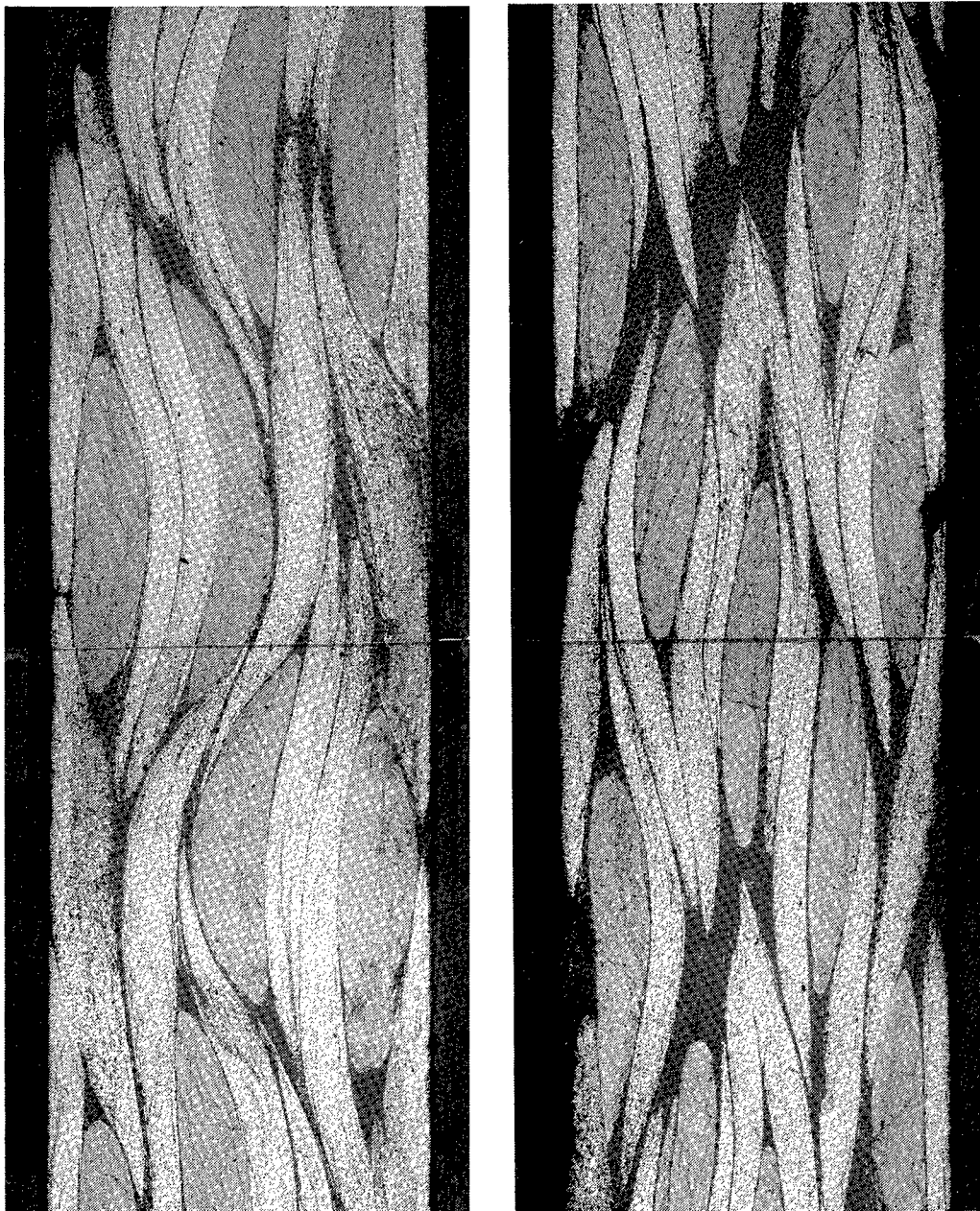


Figure 12: Cross-Section of Circumferential Hoop Frame Architecture



**Figure 13: Cross-Sections of Alternate Circumferential Hoop Frame Architectures  
(top: Architecture A1, bottom: Architecture B2)**

**Table 13: Characteristics of the 2-D Triaxially Braided Preforms**

<b>Fiber Architecture</b>	<b>A 1</b>	<b>B 1</b>	<b>B 2</b>
<b>Manufacturing Set-up</b>			
Braided Tow Size	12K	6K	6K
Longitudinal Tow Size	24K	18K	18K
Number of Braiding Carriers	144	144	144
Number of Fixed Carriers	72	72	72
Mandrel Diameter (inches)	5.50	4.80	5.25
<b>UNIT CELL Characteristics</b>			
Width of Unit Cell (inches)	0.120	0.105	0.115
Length of Unit Cell (inches)	0.061	0.046	0.042
Thickness of Unit Cell (inches)	0.037	0.026	0.027
Surface Area of Unit Cell (inches**2)	7.32e-3	4.83e-3	4.83e-3
Yarn Spacing on First Ply (inches)	0.109	0.084	0.078
Amount of Spacing/Compaction (inches)	0.011	0.006	0.012
<b>Preform Characteristics</b>			
Number of Plies (inches)	4	5	5
Braiding Angle	63 <sup>o</sup>	66.5 <sup>o</sup>	70 <sup>o</sup>
Percentage of Braided Tows	68.8%	62.6%	66.1%
Percentage of Longitudinal Tows	31.2%	37.4%	33.9%
Thickness of Inner Ply (inches)	0.037	0.026	0.027
Thickness of Outer Ply (inches)	0.036	0.026	0.026
Total Thickness of Preform (inches)	0.146	0.131	0.132
Vf of Preform (%)	54.3	54.2	54.3

A photomicrograph of the frame architecture is shown in Figure 12. Two alternate architectures were identified so that the ATCAS DBT could promptly respond to future design criteria changes and/or unforeseen preform fabrication difficulties. The additional architectures will also provide a larger data base for TECA correlation. The first alternate architecture, B2, consists of 6K tows and contains 34% longitudinal fibers with a braid angle of 70°. The second alternate architecture, A1, consists of 12K tows and contains 31% longitudinal fibers with a braid angle of 63°. Photomicrographs of the two alternate fiber architectures are found in Figure 13. A summary of the set-up variables for preform fabrication, the unit cell characteristics of the architectures, and the preform characteristics are shown in Table 12; the values contained in this table were obtained using TECA.

### **C. Manufacturing of Braided Composite Specimens**

The manufacturing of the braided composite specimens and the 3 ft frames for the manufacturing demonstration during the Direct Application Phase was performed at Fiber Innovations Inc. (FII). Braided composite manufacturing technology developed at Boeing, FII, and Shell Chemical Co. was jointly utilized during this Phase of the ATCAS Program.

#### **3.C.1 Preform Fabrication**

All preforms were formed with a 144 carrier New England Butt triaxial braider incorporating 72 longitudinal yarns in a 2/2 regular braid pattern. The preforms were formed on cylindrical mandrels and the desired preform thickness was achieved by over-braiding layers. To verify the placement of yarns in the structure, each preform was formed with one longitudinal and one braided nickel coated AS-4 carbon tracer yarn. Following braiding, the preform was cut longitudinally and removed from the mandrel. The preforms were then stabilized along the perimeter with Kevlar stitching thread to prevent the plies from shifting or distorting during insertion into the mold and also to reduce the potential for fiber wash-out during RTM.

#### **3.C.2 Resin Transfer Molding**

The RTM process at FII involves a combination of pressure and vacuum. FII has expended considerable time and energy to gain knowledge and experience in perfecting their own version of the RTM process. The details of the RTM process with the 1895 resin system are discussed in Section 3.E.2.

The target thickness tolerance of the braided composite specimens was  $\pm 0.010$  inches; the target fiber volume was 55% with a  $\pm 5\%$  variation, the tolerance of all radii was  $\pm 0.01$  inches; and the tolerance on braid angle was  $\pm 2.5^\circ$ .

#### **3.C.3 Quality Control Procedures**

The quality of the braided composite test specimens involved in the Direct Application Phase was evaluated using the same procedures as in the Technology Development Phase. The results of the quality assessment evaluations are summarized below.

Photomicrographs of the specimens showed the triaxially braided preforms were completely wet-out during the RTM process (Figure 12 and 13). The photomicrographs also showed uniform distribution of the in-laid longitudinal tows and a high degree of inter-ply nesting. Resin digestion tests proved that the braided preforms were completely wet-out; the void content of all the braided composites tested so far is under 0.5%. The fiber volume fraction of the composites was also determined via the resin digestion tests and showed that the fiber volume fractions were within the specified tolerances.

By tracing the nickel coated tracer yarns, the braid angle was measured for each of the specimens. The variation of braid angle within and between the braided composites was negligible and well within the specified tolerances. However, there was a slight variation in thickness from specimen to specimen. This



was due to the fact that two panels were RTM simultaneously and that the tool cavities were not identical. Although there is a slight variation, the dimensions of the specimens are all within the specified tolerances.

## D. Material System Performance Evaluation

### 3.D.1 Test Program Objectives

The overall objective of the braided composite material characterization study during the Direct Application Phase was to provide a data base of mechanical properties to support the preliminary design of the crown panel circumferential hoop frames. The test matrix is also being used to add to the existing braided composite data base and to further characterize the structural performance of braided composites.

### 3.D.2 Test Matrix Identification

The test matrix assembled for the Direct Application Phase is shown in Table 14. The test matrix contains three fiber architectures: the chosen frame architecture "B1", and the two alternate architectures, "A1" and "B2", whose braid angle and percentage of in-laid longitudinal fibers vary from the frame architecture.

TYPE OF TEST	FIBER ARCHITECTURES			TOTALS FOR TEST TYPE
	A1	B1	B2	
1 TENSION	3	3	3	9
2 OPEN-HOLE TENSION	3	3	3	9
3 COMPRESSION	3	3	3	9
4 OPEN-HOLE COMPRESSION	3	3	3	9
5 IN-PLANE SHEAR	4	4	4	12
6 OUT-OF-PLANE TENSION	5	5	5	15
7 COMPRESSION AFTER IMPACT	6	6	6	18
8 TENSION AFTER IMPACT	2	2	2	6
9 BEARING	8	8	8	24
10 FATIGUE	12	12	12	36
11 TENSION (UNCUT EDGES)	4	4	4	12
12 TRANSVERSE TENSION	6	6	6	18
13 WIDTH-EFFECT TENSION	0	0	12	12
14 FATIGUE (UNCUT EDGES)	0	2	0	2
15 OUT-OF-PLANE SHEAR	TBD	TBD	TBD	TBD
16 HOT-WET COMPRESSION	4	4	0	8
<b>TOTALS FOR ARCHITECTURE</b>	<b>63+</b>	<b>65+</b>	<b>71+</b>	<b>199+</b>

**Table 14: Braided Composite Direct Application Test Matrix**

In addition to providing in-plane and out-of-plane strength, stiffness, and fatigue properties, this test matrix also provides an indication of how a new material would be expected to function in a structural application. The open-hole tension and compression tests provide an indication of the material's tolerance to imperfections. The damage tolerance tests measure the material's response to impact loading and resistance to impact damage and can be used as a rough measure of thickness-direction strength. The bolt bearing data provides important parameters in structural applications where mechanical fasteners are used.

### 3.D.3 Specimen Configurations and Design

The following specimens had the same configurations as the tension specimens discussed in the Technology Development section: tension, open-hole tension, transverse tension, width-effect tension (with widths of 1.0, 2.0, 3.0, and 4.0 inches), compression, open-hole compression, hot-wet compression, and fatigue. The in-plane shear test will be a rail shear test; the test fixture for this test is currently being designed. The out-of-plane shear specimen configuration is currently under investigation. The out-of-plane tension specimen is a flange bending specimen whose configuration is identical to the circumferential hoop frame configuration. The compression after impact specimens are 6.0 inches long, 4.00 inches wide, and have a nominal thickness of 0.25 inches. The tension after impact specimens are 10.00 inches long, 4.00 inches wide, and have a nominal thickness of 0.125 inches. The specimens used for the bearing tests have the same design as discussed in the Technology Development section.

### 3.D.4 Coupon Testing Procedures/Methods

All testing is being performed on room temperature-dry specimens. All specimens are being tested in a 50 kip MTS testing machine and are being ramped to failure using a constant cross-head deflection rate of 0.05 inches per minute. The procedures discussed in the Technology Development section have been used in the tests that have been completed during the Direct Application Phase.

### 3.D.5 Test Instrumentation, Results, and Discussion

The testing involved with the Direct Application Test Matrix is on-going. The following sections will summarize the results that have been obtained so far. The failure mechanisms of the test specimens will be reported in a further publication. Tests that have been completed include: tension, transverse tension, compression, open-hole compression, hot-wet compression, out-of-plane tension, and bearing.

#### 3.D.5.a Tension

Unnotched tension tests were performed to supply strength, modulus, and Poisson's ratios for the 3 architectures involved in this study. The specimens had (0/90) strain gages of different sizes (1/16 inch, 1/8 inch, and 3/16 inch) bonded at their mid-length; an extensometer was also used to measure strain. The 1/16 inch and 1/8 inch strain gages were square and the 3/16 inch gage was 1/8 inch wide. A variety of strain gage sizes were used to observe the effect of strain gage size versus unit cell size. A comparison of strain gage sizes versus unit cell dimensions for the tension tests is shown in Table 15.

Architecture/ Direction	Unit Cell Dimension (Inches)	Ratio of 1/16 inch Gage Length/ Unit Cell Dimension	Ratio of 1/8 inch Gage Length/ Unit Cell Dimension	Ratio of 3/16 inch Gage Length/ Unit Cell Dimension
B1 Longitudinal	0.046	1.4	2.7	4.1
B1 Transverse	0.105	0.6	1.2	1.8
B2 Longitudinal	0.042	1.5	3.0	4.5
B2 Transverse	0.115	0.5	1.1	1.6
A1 Longitudinal	0.061	1.0	2.1	3.1
A1 Transverse	0.120	0.5	1.0	1.6

Table 15: Strain Gage Size versus Specimen Unit Cell Size

Results of the tension tests are summarized in Table 16. The B1 architecture possessed the highest strength and stiffness values; this was caused by the higher percentage of in-laid longitudinal tows in this architecture compared to the A1 and B2 architectures. Moduli obtained from the 1/8 inch and 3/16 inch strain gages and extensometer showed no significant differences in measured values (all moduli results reported in this study were calculated using a Least Squares Fit of the stress versus strain curve up to 2000

microstrain). This observation was expected because the gage lengths were sufficiently larger than the unit cell dimension in the loading direction. The moduli obtained from the 1/16 inch gages varied from the other gages and extensometer. The variation is due to the gage length being of the same dimensional scale as the length of the unit cell; gage lengths similar to unit cell dimensions are sensitive to localized effects within the unit cell. A wide range of Poisson's ratios was measured with the different size strain gages (the Poisson's ratios were evaluated at 2000 microstrain and calculated using a tangent method); this measurement is also sensitive to gage length versus unit cell size. The 1/16 inch and 1/8 inch gages oriented in the transverse direction were of the same dimensional scale as the unit cell width and were sensitive to localized effects. The 3/16 inch gage oriented in the transverse direction was sufficiently larger than the unit cell width and measured more accurate values.

Specimen Architecture	Stress (Ksi)	1/16 inch Gage Modulus (Msi)	1/8 inch Gage Modulus (Msi)	3/16 inch Gage Modulus (Msi)	Extensometer Modulus (Msi)	1/16 inch Gage Poisson's Ratio	1/8 inch Gage Poisson's Ratio	3/16 inch Gage Poisson's Ratio
A1	62.6	7.10	6.35	6.51	6.61	0.264	0.225	0.300
B1	80.7	7.18	6.94	6.88	6.72	0.186	0.185	0.268
B2	57.1	6.30	6.32	6.30	6.66	0.165	0.151	0.183

**Table 16: Braided Composite Axial Tension Test Results**

### 3.D.5.b Transverse Tension

Unnotched transverse tension tests were performed to supply strength, modulus, and Poisson's ratios. The same strain measurement techniques described for the unnotched tension specimens were utilized for the transverse tension tests.

Results of the transverse tension tests are summarized in Table 17. The B2 architecture possessed the highest strength and stiffness values; this is due to the higher braiding angle in this architecture as compared to the A1 and B2 architectures. Moduli obtained from the strain gages and extensometer showed variability in measured values. The variability was caused by the gage lengths being smaller or of the same dimensional scale as the length of the unit cell in the loading direction (see Table 15). The 3/16 gage showed the least amount of variability within specimens containing this size gage because it was approximately 1.5 times the unit cell dimension. A factor of 1.5 is most likely the minimum in choosing a strain gage size for accurate measurements of braided composites (thorough studies to determine the minimum factor are on-going). Similarly to the unnotched tension tests, a wide range of Poisson's ratios was measured with the different size strain gages because the gages were not of sufficient size; the 3/16 inch gage exhibited the least amount of variability in the testing.

Specimen Architecture	Stress (Ksi)	1/16 inch Gage Modulus (Msi)	1/8 inch Gage Modulus (Msi)	3/16 inch Gage Modulus (Msi)	Extensometer Modulus (Msi)	1/16 inch Gage Poisson's Ratio	1/8 inch Gage Poisson's Ratio	3/16 inch Gage Poisson's Ratio
A1	32.25	6.58	6.59	6.24	5.78	0.225	0.280	0.307
B1	41.7	7.45	6.13	6.80	6.45	0.291	0.163	0.199
B2	45.5	7.35	7.18	7.11	7.26	0.161	0.188	0.190

**Table 17: Braided Composite Transverse Tension Test Results**

### 3.D.5.c Compression

Unnotched compression tests were performed to supply strength, modulus, and Poisson's ratios for the various fiber architectures tested.

A summary of the results obtained from the compression tests are summarized in Table 18. Architecture B1 possessed the highest strength of the three architectures tested because of the higher percentage of longitudinal fibers in the B1 architecture.

Specimen Architecture	Failure Stress (psi)	% Unnotched
<b>Unnotched</b>		
A 1	44,626	----
B 1	73,634	----
B 2	56,508	----
<b>Open-Hole</b>		
A 1	43,972	99
B 1	52,399	71
B 2	45,150	80

**Table 18: Braided Composite Compression Test Results**

### 3.D.5.d Open-Hole Compression

Open-hole compression tests were performed to supply strength and modulus of braided compression specimens containing imperfections.

Results of the open-hole compression tests are summarized in Table 18. Although the B1 architecture possessed the highest notched compression strength, it also experienced the largest knock-down of the unnotched compression strength as compared to the B2 and A1 architectures. The high open-hole compression strength was due to the high percentage of longitudinal fibers. The difference in the notch sensitivity of the three architectures appears to be related to the unit cell dimensions of the architectures, specifically the longitudinal tow separation. It is speculated that if the unit cell dimensions are of the same dimensional scale as the stress concentration distribution area, different failure mechanisms occur because of increased interaction between braided and longitudinal tows thus lowering notch sensitivity. The topic of notch sensitivity as a function of unit cell size is currently being thoroughly investigated.

### 3.D.5.e Hot-Wet Compression

Hot/wet compression tests were conducted (at 180°F and 100% relative humidity after a 30 day soak) to determine the environmental effects on the crown frame material system (Architecture B1). Results of these tests show a 26.5% reduction in compression strength from room temperature/dry which is slightly better than 3501-6 hot/wet compression performance.

### 3.D.5.f Out-of-Plane Tension

Flange bending tests were performed to measure the out-of-plane tension failure stresses of the braided frame material system and configuration.

A summary of the results from the out-of-plane tension tests are given in Table 19. The transverse strengths shown in the table were calculated using the isotropic methods discussed in the Technology Development section. The results show that that the 2-D braided material system exceeds the out-of-plane

strength of quasi-isotropic tape laminates (see Figure 8). Justification for the high transverse tension strengths is discussed in the Technology Development section. Architecture A1 did not fair as well as Architectures B1 and B2 because the 12K tows do not nest as well as the 6K tows (see Figures 12 and 13).

Specimen Architecture	Failure Load (lb)	Moment (in-lb)	Strength (psi)
B1	199	223	9,486
B2	205	230	9,772
A1	157	176	7,484

**Table 19: Braided Composite Out-of-Plane Tension Test Results**

### 3.D.5.g Bolt Bearing

Bearing tests using a zero clamp-up, 35 in-lb torque, and 90 in-lb torque condition were performed to determine bearing strengths for the three architectures involved in this study.

A summary of results obtained from the bolt bearing tests is given in Table 20. The bearing stresses of the specimens contained in the Direct Application Test Matrix were much higher than the specimens previously discussed in the Technology Development Test Matrix. With a no-clamp-up condition, the bearing strengths of the 3 architectures contained in this study ranged from 90 ksi to 100 ksi. The increase in bearing strength of these braided composites can be attributed to the high percentage of axial tows, high braid angles, good preform quality, and excellent composite quality. The high braid angle provided higher tangential stiffness and restrained bearing deformation, the straight longitudinal fibers also restricted movement, and the absence of resin rich areas around the hole prevented premature yielding. The application of 35 in-lb of torque increased the bearing ultimate strengths by approximately 20% over the zero clamp-up condition while the full torque condition (90 in-lb) increased the ultimate stresses by approximately 30%. Enhanced performance of the clamp-up tests was attributed to the friction forces created by torquing the fastener.

Specimen Architecture	Torque (in-lb)	Ultimate Load (lb)	Bearing Strength (Ksi)
A1	0	3047	89.050
	35	3795	115.560
	90	4360	128.716
B1	0	3465	99.155
	35	4003	119.235
	90	4480	129.841
B2	0	3315	95.568
	35	3908	114.100
	90	4139	118.243

**Table 20: Braided Composite Bolt Bearing Test Results**

## E. 3 ft Frame Manufacturing Demonstration

The fabrication of the twelve 3 ft. frames were used to achieve the following objectives: 1) to demonstrate the proof of manufacturing concept and requirements defined in global evaluation, 2) to demonstrate batch mode processing, 3) to determine tooling and manufacturing modifications that improve part quality and producibility, 4) to assist in the local optimization of the frame configuration, and 5) to identify and address

potential problem areas that affect scale-up. The following sections describe the manufacturing details that were used to fabricate the 3 ft demonstration frames.

### 3.E.1 Manufacturing of Different Structural Configurations

Four frame configurations consisting of different combinations of flange caps and filler packs were fabricated during the manufacturing demonstration to gain manufacturing experience and to aid the design optimization; each combination is described in Table 21. More specifically, the configurations were fabricated to optimize the frame cost benefits, manufacturing process, and structural performance. Two types of radius filler packs (Narmco 1515 adhesive and dry braided fiber) and two bottom flange cap configurations (braided cap and no cap) were evaluated. The issues of compatibility between the filler packs and RTM resin processing conditions and the identification of manufacturing problems of each configuration were assessed.

Configuration Type	Filler Pack Type	Flange Cap Type
1	braided	3 plies of braided fabric
2	braided	none
3	adhesive	3 plies of braided fabric
4	adhesive	none

**Table 21: Frame Flange Configurations for the 3 ft. Manufacturing Demonstration**

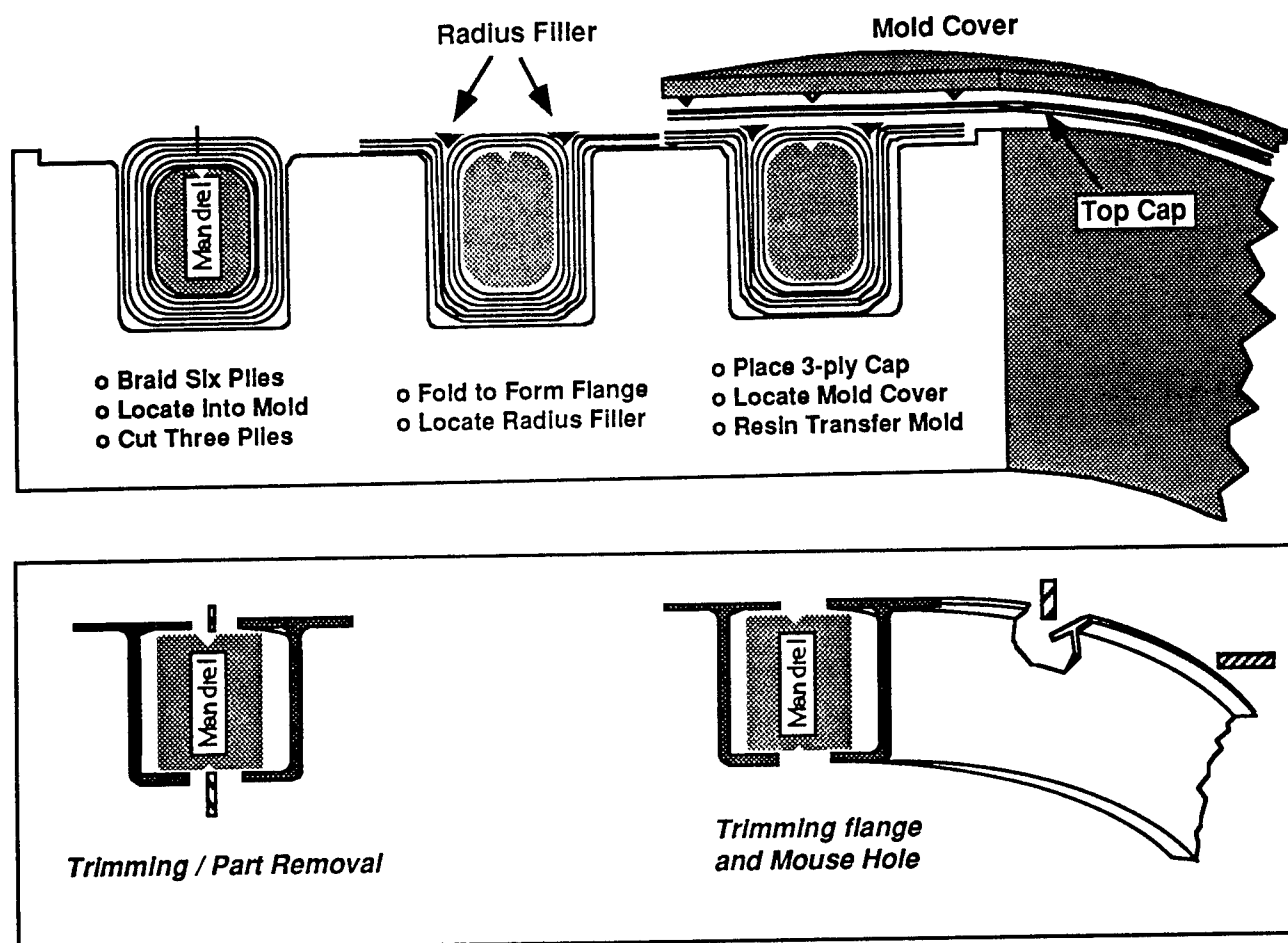
### 3.E.2 Circumferential Hoop Frame Batch Mode Manufacturing

#### 3.E.2.a Tool Design

The RTM tool was designed to demonstrate the capability of RTM long thin structural components and the batch mode concept. Although the fabrication of the 3 ft. frames demonstrated simultaneous batch mode processing of two frames, the process is still valid for multiple frames. The tool contained a single resin injection port and distributed the resin uniformly around the frame cross section using a manifold. The mandrel and mold cavity were machined out of aluminium to accommodate both of the mouse hole configurations identified in global evaluation (Section 1.B.3) and local optimization (Section 4.C). Grooves were machined into the mandrel to place the braided preforms in tension to prevent fiber movement during injection; this groove was also used as a trimming aid. The dimensions of the tool cavity were determined through process manufacturing models and preform thickness measurements. The dimensions of the tool cavity were critical because they directly control the fiber volume fraction of the composite part.

#### 3.E.2.b Frame Preform Assembly

A schematic of the crown frame fabrication procedure is shown in Figure 14. As shown in the figure, the braiding mandrels are covered with six plies of triaxial braid. The ends of the preform were trimmed and then the braided mandrel was placed into the mold cavity. To prevent preform fraying, tackifier was applied to the individual plies along the cutting area. The top three plies were then cut along the length of the mandrel and folded to form the bottom "J" flanges. Once the radius filler packs were inserted, the flange cap was laid-up and the mold was closed. To fabricate a frame without a top cap, a brass shim plate was placed between the top cover and mandrel plies prior to RTM.



**Figure 14: Crown Frame Fabrication Procedure**

### 3.E.2.c RTM with Shell's 1895 Resin

The RTM mold was oriented in a vertical position during resin injection and curing. The lower injection port of the RTM tool was connected to the resin feed system and the upper port was connected to a vacuum system. The mold was checked for vacuum integrity and preheated to 250-280°F. The proper amounts of resin and hardener were measured, mixed, and degassed for approximately 10-20 minutes. The resin system was then preheated to 180-200°F.

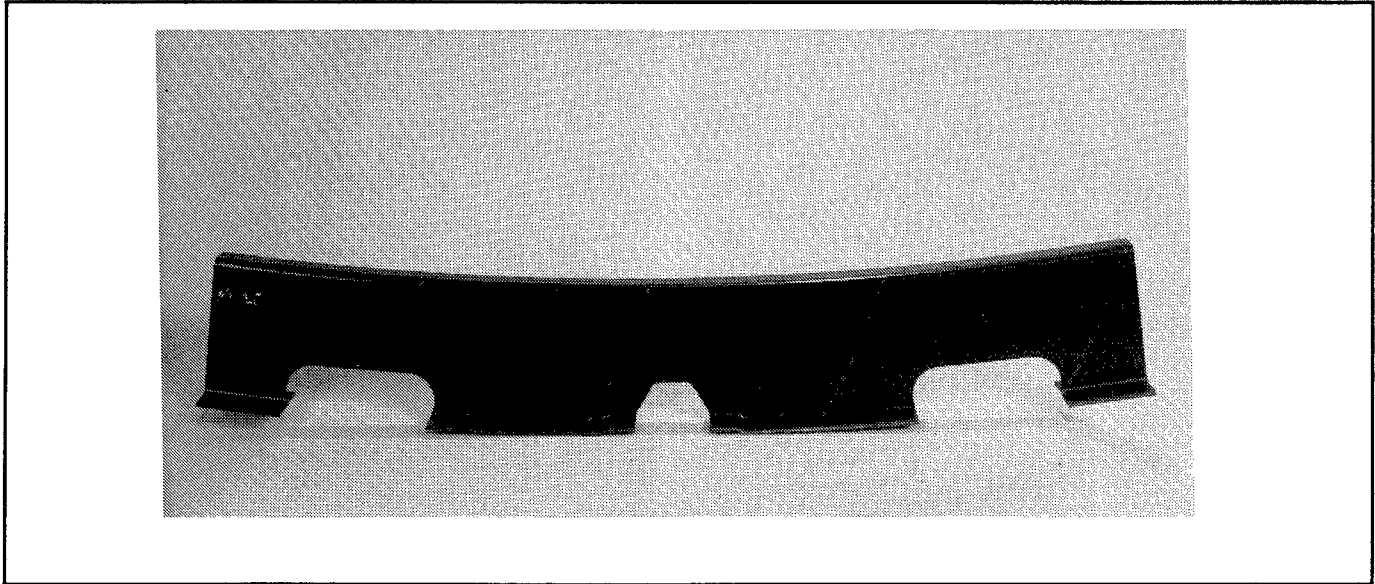
The injection cycle started with the filling of the feed system. The mold was evacuated of all air and the resin was injected at 40-90 psi into the mold through the lower port. After the mold was filled, the vacuum was relieved and the mold was pressurized at 40-90 psi for the cure cycle. The cure cycle consisted of gel stages for 30 minutes at 300°F and for 90 minutes at 350°F. Following the gel stages, the mold was cooled to 250-275°F for part removal. A freestanding post cure of two hours at 350°F was the final step prior to trimming and finishing.

Frames manufactured early on in the manufacturing demonstration possessed some surface porosity. The porosity was eliminated by increasing the injection temperature to 235°F which lowered the injection viscosity of the resin. Another processing modification was the utilization of a carbon fiber veil which acted as a breather to evacuate entrapped air. The veil eliminated surface porosity and improved the frame surface finish.

A temperature controller maintained the desired tool temperatures throughout the RTM process. Thermocouples were located inside the mold cavity and braiding mandrel in order to monitor the temperature distribution and to prevent thermal gradients.

#### *3.E.2.d Part Removal and Trimming*

The part was trimmed off the mandrel with the aid of the cutting groove in the mandrel (Figure 14). After removal of the frames from the mandrel, the mouse holes and flange edges were trimmed as shown in Figure 15.



**Figure 15: Crown Panel Frame Following Trimming**

#### *3.E.2.e Quality Control Procedures*

The same quality control procedures described in Section 2.B.2 were used to evaluate the quality of the 3 ft. frames. Photomicrographs, resin digestion tests, and ultrasonic evaluations showed that the frames possessed void contents of less than 0.5%. Measurement of the nickel coated tracers yarns showed that the braid angles were within required tolerances. Finally, coordinate measurements showed that all frame dimensions were within specified tolerances.

## **4. LOCAL DESIGN OPTIMIZATION**

The circumferential frame design issues that were addressed in the local optimization phase of the ATCAS design process were: the flange cap configuration, the cap filler pack, the mouse hole configuration, and batch-mode tooling requirements. The overall objective of the local design optimization studies was to reduce the cost and weight of the frame configuration and address the technical issues identified in the global evaluation phase of design. The following sections summarize the past and present activities in the local optimization of the circumferential hoop frames.

### **A. Dimensional Accuracy Optimization**

The four frame designs described in Section 3.E.1 were used to identify the configuration that produced the optimum dimensional stability. The main concern was thermal warpage of the frames caused by material anisotropy and structural geometry. This concern was addressed by coordinate measurements of the 3 ft.



frame manufacturing demonstrations and finite element analysis. Key elements that directly affect the thermal warpage of the frames were: geometry, anisotropic architecture, the filler pack, the resin rich areas around radii bends that are inherent to the RTM process, and the flange cap. A combination of two key elements were varied in the finite element analysis: the type of filler pack and the flange cap configuration. The analysis used three-dimensional elements because of the different material properties across the frame cross-section (plane stress or plane strain conditions could not be applied to this particular problem).

All manufactured frames were found to experience flange spring-in and a small amount of web twist caused by the frame curvature in the hoop direction. A summary of frame coordinate measurements and finite element analysis results is shown in Table 22. The spring-in of the frames varied from  $0.3^{\circ}$  to  $0.6^{\circ}$ . Configuration Type 3 experienced the least amount of spring-in because the combination of the adhesive filler pack and braided cap offer the most resistance to flange deformation. Configuration Type 2 experienced the most spring-in because to the braided filler pack offered little resistance to flange deformation. The dimensional stability finite element analysis successfully predicted the configuration that minimized the spring-in deflection; predicted values were within 10% of all measured values. It is noted that the finite element analysis did not predict web twist because the frame curvature in the hoop direction has not yet been incorporated.

Configuration Type	Measured Flange Spring-In (degrees)	FEM Predicted Flange Spring-In (degrees)	Measured Web Twist (degrees)
1	0.3	0.28	0.025
2	0.6	0.56	0.025
3	0.3	0.27	0.065
4	0.6	0.54	0.065

**Table 22: Correlation Between Measured and Predicted Flange Spring-In**

Although the configuration consisting of the adhesive filler pack and braided cap minimizes flange spring-in, the spring-in deflections of all types of configurations are within reasonable limits (under  $1^{\circ}$ ). Therefore, it was concluded that any of the four frame design configurations (with the proper tooling) would hold the necessary frame tolerances.

## **B. Frame-to-Skin Bond Issue**

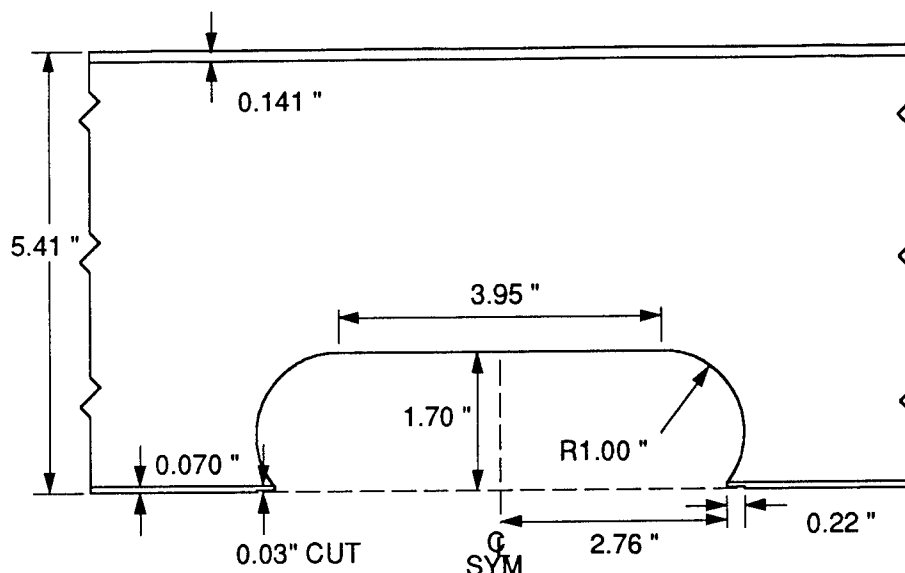
Two university subcontracts are supporting ATCAS efforts on the technical issues of frame-to-skin bond strength and durability. The University of Washington is characterizing viscoelastic properties of the adhesive. To date, time and temperature dependent properties for dry samples have been measured. Drexel University is performing three tasks: 1) time-dependent analysis development, 2) fracture toughness test characterization, and 3) frame-to-skin adhesive bond element tests. To date, significant progress has been achieved in the first two tasks. Adhesive fracture tests have been performed with braided composite plate adherends of the same architecture as the final crown frame design. Results indicate relatively high bond line fracture toughness, despite the tendency for cracks to propagate outside the toughened adhesive layer. A "rough" fracture surface that replicates the braided plate architecture appears to be responsible for the high toughness.

As a result of the test data, Type 4 was chosen as the locally optimized configuration. The skin attachment flange for frame elements of the locally optimized crown design have a thickness equal to half that of the frame web and top flange. In the original design, an additional braided plate was included as part of the frame flange that attached to the skin, resulting in a thickness equal to that of the web and similar in thickness to the skin. This additional plate was included in the design as a manufacturing aid; however,

subsequent process trials indicated that it was not needed. The reduced thickness of the current frame flange that is bonded to the skin is not only expected to reduce cost and weight, but also improve bond strength.

### C. Mouse Hole Configuration

Manufacturing costs and risks were evaluated via comparative studies for several mouse hole configurations during the local optimization process. As a result of the comparative studies, several design modifications were identified to reduce manufacturing costs and to simplify the frame/stringer/skin assembly. The most significant design modification was a larger frame mouse hole with a simplified configuration; this design modification is shown in Figure 16. The optimized configuration reduced tolerance build-up at the frame/stringer/skin interfaces, assembly time, and the manufacturing cost of the



**Figure 16: Mouse Hole Configuration Following Local Optimization**

In the optimized configuration, the frame is not directly bonded to the stringer, which minimizes the difficulty of bonding three elements (frame/stringer/skin) at one intersection. Assembly costs were reduced by 0.6% and the frame weight was reduced by 8.5% by eliminating the need for a rotisserie assembly tool. The original assembly method restricted the ability to place frames on a preassembled skin-stringer panel; the new mouse hole configuration eliminated this restriction. The DBT determined that the modification to a larger mouse hole would require further testing to evaluate the impact upon structural performance. The structural performance of the original mouse hole design (Figure 5) and the optimized configuration will be evaluated via large scale testing of the crown panel.

### D. Manufacturing Process Optimization

Batch-mode tooling requirement modifications were responsible for significant cost savings. Factory simulation studies showed that sixteen RTM tools could be reduced to five and still meet the desired crown panel production rate. This modification resulted in a 16.2% reduction in frame cost [10].

Another modification in the manufacturing process optimization was the tapering of the frame flanges. This modification was made to increase the pull-off strength of the frame-to-skin bond and to reduce the risk of manufacturing problems; this modification did not have a significant impact on frame cost or weight. Tapering the flanges minimized resin pools and reduced the stress concentrations at the edges of the flanges. It also reduced the probability of tooling interferences and cure bagging risks [10].

## E. Cost and Weight Impact of Local Design Optimization

The changes made to the circumferential hoop frame design during the local optimization phase showed a cost savings of 30.1% and weight savings of 13.3% over the original frame design selected in the global evaluation phase. These modifications reduced the overall crown panel cost by 3.2% and overall weight by 2.8% as indicated in Table 23. Although some of the frame design and manufacturing modifications did not project costs or weight savings, they were incorporated to improve the overall manufacturing process and to reduce the risk of anomalies.

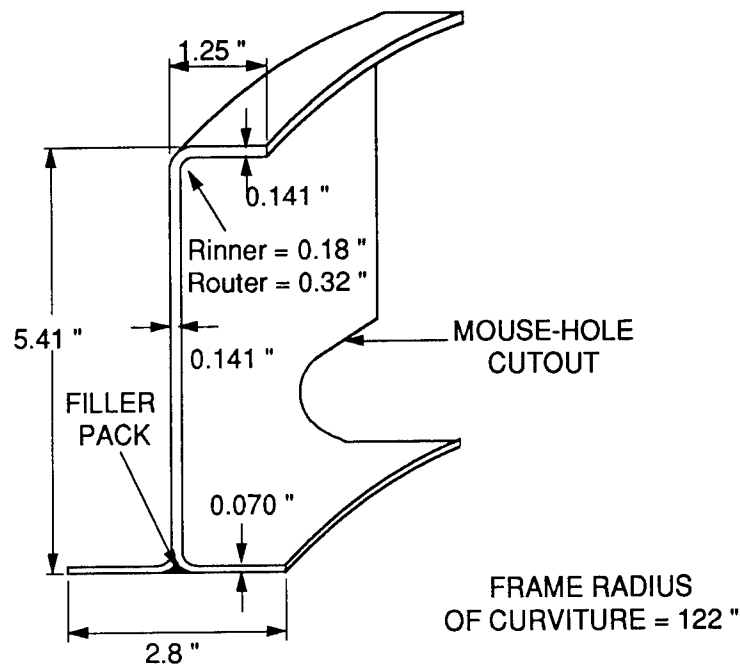
Global Evaluation	Local Optimization	Purpose of Change	Optimization Method	Cost Savings	Manufacturing Risk	Structural Performance
Small Mouse Hole	Wider Mouse Hole	- Reduce tolerance build-up - Reduce tooling cost	- DBT - Demonstration	0.6 %	Reduced	TBD
16 tools	5 tools	- Reduce tooling cost	- Factory Simulation	16.2 %	NA	NA
3 Plies of Braided Fabric	No Cap	- Increase performance - Reduce cost - Reduce weight	- DBT - Demonstration	13.3 %	Reduced	Increased
Several Potential Configurations	Adhesive Filler Pack	- Increase damage tolerance	- Design Analysis - Demonstration	0 %	Reduced	Increased
Flange Edge	Tapered Edge	- Minimize resin pools - Lower cure bagging risks - Increase pull-off strength	- Structural Tests - Demonstration	0%	Reduced	Increased

Total Frame Cost Savings	30.1 %
Total Frame Weight Savings	13.3 %
Total Crown Panel Cost Savings	3.2 %
Total Crown Panel Weight Savings	2.8 %

**Table 23: Summary of Locally Optimized Frame Cost and Weight Savings**

## F. Summary of Current Circumferential Hoop Frame Design

The current circumferential hoop frame configuration developed by the global evaluation and local optimization studies is shown in Figure 17. This is the configuration that will be manufactured during the scale-up 8 ft. frame manufacturing demonstration at the end of 1991.



**Figure 17: Circumferential Hoop Frame Configuration Following Local Optimization**

## **FUTURE WORK**

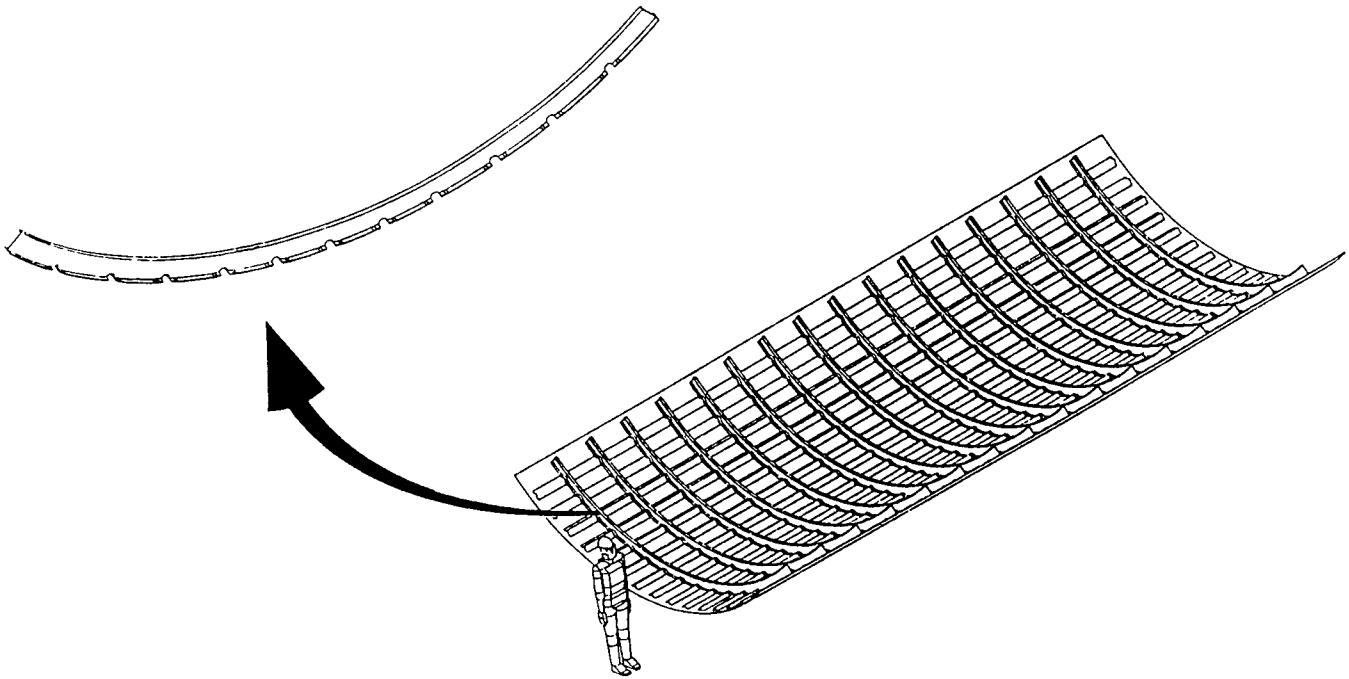
### **Approach to Scale-up**

The manufacturing demonstration of the 3 ft. frames provided processing information essential for the production of full-size 16 ft. long crown frames. The processing conditions for the Shell 1895 resin system met the manufacturing criteria, but additional work must be performed to fully understand the resin processing window and associated structural performance with triaxially braided preforms. The 3 ft. frame demonstration demonstrated the feasibility of batch mode processing with net-shape braided preforms. The frame flange spring-in, web twist, and dimensions were controlled by process optimization and tooling accuracy ( $\pm 0.010$  inch tolerance on all frame dimensions). Tooling design for longer frames must be supported by additional trials and FEM models to ensure that the frame dimensions are held to  $\pm 0.010$  inches. Although the 3 ft. frames were not fabricated with a fully automated braiding and RTM systems, the demonstration proved the manufacturing proof of concept and requirements, and provided insight for risk and cost reduction for scale-up activities.

### **8 ft. Frame Manufacturing Demonstration**

The fabrication methods that were addressed during the manufacturing demonstration of the 3 ft. frames will be utilized to develop the manufacturing process for 8 ft. frames. The RTM tool will be fabricated with Invar 36 material to minimize thermal warpage caused by tool-to-part CTE mismatch and maximize dimensional accuracy. The 3 ft. tool design will be modified to accommodate the design modifications made during the local optimization phase of the ATCAS design process. The tool will accommodate the thinner bottom frame flange and the flange spring-in effects. The stringer flange joggle that was needed for the original mouse hole configuration will be eliminated so that the tool may be used for any stringer spacing. The RTM processing parameters used to fabricate the 3 ft. frames will be used as the baseline. Additional process optimization for improved part quality will be conducted during the 8 ft. frame fabrication demonstration. The temperature control techniques that will be used to manufacture the 8 ft. frames will be similar to the techniques used in the 3 ft. manufacturing demonstration.

More than fifteen 8 ft. frames will be produced and evaluated during the last quarter of 1991. Evaluations will include: warpage measurements at -30°F, 75°F, and 130°F, void content, resin distribution, fiber orientation, and dimensional accuracy. Following inspection, the frames will be co-bonded onto three 7 ft by 10 ft. skin-stringer assemblies (Figure 18). The integrity of the entire crown panel structure will be evaluated by large panel tests.



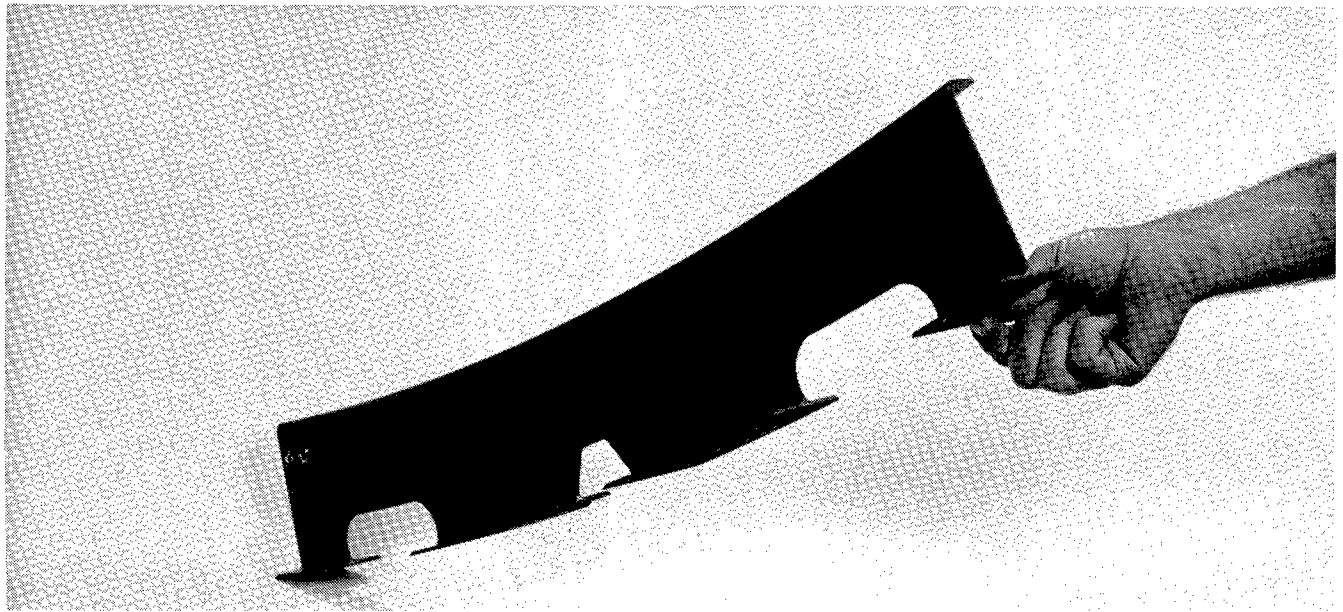
**Figure 18: Crown Panel Assembly**

#### **Verification Cost and Test**

Detailed cost and weight studies will be performed during the 8ft. frame manufacturing demonstration. The costs and weight associated with the 8 ft. frames will be utilized in the final crown panel cost and weight studies. Although the costs studies based on automation will not provide a final answer, the manufacturing and process modifications needed to meet production criteria will be determined.

### **KEY ACCOMPLISHMENTS**

The ATCAS Team has shown that textile composites can successfully be applied to primary fuselage structural components. The crown circumferential frames (Figure 19) were designed, characterized, and manufactured through the efforts summarized in this paper. The ATCAS three step design process and the DBT approach were successfully demonstrated. The state-of-the-art in textile technology was advanced in the areas of design, materials, manufacturing, analysis, and test. The technology developed in this effort was successfully applied to a direct application. The low cost manufacturing approach selected for the crown frames was demonstrated via a 3 ft. manufacturing demonstration. Finally, the scale-up issues that need to be addressed for the 8 ft. frame manufacturing demonstration were identified and are currently being analyzed.



**Figure 19: Crown Panel Frame Fabricated During Manufacturing Demonstration.**

## **ACKNOWLEDGMENTS**

The authors would like to gratefully acknowledge the efforts of the following Boeing personnel who contributed to this effort: Dr. Christian Gunther, Dr. Pierre Minguet, Dr. Larry Ilcewicz, Adam Sawicki, and Blake Flinn. The authors would also like to thank the following subcontractors and organizations for their efforts and cooperation throughout the ATCAS Program: 1) Garrett Sharpless and Steve Goodwin at Fiber Innovations Inc., 2) Ralph Hewitt, Dr. Eric Stark, and Diane Henry at Shell Chemical Co., and 3) Dr. Charlie Harris, Buddy Poe, and John Masters at the Mechanics of Materials Branch at the NASA Langley Research Center.

## REFERENCES

- 1 Walker, T.H., Smith, P., Truslove, G., Willden, K., Metschan, S., Pfahl, C., " Cost Studies for Commercial Fuselage Crown Designs", First NASA Advanced Composite Technology Conference Proceedings, Seattle, WA, October 29-November 1, 1990, NASA-CP-3104.
- 2 L.B. Ilcewicz, P. Smith, T.H. Walker, R. Johnson, " Advanced Technology Composite Aircraft Structures", First NASA Advanced Composite Technology Conference, Seattle, WA, October 29-November 1, 1990, NASA-CP-3104.
- 3 Nui, M.C., *Airframe Structural Design*, Conmilit Ltd., 1988.
- 4 Fedro, M.F., Gunther, C.K., Ko, F.K., "Mechanical and Analytical Screening of Braided Composites for Transport Fuselage Applications", *First NASA Advanced Composite Technology Conference Proceedings*, Seattle, Washington. October 29 - November 1, 1990. pp. 677 - 704.
- 5 ASTM Standards and Literature References for Composite Materials, First Edition, Editor R.A. Storer, ASTM Philadelphia, Pa., 1987.
- 6 Gause, L.W., Alper, J.M., "Structural Properties of Braided Graphite/Epoxy Composites", *Journal of Composites Technology & Research*, Vol. 9, No. 4, Winter 1987, pp. 141-150.
- 7 Whyte, D.W.: On the Structure and Properties of 3-D Braided Reinforced Composites. PhD Thesis, Drexel University, June 1986.
- 8 Adams, D.F., Walrath, D.E., "Iosipescu Shear Properties of SMC Composite Materials," *Composite Materials: Testing and Design (Sixth Conference)*. ASTM STP 787, American Society for Testing and Materials, 1982, pp 19-33.
- 9 Martin, R. "Delamination Failure in a Unidirectional Curved Composite Laminate", *NASA Contractor Report 182018*, Contract NAS1-18599, April 1990.
- 10 K.S. Willden, S. Metschan, "Composite Fuselage Crown Panel Manufacturing Technology", Ninth DoD/NASA/FAA Conference on Fibrous Composites in Structural Design, NASA CP-19 .(Paper of this compilation).

**SESSION VI**  
**DAMAGE TOLERANCE**



**THIS PAGE INTENTIONALLY BLANK**

# The Use of Impact Force as a Scale Parameter for the Impact Response of Composite Laminates

Wade C. Jackson  
US Army Aerostructures Directorate, USAARTA-AVSCOM  
Hampton, Virginia

C.C. Poe, Jr.  
NASA Langley Research Center  
Hampton, Virginia

## Abstract

The building block approach is currently used to design composite structures. With this approach, the data from coupon tests are scaled up to determine the design of a structure. Current standard impact tests and methods of relating test data to other structures are not generally understood and are often used improperly. A methodology is outlined for using impact force as a scale parameter for delamination damage for impacts of simple plates. Dynamic analyses were used to define ranges of plate parameters and impact parameters where quasi-static analyses are valid. These ranges include most low-velocity impacts where the mass of the impactor is large and the size of the specimen is small. For large-mass impacts of moderately thick (0.35-0.70 cm) laminates, the maximum extent of delamination damage increased with increasing impact force and decreasing specimen thickness. For large-mass impact tests at a given kinetic energy, impact force and hence delamination size depends on specimen size, specimen thickness, boundary conditions, and indenter size and shape. If damage is reported in terms of impact force instead of kinetic energy, large-mass test results can be applied directly to other plates of the same thickness.

## Symbols

$d_0$	diameter of damage
$E_2$	modulus transverse to the fiber direction
$E_s$	modulus of the impactor
$F$	contact force
$F_i$	contact force at initial load drop
$F_{\max}$	maximum contact force
$G_{II}$	strain energy release rate for delamination growth due to interlaminar shear

$S^*$	critical value of the average transverse shear stress to extend a delamination ( $V^*/h$ )
$h$	thickness of plate
$k$	equivalent spring constant at center of plate
$M$	mass of impactor
$n$	Hertzian contact stiffness
$r$	radial distance from center of plate
$r_c$	radius of contact
$r_i$	radius of indenter
$v$	velocity of impactor
$V$	transverse shear force per unit length
$V^*$	transverse shear force associated with the delamination front
$\alpha$	indentation
$\delta$	displacement at center of plate
$\nu_s$	Poisson's ratio of impactor

## Introduction

Composite structures are currently designed and certified by a building block approach. First, critical areas of the structure are determined, and potential failure modes are identified. Then, a series of specimens is tested that will fail in modes that represent the failure modes in critical areas. The series begins with tests of simple coupons and ends with a test on a full-scale component. In between the coupons and full-scale component, tests are conducted on specimens containing joints and other types of details, subcomponents, and components. For composites, failure modes include interlaminar failure due to both in- and out-of-plane loads. Some of the more common failure sites are at open and loaded holes, impact locations, and hard points where stiffness changes dramatically. Environmental conditions are simulated for all but the full-scale tests. Even the full-scale test specimen may have to be environmentally conditioned if changes in environment cause changes in failure mode. This experimental process has produced reliable composite structures but is very expensive and contributes significantly to the cost of composite structures. In order to reduce costs, analytical methods are needed to bridge the gap between tests of simple coupons and verification tests of full-scale structures.

One of the more important failure modes in laminated composite materials involves nonvisible impact damage. Low-velocity (large-mass) impacts can cause nonvisible impact

damage that results in significant loss of strength [1-3]. The Federal Aviation Administration (FAA) requires that a structure with nonvisible impact damage carries an ultimate load. The purpose of the present paper is to show how impact force can be used as a scale parameter for delamination damage for impacts of simple plates. The use of kinetic energy as a scale parameter is also examined. By using a scale parameter in the building block approach to design for impact damage, the number of tests can be reduced, and the reliability can be improved. The parameters considered are plate size, boundary conditions, laminate thickness, material, visibility of damage, and type of damage. The impact parameters considered are indenter diameter, mass, and velocity.

The damage resulting from an impact is considered in this paper but not the residual strength. If plate boundaries and structural elements are sufficiently remote from the impact damage, it is assumed that strength can be characterized solely by the damage state for a failure originating at the impact damage. Thus, identical damage is sufficient for identical strength. It is recognized that splices, stringers, and other structural elements are capable of arresting fractures resulting in greater strength than that of simple plates. In those cases, simple plate results are conservative.

### **Impact Analysis Models**

Three analytical methods were used to predict the impact response of rectangular plates with fixed or simply-supported boundaries and with uniform thickness and density. With two of the methods, the response was predicted by solving elasto-dynamic plate equations. The third method predicted the maximum contact force and deflection during an impact by balancing the kinetic energy of the impactor with the work performed on the plate by the impactor. For all three methods, the impactor was assumed to be spherical and rigid, and indentation was calculated assuming Hertzian contact.

A dynamic method developed by Sankar [4] predicted the impact response by the use of a dynamic Green's function. With this approach, the nonlinear contact problem was uncoupled from the linear behavior of the plate. The contact problem was modeled with Hertz's law, and the plate response was predicted by the use of plate theory with shear deformation. This particular analysis program was limited to the analysis of a rectangular plate with simply-supported boundary conditions. The other dynamic method used a finite element plate code developed by Chen and Sun [5]. This analysis program also used Hertzian contact and included the effect of shear deformation. A uniform mesh with four-noded quadrilateral elements was used to model the plate for this study. All types of boundary conditions could be modelled using the finite elements. This analysis was also used to predict the static solution. The force histories from each of the two analyses were compared for the simply-supported case and were found to be nearly identical. The analysis using the dynamic Green's function was more efficient since many solutions could be quickly obtained from the generation of a single dynamic Green's function. Thus, the impact force was calculated using the dynamic Green's function program when the boundaries were simply supported and with the finite element program when the boundaries were clamped. The finite element program was also used to calculate the transverse shear force for all boundary conditions analyzed, even for simply-supported boundaries.

In reference 6, the maximum contact force and displacement were predicted using an equation obtained from an energy balance. This technique offered a simple method to quickly obtain the impact force as well as the peak impactor and plate displacements. The basic assumption for this analysis is that all the impactor's kinetic energy is transferred into the plate at the time of maximum contact force or maximum transverse deflection of the plate. Thus, peak contact force and peak plate displacement are assumed to occur as the impactor's velocity passes through

zero. Energy losses such as material damping and vibrations are neglected. With these assumptions, the energy balance can be written as

$$\frac{1}{2} M v^2 = \int_0^{\delta_{\max}} F d\delta + \int_0^{\alpha_{\max}} F d\alpha \quad (1)$$

where  $M$  and  $v$  are the mass and velocity of the impactor and  $\delta$  and  $\alpha$  represent the plate center displacement and contact indentation, respectively. The center deflection of the plate,  $\delta$ , can be related to the contact force,  $F$ , by the linear equation

$$F = k\delta \quad (2)$$

where  $k$  is an equivalent spring constant for the plate. The spring constant can be easily calculated using plate theory or a single finite element run for more complicated boundary conditions. Since  $k$  is determined from a static analysis, the plate is assumed to deform in a static mode shape. Similarly, the contact indentation,  $\alpha$ , is related to the contact force by Hertz's Law [6,7]

$$F = n\alpha^{3/2} \quad (3)$$

where  $n$  is the Hertzian contact stiffness which can be approximated by the expression

$$n \approx \frac{4}{3} r_1^{1/2} E_2 \quad (4)$$

where  $r_1$  is the radius of the indenter and  $E_2$  is the modulus transverse to the fiber direction. By substituting (2) and (3) into (1) and integrating, the energy balance equation can be rewritten as

$$\frac{1}{2} M v^2 = \frac{1}{2} \frac{F_{\max}^2}{k} + \frac{2}{5} \frac{F_{\max}^{5/3}}{n^{2/3}} \quad (5)$$

Furthermore, the indentation and plate center deflection can be calculated through the use of (2) and (3) once  $F_{\max}$  is known.

### Force-Displacement Behavior During Impact

Instrumented impacters in falling-weight and pendulum impact tests can be used to record the contact force history. The force-displacement behavior can then be obtained by integration. Using this technique, numerous investigators have reported the contact force history and the force-displacement behavior for the impact of a composite plate [1,8-11]. A schematic of a typical force-time and force-displacement plot for a quasi-isotropic laminate with a brittle matrix is shown in Figure 1. As the impactor comes in contact with the plate, the contact force increases in a sinusoidal like manner with time and linearly with the displacement at the plate center. During quasi-static indentation tests, which have similar force-displacement plots, a crackling noise can often be heard during this phase of loading. The quasi-static indentation tests, however, do not have the small amplitude oscillations due to vibrations. Ultrasonic and microscopic inspections have revealed that matrix cracking and a small amount of delamination growth have occurred. As the force increases and a load,  $F_1$ , is reached, the force drops sharply indicating a sudden decrease in the transverse stiffness of the plate. This stiffness loss may be the result of large delamination growth. After the load drop, the contact force will increase further if the impactor has enough kinetic energy. A linear force-displacement behavior again develops where the slope after the load drop is less than the

slope prior to reaching  $F_i$ . Kwon and Sankar [8] have suggested that this linear relationship is the result of stable delamination growth. After the impactor begins to rebound, the force decreases until contact is lost. If force prediction methods do not account for the effect of damage, the predicted  $F_{MAX}$  will exceed the actual  $F_{MAX}$ . Investigators have reported a failure load,  $F_i$ , which was independent of impactor mass and velocity and of varying plate size and boundary conditions [1,8-11].

## Delamination Damage

Data from several studies [8,9,13] are analyzed to illustrate a method for predicting the maximum extent of delamination in moderately thick (0.34 - 0.70 cm) laminates. The diameter of the delaminated region, which was much larger than the contact region, was calculated in terms of the maximum contact force and the transverse shear force.

A study of impact damage in 0.70-cm-thick [45/0/-45/90]<sub>6s</sub> quasi-isotropic AS4/3501-6 and IM7/8551-7 composite laminates was conducted for static indentation and falling-weight impact tests [13]. The same indenter size (1.27-cm-diameter hemisphere) was used for all tests. The mass of the falling-weight impactor was 4.63 kg. The specimens in the static indentation tests were clamped over a 10.2-cm circular opening, whereas the specimens in the impact tests were clamped over a 12.7-cm square opening. The diameter of damage from C-scan images is plotted against impact force in Figures 2 and 3 for the AS4/3501-6 and IM7/8551-7 materials, respectively. The C-scan image depicts a cumulative planar measure of the extent of delamination. Open symbols indicate nonvisible surface damage, and filled symbols indicate visible surface damage. Initial damage was not evident on the surface. Cross-sections of some damaged specimens were examined, revealing that the damage in the contact area consisted of matrix cracks, delaminations, and broken fibers. The damage away from the contact area consisted of a combination of matrix cracks and delaminations which formed a spiral stair-case pattern involving 11 interfaces. This damage pattern was common to both the toughened (IM7/8551-7) and untoughened (AS4/3501-6) material systems. The maximum delamination diameter increased linearly with impact force for both material systems. The dashed lines represent a linear regression analysis through the origin. There was no significant difference in delamination diameter between the static and dynamic test methods for either material system.

Since there is a linear relationship between impact force and maximum delamination diameter, a constant value of transverse shear force can be associated with the delamination front. For circular isotropic plates, the shear force per unit length,  $V$ , is given by

$$V = \frac{F}{2 \pi r} \quad (6)$$

where  $F$  is the impact or contact force and  $r$  is a radial distance which is much greater than the contact radius,  $r_c$  (i.e.  $r \gg r_c$ ). This shear force expression (6) is also valid for rectangular plates where  $r$  is much greater than  $r_c$  and much less than the plate dimensions. Assuming Hertzian contact [6], the contact radius,  $r_c$ , can be calculated using the expression

$$r_c = \left( \frac{F r_i^{3/2}}{n} \right)^{1/3} \quad (7)$$

The transverse shear force,  $V^*$ , associated with the edge of the delamination can be calculated from the slope of the impact force - delamination diameter line by using the expression

$$V^* = \frac{F}{\pi d_0} \quad (8)$$

where  $d_0 = 2r$  is the maximum delamination diameter. The value of  $V^*$  for each regression line is shown. For the AS4/3501-6 data in Figure 2,  $V^*$  equals 72.1 kN/m, and for the IM7/8551-7 data in Figure 3,  $V^*$  equals 158 kN/m. For both materials, the experimental data is in good agreement with equation (8) after the delaminations have initiated. The maximum delamination diameter for a given impact force was not affected by plate size, shape, or the method of impact. The value of  $V^*$  and the contact force for delamination initiation and penetration are greater for the IM7/8551-7 than those for the AS4/3501-6 laminates. Thus, the toughened material shows superior impact resistance.

A study of impact damage [9] was conducted using a smaller 7.62- x 7.62-cm frame and an instrumented falling-weight impactor (2.74 kg) with a 1.27-cm diameter indenter. The impact specimens were 24- and 48-ply quasi-isotropic  $[-45/0/45/90]_{ns}$  laminates made of AS4/3501-6. The average thickness was 0.343 cm for the 24-ply laminates and 0.681 cm for 48-ply laminates. The results from that study are plotted in Figure 4 in the same manner as in the previous two figures. Again, a linear relationship existed between impact force and maximum delamination diameter for both the 24- and 48-ply laminates. The values of  $V^*$  computed by a linear regression for the 24- and 48-ply laminates were 40.7 and 80.2 kN/m, respectively. Also, for the 48-ply laminates, the values of  $V^*$  in Figures 2 and 4 were reasonably close (less than an 11% difference).

Another study of impact damage was reported in reference 8. In this study, both quasi-static indentation and instrumented pendulum impact tests were used. The impact specimens were 32-ply quasi-isotropic  $[0/45/90/-45]_{4s}$  laminates of AS4/3501-6. The average thickness of the laminates was 0.454 cm. The specimens were simply-supported over rings with diameters of 5.08, 7.62, and 10.2 cm. Two steel hemispherical indenters were used with diameters of 0.635 and 2.54 cm. The delamination diameter from the C-scans is plotted against impact force in Figure 5. When all of the data points are plotted together, a linear relationship is found between impact force and delamination diameter. This suggests that delamination away from the contact area is only a function of impact force and not of support diameter, indenter diameter, or method of impact. A value of  $V^* = 41.5$  kN/m was calculated using a linear regression. Equation (8) is in good agreement with the experimental data points.

The value of critical shear force,  $V^*$ , for each of the four experimental data sets is plotted against laminate thickness in Figure 6. Two curves are fitted through the data points corresponding to  $V^*$  being proportional to  $h$  or to  $h^{3/2}$  where  $h$  is laminate thickness. If  $V^*$  is proportional to  $h$ , then the delamination front can be associated with a constant value of the average transverse shear stress,  $S^* = V^*/h$ . For the data in Figure 6, a value of 10.8 MPa was calculated for  $S^*$  using a linear regression. This value of  $S^*$  is not an interlaminar shear strength since extending the delamination involves a complex interaction with matrix cracks. Hence, the delamination front is not in a state of pure shear. Also, this value of  $S^*$  is an order of magnitude less than the transverse shear strength of 124 MPa reported in reference 13 for AS4/3501-6. If the delamination front can be associated with a constant value of shear stress, then a single value of  $S^*$  may be used over a range of thicknesses as long as the material and layup sequence are kept constant. The other curve,  $V^*$  proportional to  $h^{3/2}$ , corresponds to the relationship between delamination length and thickness for an end-notched flexure specimen with constant  $G_{II}$  and applied load [14]. The three-point loading of the end-notched flexure specimen involves flexure similar to the transverse loading of a plate. Both relationships are in reasonable agreement with the data. Data over a wider range of  $h$  are required to determine the exact relationship between  $V^*$  and  $h$ .

## Dynamic Response

### The Impact Force Curve

Using a dynamic analysis program, force histories were generated for the impact of a 12.7- x 12.7-cm rectangular simply-supported quasi-isotropic plate. A few force histories at a kinetic energy of 13.6 J are shown in Figure 7. For large-mass impacts such as the 4.63-kg impact, the histories were composed of many small oscillations superimposed on the forced response. These oscillations in the force are due to the plate vibrating against the impactor during contact. For small-mass impacts such as the 0.025-kg impact, the contact duration was much shorter and the oscillations did not have time to develop. This type of response is typical of an impact from a fired projectile for a gas-gun impact test. For an impact with a mass of 0.30 kg, the force history was dominated by several large oscillations superimposed on the forced response.

A series of solutions was generated where the plate parameters were held constant, and the impactor mass and velocity were varied such that the kinetic energy remained constant. The peak contact force (referred to as impact force) from each of these runs was then plotted against the reciprocal of the impactor mass,  $M^{-1}$ , on a logarithmic scale for a given value of kinetic energy. The impact force curves at three kinetic energies for the impact of a 12.7- x 12.7-cm plate with simply-supported boundaries are shown in Figure 8. Moving to the right on a curve of constant kinetic energy corresponds to decreasing mass and increasing velocity. Approximately 20 runs were necessary to establish each impact force curve.

On the left side of the curve (large mass - low velocity), the contact duration is much longer than the time required for flexural waves to be reflected from the boundaries. It is the continual propagation and reflection of waves in the bounded plate that brings about a state of static equilibrium. During the long contact period, the flexural waves have time to propagate and reflect many times which results in a deformation mode approaching the static solution. Impact force predictions from an energy-balance analysis (eq. (4) - dashed lines) are also plotted for each kinetic energy on the figure for comparison. For large masses, the impact force approached the value predicted by the energy-balance analysis indicating a static deformation mode. In this region, the impact force is relatively constant over a range of masses and velocities at a given kinetic energy. On the right side of the curve (small mass - high velocity), the contact duration is very short. No oscillations occurred in the force history since there was insufficient time for flexural waves to reflect from the boundaries. The impact force was not independent of mass and velocity for a given kinetic energy in this region. A transitional region exists between the large-mass and small-mass region which is characterized by a force history that is dominated by a few large amplitude oscillations. Multiple contacts may also occur in this region. The impact force curve was divided into three regions (Figure 8) according to impact mechanics: static (large mass), transitional, and dynamic (small mass). These three regions are represented by the curves shown in Figure 7. For higher kinetic energies in Figure 8, the impact force curves shifted vertically, maintaining the same approximate structure. For large-mass impacts, the energy-balance analysis accurately predicted the increase of impact force with kinetic energy.

The variation of the impact force curve with changing boundary conditions and plate size is shown in Figure 9. Impact force curves for two small 12.7- x 12.7-cm plates with different boundary conditions (simply-supported and clamped) are shown. Also shown is the impact force curve for a larger 25.4- x 25.4-cm plate with simply-supported boundaries. For large-mass impacts (left side of curve), the impact force was larger for clamped boundaries than for simply-supported boundaries due to the increased transverse stiffness. Similarly, when the plate size was doubled, the impact force was less for the large-mass impact due to the decreased transverse stiffness. Also, a larger mass is required for the larger plate to deform in a static manner. This is indicated by the larger difference between the impact force for the energy-balance solution



and the impact force curve at very large masses. Quasi-static response only occurs when the impactor's mass is large and the size of the target is relatively small. During the long contact period associated with large-mass impacts, the flexural waves have time to propagate and reflect many times which results in a deformation mode approaching the static solution. However, if the plate is large, the flexural waves take much longer to reflect from the boundaries, and the deformation mode diverges from the static mode. Consequently, the impactor mass must be extremely large to ensure a contact duration long enough for the waves to reflect many times for large plates. Therefore, a static deformation mode will not develop for the impact of large plates and structures except for very large mass impactors. This failure to respond quasi-statically was also observed for the impact of large rings by very large masses [3].

For small-mass (high-velocity) impacts, the three curves converged which indicates that the impact force is independent of boundary conditions and plate size. The small difference between the curves reflects the inaccuracies of the modeling and differences between the computer codes. The convergence of the curves is due to the fact that the flexural waves do not have time to reflect from the boundaries before the peak contact force occurs. Consequently, a specific impactor mass and velocity combination will result in the same impact force regardless of plate size or boundary conditions as long as the impact response is of the dynamic type. The large plate enters the dynamic response region the earliest since the flexural waves take the longest time to reflect from the boundaries.

### Transverse Shear Force

The transverse shear force history during impact was calculated at a point 3.18 cm from the center of a 12.7- x 12.7-cm simply-supported plate. The 3.18-cm distance corresponds to the larger delamination diameters in Figures 2-5. It is also much greater than the contact diameter, eliminating the influence of the contact stresses. The finite element code was used to calculate the impact response for a range of impactor masses and velocities at two kinetic energies. The maximum shear force was normalized by the static shear force calculated for the peak contact force. This normalized shear force was then plotted against the log of the reciprocal of the impactor mass,  $\log(M^{-1})$ , to create curves for impacts of the same kinetic energy similar to the impact force curves. Figure 10 shows two shear force curves for impact energies of 13.6 and 20.3 J. Since the normalized shear force was greater than unity for all masses, the shear force increased at a faster rate than the impact force. The difference between the static and dynamic shear forces was greatest, in general, for the smaller masses. However, the shear force was within 10% of the static shear force up to  $m^{-1} = 1.6 \text{ kg}^{-1}$  (masses greater than 0.63 kg). Consequently, a static analysis, such as equation (6), should be adequate to obtain the transverse shear force for impacts in the large-mass region. In the small-mass region, however, the plate stresses and deformations tend to reach maximum values after the contact period is over. At the maximum values, the plate stresses and deformations may even be in the opposite direction of those in the static case. This phenomenon is due to the complex nature of wave propagation and reflection. The treatment of these stresses is beyond the scope of this paper.

Similar curves of normalized shear force, at a point 3.175 cm from the plate center, versus  $M^{-1}$  are plotted in Figure 11 for the impact of a 12.7- x 12.7-cm clamped plate and for a larger 25.4- x 25.4-cm simply-supported plate. Again, the shear force for the smaller two plates was within 10% of the values predicted by a static analysis for impacts in the large-mass region. However, the dynamic shear force for the large plate was more than 25% greater than the predicted static value which indicates that the large plate is not deforming in a static manner.

## Maximum Delamination Diameter

For 48-ply AS4/3501-6 plates, the diameter of delaminations was computed using an energy balance, equation (4), and the critical transverse shear force, equation (8). The results, which are applicable to large-mass impacts, are shown in Figure 12 for two values of kinetic energy, two plate sizes, two thicknesses, and for clamped and simply-supported edges. The quasi-isotropic plates were 24- or 48-ply thick, and the hemispherical indenter diameter was 1.27 cm. The critical values of the transverse shear force,  $V^*$ , were 40.7 and 72.1 kN/m for the 24- and 48-ply laminates, respectively. The predicted value of impact force is shown above each bar. For a given plate thickness, the maximum delamination diameter increased in proportion to impact force after delamination initiated. For a given value of kinetic energy, the impact force and hence maximum delamination diameter depend strongly on plate size, plate thickness, and boundary conditions for large-mass (low-velocity) impacts.

## Design Allowables from Coupon Tests

### Kinetic Energy as an Impact Parameter

For large impactor masses (low velocities) and a fixed value of kinetic energy, the analyses show that delamination damage does not vary with mass and velocity but does vary with transverse plate stiffness which is a function of plate size and boundary conditions. However, for maximum delamination diameter not to vary with mass and velocity for large plates, the mass must be much larger than for small plates. Thus, impact test results can be compared in terms of kinetic energy only when the impactor mass is large and the plates are small and have the same transverse stiffness. For small impactor masses (high velocities), on the other hand, the impact force and hence the stresses do vary with mass and velocity when kinetic energy is a constant. Therefore, kinetic energy cannot be used in general as a parameter to compare impact damage or to predict impact damage in structures from coupon tests.

### Impact Force as an Impact Parameter

When impact force is a constant and impactor mass is large, the analyses show that the maximum delamination diameter does not vary with mass and velocity nor with plate size and boundary conditions. Therefore, impact force can be used as a parameter to compare impact damage or to predict impact damage in structures from coupon tests. However, the maximum extent of delaminations must be some minimum distance from the coupon boundary and from any hard point, reinforcement, or boundary of the structure. Impact forces are routinely measured in falling-weight tests using instrumented impactors and hence are available from experiments. Impact forces can also be predicted from kinetic energy for small plates using a static analysis with a simple energy balance equation. Of course, such predictions overestimate the actual impact force when significant damage develops.

For small impactor masses (high velocities), on the other hand, the transverse shear force does vary with mass and velocity when impact force is a constant, and impact force cannot be used as a parameter to compare impact damage or to predict impact damage in structures from coupon tests. Perhaps, only plate stresses can be used in this regime. At this time, no convenient methods for measuring impact force and transverse shear force have been reported for small impactor masses like those in gas gun tests. Such a capability would assist in verifying the analyses.

## Nonvisible Damage as an Impact Parameter

As shown in the previous sections, the use of kinetic energy and impact force as impact parameters does have disadvantages. On the other hand, the use of a level of visible or nonvisible damage may eliminate the need for a dynamic analysis and the measurement of impact force or stresses. In this case, the residual strength could be determined for a certain level of visible or nonvisible damage, irrespective of kinetic energy or impact force. The maximum level of visible impact damage would be that level that is unlikely to be overlooked. Conversely, the minimum level of visible impact damage would be that level that is likely to be overlooked. Some metric for visibility like residual impression depth should be used to reduce subjectivity. For example, the United States Air Force currently defines visible damage as a 0.254-cm-deep dent [15], and Hercules demonstrated that 0.013-cm-deep depressions could be found reliably in a thick filament-wound rocket motor case [16]. Additional work needs to be done to determine the effect of impactor shape and laminate thickness on nonvisible damage.

## Concluding Remarks

Dynamic analyses were made of simple plates to calculate time histories of contact force and transverse shear force. Impactor mass and velocity and plate configuration were varied. Experimental data for quasi-isotropic laminates 0.35- to 0.70-cm thick were analyzed to determine a method for predicting delamination damage size in terms of transverse shear force. The experimental data were from falling weight and pendulum impact tests and static indentation tests. The effects of impactor and plate parameters on maximum size of delamination damage were calculated using predicted values of transverse shear force.

For large-mass (low-velocity) impacts of a given kinetic energy, the dynamic analyses indicated that the impact force (peak contact force) decreases with increasing plate size and is smaller for simply-supported plates than clamped plates. Also, impact force can be predicted using simple energy-balance equations, and transverse shear force can be predicted using a static solution. However, the mass must increase with increasing plate size in order for this static representation to remain valid. The large-mass impact tests and static indentation tests indicate that delamination damage which corresponds to a constant value of transverse shear force,  $V^*$ , at the delamination front increased in proportion to impact force. The critical shear force,  $V^*$ , increased approximately in proportion to thickness. For a constant value of  $V^*$  and kinetic energy, the dynamic analyses indicate that the size of delamination damage will decrease with increasing plate size and will be smaller for simply-supported plates than clamped plates. However, for a given impact force, size of delamination damage will be independent of plate configuration. Therefore, for large-mass (low-velocity) impacts, only impact force can be used as a sole parameter to predict the maximum size of delamination damage in simple plates or structures from that in coupons.

For small mass (high-velocity) impact, the dynamic analyses indicate that impact force increases with decreasing mass for a given plate configuration and a given value of kinetic energy and that the transverse shear force cannot be represented by static values. Furthermore, the peak shear force may occur after contact and may even be of the opposite sense as that of the static solution. Therefore, for small mass (high-velocity) impacts, neither kinetic energy nor impact force can be used as a sole parameter to predict the size of delamination damage.

## References

1. Byers, B. A.: Behavior of Damaged Graphite/Epoxy Laminates Under Compression Loading. NASA CR-159293, August 1980.
2. Rhodes, M. D.: Impact Tests on Fibrous Composite Sandwich Structures. NASA TM-78719, October 1978.
3. Poe, C. C., Jr.: Summary of a Study to Determine Low-Velocity Impact Damage and Residual Tension Strength for a Thick Graphite/Epoxy Motor Case. NASA TM-102678, June 1990.
4. Sankar, B. V.: A Modified Green's Function for Computing Structural Response due to Low-Velocity Impact. Technical Report No. AeMES-TR-1-36, Department of Aerospace Engineering, Mechanics & Engineering Science, University of Florida, October 1990.
5. Chen, J. K. and Sun, C. T.: Analysis of Impact Response of Initially Stressed and Buckled Composite Laminates. Tech. Report CML 84-6, Purdue University, April 1984.
6. Greszczuk, L. B.: Damage in Composite Materials Due to Low Velocity Impact. Impact Dynamics, edited by L. A. Zukas et al., John Wiley & Sons, New York, 1982, p. 55.
7. Sun, C. T.: An Analytical Method for Evaluation of Impact Damage Energy of Laminated Composites. Composite Materials: Testing and Design, ASTM STP 617, American Society for Testing Materials, 1977, pp. 427-440.
8. Kwon, Y. S. and Sankar, B. V.: Indentation-Flexure Damage in Graphite/Epoxy Laminates. NASA CR-187624, 1991.
9. Srinivasan, K., Jackson, W. C., and Hinkley, J. A.: Response of Composite Materials to Low Velocity Impact. NASA TM-102755, January 1991.
10. Sjöblom, P. O., Hartness, J. T., and Cordell, T. M.: On Low-Velocity Impact Testing of Composite Materials. Journal of Composite Materials, Vol. 22, January 1988, pp. 30-52.
11. Sjöblom, P. O.: Simple Design Approach Against Low-Velocity Impact Damage. Proceedings of the 32nd International SAMPE Symposium, April 6-9, 1987, pp. 529-539.
12. Poe, C. C., Jr.; Portanova, M. A.; Masters, J. E.; Sankar, B. V.; and Jackson, W. C.: Comparison of Impact Results for Several Polymeric Composites over a Wide Range of Low Impact Velocities. NASA CP-3104, 1990.
13. Sun, C. T., and Kelly, S. R.: Failure in Composite Angle Structures, Part: I, Initial Failure. J. of Reinforced Plastics and Composites, Vol. 7, May 1988, pp. 220-232.
14. Russell, A. J.: On the Measurement of Mode II Interlaminar Fracture Energies. Defense Research Establishment Pacific (DREP), Victoria, British Columbia, Canada, Materials Report 82-0, Dec. 1982.
15. Lincoln, J.: Certification of Composites for Aircraft. NASA CP-10075, March 1991, pp. 401-420.
16. Madsen, C. B., Morgan, M. E., and Nuismer, R. J.: Impacting Large Composite Structures and Scaling Impact Response and Damage. NASA CP 10075, March 1991, pp. 27-78.

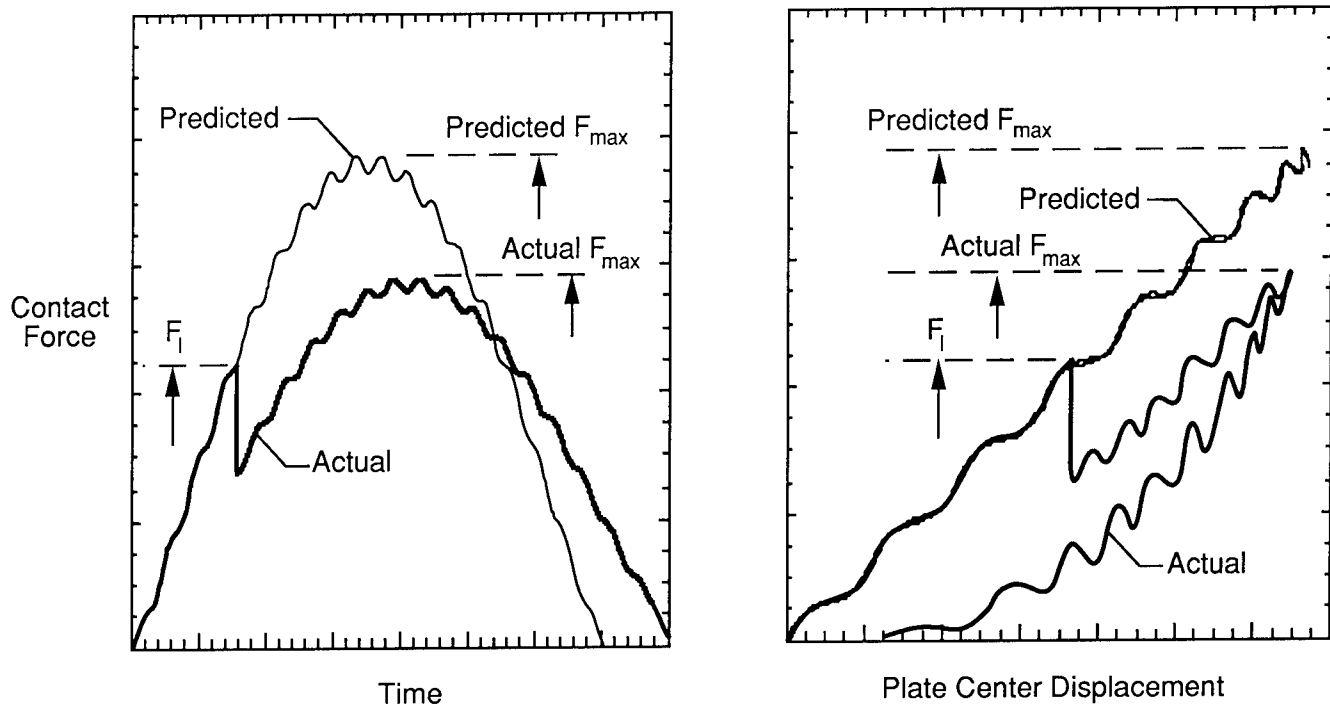


Figure 1. Schematic of a typical force-time and force-displacement plot.

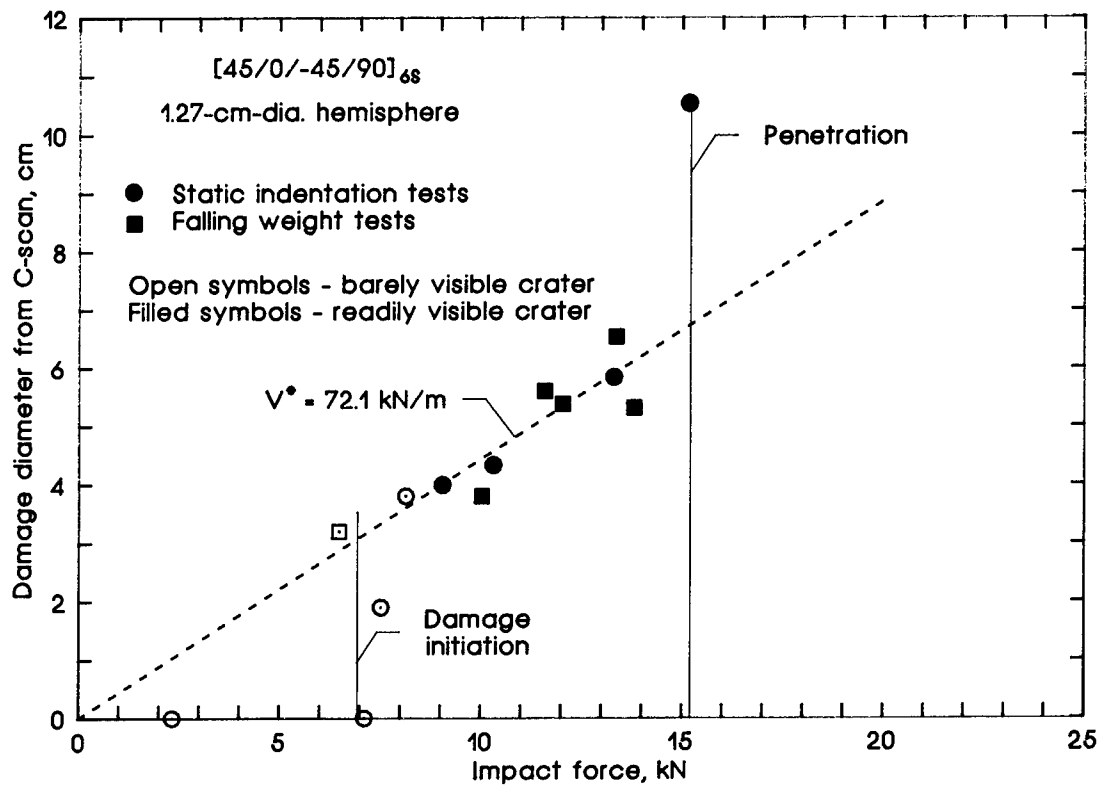


Figure 2.- Damage diameter versus impact force for 48-ply quasi-isotropic AS4/3501-6 laminates.

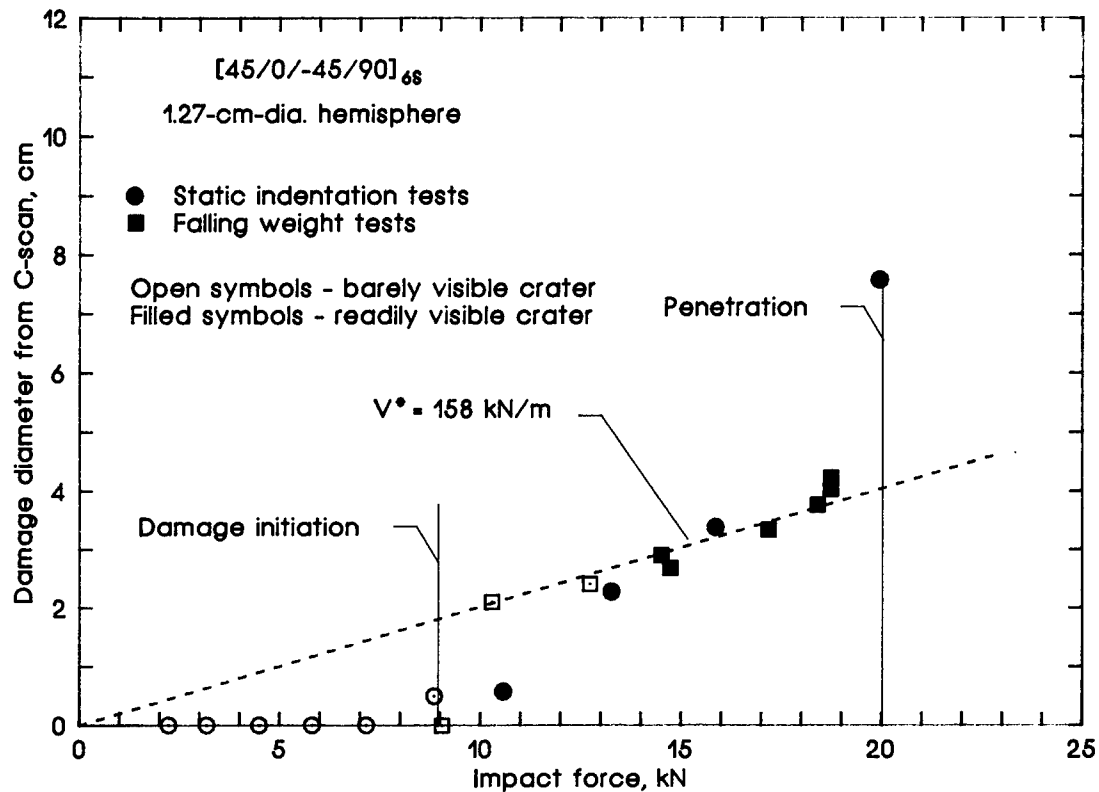


Figure 3.- Damage diameter versus impact force for 48-ply quasi-isotropic IM7/8551-7 laminates.

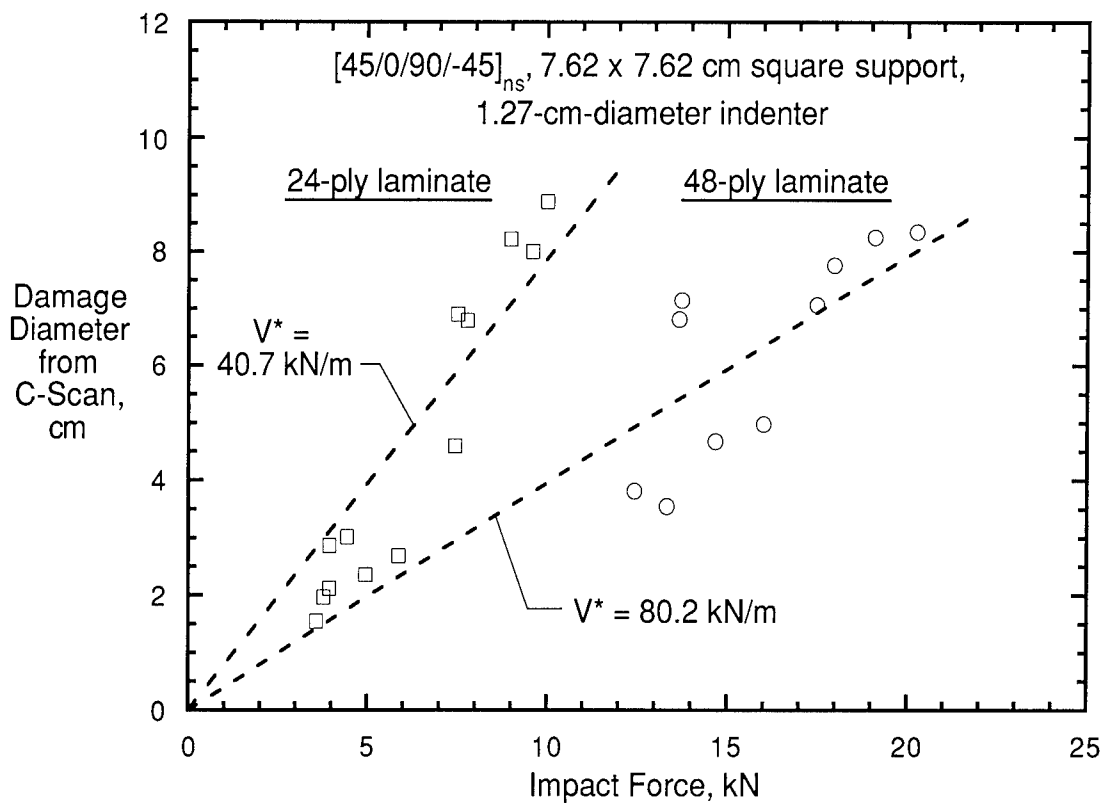


Figure 4. Delamination diameter versus impact force for 24- and 48-ply quasi-isotropic AS4/3501-6 laminates.

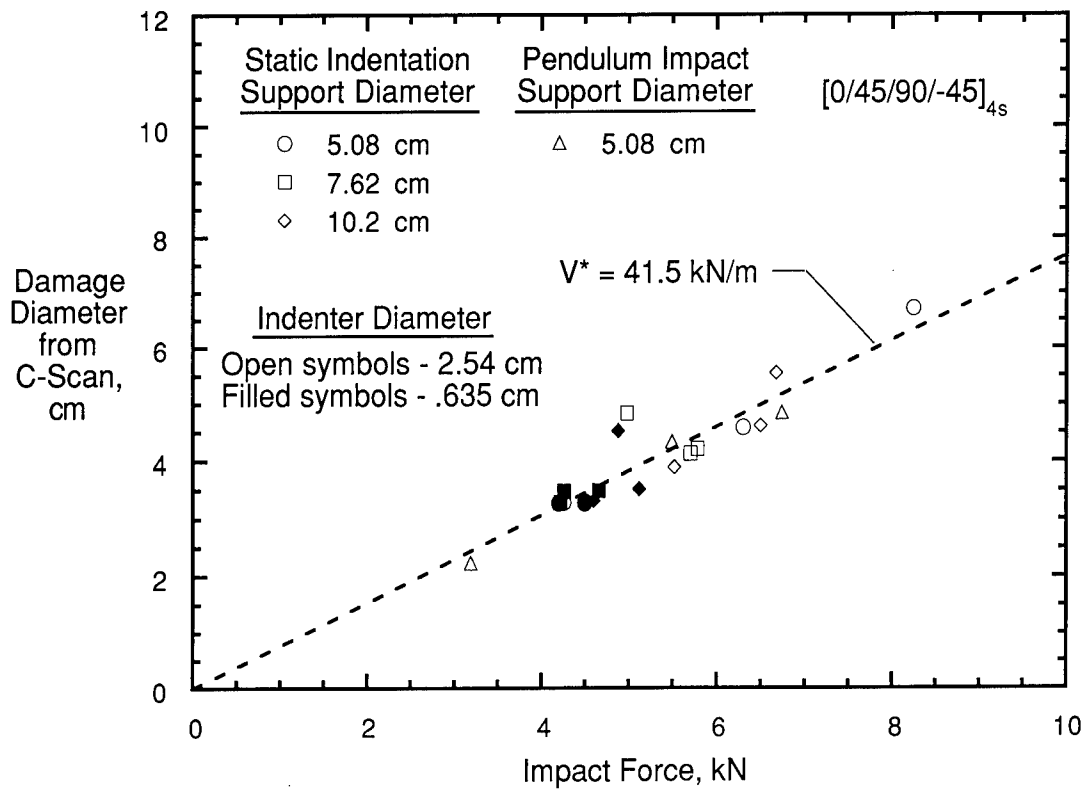


Figure 5. Delamination diameter versus impact force for 32-ply quasi-isotropic AS4/3501-6 laminates.

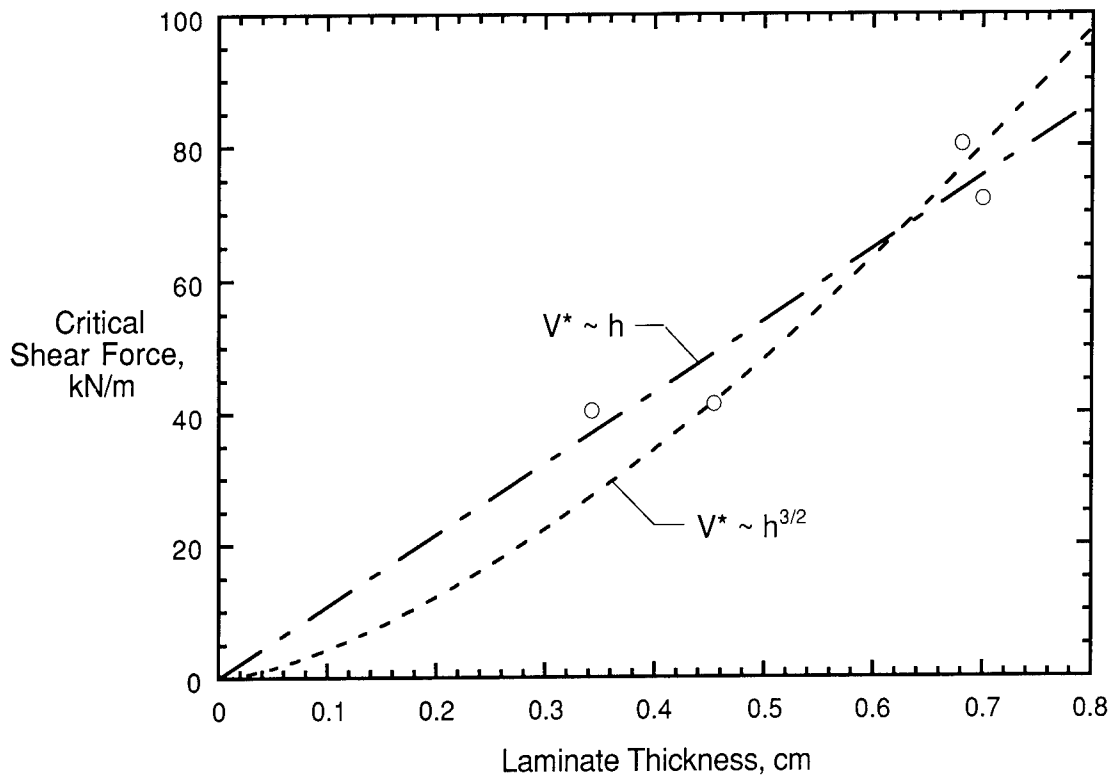


Figure 6. Effect of laminate thickness on the critical transverse shear force.

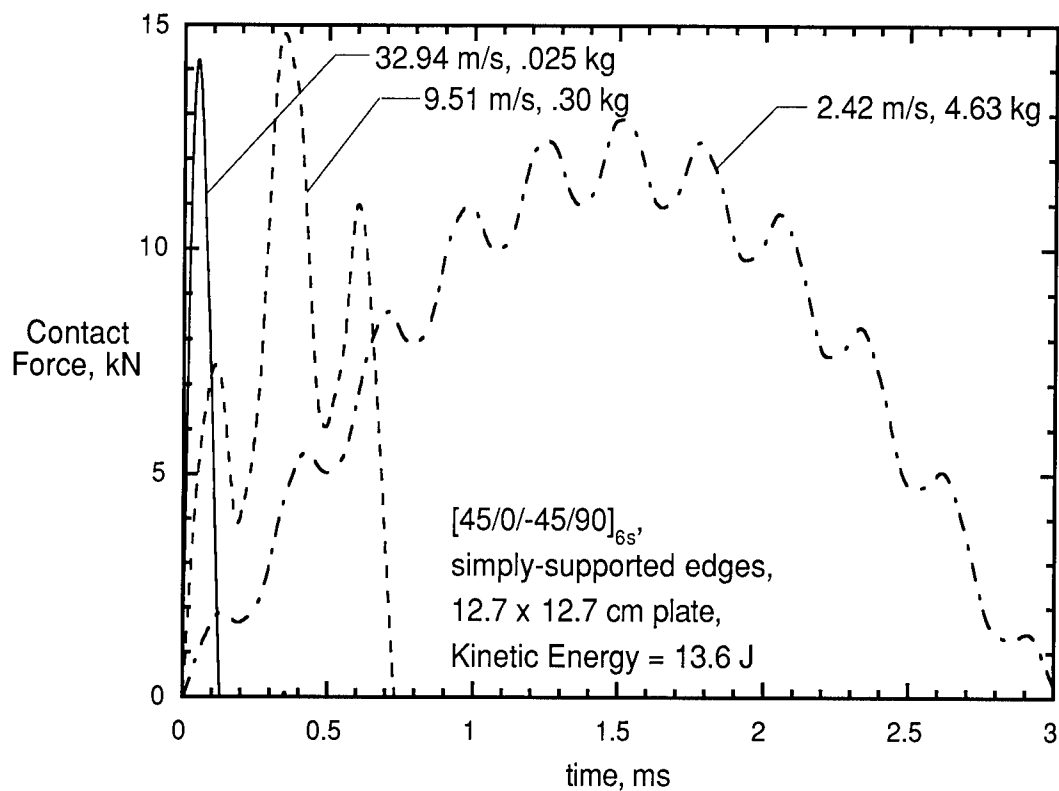


Figure 7. Predicted contact force history for several impactor mass and velocity combinations at 13.6 J.

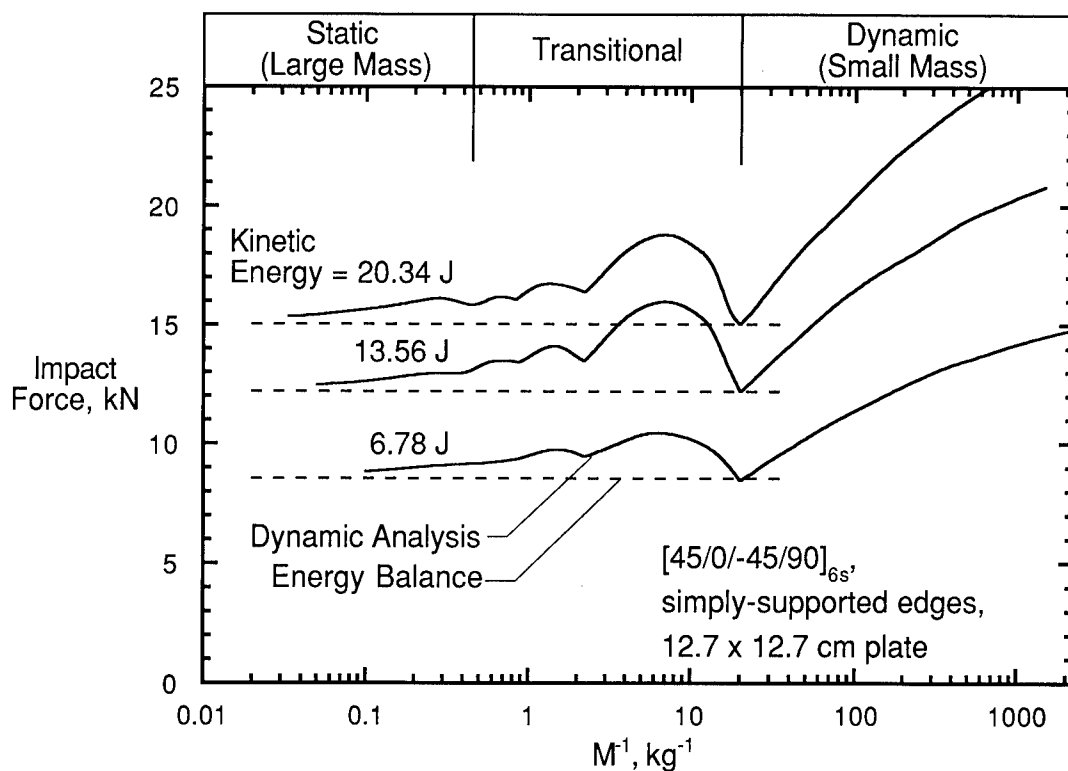


Figure 8. Predicted impact force versus impactor mass at constant kinetic energies.



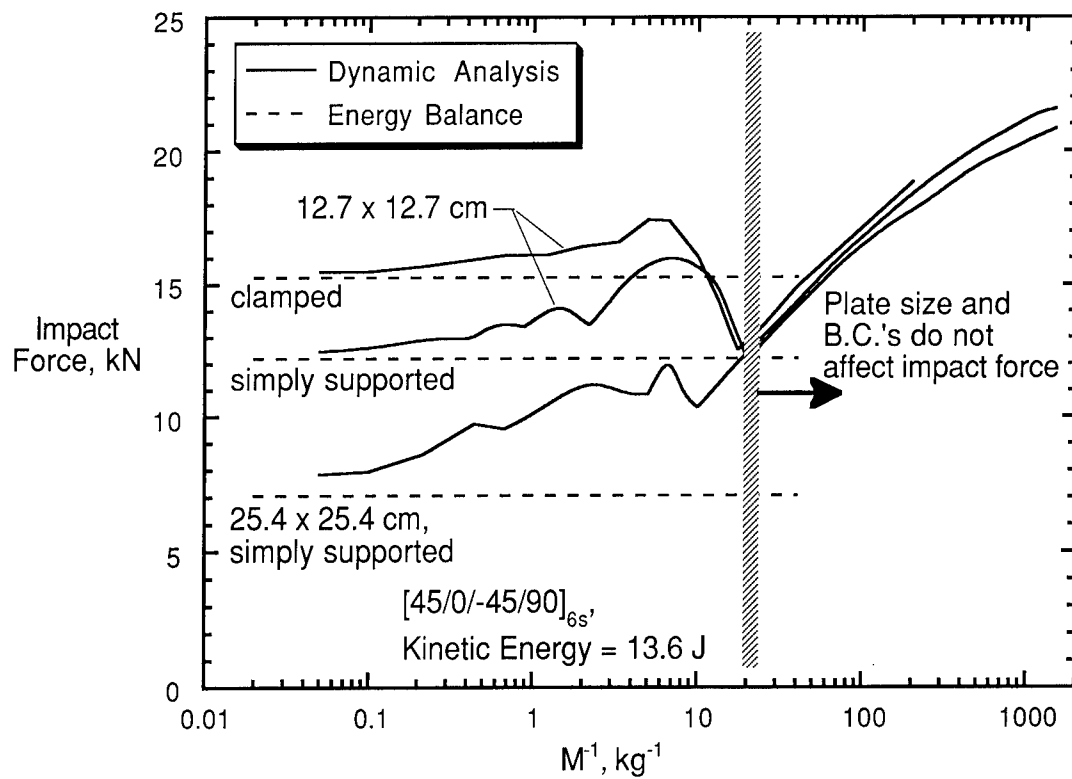


Figure 9. Impact force versus  $M^{-1}$  for various plate sizes and boundary conditions.

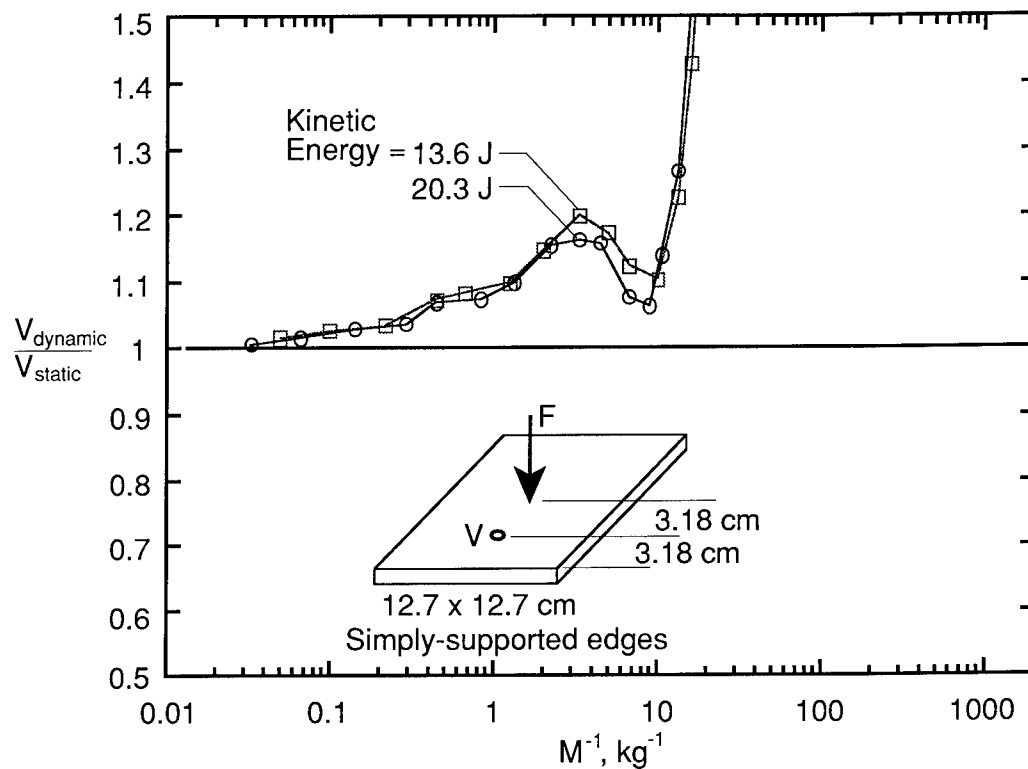


Figure 10. Normalized shear force versus  $M^{-1}$  for an impact with a kinetic energy of 13.6 and 20.3 J.

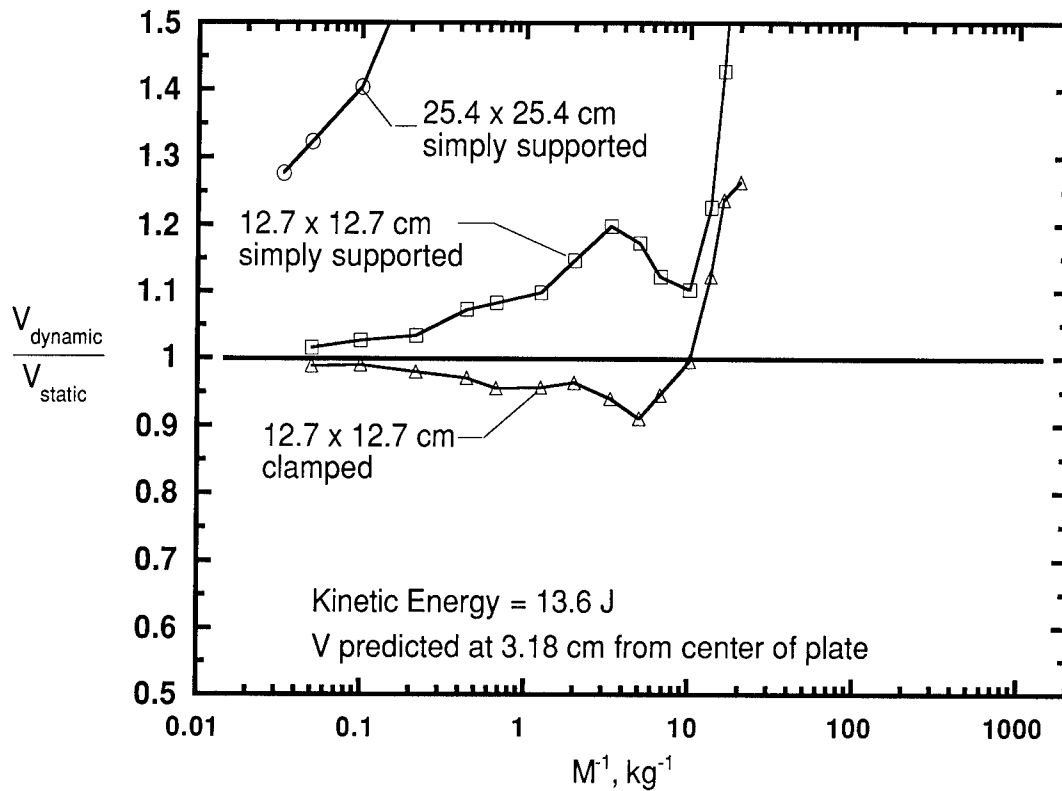


Figure 11. Normalized shear force versus  $M^{-1}$  for impacts of plates of various sizes and boundary conditions.

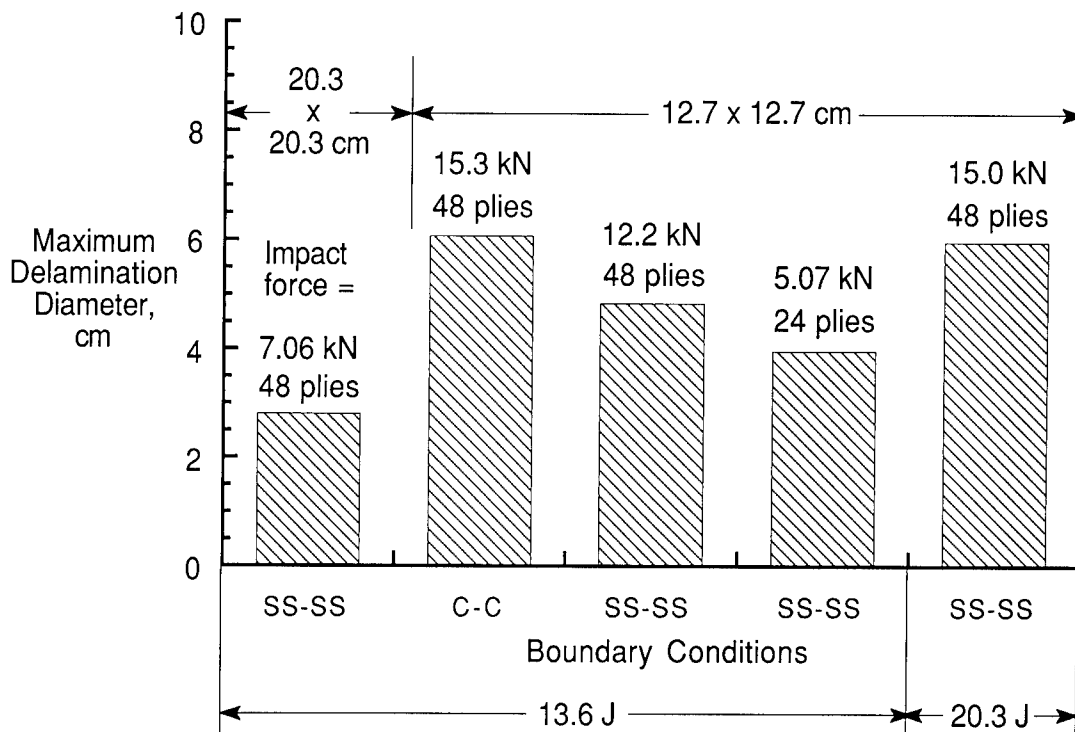


Figure 12. Predicted delamination diameters for two kinetic energies, two plate sizes, two thicknesses, and for clamped and simply-supported edges.

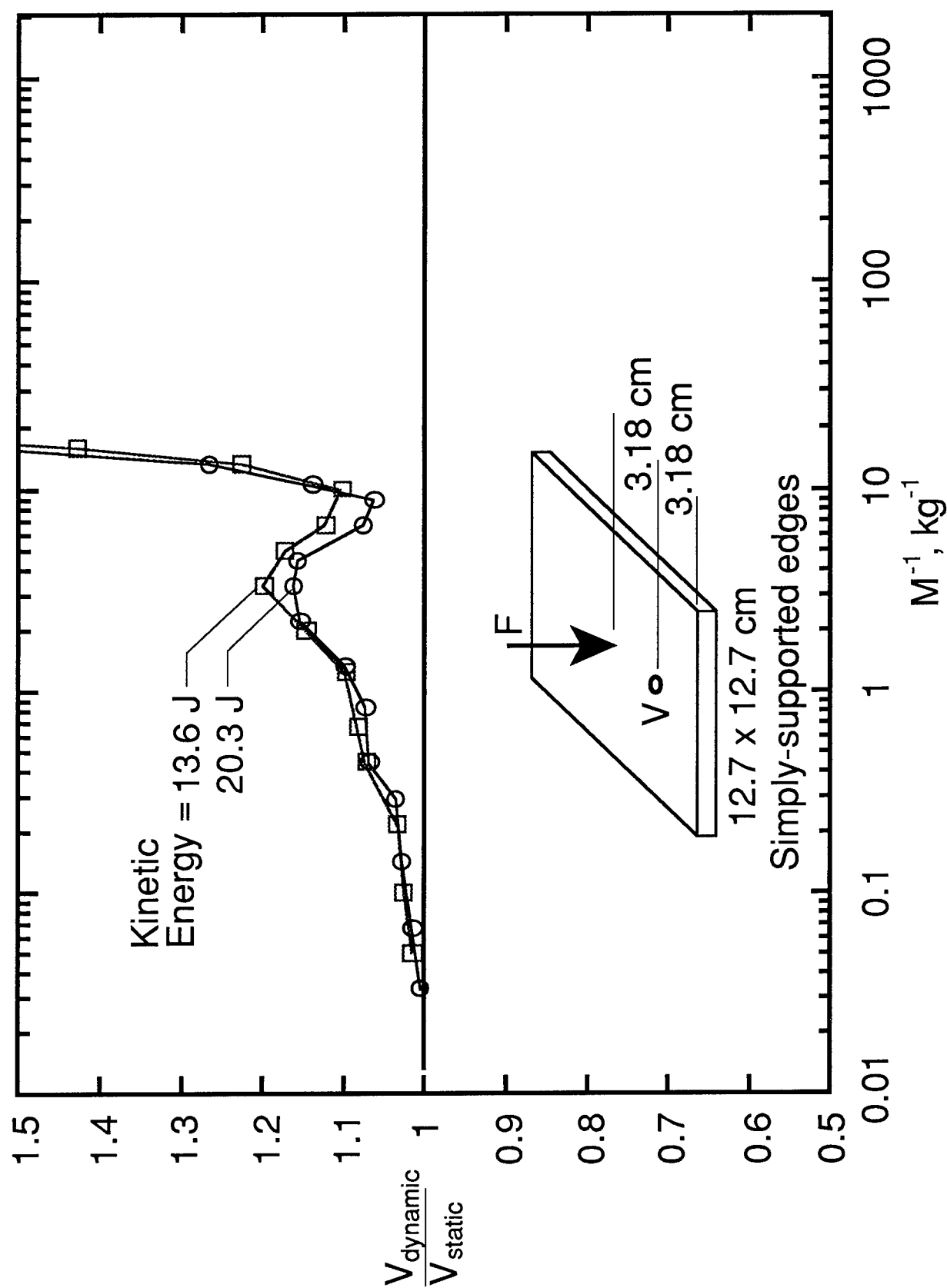


Figure 10. Normalized shear force versus  $M^{-1}$  for an impact with a kinetic energy of 13.6 and 20.3 J.

## **Application of Damage Tolerance Methodology in Certification of the Piaggio P-180 Avanti**

**Jerry Johnson  
Dow-United Technologies Composite Products, Inc.  
Wallingford, CT**

### **ABSTRACT**

The Piaggio P-180 Avanti, a twin pusher-prop engine nine-passenger business aircraft was certified in 1990, to the requirements of FAR Part 23 and Associated Special Conditions for Composite Structure.

Certification included the application of a damage tolerant methodology to the design of the composite forward wing and empennage (vertical fin, horizontal stabilizer, tailcone and rudder) structure. This methodology included an extensive analytical evaluation coupled with sub-component and full-scale testing of the structure.

The work from the Damage Tolerance Analysis Assessment was incorporated into the full-scale testing. Damage representing hazards such as dropped tools, ground equipment, handling, and runway debris, was applied to the test articles. Additional substantiation included allowing manufacturing discrepancies to exist unrepaired on the full-scale articles and simulated bondline failures in critical elements.

The importance of full-scale testing in the critical environmental conditions and the application of critical damage are addressed. The implication of damage tolerance on static and fatigue testing is discussed. Good correlation between finite element solutions and experimental test data was observed.

### **INTRODUCTION**

Advancements in the use of composites as an improved performance material in primary aircraft structure has been steadily increasing. The primary advantages of composites usage include improved fatigue life and corrosion resistance, as well as lower weight. Several business/commuter FAR 23 aircraft have been certified with composite primary structure, as well as FAR 25 transport aircraft such as the Airbus A320 and the ATR 72. The Piaggio P-180 Avanti Program is an example of a FAR 23 aircraft with extensive use of composite primary structure.

Figure 1 illustrates the composite structural components on the P-180. As the industry moves forward into the twenty-first century, composites usage will increase dramatically on aircraft like the Boeing 777/787 and the McDonnell-Douglas MD12X.

To date, all aircraft have been certified to their requisite FARs in addition to a series of Special Conditions which apply directly to the extensive use of the composites in the airframe design. Although there are different certification criteria applied to each category of aircraft, the criteria for use of primary composite structure have one aspect in common: they involve the application of a damage tolerance methodology.

## **DAMAGE TOLERANCE**

Damage Tolerance is basically the application of known damage threats to the aircraft structure during its typical lifetime usage and demonstration that this damage does not alter the safe operation of the aircraft. Failsafe Analysis should not be confused with Damage Tolerance because it deals with demonstrating adequate redundancy with critical load paths severed or incapacitated. Natural threats include runway debris, lightning strike, engine wash, bird strike, or even hail. Accidental threats typically encompass dropped objects such as tools, aircraft parts, luggage/cargo, or other maintenance related damage such as saw cuts or punctures.

These types of damages can be further quantified into the potential level of damage caused as a result of the incident. Threats which cause barely visible impact damage (BVID) may not be easily recognized and therefore not usually repaired. The application of larger threats causes visible or highly visible impact damage (VID) which would typically be repaired when discovered. Since BVID may not be easily detected, and repaired, the aircraft structure must be capable of ultimate and repeated loads, with BVID. VID is repaired but since there may be some time before the structure is inspected, aircraft structure must be capable of limit and repeated loads, with VID.

Damage threats may also exist in the form of manufacturing defects such as: cut or missing laminate plies, bondline voids or cured laminate voids (delaminations/porosity). These defects must also be evaluated in the design of composite aircraft primary structure.

Finally, the environmental effects on composite structure must also be considered in conjunction with the application of damage tolerance since material behavior is typically affected by the environment.

## **DAMAGE IDENTIFICATION AND EVALUATION**

In the case of the Piaggio P-180 program, the application of damage tolerance can be separated into three distinct phases:

1. The identification and susceptibility of perceived threats.
2. An analytical evaluation of the effect of damage threats.
3. Test evaluation of the structure including the damage threats.

By nature of composite structure design, the aircraft structure is inherently damage tolerant. Most primary composite structure is designed to a strain cut-off value indicative of the most critical environment and strength property. Additionally, the use of composite laminate analysis programs in most applications assumes part failure after one lamina ply has failed ("first ply failure").

In the identification and susceptibility analysis phase of the damage tolerance program, potential damage from any outside source was considered. The potential types of damage for the Piaggio P-180 program are tabulated in Figures 2 and 3. The types of damage can be separated into two categories: 1) Manufacturing Damage and 2) Flight Operational Damage.

Manufacturing damage was typically evaluated analytically. The analytical substantiation included a damage tolerance analysis assessment which consisted of Hazard Analysis, Damage Susceptibility Evaluations and Failure Mode Analysis. The Hazard Analysis was performed to identify and quantify the frequency and severity of the probable hazards to which the aircraft was expected to be exposed to during its service lifetime. Impact tests were performed on actual structure to quantify the levels of damage experienced from the probable hazard (Damage Susceptibility Evaluation). An analytical evaluation of potential failure modes, caused by both manufacturing defects and in-service damage, was conducted using the NASTRAN finite element model. Damage was represented in the finite element model by either removal of specific elements or removal of laminate plies in the material property cards. Strength checks were made for the new load distributions as a result of damage.

Flight operational damage, typically in the form of impacts and punctures to the aircraft structure, was analytically modelled as missing NASTRAN elements. In this case, damage representing BVID was applied to ultimate load and VID was applied at limit load.

Other analytical substantiation work included evaluating "fail-safe" design features by removing critical elements and showing load redistribution within the remaining structure, with positive margin of safety at limit load.

## **CERTIFICATION TESTING**

Usually, in a typical damage tolerance program, the testing phases of a "building-block" approach divide into coupon testing, followed by larger scale element testing, and concluding with the full-scale testing. This method is used to adequately evaluate all "unknowns and structural concerns" so surprises do not occur during the final full-scale testing phase. The "building-block" approach is not a specific FAA requirement. The original P-180 composite structure certification program included the "building-block" approach. However, after completion of the coupon testing phase, the certification program was changed to emphasize the full-scale testing.

With the changes in the certification testing, the program was re-scoped to include environmental condition of the full-scale test article. The testing of fully-saturated structure eliminates many of the analysis headaches associated with trying to correlate RTD predictions to RTD testing results and substantiating the ETW predictions by the coupon and element testing at their critical environments. The revised testing program is summarized in Figure 4.

## **FATIGUE TEST SPECTRUM**

The original fatigue spectrum proposed by Piaggio to the certification authorities was based on a FAR 25 transport category spectrum. This was not accepted because most FAR 23 aircraft fly in a more rigorous spectrum than a 767 flight from New York to Los Angeles, for example. The spectrum was revised to take into account the work NASA had developed from actual flying time in other FAR 23 aircraft. The resulting spectrum increased the numbers of take-offs and landings and increased the "G-loadings" and frequencies on many of the flight maneuvers.

The next issue to tackle was how to convert the fatigue spectrum into a full-scale test spectrum. The problem was that the aircraft was designed with a metal fuselage and wing structure and a composite canard and empennage. In metal aircraft structure, loads typically in excess of 60-

70% limit load are clipped from the spectra. This is due to the plastic behavior of metals where high loads tend to blunt the tip of any fatigue crack that may be growing as a result of the applied loads. Composites are more brittle and are affected by high end loads. Contrary to the behavior of metals, composite spectra include the high end loads but truncate the low end loads, since loads typically around 30% of limit load show no effect on the fatigue life. An example of an S/N curve for metals and for composites is depicted in Figure 5.

The composite forward wing and empennage also included several metal fittings. For FAR 23 aircraft, a fatigue analysis can be used for metal parts in lieu of testing if a life scatter factor of 8 is applied to the analysis. This analysis coupled with fail-safe redundancy features in the fitting designs was sufficient to certify the metal fittings. Therefore, a composite derived spectrum could be applied to the empennage and forward wing tests, since the fittings were certified by other means.

Using in-house coupon test data and other published literature, a truncation level of 35% of limit load was established for all the P-180 composite structures. The resulting test spectra included all high end lift loads up to and including limit load.

## **FULL-SCALE STATIC AND REPEATED LOADS TESTING**

The prototype flight articles as well as the structural test articles were fabricated in Sikorsky Aircraft's Composite Development Center. The only difference between the flight and test articles was that a higher level of manufacturing flaws were permitted on the test articles. These flaws were documented in inspection reports, and eventually allowed the inspection criteria to be updated after successful completion of all certification testing. Other flaws, in the form of simulated adhesive bondline delaminations were also introduced in the manufacturing sequence.

The manufacturing "tool-proof" articles were utilized to perform the impact testing evaluation to help distinguish between Barely Visible Impact Damage (BVID) and Visible Impact Damage (VID), and the associated energy levels and impactor geometries. BVID was considered to be at the threshold of detectability where the damage could be seen with an unaided eye at a distance of approximately 2 feet. Prior to any static testing, all BVID was applied to all the test articles. The different types of BVID are tabulated in Figure 6.

Prior to clearance of the flight test airplanes, it was necessary to successfully demonstrate Room Temperature Dry (RTD) static ultimate load. There were some initial surprises in the static



testing. The forward wing failed prematurely at 120% limit load, due to the honeycomb core being installed in the wrong ribbon direction. Another test article, with the core in the correct ribbon direction, successfully demonstrated ultimate load-RTD. There was also some "teething" problems with the empennage static test. The tailcone skins, which were designed to post-buckle above limit load, started buckling at about 90% limit load. A repair was made to the skin, and the test article made it to 120% limit load where the buckled skins caused a bulkhead to buckle and fail. The tailcone design was then changed to be shear resistant to ultimate load.

A revised design empennage assembly then successfully demonstrated RTD ultimate load with BVID. Flight testing of the aircraft was allowed to commence. All BVID on the test articles was re-measured to insure that no flaw growth had occurred during ultimate load. The test articles were then disassembled and placed into environmental conditioning chambers. The chambers were heated to 180°F and 87% relative humidity (RH) to accelerate environmental conditioning. Rider coupons representative of the thinnest and thickest laminate were periodically weighted until all specimens showed a minimum moisture uptake of 1.1% (considered saturated based upon using Fick's Law of moisture absorption).

After environmental conditioning was complete, the test articles were loaded back into the test frames. Environment tents were placed around the test structure and the test environment was brought up to 160-180°F and 82-87% RH. A life time of repeated loads was applied to the test articles. One lifetime represented 30,000 flight hours and the spectrum loads were applied in blocks of 3000 hours, with inspection at the end of each block. At the conclusion of the 30,000 equivalent flight hours of repeated loads testing, the structures were loaded back up to ultimate load at elevated temperature wet environment. Both the forward wing and empennage successfully demonstrated ETW ultimate load with no evidence of growth from the BVID.

### **FULL-SCALE DAMAGE TOLERANCE TESTING**

After careful inspection of all the structure, VID was then applied. The types of VID imposed on the test articles is tabulated in Figure 6. The VID was instrumented with strain gauges and acoustic emission sensors. Other types of damage in the form of skin cuts/tears were applied prior to commencement of damage tolerance testing. These particular locations had been selected using the finite element model output, and were indicative of the most highly loaded external structure. Skin tears/cuts were considered to be highly visible between .5 and .75 inches depending on the applicable structure. Like the VID, the skin tears were instrumented for close monitoring throughout damage tolerance testing. Skin tear damage areas are tabulated in Figure 7.

The damage tolerance testing was relatively uneventful for the VID and skin tears. All impacts and cuts were periodically inspected every 9000 equivalent flight hours, and no evidence of flaw growth was experienced. There were instances where adhesive bondlines would make noise which was picked up by adjacent AE sensors. The bondline noise was believed to be the result of the brittle behavior of the adhesive and cracks may have initiated due to previous static ultimate and fatigue testing. Since all the joints were designed with fasteners carrying ultimate load, no attempt was made to repair bondlines, and they were passively monitored.

At the conclusion of damage tolerance testing, the test articles were successfully loaded to ETW limit load to demonstrate residual strength after two lifetimes. The residual strength demonstration was conducted to comply with the FAR Special Conditions, even though the structure had seen ETW limit load three additional times during each lifetime. All VID and skin cuts were re-inspected and again no evidence of flaw growth had appeared.

Following damage tolerance testing, Severe Damage Demonstrations were conducted to further determine the damage tolerance of the structure as designed. More skin cuts/tears, as tabulated in Figure 8 were imposed on the test structure (without repairing any of the other damage) and ETW limit load was applied. The load case applied to each new severe damage was indicative of the most critical load case for that portion of structure. The new damage locations were strain gauged and acoustically monitored. No evidence of flaw growth was exhibited during the phase of testing and strain gauge trends remained basically the same.

After Severe Damage Demonstrations followed the Repair Substantiation phase of testing. In this phase, all the different types of possible field repairs were evaluated. Most of the VID and Severe Damage were repaired using repair techniques approved in the field repair service manual. These repairs included: prepreg repairs, wet lay-up repairs, and bolted/bonded joint repairs. They were typical of what could be expected in the field, whether at an authorized repair station or "in the middle of nowhere".

With the repairs in place (with added strain gauges and AE instrumentation), the structures were successfully loaded to ETW ultimate load. No evidence of any acoustic noise from the repairs was exhibited and no change in stiffness was measured as a result of these repairs. The final test phase was the most interesting. In these final tests, the structure was loaded in its most severe load environment until failure.

Since several different load cases affect the criticality of the empennage structure, the plan provided for multiple load applications until failure. The first load case application was horizontal stabilizer gust down. The test was taken to 190% limit load (limitation of test facility) and reacted load in excess of the minimum three second requirement. Since acoustic emission noise was recorded during this load excursion, the structure was re-inspected. A crack was found in the tailcone center bulkhead flange near the top of the fuselage at approximately Butt Line 0. Since it was obvious that the test results would be facility limited, it was decided to apply a hybrid load case. The hybrid load case was a combination of Engine-out side load on the vertical fin and horizontal stabilizer gust down (two singular load cases which can never occur together). The structure was loaded to facility capacity at 190% limit load. The load was kept to see if a failure would eventually precipitate. Approximately two minutes into the load application, some "oil-canning" noises were distinctly heard. The center bulkhead structure had apparently buckled, forcing load to redistribute into the aft spar. Then, the right hand side (RHS) spar cap immediately failed in column compression redistributing load into the left hand side (LHS) cap and web severing the latter from the cap and completely failing the vertical fin assembly. A post-test teardown of the ground test article helped determine the failure scenario. The failure of the aft spar cap was as anticipated. Results of post-test strain gauge surveys indicated reasonable correlation (usually within 20%) between analytical predictions and measured strain.

The results of the damage tolerance testing were utilized to determine an inspection interval for the production fleet. A life scatter factor of 3 was to be applied to the test results and was accepted by the certification authorities. Another scatter factor of 3 was established to allow an inspection two inspection intervals to miss potential damage during visual inspections. The damage tolerance testing demonstrated 30,000 hours of life with no flaw growth. After application of the various factors, the permitted inspection interval became 3300 hours ( $= 30,000/9$ ) which was further reduced to 3000 hours to be consistent with the projected service intervals for the P-180 aircraft.

## CONCLUSION

The application of damage tolerant methodology helped design an aircraft structure which demonstrated better than adequate safety margins in the presence of manufacturing defects, impact flaws, skin cuts, and bondline inclusions.

An emphasis was placed on full-scale testing demonstrations, in the most critical environment with moisture saturated structure. The certification effort was international in scope,

because the type certificate holder Piaggio had to be certified first by Registro Aeronautico Italiano (RAI), and then by bilateral agreement with the FAA.

Overall, the program was finally successful because compliance with the applicable FARs and Special Conditions was achieved with the successful completion of the full-scale testing results. As several issues regarding composite certification were addressed during the program, it is hoped that the results of the P-180 program will serve as a precedent for future composite aircraft certification programs because many issues have already been addressed.

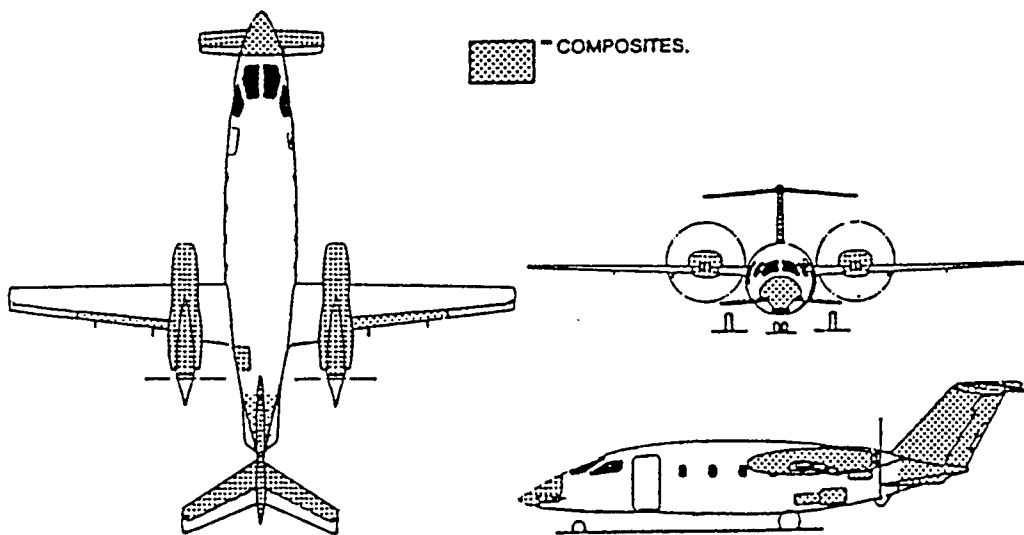


FIGURE 1. - COMPOSITE COMPONENTS ON THE PIAGGIO P-180 AVANTI.

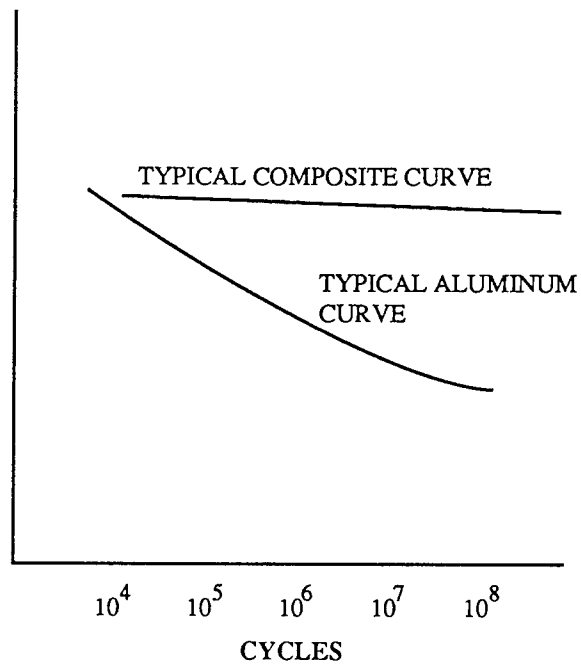
ELEMENT	DEFECT
SANDWICH SKINS	BOND VOIDS FOREIGN OBJECTS CONTAMINATION INCORRECT CORE INCORRECT RIBBON DIRECTION LAMINATE DIMPLING DARTING/MISALIGNED PLIES ON CORE RAMP
SOLID LAMINATE	VOIDS WRINKLES FOREIGN OBJECTS CONTAMINATION
ASSEMBLY/JOINTS	BOND VOIDS FOREIGN OBJECTS CONTAMINATION VOIDS/BAD CURE/DELAMINATIONS/ DAMAGE DURING ASSEMBLY

FIGURE 2. - IN-PROCESS MANUFACTURING HAZARDS.

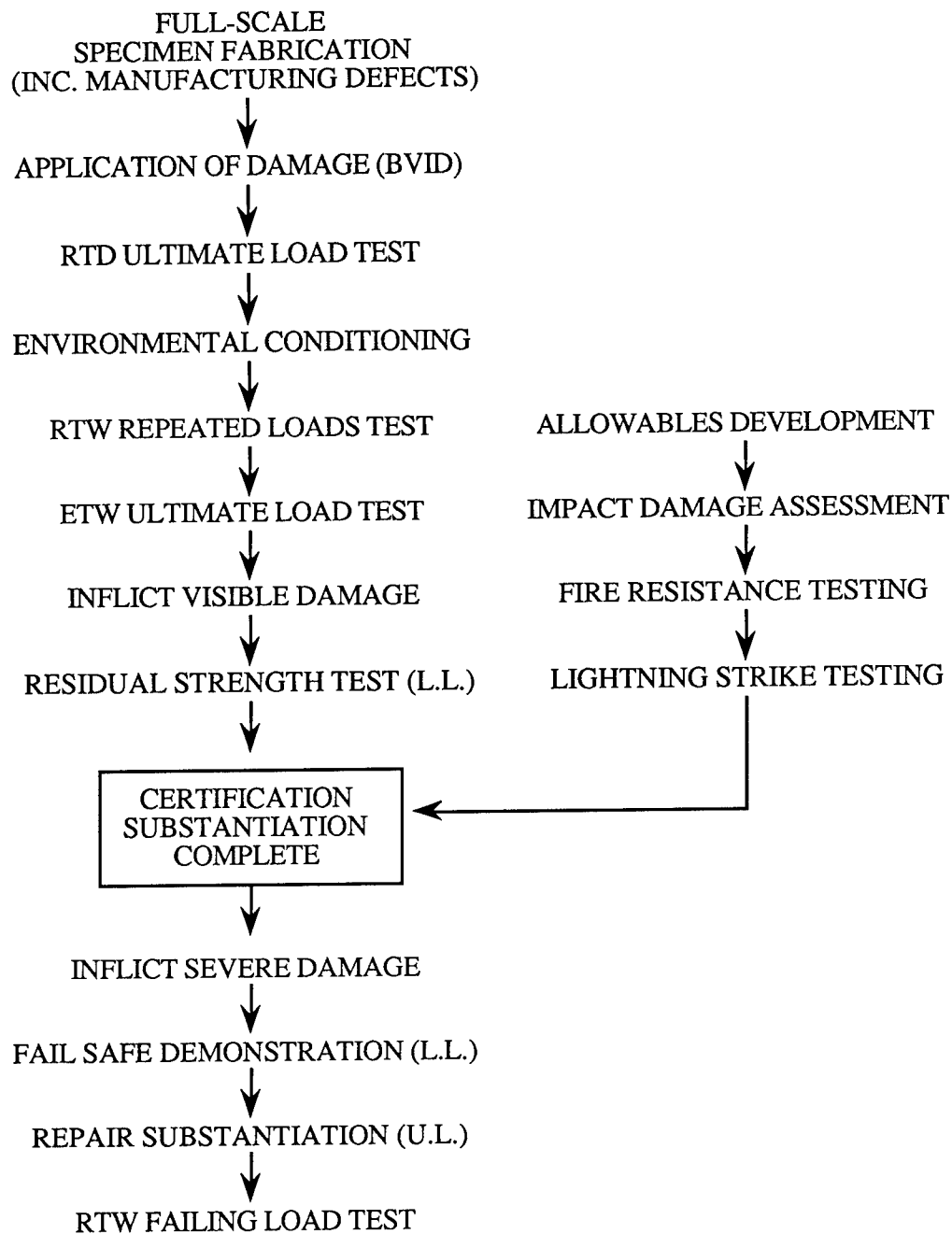
FIGURE 3. - FLIGHT OPERATIONAL HAZARDS.

STRUCTURE	HAZARD
FORWARD WING HORIZONTAL STABILIZER VERTICAL FIN/TAILCONE RUDDER	DROPPED TOOL DROPPED PART FOOT TRAFFIC GROUND EQUIPMENT HANDLING RUNWAY DEBRIS HAIL ENGINE WASH LUGGAGE

FIGURE 5. - S/N CURVE (ALUMINIUM VS. COMPOSITE).



**FIGURE 4. - REVISED CERTIFICATION TEST ACTIVITIES FLOW CHART.**



STRUCTURE	IMPACT HAZARD	IMPACTOR DIA.	IMPACT ENERGY	BYID	VID
<u>FORWARD WING</u>					
MAIN BOX	DROPPED TOOL DROPPED PART GROUND EQUIPMENT	1.5 .4 .25	180/108 108 180	NO/NO	YES YES
TRAILING EDGE	DROPPED TOOL	.5	180		YES
LEADING EDGE	HAIR GROUND EQUIPMENT	.88/25 .5	24 180	NO	YES
<u>HORIZONTAL STABILIZER</u>					
MAIN BOX	DROPPED TOOL DROPPED PART GROUND EQUIPMENT	1.5 .5 .25	180 108 180	NO YES	YES
LEADING EDGE	HAIR HAIR	.88 .25	24 24	NO	
<u>VERTICAL FIN</u>					
	DROPPED TOOL GROUND EQUIPMENT ENGINE WASH HAIR	1.5 .25 .88 .88/25	180 180 144 24	YES YES NO/NO	YES YES
<u>TAIL CONE</u>					
	DROPPED TOOL DROPPED PART GROUND EQUIPMENT ENGINE WASH/RUNWAY DEBRIS LUGGAGE HAIR	1.5 1.5 1.5/2.5 .88/25 1.5/25 .88/25	480 288 180 144 37 24	NO/NO NO/NO	YES YES YES YES
<u>RUDDER</u>	GROUND EQUIPMENT HANDLING DAMAGE	1.5 .25	180/108 180/108	YES	YES YES

FIGURE 6. - SUMMARY OF APPLIED IMPACT DAMAGE.

STRUCTURE	LOCATION
FORWARD WING	UPPER SKIN BL 2.2 LHS LOWER SKIN BL 10.25 RHS
HORIZONTAL STABILIZER	UPPER SKIN BL 10.5 RHS LOWER SKIN BL 10.5 LH
VERTICAL FIN/TAIL CONE	LHS VERTICAL FIN SKIN BETWEEN SPARS 1 AND 2 8" BELOW UPPER CLOSEOUT RIB VERTICAL FIN LEADING EDGE 36" BELOW CLOSEOUT RIB LHS VERTICAL FIN SKIN BETWEEN SPARS 3 AND 4 21" BELOW UPPER CLOSEOUT RIB TAIL CONE - LHS 3" FORWARD OF AFT BULKHEAD NEAR STRINGER 4
RUDDER	LHS SKIN - APPROX. 2" ABOVE MID-HINGE FITTING

FIGURE 7. - SUMMARY OF DAMAGE TOLERANCE SKIN CUTS.



**FIGURE 8. - SUMMARY OF SEVERE DAMAGE SKIN CUTS.**

STRUCTURE	LOCATION
<b>FORWARD WING</b>	RHS AFT SPAR WEB BL 22 LHS UPPER SPAR CAP/SKIN BL 6.5
<b>HORIZONTAL STABILIZER</b>	RHS AFT SPAR WEB BL 44 RHS UPPER FORWARD SPAR CAP/SKIN BL 6
<b>VERTICAL FIN/TAILCONE</b>	LHS TAILCONE STRINGER #5 3.5" AFT OF FORWARD BULKHEAD  RHS TAILCONE 1.9" ABOVE STRINGER #4 3.2" FORWARD OF AFT BULKHEAD  LHS VERTICAL FIN #4 SPAR CAP/SKIN CUT AT APPROX. WL 49  VERTICAL FIN #1 SPAR WEB BL 0.0 AT APPROX. WL 52
<b>RUDDER</b>	LHS SPAR CAP APPROX. 34" ABOVE BOTTOM OF L.E.  FORWARD SPAR WEB APPROX. 33" ABOVE BOTTOM OF L.E.

EFFECT OF LOW-SPEED IMPACT DAMAGE AND DAMAGE LOCATION  
ON BEHAVIOR OF COMPOSITE PANELS

Dawn Jegley

NASA Langley Research Center  
Hampton, Virginia

ABSTRACT

An investigation of the effects of low-speed impact damage on the compression and tension strength of thin (less than .05 inches thick) and moderately thick (between .12 and .17 inches thick) composite specimens was conducted. Impact speeds ranged from 50 to 550 ft/sec (impact energies from .25 to 30.7 ft-lb) and impact locations were near or away from a lateral unloaded edge. In this study, thin tension-loaded or compression-loaded specimens with only  $90^\circ$  and  $\pm 45^\circ$  plies which were impacted away from the unloaded edge suffered less reduction in maximum load-carrying capability due to impact damage than the same specimens impacted near the unloaded edge. Unlike the thin laminates, failure loads of thicker compression-loaded specimens with a similar stacking sequence were independent of impact location. Failure loads of thin tension-loaded specimens with  $0^\circ$  plies were independent of impact location while failure loads of thicker compression-loaded specimens with  $0^\circ$  plies were dependent upon impact location. A finite-element analysis of strain distributions across the panel width indicated that high axial strains occur near the unloaded edges of postbuckled panels, indicating that impacts near the unloaded edge would significantly effect the behavior of postbuckled panels.

INTRODUCTION

For composite parts to be used on aircraft primary structure, the effects of low-speed impact damage on the behavior of these structures must be understood. Impact damage followed by compression or tension loading is an important condition to be considered in the design of aircraft with composite structures. Both thicker laminates for wing panels and thinner laminates for fuselage skins must be studied. A great deal of work has been done on the effects of impact damage in the center of a relatively thick specimen (e.g., references 1-3) loaded in compression. This type of impact damage is representative of impact damage in a wing panel away from a supported edge or a stiffener. Less work has been done on impact damage near a support location or a stiffener on thinner specimens. However, impact damage near a stiffener or a supported edge can be a critical problem in compression-loaded structures (see reference 4) and damage tolerance criteria for thick specimens, such as allowable indentation depth, are not always applicable to thin specimens. Although fuselage structures carry tensile as well as compressive loads, the effect of impact location on tension-loaded panels is largely unexplored. Some data on tension-loaded specimens impacted away from a support are presented in references 5 and 6, but more work needs to be done to quantify the effects of panel thickness and impact location on structural performance.

The objective of this paper is to discuss the effects of impact damage location on failure of thin and moderately thick composite structures and to provide an

explanation for this behavior. The results of an investigation of the behavior of graphite-epoxy and graphite-thermoplastic specimens subjected to low-speed impact damage at the center of the specimen and near an unloaded edge are presented in the present paper. Tension-loaded specimens, whose behavior is dependent upon material characteristics, are discussed first. Compression-loaded specimens, whose behavior is dependent upon both material characteristics and structural parameters, are then discussed.

## TEST SPECIMENS

The graphite-epoxy specimens tested in this investigation were fabricated from commercially available Hercules, Inc., AS4<sup>+</sup> graphite fiber and 3502<sup>+</sup> thermosetting epoxy resin. The graphite-thermoplastic specimens were fabricated from commercially available Hercules AS4 graphite fiber and ICI PEEK<sup>+</sup> thermoplastic resin. All graphite-epoxy and some graphite-thermoplastic specimens were fabricated from unidirectional tape. The remaining graphite-thermoplastic specimens were fabricated from woven fabric in which the +45° and -45° fibers were woven together. The specimens tested in this study were made from the four stacking sequences  $[(\pm 45)_2/90]_s$ ,  $[(\pm 45)_2/90]_{3s}$ ,  $[\pm 45/0_2]_s$  and  $[\pm 45/0_2]_{3s}$ , which include a range of thicknesses. Specimen dimensions are shown in table I. All specimens were nominally 10 or 14 inches long and either 3, 4, or 10 inches wide with width-to-thickness ratios ranging from 18 to 240. All specimens were ultrasonically C-scanned to establish specimen quality prior to testing. Tabs were bonded to the tension-loaded specimens to prevent damage from being induced by the grips of the testing machine. The configuration of a typical tension specimen is shown in figure 1(a). The loaded ends of each compression specimen were machined flat and parallel to permit uniform end displacement.

## APPARATUS AND TESTS

### Tension Tests

Test specimens were slowly loaded in tension in an MTS testing machine using hydraulic grips. The unloaded edges were unsupported during the test. The applied load and change in specimen length were recorded at regular intervals during the test.

### Compression tests

Test specimens were slowly loaded in uniaxial compression using a hydraulic testing machine. The loaded ends of the specimen were clamped by fixtures during testing, and the unloaded lateral edges were simply supported by knife-edge restraints to prevent the specimen from buckling as a wide column. A typical compression specimen mounted in the support fixture is shown in figure 1(b). Electrical resistance strain gages were used to monitor strains, and dc differential transformers were used to monitor displacements. Typical locations of back-to-back strain gages used to monitor far-field laminate strains are shown in figure 1(b).

---

<sup>+</sup>Identification of commercial products and companies in this paper is used to describe adequately the materials. The identification of these commercial products does not constitute endorsement, expressed or implied, of such products by the National Aeronautics and Space Administration.

All specimens loaded in compression were painted white on one side to provide a reflective surface so that a moire fringe technique could be used to monitor out-of-plane deformation patterns. The applied load, the displacement of the loading platen, and the strain gage signals were recorded at regular intervals during the test.

### Impact Damage

A procedure described in reference 7 was used in the current study for impacting specimens. Aluminum spheres 0.5 inches in diameter were used as impact projectiles. The projectiles were directed normal to the plane of the specimen at speeds from 50 to 550 ft/sec. One specimen of each type was not impacted and used as a reference or control specimen while the remaining specimens were impacted prior to loading. All impacted specimens were impacted at midlength and either at midwidth or near a lateral unloaded edge. Compression-loaded specimens were placed in the test fixture prior to impact. Lateral locations of impact sites are indicated in figure 1. Since impact speed alone does not fully describe an impact event, the range of impact speeds considered and the corresponding impact energy is shown in table II.

### ANALYTICAL MODEL

Finite-element models of the graphite-epoxy compression-loaded control specimens were developed. A uniform grid of quadrilateral plate elements was used. The number of elements used to model each specimen was dependent upon the specimen dimensions but in each case the elements used were approximately square. At least 30 elements were used in the axial direction for each model. To simulate clamped conditions, no displacements or rotations were permitted on one end of the specimen and only the axial displacement was permitted on the opposite (loaded) end. The axial displacement was forced to be constant along the loaded edge. To simulate the simply supported edges, no out-of-plane displacements along the unloaded lateral edges were permitted. All analytical results are based on material properties given in table III and a nonlinear analysis using the finite-element computer code STAGS (reference 8).

### RESULTS AND DISCUSSION

Test results for specimens constructed with the four stacking sequences listed in table I are presented in this section. A comparison is made between specimens with the same stacking sequence impacted with the same impact energy in the center of the test section and impacted near a lateral unloaded edge (free for tension specimens, simply supported for compression specimens). Experimentally determined failure loads and strains are discussed for tension-loaded specimens; and then experimentally determined failure loads, buckling loads, strain distributions and out-of-plane deformations are discussed for compression-loaded specimens. Finite-element predictions of displacements and strains and experimental results are presented for specimens loaded into the postbuckling range. Results are presented in terms of a "normalized load" (load divided by specimen cross-sectional area) and "normalized end-shortening" (end-shortening divided by specimen length), and are not referred to as an "average stress" and "average strain." The terms "average stress" and "average strain" could be misleading since stresses and strains in the specimen after buckling are not constant across the width of the panel.

## Tension-loaded Specimens

Graphite-epoxy specimens constructed with two different stacking sequences were loaded in tension. One control specimen (a specimen without impact damage) of each stacking sequence was tested. Half the remaining specimens were impacted midlength and midwidth ( $x/b = .5$ , where  $x$  is the distance from the specimen unloaded edge to the impact site and  $b$  is the specimen width) and half were impacted .75 inches from an unloaded edge ( $x/b = .25$ ). All specimens were loaded to failure and showed extensive damage due to failure. Control specimens failed near the tabs while impact damaged specimens failed through the impact site. The normalized failure load (applied load at failure  $P$  divided by initial cross-sectional area  $A$ ) of the control specimens is shown in table I. The nominal impact speeds, impact locations and normalized failure loads are shown in table IV for all impacted tension-loaded specimens.

The effect of impact damage on the maximum load-carrying capability of these specimens is presented in figure 2 which shows the relationship between normalized failure load and impact speed. The circular symbols in the figure represent failures of specimens impacted near an unloaded edge and the square symbols represent failure of specimens impacted in the center of the specimen. Impacts which caused no visible damage are represented by open symbols. Impacts which caused visible damage are represented by shaded symbols if the impactor did not pass through the specimen and by filled symbols if the impactor did pass through the specimen.

The maximum reduction in load-carrying capability demonstrated in the centrally impacted specimens is 32 and 25 percent of the load-carrying capability of the corresponding undamaged (control) specimens for the  $[(\pm 45)_2/90]_s$  and  $[\pm 45/0_2]_s$  specimens, respectively. In each case, the maximum reduction for the centrally impacted specimen occurs for impact speeds of 300 ft/sec. The maximum reduction for side-impacted specimens is 49 and 30 percent of the load-carrying capability of the control specimens for the  $[(\pm 45)_2/90]_s$  and  $[\pm 45/0_2]_s$  specimens, respectively. For the  $[(\pm 45)_2/90]_s$  specimens, the centrally impacted specimens carry slightly more load at failure than the side-impacted specimens for all impact speeds considered. However, the side-impacted  $[\pm 45/0_2]_s$  specimen impacted at 400 ft/sec has a higher failure load than the centrally impacted specimen impacted at the same speed. This result suggests that impact location has no influence on maximum load-carrying capability for  $[\pm 45/0_2]_s$  specimens when loaded in tension. The 400 ft/sec impacts cause less reduction in load-carrying capability than the 300 ft/sec impacts for the  $[\pm 45/0_2]_s$  specimens. This same behavior is described for  $[0/90]_{3s}$  specimens in reference 6.

In the study described in reference 6, the most damage was caused when the impact speed was just sufficient to cause the impactor to pass through the specimen. Different types of damage are caused by impacts at different speeds. Low-speed impacts cause delaminations within the specimen. Higher-speed impacts for which the impactor does not pass through the specimen, and impacts for which the impactor barely passes through the specimen cause delaminations and severe damage to the back of the specimen, including fiber breakage. Very high speed impacts, for which the impactor passes through the specimen, cause very high stress at the impact site and less cracking away from the impact site. These different types of damage can lead to different failure modes and different amounts of reduction in maximum load-carrying capability.

## Compression-loaded Specimens

### Control Specimens

Control specimens (those without impact damage) for each stacking sequence were loaded in compression. Six control specimens with stacking sequence  $[(\pm 45)_2/90]_s$  were loaded to failure. A three-inch-wide specimen and a four-inch-wide specimen were each constructed from graphite-epoxy tape, graphite-thermoplastic tape and graphite-thermoplastic fabric. The three-inch-wide specimens buckled into one transverse and four axial half-waves of nearly equal wavelength then failed at specimen midlength (along a nodal line). The four-inch-wide specimens buckled into one transverse and three axial half-waves then failed at a nodal line. Each specimen carried load well into the postbuckling range. Normalized failure loads are shown in table I.

Two moderately thick control specimens with stacking sequence  $[(\pm 45)_2/90]_{3s}$  were constructed from graphite-epoxy tape and loaded to failure. One specimen was three inches wide and one was four inches wide. Both specimens buckled into one transverse and three axial half-waves immediately prior to failure. The three-inch-wide specimen failed through the center of the specimen (not a nodal line). The four-inch-wide specimen failed at a nodal line. Normalized failure loads are shown in table I.

One thin control specimen with stacking sequence  $[\pm 45/0_2]_s$  and one moderately thick control specimen with stacking sequence  $[\pm 45/0_2]_{3s}$  were made from graphite-epoxy tape and tested. Each specimen was 10 inches wide and 14 inches long. These control specimens buckled into one half-wave in each direction prior to failure near a loaded edge. The normalized failure load of the  $[\pm 45/0_2]_{3s}$  control specimen is shown in table I. The  $[\pm 45/0_2]_s$  control specimen was not loaded to failure.

### Impact Damaged Specimens

All remaining compression-loaded specimens were subjected to impact damage prior to loading. Nominal impact speeds, impact locations and normalized failure loads are shown in tables V-VII for the compression-loaded specimens with 3-, 4- and 10-inch widths, respectively.

$[(\pm 45)_2/90]_s$  Specimens. The relationship between impact speed and normalized failure load is shown in figures 3(a), 3(b) and 3(c) for specimens fabricated from graphite-epoxy tape, graphite-thermoplastic tape and graphite-thermoplastic fabric, respectively. The circular symbols in each figure represent the failure of the side-impacted specimens and the square symbols represent the failure of centrally impacted specimens. Impacts which caused no visible damage are represented by open symbols. Impacts which caused visible damage are represented by shaded symbols if the impactor did not pass through the specimen and by filled symbols if the impactor passed through the specimen. Specimens subjected to impact speeds less than about 200 ft/sec buckled into 4 axial half-waves and then failed at the nodal line through the impact site. Specimens subjected to impact at higher impact speeds buckled into 3, 4 or 5 axial half-waves along the length and failed through the impact site whether or not the impact site was located on a nodal line. Each specimen failed by transverse cracking and many also exhibited off-axis cracking and fiber separation on the side opposite the impact site.

Impacts at 100 ft/sec caused no reduction in maximum load-carrying capability. The results show a significant reduction in normalized failure load for each type of specimen as impact speed increases from 100 to 300 ft/sec. For the graphite-epoxy specimens, a centrally located impact can reduce the maximum load-carrying

capability of a specimen by up to 12 percent compared to that of an undamaged specimen. However, for the graphite-thermoplastic specimens, a centrally located impact can reduce the maximum load-carrying capability by 30-35 percent. The impact speed causing the most reduction in maximum load-carrying capability of the graphite-epoxy specimen is 225 ft/sec while the impact causing the most reduction in maximum load-carrying capability of the graphite-thermoplastic specimen is 300 ft/sec.

The results shown in figure 3 indicate a dependence of normalized failure load on impact location. An impact .75 inches from the lateral unloaded edge of a 3-inch-wide specimen causes a reduction in maximum load-carrying capability of about 35 percent for each type of specimen; i.e., three times the reduction in the graphite-epoxy centrally impacted specimens but about the same as the reduction in the graphite-thermoplastic centrally impacted specimens. The effect of impact location on maximum load-carrying capability is more significant for graphite-epoxy specimens than for graphite-thermoplastic specimens; however, the trend is the same for both materials. A side impact reduces the maximum load-carrying capability of the specimen by at least as much as a central impact for a given impact speed.

For these three types of specimens, nonvisible damage did not reduce their maximum load-carrying capability and the impact speed producing barely visible damage was approximately 170 ft/sec. Impacts causing visible damage caused extensive reduction in maximum load-carrying capability. In general, the most severe reduction occurred when the impact speed was approximately the speed necessary to cause the impactor to pass through the specimen. This speed was approximately 240, 325, and 275 ft/sec for the graphite-epoxy tape, the graphite-thermoplastic tape and the graphite-thermoplastic fabric specimens, respectively. An impactor that passed through the specimen at high speed (e.g., 500 ft/sec) caused less damage than an impactor that bounced off the specimen. This difference in the amount of damage is the reason that a damaged specimen with a through penetration has a higher maximum load-carrying capability than a damaged specimen without a through penetration. Ultrasonic C-scans of specimens after impact and before compressive loading indicate that there is a significant decrease in damage area for very high speed impacts compared to impacts in which the impactor barely passes through the specimen for the graphite-thermoplastic specimens. A small decrease in damage area is seen for very high speed impacts for the graphite-epoxy specimens. However, the failure load does not always correlate with the damage area determined by C-scan, as demonstrated in reference 3 for several stacking sequences. This lack of correlation is attributed to the fact that C-scan indicates a total damage area in a qualitative manner, not a specific amount and type of damage (i.e., number and location of delaminations) in the area.

The relationship between normalized failure load and impact location is shown in figure 4 for a four-inch-wide specimen impacted at several locations across the width at a speed of approximately 450 ft/sec (the impactor passed through the specimens). In each case the central impact caused little reduction in maximum load-carrying capability but the side impacts caused a significant reduction. The closer the impact was to the edge of the specimen, the more the reduction in maximum load-carrying capability. A discussion of why a side impact causes more reduction in maximum load-carrying capability than a center impact is presented later in this paper.

The experimentally determined normalized load versus normalized end-shortening of four impacted graphite-epoxy specimens is shown in figure 5. The load is normalized by the specimen cross-sectional area and the end-shortening is normalized

by the specimen length. Two specimens were impacted at 175 ft/sec (damage which was barely visible) and two specimens were impacted at 250 ft/sec (the impactor passed through the specimen). Each specimen buckled at a normalized load of approximately 10 ksi. There is no difference between the prebuckling response of the side- and center-impacted specimen in either case. The primary difference in the postbuckling response is that the side-impacted specimens fail at much lower loads than the center-impacted specimens.

The displacements and strains in the four-inch-wide control specimen are shown in figure 6. The experimentally determined normalized load versus normalized end-shortening relationship for three four-inch-wide specimens and the analytically determined normalized load versus normalized end-shortening relationship for a four-inch-wide control specimen are shown in figure 6(a). The analytical and experimental results for the control specimen agree quite well. The control specimen fails at a load 2.61 times the buckling load. Little difference is seen between the results for the centrally impacted specimen and the control specimen but the side-impacted specimen failed at a much lower load, although the overall specimen stiffness seems to be unaffected by the impact damage.

The analytically determined out-of-plane displacements  $w$  (normalized by the specimen thickness  $t$ ) along the specimen length  $L$  at the center, at one quarter of the width and near an unloaded edge, for a specimen loaded in the postbuckling range is shown in figure 6(b). The buckling load of the specimen is represented by  $P_{cr}$  and the specimen buckled into one transverse and three axial half-waves. Displacements for 1.22 and 2.55 times the buckling load are shown. The maximum out-of-plane displacement is at the center of the specimen. The highest gradient in out-of-plane deformation is at the nodal lines, at approximately  $y/L = .33$  and  $.66$  ( $y$  is distance from the loaded edge).

The experimentally determined axial membrane strain (average of back-to-back strain gages) across the specimen at a nodal line is shown in figure 6(c) for several values of load  $P$ , normalized by the buckling load  $P_{cr}$ , in the pre- and postbuckling range. In the postbuckling range, the higher the value of  $P/P_{cr}$ , the higher the membrane strain near the unloaded edge of the specimen and the lower the membrane strain near the center of the specimen. The strain distribution across the specimen width at a nodal line just before failure is shown in figure 6(d). The dashed and solid curves represent membrane strains determined analytically and experimentally, respectively (a least squares fit to the data points was used). The open and filled symbols represent surface strains determined analytically and experimentally, respectively. Slight differences in results at the unloaded edges can be attributed to anisotropic effects since the ratios of the anisotropic terms to the bending stiffnesses are relatively large, i.e.,  $D_{16}/D_{11} = .22$ , and  $D_{26}/D_{22} = .31$ . Front and back surface strains differ significantly in the postbuckled specimen, and much higher strains occur at the edges of the specimen than at the center.

The strain and displacement distributions presented in figure 6 indicate why side impacts have more effect on failure loads than central impacts for these buckled specimens. Prior to buckling, the axial strain is relatively constant across the width of the panel so impact location has little effect on specimen behavior. At buckling, the loads in the panel redistribute and more load is carried near the supported unloaded edges. The high deformation gradients at the nodal lines and the higher strains near the specimen edges induce transverse shearing loads which cause failure at the nodal lines in undamaged specimens. Impact damage in a region of high strain near an unloaded edge has more effect on strength than impact damage in a region of low strain at the specimen center.



$[(\pm 45)_2/90]_{3s}$  Specimens. - A series of moderately thick three-inch-wide specimens were impacted either in the center of the specimen or .7 inches away from an unloaded edge. The relationship between normalized failure load and impact speed is shown in figure 7 for these specimens. The specimen impacted midwidth at 100 ft/sec buckled into three axial half-waves immediately prior to failure. No other impacted specimen buckled. The most severe reduction in maximum load-carrying capability due to impact damage occurs at a speed of 400 ft/sec, but there appears to be no difference between the effect of side impact and center impact. The impactor passed through the specimen at speeds greater than about 425 ft/sec and the failure load increased slightly for speeds of 525 ft/sec since a more ballistic type of damage is induced at very high speeds (ref. 6). Nonvisible damage does not cause a reduction in maximum load-carrying capability, but barely visible damage (impact speeds of 150 ft/sec) causes more than a 40 percent reduction in maximum load-carrying capability compared to the control specimen.

The relationship between normalized failure load and impact location for four four-inch-wide specimens impacted at a speed of 500 ft/sec is shown in figure 8. Impact location appears to have little effect on failure load. The normalized load versus normalized end-shortening for three specimens impacted at 540 ft/sec is shown in figure 9. The control specimen buckles just before failure while the impacted specimens fail well before buckling occurred. The fact that these specimens do not buckle means that the strain distribution across the specimen width is almost constant at failure. The measured surface strains, membrane surface strains based on an average of the surface strains, and analytical membrane strains are shown in figure 10 for the control specimen just prior to failure. Surface strains are represented by data points and membrane strains are represented by curves. The results show that there is no significant difference in strain across the specimen width so impact location does not affect maximum load-carrying ability.

$[\pm 45/0_2]_{3s}$  specimens. - Two ten-inch-wide specimens were impacted with an impact speed of 150 ft/sec and loaded to failure. Impact locations were at midlength and at the center or one inch from the specimen unloaded edge. Each specimen buckled into one transverse and two axial half-waves then continued to carry the load well into the postbuckling range. The specimens then exhibited a mode shape change to three axial half-waves and failed at a loaded edge. The normalized load versus normalized end-shortening relationship for these two specimens is shown in figure 11. The impact has little effect on the specimen prebuckling behavior, buckling load or postbuckling behavior.

$[\pm 45/0_2]_{3s}$  specimens. - Nine specimens were constructed from graphite-epoxy tape and loaded to failure. Each specimen was 14 inches long and 10 inches wide. Each specimen buckled into one half-wave in each direction prior to failure. Failures occurred at a loaded edge in all cases and caused damage growth at the impact sites for the specimens impacted at high impact speeds. Visible damage was caused by impacts of 300 ft/sec and the impactor passed through the specimen for impacts with speeds greater than 400 ft/sec. Three specimens were impacted at the center, two were impacted two inches from an unloaded edge and two were impacted one inch from an unloaded edge, providing results for impact sites at  $x/b=.5$ ,  $.2$ , and  $.1$ , respectively.

The relationship between normalized failure load and impact speed is shown in figure 12. Centrally located impacts and impacts at  $x/b=.2$  do not cause a reduction in maximum load-carrying capability at impact speeds up to 450 ft/sec. However, impacts at speeds above 300 ft/sec at  $x/b=.1$  cause significant reduction in maximum

load-carrying capability. An impact at 450 ft/sec at  $x/b=.1$  can cause a 30 percent reduction in failure load compared to the control specimen.

The experimentally and analytically determined normalized load versus normalized end-shortening relationships for the control specimen are shown in figure 13. The analytical and experimental results for the control specimen agree quite well and each method predicts a normalized buckling load of about 6500 psi. Specimen failure is at 3.1 times the buckling load. The normalized load versus normalized end-shortening behavior of the centrally impacted and both of the side-impacted specimens that were impacted at 450 ft/sec are shown in figure 14. Once again, prebuckling behavior is approximately the same for the three specimens and initial postbuckling behavior is also the same for the three specimens.

The axial strain distribution across the width of a control specimen at midlength is shown in figure 15. The change in analytically determined strain distribution as the load is increased past the buckling load to specimen failure is shown in figure 15(a) and the experimental and analytical membrane strains at failure are shown in figure 15(b). The data points represent surface strains measured by strain gages. The solid and dashed curves represent membrane strains determined from averaging back-to-back surface strain gage results and from finite-element analysis, respectively. Higher strains occur at the specimen edges than in the center, as seen before. However, the section of the specimen which experiences higher strains is smaller than that in the previous case. In  $[\pm 45/0_2]_{3s}$  specimens, an impact at width position  $x/b=.2$  is not as far into the region of high strain as an impact at width position  $x/b=.25$  in the  $[(\pm 45)_2/90]_s$  specimens, so the impact at  $x/b=.2$  in the  $[\pm 45/0_2]_{3s}$  specimens causes less reduction in maximum load-carrying capability than the impacts at  $x/b=.25$  in the  $[\pm 45/0_2]_{3s}$  case. However, an impact at  $x/b=.1$  in the  $[\pm 45/0_2]_{3s}$  specimens is in the region of high axial strain so this impact does significantly affect the maximum load-carrying capability of the specimen. Impact damage location has more effect on maximum load-carrying capability for specimens without  $0^\circ$  plies than for specimens with  $0^\circ$  plies since stacking sequence influences how the load is redistributed after buckling.

#### CONCLUDING REMARKS

An investigation of the behavior of laminated thin and moderately thick graphite-epoxy and graphite-thermoplastic specimens subjected to impact damage and loaded in compression and tension was conducted. Specimens were impacted with a 0.5-inch-diameter aluminum sphere at impact speeds up to 550 ft/sec (impact energy 30.7 ft-lb) either in the center of the specimen or near an unloaded edge prior to loading.

The results of this investigation indicate that impact location in thin tension-loaded specimens dominated by angle plies influences failure load. In these specimens, impacts near an unsupported edge reduced specimen maximum load-carrying capability more than central impacts (away from an unsupported edge) reduced specimen maximum load-carrying capability. However, the failure load of thin tension-loaded specimens with 50 percent  $0^\circ$  plies was independent of impact location. Experimental results and finite-element analysis results of compression-loaded specimens indicate that high axial strains occur near the simply-supported unloaded edges of a postbuckled specimen. These strains lead to lower failure loads in specimens impacted near the unloaded edge than in specimens impacted away from an edge. The failure load for damaged specimens that fail prior to buckling is unaffected by the widthwise location of the impact damage. Impact damage to

specimens with 0° plies is less dependent upon impact location than impact damage to specimens without 0° plies.

#### References

1. Starnes, J. H., Jr.; and Williams, J. G.: Failure Characteristics of Graphite-Epoxy Structural Components Loaded in Compression. *Mechanics of Composite Materials*, Pergamon Press, 1982, pp. 283-306.
2. Jegley, Dawn C.: Compression Behavior of Graphite-Thermoplastic and Graphite-Epoxy Panels with Circular Holes or Impact Damage. NASA TP 3071, March 1991.
3. Guynn, E. G.; and O'Brien, T. K.: The Influence of Lay-Up and Thickness on Composite Impact Damage and Compression Strength. A Collection of Technical Papers--AIAA/ASME/ASCE/AHS 26th Structures, Structural Dynamics and Materials Conference, Part 1, April 1985, pp. 187-196. AIAA Paper No. 85-0646.
4. Starnes, James H., Jr.; and Rouse, Marshall: Post-buckling and Failure Characteristics of Selected Flat Rectangular Graphite-Epoxy Plates Loaded in Compression. A Collection of Technical Papers--AIAA/ASME/ASCE/AHS 22nd Structures, Structural Dynamics and Materials Conference, Part 1, April 1981, pp. 423-434. AIAA Paper No. 81-0543.
5. Avva, V. S.: Fatigue/Impact Studies in Laminated Composites. AFWAL-TR-3060, May 1983.
6. Dorey, Graham: Damage Tolerance and Damage Assessment in Advanced Composites. Advanced Composites, edited by Ivana Partridge, Elsevier Applied Science, 1989, pp. 369-398.
7. Starnes, J. H., Jr.; Rhodes, M. D.; and Williams, J. G.: Effect of Impact Damage and Holes on the Compression Strength of a Graphite/Epoxy Laminate. Nondestructive Evaluation and Flaw Criticality for Composite Materials, edited by R. B. Pipes, ASTM STP 696, 1979, pp. 145-171.
8. Almroth, B.O.; and Brogan, F.A.: The STAGS Computer Code. NASA CR-2950, 1980.

Table I. Stacking Sequence, Average Specimen Dimensions and Control Specimen Normalized Failure Load

Stacking Sequence	Material*	Average Thickness, t (in.)	Average Width, b (in.)	Average Length, L (in.)	Number of Specimens Tested	Normalized Failure Load, P/A (ksi)
Tension-Loaded Specimens						
$[(\pm 45)_2/\overline{90}]_s$	ge, tape	.0498	3.00	10.01	7	32.8
$[\pm 45/\overline{0}_2]_s$	ge, tape	.0435	3.00	10.00	8	128.
Compression-Loaded Specimens						
$[(\pm 45)_2/\overline{90}]_s$	ge, tape	.0481	3.00	10.00	12	19.7
$[(\pm 45)_2/\overline{90}]_s$	ge, tape	.0479	4.00	10.00	4	15.6
$[(\pm 45)_2/\overline{90}]_s$	gt, tape	.0491	2.99	9.92	14	20.6
$[(\pm 45)_2/\overline{90}]_s$	gt, tape	.0495	4.00	10.00	3	16.4
$[(\pm 45)_2/\overline{90}]_s$	gt, fabric	.0470	3.00	10.00	12	21.2
$[(\pm 45)_2/\overline{90}]_s$	gt, fabric	.0461	4.00	10.00	4	17.8
$[(\pm 45)_2/\overline{90}]_{3s}$	ge, tape	.1626	3.00	10.00	12	53.0
$[(\pm 45)_2/\overline{90}]_{3s}$	ge, tape	.1610	4.00	10.00	4	49.4
$[\pm 45/\overline{0}_2]_s$	ge, tape	.0428	10.00	14.00	3	Not Available
$[\pm 45/\overline{0}_2]_{3s}$	ge, tape	.1280	10.00	14.00	9	20.4

\* ge represents graphite-epoxy, gt represents graphite-thermoplastic, tape represents unidirectional tape and fabric represents woven fabric with #45 fibers.

\* Normalized failure load of control specimen (failure load/cross-sectional area).

Table II. Relationship Between Impact Speed and Energy

Impact Speed (ft/sec)	Impact Energy (ft-lb)
0.	0.00
50.	0.25
100.	1.02
150.	2.29
200.	4.07
250.	6.35
300.	9.15
350.	12.4
400.	16.3
450.	20.6
500.	25.4
550.	30.7

Table III. Graphite-epoxy Material Properties

Longitudinal Young's modulus, Msi	18.5
Transverse Young's modulus, Msi	1.64
Shear modulus, Msi	.89
Major Poisson's ratio	.30

Table V. Compression-loaded Three-inch-wide Specimens

Nominal Impact Speed, v (ft/sec)	Normalized Failure Load, P/A* (ksi)					
	stacking sequence $[(\pm 45)_2/90]_s$					
	graphite-epoxy, tape		graphite-thermoplastic, tape		graphite-thermoplastic, fabric	
	x/b* = .5	x/b* = .25	x/b* = .5	x/b* = .25	x/b* = .5	x/b* = .25
100.	20.2	20.5	21.6	21.9	22.9	23.8
175.	20.7	15.6	21.5	18.4	23.7	22.0
225.	17.8	-	-	-	-	-
250.	18.5	12.9	17.5	16.4	19.1	17.8
300.	18.8	-	12.7	-	-	-
325.	-	15.6	13.6	12.3	17.8	14.8
350.	17.8	-	16.2	-	-	-
375.	-	-	-	-	16.5	-
400.	19.2	-	16.3	-	18.1	13.6
400.	-	-	13.9	-	-	-
500.	-	-	17.6	-	-	-
	stacking sequence $[(\pm 45)_2/90]_{3s}$					
	graphite-epoxy, tape		graphite-thermoplastic, tape		graphite-thermoplastic, fabric	
	x/b* = .5	x/b* = .25	x/b* = .5	x/b* = .25	x/b* = .5	x/b* = .25
100.	51.4	50.7	-	-	-	-
175.	27.0	29.0	-	-	-	-
250.	19.6	22.7	-	-	-	-
325.	16.0	-	-	-	-	-
400.	15.2	15.5	-	-	-	-
540.	20.2	17.0	-	-	-	-

\* P is the failure load; A is the average cross-sectional area and is .144, .147 and .141 in.<sup>2</sup> for the graphite-epoxy, graphite-thermoplastic tape, and graphite-thermoplastic fabric  $[(\pm 45)_2/90]_s$  specimens, respectively. Average cross-sectional area is .488 in.<sup>2</sup> for the  $[(\pm 45)_2/90]_{3s}$  specimens.

+ Panel width (b) is 3 inches, x is distance from specimen unloaded edge.

Table IV. Tension-loaded Specimens

Nominal impact speed, v (ft/sec)	Normalized Failure Load, P/A* (ksi)	
	x/b* = .5	x/b* = .2
	stacking sequence $[(\pm 45)_2/90]_s$	
	200.	27.2
	300.	23.2
	400.	22.6
	stacking sequence $[(\pm 45)/0_2]_s$	
	100.	116.
	200.	103.
	300.	98.
	400.	105.
		116.

\* P is the failure load; A is the average cross-sectional area and is .149 in.<sup>2</sup> for  $[(\pm 45)_2/90]_s$  specimens, and is .131 in.<sup>2</sup> for  $[(\pm 45)/0_2]_s$  specimens.

+ Panel width (b) is 3 in., x is distance from specimen unloaded edge.

Table VI. Compression-loaded Four-inch-wide Specimens

Material	Nominal impact speed, v (ft/sec)	Normalized Failure Load, P/A* (ksi)		
graphite-epoxy, tape  graphite-thermoplastic, tape  graphite-thermoplastic, fabric	stacking sequence $[(\pm 45)_2/\overline{90}]_s$			
	450.	x/b <sup>+</sup> =.5	x/b <sup>+</sup> =.3	x/b <sup>+</sup> =.2
		15.9	17.0	8.7
		18.2	-	9.5
	450.	18.1	13.8	12.2
	stacking sequence $[(\pm 45)_2/90]_{3s}$			
graphite-epoxy, tape	500.	21.0	18.3	15.5

\*  $P$  is the failure load;  $A$  is the average cross-sectional area and is .192, .198, and .184 in.<sup>2</sup>, for the graphite-epoxy, graphite-thermoplastic tape, and graphite-thermoplastic fabric  $[(\pm 45)_2/\overline{90}]_s$  specimens, respectively. Average cross-sectional area is .644 in.<sup>2</sup> for the  $[(\pm 45)_2/90]_{3s}$  specimens.

+ Panel width ( $b$ ) is 4 inches,  $x$  is distance from specimen unloaded edge.

Table VII. Compression-loaded Ten-inch-wide Specimens

Nominal impact speed, v (ft/sec)	Normalized Failure Load*, P/A (ksi)		
stacking sequence $[\pm 45/0_2]_{3s}$			
250. 350. 450.	x/b <sup>+</sup> =.5	x/b <sup>+</sup> =.2	x/b <sup>+</sup> =.1
	23.4	21.8	-
	21.0	21.6	16.2
	20.9	21.2	14.3
stacking sequence $[\pm 45/0_2]_s$			
150.	9.98	-	9.1

\*  $P$  is the failure load;  $A$  is the average cross-sectional area and is .428 in.<sup>2</sup> for  $[\pm 45/0_2]_s$  specimens, and 1.28 in.<sup>2</sup> for  $[\pm 45/0_2]_{3s}$  specimens.

+ Panel width ( $b$ ) is 10 in.,  $x$  is distance from specimen unloaded edge.

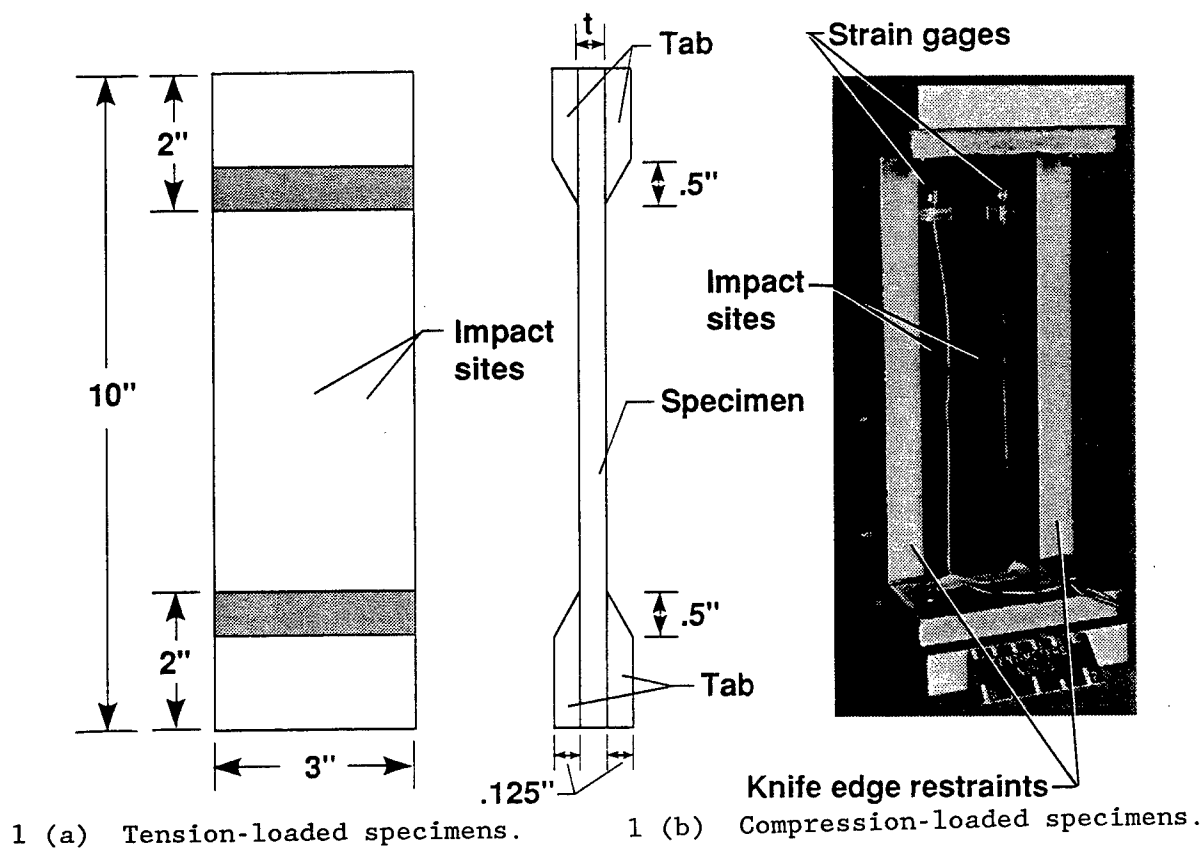


Figure 1. Specimen configuration.

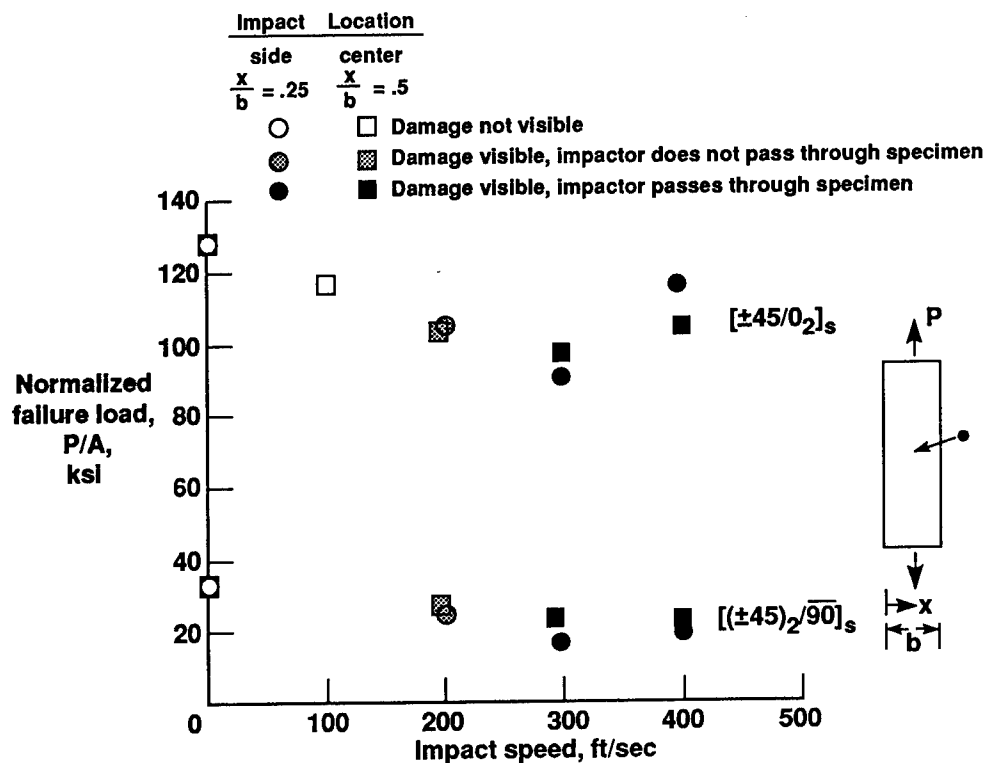
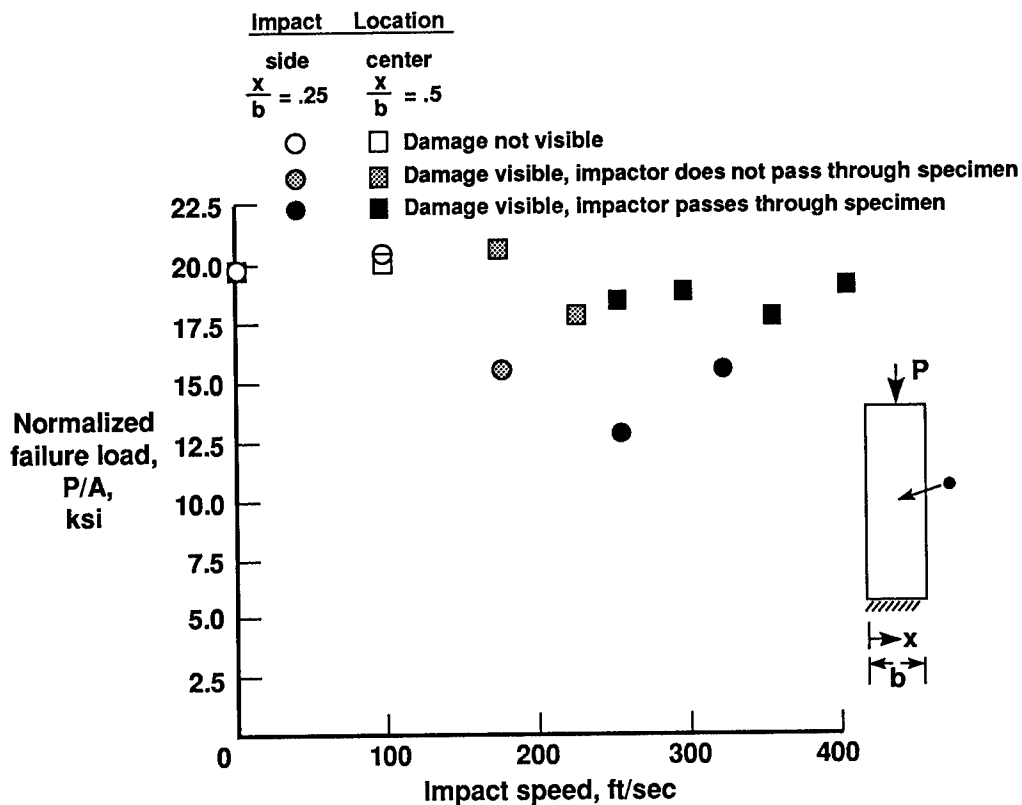
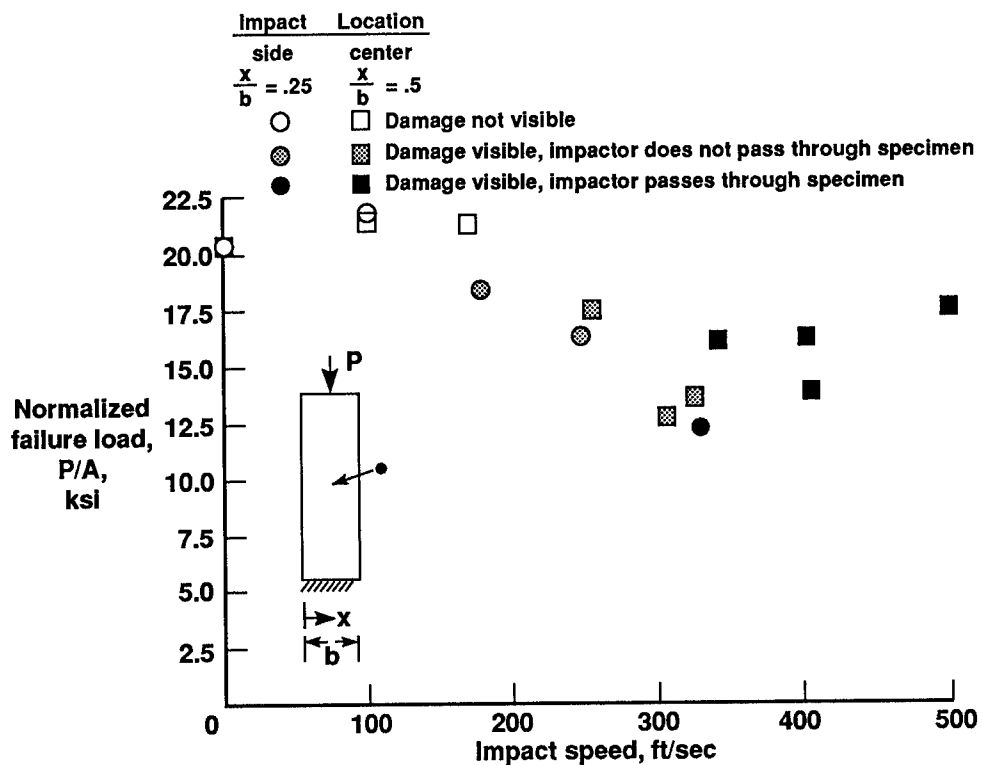


Figure 2. Effect of impact speed on normalized tensile failure load for panels with stacking sequences  $[(\pm 45)_2/90]_s$  and  $[\pm 45/0_2]_s$  impacted in the center and at the side.  $A$  is cross-sectional area.

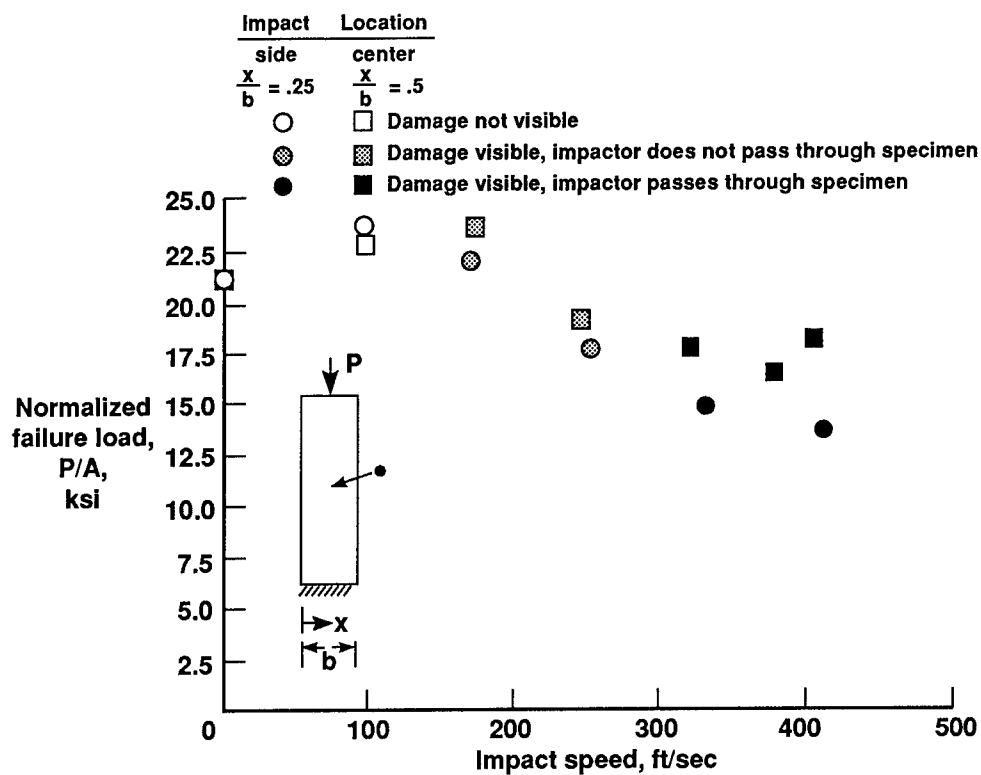


3 (a) Graphite-epoxy tape specimens.



3 (b) Graphite-thermoplastic tape specimens.





3 (c) Graphite-thermoplastic fabric specimens.

Figure 3. Effect of impact speed on compressive failure load for panels with a  $[(\pm 45)_2/90]_s$  stacking sequence impacted in the center and at the side. A is cross-sectional area.

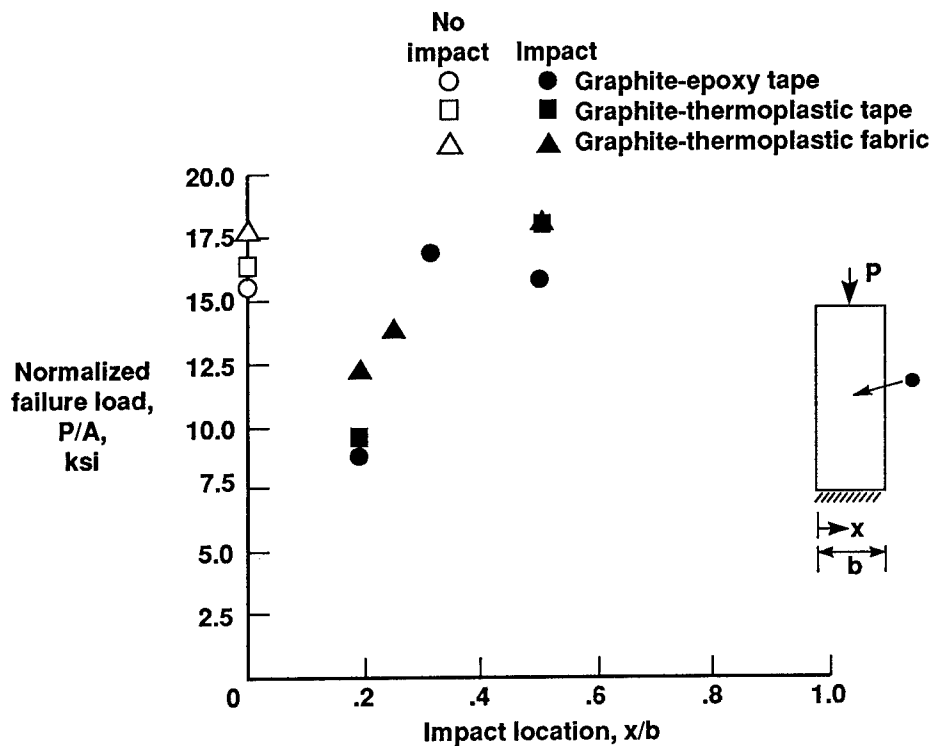
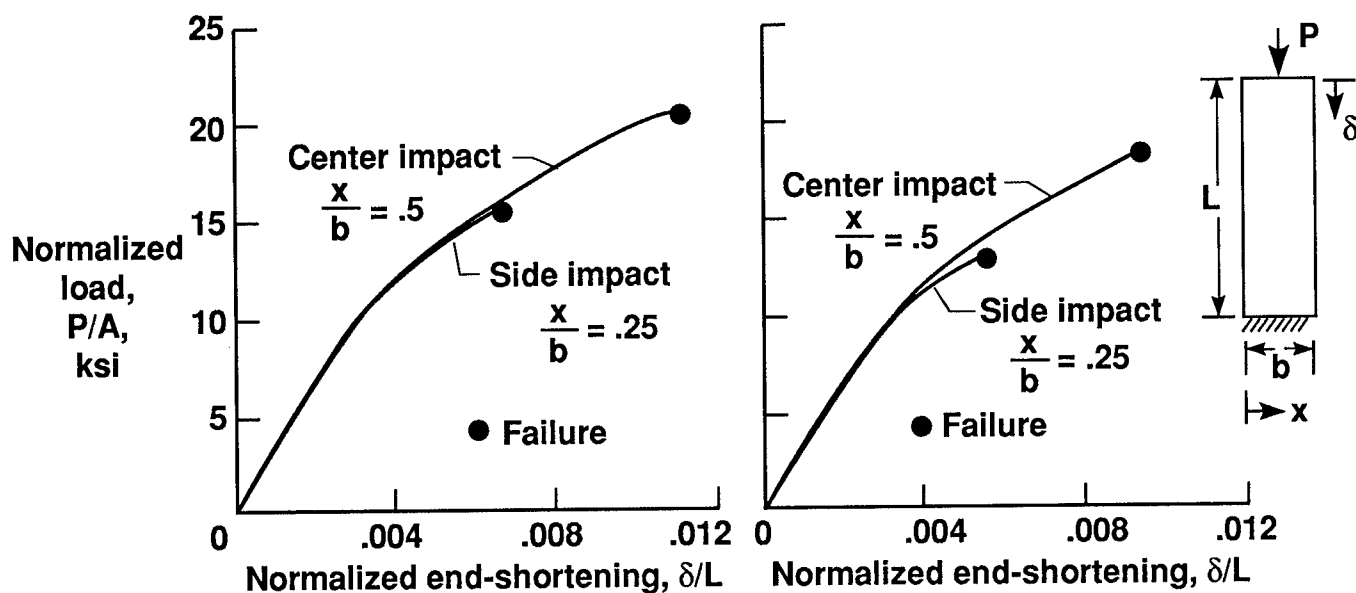


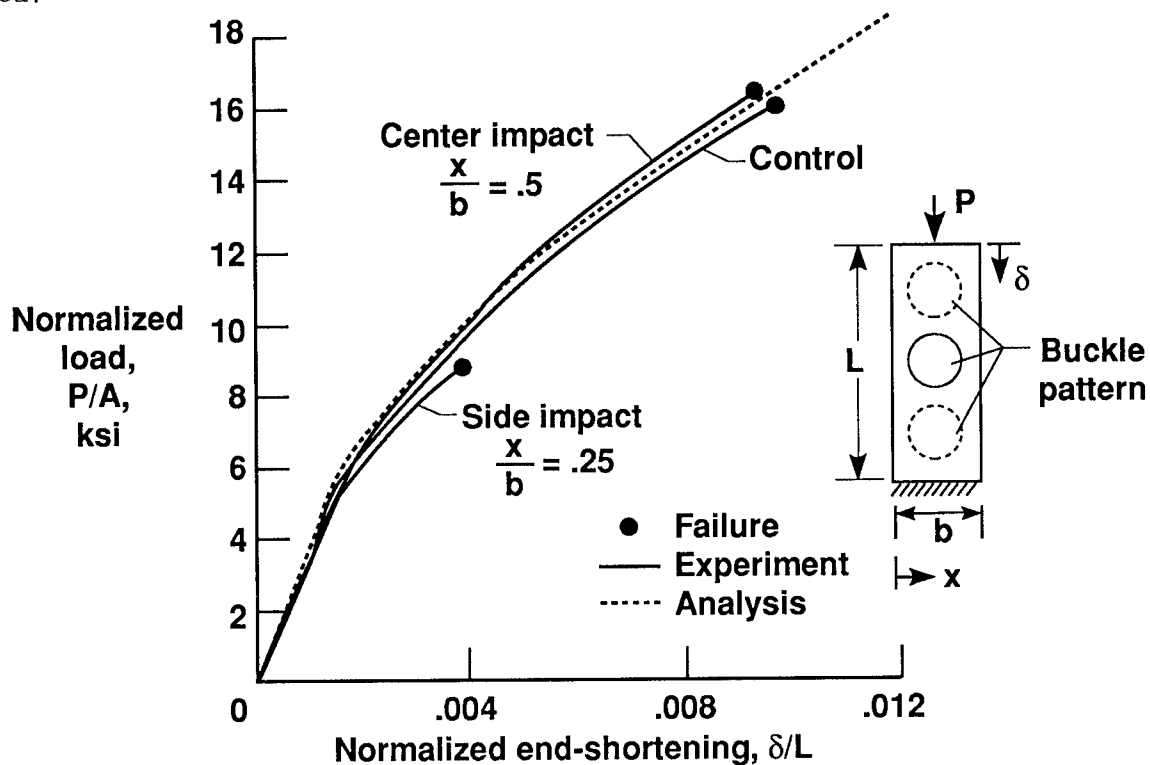
Figure 4. Normalized compressive failure load as a function of impact location for panels with a  $[(\pm 45)_2/90]_s$  stacking sequence impacted at 450 ft/sec. A is cross-sectional area.



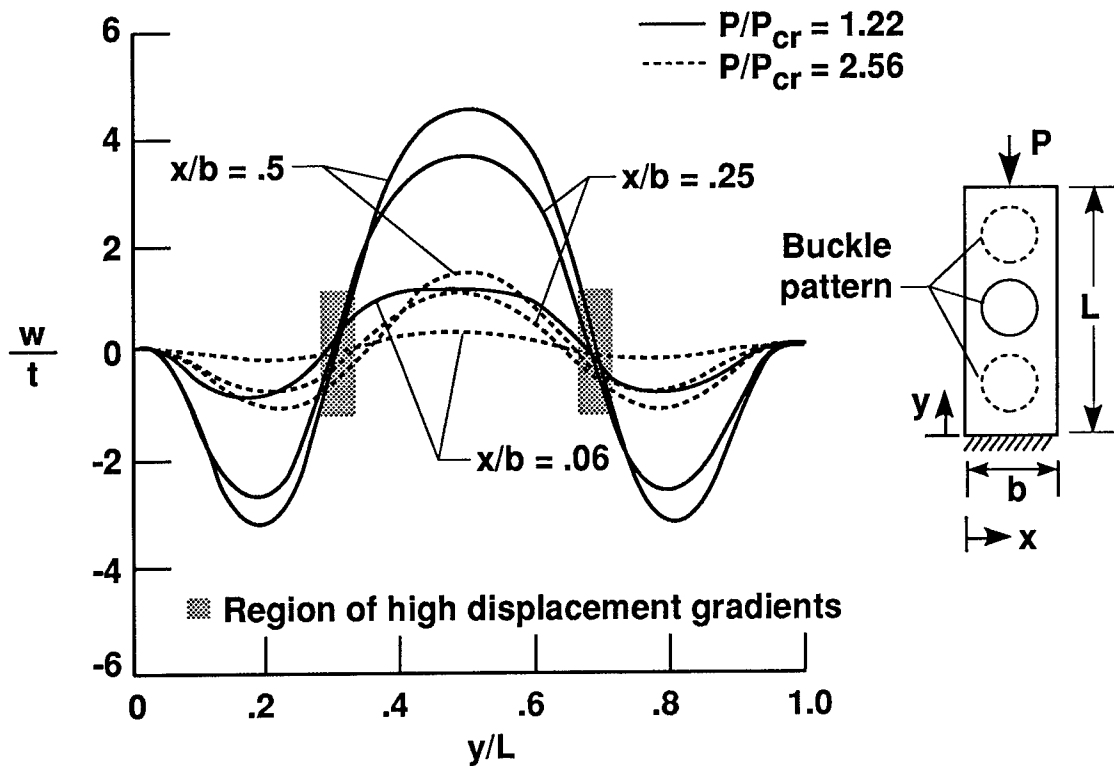
5 (a) Impact damage barely visible prior to load (impact speed 175 ft/sec).

5 (b) Severe impact damage (impact speed 250 ft/sec).

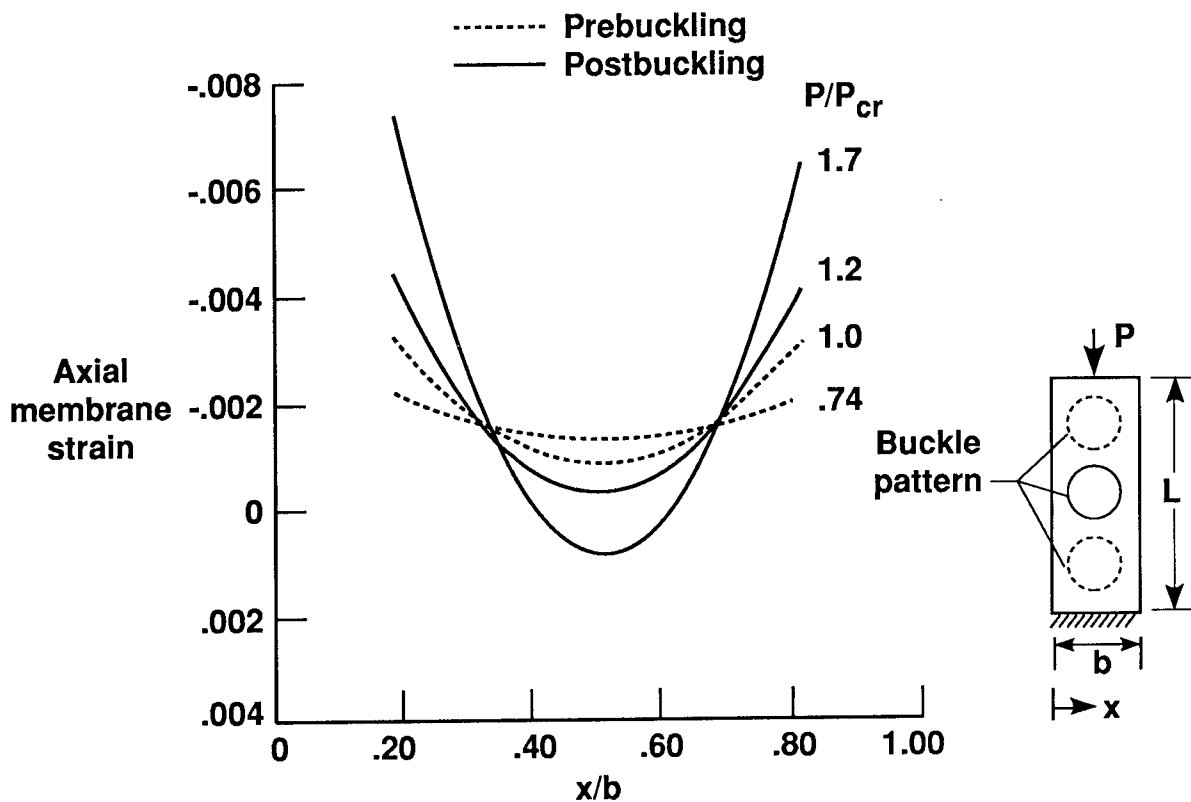
Figure 5. Normalized load versus normalized end-shortening for graphite-epoxy panels with a  $[(\pm 45)_2/90]_s$  stacking sequence impacted at the center or side with the same impact speed.  $A$  is cross-sectional area.



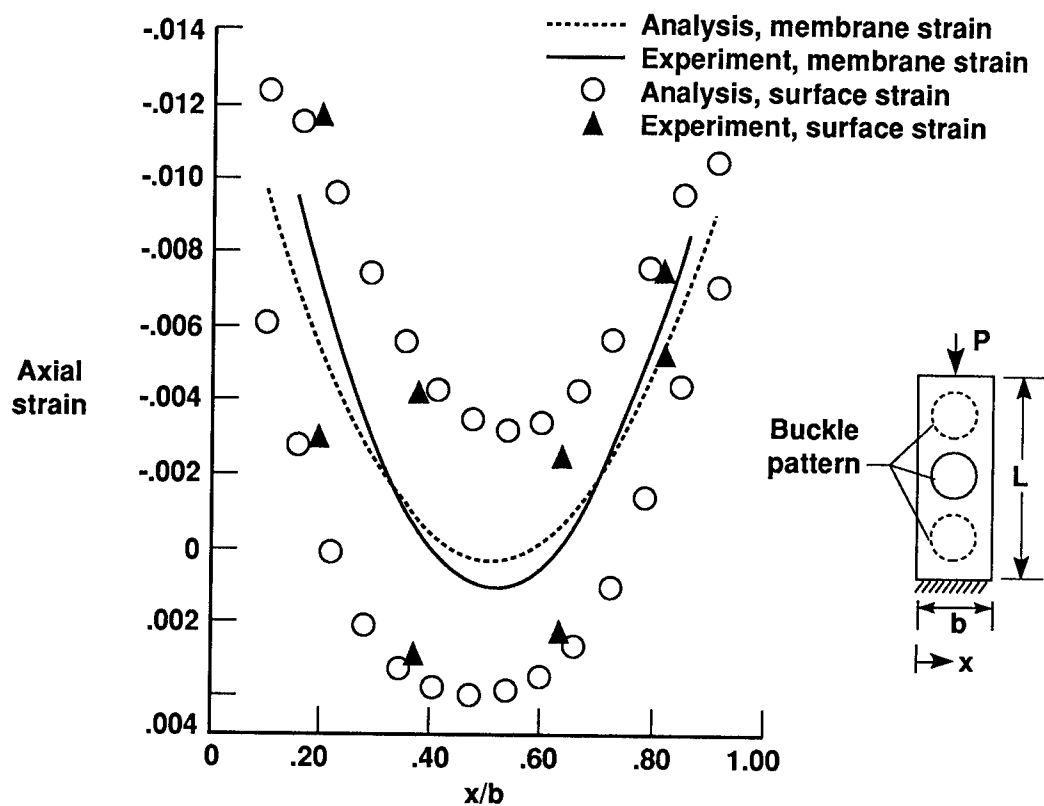
6 (a) Normalized load versus normalized end-shortening.  $A$  is cross-sectional area.



6 (b) Normalized out-of-plane displacement versus axial location at two values of load.



6 (c) Axial membrane strain versus normalized width location for various load levels at a nodal line.



6 (d) Strain versus width location at failure.

Figure 6. Analytically determined displacements and strains for four-inch wide control panels with a  $[(\pm 45)_2/\overline{90}]_s$  stacking sequence.

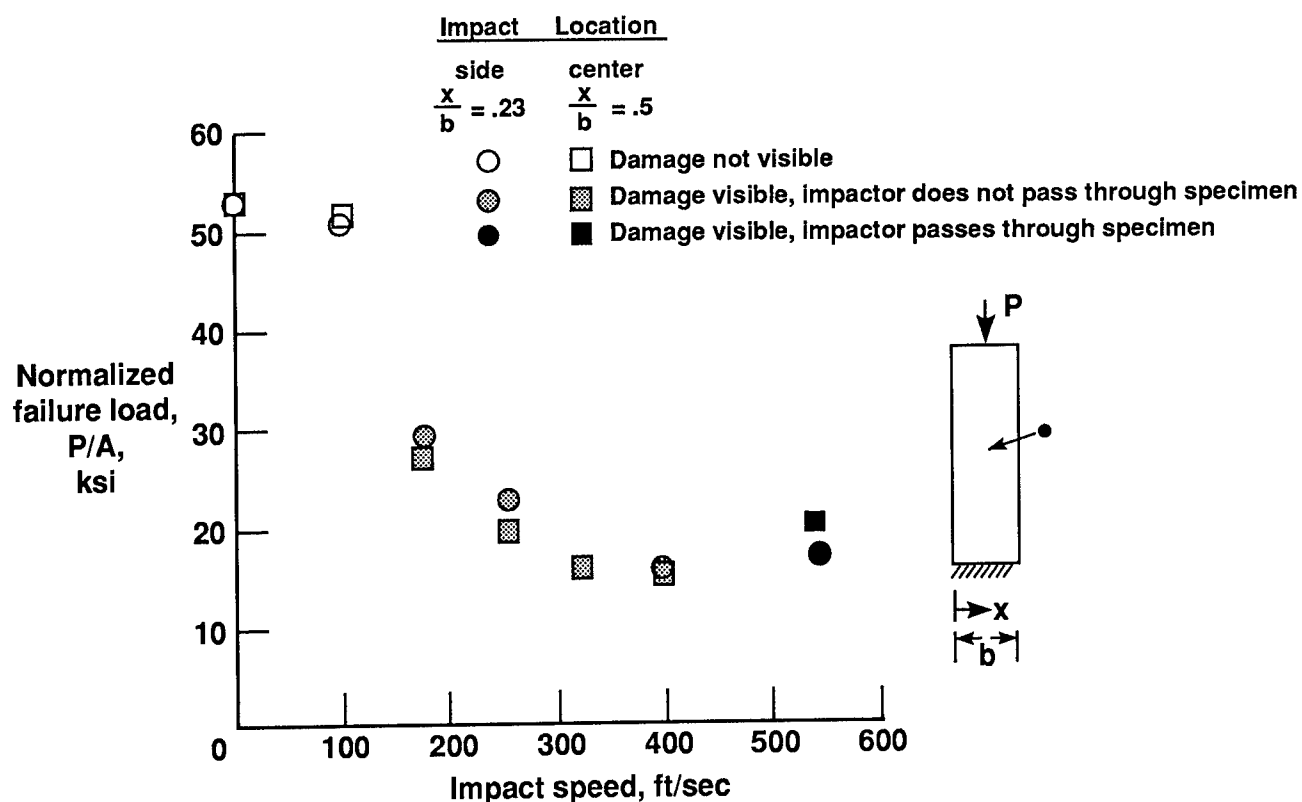


Figure 7. Effect of impact speed on normalized compressive failure load for panels with a  $[(\pm 45)_2/90]_{3s}$  stacking sequence impacted in the center and at the side. A is cross-sectional area.

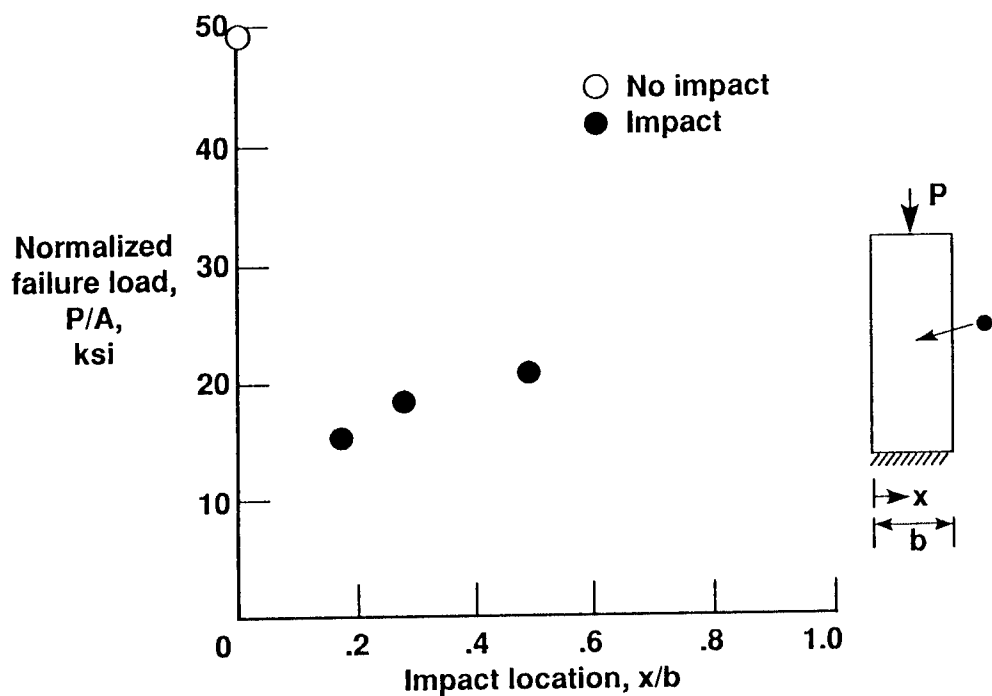


Figure 8. Normalized compressive failure load as a function of impact location four-inch wide panels with a  $[(\pm 45)_2/90]_{3s}$  stacking sequence impacted at 500 ft/sec. A is cross-sectional area.

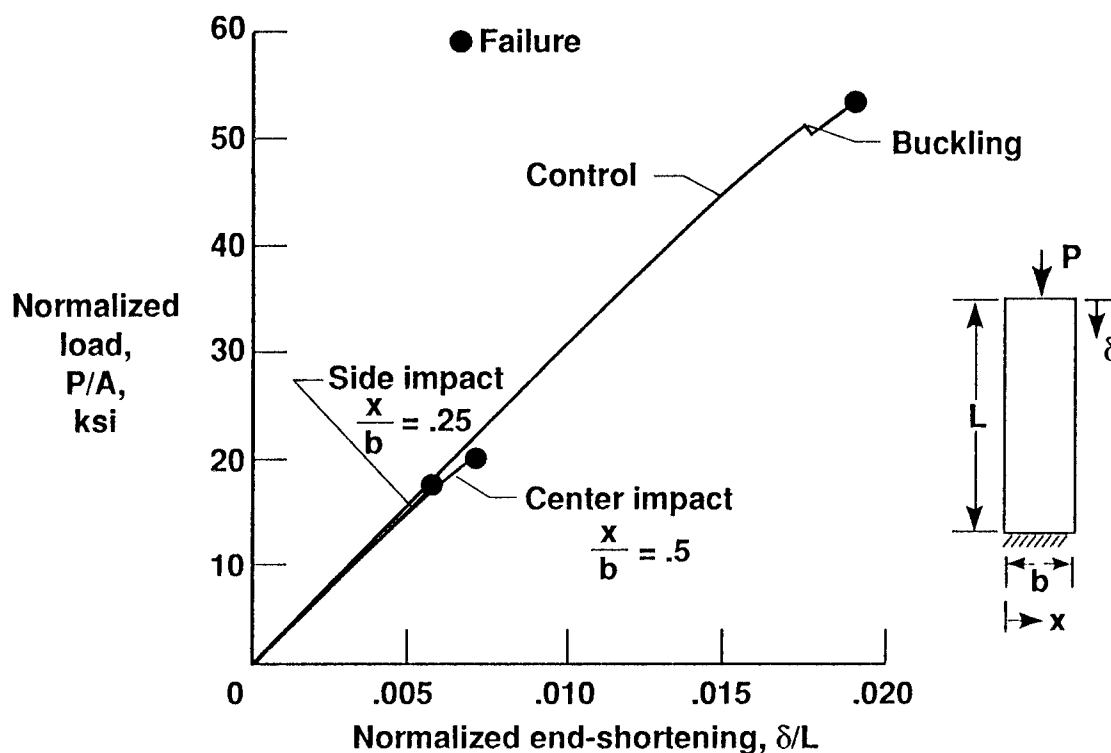


Figure 9. Normalized load versus normalized end-shortening for graphite-epoxy panels with a  $[(\pm 45)_2/90]_{3s}$  stacking sequence with no impact and impacted at the center or side at 540 ft/sec. A is cross-sectional area.

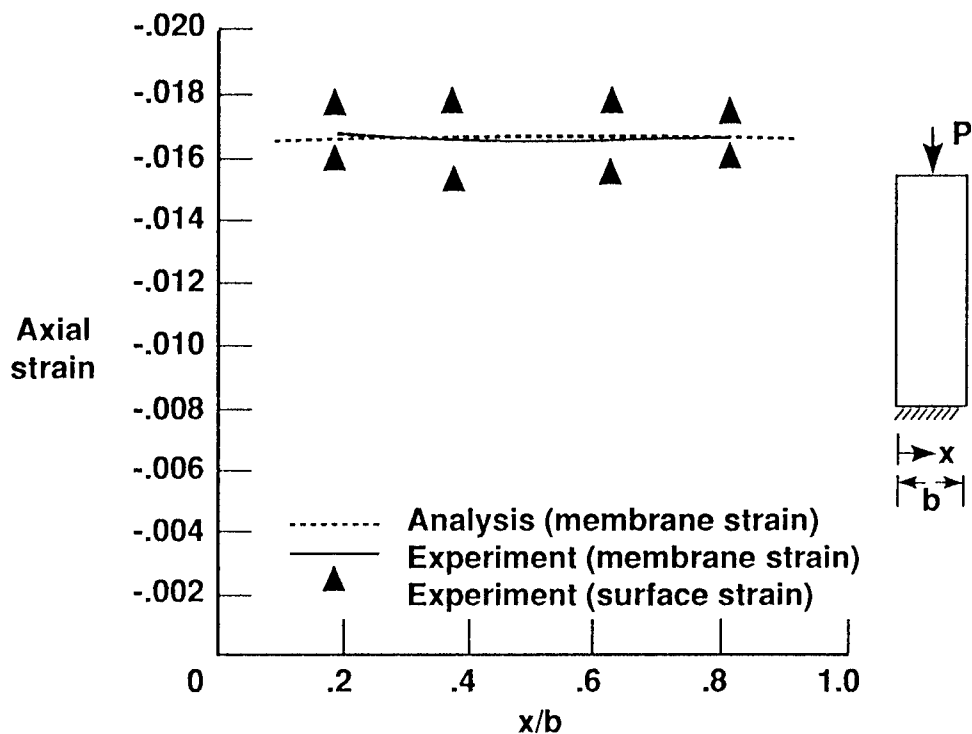


Figure 10. Strain versus normalized width location at failure of four-inch wide control panel with a  $[(\pm 45)_2/90]_{3s}$  stacking sequence.

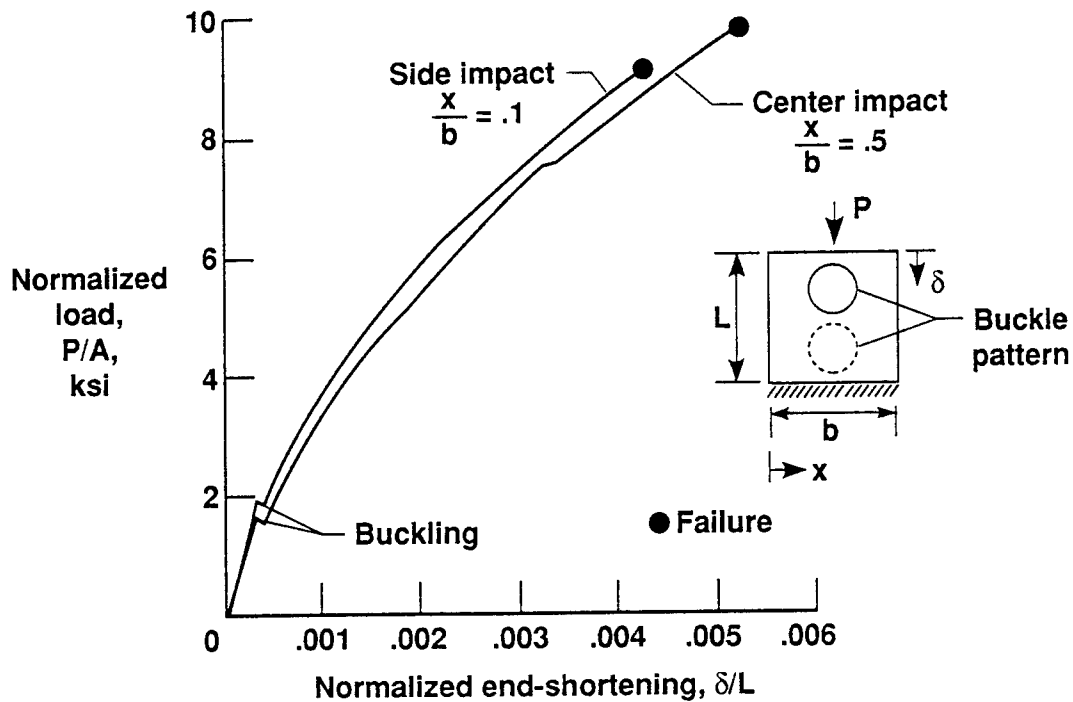


Figure 11. Normalized load versus normalized end-shortening for graphite-epoxy panels with a  $[\pm 45/0_2]_s$  stacking sequence impacted at the center or side with an impact speed of 150 ft/sec, causing barely visible damage prior to load. A is cross-sectional area.

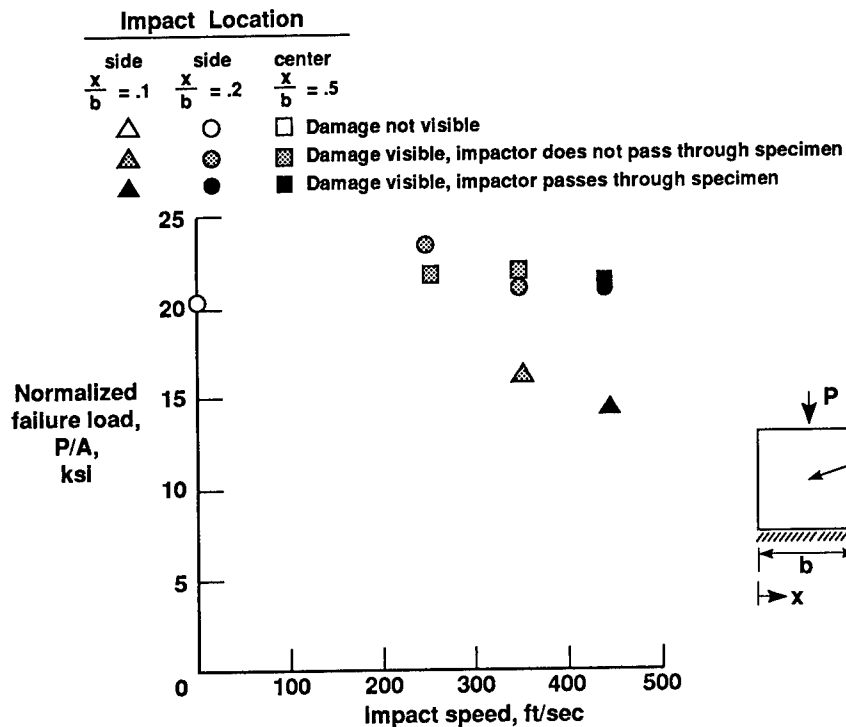


Figure 12. Effect of impact speed on normalized compressive failure load of graphite-epoxy panels with a  $[\pm 45/0_2]_{3s}$  stacking sequence. A is cross-sectional area.

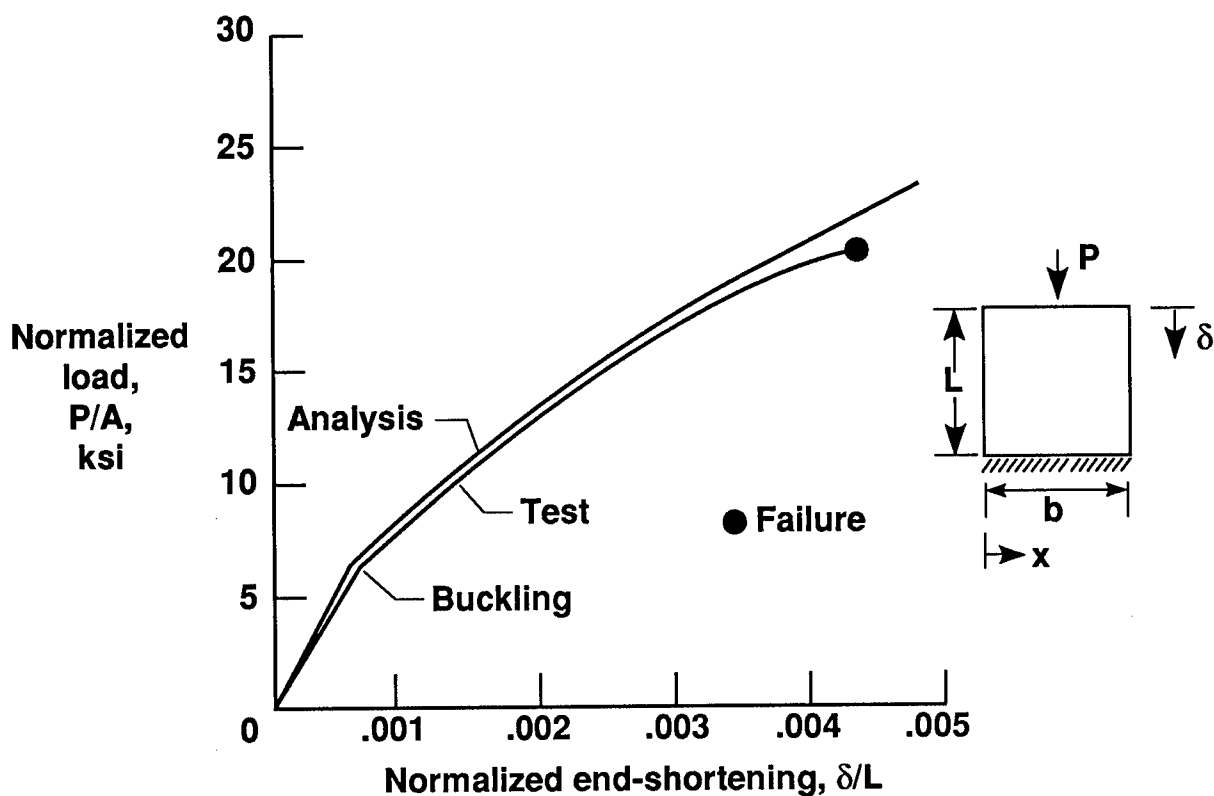


Figure 13. Normalized load versus end-shortening for control panel with a  $[\pm 45/0_2]_{3s}$  stacking sequence.  $A$  is cross-sectional area.

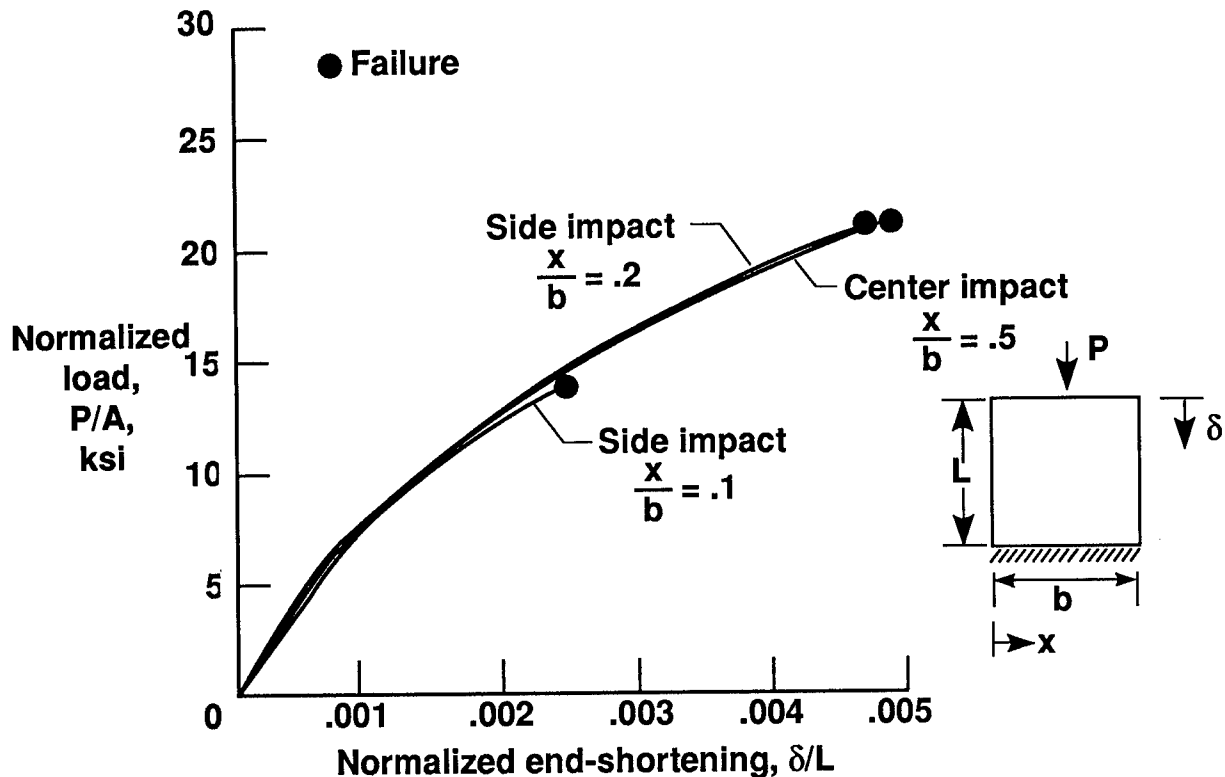
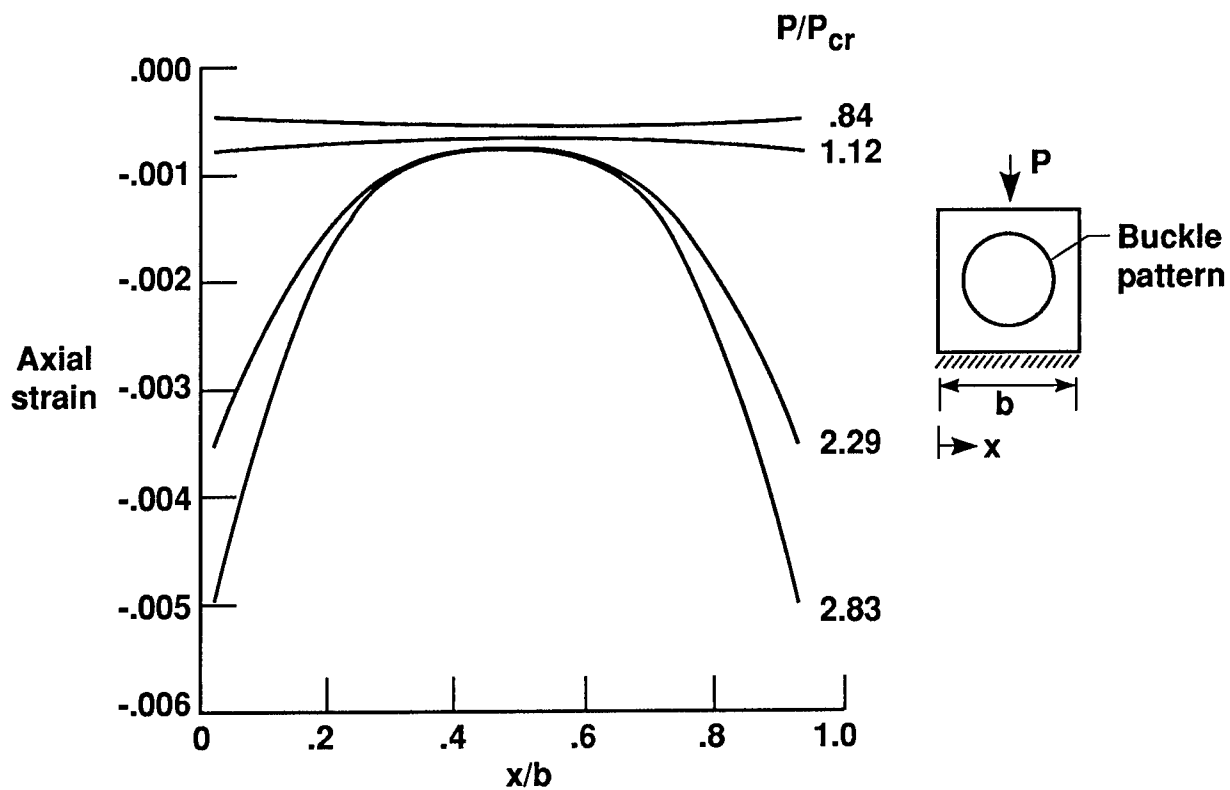
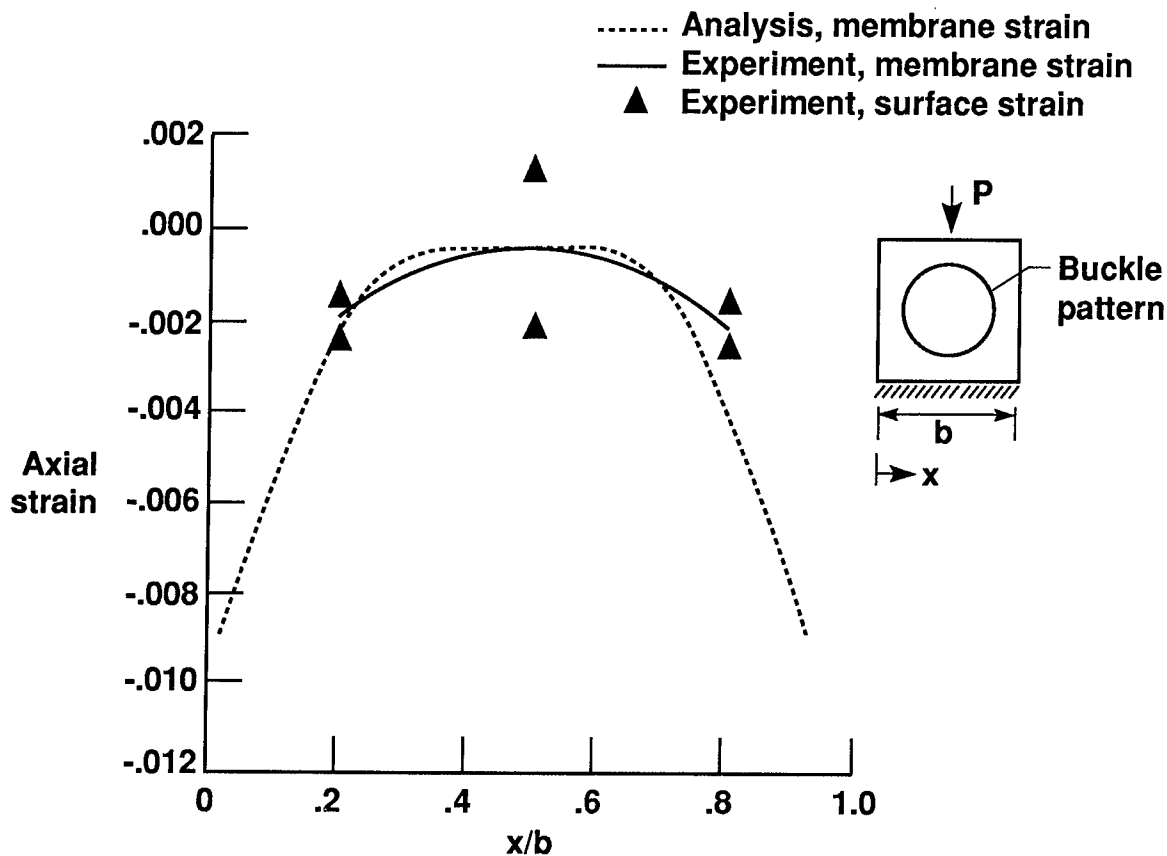


Figure 14. Normalized load versus normalized end-shortening for panels with a  $[\pm 45/0_2]_{3s}$  stacking sequence impacted at 450 ft/sec in the center and at two side locations.  $A$  is cross-sectional area.





15 (a) Strain for several load levels.



15 (b) Strain at failure.

Figure 15. Strain versus width location of ten-inch wide control panel at axial centerline with a  $[\pm 45/0_2]_{3s}$  stacking sequence.

# **IMPACT DAMAGE RESISTANCE OF COMPOSITE FUSELAGE STRUCTURE, PART I<sup>1</sup>**

**E. F. Dost, W. B. Avery, L. B. Ilcewicz, and D. H. Grande**

**Boeing Commercial Airplane Group, Seattle, WA.**

**B. R. Coxon**

**Integrated Technologies, Inc., Bothell, WA.**

## **ABSTRACT**

Impact damage resistance of laminated composite transport aircraft fuselage structure was studied experimentally. A statistically based designed experiment was used to examine numerous material, laminate, structural, and extrinsic (e.g., impactor type) variables. The relative importance and a quantitative measure of the effect of each variable and variable interactions on responses including impactor dynamic response, visibility, and internal damage state were determined. The study utilized 32 three-stiffener panels, each with a unique combination of material type, material form, and structural geometry. Two manufacturing techniques, tow placement and tape lamination, were used to build panels representative of potential fuselage crown, keel, and lower side-panel designs. Various combinations of impactor variables representing various foreign-object-impact threats to the aircraft were examined. Impacts performed at different structural locations within each panel (e.g., skin midbay, stiffener attaching flange, etc.) were considered separate parallel experiments. The relationship between input variables, measured damage states, and structural response to this damage are presented including recommendations for materials and impact test methods for fuselage structure.

## **INTRODUCTION**

Carbon fiber composites have the potential of reducing both the weight and cost of primary aircraft structure. The high specific stiffness and strength along with corrosion and fatigue resistance have been cited by many researchers as benefits of composite materials. One major weakness of laminated composites is their reduced strength when subject to foreign object impact. This susceptibility to impact damage has been studied by many investigators. Impact induced matrix damage has been found to reduce the compressive strength [1, 2], while fiber damage reduces both the compressive and tension strengths [3, 4].

Impact studies conducted by NASA and other researchers in the past [e.g., 1, 2, 5-7] concentrated on wing type structure. Impact testing was performed on both coupons and subcomponents using simulated impact threats, usually with a hemispherical tip. Internal Boeing studies involving various shop tools dropped onto test articles were correlated to these assumed impact threats. The coupons and subcomponents were then tested in axial compression (to simulate upper wing surface loads) to determine the effect of the damage.

---

<sup>1</sup> This work was funded by Contract NAS1-18889, under direction of J.G. Davis and W.T. Freeman of NASA Langley Research Center.

The damage states and residual strengths observed in these early tests were found to be a strong function of impact energy and relatively independent of the impactor shape. Matrix damage (i.e., delaminations and transverse cracks) was found to be the primary failure mechanism for the "brittle" epoxy laminates under study at that time. The areal extent of the matrix damage was a strong function of the impact energy. Local fiber failures were suppressed by the formation of large delaminations which reduced local contact forces by locally softening the laminate. Matrix damage dominated compression-after-impact (CAI) strength [6], while fiber failure, which would be strongly influenced by impactor geometry, was not found to be a strong contributor to the observed compression strength degradation. These findings along with ease of analytical modeling lead to the use of spherically shaped impactors with diameters between 12.7 mm and 25.4 mm for the majority of studies on impact on fibrous composites to date.

Coupon level tests such as the 6.35 mm thick NASA ST-1 [8] and the 4.6 mm thick Boeing 4"x6" CAI [6] were developed based on results and observations from these early impact studies. The design of these specimens and tests emphasized the effects of matrix damage. Much of recent composite material development efforts have concentrated on improving CAI while keeping some minimum hot/wet compression strength. Approaches for improving CAI have included toughened (high elongation) thermoset matrices [9], addition of discrete interlayers (e.g., adhesive or elastomeric particle) [10, 11], through-thickness stitching [12, 13], and braided fiber architectures [14].

Improvements in CAI by the first and second methods stated above have been accomplished by reducing the areal extent of matrix damage [15]. This reduction of delamination planar area would tend to increase local contact forces during an impact event. Braided composites may absorb some energy through matrix cracking, but delamination is suppressed by the fiber architecture [14]. Both may have a stronger tendency toward fiber failures under the impactor and have post-impact strengths influenced by impactor geometry.

An experimental study to investigate impact damage that may occur in laminated composite aircraft fuselage structure was performed. Material, laminate, structural, and numerous impact variables were considered. A design of experiments (DOE) technique was used to study the large number of variables. The relative importance and a quantitative measure of the effect of variables and variable interactions with respect to specific responses were determined. The current study utilized 32 three-stiffener panels, each with a distinct combination of material type, material form, and structural geometry to study the impact damage resistance of fuselage structure. Laminate and structural variable levels were representative of potential fuselage crown, keel, and lower side-panel designs.

## TEST MATRIX DEVELOPMENT

### Variable Identification

**Intrinsic Variables.** Aircraft fuselage can be designed with many different combinations of material, layup, and structural geometry depending on specific requirements. An aircraft fuselage may be considered as four separate quadrants, each having different design drivers. The crown (top) is dominated by tension loads, the keel (bottom) is predominantly designed by compression, and the side panels have combined shear and axial loads. The entire fuselage cylinder is subjected to hoop tension from internal pressure. An aircraft designer must choose specific values (levels) from each potential variable (e.g., fiber/matrix type, stiffener geometry, skin thickness/layup, etc.) to design the structure in each quadrant. The variables associated with the structure are termed *intrinsic* variables. Table 1 lists all intrinsic variables studied along with their respective levels.

Variable	Low Level	High Level
Fiber Type	AS4	IM7
Matrix Type	938	977-2
Fiber Volume	48%	56.5%
Material Form (Stiffener Layup)	Tow (Soft)	Tape (Hard)
Skin Layup	Soft	Hard
Stiffener Type	Blade	Hat
Stiffener Spacing	17.8 cm (7 in)	30.5 cm (12 in)
Laminate Thickness	2.26 mm (0.0888 in)	4.51 mm (0.1776 in)

Layups	
Hard Skin (Thin)	(45/ 90/ -45/ 0/ 90/ 0) <sub>S</sub>
Soft Skin (Thin)	(45/ 90/ -45/ 45/ 0/ -45) <sub>S</sub>
Hard Skin (Thick)	(45/ 90/ -45/ 0/ 45/ 90/ -45/ 0/ 90/ 0/ 90/ 0) <sub>S</sub>
Soft Skin (Thick)	(45/ 90/ -45/ 45/ 0/ -45/ -45/ 0/ 45/ -45/ 90/ 45) <sub>S</sub>
Hard Stiffener (Thin)	(22.5/ 90/ -22.5/ 0) <sub>S</sub>
Soft Stiffener (Thin)	(30/ 90/ -30/ 0) <sub>S</sub>
Hard Stiffener (Thick)	(22.5/ 90/ -22.5/ 0) <sub>2S</sub>
Soft Stiffener (Thick)	(30/ 90/ -30/ 0) <sub>2S</sub>

**Table 1: Intrinsic Variables**

Material variables may include fiber, matrix, and their combined architecture. Graphite or carbon fiber properties may be quantified in terms of axial stiffness, tensile strength, and cross-sectional size/shape. The matrix is generally classified by its stiffness, strengths, and in-situ composite toughness (i.e., inter- and intra-laminar toughness). The performance of the composite is influenced by the fiber/matrix architecture. This is characterized by the overall fiber volume, fiber/resin distribution, interlayer structure, amount of fiber waviness, void content, and fiber-matrix interface. Many of these material attributes are not controllable when two or more of are studied simultaneously. Variables considered for study were fiber type, matrix type, and overall fiber volume.

Various schemes for manufacturing laminates exist, including hand layup, automatic tape layup (ATL), filament winding, advanced tow placement (ATP), and resin transfer molding (RTM). Cost effective fabrication of large fuselage quadrants requires lamination flexibility including the ability to tailor thickness and follow surfaces with complex contours. Hand layup and ATP were chosen for this study because both meet these lamination flexibility requirements. In addition, hand layup offers a well understood material form and part performance, while ATP offers reduced manufacturing and raw material costs. Laminate layup and thickness were also included as variables in these experiments.

Structural configuration has a strong influence on the cost, weight, and assembly of the fuselage [16]. Structural performance; including local skin buckling, overall panel stability, impact damage resistance, and damage tolerance, is governed by the skin thickness and stiffness; stiffener geometry, layup, and spacing; and the applied loads. Blade and closed hat stiffeners were studied because they provide a distinct range in structural response for stiffened-skin panel construction.

**Extrinsic Variables.** The potential for foreign-object impact on aircraft primary structure starts the day the first element is cured and continues until the aircraft is retired from service. Threats include

dropped hand and power tools, tool boxes, hail, runway debris, engine-burst fragments, ground handling equipment [17]. Generally, impacts may occur at any location on both the inner and outer surfaces of the structure, although certain types of impacts will be constrained to specific regions of the aircraft (e.g., hail will generally strike the crown, other horizontal surfaces, leading edges, and nose of the aircraft). The environment during an impact event is governed by those the aircraft may see while in service. Variables associated with an impact event including when, how, and where, are classified as *extrinsic* variables.

Impact threats may be categorized by the mass, shape, size, stiffness, velocity, and incidence angle of the impactor. The current experiment considered all of these impactor variables, except incidence angle and velocity. Impacting at oblique angles was found to be experimentally difficult with the equipment available. Impact energy was substituted for impact velocity because unrealistically high impact energies result when velocity and mass are combined in a partially crossed experiment. Temperature at impact was chosen to examine the effect of environment on impact damage. All extrinsic variables and the associated levels are listed in Table 2.

Variable	Low Level	High Level
Impactor Stiffness	2.8 GPa (0.4 Msi)	210 GPa (30 Msi)
Impactor Mass	0.28 kg (0.62 lbm)	6.31 kg (13.9 lbm)
Impact Energy	23 J (200 in-lb)	136 J (1200 in-lb)
Impactor Shape	Flat	Spherical
Impactor Diameter	6.35 mm (0.25 in)	25.4 mm (1.00 in)
Temperature at Impact	21°C (70°F)	83°C (180°F)

**Table 2: Extrinsic Variables**

**Design of Experiments.** The final experiment examined fourteen variables to determine their relationship to fuselage impact damage resistance. The examination of this large number of variables within one comprehensive study required the use of a statistical technique known as *Design of Experiments (DOE)* [18, 19]. A DOE provides a systematic way to design an efficient experiment, collect data, and analyze the results. The DOE used for this study, a 32 run, split-plot fractional factorial design, provided information on the main variables and indicated whether variable interactions existed.

The use of this DOE put limitations on the number of variable levels and the types of variables which could be studied. The number of variable levels was restricted to two, and had to be chosen so that unrealistic combinations were avoided, yet were representative of potential fuselage designs. Decisions on conflicting variables were made based on practical considerations and our knowledge and intuition of impact damage resistance. Table 3 contains a list of the variables studied with their respective levels as they fit into the DOE.

The design of experiments technique required quantifiable response measurements for all 32 runs to evaluate the effect of variables and interactions. Responses measured and studied via the DOE included: indentation depth, planar damage area, and fiber damage average length and through-thickness distribution. Preliminary results of flexural wave propagation measurements are presented, but not analyzed in the context of the DOE.

Table 3: Thirty-Two DOE Runs with Variable Levels

Run #	Panel ID	Fiber Type	Matrix Type	Fiber Volume	Material Form (Stiffener Layup)	Skin Layup	Stiffener Type	Stiffener Web Spacing	Laminate Thickness	Impact Stiffness	Impact Mass	Impact Energy	Impact Shape	Impact Diameter	Temperature
1	28-1B	AS4	938	0.480	Tow (Soft)	Soft	Blade	17.8 cm	2.26 mm	3 GPa	0.28 kg	23 J	Flat	6.35 mm	210C
2	28-1A	AS4	938	0.480	Tow (Soft)	Soft	Blade	17.8 cm	4.51 mm	3 GPa	6.31 kg	136 J	Spherical	25.4 mm	830C
3	28-7A	AS4	938	0.480	Tow (Soft)	Hard	Hat	30.5 cm	4.51 mm	210 GPa	6.31 kg	136 J	Flat	6.35 mm	210C
4	28-7B	AS4	938	0.480	Tow (Soft)	Hard	Hat	30.5 cm	2.26 mm	210 GPa	0.28 kg	23 J	Spherical	25.4 mm	830C
5	28-2B	AS4	938	0.565	Tape (Hard)	Hard	Blade	17.8 cm	2.26 mm	210 GPa	0.28 kg	136 J	Spherical	25.4 mm	210C
6	28-2A	AS4	938	0.565	Tape (Hard)	Hard	Blade	17.8 cm	4.51 mm	210 GPa	6.31 kg	23 J	Flat	6.35 mm	830C
7	28-8A	AS4	938	0.565	Tape (Hard)	Soft	Hat	30.5 cm	4.51 mm	3 GPa	0.28 kg	23 J	Spherical	25.4 mm	210C
8	28-8B	AS4	938	0.565	Tape (Hard)	Soft	Hat	30.5 cm	2.26 mm	3 GPa	6.31 kg	136 J	Flat	6.35 mm	830C
9	28-1B	AS4	977-2	0.565	Tow (Soft)	Soft	Hat	17.8 cm	2.26 mm	210 GPa	0.28 kg	136 J	Flat	6.35 mm	830C
10	28-1A	AS4	977-2	0.565	Tow (Soft)	Soft	Hat	17.8 cm	4.51 mm	210 GPa	6.31 kg	23 J	Spherical	25.4 mm	210C
11	28-7A	AS4	977-2	0.565	Tow (Soft)	Hard	Blade	30.5 cm	4.51 mm	3 GPa	0.28 kg	23 J	Flat	6.35 mm	830C
12	28-7B	AS4	977-2	0.565	Tow (Soft)	Hard	Blade	30.5 cm	2.26 mm	3 GPa	6.31 kg	136 J	Spherical	25.4 mm	210C
13	28-2B	AS4	977-2	0.480	Tape (Hard)	Hard	Hat	17.8 cm	2.26 mm	3 GPa	0.28 kg	136 J	Flat	6.35 mm	830C
14	28-2A	AS4	977-2	0.480	Tape (Hard)	Soft	Blade	30.5 cm	4.51 mm	210 GPa	6.31 kg	23 J	Spherical	25.4 mm	210C
15	28-8A	AS4	977-2	0.480	Tape (Hard)	Soft	Blade	30.5 cm	2.26 mm	210 GPa	0.28 kg	136 J	Flat	6.35 mm	830C
16	28-8B	AS4	977-2	0.480	Tape (Hard)	Soft	Hat	30.5 cm	4.51 mm	3 GPa	0.28 kg	23 J	Spherical	25.4 mm	210C
17	28-5B	IM7	977-2	0.480	Tow (Soft)	Soft	Hat	30.5 cm	2.26 mm	3 GPa	6.31 kg	136 J	Flat	6.35 mm	830C
18	28-5A	IM7	977-2	0.480	Tow (Soft)	Soft	Hat	30.5 cm	4.51 mm	3 GPa	0.28 kg	23 J	Spherical	25.4 mm	210C
19	28-3A	IM7	977-2	0.480	Tow (Soft)	Hard	Blade	17.8 cm	2.26 mm	210 GPa	6.31 kg	136 J	Flat	6.35 mm	830C
20	28-3B	IM7	977-2	0.480	Tow (Soft)	Hard	Blade	17.8 cm	4.51 mm	210 GPa	0.28 kg	23 J	Spherical	25.4 mm	210C
21	28-6B	IM7	977-2	0.565	Tape (Hard)	Hard	Hat	30.5 cm	2.26 mm	210 GPa	6.31 kg	136 J	Flat	6.35 mm	830C
22	28-6A	IM7	977-2	0.565	Tape (Hard)	Hard	Hat	30.5 cm	4.51 mm	3 GPa	0.28 kg	23 J	Spherical	25.4 mm	210C
23	28-4B	IM7	977-2	0.565	Tape (Hard)	Soft	Blade	17.8 cm	2.26 mm	210 GPa	6.31 kg	136 J	Flat	6.35 mm	830C
24	28-4A	IM7	977-2	0.565	Tape (Hard)	Soft	Blade	17.8 cm	4.51 mm	210 GPa	0.28 kg	23 J	Spherical	25.4 mm	210C
25	28-5B	IM7	938	0.565	Tow (Soft)	Soft	Blade	30.5 cm	2.26 mm	3 GPa	6.31 kg	136 J	Flat	6.35 mm	830C
26	28-5A	IM7	938	0.565	Tow (Soft)	Soft	Blade	30.5 cm	4.51 mm	3 GPa	0.28 kg	23 J	Spherical	25.4 mm	210C
27	28-3A	IM7	938	0.565	Tow (Soft)	Hard	Hat	17.8 cm	2.26 mm	210 GPa	6.31 kg	136 J	Flat	6.35 mm	830C
28	28-3B	IM7	938	0.565	Tow (Soft)	Hard	Hat	17.8 cm	4.51 mm	210 GPa	0.28 kg	23 J	Spherical	25.4 mm	210C
29	28-6B	IM7	938	0.480	Tape (Hard)	Hard	Blade	30.5 cm	2.26 mm	3 GPa	6.31 kg	136 J	Flat	6.35 mm	830C
30	28-6A	IM7	938	0.480	Tape (Hard)	Hard	Blade	30.5 cm	4.51 mm	3 GPa	0.28 kg	23 J	Spherical	25.4 mm	210C
31	29-4A	IM7	938	0.480	Tape (Hard)	Soft	Hat	17.8 cm	2.26 mm	210 GPa	6.31 kg	136 J	Flat	6.35 mm	830C
32	29-4B	IM7	938	0.480	Tape (Hard)	Soft	Hat	17.8 cm	4.51 mm	210 GPa	0.28 kg	23 J	Spherical	25.4 mm	210C

## EXPERIMENTAL TECHNIQUE

### Specimen Preparation

The intrinsic variables in the test matrix were implemented in 32 three-stiffener panels, one for each of the 32 runs of the DOE test matrix and each having a distinct combination of variable levels. Careful placement of variables into the DOE test matrix resulted in identical panel configurations except for laminate thickness for every two runs (e.g., 1 & 2, 3 & 4). Sixteen 2.79 meter long panels with a 1.27 meter long thick constant gage section, a 0.25 meter long thickness transition zone, and a 1.27 meter long thin constant gage section were designed. Formal drawings of these 16 panels were created, describing all material and fabrication requirements. An abbreviation of the drawing number followed by an "A" for the thick section and a "B" for the thin section was used to identify each panel as shown in Table 3.

**Materials.** Eight distinct combinations of fiber type, matrix type, fiber volume, and material form were specified by the implementation of these variables into the DOE matrix. All eight materials, four pre-impregnated tow and four pre-impregnated tape, were manufactured by ICI Fiberite. The tow was made using solvent impregnation, while tape was created using hot-melt impregnation. Minimum property requirements for acceptance tests were established from known fiber and matrix properties using micromechanics [20]. The material constitutive properties along with calculated lamina properties are given in Table 4.

**Tape Hand Layup.** Panels fabricated using prepreg tape hand layup were manufactured at Boeing's composite fabrication facility in Auburn, Washington. Individual plies were laminated into flat skin panels and stiffener charges using a ply layup template (PLT) created from the formal drawings. Skin and stiffener layups were vacuum compacted following application of every ply. Skin panels were stored under vacuum, while the stiffeners were being prepared.

The flat stiffener charges were formed into appropriate stiffener cross-sections following layup. Closed-hat stiffeners were formed to their final shape using one forming operation over elastomeric mandrels (Figure 1). Blade stiffeners required four major fabrication steps: first, angles were formed over polished-steel-angle mandrels; second, the angles were assembled into a blade section; third, a radius filler was formed from the pre-impregnated graphite; and fourth, the radius filler was placed into the blade between the two angles (Figure 2). The stiffeners were assembled to the skin panel per PLT markings and the assembled panel was bagged and cured per Boeing specifications.

The panel periphery and blade stiffener tops were trimmed to their final dimensions following cure. The 2.79 meter long panels were machined into the three sections described above. All panels were non-destructively inspected using 10 MHz pulse-echo ultrasonics for the skins and 5 MHz through-transmission ultrasonics for the stiffeners. The trimmed panel ends were polished and the cross-section inspected via optical microscopy to validate the ultrasound results.

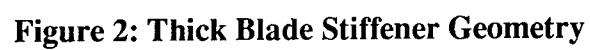
MATERIAL SYSTEM	AS4/3501-6 (6k tow)	AS4/3501-6 (tape)	IM7/977-2 (12k tow)	IM7/977-2 (tape)	IM7/3501-6 (12k tow)	IM7/3501-6 (tape)	AS4/977-2 (6k tow)	AS4/977-2 (tape)
R.C.	44.4%	35.7%	44.8%	36.8%	34.9%	44.1%	37.3%	44.9%
F.V.	48.5%	56.8%	47.1%	56.3%	57.4%	48.8%	55.8%	47.3%
CONSTITUTIVE PROPS.								
fiber:								
E(1)t	3.400E+07	3.400E+07	3.800E+07	3.800E+07	3.800E+07	3.800E+07	3.400E+07	3.400E+07
E(1)c	3.250E+07	3.250E+07	3.450E+07	3.450E+07	3.450E+07	3.450E+07	3.250E+07	3.250E+07
E(2)	2.300E+06	2.300E+06	2.300E+06	2.300E+06	2.300E+06	2.300E+06	2.300E+06	2.300E+06
G(12)	2.700E+06	2.700E+06	2.600E+06	2.600E+06	2.600E+06	2.600E+06	2.700E+06	2.700E+06
NU(12)	0.300	0.300	0.310	0.310	0.310	0.310	0.300	0.300
alpha(1)	-2.000E-07	-2.000E-07	-5.100E-07	-5.100E-07	-5.100E-07	-5.100E-07	-2.000E-07	-2.000E-07
alpha(2)	5.000E-06	5.000E-06	5.200E-06	5.200E-06	5.200E-06	5.200E-06	5.000E-06	5.000E-06
density	1.73	1.78	1.80	1.73	1.80	1.73	1.73	1.78
matrix:								
E	6.200E+05	6.200E+05	5.200E+05	5.200E+05	6.200E+05	6.200E+05	5.200E+05	5.200E+05
G	2.200E+05	2.200E+05	1.800E+05	1.800E+05	2.200E+05	2.200E+05	1.800E+05	1.800E+05
NU	0.350	0.350	0.410	0.410	0.350	0.350	0.410	0.410
alpha	2.630E-05	2.630E-05	2.470E-05	2.470E-05	2.630E-05	2.630E-05	2.470E-05	2.470E-05
density	1.30	1.30	1.30	1.30	1.30	1.30	1.30	1.30
LAMINA PROPERTIES								
E(1)t	1.680E+07	1.958E+07	1.817E+07	2.164E+07	2.207E+07	1.886E+07	1.921E+07	1.634E+07
E(1)c	1.608E+07	1.873E+07	1.652E+07	1.966E+07	2.007E+07	1.715E+07	1.837E+07	1.564E+07
E(2)	1.262E+06	1.379E+06	1.109E+06	1.241E+06	1.388E+06	1.266E+06	1.233E+06	1.111E+06
G(12)	6.103E+05	7.150E+05	4.982E+05	5.973E+05	7.178E+05	6.100E+05	5.946E+05	5.023E+05
NU(12)	0.326	0.322	0.363	0.354	0.327	0.330	0.349	0.358
alpha(1)	3.266E-07	1.788E-07	-9.011E-08	-2.190E-07	-1.571E-07	-1.354E-08	1.115E-07	2.367E-07
alpha(2)	1.421E-05	1.248E-05	1.444E-05	1.256E-05	1.252E-05	1.429E-05	1.251E-05	1.427E-05

Units: Moduli in psi, Densities in kg/m3, CTE's per degree F

Room Temperature Properties

Table 4: Micromechanics Based Ply Properties





**Tow Placement.** Panels manufactured using advanced tow placement were fabricated by Hercules Incorporated's Composite Products Group. A seven-axis numerically-controlled robot was used to fabricate flat skin and stiffener charges from pre-impregnated tow. This machine collimated and spread twelve individual tows into 25 mm wide bands of the appropriate thickness. Pressure applied by the cylindrical-rolling applicator of the tow-placement head helped to compact the laminate. Additionally, the laminate was vacuum compacted following application of every fourth ply. Stiffener forming, panel assembly, bagging, and cure procedures used by Hercules were identical to those performed by Boeing.

### **Impact Testing**

Impact testing was divided into two portions; high mass (6.31 kg) impacts and low mass (0.28 kg) impacts. The equipment used to perform these two types of impacts were of differing design. Nominally, ten impacts were performed on each panel, eight of which were based on the extrinsic variables listed in Table 2. Two additional impacts, one on the skin midbay and one over the stiffener centerline, were performed using a 63.5 mm (2.5 in) diameter lead ball dropped at 56.5 Joules (500 in-lb) to simulate 63.5 mm diameter hail at terminal velocity.

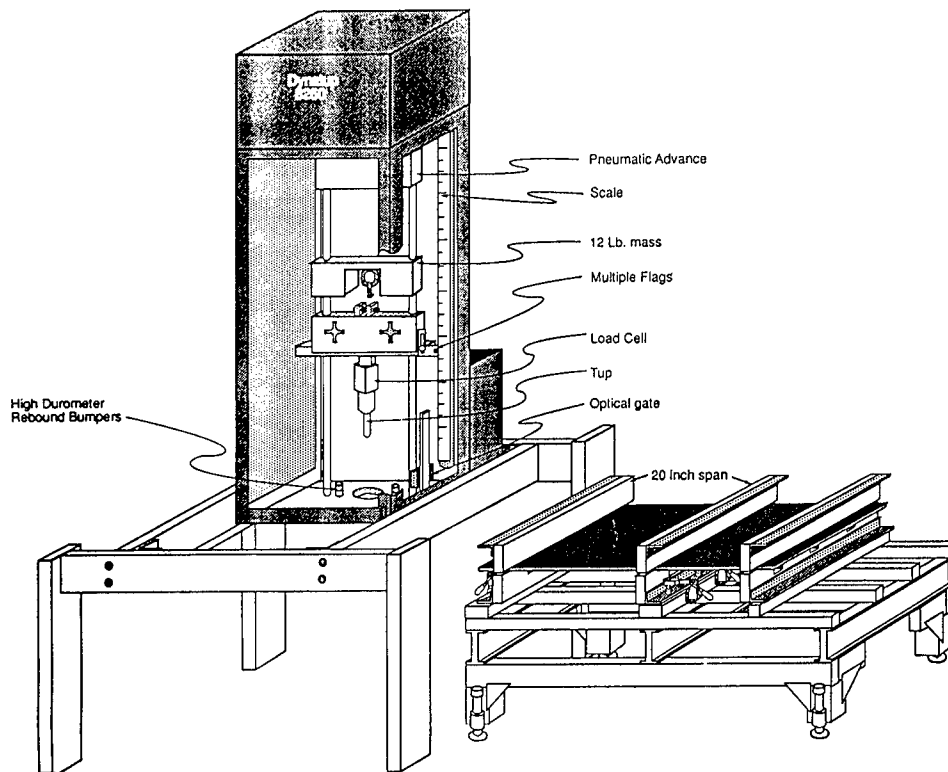
**Boundary Conditions.** The boundary conditions applied to all panels were designed to simulate the circumferential frames found in aircraft fuselage. Supports were placed with a span of 0.51 meter between their inner edges to simulate the fuselage 0.56 meter (22 in) centerline to centerline frame spacing. Three sets of 44.5 mm by 89.9 mm (2" X 4") fir boards were notched to provide clearance for the three stiffeners. The boards were shaved slightly at the stiffener attaching flange locations so that both the skin and attaching flanges were supported during impact. Unnotched boards were placed over the skin side and bolted to the opposing notched board to restrict panel z-axis motion.

Impacts were performed 76.2 mm (3 in) from a support. This distance allowed clearance for the impactor and was probably close to the worst case location. Additionally, it allowed maximum post-impact test of these panels by minimizing the area of panel affected by impact damage. The free end of the panel was restrained with a third pair of supports.

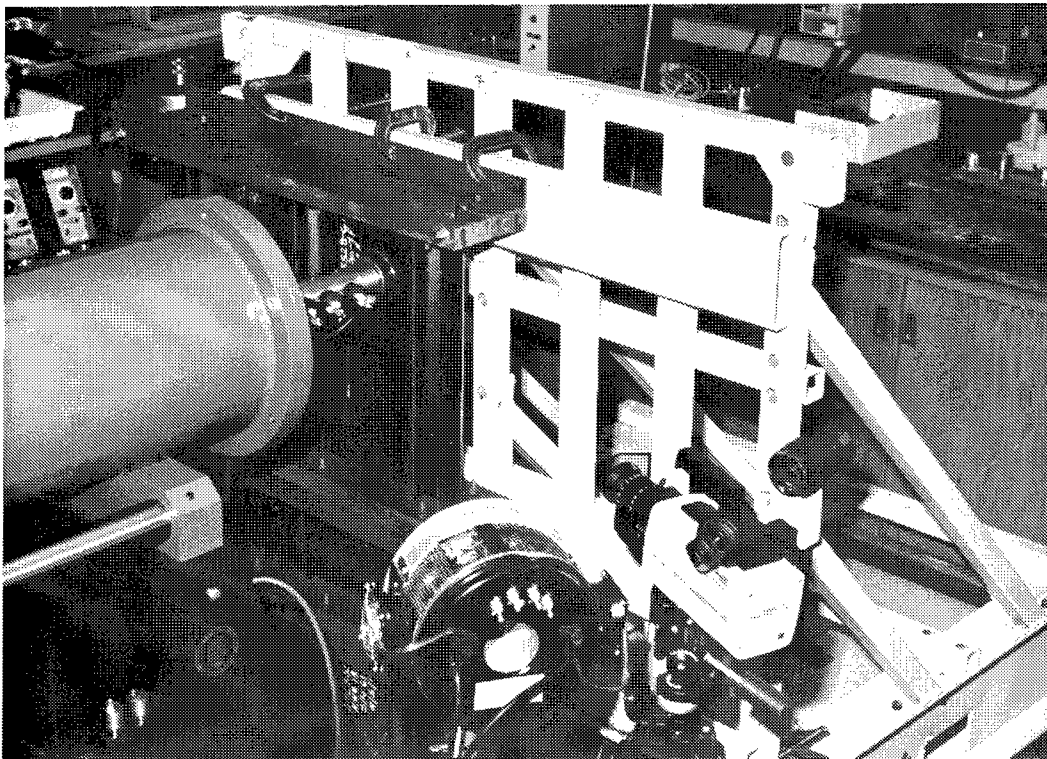
The panel with simulated frames was held in place by steel fixtures which were solidly mounted to cement floors. Figure 3 shows the general fixture configuration of the high mass support fixture. The low mass panel support fixture held panels vertically and is shown in Figure 4. Impact alignment was achieved by aligning crosshairs marked at the desired impact location on the panel with a pointed alignment tup mounted in the impactor. The panel was clamped in place when alignment was within  $\pm 1.27$  mm.

**Impact Tups.** The implementation of impactor variables into the DOE defined eight different impact tups. Materials used to fabricate these tups were steel for hard impactors and graphite/epoxy cut transverse to the plane of lamination for soft impactors. All low and high mass impactor tups were designed with sufficient length to allow panel perforation under maximum deflection.

Steel impacting tups for the high mass impactor were manufactured out of A2 steel and machined to dimensional tolerance of  $\pm 0.051$  mm and a mass of  $226.8 \pm 9.1$  grams. The low mass impactor steel tups were machined from 4140 steel with a dimensional tolerance of  $\pm 0.051$  mm and a mass of  $35.2 \pm 0.2$  grams. All steel tups were hardened to 55-60 Rockwell C.



**Figure 3: High Mass (Dynatup) Impact Apparatus**

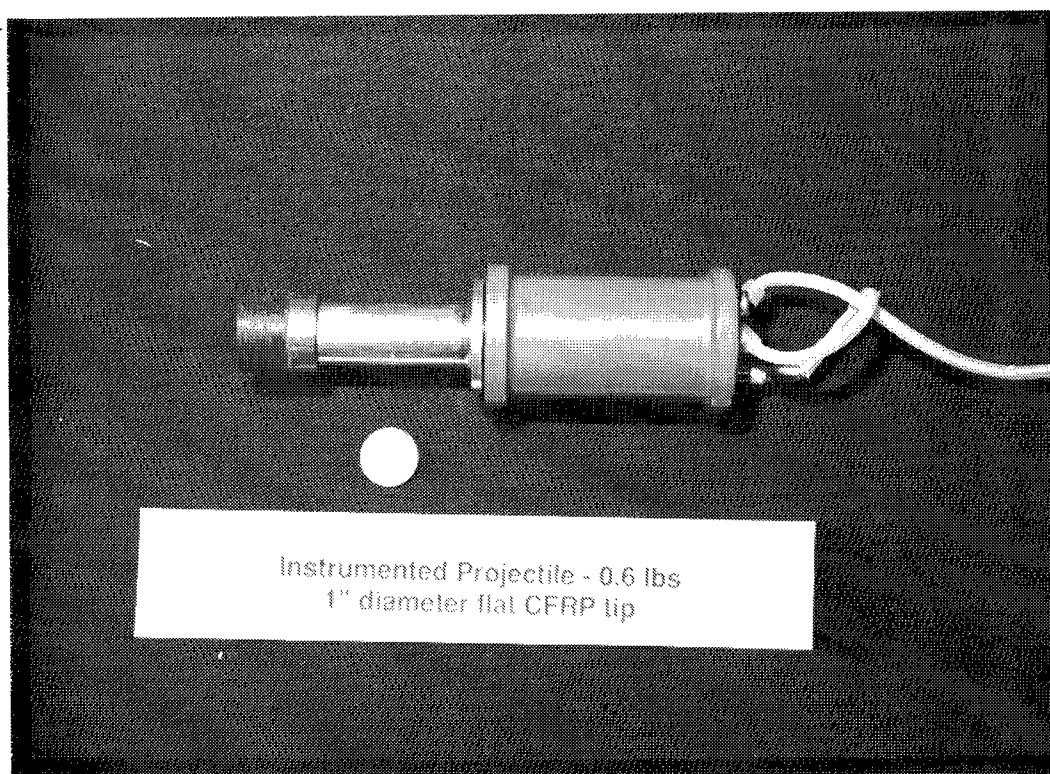


**Figure 4: Low Mass (University of British Columbia) Impact Apparatus**

Graphite tups were rough cut, using a waterjet cutter, from a 31.75 mm thick block of tool grade graphite-epoxy (Toolrite MXG-7650 style 2577). The 25.4 mm tups were machined to a tolerance of  $\pm 0.76$  mm in diameter. Tolerances for these graphite tups were less strict due to difficulty in lathe cutting a hemisphere without chipping or scarring the graphite/epoxy. The 6.35 mm tups were ground rather than lathe cut because of their tendency to break under lateral load. Grinding yielded tolerances of  $\pm 0.051$  mm.

**Low Mass Impacts.** Low mass impacts were performed at the University of British Columbia, using a horizontally oriented nitrogen gas gun. The projectile consisted of the steel or graphite tip, an aluminum shaft, a PCB 208M88 5 kip load cell, and a torlon shell as shown in Figure 5. The load cell was connected through a trailing wire to a Tektronix 2230, 100 MHz, 8 bit digital storage oscilloscope capable of storing 4096 points of data. Impact and rebound velocities were computed using three pairs of optical gates placed just before the point of impact. Data acquisition was triggered by the last optical gate with an experimentally calibrated electronic time delay circuit to assure data collection started just prior to contact. Impact velocity was calibrated as a function of firing pressure.

The impact tups were created with sufficient length to allow full penetration during impact including an allowance for panel deflection. The larger diameter backup structure was prevented from striking the panel by placing an elastomeric-ring bumper in the end of the air-gun barrel. Each panel was then carefully placed a specified distance from the end of the barrel. Secondary impacts were prevented by activating a pressure release valve which vented barrel after the gun was fired. This prevented back pressure from forcing the rebounding tup into the panel.



**Figure 5: Low-mass Impact Projectile**

**High Mass Impacts.** High mass impacts were performed on the Dynatup 8250 drop weight impactor schematically shown in Figure 3. Data acquisition was accomplished using a Macintosh IICx computer equipped with a National Instruments model A2000 high speed data acquisition board operating at 500 kHz and Integrated Technologies, Inc. proprietary software. A Dynatup 10 kip load cell was conditioned using a Measurements Group 2210A signal conditioner. The range of the load cell could be changed from 44.5 MN to 22.25 MN (10 kips to 5 kips) to improve resolution using the appropriate gain settings. Impact and rebound velocities were computed using a precision machined flag which passed through an optical gate placed just before the point of impact.

Impact velocities for low energy impacts of 11.3 J (100 in-lb) to 56.5 J (500 in-lb) on the Dynatup 8250 impactor were generated by setting the impactor at an initial height, (h) and using gravitational acceleration (g) to achieve the desired energy, (E). The value of (h) was back calculated using the potential energy equation:

$$E = mgh$$

where m is the mass of the impactor. High energy impacts (< 56.5 J), which could not be achieved by gravity drops, were generated by a calibrated pneumatic system which compressed springs against the impactor. The springs imparted an initial velocity to the impacting mass when released.

High durometer elastomeric rebound bumpers were placed at a specified height to stop the impactor following perforation of a panel. The constant diameter portion of the tup was long enough to allow full penetration into the panel, again, including an allowance for panel deflection. Secondary impacts were prevented by a ratchet device which was triggered on the first pass of the impactor. This device stopped the impactor on its second pass through following rebound.

**Hail Simulation.** An experiment to study damage created by 63.5 mm (2.5 in) hail was performed in parallel with the full experiment. Hail of this size at terminal velocity has 500 in-lb of energy. A 63.5 mm lead ball was dropped from 3.43 meters to achieve an equivalent energy. Impacting the desired location was accomplished by aligning the base of a 76.2 mm diameter PVC tube with the impact site. The lead ball was dropped inside the tube to impact the panel. A rubber lined aluminum plate was placed between the tube and panel immediately after impact to catch the lead ball and prevent a second impact. Lead ball impacts were not instrumented and were performed at ambient temperature.

### Damage Characterization

The fundamental understanding between the variables studied and resulting impact damage is accomplished by comparing measured responses. Many responses may be associated with a given impact event, including measures of the dynamic event, damage area, fiber breakage, and strength-after-impact. These responses may be broken into two major categories: discrete measurements which quantify details of the damage (e.g., delamination area) and non-discrete measurements which relate directly to structural response (e.g., compression-after-impact strength).

Discrete measurements considered in this study were the through-thickness location and extent of matrix damage, through-thickness location and extent of fiber breakage, dynamic response during impact, and surface indentation. A non-discrete measure of the damage investigated was local flexural stiffness of the damage region. The experimental technique associated with obtaining each of these responses is discussed below.

**Surface Indentation.** The indentation depth of all impact damage sites was measured with a dial indicator centrally mounted in a support base designed to set away from influence of the damage on flat panels. The accuracy of these readings was  $\pm 0.025$  mm.

**Matrix Damage.** Internal matrix damage consisted of interconnecting arrays of delaminations and transverse cracks. Ultrasonic inspections of the damage at each impact site were performed to determine the planar dimensions of matrix damage created. Additionally, the through-thickness location of matrix damage for the soft layup-thick laminate variable combination was mapped out in detail using a combination of non-destructive detailed 3-dimensionally imaged ultrasonic inspection and destructive cross-sectioning techniques. Detailed mapping of the through-thickness location of matrix damage for the three other stacking sequences (i.e., hard-thick, hard-thin, and soft thin) will be presented in the future.

Pulse-echo ultrasonics was used to locate internal delaminations by examining the amplitude and time-of-flight of a high frequency (10 MHz) short duration pulse sent into the laminate perpendicular to the surface and then received back at that surface by the same transducer. Initial investigations consisted of a coarse planar inspection of each panel to map planar location of damage created during impacting. The time-of-flight data from the overall panel scans were presented as planar (C-scan) damage maps, with various colors representing different depths of delamination.

Damage sites observed in the overall panel C-scans were further investigated by performing more detailed ultrasound mappings by collecting data every 0.25 mm or 0.50 mm (depending on damage size) with a narrowly focused transducer. The damage found in these detailed scans provided information on the first levels of delamination in the laminate. Damage occurring below the first delamination encountered by a pulse at a particular point was shielded from detection because the pulse is not transmitted past that point. Planar damage area was among the data collected in these scans and was analyzed as a response below.

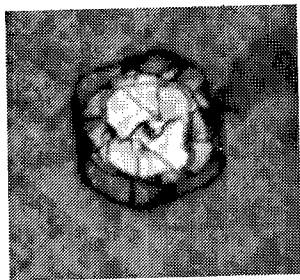
Two damage sites were visualized with Voxel View<sup>2</sup>, a computer graphics program which allows three-dimensional viewing of volume data sets. Three-dimensional viewing helped conceptualize the extent and depth of delaminations. Data from individual through-thickness slices were plotted individually as shown in Figure 6 for panels 29-8A (soft layup-thick laminate-full experiment) and 28-2A (hard layup-thick laminate-hail simulation).

Destructive cross-section examination of an impact site from panel 29-8A was performed to determine the through-thickness location of matrix damage hidden from ultrasound inspection. The cross-section study began by waterjet cutting the impact site from the panel using the shape shown in Figure 7. The hemispherical protuberance was cut from the coupon and the edges around the circumference carefully ground down to reveal the sublaminates created by the matrix damage. Matrix damage was highlighted through the use of fluorescent-dye penetrant to aid in visual interpretation. This technique was termed cylindrical-sectioning by the authors. The sublaminate structure revealed by the cylindrical-section is shown in Figure 8. The rectangular portion was again cut 7.62 mm from the impact centerline and both these flat sections polished to further aid in interpretation of the damage state.

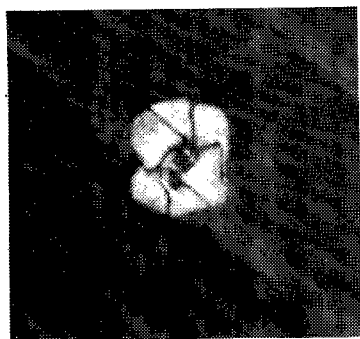
The accumulated matrix damage findings for panel 29-8A were summarized in schematic form as shown in Figure 9. The damage found in the vicinity of a given ply was sketched onto paper with each ply in the stack sequence represented by a sheet of paper. Transverse cracks through the ply being observed were drawn as dashed lines, the "shadow" of transverse cracks through the ply above were plotted as solid lines, and delamination between the ply being observed and the one above were represented by a shaded region. Characterization of additional impact sites in this manner will be performed in future work.

---

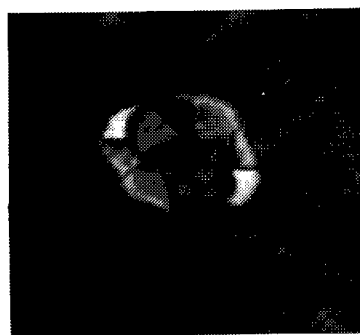
<sup>2</sup> Vital Images, Inc., 505 N. 3rd, Suite 205, Fairfield, IA, 52556.



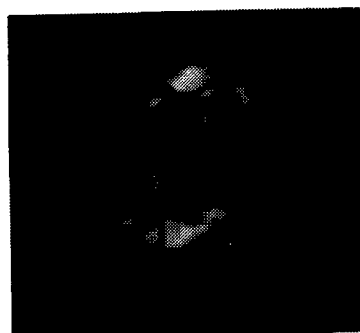
Overall



25%

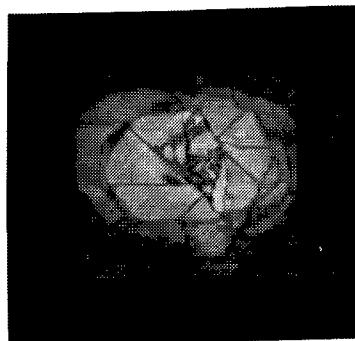


63%



88%

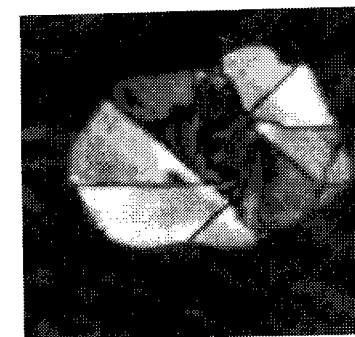
29-8A, Soft Layup



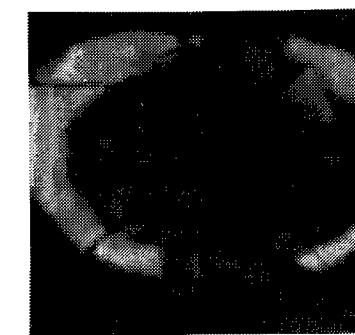
Overall



24%



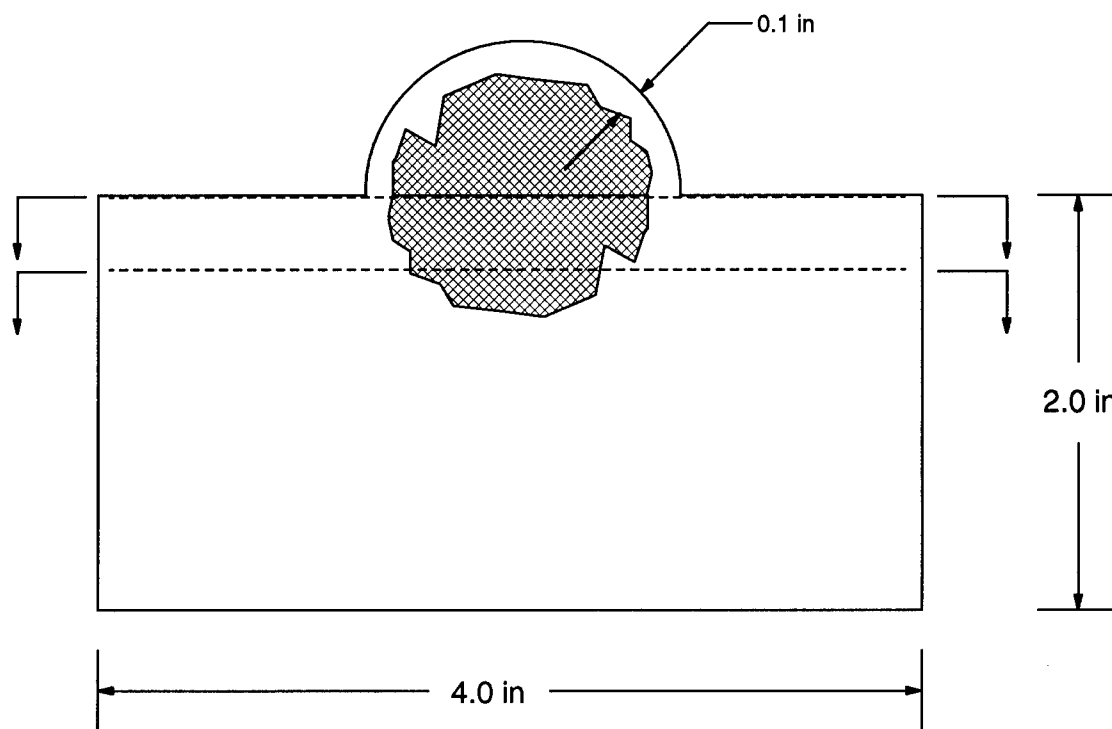
34%



88%

28-2A, Hard Layup

Figure 6: Through-Thickness C-scan Images for Panels 28-2A and 29-8A.



**Figure 7: Cross-section and Cylindrical-section Coupon Geometry.**

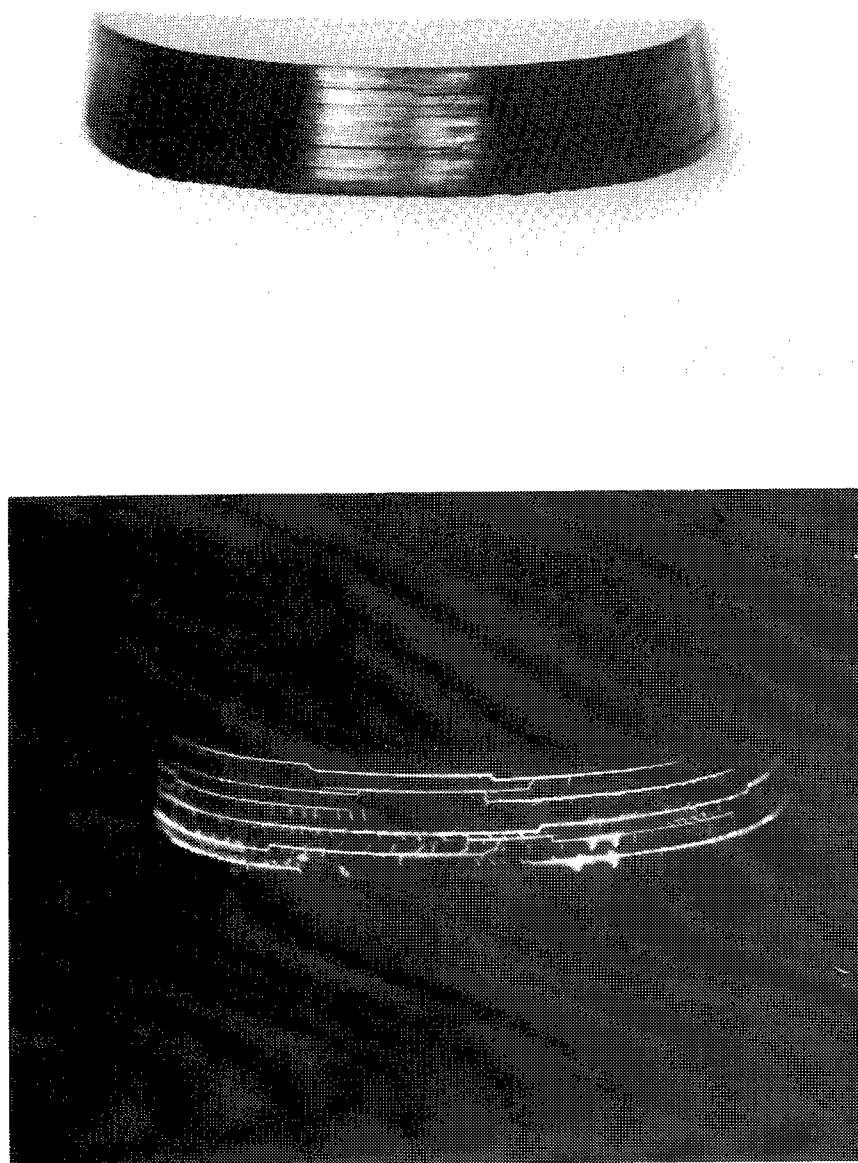
Mapping out the delamination planes and interconnecting transverse cracks for typical panels will provide information applicable to all panels of a given stacking sequence. The through-thickness location of matrix damage within a given stacking sequence was found in earlier studies to be chiefly a function of the stacking sequence [21]. These matrix damage maps will aid in developing an understanding of the through-thickness distribution of matrix damage as related to the intrinsic and extrinsic variables.

**Fiber Failure.** Fiber failures in the skin midbay impacts were measured by thermally deplying a damage site from each of the 32 panels and measuring the length of broken fibers in each ply. A numerically controlled waterjet-cutter machined 101.6 mm by 101.6 mm (4 in x 4 in) square plates with one corner cut diagonally to preserve orientation. Prior to burn-off, specimens were examined for visual damage, exact impact site location within the square, and any surface irregularities.

The deply technique consisted of placing the specimens on sheet steel shelves in a Sybron model FB1415M muffle furnace set at a temperature of 394°C to 402°C. The specimens were removed from heat after 3 hours and cooled at room temperature. Each specimen was immediately labeled and deply attempted when sufficiently cooled. If significant resin was still present, the specimen was placed back in the oven in 45 minute intervals until the resin was sufficiently burned-off.

Upon successfully deplying the first ply, each successive layer, with the impacted surface as layer one, was placed face up on a paper template imprinted with the specimen outline including orientation mark, specimen number, resin type, fiber type, stacking sequence, and date of deply. Specimens were held in place with cellophane tape placed around the periphery, taking care not to cover the impact zone.





**Figure 8: Cylindrical-Section Results for Panel 29-8A.**

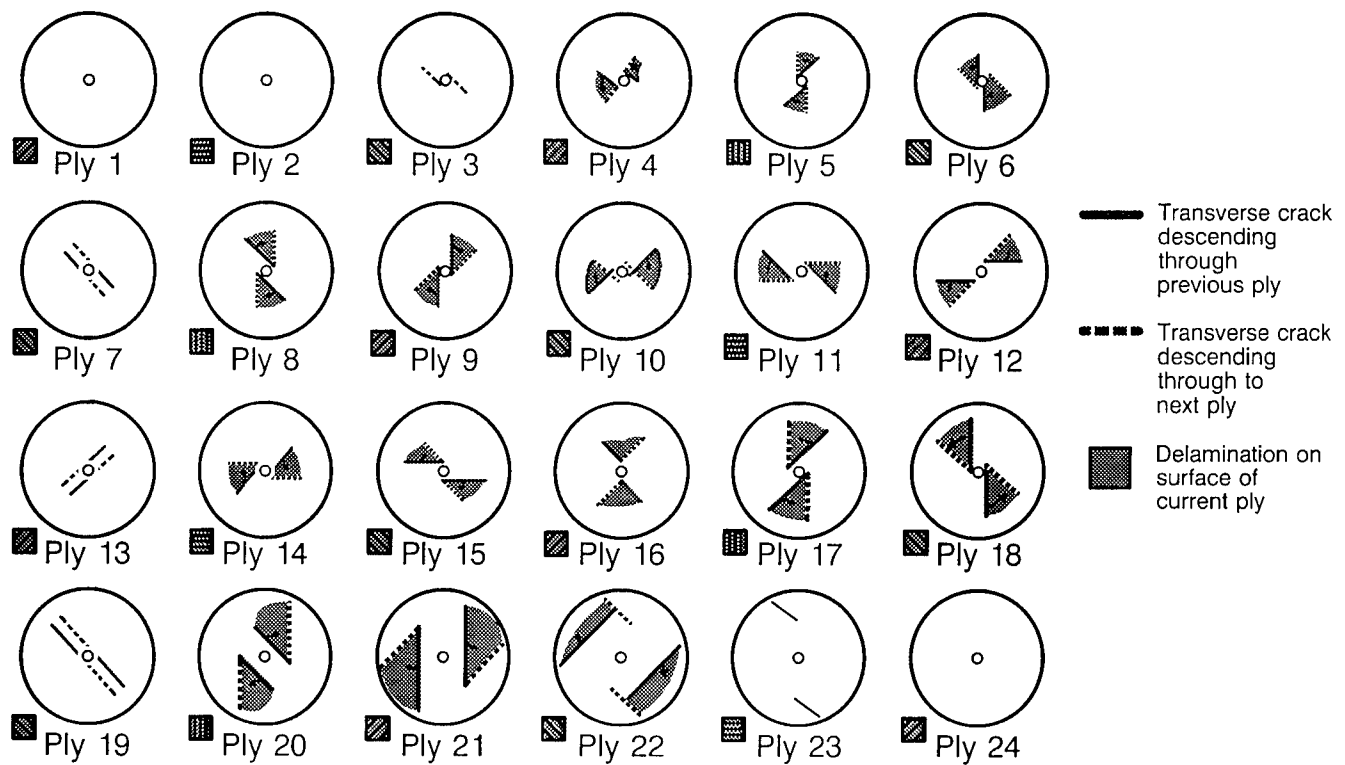


Figure 9: Ply by Ply Matrix Damage Maps for Panel 29-8A.

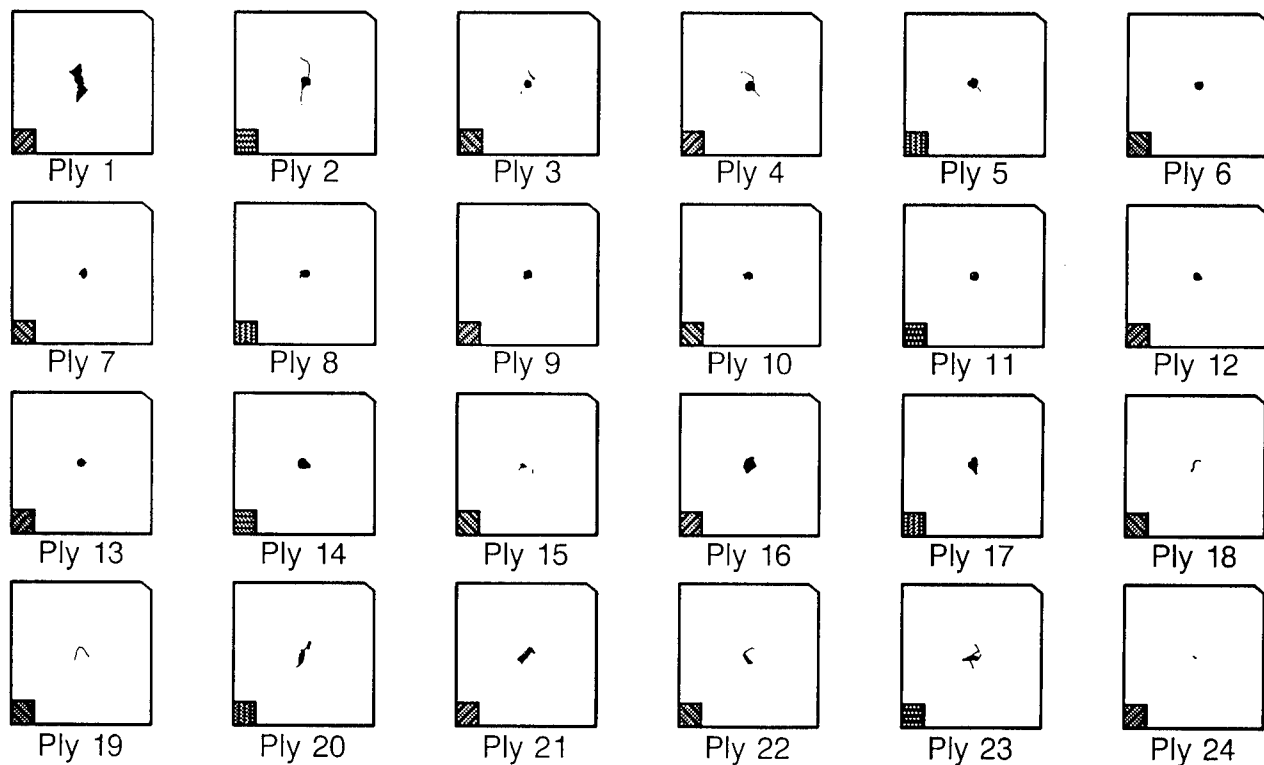


Figure 10: Ply by Ply Fiber Failure Maps for Panel 28-4A.

The length and orientation of cracks (failed fibers) in each ply were traced onto a transparency using indelible black ink. All transparencies had previously been marked with specimen outlines to maintain alignment between the transparency boundary, specimen boundary, and traced on fiber break locations. The lines of fiber breakage for each ply of panel number 28-4A are shown in Figure 10.

The data contained on the transparencies for each impact site were digitized to ease data processing. Each transparency was placed on an Apple A9M0337 scanner in a specified orientation and location and scanned into a bitmap file. The bitmap data for all plies in a specimen were transformed into a three-dimensional scientific data set and stored in Hierarchical Data Format (HDF) with a Spyglass<sup>3</sup> utility. A utility was written to calculate the length of fiber breakage perpendicular to the fiber orientation (i.e., the length of fiber removed from the load path) in each ply. Figure 11 summarizes the fiber breakage lengths for all plies of panel number 28-4A. The slope of a best fit straight line was used to describe through-thickness distribution, although not all distributions were linear.

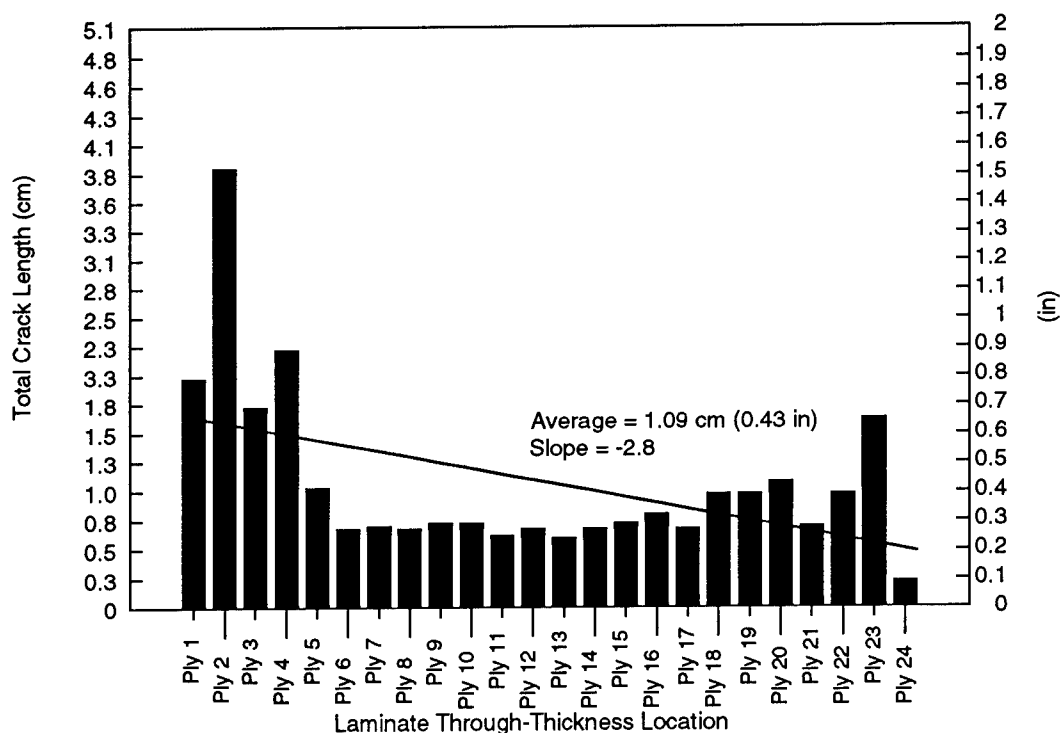
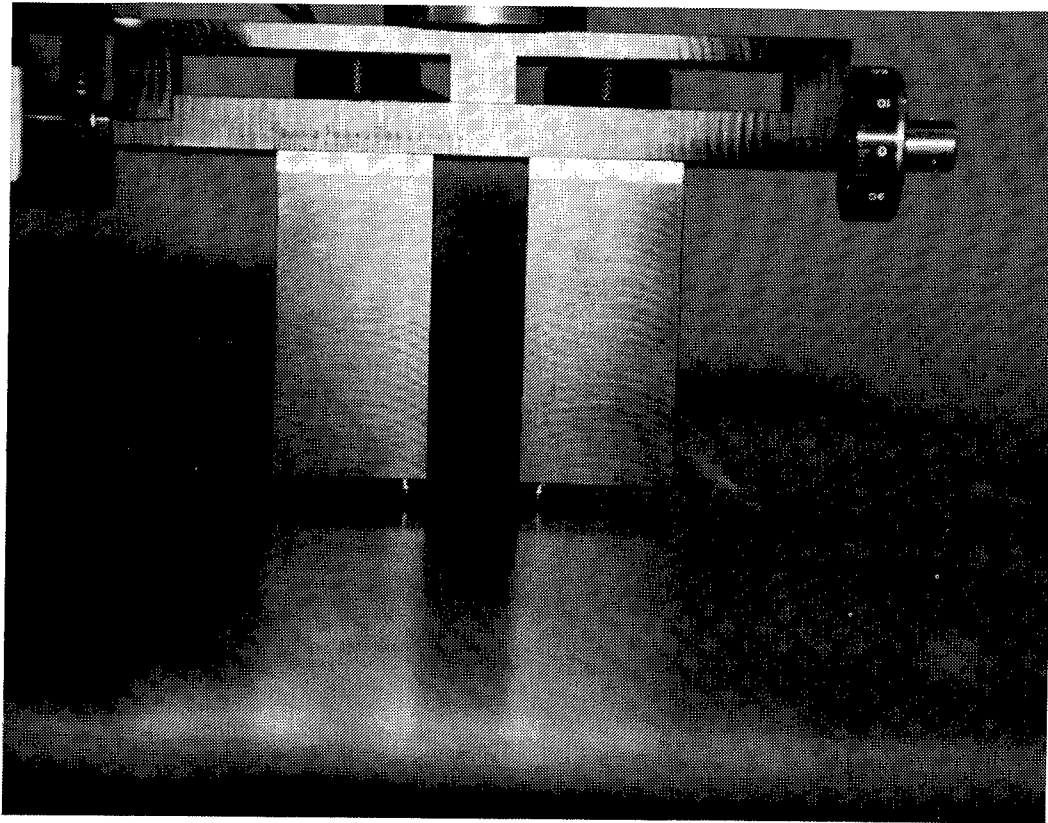


Figure 11: Summarized Fiber Failures for Panel 28-4A.

**Non-discrete Measurements.** A non-discrete inspection method using characteristics of flexural (Lamb) wave propagation to quantify impact damage in laminated composites was investigated. A fixture to accurately locate a sending transducer and a receiving transducer on the test panels, as shown in Figure 12, was designed and built by ZETEC of Issaquah, WA. The velocity of flexural-waves (phase velocity) propagating from the sending transducer to the receiving transducer were measured experimentally using a prototype of ZETEC's new S-9 sondicator. The measurements of phase

<sup>3</sup> Spyglass, Inc., 701 Devonshire Dr., Champaign, IL, 61820.

velocity were made both in undamaged and damaged mid-bay regions of the panels in directions both parallel and perpendicular to the stiffeners using several excitation frequencies.



**Figure 12: Apparatus for Measuring Flexural Wave Propagation through Impact Damage**

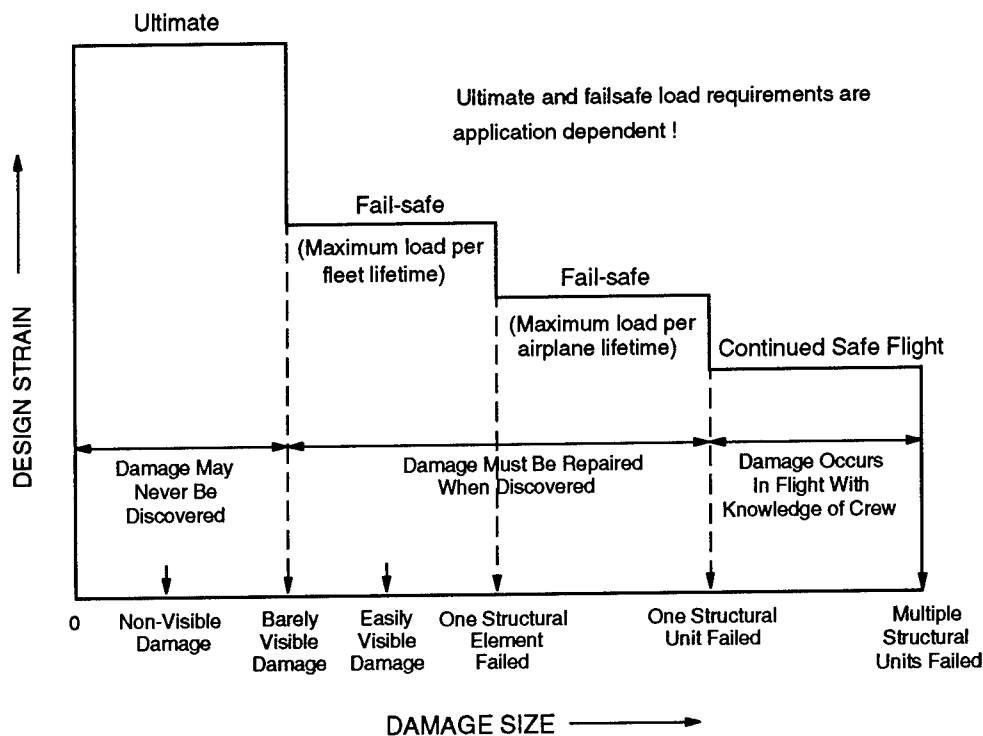
## **RESULTS AND DISCUSSION**

The full experiment and the hail simulation experiment were separate parallel studies on the same panels. These experiments were both based on the design of experiments statistical technique. The full experiment studied 14 variables (8 intrinsic and 6 extrinsic) while the hail simulation experiment studied the 8 intrinsic variables with respect to one impactor, a lead ball with 56.5 Joules of kinetic energy.

A comprehensive statistical evaluation of the experimental results which considered the complexities of these designed experiments has not yet been completed. The data analysis performed below studied the DOE results using engineering evaluation coupled with a coarse statistical analysis. The process by which the data was evaluated is described in the indentation depth discussions.

Data evaluation initially focused on studying each experiment individually to determine important effects. The results from the full and hail simulation experiments were found to complement one another and the combined study of both sets of results aided in overall data interpretation. Presentation of results and discussions of the findings will be done for each measured response using data from both experiments for justification.

**Indentation depth/Visibility.** Visibility of impact damage is directly related to post-impact strength requirements as illustrated in Figure 13 for commercial aircraft. The different load levels defined in this illustration are based on the amount of visible damage. Ultimate load is applicable for damage defined as nonvisible per the defined inspection technique. The Boeing Commercial Airplane Group interpretation of FAA requirements led to the definition of a 0.25 mm (0.01 in) indentation as the threshold of visibility (i.e., barely visible impact damage) based on visual inspection from 5 feet. The United States Air Force quantified the threshold for damage visibility at a 2.5 mm (0.10 inch) dent [21], based on their inspection requirements. Lower load requirements exist for structures having damage that is easily visible. The absolute levels of these loads and requirements defining them are application dependent.



**Figure 13: Structural Load Requirements as a Function of Damage Size.**

Impact damage created in this study spanned the range from completely nonvisible by visual inspection to quite easily visible. Figures 14 and 15 show examples of "visible" damage (as defined by the authors inspection technique) created by simulated hail impacts. The surface indications range from a slight amount of back surface breakout (and a 0.08 mm front surface indentation) to a front surface crater larger than 2.5 mm (0.10 in) in depth.

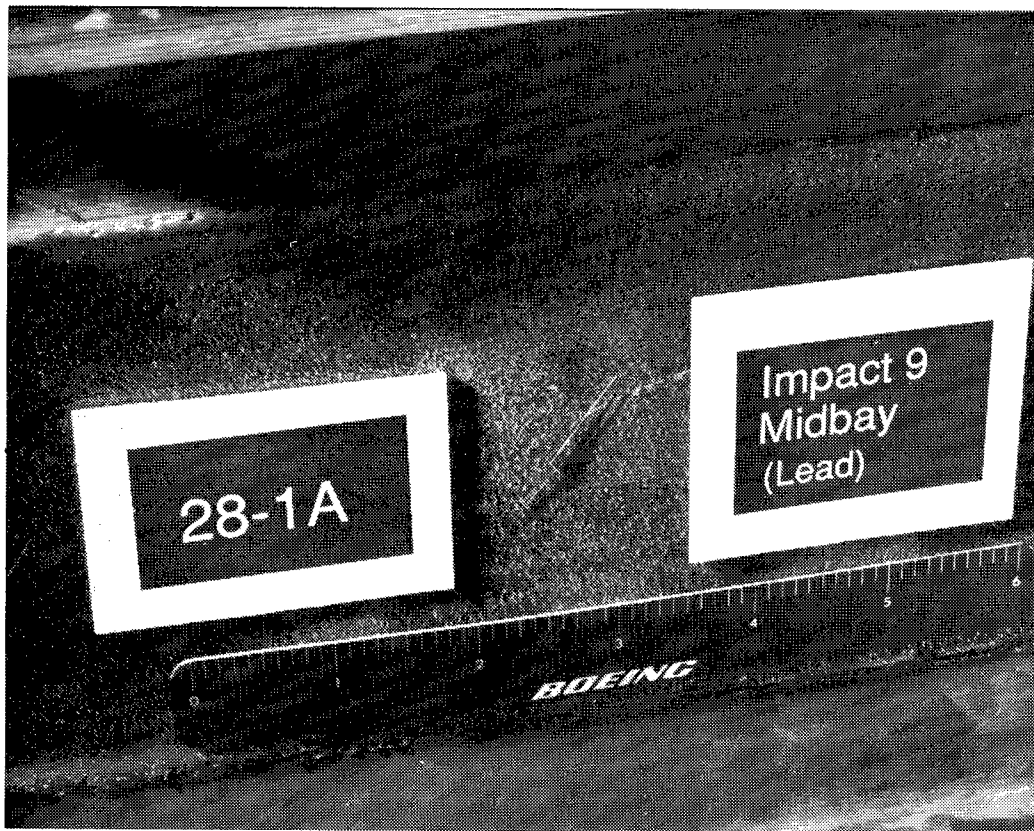


Figure 14: Barely Visible Damage.

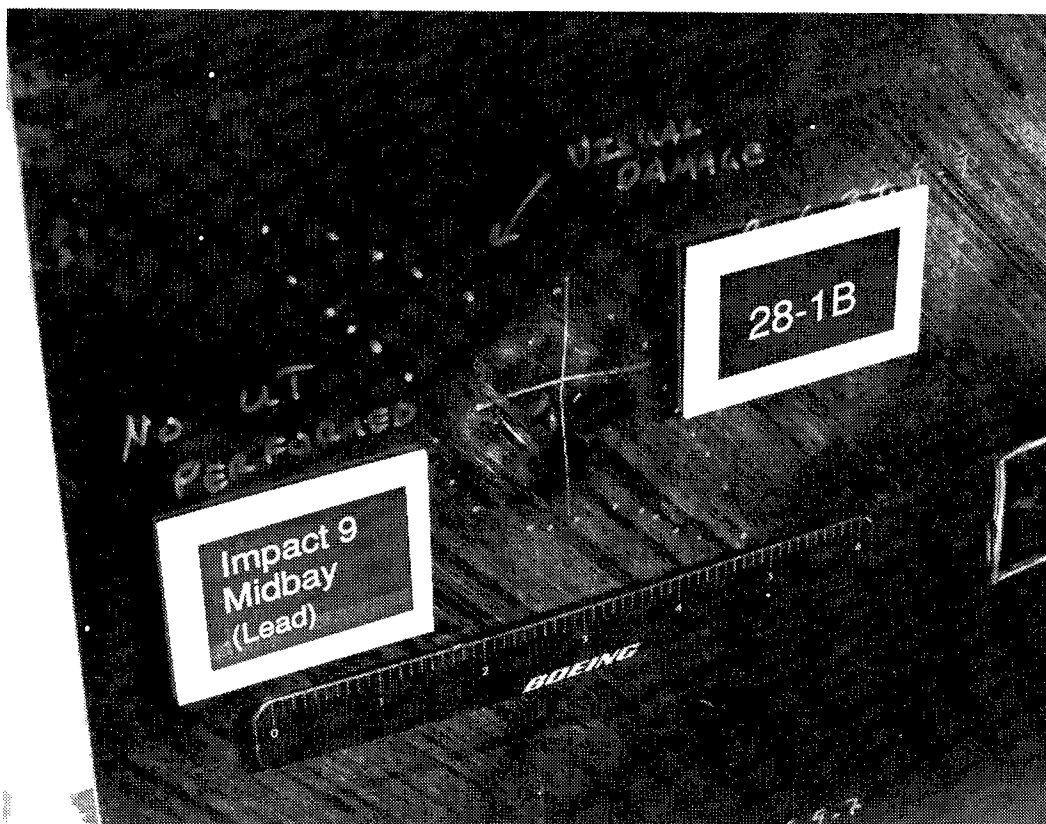


Figure 15: Clearly Visible Damage.

The indentation depth data from the hail simulation and full experiment impacts were initially evaluated using "scree plots," as defined in [18]. Scree plots displayed statistical data about each run in a histogram format to identify potentially important variables and variable interactions. The average response for each substantial variable or variable interaction was calculated to determine its effect (on indentation). Those with large effects compared to the majority of measured effects were considered important.

Figure 16 illustrates effect calculation for the "Laminate thickness" variable using hail simulation data. The measured indentation depth is represented on the y-axis and the run numbers, as defined in Table 3, are along the x-axis. Each vertical bar represents the indentation depth for the listed run number. These data were grouped into two halves, runs with thin laminate panels and runs with thick laminate panels. The average level of each half was calculated, and the difference between the two halves divided by 2 to estimate the effect.

Two-factor interactions were evaluated in a similar manner, as illustrated in Figure 17 for the "Fiber type-Fiber volume" interaction. The data were first grouped according to "Fiber type." Within each "Fiber type" group the data were sub-grouped according to "Fiber volume," and the average level for each quarter of the runs, as defined by these divisions, was calculated. The sum of the average level for the AS4, 56% fiber volume (FV) group and the IM7, 48% FV subgroup was subtracted from the sum of the average level for the AS4, 48% FV subgroup and the IM7, 56% FV. The resulting value was divided by 4 to obtain an estimate of the effect of this interaction.

Half the data in the AS4, 48% FV subgroup were observed to be higher than the rest. These runs were studied to determine if one variable could account for the differences, and "Laminate thickness" was found to correlate with the observed variations. Bars representing data from runs with thin laminate panels were crosshatch shaded, while runs from thick laminate panels were solid shaded. It is apparent in Figure 17 that the high values in this subgroup are all thin laminate panels, suggesting that a three-way interaction between "Laminate thickness"- "Fiber type"- "Fiber volume" may exist.

Two factor interactions such as the one illustrated in Figure 17 are often confounded with other two factor interactions. The patterns and levels of confounding were defined by the method of statistical experimental design and number of variables studied [18, 19]. The design of this experiment resulted in the "Fiber type-Fiber volume" interaction being confounded with the "Matrix type-Material form" interaction shown in Figure 18 and the "Skin layup-Stiffener type" interaction (not shown). Statistically, the estimated effect for this set of three potential interactions is the sum of the estimated effects for these interactions, and is not separable. Engineering judgement and/or further experimentation must be used to sort out the true significant interactions.

Deduction of some confounded interactions was accomplished by the examination of results from both experiments. An example of this process is illustrated with the aid of Table 5. Listed are the confounded interactions that made up the second most important effect for indentation depth in both experiments. The first three potential interactions listed are identical for the two experiments; therefore, one can hypothesize that it is unlikely that interactions 4 through 6 of the full experiment are significant, since they do not occur in the hail simulation experiment. The "Skin layup-Stiffener type" interaction is improbable because "Stiffener type" relates to the stiffness of the panel during impact, and should not interact with "Skin layup." The most likely candidates for the actual interaction are "Fiber type-Fiber volume" or "Matrix type-Material form".

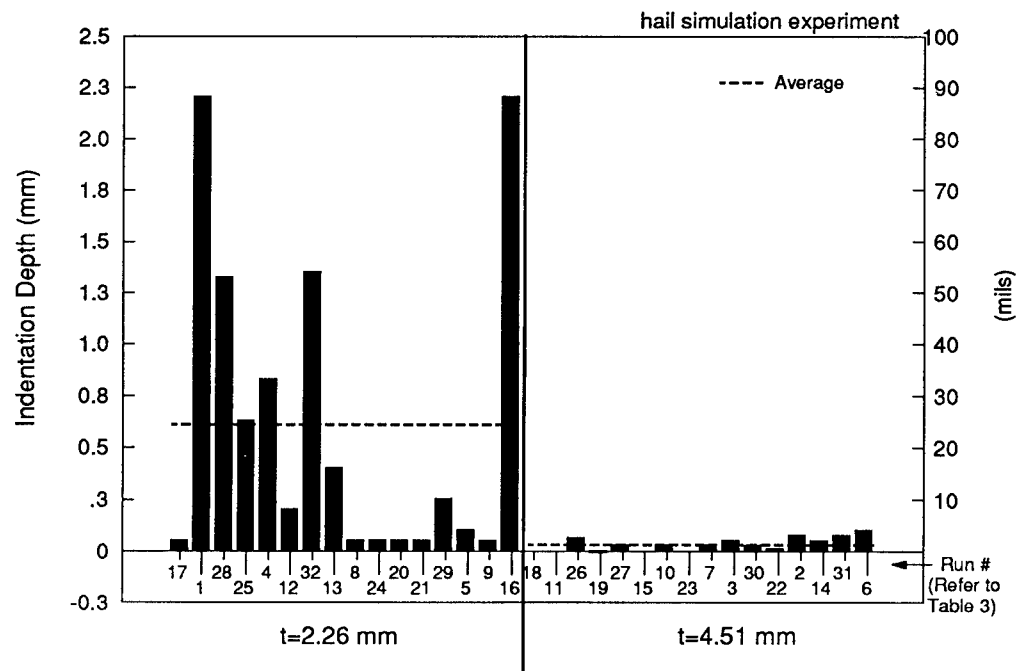


Figure 16: Laminate thickness Effect for Hail Simulation Experiment Indentation Depth

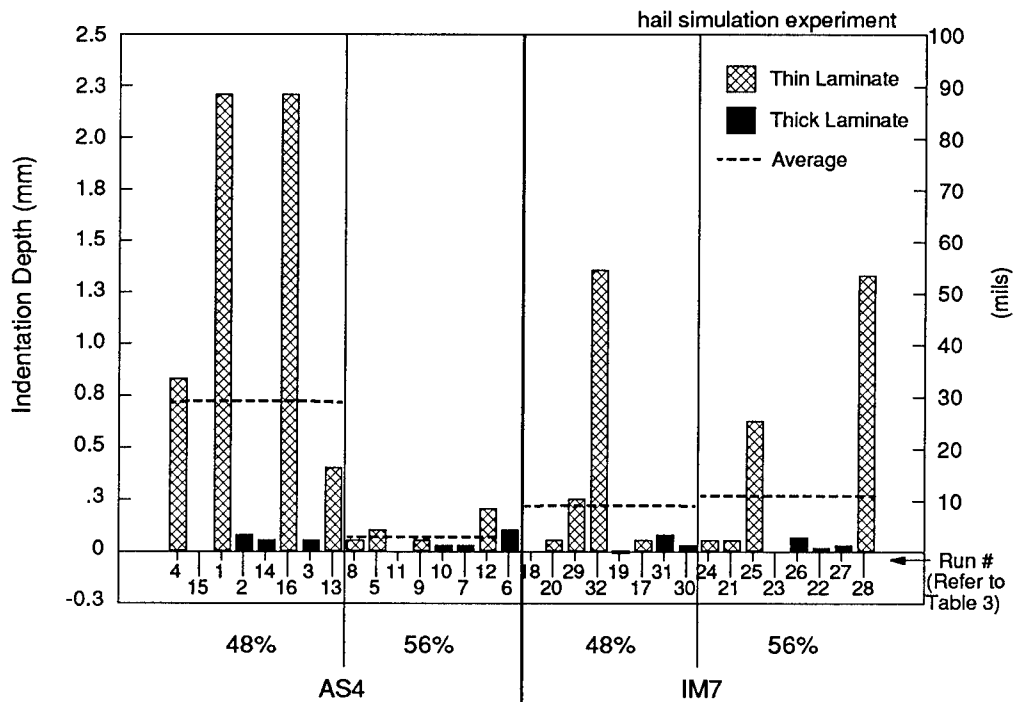
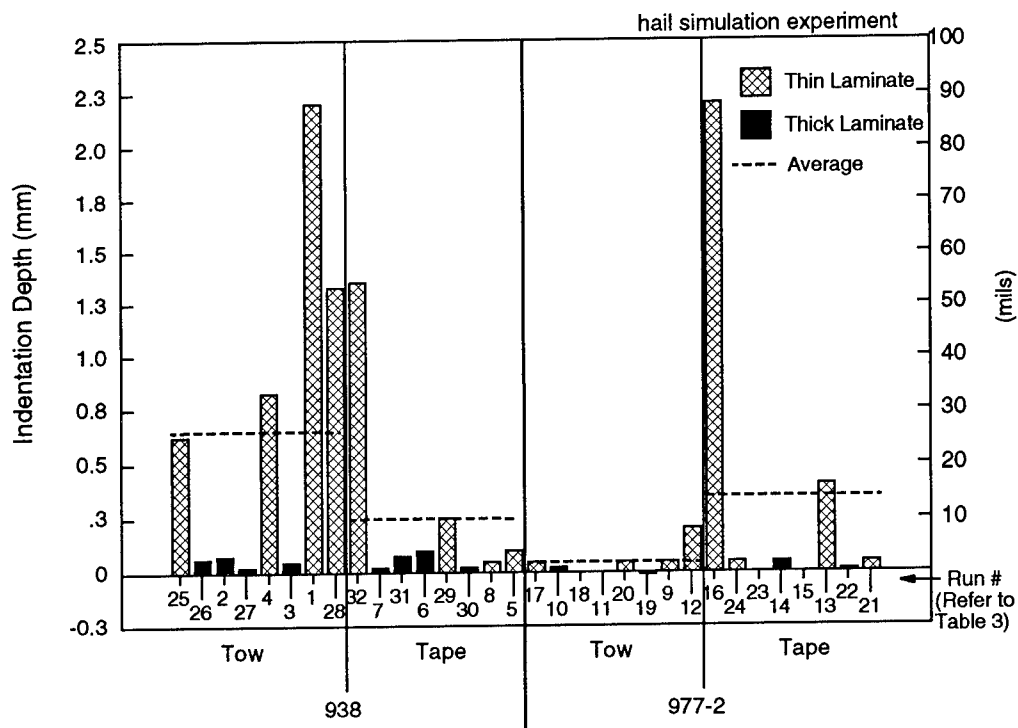


Figure 17: Fiber type-Fiber volume Interaction for Hail Simulation Experiment Indentation Depth.





**Figure 18: Matrix type-Material form Interaction for Hail Simulation Experiment Indentation Depth.**

Full Experiment	Hail Simulation
1) Fiber type-Fiber volume 2) Matrix type-Material form 3) <del>Skin layup-Stiffener type</del> 4) <del>Impactor stiffness-Stiffener spacing</del> 5) <del>Laminate thickness-Impact energy</del> 6) <del>Impactor shape-Temperature</del>	1) Fiber type-Fiber volume 2) Matrix type-Material form 3) <del>Skin layup-Stiffener type</del>

**Table 5: Interaction Deduction for the Indentation Depth Response**

A summary of the most important variables (main effects) and variable interactions (interaction effects) as related to indentation depth from both the hail simulation and the full experiment is listed in Table 6. These effects are ranked according to their importance based on the full experiment. Interactions were listed below the main effects for clarity, and not to suggest a lesser importance of the effect. Ranking of important variables identified in the hail simulation experiments are shown in parentheses.

Rank	Variable	Low Level	High Level	Result
1	Impact energy	23 Joules	136 Joules	Increased
3	Impactor diameter	6.35 mm	25.4 mm	Decreased
4	Impactor shape	Flat	Spherical	Increased
11 (1)	Laminate thickness	2.26 mm	4.51 mm	Decreased
Important Interactions				
2 (2)	Fiber type-Fiber volume or Matrix type-Material form			

Note: Ranking of hail simulation results shown in parentheses.

**Table 6: Important Effects for the Indentation Depth Response.**

Impact energy was found to be the most important variable influencing indentation depth for the full experiment, as might be expected. The second most important effect was the set of confounded interactions discussed previously. Variables associated with impactor geometry were found to have a pronounced effect on the observed indentations, while laminate thickness was most important when all other impactor variables were ignored.

The strong influence of impactor geometry on indentation comes as no surprise. The relative importance of these variables on the results suggests that attempting to relate surface indentation to the internal damage state or residual strength to be a formidable task. The load requirements, as illustrated in Figure 13, are a strong function of the "visibility;" therefore, studies on impact must consider the wide range of potential threats at all realistically possible impact energies to determine worst case scenarios for each load requirement.

**Matrix Damage.** Measurements of planar damage area as determined from ultrasonic inspection were studied using the designed experiment. The results summarized in Table 7 were found to have the most important effects, with the ranking based on importance determined in the full experiment. Ranking of important effects from the hail simulation experiment are labeled with parentheses. Three-dimensional characterization of the sublamine structure which relates directly to the compression after impact strength [2, 22] was attempted but has not yet been completed for all runs. The study of the data using the designed experiment required a completed data set.

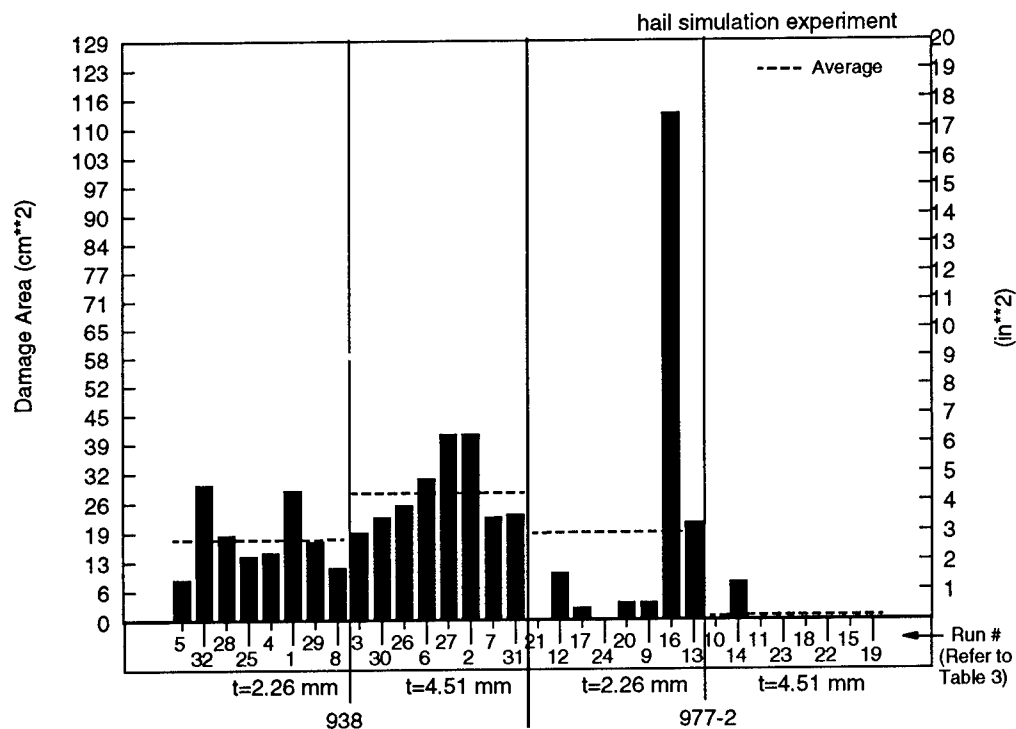
Impact energy was found to be the most important variable effecting planar damage area, as expected. Following this was the set of six confounded interactions. Impactor diameter was found to have a stronger effect than the matrix type, with large diameter impactors creating larger damage areas. Higher interlaminar toughness of the matrix tended to restrict the damage size, but an examination of the "Matrix type-Laminate thickness" interaction for both the hail simulation and full experiments, shown in Figures 19 and 20, respectively, indicates that effect of toughness was most notable for thick laminates.

Rank	Variable	Low Level	High Level	Result
1	Impact energy	23 Joules	136 Joules	Increased
3	Impactor diameter	6.35 mm	25.4 mm	Increased
4 (2)	Matrix type	938	977-2	Decreased

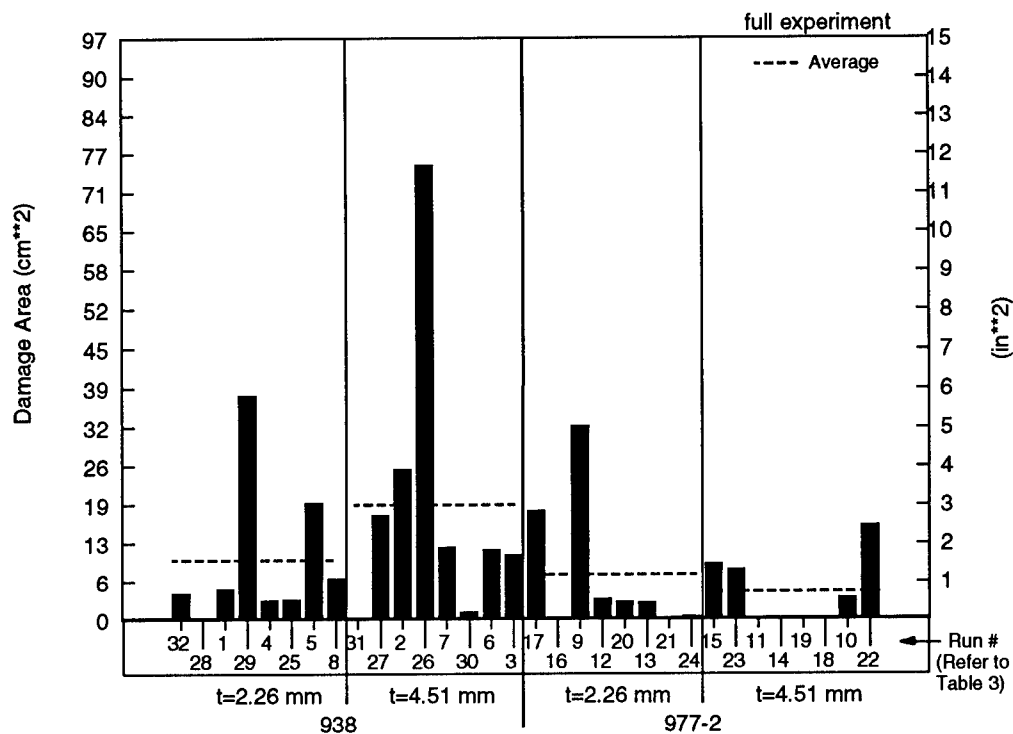
	Important Interactions
6 (1)	Matrix type-Laminate thickness
2	Impact energy-Impactor diameter or Impactor mass-Temperature at impact or Fiber volume-Impactor stiffness or <del>Fiber type</del> Stiffener spacing or <del>Matrix type</del> Stiffener type or <del>Material form</del> Skin layup
5 (3)	Fiber volume-Laminate thickness

Note: Ranking of hail simulation results shown in parentheses.

**Table 7: Important Effects for the Planar Damage Area Response.**



**Figure 19: Matrix type-Laminate thickness Interaction for Hail Simulation Experiment Planar Damage Area.**

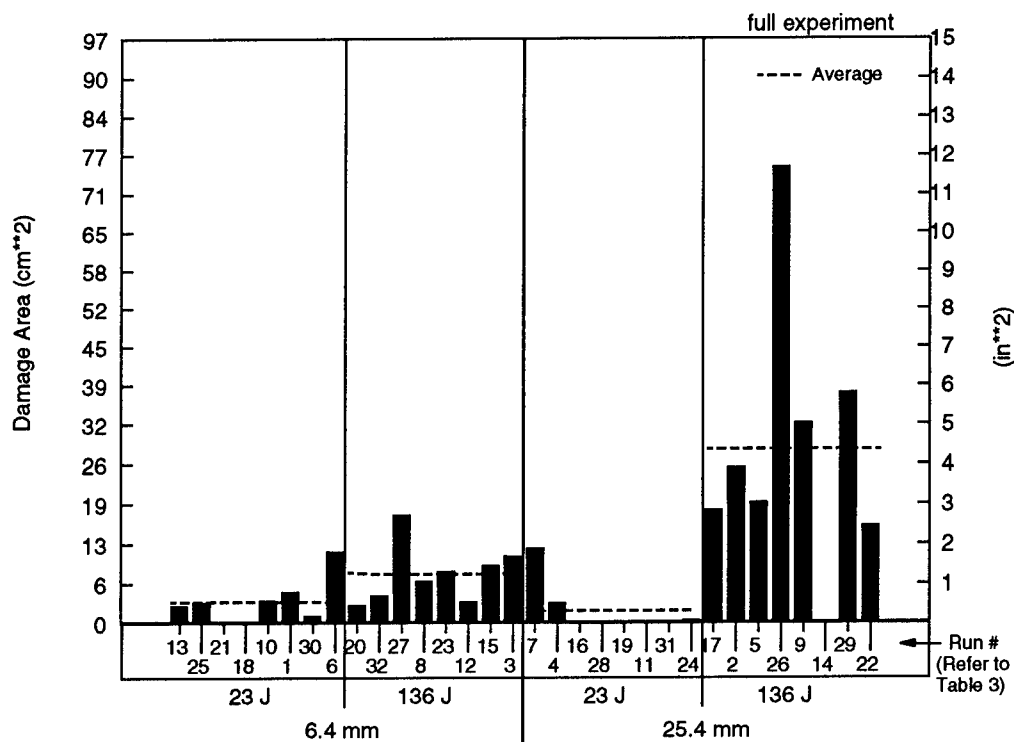


**Figure 20: Matrix type-Laminate thickness Interaction for Full Experiment Planar Damage Area.**

The set of six interactions, ranked 2 in Table 7, only appeared in the full experiment. "Fiber type-Stiffener spacing," "Matrix type-Stiffener type," and "Material form-Skin Layup" are interactions which do not involve impactor variables and are therefore unlikely. "Impact energy-Impactor diameter" is thought to be the likely interaction of the remaining three, because "Impactor diameter" was found to have a strong effect. Figure 21 illustrates this interaction. The average damage area for the low impact energy appears insensitive to impactor diameter, but damage area increases significantly with impactor diameter for higher levels of impact energy. The occurrence of fiber failures and subsequent perforation may explain these observations, illustrating the failure mechanism interplay between fiber and matrix damage during impact.

Planar damage areas in the hail simulation experiment were strongly influenced by a "Fiber volume-Laminate thickness" interaction. The thin laminates with high fiber volumes were found to have smaller damage areas than thin laminates with a low fiber volume. Damage areas in the thick laminate panels were not significantly influenced by fiber volume for this experiment, although the full experiment and past internal Boeing studies have found that decreased fiber volume decreased damage area for thicker laminates. This trend may have been obscured in the hail simulation by the range of variables studied.

**Fiber Failure.** Impact induced fiber failures were quantified both by their average length and through-thickness distribution for the full experiment impacts. The data on broken fibers may further be quantified in terms of their effect on the local load paths and strength as discussed in [3, 4, and 23], but has not yet been attempted. Table 8 lists the important observations for the fiber failure average length response.



**Figure 21: Impactor diameter-Impact energy Interaction for Full Experiment Planar Damage Area.**

Rank	Variable	Low Level	High Level	Result
1	Impact energy	23 Joules	136 Joules	Increased
3	Laminate thickness	2.26 mm	4.51 mm	Decreased
4	Impactor diameter	6.35 mm	25.4 mm	Increased
5	Impactor shape	Flat	Spherical	Increased

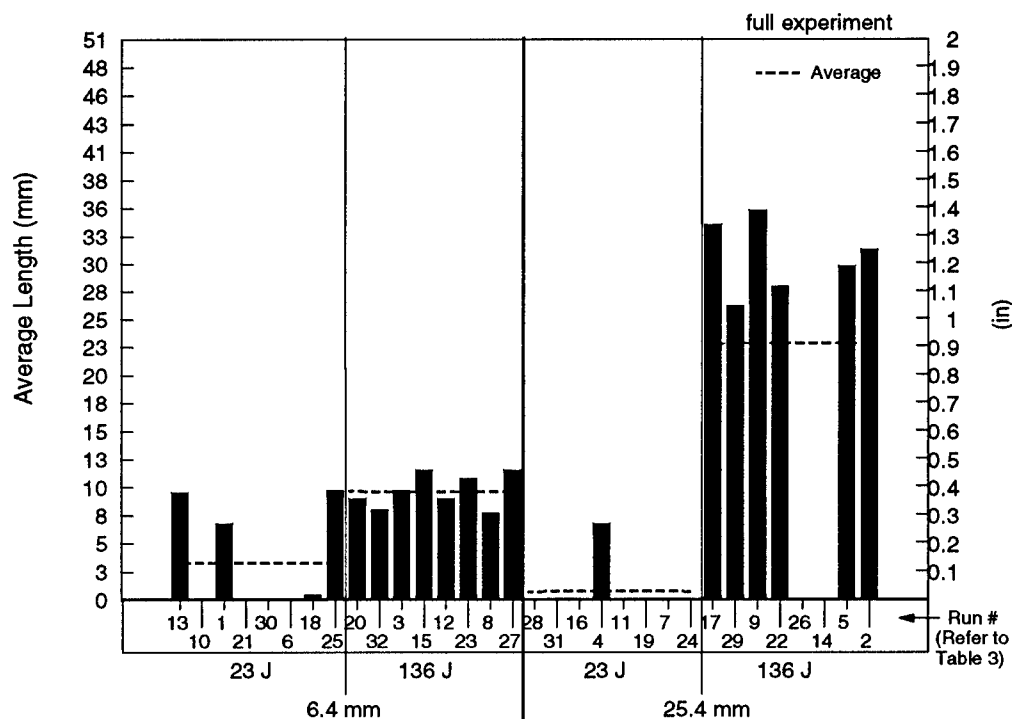
  

	Important Interactions
2	Impactor diameter-Impact energy or Impactor mass-Temperature at impact or Fiber volume-Impactor stiffness or Fiber type-Stiffener spacing or Matrix type-Stiffener type or Material form-Skin layout

**Table 8: Important Effects for the Fiber Failure Average Length Response.**

Impact energy was again found to be the strongest variable, with higher energies leading to more fiber failure. Second was a set of confounded two-factor interactions. Interaction deduction was not aided by results from the hail simulation experiment because fiber failure data was not collected. Increasing the laminate thickness tended to decrease the amount of fiber failure while an increase was found for the larger impactor diameters. Spherical impactors generally created more fiber failure than the flat impactors because of higher contact pressures.

The "Impactor diameter-Impact energy" interaction is illustrated in Figure 22. Although the six interactions are statistically confounded, common sense evaluation led the authors to believe this to be the most likely of these two-factor interactions. The contact pressures, and hence local fiber breaks, were larger for the 6.35 mm (0.25 in) diameter impactor for energies below the perforation threshold, while large diameter impactors created more fiber failure at high impact energies which caused perforation.



**Figure 22: Impact diameter-Impact energy Interaction for Full Experiment Fiber Failure Average Length.**

Results for through-thickness distribution of fiber failures are listed in Table 9. Although these results have not yet been studied in detail, it is of interest that the material form may influence the damage state. Thinner laminates tended to have a more uniform fiber breakage distribution, while higher impact energies decreased the uniformity. A two-way interaction is again among the important effects.

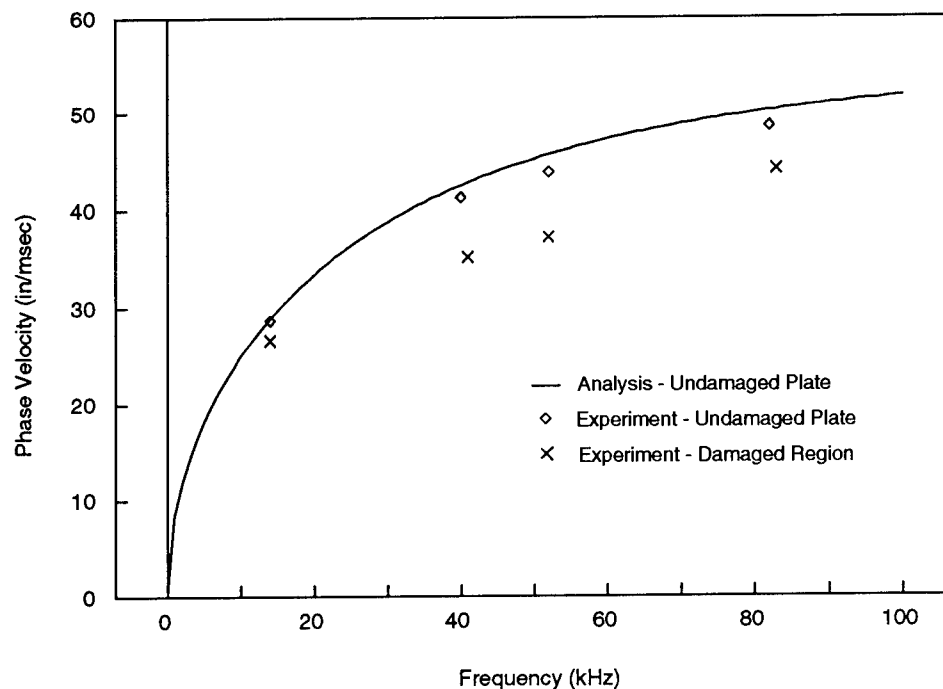
**Non-discrete Measurements.** The reduction in compression strength of laminated composites has been attributed to the buckling of sublaminates created by impact induced matrix damage followed by local load redistribution [2]. Sublaminates buckling is directly related to the flexural stiffnesses of these sublaminates. Flexural wave propagation in a plate is also a function of the bending and shear stiffnesses. It was theorized that the presence of impact damage would result in reduced flexural wave speeds, allowing both detection of the damage and assessment of the associated stiffness reduction.

Dispersion curves, which relate phase velocity to frequency, were generated for the undamaged laminates using the theoretical formulation found in [24]. This formulation was based on laminated plate theory and included the effects of shear deformation and rotary inertia. Experimental measurements of phase velocity as a function of frequency for undamaged regions of the panels were compared to the theory for mutual verification. Measurements and comparisons were made both 0° and 90° to the stiffeners because the phase velocity in a composite laminate is dependent on the direction of propagation due to material anisotropy.

The measured phase velocities in the undamaged regions agreed well with theoretical predictions. Phase velocities in damaged regions were less than those in the undamaged regions as theorized. Figure 23 shows the comparison between theory and experiment for the undamaged laminate along with data from the damaged region . Damage sites with extreme amounts of damage proved difficult to measure experimentally with the current techniques. This difficulty was probably caused by excessive attenuation of the signal and by waves reflected from the damage boundary.

Rank	Variable	Low Level	High Level	Result
1	Laminate thickness	2.26 mm	4.51 mm	Decreased
2	Material form	Tow	Tape	Decreased
3	Impact energy	23 Joules	136 Joules	Increased
Important Interactions				
4	Fiber type-Impactor mass or Matrix type-Laminate thickness or Material form-Impact energy or Layup-Impactor diameter or Impactor stiffness-Impactor shape or Stiffener spacing-Temperature			

**Table 9: Important Effects for the Fiber Failure Through-Thickness Distribution Response.**



**Figure 23: Theoretical Dispersion Curve and Experimentally Measured Data for Panel 28-6A**

## CONCLUSIONS

This experiment resulted in a relative ranking of the important variables and variable interactions studied. Variables found to have little effect are not necessarily unimportant, but were overshadowed by the effects of others. Future studies on impact should consider the important variables and interactions. These results are meant to guide future studies, and are not the final judgement. The important findings are summarized below.

Impact energy and impactor geometry were the chief extrinsic variables affecting both internal damage and surface visibility. Important variables associated with impactor geometry were the diameter and shape. Larger diameter impactors were found to create more damage (impact energy not being held constant) and less surface indication, while impact energy had direct correspondence to the damage state and external indications. The strong couplings between these extrinsic impact variables and damage characteristics suggest the need for a more comprehensive material and design screening approach.

Intrinsic material variables were generally less important than extrinsic variables when considering the range of variables and variable levels studied in the full experiment. Matrix toughness appeared to have little effect on impact damage in minimum gauge structure (i.e., 0.09 in thick), which is characteristic of 70% of fuselage shell, but did reduce the damage in thicker fuselage skin gauges characteristic of compression loaded keel structures. Fiber type, by itself, was found to have little effect on impact damage.

Interactions between variables were found to have a stronger influence on the damage state than most variables by themselves. These two- and possibly three- factor interactions must be better understood and accounted for in future impact studies. An understanding of important interactions between laminate and material variables may lead to breakthroughs in damage resistant composite design.

Laminate thickness was the critical design variable when considering the indentation created by simulated hail impacts. Economic considerations on hail induced damage have led to minimum fuselage gauge requirements to avoid frequent repairs. Increased laminate thickness reduced indentation/visibility of damage created by hail impact, while higher fiber volumes reduced internal damage for the thin gauge laminates. Efficient hail damage resistant structure should result from further study and understanding of these effects.

Ultrasonic Lamb wave propagation has potential as a quantitative method of characterizing impact damage in fuselage structure. Experimental results were within 5% of theory for undamaged laminate measurements and demonstrated the expected trends for measurements of the damage.

## ACKNOWLEDGMENTS

The authors wish to acknowledge G. Cox, S. Finn, R. Horton, J. Linn, W. Motzer, L. Nuanez, P. Puzon, P. Smith, K. Willden, and M. Wood of The Boeing Company; T. Brown and C. Grant of Hercules, Inc.; R. Wishart of Integrated Technologies, Inc.; R. Bennett, D. Delfosse, A. Poursartip, G. Pageau, and R. Vaziri of the University of British Columbia; and R. Groh and D. Newkirk of the University of Washington for technical support.

## NOTICE

Use of commercial products or names of manufacturers in this report does not constitute official endorsement of such products or manufacturers, either expressed or implied, by The Boeing Company or The National Aeronautics and Space Administration.



## REFERENCES

1. Rhodes, M. D., Williams, J. G., and Starnes, J. H. Jr., "Effect of Impact Damage on the Compression Strength of Filamentary-Composite Hat-Stiffened Panels," Society for the Advancement of Material and Process Engineering, Vol. 23, May 1978.
2. Dost, E. F., Ilcewicz, L. B., and Gosse, J. H., in Proc. of 3rd Tech. Conf. of American Soc. for Composites, Technomic Publ. Co., 1988.
3. Cantwell, W. J., Curtis, P. T., and Morton, J., "An Assessment of the Impact Performance of CFRP Reinforced with High Strain Carbon Fibres," Composite Science and Technology, Vol. 25, 1986.
4. Cairns, D. S. and Lagace P. A., "Residual Tensile Strength of Graphite/Epoxy and Kevlar/Epoxy Laminates with Impact Damage," Massachusetts Institute of Technology, TELAC Report 88-3, 1988.
5. Rhodes, M. D., Williams, J. G., and Starnes, J. H. Jr., "Low-Velocity Impact Damage in Graphite-Fiber Reinforced Epoxy Laminates," Proceedings of the 34th Annual Technical Conference of the Reinforced Plastics/Composite Institute, The Society of the Plastics Industry, Inc., 1979.
6. Byers, B. A., "Behavior of Damaged Graphite/Epoxy Laminates Under Compression Loading," NASA Contractor Report 159293, 1980.
7. Smith, P. J. and Wilson, R. D., "Damage Tolerant Composite Wing Panels for Transport Aircraft," NASA Contractor Report 3951, 1985.
8. Chapman, A. J., "Standard Test Evaluation of Graphite Fiber/Resin Matrix Composite Materials for Improved Toughness," NASA Technical Memorandum 86298, 1984.
9. Palmer, R. J., "Investigation of the Effect of Resin Material on Impact Damage to Graphite/Epoxy Composites," NASA Contractor Report 165677, 1981.
10. Masters, J. E., "Characterization of Impact Damage Development in Graphite/Epoxy Laminates," Fractography of Modern Engineering Materials: Composites and Metals, ASTM STP 948, ASTM, Philadelphia, PA, 1987.
11. Evans, R. E., and Masters, J. E., "A New Generation of Epoxy Composites for Primary Structural Applications: Materials and Mechanics," Toughened Composites, ASTM STP 937, ASTM, Philadelphia, PA, 1987.
12. Dow, M. B. and Smith, D. L., "Damage-Tolerant Composite Materials Produced by Stitching Carbon Fabrics," International SAMPE Technical Conference Series, Volume 21, 1989.
13. Palmer, R. J., Dow, M. B., and Smith, D. L., "Development of Stitching Reinforcement for Transport Wing Panels," NASA Conference Publication 3104, 1990.
14. Ko, F. K. and Hartman, D., "Impact Behavior of 2D and 3D Glass-Epoxy Composites," SAMPE Journal, July/Aug 1986.
15. Boll, D. J., Bascom, W. D., Weidner, W.C., and Murri, W.J., "A Microscopic Study of Impact Damage of Epoxy-Matrix Carbon-Fibre Composites," Journal of Material Science, Vol 21, 1986.

16. Swanson, G. D., Ilcewicz, L. B., Walker, T. H., Graesser, D., Tuttle, M., and Zabinski, Z., "Local Design Optimization for Transport Fuselage Crown Panels," in Proceedings of Ninth DoD/NASA/FAA Conference on Fibrous Composites in Structural Design, FAA Publication, 1991.(Paper of this compilation.)
17. Joynes, D., "Inservice Experience and Maintenance of Advanced Composite Structures in Airline Service," International SAMPE Technical Conference Series, Volume 22 ,1990.
18. Wheeler, D. J., Understanding Industrial Experimentation, Statistical Process Controls, Inc., Knoxville, TN, 1988.
19. Wheeler, D. J., Tables of Screening Designs, Second Edition, SPC Press, Inc., Knoxville, TN, 1989.
20. Chamis, C. C., "Simplified Composite Micromechanics Equations for Hygral, Thermal, and Mechanical Properties," NASA TM-83320, National Aeronautics and Space Administration, Feb., 1983.
21. Horton, R., Whitehead, R., et al, "Damage Tolerance of Composites, Final Report," AFWAL-TR-87-3030, Vol. 3, May 1988.
22. Dost, E. F., Ilcewicz, L. B., and Avery, W. B., "The Effects of Stacking Sequence On Impact Damage Resistance and Residual Strength for Quasi-Isotropic Laminates," in Composite Materials: Fatigue and Fracture, ASTM STP 1110, 1991.
23. Walker, T. H., Avery, W. B., Ilcewicz, L. B., Poe, C. C., Jr., and Harris, C. E., "Tension Fracture of Laminates for Transport Fuselage, Part I: Material Screening," in Proceedings of Ninth DoD/NASA/FAA Conference on Fibrous Composites in Structural Design, FAA Publication, 1991.(Paper of this compilation.)
24. Tang, B., Henneke, E. G., and Stiffler, R. C., "Low Frequency Flexural Wave Propagation in Laminated Composite Plates," published in the Proceedings of Acousto-Ultrasonics: Theory and Application, 1988.

**THIS PAGE INTENTIONALLY BLANK**

# **APPLICATIONS OF A DAMAGE TOLERANCE ANALYSIS METHODOLOGY IN AIRCRAFT DESIGN AND PRODUCTION**

Copyright © 1991  
by General Dynamics Corporation  
All rights reserved.

M. R. Woodward and S. D. Owens,  
G. E. Law; L.A. Mignery  
General Dynamics Fort Worth Division

## **ABSTRACT**

Objectives of customer mandated aircraft structural integrity initiatives in design are to guide material selection, to incorporate fracture resistant concepts in the design, to utilize damage tolerance based allowables and planned inspection procedures necessary to enhance the safety and reliability of manned flight vehicles. However, validated fracture analysis tools for composite structure are needed to accomplish these objectives in a timely and economical manner. This paper briefly describes the development, validation, and application of a damage tolerance methodology for composite airframe structures.

A closed-form analysis code, entitled SUBLAM was developed to predict the critical biaxial strain state necessary to cause sublaminar buckling-induced delamination extension in an impact damaged composite laminate. An embedded elliptical delamination separating a thin sublaminar from a thick parent laminate is modelled. Predicted failure strains were correlated against a variety of experimental data that included results from compression after impact coupon and element tests. An integrated analysis package has been developed to predict damage tolerance based margins-of-safety (MS) using NASTRAN generated loads and element information. Damage tolerance aspects of new concepts are quickly and cost-effectively determined without the need for excessive testing.

## **INTRODUCTION**

Emerging military aircraft contain higher percentages of advanced composite materials in flight critical primary structure applications to meet demanding weight and performance goals. Examples include the B-2 stealth bomber, the F-22 advanced tactical fighter, the F-117A stealth fighter, and the V-22 tilt-rotor. These new aircraft must meet demanding requirements for durability and damage tolerance. There is a need for validated analysis tools that can be used in a production environment to assess the effects of delamination damage on the residual strength of composite structure in a timely and efficient manner. In addition, analysis tools are also needed to aid in the disposition of discrepant parts during manufacture, and to develop accept/reject criteria necessary for quality control. In this paper, applications of

a damage tolerance methodology in the design and analysis of composite airframe structure will be emphasized. The development of the fracture analysis model will be briefly discussed.

The certification of airframe structures for durability and damage tolerance has been the impetus for the development and application of fracture analysis methods at General Dynamics to improve product reliability, safety, and supportability. The goal has been to develop and validate efficient, closed-form analysis tools that are readily available to the designer and the analyst. A damage tolerance analysis (DTA) methodology for composite structures was developed and validated under a General Dynamics IR&D task. The methodology is embodied in a computer program entitled SUBLAM. SUBLAM calculates the critical biaxial strains required to cause sublamine buckling-induced delamination extension in a composite plate.

Applications of this damage tolerance methodology in the design and manufacture of military aircraft are described. The new military damage tolerance requirements and their relationship with the analysis methodology are discussed. The use of SUBLAM to establish damage tolerance based compression strain allowables, optimize laminate stacking sequences, size structure, and develop quality control criteria for composite structure is addressed.

## METHODOLOGY DEVELOPMENT

### Background

Sublamine buckling induced delamination growth produced by compressive loading has been recognized as a worst case failure mode in composite structures (ref. 1). In this failure mode, delamination damage causes the sublaminates to buckle under compressive loading. As the compressive loading increases, strain energy stored in the buckled sublamine also increases until reaching a critical level (denoted as  $G_c$ , the critical strain-energy release rate). At this critical strain level, the delamination is assumed to propagate when  $G \geq G_c$ . Since failure occurs at the initiation of delamination growth, this failure mode is treated as a static problem. This behavior has been experimentally observed in a large number of impact damaged component fatigue tests at General Dynamics and elsewhere (ref. 1).

The finite element modeling (FEM) technique has been extensively utilized to address local instability-induced fracture behavior in composite materials. However, the application of complex two- and three-dimensional FEM's to solve fracture problems is not ideally suited for the aircraft industry due to time and cost constraints. In addition, the number of parts that must be efficiently analyzed during design is staggering. Thus, a fast, closed-form delamination analysis tool was developed to aid the analyst in assessing the damage tolerance of composite structure.

The SUBLAM computer program was formulated in 1988 and 1989 using the model developed by Chai and Babcock (ref. 2) as the baseline. The model treats the problem illustrated in Figure 1 in which a thin sublaminate disbonds from a thick parent laminate. The buckled sublaminate is assumed to be elliptically shaped with clamped boundary conditions. The elliptical shape can be varied by changing the aspect ratio, defined as  $(a/b)$ .

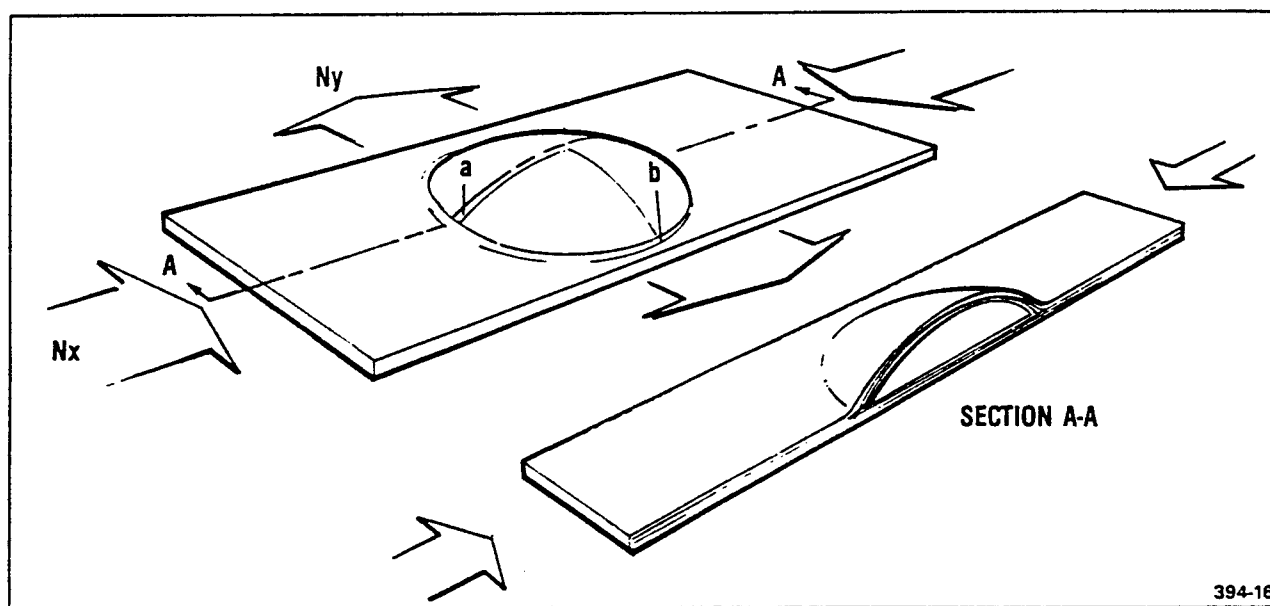


Figure 1 SUBLAM Models A Delaminated Region In A Biaxially Loaded Composite Plate

A single-term Rayleigh-Ritz solution technique is used to describe the buckled shape of the sublaminate. Through differentiation of the total potential energy with respect to the delamination ellipse major and minor dimensions, "a" and "b" respectively, the total strain-energy release rate ( $G$ ) is calculated as an average around the perimeter of the delamination. When  $G_a$  or  $G_b$  is  $\geq G_c$  (the critical strain-energy release rate), delamination growth is assumed to occur in a self-similar fashion. Thus, the biaxial strains required to cause buckling induced delamination growth in a composite plate are calculated. Predictions are made at every ply interface and can be performed for different in-plane loadings ( $N_x$ ,  $N_y$ , and  $N_{xy}$ ), flaw aspect ratios, and sizes. Program inputs include laminate stacking sequence, critical  $G$ , flaw sizes and aspect ratios, and lamina mechanical properties. Additions to Chai and Babcock's model were incorporated in SUBLAM. Both the sublaminate and the parent laminate are represented as homogeneous anisotropic layers. To predict failure strains produced by low velocity impact damage (LVID), the extensional and bending stiffness terms ( $A_{ij}$  and  $D_{ij}$ ) were assumed to be degraded using a rule-of-mixtures approach.

SUBLAM was integrated into an overall damage tolerance analysis (DTA) methodology that utilizes information from the NASTRAN finite element model of the aircraft structure. Several codes used to extract load and stacking sequence data, as well as format results for post-processing were packaged into a large command file program entitled "DTC". The application of these codes in structural design and analysis are described in the following section.

### Validation

General Dynamics has conducted numerous experiments to correlate and validate fracture analysis models. Durability and damage tolerance (DADT) testing has been conducted using coupon, element, and component size articles, as well as full-scale flight hardware. This effort has created a sizeable amount of data on the impact damage problem and its effects on the residual compressive strength of composite structures.

SUBLAM predicted failure strains were correlated against a variety of experimental data. Predictions were made for coupons, single-bay box-beam components, and stiffened panels subjected to compression after impact (CAI) testing. Additional stiffened panel tests data were obtained from contractor reports (ref. 1). Different laminate ply-percentages, layups, thicknesses, panel geometries, and material systems were used in the correlation. SUBLAM generally predicted conservative values, as shown in Figure 2. In some cases, the  $G_c$  was unknown, and therefore was estimated.

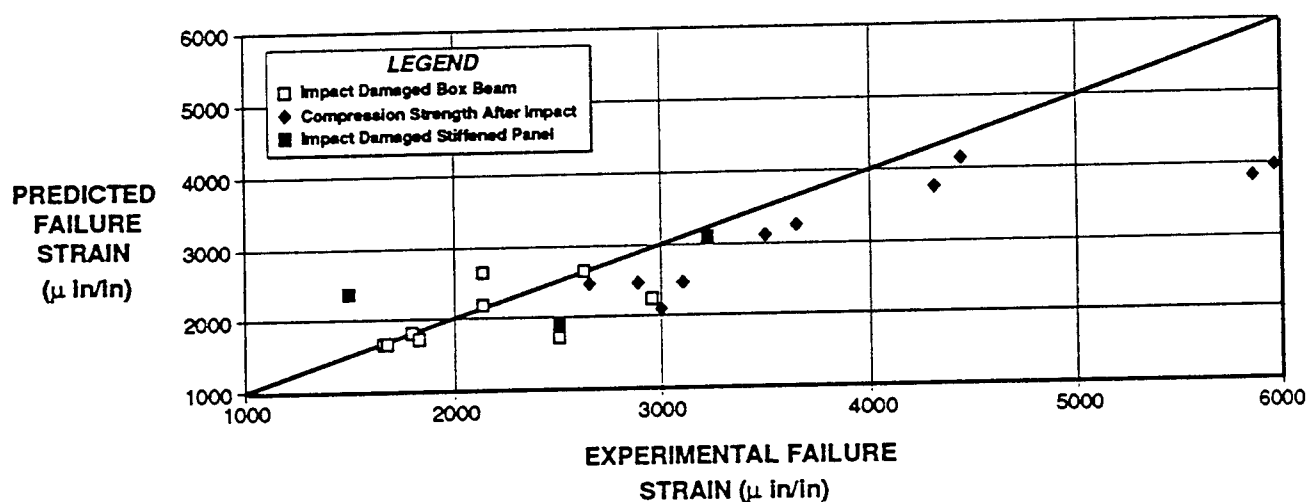


Figure 2 SUBLAM Predictions Correlate Well With Experimental Results

## DAMAGE TOLERANCE REQUIREMENTS

Air Force and Navy damage tolerance specifications for composites dictated the approach taken during development, validation, and implementation of General Dynamics' damage tolerance analysis methodology. General requirements and the implications of these specifications on the methodology are described below.

Specific damage tolerance requirements and design criteria for organic matrix composite materials were not specified during design and development of various military aircraft introduced in the 1970's and early 80's, such as the F-16, F-15, and F/A-18. Instead, composite structures were certified on an ad hoc basis, usually via full-scale component testing. Typical manufacturing and in-service threats were identified, but a consensus for design purposes was not established. These early composite airframe structures are primarily damage tolerant due to the use of low design strain allowables. Strain allowables for carbon/epoxy composites are usually established by low bolted joint strength, global buckling, flutter, stiffness, and strength considerations. Fatigue has not been an issue since the operational strain levels are safely below the fatigue threshold for graphite/epoxy composite materials.

New and emerging aircraft fabricated using advanced composite materials in fracture critical airframe applications are designed to meet new damage tolerance requirements for organic matrix composites such as those contained in Air Force Guide Specification 87221A (ref. 3). Damage tolerance requirements can vary considerably depending on the customer, i.e., Air Force, Navy, Army, and FAA. Although the philosophy of designing fracture critical structure to safely tolerate the presence of damage produced either during manufacture or from an in-service event for a period of time while maintaining a specified residual strength is uniformly embraced by both government and industry.

Delamination produced by low-velocity impact damage (LVID) has been demonstrated to represent a worst case threat in terms of reductions in static and fatigue residual strength (ref. 1). Single and multiple delaminations are not as serious as impact damage. Thus, certification specifications address delamination damage produced by LVID as a worst case threat for design purposes. For instance, (dependent on the customer) fracture critical, primary load path structures are designed to sustain design ultimate load in the presence of visible impact damage with no progressive flaw growth for two lifetimes (Navy), or to sustain the once-per 20 lifetimes maximum spectrum load in the presence of damage produced by the energy necessary to create a 0.1 inch deep dent to a maximum of 100 ft-lb of energy after two design lifetimes (Air Force). The impact damage is assumed to exist in the worst possible location and orientation. Impact damage is typically produced by either a 0.5 or a 1.0 inch diameter hemispherical steel impactor.

For the composite material systems used date, the above criteria has been satisfied using a static analysis. Damage tolerance testing has verified that this approach for the certification of composite airframe



structure is sound. Composite structure designed to sustain maximum design flight loads in conjunction with end-of-life environmental properties will tolerate the presence of low-velocity impact induced delamination damage without threat of subcritical growth. This approach to the design and certification of composite airframe structures for damage tolerance is considered to be conservative.

## **APPLICATIONS IN DESIGN AND ANALYSIS**

### Design Information

Our overall objective during design is to guide material selection, to incorporate fracture resistant concepts in the design, and to establish damage tolerance based strain allowables and planned inspection procedures necessary to enhance the safety, reliability, and supportability of manned flight vehicles. The use of a damage tolerance analysis methodology to accomplish these goals is described. The importance of addressing damage tolerance early in the design process is emphasized. Otherwise, cost and schedule can be adversely impacted due to drawing and/or tooling changes necessary to meet customer damage tolerance requirements.

The demand for tougher, more damage tolerant composite materials has led suppliers in recent years to introduce a variety of new material systems, including thermoplastic, toughened epoxy, and toughened bismaleimide resins. The toughness issue is still debated throughout the aerospace industry. As in metallic materials, the price paid for increased toughness has been at the expense of strength. Specifically, for composites the hot/wet compression strength is decreased. The material selection process for new flight vehicles has become one of the most challenging, divisive, important, and sometimes political decisions made during the development stage. There are sometimes misconceptions concerning the importance of toughness in aircraft design. Historically speaking, damage tolerance strain allowables have been a factor in the sizing of less than 10 percent of the total number of composite parts on some recent aircraft programs. In other words, damage tolerant materials are desirable, but not at the expense of weight and cost. SUBLAM can be used in trade studies to predict failure strains for different material systems. Thus, fracture toughness requirements can be methodically assessed, and help in making good material selections.

During preliminary design, SUBLAM can be used to optimize stacking sequences for enhanced damage tolerance and to establish compression strain allowables. For buckling critical structure, the optimum stacking sequence can conflict with the best layup for enhanced damage tolerance. Laminates with grouped, major load bearing plies placed near the surface are prone to delaminate due to large stiffness changes through the thickness (creating high energy interfaces). As shown in Figure 3, the damage tolerance based compression strain allowable is increased by "softening" (incorporating angle-ply material) the outside laminae in the direction of the primary compression load. In addition, the benefits of subsymmetry on laminate design in reducing transverse shear are also predicted to increase the damage tolerance

strain allowable. If strength deficiencies are predicted, solutions may include rearranging the existing stacking sequence (increasing the strain allowable), or by the addition of plies (reducing the applied strain). It has been shown analytically and verified through test that the compression after impact strain allowable (for a laminate with fixed ply percentages) is highly dependent on the stacking sequence.

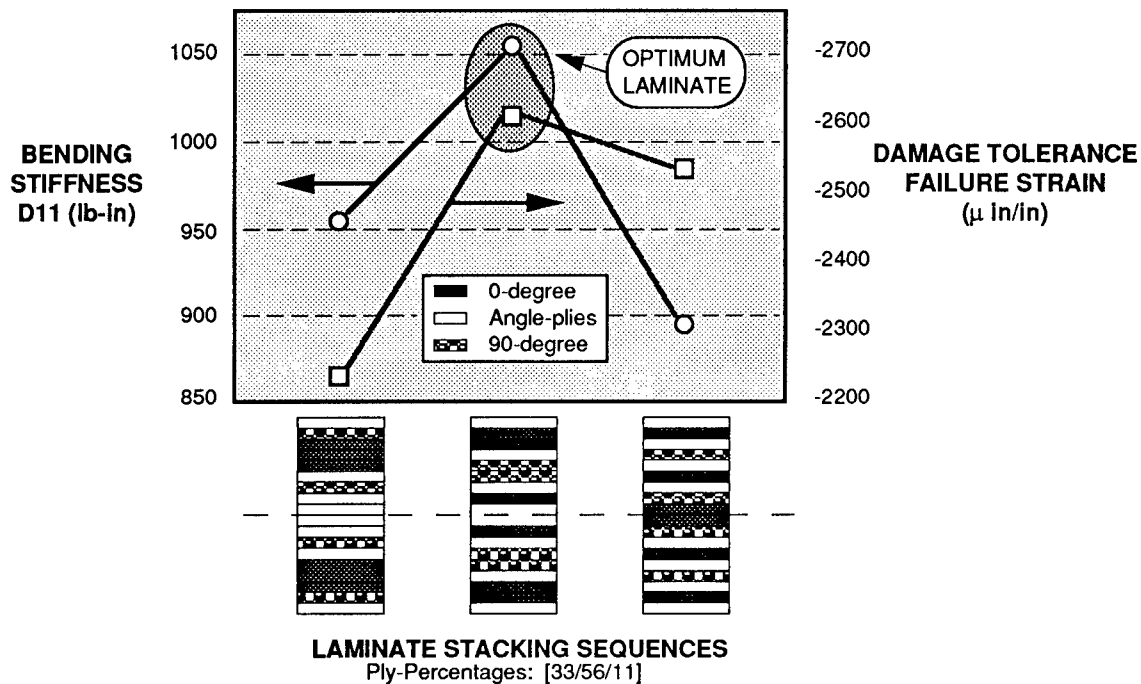


Figure 3 SUBLAM Is Used In Optimization Trade Studies

### Damage Tolerance Analysis

Validated analysis tools used for the design and analysis of damage tolerant composite structure have been successfully implemented at General Dynamics. The application of these tools to certify primary composite airframe structure for damage tolerance by analysis is described. The analysis procedure is highly automated. A flowchart of the basic processing steps is shown in Figure 4. The first task is to obtain mid-plane loads, element identification, and material properties from the finite element model. Data is typically extracted via the NASTRAN portable file used for post-processing. Models of the entire aircraft or a component thereof can be selected. Next, the element and load information is matched to a stacking sequence from the engineering drawing. If the correct laminate stiffness data is included in the finite element model, the laminate stiffness matrices can be obtained directly. A conservative assumed flaw size is typically selected based on delamination area associated with visible impact damage. The optimum value for  $G_c$  is determined via correlations with experimental data. In

the absence of an empirically correlated  $G_c$  value, the mode I fracture toughness, measured using the double cantilever beam test is utilized. Not surprisingly, experience has shown that use of the mode I  $G_c$  in SUBLAM typically results in unconservative predictions. Damage tolerance based margins-of-safety are calculated for each element by comparing the SUBLAM predicted critical principal strain to that from the FEM at 120% of design limit load (or 125% of the maximum spectrum stress, whichever is greater). Both tabular listings and computer files for post-processing are created to expedite the data review process. As an example, a contour plot of damage tolerance based margins-of-safety for a horizontal empennage skin at static design ultimate load is shown in Figure 5. Hot spots are easily identified for more detailed analysis if required. In some cases when a negative MS is predicted, the assumed flaw size can be larger than representative elements. Thus loads are averaged in a detailed analysis to more adequately represent the actual situation.

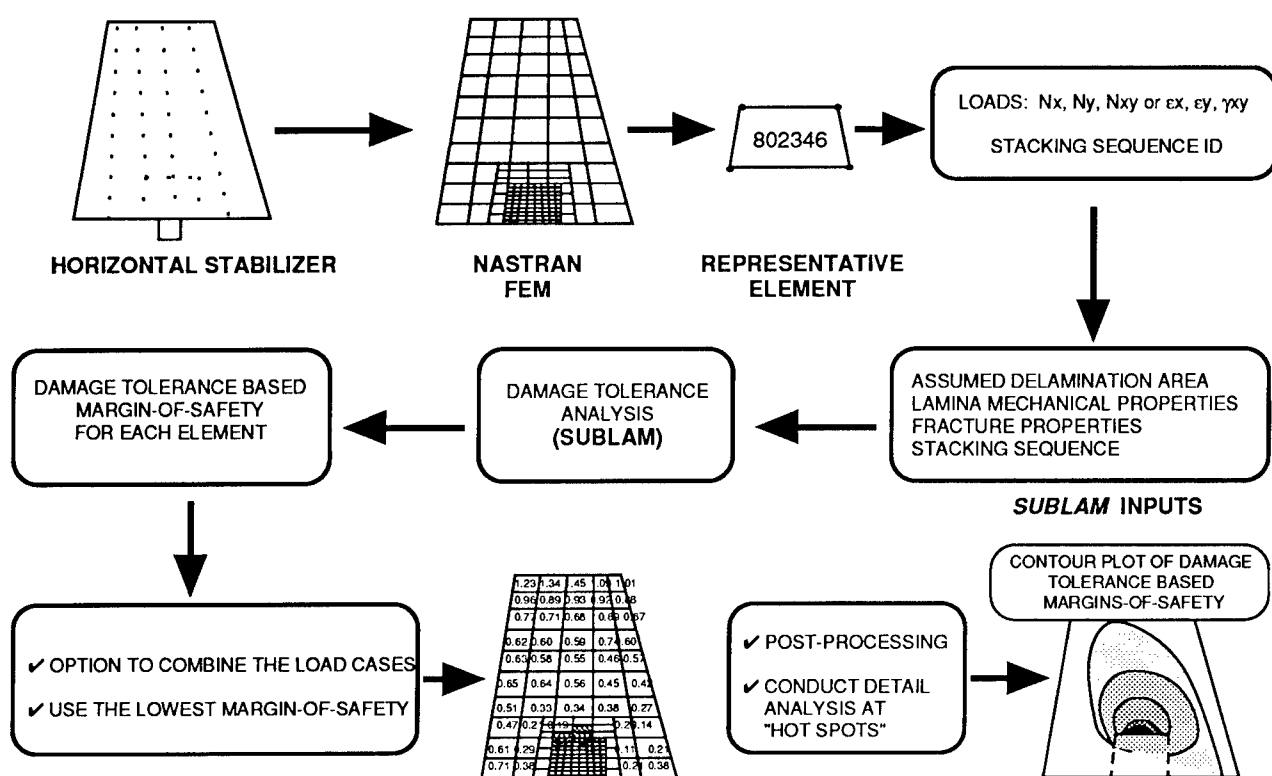


Figure 4 Damage Tolerance Methodology Flowchart

Once problem areas are identified, and the loads verified, several courses of action can be taken to increase the MS. The first option is to rearrange the laminate stacking sequence. Advantages are that no weight penalty is incurred and that no tooling changes are required. Another choice is to simply add plies in the direction of the primary compressive load. Unfortunately, the analyst becomes the bad guy by causing weight increases! Other potential problems are increases in load attracted to the area caused by increased stiffness.

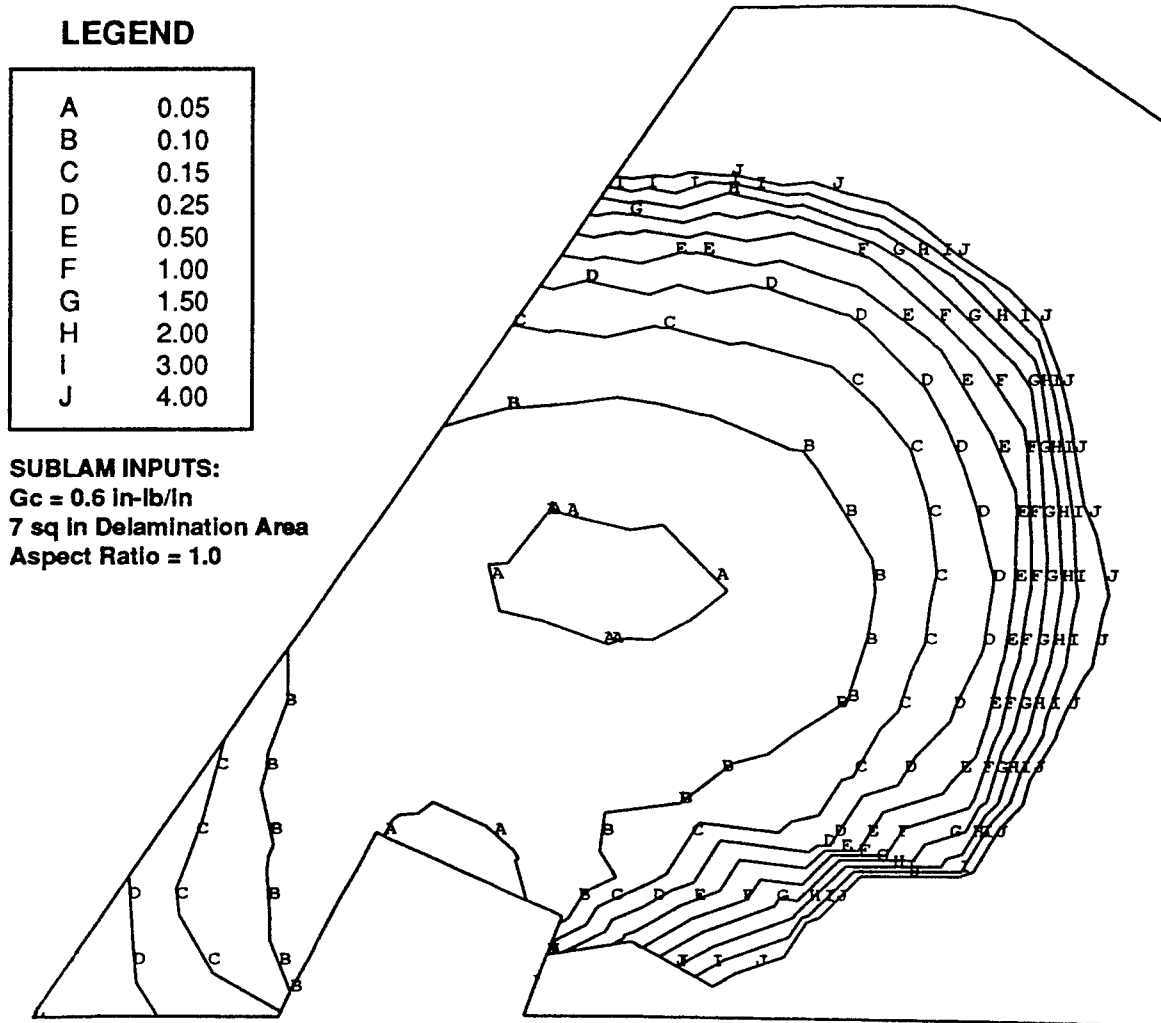


Figure 5 Contour Plot of Damage Tolerance Based Margins-of-Safety For A Composite Horizontal Empennage Skin

The delamination analysis methodology can also be used to perform updated damage tolerance analyses of composite structures. Loads and part geometries can change to meet updated mission profiles, design changes, or usage variations. The simplicity of the model allows an analyst to perform an expedient damage tolerance analysis. The model can be used to extend beyond the verification database when new materials and loads are introduced. In addition, the methodology can be utilized to reduce time involved in conducting analyses in support of engineering changes to production drawings. Design changes are costly in terms of labor hours and potential schedule impacts. Revised parts are reanalyzed to meet certification specification requirements. Again, application of efficient fracture analysis tools reduces time and labor costs.

### **Applications in the Quality Assurance Process**

#### Development of Accept/Reject Criteria

In the design and development stage of an aircraft program, SUBLAM can be effectively utilized to establish quality control accept/reject criteria for manufactured parts. On a recent aircraft program, all of the composite parts were "zoned" for maximum allowable delamination sizes. Five zones were established based on predicted maximum allowable delamination sizes. Allowable delamination sizes were calculated using ultimate loads. Flaw depth was not specified in the criteria, only flaw area for the sake of conservatism, inspectability, and brevity. It was assumed that the flaw was located at the critical interface. Zoning of composite parts effectively reduces the time, cost, and complexity associated with nondestructive inspection.

#### Disposition of Discrepant Manufactured Parts

During the manufacture and assembly of composite airframe structures, delaminations can be induced by improper machining techniques, forcing together improperly shimmed parts, and foreign object damage (FOD). It is imperative to determine the significance of delaminations that are induced during the manufacturing process in a timely manner. SUBLAM has been effectively utilized in the quality control process at General Dynamics to aid engineering in the disposition of discrepant parts.

Typical procedures include a thorough nondestructive inspection to assess the depth(s) and area(s) of each delamination. The local stacking sequence, lamina mechanical properties, critical G, strain state at 120% of design limit load, and the flaw dimensions are input to SUBLAM. High aspect ratio delamination shapes are conservatively represented using a circular shape. A margin-of-safety is calculated at the specific ply interface of concern. A disposition is made based not only on results from the delamination analysis, but on the flaw location, repair options, dollar value of the part or assembly, and part classification (fracture critical parts require special attention). The part is either scrapped, returned to print via a remove and replace operation, or repaired.

## Disposition of Service-Induced Damage

Similarly, the severity of service-induced delamination damage must be quickly and effectively assessed by field and depot level operations personnel. A number of disposition options are normally considered depending on part function, location, and classification. With proper guidance, fracture analysis tools similar to SUBLAM could be confidently used by field-level personnel to determine whether to operate as is, ferry flight the aircraft to a repair depot, remove the part from service, or specify standard repairs.

### SUMMARY

An efficient damage tolerance analysis methodology has been developed that is useful during the design, development, and production stages of an aircraft program to establish damage tolerance based strain allowables, conduct damage tolerance analyses, aid in the disposition of discrepant parts both in manufacturing and in service environments, and establish acceptance and rejection criteria for composite structure. Incorporating damage tolerance in the design process will enhance product reliability, supportability, and maintainability without significant cost or weight implications.

### REFERENCES

1. Kan, H.P., Graves, M.J., et. el., "Damage Tolerance of Composites," Vol. I Final Report, AFWAL-TR-87-3030, 1988.
2. Chai, H., Babcock, C.D., "Two-Dimensional Modelling of Compressive Failure in Delaminated Laminates," J. of Composite Materials, Vol. 19, 1985.
3. AFGS-87221A, "Air Force Guide Specification - General Specification For Aircraft Structures," pp 332-342, June 1990.

**THIS PAGE INTENTIONALLY BLANK**

## COMPRESSIVE STRENGTH OF DAMAGED AND REPAIRED COMPOSITE PLATES

Scott R. Finn and George S. Springer

Department of Aeronautics and Astronautics  
Stanford University, Stanford, California

### ABSTRACT

Tests were performed assessing the effectiveness of repair in restoring the mechanical properties of damaged, solid composite plates made of Fiberite T300/976 graphite-epoxy. Some (75 percent) or all (100 percent) of the damaged zone was cut out, and the plate was repaired by plugging and patching the hole. The effectiveness of the repair was evaluated by measuring the compressive strengths of undamaged plates, damaged plates with no cutout, damaged plates with a cutout, and plates having been repaired.

### INTRODUCTION

In this paper, data are presented showing the benefits, as represented by the in-plane compressive strength, which can be gained by repairing damaged composite plates. To this end, solid (as opposed to honeycomb) composite plates were subjected to impact or transverse static loads. Some or all of the damaged zone was removed, and the plate was then repaired. The in-plane compressive strengths of the plates were determined 1) prior to impact, 2) after impact, before repair, 3) after impact, with some or all of the damaged zone removed, and 4) after impact, with the damaged zone repaired.

These compressive strengths were then compared, and the effectiveness of the repair was assessed from these comparisons.

### EXPERIMENTS

Four inches long and 3 inches wide plates made of Fiberite-T300/976 unidirectional graphite-epoxy tape were used in the tests. After manufacture, each plate was inspected by a pulse-echo ultrasonic technique (C-scan) to establish that they were undamaged. Damage was introduced in the plates in one of two ways. Either the plates were impacted with a projectile (impactor) fired from an air gun, or a transverse load was applied via an indenter and a mechanical tester. In both cases, the load was applied at the center of the plate by a hemispherical steel impactor (indenter) having a 0.25 inch radius. The damaged plates were inspected by X-ray and, some of the plates, also by pulse-echo C-scan. In this manner, the sizes of the damaged zones were determined.

The damaged zone was removed by grinding out an elliptical hole through the entire thickness of the plate (Figure 1). After grinding, the plate was again X-rayed to establish that the process did not damage the plate further.



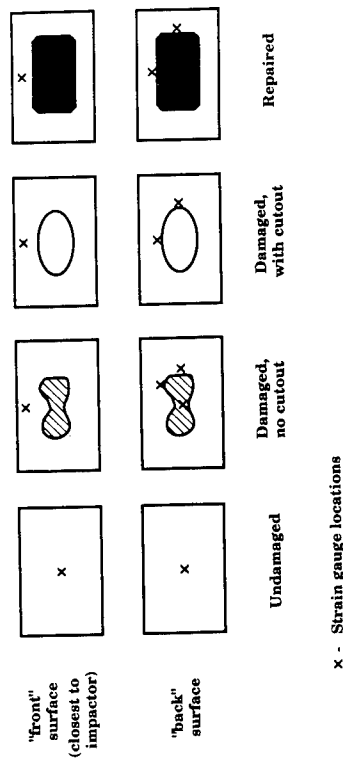


Figure 3. Locations of the strain gauges.

Figure 1. Description of the plate a) before cutout, b) with cutout, c) with plug inserted in cutout, and d) with patch placed over plug.

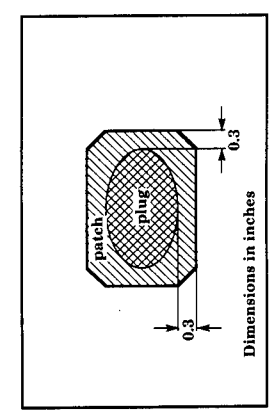
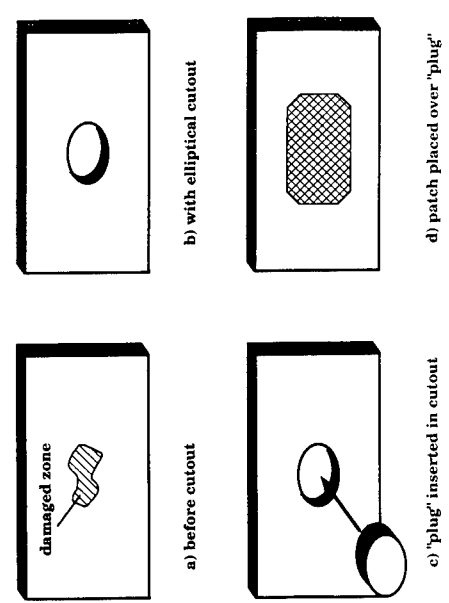


Figure 2. Dimensions of the patch used in repairing the plate.

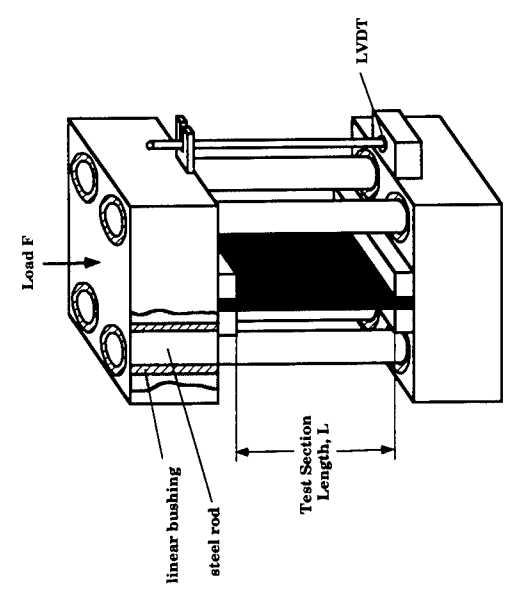


Figure 4. Compression test fixture.

After holes were cut in the plates, the plates were repaired by placing a "plug" (made of the same material as the plate) in the hole (Figure 1). This plug had the same shape and size as the hole, and had the same layup as the plate. American Cyanamid FM300 adhesive was placed between the plug and the plate. One layer of Fiberite T300/976 graphite-epoxy cloth "patch" was placed above the plug on each side of the plate. The dimensions of the patch are given in Figure 2. The plates were vacuum bagged and cured. Strain gauges were then mounted on the plates (Figure 3).

The compressive strength of each plate was measured by clamping the two short edges of the plate in a specially built fixture (Figure 4). The compressive load was applied at a displacement rate of  $2 \times 10^{-5}$  in/sec, and the load versus strains and the load versus displacement were measured.

The following information was deduced from the data.

- 1) "Delamination buckling" load  $F_{db}$  is defined as the load at which the plate locally buckles above the damaged area. The load at which this occurs was determined from the output of the strain gauge placed at the center of the damaged region on the "back" surface.
- 2) "Damage growth" load  $F_g$  is defined as the load at which the damaged area starts to grow. The load at which this occurs was determined from the strain gauges on the "back" surface of the plate located at the edge of the damaged area (plates without cutout), near the edge of the hole (plates with cutout), or near the edge of the repaired zone (repaired plates). The damage growth load data for plates with cutout or with repair were normalized with respect to the damage growth loads of damaged plates with no cutout  $F_g^{nc}$ .
- 3) "Buckling" load  $F_b$  is defined as the load at which the entire plate buckles. The load at which this occurs was determined from the displacement and from the strain gauge on the "front" surface of the plate. The buckling load data for damaged plates were normalized with respect to the buckling loads of undamaged plates  $F_b^0$ .
- 4) "Ultimate" load  $F_u$  is defined as the maximum load which the plate can support before collapse. This load could be determined from any of the plots of load versus displacement or load versus strain. The ultimate load data for damaged plates were normalized with respect to the ultimate loads of the undamaged plates  $F_u^0$ .

## RESULTS

The results presented below are grouped into four categories 1) delamination buckling load,  $F_{db}$ , 2) damage growth load,  $F_g$ , 3) buckling load,  $F_b$ , and 4) ultimate load,  $F_u$ . The measured loads are presented in terms of four variables, the number of plies  $n$  in the  $0^\circ$  ply groups, the mismatch angle  $q$ , and the initial damaged zone length  $l_D$ .

Below, data are presented for plates a) with no damage, b) with damage, c) with all (100%) or some (75%) of the damaged zone removed, and d) with the damaged zone repaired. For 100% of the damaged zone removed, the major axis of the elliptical cutout was equal to the maximum length of the damaged zone, and the minor axis was equal to the maximum width of the damaged zone. For 75% of the damaged zone removed, the above major and minor axes of the cutout ellipse were reduced to 75% of their original lengths. Obviously, in this case some of the damaged zone was not removed. All of the repaired plates had a 100% cutout before plugging and patching.

## Delamination Buckling Load

The measured delamination buckling loads are given in Figures 5-7. Data are only presented for damaged plates with no cutout or repair, as delamination buckling was not observed in the plates with cutout or repair.

The load (delamination buckling load  $F_{db}$ ) at which a sublaminate in the damaged zone buckles increased as the number  $n$  of plies in the  $0^\circ$  ply groups increased, i.e., as the thickness of the back ply group increased (Figure 5). This can be explained by observing that when the load was applied, the sublaminate below the damaged zone (at the "back" side of the plate) buckled. A thicker back ply group corresponds to a sublaminate which is stiffer and thus more resistant to buckling.

The delamination buckling load  $F_{db}$  decreased with mismatch angle  $q$  (Figure 6). To explain the reason for this, we observe that the data shown in this figure apply to plates in which the damage length was constant ( $l_D = 1.5$  in), while the width was not controlled independently. In fact, the damage width  $w_D$  (and consequently the damaged area) increased with the mismatch angle  $q$  (Figure 6). Thus the size of the damaged area increased resulting in a decrease in the delamination buckling load  $F_{db}$  with increasing mismatch angle  $q$ .

The delamination buckling load  $F_{db}$  as a function of the initial damaged zone length  $l_D$  is shown in Figure 7. For these  $[0_4/90_4]_S$  plates, the width  $w_D$  of the damaged zone was approximately equal to one half of the damage length  $l_D$ . As the length  $l_D$  increased (and with it, the size of the damaged zone), the load required to buckle the sublaminate decreased.

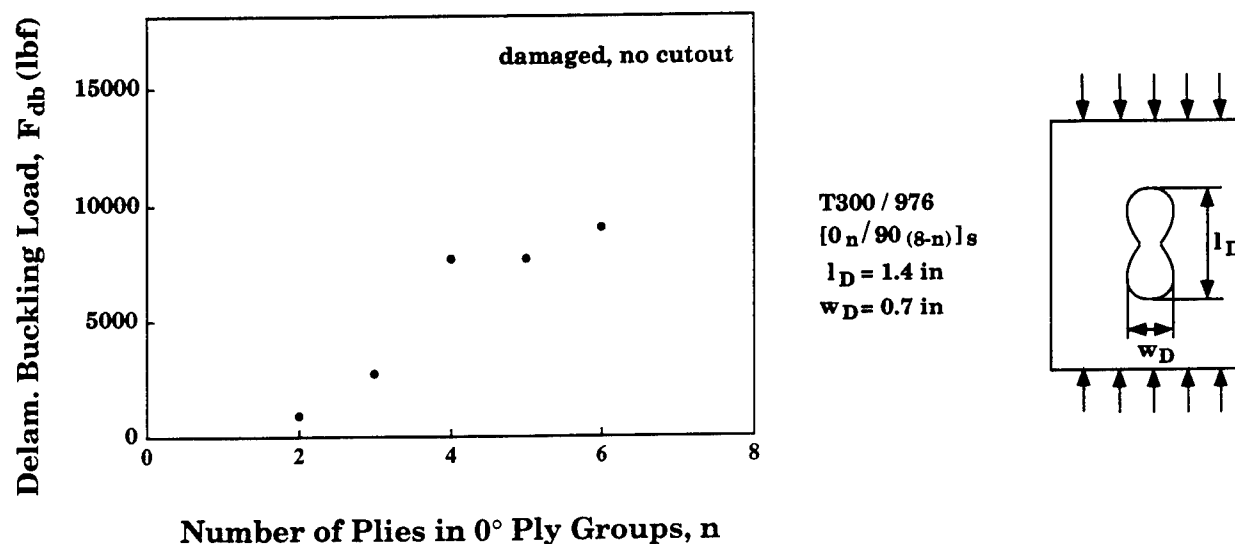


Figure 5. Delamination buckling load  $F_{db}$  as a function of the number of plies  $n$  in the  $0^\circ$  ply groups. Test section length  $L = 3$  in.

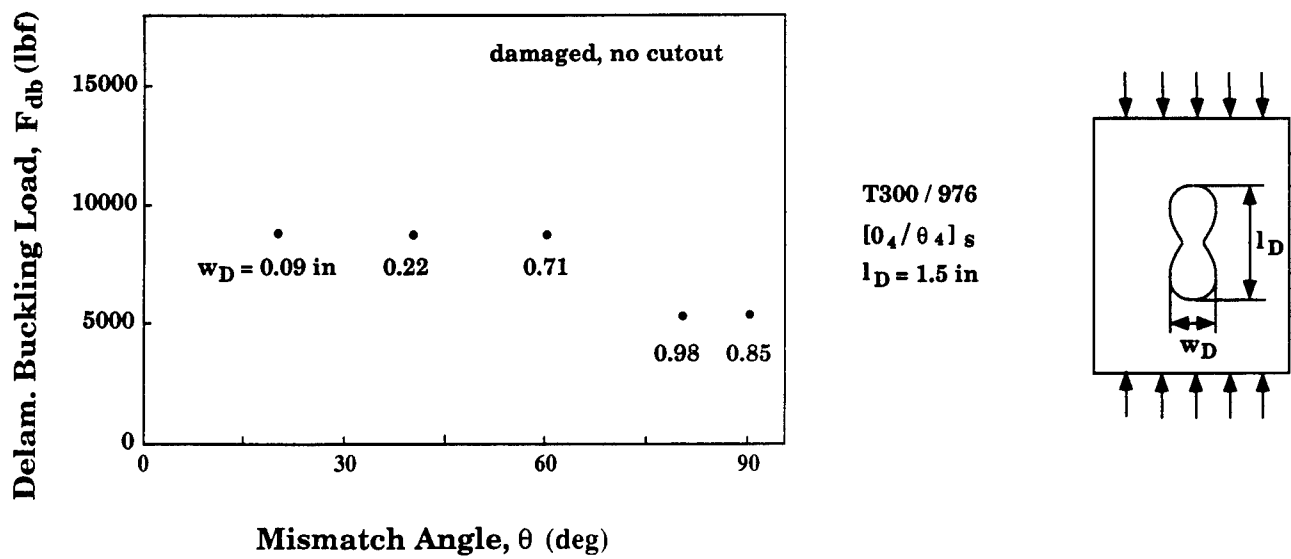


Figure 6. Delamination buckling load  $F_{db}$  as a function of the mismatch angle  $\theta$ . Test section length  $L = 3$  in.

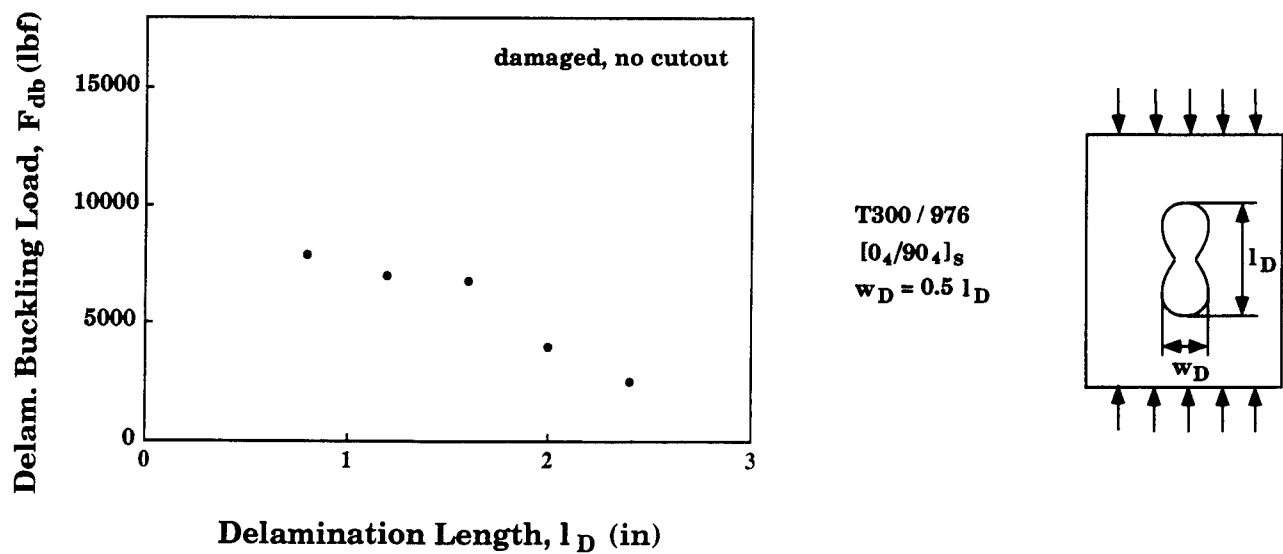


Figure 7. Delamination buckling load  $F_{db}$  as a function of the initial damaged zone length  $l_D$ . Test section length  $L = 3$  in.

## Damage Growth Load

The damage growth load  $F_g$  as a function of the number of plies  $n$  in the  $0^\circ$  ply groups is shown in Figure 8. For damaged plates with no cutout, the growth load increased with the number of plies in the  $0^\circ$  ply groups. To explain this trend it is again noted that the buckled sublaminate was at the back of the plate. Accordingly, an increase in the number of plies  $n$  in the back  $0^\circ$  ply group corresponded to an increase in the stiffness of the sublaminate and an increase in the delamination buckling load  $F_{db}$  (Figure 5). For the plates with no cutout or repair, damage growth was always preceded by delamination buckling. Therefore, the damage growth load  $F_g^{nc}$  also increased with increasing number of plies  $n$  in the  $0^\circ$  ply groups.

Cutting out the damage resulted in an increase in the damage growth loads  $F_g$  provided the back ply groups were relatively "thin" ( $n=2,3$ ). The reason for this is that removal of the damaged zone prevented delamination buckling and delayed damage growth. Furthermore, plates with 100% cutout had higher growth loads than those with 75% cutout because, in the latter case, not all the damaged zone was removed. Cutting out the damaged zone did not affect the damage growth loads  $F_g$  of plates with "thick" back ply groups ( $n=4-6$ ). Because of the large back ply group thickness (corresponding to high stiffness of the sublaminate), in these plates, the damage started to grow even before the sublaminate buckled.

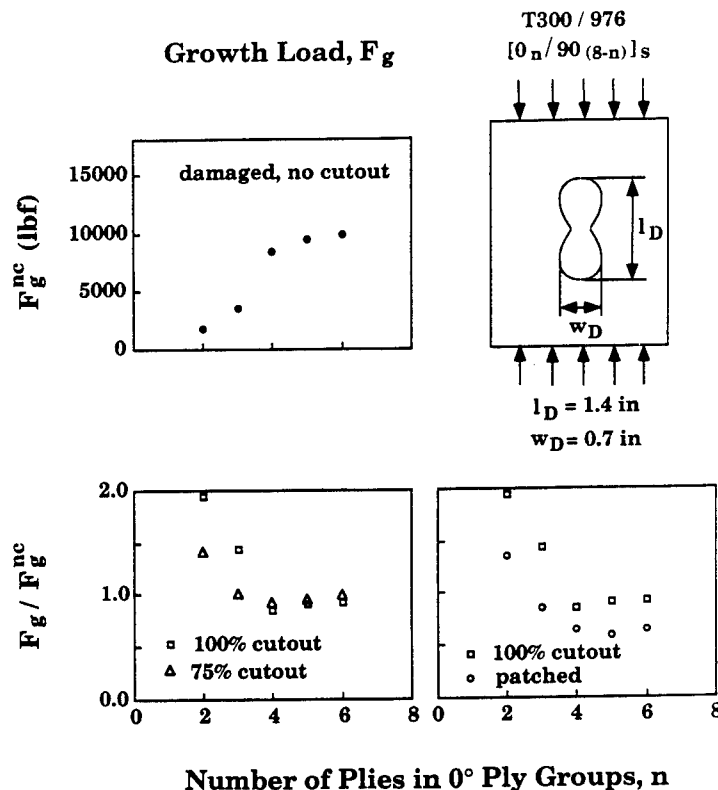


Figure 8. Damage growth load  $F_g$  as a function of the number of plies  $n$  in the  $0^\circ$  ply groups. Test section length  $L = 3$  in.

Repaired plates had lower damage growth loads than plates with 100% cutouts (Figure 8, right). The reason for this is unclear, but it is likely that damage could initiate at the interface between the plate and the plug.

The damage growth load  $F_g$  as a function of the mismatch angle  $q$  is shown in Figure 9. For damaged plates with no cutout, the growth load decreased as the mismatch angle increased (Figure 9, top). The reason for this decrease was that larger mismatch angles were accompanied by larger initial damaged zones (as was discussed in Section 3.1) and lower delamination buckling loads  $F_{db}$  (Figure 6). Since the size of the damaged zone increased with increasing mismatch angle  $q$ , the growth load  $F_g^{nc}$  decreased. Neither removing the damaged zone nor repairing it had a significant effect on the damage growth loads, as shown in Figure 9, bottom.

The damage growth load  $F_g$  as a function of the initial damaged zone length  $l_D$  is shown in Figure 10. For plates with no cutout or repair, the damage growth load  $F_g^{nc}$  decreased with the damage length  $l_D$ . Since the damage width  $w_D$  increased along with the damage length, the overall size of the damaged zone increased. This increase in the size of the damaged zone resulted in the decrease in growth load  $F_g^{nc}$ .

For plates with relatively "small" initial damage lengths ( $l_D < 2$  in), the damage started to grow before the sublaminates buckled. Hence, in this case, cutting out the damaged zone did not change significantly the damage growth load, i.e. the damage growth loads for plates with and without cutouts were nearly the same (Figure 10, middle). For plates with larger initial damage lengths ( $l_D \geq 2$  in), the sublaminates buckled, and this event governed the damage growth. In this case, cutting out the damaged zone resulted in an increase in the damage growth loads  $F_g$ . Repairing the plates seemed to produce little or no change in the growth load compared with plates with 100% cutout (Figure 10, right).

### Buckling Load

The global buckling load  $F_b$  as a function of the number of plies  $n$  in the  $0^\circ$  ply groups is shown in Figure 11. For initially undamaged plates, the buckling load  $F_b^0$  increased slightly as  $n$  (and hence the number of  $0^\circ$  plies in the plate) increased. As the number of  $0^\circ$  plies in the plate increased, so did the bending stiffness of the plate in the lengthwise direction. This resulted in an increase in the buckling load  $F_b^0$ .

As expected, damaged plates, with or without cutout, generally had lower buckling loads  $F_b$  than undamaged plates. The removal of all or part of the damaged zone generally produced a small decrease in the buckling load compared to the buckling load of damaged plates with no cutout. Although the material in the damaged zone was not as strong as the undamaged material, it still provided some resistance to buckling. For this reason, removal of the damaged material caused a decrease in the buckling loads  $F_b$ .

Repaired plates had slightly higher buckling loads than plates with 100% cutout. However, repaired plates had practically the same buckling loads as damaged plates with no cutout. Inserting new material into the damaged zone provided more buckling resistance than a cutout, but not more than the original damaged material.

The global buckling load as a function of the mismatch angle  $q$  is shown in Figure 12. For initially undamaged plates, the buckling load  $F_b^0$  exhibited a slight decrease with mismatch angle (Figure 12, top). As the angle  $q$  increased, the stiffness of the laminate in the lengthwise direction decreased leading to the decrease in the buckling load.

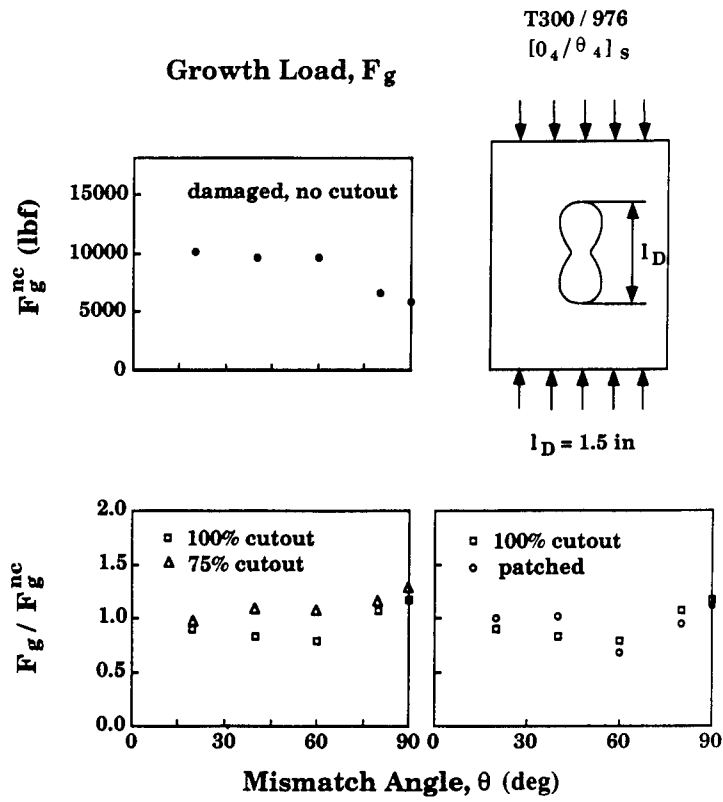


Figure 9. Damage growth load  $F_g$  as a function of the mismatch angle  $\theta$ . Test section length  $L = 3$  in.

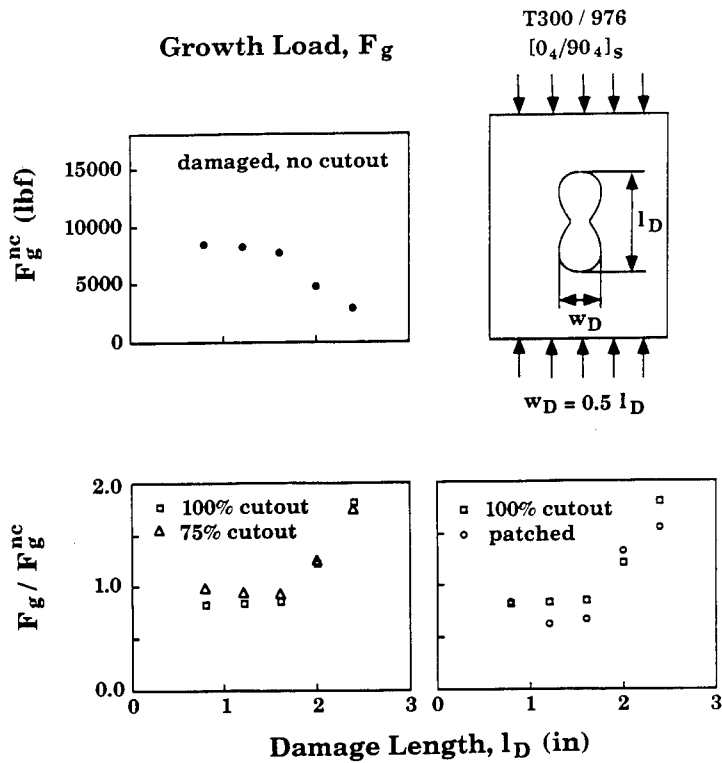


Figure 10. Damage growth load  $F_g$  as a function of the initial damaged zone length  $l_D$ . Test section length  $L = 3$  in.

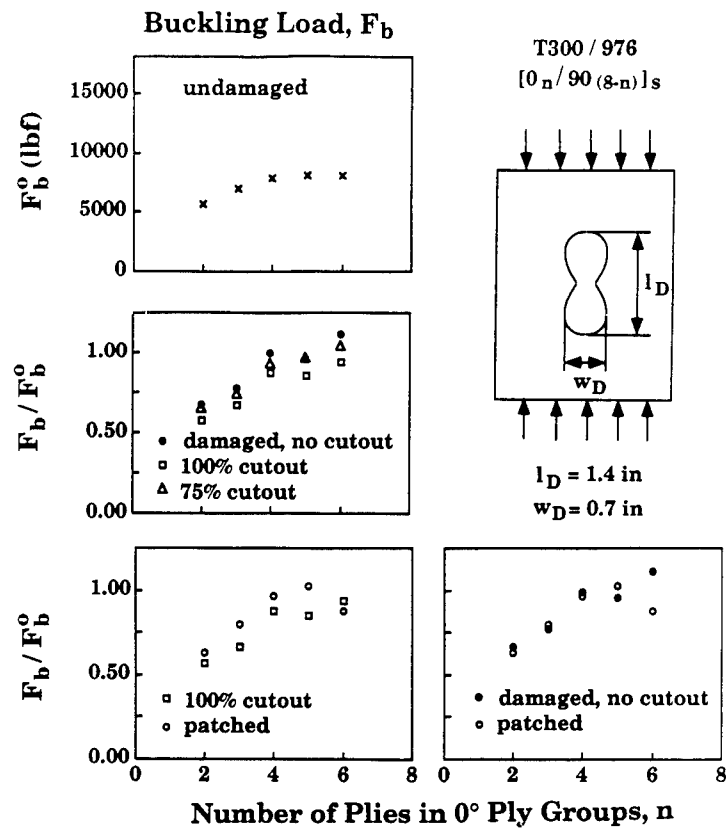


Figure 11. Buckling load  $F_b$  as a function of the number of plies  $n$  in the 0° ply groups. Test section length  $L = 3$  in.

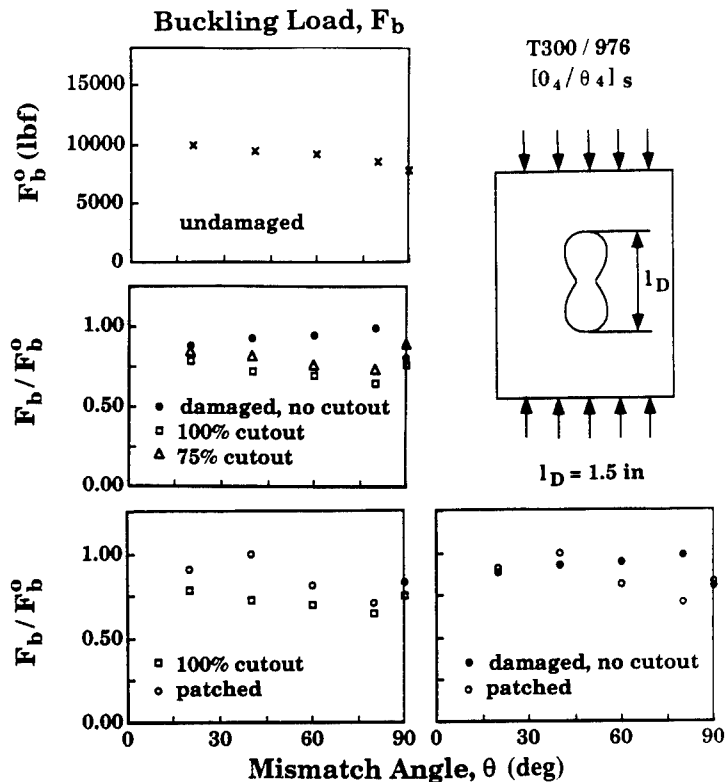


Figure 12. Buckling load  $F_b$  as a function of the mismatch angle  $\theta$ . Test section length  $L = 3$  in.



Damaged plates with no cutout had lower buckling loads than undamaged plates ( $F_b/F_b^0 < 1$ ), but higher buckling loads than plates with the damaged zone removed. Removal of the material, even though it was damaged, resulted in less resistance to plate buckling. Repaired plates had higher buckling loads  $F_b$  than plates with a 100% cutout, but only about the same buckling loads as damaged plates with no cutout.

For damaged plates with and without cutouts, the buckling load  $F_b$  decreased as the initial damaged zone length  $l_D$  increased (Figure 13). Since the damage width  $w_D$  increased with the damage length  $l_D$ , the size of the damaged zone also increased. This increase in the size of the damaged zone caused a decrease in the global buckling load  $F_b$ . Again, damaged plates without a cutout generally had higher buckling loads than the plates with either 100% or 75% cutouts.

Repaired plates had higher buckling loads than plates with 100% cutout but only about the same buckling loads as damaged plates with no cutout.

### Ultimate Load

The ultimate load  $F_u$  as a function of the number of plies  $n$  in the  $0^\circ$  ply groups is shown in Figure 14. For initially undamaged plates, the ultimate load  $F_u^0$  increased as  $n$  (and correspondingly, the number of  $0^\circ$  plies in the plate) increased. There are two reasons for this trend. First, the plate buckling load  $F_b$  increased with  $n$  (Figure 11), and higher buckling loads generally cause higher ultimate loads. Second, for a load applied in the lengthwise direction, a higher number of  $0^\circ$  plies in the plates corresponds to a lower longitudinal stress in each ply. Since the ply stresses decreased with the number  $n$  of plies in the  $0^\circ$  ply groups, the ultimate load  $F_u^0$  increased.

Damaged plates, of course, had lower ultimate loads than undamaged plates. Cutting out some or all of the damaged zone further reduced the ultimate loads. It is interesting to note that while, in general, cutting out the damaged zone increased the damage growth loads  $F_g$  (Figure 8), it reduced the ultimate loads. Thus, cutting out the damaged zone may not always be advantageous.

Repaired plates had higher ultimate loads  $F_u$  than plates with 100% cutout, but about the same ultimate loads as damaged plates with no cutout. Hence, repair does not seem to enhance the ultimate load.

The ultimate load  $F_u$  is shown in Figure 15 as a function of the mismatch angle  $q$ . For undamaged plates, the ultimate load  $F_u^0$  decreased with the mismatch angle. Again, there are two reasons for this decrease. First, the buckling load  $F_b^0$  decreased with mismatch angle (Figure 12). Lower buckling loads lead to a decrease in the ultimate load. Second, increasing the angle  $q$  in the  $[0_4/q_4]_S$  plates moved the fiber direction of the middle ply group farther out of alignment with respect to the applied axial load  $F$ . This resulted in higher longitudinal stresses for a given applied load, and hence to a decrease in the ultimate load  $F_u$  with increasing mismatch angle  $q$ .

Damaged plates had lower ultimate loads  $F_u$  than corresponding undamaged plates. Cutting out some or all of the damaged zone further reduced the ultimate loads, because cutouts decreased the buckling loads of the plates (Figure 12). Repair of the plates did not change significantly the ultimate loads  $F_u$ .

For damaged plates with no cutout, the ultimate load  $F_u$  decreased as the initial damaged zone length  $l_D$  increased for all three materials (Figure 16). Since the damage width  $w_D$  increased with the damage length  $l_D$ , the overall size of the damaged zone also increased. The increase in the size of the

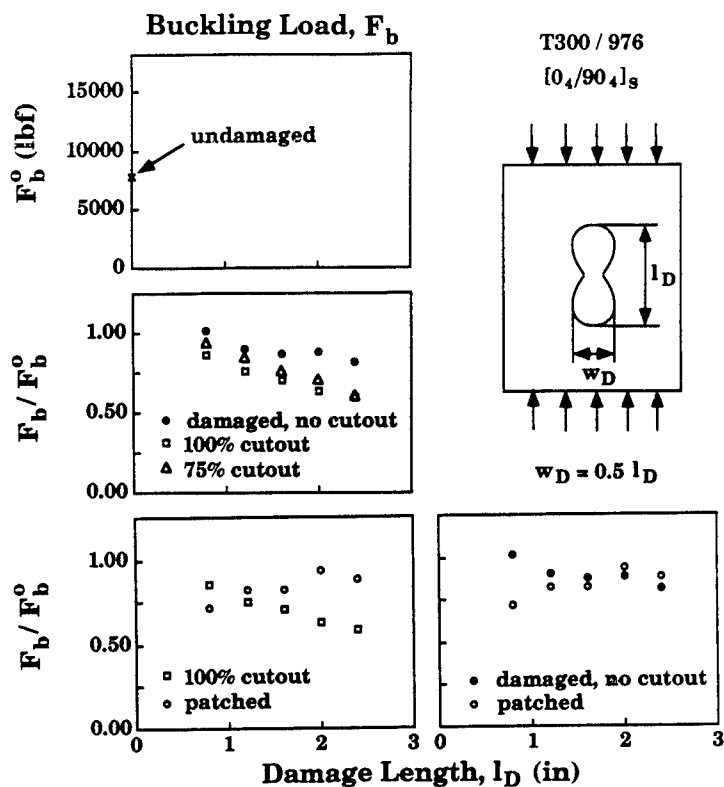


Figure 13. Buckling load  $F_b$  as a function of the initial damaged zone length  $l_D$  for T300/976 graphite/epoxy. Test section length  $L = 3$  in.

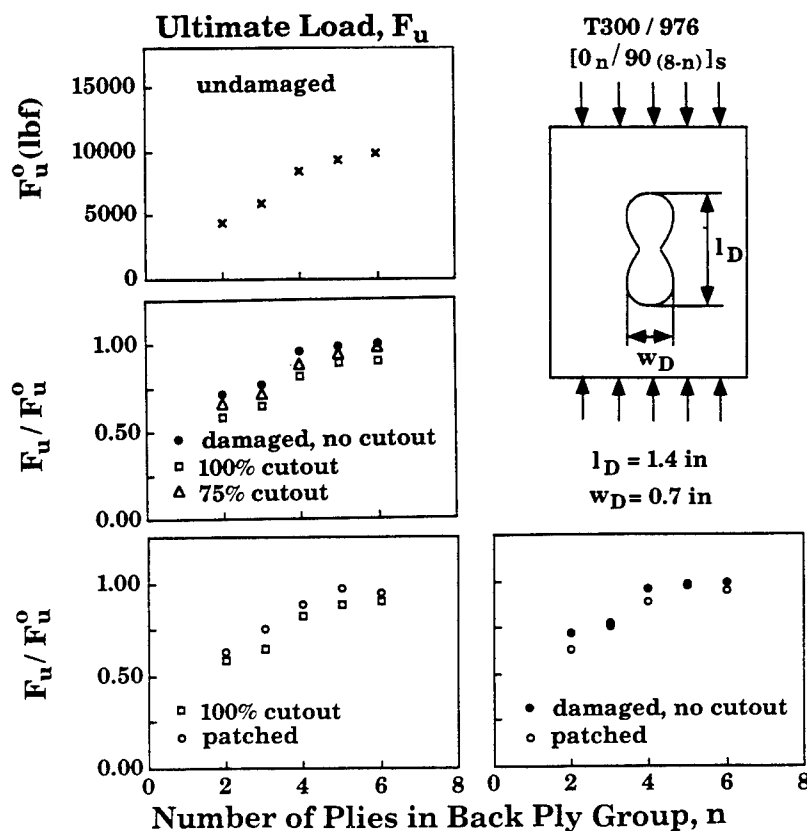


Figure 14. Ultimate load  $F_u$  as a function of the number of plies  $n$  in the 0° ply groups. Test section length  $L = 3$  in.

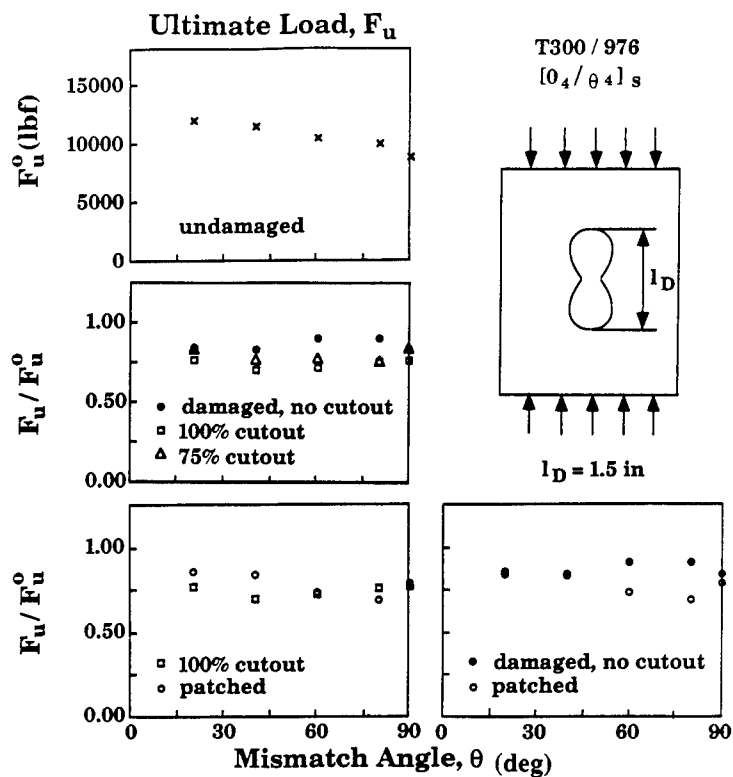


Figure 15. Ultimate load  $F_u$  as a function of the mismatch angle  $\theta$ . Test section length  $L = 3$  in.

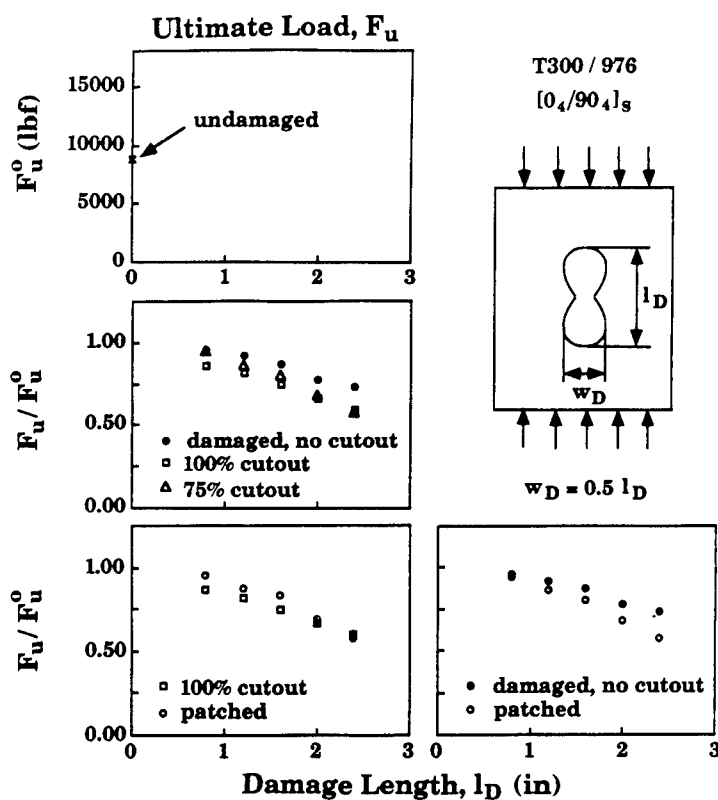


Figure 16. Ultimate load  $F_u$  as a function of the initial damaged zone length  $l_D$  for T300/976 graphite/epoxy. Test section length  $L = 3$  in.

damaged zone caused a decrease in the ultimate load  $F_u$ . For all three materials, the removal of part or all of the damaged zone resulted in the plates having lower ultimate loads  $F_u$  than damaged plates with no cutout.

Repaired plates had slightly higher ultimate loads  $F_u$  than plates with 100% cutout. However, repaired plates had lower ultimate loads than damaged plates with no cutout.

### CONCLUDING REMARKS

The data presented in this paper provide information regarding the in-plane compressive strengths of damaged plates. In general, the compressive strength was further reduced if all or part of the damaged zone was removed. Repairing the damaged plates, by cutting out the damaged zone and replacing it with a plug, did not necessarily improve the compressive strength of a plate. In most cases, the highest compressive strength was retained if the damaged zone was simply left in the plate. Care should be exercised in extending the results to sandwich panels.

### ACKNOWLEDGMENTS

This work was supported by NASA Langley Research Center under contract number NAS1-18778, with Mr. C.C. Poe acting as the project engineer. Messrs. Y.F. He and H.J. Lee assisted with tests.

**THIS PAGE INTENTIONALLY BLANK**

## POST IMPACT COMPRESSIVE STRENGTH IN COMPOSITES

Edvins Demuts, Raghubir S. Sandhu and John A. Daniels  
Flight Dynamics Directorate, Wright Laboratory, USAF

### SUMMARY

Presented in this paper are the plan, equipment, procedures and findings of an experimental investigation of the tolerance to low velocity impact of a graphite epoxy (AS4/3501-6) and graphite bismaleimide (IM6/CYCOM3100) advanced composites. The applied impacts were governed by the Air Force Guide Specification 87221. Specimens of each material system having a common nominal layup ( $10\%0^\circ$ ;  $80\% \pm 45^\circ$ ;  $10\% 90^\circ$ ), a common 7 inch (17.78 cm) by 10 inch (25.40 cm) size, five different thicknesses (9, 26, 48, 74 and 96 plies) and ambient moisture content were impacted and strength tested at room temperature. Damaged areas and post impact compression strengths (PICS) were among the most significant findings obtained. While the undamaged per ply compression strength of both materials is a strong function of laminate thickness, the per ply PICS is not. The average difference in per ply PICS between the two material systems is about seven percent. Although a smaller percentage of the applied kinetic energy was absorbed by the Gr/BMI than by the Gr/Epoxy composites, larger damaged areas were produced in the Gr/BMI than in Gr/Epoxy. Within the limitations of this investigation, the Gr/BMI system seems to offer no advantage in damage tolerance over the Gr/Epoxy system examined.

### INTRODUCTION

The US Air Force, in its aim to provide a desired degree of structural integrity that would preclude catastrophic failures due to barely visible impact damage, currently requires that a damage tolerant design of an airframe incorporates an initial damage due to either a 0.1 inch (2.54 mm) deep dent or a 100 ft-lb (136 joules) impact, whichever is less, both caused by a 1 inch (2.54 cm) diameter impactor traveling at 16 ft/sec (4.88 m/sec). This requirement is based on data obtained in an Air Force sponsored damage tolerance program where a graphite epoxy (AS4/3501-6) composite was investigated. Also, in this program it was found that among various common types of damage the barely visible damage due to low velocity impact was the worst type and that it could reduce the original compression strength by as much as 60%. Assuming that different damage tolerance findings may be obtained in composites of different material systems, the need for investigating impact responses by different composites was recognized.

## OBJECTIVE AND SCOPE

The main objective of the investigation presented in this paper is to experimentally determine the room temperature post impact compressive strength (PICS) of moisture non-preconditioned ("dry") AS4/3501-6 graphite epoxy (Gr/Ep) and IM6/CYCOM 3100 graphite bismaleimide (Gr/BMI) specimens that had been subjected to low velocity impact in accordance with the above US Air Force requirements. The paper will also present the description of the test plan, including the selected layup, stacking sequences, and thicknesses; the non-destructive inspection of specimens before and after impact; the apparatus for inducing impact; and the residual strength test procedures. The discussion of test results and conclusions will be presented here as well.

## TEST PLAN

The following is the rationale for selecting AS4/3501-6 graphite epoxy and IM6/CYCOM3100 graphite bismaleimide as the composite material systems for the low velocity impact resistance investigation presentation in this paper. The Gr/Ep, being one of the most characterized and hence popular systems, was to serve as the base line. The low velocity impact resistance of the Gr/BMI system represents a modified and allegedly more damage tolerant system, and was to be observed and compared with that of the baseline. The nominal laminate layup for each of the two selected material systems was chosen as 10/80/10 (10% 0°, 80% ±45° and 10% 90° plies) for the reason that such a layup, due to its relatively high potential ultimate strain in the 0° direction, would buy maximum damage tolerance while still maintaining a reasonable strength in the 0° direction. To investigate the effect of laminate thickness on impact resistance, test specimen thicknesses of 9, 26, 48, 74 and 96 plies were selected. Using the selected number of plies, most of the resulting layups were slightly different than the nominal 10/80/10 as shown in Table I. Panels from both material systems were cured in an autoclave. The total cure cycle for Gr/Ep, including heat-up and cool-down ramps, lasted six hours, two of which included 100 psi (0.689 MPa) pressure and 350°F (177°C) temperature. There was no post cure for Gr/Ep. The Gr/BMI panels were cured at 85 psi (0.586 MPa) pressure and 350°F (177°C) temperature for four hours. Including heat-up and cool down ramps, it took 7 3/4 hours to complete the cure cycle. The Gr/BMI was subsequently postcured at 400°F (204°C) and atmospheric pressure for four hours. The resulting fiber volumes for each of the two composites were 63% for AS4/3501-6 and 57% for IM6/CYCOM3100. The cured panels were ultrasonically inspected for manufacturing quality and those with acceptable quality were then cut into specimens with an eight-inch diameter and 1/8 inch wide diamond saw. The size of the test specimens varied depending on the purpose of the test. Specimens for characterizing the material systems (Table II) were of the following sizes: 3/4" (1.905 cm) x 10" (25.4 cm) for 0° tension; 1" (2.54

cm) x 10" (25.4 cm) for 90° tension; 1" (2.54 cm) x 10" (25.4 cm) for in-plane shear; 3/4" (1.905 cm) x 5" (12.7 cm) for 0° compression and 3/4" (1.905 cm) x 5" (12.7 cm) for 90° compression. Those specimens for determining virgin compressive strength of the impact specimens were 5" (12.7 cm) by 10" (25.4 cm) while the size of the low velocity impact test specimens was 7" (17.8 cm) wide and 10" (25.4 cm) long. Since the specimens were neither desiccated nor deliberately moisture preconditioned, their moisture content at the times of impact introduction and residual strength determination was ambient, i.e., specimens had absorbed moisture from surrounding air only. A commercially available Dynatup drop tower was employed to introduce impact to the specimen. This was achieved by a vertically falling steel impactor with a 1 inch (2.54 cm) diameter hemispherical end. The specimen was placed between a 1 inch (2.54 cm) thick steel plate and a 0.75 inch (1.90 cm) thick aluminum cover plate, each having in its center a 5 inch (12.70 cm) square opening whose center coincided with those of the specimen and the impactor. The assembly of the plates and the specimen was held together by clamps at the four corners (Reference 1). The resulting boundary conditions for the specimen were neither hinged nor fixed but somewhere between the two. Before proceeding with impact introduction, a velocity check of the free falling impactor was performed. This check consisted of comparing the theoretical free falling velocity evaluated from the impactor's drop height ( $h = V^2 / 2g$ ) with the recorded velocity sensed by a velocity detector built into the drop tower. In case of a significant disagreement, the guide bars were cleaned to reduce friction between the bars and the falling impactor until there was no significant difference between the two velocities. Since the drop height was limited to the available maximum of 3.5 ft (1.07 m), the maximum velocity of the free falling impactor was also fixed. Thus the impactor weight was the only variable in those series of tests governed by the 0.1 inch (2.45 cm) deep dent (9, 26, 48 plies thick specimens) and 100 ft-lbs (136 joules) for 74 and 96 plies thick specimens.

Among the quantities recorded during the short impact event (6-7 milliseconds) were: the histories of contact load and energy absorbed by the specimen, test temperature, impactor velocity just before touching the specimen, and other important useful load and energy quantities that are post-test calculated (Figure 1). An accelerometer built into the impactor sensed the magnitude of the contact load that was used to calculate the energy absorbed by the specimen.

All testing was conducted at room temperature. Dent depths were found using shadow Moire techniques (References 2 and 3). The impacted specimens were ultrasonically examined to determine the damaged areas (Table I). The residual post impact compression strength (PICS) of each specimen was found in a test conducted in an INSTRON test machine. The specimen that was cut to a 5 inch (12.7 cm) by 10 inch (25.4 cm) size was supported in a compression fixture that prevented lateral displacement of the specimen edges. This fixture, originally known as the NASA-Boeing fixture, was modified by Dr R. S. Sandhu who provided a lateral restraint to the top portion of specimen edge that previously did not have such restraint.



## DISCUSSION OF RESULTS

Table I summarizes the more significant results of this investigation. In addition, Figures 1, 2 and 3 exemplify some of these findings graphically. The values shown in Table I for each of the five specimen thicknesses are the averages of a number of replicates varying between three and ten. It must be emphasized that the impact intensity in this investigation was governed by current US Air Force suggested requirements to assure a damage tolerant airframe as described in the INTRODUCTION of this paper. One exception to the requirements is the 9-ply laminate where it is impossible to achieve the required 0.1 inch (2.54 mm) deep dent without penetration since the laminate itself is only 0.0468 inch (1.189 mm) thick. Hence in this case the impact intensity was selected such as to cause an indentation approximately equal to the thickness of the 9-ply specimens (Reference 3). Among the most significant data were the absorbed energy, damaged areas and post impact compressive strength (PICS). Since the applied kinetic energies for laminates of both material systems had been selected according to the requirements of the Air Force Guide Specification 87221, for the same thickness they were almost the same (columns 7 and 16 of Table I). While the graphite epoxy thinner laminates absorbed more energy than the thicker ones (column 9, Table I), the graphite bismaleimide did not show such a trend as the percentages were fairly uniform for all thicknesses (column 18, Table I). It is quite obvious though that the Gr/Ep specimens absorbed a greater percentage of applied kinetic energy than the Gr/BMI specimens. In spite of this observation and possible intuitive conclusion, the damaged areas in Gr/Ep were smaller than those in Gr/BMI. A possible explanation for this is the generally greater brittleness for bismaleimides of the type similar to CYCOM3100. As Figure 3 clearly depicts, the per ply compressive strength of the undamaged specimens of both material systems strongly depends on the thickness of the specimen. The undamaged Gr/BMI strength exceeds that of Gr/Epoxy by an average of 20%. However, the per ply PICS of both composites is essentially the same for all thicknesses. The loss of per ply compressive strength is greater in the Gr/BMI composites than in the Gr/Epoxy composites. This is reflected graphically in Figure 3 and numerically in columns 13 and 22 of Table I.

## CONCLUDING REMARKS

Based on the data obtained in this experimental investigation, it may be concluded that the per ply post impact compressive strength for either the graphite epoxy or the graphite bismaleimide composites is fairly constant for all thicknesses investigated. Thus there appears to be no strength advantage to prefer the Gr/BMI system over the Gr/Epoxy system for designs governed by damage tolerance.

## REFERENCES

1. NASA Reference Publication 1092, 1982.
2. Handbook of Experimental Mechanics, Society for Experimental Mechanics, Prentice-Hall, 1987.
3. Demuts, E.; Sandhu, R. S.; Maddux, G. E.: Barely Visible Damage Threshold In Graphite Epoxy. Proceedings of the Eighth International Conference on Composite Materials, July 1991, SAMPE, Vol 4, pp 32- N -1 to 32 -N -12.

TABLE I - SUMMARY OF TEST RESULTS

AS4/3501-6 GRAPHITE EPOXY												
NO. OF PLIES	STK SEQ	ACTUAL LAYUP  % (0°/±45°/90°)	IMPACT GOVERN- NOR									
				NO. OF REPLI- CATES	MEASURED		ABSORBED ENERGY		DAMAGED AREA	UNDAM. COMPR. STRTH	PICS	
					VELO- CITY m/sec	ENERGY joules	joules	%			N/ply	% OF UNDAM %
(1)	(2)	(3)	(4)	(5)	(6)	(7)	(8)	(9)	(10)	(11)	(12)	(13)
9	C	22.2/66.7/11.1	D1	10	2.51	12.34	10.02	81	6.45	1,561	1,753	123
26	D	11.5/77.0/11.5	D2	3	4.48	48.28	39.96	83	19.35	3,345	2,522	75
48	E	12.5/75.0/12.5	D2	8	3.71	123.82	97.65	79	103.23	6,241	1,908	31
74	F	12.2/75.6/12.2	E	8	3.88	135.78	66.04	49	116.13	6,610	2,082	31
96	G	12.5/75.0/12.5	E	5	3.88	135.81	51.57	38	116.13	5,551	2,340	42

IM6/CYCOM3100 GRAPHITE BMI												
NO. OF PLIES	STK SEQ	ACTUAL LAYUP  % (0°/±45°/90°)	IMPACT GOVERN- OR									
				NO. OF REPLI- CATES	MEASURED		ABSORBED ENERGY		DAMAGED AREA	UNDAM. COMPR. STR' TH	PICS	
					VELO- CITY m/sec	ENERGY joules	joules	%			N/ply	% OF UNDAM %
(1)	(2)	(3)	(4)	(5)	(6)	(7)	(8)	(9)	(10)	(11)	(12)	(13)
9	C	22.2/66.7/11.1	D1	4	2.43	12.40	4.62	37	6.27	1,842	1,997	108
26	D	11.5/77.0/11.5	D2	4	3.74	48.15	17.54	36	132.97	4,675	2,229	48
48	E	12.5/75.0/12.5	D2	4	4.22	124.07	33.58	27	169.62	7,175	1,922	27
74	F	12.2/75.6/12.2	E	5	4.42	136.28	51.93	38	151.02	7,215	1,957	27
96	G	12.5/75.0/12.5	E	4	4.42	136.12	58.64	43	138.26	6,597	2,318	35

STACKING SEQUENCES (COLUMN 2)

C: ( $\pm 45/0/45/90/45/0/\pm 45$ )D: ( $\pm 45/0/\pm 45/90/\pm 45/0/90/\pm 45/90/\pm 45/0/\pm 45$ )E: ( $\pm 45/0/\pm 45/90$ )<sub>3a</sub>F: [ $\pm 45/0/\pm 45/90$ ]<sub>4</sub>  $\pm 45/0/90/\pm 45/90/\pm 45/0/\pm 45$ ]<sub>4</sub>G: ( $\pm 45/0/\pm 45/90$ )<sub>3a</sub>

IMPACT GOVERNOR (COLUMN 4)

D1 - DENT = SPEC. THICKNESS

D2 - DENT = 0.1 in. (2.54 mm)

E - ENERGY = 100 ft-lb (136 joules)

TEST TEMPERATURE: ROOM TEMPERATURE (RT)

SPECIMEN MOISTURE: AMBIENT (D)

TABLE II - ELASTIC CONSTANTS OF GR/EP AND GR/BMI

	ET1	EC1	ET2	EC2	G12	$\mu_{T12}$	$\mu_{C12}$	$\sigma_{T1u}/$ $\epsilon_{T1u}$	$\sigma_{C1u}/$ $\epsilon_{C1u}$	$\sigma_{T2u}/$ $\epsilon_{T2u}$	$\sigma_{C2u}/$ $\epsilon_{C2u}$	$\tau_{12u}/$ $\gamma_{12u}$
Gr/Epoxy	22.0	20.2	1.48	1.55	0.83	0.277	0.332	289.3/ 1.302%	188.1/ 1.05%	8.57/ 0.57%	34.19/ 2.21%	14.5/ 14.4%
Gr/BMI	22.2	20.7	1.54	1.50	0.85	0.313	0.379	280.0/ 1.18%	209.0/ 1.15%	7.36/ 0.55%	33.0/ 2.24%	10.6/ 2.40%

NOTE: Youngs' modulii and stresses are in ksi (1.0 ksi = 6.895 MPa)

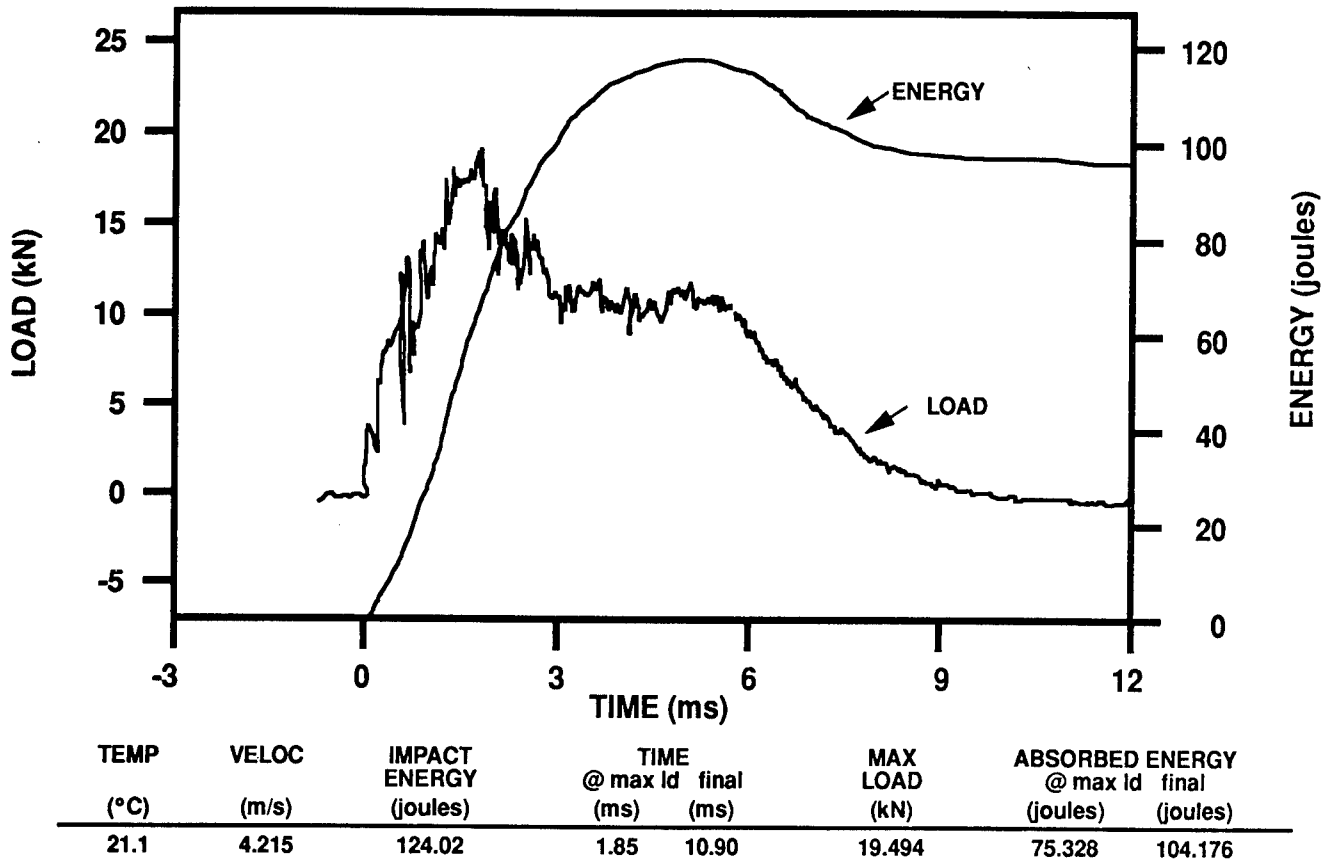


Figure 1. Impact Load and Energy Histories

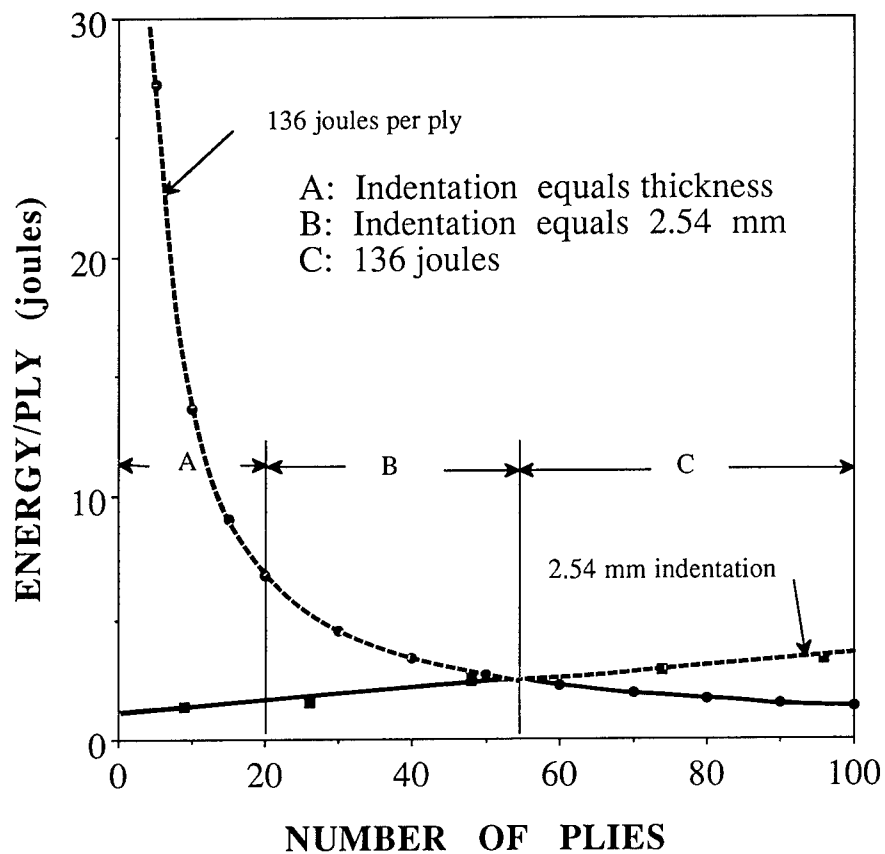


Figure 2. Initial Damage Assumption

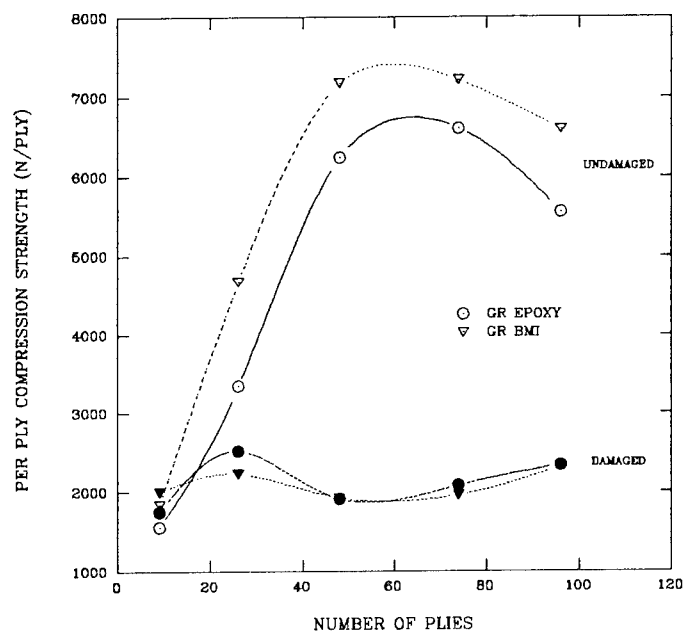


Figure 3. Laminate Compression Strengths - Undamaged and PICS

# FUNDAMENTAL CONCEPTS IN THE SUPPRESSION OF DELAMINATION BUCKLING BY STITCHING

B.N. Cox

Rockwell International Science Center  
Thousand Oaks, CA

## ABSTRACT

Elementary results are presented for the buckling of stitched, laminated composites containing delamination cracks. The stitching fibers are assumed to provide continuous, linear restoring tractions opposing the deflection of the delaminated layer adjacent to the crack. It is shown that there exists a characteristic length  $a_0$  for buckling: if the length,  $2a$ , of the delamination crack exceeds  $2a_0$ , then, when buckling occurs, it will consist of waves of period  $2a_0$  and will usually not span the whole delamination. Simple expressions are derived for the critical buckling load and the minimum stitching density required to suppress buckling of the delaminated layer.

## INTRODUCTION

One of the principal obstacles to using relatively cheap graphite epoxy laminates in the commercial aircraft industry is their susceptibility to delamination, especially during impact, and the subsequent catastrophic growth of the delamination crack when the delaminated layer buckles under in-plane compression [see, for example, ref. 1]. One promising solution to this problem is the incorporation of fiber tows normal to the laminate plane by stitching. While stitching tows do not eliminate delamination during impact, they do minimize loss of strength under subsequent compression [refs. 2,3]. It appears that the stitching tows bridge the delamination crack and prevent or reduce buckling of the adjacent delaminated layer. The in-plane stiffness then survives relatively unimpaired and, if the delaminated layer remains flat, the delamination crack does not grow, since it experiences no driving force. Failure under compressive loading occurs by some other mechanism and the compressive strength after impact is restored to an acceptably high value.

This paper presents the simplest possible description of the mechanics of this buckling problem, which can be modeled as that of a buckling plate on a Winkler foundation of damping springs [e.g., refs. 4,5]. However, in contrast to the usual assumption, buckling deflections in the present problem can occur in one direction only. This constraint gives rise to a characteristic length for buckling and an enhanced value of the critical force for buckling. Simple arguments are presented to show how these fundamental quantities vary with stitching fiber density and the thicknesses of the delaminated layer and the substrate beneath it.

## BUCKLING IN THE PRESENCE OF LINEAR DAMPING

Consider a delamination crack of length  $2a$  lying along the  $x$ -axis, as shown in Figure 1. Let the crack be in a state of plane strain. Suppose the body containing the crack is subject to a compressive load that results in the compressive force  $F$  per unit length being imposed on the thin layer of delaminated material above the delamination crack. Buckling of the thin layer will result in the deflection  $w(x)$ , which can be determined if the layer is thin enough by consideration of the balance of forces according to the elementary theory of bending plates [refs. 5,6]. If the delamination crack is bridged by stitching fibers, as shown schematically in Figure 1, the problem is modified by the lateral tractions those fibers impose.

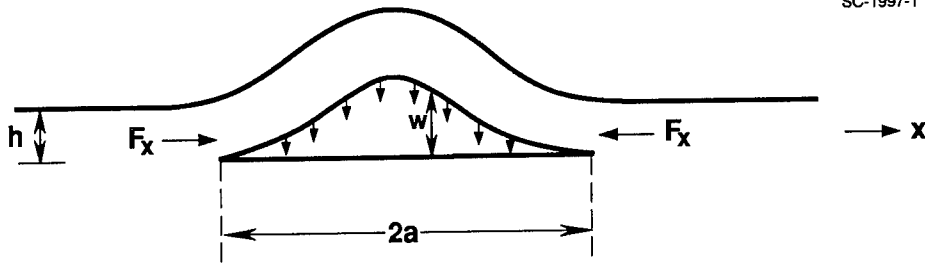


Fig. 1. Schematic of a delaminated and buckled layer, showing lateral tractions opposing the buckling deflection.

If the stitching fiber spacing is appreciably smaller than  $2a$ , the lateral tractions can be considered continuous over  $x$ . Furthermore, if the stitching fibers are debonded from the matrix or are much stiffer than the matrix, then the tractions, denoted  $q$ , will be a linear function of the deflection:

$$q(x) = \beta w(x), \quad (\beta > 0) \quad (1)$$

The spring constant  $\beta$  will be related below to the properties of the stitching tows. The deflection profile is given by the linear differential equation [refs. 4-6]

$$\frac{d^4 w}{dx^4} + \frac{F}{D} \frac{d^2 w}{dx^2} + \frac{\beta}{D} w = 0 \quad (2)$$

where  $F > 0$  denotes a compressive force and  $D$  is the flexural rigidity of the delaminated layer. (The body has been assumed to be isotropic and homogeneous, a crude representation of a stitched laminate but a useful simplification when exploring fundamental aspects of the problem.) The deflection must also satisfy clamped end boundary conditions and be positive, since negative deflections would imply interpenetration. Equation (2) has both symmetric and antisymmetric solutions, but only the symmetric solutions can satisfy  $w > 0$ . The symmetric solutions have the form

$$w(x) = A_+ \cos \xi_+ x + A_- \cos \xi_- x \quad (3a)$$

$$\text{where } \xi_{\pm} \equiv \sqrt{f(1 \pm \sqrt{1 - b/f^2})} \quad (3b)$$

$$\text{with } f \equiv F/2D \text{ and } b \equiv \beta/D \quad (3c)$$

The boundary conditions determine both the ratio  $A_+/A_-$  and the critical buckling load  $f_c^{(m)}(a)$  for the  $m^{\text{th}}$  buckling mode for delamination crack length  $2a$ . Numerically determined values of  $f_c^{(m)}(a)$  are shown for the first few modes in Fig. 2 (see also [Ref. 4]). Each  $f_c^{(m)}$  is a monotonically decreasing function of  $a$ , in contrast to the case of a plate with simply supported ends, for which the buckling load decreases for small  $a$  and then increases as  $a^2$  for large  $a$  [e.g., ref. 5].

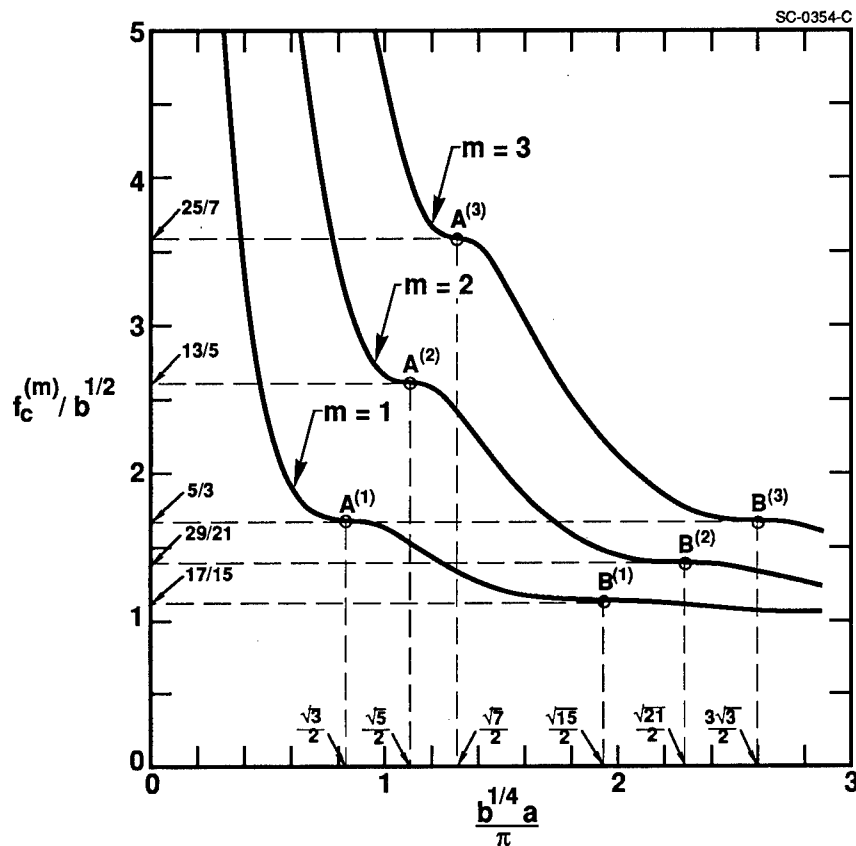


Fig. 2 The critical force for buckling for the first few symmetrical buckling modes as a function of delamination crack length.

With  $f_c^{(m)}$  determined, the corresponding deflection  $w^{(m)}(x)$  is also determined to within a multiplicative constant by the boundary conditions. To the left of the points  $A^{(m)}$  in Fig. 2,  $w^{(m)}(x)$  is of one sign, i.e. it contains no zeroes in  $(-a, a)$ ; and, if it is taken to be positive, it contains  $m$  maxima. At the points  $A^{(m)}$ ,  $B^{(m)}$ , etc.,  $d^2w^{(m)}/dx^2$  evaluated at  $x = \pm a$  passes through zero and  $w^{(m)}(x)$  acquires two zeroes, which begin at  $x = \pm a$  and move into the interval  $(-a, a)$  as  $a$  increases. At all values of  $a$  to the right of  $A^{(m)}$ ,  $w^{(m)}(x)$  possesses at least two zeroes, i.e. it is no longer of one sign.

For  $w > 0$ , the minimum buckling load,  $f_0$ , is thus found at the point  $A^{(1)}$ , i.e.

$$f_0 = \frac{5}{3} b^{\frac{1}{2}} \quad (4)$$

The crack length corresponding to point  $A^{(1)}$  is given by

$$a_0 = \frac{\sqrt{3}}{2} \frac{\pi}{b^{\frac{1}{4}}} \quad (5)$$

It denotes a characteristic buckling length: whenever  $a > a_0$ , buckling will occur not over the whole delamination  $(-a, a)$ , but over some subinterval or series of subintervals of length  $2a_0$ . The buckling profile over each subinterval is that for  $\xi_+ a = 3\pi/2$  and  $\xi_- a = \pi/2$ , i.e.

$$w_0(x) = A \left[ \cos \frac{3\pi x}{2a} + 3 \cos \frac{\pi x}{2a} \right] \quad (6)$$



with  $A$  an undetermined constant. The appearance of buckling when  $a > a_0$  is therefore qualitatively different from the case of an unbridged delamination crack. If  $a < a_0$ , buckling occurs over the whole interval  $(-a, a)$  and the critical load rises with decreasing  $a$  as in Fig. 2.

### STITCHED LAMINATES

For stitched laminates, the stiffness parameter  $\beta$  depends on how the delaminated layer is coupled to the rest of the material. Figure 3(a) shows the case of a delamination crack lying in the mid-plane of a thin panel. Buckling upon compressive loading occurs in a symmetric manner. Figure 3(b) shows the case of a thin delaminated layer lying over a thick substrate, which remains straight while the delaminated layer buckles. If the stitching fiber tows pass from top to bottom of the panel and they are initially unstrained, then the stiffness parameter is approximately

$$\beta = \begin{cases} \frac{v_s E_f}{h} & \text{(case I)} \\ \frac{v_s E_f}{t} & \text{(case II)} \end{cases} \quad (7a)$$

$$\quad \quad \quad (7b)$$

where case I refers to the case of Fig. 3(a) and case II to that of Fig. 3(b),  $v_s$  is the volume fraction of the stitching fibers,  $E_f$  is the fiber modulus, and the dimensions  $h$  and  $t$  are defined in Figure 3.

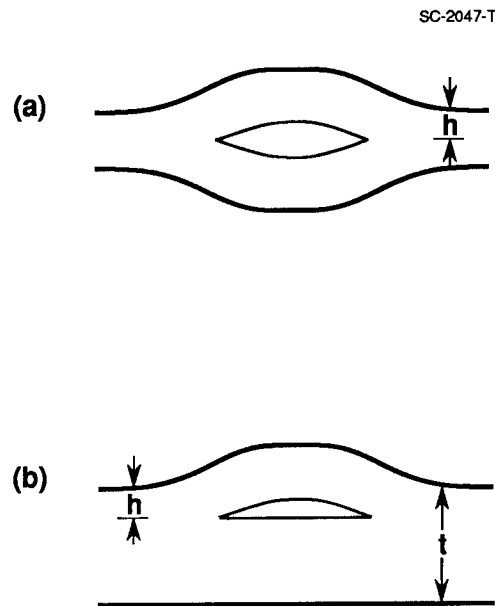


Fig. 3 (a) Symmetric buckling. (b) Buckling of a thin layer over a thick substrate.

Now the results of Section 2 were obtained for an isotropic material, whereas a stitched laminate is more closely orthotropic. Nevertheless, useful results in terms of orders of magnitude can be obtained by making some crude approximations concerning elastic properties. Since buckling of thin plates is determined mainly by in-plane elastic properties, the flexural rigidity of Eq. (3) can be approximated by

$$D = \frac{v_f E_f h^3}{12(1 - \nu^2)} \quad (8)$$

where  $\nu$  is Poisson's ratio,  $v_f$  is the volume fraction of fibers lying in the axial direction (parallel to the x-axis and the applied compressive load), and it has been assumed that these fibers have the same modulus as the stitching fibers. The stitching and axial fibers are indeed often of the same kind. The characteristic buckling length can now be approximated by

$$a_0 = \begin{cases} c_1 \left(\frac{v_f}{v_s}\right)^{\frac{1}{4}} h & \text{(case I)} \\ c_1 \left(\frac{v_f}{v_s}\right)^{\frac{1}{4}} \left(\frac{t}{h}\right)^{\frac{1}{4}} h & \text{(case II)} \end{cases} \quad (9a)$$

$$(9b)$$

$$\text{with } c_1 = \frac{3^{\frac{1}{4}}}{2^{3/2}} \frac{\pi}{(1-\nu^2)^{\frac{1}{4}}} \approx 1.5 \text{ when } \nu = 0.3 \quad ; \quad (9c)$$

and the critical force  $f_0$  of Eq. (4) is approximately

$$f_0 = \begin{cases} c_2 (v_f v_s)^{\frac{1}{2}} E_f h & \text{(case I)} \\ c_2 (v_f v_s)^{\frac{1}{2}} \left(\frac{h}{t}\right)^{\frac{1}{2}} E_f h & \text{(case II)} \end{cases} \quad (10a)$$

$$(10b)$$

$$\text{with } c_2 = \frac{5}{3^{3/2} (1-\nu^2)^{\frac{1}{2}}} \approx 1.0 \text{ when } \nu=0.3 \quad . \quad (10c)$$

Equations (9) and (10) illustrate in a simple way how geometry and fiber density control the efficacy of stitching in suppressing buckling. In particular, Eq. (9) shows that the characteristic buckling length in stitched materials will usually be no more than an order of magnitude greater than the thickness,  $h$ , of the delaminated layer. Even if  $v_s \sim 10^{-2} v_f$ , i.e., sparse stitching, one still has  $a_0 \approx 5h$  for case I, since the ratio  $v_f/v_s$  appears to the power  $\frac{1}{4}$ . The additional factor  $(t/h)^{\frac{1}{4}}$  in case II is also unlikely to be much greater than 2 in practice.

In the absence of impact damage, stitched laminates generally fail under in-plane compression by the formation of a kink band of buckled and broken axial fibers. The stress at which this occurs corresponds to a particular value,  $f'_0$ , of the force acting on the ends of a delaminated layer if it has not yet buckled. Substituting  $f'_0$  for  $f_0$ , Eq. (10) provides a simple estimate of the stitching fiber density required to suppress buckling and eliminate delamination crack growth as a potential failure mechanism. Thus the required value of  $v_s$  is proportional to  $(f'_0/h)^2$ . Conversely, the critical force,  $f_0$ , is more sensitive to fiber volume fractions than is the characteristic buckling length, being proportional to  $v_s^{\frac{1}{2}}$ .

Equation (10) also shows that  $f_0$  in case II varies as  $t^{\frac{1}{2}}$ , which simply reflects the fact that stitching fibers of shorter initial through-thickness length experience greater strain for a given buckling deflection. Thus an effective method of raising  $f_0$  for a given density of stitching fibers and laminate thickness is to pass stitching tows only part way through the laminate, achieving through-thickness reinforcement by staggering the stitching at different depths. Laminates with such stitching patterns are indeed available, but no results concerning their delamination and buckling behavior have yet been published.

## CONCLUSIONS

The presence of stitching tows introduces a minimum compressive load,  $f_o$ , required to buckle a delaminated layer in a stitched laminate, regardless of the length of the delamination crack; and a characteristic buckling length,  $a_o$ . If the delamination crack length  $2a$  exceeds  $2a_o$ , buckling has the form of waves of length  $2a_o$ , which arise when the load exceeds  $f_o$ . In typical stitched laminates, the length  $a_o$  will not exceed the thickness,  $h$ , of the buckling delaminated layer by more than one order of magnitude. The critical force,  $f_o$ , can be enhanced by increasing stitching density or passing stitching tows only part way through the laminate.

## ACKNOWLEDGEMENTS

Work supported by Rockwell International Independent Research and Development funds. The author is indebted to Drs. John Hutchinson, Larry Ilcewicz, David Marshall, Buddy Poe, and Francis Rose for enlightening discussions.

## REFERENCES

1. Horton, R.E., and McCarty, J.E., 1987, "Damage Tolerance of Composites," in *Engineered Materials Handbook*, Vol. 1: Composites (ASM International, Metals Park, OH).
2. Dow, M.B., and Smith, D.L., 1989, "Damage Tolerant Composite Materials Produced by Stitching Carbon Fabrics," *Int. SAMPE Technical Conf. Series*, Vol. 21, pp. 595-605.
3. Smith, P.J., and Wilson, R.D., 1985, "Damage Tolerant Composite Wing Panels for Transport Aircraft," Boeing Commercial Airplane Company, NASA Contractor Report 3951.
4. Hetényi, M., "Beams on Elastic Foundation," University of Michigan Press, Ann Arbor, MI, 1946.
5. Timoshenko, S.P., and Gere, J.M., 1961, "Theory of Elastic Stability," 2nd edition, McGraw-Hill, New York, p. 94 and Chap. 8.
6. Saint Venant, B. de, 1883, discussion in "Théorie de l'Elasticité des Corps Solides," by A. Clebsch, Gauthier-Villars, Paris, p. 704.

# DAMAGE TOLERANCE OF A GEODESICALLY STIFFENED ADVANCED COMPOSITE STRUCTURAL CONCEPT FOR AIRCRAFT STRUCTURAL APPLICATIONS

Marshall Rouse and Damodar R. Ambur  
NASA Langley Research Center  
Hampton, VA 23665-5225

## INTRODUCTION

Geodesically stiffened structures that utilize continuous filament composite materials for stiffener construction are very efficient for aircraft fuselage applications since this structural concept is very effective in carrying loads due to bending, shear, torsion, and internal pressure. Structural efficiency combined with cost effective methods of manufacturing make geodesically stiffened structures very attractive for commercial transport structural applications. Geodesically stiffened structures are also very damage tolerant since there are multiple load paths available due to the nonprismatic nature of the structure that can help redistribute the load. The potential of geodesically stiffened composite structures for a fuselage application that utilizes advanced manufacturing processes needs to be demonstrated to add to the information base on these structural concepts for aircraft.

This paper describes the features of a geodesically stiffened panel concept that was designed for a fuselage application with a combined axial compression loading of 3,000 lb/in. and a shear loading of 600 lb/in. Specimens representative of this panel concept have been tested in uniaxial compression both without and with low-speed impact damage to study the buckling and postbuckling response of the structure. Experimental results that describe the stiffness and failure characteristics of undamaged and impacted damage specimens are presented. A finite element analysis model that captures the principal details of the specimens has been developed and used to predict the panel response. Analytical results on panel end-shortening are compared with the experimental results. Analytical results that describe panel end-shortening, out-of-plane displacement and stress resultants are presented.

## SPECIMEN DESCRIPTION

The specimens tested in this investigation were fabricated from commercially available Hercules Incorporated AS4 graphite fiber preimpregnated with Hercules 3502 epoxy resin (AS4/3502). The skins of the specimens were made from 12 K tow material with a  $[\pm 45/90/\mp 45]$  stacking sequence. The skins of the specimens had a fiber cross-over pattern across the mid-section of the panel to simulate a filament wound skin feature. The stiffeners were placed at  $\pm 20^\circ$  to the longitudinal axis of the test panel. The stiffeners were made of unidirectional tows of graphite-epoxy material overwrapped with graphite-epoxy fabric material and were secondarily bonded to the skin. Two frame clips were made of woven graphite-epoxy fabric and secondarily bonded to the skin at a distance of 10 inches on either side of the horizontal centerline of the specimen. Also, a buffer strip made from unidirectional tow material was embedded in the skin at the location of the frame clips to simulate a fail-safe strap in a fuselage. A total of three specimens was tested in this investigation. All of the specimens had a 40-inch length. Two of the specimens were 14.56 inches wide and the third was 29.12 inches wide. The ends of the specimens were potted and ground flat and parallel for uniform load introduction. The sides of the specimens were supported with knife-edges. A sketch of the test specimen including the local details is shown in figure 1.

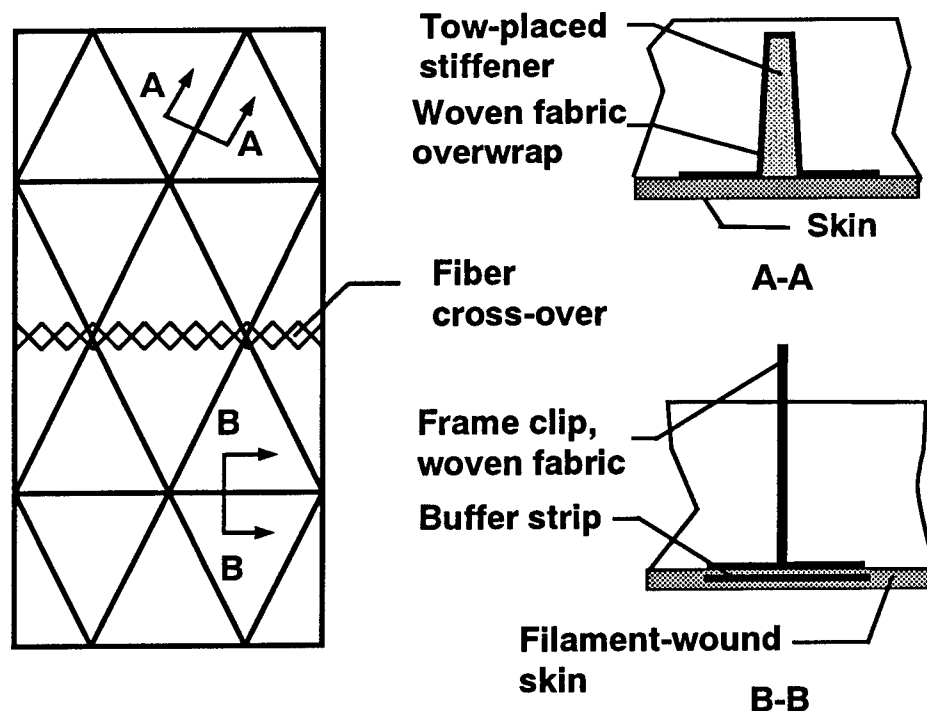


Figure 1. Specimen description

## END-SHORTENING RESPONSE OF GEODESICALLY STIFFENED COMPRESSION PANELS

A summary of results for all of the panels that was tested without impact damage is shown in Figure 2. The panels were loaded in compression using a one million pounds capacity hydraulic test machine. Applied load  $P$  normalized by the width of the test section  $b$  plotted as a function of end-shortening  $u$  normalized by the length of the test section  $L$  is shown on the left of the figure. Results for the 29.12- and 14.56-inch-wide panels are represented by the circles and the squares, respectively. The theoretical buckling load is indicated by the open symbols. The experimental failure load of the panel is indicated by the filled symbols. The panels buckled at a normalized applied load of approximately 1400 lb/in. All of the panels tested without damage failed at a value of applied load greater than the analytical buckling load. The 29.12-inch-wide panel failed at a value of normalized applied load of 3,312 lb/in. The 14.56-inch-wide panel failed at a value of normalized applied load of 3,540 lb/in.

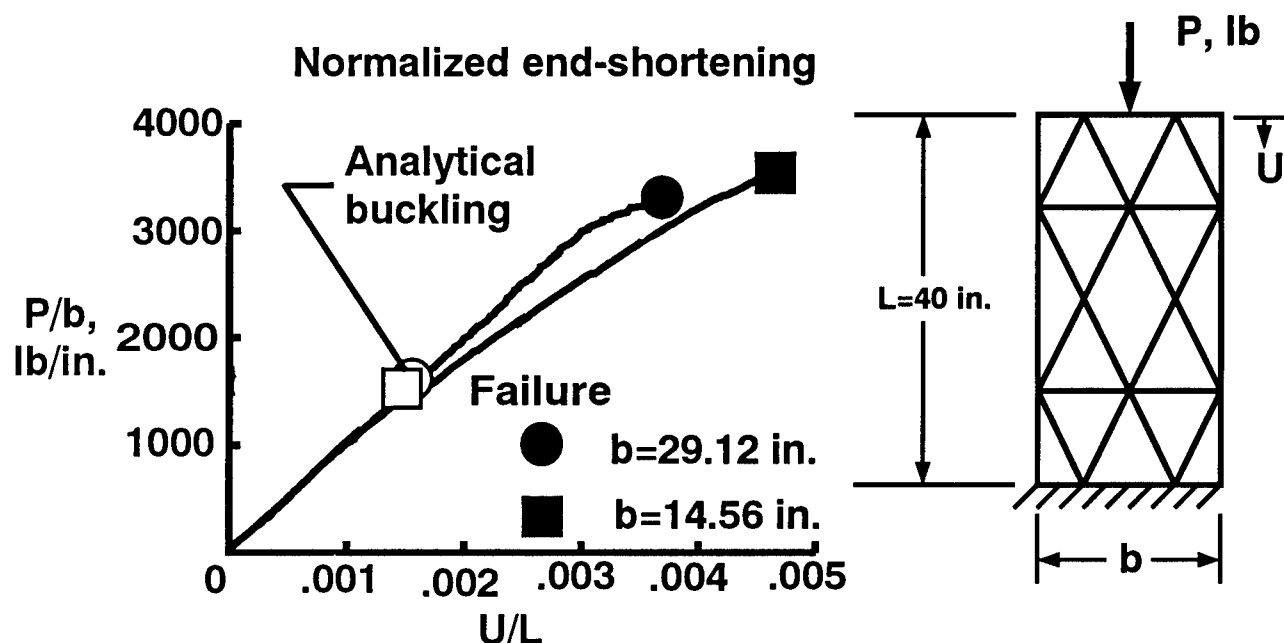


Figure 2. Summary of results for specimens tested without impact damage

## OUT-OF-PLANE DEFLECTION OF GEODESICALLY STIFFENED COMPRESSION PANELS

Out-of-plane deflection  $w$  measured at the intersection of a frame and stiffeners located at the midlength of the panel normalized by the skin thickness  $t$  is shown in Figure 3 as a function of normalized load. Failure of the panels is indicated by the filled circles. All of the panels deformed out of plane prior to buckling when loaded. The 29.12-inch-wide specimen exhibited the most out-of-plane deflection during loading with a maximum value of over 6 times the skin thickness. The 14.56-inch-wide panel had a maximum out-of-plane deflection of approximately 4 times the skin thickness.

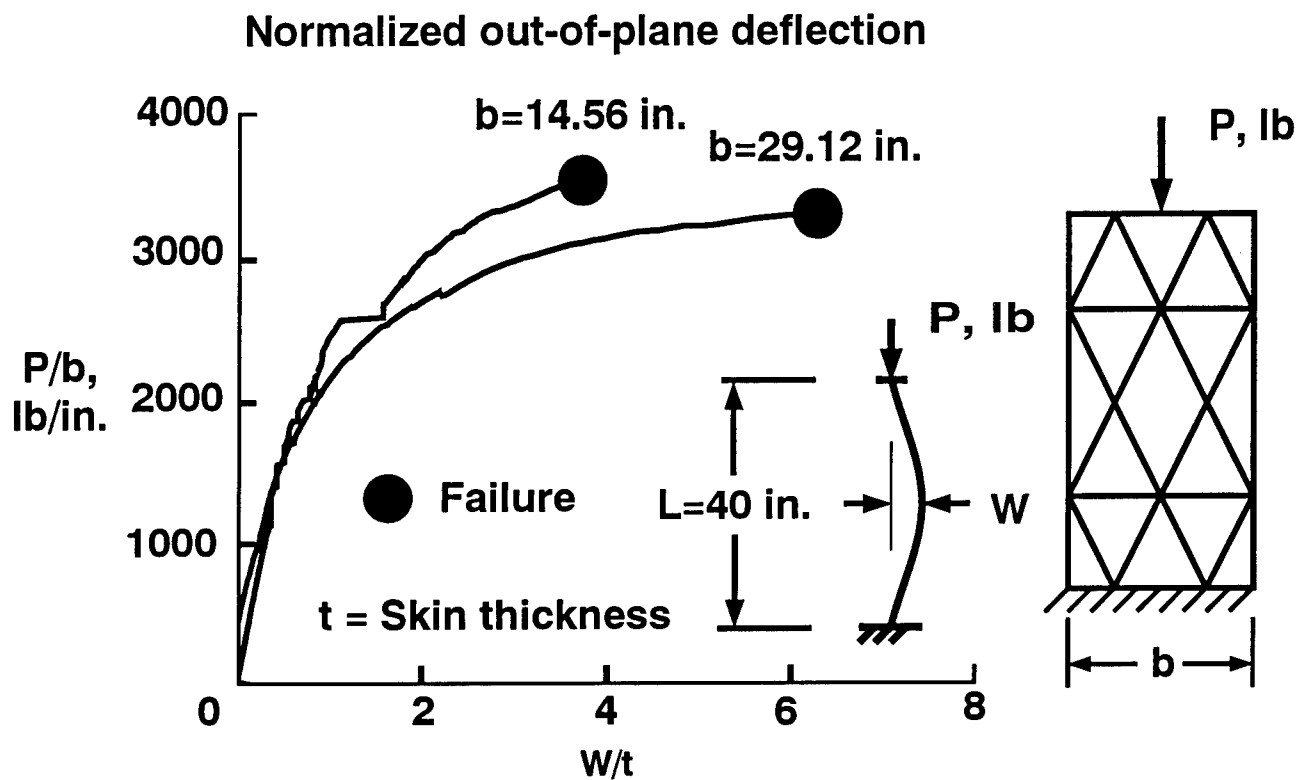


Figure 3. Out-of-plane deflection results for specimens tested without impact damage

## SKIN SURFACE STRAIN

A comparison of typical surface strain results for a 14.56-inch-wide panel tested without impact damage is presented in Figure 4 as a function of normalized load. The surface strain  $\epsilon_x$  results were recorded from back-to-back strain gages oriented parallel to the direction of applied loading at two locations on the skin. Surface strain results from back-to-back strain gages at location A, which is at the center of the specimen on the skin, are indicated by the filled circles. Surface strain results from back-to-back strain gages at location B, which is away from the center of specimen on the skin, are indicated by the filled square. The panel had a maximum compressive strain of approximately 0.008 in./in. and a maximum tensile strain of approximately 0.002 in./in. at the center of the specimen at failure. The divergence of the back-to-back strain gage results at the center of the panel suggests that bending strain at the center of the specimen is due to local buckling of the skin as the panel was loaded to failure. The discontinuities in the surface strain results measured at the center of the panel suggest that a redistribution of load occurred at approximate values for normalized load of 1,500 lb/in. and 2,500 lb/in. The redistribution of load was due to a combination of changes in skin local buckling mode and local failures at the skin-stiffener interface and fiber cross-over region. This local damage could have resulted in redistribution of load near location B which is indicated by sudden reductions in strain at 1500 lb/in. and 2,500 lb/in. The panel had a maximum compressive strain of approximately 0.001 in./in. at location B. The discontinuities in the load-strain curve for surface strain results measured at location B suggest that local failures caused redistribution of load in the panel as it was loaded to failure.

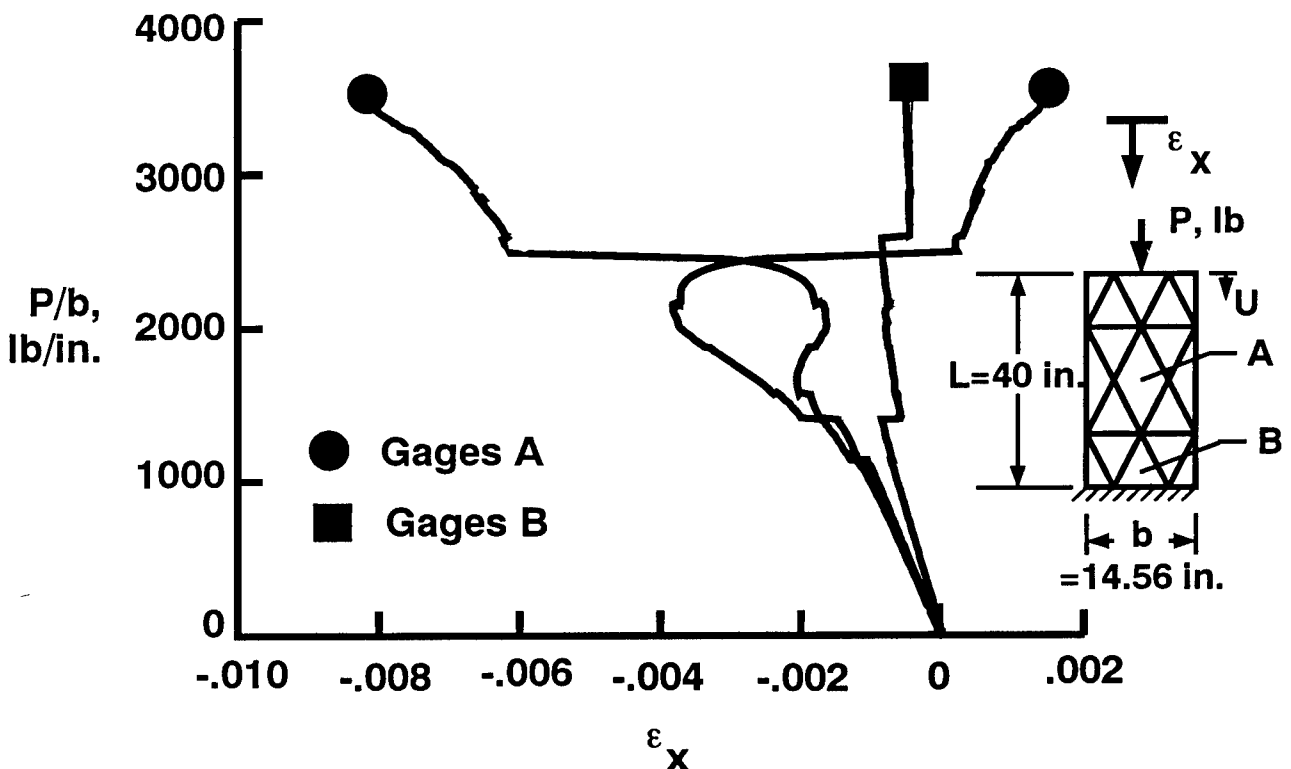


Figure 4. Typical surface strain results for a 14.56-inch-wide panel



## STIFFENER AXIAL STRAIN

Typical stiffener axial strain results for a 14.56-inch-wide panel tested without impact damage are presented in Figure 5 as a function of the normalized applied load. The axial strain  $\epsilon$  results were recorded from strain gages oriented parallel to the direction of the stiffener at locations midway between stiffener intersections. Axial strain data at location A on the crown of the stiffener are indicated by the filled circle. Surface strain data on the skin below the stiffener are indicated by the filled square. Axial strain data at locations C on the sides of the stiffener are indicated by the filled diamond. A maximum tensile strain at failure of approximately 0.0005 in./in. was measured at location A. The panel had a maximum compressive strain at Location B of approximately 0.0047 in./in. at failure. Divergence of the axial strain data at locations A and B suggests that bending strains occurred about a plane parallel to the mid plane of the skin as it was loaded into the postbuckling range. The panel had a maximum compressive strain value at locations C of approximately 0.002 in./in. at failure. The results at locations C also suggest that no lateral bending of the stiffener occurred. Also, the discontinuities in the load-strain curves shown in Figure 5 suggest that a redistribution of load occurred in the panel due to local failures prior to the failure of the panel.

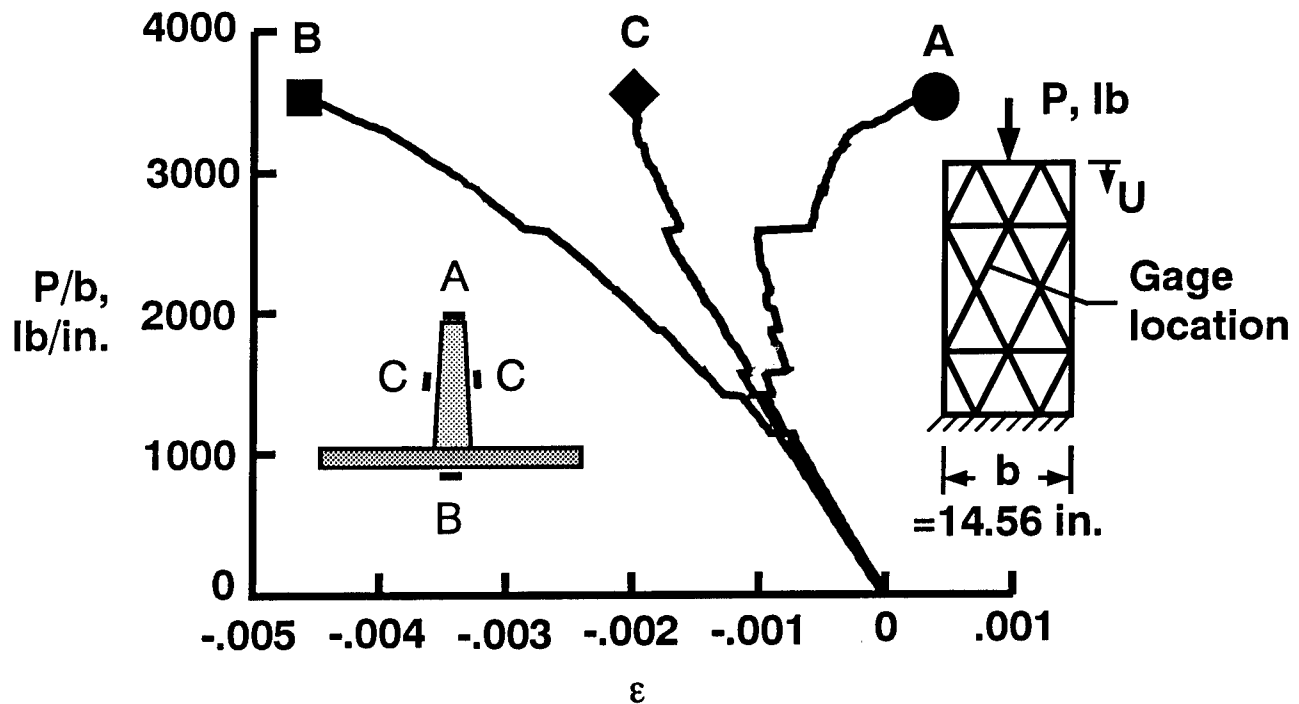


Figure 5. Typical axial strain results for a 14.56-inch-wide panel

## FAILURE OF GEODESICALLY STIFFENED COMPRESSION PANELS

Typical failure characteristics of the geodesically stiffened compression panel tested without impact damage are shown in Figure 6. The photograph on the left of the figure shows the skin side of the failed panel. The panel failed due to separation of the skin from the stiffeners across the middle of the panel in addition to the failure along the fiber cross-over region. The photograph on the right of the figure shows a close-up of the local failure mode of the panel. The skin-stiffener separation at a stiffener intersection is shown here.

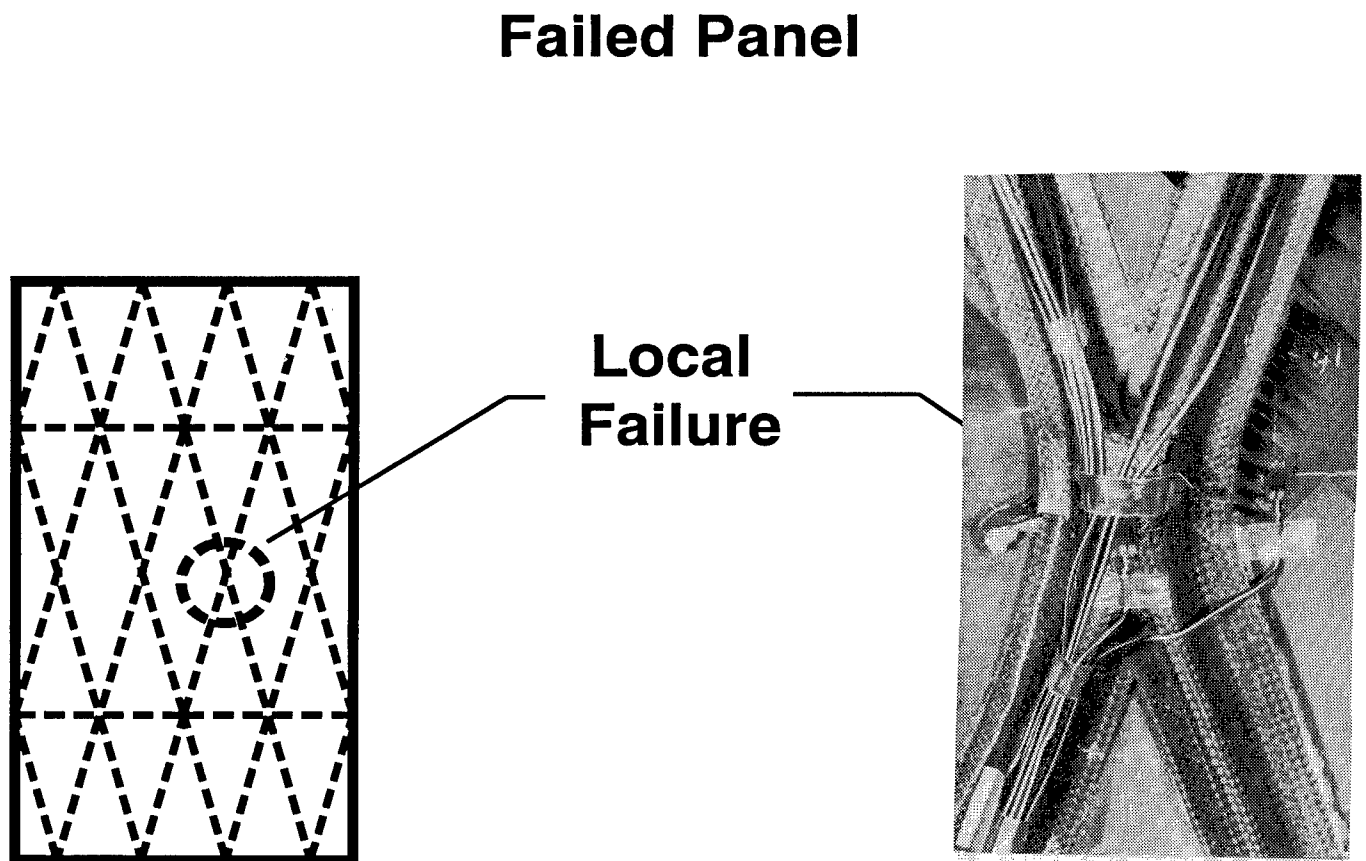


Figure 6. Failure characteristics of a geodesically stiffened compression panel

## LOW-SPEED IMPACT DAMAGE OF GEODESICALLY STIFFENED COMPRESSION PANELS

Experimental results for a geodesically stiffened compression panel subjected to low-speed impact damage are presented in Figure 7. A 14.56-inch-wide panel was subjected to low-speed impact damage at two locations near the skin-stiffener interface prior to testing. Aluminum spheres 0.5 inches in diameter were used as the impact projectile in this investigation. The panel was impacted at a point midway between intersecting stiffeners at a velocity  $V_1$  of 345 ft/sec and at the intersection of two stiffeners at a velocity  $V_2$  of 350 ft/sec. The plot on the left of the figure shows normalized end-shortening as a function of normalized applied load. Failure of the undamaged and impact damaged panels are represented by the filled circles. The analytical buckling load of an undamaged panel is represented by the open circle. The results show that the impact damaged panel failed at a value of normalized load of approximately 2,900 lb/in. which is slightly lower than the failure load of the panel tested without low-speed impact damage. The photograph on the right of the figure shows the failed impact damaged panel. The photograph shows that the panel failed in a similar mode to the undamaged panel that was described in Figure 6. The results presented in figure 7 suggest that the presence of low-speed impact damage did not significantly influence the stiffness or strength of this geodesically stiffened compression panel.

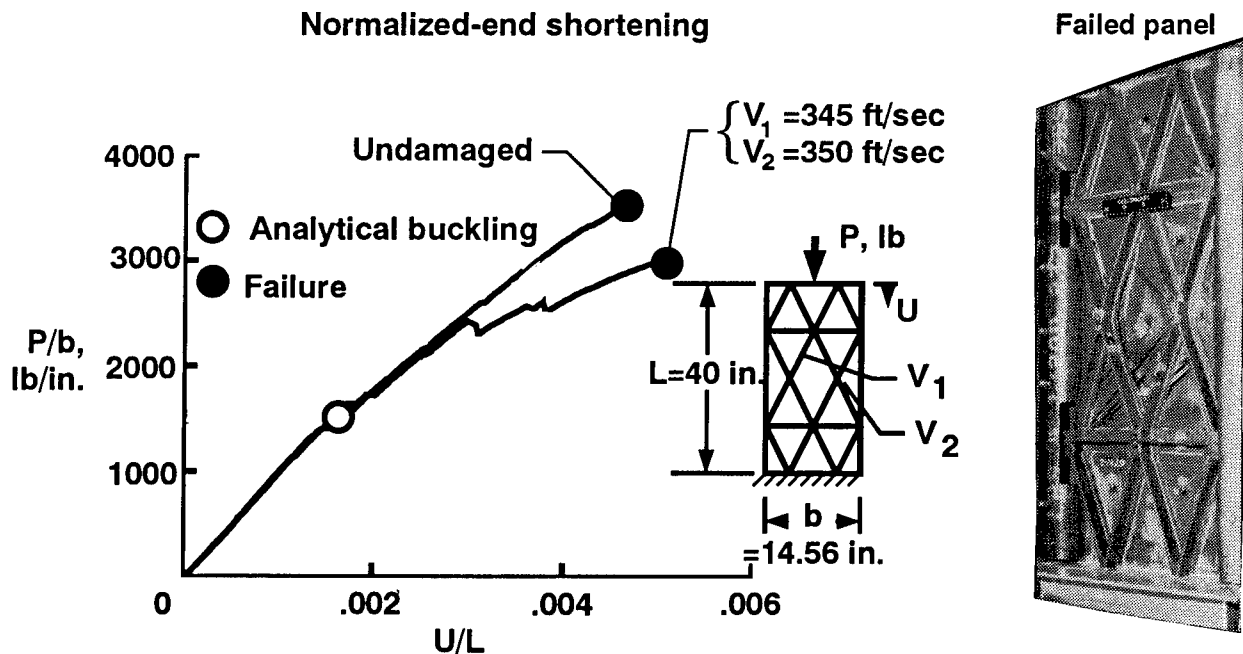


Figure 7. Summary of results for panels tested with low-speed impact damage

## GEODESICALLY STIFFENED COMPRESSION PANEL TEST AND ANALYSIS CORRELATION

A comparison between test results and analytical results obtained using the Computational Mechanics Testbed (COMET) finite element computer code (ref. 1) is presented in Figure 8. A finite element analysis was used to perform linear and geometrically nonlinear calculations. The skin, stiffeners, and frame clips were modeled with quadrilateral plate elements that allow transverse shear deformations. The finite element model of the 14.56-inch-wide panel had approximately 18,000 degrees of freedom. Boundary conditions shown in Figure 8 were assumed along the loaded edges of the panel. A uniform edge displacement  $u$  was applied to the loaded edge of the panel and this degree of freedom was constrained at the opposite edge. The applied load was calculated by summing the reactions along the constrained edge of the panel. Out-of-plane deflections  $w$  were constrained along the edges of the panel. Normalized end-shortening results as a function of normalized load are shown on the left of the figure. The circles represent experimental results and the line represents analytical results. The filled circle denotes failure of the panel and the filled square denotes the analytical buckling load obtained from linear buckling calculations. End-shortening contours calculated from a geometrically nonlinear finite element analysis are shown on the right of the figure. The contour results indicate that end-shortening was uniform across the width at the loaded edges of the panel. However, the end-shortening contours were not uniform across the width of the panel away from the loaded edges. The results suggest that the end-shortening contours were influenced by the stiffeners and stiffener intersection points. The results presented in Figure 8 indicate that the analysis accurately predicts buckling and postbuckling response of the panel up to about two times the buckling load.

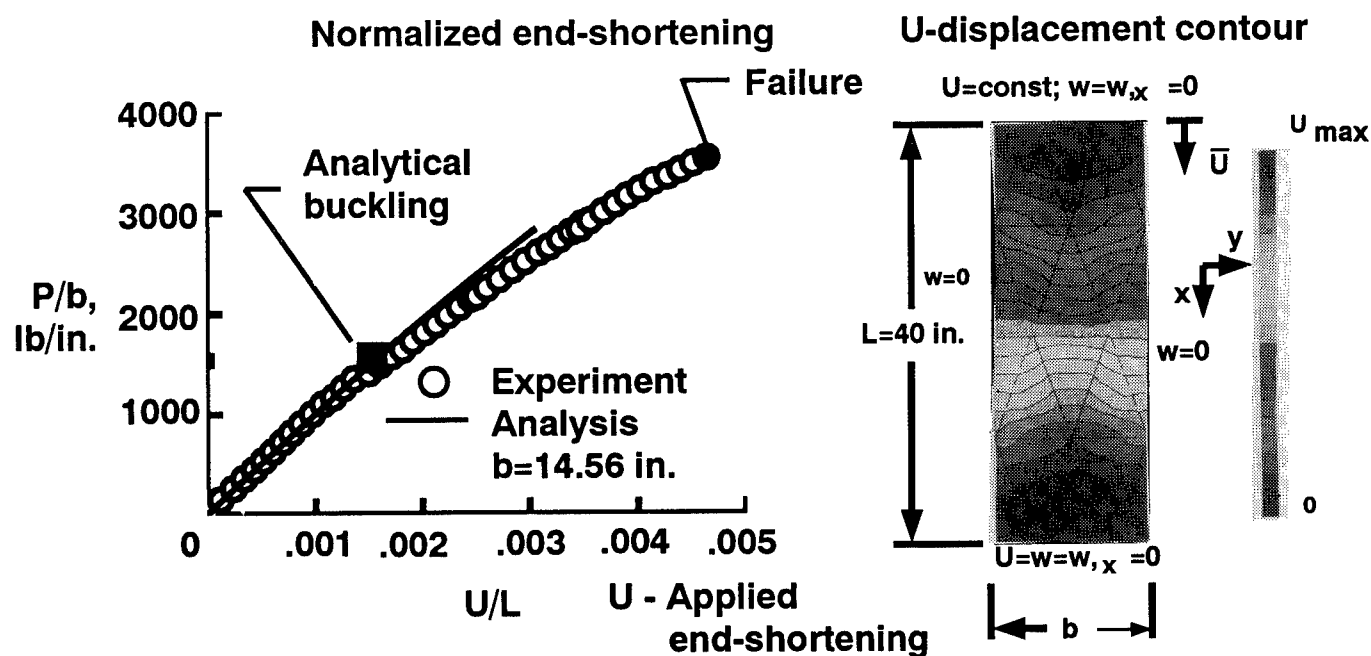


Figure 8. Comparison of experimental and analytical end-shortening results

## GEODESICALLY STIFFENED COMPRESSION PANEL OUT-OF-PLANE DEFLECTION CONTOURS

Finite element results of out-of-plane deflections  $w$  at approximately 1.5 times the buckling load and a photograph of the corresponding moire-fringe pattern are presented in Figure 9. A photograph of the moire-fringe pattern on the skin side of a 14.56-inch-wide panel is shown on the left of the figure. This photograph shows that the rhombic skin panel buckled into three halfwaves at the center of the panel. The analytical out-of-plane deflection contours viewed from the stiffener side of the panel presented on the right of the figure compare well with experimental results. The out-of-plane deflection results presented in the figure also indicate that the center region of the entire panel deformed out-of-plane during loading. Also, the buckle pattern exhibits a noticeable skew.

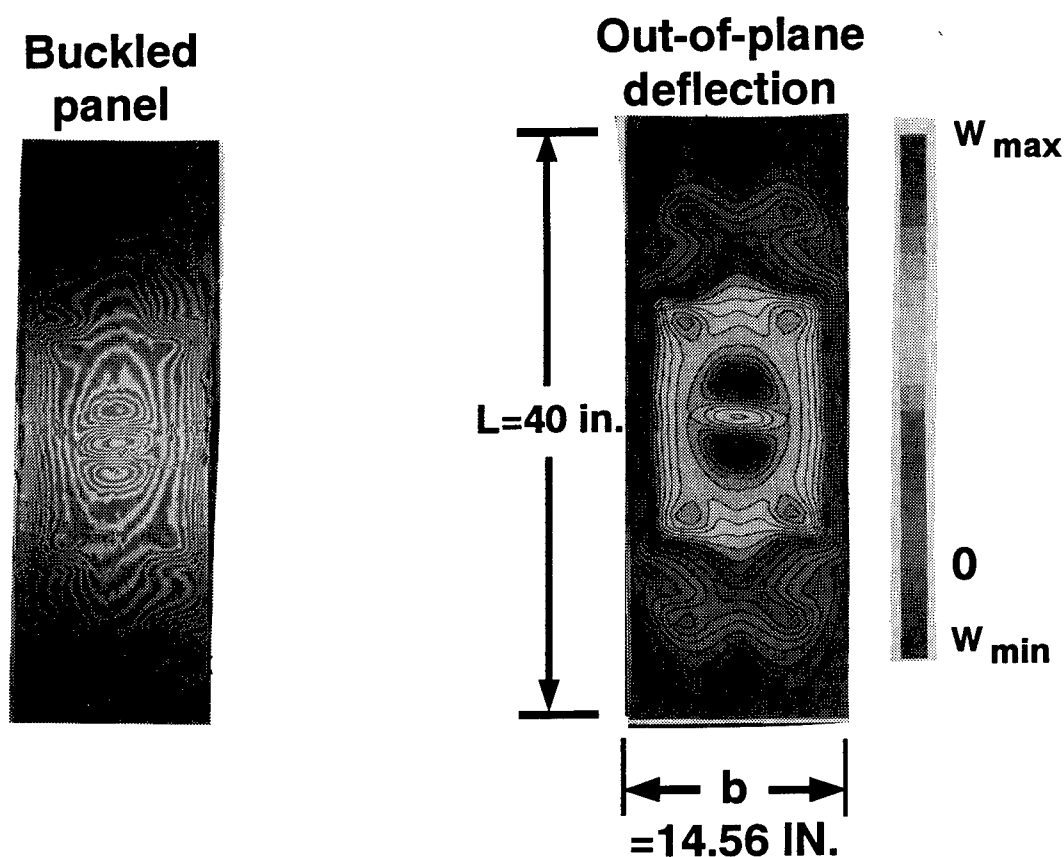


Figure 9. Experimental and analytical out-of-plane deflection results.

## TYPICAL STRESS RESULTANT CONTOUR RESULTS

Typical stress resultant contours for a 14.56-inch-wide specimen calculated from a geometrically nonlinear finite element analysis at approximately 1.5 times the buckling load are presented in Figure 10. Contour plots of the inplane normal stress resultants  $N_x$  in a direction parallel to the longitudinal axis of the panel and along the axis of the stiffeners and frame clips are shown on the left of the figure. The contour results indicate that most of the compression load is carried by the stiffeners of the geodesic compression panel. Contour plots of the inplane normal stress resultants  $N_y$  (in a direction normal to the longitudinal axis of the panel) are shown on the middle of the figure. These results indicate that the stress resultants normal to the longitudinal axis of the panel are a maximum near the location of frame clips where the  $0^\circ$  material buffer strip was embedded into the skin laminate. The high  $N_y$  stress resultants at the location of the frame clips is due to the buffer strips resisting the lateral movement of the stiffeners at the stiffener intersections. Contour plots of the inplane shear stress resultants  $N_{xy}$  are shown on the right of the figure. Inplane shear stress resultant contour results indicate that shear stresses are generated in the skin although the panel is loaded in uniaxial compression. These inplane shear stresses in the skin caused the skewed buckle pattern described in Figure 9.

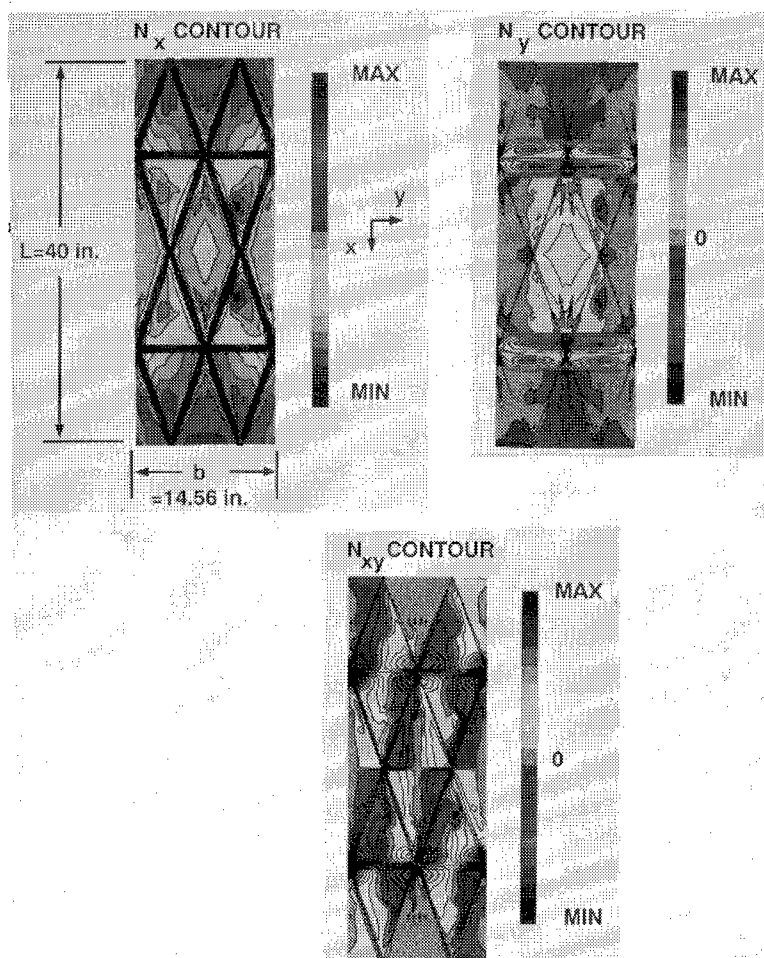


Figure 10. Typical stress resultant contour results.

**THIS PAGE INTENTIONALLY BLANK**

ADVANCED WING DESIGN  
SURVIVABILITY TESTING AND RESULTS

J. Bruno  
Grumman Aircraft Systems  
Bethpage, NY

M. Tobias  
Naval Air Development Center  
Warminster, PA

SUMMARY

Composite wings on current operational aircraft are conservatively designed to account for stress/strain concentrations, and to assure specified damage tolerance.

The technology that can lead to improved composite wing structures and associated structural efficiency is to increase design ultimate strain levels beyond their current limit of 3500 to 4000 micro-in./in. ( $\mu\text{in./in.}$ ) to 6000  $\mu\text{in./in.}$  without sacrificing structural integrity, durability, damage tolerance, or survivability. Grumman, under the sponsorship of the Naval Air Development Center (NADC), has developed a high-strain composite wing design for a subsonic aircraft wing using novel and innovative design concepts and manufacturing methods, while maintaining a state-of-the-art fiber/resin system. The current advanced wing design effort addressed a tactical subsonic aircraft wing using previously developed, high-strain wing design concepts in conjunction with newer/emerging fiber and polymer matrix composite (PMC) materials to achieve the same goals, while reducing complexity. Two categories of advanced PMC materials were evaluated: toughened thermosets, and engineered thermoplastics. Advanced PMC materials offer the technological opportunity to take maximum advantage of improved material properties, physical characteristics, and tailorability to increase performance and survivability over current composite structure.

Damage tolerance and survivability to various threats, in addition to structural integrity and durability, were key technical issues addressed during this study, and evaluated through test. This paper focuses on the live-fire testing, and the results performed to experimentally evaluate the survivability of the advanced wing design.

The objective of the live-fire testing is to demonstrate the ability of the advanced wing design/material combination to survive a 23-mm high-energy incendiary (HEI) single hit (while under load) without the use of S-glass/epoxy (S-Gl/Ep) crack-arrestment strips. The intended purpose of the S-Gl/Ep strips is to increase the design's overall damage tolerance to ballistic impact by arresting the growth of damage and preventing it from growing to catastrophic proportions. Inclusion of these strips within the laminate is labor intensive and adds both weight and cost to



the design. Ballistic testing of toughened thermoset panels (with and without crack-arrestment strips) and a thermoplastic panel (without crack-arrestment strips) provides a direct comparison of realistic data to evaluate the effectiveness of the design/material combination to eliminate the crack-arrestment strips and simplify the overall design.

## INTRODUCTION

PMC materials have found increasing application in the aerospace industry because of their high strength and stiffness-to-weight ratios and potentially lower unit costs. While attractive weight savings have been realized, on a component basis, PMC structures have not yet met their full potential in terms of weight savings. This has been due in part to conservatism in design, which has resulted in strain levels being suppressed to account for reduced performance under hot/wet conditions and the presence of notches and/or damage.

The technology that can lead to improved wing structures and associated structural efficiency by increasing design ultimate strain levels beyond their current limit of 3500 to 4000  $\mu\text{in./in.}$  has been demonstrated through the development of novel and innovative design concepts and manufacturing techniques, while maintaining the same fiber/non-toughened resin system, without sacrificing structural integrity, durability, damage tolerance, or survivability (battle damage tolerance). Concepts/features considered included the use of compliant high-strain-to-failure laminates, locally concentrated and banded 0-deg plies, integral cover-to-substructure concepts to minimize/eliminate fastener holes, and S-GI/Ep softening strips at locations where holes are required to accommodate fasteners. Damage tolerance was achieved through a multi-path design utilizing S-GI/Ep crack-arrestment strips to isolate and contain battle damage. In addition, Kevlar stitching was incorporated through the crack-arrestment strips to stop growth of delaminations (at the high operating strain level) resulting from low-energy impact damage (LEID).

An extensive design, development, and verification test effort has been an integral part of this development program. Design development testing consisted of over 140 coupons and 32 major elements prior to the design, fabrication, and test of a full-scale wing box subcomponent. The development testing successfully met their objectives to:

- Derive material allowables for notched high-strain laminates with S-GI/Ep softening strips
- Correlate and confirm the adequacy of the analytical procedures used to define and analyze the design concept
- Demonstrate structural integrity of critical design areas
- Demonstrate the ability of the high-strain wing to sustain cyclic loading consistent with the aircraft's design life

- Demonstrate the effectiveness of the stitched S-Gl/Ep crack-arrestment strips for LEID and battle damage
- Establish the confidence to proceed to the fabrication and test of the full-scale wing box subcomponent.

The successful fabrication and testing of the four-spar subcomponent [a 241-cm (95-in.)-long, 91.4-cm (36-in.)-wide, 33-cm (13-in.)-deep representative segment of the high-strain wing box center section] verified the structural integrity, durability, and LEID tolerance of the high-strain wing design under combined loading and fuel pressure. It also demonstrated the manufacturing approach, and the battle damage tolerance while under load and pressurized.

Coincident with this effort, the trend toward increased structural efficiency and damage-tolerant structures emphasized the need for, and vigorous development of, new/improved composite materials consisting of high-performance graphite fibers in combination with toughened resin systems. Compared with composite material systems used on operational aircraft, these emerging new/improved fibers offer increased strength, stiffness, and strain-to-failure in the presence of a notch. New/emerging resin systems--both toughened thermosets and thermoplastics--have increased toughness, and improved elevated temperature/wet retention of properties. The potential benefits that can be realized by combining these newer/emerging fibers and tougher resin systems with previously developed high-strain wing design to maximize structural efficiency and simplify the design to reduce fabrication costs (while maintaining to greatest extent possible the durability, damage tolerance, and survivability demonstrated by the original high-strain wing design) were evaluated during a subsequent advanced wing design and experimental evaluation effort also sponsored by the NADC. Coupon and element testing, similar to that of the high-strain wing effort, was performed and addressed the same key issues: structural integrity, durability, damage tolerance, and survivability. This paper focuses on the battle damage tolerance testing accomplished, and presents the results.

## ADVANCED WING DESIGN DEVELOPMENT

The planform and basic geometry for the Grumman/Navy A-6E attack aircraft wing baselined for this design and experimental evaluation effort is illustrated in figure 1. The wing has a span of 16.2 m (53 ft), a fold span of 7.7 m (25.3 ft), and a total area of 49.1 sq m (528.9 sq ft). The thickness-to-chord (T/C) ratio is 9% at the root and 5.9% at the tip, with a maximum thickness of 30.5 cm (12 in.) at the root. Wing control surfaces include inboard and outboard slats, flaps, flaperons, and speedbrakes at the wing tips. The wing is comprised of three major sections: an inner panel/center section that is one piece from fold joint to fold joint, and two outer panel sections. The structural torque box is a multi-spar construction with seven spars in the center section, nine in the inner panel, and seven in each outer panel. There is a total

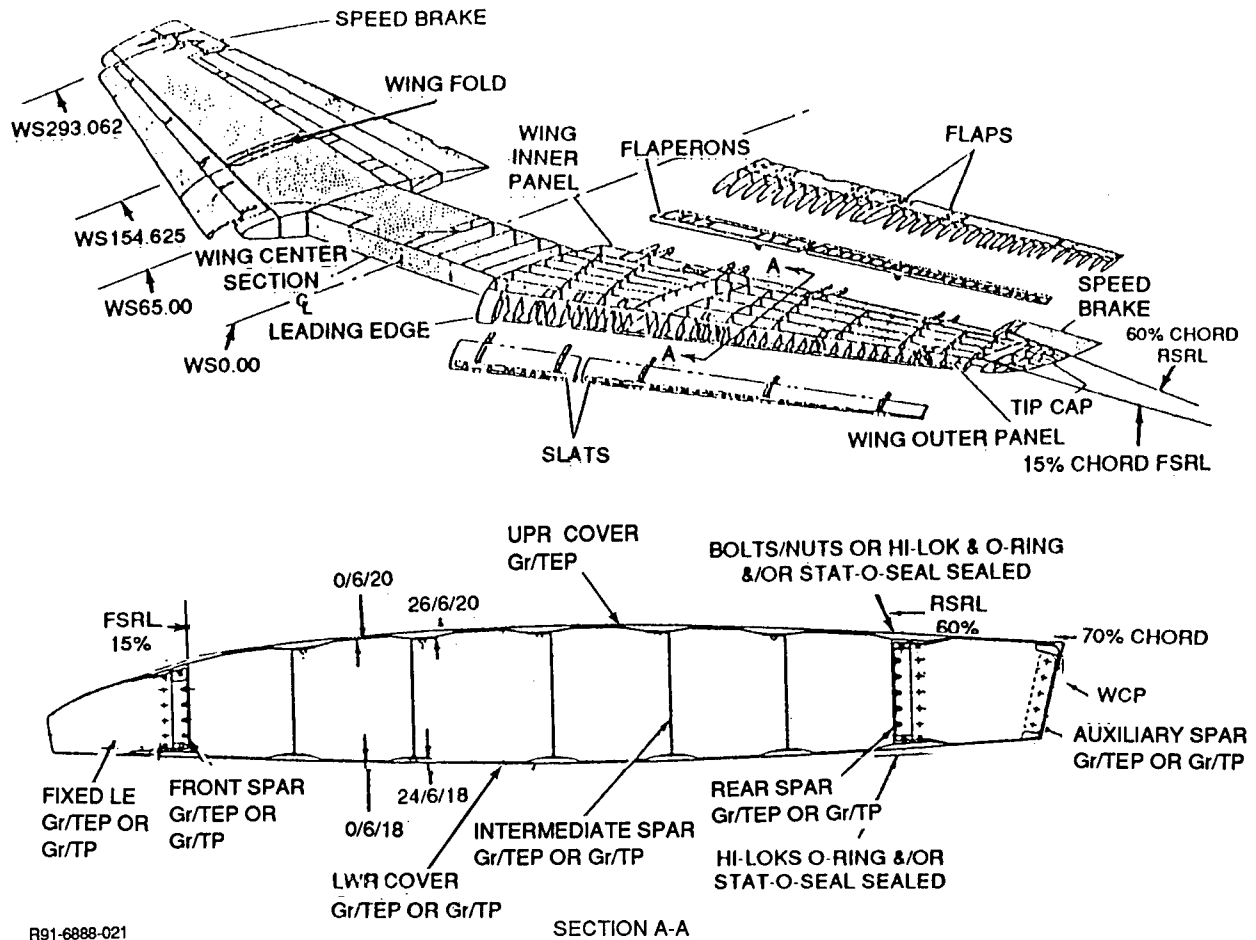


Figure 1 Baseline Wing Structural Arrangement

of 27 ribs, 13 of which are in the inner panel/center section, and 7 in each outer panel.

Design criteria established for this effort are presented in table I. The environmental conditions were based on the operational temperatures, mission profiles, and typical deployment areas. Damage tolerance requirements are similar to current composite wing requirements, i.e., ultimate load capability with the presence of LEID. Survivability requirements, for battle damage, required the structure to carry design limit load (DLL) following a single hit from a 23-mm HEI projectile with a super-quick fuse, and withstand the hydrodynamic ram effects due to the high-energy impact of the fuel-filled wing. Supportability requirements dictated that one cover be removable for maintenance and repair. In addition, removable access panels for maintenance of internal wing systems were included in the design. Finally, the wing box is an integral fuel-containing structure and was therefore designed to withstand maximum fuel pressures encountered during refueling or flight conditions.

The type of construction selected for the design and experimental evaluation effort is also illustrated in figure 1. The upper and lower

**TABLE I. - AWD Design Criteria**

WEIGHT:	20% WEIGHT REDUCTION FROM CURRENT SOA COMPOSITE DESIGN
STRAIN LEVEL:	6000 MICRO-IN./IN. DESIGN ULTIMATE STRAIN FOR TENSION & COMPRESSION COVERS
ENVIRONMENTAL CONDITIONS:	71°C (160°F) & 1.3% MOISTURE
DAMAGE TOLERANCE:	SUSTAIN DUL AFTER LOW-ENERGY IMPACT
SURVIVABILITY:	EXPERIENCE SINGLE HIT BY 23-MM HEI PROJECTILE & RETAIN CAPABILITY TO CARRY DESIGN LIMIT LOAD
MAINTENANCE:	ONE COVER REMOVABLE FOR INSPECTION & REPAIR
FUEL CONTAINMENT:	DESIGNED TO WITHSTAND MAX FUEL PRESSURES; HYDRODYNAMIC RAM EFFECTS CONSIDERED
MR91-6888-008	

covers are designed as discrete cap laminates with the outer fibers working to a design ultimate strain level of 6000  $\mu$ in./in. The basic cover between spar supports is a compliant high-strain-to-failure laminate consisting of  $\pm 45^\circ$ - and  $90^\circ$ -deg plies only. This type of laminate has the advantages of minimizing load in the unsupported region of the cover, while maximizing buckling coefficients and being highly damage tolerant. The required  $0^\circ$ -deg axial load-carrying plies are concentrated and banded at discrete locations over spar supports. The lower cover is attached to the substructure using blind composi-lok fasteners with O-rings under the heads for sealing. To satisfy the Navy requirement to have one cover removable for maintenance and repair, the upper cover is attached to the substructure using mechanical fasteners through nut-plates attached under the spar flanges.

The front and rear spars are unstiffened channel sections designed to be non-buckled to ultimate load. The front spar is fabricated in five segments: one in the center section, and one for each inner and outer panel. The rear spar is fabricated in three segments: one for each outer panel, and a one-piece segment on the center section/inner panel from fold to fold. The front and rear spars also serve as fuel tank boundary elements and seal the tank. An integrally molded groove seal in the flanges of the front and rear spars provides sealing and adequate structural behavior at minimum cost. The intermediate spars are channel sections with flat unstiffened webs non-buckled to ultimate load. Of the 27 ribs, 17 are composite and 10 are titanium. Titanium ribs are used at the two wing fold locations, the outboard tank boundaries, and at store locations.

The wing box attaches to the fuselage at four locations. Titanium fittings are bolted to the front and rear spars in the center section and

are backed up by ribs. Single large-diameter fail-safe pins engage the titanium fittings through the fuselage bulkheads.

Major materials of construction considered consisted of two categories of new and/or improved graphite fibers: high strain (1.8% elongation or greater) and higher modulus [275.8 MPA (40 MSI) or greater with at least 1.5% elongation], in combination with two categories of toughened matrices: toughened thermosets and "engineered thermoplastics". A total of 28 toughened thermoset and nine thermoplastic material systems, summarized in tables II and III, respectively, have been screened for selection and evaluation of the most promising material systems. Grumman's extensive data base and material supplier data were used, in part, to perform the screening. In addition, industry-standard coupon tests were performed to obtain sufficient data where lacking, and to characterize the material systems to permit comparison on a common basis. Four toughened thermoset (IM8/8551-7A, T800/F3900, HITEK45-9B/E7T1-2, and G40-800/F584) and two thermoplastic (T650-42/RADEL-8320 and IM7/APC-II) material systems exhibited an overall balanced improvement in mechanical properties and toughness, and were therefore selected for characterization testing and further consideration for the preliminary design and trade study effort. Two toughened thermosets (IM8/8551-7A and HITEK45-9B/E7T1-2) and one thermoplastic (T650-42/RADEL-8320) were further down selected for battle damage tolerance testing.

## TEST OBJECTIVE

The objective of the battle damage tolerance element testing was to demonstrate the ability of the advanced wing cover design concept/material combination to survive a single hit from a 23-mm HEI (with super-quick fuse) while under load without the use of S-GI/Ep crack-arrestment strips. The intent of the S-GI/Ep strips is to increase the overall damage tolerance of the design to ballistic impact by isolating the damage and preventing its growth to catastrophic proportions. Inclusion of these strips within the laminate, however, is labor-intensive and adds both cost and weight to the design. Ballistic testing of the toughened thermoset panels (with and without S-GI/Ep strips) and the thermoplastic panel (without S-GI/Ep strips) provided a direct comparison of realistic data to evaluate effectiveness of the material/design combination to eliminate the crack-arrestment strips and simplify the overall design.

## COMPONENT DESCRIPTION AND DESIGN

The wing cover component, illustrated in figure 2, is a 53.3-cm (21-in.)-wide and 190.5-cm (75-in.)-long discrete cap laminate consisting of two cover-bays and three discrete caps, and is fully representative of

**TABLE II. – Candidate Toughened Thermoset Prepregs**

FIBER MANUFACTURER	FIBER TYPE	FIBER TENSILE STRENGTH (KSI)	FIBER TENSILE MODULES (MSI)	R6376/CIBA	CYCOM 1827/CYAN	XU71787/DOW	F584/HEXCEL	8551/HERCULES	HG9105-2/HYSOL	5745C/NARMCO	E7K8/US POLY	974/FIBERITE	ERLIX 1928/AMOCO	E7T1-2/US POLY	F3900/HEXCEL	AVAILABILITY
BASF/CELION	G-40 -600	600	43.5	√			√			√		√				DEVELOPMENTAL
BASF/CELION	G-40 -700	690	49													DEVELOPMENTAL
BASF/CELION	G-40 -800	820	43.5				√									DEVELOPMENTAL
BASF/CELION	CELION-ST	580	35	√												FULL PRODUCTION
HERCULES	IM6	635	40		√		√	√		√						FULL PRODUCTION
HERCULES	IM7	680	41			√		√								FULL PRODUCTION
HERCULES	IM8	750	45					√								FULL PRODUCTION
HERCULES	AS6	650	35					√								FULL PRODUCTION
HITCO	HITEX-42	600	42							√	√					FULL PRODUCTION
HITCO	HITEX-46	900	46								√			√		FULL PRODUCTION
AMOCO	T-650	650	42										√			FULL PRODUCTION
AMOCO	T-40X	820	41	√			√				√		√			FULL PRODUCTION
HYSOL	IM-S	820	43						√							LTD PRODUCTION QTY
HYSOL	APPOLLO-M	820	53				√		√							LTD PRODUCTION QTY
HEXCEL MR91-6888-009	T-800	850	42												√	LTD PRODUCTION QTY

the selected advanced-wing lower-cover design at the one-third semi-span location of the wing outer panel. The component consists of a 0/6/18 (number of plies in the 0-, 90-, and  $\pm 45$ -deg orientations, respectively) basic cover laminate between discrete caps/spar supports, and builds up locally to a 26/6/18 discrete cap laminate. A single row of high-tensile-strength-Kevlar stitches was incorporated through the basic cover laminate (prior to cure) adjacent to both sides of each discrete cap. The rows of stitches were included to provide translaminar reinforcement to arrest delamination growth, if necessary, due to the high operating strain level. The stitches were also an integral part of the overall design approach to address survivability for battle damage tolerance and hydrodynamic ram effects, and were incorporated into the toughened thermoset components for design realism. The spacing between discrete caps/spar supports at this location is 18.7 cm (7.35 in.), and the cover load intensities are 1609 kN/m (9190 lb/in.) axial (Nx), and 128 kN/m

TABLE III. – Candidate Thermoplastic Prepregs

FIBER MANUFACTURER	FIBER TYPE	FIBER TENSILE STRENGTH (KSI)	FIBER TENSILE MODULES (MSI)	APC-2(PEEK)/ICI	PPS(RYTON)/PHILLIPS	KII(AVIMID)/DUPONT	PAI(TORLON)/AMOCO	KIII(AVIMID)/DUPONT	RADEL-8320/AMOCO	AVAILABILITY
BASF/CELION	G-40-600	600	43.5		✓					DEVELOPMENTAL
HERCULES	IM6	635	40		✓	✓	✓		✓	FULL PRODUCTION
HERCULES	AS6	650	35				✓		✓	FULL PRODUCTION
HYSOL	APPOLLO-M	820	53		✓					LIMITED PRODUCTION QTY
AMOCO	T650-42	650	42						✓	FULL PRODUCTION

MR91-6888-010

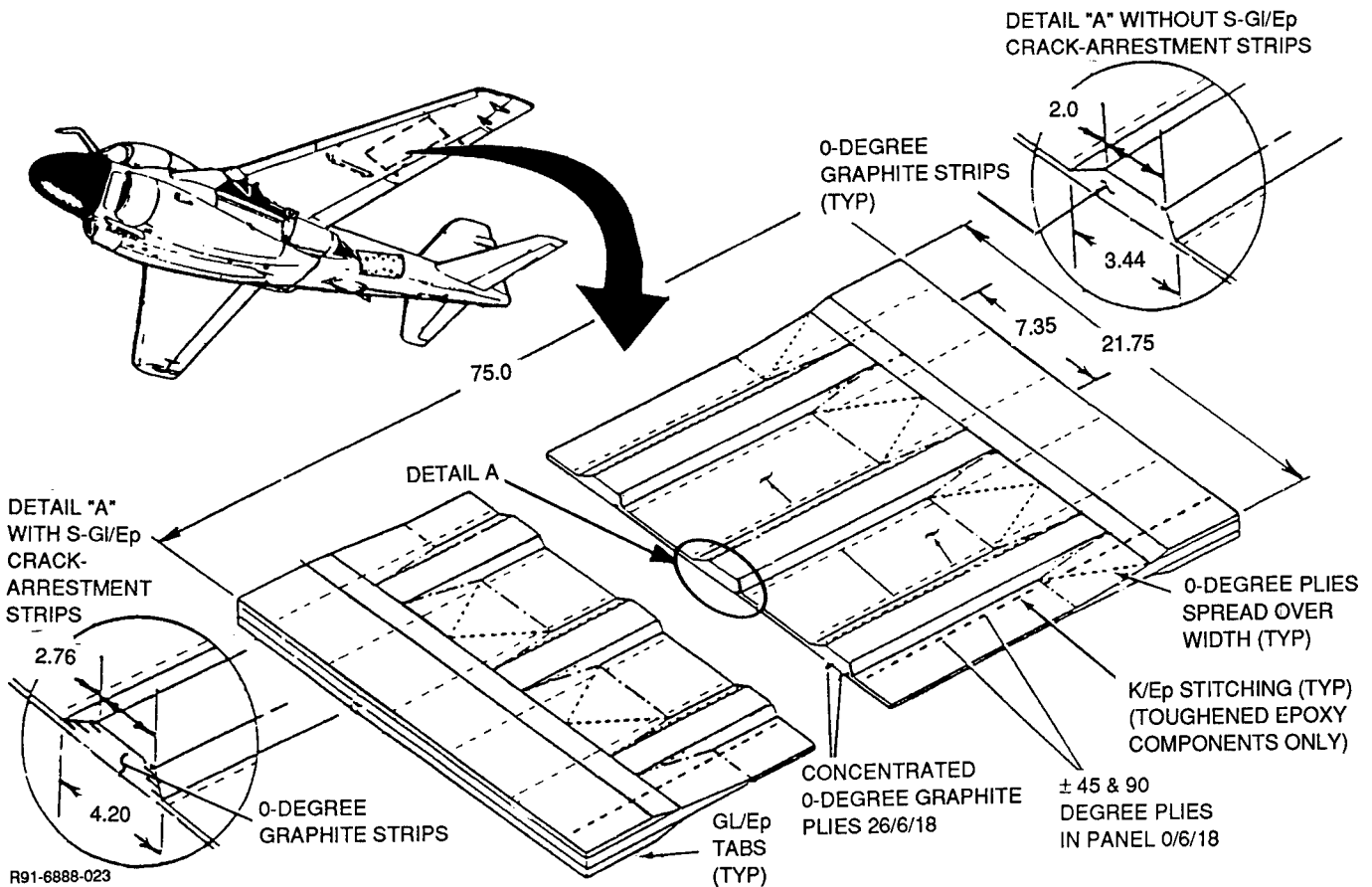


Figure 2 Wing Component Configuration

(731 lb/in.) shear ( $N_{xy}$ ). The components were designed to be of sufficient size to provide a realistic demonstration of the survivability of the material/design for the ballistic threat--while under load--and make possible the incorporation of a repair. Detail laminate design, an integral part of the overall structural design process, was performed by extending basic material properties data through classical lamination theory to predict multi-directional laminate behavior. As previously mentioned, laminates representative of the advanced wing cover design contain a high percentage of 0-deg plies or none at all. In either case, careful attention was given to stacking sequence for both the basic-cover and discrete-cap laminates.

Four fiberglass gripper tabs were fabricated as separate details and adhesively bonded to each side of the load introduction areas at both ends of the component.

In preparation for test, the components were drilled and countersunk in the discrete cap areas to accommodate attachment of a simulated substructure support using 0.635-cm (0.25-in.)-diameter Hi-lok fasteners. Steel load introduction gripper plates were bolted to the fiberglass tabs at each end of the component.

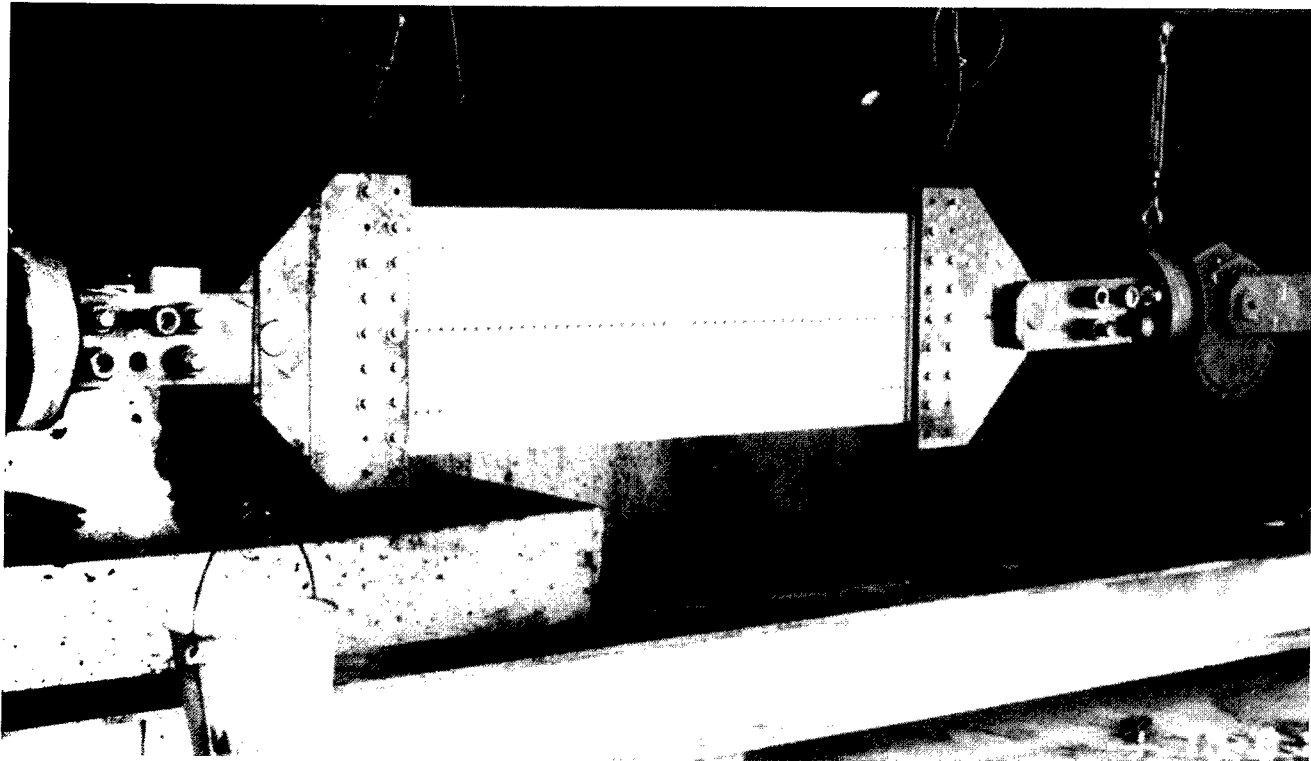
#### SURVIVABILITY TESTING

The cover components were live-fire tested at the USA Ballistic Research Lab, Aberdeen Proving Grounds, MD. The test setup shown in figure 3 consisted of a hydraulic cylinder attached to an adjustable frame, which in turn was attached to the test specimen's gripper plates via single, large-diameter clevis pins at each end. The gripper plates, bolted to each end of the cover component, transfer the tensile load applied by the hydraulic cylinder/adjustable frame combination to the specimen. A tensile load of 400.3 kN (90,000 lb) was applied to attain the required 55% DLL level while subjecting the components to the ballistic hit. The gun used was a 23-mm rifled barrel clamped to a recoil-absorbing mount. It was fired remotely by electrical impulse. The 23-mm projectile was fired at a nominal velocity of 607 m/s (2000 ft/s) into the center of the mid-discrete cap at 0-deg obliquity while the components were loaded in tension to 55% DLL.

#### TEST RESULTS

All cover components were able to maintain the applied load both during and after the ballistic hit; however, an approximate 10% reduction in applied load was recorded subsequent to the hit, which has been attributed to flexibility in the test setup. The applied load was maintained at this level (48% DLL) for a sufficient length of time after





R91-6888-003

**Figure 3 Wing Component Set Up for Test**

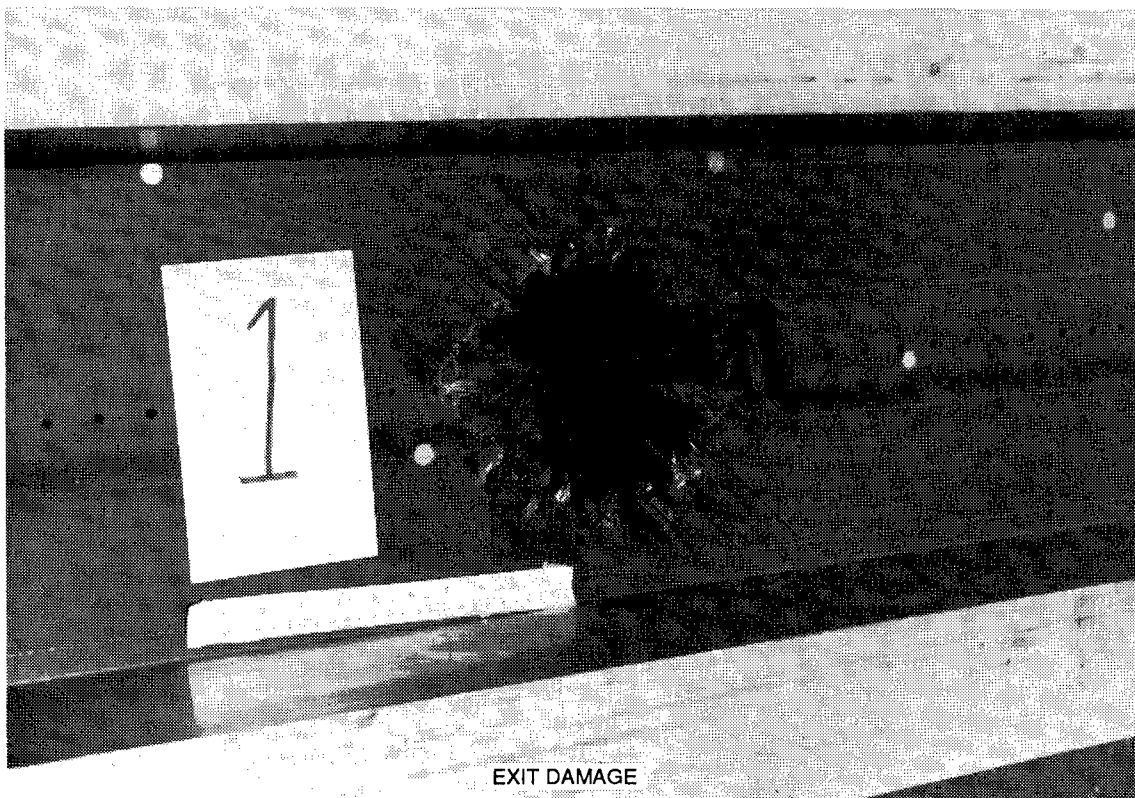
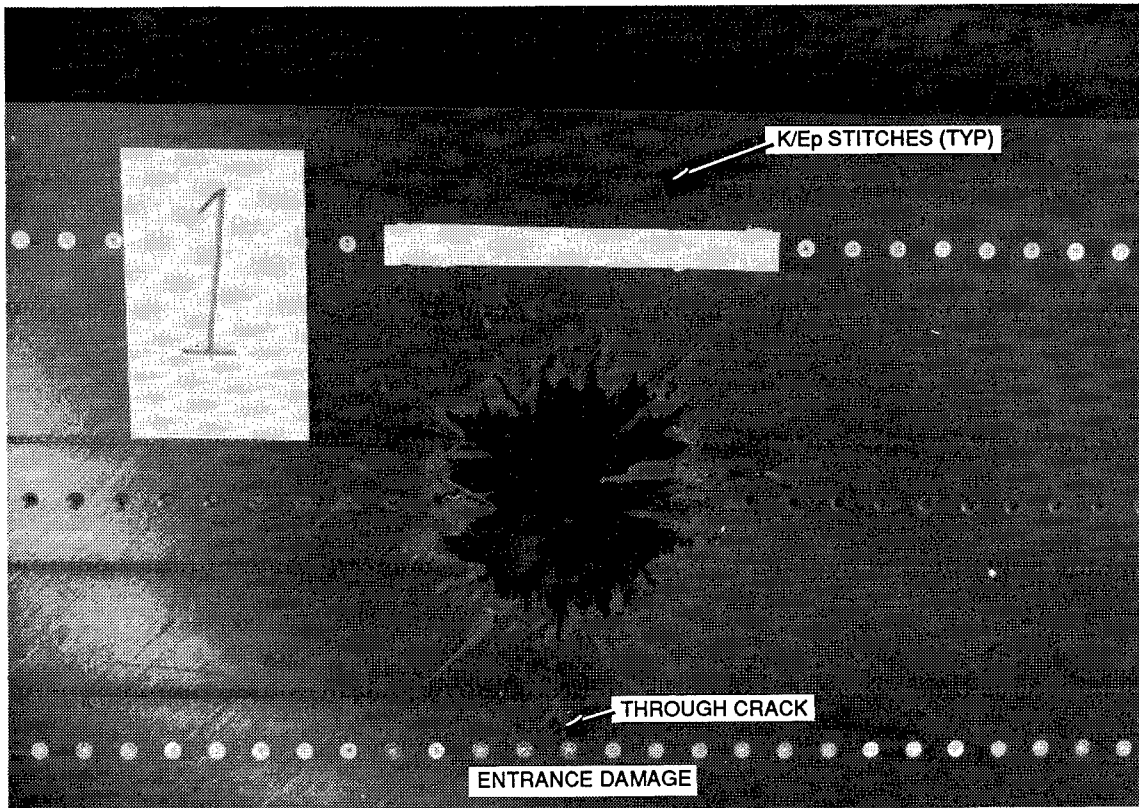
the impact. The following observations, based on visual examinations, were made regarding the damage of each panel subsequent to the ballistic hit.

**Panel No. 1 (IM8/8551-7A without crack-arrestment strips)**

The round impacted the center of the panel as planned, thus hitting the center of the mid-discrete cap. Upon detonation, it completely severed the cap and blew a jagged hole approximately 22.9 cm (9 in.) in diameter in the panel. Numerous strips of  $\pm 45$ -deg material delaminated and peeled back from the edges of the jagged hole, but were prevented from delaminating further by the rows of Kevlar stitches (see figure 4). However, a crack that originated at the bottom edge of the hole propagated chordwise for approximately 20.3 cm (8 in.), through the row of stitches at the lower adjacent discrete cap, through a bolt hole in the adjacent discrete cap, and then through the second row of stitches on the other side of the discrete cap. The running crack was through the thickness of the specimen from front to back.

**Panel No. 2 (HITEX 45-9B/E7T1-2 without crack-arrestment strips)**

The entry damage size was similar to panel no. 1 [approximately 22.9-cm (9-in.)-diameter jagged hole] except that only the impacted mid-discrete cap was severed; i.e., no cracks extended from the hole to



R91-6888-004

**Figure 4 Panel No. 1 Entrance and Exit Damage**

adjacent caps. Exit damage differed from panel no. 1 in that there was more delamination and peeling of surface  $\pm 45$ -deg plies, which stopped at the adjacent rows of stitching. There seemed to be more damage longitudinally, along the cap, than panel no. 1, with more of the cap material peeled back (see figure 5).

#### Panel No. 3 (IM8/8551-7A with crack-arrestment strips)

The third panel in this series of tests differed from the first two in that it had S-Gl/Ep strips incorporated within the laminate adjacent to both sides of each discrete cap. The entry side damage (see figure 6) is nearly identical to panels no. 1 and 2. However, the exit side damage (also shown in figure 6) extended further spanwise along the length of the panel. The S-Gl/Ep crack-arrestment strips arrested any chordwise growth of damage. However, the S-Gl/Ep crack-arrestment strip adjacent to both sides of the mid-discrete cap were severed (along with the cap) and pulled out of the laminate, thereby pulling loose a section of Gr/Ep material approximately 10.2 cm (4 in.) wide by 22.9 cm (9 in.) long, resulting in more extensive spanwise damage. No through-the-thickness cracks, as seen on panel no. 1, were evident in this specimen.

#### Panel No. 4 (T650-42/RADEL-8320)

The fourth panel, fabricated from a thermoplastic material without crack-arrestment strips and without Kevlar stitching, responded differently to the ballistic hit than did the three previous toughened thermoset panels. The ballistic projectile impacted the center of the mid-discrete cap as planned. Upon detonation, the ballistic projectile blew a 20.3-cm (8-in.)-diameter jagged hole in the center of the panel. There was minimal ply breakout and surface damage on either the entrance or exit sides (see figure 7). As such, exit side damage was virtually the same as the entrance side damage. Furthermore, the damage was limited to the jagged hole with no through-the-thickness cracks or delaminations extending beyond the hole thus making the component easier to repair. Based on observations at the time of the live-fire test, the resulting damage and overall response of the panel to the ballistic hit was very much like that of aluminum, except that there were no cracks, tears, or permanent deformations evident.

### CONCLUSIONS

Conclusions reached as a result of the experimental effort described in this paper have been encouraging. In general, toughened thermoset and thermoplastic materials appear to provide improvements in wing primary structures for future military aircraft to potentially reduce fabrication costs and increase structural efficiency, while providing advantages for

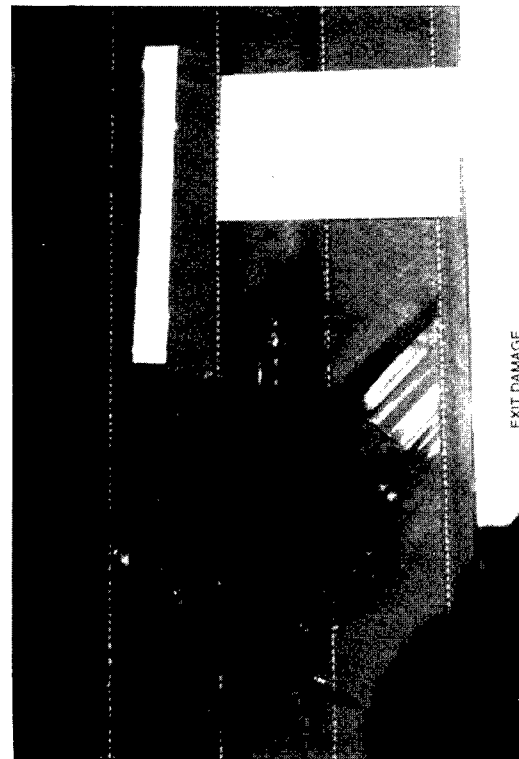
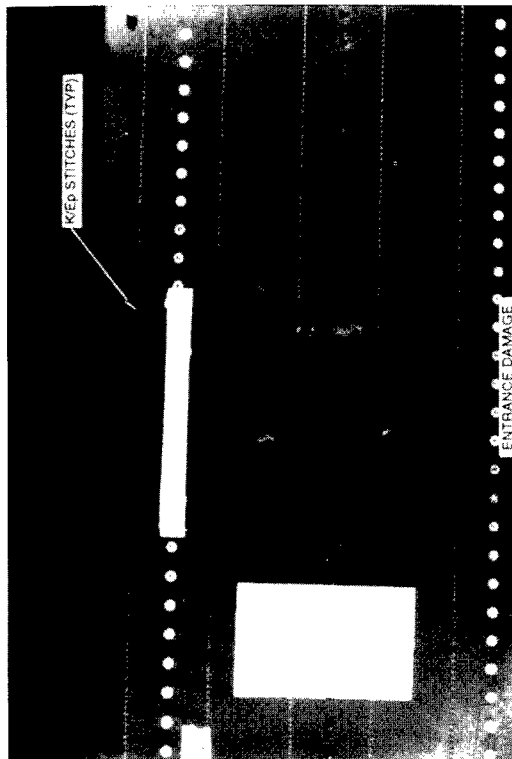


Figure 5 Panel No. 2 Entrance and Exit Damage

RG1-6888-005

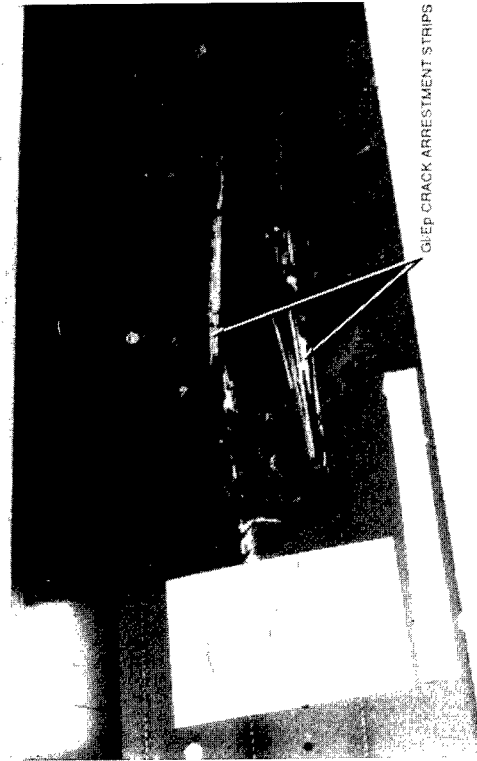
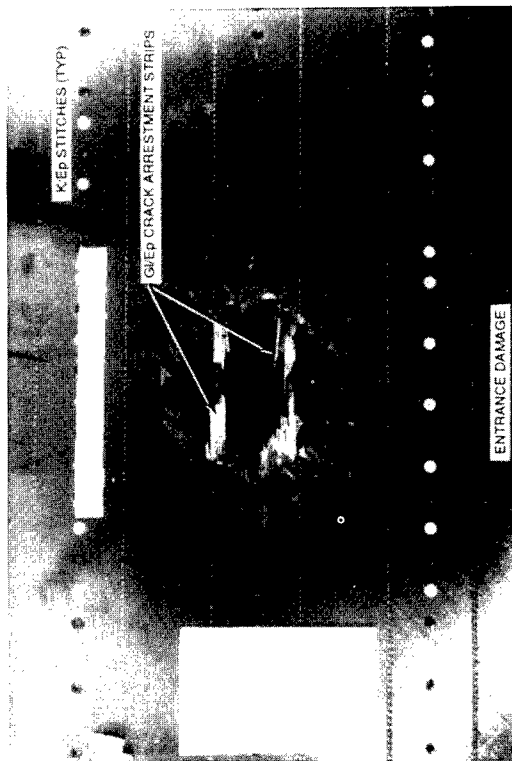
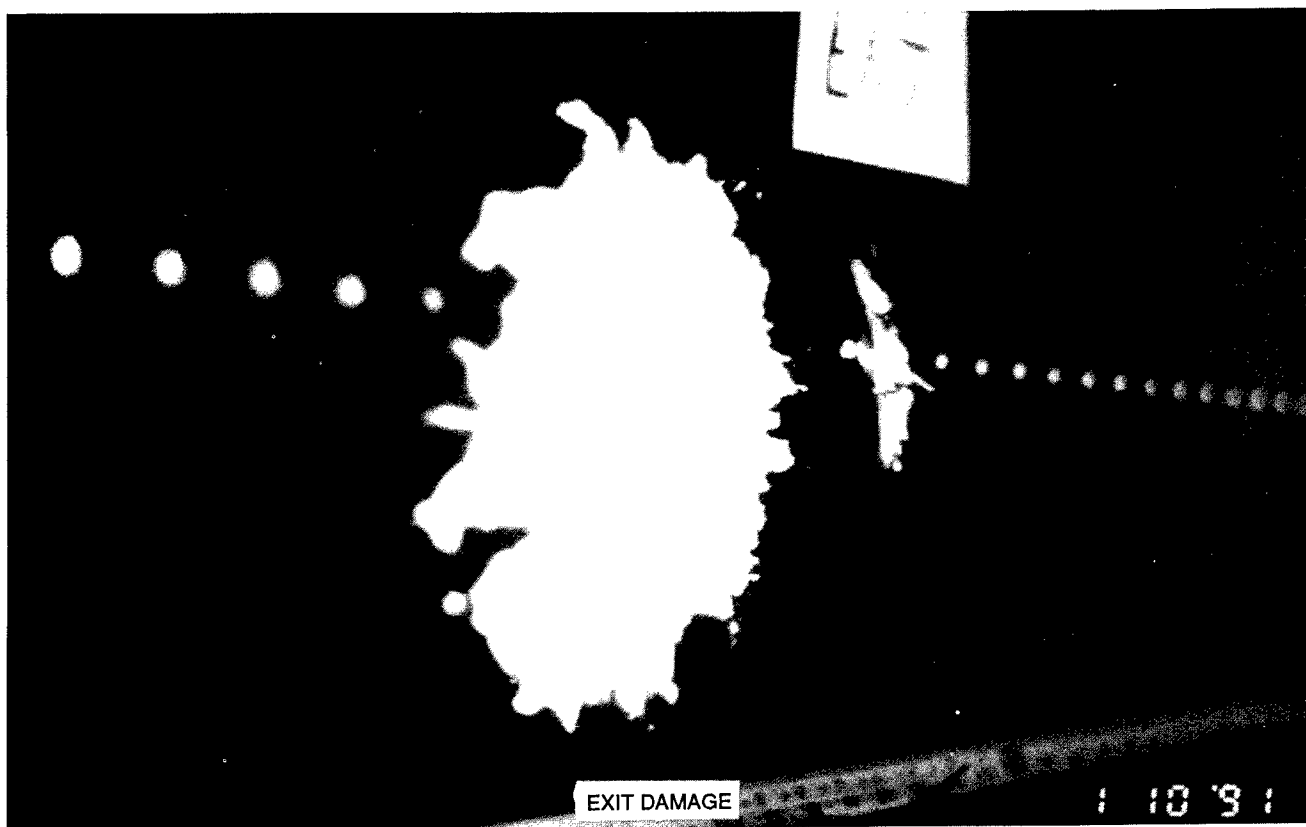
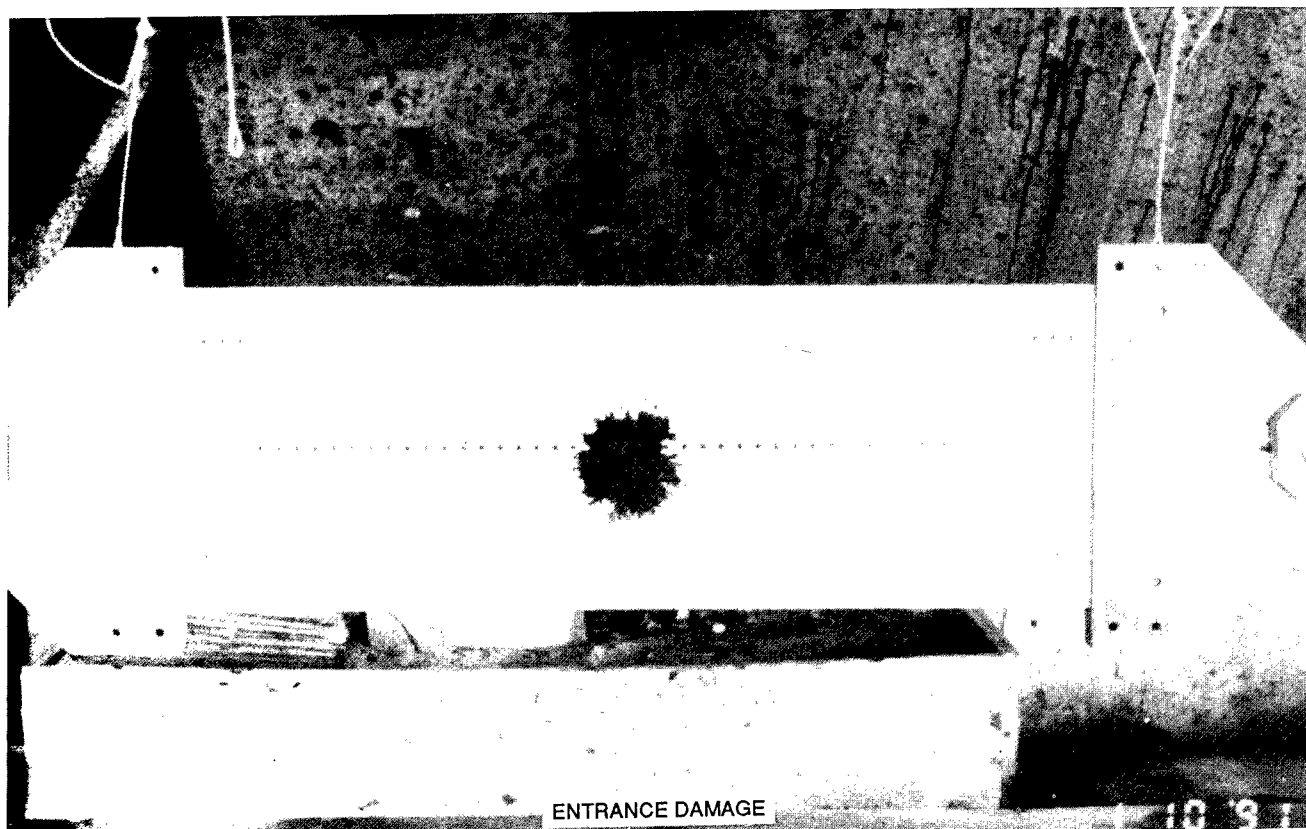


Figure 6 Panel No. 3 Entrance and Exit Damage

RG1-6888-006



R91-6888-007

Figure 7 Panel No. 4 Entrance and Exit Damage

battle damage tolerance and survivability. Specific conclusions based on the live-fire testing are discussed in the following paragraphs.

The IM8/8551-7A (both with and without S-G1/Ep crack-arrestment strips), HITEK 45-9B/E7T1-2, and T650-42/RADEL-8320 discrete cap cover components survived a single hit from a 23-mm HEI projectile and continued to carry 55% DLL (in tension) during and after the ballistic hit.

Panel no. 1, constructed of IM8/8551-7A (without crack-arrestment strips), suffered the most chordwise damage, which consisted of a through-the-thickness propagating through two rows of stitching and an adjacent discrete cap. However, the surface delamination and peeling was not as severe, resulting in a smaller damage area on the exit side compared with panel no. 3. Panel no. 3, which contained the crack-arrestment strips, showed significant exit side spanwise damage due to the pulling out of the severed crack-arrestment strips peeling back a significant amount of cap material when the round detonated.

Panel no. 2, constructed of HITEK45-9B/E7T1-2 (without crack-arrestment strips), experienced much greater exit side damage, consisting of a great deal of delamination/peeling, but with all chordwise damage arrested by the stitching; no through-the-thickness cracks appeared to propagate beyond the rows of stitches.

Panel no. 4 constructed from the T650-42/RADEL-8320 thermoplastic material system exhibited the least damage of all the panels tested. This damage was limited to a jagged 20.3-cm (8-in.)-diameter hole. The resulting damage and response of the panel to the ballistic hit was very much like that of aluminum, without the tearing, cracking, and permanent deformations indicative of aluminum.

The T650-42/RADEL-8320 panel satisfied the ballistic requirements without the need for translaminal reinforcement (stitching). However, overall suitability for stitch-free delamination failure modes needs to be evaluated.

Discrete cap cover designs, combined with toughened epoxy or thermoplastic matrices, appear to be an efficient approach to satisfy live-fire wing requirements.

Repair of the toughened thermoset and thermoplastic cover components using battle damage repair methods and criteria is being considered.

**THIS PAGE INTENTIONALLY BLANK**

# NASA-ACEE/BOEING 737 GRAPHITE-EPOXY HORIZONTAL STABILIZER SERVICE

By: J. T. Quinlivan, Ph.D., Program Manager  
J. A. Kent, Structures Manager  
D.R. Wilson, Senior Principal Engineer

777 Empennage Structures  
Boeing Commercial Airplane Group  
Seattle, Washington 98124

## INTRODUCTION

The 737 graphite-epoxy horizontal stabilizer was developed by Boeing as part of the NASA-ACEE (Aircraft Energy Efficiency) Advanced Composite Structures Program. NASA-ACEE programs challenged large-transport manufacturers to use graphite material in redesigning existing aircraft components. The goal of the program was to develop the necessary data and technology to achieve production commitments to advanced composites. Boeing designed, fabricated, and certified five shipsets of horizontal stabilizers for the 737-200 airframe. The program was initiated in July 1977 and certification was achieved in August 1982. Schedule highlights are shown in Figure 1. The work performed on this program is reported in NASA technical summaries and final reports, (ref. 1 thru 4).

Boeing introduced the stabilizer into commercial operation in 1984, and has maintained surveillance for seven years of in-service evaluation. Outstanding performance has been demonstrated with no service incidents attributed to the graphite-epoxy structure. Boeing will continue to monitor and support these aircraft, adding to the data base of commercial composite experience.

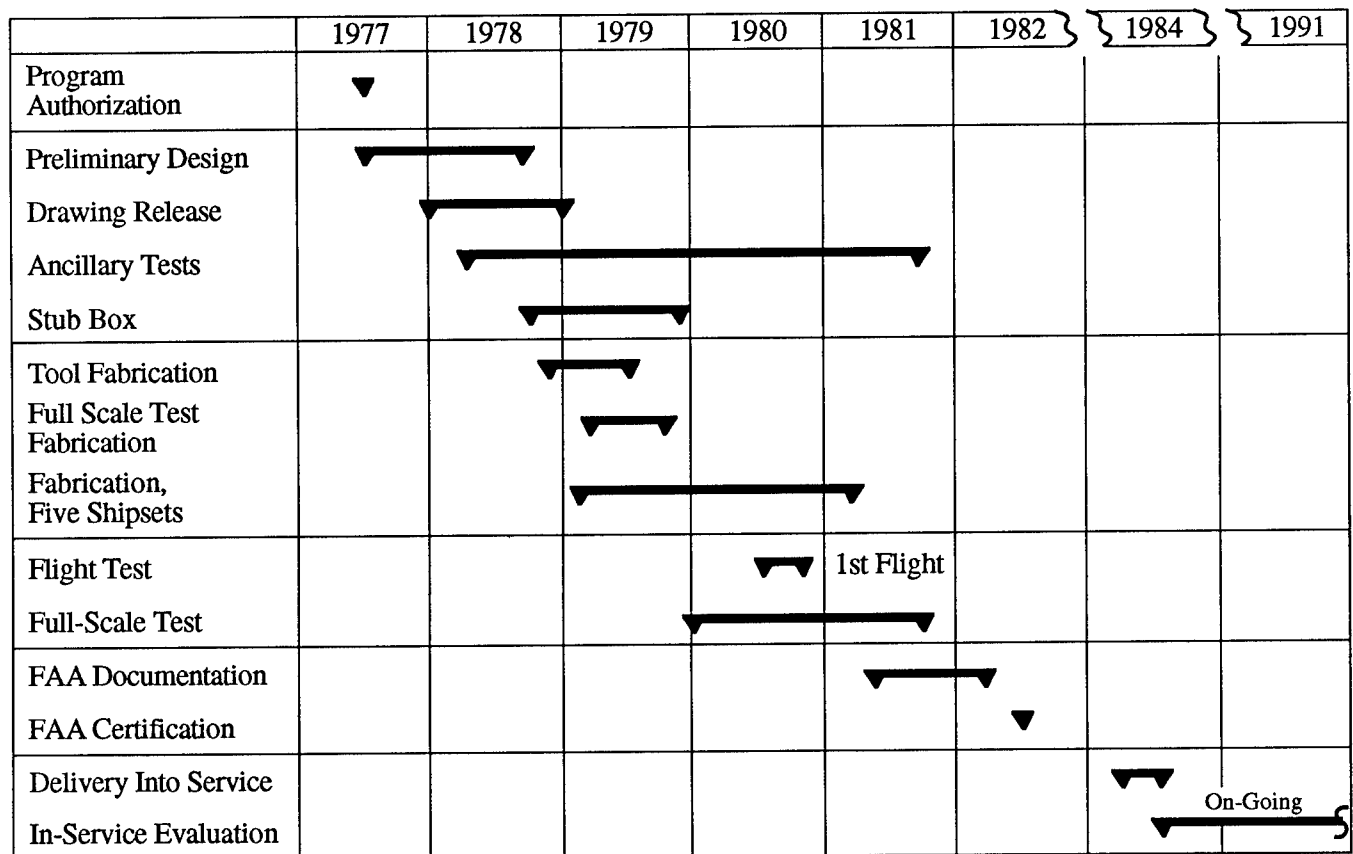


Figure 1. Program Schedule



## STRUCTURAL ARRANGEMENT

Design and contract requirements specified that the graphite-epoxy structure would be interchangeable, both geometrically and functionally with the existing flying hardware. These criteria defined the structural interface, stiffness, aerodynamic shape, planform, and elevator interface. The general structural arrangement is shown in Figure 2. Trade-off considerations were given to element designs within the box. Details were selected that could be produced with the then current material systems and manufacturing technology while looking to future applications such as a wing design. The selected configuration, shown in Figure 3, was comprised of:

- a) I-stiffened, co-cured laminate panels.
- b) Shear-tied ribs using honeycomb webs and graphite-epoxy faces.
- c) I-section solid laminate spars.

The material system selected was Narmco T300/5208. The predominant material form was fabric with selected use of tape. The structural details used hand-layup procedures throughout. Conventional fastening systems were used for assembly.

A requirement of the program was to use existing hardware to the greatest extent possible. Since the parts that were available for use were predominantly aluminum alloy, a protection system was developed to prevent corrosion. The protection system was designed to isolate graphite-epoxy surfaces from aluminum structure, minimizing the cathodic area (graphite) available for electro-chemical reaction. The system, shown in Figure 4, isolated the graphite-epoxy side of the interface with either co-cured fiberglass or primer and epoxy paint. The aluminum alloy was anodized or alodine treated, primed and enameled. Polysulfide sealant was applied to faying surfaces and fasteners at installation.

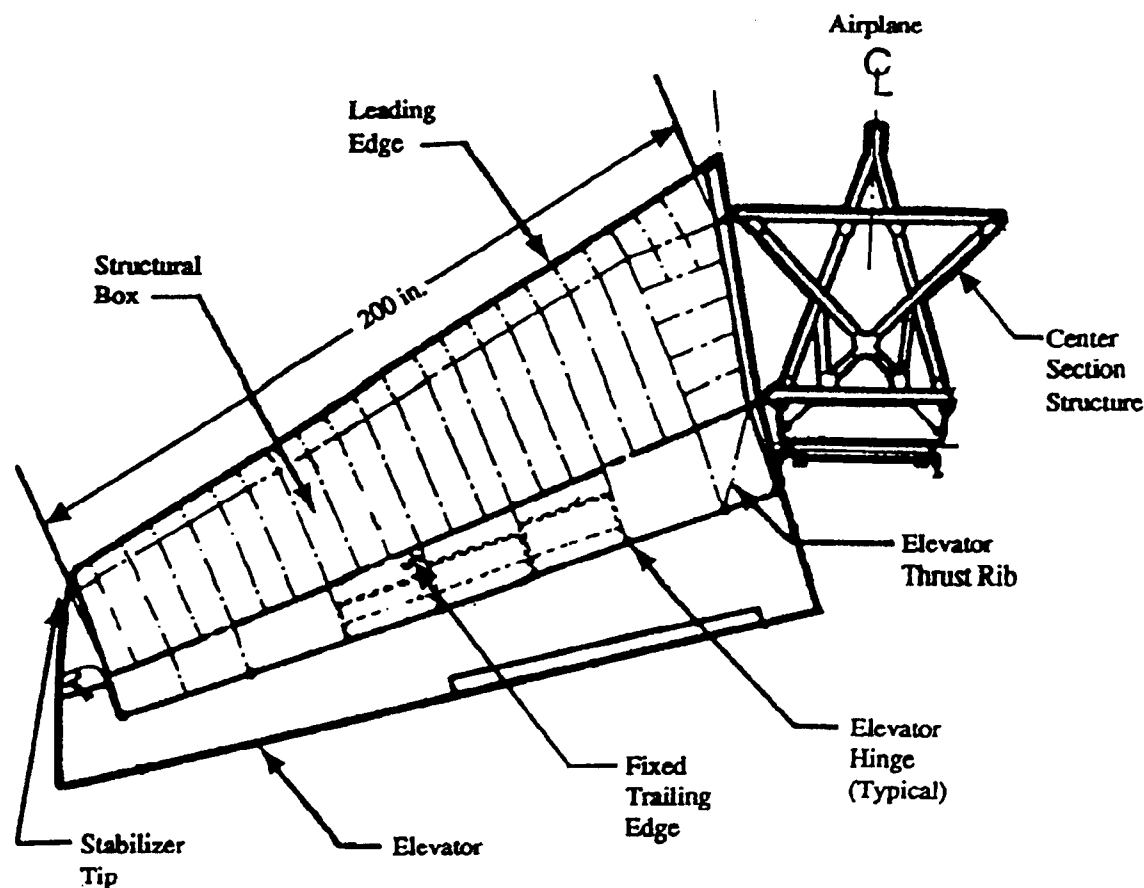


Figure 2. Horizontal Stabilizer - General Arrangement - Aluminum Alloy Baseline

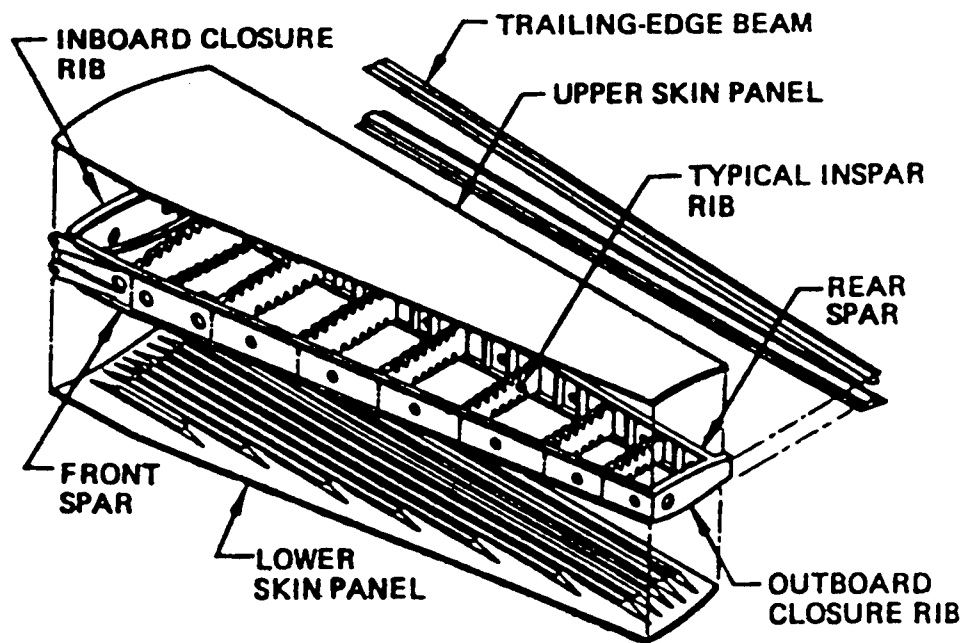


Figure 3. Advanced Composite Stabilizer Inspar Structural Arrangement

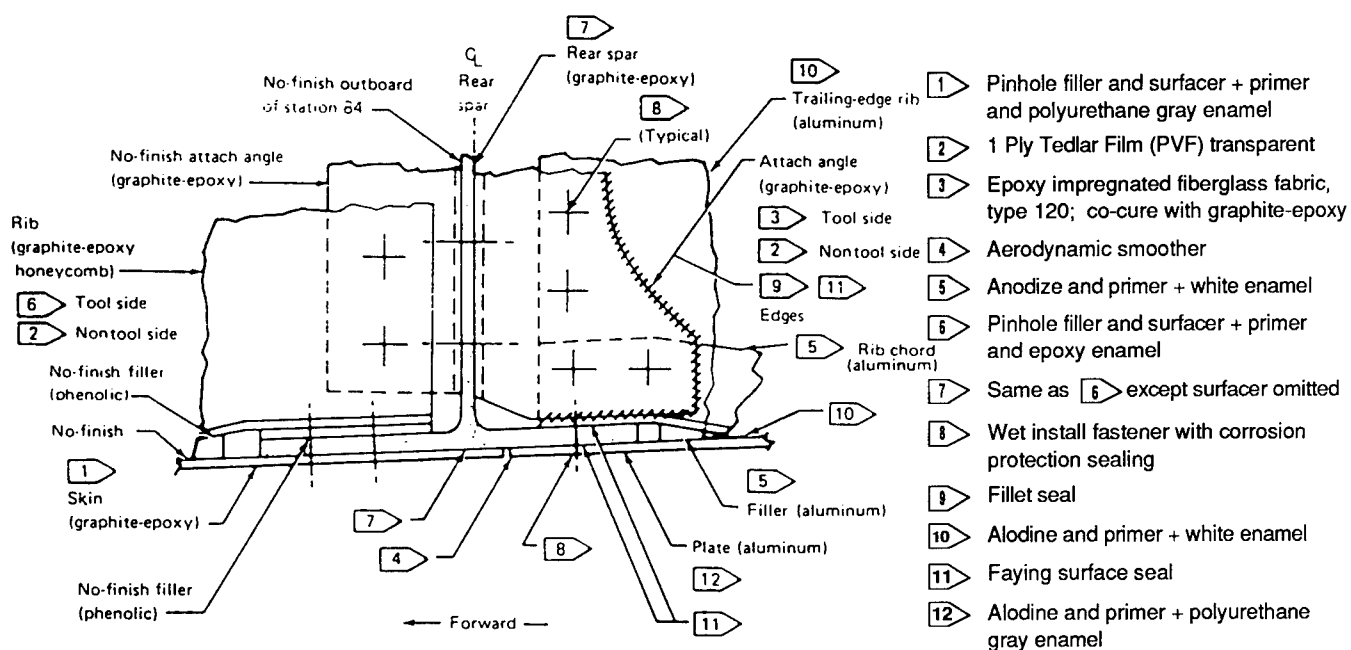


Figure 4. Corrosion Protection System

## CERTIFICATION

Certification requirements for commercial transport aircraft are defined in Code of Federal Regulations, FAR Part 25, (ref. 5). An FAA advisory circular, AC 20-107, (ref. 6) set forth a recommended means of compliance with the regulations.

Boeing's certification approach, presented in detail in reference 7, was based on current and accepted practices and procedures. "Simply stated, the primary means of commercial aircraft certification is by the analytical process supported by appropriate test evidence" (ref. 7). Early coordination with the FAA established a detailed plan to certify the 737 hardware.

**ANALYSIS** - Analyses were performed during the program that encompassed external static and dynamic loads, sonic environment, electro-dynamic effects and environment. An extensive finite element model was developed to perform stress/strain analyses that addressed applied loads and environmental effects. Strains were calculated for static and residual strength including bird strike damage. Compliance with the requirements of the regulations was then demonstrated by comparing the maximum calculated strain to the allowable design value for a particular environmental condition.

**TEST PROGRAM** - A test program was implemented to provide the necessary supporting data for compliance with FAR Part 25. A "building block approach", (Figure 5) was developed that utilized:

- Coupon, element, and panel tests that addressed material properties and point design characteristics and included the effects of environment.
- An early stub box test that subjected critical structure to three-dimensional strain and validated design concepts.
- A highly strained, bi-directionally loaded panel tested in various environments to demonstrate the validity of the analysis techniques used to calculate environmental strains.
- A full scale ground test that verified calculated strain distributions, functional performance, durability, damage tolerance and ultimate load carrying capability.
- A flight test that demonstrated equivalency to the aluminum stabilizer from a flutter and a stability and control standpoint.

References 7 and 8 discuss these elements in further detail.

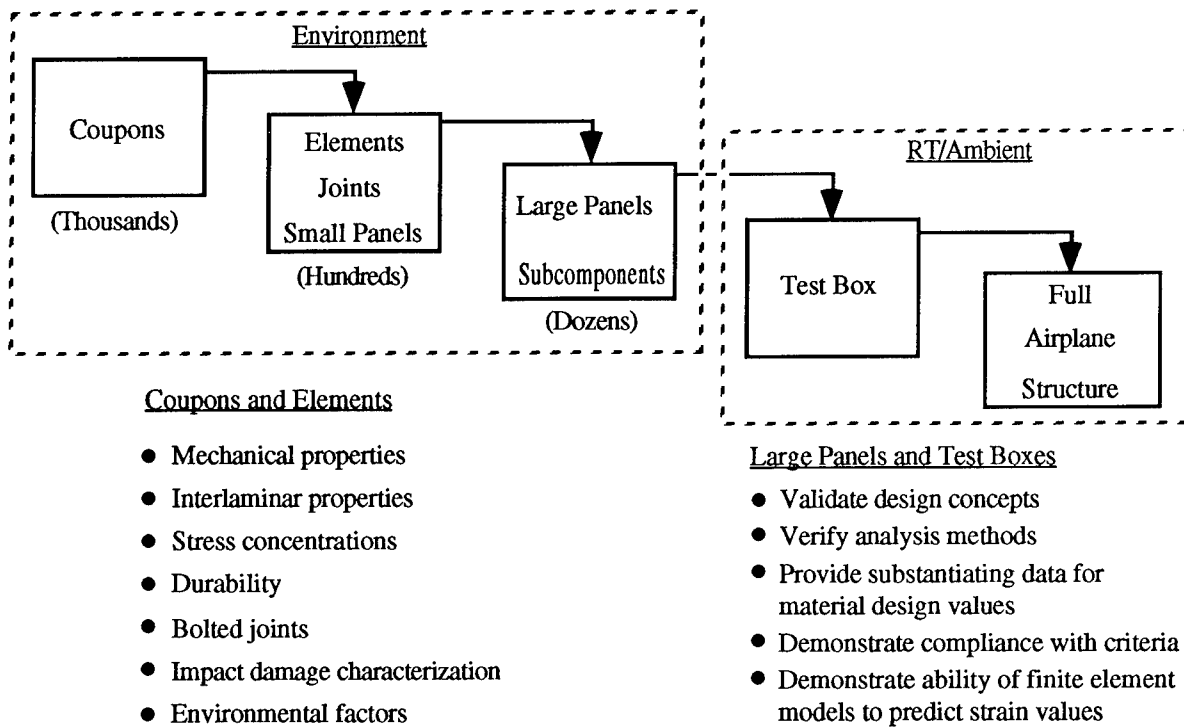


Figure 5. The Building Block Approach

## IN-SERVICE EXPERIENCE

**MAINTENANCE PLANNING PROGRAM** - A maintenance planning program was defined to assist the operator in establishing procedures that would insure continued safety and performance. The Boeing 737 had been in service for over ten years, therefore a primary groundrule for introducing a graphite-epoxy stabilizer was to provide the same level of safety while recognizing the unique characteristics of composite structure and creating a minimum impact on the operator.

A basic plan, (ref. 8) adjustable to the individual airline's existing procedure was established and FAA approval was received. Details of this plan were presented in references 2 and 9. The Maintenance Planning Schedule recommended by Boeing is shown on Table 1. As part of the certification proceedings Boeing agreed to support an additional (early) structural inspection that would be performed on the first two airplanes to reach 7000 hours of service. Non-destructive inspection techniques were developed that used equipment common to most operator maintenance depots. Repairs were designed and tested to demonstrate that the structure could be restored to a pre-damaged level of strength and durability in the event of in-service damage. A repair manual was prepared, and in combination with the maintenance plan and inspection techniques, provided the concluding data for certification.

Table 1. Maintenance Planning Schedule

Check	Inspection Interval (Flight Hr) <sup>a</sup>	Description
Preflight/transit	---	<ul style="list-style-type: none"> <li>• Walk around</li> </ul>
A	75	<ul style="list-style-type: none"> <li>• Visual inspection of exterior surface, from ground level</li> </ul>
B	300	<ul style="list-style-type: none"> <li>• Visual inspection of external surfaces</li> </ul>
C	1,200	<ul style="list-style-type: none"> <li>• External visual inspection</li> <li>• Exposed rear spar area</li> <li>• Exposed hinge fittings and thermal linkage</li> </ul>
	2,400	<ul style="list-style-type: none"> <li>• Front and rear spar-to-center section attachment lugs</li> <li>• Inboard edge of rear spar web</li> <li>• Trailing-edge cavities</li> </ul>
Structural	14,000 <sup>b</sup>	<ul style="list-style-type: none"> <li>• External visual inspection</li> <li>• NDT inspection upper and lower skin from the rear spar forward to stringer 3 between the side-of-body and the rib at stabilizer station 111.1</li> <li>• Front and rear spar attachment lugs, pins, bushing, and fittings</li> <li>• Internal trailing-edge structure</li> <li>• Internal structure, spars, stiffeners, closure ribs; access by removing gap covers, access hole covers, removeable leading edge, removeable lower trailing-edge panels and removeable tip</li> </ul>

a) Boeing recommended for new operators      b) Early inspection on the first two units to reach 7000 flight hours

**SERVICE BEHAVIOR** - The stabilizers were introduced into service in 1984 with Boeing committed to supporting the inspection and maintenance program. The current in-service status is shown on Table 2. Continued effort has been expended to ensure that the composite structure provides satisfactory service and meets design requirements. The objective of minimized corrosion and fatigue damage has been demonstrated. There have been no service reports of problems related to the composite material.

Table 2. In-Service Status May 31, 1991

Tail No.	Airline	Installation	Hours	Landings
N314DL	Delta	3-13-84	19622	19097
N307DL	Delta	3-16-84	19216	18690
① N670MA	Markair	5-11-84	17318	19308
N671MA	Markair	6-22-84	19175	19001
N672MA	Markair	8-18-84	19568	20966

① Status on 6-2-90

**INSPECTION RESULTS** - The early 7000 hour structural inspections of the composite stabilizers were performed on Delta Airlines aircraft N314DL and Markair aircraft N670MA as part of a regular "C" check per Table 1. Inspections were performed per the recommended plan (Table 1 and Figure 6). There were no structural problems or in service wear reported. The inspections required 24 and 17 hours down-time respectively, which is consistent with the inspection of metal structure. The Markair aircraft inspection showed no problems other than a debris strike on the lower surface. Damage was limited to the protective finish.

Both operators have continued to perform regularly scheduled "C" checks. No structural problems have been reported.

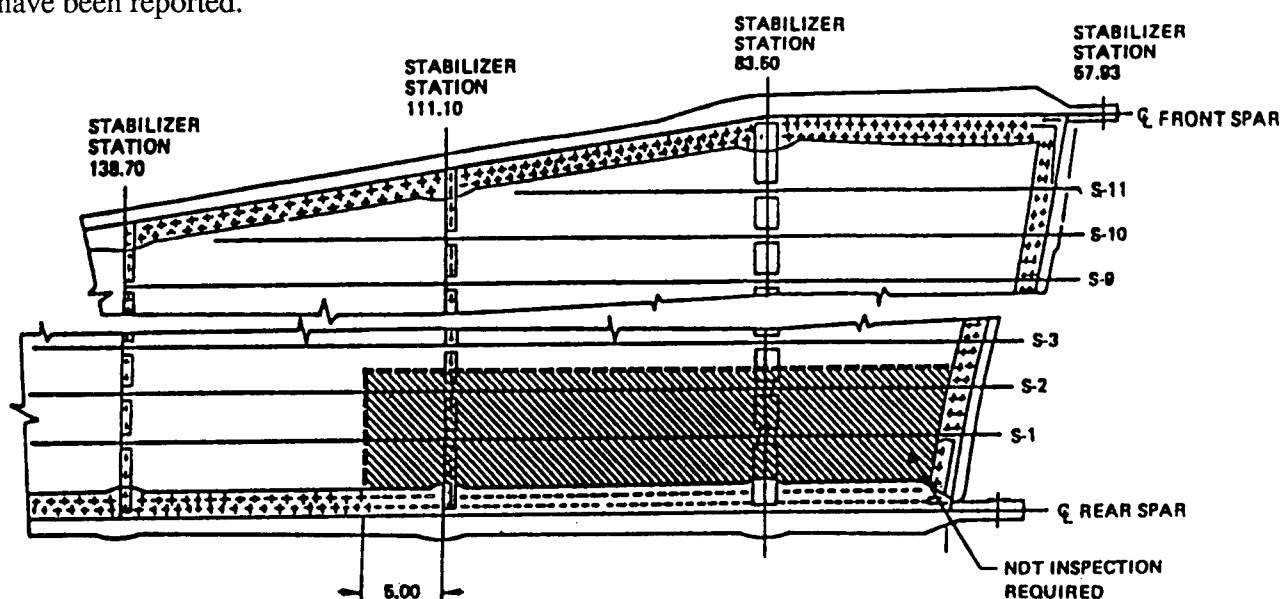


Figure 6. Upper and Lower Skin Panel NDT Inspection Requirements

### IN-SERVICE DAMAGE

Markair has experienced two incidents that required repair. Damage to the skin panels occurred due to impact by a foreign object. Both damages were repaired using techniques developed during the test program. For example, the damage shown in Figure 7 was caused by debris resulting from an engine failure. Pulse-echo NDT inspection of the surrounding area determined that the damage was limited to the penetration through the skin and did not affect the stringers attached to the skin. The skin was scarfed and prepared for repair (Figure 8). The repair used a hot bond/vacuum bag procedure (Figure 9) that required tools readily available at maintenance depots. The completed patch (Figure 10) constituted terminating action and returned the structure to unrestricted flying status.

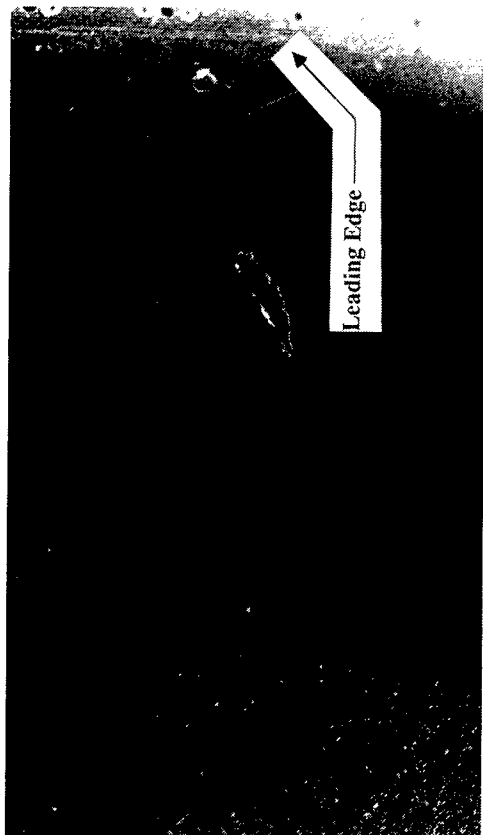


Figure 7. Damage from Runway Debris

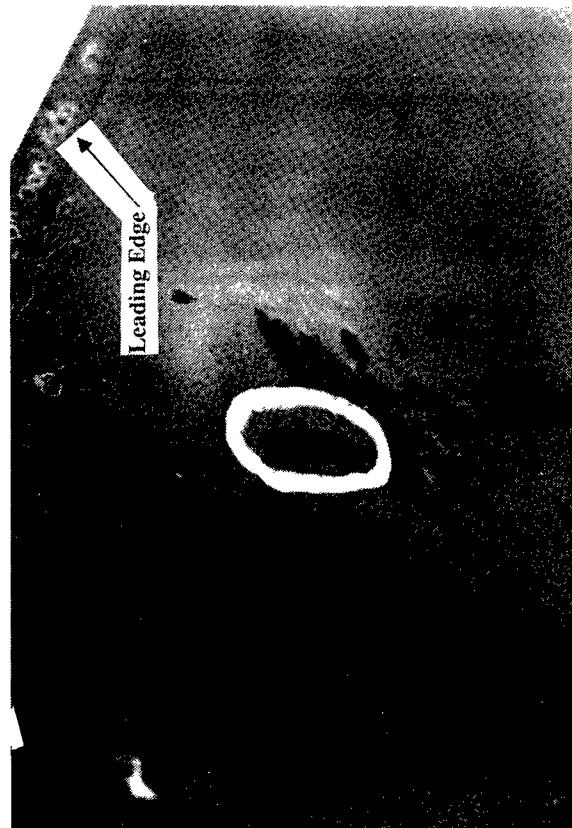


Figure 8. Damage Prepared for Repair

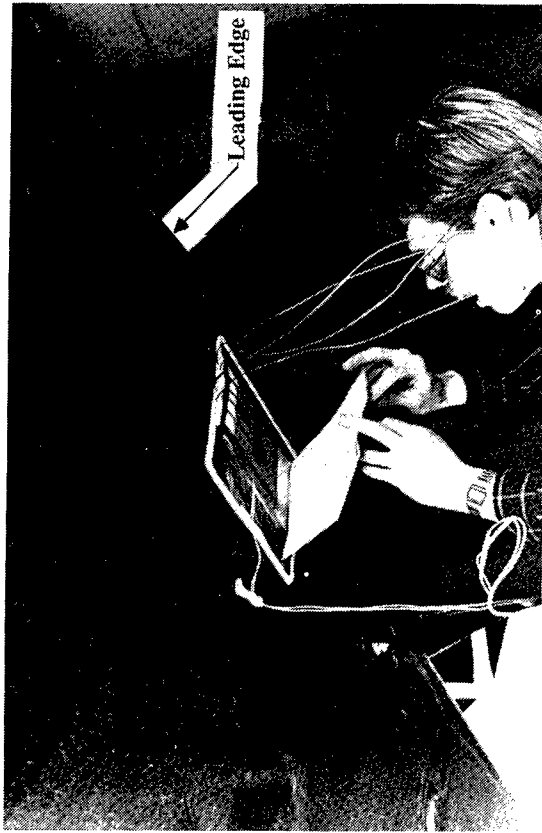


Figure 9. Installation of Heat Blanket

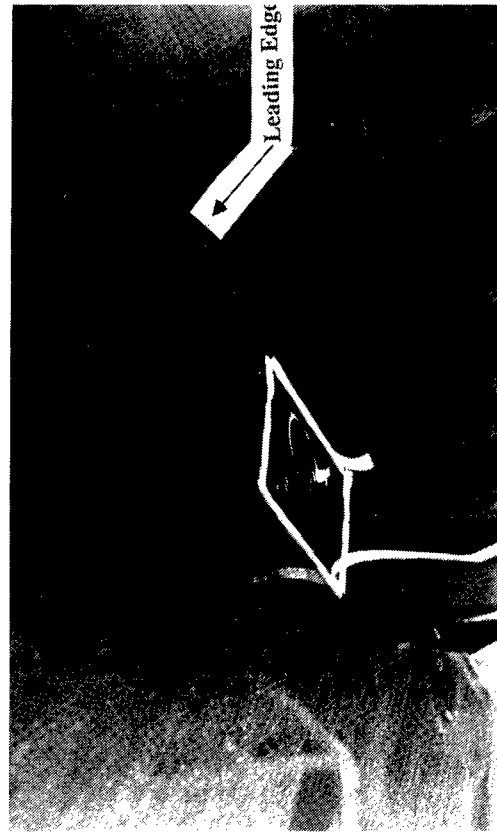


Figure 10. Finished Repair

### TEARDOWN

In June 1990 a shipset of stabilizers became available for a teardown inspection. Markair, N670MA, crashed on landing approach to Unalakleet, Alaska. It was a non-revenue flight and there were no fatalities. The total time was 17318 hours and 19308 landings. The empennage portion of the airplane separated from the fuselage after impact, (Figure 11 and 12), with the left hand stabilizer receiving minimal damage.

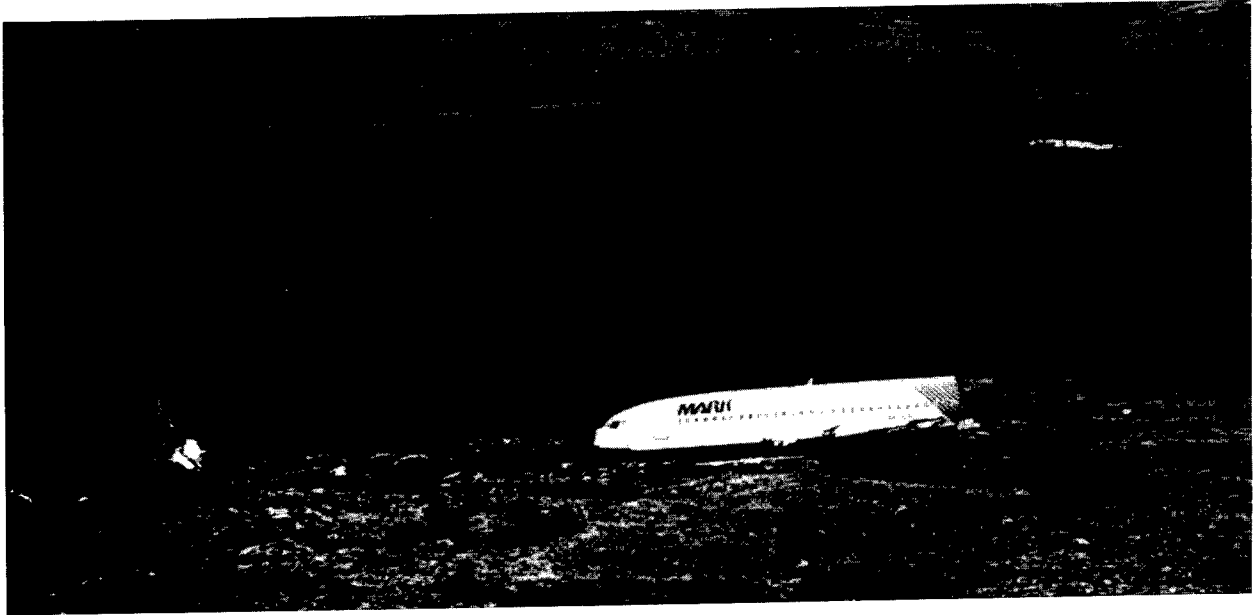


Figure 11. Markair N670MA



Figure 12. Markair N670MA Empennage

Boeing purchased the stabilizers and proceeded with a tear-down inspection. The left hand stabilizer was mounted in a fixture as shown in Figures 13-A and 13-B.

The initial inspection followed the Maintenance Planning Schedule, Table 1, for a structural check. Pulse-echo inspection of the critical areas of the upper and lower skin panels detected no damage (Figure 6). An extensive visual examination of the remainder of the structure revealed no evidence of service deterioration.

The inspection continued by systematically dismantling the box and inspecting each joint, the focus being directed to identify:

1. Any structural damage, delaminations, wear, fretting, etc., or
2. Any corrosion at the aluminum/graphite interfaces.

No structural damage or delaminations were found except for those resulting from the crash. The majority of the aluminum parts are located at the leading edge, trailing edge, and the inboard closure rib. The rib was removed (Figure 14). No corrosion was detected at any of the aluminum/graphite interfaces. The interior area of the box (Figure 15) was clean with no apparent moisture accumulation. All joints had the original protective system in place with no visual degradation or cracking. Fretting or wear was not apparent.

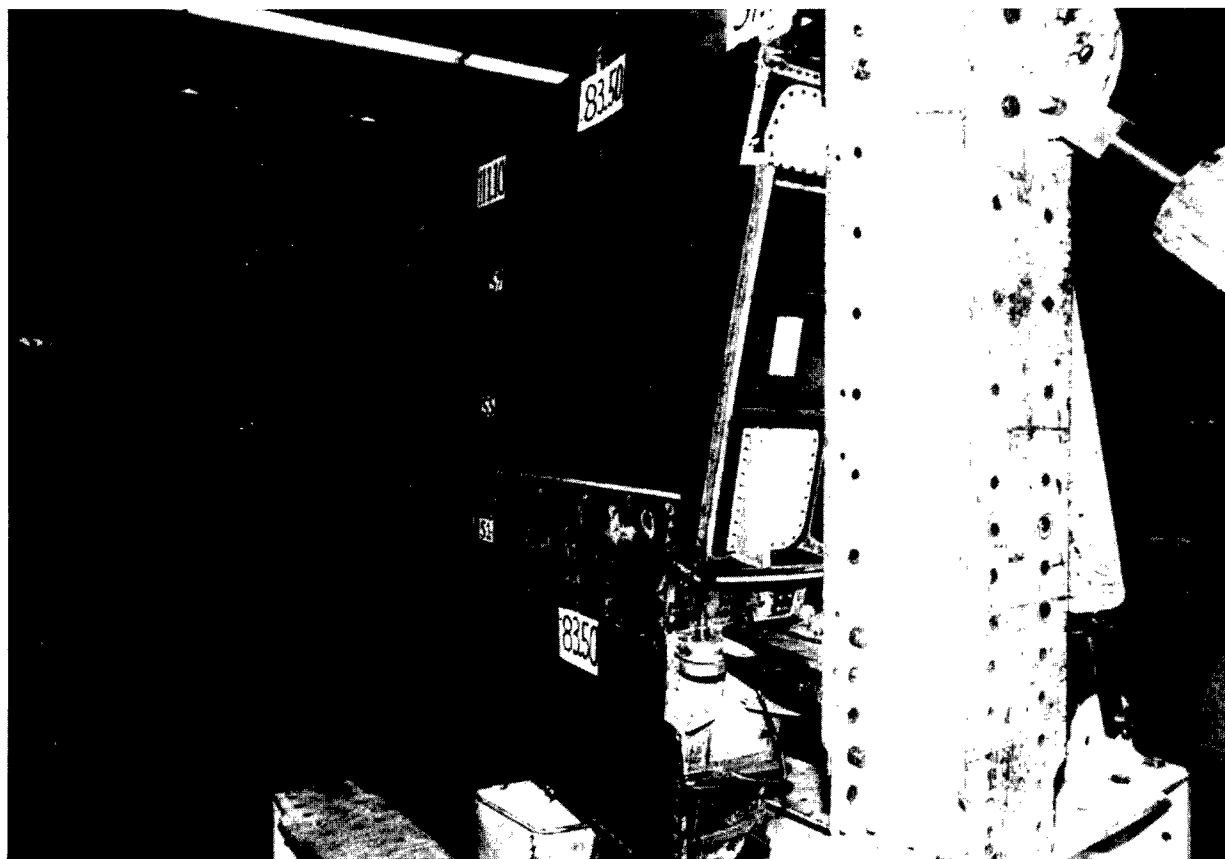


Figure 13-A. Stabilizer Mounted for Inspection, Upper Surface



The damage inflicted on the left hand stabilizer during the crash/skid was limited to abrasion of the tip structure and an impact on the lower surface. The results of lower surface impact are shown in Figure 13-B. Close visual examination of the structure verified that damage was limited to the immediate area adjacent to the impact. The skin panel laminate did not shatter or exhibit extensive delamination.

### SUMMARY

The Boeing 737 graphite-epoxy horizontal stabilizer program has achieved its goals. Five shipsets were designed, fabricated, certified, and introduced into service. The graphite-epoxy structural box demonstrated a weight savings of 22% over the aluminum counterpart.

After six years of commercial airline service, the 737 graphite-epoxy horizontal stabilizers are demonstrating excellent performance. A thorough teardown inspection of one shipset of stabilizers found no signs of deterioration due to wear, fatigue or environmental factors. The corrosion protection system developed to protect mating aluminum surfaces performed as intended and no corrosion was detected. Composite repairs in the field were easily installed and inspections used equipment and techniques familiar to the operators. The 737 graphite-epoxy stabilizers continue to demonstrate the advantages of advanced composite materials in terms of outstanding performance at reduced weight.

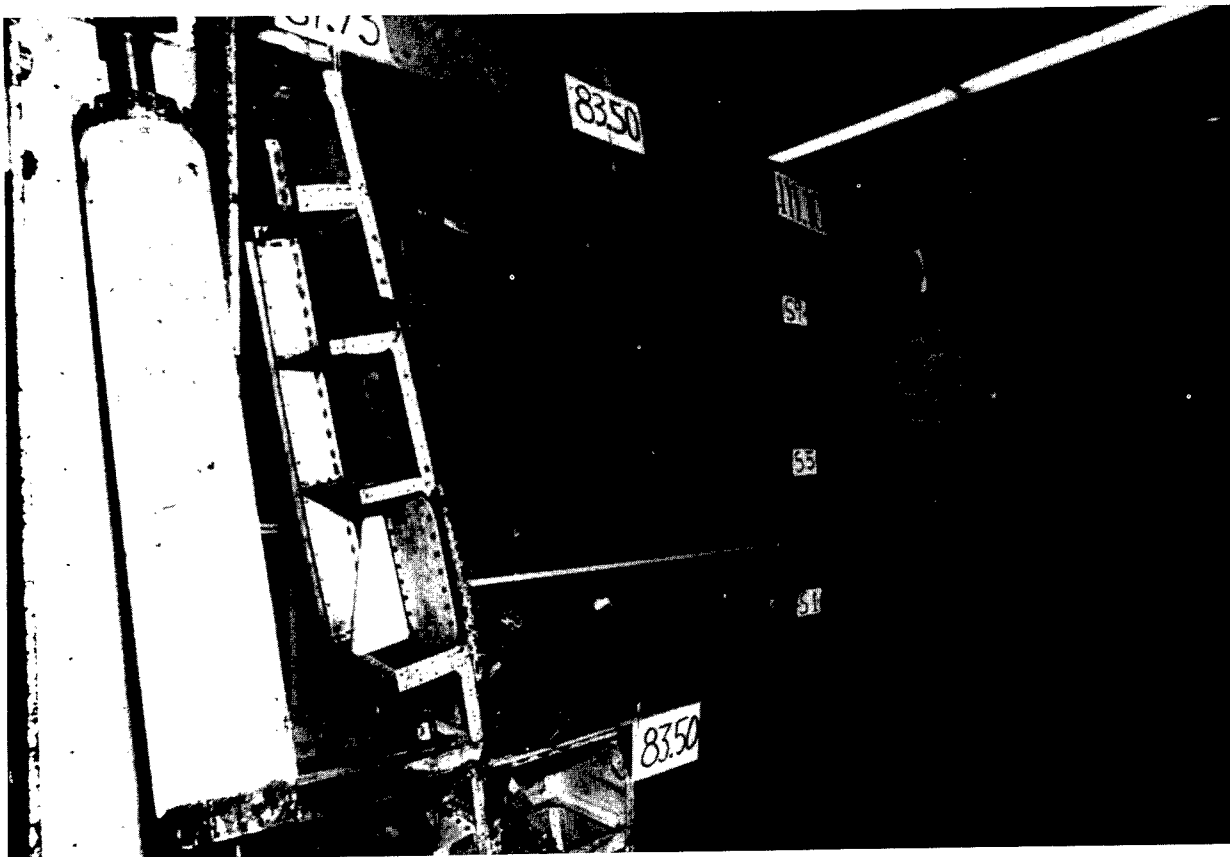


Figure 13-B. Stabilizer Mounted for Inspection, Lower Surface

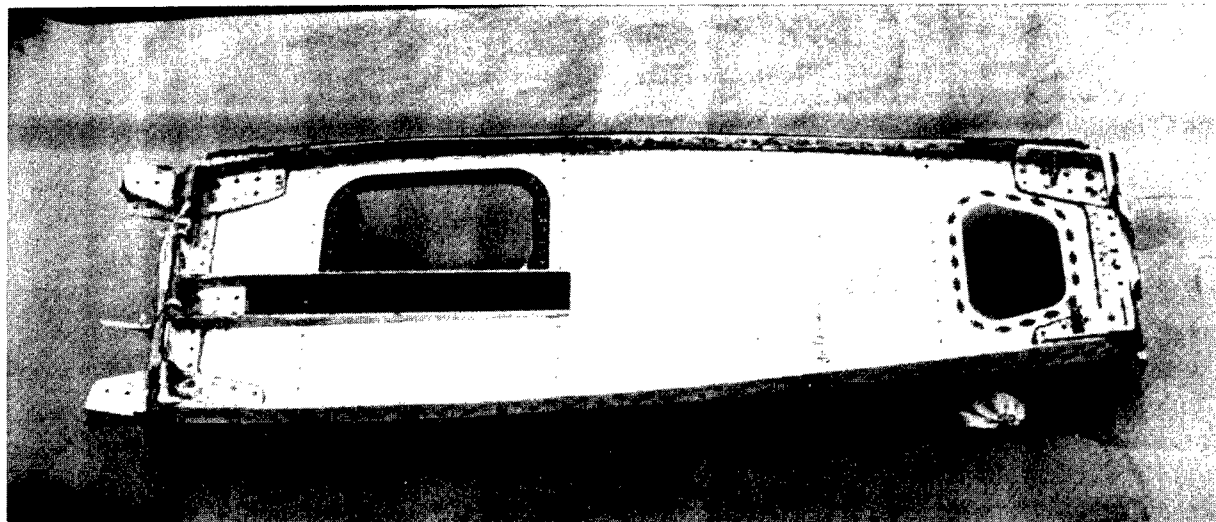


Figure 14. Inboard Closure Rib

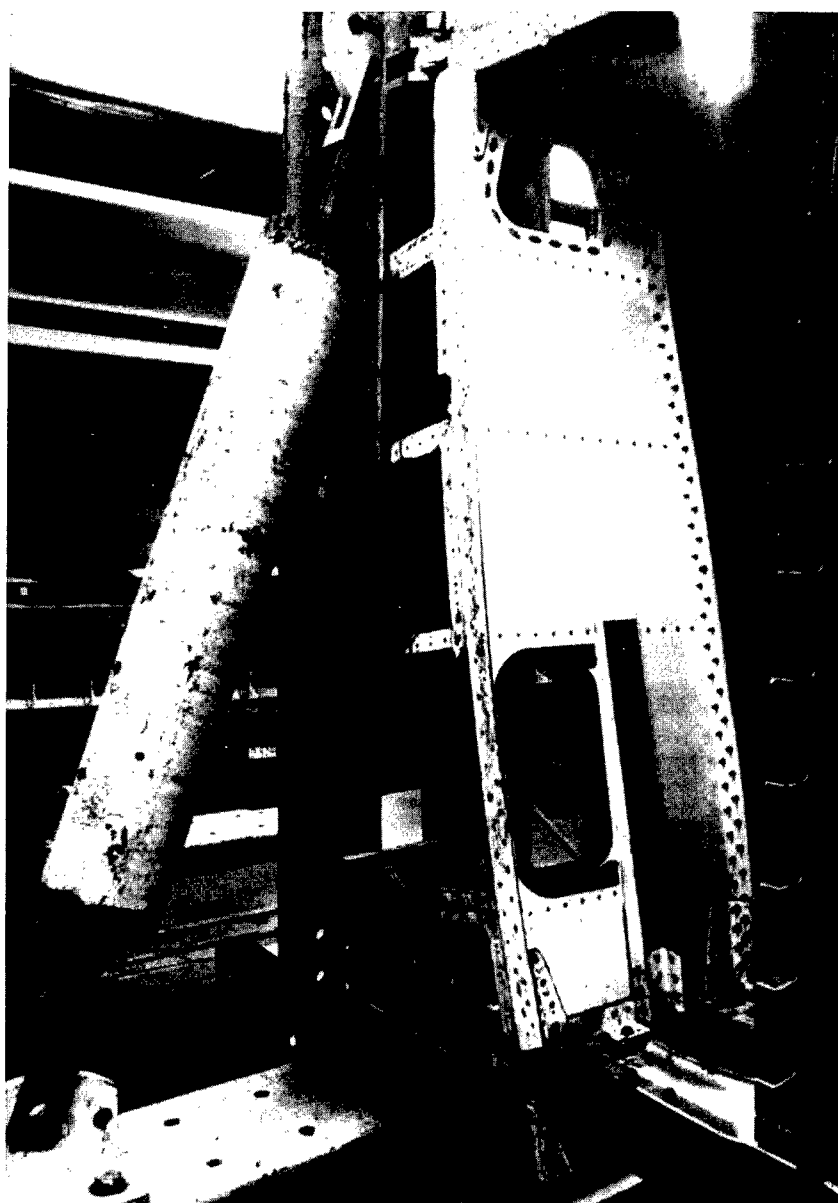


Figure 15. Interior of Box

## REFERENCES

1. Aniversario, R.B. et al., "Design, Ancillary Testing, Analysis, and Fabrication Data for the Advanced Composite Stabilizer for Boeing 737 Aircraft", Volume I-Technical Summary, NASA CR-3648, December 1982.
2. Aniversario, R.B. et al., "Design, Ancillary Testing, Analysis, and Fabrication Data for the Advanced Composite Stabilizer for Boeing 737 Aircraft", Volume II-Final Report, NASA CR-166011, December 1982.
3. Aniversario, R.B. et al., "Full Scale Testing, Production, and Cost Analysis Data for the Advanced Composite Stabilizer for Boeing 737 Aircraft", Volume I-Technical Summary, NASA CR-3649, December 1982.
4. Aniversario, R.B. et al., "Full Scale Testing, Production, and Cost Analysis Data for the Advanced Composite Stabilizer for Boeing 737 Aircraft", Volume II-Final Report, NASA CR-166012, December 1982.
5. Federal Aviation Regulations, Part 25, Airworthiness Standards: Transport Category Airplanes, Department of Transportation, Federal Aviation Administration, December 1978.
6. Advisory Circular 20-107, Composite Aircraft Structure, Federal Aviation Administration, July 1978.
7. McCarty, J. E., Johnson, R.W., and Wilson, D. R., "737 Graphite-Epoxy Horizontal Stabilizer Certification, A Collection of Technical Papers," Part 1: Structures and Materials, AIAA No. 82-0745, AIAA/ASME/ASCE/ AHS 23rd Structures, Structural Dynamics and Materials Conference, New Orleans, May 1982.
8. D6-46036, Maintenance Planning Data, 737 Aircraft Structural Inspection, Composite Horizontal Stabilizer, The Boeing Company, December 11, 1981.
9. McCarty, J. E., Wilson, D. R., Advanced Composite Stabilizer for Boeing 737 Aircraft, Proceedings of the Sixth DOD/NASA Conference on Fibrous Composite in Structural Design, New Orleans, LA., January 24-27, 1983.